# Pore-scale imaging and determination of relative permeability and capillary pressure in a mixed-wet carbonate reservoir rock at subsurface conditions

*Amer M.* Alhammadi*, *Ying* Gao, *Takashi* Akai, *Martin J.* Blunt, and *Branko* Bijeljic

Department of Earth Science and Engineering, Imperial College London, SW7 2AZ, United Kingdom

**Abstract.** We use X-ray micro-tomography combined with a high-pressure high-temperature steady-state flow apparatus to simultaneously measure relative permeability and capillary pressure in a carbonate core from a producing oil field from the Middle East. The native reservoir wettability conditions were restored by ageing the sample at 10 MPa and 80 °C. Imaging and measurement of steady-state relative permeability were performed at eight water fractional flows ($f_w = 0, 0.15, 0.3, 0.5, 0.7, 0.85, 0.95, 1$), while measuring the pressure differential across the sample. The formation brine was doped with 30 weight % KI to resolve the fluid saturation in the macro- and the sub-resolution pores. The measured relative permeabilities indicated favourable oil recovery with a cross-over saturation above 60%. Below this saturation the water relative permeability is low, while above it oil still flows through thin layers resulting in additional recovery. We quantify oil recovery from both macro-pores and micro-pores. The measurements of the interfacial curvature indicated negative capillary pressure that decreased with an increase in fractional flow, which is a signature of predominantly oil-wet media. Overall, this work has important implications for improved oil recovery in mixed-wet reservoirs. The measured relative permeability, capillary pressure and fluid distribution can also be used to benchmark and validate pore-scale models.

## 1 Introduction

Designing subsurface processes such as hydrocarbon recovery and geological carbon dioxide storage requires an understanding of multiphase fluid flow in natural porous media [1-3] which is described by relative permeability and capillary pressure [1,4-6].

Conventionally, three main special core analysis (SCAL) methods are used to measure capillary pressure. These methods include the centrifuge, the porous plate method, and mercury intrusion capillary pressure, MICP method [5, 7-9]. All of the three methods have advantages and limitations. The centrifuge method, for instance, is difficult to conduct at subsurface conditions and boundary conditions influence the measured data [8]. On the other hand, the porous plate method can produce a homogeneous saturation profile using reservoir fluids. It is also considered reliable for both drainage and waterflood [6, 10]. However, the porous plate method takes a relatively long time to reach capillary equilibrium at every point in the measurement [11]. MICP is cost-effective and can be conducted in a relatively short period of time. However, the sample can be used only once as this method is destructive. In addition, mercury has a different wettability than reservoir rocks and is used to perform drainage only. Finally, this method is limited to small rock samples.

Relative permeability is accurately measured by the steady-state method which applies a sequence of fractional flows ($f_w$) at which the pressure differential due to flow is recorded and the saturation measured from either mass balance or imaging [4, 12]. The relative permeability is usually measured on a different rock sample from the capillary pressure with experiments that employ different displacement methods. Capillary pressure and relative permeability could be measured on the same sample using the semi-dynamic method, however, it is time consuming.

Recently, non-destructive three-dimensional imaging using X-ray micro-tomography has been improved and combined with high-pressure and high-temperature injection to study multiphase flow in permeable media [13-23]. This has facilitated the measurement of relative permeability by accurately measuring the pressure differential across a small rock sample during a steady-state displacement combined with pore-scale imaging. This method has been used to measure relative permeability of a water-wet Bentheimer sandstone [24].

The same pore-scale images used to quantify brine saturation can be used to measure interfacial curvature by capturing the fluid-fluid interface [20, 25] which can then be used to calculate capillary pressure using the Young-Laplace equation. Recently, both capillary pressure and relative permeability have been measured simultaneously

---

* Corresponding author: a.alhammadi15@imperial.ac.uk

on the same water-wet Bentheimer sample during a steady-state experiment [26].

However, hydrocarbon reservoirs are rarely water-wet, but instead have mixed-wettability as a result of contacting crude oil [27-29], where parts of the pore space remain water-wet while others through direct contact with the polar components become more oil-wet or neutrally-wet [29, 30]. Relative permeability and capillary pressure are affected by the wettability state of the rock [31-35]. Recently, both water-wet and mixed-wet relative permeability were measured using X-ray images on Bentheimer sandstone saturated with Soltrol-130 as an oil phase [36] which showed an evidence of increased ganglion dynamics at low water saturation. Another complexity arises when studying carbonates, for which characterisation of micro-porosity is necessary since it can enhance pore space connectivity. For this purpose, a differential imaging method was developed for studying single-phase flow [37, 38] and multiphase flow [24, 39]. Gao et al. [40] studied steady-state relative permeability in a water-wet micro-porous limestone. Using differential imaging to characterise fluid occupancy in micro- and macro pore space, it was demonstrated that relative permeability and oil recovery were impacted by water-wet micro-porosity which provided additional connectivity to the water phase.

Nevertheless, all of the studies that used pore-scale imaging to measure relative permeability were conducted on quarry samples and used refined oil at room temperature. To have a thorough understanding of the multiphase flow properties in a mixed-wet reservoir, it is vital to carry out experiments on heterogeneous reservoir rock systems at subsurface conditions.

In this study, we use a complex carbonate reservoir rock extracted from a very large producing oilfield which has a heterogeneous pore structure that is saturated with crude oil and the prepared formation brine from the same reservoir at subsurface conditions. We use the X-ray micro-tomography to acquire pore-scale images from which brine saturation was calculated while measuring pressure drop across the sample to obtain the relative permeability. The same pore-scale images are used to determine the local capillary pressure and fluid occupancy in the pore space.

# 2 Materials and methods

## 2.1 Materials

### *2.1.1 Porous media*

Two carbonate reservoir rock samples were drilled and assembled together to make a longer sample (50.1 mm in length) and 6.2 mm in diameter. The rock was mostly calcite 99.8 ± 0.5 weight% with small amounts of quartz 0.2 ± 0.1 weight%. The chemical composition was measured by X-ray diffraction analysis performed at the Natural History Museum, London, UK. The rock had a total porosity of 27.4% (measured on the X-ray segmented image) and a brine permeability of 292 mD.

### *2.1.2 Oil phase*

Crude oil from the same reservoir was used as an oil phase to saturate the sample. The crude oil had a density and viscosity of 812 kg/m$^3$ and 1.94 mP·s respectively, measured at 60 °C. The crude oil contained 55.23% saturates, 38.07% aromatic, 6.22% resins and 0.46% asphaltenes, measured by Weatherford Laboratories.

### *2.1.3 Water (brine) phase*

Prepared formation brine was used as the aqueous (water) phase, containing Sodium, Calcium, Magnesium, Chloride, Sulphate and Bicarbonate. After preparing the formation brine, it was doped with 30 weight% Potassium Iodide to resolve water and oil in the sub-resolution pore space. The density and viscosity of the used brine were 1,344 kg/m$^3$ and 0.83 mP·s, respectively measured at 60 °C.

## 2.2 Methodology

### *2.2.1 Core holder assembly and high-pressure high-temperature flow apparatus*

Before commencing the flow experiment the carbon fibre core holder assembly had been prepared with dry and clean rock sample, which is described as follows and shown in Figure 1.

- Firstly, two reservoir rock samples were drilled while running tap water as a coolant fluid.

- Both ends of the samples were made flat to have a perfect fit with each other and with the metal end-pieces.

- The samples were solvent-cleaned with a mixture of 50/50 volume% methanol and toluene [41] and dried overnight.

- The dry samples were inserted inside a Viton sleeve.

- The Viton sleeve was connected to the co-injection metal end-piece from the base side and to the top metal end-piece from the top side, which had a tight fit over both end-pieces to avoid confining fluid leaking into the sample.

- The thermocouple was inserted through the base of the core holder and placed carefully next to the sample to measure the pore space temperature.

- A flexible heating jacket was wrapped around the carbon fibre sleeve to elevate the sample temperature.

- Both end-pieces were connected to polyether ether ketone (PEEK) tubing through which crude oil, formation brine and confining DI water were injected. The PEEK tubing was used to allow smooth and flexible rotation of the whole core holder assembly while acquiring X-ray images without shifting the sample.

- Three-way valves were connected to all oil, brine and receiving lines which is considered as a crucial component for the success of the experiment. The combination of three-way valves was used to divert air out of the lines and avoid having any air in the sample.

- Furthermore, the three-way valves were used to isolate the whole core holder assembly in preparation for its transfer into an oven for the ageing process at high pressure and temperature followed by the transfer of the core holder assembly back to the micro-CT enclosure to perform the steady state experiment on the aged sample.

- The completed core holder assembly containing a dry sample is shown in Figure 1.

The next step was performing the steady-state flow experiment using the experimental apparatus shown in Figure 2. A combination of four high pressure syringe pumps was used to apply constant oil and brine flow rates and maintain high pore and confining pressure. The core holder can withstand high pressure and temperature, yet is almost transparent to X-rays [42]. A co-injection end-piece was used to inject both crude oil and formation brine simultaneously into the reservoir rock sample. A proportional-integral-derivative controller (PID) was used to apply constant elevated temperature through a flexible heating jacket. The pressure differential across the rock sample was measured by a 300 kPa pressure transducer.

- Firstly, a confining pressure of 2 MPa was applied to squeeze the Viton sleeve onto the sample to prevent fluids flow on the side of the rock sample. At this stage a dry reference scan was taken.

- The air was removed out of the pore space by injecting carbon dioxide which was followed by brine injection to fully saturate the pores. At this stage a brine reference scan was acquired.

- The absolute permeability was measured by applying five flow rates in single phase brine injection.

- After that the core holder assembly was isolated using the three-way valves and moved to an oven at which primary drainage and ageing was performed at 10 MPa and 80 °C over a period of two weeks to establish the mixed-wettability conditions known to exist in hydrocarbon reservoirs [27-29].

- After completing ageing, the core holder assembly was isolated and moved back carefully into the X-ray micro-tomography scanner.

- The PID controller was connected to the core holder assembly to maintain pore space temperature of 60 ± 1 °C. The back pressure valve was set to maintain a pore pressure of 1 MPa while the confining pump applied a confining pressure of 3 MPa.

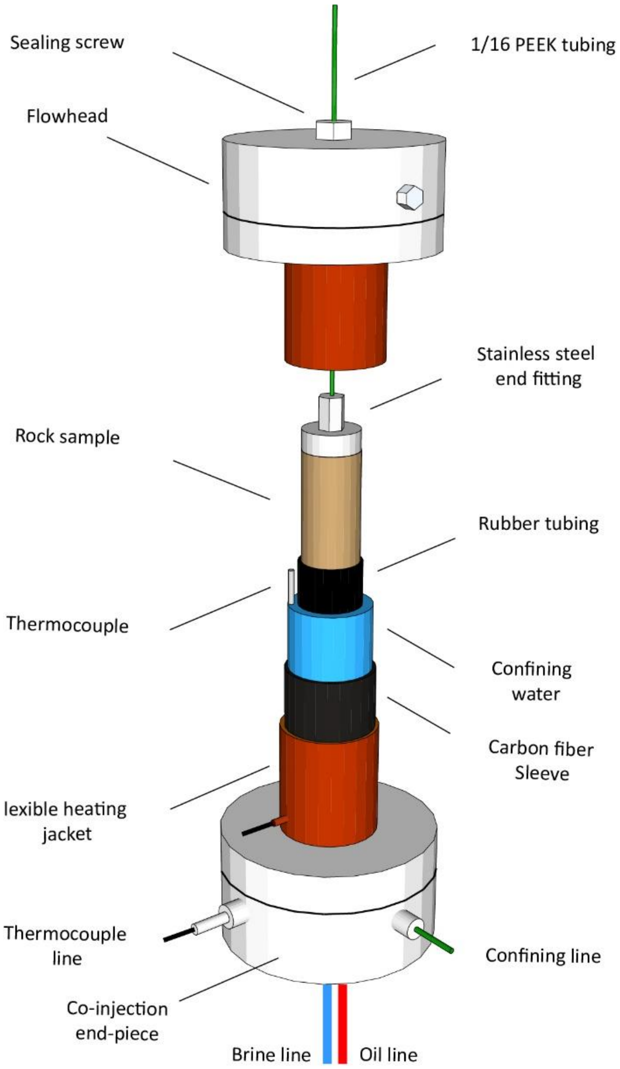

**Fig. 1.** A schematic demonstration of the core holder assembly with the rock sample. All of the core holder assembly components are labelled with the internal cross-section view of the core holder.

- A total of eight brine (water) fractional flows were imposed to measure the relative permeability ($f_w$= 0, 0.15, 0.3, 0.5, 0.7, 0.85, 0.95 and 1). The total co-injection flow rate was 0.02 mL/min. At the first fractional flow point ($f_w$=0), only oil was injected at 0.02 mL/min. Then, the water fractional flow was increased to 0.15 with water rates of 0.003 mL/min and oil rate of 0.017 mL/min. The water fractional flow was increased in steps to 100%. At $f_w$=1, the water flow rate was increased (from 0.02 mL/min to 2 mL/min) to reach residual oil saturation, which was then decreased back to 0.02 mL/min at which the pressure drop was measured.

The co-injection of crude oil and formation brine at each water fractional flow continued for at least 20 hr. Two overlapping scans (one hour each) were taken at a stabilized pressure drop at the end of the flow period.

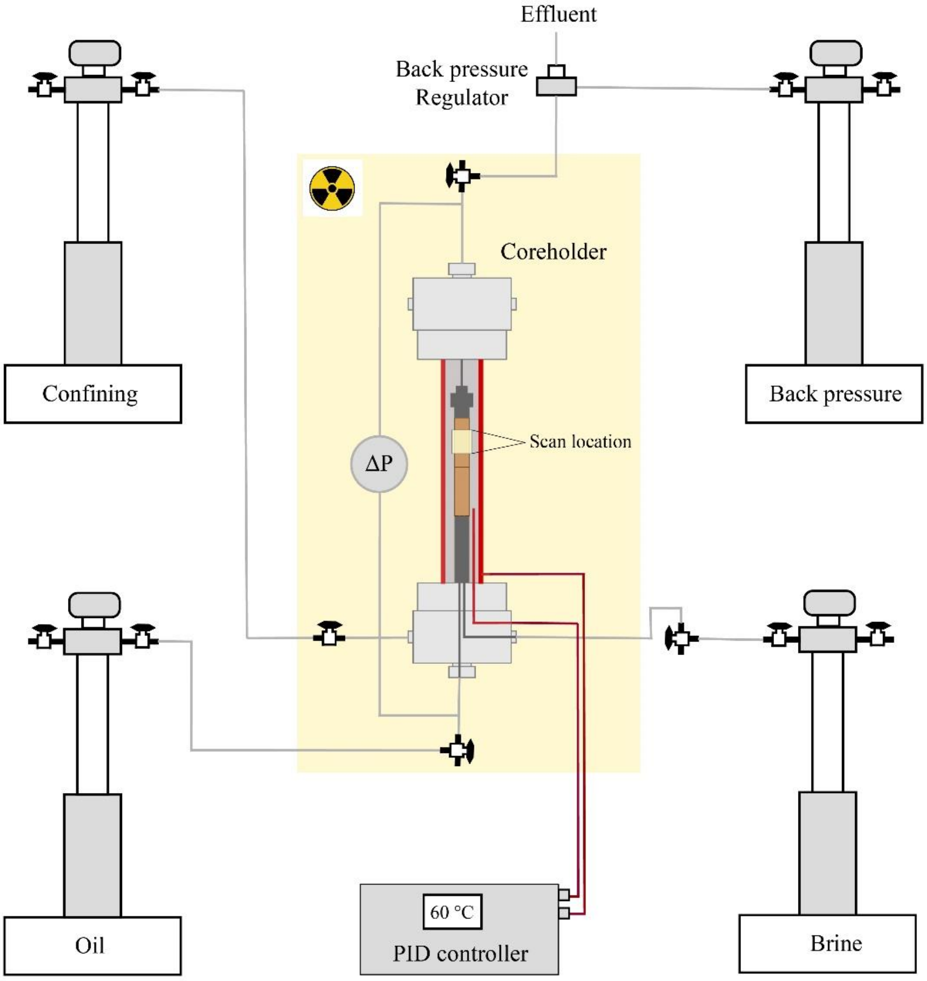

**Fig. 2 :** The high-pressure high-temperature flow apparatus consists of five main components. 1. Core holder assembly. 2. High pressure syringe pumps to control the flow rates, confining pressure and back pressure. 3. Back pressure regulator. 4. PID controller to control the applied temperature. 5. Pressure transducer recording the pressure differential across the sample.

### *2.2.2 Three-dimensional X-ray imaging and image processing.*

We used a Zeiss Xradia 510 Versa X-ray micro-tomography scanner to take the high resolution three-dimensional X-ray images. All scans were acquired at an energy and power of 75 keV and 6.5 W, respectively. A flat panel detector was used to obtain a large field of view with a voxel size of 3.567 μm with a total number of projections of at least 3,200 to acquire good quality images. All tomograms were reconstructed using the Zeiss Reconstructor Software and the most appropriate centre shift correction value was applied.

The two overlapping images were all normalized to the brine reference scan and stitched together to form a larger image with a total size of 6 × 6 × 9 mm$^3$, with 7.1 billion voxels. The stitched images were then registered to the stitched dry reference image to have the same spatial orientation that facilitates an accurate fluid quantification at the same location by differential imaging. The grey-scale images were filtered using the non-local means filter [43, 44]. To quantify oil and brine saturation accurately, the differential imaging technique was used [24, 37, 39] to segment the 6 × 6 × 9 mm$^3$ images. This method allows us to quantify oil and brine volumes in small pores that cannot be explicitly resolved in the image. The pore space and rock phases were segmented at the beginning from the difference between the two reference scans (dry and high contrast brine scans). The 30 weight % KI added to brine had an even higher grey-scale value than the solid grains. The difference images were able to identify low density minerals or isolated micro-pores. Then, a two-step watershed segmentation [45] was used to segment solid, micro-porous grains and macro-pores. The next step was to segment the oil phase in macro-pores (pores that could be resolved in the image) and micro-pores (pore space below the image resolution) by applying the image difference between the multiphase scans and the high contrast brine scan. The oil and brine phase were segmented using grey-scale interactive thresholding for all water fractional flows.

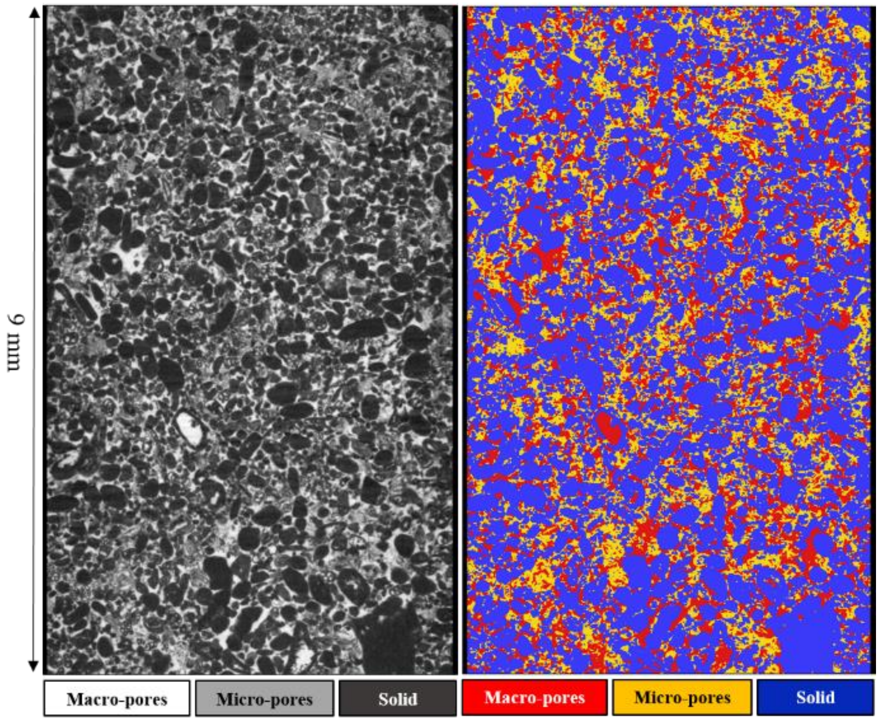

**Fig. 3:** Three-phase segmentation of the rock and pore space. On the left, the difference image between high contrast brine reference scan and the dry scan is presented. On the right, the segmented solid, micro-porous grains and macro-pores are shown.

A smaller sub-volume was extracted with an image size of 2 × 2 × 2 $mm^3$ to measure the oil-brine interfacial curvature from which capillary pressure was calculated. The smaller sub-volume image was segmented using the same method described above, but the image difference was applied between the multiphase scans and the dry reference scan to generate very sharp brine-oil interfaces that could capture the shape of the fluids and interfaces in the pore space.

### *2.2.3 Pore-space characterization*

The reservoir rock is made up of a complex and heterogeneous pore space with a wide range of pore sizes from sub-microns to millimetres. To accurately characterize such heterogeneous porous media in 3D, we use differential imaging between the high contrast brine reference scan and the dry reference scan which provides an accurate segmentation of solid, micro-porous grains and macro-pores, Figure 3. The total pore volume was quantified by

$$PV = 1 \times V_{macro} + \phi_{sub} \times V_{micro} \tag{1}$$

$$\phi_{sub} = \frac{CT_{sub} - CT_{grain}}{CT_{macro} - CT_{grain}} \tag{2}$$

which is simply the summation of the macro-pore and micro-pore volumes.

The contribution to porosity of the micro-porous space was determined by plotting the histograms for the grey-scale voxels in the brine reference image to find the peak (CT) in each phase and calculating the sub-resolution porosity fraction ($\phi_{sub}$), Figure 4. The total of macro- and micro-porosity measured from X-ray differential imaging was 27.4 % (where the macro-pores contributed 65.8% to the total porosity with 34.2% from the micro-pores) compared to a helium porosity of 27.8 % measured on the 1.5 inch (38 mm) core plug from which the rock sample was drilled. The MICP porosity was 27.0 % measured on a trim of the larger plug. The consistency of these values indicates that we have imaged a representative elementary volume of this rock.

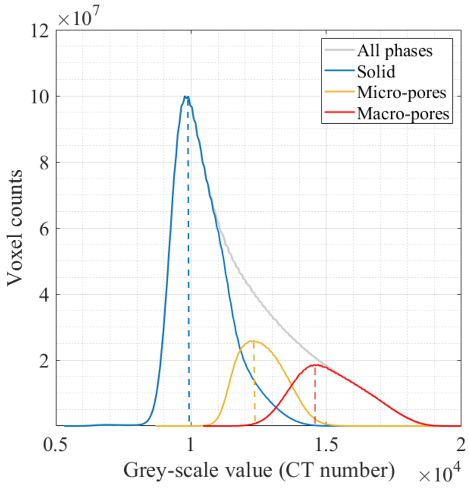

**Fig. 4:** The histograms of the grey-scale voxels in the brine reference image used to calculate the sub-resolution fraction in the micro-porous matrix.

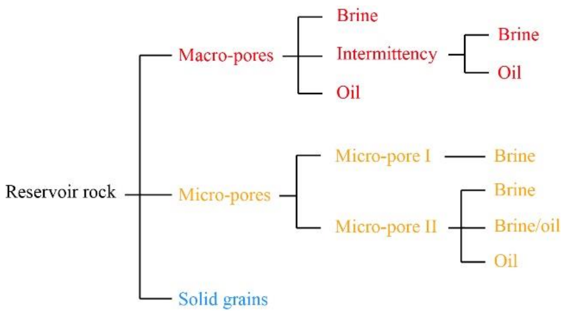

**Fig. 5:** A schematic diagram shows the brine quantification diagram in all phases of the reservoir rock.

### *2.2.4 Water saturation quantification*

The water saturation was quantified in both macro-pores (pores that can be resolved by the image resolution) and micro-pores (pores that have sizes smaller than the image resolution). The difference image between the multiphase scans at different fractional flows and the high contrast brine reference image accurately distinguished between the oil and brine phases in micro-and macro pore space. Figure 5 shows a schematic diagram of how the brine and oil were quantified.

Firstly, by differential imaging we were able to distinguish the intermittent phase in macro pores in which both oil and brine periodically existed as a single phase during the one-hour scan. The brine saturation in the intermittent phase that existed in the first two fractional flows was quantified by

$$S_{w\_inter\_macro} = \phi_{inter} \frac{CT_{inter} - CT_{oil}}{CT_{brine} - CT_{oil}} \qquad (3)$$

where $\phi_{inter}$ is the fraction of the intermittent phase in the total pore volume. CT refers to the peak grey-scale value found for each phase in the histogram of the raw multi-phase image.

Similar to the recent study by Gao et al. [40] on Estaillades limestone we observed that with increased fractional flow some voxels in micro-porosity did not change their grey scale value (their difference image value was zero), while the grey-scale value of other voxels decreased since some of the initially residing oil was displaced. We therefore infer that the former were always occupied by brine as micro-pore phase I, while the latter was micro-porous phase II consisting of both brine and oil. This is illustrated for $f_w$=0.5 in Figure 6.

The brine saturation in micro-pore phase I is equal to the pore space fraction in micro-pore phase I ($\phi_I$) that is fully saturated with brine. Whereas, the brine saturation in micro-pores II is quantified by

$$S_{w\_PF\_micropore\mathrm{II}} = \phi_{PFM} \frac{CT_{PFmicropores} - CT_{oil}}{CT_{brine} - CT_{oil}} \qquad (4)$$

where $\phi_{PFM}$ represents the fraction of the partially filled micro-pore space. CT refers to the peak grey-scale value found for each phase in the histogram of the raw multiphase image. The quantified brine saturation in macro and micro pore space at fractional flow 0.5 is shown over the length of the sample in Figure 7.

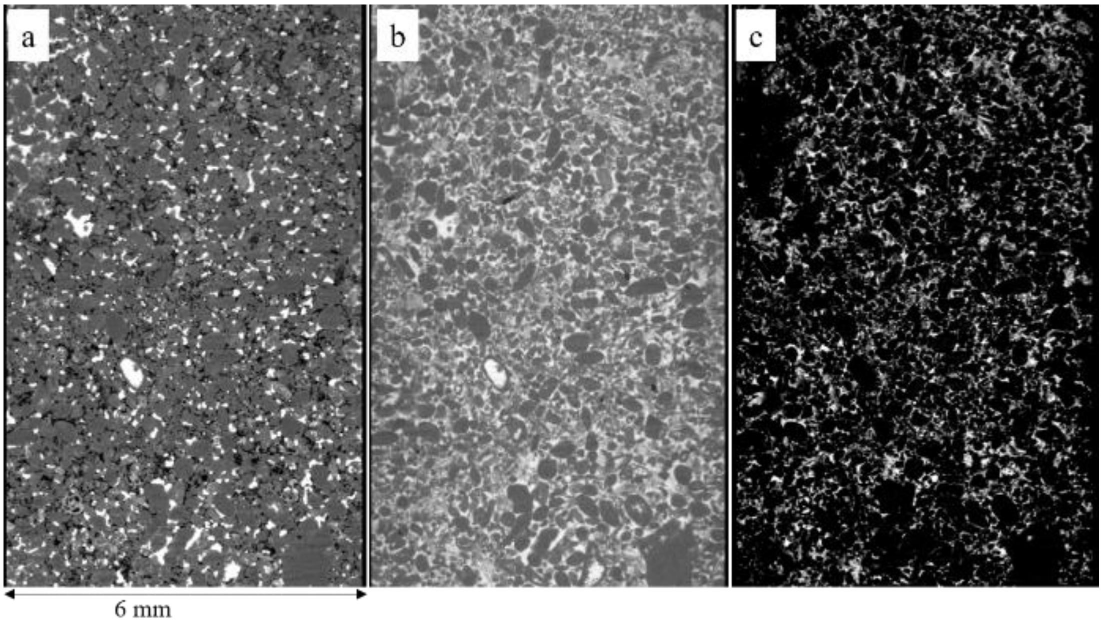

**Fig. 6:** a. Multiphase scan at $f_w$=0.5 where oil, rock and brine are shown in black, grey and white respectively. b. High contrast brine reference scan. c. Difference image between multiphase scan and the high contrast scan, where oil is shown in white and, rock and brine are shown in black.

## 3 Results and Discussion

We focus attention on the measured relative permeability and capillary pressure in the mixed-wet carbonate sample and interpret the behaviour based on the pore occupancy obtained from micro-CT images.

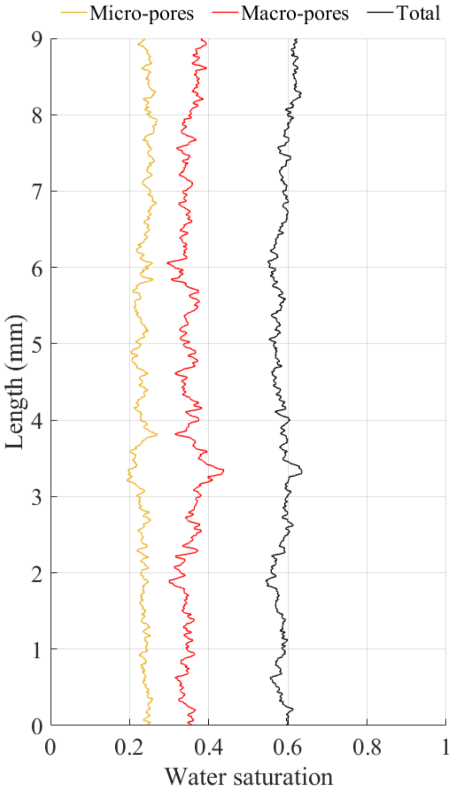

**Fig. 7:** Brine saturation profile of $f_w$=0.5 in macro-pores (red), micro-pores (orange) and total (black).

### 3.1 Relative permeability

The relative permeability of brine and oil were calculated using Darcy's law. The brine saturation at each fractional flow was measured on the segmented X-ray images while the pressure differential across the sample was measured using the pressure transducer. The *in situ* wettability was measured at $f_w$=0.5 on the segmented image showing a mixed-wet system with predominantly oil-wet surfaces with a mean contact angle of 113° ± 20°, [29, 46, 47]. As observed from Figure 8, the brine relative permeability is low and approximately constant until the cross-over point which occurs at $S_w$=63%. This means that, despite increasing fractional flow and saturation of water, there is no increase in water connectivity in the pore space. Approximately just before the cross-over point, water permeability starts to increase and above $f_w$=0.7 rises more steeply to high values, which is an indication of the enhanced connectivity in both macro- and micro-pore space.

The oil relative permeability remains finite after the cross-over point until the residual oil saturation, $S_{or}$ is attained. This is an indicator of oil connectivity at low oil saturations that is achieved through layer flow and has very important implications for favorable oil recovery. This finding is also supported in Figure 9 showing one-dimensional water saturation profiles along the core. We observe a significant additional oil recovery when $f_w$ is increased from 0.95 and 1 to reach residual oil saturation. In addition, significantly higher oil recovery is observed for fractional flow changes between 0 and 0.5, which is consistent with the previously explained observation of approximately constant water relative permeability. More detailed pore-scale observations associated with favorable oil recovery in the mixed-wet carbonate reservoir rock are presented elsewhere [48].

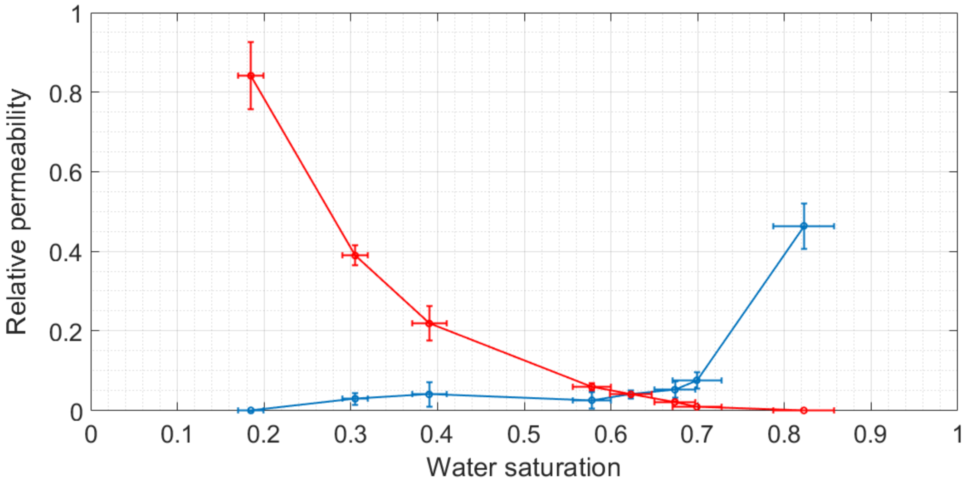

**Fig. 8:** Relative permeability measured for a steady state oil-brine waterflood in the mixed-wet reservoir carbonate sample. The error bars account for pump accuracy that controls flow rates and pressure measurement across the sample, and the uncertainty in the measurement of saturation from the images.

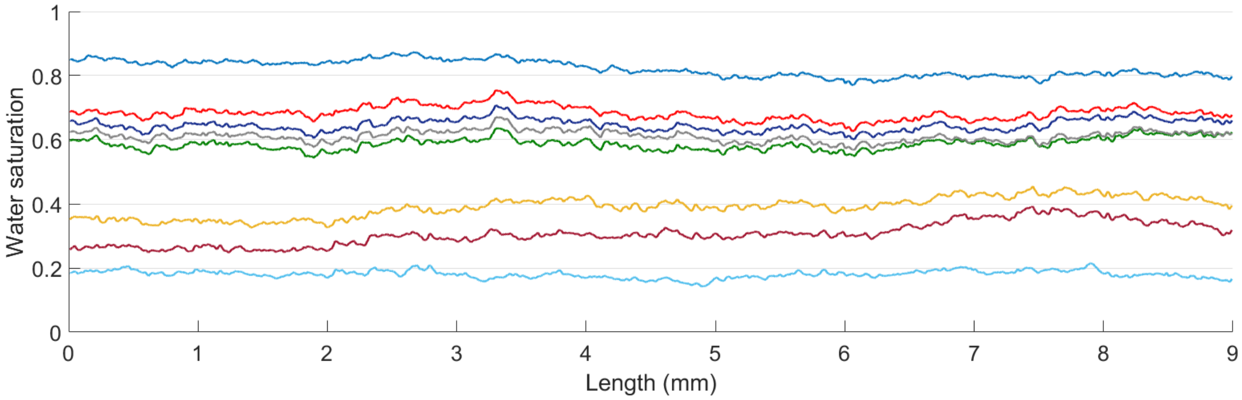

**Fig. 9:** Total brine (water) saturation profiles averaged in slices perpendicular to the flow direction for all of the eight water fractional flows over the length of the analyzed image. The lowest profile is for $f_w$=0 and the top is $f_w$=1.

The pressure differentials across the sample at the eight fractional flows are shown in Table 1. The sample pressure drop gradually increases with fractional flow increase until around the cross-over point. Here the pressure differential is highest as oil and brine have similar saturations and compete to flow through the same pores.

**Table 1.** Pressure differential across the sample at the eight fractional flows. SD indicates standard deviation and represents the fluctuations observed in the pressure recordings.

| $f_w$ | 0 | 0.15 | 0.3 | 0.5 | 0.7 | 0.85 | 0.95 | 1 |
|---|---|---|---|---|---|---|---|---|
| Total pressure drop (kPa) | 6.61 | 10.30 | 18.04 | 42.61 | 40.88 | 36.04 | 25.74 | 5.81 |
| Line pressure drop (kPa) | 2.18 | 2.16 | 6.11 | 10.28 | 13.11 | 9.91 | 5.68 | 2.36 |
| Sample pressure drop (kPa) | 4.43 | 8.14 | 11.93 | 31.33 | 27.77 | 26.13 | 20.06 | 3.45 |
| Sample pressure drop SD (kPa) | 0.13 | 0.22 | 1.89 | 0.36 | 0.32 | 0.29 | 0.25 | 0.13 |

### 3.2 Capillary pressure

Understanding capillary pressure, which controls fluid configurations at the pore-scale is essential to quantify the performance of hydrocarbon reservoirs at the macro-scale. The local capillary pressure was calculated from the measured mean interfacial curvature using the Young-Laplace law

$$P_c = 2\sigma\kappa \tag{5}$$

The interfacial tension, $\sigma$, was measured to be 27.9 ± 0.64 mN/m at 60 °C. The curvature was determined on the smoothed oil/brine interfaces by the average of the two principal curvatures: $\kappa = (\kappa_1 + \kappa_2)/2$, [20, 21, 25, 26]. The brine/oil interfacial curvature at $f_w$=0.5 measured on the sample volume of 2 × 2 × 2 mm$^3$ is shown in Figure 10. We observe both positive and negative values. The curvature histogram of 4.5 million measured values at $f_w$=0.5 is shown in Figure 11, with a negative average value (-0.011 ± 0.042 μm$^{-1}$) which results in the negative capillary pressure of -590 Pa.

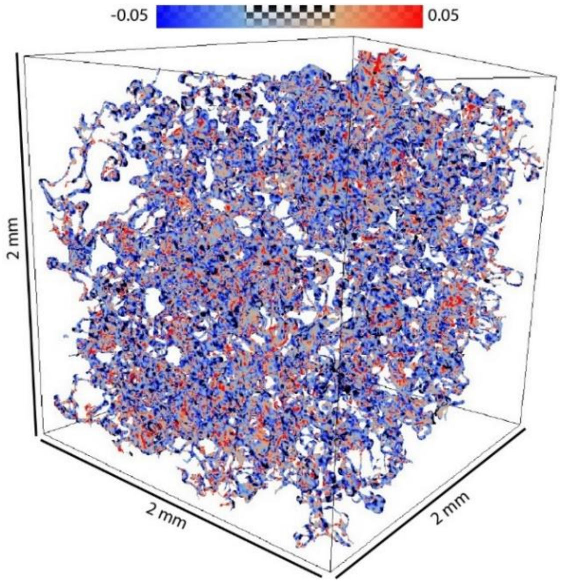

**Fig. 10:** Interfacial curvature (μm$^{-1}$) at $f_w$=0.5 where blue shows negative values and red shows positive values.

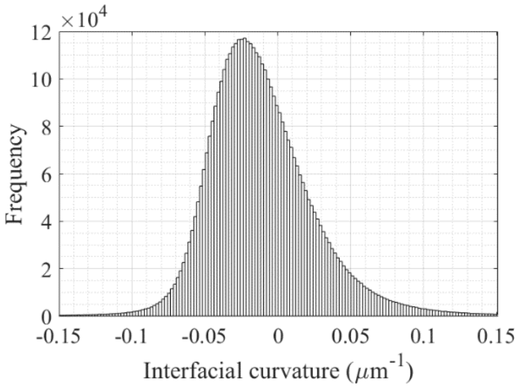

**Fig. 11:** Interfacial curvature distribution of 4.5 million measured values at $f_w$=0.5.

Capillary pressures calculated from the brine/oil interfacial curvature measurements for $f_w$ ranging from 0 to 0.95 are presented in Figure 12. They all have negative values ranging from -150 Pa to -630 Pa. This confirms that the fluid pressures are higher in brine than in oil, which is a characteristic of predominantly oil-wet media. Moreover, capillary pressure decreases with increasing water fractional flow.

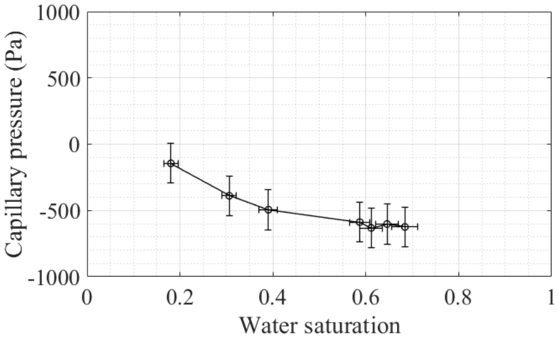

**Fig. 12:** The capillary pressure estimated from the average curvature of the oil-water interfaces plotted as a function of water saturation.

## 4 Conclusions and implications

Relative permeability and capillary pressure were measured simultaneously on a mixed-wet carbonate reservoir rock by conducting a steady-state experiment using crude oil and prepared doped formation brine from the same reservoir at subsurface conditions. Our main conclusions and implications from this work are:

- The relative permeability was measured by using water saturation quantified on X-ray segmented images and by measuring the pressure differential measured across the sample by a pressure transducer. The cross-over of the relative permeability was above 60% indicating favourable oil recovery.
- The capillary pressure was determined from the average of the local interfacial curvature. As expected for a predominantly oil-wet system, the capillary pressure was negative and decreased with increasing water fractional flow.
- Differential imaging was used to quantify fluid saturation in both macro-porosity and micro-porosity (sub-resolution). Hence, this work presents a procedure to perform oil and brine saturation quantification in micro-porous carbonate reservoir rocks, facilitating further studies to quantify oil recovery from macro- and micro-porosity for different reservoir systems.
- The results from this work could be used in future to benchmark pore-scale modelling to enhance the prediction of the multiphase flow in complex carbonate reservoirs

## Acknowledgement

We thank Abu Dhabi National Oil Company (ADNOC) and ADNOC Onshore for funding this work.

## References

1. M. J. Blunt, “Multiphase flow in permeable media: A pore-scale perspective”, *Cambridge University Press* (2017).
2. P. P. Jadhunandan, N. R. Morrow, “Effect of wettability on waterflooding recovery for crude oil/brine/rock systems”. *SPE Reservoir Engineering*. **10** (1), 40-46 (1995).
3. S. Bachu, “$CO_2$ storage in geological media: Role, means, status and barriers to deployment”. *Progress in Energy and Combustion Science*, **34** (2), 254-273 (2008).
4. M. R. Dernaika, M. A. Basioni, A. M. Dawoud, M. Z. Kalam, S. M. Skjaeveland, “Variations in Bounding and Scanning Relative Permeability Curves With Different Carbonate Rock Type”. *SPE Reservoir Evaluation & Engineering*, **16** (3), 265-280 (2013).
5. S. K., Masalmeh, X. D. Jing, W. van Vark, S. Christiansen, H. Van der Weerd, J. Van Dorp, “Impact of SCAL (special core analysis) on carbonate reservoirs: How capillary forces can affect field performance predictions”. *Petrophysics,* **45**, 403–413. (2004).
6. J. C. Parker, “Multiphase flow and transport in porous media”. *Reviews of Geophysics*, **27**(3), 311 (1989).
7. G. L. Hassler, E. Brunner, “Measurement of capillary pressures in small core samples”. *Transactions of AIME*, **160**(01), 114–123 (1945).
8. M. Z. Kalam, K. Al Hammadi, O. B. Wilson, M. Dernaika, H. Samosir, “Importance of porous plate measurements on carbonates at pseudo reservoir conditions”, *SCA2006-28, Proceedings of the 2006 SCA International Symposium, Trondheim, Norway*. (2006).
9. S. K. Masalmeh, X. D. Jing, “The importance of special core analysis in modelling remaining oil saturation in carbonate fields”. *SCA2008-03. In*

*Proceedings of the International Symposium of the Society of Core Analysis.* (2008).

10. M. R. Dernaika, M. S. Efnik, S. Koronfol, S. M. Skjaeveland, M. M. Al Mansoori, H. Hafez, M. Z. Kalam, "Capillary Pressure and Resistivity Index Measurements in a Mixed-Wet Carbonate Reservoir". *Petrophysics*, **55**(01), 24-30 (2014).
11. M Kennedy, "Practical petrophysics". *Netherlands: Elsevier* (2015).
12. C. McPhee, J. Reed, I. Zubizarreta, "Best practice in coring and core analysis". *In Developments in Petroleum Science,* 1–15 (2015).
13. D. Wildenschild, A. P. Sheppard, "X-ray imaging and analysis techniques for quantifying pore-scale structure and processes in subsurface porous medium systems". *Advances in Water Resources*. **51**, 217-246. (2013).
14. M. Andrew, B. Bijeljic, M. J. Blunt, "Pore-scale imaging of geological carbon dioxide storage at in situ conditions". *Geophysical Research Letters*. **40**, (15), 3915-3918 (2013).
15. M. J. Blunt, B. Bijeljic, H. Dong, O. Gharbi, S. Iglauer, P. Mostaghimi, A. Paluszny, C. Pentland, "Pore-scale imaging and modelling". *Advances in Water Resources*, **51**, 197–216 (2013).
16. S. Berg, H. Ott, S. Klapp, A. Schwing, R. Neiteler, N. Brussee, A. Makurat, L. Leu, F. Enzmann, j. Schwarz, M. Kersten, S. Irvine, M. Stampanoni, "Real-time 3D imaging of Haines jumps in porous media flow". *Proceedings of the National Academy of Sciences.* **110**, (10), 3755-3759 (2013).
17. S. Schlüter, A. Sheppard, K. Brown, D. Wildenschild, "Image processing of multiphase images obtained via X-ray microtomography: a review". *Water Resources Research*. **50**, (4), 3615-3639 (2014).
18. C. A. Reynolds, H. Menke, M. Andrew, M. J. Blunt, S. Krevor, "Dynamic fluid connectivity during steady-state multiphase flow in a sandstone". *Proceedings of the National Academy of Sciences*. **114**, (31), 8187-8192 (2017).
19. A. M. Alhammadi, A. AlRatrout, B. Bijeljic, M. J. Blunt, "Pore-scale Imaging and Characterization of Hydrocarbon Reservoir Rock Wettability at Subsurface Conditions Using X-ray Microtomography". *Journal of Visualized Experiments*, (140), e57915 (2018).
20. R. T. Armstrong, M. L. Porter, D. Wildenschild, "Linking pore-scale interfacial curvature to column-scale capillary pressure". *Advances in Water Resources*, **46**, 55–62 (2012).
21. K. Singh, H. Menke, M. Andrew, Q. Lin, C. Rau, M.J. Blunt, B., Bijeljic, "Dynamics of snap-off and pore-filling events during two-phase fluid flow in permeable media". *Scientific Reports*. **7**, (1), 5192 (2017).
22. A. L. Herring, L. Andersson, D. Wildenschild, "Enhancing residual trapping of supercritical $CO_2$ via cyclic injections". *Geophysical Research Letters.* **43**, (18), 9677-9685 (2016).
23. A. L. Herring, J. Middleton, R. Walsh, A. Kingston, A. Sheppard, "Flow rate impacts on capillary pressure and interface curvature of connected and disconnected fluid phases during multiphase flow in sandstone". *Advances in Water Resources*, **107**, 460–469 (2017).
24. Y. Gao, Q. Lin, B. Bijeljic, M. J. Blunt, "X-ray Microtomography of Intermittency in Multiphase Flow at Steady State Using a Differential Imaging Method". *Water Resources Research* **53**, 10274–10292 (2017).
25. M. Andrew, B. Bijeljic, M. J. Blunt, "Pore-by-pore capillary pressure measurements using X-ray microtomography at reservoir conditions: Curvature, snap-off, and remobilization of residual $CO_2$". *Water Resources Research*, **50**, 8760–8774. (2014a).
26. Q. Lin, B. Bijeljic, R. Pini, M. J. Blunt, S. Krevor, "Imaging and measurement of pore-scale interfacial curvature to determine capillary pressure simultaneously with relative permeability". *Water Resources Research*, **54**(9), 7046-7060 (2018).
27. R. A. Salathiel, "Oil recovery by surface film drainage in mixed-wettability rocks". *Journal of Petroleum Technology*. **25**, 1216–1224 (1973).
28. A. R. Kovscek, H. Wong, C. J. Radke, "A pore-level scenario for the development of mixed wettability in oil reservoirs". *AIChE J.* **39**, 1072–1085 (1993).
29. A. M. Alhammadi, A. AlRatrout, K. Singh, B. Bijeljic, M. J. Blunt, "In situ characterization of mixed-wettability in a reservoir rock at subsurface conditions". *Scientific Reports*, **7**(1), 10753 (2017).
30. J. S. Buckley, Y. Liu, S. Monsterleet, "Mechanisms of wetting alteration by crude oils". *SPE Journal*. **3**, 54–61 (1998).
31. W. G. Anderson, "Wettability literature survey-part 2: Wettability measurement". *Journal of Petroleum Technology.* **38**, (11), 1246-1262 (1986).
32. Anderson, W. G. "Wettability literature survey - part 5: The effects of wettability on relative permeability". *Journal of Petroleum Technology*. **39**, (11), 1453-1468 (1987a).
33. W. G. Anderson, "Wettability literature survey - part 6: The effects of wettability on waterflooding". *Journal of Petroleum Technology*. **39**, (12), 1605-1622 (1987b).
34. L. E. Cuiec, "Evaluation of reservoir wettability and its effect on oil recovery". *Interfacial Phenomena in Petroleum Recovery*. 319-375 (1990).
35. Morrow, N. R. "Wettability and its effect on oil recovery". *Journal of Petroleum Technology*. **42**, (12), 1476-1484 (1990).
36. S. Zou, R. T. Armstrong, J. Y. Arns, C. H. Arns, F. Hussain, "Experimental and Theoretical Evidence for Increased Ganglion Dynamics During Fractional Flow in Mixed-Wet Porous Media". *Water Resources Research*. **54** (5), 3277-3289 (2018).
37. Q. Lin, Y. Al-Khulaifi, M.J. Blunt, B. Bijeljic, "Quantification of sub-resolution porosity in carbonate rocks by applying high-salinity contrast brine using X-ray microtomography differential imaging". *Advances in Water Resources*, **96**, 306–322 (2016).

38. B. Bijeljic, A. Q. Raeini, Q. Lin, M. J. Blunt, "Multimodal Functions as Flow Signatures in Complex Porous Media" (2018). arXiv Prepr. arXiv1807.07611.
39. Q. Lin, B. Bijeljic, H. Rieke, M. J. Blunt, "Visualization and quantification of capillary drainage in the pore space of laminated sandstone by a porous plate method using differential imaging X-ray microtomography". *Water Resources Research* **53**, 7457–7468 (2017).
40. Y. Gao, A. Q. Raeini, M. J. Blunt, B. Bijeljic, "Pore Occupancy, Relative Permeability and Flow Intermittency Measurements Using X-Ray Micro-tomography in a Complex Carbonate", *Advances in Water Resources*, **129**, 56-69 (2019).
41. P. L. Gant, W. G. Anderson, "Core cleaning for restoration of native wettability", *SPE Formation Evaluation*, **3**(1), 131–138 (1988).
42. M. Andrew, B. Bijeljic, M. J. Blunt, "Pore-scale imaging of trapped supercritical carbon dioxide in sandstones and carbonates". *International Journal of Greenhouse Gas Control*. **22**, 1-14 (2014b).
43. A. Buades, B. Coll, J. M. Morel, "A non-local algorithm for image denoising". *Proceedings / CVPR, IEEE Computer Society Conference on Computer Vision and Pattern Recognition*. **2** (7), 60-65 (2005).
44. A. Buades, B. Coll, J. M. Morel, "Nonlocal image and movie denoising". *International Journal of Computer Vision*. **76** (2), 123-139 (2008).
45. A.C. Jones, C.H. Arns, A.P. Sheppard, D.W. Hutmacher, B.K. Milthorpe, M.A. Knackstedt, "Assessment of bone ingrowth into porous biomaterials using micro-CT". *Biomater*. **28**, 2491–2504 (2007).
46. A. AlRatrout, M. J. Blunt, B. Bijeljic, "Wettability in complex porous materials, the mixed-wet state, and its relationship to surface roughness". *Proceedings of the National Academy of Sciences*, **115** (36), 8901-8906 (2018).
47. A. AlRatrout, A. Q. Raeini, B. Bijeljic, M. J. Blunt, "Automatic measurement of contact angle in pore-space images". *Advances in Water Resources*. **109**, 158-169 (2017).
48. A. M. Alhammadi, Y. Gao, T. Akai, M. J. Blunt, B. Bijeljic, "Pore-scale X-ray imaging with measurement of relative permeability, capillary pressure and oil recovery in a mixed-wet micro-porous carbonate reservoir rock". *Fuel* (Under Review) (2019).

# Density Functional Hydrodynamics in Multiscale Pore Systems: Chemical Potential Drive

*Oleg* Dinariev[1], *Nikolay* Evseev[1,*], and *Denis* Klemin[2]

[1] Schlumberger, Schlumberger Moscow Research, 113, Pudovkina Street, Moscow 119284, Russia
[2] Schlumberger, Schlumberger Reservoir Labs, 6350 West Sam Houston Pkwy N, Houston, TX 77041, Houston, USA

**Abstract.** We use the method of density functional hydrodynamics (DFH) to model compositional multiphase flows in natural cores at the pore-scale. In previous publications the authors demonstrated that DFH covers many diverse pore-scale phenomena, starting from those inherent in RCA and SCAL measurements, and extending to much more complex EOR processes. We perform the pore-scale modelling of multiphase flow scenarios by means of the direct hydrodynamic (DHD) simulator, which is a numerical implementation of the DFH. In the present work, we consider the problem of numerical modelling of fluid transport in pore systems with voids and channels when the range of pore sizes exceed several orders of magnitude. Such situations are well known for carbonate reservoirs, where narrow pore channels of micrometer range can coexist and interconnect with vugs of millimeter or centimeter range. In such multiscale systems one cannot use the standard DFH approach for pore-scale modeling, primarily because the needed increase in scanning resolution that is required to resolve small pores adequately, leads to a field of view reduction that compromises the representation of large pores. In order to address this challenge, we suggest a novel approach, in which transport in small-size pores is described by an upscaled effective model, while the transport in large pores is still described by the DFH. The upscaled effective model is derived from the exact DFH equations using asymptotic expansion in respect to small-size characterization parameter. This effective model retains the properties of DFH like chemical and multiphase transport, thus making it applicable to the same range of phenomena as DFH itself. The model is based on the concept that the transport is driven by gradients of chemical potentials of the components present in the mixture. This is a significant generalization of the Darcy transport model since the proposed new model incorporates diffusion transport in addition to the usual pressure-driven transport. In the present work we provide several multiphase transport numerical examples including: a) upscaling to chemical potential drive (CPD) model, b) combined modeling of large pores by DFH and small pores by CPD.

## 1 Introduction

In recent years we witnessed an increasing level of capability and acceptance of digital rock as a complementary tool in core analysis. This tendency is following a gradual increase in both resolution of rock imaging techniques and the power of high-performance computing that are the key to unlock the potential in the core analysis by digital rock. As an answer to the growth in the hardware possibilities various modeling methods applicable in digital rock also evolve; see reviews in [1-6]. One of such methods, which the authors are actively developing, is the density functional hydrodynamics (DFH).

DFH is essentially a pore scale multi-phase, multi-compositional approach. As it has been demonstrated in previous publications [7-10], various multiphase compositional problems can be described in the frame of the DFH. The DFH method has found many applications in direct pore-scale modeling of various hydrodynamic and petrophysical phenomena on digital rock models obtained by X-ray micro-CT and SEM [11-21]. The practical usefulness of a standard workflow is very much dependent on the possibility to resolve necessary pore structure adequately, as well as on the rock sample being representative for the considered formation. There are specific ways to meet both of these requirements, but in this work, we discuss the resolution problem only.

In many cases the natural rocks are characterized by a wide range of pore sizes making the choice of X-ray micro-CT resolution very difficult if not altogether impossible. Indeed, if pores of both micrometer and millimeter range coexist within one piece of rock then, at present, it is not always possible to develop 3D model of rock microstructure, which can represent all pores. In situations like this we propose a combined approach, when several 3D digital rock models having different resolutions are integrated into one synthetic model. Combined multiscale approach is also being developed in the frame of pore-network modelling [1], but we follow image-based approach as it is inherent in DFH. High-resolution sub-models with explicitly resolved small

---

[*] Corresponding author: nevseev@slb.com

pores are used for direct modeling of transport processes by DFH to obtain effective flow characteristics. Then these results are incorporated into low-resolution model with explicit imaging of large pores while small pores are not necessarily resolved. At this stage the hydrodynamics in large pores is still simulated directly by DFH, while the transport in matrix is simulated using the previously computed effective transport properties. All these operations are done by the DFH pore-scale simulator called DHD (Schlumberger).

In effect, the described procedure represents upscaling from pore-scale DFH equations to macroscopic porous medium equations. As concerned with the single-phase flow, our idea is similar to the one described in [22, 23]. However, in addition to being applicable in general multiphase compositional scenarios, the rigorous upscaling starting with the DFH equations leads to the transport equations, which constitute the significant extension of the Darcy model. The driving force for the fluid flow happens to be gradients of chemical potentials of fluid chemical components that gives the model its name Chemical Potential Drive (CPD). Because change in pressure is directly related to change in chemical potential, this new model is consistent with pressure-drive Darcy approach as will be shown below. On the other hand, the CPD approach covers certain physical phenomena outside the scope of the Darcy model. Here are two examples in relation to the latter assertion. First, there are cases, when definition of pressure in confined fluid is problematic, e.g., when gas mean free path length is comparable to pore size (high Knudsen number), or liquid in pores with significant disjoining pressure; at the same time, the definition of chemical potential is still correct in both said instances. Second, there is an easy to derive exact solution for two-phase water-oil transport velocities in a hydrophilic circular capillary

$$u_{\mathrm{w}} = -(8\eta_{\mathrm{sw}})^{-1} R^2 (1-(r/R)^2)^2 G \tag{1}$$

$$u_{\mathrm{o}} = -(8\eta_{\mathrm{so}})^{-1} R^2 (2(r/R)^2 (1-(r/R)^2)^2 (\eta_{\mathrm{so}}/\eta_{\mathrm{sw}}) + (r/R)^4) G \tag{2}$$

where the water and oil velocities $u_{\mathrm{w}}, u_{\mathrm{o}}$ are defined as phase fluxes per capillary cross-section, $\eta_{\mathrm{sw}}, \eta_{\mathrm{so}}$ are the shear viscosities of water and oil, respectively, $R$ is the capillary radius, $r$ is the radius of the central region occupied by oil, and $G$ is the pressure gradient. An important observation following from Eqs. (1), (2) is that the transport of oil is influenced by viscosity of water, because oil, being the central phase, is carried by water. This cross-phase friction is in direct contradiction with the routine concept of phase permeabilities indicating the possible role of cross-terms in phase permeability matrix [24]. At the same time the cross-component influence is inherent in CPD, as it will be demonstrated below. Limitations of the Darcy law are discussed in the literature and deviations from it are observed in both high-accuracy 4D visualization of pore-scale fluid dynamics as well as in numerical simulations of pore-scale flows [25]. One may expect more deviations when dealing with complex fluids.

In Sec. II we give a brief reminder of the DFH equations, as well as a derivation of upscaling from DFH to CPD. Numerical demonstration of combined DFH and CPD models is presented in Sec. III. The overall summary and discussion of results is in Sec. IV.

The summation over repeated indices is implied everywhere. The indices $a, b, c = 1, 2, 3$ are related to Cartesian coordinates $x^a$, the indices $i, j, k = 1, ..., M$ are related to chemical components in the fluid mixture. We consider isothermal processes, so the temperature is assumed to be fixed, and dependence of certain variables on temperature is omitted. We use short symbols for partial derivatives: $\partial_a = \partial / \partial x^a$ and $\partial_t = \partial / \partial t$, where $t$ is time.

## 2 Theoretical concepts and equations

### 2.1 Density functional hydrodynamics

Here we provide only some of the basic definitions necessary to evolve the step from the DFH equations to the CPD ones. A detailed exposition of the DFH can be found in [7-10].

We consider continuum mechanics description of a mixture of $M$ chemical components present inside a spatial region $D$ having volume $V_D$. The region contains $N_{iD}$ of each type of molecules. To avoid large numbers, the quantities $N_{iD}$ are measured in moles. In case of homogeneous and static mixture we define chemical component molar densities by $n_i = N_{iD} / V_D$. If the mixture is inhomogeneous and possibly evolving, one can define $n_i$ as a dynamic variable at time $t$ and spatial point $x^a$ by establishing a small volume limit, such as $n_i = n_i(t, x^a) = \lim_{V_D \to 0} (N_{iD} / V_D)$. Like elsewhere in continuum mechanics, the small volume limit is understood as the convergent procedure with $V_D$ being small, but still larger than the molecular volume.

By counting the flow rate of molecules through a small area inside the mixture, one can define the component flux $I_{ia} = I_{ia}(t, x^b)$. The component fluxes are used to calculate the mass flux $I_a = m_i I_{ia}$, where $m_i$ is the molar mass of the $i$th component. By introducing mass density $\rho = m_i n_i$ it is possible to define mass velocity $v_a = \rho^{-1} I_a$. Component flux $I_{ia}$ can be represented as a combination of transport term $n_i v_a$ and diffusion flux $Q_{ia}$:

$$I_{ia} = n_i v_a + Q_{ia} \tag{3}$$

where by definition diffusion flux does not influence net mass transfer $m_i Q_{ia} = 0$. We assume the existence of the Helmholtz energy functional

$$F_D = F_D[n_i] = \int_D \omega dV + \int_{\partial D} f_* dA, \qquad (4)$$

$$\omega = f(n_i) + 2^{-1} \nu_{ij}(n_k) \partial_a n_i \partial_a n_j, \qquad (5)$$

where $\partial D$ is the boundary surface of the region $D$ (when the region is finite), $f = f(n_i)$ is the bulk Helmholtz energy density of homogeneous mixture, $\nu_{ij}$ is the positive-definite symmetric matrix, and $f_* = f_*(n_i)$ is the surface Helmholtz energy density, which is not equal to zero if $\partial D$ is a contact surface with some immobile solid. It is convenient to recollect certain thermodynamic equations involving Helmholtz energy

$$f = \kappa_i n_i - p, \; df = \kappa_i dn_i, \; dp = n_i d\kappa_i, \qquad (6)$$

where $\kappa_i$ is the chemical potential of the $i^{\text{th}}$ component, and $p$ is the hydrostatic pressure.

The model in Eqs. (4) and (5) is adequate for description of many important phenomena involving multiphase multicomponent mixtures. Up to now, it was successfully used to simulate multiphase multicomponent phenomena with or without phase transitions, surfactants, and mixtures with solid phases such as gas hydrates or solid particles [9-21, 26].

Now we list the DFH statements necessary to move forward to CPD.

The multiphase compositional transport in case of isothermal flow of fluids with Newtonian rheology is governed by the following equations written in a form of conservation laws for chemical components and momentum

$$\partial_t n_i + \partial_a (n_i v_a + Q_{ia}) = 0, \qquad (7)$$

$$\partial_t (\rho v_a) + \partial_b (\rho v_a v_b - p_{ab}) = 0, \qquad (8)$$

together with the relations

$$p_{ab} = \sigma_{ab} + \tau_{ab}, \qquad (9)$$

$$\sigma_{ab} = (\omega - \Phi_i n_i) \delta_{ab} - \nu_{ij} \partial_a n_i \partial_b n_j, \qquad (10)$$

$$\tau_{ab} = \eta_{\text{v}} \delta_{ab} \partial_c v_c + \eta_{\text{s}} (\partial_a v_b + \partial_b v_a - \frac{2}{3} \delta_{ab} \partial_c v_c), \qquad (11)$$

$$Q_{ia} = -D_{ij} \partial_a \Phi_j, \qquad (12)$$

$$\Phi_i = \kappa_i + 2^{-1} \frac{\partial \nu_{jk}}{\partial n_i} \partial_a n_j \partial_a n_k - \partial_a (\nu_{ij} \partial_a n_j), \qquad (13)$$

and subject to the boundary conditions at $\partial D$, when it is a contact surface with some immobile solid

$$v_a = 0, \qquad (14)$$

$$l^a Q_{ia} = 0, \qquad (15)$$

$$\frac{\partial f_*}{\partial n_i} - l^a \nu_{ij} \partial_a n_j = 0, \qquad (16)$$

where $p_{ab}$ is the stress tensor, $\sigma_{ab}$ is the static stress tensor, $\tau_{ab}$ is the viscous stress tensor, $\Phi_i$ is the generalized chemical potential of the $i^{\text{th}}$ mixture component, $\eta_{\text{v}}$ and $\eta_{\text{s}}$ are nonnegative bulk and shear viscosity coefficients, respectively, $D_{ij}$ is the nonnegative definite symmetric matrix subject to $D_{ij} m_j = 0$, $l^a$ is the internal normal unit vector at the boundary surface $\partial D$, and $\delta_{ab}$ is the Kronecker symbol. We also note that there is the identity $\partial_b \sigma_{ab} = -n_i \partial_a \Phi_i$, which reduces to $\partial_b \sigma_{ab} = 0$ in static equilibrium.

It is possible to derive the differential equation for the total energy (that includes both Helmholtz and kinetic energy) with energy flux $J_a$ and dissipation rate function $\chi$:

$$\partial_t (\omega + 2^{-1} \rho v_a v_a) = -\partial_a J_a + \chi, \qquad (17)$$

$$J_a = \frac{1}{2} \rho v_b v_b v_a - \nu_{ij} \partial_t n_i \partial_a n_j - \tau_{ab} v_b + \Phi_i I_{ia}, \qquad (18)$$

$$\chi = -\tau_{ab} \partial_a v_b + Q_{ia} \partial_a \Phi \qquad (19)$$

In accordance with Eqs. (11), (12), and (22) the inequality $\chi \le 0$ holds. Also, in accordance with Eqs. (14)-(16) the energy flux vanishes at the boundary $\partial D$: $l^a J_a = 0$. This signifies that in absence of external sources and forces the total energy decreases $\frac{d}{dt} \int_D (\omega + 2^{-1} \rho v_a v_a) dV \le 0$ in consistency with the second law of thermodynamics.

### 2.2 Upscaling to macroscopic transport in porous medium: chemical potential drive

Now we consider transition from microscopic DFH to macroscopic CPD description of fluid transport in porous medium. We use variables related to microscopic pore-scale description in parallel to similar variables related to macroscopic description. If $a$ is a microscopic variable, then similar macroscopic variable is denoted by symbol $\bar{a}$. The latter variable is usually obtained from the former by using certain averaging procedure. For example, we define component molar density by $\bar{n}_i = \bar{n}_i(t, x^a) = \lim_{V_D \to 0} (N_{iD} / V_D)$, where the pore volume $V_D$ is now sufficiently large to contain representative piece of saturated porous medium. The respective spatial region $D$ encompasses pores belonging to a porous medium region $\Delta$ containing both solid skeleton and pores. This porous medium region $\Delta$ is supposed to be representative of pore structure in statistical terms but not necessarily identical to the neighbor regions of porous medium. This is different from homogenization approach with periodic geometry of pore system [27]. The volumes of two regions $D$ and $\Delta$ are related by $V_D=\phi V_\Delta$, where $\phi=\phi(x^a)$ is porosity. The processes in a porous medium are assumed to be sufficiently slow in respect to the changing macroscopic component molar densities, so that the local distribution of chemical components and phases in pores are close to the equilibrium. Therefore, it is possible to define the macroscopic Helmholtz energy density $\bar{f}=\lim_{V_D\to 0}(F_D/V_D)$ as a function of parameters $\bar{n}_i$ since the equilibrium state of the mixture is determined by the functional (4) together with the components conservation condition $N_{iD}=\int_D n_i\, dV$. Using $\bar{f}$ it is possible to define macroscopic chemical potentials $\bar{\kappa}_i=\frac{\partial \bar{f}}{\partial \bar{n}_i}$.

Let us study transport through the spatial porous region *D*. Transport is possible only if there are free subregions of the boundary $\partial D$, which are not associated with solid surface. We designate $\partial D=\Gamma_{\mathrm{f}}\cup\Gamma_{\mathrm{s}}$, where $\Gamma_{\mathrm{f}}$, $\Gamma_{\mathrm{s}}$ are free and solid boundary, respectively. At the free boundary $\Gamma_{\mathrm{f}}$ the so-called free boundary condition for velocity is used in the form of $l^b\partial_b v_a=0$ instead of the no-slip condition in Eq. (14) of the DFH. The diffusion transport is generated by gradients of generalized chemical potentials $\partial_a\Phi_i$ (see Eq. (12)). The convective transport is determined by mass velocity, which under current assumptions satisfies the reduced momentum equation

$$\partial_b\tau_{ab}=n_i\partial_a\Phi_i . \tag{20}$$

with mixed no-slip and free boundary conditions. In terms of differential operations Eq. (20) can be represented as follows

$$L_{ab}v_b=-\eta_a=-n_i\partial_a\Phi_i , \tag{21}$$

where the left side is positive elliptic self-adjoint operator in $L_2(D)$ acting on the velocity field. It admits the solution with a Green's function, which can also be represented in operator form

$$v_a=-G^{ab}\eta_b=-G^{ab}(n_i\partial_a\Phi_i) . \tag{22}$$

Here the integral operator in $G^{ab}$ is positive definite, and also $G^{ab}=G^{ba}$. Now combining Eqs. (12) and (22) we arrive to the expression for the component flux generated by the gradients $\partial_a\Phi_i$

$$I_{ia}=n_i v_a+Q_{ia}=-(n_i G^{ab}n_j+\delta_{ab}D_{ij})\partial_b\Phi_j . \tag{23}$$

Averaging Eq. (23) over different cross-sections of the region $\Delta$ produces the macroscopic flux of components generated by gradients of chemical potentials (Chemical Potential Drive or CPD)

$$\bar{I}_{ia}=<I_{ia}>=-K_{ij}^{ab}\partial_b\bar{\kappa}_j , \tag{24}$$

where the transport matrix $K_{ij}^{ab}=K_{ij}^{ab}(x^c)$ is positive definite and satisfies the symmetry conditions $K_{ij}^{ab}=K_{ij}^{ba}=K_{ji}^{ab}$. The component conservation equation together with the CPD transport law in Eq. (24) that constitutes the closed formulation of macroscopic fluid transport model is as follows

$$\partial_t(\phi\bar{n}_i)+\partial_a\bar{I}_{ia}=0 . \tag{25}$$

Direct calculations lead to the macroscopic equivalent of Eq. (17)

$$\partial_t(\phi\bar{f})=-\partial_a\bar{J}_a+\bar{\chi} \tag{26}$$

$$\bar{J}_a=\bar{\kappa}_i\bar{I}_{ai} , \tag{27}$$

$$\bar{\chi}=\bar{I}_{ai}\partial_a\bar{\kappa}_i\le 0 . \tag{28}$$

### 2.3 Boundary conditions between DFH and CPD domains

In highly heterogeneous porous material there can be situations when there are adjacent spatial regions where one can use alternatively DFH or CPD. It is necessary to discuss what boundary conditions should be set at the common boundary $\Gamma=\partial D_1\cap\partial D_2$ between the DFH region $D_1$ and the CPD region $D_2$. Eq. (16) is still valid at $\Gamma$ in $D_1$, while Eqs. (14) and (15) are not because there can be transport of components through the boundary.

One evident boundary condition follows from conservation of component fluxes

$$l^a I_{ai}=l^a\bar{I}_{ai} . \tag{29}$$

The next condition can be derived from energy conservation at the boundary

$$l^a J_a=l^a\bar{J}_a . \tag{30}$$

Using Eqs. (18), (29), and (30) one can satisfy Eq. (27) by imposing boundary condition for chemical potentials

$$\bar{\kappa}_i=\Phi_i-m_i X , \tag{31}$$

where variable $X$ is determined by the additional boundary equation

$$X\rho l^a v_a+\frac{1}{2}\rho v_b v_b l^a v_a-l^a\tau_{ab}v_b=0 . \tag{32}$$

### 2.4 Examples of CPD models

For the first example we assume that the porous medium is homogeneous and isotropic, and there is single-phase single-component flow. In this case the CPD transport law is equivalent to the Darcy law (see the last equation in (6))

$$\bar{I}_{1a} = -K \partial_a \bar{\kappa}_1 = -K \bar{n}_1^{-1} \partial_a \bar{p}_1 \tag{33}$$

with CPD transport coefficient $K$ being proportional to the absolute permeability $k$, $K = k \bar{n}_1^2 \eta_s^{-1}$, where coefficient $\eta_s$ is the shear viscosity.

Second, we consider two-phase two-component mixture modeling water and oil. Here we have the following definitions

$$\bar{n}_1 = \bar{s}_w \bar{n}_w,\; \bar{n}_2 = (1-\bar{s}_w)\bar{n}_o, \tag{34}$$

$$\bar{f} = \bar{f}(\bar{n}_i) = \bar{s}_\mathrm{w} \bar{f}_\mathrm{w}(\bar{n}_\mathrm{w}) + (1-\bar{s}_\mathrm{w}) \bar{f}_\mathrm{o}(\bar{n}_\mathrm{o}) + \bar{f}_\mathrm{cap}(\bar{s}_\mathrm{w}), \tag{35}$$

$$\bar{p}_\mathrm{w} - \bar{p}_\mathrm{o} = \bar{p}_\mathrm{cap}(\bar{s}_\mathrm{w}) = \bar{f}_\mathrm{cap}'(\bar{s}_\mathrm{w}), \tag{36}$$

where $\bar{s}_\mathrm{w}$ is the water saturation, $\bar{f}_\mathrm{w}, \bar{p}_\mathrm{w}$ are the Helmholtz energy density and pressure of water, $\bar{f}_\mathrm{o}, \bar{p}_\mathrm{o}$ are the Helmholtz energy density and pressure of oil, and $\bar{f}_\mathrm{cap}(\bar{s}_\mathrm{w})$, $\bar{p}_\mathrm{cap}(\bar{s}_\mathrm{w}) = \bar{f}_\mathrm{cap}'(\bar{s}_\mathrm{w})$ are the Helmholtz energy density and pressure for capillary forces. Eqs. (34)-(36) determine variables $\bar{s}_\mathrm{w}, \bar{n}_\mathrm{w}, \bar{n}_\mathrm{o}$ when variables $\bar{n}_1, \bar{n}_2$ are known. The transport model in Eq. (24) is consistent with the generalized Darcy law if there are the following additional conditions:

$$K_{12} = K_{21} = 0,\; K_{11} = k_\mathrm{w} \bar{n}_\mathrm{w}^2 \eta_\mathrm{sw}^{-1}, \quad K_{22} = k_\mathrm{o} \bar{n}_\mathrm{o}^2 \eta_\mathrm{so}^{-1}, \tag{37}$$

where $k_\mathrm{w}, k_\mathrm{o}$ are water and oil phase permeabilities. If conditions in Eq. (37) are not satisfied, CPD model can demonstrate some phenomena outside traditional Darcy transport.

## 3 Numerical examples

To demonstrate application of a workflow based on the joint DFH modeling within resolved porosity and CPD modeling within matrix containing unresolved smaller pores (DFH+CPD workflow) we chose a heterogeneous, but relatively well characterized chalk sample. The sample is grainstone composed of pelloids, skeletal grains and ooids. The grains are cemented by equant calcite spar cement. Intergranular porosity is the dominant pore system, additionally some moldic and micropores are present in partially leached grains. Pore throats are ranging between approximately 1 and 10 microns. Pore throat distribution is skewed to smaller pore throat sizes. Measured gas porosity of the sample is 26.2%, and gas permeability is 19.4 mD.

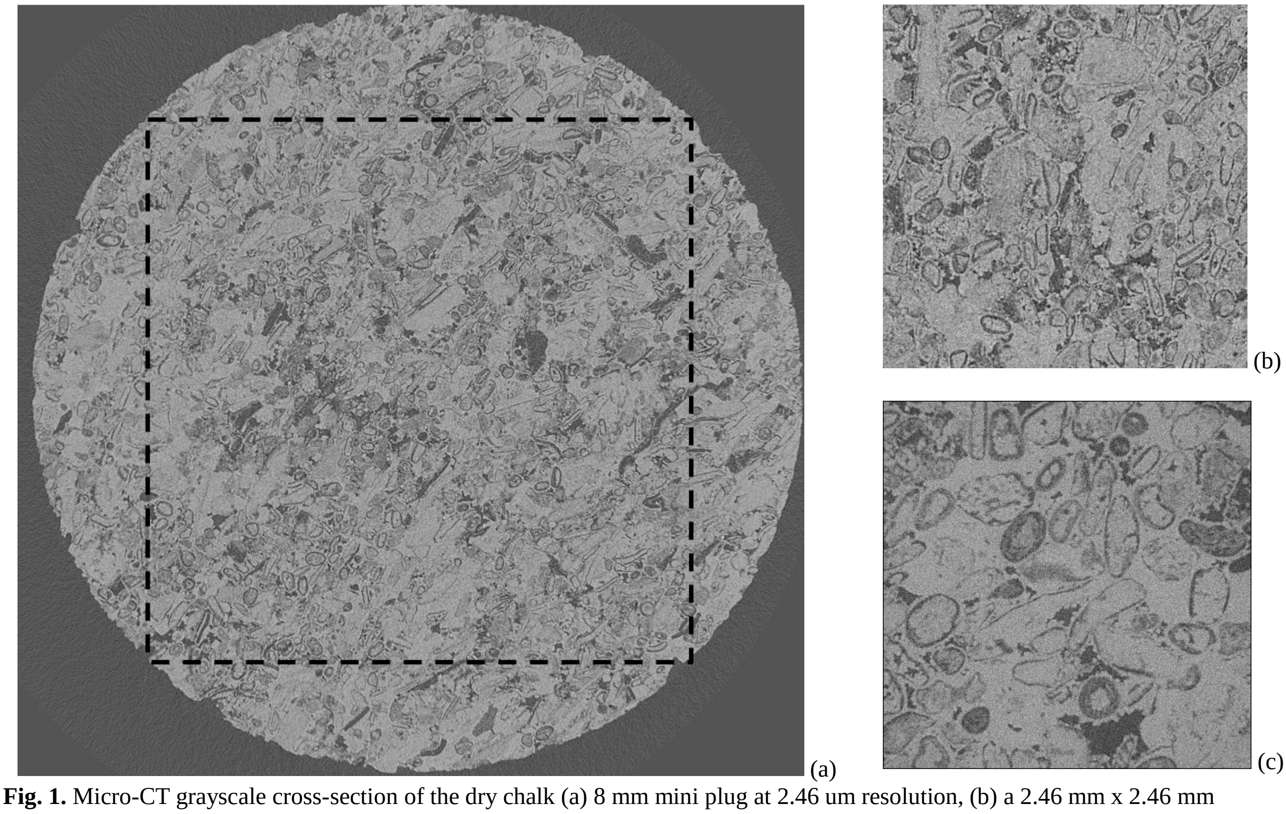

**Fig. 1.** Micro-CT grayscale cross-section of the dry chalk (a) 8 mm mini plug at 2.46 um resolution, (b) a 2.46 mm x 2.46 mm fragment of a cross-section at 2.46 um resolution, and (c) a 0.82 mm x 0.82 mm fragment of a cross-section at 0.82 um resolution; the dashed line in (a) shows the position of the maximum size parallelepiped model extracted from the mini plug.

An 8 mm diameter mini plug was scanned with 2.46 um per voxel resolution, and a portion of the mini plug was scanned with higher resolution of 0.82 μm per voxel (Fig. 1).

Two 3D digital rock models (DRM) with these two different resolutions were constructed (Fig. 2). Both models cover the same spatial region with the size 0.82 mm x 0.82 mm x 0.82 mm, but they have different number of cells (voxels). The high-resolution DRM has $1000^3$ (1000x1000x1000) cells and the low-resolution DRM has $333^3$ (333x333x333) cells so that the cell sizes are 0.82 um and 2.46 um, respectively. In either model some portion of pores fell below resolution. However, it is evident from Fig. 2 that significantly higher proportion of pores remains below resolution in the low-resolution DRM than it does in the high-resolution DRM. The data on the resolved and unresolved porosity is shown in Table 1.

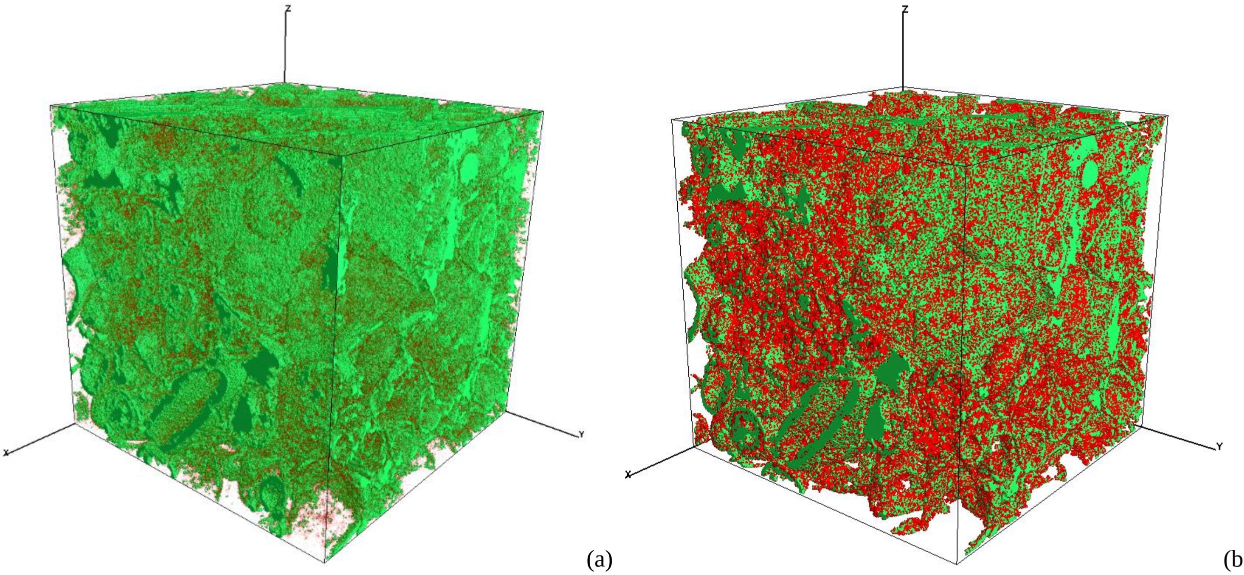

(a) (b)

**Fig. 2.** 3D view of the pore space of the (a) high-resolution $1000^3$ and (b) low-resolution $333^3$ DRMs. The resolved pores are shown in green, the unresolved pores (subresolution matrix) are shown in red, and the skeleton is made transparent.

**Table 1.** The portion of resolved porosity and unresolved porosity (subresolution matrix) within digital rock models of different spatial resolution.

| Model | Resolved porosity | Subresolution matrix |
|---|---|---|
| $1000^3$, 0.82 um | 0.166 | 0.073 |
| $333^3$, 2.46 um | 0.091 | 0.157 |

In addition to X-ray micro-CT, we have done scanning electron microscopy (SEM) of parts of the sample to reveal the pores below micro-CT resolution down to 50 nm. Using both micro-CT high-resolution (0.82 um) and SEM data we performed digital modeling of MICP experiment and reconstructed pore throat size distribution that is compared to the standard experimental MICP measurements in Fig. 3. The two curves in Fig. 3 match well meaning that most of the controlling pore throats have been adequately resolved on the corresponding scales.

In modeling on the high-resolution DRM, we assumed that the subresolution matrix portion of the model is effectively impermeable for oil at relevant oil-water capillary pressure levels so that only the DFH equations need to be solved within the resolved pore space. On the other hand, in modeling on the low-resolution DRM, we assumed that the subresolution matrix is permeable and therefore the full DFH+CPD simulation needs to be done. To set up a single-phase DFH+CPD simulation it is necessary to provide absolute permeability in the subresolution matrix cells so that the single-phase CPD transport law given in Eq. (33) could be resolved. In order to do this, we first simulated single-phase flow on the high-resolution DRM to obtain velocity distribution (Fig. 4a).

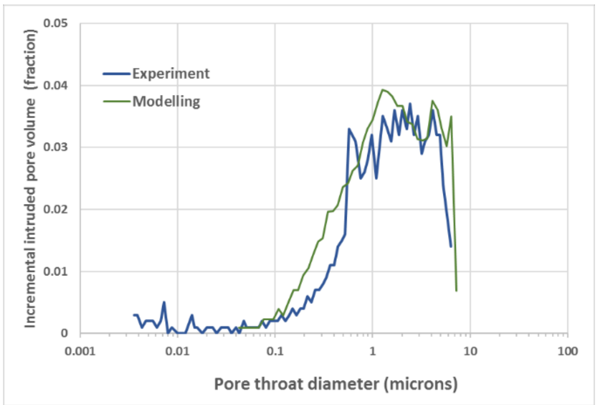

**Fig. 3.** Reconstructed numerically from the micro-CT and SEM data (green curve) and obtained from the MICP measurements (blue curve) pore throat size distributions.

Then, by interpreting the simulation results in terms of Eq. (33) and linking them with the gray scale distribution from the high-resolution images such as those shown in Fig. 1c, we established a correlation between the gray scale and absolute permeability values. We then applied the same correlation to the low-resolution gray scale images to inform the low-resolution DRM about the subresolution matrix permeability. The velocity

---

* Corresponding author: nevseev@slb.com

distribution obtained on this $333^3$ low-resolution DRM is presented in Fig. 4b. The absolute permeabilities calculated on the high- and low-resolution DRMs are 17.3 mD and 18.2 mD, correspondingly.

The next step was simulating two-phase flow and the steady-state relative permeability experiment. The two immiscible phases were assumed to be water and oil with the properties as follows: $\rho_{\mathrm{w}} = 1000\,\mathrm{kg/m^3}$, $\rho_{\mathrm{o}} = 800\,\mathrm{kg/m^3}$, $\eta_{\mathrm{sw}} = 0.001\,\mathrm{Pa{\times}s}$, $\eta_{\mathrm{so}} = 0.004\,\mathrm{Pa{\times}s}$, $\gamma_{\mathrm{ow}} = 0.03\,\mathrm{N/m}$, where $\rho_{\mathrm{w}}, \rho_{\mathrm{o}}$ are the water and oil mass densities, $\eta_{\mathrm{sw}}, \rho_{\mathrm{so}}$ are the water and oil viscosities, and $\gamma_{\mathrm{ow}}$ is the oil-water interfacial tension. Since the sample is carbonate, it was assumed that it has mixed wettability. To model this, we first injected oil into initially water-wet 100% water saturated high-resolution DRM using our standard DFH workflow [11, 14-17, 19-21]. (In all cases here and below injection was arranged in direction from bottom to top as shown in the 3D views.) Then at those places where oil touched the pore walls we switched wettability to moderately oil-wet while leaving the untouched pore walls water-wet. In this way most of the smaller pores as well as the pores isolated by thin pore throats remained water-wet, while the larger pores attained wettability towards oil. The distribution of water and oil at the residual water saturation state is shown in Fig. 5a. Using the obtained mixed-wet wettability distribution we simulated the steady-state relative permeability experiment by injecting oil and water mixture in several steps different in water content in the influx; at the final step, with only water injected, the residual oil saturation was obtained (Fig. 5c).

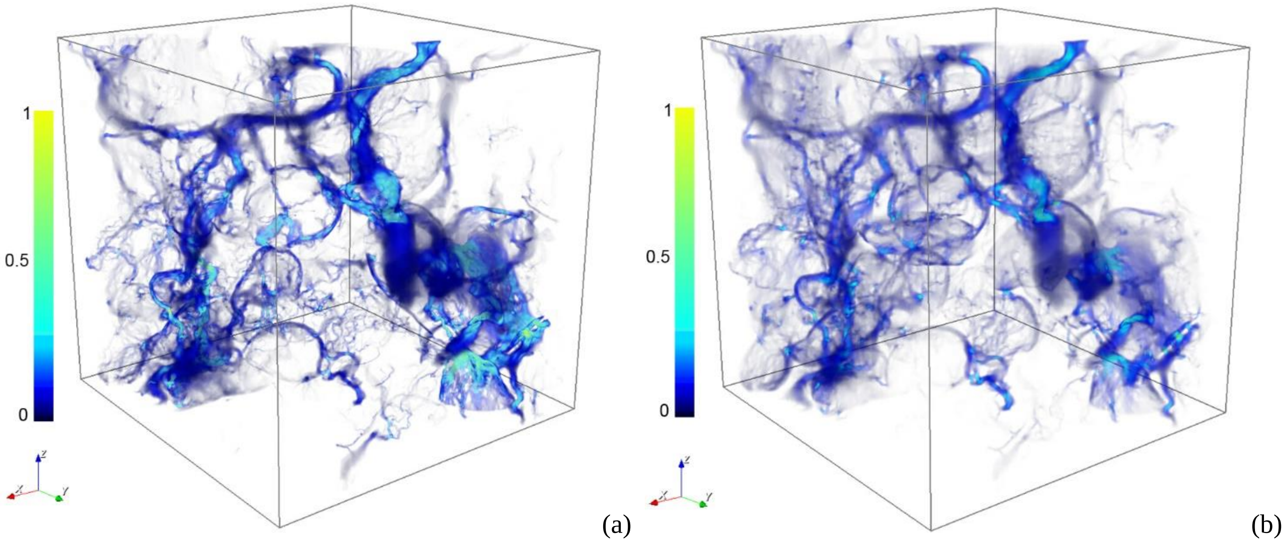

(a) (b)

**Fig. 4.** 3D view of the velocity absolute value distribution in (a) the high-resolution $1000^3$ DRM and (b) the low-resolution $333^3$ DRM of the same location within the core. The shown distribution was scaled to the [0; 1] range. The velocity corresponds to flow in vertical ($z$) direction.

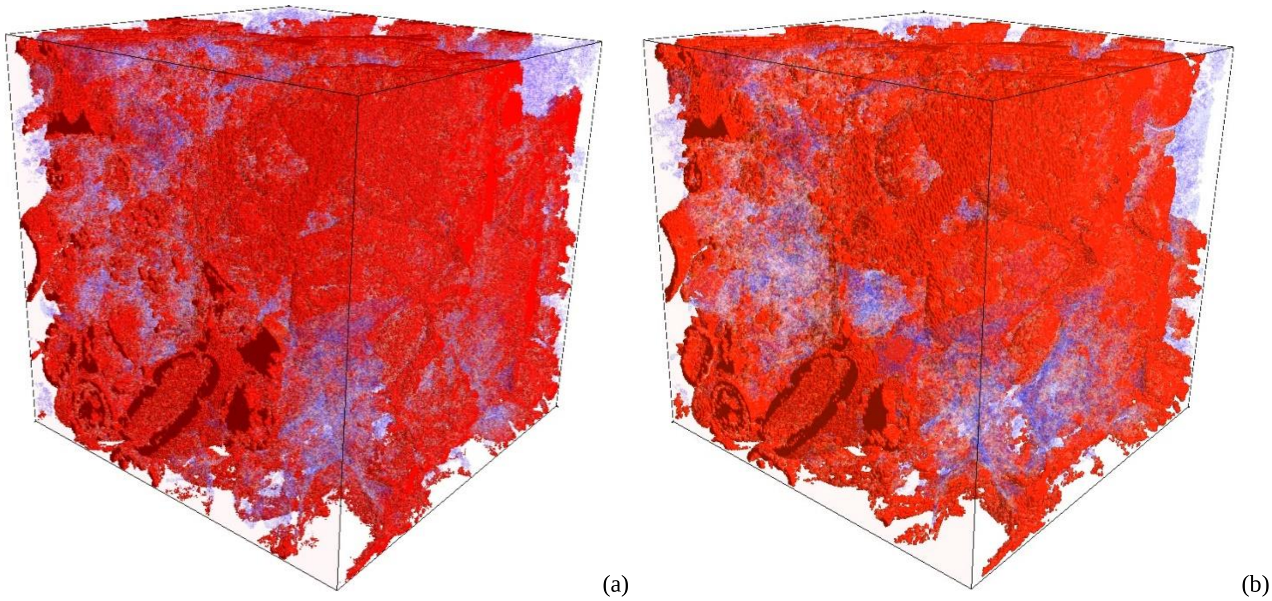

(a) (b)

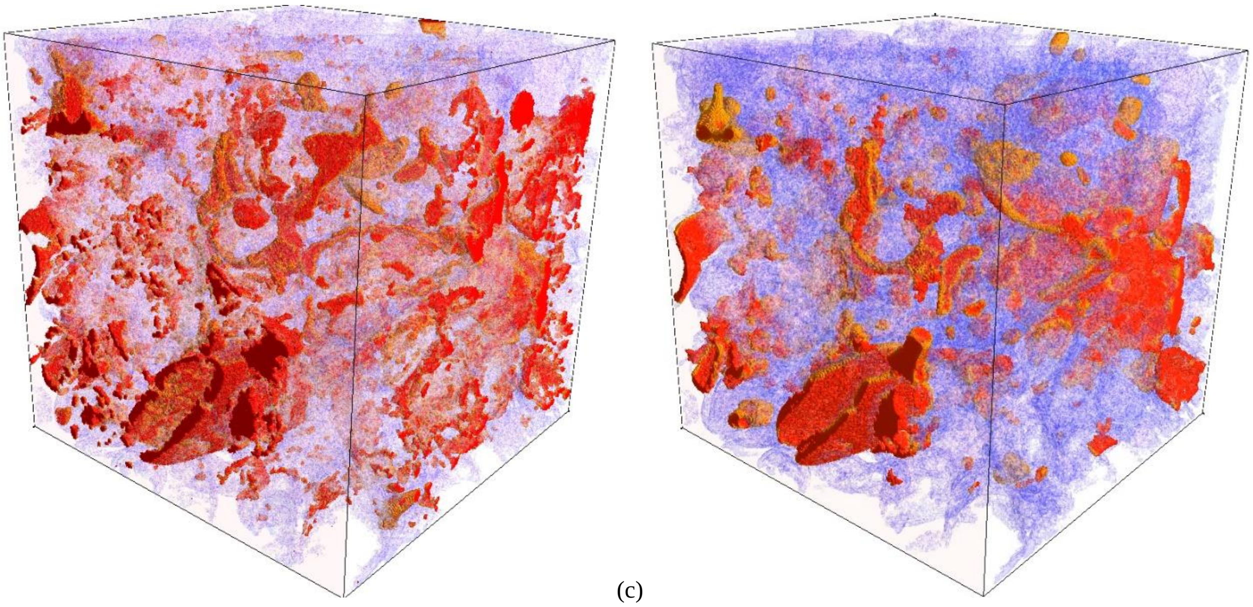

(c) (d)

**Fig. 5.** 3D view of the distribution of water and oil in the **high-resolution DRM** (left column) and the **low-resolution DRM** (right column) at the initial conditions corresponding to the residual water saturation (a, b), and the final state corresponding to the residual oil saturation (c, d). Water is shown in semitransparent blue, oil is shown in red, and skeleton is completely transparent.

To run DHD+CPD two-phase simulation, it is necessary to provide CPD transport matrix of Eq. (24) in subresolution matrix cells. Alternatively, when dealing with immiscible phases like oil and water that are each described by just one pseudo-component, it is possible to use simplified CPD transport model provided in Eq. (37) and based on the concepts of absolute and relative permeabilities and capillary pressure. We already discussed how absolute permeability was assigned to the subresolution matrix cells of the low-resolution DRM. The relative permeability was assigned in a similar way since all the velocity distribution, pressure, and water saturation for the subresolution matrix cells are known from the simulation on the high-resolution model. The capillary pressure function was constructed using the Young-Laplace equation and then scaled to the pore size distribution correlated by the gray scale values.

The distributions of oil and water obtained in simulation of the two-phase steady-state relative permeability experiment modeled using the DFH+CPD workflow on the low-resolution DRM are presented in Fig.5b,d. The chart in Fig. 6 compares the relative permeability curves obtained on both high- and low-resolution DRMs.

The final example we wish to present here is the simulation of both absolute and steady-state relative permeabilities on another low-resolution DRM with the size of 4.92 mm x 4.92 mm x 2.46 mm approximated with 500 x 500 x 250 cells with the cell size of 9.84 um. This model covers maximum size parallelepiped that can be extracted from the micro-CT scans of the 8 mm mini plug as shown by the dashed line in Fig. 1a. All of the parameters necessary to set up the DFH+CPD model were taken from the previous calculations on the high-resolution DRM as described previously.

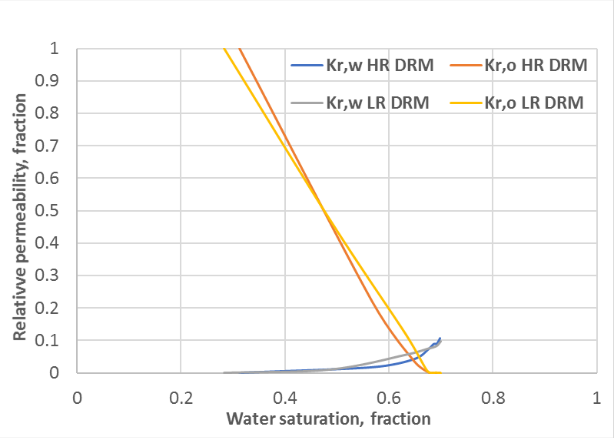

**Fig. 6.** Comparison of the simulated steady-state relative permeability curves obtained on the high-resolution (orange and blue curves) and low-resolution (yellow and gray curves) DRMs of the same spatial region within the sample.

Simulated absolute permeability of this model is 19.8 mD. The distributions of water and oil corresponding to the residual water saturation and residual oil saturation as obtained during the steady-state relative permeability simulation are shown in Fig. 7. The simulated relative permeability curves are presented in Fig. 8.

In this work, the simulation results were interpreted in consistency with the conditions in Eq. (37) that is with the traditional Darcy transport. However, in complex fluid problems deviations from relative permeability concept are expected, which then must be treated in the frame of the wider CPD model.

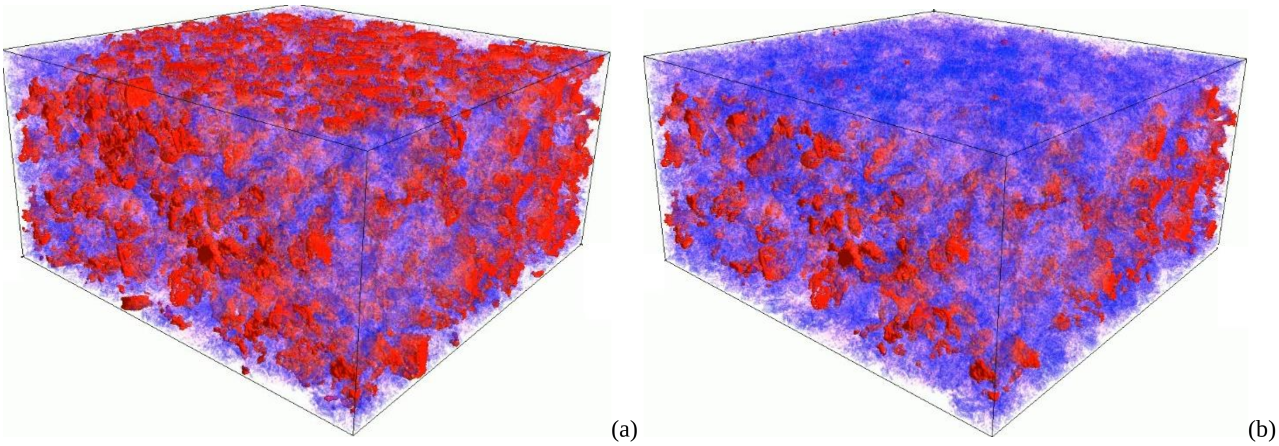

**Fig. 7.** 3D view of the distribution of water and oil in the upscaled low-resolution DRM at (a) initial conditions corresponding to the residual water saturation, and (b) final state corresponding to the residual oil saturation. Water is shown in semitransparent blue, oil is shown in red, and skeleton is transparent.

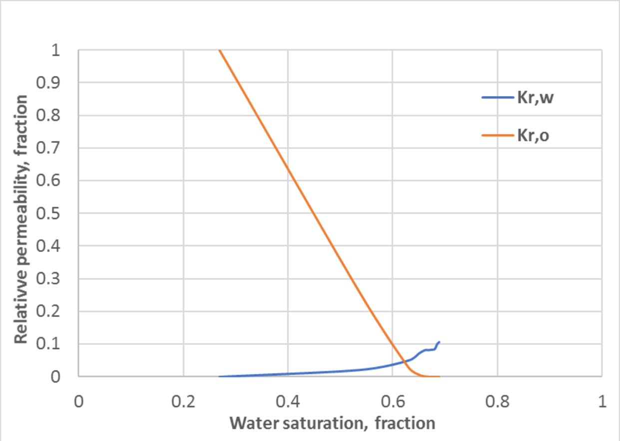

**Fig. 8.** Simulated steady-state relative permeability curves obtained on the upscaled low-resolution model.

## 2 Conclusion

We developed a new digital rock workflow applicable for simulation of multiphase flow on multiscale models representing heterogeneous core samples. The workflow called DFH+CPD is based on solving the standard DFH equations within resolved porosity and solving the new CPD equations within unresolved porosity or subresolution matrix. The CPD equations are derived in mathematically rigorous way from the DFH equations averaged over statistically representative ensemble of pores. The new workflow amounts to an effective upscaling procedure allowing multiphase simulation on coarse resolution digital rock models that include information that can be obtained on high-resolution models. The DFH+CPD workflow was implemented within the Schlumberger DHD simulator.

To validate the new workflow, we compared absolute and steady-state relative permeabilities simulation results on the high-resolution model and the low-resolution model of the same region within the heterogeneous carbonate core. Then we demonstrated simulation of the steady-state relative permeabilities on the upscaled digital rock model that covers almost entire 8 mm mini plug.

We thank Schlumberger for permission to publish this work.

## References

1. Blunt, M.J., *Multiphase Flow in Permeable Media: A PoreScale Perspective*, (Cambridge University Press, Cambridge, 2017). ISBN 978-1-107-09346-1
2. C.F. Berg, O. Lopez, H. Berland, J. Petrol. Sci. Eng. **157**, 131 (2017)
3. T. Bultreys, W. De Boever, V. Cnudde, Earth Sci. Rev., **155**, 93 (2016)
4. M.J. Blunt, B. Bijeljic, H. Dong, O. Gharbi, S. Iglauer, P. Mostaghimi, A. Paluszny, C. Pentland, Adv. Water Resour. **51**, 197 (2013)
5. V. Joekar-Niasar, M.I.J. van Dijke, S.M. Hassanizadeh, Transp. Porous Med. **94**, 461 (2012)
6. P. Meakin, A.M. Tartakovsky, Rev. Geophys., **47**, RG3002 (2009)
7. O. Dinariev, J. Appl. Math. Mech. **59**, 745 (1995)
8. O. Dinariev, J. Appl. Math. Mech. **62**, 397 (1998)
9. A. Demianov, O. Dinariev, N. Evseev, Can. J. Chem. Eng., **89**, 206 (2011)
10. A.Yu. Demianov, O.Yu. Dinariev, N.V. Evseev, *Introduction to the density functional method in hydrodynamics* (Fizmatlit, Moscow, 2014). ISBN 978-5-9221-1539-1
11. D. Koroteev, O. Dinariev, N. Evseev, D. Klemin, A. Nadeev, S. Safonov, O. Gurpinar, S. Berg, C. van Kruijsdijk, R. Armstrong, M. T. Myers, L. Hathon, H. de Jong, Petrophysics **55**, 294 (2014).
12. R.T. Armstrong, N. Evseev, D. Koroteev, S. Berg, Adv. Water Resour., **77**, 57 (2015)
13. R.T. Armstrong, S. Berg, O. Dinariev, N. Evseev, D. Klemin, D. Koroteev, S. Safonov, Transp. Porous Med., **112**, 577 (2016)
14. N. Evseev, O. Dinariev, M. Hürlimann, S. Safonov, Petrophysics, **56**, 32 (2015)
15. A. Shandrygin, V. Shelepov, R. Ramazanov, N. Andrianov, D. Klemin, A. Nadeev, Yakimchuk, SPE-176629-MS (2015)

16. A. Shandrygin, V. Shelepov, R. Ramazanov, N. Andrianov, D. Klemin, A. Nadeev, S. Safonov, I. Yakimchuk, SPE-182037-MS (2016)
17. O. Dinariev, N. Evseev, Computat. Geosci., **20**, 835 (2016)
18. O. Dinariev, N. Evseev, Phys. Rev., **E95**, 063307 (2017)
19. S.I. Geetan, R.M. MacDonald, D. Klemin, 2461115-MS URTeC Conference Paper (2016)
20. S.I. Geetan, R.M. MacDonald, D. Klemin, 2671283-MS URTeC Conference Paper (2017)
21. R.M. MacDonald, S.I. Geetan, D. Klemin, B. Hill, 2902911-MS URTeC Conference Paper (2018)
22. T.D. Scheibe, W.A. Perkins, M.C. Richmond, M.I. McKinley, P.D.J. Romero-Gomez, M. Oostrom, T.W. Wietsma, J.A. Serkowski, J.M. Zachara, Water Resour. Res., 51, 1023 (2015)
23. C. Soulaine, P.Creux, H.A. Tchelepi, Transp. Porous Med. **127**, 85 (2019)
24. O.Yu. Dinariev, J. Appl. Math. Mech. **69**, 213 (2005).
25. R.T. Armstrong, J.E. McClure, M.A. Berrill, M. Rücker, S. Schlüter, S. Berg, Phys. Rev. **E94**, 043113 (2016)
26. O.Yu. Dinariev, N.V. Evseev, Miner. Eng., **125**, 239 (2018)
27. K.R. Daly, T. Roose. Proc. R. Soc. **A 471**, 20140564 (2015)

# Uncertainty span for relative permeability and capillary pressure by varying wettability and spatiality flow directions utilizing pore scale modelling

*Thomas* Ramstad, *Anders* Kristoffersen, and *Einar* Ebeltoft

Equinor ASA, Norway

**Abstract.** Relative permeability and capillary pressure are key properties within special core analysis and provide crucial information for full field simulation models. These properties are traditionally obtained by multi-phase flow experiments, however pore scale modelling has during the last decade shown to add significant information as well as being less time-consuming to obtain.

Pore scale modelling has been performed by using the lattice-Boltzmann method directly on the digital rock models obtained by high resolution micro-CT images on end-trims available when plugs are prepared for traditional SCAL-experiments. These digital rock models map the pore-structure and are used for direct simulations of two-phase flow to relative permeability curves.

Various types of wettability conditions are introduced by a wettability map that opens for local variations of wettability on the pore space at the pore level. Focus have been to distribute realistic wettabilities representative for the Norwegian Continental Shelf which is experiencing weakly-wetting conditions and no strong preference neither to water nor oil. Spanning a realistic wettability-map and enabling flow in three directions, a large amount of relative permeability curves is obtained. The resulting relative permeabilities hence estimate the uncertainty of the obtained flow properties on a spatial but specific pore structure with varying, but realistic wettabilities.

The obtained relative permeability curves are compared with results obtained by traditional SCAL-analysis on similar core material from the Norwegian Continental Shelf. The results are also compared with the SCAL-model provided for full field simulations for the same field. The results from the pore scale simulations are within the uncertainty span of the SCAL models, mimic the traditional SCAL-experiments and shows that pore scale modelling can provide a time- and cost-effective tool to provide SCAL-models with uncertainties.

## 1 Introduction

Wettability is a key factor for multiphase flow behaviour in porous media in general, and for reservoir rocks especially. In the origin of the petroleum industry, clastic reservoir rocks where assumed to behave water-wet due to the water-wetting minerals composing the rock and pore surface. Since the 70'ties, several papers [see i.e 1,2] have questioned this assumption by adsorption of oil components on the pore surface due to braking the thin water-film established between the oil-phase and the rock surface [3]. It is now well acknowledged that the wettability of clastic reservoir rocks experiences weakly wetting behaviour and generally no strong preference to neither oil nor water.

Wettability can be determined and studied by different approaches [2-8]. The most common for the petroleum industry have been either measurements of contact angles, θ, and interfacial tension, σ/IFT, [4] or macroscopic experiments and measurements on core samples by the traditionally Amott/Amott-Harvey and USBM methods [9,10,11]. The benefit of the first approach is that the wetting preference is well defined, however the major – and crucial - drawback is that the measurements must be done on a flat surface with a geometry far from the geometry and shape of the pore structure in porous media. Macroscopic measurements are done on core samples exposed to real fluids at reservoir conditions, however the measurements are not regarded as well-suited to define the specific wettability where limited preferences to neither of the phases are experienced – which is the case for most clastic reservoir rocks. Even though the macroscopic approach has its limitation, it is the most used method by the industry due to its pragmatic approach and it provides reliable quality information of the wettability preference.

A huge amount of wettability definitions has been suggested during the years: mixed-wet, intermediate-wet, neutral-wet, weakly water-wet, weakly to strongly water-wet etc. Even though the origin of these definitions was intended to be well-defined, the pragmatic use of the terms is not. When providing SCAL-models for full-field applications, the methods and pragmatic understanding described in ref. [3-8] are generally applied. The core sample is generally cleaned, irreducible water saturation, $S_{wir}$, is established, the core sample is then saturated with reservoir oil at reservoir conditions – and subsequently aged for two to three weeks at irreducible water saturation. The core is then, by definition,

---

* Corresponding author: trams@equinor.com

restored to its original wetting conditions. This approach is well established, even though the distribution of the (irreducible) water-film is not known and the local wettability in the pore space, pore throats, body and pore necks are not known.

SCAL data for use in reservoir modelling are commonly obtained through core flooding experiments. Detailed information about wettability is distributed in the core sample, and how that influence the fluid distributions inside the pore space, is limited. Recent advances in X-ray CT technology have made non-destructive imaging of core material readily available in the petroleum industry. High resolution micro-computed tomography (micro-CT) enables both resolving the pore space to a high degree of accuracy and visualize the distribution of fluids at the pore level – before and after a flooding. Such technology provides a valuable tool for interpreting and augmenting SCAL data. Micro-CT images can in addition be segmented into pore scale models that can be used for flow simulations. To optimally utilize the results from this new imaging equipment, a digital workflow that combines experimental imaging with simulations directly on these images will be essential.

In this paper we combine the approach of using the well-defined wettabilities by contact angles and interfacial tension distributed on the porous structure of the rock surface obtained by micro-CT imaging and direct pore scale simulations.

Wettability maps are generated, where wettabilities can be varied for different parts of the pore structure and/or varied from sample to sample, experiencing identical pore structure. This will provide additional and important information how the various definitions of wettabilities influence the dynamic flow behaviour, i.e. relative permeability and capillary pressure.

## 2 Methods

In this section we present the background and techniques for the different steps in the workflow. Every step provides useful information, but ultimately, we wish to gain direct information about essential SCAL data like relative permeability and capillary pressure for different wettability and orientations.

The total workflow contains the following steps:

- Sample selection and preparation
- High resolution Micro-CT imaging
- Image segmentation
- Direct pore scale flow simulations in the segmented images

### 2.1 Samples and preparation

End trims from representative core material were selected as starting point for the workflow. The core material has been part of a SCAL program and comes from two different wells in the same formation on the Norwegian Continental Self (NCS).

The end-trims themselves are incomplete and otherwise not suited for flooding experiments. However, they can be imaged in micro-CT and thus provide pore scale images used for further modelling.

Examples of overview scans and sample selection area are shown in Figure 1. Coarse micro-CT were first done to evaluate the integrity of the material and find suited parts for sub-sampling. The samples were embedded in epoxy solution before further handling to avoid alterations in the pore space of loosely consolidated grains. After epoxy treatment, micro-plugs with diameter 5 mm were drilled for further imaging. Presently, no confining pressure can be applied which may affect the pore throats and measured permeability.

The plug preparation and scanning were carried out by a FEI HeliScan® micro-CT instrument.

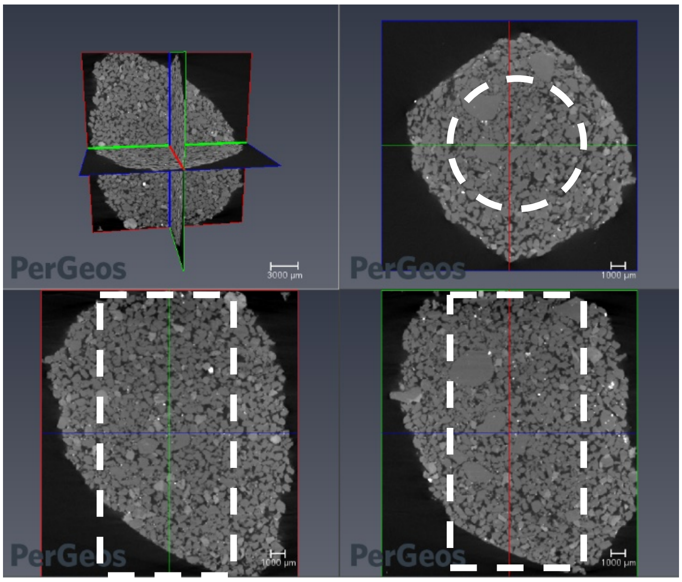

**Fig. 1** Overview micro-CT scan of an end-trim sample. The micro-plug selection is marked.

### 2.2 MCT, segmentation and downsampling

The 5 mm samples were scanned at a photon energy of 100 kV and the resolution was 4.2 µm/pixel.

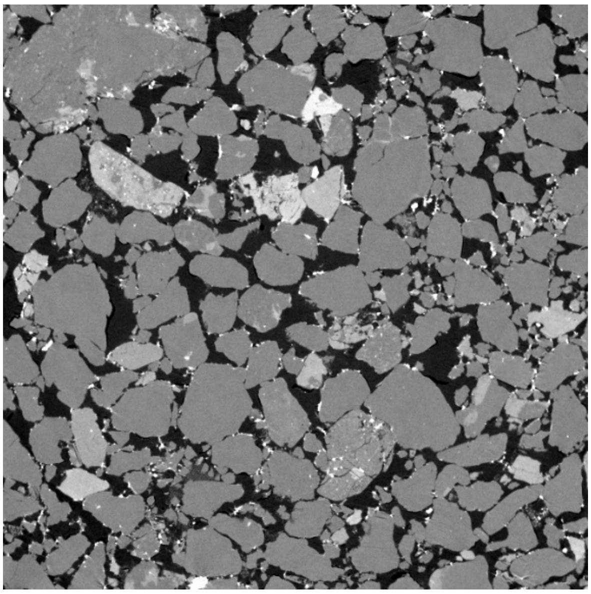

**Fig. 2** High resolution micro-CT scan of an end-trim sample.

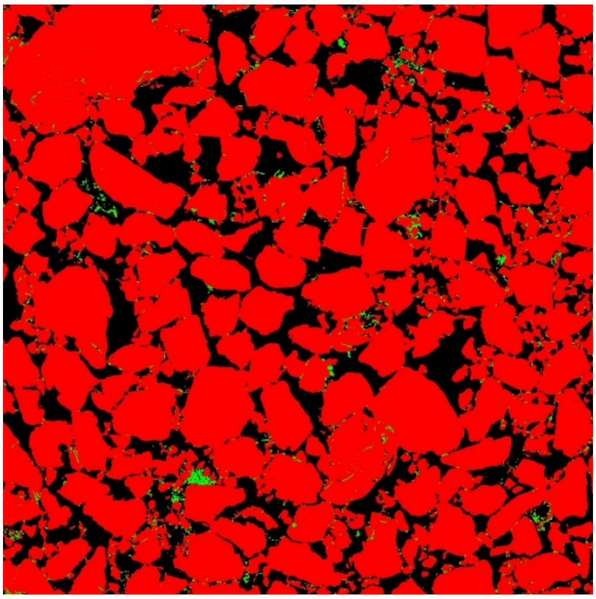

**Fig. 3** The image in **Fig. 2** segmented into a solid phase (red), pore phase (black) and a sub-resolution porosity phase, which mainly corresponds to clay (green).

The segmentation was performed in the Avizo® software, using a marker-controlled watershed algorithm. An example of a raw image and the corresponding label image is shown in Fig. *2* and Fig. *3*, respectively. The image is segmented into three phases (solid, pore and sub-resolution porosity). The lattice-Boltzmann algorithm inputs a binary map (solid/pore). Therefore, the sub-resolution porosity was assigned to the solid phase. The reason is that the sub-resolution porosity is clay, and we do not expect clay-bound water to contribute to the flow. It should also be noted that the clay content was small in all of the examined samples as can be seen in Fig. *3*.

Lattice Boltzmann modelling is computationally intensive, and it is crucial to limit the size of the grid. Therefore, it was decided to downsample the images prior to the flow simulations. By downsampling to a coarser resolution, it is possible to model a larger physical section of the plug, thus coming closer to a representative elementary volume. Figure 4 shows a slice at the original resolution and one that is downsampled. Visually, there seems to be no significant loss of information. To verify this, the relative permeabilities were calculated on the same physical sample at three different resolutions; 7 µm, 10 µm and 15 µm (data not shown). Indeed, the results were equal. It was therefore concluded that the downsampling approach was justified. The length dimensions of the samples are listed in Table 1.

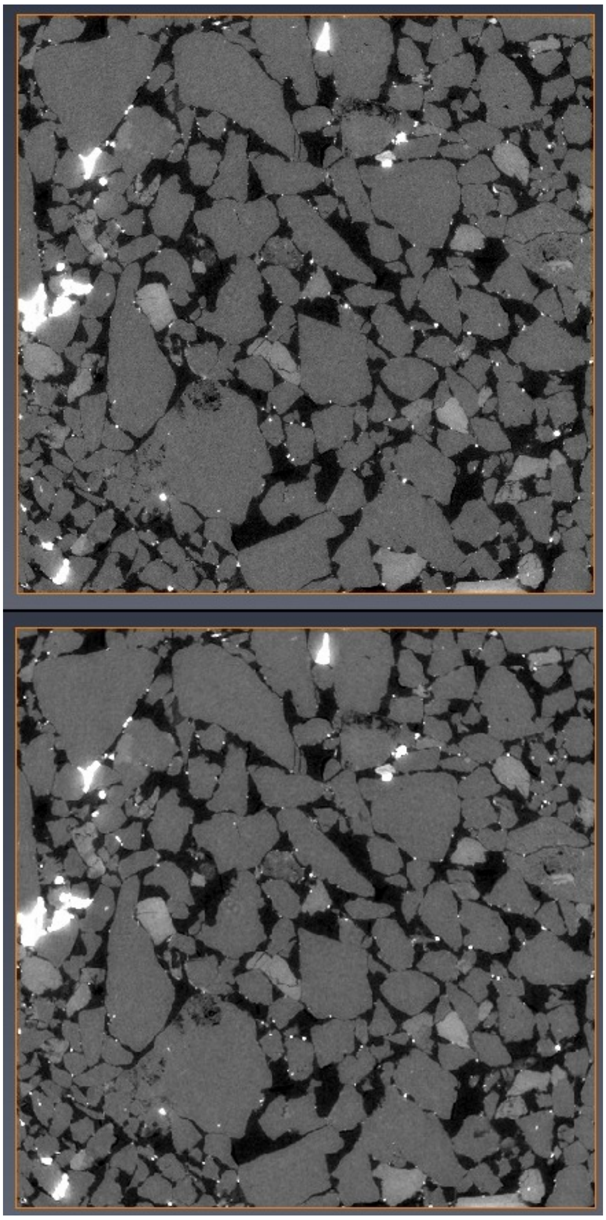

**Fig. 4.** An image slice at the original resolution of 4.2 µm (top) and the corresponding slice downsampled to a resolution of 15 µm (bottom).

## 2.3 Direct pore scale simulations

Multiphase flow is simulated directly on the segmented images from the micro-CT scans. We use a multiphase lattice Boltzmann method (LBSIM) for this purpose, and the simulations perform the basis for the SCAL results produced.

The lattice Boltzmann method is a kinetic approach to fluid dynamics and is well documented in the literature [16]. The method is well suited for simulating multiphase flow in complex geometries and fluid interfaces that are the cases for flow in porous media. From such simulations it is possible to obtain capillary pressure and relative permeability that can be compared to different experimental set-ups.

For the multiphase simulations presented in this paper we use the following set-up:

1. Irreducible water saturation is established through primary drainage simulations
2. Wettability in the model is established either as a uniform wettability or through a local wettability distribution on the pore space, i.e. wettability map
3. Water flooding capillary pressure curves are obtained through forced imbibition
4. Relative permeability points are generated from a steady-state set-up. The results are then analysed using the software Sendra® [12] with the end-point obtained from the capillary pressure simulations.

The different steps of the workflow can be repeated with different conditions, and the simulations thus provide a fast tool for sensitivity testing, such as wettability and spatial flow direction.

The forced imbibition capillary pressure simulations are done by injecting water with a fixed pressure drop over the model. When the water saturation has converged, the capillary pressure is recorded, and the applied pressure drop increased. This way we obtain the capillary pressure curve and the end-point residual saturations.

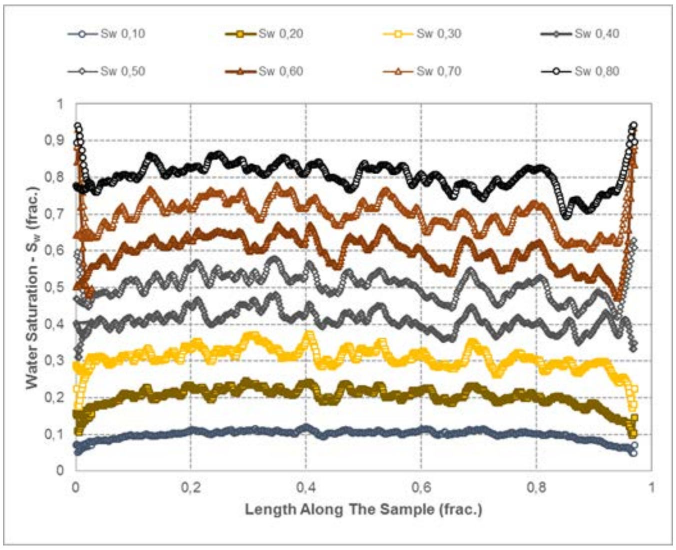

**Fig. 5.** Water saturation profile at steady state in the simulations.

The steady state relative permeability curves are done with periodic boundary conditions to minimize end-effects. When the effective permeability of each phase has converged, the saturation is changed to preserve the fluid distribution history. This is done to model the proper effect of steady state water flooding with increasing water saturation.

As shown in Fig. ***5***, the saturation distribution in the sample is close to uniform, and end-effects are relatively small despite the limited physical size of the sample.

Steady state effective permeability values are normalized with the initial oil effective permeability at irreducible water saturations to get relative permeability. The steady state set-up is suited for obtaining the relative permeability in the mid saturation region. However, it suffers from resolution limitations closer to low end-point values. To compensate for this, a curve fit is done combining steady state points with residual points from the capillary pressure simulations.

## 2.4 Wettability distribution

One of the main aims of this study is to investigate the effects of wettability and to clarify some of the concepts related to wettability distribution. With the use of rock images and modelling, we can set the wettability locally on the grains and investigate the resulting fluid distributions.

In LBSIM the wettability is defined through a scalar affinity value that controls the local wettability. The local affinity values range from 1.0 to -1.0. On a plain surface, this correlation can be translated into a contact angle between the fluid and solid pore walls. However, for complex and rugged grain surface it is difficult to define unique contact angle. Hence, it is common to refer a local wettability of 1.0 to strongly water wet (WW) while a value of -1.0 relates to strongly oil wet (OW). In terms of global wettability for the sample, there are two ways of setting that in the simulations, which we refer to as: Uniform wettability and non-uniform wettability.

For a uniform wettability the local wetting parameter is constant throughout the sample. This is indeed a special case, as there are many local effects that can alter wettability, like e.g. fluid composition and mineralogy. However, a uniform wettability can be justified in cases of a clear wettability trend in the entire sample like strongly WW or strongly OW.

A more sophisticated way of handling the wettability is by distribution of the local wettability parameters in the pore space. Such a control of the local wettability opens for a more in-depth treatment of wettability effects in a setting of non-uniform wettability.

There are many ways to define the wettability in the samples, but in this study, the local wettability parameters are limited to a static binary wettability map as shown in Fig. ***6***.

The wettability maps consist of two affinity parameters: OW and WW, and they only apply to the fluid grid voxels that border to solid. The OW and WW are distributed according to the fluid distribution at initial water saturation, $S_{wi}$. Grid voxels where the oil is in contact with the grain is set to OW while the WW is applied elsewhere.

We chose to set the WW parameter to WW = 1.0 while the OW will vary from 1.0 to -1.0. This to mimic an aging process. Changing wettability though an aging is a slow process that usually takes weeks. Hence, the values of OW and WW are kept static and do not change throughout a simulation.

A resulting fluid distribution is shown in Figure 7. We can observe the curvature of droplets and the contact with grains. This is further magnified in Figure 9 and Figure 10. Such fluid distributions can again be compared directly to micro-CT images of flooding experiments (see e.g. ref [19]).

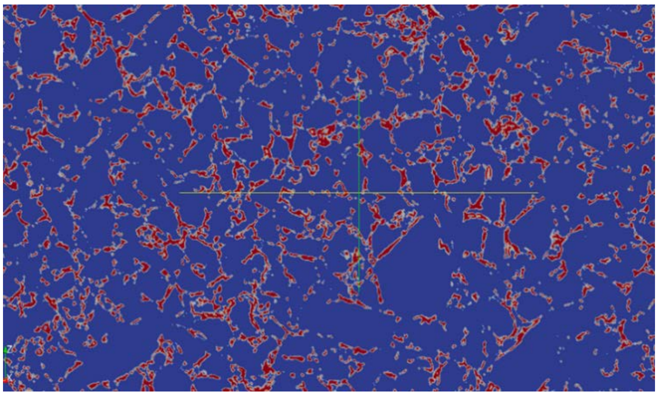

**Fig. 6** Binary wettability map where red denotes OW index and blue is WW index. Only voxels that border to solid grains will be affected by the wettability index.

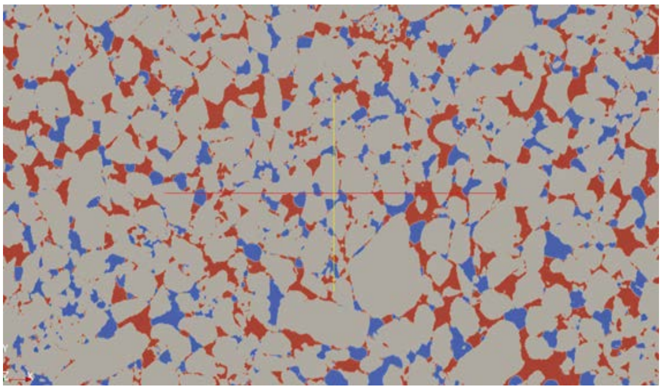

**Fig. 7.** A resulting fluid distribution from the wettability map in Fig. **6**. The water saturation is $S_w = 0.5$. Water is blue and oil is red.

## 3 Results

This section provides the results obtained by combining Micro-CT images, spatially pore scale simulations combined with wettability distribution within the porous structure.

### 3.1 Models and Set-up

We have used the workflow and tools listed in Section 2 to build pore scale models and run two-phase direct flow simulations with LBSIM. The dimensions and properties of the models are listed in Table 1:

**Table 1**. Basic properties of the digital models

| Sample | A | B | C |
|---|---|---|---|
| Size [voxels] | 485 x 485 x 1085 | 485 x 485 x 878 | 485 x 485 x 878 |
| Resolution [microns] | 15 | 15 | 15 |

Dynamic SCAL-experiments utilizing either the steady state- or the unsteady state techniques are generally exposed to capillary end-effects and are not well suited to provide estimates of the residual oil saturation, $S_{orw}$. A common approach is to combine such flow experiments with comparable centrifuge or porous plate techniques which are well suited to provide estimates of residual saturations [13]. This behaviour is also experienced for steady state pore scale modelling on digital images. Hence, it tends to be unsuited for determination of very low relative permeabilities close to residual saturations, $S_{wir}$ and $S_{orw}$, both because of low fractional flow and limited resolution. The steady state dynamic simulations are here done at typical capillary numbers of Ca = $10^{-5}$.

Pore network analogues can reduce some of the problems related to limited resolutions, but these come at the cost of simplifying the pore scale micro structure and reducing dynamic effects for low capillary numbers [18].

Similar approach as for traditional SCAL-experiments have been utilized in the simulations. Capillary pressure with the coherent saturation end-points are determined prior to determination of the relative permeabilities. These latter simulations are performed with steady state conditions and anchored in the saturation end-points, $S_{orw}$, determined from the capillary pressure simulations.

When the pore scale models are built, it is straight forward to change input parameters related to wettability and sample orientation and re-run simulations from the same starting point, i.e. the configuration after primary drainage. With the data points obtained from capillary pressure and relative permeability simulations, we have used the software Sendra® for further curve fitting.

The simulations have been done on end-trims from core material defining the SCAL-model used for full-field simulations. The obtained curved are then compared to relevant field SCAL model with uncertainty bands [20].

From the samples listed in Table 1 with sensitivity on wettability and orientation for each sample, we obtain a total of 54 relative permeability curves and 9 capillary pressure curves. These are used to in-depth analyse the impact by wettability on SCAL data and the associated uncertainty in interpretation of SCAL data.

### 3.2 Capillary pressure and end-points

All capillary pressure data points from the simulations are obtained through a forced imbibition set up. The pressure drop over the model is fixed, and when the time dependent saturation profile has converged, both the resulting saturation and pressure are recorded.

Figure 8 shows the capillary pressure points determined by pore scale modelling and subsequently curve fitted by the LET-correlation for capillary pressure [14]. This provide guidelines for where to anchor residual oil saturation, $S_{orw}$, for the relative permeabilities shown in the next section. In addition, the capillary pressure curves are also determined.

The forced imbibition simulations were done with uniform wettability distribution in the intermediate wet range. From the curves, there is a relatively long range of water saturations with negative Pc values.

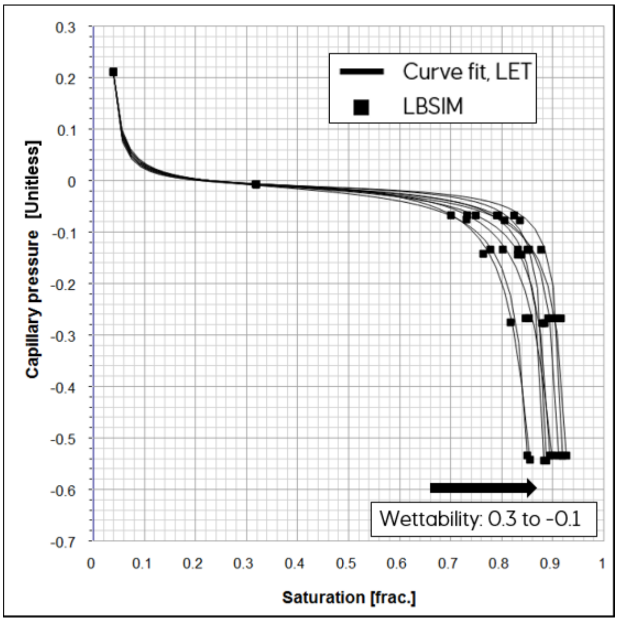

**Fig. 8** Capillary pressure curves for all samples with different wettabilities on the intermediate wet range. The end-points are listed in Table 2.

The residual oil saturation, $S_{orw}$, experiences reliable values for $S_{orw} \in [0.06 – 0.15]$ and are listed in Table 2. These end-points are used in further interpretation of steady state relative permeability curves.

**Table 2**. End-point saturations from the capillary pressure curves.

| Sample | A | B | C |
|---|---|---|---|
| $S_{wir}$ | 0.04 | 0.04 | 0.04 |
| $S_{orw}$, OW = -0.5 | 0,088 | 0,105 | 0,149 |
| $S_{orw}$, OW = 0.3 | 0,080 | 0,073 | 0,101 |
| $S_{orw}$, OW = 0.5 | 0,112 | 0,116 | 0,144 |

### 3.3 Relative permeabilities

Relative permeabilities are obtained by pore scale simulations (LBSIM) with steady state flow conditions.

Each of these samples utilized different wettabilities, and simulations have been done for three spatial directions

A total of six different wettabilities have been used, three cases of uniform wettability and three cases of non-uniform wettability where a binary wettability maps, as described in section 2.4, have been applied. For the uniform wettability cases, the local wettability constant takes the values 0.3, 0.1 and -0.2 giving intermediate global wettabilities. These correspond to the capillary pressure curves shown in Figure 8.

In the cases of the non-uniform wettability the parameter WW (see Section 2.4) has been defined to strictly 1.0 and the OW parameter takes the values 0.5, 0.3 and -0.5. The wettability maps are generated from the $S_{wir}$ distributions, and hence the WW only applies to small pores and corners in pore bodies.

With the OW index taking the value -0.5, the resulting fluid distribution can be observed in detail Figure 10. A wetting configuration that is more towards a global oil wet condition is observed, and water droplets forming on the grain walls are observed.

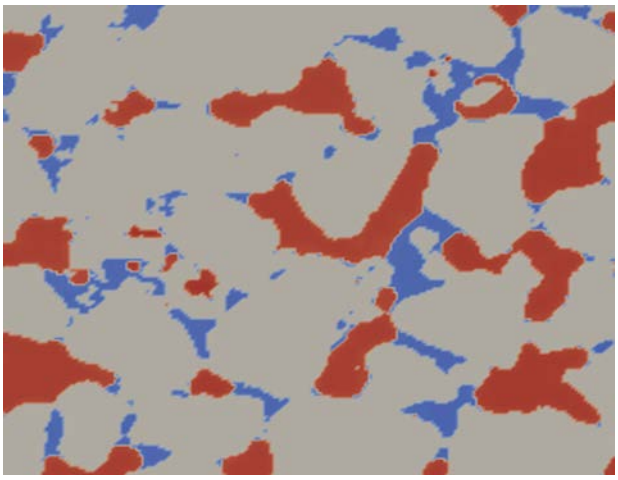

**Fig. 9** Different fluid distributions from non-uniform wettability OW = 0.5

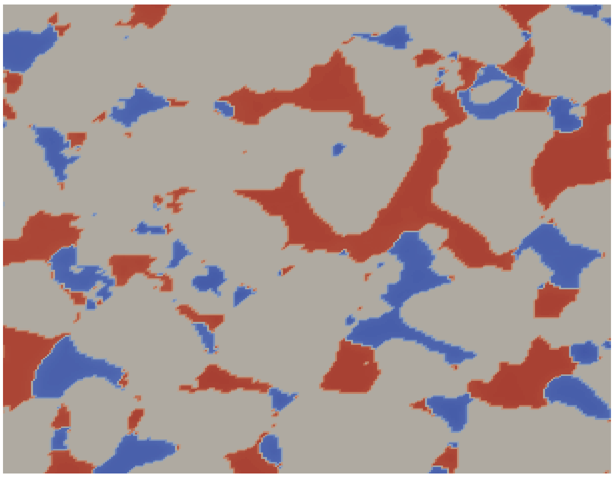

**Fig. 10** Different fluid distributions from non-uniform wettability OW = -0.5

With OW = 0.5, the oil resides on the pore bodies as droplets formed by the water wet films and corners, but there is not a large curvature for the interfaces between water and oil in large pores (Figure 9).

These two wettability settings have been compared to the SCAL models in Figure 11 and

Figure 12. All relative permeabilities obtained by LBSIM have been curve fitted by the LET-correlation for relative permeability [15]. The observation is that the uniform wettability case produces more symmetric relative permeability curves and the relative permeability of water ($K_{rw}$) is consistently higher than the SCAL model close to residual oil saturation, see Figure 11. For the non-uniform wet cases the bundle for curves stay within the uncertainty of the SCAL model, $K_{rw}(S_{wir})$ is lower than for the uniform wettability case, albeit on the pessimistic side of the SCAL model, see Figure 12.

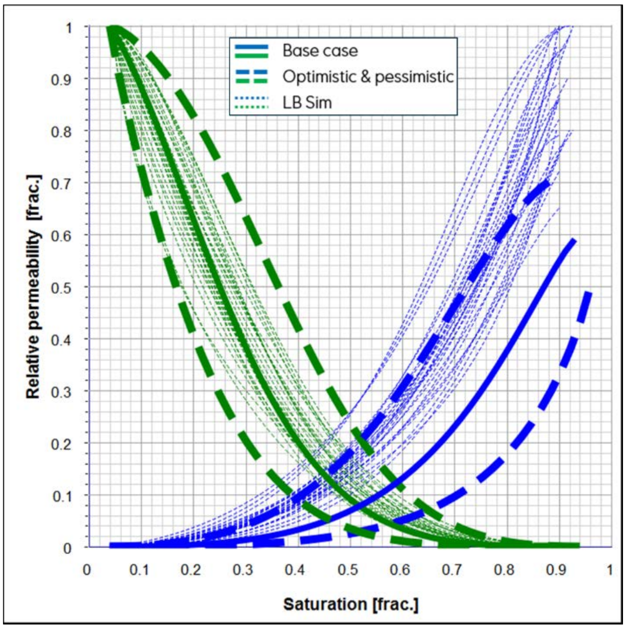

**Fig. 11** All relative permeability for curves for the uniform wet cases.

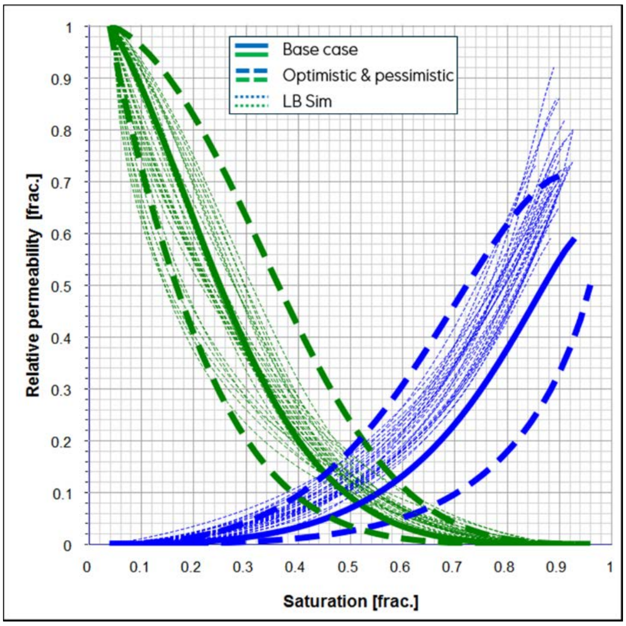

**Fig. 12** All relative permeability for curves for the non-uniform wet cases.

In the following we will focus on the sensitivity to wettability using the approach of wettability maps with non-uniform wettability. All results from pore scale modelling non-uniform wet conditions are within the provided uncertainty span for the SCAL-model, even though it can be argued that the water relative permeabilities and oil relative permeabilities are on the pessimistic and optimistic side, respectively. This observation is similar to the results for the comparison to steady state experiments from one individual core - Figure 13 and Figure 14 - and is considered for further work when defining the wettabilitiy maps.

As for the individual interpretation the results are within the expected uncertainty for SCAL-experiments and multi-phase flow behaviour in general. The steady state experiments were performed with the following fraction flow of water, $f_w$ = 0.008; 0.06; 0.22; 0.5; 0.78; 0.94; 0.992; 1.

The relative permeablity curves tend to be overestimated for low values - toward the residuals - compared to the experimental results. This is due to limited resolution and finite-size effects in the models and fluid dynamics.

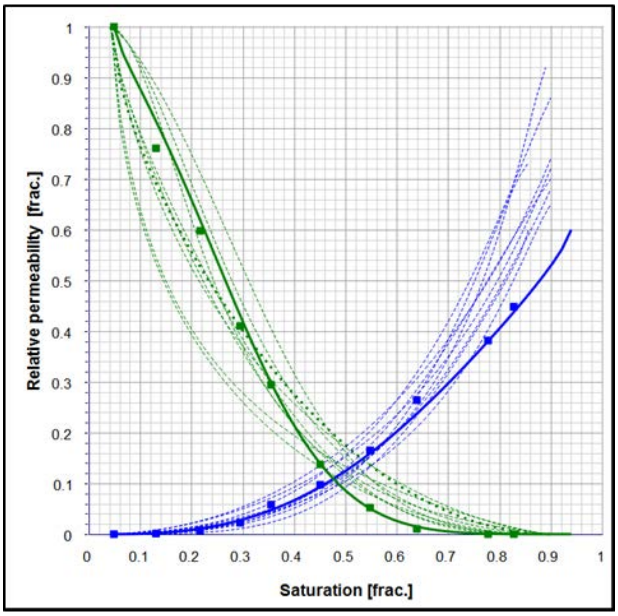

**Fig. 13** Experimental steady state relative permeability curves compared to different non-uniform wet conditions and orientations, lin-lin.

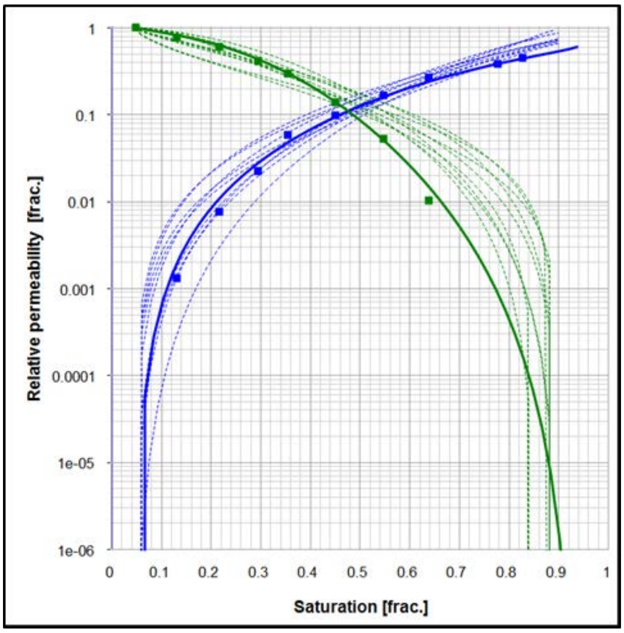

**Fig. 14** Experimental steady state relative permeability curves compared to different non-uniform wet conditions and orientations, semilog.

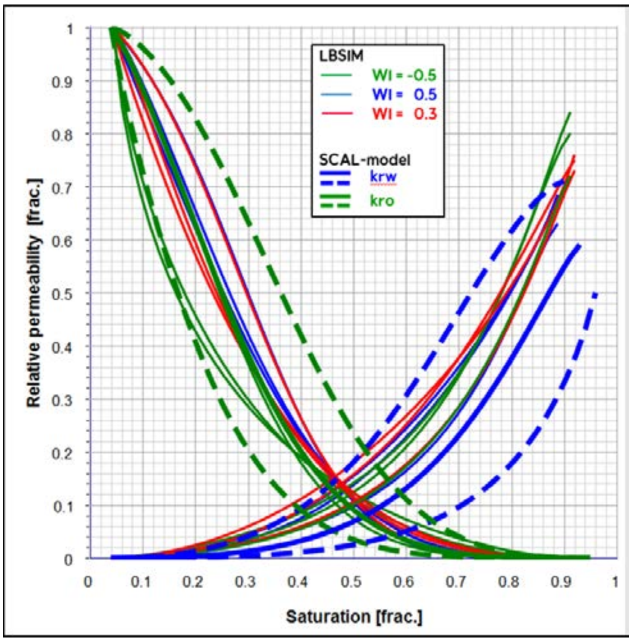

**Fig. 15** Wettability sensitivity in relative permeability for Sample A. The data are compared to the SCAL model with uncertainty span (bold lines).

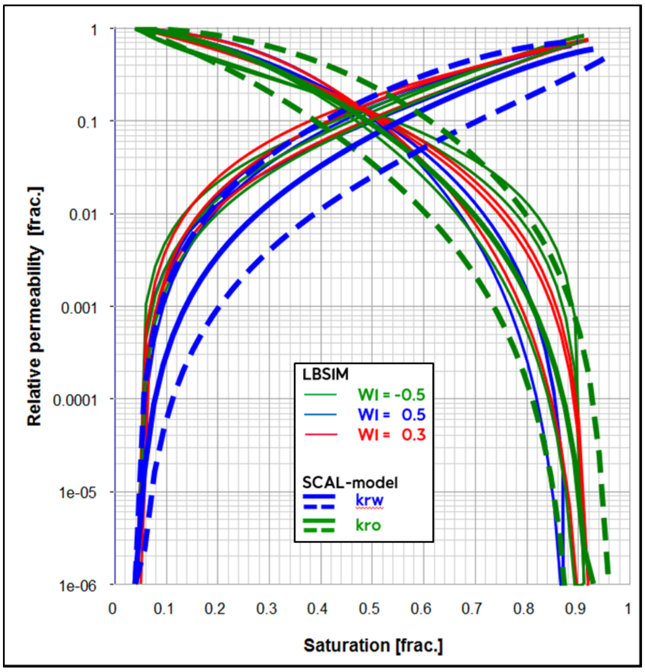

**Fig. 16** Wettability sensitivity in relative permeability for Sample A. The data are compared to the SCAL model with uncertainty span (bold lines).

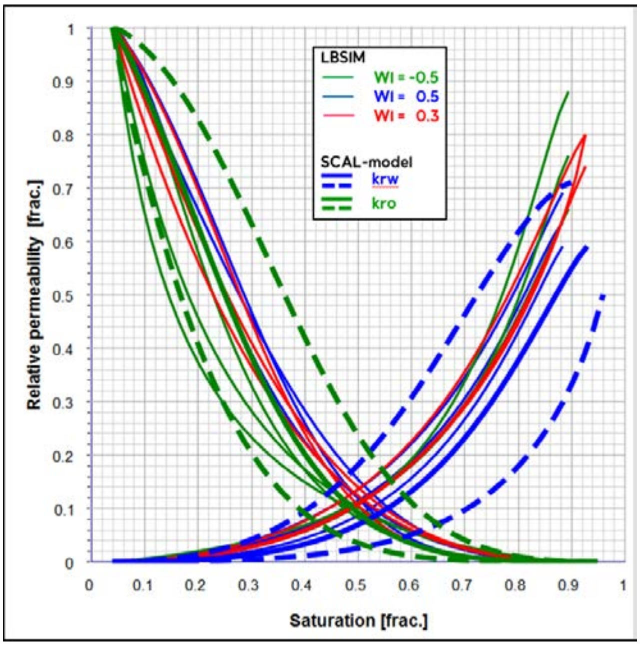

**Fig. 17** Wettability sensitivity in relative permeability for Sample B. The data are compared to the SCAL model with uncertainty span (bold lines).

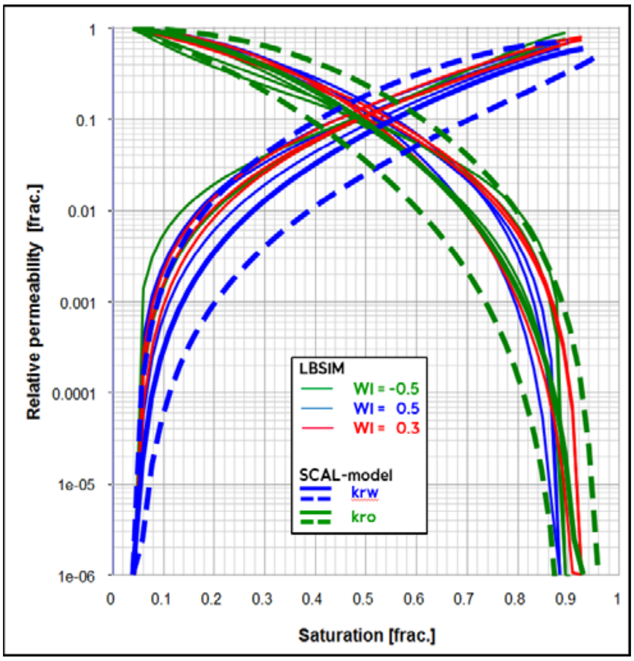

**Fig. 18** Wettability sensitivity in relative permeability for Sample B. The data are compared to the SCAL model with uncertainty span (bold lines).

In terms of analysis of uncertainty on relative permeability measurements that owe to wettability, we have plotted the results for each sample in Fig. **16** to Figure 20. The results are differentiated on sample with three different non-uniform wetting conditions. The samples are homogeneous and isotropic. Hence, the

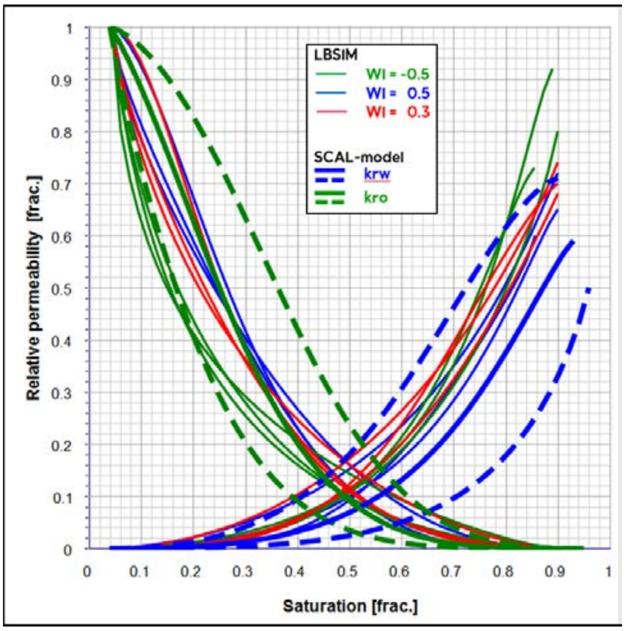

**Fig. 19** Wettability sensitivity in relative permeability for Sample C. The data are compared to the SCAL model with uncertainty span (bold lines).

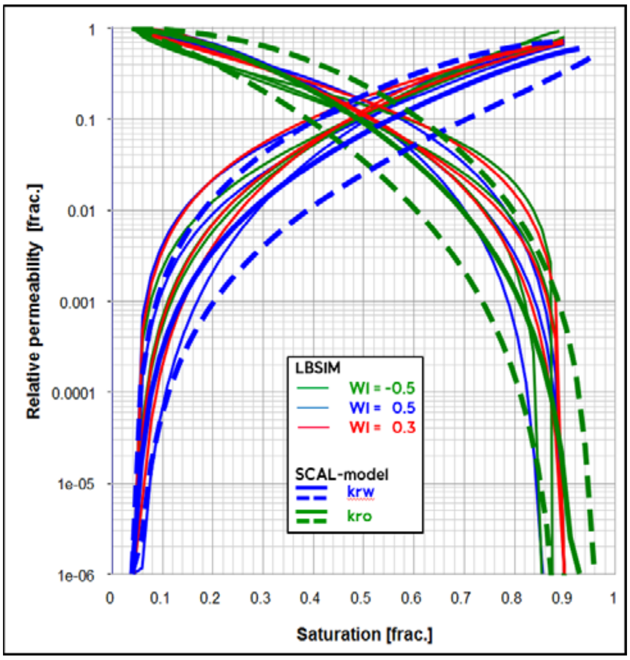

**Fig. 20** Wettability sensitivity in relative permeability for Sample C. The data are compared to the SCAL model with uncertainty span (bold lines).

results from orientation should not be systematically different although we expect a certain degree of spreading in the results. Also, the SCAL models with uncertainty span should apply to all samples.

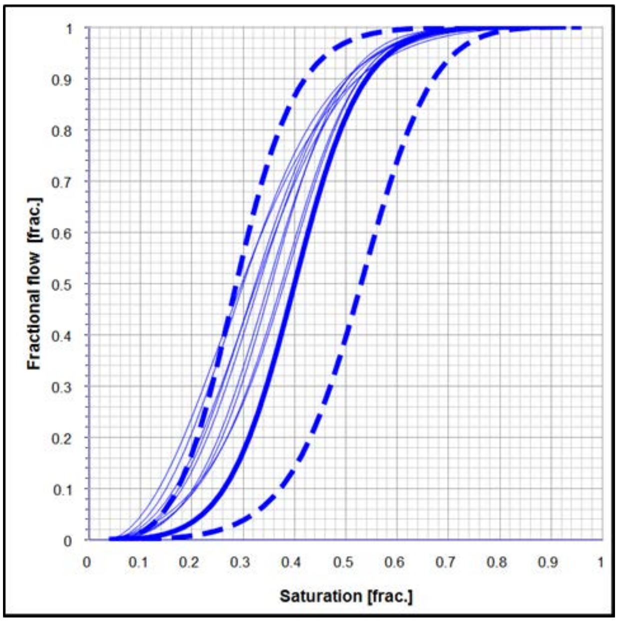

**Fig. 21** Fractional flow curves for all non-uniform wettability cases Sample A.

However, we expect to see a certain trend in relative permeability owing to different wettability. With wettability towards more oil wet, the curves tend to be more pessimistic. As the wettability tends more towards the neutral wet regime, the curves are more in agreement with the SCAL model also for the end-points.

Fraction flow curves for all samples are shown in Figure 21 to Figure 23. Most curves fall within the uncertainty span of the SCAL model, but towards more mobile water.

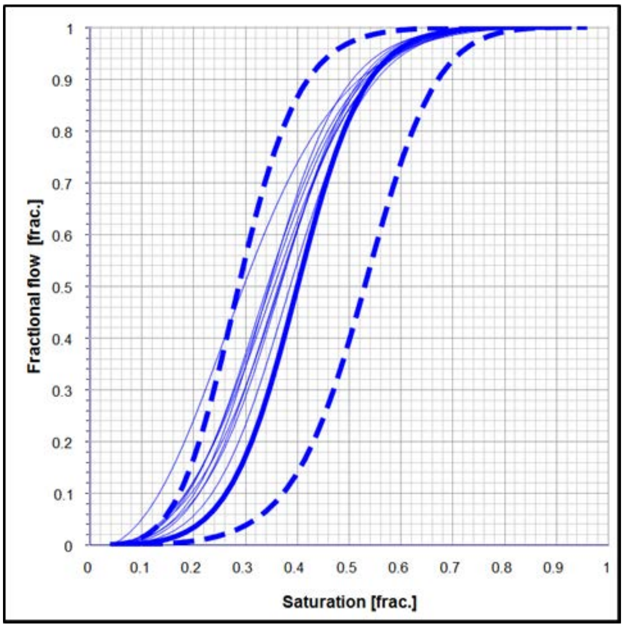

**Fig. 22** Fractional flow curves for all non-uniform wettability cases Sample B.

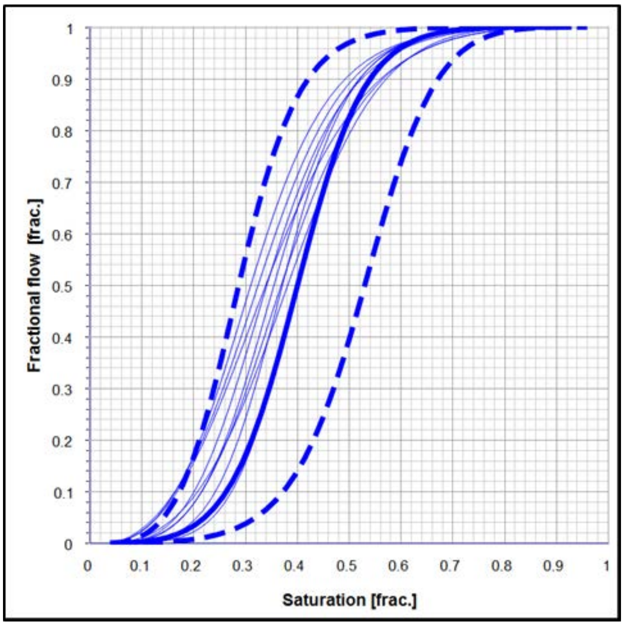

**Fig. 23** Fractional flow curves for all non-uniform wettability cases Sample C.

## 4 Discussion

Pore scale simulations of the individual sample maps the steady state experiment reasonably. It also provides an estimate of the uncertainty span due to spatial- and wettability variations as shown in Figure 11 and Figure 12. Even though we have compared with the steady state experiment, it is not - a priori - expected that the results should map each other perfectly. The core samples used for the composite core in the steady state experiments have undergone the common "recommended practice" preparation prior to experimentation – restored state, $S_{wir}$ establishment and aging with live oil. There is no guarantee that this procedure provides the "correct" wettability-state of the core sample prior and during the flow experiment.

The relative permeability to oil and water are slightly over-estimated toward residual oil saturation, $S_{orw}$, interpreting the water relative permeability, $k_{rw}$, slightly too pessimistic and the oil relative permeability, $k_{ro}$, slightly too optimistic compared to the steady state experiment. However, this is within the expected uncertainty for SCAL-experiments and multi-phase flow behaviour in general.

It needs to be emphasized, that the digital models are restrained by the resolution of the micro-CT images. Low relative permeability values close to the saturation end-points and residuals tend to be over-estimated. It is a general short-coming of direct simulation techniques to handle very low fractional flows. There will be a certain amount of finite size effects linked to fluid-fluid interfaces and fluid-solid interactions. In general, these will lead to noise and small-scale currents that contribute relatively stronger to small fractional flow rates. Nevertheless, steady state set-ups are in general not the best candidate for end-point estimations and a combination with additional centrifuge experiments/set-up is advised.

With a detailed mapping of local wettability, we can reproduce expected trends, but also categorize properties on the pore space that are considered "Black Box" in ordinary core flooding experiments. More sophisticated wettability maps should preferably be considered for further work. A wettability map that distribute various in-situ contact angels throughout a mixed-wet pore structure with local varieties depending upon pore-shapes [19]. Further the traditional classifications of wettability - intermediate-wet, neutral-wet, weakly water-wet, weakly to strongly water-wet etc. - can be distributed by defining in-situ contact angels and interfacial tensions to further study variations of realistic wettabilities where none of the fluids have strong wetting preferences.

## 5 Conclusion

In this paper the following conclusions are drawn:

- LBSIM combined with wettability mapping and spatial directions provides reliable uncertainty span for the relative permeability curves.

- LBSIM and wettability mapping has the potential to provide basic understanding of mechanisms that influence the flow behaviour.

- Non-uniform wettability defined from irreducible oil distribution leaves corners and small pores water wet. Such wettability distribution lowered the water relative permeability curves compared to a uniform wettability distribution. A non-uniform wettability distribution is considered a more realistic scheme.

- Uniform wettability with a weak overall wetting preference produces almost symmetric oil and water relative permeability curves and thus a more pessimistic case compared to SCAL models.

- For a fruitful and possible concluding approach, we need to properly define contact angle and interfacial tension for wettabilities.

## References

1. Morrow, N.R. (editor): "Interfacial phenomena in petroleum recovery", 1991, Marcel Dekker Inc., New York.
2. Radke, C.J., Kovscek, A.R. and Wong, H.: "A Pore-Level Scenario for the Development of Mixed Wettability on Oil Reservoirs", SPE 24880, presented at the 67th Annual Technical Conference and Exhibition of the Society of Petroleum Engineers, Washington. DC, October 4-7, 1992.
3. Anderson, W.G.: "Wettability Literature Survey – Part 1; Rock/Oil/Brine Interactions, and the Effects of Core Handling on Wettability" JPT (Oct. 1986), 1125-44.
4. Anderson, W.G.: "Wettability Literature Survey – Part 2; Wettability Measurements" JPT (Nov. 1986), 1246-62.
5. Anderson, W.G.: "Wettability Literature Survey – Part 3; The Effects of Wettability on the Electric Properties in Porous Media" JPT (Dec. 1986), 1371-78.
6. Anderson, W.G.: "Wettability Literature Survey – Part 4; The Effects of Wettability on Capillary Pressure" JPT (Oct. 1987), 1283-1300.
7. Anderson, W.G.: "Wettability Literature Survey – Part 5; The Effects of Wettability on Relative permeability" JPT (Nov. 1987), 1453-68.
8. Anderson, W.G.: "Wettability Literature Survey – Part 6; The Effects of Wettability on Waterflooding" JPT (Dec. 1987), 1605-22.
9. Amott, E.: "Observations Relating to the Wettability of Porous Rock", Trans., AIME (1959) **216**, 156-62.
10. Boneau DF and Clampitt RL: "A Surfactant System for the Oil-Wet Sandstone of the North Burbank Unit" Journal of Petroleum Technology 29, no. 5 (May 1977): 501–506.
11. Donaldson EC, Thomas RD and Lorenz PB: "Wettability Determination and Its Effect on Recovery Efficiency" SPE Journal 9 (March 1969): 13–20.
12. Sendra User guide 2018.5, ProRes AS, 2019.
13. Sylte, A., Ebeltoft, E. and Petersen, E.B.: "Simultaneous Determination of Relative Permeability and Capillary Pressure Using Data from Several Experiments". Paper SCA 2004-08 presented at the International Symposium of the Society of Core Analysts, Abu Dhabi, UAE, 5-9 October 2004.
14. Lomeland, F., and Ebeltoft, E.: "A New Versatile Capillary Pressure Correlation". Paper SCA 2008-08 presented at the International Symposium of the Society of Core Analysts, Abu Dhabi, UAE, 29 October – 2 November 2008.
15. Lomeland, F., Ebeltoft, E., and Thomas, W.H.: "A New Versatile Relative Permeability Correlation". Paper SCA 2005-32 presented at the International Symposium of the Society of Core Analysts, Toronto, Canada, 21-25 August 2005.
16. T. Ramstad, I. Nasiru, C. Nardi, P. E. Øren, "Relative permeability calculations from two-phase flow simulations directly on digital images of porous rocks", Transport in Porous Media **94**, 487 - 504 (2012)
17. Lopez, O., Mock, A., Skretting, J., Pedersen EB., Øren, P., Rustad, AB., "Investigation into the Reliability of Predictive Pore-Scale Modeling for Siliciclastic Reservoir Rocks", Proceedings of the 2010 International Symposium of Core Analysts, SCA2010-23 (2010)
18. Ruspini, LC., Farokhpoor, R., Øren, P., "Pore-scale modeling of capillary trapping in water-wet porous media: A new cooperative pore-body filling model". Adv. Water Resources, (2017), **108**, 1-14.
19. Lin, Q, Bijeljic, B., Krevor, S.C., Blunt, M. J., Berg, S., Coorn, A., van der Linde, H., Georgiadis, A., Wilson, O.B.: "A New Waterflood Initialization Protocol for Pore-Scale Multiphase Flow Experiments". Paper SCA 2018-32 presented at the International Symposium of the Society of Core Analysts, Trondheim, Norway, 27-30 August 2018.
20. Ebeltoft, E., Lomeland, F., Brautast, A., Haugen, Å.: "Parameter Based SCAL - Analysing Relative Permeability for Full Field Application", reviewed Proceedings of the 2014 International Symposium of the SCA, Avignon, France, September 8-11, 2014.

# Permeability alteration by salt precipitation: numerical and experimental investigation using X-Ray Radiography

*Olivier* Lopez[2], *Souhail* Youssef[1], *Audrey* Estublier[1], *Jostein* Alvestad[2], *Christin* Weierholt Strandli[2]

[1]IFP Energies Nouvelles, Rueil-Malmaison France
[2]Equinor, Trondheim, Norway

**Abstract.** The injection of a gas phase through a water saturated porous medium can reduce the water saturation not only by displacement mechanisms but also by evaporation mechanisms. In the presence of brine, this process can induce salt crystallization and precipitation within the porous medium with a risk of permeability alteration. In the field of gas production and storage, the occurrence of such a phenomenon can have detrimental consequence on the well productivity or injectivity. In this work, we investigated experimentally and numerically the effect of dry gas injection on salt precipitation and permeability impairment. State of the art equipment designed for high throughput coreflood experimentation was used to capture the dynamic of salt migration using X-Ray radiography. A set of experiments have been conducted on a sample of Bentheimer sandstone (10mm in diameter and 20 mm in length) as well as a two layers composite sample with a significant permeability contrast. Experiments were conducted using Nitrogen and KBr brine with different boundary conditions (i.e. with and without capillary contact). Results showed that salt precipitation results from the interplay of different parameters, namely pressure gradient, brine salinity, capillary forces and vapor partial pressure. Experimental observations indicate that in the case of dry gas injection, salt systematically precipitates but permeability alteration is observed only if a capillary contact is maintained with the brine. We built a 2D flow model integrating two-phase Darcy flow, capillary forces, salt effect on vapor partial pressure, dissolved salt transport, as well as the different PVT equilibria needed to describe properly the systems. Once calibrated, the model showed good predictability of lab scale experiment and thus can be used for parametrical study and upscaled to the well bore scale.

## 1. Introduction

In the field of natural gas production as well as gas storage in aquifer, salt deposition is considered as a potential risk for gas wells. In Northern Germany, field evidences of mainly halite precipitation have been reported during gas production [1]. A synthetic review of gas well productivity impairment by salt plugging can be found in [2]. Injection of a gas phase through a water saturated porous medium can reduce the water saturation not only by displacement mechanisms but also by evaporation mechanisms. To understand the phenomena of drying induced by gas production, Mahadevan *et al.* [3] did an extensive experimental and theoretical study to show that injection of vapor saturated gas (i.e., humid gas) in a rock sample can induce drying [3-4]. The origin of the drying is that the water mole fraction in the gas phase at equilibrium depends on pressure. In the context of gas storage in aquifer, experiments have been conducted by [5-6] where dry gas was injected in brine saturated sandstone samples with different salt concentrations in the brine. They showed that the drying rate is proportional to the gas velocity and that any dissolved salt in the water can be transported by capillary flows induced by drying and can even accumulate near the injection surface. The permeability can then be reduced by pore clogging. They conclude that all these mechanisms must be included in models to calculate the near wellbore permeability and porosity changes with time, to correctly determine well injectivity.

A first attempt to model the drying process in a porous media at the laboratory scale was proposed by Mahadevan *et al.* [4]. The authors considered two different models, one to model the first stage of the immiscible displacement, and another during the evaporation regime. The first part is described by a standard two-phase Darcy model. The second accounts for compressibility-driven drying and capillarity effects. The two models were not coupled. The evaporation model was then extended in [7] to consider the impact of capillary-driven liquid film flow on the evaporation rates as well as the rate of transport of salt through those films. TOUGH2 family of reservoir simulators was also used by [8-9] to simulate two-phase flow of a gas mixture in equilibrium with a sodium chloride brine, including the modeling of halite precipitation/dissolution. The simulations were conducted for near well bore model in the context of $CO_2$ injection at laboratory scale.

In this study, we present a comprehensive experimental investigation of the effect of gas flow in a

---

[*] Corresponding author: ollop@equinor.com

sandstone sample initially saturated with water or brine. A set of experiments have been conducted on a Bentheimer sandstone sample (10mm in diameter and 20 mm in length) as well as on a two layers composite sample of different permeability (high and low) with the aim of investigating the effect of salt precipitation on permeability impairment at different boundary conditions. Experiments were then simulated using an in-house advanced compositional model (CooresFlow).

## 2. Materials and methods

### 2.1. Experimental set-up

The experimental set-up used in this study is shown in **Fig. 1**. Nitrogen was injected at a constant pressure using a downstream pressure regulator. Its flow rate was monitored by a Coriolis mass flow meter Brine solution was injected using an Isco Pump. The different lines were connected to an X-ray transparent hassler type cell equipped from each side with three connections (inlet, outlet and static line for the pressure transducer). A data acquisition system was used to monitor the pressure, mass flow and temperature. Finally, the set-up was installed in dedicated radiography facility equipment for in-situ saturation monitoring.

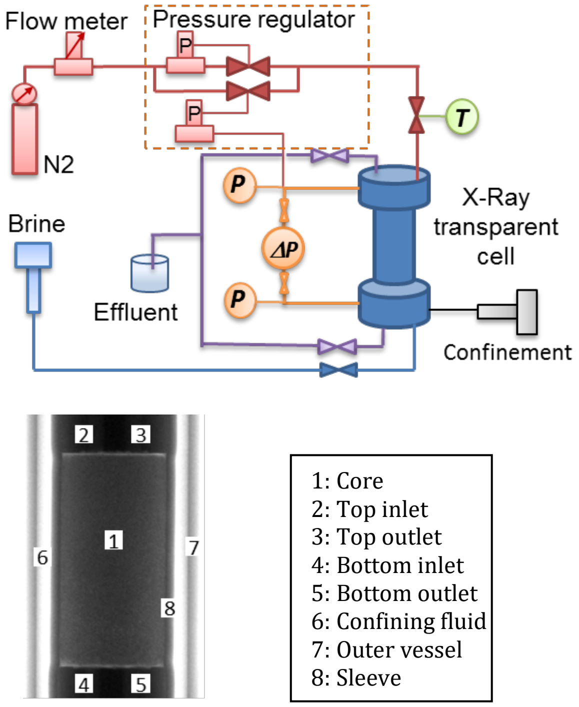

**Fig. 1** Experimental set-up and radiograph showing the sample shape and the basic components of the Hassler injection cell.

During fluid injection, the sample was imaged using an X-ray radiograph equipment. The system consists of an X-ray source, a flat panel and a data processing unit for computation, visualization and data analysis. The radiographs were captured with a resolution a 20 µm at a rate of one frame per second. Radiographs were then cropped to show only the sample (see zone 1 in Figure 1). The stack of images was processed to monitor water saturation and salt concentration evolution during gas injection [10]. Indeed, image gray levels are proportional to the transmitted X-ray intensity which is defined by the Beer Lambert's law in the case of a multicomponent material as:

$$I_t = I_o\, e^{-(\mu_{bt} X_b + \mu_g X_g) + \alpha}$$

where $I_o$ and $I_t$ are respectively the incident and the transmitted X-ray intensity, $\mu_{bt}$ and $\mu_g$ are respectively the brine and the gas attenuation coefficients, $X_w$and $X_g$ are respectively the brine and the gas portions in the linear path of the X-ray and α is the attenuation of the structure. Considering two references states, 100% brine saturated and dry images the above equation can be written as:

$$I_b = I_o\, e^{-\mu_{b0} X + \alpha} \text{ and } I_g = I_o\, e^{-\mu_g X + \alpha}$$

where X is the linear path of the X-ray that corresponds to the total porosity and $\mu_{b0}$ is the initial brine attenuation coefficient.

By construction we obtain:

$$X_b + X_g = X$$

Afterward, normalizing the X-ray intensity $I_t$ by both the 100% brine and the dry case, and considering $\mu_b \gg \mu_g$ we obtain:

$$\frac{\ln\left(\frac{I_b}{I_0}\right) - \ln\left(\frac{I_t}{I_0}\right)}{\ln\left(\frac{I_b}{I_0}\right) - \ln\left(\frac{I_g}{I_0}\right)} = \frac{-\mu_{b0} X + \mu_{bt} X_b}{-\mu_{b0}\, X}$$

When salt concentration is constant we have:

$$\mu_{bt} = \mu_{b0} \text{ and } \frac{X - X_b}{X} = S_g$$

where $S_g$ is the gas saturation. If the salt concentration changes, $\mu_{bt}$ will vary with an upper limit equal to the KBr attenuation coefficients. If we normalize the X-ray transmitted intensities (i.e. relative X-ray absorption) by the mean intensity of a dry sample with precipitated salt, we can assess qualitatively the variation of salt quantity compared to the initial distribution.

### 2.2. Experimental procedure

A set of experiments has been conducted using the set-up described above. The experiments have been conducted on the Bentheimer sandstone sample and the Bentheimer/Molière composite core. Four steps have been applied to investigate the effect of salt on the drying dynamics and the effect of capillary contact on salt accumulation and permeability alteration. the sequence of injection consisted in:

1-Saturating the sample with the wetting phase by injecting the water (or brine) from the bottom inlet and opening the top outlet (the bottom outlet and top inlet are closed). To ensure a full saturation, we have imposed a back pressure of 4 bar and monitored the saturation by X-ray.

2-Lowering the pore pressure to 1 bar, opening the bottom outlet and top inlet and closing the top outlet. The water injection is maintained allowing a sweeping of the bottom face of the sample.

3-The gas is then injected at a constant pressure. The variation of the saturation and the local concentration of salt is monitored by the X-ray radiographs and the gas flow rate is monitored by the Coriolis flow meter. The injection is stopped once no more variations are observed on the radiograph and the flow rate.

4-The sample is finally cleaned by injecting deionized water until the reference X-ray absorption is reached.

### 2.3. Sample properties and fluids

The experiments were conducted using two consolidated water-wet sandstones: Bentheimer, and Molière. Bentheimer sandstone is a high porosity (23%) permeable (1350 mD) rock composed mainly of quartz; while Molière sandstone is a medium porosity (14%) with very low permeability (0.05 mD) composed of quartz and pore filled clay.

In the three first experiments a Bentheimer core of 1 cm in diameter and 2 cm in length was used. In the last experiment and to reproduce a lateral capillary contact parallel to the flow direction, a composite sample was shaped using Bentheimer and Molière sample. The plugs were first half cut in the longitudinal direction using a diamond saw. The two half pieces were then gathered by using a nonwoven fabric reinforced by a wet ceramic powder (see **Fig. 2** a) to improve capillary contact. The Bentheimer half core is made shorter than the Molière one to avoid outlet capillary contact with the distributor (see **Fig. 2**.b).

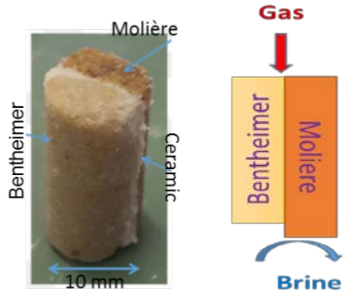

(a) (b)

**Fig. 2** (a) Photographs of the composite core composed of Bentheimer and Molière half cores contacted with nonwoven fabric reinforced by a wet ceramic powder. (b) Sketch of the composite sample during fluids injection.

To perform the different experiments, we have used dry nitrogen and 100 g/l KBr brine. KBr salt was chosen as it has a high electronic density allowing a good X-ray contrast with water and gas. The solubility limit of KBr in water at 20°C is 560 g/l.

## 3. Experimental observations

As pointed out in the introduction, drying and salt precipitation result from the interplay of different parameters. To separate the effect of these parameters, we have conducted a non-exhaustive number of experiments that focus on the effect of salt on permeably alteration with three different boundary conditions: no capillary contact at the outlet face, capillary contact at the outlet by brine seeping and lateral capillary contact using a composite sample as described in the previous section. In the following, we discuss the impact of these parameters.

### 3.1. Effect of salt

To study the effect of salt on permeability alteration, we have conducted two experiments where we have first injected dry gas in a Bentheimer sample initially saturated with deionized water (Exp 1). The purpose of this first experiment is to observe the drying dynamics without the interference of the salt. The inlet relative gas pressure was set to 100 mbar. The pressure drop was chosen to be above the entry pressure of 70 mbar and corresponds to a pressure gradient of 5 bar/m which is representative of near well bore pressure gradient. **Fig. 3** shows the evolution of the mean gas saturation within the sample as well as the mass flow rate of the gas for Exp 1.

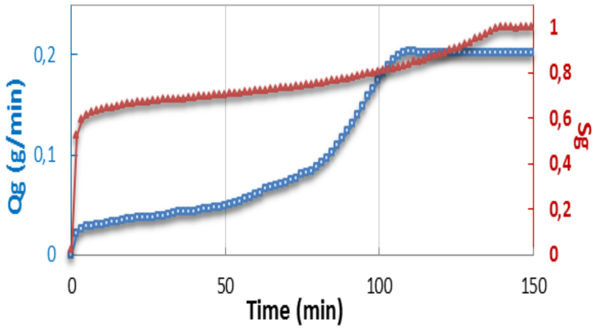

**Fig. 3** Exp 1 Gas saturation (red curve) and mass flow rate (blue curve) evolution as a function of time for gas injection in sample initially saturated with deionized water.

Four regimes can be distinguished:

- In the first few minutes (between 0 and 10 min) the gas drains the sample until it reaches the residual water saturation that was established to 40%. **Fig. 4** shows the local saturation of the sample after 10 min. The longitudinal profile as well as the 2D saturation map show a typical drainage profile with a quite constant saturation on the first 2/3 of the sample (around 30% of water) followed by an increasing water saturation toward the outlet due to capillary end effects.
- The next regime (between 10 and 70 min) exhibits a smooth increase in the gas saturation that reaches 74% as well as in the flow rate that establishes at 35% of the final rate (cf. **Fig. 3**). The profile at 70 min displays a constant shift of the initial profile. This observation can be explained by an apparent homogeneous drying all along the sample which means that the equilibrium between the gas and the water is not instantaneous. Or by an equilibrium reached between the water evaporation and capillary forces that tends to redistribute liquid from regions of high-water saturation to region of low-water saturation.
- Following this second regime that ends at 70 min and at water mean saturation of 26% we observe a noticeable increase in the gas flow rate until 110 min as well as in the gas saturation until 140 min. This change in the drying rate corresponds to the progression of a discontinuity and a sharp front on the saturation profile and 2D map. This front propagates through the sample toward the outlet allowing a subsequent increase in the flow rate until it reaches a plateau.

- The final stage corresponds to the dry state (above 140 min). It is to be noticed that the flow rate reaches its limit before the gas saturation.

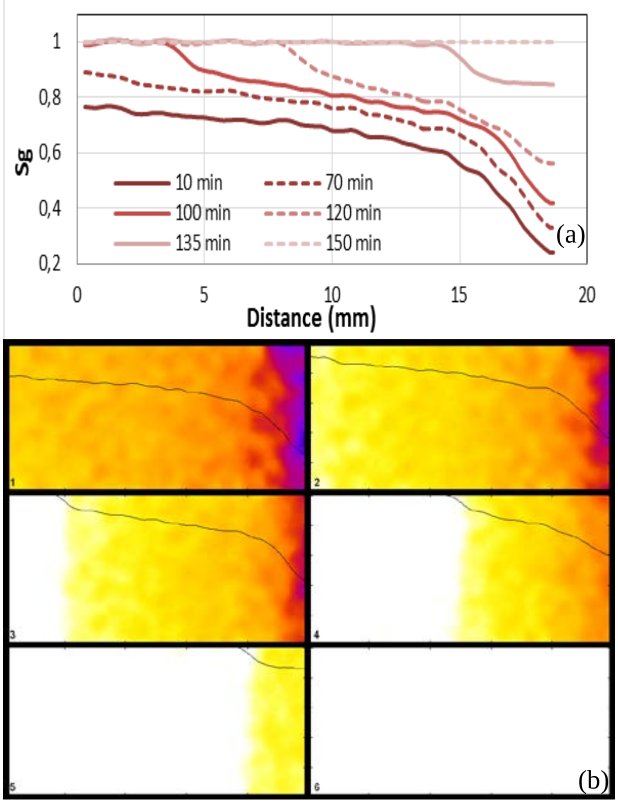

**Fig. 4** Exp 1 evolution of gas saturation (a) 1D profile et (b) 2D map as a function of time (gas is injected from left) in sample initially saturated with deionized water.

This first experiment shows that injecting a dry gas in a porous media containing only deionized water allows to evaporate the total content of water without altering the permeability of the sample. The observation of the saturation profiles shows that the drying effect takes place first at the inlet of the sample and then propagates throw a sharp front downstream. The two first regimes involved in this particular case are most likely an instantaneous phase equilibrium between gas and water coupled with a capillary equilibrium generated by the gas flow and the water saturation.

The drying scenario would probably be first the gas vaporizes water at the entrance of the sample creating a capillary disequilibrium and decreasing the water saturation. This results in water redistribution by counter-current imbibition to compensate for the water evaporation at the inlet. Once the mean water saturation reaches a minimum (26%), the capillary disequilibrium cannot be compensated anymore. The evaporation front appears and propagates in the sample until the total drying of the sample.

In a second experiment (Exp 2) dry gas was injected in the same sample initially saturated with KBr brine at a relative gas pressure of 150 mbar. **Fig. 5** shows the evolution of the gas flow rate as a function of time as well as the relative X-ray absorption that was normalized by the final stage of Exp 3. The flow rate exhibits the same behavior as for the first experiment (i.e. a first increase corresponding to the drainage phase, a smooth increase slope followed by a more pronounced rise till flow rate reaches a constant plateau corresponding to the dry state). The relative X-ray absorption that corresponds in this particulate case to the mean gas saturation shows an asymptotic behavior with a smooth increase of the gas saturation. The final flow rate did not show any evidence of permeability alteration due to salt precipitation.

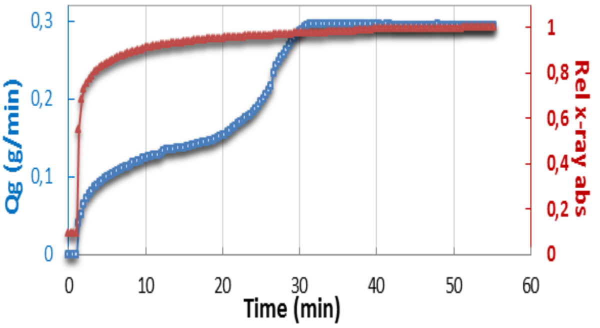

**Fig. 5** Exp 2 X-ray relative absorption (red curve) and gas mass flow rate (blue curve) evolution as a function of time for gas injection in sample initially saturated with 100 g/l KBr brine.

The observation of the local profiles shows a more complex behavior (see **Fig. 6**). As the relative X-ray absorption was normalized by the gray level of the final sate, the profile can be qualitatively interpreted as the relative variation in salt localization (i.e. when the profile goes over or under one, it means that the quantity of salt decreases or increases respectively). Thus, we can observe that the salt concentration slightly decreases in the first half of the sample while it considerably increases at a specific location situated 5 mm from the outlet, corresponding to the location of the capillary end effects.

This behavior can be explained by the competition between drying and capillary rise. Actually, as drying decreases the saturation from the inlet toward the outlet as shown by case 1, capillary forces tend to equilibrate the saturation by displacing brine toward the inlet. As a consequence, the salt concentration locally increases and once it reaches the solubility limit, it precipitates.

The measured gas flow rate shows that, even if salt has precipitated, it did not affect the permeability. This could be explained by the low quantity of salt initially present in the sample after the drainage. An estimation of the initial volume of dissolved salt after the drainage gives a value 0.003 cc which corresponds to 0.01PV (PV is the pore volume). This reduction of the pore volume does not seem sufficient to reduce the absolute permeability. To confirm this observation, a 3D images of the sample was taken at initial dry state and after salt precipitation. **Fig. 7** shows a slice picked at the level of maximum salt precipitation. We can distinguish almost no difference between the two images apart few bright points corresponding to solid salt in some locations.

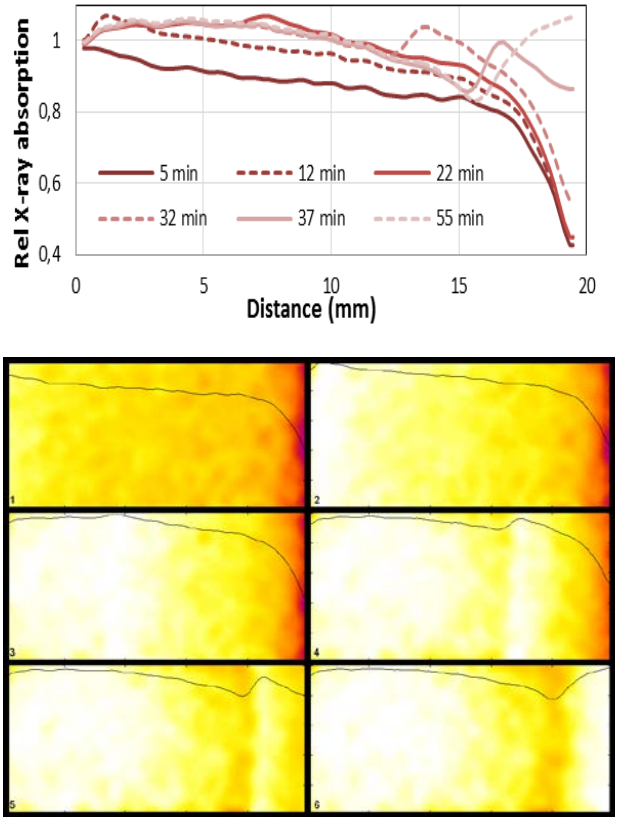

**Fig. 6** Exp 2 evolution of X-ray relative absorption (a) 1D profile and (b) 2D map as a function of time (gas is injected from left) in sample initially saturated with 100 g/l KBr brine.

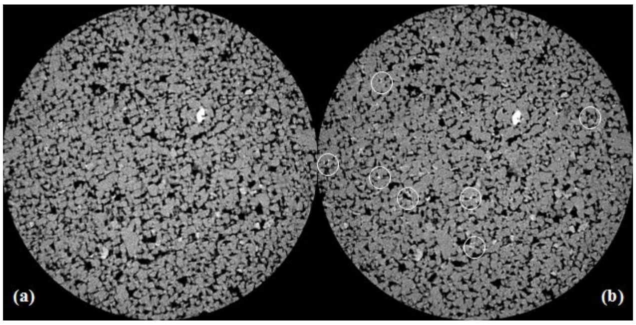

**Fig. 7** 2D slices picked at the maximum salt precipitation location (4 mm from the outlet) (a) at the initial dry state and (b) at the final state of the experiment corresponding to a dry state with precipitate salt. Some locations where salt has precipitated are indicated by circles.

### 3.2. Outlet capillary contact effect

To investigate the capillary effect, dry gas was injected in a sample initially saturated with a 100g/l KBr brine while contact with brine was maintained by sweeping the bottom face of the sample at a relative gas pressure of 150 mbar. **Fig.8** shows the evolution of the gas flow rate and the relative X-ray absorption as a function of time. In this case, we observe a completely different behavior than in the previous cases. After an initial increase due to drainage, the gas flow rate experiences successive decline and rise cycles with increasing amplitude before it reaches zero after six hours of injection. The relative X-ray absorption shows a constant decrease which corresponds to an increase of the sample density. This observation suggests an accumulation of additional salt within the sample that is supplied by the brine in contact with the bottom face of the sample.

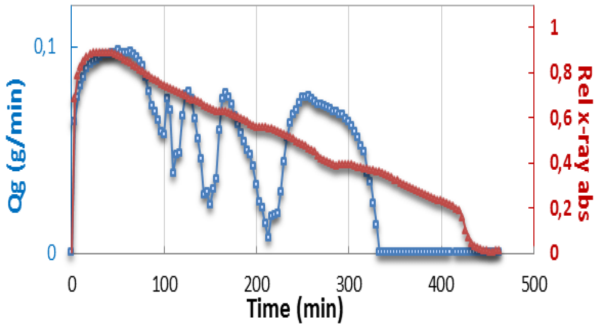

**Fig. 8** Exp 3 X-ray relative absorption (red curve) and gas mass flow rate (blue curve) evolution as a function of time for gas injection in sample initially saturated with 100 g/l KBr brine and with outlet capillary contact.

The profiles illustrated in **Fig. 9** give more insight into the mechanisms that take place during this experiment. We observe first a local decrease in the relative X-ray attenuation at 8 mm from the inlet at 63 min that suggests an increase in salt concentration. The advent of this salt strip is correlated with a decrease in the gas flow rate and corresponds most probably to salt precipitation that alters permeability to gas. We observe then an alternation of dilutions and precipitation corresponding respectively to the increase and the decline of the gas flow rate with an intensification of the relative X-ray attenuation along the salt strip. Finally, we observe a displacement of the salt strip during the successive cycles of dilution precipitation toward the inlet of the sample. At the end of the experiment the salt strip is located 5 mm far from the inlet. The observed phenomena can be explained by the competition between drying and capillary rise. Indeed, the gas flow dries out the sample, which is manifested by a decrease in the water saturation. However, as we have an active capillary contact, capillary suction compensates for the decrease of water saturation to maintain a capillary equilibrium, which in turn leads to an increase of local salt concentration. At one point the salt concentration is sufficiently high to precipitate salt and altering the gas permeability. As the gas flow rate declines, the capillary rise becomes predominant, allowing the dilution of the precipitated salt and a regeneration of the gas permeability. The alternation of this instable equilibrium leads to an increase of the precipitated salt after each stage till a point of no return is reached where the volume of precipitated salt is sufficiently high to stop the gas flow and the capillary suction.

At the end of the experiment a 3D image of the sample was taken to evidence salt precipitation. **Fig. 10** shows a slice picked up at the maximum salt precipitation location. The accumulation of solid salt is clearly observable all over the porous space of the sample (white part). The solid salt plugs the pores and is responsible of the permeability alteration.

.

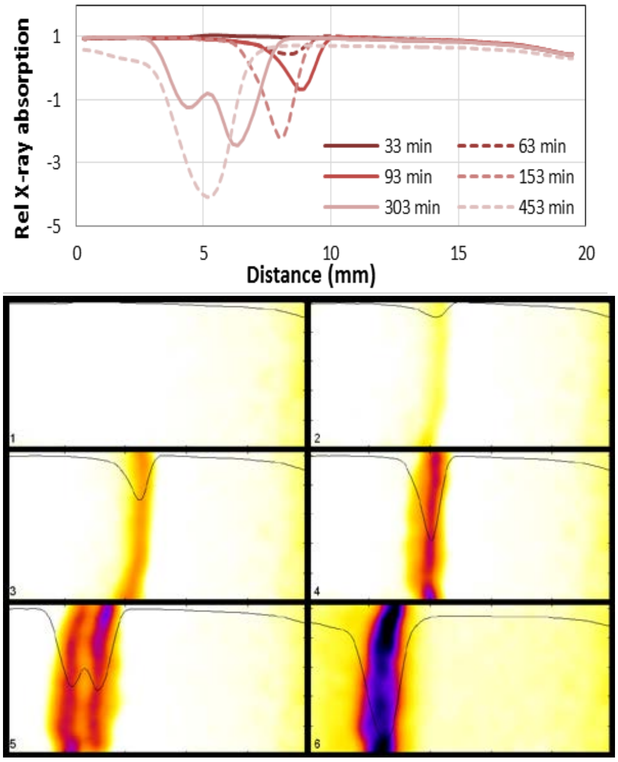

**Fig. 9** Exp 3  X-ray relative absorption (a) 1D profile and (b) 2D maps (gas is injected from left) as a function of time for dry gas injection in sample initially saturated with 100 g/l KBr brine and with outlet capillary contact.

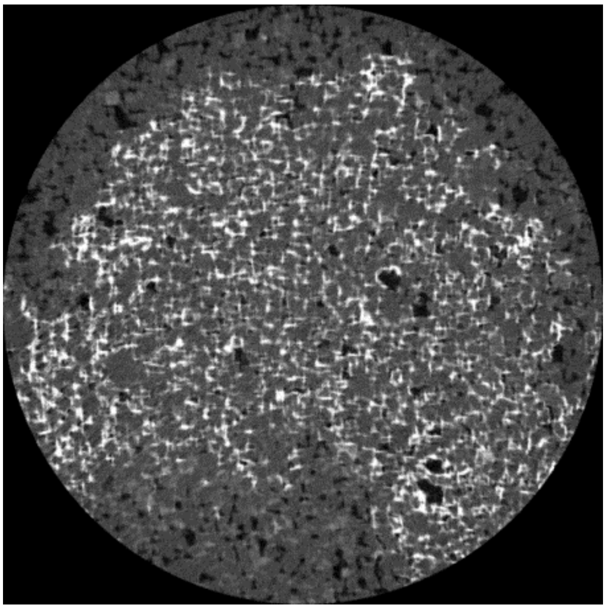

**Fig. 10** 2D slice picked at the maximum salt precipitation location (5 mm from the inlet) at the final state of the experiment. Light gray level corresponds to solid salt that has precipitate due to gas drying out.

### 3.3. Lateral capillary contact effect

In this last experiment (Exp 4), we have injected dry nitrogen in the composite sample initially saturated with 100 g/l KBr brine. The inlet gas pressure was set to 450 mbar (the outlet was opened to atmosphere). **Fig. 11** shows the evolution of the gas flow rate as a function of time as well as the relative X-ray absorption that was normalized by the finale stage within the Bentheimer half core. We can observe that when gas is injected, the relative X-ray absorption and the gas flowrate rise rapidly to a maximum that correspond probably to the residual water saturation state. Following this first stage, we note a monotonous decrease in the relative X-ray adsorption which means salt accumulation within the sample. As consequence, the gas flow rate decreases which corresponds to a progressive permeability alteration.

**Fig. 12** shows the 1D and 2D locale relative X-ray absorption. The Bentheimer half core is positioned on the upper part of the images. The first image at 26 min shows that when gas is injected, a preferential path is created throw the Bentheimer sample that goes to Swi whereas the Molière half core remains fully brine saturated. The second image shows the advent of salt precipitation that is located almost at the middle of the sample and near the Bentheimer and sleeve boundary. However, the shape of the precipitate salt zone is completely different from the one observed in the previous experiment.  Indeed, we do not observe a strip perpendicular to the gas flow direction but rather an arrow like spot. The next images show that salt precipitates and accumulates in parallel to the flow direction. As the Bentheimer half plug is only in contact with the Moliere one, this observation confirms that the lateral capillary contact is active and can provide enough salt to plug completely the permeable zone.

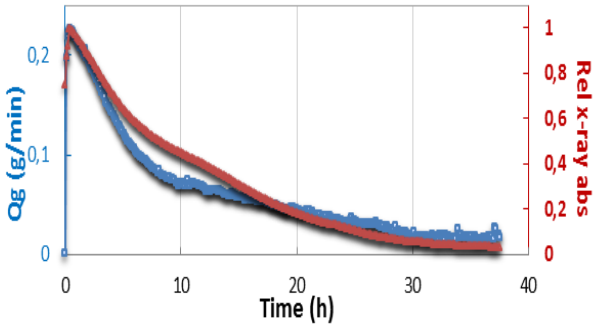

**Fig. 11** Exp 4  X-ray relative absorption (red curve) and gas mass flow rate (blue curve) evolution as a function of time for gas injection in sample initially saturated with 100 g/l KBr brine and with outlet capillary contact.

To better observe the shape of the salt precipitate zone, a 3D image was taken at the end of the experiment.  Fig. 13 shows 2D sagittal and axial images of the sample. We can clearly see the solid salt barrier that cause permeability alteration. It is interesting to note that this barrier lies in diagonal to the Bentheimer sample and extend on the two third of the length. This shape reveals the complexes interplay of the different mechanisms involved in salt precipitation.

In this case, the drying front is opposed not only to parallel capillary forces coming from the capillary end effect in the Bentheimer half core (as described in Exp 2) but also to perpendicular capillary forces resulting from the contact with the Moliere half core. This configuration can then explain the shape of the precipitated salt that results from the competition between the two perpendicular drying fronts.

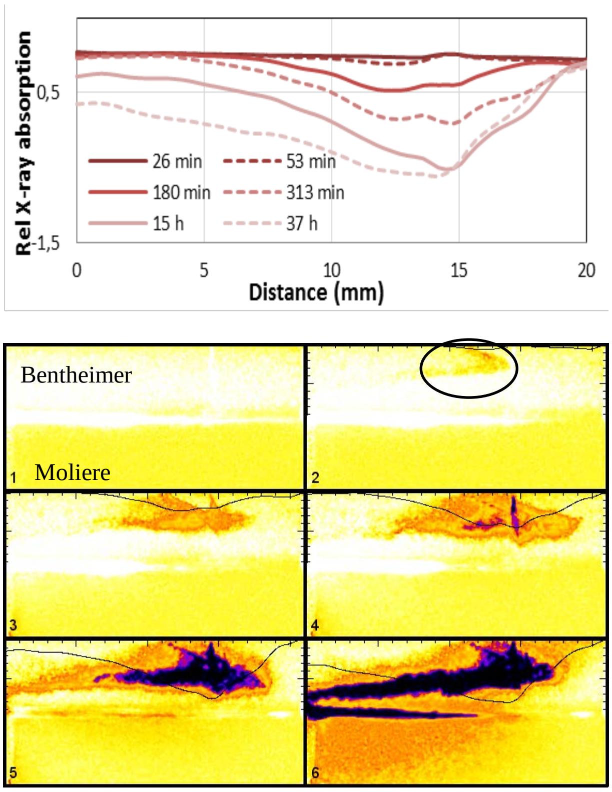

**Fig. 12** Exp 4 X-ray relative absorption (a) 1D profile and (b) 2D maps (gas is injected from left) as a function of time for dry gas injection in sample initially saturated with 100 g/l KBr brine and with lateral capillary contact.

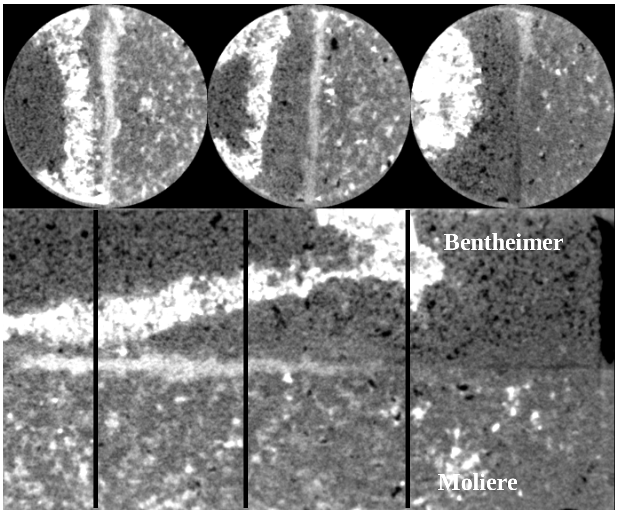

**Fig. 13** 2D sagittal slice (bottom) and 2D axial slices picked at three different salt precipitation location at the final state of the experiment. Bright zone corresponds to solid salt that has precipitated due to gas drying out.

## 4. Numerical interpretation

In this study we used CooresFlow an in-house simulator designed for reactive flows in porous media. It was developed to model multiphase transport processes coupled with fluid-rock interactions, for various applications including $CO_2$ underground storage as well as enhanced recovery of hydrocarbon reservoirs.

### 4.1. General characteristics

CooresFlow is a THC (thermal hydro-chemistry) simulator that consider the following phenomena:

- multiphase flow in porous media, with viscous and capillary forces,
- transport of chemical components by advection, diffusion and dispersion,
- transfers within the fluids or on the surface of the rock governed by local equilibrium,
- chemical equilibrium or kinetic reactions to describe geochemical exchanges,
- dynamic modification of the porosity and permeability of the porous medium over time.

In the case of gas production or storage, it allows to consider:

- the phenomena of mass transfer between liquid water and water vapor (drying),
- the transport and precipitation of dissolved species (salts),
- the coupling between porosity and permeability changes.

The mathematical formulation used in the simulator is a generalization of the compositional formulation based on material and energy balance equations and chemical equilibrium equation (for more see [11])

### 4.2. Physical and numerical model

In this study we consider a multiphase compositional system composed of four phases: two fluids (water and gas) and two solids (rock and salt). As the system is compositional, each phase can contain one or several species. In the studied case, the species are:

- H2Ow and KBrw (the dissolved salt) in water,
- N2g (nitrogen) and H2O vapor (H2Og) in gas,
- Precipitated salt (KBrs) in salt.
- The Rock phase (Quartz) considered inert in this study (no exchange with other phases)

The rock sample is modelled by a vertical parallelepiped of 100 cells in Z direction. Its sizes are 0.86 cm in X and Y directions and 1.98 cm vertically. Initially, the sample is saturated with either deionized water or a 100 g/l KBr brine. The temperature is constant within the sample and does not evolves with time. The pressure is also initially constant and equal to the atmospheric pressure. The boundary conditions were defined in accordance to the experimental design.

The thermodynamic model computes the density and viscosity of the fluids. The brine density evolves with the salt concentration (KBr molar fraction) using a linear relation based on experimental data from the Detherm 2015 database, for a temperature of 25°C. In the same way, the brine viscosity evolves with the salt concentration by interpolating linearly experimental data of the Detherm 2015 database for a temperature of 25°C. The gas properties are assumed constant since the pressure is closed to 1 bar and the humidity rates are low (<2%). We consider a gas density of 1.2 kg/m3 and viscosity of 1.758 $10^{-5}$ Pa.s.

In this work, two phase transfers are modelled: Water evaporation and condensation, and salt dissolution and precipitation. The salt dissolution/precipitation is considered instantaneous. It is modelled by an equilibrium constant with a linear dependency on temperature. The equation is based on the experimental data of the Detherm 2015. The water evaporation/condensation is also considered instantaneous. This hypothesis is confirmed by a Peclet number higher than 1 that means the water advection dominates the water diffusion in gas. The model is defined by a table of equilibrium constants with a dependency to temperature, pressure and salt concentration. This table is based on experimental data from the Carnot and Detherm 2015 databases.

## 4.3. Flow through drying modelling

To generate the petrophysical model, we have first considered a homogeneous sample with a constant porosity of 23% and permeability to water of 1450 mD. Relative permeabilities and capillary pressure were then estimated by history matching the mean saturation profiles and gas flow rate end point from Exp1. The resulting relative permeability to water and to gas as well as water/gas capillary pressure are illustrated in **Fig. 14**. It is to be noted that the resulting absolute permeability to gas was estimated to 2450 mD which is much higher than the water permeability. This can be explained by the inertial effect. This effect was not considered in this study. Irreducible water saturation was estimated to 12%. In the domain of 0 to 12% of water saturation, the relative permeability to gas is found to be constant while the capillary pressure increases slightly.

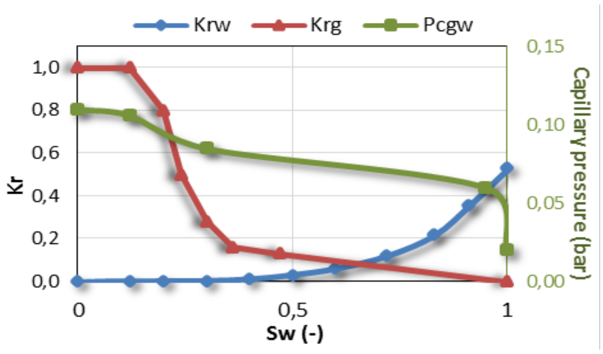

**Fig. 14** Water (Krw), gas (Krg) relative permeability and Gas-water capillary pressure (Pcgw) versus water saturation

By comparing the simulation results with the experimental data in the case of Exp 1 (see **Fig. 15**), we observe that the simulated system exhibits the same behavior than the experimental case. Indeed, we observe the same behavior of the gas rate with an initial important increase corresponding to the drainage phase, then a smoother increase followed by a greater increase during the drying phase within the sample until the gas rate reaches a plateau

The model succeeds to fit properly the mean saturation and gas flow rate end point as well as the major part of saturation profiles. However, differences are observed on the gas flow rate dynamic. This discrepancy can be explained by the uncertainties on capillary effects and saturation at the outlet boundary that induce a difference on the gas saturation profiles near the outlet. Nevertheless, the reactive transport model succeeds to simulate the same physical phenomena such as the drying effect, the capillary counter-current, the disappearance of a phase with similar characteristic times.

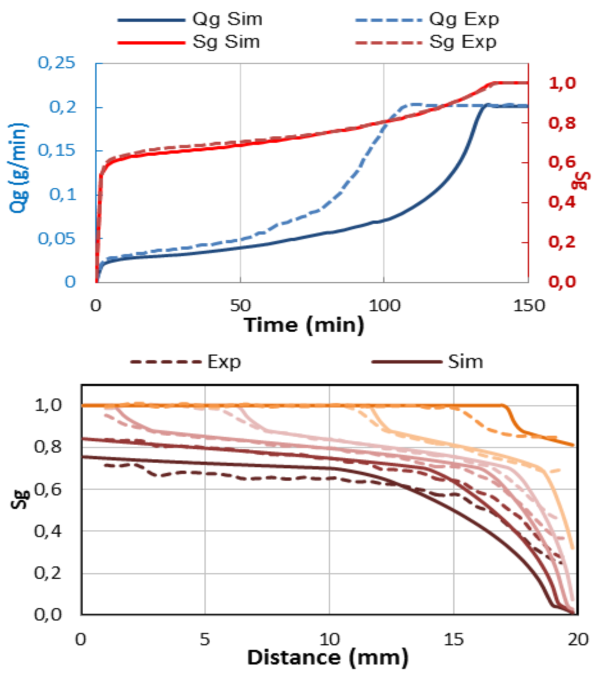

**Fig. 15** Comparison of the experimental and simulated results of Exp 1 (dry gas injection in sample initially saturated with deionized water)

## 4.4. Salt precipitation modelling

To consider the effect of salt precipitation on permeability to gas, the porosity is allowed to evolve over time with the volume of precipitated or dissolved salt. The permeability can change accordingly using a Kozeny Carman model with critical porosity:

$$k = k_0 \left(\frac{\emptyset - \emptyset_c}{\emptyset_0 - \emptyset_c}\right)^a \left(\frac{1 - \emptyset_0 + \emptyset_c}{1 - \emptyset + \emptyset_c}\right)^b$$

Where $k$ and $\emptyset$ are respectively dynamic permeability and porosity, $k_0$ and $\emptyset_0$ are respectively initial permeability and porosity and $\emptyset_c$ is a critical porosity beyond which permeability is null. Exponents a and b as well as $\emptyset_c$ were history matched using data from Exp 3. Best match was found with 0.08 for $\emptyset_c$ , 2.5 for a and 1.5 for b. Experiment 2 was simulated using the same model parameters defined in experiment 1 apart from the initial saturation where the salt concentration was set to 100 g/l and the relative gas pressure at the inlet of 150 mbar.

**Fig. 16** shows the evolution of the simulated (continuous line) gas flow rate, mean gas saturation within the sample and the inverse of the normalized KBr quantities. Experimental data (dashed line) were added for comparison. Simulated gas flow rate shows the same behaviour as for previous case with also a slower dynamic than the experimental data due probably to the same reason mentioned previously. However, comparison of simulated gas saturation and relative X-Ray attenuation is not straightforward as X-Ray attenuation is sensitive not only to water saturation but also to salt quantities. Still the two quantities decrease monotonically which agrees with the increase of the X-Ray attenuation. We also observe that the salt quantity reaches a plateau after about 20 min indicating that no more salt is evacuated from the sample which mean that no more water convection is active. This time corresponds also to a change in the flow rate slop indicating a change in the water transport mechanism which becomes dominated by the evaporation and drying mechanisms.

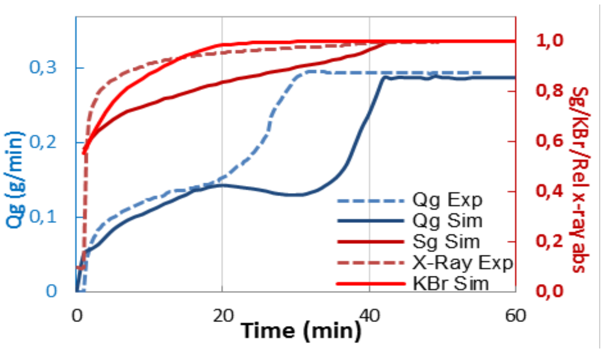

**Fig. 16** Comparison of the experimental and simulated results of Exp 2 (dry gas injection in sample initially saturated with 100 g/l brine)

Simulation results show also a similar KBr salt profile evolution with the experimental data as well as a salt accumulation near the outlet of the sample. **Fig. 17** shows four different profiles taken at four different time and corresponding to (a) experimental X-Ray attenuation normalized by the final mean X-Ray attenuation, (b) the KBr quantity along the sample normalized by the final one, (c) dissolved KBr concentration and (d) gas saturation along the sample. For each date, we observe on the KBr quantity a front similar to the experimental data that separates the precipitated-salt zone from the dissolved-salt zone. This front has a characteristic shape that is induced by the combination of an increasing water saturation (cf. **Fig. 17**.d) with a decreasing KBr concentration (cf. **Fig. 17**.c) that reaches a maximum at the interface between the dry zone and the wet zone. The front moves towards the outlet at the same velocity as the evaporation front. It is to be noted that simulation shows no evidence of overconcentrated zone (i.e. zone where concentration is greater than solubility limit). At 55 min, the sample is completely dried and all the KBr salt is precipitated. Within the sample, the KBr amount corresponds to the amount that was included in the residual water saturation (after 20 min). But near the outlet boundary, we observe an accumulation of salt. It results from the initial capillary end effect and very close to the outlet, from the competition between the drying effect and the capillary re-imbibition.

This salt precipitation occurs when the solubility threshold is reached. It reduces the porous volume in proportion with the solid KBr density. The final average porosity was estimated at 0.228 with a minimum of 0.225 which is very closed to the initial 0.23 value. The initial salt amount of the sample is not sufficient to drastically reduce the porosity. This porosity decrease induces a small permeability decrease that has a little effect on the gas rate. The average permeability to gas was 2000 mD compared 2450 mD at the initial state.

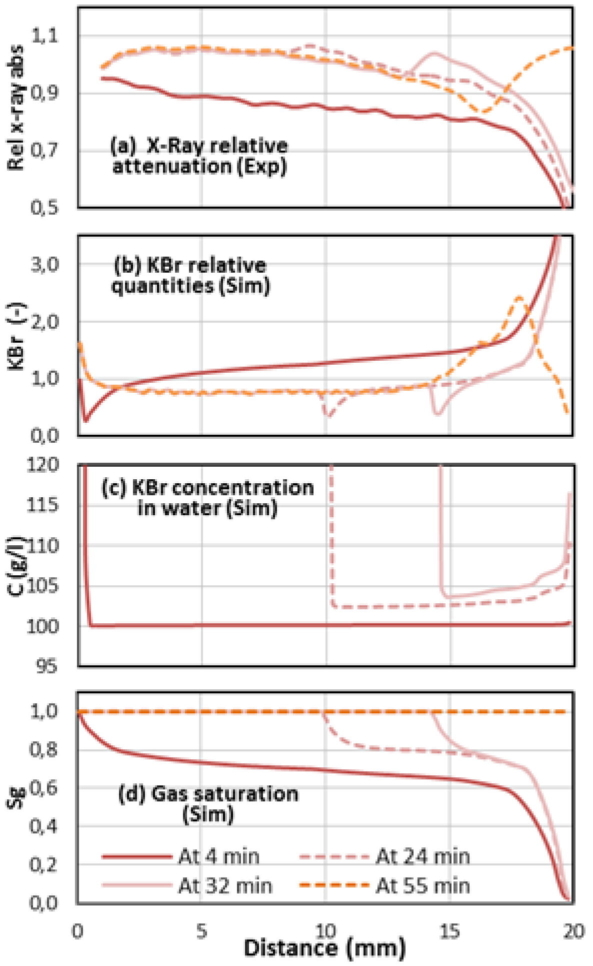

**Fig. 17** Comparison of (a) experimental X-Ray attenuation profiles normalized by the final mean X-Ray attenuation and simulated profiles of (b) the KBr quantity along the sample normalized by the finale one, (c) the dissolved KBr concentration and (d) the gas saturation along the sample at four different date for Exp 2.

### 4.5. Capillary contact modelling

To simulate capillary contact effect, the numerical model was modified by adding an infinite water reservoir in contact with the outlet boundary to reproduce Exp 3 boundary condition. Water was set free to flow through the outlet in the two directions. In the two cases dry gas is injected in a sample initially saturated with a 100 g/l KBr brine.

**Fig. 18** (a) shows that the simulated gas flow rate for the third experiment (Exp 3) was comparable to the experimental one. Indeed, we observe four successive cycles of gas flow rate increase and decrease corresponding drainage/dissolution (increasing flow rate) and drying/precipitation phase (decreasing flow rate). The gas rate decreases for the last time at 327 min and reaches a value close to zero.

To get more insight in the cycling behavior, we have reported in **Fig. 18** (b) the simulated mean gas saturation within the sample, the precipitated solid KBr quantities normalized by the maximum KBr quantity and the KBr concentration in water normalized by the initial concentration. Experimental data corresponding to the X-Ray normalized attenuation was added for comparison. The KBr curve shows clearly that the quantity of precipitate salt is increasing over time during each cycle with alternation of stagnation intervals that correspond to gas rate local minima. During those stagnation periods, we observe also a decrease in gas saturation as well as a slight increase in the brine concentration that is probably due to solid salt dissolution. However, as we do not observe any significant decrease in the solid KBr quantity curve, this means that during the stagnation period, an equilibrium is reached between dissolution and precipitation reaction. Salt is dissolved at the contact of brine and precipitate at the drying front.

The simulated KBr normalized quantity profiles at four different date are illustrated in **Fig. 19**. They show where salt forms a deposit. The four times correspond to the four gas local minimum rates. At these times, the salt amount is mainly located in the first 7 mm of the sample with a tendency to move towards the inlet over time. It is characterized by one or several peaks with an increasing base. At these zones, the porosity and the permeability are altered and reach a minimum value of respectively 9% and 1-10 mD. All these figures clearly show a correlation between the increase of the salt amount, the permeability alteration and the decrease of the gas rate.

The following process can explain the different observations made above. As in the case 2, the dry gas injection locally induces a decrease of water saturation due to water evaporation and a capillary re-imbibition from the high-water saturation zone to the low-water saturation zone to compensate the water loss. While the porous medium dries, the brine salt concentration increases until it reaches the solubility threshold. Then, it precipitates with an impact on the porosity and the permeability. The gas front on the saturation profile continues to propagate towards the outlet, leaving behind it, a dried porous medium containing a small amount of precipitated salt. At a specific location defined by the competition between the drying effect and the capillary re-imbibition, a salt accumulation starts, fed by the capillary contact, and alters the petrophysical properties. In that case, the gas rate strongly decreases until the capillary re-imbibition becomes preeminent. Then, the brine supplied by the capillary counter-current partially dissolves the precipitated salt. Indeed, the salt dissolution quickly saturates the brine that cannot dissolve an additional amount of salt. Consequently, the porosity and the permeability are also partially restored, and the gas rate increases again, until a maximum reduction. This is the end of the first cycle. Then, the process starts again with altered petrophysical conditions that impact the competition between the drying effect and the capillary re-imbibition. It explains the displacement of the salt accumulation observed in **Fig. 19**. The cycling process continues and stops when the pressure forces dominate the capillary forces and block the capillary flow.

In conclusion, the simulations results show a similar gas rate evolution with the experimental data as well as a salt accumulation that behaves in the same way. The reactive transport model succeeds to simulate the drying effect and the salt precipitation associated to a petrophysical properties change. The dynamic permeability model used in this study reveals adapted to model the main effects of salt precipitation.

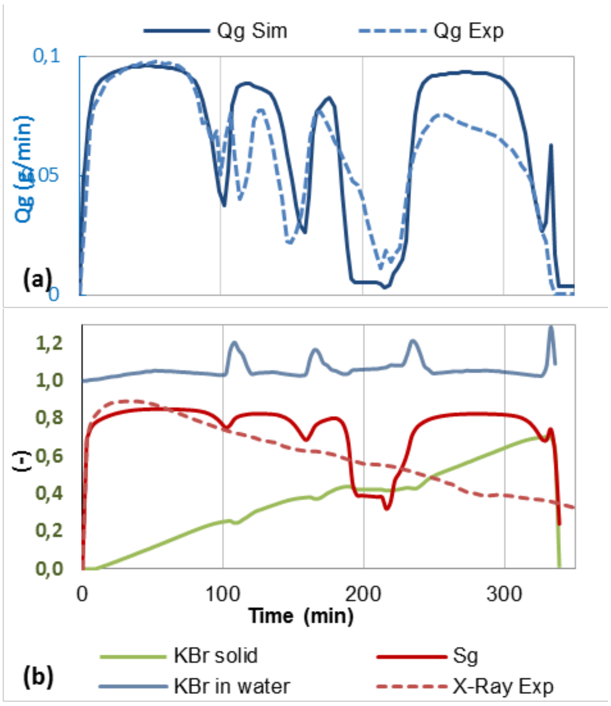

**Fig. 18** Comparison of (a) experimental and simulated gas flow rate, (b) experimental X-Ray attenuation normalized by the final mean X-Ray attenuation and simulated evolution of (b) solid (precipitated) KBr quantity normalized by the finale total KBr quantity, the dissolved KBr concentration and the mean gas saturation Exp 3.

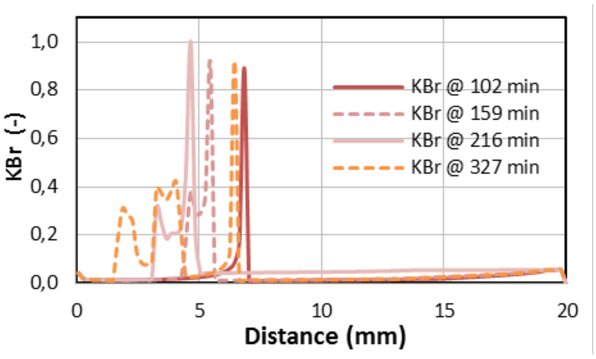

**Fig. 19** KBr quantity profile along the sample normalized by the maximum quantity at four different date for Exp 3.

In the case of Experiment 4 a two-layers mode parallel to the pressure gradient, (see **Fig. 2** (b)) was built with high permeability contrast. In this case outlet capillary contact was only maintained for the low permeability layer. **Fig. 20** shows the evolution of the simulated gas flow rate for Exp 4. We observe the same behavior the experimental case (see **Fig. 11**). The curve strongly increases due to the drainage phase then quickly decreases probably due to an alteration of the permeability. However, and as for experiment 1 and 2, the simulated flow rate exhibits a faster dynamic that can also be explained in this case by the uncertainty on the capillary contact description.

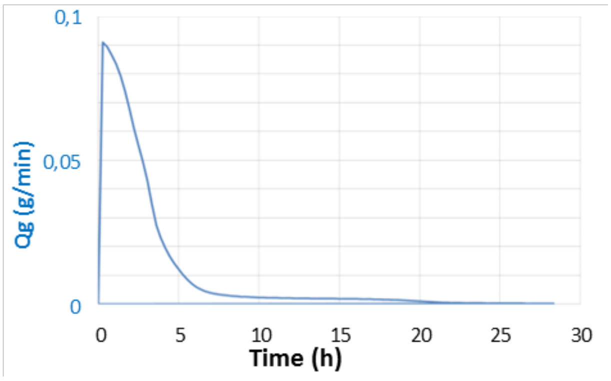

**Fig. 20** Simulated gas flow rate in the case of Exp 4.

Within the property maps shown in **Fig. 21**, we observe the result of the longitudinal capillary contact effect. The third experiment has shown that the capillary contact at the bottom of the sample induces a salt deposit that is perpendicular to the fluid flow. In the case of Exp 4, the result is different. The re-distribution of brine from the high-water saturation zone to the low-water saturation zone mainly occurs near the contact surface between the two porous media, that induces a 2D profile of salt deposit that spread over a diagonal in the Bentheimer half core. As in the previous case, the brine feeding induces a salt accumulation that strongly alters the porosity (decrease from 23% to 8.06%) and the permeability (decrease from 1350 mD to 1.2 mD). The sample is plugged in 7 hours. This simulation case shows that the plugging of a permeable rock can be caused by the combination of the drying and a brine supply coming from a low-permeability rock that contains enough volume of mobile brine.

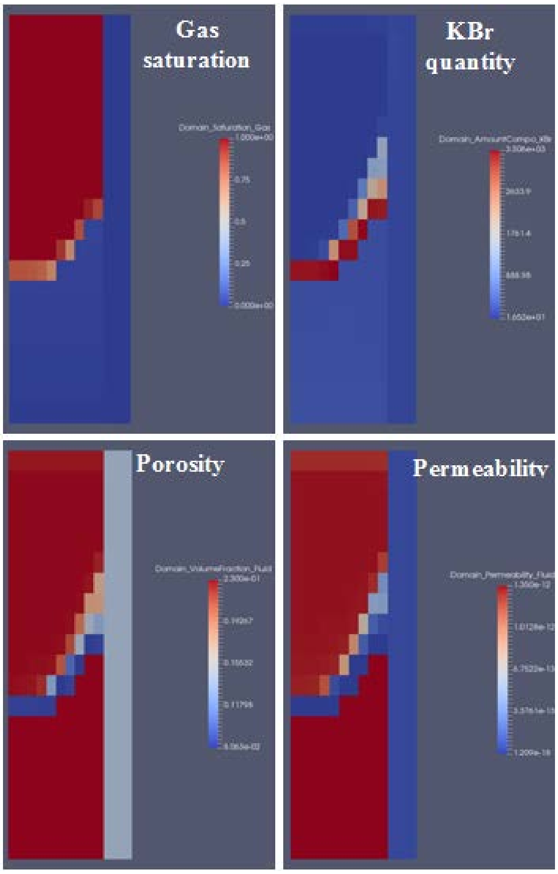

**Fig. 21** 2D map simulation results of gas saturation, KBr quantity, porosity and permeability within the sample at 25 hours for Exp 4. The low permeable zone representing the Moliere is on the left zone of the maps.

## 5. CONCLUSIONS

In this study, we have shown the importance and interplay of different parameters that govern brine drying and salt precipitation in porous media subject to dry gas injection. When dry gas is injected in a sample saturated with brine, the water is dried out near the inlet first and then a drying front propagate toward the outlet. As a consequence, salt precipitates in the porous media and can lead to pore plugging. The pore plugging will either completely block the pore space or heavily reduce the rock permeability depending on the boundary conditions.

Indeed, the experimental study showed that dry gas injection combined with a capillary water contact can trigger salt precipitation and possibly block the pore space. These experiments establish the basis for simulation models that can be used to integrate the different physical phenomena that take place during water displacement, evaporation and possibly precipitation.

Results from the experimental study have been modeled using an in-house simulator to interpret the drying and salt precipitation mechanisms. The governing equations consider various coupled mechanisms like flow-through drying, capillary forces, salt displacement, salt precipitation and porosity/permeability alteration. This reactive transport model succeeded in simulating the main effects observed in experimental cases:

- drying of the sample by dry gas injection, and salt precipitation
- salt accumulation supplied by capillary re-imbibition until plugging of the sample,
- successive alteration and improvement cycles of the petrophysical properties due to precipitation and dissolution of salt.

Future work includes:

- improving the simulation approach by integrating
    - modeling of hysteresis in the drainage/imbibition curves of relative permeability and capillary pressure,
    - modeling of the capillary pressure evolution with porosity,
    - modeling of the thermal transfer due to evaporation,
- investigating the effect of other parameters like pressure gradient, salt concentration and/or gas relative humidity to assess the induced risk of salt precipitation on permeability alteration,
- adaptation and application of the model to near well and reservoir scale problems. In particular, radial flow conditions imply rapidly changing pressure gradients close to wellbore, contrary to the uniform pressure gradient characterizing linear flow in a core.

## 6. References

1. W. Kleinitz, G. Dietzsch, and M. Köhler, "Halite scale formation in gas-producing wells," Chemical Engineering Research and Design, vol. 81, no. 3, pp. 352-358, 2003.
2. P. M. Aquilina, "Impairment of gas well productivity by salt plugging: A review of mechanisms, modeling, monitoring methods, and remediation techniques," in SPE Annual Technical Conference and Exhibition, 2012: Society of Petroleum Engineers.
3. J. Mahadevan, M. M. Sharma, and Y. C. Yortsos, "Flow-through drying of porous media," AIChE journal, vol. 52, no. 7, pp. 2367-2380, 2006.
4. J. Mahadevan, M. M. Sharma, and Y. C. Yortsos, "Water removal from porous media by gas injection: experiments and simulation," Transport in Porous Media, vol. 66, no. 3, pp. 287-309, 2007.
5. Y. Peysson, B. Bazin, C. Magnier, E. Kohler, and S. Youssef, "Permeability alteration due to salt precipitation driven by drying in the context of CO2 injection," Energy Procedia, vol. 4, pp. 4387-4394, 2011.
6. Y. Peysson, L. André, and M. Azaroual, "Well injectivity during CO2 storage operations in deep saline aquifers—Part 1: Experimental investigation of drying effects, salt precipitation and capillary forces," International Journal of Greenhouse Gas Control, vol. 22, pp. 291-300, 2014.
7. D. Le, H. Hoang, and J. Mahadevan, "Impact of capillary-driven liquid films on salt crystallization," Transport in porous media, vol. 80, no. 2, p. 229, 2009.
8. T. Giorgis, M. Carpita, and A. Battistelli, "2D modeling of salt precipitation during the injection of dry CO2 in a depleted gas reservoir," Energy Conversion and Management, vol. 48, no. 6, pp. 1816-1826, 2007.
9. L. André, Y. Peysson, and M. Azaroual, "Well injectivity during CO2 storage operations in deep saline aquifers–Part 2: Numerical simulations of drying, salt deposit mechanisms and role of capillary forces," International Journal of Greenhouse Gas Control, vol. 22, pp. 301-312, 2014.
10. S. Youssef, M. Mascle, Y. Peysson., O. Vizika "CAL-X: An X-Ray Radiography tool for high throughput coreflood experimentation. Applications in the EOR context," in International symposium of SCA, 2017: Society of core analysist.
11. O. Gassara, A. Estublier, B. Garcia, S. Noirez, A. Cerepi, C. Loisy, O. Le Roux, A. Petit, L. Rossi, S. Kennedy, T. Brichart, P. Chiquet, L. Luu Van Lang, F. André Duboin, J. Gance, B. Texier, Lavielle, B. Thomas, "The Aquifer-CO2 Leak project: numerical modeling for the design of a CO2 injection experiment in the saturated zone of the Saint-Emilion", to be submitted.

# Steady-State Two-Phase Flow in Porous Media: Laboratory Validation of Flow-Dependent Relative Permeability Scaling

*Marios S.* Valavanides[1,*], *Matthieu* Mascle[2], *Souhail* Youssef[2] and *Olga* Vizika[2]

[1]Civil Engineering Department, University of West Attica, 12243 Attica, Greece
[2]IFP Energies Nouvelles, Rueil-Malmaison, France

**Abstract.** The phenomenology of steady-state two-phase flow in porous media is recorded in SCAL relative permeability diagrams. Conventionally, relative permeabilities are considered to be functions of saturation. Yet, this has been put into challenge by theoretical, numerical and laboratory studies that have revealed a significant dependency on the flow rates. These studies suggest that relative permeability models should include the functional dependence on flow intensities. Just recently a general form of dependence has been inferred, based on extensive simulations with the DeProF model for steady-state two-phase flows in pore networks. The simulations revealed a systematic dependence of the relative permeabilities on the local flow rate intensities that can be described analytically by a universal scaling functional form of the actual independent variables of the process, namely, the capillary number, *Ca*, and the flow rate ratio, *r*. In this work, we present the preliminary results of a systematic laboratory study using a high throughput core-flood experimentation setup, whereby SCAL measurements have been taken on a sandstone core across different flow conditions -spanning 6 orders of magnitude on *Ca* and *r*. The scope is to provide a preliminary proof-of-concept, to assess the applicability of the model and validate its specificity. The proposed scaling opens new possibilities in improving SCAL protocols and other important applications, e.g. field scale simulators.

## 1. Introduction

The conventional use of saturation as the independent variable in two-phase flow in *porous media* (PM) is based on the oversimplifying assumption that disconnected fluidic elements of the *non-wetting phase* (NWP) (ganglia and droplets) do not move with the average flow but remain stranded in the pore medium matrix. This situation arises when flow conditions of 'relatively small values' of the capillary number are maintained. In those cases the disconnected NWP fluidic elements block part of the available flow cross-section by a fraction analogous to the average saturation and effect a relative reduction of the permeability of both the NWP and the *wetting phase* (WP). Nevertheless, there is ample experimental evidence that disconnected flow is a substantial and sometimes prevailing flow pattern [1-8].

Treating relative permeabilities as functions of the saturation is inefficient in providing a correct and specific-enough description of the process across the domain of all possible flow conditions. The issue is extensively discussed in [9]. A particular value in saturation does not necessarily imply that a unique disconnected structure (arrangement) of the NWP will settle-in. Disconnected structures of the NWP can be coarsely described by a spectrum of population density distributions, extending from distributions of 'many-and-small' fluidic elements (droplets and small ganglia) to 'fewer-and-larger' fluidic elements (small and large ganglia). For any one of those cases, the corresponding superficial velocity of the disconnected NWP would not necessarily attain the same value. The latter would be the result of the 'negotiation' between the two factors inhibiting the transport of each phase, i.e. viscosity and capillarity, over the mass and momentum balances. Moreover, this 'negotiation' takes place within the 'regulatory framework' conformed by two critical 'stakeholders' or 'regulators', namely the particular structure of the PM and the externally imposed, flow conditions.

The term 'structure of the PM' comprises some appropriate, modeling ensemble of geometric /topologic characteristics of the pore network (dimensionality, genus, tortuosity, pore geometry etc.) as well as a set of physicochemical characteristics of the N/W/PM system, pertaining to- or associated with- *wettability* or to the favoring of interstitial, *emulsion* type flows. Wettability may be accounted by the values of the *static* contact angles of the N/W (NWP/WP) menisci against the pore walls. In that context, wettability conforms to the combination of the NWP, WP and PM surface characteristics and tripartite physicochemical affinities, as well as to *hysteresis*, expressed by the difference between the *dynamic receding* and *advancing* contact angles, pertaining to the motion of N/W menisci during drainage or imbibition of the WP within pores [10, 14].

---

[*] Corresponding author: marval@uniwa.gr

Flow conditions have an adverse effect on the momentum balance and, in particular, on the relevant magnitude of the Stokes flow resistances (due to bulk viscosity of the NWP and WP) and to Young-Laplace resistances (due to the contact forces between the N/W menisci and the pore walls). The former depend on local (micro /pore scale) velocity gradients (rates of deformations), in contrast to the latter that are relatively independent of rates of displacement of the menisci. From an energy point of view, the power dissipation due to bulk viscosity scales with the square of the local velocity gradients, whereas the capillarity-induced dissipation scales with the rates of displacement of the menisci. At relatively low values of the flow intensity (superficial velocity) viscosity effects are insignificant to capillarity effects; as flow intensity is progressively increased, viscosity takes over from capillarity and the flow progressively mutates from capillarity-dominated to transient capillary-viscosity- to viscosity-dominated characteristics [9].

As a consequence, for any two different cluster configurations (any two different population density distributions) of disconnected phase, the effective permeabilities of the WP and the NWP would differ and, therefore, the corresponding values of the relative permeability to the NWP would be different. Yet, those different cluster configurations (population distributions) and different values of the relative permeability could -in general- correspond to the same saturation value. In such situations, a universal, saturation-dependent description of the flow would be weak.

In addition, during core analysis, saturation is measured indirectly and cannot be externally imposed directly; it is only through control of a combination of pressure difference and/or flow rate of the NWP or WP that the system will attain an average saturation. If one wants to consistently and systematically describe the process in the entire flow regime (extending across extreme values in the capillary number and the viscosity ratio), one has to consider those variables that describe the externally imposed conditions and contain macroscopic *kinematic* information, e.g. the superficial velocity of each phase or, equivalently, the capillary number and the flow rate ratio. Moreover, saturation cannot adequately (or uniquely) describe the flow conditions. This is because saturation alone brings no definite input to the momentum balance, therefore it is questionable if it can provide any information on the *kinetics* of the macroscopic flow.

Observations of single phase flows within pore networks confirm that the macroscopic pressure gradient scales linearly with the superficial fluid velocity (Darcy's law). This seems to be a quite trustworthy modeling consideration in the case of two-phase flow as well, but only when very high superficial velocities are considered and capillary forces are negligible. However, at moderate/low velocities, when capillary forces are comparable to viscous forces, the macroscopic pressure gradient does not scale linearly with the flow rate. Experimental studies on steady-state two-phase flows in glass beads [3, 5, 6], in glass bead columns [11], as well as in sand-pack columns [12], revealed that the non-linear relation between pressure gradient and flow rate can be described by generic power laws with different exponent values. The discrepancy between the values of the scaling exponents is attributed to differences associated with dimensionality of the pertinent variables, measurements pertaining to different flow conditions, dimensionality of the NWP/WP/PM system etc. Therefore, it is worth the effort to examine if these 'different' observations can be integrated in a universal power law relating appropriate, dimensionless variables of the process.

To this end, a first attempt in deriving a universal scaling functional form describing the flow dependency of relative permeability was recently proposed [13]. It is based on the results stemming from systematic, extensive simulations spanning 5 orders of magnitude in both the capillary number and flow rate ratio, implementing the DeProF model algorithm, build around a hybrid, true-to-mechanism, stochastic scale-up model for steady-state two-phase flows in pore networks [14].

The objective of the present work is three-fold:

(a) to examine the applicability of the proposed scaling on the basis of using typical R/SCAL measurements;

(b) to verify the existence, uniqueness and form of the locus of critical flow conditions, an inherent characteristic of such processes in terms of energy efficiency (see next section and [9]);

(c) to examine the potential of the proposed scaling and the underlying theoretical framework, in revealing the flow structure and/or network structure characteristics of any set of R/SCAL measurements (R/SCAL forensics).

To do so we have used a set of SCAL measurements on a typical sandstone core. Data were collected over a grid of specially selected flow conditions, spanning across up to 5 orders of magnitude on *Ca* and up to 10 orders on *r*. The laboratory study was performed independently, i.e. prior to the publication of the recently proposed flow-dependent relative permeability scaling; in that sense it can be characterized as a "blind study". With respect to (b), the existence of critical flow conditions (CFCs) has been already verified in an extensive review of published R/SCAL relative permeability diagrams [15]; nevertheless, verification of the universal form of the locus of CFCs proposed in [9] was lacking a laboratory verification using the same core and across a broad domain of flow conditions (*Ca* and *r*).

The paper deploys in 3 sections. We start by providing the basic modeling assumptions for concurrent, immiscible, steady-state two-phase flows in porous media and present the basic structure of the proposed, flow-dependent relative permeability scaling. We continue with describing the SCAL experiments we have tapped-on (methods and materials). Then, we present the results of the laboratory examination and associated raw data calculations. Finally, we discuss "points of agreement/disagreement" between scaling predictions and actual measurements and we draw conclusions on the applicability of the proposed scaling or its potential exploitation in SCAL technology.

## 2. Basic Theoretical Background

Consider the simultaneous, one-dimensional concurrent flow of a non-wetting phase (NWP, index n) and a wetting phase (WP, index w) across a porous medium control surface, $\tilde{A}$, at flow rates equal to $\tilde{q}_n$ and to $\tilde{q}_w$ respectively. (A tilde ~ is used to indicate a dimensional variable, no tilde indicates a dimensionless variable.) The phenomenological fractional flow Darcy relations that describe the steady-state, fully developed process, whereby the pressure gradient, $(\Delta\tilde{p}/\Delta\tilde{z})$, is common in both fluids ([9], Appendix I), are given by eqn (1)

$$\tilde{U}_i = \frac{\tilde{q}_i}{\tilde{A}} = \frac{\tilde{k}}{\tilde{\mu}_i} k_{ri} \left(\frac{\Delta\tilde{p}}{\Delta\tilde{z}}\right) \quad , \qquad i = n, w \qquad (1)$$

In one-dimensional flow under steady-state conditions, especially when the flow is fully developed, the common pressure gradient in both phases can be expressed in reduced form as

$$x = \frac{\Delta\tilde{p}/\Delta\tilde{z}}{(\Delta\tilde{p}/\Delta\tilde{z})^{1\Phi}} = \frac{\Delta\tilde{p}/\Delta\tilde{z}}{\tilde{\gamma}_{nw} Ca/k} = \frac{\Delta\tilde{p}}{\Delta\tilde{z}} \frac{\tilde{k}}{\tilde{\mu}_w \tilde{U}_w} = \frac{1}{k_{rw}} \qquad (2)$$

where
$(\Delta\tilde{p}/\Delta\tilde{z})^{1\Phi}$ is the pressure gradient corresponding to an equivalent saturated one-phase flow ($1\Phi$) of the WP at the same superficial velocity ($\tilde{U}_w$).
*Ca* is the capillary number, conventionally defined as

$$Ca = \tilde{\mu}_w \tilde{U}_w / \tilde{\gamma}_{nw} \qquad (3)$$

$\tilde{\mu}_w$ is the viscosity of the WP and $\tilde{\gamma}_{nw}$ is the NWP/WP interfacial tension.

In eqn (2) the actual pressure gradient is divided by the pressure gradient of an equivalent one-phase flow of water at superficial velocity equal to $\tilde{U}_w$ (the 2nd component of the product). Note that, by definition, it is straightforward to verify that the reduced pressure gradient is essentially the inverse of the relative permeability of the WP.

The set of superficial velocities in eqn (1) may be appropriately reduced and replaced by a set of dimensionless variables, namely, the capillary number, *Ca*, as defined previously in eqn (3), and the N/W flow rate ratio,

$$r = \tilde{q}_n / \tilde{q}_w = \tilde{U}_n / \tilde{U}_w \qquad (4)$$

At steady-state conditions in one-dimensional flow, the flow rate ratio, *r*, is equal to the mobility ratio, $r_\lambda$. The equivalence, expressed in the first part of eqn (5), is a conjecture resulting from direct flow analysis (see Appendix I in [9]).

$$r = \frac{U_n}{U_w} \equiv \frac{1}{\kappa} \frac{k_{rn}}{k_{rw}} = r_\lambda \quad \Leftrightarrow \quad k_{rn} = \kappa r k_{rw} \qquad (5)$$

where

$$\kappa = \tilde{\mu}_n / \tilde{\mu}_w \qquad (6)$$

is the NWP/WP bulk viscosity ratio.

Eqn (5) is very useful, as we may easily recover the $r_i$ value pertaining to any pair *i* of measured $\{k_{rn}, k_{rw}\}_i$ values from a conventional (saturation dependent) relative permeability diagram. We may also recover a relative permeability by knowing the values of the other relative permeability and the flow rate ratio. Therefore, switching to the approach of flow-dependency may be readily applicable as all conventional relative permeability diagrams can still be used.

The conjecture that both fluids share a common pressure gradient, eqn (1), is also based on experimental evidence. In particular, eqn (5), i.e. the direct result of assuming a common pressure gradient, is verified by experiment. When measured values of flow rate ratio are plotted against calculated values of mobility ratio, they align on a straight line. Ample experimental evidence is provided in a recent work whereby ~180 relative permeability diagrams pertaining to steady-state conditions for a variety of N/W/PM systems have been reviewed [15]. The conjecture proves to be valid also in the present work, see the diagrams in **Fig. 7**. Because of the common pressure gradient [eqn (1)] and the equivalence between flow rate ratio and mobility ratio [eqn (5)], relative permeability curves intersect at a fixed value of the flow rate ratio, the so-called cross-over flow rate ratio value, $r_x$. The latter is reciprocal to the viscosity ratio, $r_x = (1/\kappa)$, as provided by eqn (5). This inherent characteristic of steady-state flows is universally observed in all relative permeability vs flow rate ratio diagrams ([9], [15] and **Fig. 7**).

In the line of the present work we will also analyze the results from an energy efficiency perspective. In this context, we will use the reduced (normalized) measure of the energy efficiency of the process, considered as the flow rate of the NWP per unit of total hydraulic power spent, or equivalently, provided externally to the N/W/PM system (say by the “pumps”), to maintain two-phase flow (an essentially dissipative process) at any set of externally imposed flow conditions, *Ca* and *r*. The associated energy utilization factor, or energy efficiency index, $f_{EU}$, can be readily calculated in terms of macroscopic measurements [9], as

$$f_{EU} = \frac{k_{rn}}{\kappa(r+1)} = \frac{r k_{rw}}{r+1} = \frac{r}{x(r+1)} \qquad (7)$$

For every fixed value of the capillary number, *Ca*, there exists a single value of the flow rate ratio, *r**, for which the energy efficiency index, $f_{EU}^*$, attains a maximum value [9, 15]. Moreover, for every N/W/PM system, a unique locus of energy efficiency maxima is formed, $r^*(Ca)$. Flow conditions matching the $r^*(Ca)$ locus are called *critical flow conditions* (*CFCs*). Critical flow conditions can be measured and identified by R/SCAL. The efficiency index provides a strong flow analysis and characterization tool [9].

Closing this passage, we need also to address the issue of selecting and using the flow rate ratio, *r*, instead of the fractional flow of the WP, $f_w$, as one of the two independent variables of the process – the other being the capillary number, *Ca*. In the core analysis community the applicable standard is to refer to one of the fractional flow of the WP, $f_w$. Switching between *r* and $f_w$ (or $f_n$) is readily provided through the transformation $f_w = r/(1+r)$. The use of the flow rate ratio, *r*, instead of the fractional flow, $f_w$, as independent variable, has the advantage of a more convenient description of the sought physical process, especially (or at least) around the critical flow conditions, whereby the identification of the critical flow rate ratio, $\log r^*(Ca)$, becomes more evident and obvious. The implications in using $f_w$, or $f_n$, instead of *r* are extensively discussed in [15**]**. As a general observation all energy efficiency diagrams ($\{r, f_{EU}\}_i$) show a more uniformly smooth trend irrespective of the particular values of the system parameters and flow conditions examined in that review.

## 2.1 Prediction of Steady-State Relative Permeabilities

The mechanistic model *DeProF* for immiscible, steady-state two-phase flow in pore networks may be used to predict the reduced macroscopic pressure gradient, *x*, given the flow conditions and system properties. The model is based on the concept of decomposition in prototype flows, hence the acronym *DeProF*. It takes into account the pore-scale mechanisms and the sources of non-linearity caused by the motion of interfaces, as well as other complex, network-wide cooperative effects, to estimate the conductivity of each class of pore unit cells in a statistical sense. It implements effective medium theory with appropriate expressions for pore-to-macro scale consistency for NWP and WP mass transport, to derive an implicit algebraic relation invoking the macroscopic pressure gradient, the capillary number, *Ca*, the flow rate ratio, *r*, the viscosity ratio, $\kappa$, the dynamic advancing and receding contact angles, $(\theta_A, \theta_R)$ (wettability), and a set of parameters that describe the geometrical, topological and structural characteristics of the pore network, $\mathbf{x}_{pm}$ [14].

Using the *DeProF* model, one can obtain the solution to the problem of steady-state two-phase flow in porous media in the form of the following transfer function,

$$x = x(Ca, r; \kappa, \theta_A, \theta_R, \boldsymbol{x_{pm}}) \qquad (8)$$

Implementation of the DeProF model is possible when analytical expressions of the pore network geometry are plausible and general expressions for the cell conductivities can be calculated for all possible flow configurations. In general, this is not the case for real porous media, but only for a certain class of model pore networks with analytically tractable pore geometry. Yet, one can benefit by scanning entire domains of flow conditions at relatively short times and therefore get a systematic and consistent overview of the behavior of the flow across orders of magnitude on flow conditions. In that context, DeProF can be used as a virtual,large core SCAL simulator.

In a recent work, extensive simulations implementing the *DeProF* algorithm have been carried out to derive maps that describe the dependence of the flow structure on the independent flow variables, namely the capillary number, *Ca*, and the flow rate ratio, *r*, or, equivalently, to the reduced, superficial velocities of NWP and WP [14]. The simulations span 5 orders of magnitude in *Ca* $(-9 \le \log Ca \le -4)$ and *r* $(-2 \le \log r \le 2)$ over sufficiently fine steps. Fluid systems with various viscosity ratios (9 in total), have been examined.

Indicative DeProF model predictions of the reduced pressure gradient, *x*, are presented in **Fig. 1** for a typical NWP/WP/PM system with viscosity ratio $\kappa = 1.5$. The diagrams furnish the projections of the $x_{ij}(Ca_i, r_j)$ predicted values on many constant-log$Ca_i$ planes in (a) and constant-log$r_j$ planes in (b). In that context, markers are connected into iso-*Ca* and iso-*r* groups.

Referring to **Fig. 1**(a), at the high-end of the log*r* domain, all curves pertaining to constant-*Ca* values tend to bundle and align asymptotically to the straight (dashed) line. The corresponding functional form, eqn (9), states that at sufficiently large *Ca* values the reduced pressure gradient becomes a linear function of the flow rate ratio, with the linearity constant equal to the viscosity ratio, $\kappa = 1.5$.

$$\text{As } r \to \infty, \quad \log x = \log\kappa + \log r \quad \Leftrightarrow \quad x = \kappa r \qquad (9)$$

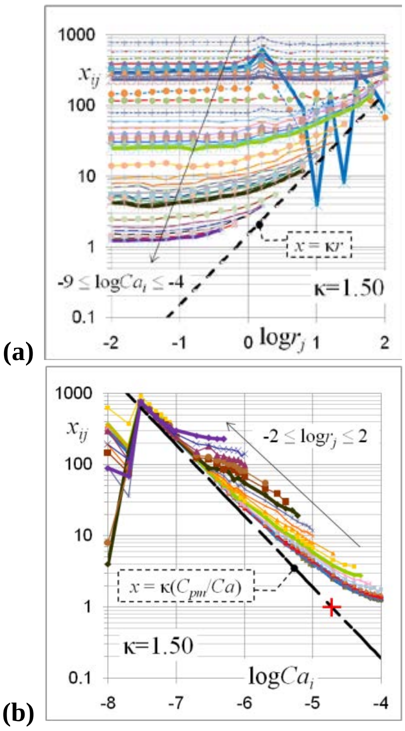

**Fig. 1** Reduced pressure gradient values, *x*, for different values, **(a)** of the capillary number, *Ca*, and **(b)** of the flow rate ratio, *r*. Both diagrams pertain to a typical value of the viscosity ratio, $\kappa = 1.5$ function

We may observe a similar trend in **Fig. 1**(b). At the low-end of the *Ca* domain, all iso-*r* curves tend to bundle and align asymptotically to a straight line, also illustrated with a dashed line. Now the functional form is given by the expression, up to a constant value, $C_{pm}$, associated to the N/W/PM system [13].

$$\log Ca \ll 0, \ \log x = \log\kappa - \log C_{pm} - \log Ca \ \Leftrightarrow x = \kappa/(C_{pm} Ca) \qquad (10)$$

### 2.2 Universal Functional Form of Relative Permeabilities

Based on these simulations it was possible to derive a universal function that can describe the dependence of the DeProF model predicted values $x_{ij}(Ca_i, r_j)$ of the reduced pressure gradient for different values of the capillary number, *Ca*, and the flow rate ratio, *r*, by the universal scaling form [13],

$$x(\log Ca, \log r) = A(\log Ca) + \kappa r \tag{11}$$

where the functional $A(\log Ca)$ may be determined by any fitting procedure. The set of ($A_i$, $Ca_i$) values is plotted on the diagram of **Fig. 2**. The cross-markers are lined-up against two straight line asymptotes; one with negative inclination and the other coinciding with the horizontal axis; these meet at an oblate angle.

We may fit the set of $(\log Ca_i, \log A_i)$ values by a function of the form,

$$\log Ca = \log Ca_0 + C_0/(\log A)^2 - C_3 \log A \tag{12}$$

where $-1/C_3$ is the gradient of the inclined asymptote, and $\log Ca_0$ is the abscissa of the intersection of the two asymptotes and coefficient $C_0$ is a measure of the overall distance (approach) to the two asymptotes (the higher this value, the greater the distance of the apex of the swarm of markers to the asymptotes' intersection).

The coefficients values pertaining to the particular NWP/WP/PM model system (examined in the DeProF simulations) are: $C_3 = 1.1474$, $\log Ca_0 = -4.3$, and $C_0 = 0.003$. The thick red line is the curve log*A*(log*Ca*) that has been fitted to the raw data log$A_i$ using eqn (12). Note, eqn (12) is an implicit function of log*A* in terms of log*Ca*. In particular, it is a cubic equation of log*A*, which can be solved analytically to provide an explicit analytical expression $\log A(\log Ca/Ca_0\,; C_0, C_3)$.

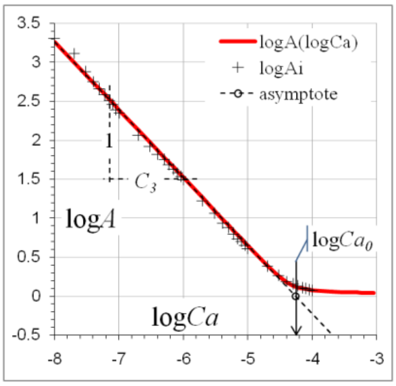

**Fig. 2** Kernel function values *A*, in terms of *Ca*. Cross-markers indicate values (log$A_i$, log$Ca_i$) of the kernel function used in eqn (11), calculated to fit the DeProF predicted data, **Fig. 1**(b). These have been fitted by the thick red line, using eqn (12). The black dashed line is an asymptote with gradient (-1/$C_3$).

Using the analytical expressions from eqs (11) and (12) with the aforementioned coefficient values, we may plot the reduced pressure gradient in terms of *Ca* and *r*, $x(\mathrm{Ca}, r)$. Comparing the diagrams of **Fig. 2** to those of in **Fig. 1**, we observe that the DeProF predicted values $x_{ij}(Ca_i, r_j)$ are recovered with great specificity, and that the trend at extreme flow conditions, maintains its physically-true characteristics (NWP flow is decoupled to the WP flow). Similar plots for other systems can be found in [13].

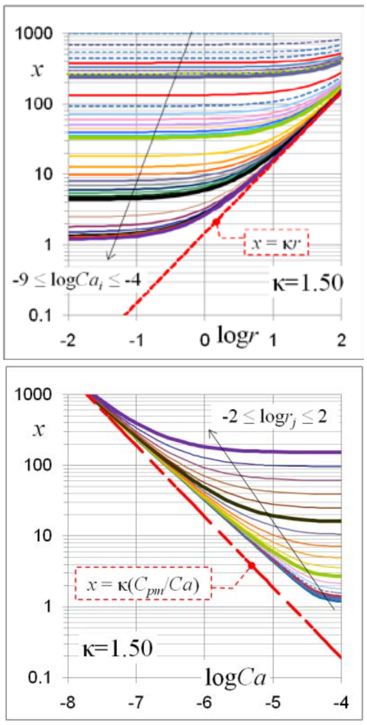

**Fig. 3** Plots of the reduced pressure gradient values, *x*, in terms of the flow conditions, *Ca* and *r*. based on eqs (11) and (12); **(a)** iso-*Ca* curves; **(b)** iso-*r* curves.

We also need to stress here that the particular form/shape of the kernel function log*A*(log*Ca*) produced in Fig. 2, as well as the form of eqn (12), come as a result of fitting the log$A_i$ values produced by the DeProF model simulations of a NWP/WP/PM system of intermediate wettability. Yet, the system we examined in the laboratory is water wet. To this end, it needs to be investigated if we may implement the same type of functional form for the kernel function [as eqn (12)] or we will have to derive a different one.

## 3. Laboratory Materials and Methods

A set of SCAL measurements was ran on a typical sandstone core, over a grid of specially selected flow conditions (88 in total), spanning across ~6 orders of magnitude on *Ca* and ~6 orders on *r*.

### 3.1 Rock samples and fluids

Sample used in this work is water-wet outcrop sandstone from a Clashach quarry, with porosity of 13% and mean permeability of 672 mD. Sample was cored with a diamond core drill with 1 cm internal diameter and cut to a length of 2 cm. After being cored, the sample was dried in an oven for at least 48 hours at a temperature of 60 °C.

Two-phase flow measurements were conducted using synthetic dodecane oil and brine at 5 g/l NaCl (Sodium Chloride) for the low to intermediate capillary number. Viscosity at 20°C were respectively for oil and brine 1.5 cp and 1.07 cp. Interfacial tension was measured at $\tilde{\gamma}_{nw} = 50\mathrm{mN/m}$. For intermediate to high capillary number, i.e. for 1 g/lt of SDBS (sodium dodecyl-benzene-sulfonate) was added to the brine to lower the interfacial tension to 1% of the original, i.e. to $\tilde{\gamma}_{nw} = 0.5\mathrm{mN/m}$. According to Graue *et al* [16], Clashach sandstone exhibits an Amott index of 0.45 which is typical of strongly water wet rock. During our experiments we have checked that the sample do not spontaneously imbibe oil.

### 3.2 Experimental set-up and procedure

Two phase flow measurements were conducted using the CAL-X set-up that has been recently designed for high throughput core-flood experimentation [17]. It is composed of an X-ray radiography facility, a fully instrumented multi-fluid injection platform and a dedicated X-ray transparent beryllium core holder. The local and averaged saturation $S_w$ is derived from the radiographs, captured every 10 seconds, using Beer-Lambert law for multi-material.

Steady State Method (SSM) was used to derive relative permeability. The SSM method involves the injection of both fluids at the inlet of the plug while measuring the differential pressure and the saturation within the core. Eqn (1) can be solved analytically if capillary pressure gradient is constant and end effects are neglected. This condition can be assessed when fluids are injected at high flow rate. Yet, these assumptions as well as laminar flow (i.e Reynolds number less than 10) have to be confirmed. Laminar condition is verified since a linear relation between flow rate and pressure drop is respected in mono-phasic injection. To validate the constant capillary pressure gradient and negligible capillary end effect, we verify that the saturation at steady state condition is uniform along the sample, see example on **Fig. 4**.

The core has been systematically flooded, by successive cycles of drainage and imbibition at practically constant values of the nominal capillary number, $N_{Ca}$, defined over total flow and average viscosity as

$$N_{Ca} = \left(\tilde{U}_n + \tilde{U}_w\right)\left(\tilde{\mu}_n + \tilde{\mu}_w\right)/(2\tilde{\gamma}_{nw}) \tag{13}$$

The diagram in **Fig. 5** illustrates a map of the broad range of scanned flow conditions – spanning across 5 orders of magnitude over $Ca$ and 10 orders of magnitude over $r$. Markers connected with lines group successive cycles of drainage /imbibition, at nominal capillary number values, $N_{Ca}$, as indicated in the legend.

Note, $Ca$ is defined by eqn (3) whereas $N_{Ca}$ is defined by eqn (13). Therefore,

$$N_{Ca}/Ca = (1 + r)\,(1 + \kappa)/2 \tag{14}$$

In total, 14 cycles of drainage and imbibitions have been run and 88 measurements have been taken. The source data measurements are presented in Table 1.

**Table 1** The 88 source data measurements taken for each of the 14 cycles of drainage and imbibitions type injections of the core floods. The panel on the left is for high-IFT set-up, the panel on the right for low-IFT set-up.

| Cycle | Type | <$N_{Ca}$> [×10$^{-6}$] | k [md] | WP | NWP | IFT [mN/m] | $q_n$ [cc/min] | $q_w$ [cc/min] | $S_w$ [-] | $\Delta p$ [mbar] |
|---|---|---|---|---|---|---|---|---|---|---|
| 01 | 1st Dr | 0.54 | 620 | 5 g/l NaCl | Dodecane | 50 | 0.00001 | 0.097 | 0.98 | 11 |
| | | | | | | | 0.002 | 0.088 | 0.67 | 64 |
| | | | | | | | 0.048 | 0.044 | 0.55 | 98 |
| | | | | | | | 0.105 | 0.00001 | 0.28 | 80 |
| 02 | 1st I | 0.54 | | | | | 0.0934 | 0.00001 | 0.28 | 80 |
| | | | | | | | 0.073 | 0.021 | 0.4 | 124 |
| | | | | | | | 0.048 | 0.045 | 0.49 | 153 |
| | | | | | | | 0.004 | 0.091 | 0.51 | 199 |
| | | | | | | | 0.00001 | 0.097 | 0.52 | 192 |
| 03 | 2nd Dr | 0.56 | | | | | 0.00001 | 0.097 | 0.555 | 191 |
| | | | | | | | 0.028 | 0.091 | 0.545 | 189 |
| | | | | | | | 0.046 | 0.046 | 0.492 | 164 |
| | | | | | | | 0.072 | 0.021 | 0.452 | 130 |
| | | | | | | | 0.092 | 0.004 | 0.389 | 97 |
| | | | | | | | 0.096 | 0.00001 | 0.27 | 82 |
| 04 | 1st Im | 5.55 | 823 | | | | 1 | 0.00001 | 0.19 | 174 |
| | | | | | | | 0.929 | 0.044 | 0.345 | 407 |
| | | | | | | | 0.736 | 0.246 | 0.42 | 587 |
| | | | | | | | 0.488 | 0.491 | 0.46 | 670 |
| | | | | | | | 0.239 | 0.736 | 0.48 | 722 |
| | | | | | | | 0.04 | 0.933 | 0.51 | 682 |
| | | | | | | | 0.00001 | 0.974 | 0.53 | 653 |
| 05 | 2nd Dr | 5.58 | | | | | 0.00001 | 0.974 | 0.54 | 650 |
| | | | | | | | 0.043 | 0.933 | 0.52 | 695 |
| | | | | | | | 0.246 | 0.736 | 0.5 | 713 |
| | | | | | | | 0.501 | 0.49 | 0.473 | 712 |
| | | | | | | | 0.746 | 0.245 | 0.441 | 629 |
| | | | | | | | 0.946 | 0.046 | 0.384 | 400 |
| | | | | | | | 0.99 | 0.00001 | 0.23 | 180 |
| 06 | 1st Dr | 5.60 | 521 | | | | 0.00001 | 0.998 | 0.964 | 97 |
| | | | | | | | 0.046 | 0.932 | 0.75 | 403 |
| | | | | | | | 0.245 | 0.735 | 0.65 | 561 |
| | | | | | | | 0.502 | 0.491 | 0.574 | 630 |
| | | | | | | | 0.748 | 0.237 | 0.51 | 612 |
| | | | | | | | 0.944 | 0.046 | 0.415 | 435 |
| | | | | | | | 0.996 | 0.00001 | 0.225 | 243 |
| 07 | 1st Im | 5.57 | | | | | 0.996 | 0.00001 | 0.225 | 243 |
| | | | | | | | 0.942 | 0.045 | 0.39 | 430 |
| | | | | | | | 0.743 | 0.244 | 0.464 | 726 |
| | | | | | | | 0.496 | 0.49 | 0.505 | 871 |
| | | | | | | | 0.232 | 0.733 | 0.525 | 876 |
| | | | | | | | 0.041 | 0.93 | 0.55 | 828 |
| | | | | | | | 0.00001 | 0.982 | 0.561 | 760 |
| 08 | 2nd Dr / | 5.56 | | | | | 0.00001 | 0.982 | 0.572 | 760 |
| | | | | | | | 0.041 | 0.932 | 0.561 | 811 |
| | | | | | | | 0.236 | 0.734 | 0.533 | 945 |
| | | | | | | | 0.486 | 0.49 | 0.504 | 890 |
| | | | | | | | 0.742 | 0.243 | 0.46 | 817 |
| | | | | | | | 0.947 | 0.043 | 0.387 | 500 |
| | | | | | | | 0.994 | 0.00001 | 0.19 | 245 |

| Cycle | Type | <$N_{Ca}$> [×10$^{-6}$] | k [md] | WP | NWP | IFT [mN/m] | $q_n$ [cc/min] | $q_w$ [cc/min] | $S_w$ [-] | $\Delta p$ [mbar] |
|---|---|---|---|---|---|---|---|---|---|---|
| 09 | 1st Dr | 55.17 | 693 | 5g/l NaCl + 1 g/l SDBS | Dodecane | 0.5 | 0.00001 | 0.98 | 0.98 | 86 |
| | | | | | | | 0.0044 | 0.093 | 0.58 | 58 |
| | | | | | | | 0.048 | 0.047 | 0.385 | 183 |
| | | | | | | | 0.099 | 0.00001 | 0.14 | 40 |
| 10 | 1st Im | 55.35 | | | | | 0.099 | 0.00001 | 0.14 | 40 |
| | | | | | | | 0.094 | 0.004 | 0.15 | 576 |
| | | | | | | | 0.074 | 0.022 | 0.211 | 390 |
| | | | | | | | 0.049 | 0.048 | 0.311 | 180 |
| | | | | | | | 0.005 | 0.093 | 0.413 | 56 |
| | | | | | | | 0.00001 | 0.098 | 0.431 | 28 |
| 11 | 2nd Dr / | 56.02 | | | | | 0.00001 | 0.098 | 0.43 | 28 |
| | | | | | | | 0.005 | 0.093 | 0.421 | 32 |
| | | | | | | | 0.026 | 0.073 | 0.41 | 51 |
| | | | | | | | 0.05 | 0.047 | 0.35 | 105 |
| | | | | | | | 0.074 | 0.022 | 0.25 | 385 |
| | | | | | | | 0.096 | 0.004 | 0.172 | 746 |
| | | | | | | | 0.104 | 0.00001 | 0.165 | 82 |
| 12 | 1st Dr | 558.12 | 823 | | | | 0.00001 | 0.988 | 0.974 | 86 |
| | | | | | | | 0.041 | 0.937 | 0.9 | 108 |
| | | | | | | | 0.236 | 0.74 | 0.729 | 230 |
| | | | | | | | 0.493 | 0.494 | 0.47 | 506 |
| | | | | | | | 0.74 | 0.247 | 0.234 | 1170 |
| | | | | | | | 0.94 | 0.048 | 0.143 | 1449 |
| | | | | | | | 0.99 | 0.00001 | 0.122 | 250 |
| 13 | 1st Im | 558.11 | | | | | 0.98 | 0.00001 | 0.122 | 255 |
| | | | | | | | 0.937 | 0.0439 | 0.125 | 1572 |
| | | | | | | | 0.739 | 0.239 | 0.191 | 1340 |
| | | | | | | | 0.494 | 0.493 | 0.41 | 520 |
| | | | | | | | 0.247 | 0.744 | 0.624 | 270 |
| | | | | | | | 0.048 | 0.935 | 0.738 | 134 |
| | | | | | | | 0.00001 | 0.994 | 0.783 | 105 |
| 14 | 2nd Dr | 558.69 | | | | | 0.00001 | 0.995 | 0.787 | 105 |
| | | | | | | | 0.049 | 0.935 | 0.746 | 133 |
| | | | | | | | 0.236 | 0.739 | 0.639 | 267 |
| | | | | | | | 0.493 | 0.494 | 0.437 | 530 |
| | | | | | | | 0.74 | 0.247 | 0.2 | 1350 |
| | | | | | | | 0.935 | 0.048 | 0.111 | 1599 |
| | | | | | | | 0.99 | 0.00001 | 0.11 | 280 |

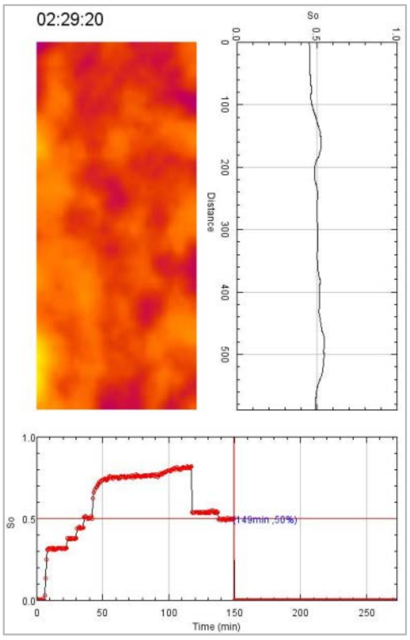

**Fig. 4** Example of real-time saturation monitoring: 2D saturation map (upper left) and corresponding saturation profile (upper right); evolution of mean saturation as a function of time (low central)

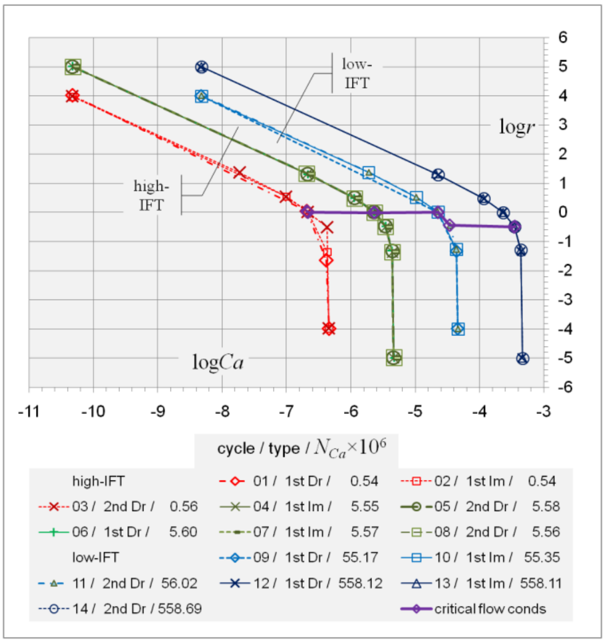

**Fig. 5** Mapping of the 88 imposed flow conditions scanned during the 14 core-floods. Markers connected with lines are grouped into successive cycles of drainage/imbibitions, at constant values of the nominal capillary number, $N_{Ca}$, as indicated in the legend.

## 4. Results and discussion

Pairs of NWP and WP relative permeability values $\{k_{rn}, k_{rw}\}_i$, were computed using eqn (1) for each measurement $i$ $(i = 1, 88)$. These were then drawn into standard relative permeability diagrams in terms of the WP saturation, $S_{wi}$, for each one of the 14 different core flood cycles (or iso-$N_{Ca}$ groups). These diagrams are not presented here because of space limitation. For the record, they have been merged into a single diagram, see **Fig. 6**(a). No evidence of grouped correlations between $k_{rn}$, $k_{rw}$ and $S_w$ is observed (as expected). Yet, the picture becomes more clear when values of relative permeabilities, $\{k_{rn}, k_{rw}\}_i$, are plotted against corresponding values of the flow rate ratio, $r_i$. The diagram in **Fig. 6** (b) is the result of merging the corresponding source diagrams in **Fig. 7**.

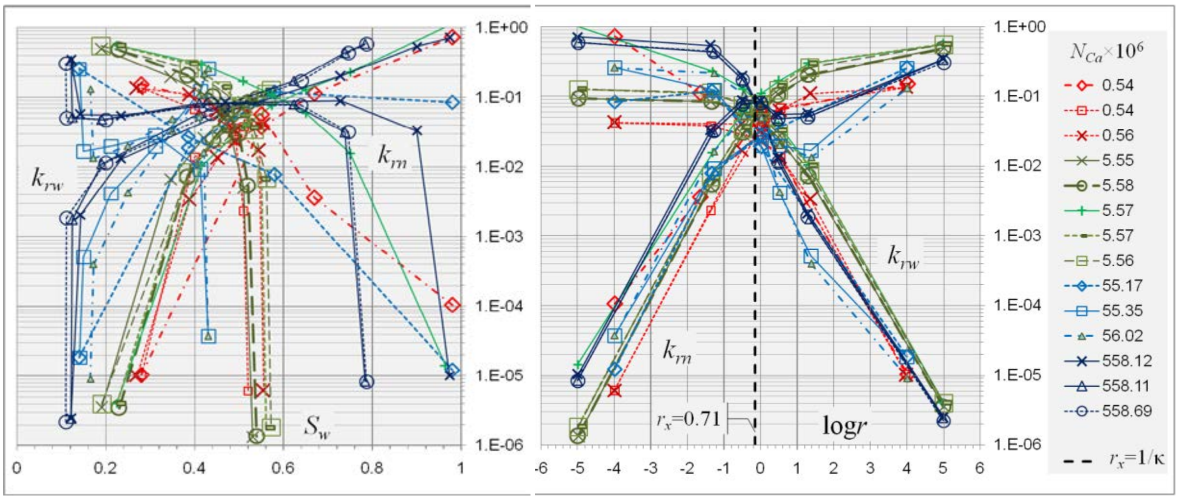

**(a)** **(b)**

**Fig. 6** Core-flood measured relative permeabilities, $k_{rn}$, $k_{rw}$, against corresponding mean values of WP saturation, $S_w$. **(a)** and flow rate ratio values, log$r$ **(b)**. In both diagrams, a total of 88 markers connected with lines are grouped into 14 successive cycles of drainage /imbibition, at constant values of the nominal capillary number, $N_{Ca}$, as indicated in the legend.

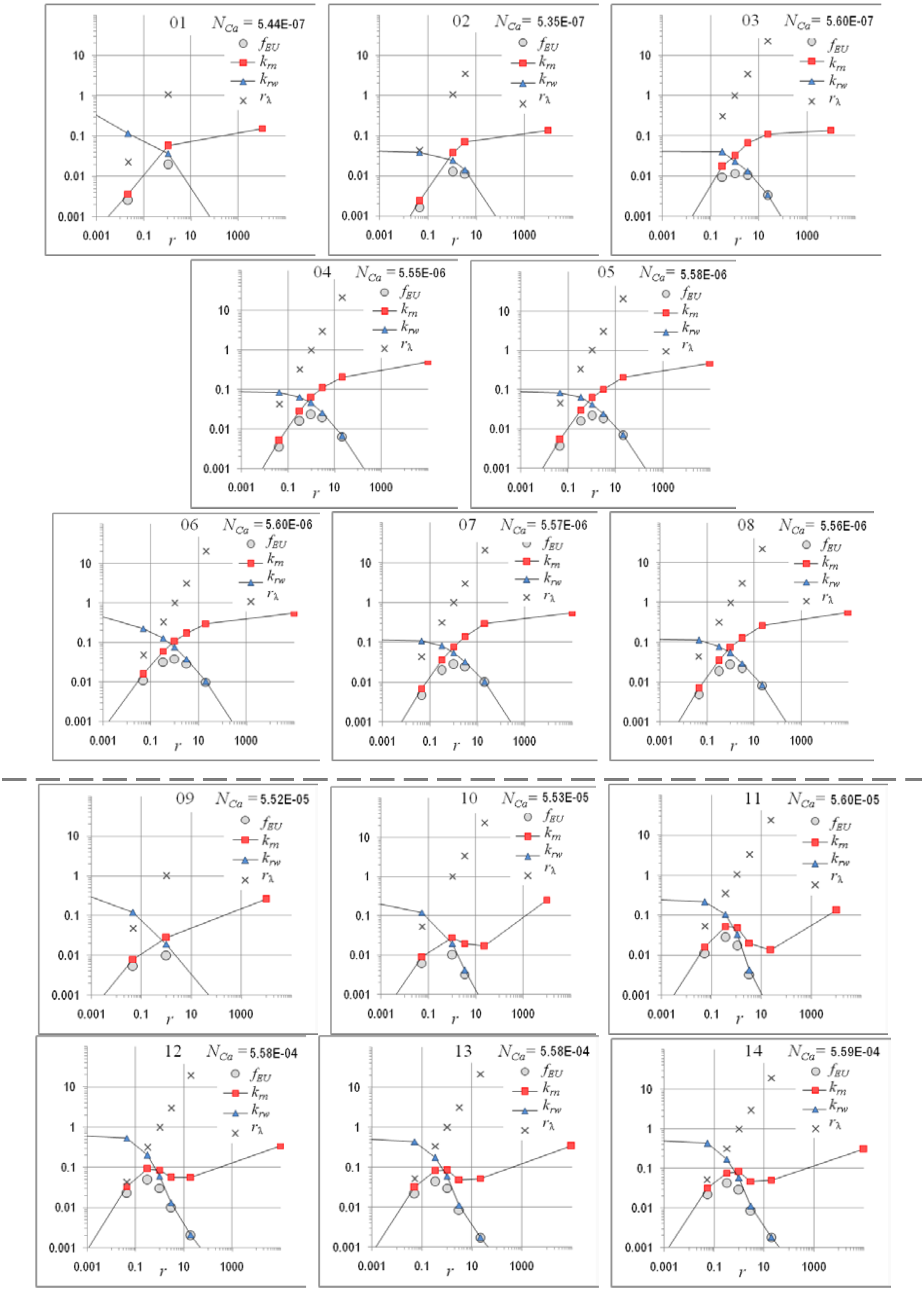

**Fig. 7** Measured values of relative permeabilities, $k_{rw}$ (▲) and $k_{rn}$ (■), mobility ratio, $r_\lambda$ (×) and energy efficiency, $f_{EU}$ (○) against flow rate ratio values, $r$, for the 88 different steady-state flow conditions imposed during the 14 core floods (see **Fig. 5**). Diagrams 01-08 (above the dashed line) pertain to high IFT (50 mN/m) core-floods whereas 09-14 to low-IFT (0.5 mN/m) floods.

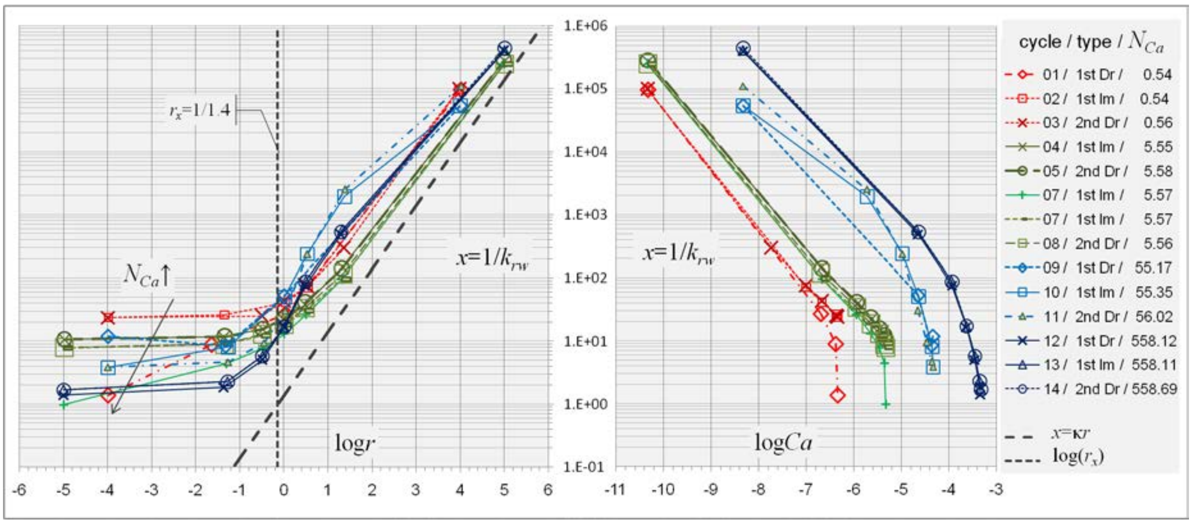

**(a)** **(b)**

**Fig. 8** Reduced pressure gradient values, *x*, measured during the core-floods. Data markers are organized in iso-$N_{Ca}$ groups. **(a)** Dashed inclined line indicates the asymptotic line for flow decoupling provided by eqn (9). **(b)** Data group markers are clustered into two formations, each pertaining to a value of the interfacial tension (IFT = 50 mN/m (left cluster) and 0.5 mN/m (right cluster).

## 4. Results and discussion

Pairs of NWP and WP relative permeability values $\{k_{rn}, k_{rw}\}_i$, were computed using eqn (1) for each measurement $i$ $(i = 1,\ 88)$. These were then drawn into standard relative permeability diagrams in terms of the WP saturation, $S_{wi}$, for each one of the 14 different core flood cycles (or iso-$N_{Ca}$ groups). These diagrams are not presented here because of space limitation. For the record, they have been merged into a single diagram, see **Fig. 6**(a). No evidence of grouped correlations between $k_{rn}$, $k_{rw}$ and $S_w$ is observed (as expected).

Yet, the picture becomes more clear when values of relative permeabilities, $\{k_{rn}, k_{rw}\}_i$, are plotted against corresponding values of the flow rate ratio, $r_i$. The diagram in **Fig. 6** (b) is the result of merging the corresponding source diagrams in **Fig. 7**.

Note, in the latter diagrams (**Fig. 7**), measured values of the actual flow rate ratio, *r* [eqn (4)], and the calculated mobility ratio, $r_\lambda$ [eqn (5)], are aligned along a straight line with gradient 1. Therefore, the conjecture of common pressure gradient in both fluids, as well as the transformation expressed in eqn (5), because of the underlying equivalence between $r$ and $r_\lambda$, are also verified. Note, in **Fig. 6**(b) and **Fig. 7**, all pairs of NWP and WP relative permeability curves intersect at the, so-called, cross-over flow rate ratio value, $r_x = (1/\kappa)$, eqn (5). That value is indicated by the black short-dash line at $\log r_x = -\log(\kappa)$ in **Fig. 6** (b).

Reduced pressure gradient values, *x*, calculated as the reciprocal to the WP relative permeability, $k_{rw}$, [eqn (2)], are presented in **Fig. 8**. The diagram in **Fig. 8** (a) presents data values in terms of log*r*, classified into 14 iso-$N_{Ca}$ groups. The general trend is similar to that provided by the proposed functional form, eqs (11) and (12), **Fig. 1** and **Fig. 3**. Note, with increasing *r*, the asymptotic trend aligns to the dashed inclined line to a virtually decoupled flow state, as provided by eqn (9).

In **Fig. 8** (b) reduced pressure gradient values, *x*, in terms of log*Ca* are also presented in iso-$N_{Ca}$ groups. The groups are clearly clustered into two formations (or "islands"). Each pertains to core floods performed with the same fluids but under different interfacial tensions (Section 3.1). The cluster on the left pertains to an interfacial tension (IFT) value $\tilde{\gamma}_{nw} = 50\mathrm{mN/m}$, while the cluster on the right (higher $N_{Ca}$) to an IFT reduced by 1%, $\tilde{\gamma}_{nw} = 0.5\mathrm{mN/m}$. On the high-*Ca* region the trend is different when compared to that observed in the diagram of **Fig. 1**(b) [also **Fig. 3** (b)]. Specifically, the mild and progressive drop of the *x* values, as flow conditions shift to high-*Ca* regimes, contradicts the smooth but very steep (abrupt) drop of the pressure gradient measured in the core-floods (**Fig. 8**). Moreover, we may distinguish two similar behaviors. In the high-IFT set-up (left cluster, groups 01- 08) the drop in *x* observed at increasing values of *Ca* is steeper when compared to the low-IFT set-up. In that same set-up (groups 09-11 and 12-14) the drop in *x* is progressive, yet its onset is practically independent of the $N_{Ca}$. We will comment on this later on.

Using eqn (11), for every pair $\{x, r\}_i,\ i = 1, 88$ of the measured values, we may calculate a corresponding $A_i$ value for each flow condition imposed during the core-floods. The $A_i$ values are plotted in terms of log$Ca_i$ values on the diagram in **Fig. 9**. Comparing with **Fig. 2**, we observe the same differences in the trend (drop) of the $A_i$ values at high-*Ca* regimes. The trend in **Fig. 9** is similar to that observed in **Fig. 8**(b). Note, also, data markers of the high-IFT set-up are aligned within a narrow band in the low-*Ca* regime, in contrast to the high-IFT set-up where markers are aligned to a wider band. The gradients of these bands in the low-*Ca* regime, could be considered as a "system identity" (compare with **Fig. 2**).

The overall trend indicates a drop of the effect of capillary forces at high-*Ca* regimes. The cause may probably be associated to interstitial, emulsion type flow, setting-in at high-*Ca* flow conditions.

Fitting the $A_i$ data using the functional form expressed by eqn (12) does not succeed in capturing the trend at the high-*Ca* regime. An expression describing more consistently the trend at the high-*Ca* regime is

$$\log A = A_0\left(1-\frac{|log(Ca/Ca_0)|}{|log(Ca_m/Ca_0)|}\right)^{\frac{1}{n}} - C_g \log\frac{Ca}{Ca_0} \qquad (15)$$

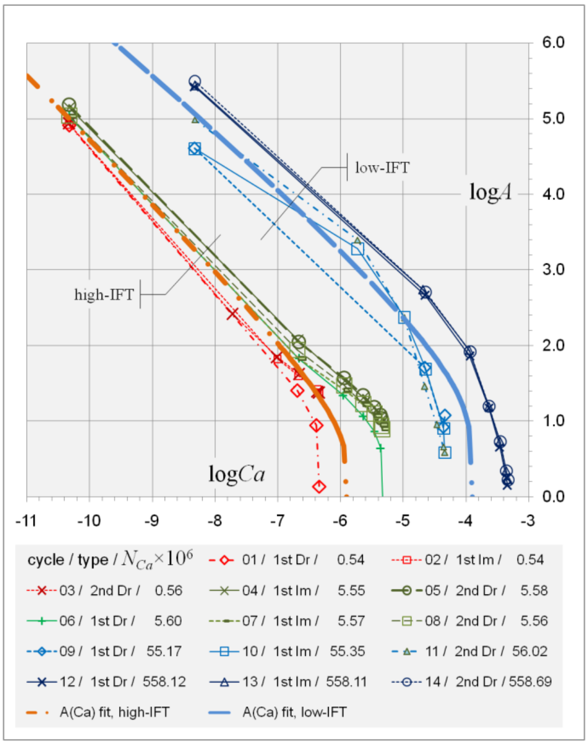

**Fig. 9** The log*A* values in terms of log*Ca*, calculated from the core-flood data using eqn (11). The continuous orange dash-dotted line fits high-IFT data, the blue dashed line fits low-IFT data, both using eqn (15).

The orange dash-dotted and the blue dashed lines fit the high-IFT and low-IFT data (**Fig. 9**). Coefficient values of the two fitting curves are presented in **Table 2**.

**Table 2.** Values of the log*A* fitting expressions coefficients

| IFT | $A_0$ | $\log Ca_m$ | $\log Ca_0$ | $C_g$ | $n$ |
|---|---|---|---|---|---|
| High | 1.7 | -13 | -5.9 | 0.78 | 5 |
| Low | 2.4 | -11 | -3.9 | 0.65 | 5 |

We may now compare the dissimilar trends at high-*Ca* regimes between the DeProF model predictions for a system of intermediate wettability, eqn (12), and the water wet system examined in the core-floods, eqn (15). To reveal any latent systematic trend and eventually get a better image of the interstitial flow structure, we have further investigated energy efficiency aspects of the core-floods within the particular N/W/PM system.

The diagram in **Fig. 10**(a) provides the map of the *critical flow conditions* (CFCs) identified from the core floods. The diagram is actually a blow-up of the central part of the diagram in **Fig. 5** -focusing on the layout of the CFCs. The line connecting the CFCs attains a clearly formed S-shape, consistent to the *r**(*Ca*) shape of the CFC locus on the universal energy efficiency map illustrated in [9] (cf. reference Figure 6 and 7). The dashed red horizontal line indicates the *nominal* value of the critical flow rate ratio for fully viscous flow conditions (as $Ca \to \infty$). Provided the viscosity ratio value of the examined N/W system [9], this CFC *nominal* value is estimated to be $r^*_\infty = 1/\sqrt{\kappa} = 0.845$ ($\log r^*_\infty = -0.073$). The *actual value* attained within the lower part of the S-shape form, indicates an asymptotic trend ($Ca \to \infty$) towards $r^*_\infty \cong 0.32$. ($\log r^*_\infty = -0.496$).

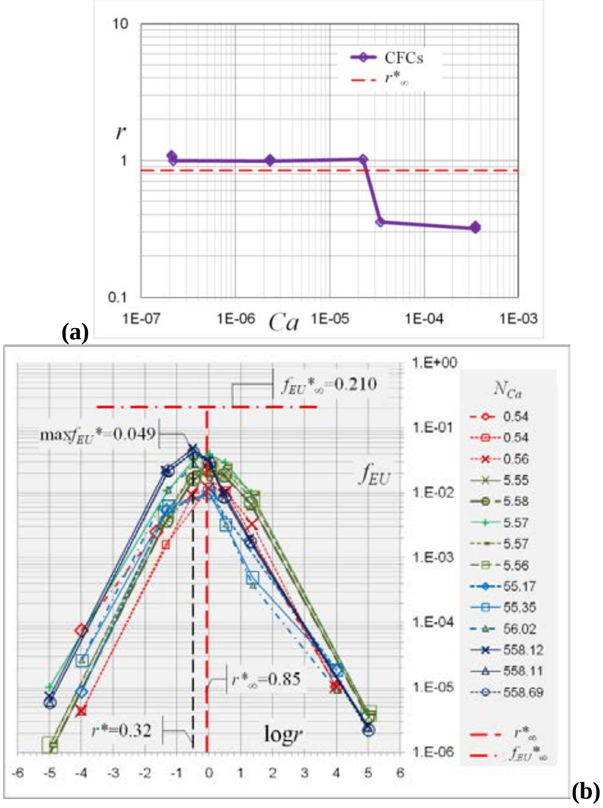

**Fig. 10** Energy efficiency characteristics of the examined core-floods. **(a)** Detected critical flow conditions for various values of the capillary number, *r**($N_{Cai}$), attaining an S-shape form. The diagram is a blow-up of the diagram in **Fig. 5**. **(b)** Energy efficiency values attained in terms of the flow rate ratio, *r*, grouped in iso-$N_{Ca}$ core floods.

We may further examine the energy efficiency characteristics of the core floods, presented in the diagram of **Fig. 10**(b). The dash-dotted red horizontal line indicates the *nominal* value of the maximum attainable energy efficiency for the particular N/W system, the "ceiling of efficiency", toping at $f^*_{EU\infty} = 1/\left(1+\sqrt{\kappa}\right)^2 = 0.2096$ as $Ca \to \infty$ (cf. eqn (30) in [9]), expected to be met at $r^*_\infty = 1/\sqrt{\kappa} = 0.845$ ($\log r^*_\infty = -0.073$). Yet, the energy efficiency of the examined core floods reached an *actual* maximum value, $\max f^*_{EU} = -0.049$, at $r \cong 0.32$ ($\log r = -0.496$). It is obvious that the *actual* values of energy efficiency attained at large *Ca*, are rather low when compared to the nominal, maximum values pertaining to the particular N/W system.

Overall, the observed differences are associated to high-*Ca* flow conditions. This strange behavior may be correlated to two factors favoring the setting of emulsion type flow: wettability (the examined system is 100% water wet) and emulsification, affecting the structure of the interstitial flow(s). The aforementioned nominal values ($r^*_\infty, f^*_{EU\infty}$) are estimated considering the ideal case of minimization of capillarity effects at very large *Ca* values (see eqn (30) and Appendix II in [9]). In that modeling approach, capillarity effects are mainly attributed to the net Young-Laplace resistances at the contact lines, when menisci migrate downstream, by taking into account the hysteresis between the dynamic advancing and receding contact angles of menisci. If the flow intensities (superficial velocities) are large, power dissipation due to viscosity resistances prevails over power dissipation due to capillarity hysteresis –as the former depends quadratically on flow intensity, whereas the latter linearly. In that situation the flow is decoupled of capillarity effects and a nominal value of the flow rate ratio maximizing the energy efficiency can be estimated analytically (assuming a rather oversimplifying modeling hypothesis of negligible menisci resistances, [9]), as $r_\infty^* = 1/\sqrt{\kappa}$.

Nevertheless, in reality, e.g. during core floods in R/SCAL measurements, the NWP may disconnect in tiny droplets. (This is also taken into account in the DeProF model simulations albeit the system is of intermediate wettability.) The onset of emulsification is not only due to the reduction of the interfacial tension between the NWP and the WP, but also due to the pore scale flow dynamics and the pore network characteristics [18]. In general, there are two classes of emulsion flows in porous media depending on the size of the drops compared to the capillary throat diameter. For emulsions with smaller drops, the extra-pressure drop does not vary with capillary number and it is a function of the viscosity ratio, dispersed phase concentration and drop size distribution. For emulsions with larger drops, these may partially block the capillaries, leading to higher extra pressure differences at low capillary numbers [1, 19]. Likewise, part of the NWP droplet population may pass through larger throats without contacting the pore walls. In that case a significant fraction of the NWP flows free of contact-line resistances. The associated energy cost is reduced, allowing for a shifting of the critical flow rate ratio to lower values in order to reduce also the power dissipation due to the bulk viscosity of the NWP [9].

Moreover, in water-wet systems, the hysteresis effects are pronounced due to the large differences occurring between receding and advancing dynamic contact angles that, in turn, burden the flow with substantial capillarity-induced resistances at the low-*Ca* regimes. Nevertheless, there is a cut-off limit in pore scale velocities above which lubricating-films are formed and capillarity induced resistances may drop significantly. This is expressed as the steep drop in reduced pressure gradient values pertaining to the examined core-floods systems.

## 5. Conclusions

We have performed a preliminary assessment/validation of the specificity and applicability of a new flow-dependent relative permeability scaling law that takes explicitly into account capillarity effects. Flow dependency is associated to the flow intensities of the NWP and WP or, equivalently to the capillary number of the WP, *Ca*, and the NWP/WP flow rate ratio, *r*. The proposed scaling is built around a kernel function, log*A*(log*Ca*), that provides a “transitioning bridge” between the decoupled character of the flow at the two extreme flow regimes (low-*Ca*/low-*r* to high-*Ca*/high-*r* flows). The validation was based on a set of 14 core-floods of a typical water-wet sandstone and for a variety of flow conditions spanning across 5 orders of magnitude on *Ca* and 10 orders of magnitude on *r*.

The results suggest that it is possible to derive and implement universal, true-to-mechanism functions of flow-dependent relative permeabilities. The critical step here is to guess or data-fit an appropriate form of the kernel function, log*A*(log*Ca*). The latter is associated to the complex character of the NWP/WP/PM system rheology manifesting itself across the entire *Ca* domain.

The specificity /applicability of the proposed scaling is substantial and deserves further investigation, mainly towards understanding the universal structure of the kernel function log*A*(log*Ca*). Because of the structure of the scaling, eqn (11), the mode of decaying of log*A* at high-*Ca* regimes, whether expressed by eqn (12) or eqn (15), is equally applicable and depends on the physicochemical properties of the N/W/PM system, e.g. wettability. The critical property of the kernel function should be a monotonous decay at the high-*Ca* regime.

Implementing the proposed flow-dependency analysis it was possible to get a consistent and well structured view of the flow in the examined core-floods. The calculated values of reduced quantities (reduced pressure gradient, kernel function) show a *consistent dependency on flow conditions* and can be used to reveal the underlying flow mechanisms. In particular, considering the physicochemical properties of the two fluids, the results suggest that emulsion type flow settles-in above a threshold value of the capillary number. This threshold value depends on the flow conditions and the interfacial tension between the two fluids.

Reviewing the present work in terms of reaching its objectives, we may conclude:

(a) Implementation of the proposed scaling is possible using typical R/SCAL measurements; moreover it was possible to rely on superficial measurements only, i.e. flow rates of the two phases, pressure drop across the core length, IFT, absolute permeability.

(b) the existence, uniqueness and form of the locus of critical flow conditions, *r**(*Ca*), was confirmed. The S-shape type, confined between two asymptotic lines, $r_0^*$ and $r_\infty^*$ as proposed in [9] is also confirmed. Differences between nominal (expected) and actual (measured) values, of $r_\infty^*$ and $f_{EU\infty}^*$, are justified on the basis of the induced emulsification of the flow occurring at very high *Ca* values. In order to reveal the S-shaping in greater detail, in follow-up studies the flow conditions should be finely scanned /tuned in proximity to the transition zone of the CFC locus.

(c) By implementing the proposed scaling and considering the underlying mechanisms of the interstitial flows, it was possible to explain the flow behavior as described by the macroscopic measurements. That was possible by examining the structure of the WP relative permeability, $k_{rw}$, and of the kernel function *A*, without any need to examine the flow at the pore scale using sophisticated equipment. Therefore, the proposed scaling could potentially serve as an additional tool for quality assessment of measurements (R/SCAL forensics).

Based on the results of this preliminary assessment, it would make sense to consider designing and deploying a systematic laboratory to investigate and reveal the effects of wettability, pore network structure, core size, etc. on the form of $A(\log Ca)$. The scope would be to improve R/SCAL protocols, and develop more robust and accurate macroscopic scale models.

The authors thank the reviewers for their constructive comments. MSV acknowledges partial support by the Research Council of Norway through its Centres of Excellence funding scheme, project number 262644.

## References

1. C.T. Tsakiroglou, D.G. Avraam, A.C. Payatakes, “Transient and steady-state relative permeabilities from two-phase flow experiments in planar pore networks”, *Adv. Wat. Res.*, vol. 30, pp. 1981–1992, 2007, doi:10.1016/j.advwatres.2007.04.002
2. V.R. Guillen *et al.*, “Capillary-driven mobility control in macro emulsion flow in porous media”, *Int. J. Multiphase Flow*, vol. 43, pp. 62-65, 2012, doi:10.1016/j.ijmultiphaseflow.2012.03.001
3. K.T. Tallakstad *et al.*, “Steady-State Two-Phase Flow in Porous Media: Statistics and Transport Properties”, *Phys. Rev. Let.*, vol. 102, 074502, pp. 1-4, 2009, doi:10.1103/PhysRevLett.102.074502
4. A. Georgiadis *et al.*, “Pore-scale micro-computed-tomography imaging: Nonwetting-phase cluster-size distribution during drainage and imbibition”, *Phys. Rev. E*, vol. 88, 033002, pp. 1-9, 2013, doi:10.1103/PhysRevE.88.033 002
5. O. Aursjo *et al.*, “Film flow dominated simultaneous flow of two viscous incompressible fluids through a porous medium”, *Frontiers in Physics*, vol. 2, no. 63, pp. 1-9, 2014, doi:10.3389/fphy.2014.00063
6. S.S. Datta, T.S. Ramakrishnan, D.A. Weitz, “Mobilization of a trapped non-wetting fluid from a three-dimensional porous medium”, *Phys. Fluids*, vol. 26, 2014, 022002, 2014, doi:10.1063/1.4866641
7. R. Oughanem *et al.*, “A Multi-Scale Investigation of Pore Structure Impact on the Mobilization of Trapped Oil by Surfactant Injection” *Transp. Porous Media* vol. 109, pp. 673-692, 2015, doi:10.1007/s11242-015-0542-5
8. R.T. Armstrong, J.E. McClure, M.A. Berrill, M. Rücker, S. Schlüter, S. Berg, “Beyond Darcy’s law: The role of phase topology and ganglion dynamics for two-fluid flow”, *Phys. Rev. E*, vol. **94**, 043113, 2016, doi: 10.1103/PhysRevE.94.043113
9. M.S. Valavanides, “Review of Steady-State Two-Phase Flow in Porous Media: Independent Variables, Universal Energy Efficiency Map, Critical Flow Conditions, Effective Characterization of Flow and Pore Network”, *Transp. in Porous Media*, vol. 123, no. 1, pp. 42-99, 2018, doi:10.1007/s11242-018-1026-1
10. R.E. Hinkley, M.M. Dias, A.C. Payatakes, “On the motion of oil ganglia in porous media”, *PhysicoChemical Hydrodynamics*, vol. **8**, no.2, pp. 185-211, 1987
11. S. Sinha *et al*, “Effective Rheology of Two-Phase Flow in Three-Dimensional Porous Media: Experiment and Simulation”, *Transp. in Porous Media*, vol. 119, no. 1, pp. 77-94, 2017, doi:10.1007/s11242-017-0874-4
12. C.D. Tsakiroglou *et al.*, “Steady-state two-phase relative permeability functions of porous media: A revisit”, *Int. J. Multiphase. Flow*, vol. 73, pp. 34–42, 2015, doi:10.1016/j.ijmultiphaseflow.2015.03.001
13. M.S. Valavanides, “Universal, Flow Dependnet Relative Permeability Scaling for Steady-State Two-Phase Flows in Porous Media”, SCA2018-066, in *Int. Symp. of the Society of Core Analysts*, Trondheim, Norway, Aug. 27-30, 2018, pp.1-9
14. M.S. Valavanides, “Oil Fragmentation, Interfacial Surface Transport and Flow Structure Maps for Two-Phase Flow in Model Pore Networks. Predictions Based on Extensive, DeProF Model Simulations”, *Oil Gas Sci. Tech.*, vol. 73, no.6, pp. 1-36, 2018, doi:10.2516/ogst/2017033
15. M.S. Valavanides, E. Totaj, M. Tsokopoulos, “Energy efficiency characteristics in steady-state relative permeability diagrams of two-phase flow in porous media”, *J. Pet. Sci. Eng.*, vol. 147, pp. 181-201, 2016, doi:10.1016/j.petrol.2016.04.039
16. A. Graue *et al*, “Imaging Fluid Saturation Development in Long-Core Flood Displacements”, SPE 17438-PA, in *Proc. SPE 58th California Regional Meeting*, Long Beach, California, 1988, pp. 363-372, doi:org/10.2118/17438-PA
17. S. Youssef, M. Mascle, O. Vizika., “High Throughput Coreflood Experimentation as a Tool for EOR Project Design”, SPE-190166-MS, in *SPE Improved Oil Recovery Conf.*, Tulsa, Oklahoma, USA, 14-18 April, 2018
18. E. Unsal, M. Broens, R.T. Armstrong, “Pore Scale Dynamics of Microemulsion Formation”, *Langmuir*, vol. 32, pp. 7096-7108, 2016, doi: 10.1021/acs.langmuir.6b00821
19. S. Cobos, M.S. Carvalho, V. Alvarado, “Flow of oil–water emulsions through a constricted capillary”, *Int. J. Multiphase Flow*, vol. 35, pp. 507-515, 2009, doi: 10.1016/j.ijmultiphaseflow.2009.02.018

# Improved method for complete gas-brine imbibition relative permeability curves

*M. Ben* Clennell[1,*], *Cameron* White[1], *Ausama* Giwelli[1], *Matt* Myers[1], *Lionel* Esteban[1], *Michael* Cullingford[2], *William* Richardson[3], *Gavin* Ward[2], *Matt* Waugh[2], *Scott* Cole[2], *Ashley* Hunt[2] and *Peter* Bright[2§]

[1]CSIRO Energy, Australian Resources Research Centre, Kensington, Western Australia 6076
[2]Chevron Australia, QV1, 250 St George's Terrace Perth, Western Australia, 6000.
[3]Chevron Energy Technology Centre, 3901 Briarpark Drive, Houston, Texas 77042 USA

**Abstract.** Standard test methods for measuring imbibition gas-brine relative permeability on reservoir core samples often lead to non-uniform brine saturation. During co-current flow, the brine tends to bank up at the sample inlet and redistributes slowly, even with fractional flow of gas to brine of 400:1 or more. The first reliable Rel Perm point is often only attained after a brine saturation of around $S_w$=40% is achieved, leaving a data gap between $S_{wirr}$ and this point. The consequent poor definition of the shape of the Rel Perm function can lead to uncertainty in the performance of gas reservoirs undergoing depletion drive with an encroaching aquifer or subjected to a water flood. We have developed new procedures to pre-condition brine saturation outside of the test rig and progress it in small increments to fill in the data gap at low $S_w$, before continuing with a co-current flood to the gas permeability end-point. The method was applied to series of sandstone samples from gas reservoirs from the NW Shelf of Australia, and a Berea standard. We found that the complete imbibition relative permeability curve is typically 'S' shaped or has a rolling over, convex-up shape that is markedly different from the concave-up, Corey Rel Perm curve usually fitted to SCAL test data. This finding may have an economic upside if the reservoir produces gas at a high rate for longer than was originally predicted based on the old Rel Perm curves.

## 1 Introduction

When using standard, best-practice SCAL testing methods for measurement of imbibition gas-brine relative permeability on reservoir core samples, e.g., as recommended by McPhee et al. [1], it is very difficult to establish a uniformly progressing brine saturation. This difficulty in establishing stable co-current flow conditions leads to poor definition of the shape of the Rel Perm function at lower brine saturations when gas has the highest mobility.

Typically, during co-current flow with forced imbibition of brine along with gas, the saturation within the sample does not advance uniformly along the sample length but will bank up at the inlet end of the sample (Figure 1). The brine largely builds up by spontaneous imbibition from the restricted supply available and owing to low $k_{rw}$ it takes hours or days for brine to redistribute along the sample length, even with high fractional flow of gas to brine of 400:1 or more. Moreover, the first reliable co-current gas-brine relative permeability point (stable differential pressure and uniform saturation) is often only attained after a brine saturation of $S_w$=40% or more is achieved, leaving a significant data gap between $S_{wirr}$ and this point (Figure 2).

The data in Figure 2 can be interpolated with a concave-up Corey function curve [2], but this may be incorrect. The lack of valid data can lead to questionable inputs to (and outputs of) reservoir simulation models and flow on to uncertainty in the performance of gas reservoirs undergoing depletion drive with an encroach-

**Fig. 1.** Berea sandstone sample taken from test rig at the early stage of an imbibition Rel Perm measurement using standard, co-current SCAL methods. A large brine bank has formed at the inlet that blocks the permeability to gas.

---

[*] Corresponding author: Ben.Clennell@csiro.au [§] Present Address: BHP Petroleum, 125 St George's Terrace, Perth W.A. 6000.

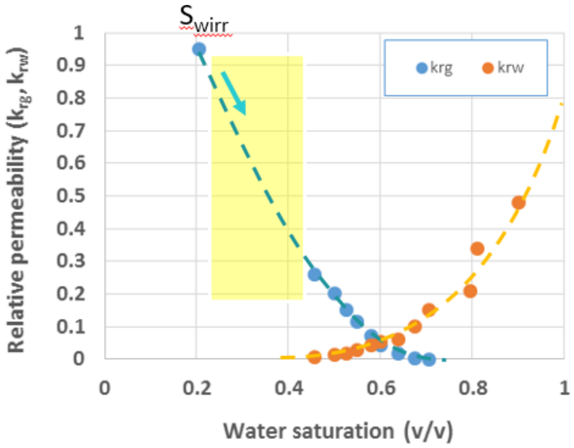

**Fig. 2.** Example of a good quality, but incomplete imbibition relative permeability curve. There is a large data gap (yellow) in the gas Rel Perm data between the gas-only flow point at $S_{wirr}$ and the first co-current flow point at $S_w$=0.43. Data from [3].

-ing aquifer or subjected to a water flood.

The general problem of incomplete imbibition Rel Perm curves available for conventional gas field development planning has been pointed out previously at this forum [2] but it has not so far been resolved in the form of a more practical measurement method that can obtain accurate and complete Rel Perm curves at low to intermediate $S_w$.

In 2016 CSIRO was engaged by industry partners to investigate improvements to Special Core Analysis (SCAL) test methods for the purpose of reducing uncertainties in the development of major gas fields in the Northwest Shelf of Australia. During the ensuing research project, CSIRO worked with the operating company and in-house domain experts to devise and test new laboratory methods. We were able to collect a series of much more complete imbibition gas-brine relative permeability curves on several sandstone samples of moderate to excellent quality. The methods were applied to five NWS gas reservoir sandstones and also to a Berea sandstone, a well characterized "standard" rock, which produced similar results.

## 2 Materials and Methods

Experiments were conducted on reservoir sandstone samples ranging in dry gas permeability from 10 mD to around 670 mD, and with porosity ranging from 17% to 23% (see Figure A1). The reservoir sandstones are all quartz arenites (Q > 78%) with 6-10% feldspar and 3-4% kaolinite as the only clay mineral. The Berea sandstone outcrop sample used was quartz rich (Q >90%) and well sorted with dry gas permeability of 665 mD and porosity of 21.8%. Core plugs of around 50-60 mm length and 38 mm in diameter were cleaned prior to measurement, and then saturated with synthetic formation brine.

The samples were drained to irreducible brine saturation using a petrophysical centrifuge up to either 100 psi or 250 psi air-brine capillary pressure. The imbibition Rel Perm experiments were commenced from close to the value of irreducible brine saturation $S_{wirr}$, which in the case of the Berea sample and the most permeable reservoir sample, was around 2%, for the other reservoir samples $S_{wirr}$ ranged from 10 to 15%.

Samples were loaded into the CSIRO x-ray CT monitored core flooding rig (Figure 3). The system uses accurate differential (Keller, Switzerland) and absolute (Quartzdyne, USA) pressure transducers capable of resolving a very small pressure drop across the sample, and gas (Teledyne ISCO, USA) and brine (Quizix, Chandler USA) pumps with high accuracy and a wide range of allowable flow rates (0.001 to 120 cc/min). Flow into and out of the sample is by means of two porous end stones that are removable for cleaning and for controlling their initial brine content. The pressure drop for flow calculations is across the sample only, with the end stones bypassed by thin peek tubes and attached to the differential pressure transducer (Figure 4).

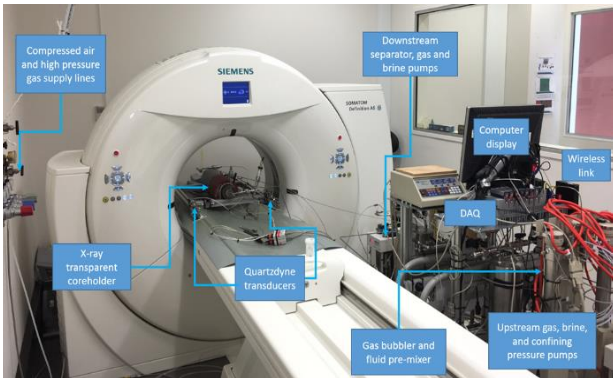

**Fig. 3**. CSIRO x-ray CT monitored core flooding rig.

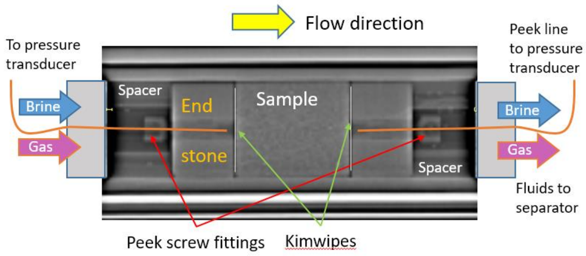

**Fig. 4**. Configuration of the core holder with removeable end stones made of Bentheimer sandstones that served as flow distributors for gas and brine. Pressure drop is measured only across the sample itself via a thin PEEK tube. Single ply tissue was used for capillary continuity at the ends of the sample.

In all the tests reported here a confining pressure of 2500 psi and a pore pressure of 500 psi were used. The gas used was nitrogen rather than methane for safety reasons. A sodium iodide-based brine was used to enhance x-ray contrast, though the overall composition was tested to be compatible with any clays in the rocks. The saturation computations from x-ray CT numbers used calibrations from dry and brine-saturation samples loaded to the same net overburden pressure of 2000 psi used in the test. Moreover, we also used intermediate points of known saturation before applying back pressure, to better constrain the calibration. The saturation from XCT is determined to within 3%, with errors from inexact repositioning of the sample, and drift in beam energy.

When using the standard technique of high gas fraction/ low brine fraction co-current flow to introduce the water in sample S22B, we encountered the same problem that has been reported previously. The brine entering the rock accumulated at the inlet and did not distribute uniformly until $S_w$ of over 50% had been achieved. By this stage, the gas was nearly immobile. The relative permeability is poorly defined (Figures 5 & 6).

In these figures the valid Rel Perm data points are shown in solid colour. The data point at $S_w$=49% was collected when pressure was stable and the flow rates into and out of the sample were equal. However, the x-ray images (Figures A7-A9) show that the saturation profile was not even at that time. A brine bank formed at the inlet had not yet dissipated (Figure A7 image 2). The high brine saturation blocked gas flow through the sample, so that its relative permeability was only 2.2 mD. This banked point is labelled with a black border. During continued co-current flow at 400:1 gas to brine ratio the bank spread out through the sample (in fact there was locally, some secondary drainage of excess brine) and a valid point was eventually achieved at $S_w$=53%, with $k_{rg}$ = 7.6 mD.

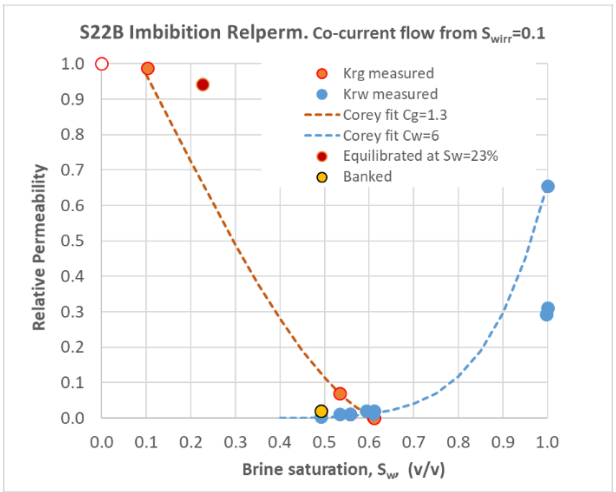

**Fig. 5**. Relative permeability curve for reservoir sandstone of good quality, (dry gas permeability 107 mD), collected using standard co-current test method. A Corey function with small exponent $C_g$= 1.3 can be used to fit the valid data points but there is a large gap between $k_{rg}$ at $S_{wirr}$, around 103 mD, and the next point where the brine was seen on the x-ray CT to be evenly distributed along the length of the sample.

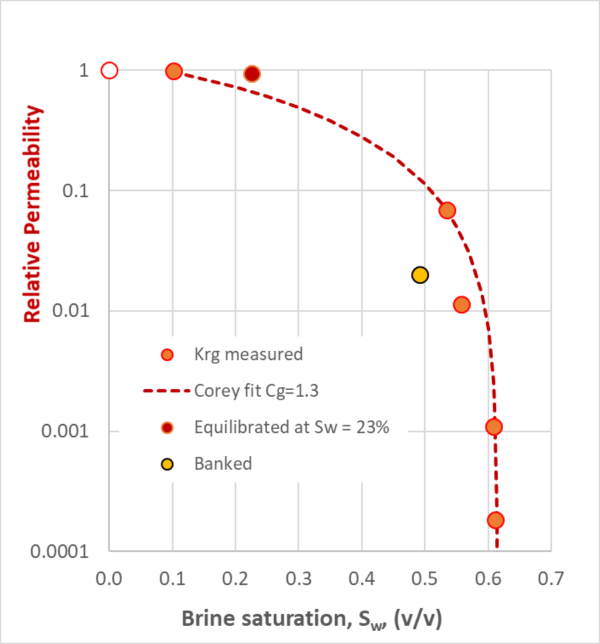

**Fig. 6**. Gas-only Rel Perm data in Figure 5, plotted in an expanded logarithmic scale. Points at $S_w$=0.23 (imbibed) and 0.49 (banked) are discussed in the text.

To overcome the problems described above, we developed simple procedures to create a more uniform brine saturation in the low $S_w$ region, but otherwise retain the desirable features of steady-state Rel Perm procedures established as best practice and outlined, e.g. in McPhee et al. [1]. The new step is to control the early imbibition process in small increments of 5-10% $S_w$ outside of the test cell. We achieved this by blotting brine slowly into the rock plug from all sides with lint-free laboratory tissue (green Kimwipe$^{TM}$), wrapping the sample plus tissue in impermeable film and allowing it to imbibe and redistribute evenly over a period of several hours (permeable samples) to several days (found necessary for the least permeable samples). Several samples were treated in parallel so that they could be loaded sequentially into the test rig and then each advanced further. This means that test rig throughput remains high.

The use of removeable end stones made from highly uniform Bentheimer sandstone meant that the brine saturation in the sample could be pre-equilibrated with the flow boundary materials, also outside of the rig, for each particular sample. We used hand-tightened ‘G’ clamps to press the end stones against the test samples, while imbibition of the inlet-sample-outlet composite took place. We used mouldable wax film (Parafilm$^{TM}$) wrapped around the polyethyene cling film to keep the blotting tissue firmly in place around the samples and stones, and the whole assembly was stored horizontally in the refrigerator.

Uniform brine saturation throughout the rock was

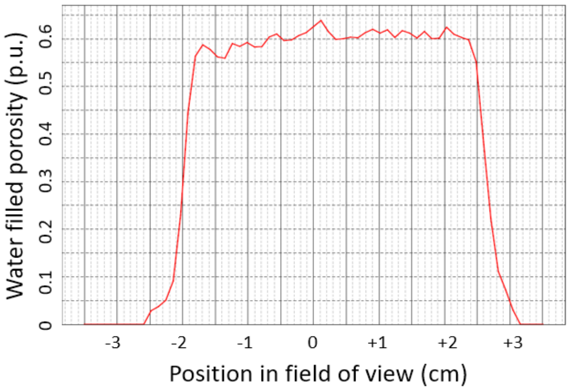

**Fig. 7**. Example of NMR saturation profile through core plug of high permeability sandstone after blotting with tissue and equilibration. Tissue was removed prior to NMR scan acquisition. Good uniformity in water filled porosity along the core length shows that an even saturation of brine through the sample has been achieved.

validated using NMR $T_2$ spectroscopy and profiling along the axis of the cling film-wrapped sample (Figure 7).

The equilibrated samples were loaded into the x-ray imaging flow rig and confining pressure and back pressure were applied slowly. Figure A2 shows an example of a high permeability sandstone together with its end stones loaded into in the test rig.

With the blotting procedure, a series of data points was collected to fill in the data points from the starting point, at or close to $S_{wirr}$, up to intermediate brine saturations.

At low $S_w$, before brine became substantially mobile, we injected gas-only, at four or more rates, to define accurate gas relative permeability values that we also found to be highly repeatable. That is, we avoided co-current flow to avoid banking and we used humidified gas to prevent drying of the samples. Using multiple rates, the linearity of the flow (obeying Darcy's Law) could be confirmed, and any offsets in the transducer values (instrument drift and capillary effects not indicative of the flow-induced pressure drop; e.g. see [5], [6]) could be tracked. Generally, we found that capillary effects close to the inlet or outlet upset the stability of the pressure records to such an extent that the data was unusable (Figure A3). Therefore, we developed a procedure to bleed out any brine droplets that were trapped in the inlet of the PEEK tubes and were able to collect very stable pressure readings resolving pressure drops smaller than 0.02 psi. Figure A4 shows an example of a good quality record in a high permeability sample where very small differential pressure signals can be resolved.

Once saturation had advanced sufficiently for brine to be detectably mobile, we progressed into co-current flows with the fractions of gas and brine adjusted to maintain near stable, but slowly advancing $S_w$. We note that commonly, onset of brine mobility coincided with non-linearity of the pressure response to increased flow rate: in these cases, we used the linear portion of the curve at lower gas flow rates to compute the relative permeability.

The use of paired syringe pumps at inlet and outlet allowed close control of both inflow and outflow brine rates, such that true steady state conditions were verified. We define a point as "valid" when flow rates in and out of the sample are equal, the differential pressure is steady, and the saturation is uniform to within five percent. Points that are invalid or suspect are shaded grey on the plots.

Ideally, the brine saturation should be completely uniform and, in many cases, $S_w$ did vary by less than 2% along the sample length. We found that in the highly permeable sandstones, the brine was easily moved within the sample during loading and pressurization in the rig. As $S_w$ was increased beyond about 50%, brine became more mobile, and there was a tendency to see some end effects so that brine either accumulated at, or retracted from, the sample boundaries: if this led to a saturation range greater than 5% within the sample we consider it invalid. Note that "invalid" points happen to lie on the curves eventually fitted through the valid data points.

The x-ray images of the experiments taken in the medical CT system included the end stones and this gave us advanced warning of potential saturation changes that could be balanced with a higher or lower brine flow rate. In this way, the progression of saturation was made as smooth as possible and the imbibition was controlled to be monotonic (meaning without any regressions in water saturation owing to too-rapid drainage of brine out of the sample). Even so, the experiments are quite challenging to perform as uneven brine saturation can still occur due to brine accumulating at the inlet (banking, as described above, owing to spontaneous imbibition from the upstream stone) or the outlet end of the sample (likely due to poor capillary continuity between the sample and the downstream stone).

## 3 Results

We present representative results from our study for three samples representing low, intermediate and good quality gas reservoir types.

In Figures 5 and 6 we illustrate the effect of resetting the saturation of Sample S22B from $S_{wirr}$ and advancing $S_w$ to ~23 % using the blotting method to collect just one

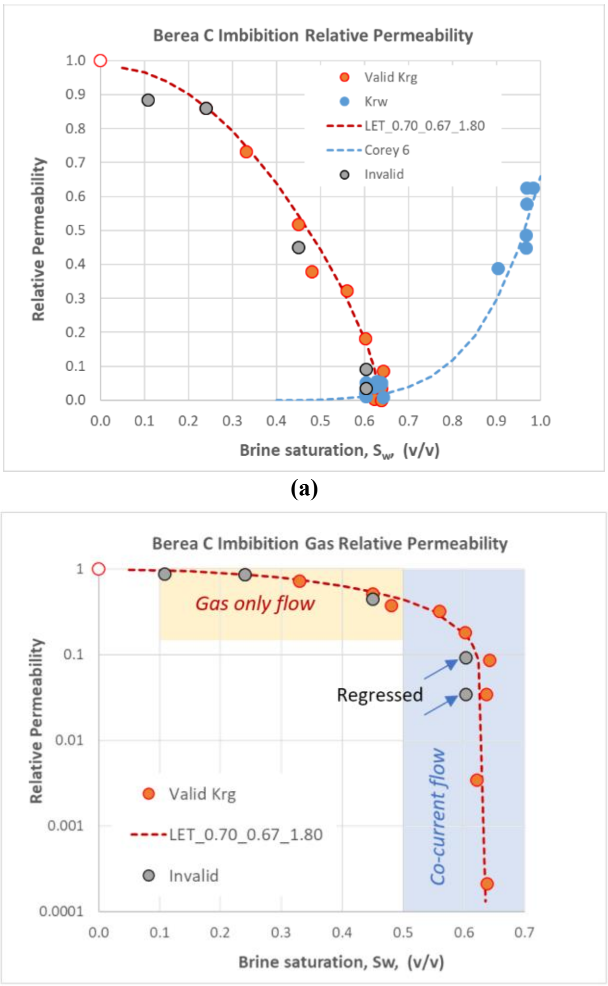

(a)

(b)

**Fig. 8.** Gas relative permeability (orange dots are valid points) and brine relative permeability (blue dots) for Berea C sample. The red dashed line is the LET function fit to gas permeability. Brine data in (a) fit a Corey function. In the expanded, logarithmic-scale plot (b), the location of two stable and equilibrated points that lie below the main Rel Perm curve are labelled. They were acquired after a period of regression in the brine saturation during co-current flow.

additional equilibrated imbibition Rel Perm point within the gap region. This point is shown in darker solid colour, and it lies well above the Corey curve fitted through the other points acquired earlier with the standard methodology. The Corey fit was allowable when there was a large data gap, but the new point makes this type of curve impossible. By collecting more points with sequential blotting, we can trace a more complete curve towards $S_w$ values of around 50% brine when the co-current data are again reliable.

Figure 8 shows the full results for Berea sandstone, which has a dry gas permeability of around 665mD. The evolution of brine distribution for this sample is shown in Figure A5. This sample was challenging owing to high water mobility, which was near the limit of causing gravitational segregation during horizontal core floods. Two points at around 11 and 24% brine saturation showed more brine in the middle part of the core than at the ends, and therefore are coloured grey in Figure 8.

These two values were collected immediately after loading the samples into the rig, from an original state that did have uniform brine distribution, in equilibrium with the end stones. We presume that application of the gas pressure from both ends of the sample caused some retraction of the brine towards the middle of the core plug.

Figure 9 shows the gas relative permeability curve for the poorest quality reservoir sample, S26B (porosity 17%, dry gas permeability of 9.4 mD). The first point was collected at $S_w$=25%, following centrifugation to 100 psi. The general shape of the Rel Perm curve is similar to the Berea and S22B but with slower fall-off and a gas end point at higher water saturation ($S_w$=73%, $S_{gr}$=27%).

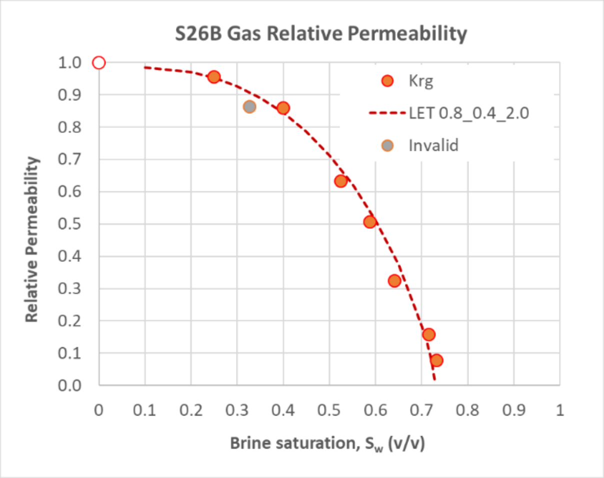

**Fig. 9.** Gas relative permeability (orange dots are valid points) for sample S26B. The red dashed line is the LET function fit.

For five reservoir sandstones and for the Berea "standard" rock we found that the shape of the more complete gas relative permeability curve, now extending through to low $S_w$ values, is convex upwards and does not show the concave-up or "Corey" type profile that is conventionally expected. The gas Rel Perm function may have an 'S' shaped form or simply roll over to a sharp drop-off without tapering at high $S_w$. The experimental gas Rel Perm curves can be fitted with the LET function [7], while the water Rel Perm curves still show a classic Corey function shape, as expected from established theory for strongly water wet conditions. The properties and LET fitting values for three representative samples are summarised in Table 1.

We note that during the co-current test periods, we saw several of the phenomena mentioned by Cense et al. [2] for gas-brine imbibition experiments, such as the development of a gradient in brine saturation along the sample near the permeability end point owing to greater compression of trapped gas bubbles at the inlet end than at the outlet end, and also a small amount of "carry-over" of gas in solution or as disconnected bubbles. We therefore used recommended procedures not allowing the differential pressure to exceed 50 psi (10% of the back pressure applied). Usually ΔP was less than 5 psi.

When regressions in saturation occurred, the gas relative permeability for the subsequent point lay below the curve for progressive imbibition, suggesting that additional blocking of gas pathways by displaced brine was occurring. The "invalid" grey points labelled with arrows between $S_w$=0.4 and $S_w$=0.64 in Figure 8b were acquired after such episodes of regression in saturation during the co-current flow period in the Berea C sample.

## 4 Discussion and Implications

Our findings question the adequacy of current "best practice" relative permeability testing methods and reporting in SCAL programs for gas reservoirs. While every Rel Perm point reported may be valid, the limited data available are often fitted through the "gap" at intermediate $S_w$ values using a Corey-type curve that may not be applicable. (Figures A7 to A9 show how this gap came about in sample S22B using co-current flow at 1000:1 gas to brine ratio). Therefore, completing the curve in this region can reduce the uncertainty in what the permeability trajectory during brine imbibition will be.

The results that we obtained for a range of sandstones from good and poor-quality reservoirs suggest that the shape of gas-brine imbibition relative permeability curves should not be assumed to have a concave-up shape, at least for water wet systems such as those investigated in this research project. Considering that in a water wet rock, the brine has a strong affinity for surfaces, it is not surprising to us that the brine does not start to have a marked effect on the gas permeability until it has built up to a level where it blocks the gas pathways in the centres of pores and throat regions. Once the pathways start to block up however, the permeability to gas drops more precipitously in a process akin to the removal of conducting bonds in a percolating network.

Sigmoidal-shaped [imbibition] relative permeability curves for oil-brine and gas-brine system have been reported in the literature, e.g. [8-12], hence the derivation of fitting functions such as LET [7] to describe them. The shape is likely to relate to the pore structure and the "roll-over" shape that has been termed "reverse hysteresis" is sometimes cited as being typical of a sand-pack rather than a heavily consolidated rock [13]. In simple network simulations of two-phase displacements, the shape is typical of low aspect ratio pore structures, and well-connected topology [14,15]. We note that the porosity of the samples that we tested is from ~17%-22%, and microscopic examination shows moderate consolidation and quartz cementation, but in general that sandstones all have an "open" and well-connected type of pore structure.

The Berea sandstone sample that we tested here, is homogeneous in the along-core direction, and looks uniform on visual inspection but has discernible lamination in the x-ray images (Figure A6), whose contrast increases at intermediate brine saturations when the finer layers imbibe more brine relative to the coarse layers. Thus, for Berea C, there are likely to be some relatively unrestricted channels for gas flow at intermediate brine saturation, that remain free flowing until those laminae with large pore apertures also become invaded by brine. This would act to maintain high gas of Rel Perm to a larger value of $S_w$ and generate a "roll over" curve shape thereafter. However, we should point out that all the other samples were chosen for their homogeneity and the overall shape of the permeability decline in laminated Berea C is rather similar to that measured for the highly uniform sample S26B.

Other factors such as interfacial tension, wettability and flow rates affecting the viscous force balance are likely to be as important as the pore structure in controlling the Rel Perm curve shapes. Kjosavic et al. [16] suggest that strong water wetting can produce a sigmoidal shape of Rel Perm curves and leads to an increase in hysteresis between drainage and imbibition processes. A decrease in the exponent describing the non-wetting phase tortuosity (which depends on pore structure, IFT and wettability) is shown by Gerhard and Keuper [13] to generate a convex-up shape for the first imbibition curve and for imbibition scanning curves: physically this implies that the gas flow pathways are relatively simple and dominant with the water phase forced to the margins of the pore space. More sophisticated measures of non-wetting phase continuity and connectedness now being made possible with x-ray microCT image analysis at pore scale may help to put these measures on a more quantitative and predictive footing [17]. Indeed, digital rock simulations with realistic physics can already predict a range of Rel Perm curve shapes, and they can produce output continuously across the full range of saturations [18,19].

Our results apply to the water wet conditions tested in the gas-brine system having high interfacial tension (around 70 $\mathrm{mNm^{-1}}$) in quartzo-feldspathic sandstones with a small proportion of clay, and moderate to high permeability. The prevailing conditions of our tests are representative of the interior of the reservoir (far from a well) and involve small capillary numbers (ratio of viscous (drag) forces to capillary (surface) forces of around $10^{-6}$ or $10^{-7}$. At higher velocity, and capillary number $>10^{-5}$, the viscous forces and momentum transfer will change the shape of the gas Rel Perm curve, which is likely to straighten as the gas can more effectively push brine out of the way. Therefore, prediction of gas flow dynamics close to the wellbore would require a different style of lab test and would most likely lead to differently shaped Rel Perm curves than the examples reported here.

Considering the true sigmoidal or roll-over profile of the gas Rel Perm curves at low capillary number, one can see that the gas flow rates predicted for the earlier stages of brine invasion into the reservoir (away from the near wellbore region) as it is depleted or swept, will be higher than would be predicted by defaulting to the concave-up "Corey" shape. (Figure 5 shows an example a good Corey curve fit to limited data). The Corey and LET type curves only merge towards the tail end of gas mobility, when the relative permeability is less than 10 percent of the starting values at $S_{wirr}$. Therefore, one would predict that higher gas flow rates are possible in the reservoir during the early stages of water ingress, before a steeper drop-off in $k_{rg}$. The consequences for reservoir planning are likely to be more important for a water drive situation, and be less important for reservoirs only undergoing depletion.

This new understanding of the true gas-brine relative permeability curve shapes may influence the development concept for gas reservoirs, the placement of wells and even the ultimate economics of a project. At the least, having complete and reliable relative permeability curves as inputs will improve the accuracy of reservoir simulation models and increase the level of confidence in their predictions of reservoir performance over time.

## Acknowledgements

Chevron Australia and joint venture partners Exxon Mobil Australia and Shell Australia are thanked for funding this research. Dr Ali Saeedi from Curtin University provided important guidance in setting up this project, and advice as to experimental methods. Dr Lincoln Paterson and Dr Tara La Force from CSIRO are thanked for providing internal peer reviews. P. Egermann and K. Flynn are thanked for thoughtful reviews that improved the quality of the paper. This research utilized the x-ray CT and Advanced Core flooding facilities of the National Geosequestration Laboratory (ngl.org.au).

## References

1. C. McPhee, J. Reed and I. Zubizarreta, *Core Analysis: A Best Practice Guide*. Elsevier (2015).
2. A. Cense, J. Reed and P. Egermann. "SCAL for gas reservoirs: a contribution for better experiments". SCA 2016-023 (2016).
3. D. Maloney, K. Doggett and R. Gilliland. "New procedure and apparatus for combined reservoir condition gas-brine relative permeability, capillary pressure and electrical property measurements". SCA-9427 (1994).
4. A. T. Corey. "The interrelation between gas and oil relative permeabilities". Producers Monthly, **19**, 38-41, (1954).
5. R. Pini, and S. Benson. "Simultaneous measurement of capillary pressure and relative permeability drainage curves". Water Resources Research, **49**, 3516-3530, (2013).
6. R. Gupta, and D. Maloney. "Intercept Method—A novel technique to correct steady-state relative

permeability data for capillary end effects". SPE171797-PA (2014)

7. F. Lomeland, E. Ebeltoft, and W.H. Thomas, "A new versatile relative permeability correlation". SCA 2005-32. (2005).
8. J. Osoba, J. Richardson, J. Kerver, J. Hafford, and P. Blair. "Laboratory Measurements of Relative Permeability". Petroleum Transactions AIME, 192, 47–56 (1951).
9. J. Batycky and F. McCaffery. "Low interfacial tension displacement studies". Petroleum Society of CIM, Calgary, Canada, Paper 78.29.26. 1978.
10. Raimondi, P. "Distribution of the oil phase obtained upon imbibition of water". *Society of Petroleum Engineers Journal*, 49–55 (1964)
11. J. Colonna, F. Brissaud, and J.L. Millet. "Evolution of capillarity and relative permeability hysteresis". Society of Petroleum Engineers Journal, **12**, 28–38 (1972).
12. R. Fulcher, E. Turkay and C. Stahl. "Effect of capillary number and its constituents on two-phase relative permeability curves". SPE 21170-PA (1985)
13. J. Gerhard and B. Keuper. "Relative permeability characteristics necessary for simulating DNAPL infiltration, redistribution and immobilization in saturated porous media". Water Resources Research **39**, W1213 (2003)
14. G. Jerauld, and S. Salter, S. J. "The effect of pore-structure on hysteresis in relative permeability and capillary pressure". Transport in Porous Media, **5**, 103–151 (1990).
15. P. Valvatne and M. Blunt. "Predictive pore-scale modelling of two-phase flow in mixed-wet media". Water Resources Research **40**, W07406, (2004).
16. A. Kjosavik, J. Ringen, and S. Skjaeveland. "Relative Permeability Correlation for Mixed-Wet Reservoirs". SPE Journal, **7**, 49–58 (2007).
17. L. Andersson, S. Schlueter, and D. Wildenshild. "Defining a novel pore-body to pore-throat 'Morphological Aspect Ratio' that scales with residual non-wetting phase capillary trapping in porous media". Advances in Water Resources, **122**, 251–26. (2018)
18. Schembre-McCabe, R. Salazar-Tio, and J. Kamath, 2012. "Two examples of adding value through Digital Rock Technology". SCA 2012-081 (2012)
19. R. Farokhpoor, E. Westphal, N. Idowu, P. Oren and B. Fletcher. "Gas-water steady-state relative permeability determination with two approaches; experimental and digital rock analysis, strengths and weaknesses". SCA2016-12. (2016)

**Table 1.** Properties of the three representative sandstones, and their LET function parameters for the gas Rel Perm [7]

| | Porosity p.u. | Dry Gas Perm. mD | L,E,T for $k_{rg}$ |
|---|---|---|---|
| S22B | 20.2 | 107 | 2.2, 0.09, 1.5 |
| S26B | 17.1 | 9.4 | 0.8 ,0.4 ,2.0 |
| Berea C | 21.8 | 665 | 0.7, 0.67, 1.8 |

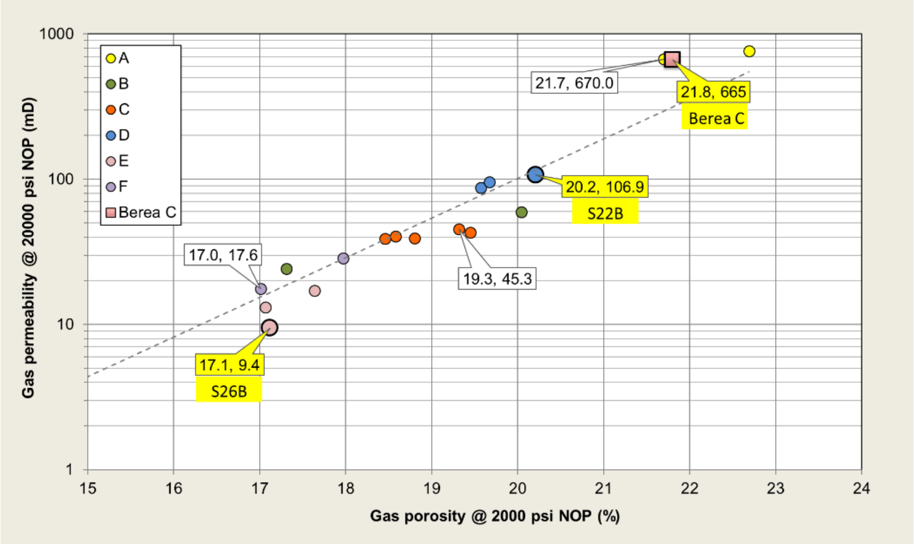

**Fig. A1**. Dry nitrogen porosity and permeability of the five tested samples from NWS gas field, measured at 2000 psi net overburden pressure. The set of samples represents the range of routine core analysis values of medium to good reservoir quality. The Berea C sandstone has a porosity and permeability very similar to the highest permeability sample among those tested from the reservoir set. The three samples for which relative permeability results are presented in this paper are highlighted in yellow.

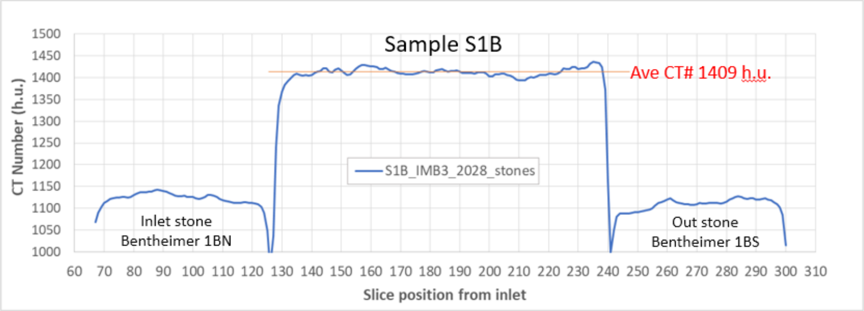

**Fig. A2**. Profile of average X-ray CT numbers through the assembly of inlet stone-sample-outlet stone mounted in the test rig, prior to commencing measurements. The sample has a uniform brine saturation of 30% and is in capillary equilibrium with the stones. The dip in CT number at the boundary marks the position of the single ply Kimwipe tissue used to maintain good continuity of the brine phase between the end faces of rocks.

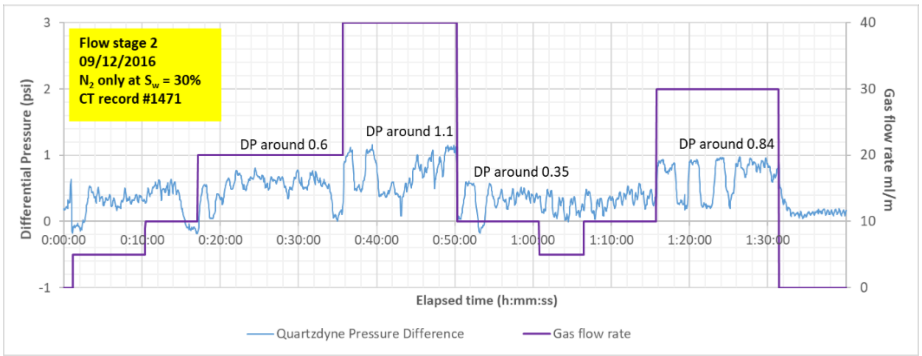

**Fig. A3**. Example of a completely unstable pressure record during multiple rate gas flow experiments in sample S22B. This problem was rectified by bleeding off any brine droplets that had entered the PEEK tubes connected to the flow transducers.

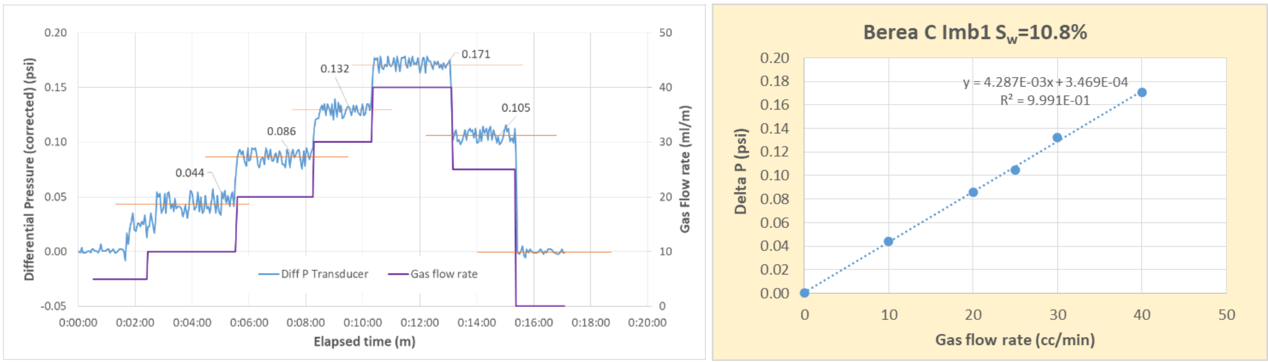

**Fig. A4**. Example of stable flow-pressure record in sample Berea C, at multiple gas flow rates and a plot showing linearity of the Darcy flow regime. The static periods of no flow show the very high resolution and low noise level of the differential transducer. The fluctuations around the mean pressure values during gas flow are real "flutter" in the multiphase flow process.

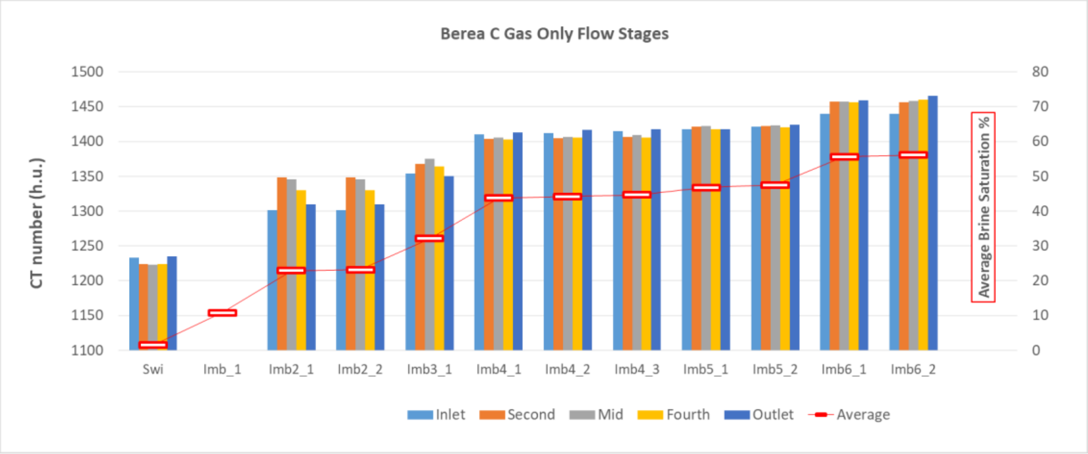

**Fig. A5**. Saturation distribution through the Berea C sample during tests with gas-only flow. The average CT values for 5 regions running from inlet through to outlet are shown here for simplification, although the data were collected with a slice thickness of around 0.5mm, as seen in the following figure. For Imb 1, x-ray CT data was not collected owing to machine failure, but the brine distribution was measured before loading into the rig, when it was uniform, and after testing, blow-down and extraction, when it the brine was found to have retracted towards the mid-point of the plug. For the two CT scans in Imb2, brine again was initially uniform as determined by NMR profiling, prior to loading into the rig, but retracted away from the core ends. This is seen very slightly in the third imbibition stage, and thereafter the brine distributions were highly uniform apart from small end effects, as seen in the following figure.

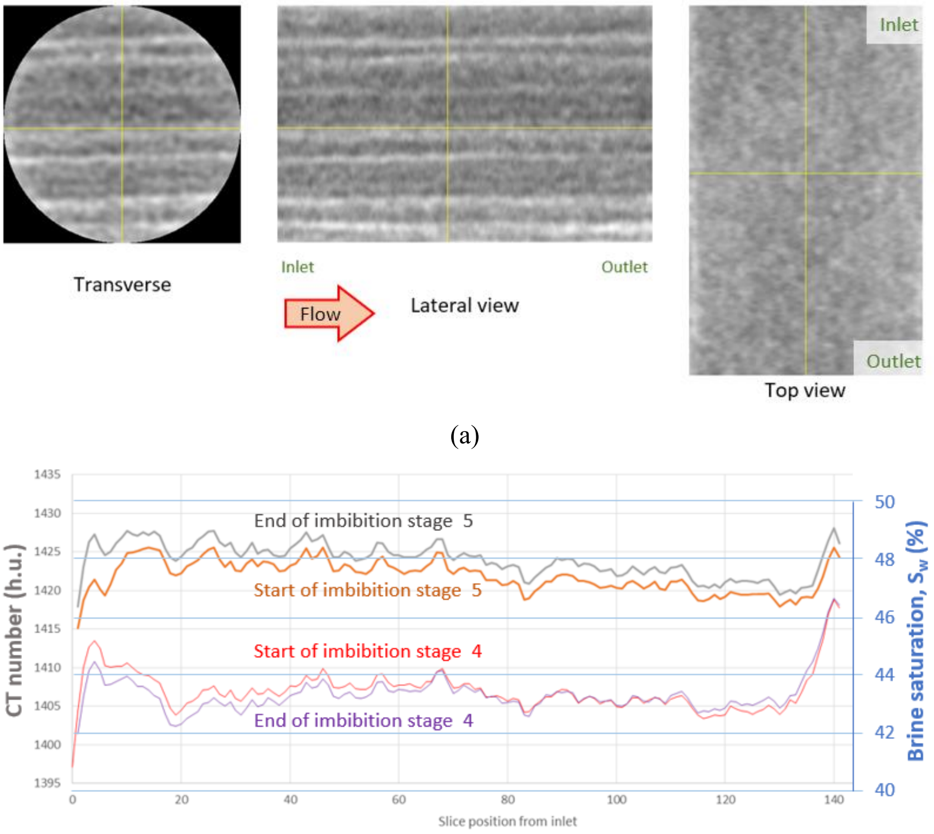

(a)

(b)

**Fig. A6**. (a) X-ray CT images of Berea C Sample during imbibition stage 4, at around 43% average brine saturation. The distribution of brine appears to be very uniform. The horizontal laminations are well defined, and the contrast between them is highest at intermediate saturations owing to the finer laminae having a higher brine content than the coarser-grained laminae. (b) Detail of x-ray profiles showing average CT number variations from inlet to outlet in imbibition stage 4, and the subsequent stage after a further increment of blotting. Small capillary end effects are evident that do not seem to have affected flow or pressure data. While there was essentially no change in brine saturation during stage 4, there was a small net transfer of brine into the sample from the end stones during stage 5, even during gas-only flow, but this amounted to an overall increase in saturation of less than 1 percent.

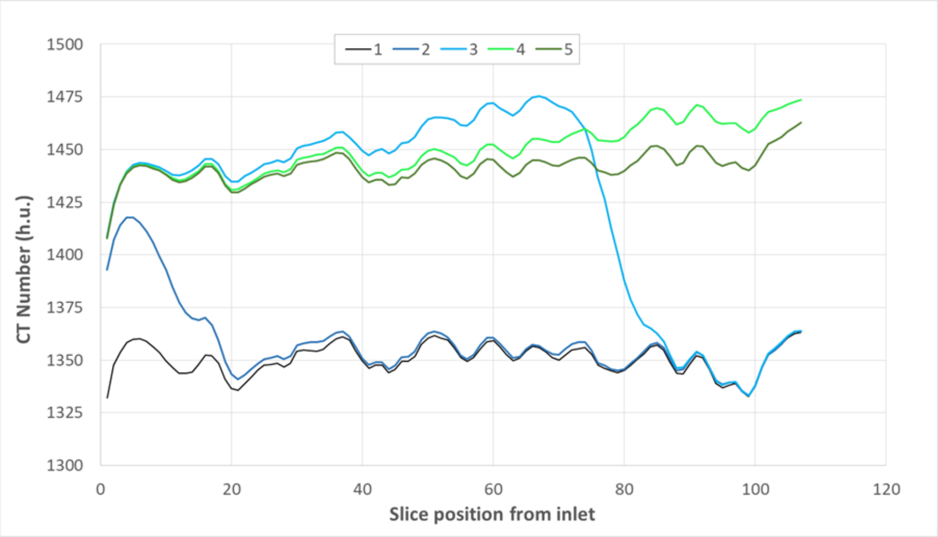

**Figure A7**. CT value evolution during brine imbibition stages from $S_w$=22% in sample S22B, during co-current flow at 1000:1. The initial uniform distribution of brine in Image 1 becomes banked at the inlet (2), and a large front progresses two thirds of the way into the sample (3) before reaching the outlet and dissipating (4) and becoming nearly uniform again by Image 5. This figure illustrates the development of the significant gap in relative permeability data for situations with an even brine saturation when using co-current flow, even at high gas rate (60 ml/min) and very low brine fraction.

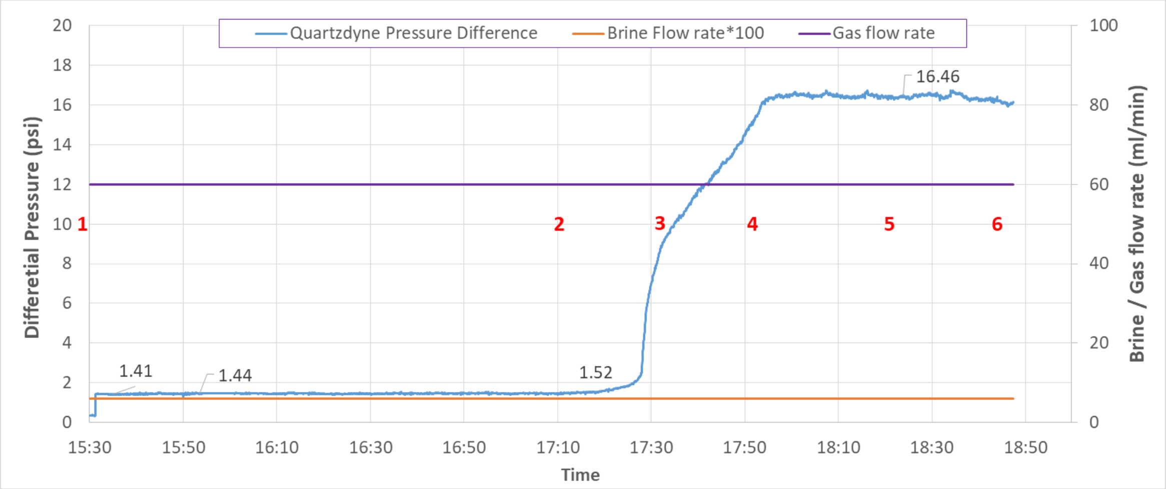

**Figure A8**. Pressure record for initial gas flow in sample S22B commencing from $S_w$=22%, followed by high gas fraction co-current flow (1000:1 ratio) that matches to the saturation history shown in the previous figure. There are no good Rel Perm data points between an initial gas permeability of 103 mD, and the drop right down 2.2 mD after the brine spreads out at an average brine saturation of 49% (Image 5 in the previous figure, banked point in Figures 5 and 6).

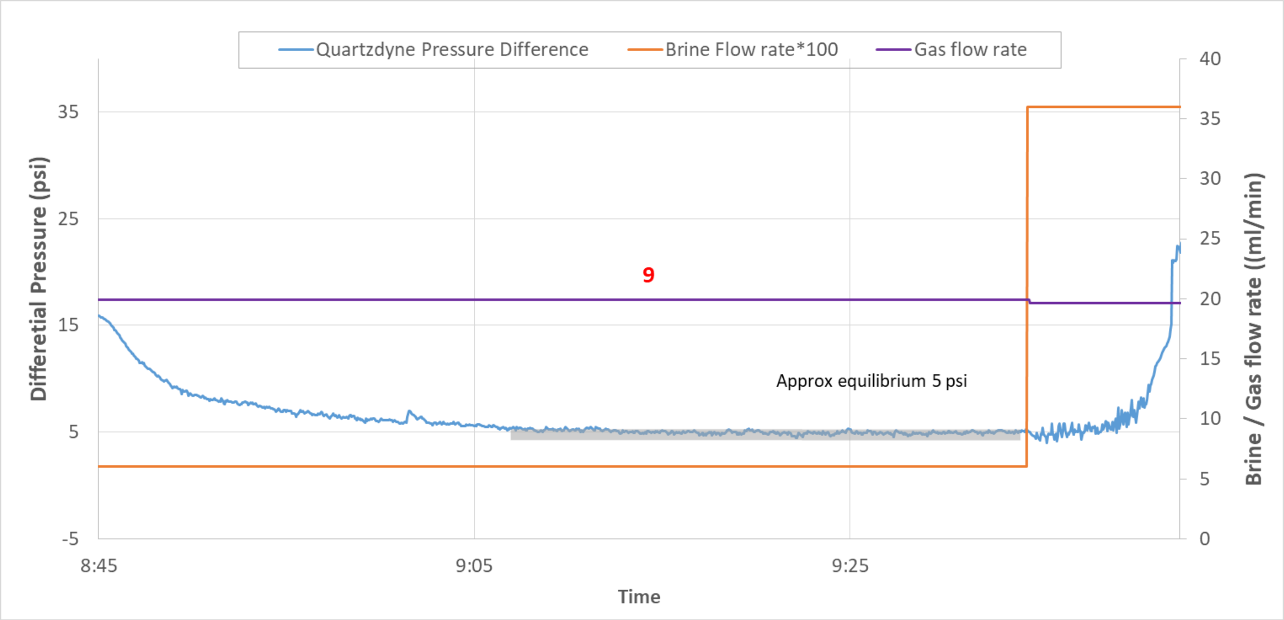

**Figure A9** After the sample S22B was left overnight, co-current flow was recommenced at a ratio of 333:1. The permeability to gas recovered to 7.6 mD and flow was very stable. Brine saturation was uniform and had progressed slightly to 53% (the next valid Rel Perm point in Figures 5 and 6). A relatively small redistribution of the brine in the sample significantly affected its gas permeability, as can be seen from the drop off in differential pressure from the peak of 16.5 psi down to 5 psi during this flow stage.

# Workflow for upscaling wettability from the nano- to core-scales

*Maja* Rücker[1,3], *Willem-Bart* Bartels[2,3], *Tom* Bultreys[1,4,6], *Marijn* Boone[7], *Kamaljit* Singh [5,6], *Gaetano* Garfi [6], *Alessio* Scanziani [6], *Catherine* Spurin[6], *Sherifat* Yesufu [1], *Samuel*. Krevor[6], *Martin. J.* Blunt[6], *Ove* Wilson[3], *Hassan* Mahani[3], *Veerle* Cnudde[2,4], *Paul F.* Luckham[1], *Apostolos* Georgiadis[1,3] and *Steffen* Berg[1,3,6]

[1]Department of Chemical Engineering, Imperial College London, UK
[2]Earth Sciences Department, Utrecht University, NL
[3]Shell Global Solutions International B.V., Grasweg 31, 1031 HW Amsterdam, NL
[4]UGCT- PProGRess, Ghent University, BE
[5]Institute of Petroleum Engineering, Heriot-Watt University, Edinburgh, UK
[6]Department of Earth Science and Engineering, Imperial College London, UK
[7]Tescan XRE, Bollenbergen 2B bus 1, 9052 Ghent, BE

**Abstract.** Wettability is a key factor influencing multiphase flow in porous media. In addition to the average contact angle, the spatial distribution of contact angles along the porous medium is important, as it directly controls the connectivity of wetting and non-wetting phases. The controlling factors may not only relate to the surface chemistry of minerals but also to their texture, which implies that a length-scale range from nanometres to centimetres has to be considered. So far, an integrated workflow addressing wettability consistently through the different scales does not exist. In this study, we demonstrate that such a workflow is possible by combining micro-computed tomography imaging with atomic force microscopy (AFM). We find that in a carbonate rock, consisting of 99.9% calcite with a dual porosity structure, wettability is ultimately controlled by the surface texture of the mineral. Roughness and texture variation within the rock control the capillary pressure required for initializing proper crude-oil-rock contacts that allow ageing and subsequent wettability alteration. AFM enables us to characterize such surface-fluid interactions and to investigate the surface texture. In this study, we use AFM to image nano-scale fluid-configurations *in situ* in 3D at connate water saturation and compare the fluid configuration with simulations on the rock surface assuming different capillary pressures.

## 1 Introduction

Wettability is the preference of a solid to be in contact with one fluid over another fluid. In petroleum applications, rock represents the solid phase, crude oil the first fluid phase and brine, which may be either present in the reservoir (formation water) or injected for oil recovery, the second fluid phase. A rock surface is called water-wet when the water tends to cover it and is called oil-wet when it prefers to be in contact with the oil phase. Furthermore, wettability may vary from location to location with a mixture of water-wet and oil-wet regions. In this case the rock is called mixed-wet [1-5].

Wettability by itself is not a property used as a direct input parameter for reservoir models. Yet, it is known to significantly impact input values such as relative permeability- and capillary pressure-saturation functions [6-8]. So far, these relationships can only be determined with core-scale experiments. To predict these parameters for a specific reservoir a better understanding of the principles behind wettability is crucial.

In a reservoir the wettability depends on various properties which act at different length scales. An overview of the different properties over increasing length scales is shown in Fig. 1. Brine and crude oil composition, surface chemistry and the P-T conditions affect molecular interactions, which can be assessed for instance through adhesion force measurements obtained with atomic force microscopy (AFM) [9-11].

At the sub pore scale, roughness, which may facilitate formation of thin water- or oil-films, becomes an additional factor. On this length scale the contact angle forming along three-phase contact lines may be measured [12].

At the larger pore and pore-network scale ($\mu m$ to mm), the confined space within a porous medium is taken into account. Mineralogy and mineral distribution as well as the saturation history need to be considered. On this length scale wettability can be characterized through contact angle distributions [13], fluid distributions [14], by defining local capillary pressure [15, 16] and small scale relative permeability [17, 18].

To predict wettability at the core scale the contribution of each consecutive scale to the overall wettability of the system needs to be considered.

---

[*] Corresponding author: m.rucker15@imperial.ac.uk

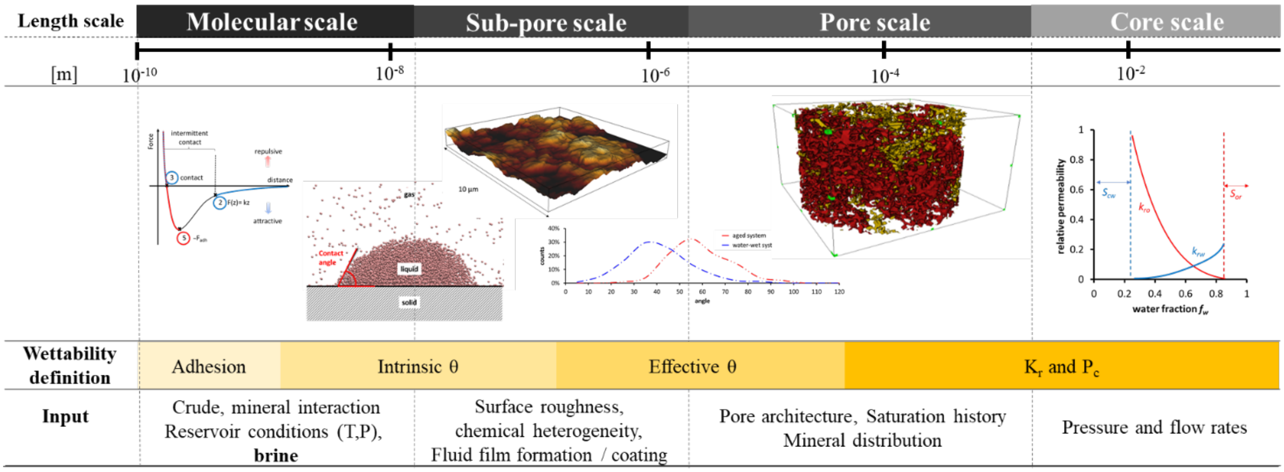

**Fig. 1.** Wettability depends on various properties acting at different length scales such as brine- and crude-oil composition, reservoir pressure and temperature (P-T) conditions, surface chemistry associated with mineralogy at the molecular scale, surface structure and fluid-film formation at the sub-pore scale as well as saturation history and mineral distribution at the pore scale. They all influence wettability, and thereby the pore-dynamics during two-phase flow and the relative permeability. [71]

### 1.1 Wettability at the molecular scale

Most minerals of reservoir rock are originally strongly water-wet [4, 9, 19]. However, the adsorption of surface active components or the precipitation of asphaltenes present in the crude oil may alter the wettability towards more oil-wet [4, 20-23]. Correspondingly, crude oils are usually classified by assessing their acid (TAN) and base (TBN) numbers as well as saturate, aromatics, resins and asphaltene (SARA) fractions, which indicate the stability of asphaltenes within the crude [24, 25].

In addition to the chemistry of the crude oil and the rock, the brine composition may also impact the wettability. Along a mineral surface, the balance between electro-static forces and van der Waals forces leads to a double layer of counter ions of the brine phase in correspondence with Derjaguin-Landau-Verwey-Overbeek [26, 27] (DLVO theory), which impacts the repulsive/attractive forces of approaching oil molecules [28, 29].

Various studies addressed the impact of these different components [30-33]. In this work, we keep these values constant by focussing on specific crude oil/rock/brine systems to assess the impact of various parameters controlling wettability at larger length scales.

### 1.2 Wettability at the sub-pore scale

At the sub-pore scale the measure of wettability is the contact angle, which can be obtained by imaging a droplet on a surface e.g. with a contact angle goniometer [34-41]. However, sub-resolution features are known to impact the observed response. Surface roughness may lead to pinning and therewith to a range of possible equilibrium contact angles [12, 42, 43]. This effect even occurs on surfaces considered atomically flat [42, 44]. Correspondingly, any contact angle measured represents an effective contact angle $\theta_e$. The intrinsic contact angle $\theta_i$, which is solely related to the molecular interactions, is only a theoretical descriptor obtained e.g. through

**Table 1.** TAN, TBN, SARA fractions, viscosity and density of the crude oils used.

| | TAN [mg KOH $g^{-1}$] | TBN [mg $kg^{-1}$] | Saturates [wt %] | Aromatics [wt %] | Resins [wt %] | Asphaltenes [wt %] | Viscosity 20 °C [mPa s] | Density 20 °C [g $cm^{-3}$] |
|---|---|---|---|---|---|---|---|---|
| crude A | 0.07 | 83.9 | 58.45 | 44.00 | 4.36 | 0.28 | 4.87 | 0.83 |
| crude B | 0.38 | 2.86 | 52.08 | 39.06 | 7.96 | 0.91 | 17.03 | 0.85 |

**Table 2.** Composition of formation water (FW) and a high salinity brine (HS) used.

| ION [mg/L] | $Na^+$ | $K^+$ | $Mg^{2+}$ | $Ca^{2+}$ | $Cl_-$ | $SO_4^{2-}$ | $HCO^{3-}$ | $I^-$ | Ionic strength [mol/L] | pH |
|---|---|---|---|---|---|---|---|---|---|---|
| FW | 49898 | 0 | 3248 | 14501 | 111812 | 234 | 162 | 0 | 3.659 | 6.9 |
| HS (doped) | 0 | 47106 | 0 | 0 | 0 | 0 | 0 | 152894 | 1.205 | - |
| S (doped) | 0 | 21198 | 0 | 0 | 0 | 0 | 0 | 68802 | 0.542 | - |

molecular models assuming a perfectly smooth surface with the fluid phases being equilibrated [12, 45].

Dynamic contact angle measurements allow the assessment of roughness through an advancing contact angle $\Theta_a$ and receding contact angle $\Theta_r$, which represent the upper and lower boundary of possible contact angles for the studied surface. The detected contact angle hysteresis depends on the intrinsic contact angle, the surface roughness and velocity of the moving contact line [12].

Furthermore, grooves on a rough surface lead to entrapment of the wetting phase [46-48]. This can have large effects on the wettability alteration process. During drainage, in most cases the aqueous phase is wetting and forms water-films and layers within such grooves. These water-films and layers prevent the intimate contact between the oil and the solid and therewith wettability alteration in this regions Correspondingly, such water films may lead to mixed wettability patterns along the surface [3, 22, 49, 50].

### 1.3 Wettability at the pore scale

So far, most 3D studies on mixed-wet and oil-wet rock systems have focussed on wettability characterization. Andrew et al. [13] introduced *in situ* measurements of contact angles in rock and Scanziani et al. [51] and AlRatrout et al. [52] automated the process. Contact angle distributions are sensitive to image resolution and may vary in case of non-equilibrium conditions [13]. However, they provide an indication of the wettability and wettability changes of the system. Alhammadi et al. [53] showed a shift of the contact angle distribution when the wettability of the rock is altered by aging. Yet, these contact angles are not sufficient for prediction of larger scale relative permeabilities. The obtained distribution does not necessarily cover the advancing contact angle $\Theta_a$, which is used as input for most multiphase flow models in porous media, nor for its spatial distribution in case of a mixed-wet rock [17].

Another way to characterize wettability is through fluid distribution. In oil-wet and mixed-wet systems the oil clusters appear sheet-like and flat compared to the more spherical geometry in water-wet systems [54, 55]. Singh et al. [56] observed oil layer formation on the rock surface and between two water interfaces, which provides a conductive flow path for the oil phase in mixed-wet systems. Lin et al. [57] observed the formation of minimal fluid-fluid interfaces with a mean curvature of approximately zero and deviating principal curvatures. The fluid phase distribution or geometry may be fully characterized through morphological descriptors known as the four Minkowski functionals: volume, surface area, integrated mean curvature and Euler characteristic [14, 58-62].

Recent work focuses on linking the pore scale wettability parameter to core scale properties such as capillary pressure -saturation and relative permeability -saturation relationships [16, 18, 63-65].

### 1.4 Wettability at the core scale

In conventional special core analysis (SCAL) experiments, the capillary pressure - saturation relationship is used to assess the wettability of a system. This relationship can be obtained by combining the Amott spontaneous imbibition test, in which the cumulative production of the displaced phase versus time is recorded as well as waterfloods to obtain the forced part of the capillary pressure. Various indices, with the Amott and USBM index being the most common, have been introduced to derive wettability from the capillary pressure - saturation relationship [66, 67]. However, the results of such experiments are difficult to interpret as other factors besides wettability may impact the results. These factors include, for instance, viscosity, interfacial tension and flow dynamics [68-70]. An alternative is the wettability characterization by re-scaling the Leverett J function to provide an average contact angle [71, 72]. Yet, this method is not able to account for mixed wettability.

The wettability of a system can also be inferred from the relative permeability- saturation functions using the end-point water relative permeability, oil-layer drainage and shape of the water relative permeability: An end point permeability $\boldsymbol{k_{rw}^{max}} < 0.3$ indicates a water-wet system, $0.3 < \boldsymbol{k_{rw}^{max}} < 0.6$ a mixed wet and $\boldsymbol{k_{rw}^{max}} > 0.6$ an oil-wet system. Oil-layer drainage can be assessed from $k_{ro}$ near to the end-point: If $k_{ro} < 0.05$, while the saturation is still decreasing, oil is moving through a continuous oil layer, which is indicative of a mixed- or oil-wet system. If the shape of $k_{rw}$ shows a sharp rise with a cross over saturation $\boldsymbol{S_w^{cross}} < 0.5$ the system is often oil-wet. A low $k_{rw} < 0.2$ for $S_w = S_{wi} + 0.2$ is indicative of a water-wet system [73].

To predict the described core-scale output using computational models this behaviour needs to be linked to the smaller scale wettability responses. In this work we combine the results of various experiments across length scales using similar systems to describe this relationship.

## 2 Methodology

In this work, we compiled the results of previous studies addressing wettability in similar systems [49, 74-77] and complemented the results with additional measurements to obtain wettability descriptions across all length scales.

### 2.1 Sample selection

#### *1.1.1 Crude oil*

The crude oils were chosen based on their high wettability alteration potential. The corresponding total acid number (TAN) and total base number (TBN) as well as the Saturates, Aromatics, Resins, Asphaltene (SARA) analysis are listed in Table 1. The crude oils are rich on surface active components and asphaltenes, which represent the components that are expected to change the wettability of the rock.

Crude oil B was doped with 20% - iododecane, to enhance the contrast to the brine phase for µCT imaging.

In all experiments with crude oil A, the brine phase was doped with potassium iodide. In one experiment, n-decane was used as a model oil.

### 1.1.2 Brine

The brine composition used in the current studies is listed in Table 2. The formation water (FW) recipe, typical for a carbonate reservoir, was taken from Mahani et al. [78]. For the first study with a doped brine a 17 wt% KI-brine was chosen. Based on the ionic strength this corresponds to 70400 ppm NaCl and therefore is considered a high salinity solution (HS). For the other experiment a 9 wt% KI-brine (S) was chosen to obtain better contrast between the two fluid phases.

### 1.1.3 Rock

Ketton rock is a middle Jurassic oolithic carbonate rock consisting of round grains (ooids and peloids) ranging from 100 µm – 1 mm size. Oolites are marine sediments, which form during evaporation. Dissolved carbonate precipitates along nuclei floating in the seawater, which leads to concentric growth and to the round shape of the grains. Once the particles become too heavy they accumulate at the seafloor, where they become cemented [79]. The geological history of the formation leads to a homogeneous and simple structure of the rock, which makes the rock highly suitable for µCT flow experiments [49, 80, 81].

The rock has a porosity of $\varphi = 23\%$ with a bimodal pore size distribution and permeability of 3 – 6 D. It consists predominantly of calcite (99.1%) with minor quartz (0.9%) components [82].

## 2.2 Core scale wettability assessment

At the core scale, wettability can be derived from relative permeability-saturation and capillary pressure-saturation functions. These can be obtained through special core analysis (SCAL) experiments such as steady-state core floods or Amott spontaneous imbibition tests.

### 2.2.1 Steady-state core flood experiment

Experiments to determine relative permeability were performed in a custom-built X-ray saturation measurement apparatus at Shell [18, 83, 84] following the steady-state method [85, 86].

The Ketton sample (SCAL-plug: diameter d = 2.5 cm and length L = 5 cm) was first saturated with HS-brine and then mounted inside an X-ray transparent core holder and placed in the flow apparatus for steady-state relative permeability measurement. Afterwards, the sample was desaturated with crude oil A by flooding at 1 ml/min until no further change in saturation was detected. The sample was then aged at 30 bar and 70˚ C for 1 week. The measurements were conducted at a constant flow rate, where the fractional flow $f_w$ was systematically changed from 100% crude oil to 100% brine in 10 steps ($f_{w1} = 0{,}01$; $f_{w2} = 0{,}05$; $f_{w3} = 0{,}1$; $f_{w4} = 0{,}3$; $f_{w5} = 0{,}5$; $f_{w6} = 0{,}7$; $f_{w7} = 0{,}9$; $f_{w8} = 0{,}95$; $f_{w1} = 0{,}99$; $f_{w10} = 1$). At each step saturation (and spatial profile along the core) and phase pressures were recorded after steady-state was reached. The SCAL data (pressure drop over the core and *in situ* saturation profiles at each fractional flow step) were matched numerically using Shell's in-house simulator (MoReS) to estimate the relative permeability as a function of saturation.

### 2.2.2 Amott spontaneous imbibition tests

In an Amott spontaneous imbibition test an oil-saturated rock sample is placed into a vessel containing brine. In water-wet and mixed-wet samples the water starts to spontaneously imbibe into the rock sample replacing the oil, which then gets produced, collected and monitored over time. The production rate and the cumulative production are used as a measure for wettability [67].

Bartels et al. [77] conducted an Amott spontaneous imbibition test on a SCAL plug sample and a mini plug sample commonly used for µCT studies (mini-plug: diameter $d = 4$ mm and length $L = 20$ mm).

Both samples were cleaned, saturated with brine and then desaturated with crude oil B. The SCAL plug was desaturated by centrifugation (URC-628, 129 Coretest Systems Inc., used at 3500 RPM) for 24 hours while the temperature was kept constant at 40˚C. The mini plug was desaturated by flooding 0.5 ml/min and then placed into an oven at 40 ˚C for 24 h.

Consecutively the samples were placed into Amott vessels. The production of the SCAL plug was monitored with HECTOR, a high energy µCT scanner at the Centre for X-ray Tomography (UGCT) in Ghent, Belgium [87] and the production of the mini plug with the Environmental MicroCT scanner (EMCT) also at UGCT [88]. The scans were reconstructed using dedicated reconstruction tools in the Acquila software package from Tescan XRE. Visualization and additional post-processing of the data were performed with Avizo 9.2.0 (Thermo Fischer Scientific).

The detailed experimental procedures can be found in Bartels et al. [77].

## 2.3 Pore scale wettability assessment

Lin et al. [89] stated that sample initialization, especially flooding as opposed to centrifugation may have a significant impact on the outcome. For this reason, both initialization protocols (centrifugation and flooding) were assessed at the pore scale.

### 2.3.1 Unsteady-state waterflood experiments initialized by flooding

The unsteady-state waterflood experiment was obtained from Rücker et al, [90]. The mini plug samples were first saturated with HS brine and then desaturated with crude A by flooding 0.5 ml/min using the flow cell described in Armstrong et al. [13]. The samples were aged at 3MPa and 70 ˚C for one week. The waterflood was performed at a flow rate of 0.03 ml/min. During the experiment the fluid distributions within the sample were monitored using fast µCT facility at the TOMCAT-SLS beamline at the Paul Scherrer Institute, PSI, in Switzerland, while the HS brine was injected into the sample.

The images were reconstructed using the Paganin method [91] and processed and segmented with Avizo 9.0. The wettability of the system was assessed visually and by contact angle measurements following the workflow described in Andrew et al. [13] using the filtered grey scale image of the final timestep measured during this flooding sequence.

### *2.3.1 Unsteady-state waterflood experiments initialized by centrifugation*

The unsteady-state waterflood performed on a centrifuged sample was prepared following the protocols from Lin et al. [89]. 8 subsamples with a diameter ø = 6 mm and length L = 20 mm were predrilled in a SCAL plug with a diameter ø = 3.8 cm and length $L$ = 4 cm. Subsequently, the plug was saturated with HS-brine, desaturated in a centrifuge with crude A (URC-628, 129 Coretest Systems Inc., used at 3500 RPM for 24h) and then stored under elevated pressure of 3 MPa and temperature of 70 °C for 4 weeks. Afterwards, the smaller sample was chopped off the SCAL plug and fitted into the Viton sleeve while being kept in the crude oil and placed into a core holder described in Singh et al. [56]. Consecutively, a waterflood experiment was performed by injecting HS-brine at a flow rate of 0.03 ml/min for 2 h. µCT scans with a voxel size of 6.1 µm were taken for the full sample and two smaller (988 ×1014 × 997) subsamples with a voxel size of 2 µm prior to and after the experiment using a Xradia µCT-scanner (Zeiss).

The images were reconstructed using the proprietary software provided by Zeiss, filtered with a non-local means filter and segmented with the trainable WEKA segmentation tool [92] provided by Fiji [93]. The contact angle distribution was measured manually using the filtered image obtained after the waterflood following the procedure described in Andrew et al. [13]

### 2.3 Topographical measurements with AFM

At the sub-pore scale the impact of the surface structure of a rock was assessed with atomic force microscopy (AFM). As illustrated in Fig. 2., AFM images the topography of a surface mechanically. The surface of the rock is raster scanned by an atomically sharp tip attached to the end of a cantilever. Close to the surface, intermolecular forces acting on the tip lead to a bending of the cantilever, which is monitored by a laser. For the measurements presented, special attention was given to the location at which the rock was scanned, to avoid spots affected by drilling or breakage. The rock surface was scanned with a silicon tip (PPP-NCHAuD from NANOSENSORS$^{TM}$) along a 10 µm x 10 µm area (128 × 128 pixels) using the Quantitative Imaging mode (QI$^{TM}$-mode). In this mode at each pixel a full force distance profile is obtained (i.e. the force between the AFM tip and the surface is monitored as the tip approaches the surface). The rock sample was first saturated with brine and then desaturated with n-decane by flooding (500 µl/min) to mimic the distribution of fluid films and layers at the end of drainage. In addition, test experiments were performed on calcite minerals cleaved in oil and cleaved in brine and then submerged in oil.

The image was analyzed with JPKSPM data processing software (JPK instruments) and then transformed into a 3D image using MATLAB (R2018b). These 3D images were then further processed with Geodict 2015 (Math2Market). A morphological drainage simulation assuming a water-wet contact angle of 30˚ [94] was applied. Avizo 9.0 (a) was used for visualization.

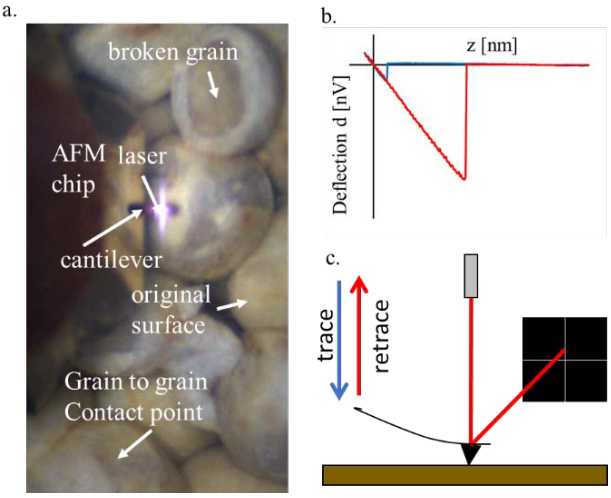

**Fig. 2.** AFM was used to image the surface of the original rock surface within a pore (a) using QI$^{TM}$-mode, which creates a force distance curve at each pixel (b) by monitoring the deflection of a cantilever with an atomic sharp tip as it approaches and disengages from the surface (c) [71].

## 3 Results and discussion

### 3.1 Wettability at the core scale

Fig. 3 shows the core-scale responses obtained from the core-scale steady-state flooding experiment and the Amott spontaneous imbibition test. The results show a difference in wettability depending on the sample initialization.

The samples prepared by flooding appear mixed-wet to water-wet. Following the guidelines to assess wettability from relative permeabilities by Blunt [73], the steady-state experiment initialized by flooding appears with a water permeability end-point of $\boldsymbol{k_{rw}^{max}}$ = 0.2 at the upper limit for a water-wet system, but would not yet be considered mixed-wet. However, with a very low residual oil saturation of $\boldsymbol{S_{res,o}}$ = 0.06 and a low water relative permeability at low water saturations (< $\boldsymbol{S_{wi+0.2}}$) of $\boldsymbol{k_{rw}(S_{wi}+0.2)}$ = 0.03, this system fulfils two of three criteria proposed to identify a mixed-wet system and

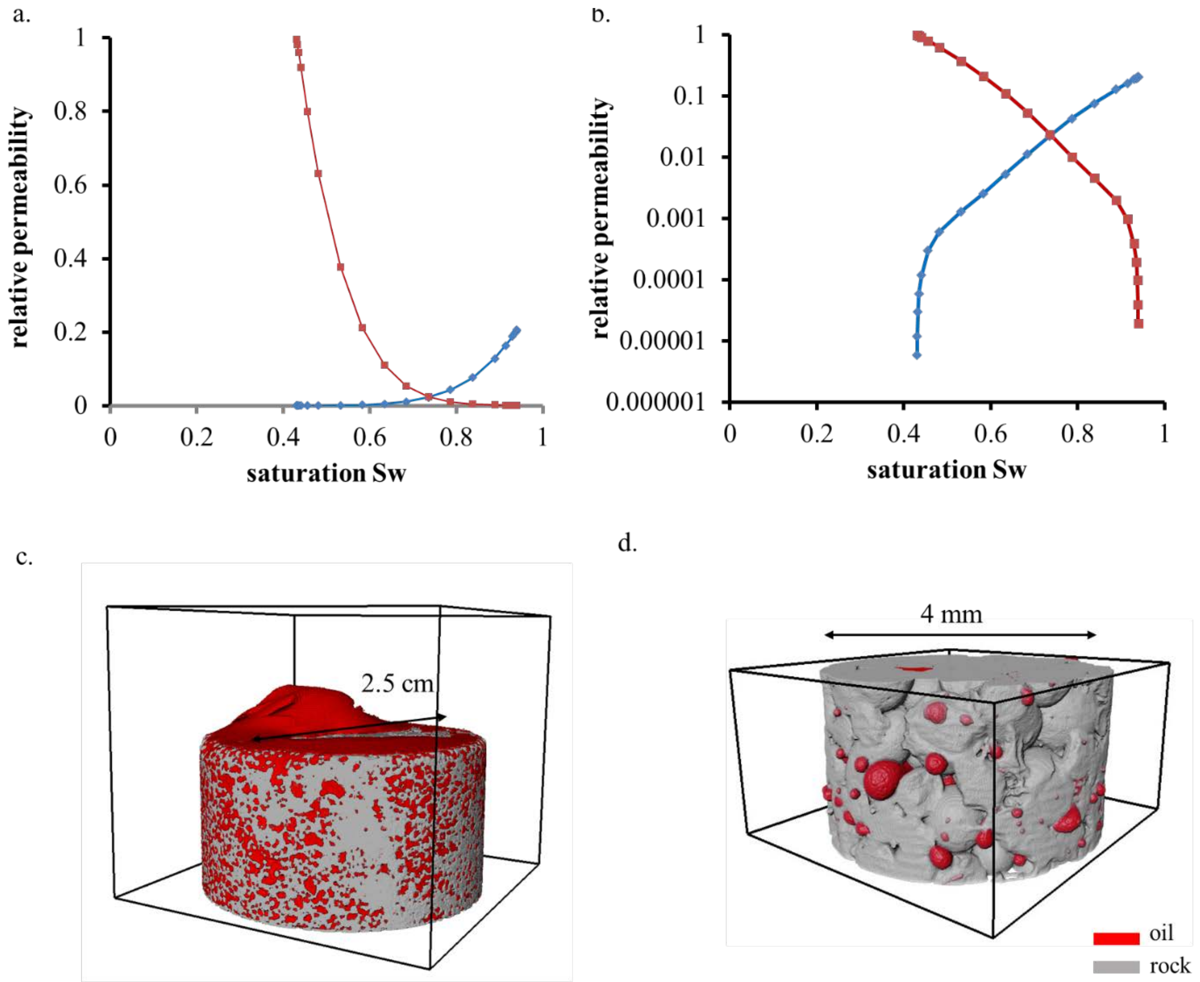

**Fig. 3.** The core scale steady-state SCAL experiment initialized by flooding shows a relative permeability, here displayed on an arithmetic (a) and semi-logarithmic scale (b), which is typical for a mixed-wet system leaning towards the water-wet side [71]. As the oil droplets (red) emerging from the rock illustrate, the Amott spontaneous imbibition tests show an oil-wet behaviour for the sample initialized by centrifugation (c, imaged using HECTOR) and water-wet behaviour for the sample initialized by flooding (d, imaged using EMCT). [74]

correspondingly is considered mixed-wet leaning to the water-wet side.

The Amott spontaneous imbibition test of the sample initialized by flooding also showed a water-wet response. As illustrated in Fig. 3d the oil droplets emerging while the brine invades the pore space show a water-wet shape. Similar observations for a Ketton rock initialized by flooding have been reported by Alyafei et al. [95].

The sample initialized by centrifugation, however, showed only a little oil production from the pore space (1%) and the oil droplets accumulating at the top of the sample showed an oil-wet structure (Fig. 3c) [77].

The difference between the initialization by flooding and the initialization by centrifugation is the capillary pressure applied during drainage.

Based on the Young-Laplace equation, a higher capillary pressure leads to the invasion of smaller pores by oil compared to a lower capillary pressure. As the rock surface is altered in contact with the crude [22], only the pores invaded by oil are expected to change wettability.

Fig. 4 shows the pore (inlet) diameter distribution of Ketton rock obtained by mercury porosimetry and the estimated pore (inlet) diameter invaded by centrifugation and flooding respectively for the Amott test examples [77]. The pore sizes invaded by centrifugation were estimated based on the rotation speed, interfacial tension and fluid densities assuming an advancing contact angle of 30˚. Based on this calculation pores down to a diameter of 0.3 µm are expected to be filled with oil [77]: this is sufficient to invade some micro-porosity and hence make the solid surfaces oil-wet. As no porous plate was used during flooding the maximum capillary pressure achieved is controlled by the pore structure itself. An exact value cannot be determined. However, the capillary pressure is expected to be at the lower end of the peak pore (inlet) diameter. µCT images obtained with the EMCT scanner after drainage were used for validation. In these images, all the resolved pore sizes showed occupancy with oil. The small amounts of water detected did not show a correlation with the pore diameter. However, it is likely that the micro-porosity in the grains remained water-saturated and water-wet. This is evident in the high initial water saturation of approximately 0.4 in the results shown in Fig. 3. The solid grains are micro-porous – if they are water-filled, they act like a wet sponge and may prevent contact of oil with the surface of the grains even in the larger pores, and hence retaining water-wet characteristics in this case. We will test this directly later in the paper by measuring water film thicknesses in the corners of the macro-pore space using AFM.

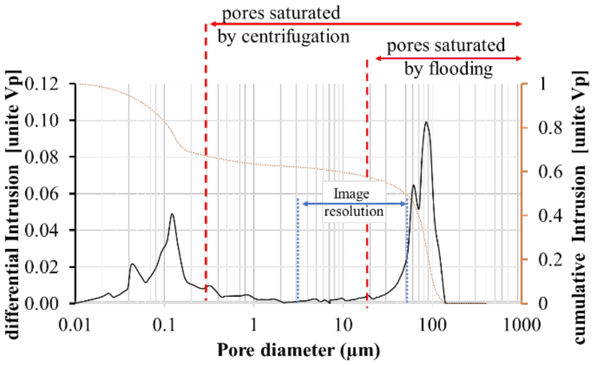

**Fig. 4.** Pore size distribution of Ketton rock. Based on the oil-saturations obtained from the experiments, initialization by flooding filled pores down to a diameter of 20 µm and centrifugation down to 0.3 µm [77].

Correspondingly, the estimated minimum pore radius accessed during flooding was set at 20 µm at the image resolution boundary (4 voxel lengths) and below the larger peak pore (inlet) diameter (Fig. 4). Smaller scale imaging techniques such as µCT and AFM can give further insights into the core-scale wettability response and will be discussed below in more detail.

### 3.2 Wettability at the pore scale

The µCT unsteady-state waterflood experiments were used to compare the impact of centrifugation and flooding on sample initialization at the pore-scale.

The images Fig. 5 and Fig. 6 show some examples of the fluid distribution at the pore-scale before and after an unsteady-state waterflood for a sample initialized by flooding (Fig. 5, measured at SLS) and by centrifugation (Fig. 6, measured with Xradia).

Next to the brine phase (white), the oil phase (black) and the rock (light grey) both figures also show the presence of a water-in-oil emulsion. In the sample initialized by flooding the emulsion appears as a third phase (dark grey) [76]. In the sample initialized by centrifugation, the emulsion appears in distinct droplets with a diameter of up to 100 µm. The emulsion forms due to the presence of surface active components in the crude, which are also responsible for the wettability alteration of the system itself. The identification and image processing of this third phase was discussed in detail by Bartels et al. [76].

Furthermore, both figures show the presence of oil films along the grain surface and in the crevices in between after the waterflood. However, for the centrifuged sample, this oil appears continuous, while the oil films in the flooded sample appear discontinuous (comparison Fig. 5 and Fig. 6). This supports the findings observed at the core-scale. The discontinuous oil films observed in the µCT images hint to a mixed-wet sample, while the continuous oil films indicate a predominantly oil-wetting surface. The difference in the emulsion phase can be explained in the same way. As the surface is oil-wet after centrifugation, large water droplets may form and remain stable, while in a mixed-wet system larger droplets are likely to collapse as they get in contact with the preserved water films in a mixed-wet system and only small droplets, (below the image resolution) remain stable.

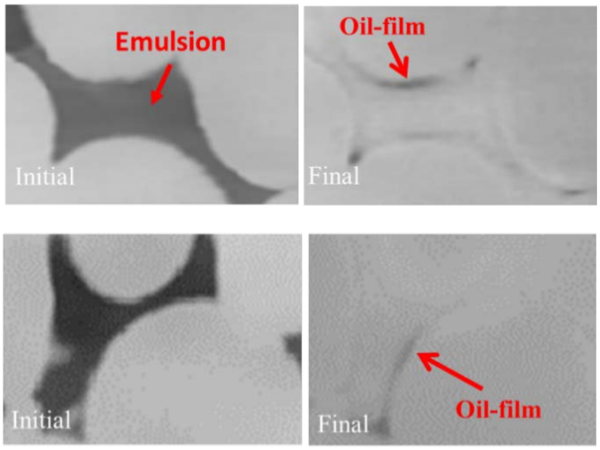

**Fig. 5.** µCT images obtained before (left) and after the waterflood experiment (right) of a Ketton rock sample (grey) initialized by flooding. Next to the oil (black) and brine (white), the images show the presence of emulsion (dark grey). Furthermore, the images show the presence of discontinuous oil films along the surfaces and in crevices [47, 71]. The images were obtained at the SLS.

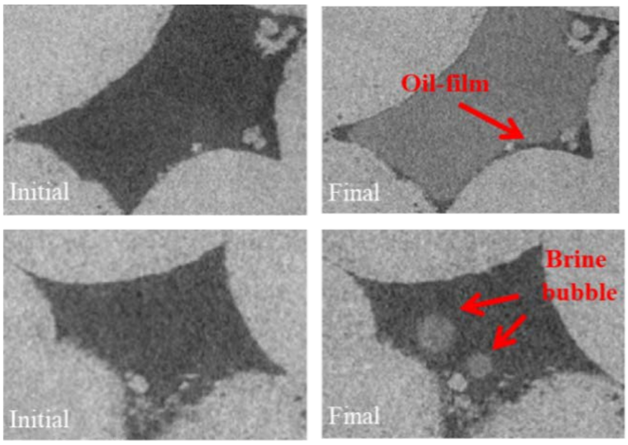

**Fig. 6.** µCT images obtained before (left) and after the waterflood experiment (right) of a Ketton rock sample initialized by centrifugation. The emulsion phase appears in form of distinct brine droplets. The oil films appear continuous. The images were obtained with Xradia [71].

The images obtained at the end of each waterflood experiment were further used to measure the contact angle distribution displayed in Fig. 6. The contact angle distribution obtained for the Ketton sample indicates a water-wet system with a peak < 90 °. However, compared to the contact angle distribution for the strongly water-wet decane-brine-Ketton rock sample reported by Scanziani et al. [51], this system seems shifted by 30° towards more oil-wet conditions.

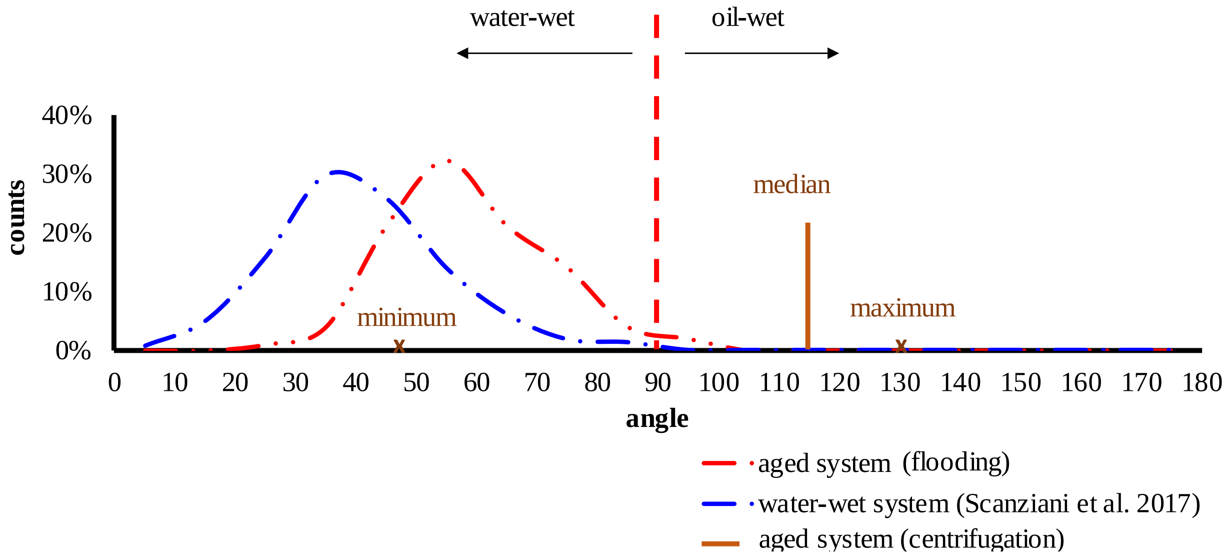

**Fig. 7.** The contact angle distribution (100 contact angles) for the unsteady-state waterflood μCT experiment with a rock sample initialized by flooding indicates a water-wet state even though more oil-wet than the water-wet reference obtained from Scanziani et al. (2017). Due to the low number of contact angles (21 contact angles) obtained for the unsteady-state waterflood μCT ex-periment performed on a centrifuged sample flooding, solely the median value, the maximum and minimum are plotted [47, 49, 71].

Yet, the contact angle distribution does not show the mixed-wet system observed in the image. The reason might be the patchy small-scale wettability pattern, which leads to pinning of the fluid-fluid interface, when the surface changes from water-wet to oil-wet.

The contact angles detected in the sample initialized by centrifugation varied from 50 ˚ to 130˚, with a median value of 115˚ (Fig. 7). Only 21 contact angles could be obtained for this sample. The reason was that the oil remained predominantly in the poorly resolved pore throats, which are less suitable for contact angle measurements. For the same reason, the contact angles obtained may be more affected by measurement errors, which needs to be considered for the following interpretation: The low values of 50˚ might be a sign of a mixed-wettability pattern. However, as the oil-phase in this sample is continuous, the pinning of the fluid-fluid interface is less pronounced.

The sample initialization of the two cores investigated were subject to different capillary pressures applied during the drainage process and aging time. However, the impact of aging time was assumed to be minor for the following reasons. First, the core-scale studies indicate that the wettability alteration of Ketton rock appears already after 24h. Second, previous studies indicated that the water-wet appearance of Ketton rock is preserved for even longer aging periods [95]. Third, oil layers, present in the flooded sample, show that wettability alteration happened where the oil was in contact with the surface. The oil layer, however, was discontinuous, which might have been caused by sub-resolution surface features, which can be investigated with AFM.

### 3.3 Wettability at the sub-pore scale

AFM was utilized to investigate the water films and layers present within the Ketton rock sample initialized by flooding.

The water-decane interface and the height of the rock surface were obtained from the force distance curves collected for all of the 128 × 128 pixels along the 10 µm × 10 µm area. Fig. 8 shows examples for such force distance curves obtained from measurements on calcite surfaces prepared with and without water.

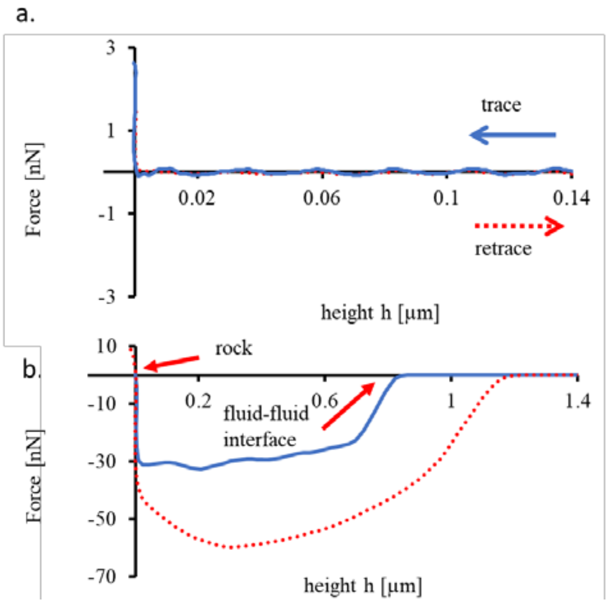

**Fig. 8.** Representative force distance curves obtained from a calcite surface without (a) and with the presence of a water film (b). As the tip passes through the brine-decane interface the cantilever is bending towards the surface, which is recorded as a negative force. Once the cantilever reaches the rock surface it gets bent in the opposite direction [71].

As the tip is water-wet, the cantilever bends towards the surface when it passes through the fluid-fluid interface during the approach, which is displayed in form of a negative force. The height of the rock surface is obtained from the bending of the tip in the opposite direction recorded as a positive force on the cantilever.

In the resulting image shown in Fig. 9, 60% of the surface was covered with brine. Only 40% of the surface were directly in contact with decane.

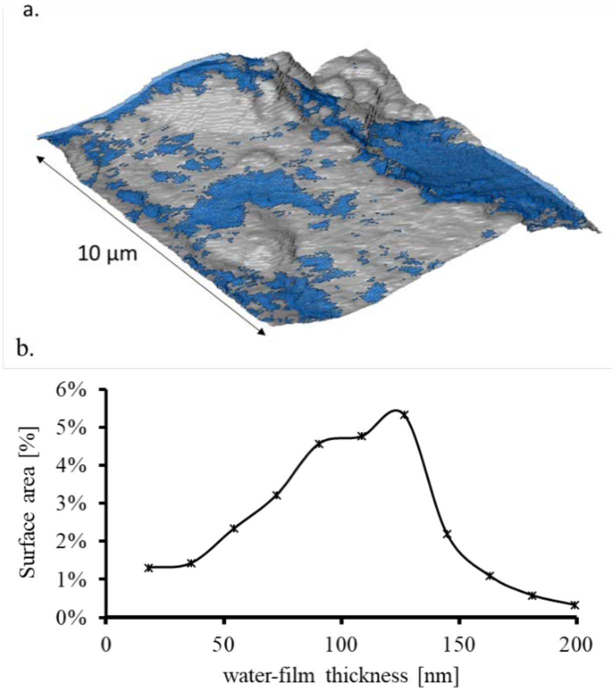

**Fig.10.** a Water film (blue) on top of a rock surface (grey) measured in decane. The water layer shows a film thickness ranging between 0 nm and 200 nm with a peak film thickness of 125nm (b) [71].

The 3D measurement of the wetting film also allows to quantify fluid film thickness. Fig.9b shows that the film thickness ranges between 0 nm and 200 nm with a peak film thickness of 125 nm.

Furthermore, the rock surface obtained was used to simulate the coverage of the rock for different capillary pressures applied using a morphological drainage simulation. The algorithm fits spheres of different radii, representing different capillary pressures, onto the surface to model the drainage process as it is applied prior to the wettability alteration in a rock.

The result is shown in Fig. 10. Fig. 10d shows the surface area coverage as a function of sphere diameter. The higher the diameter – and the lower the corresponding capillary pressure – the larger the surface area covered with brine. 50% of the surface was covered with water for a sphere diameter of 7 µm. For sphere diameters below 1.5 µm only 1.5% of the surface remained in contact with the aqueous phase. These results are in line with the detected water films.

These findings show that surface roughness of a rock can facilitate the formation of water-layers. Different capillary pressures applied on the rock during drainage result in different water coverage of the rock surface. Based on the assumption that wettability alteration occurs predominantly when the surface is in direct contact with the oil, the difference in coverage would result in a sub-pore-scale wettability pattern as indicated in section 3.2 and explain the different wettability responses observed at the core-scale.

## 4 Conclusions

In this study we assessed the wettability across the length scales using similar oil-brine-rock system, including AFM at the sub-pore scale, µCT imaging and *in situ* contact angle distributions at the pore-scale combined with Amott spontaneous imbibition tests and steady-state relative permeability measurements at the core-scale, demonstrating that upscaling is possible.

For this crude oil-brine-rock system, surface roughness and the capillary pressure applied during initialization were found to control the larger scale wettability response after aging.

AFM studies showed the formation of water films along the rock surface preventing a direct contact of the oil and the rock which lead to a patchy sub-pore scale

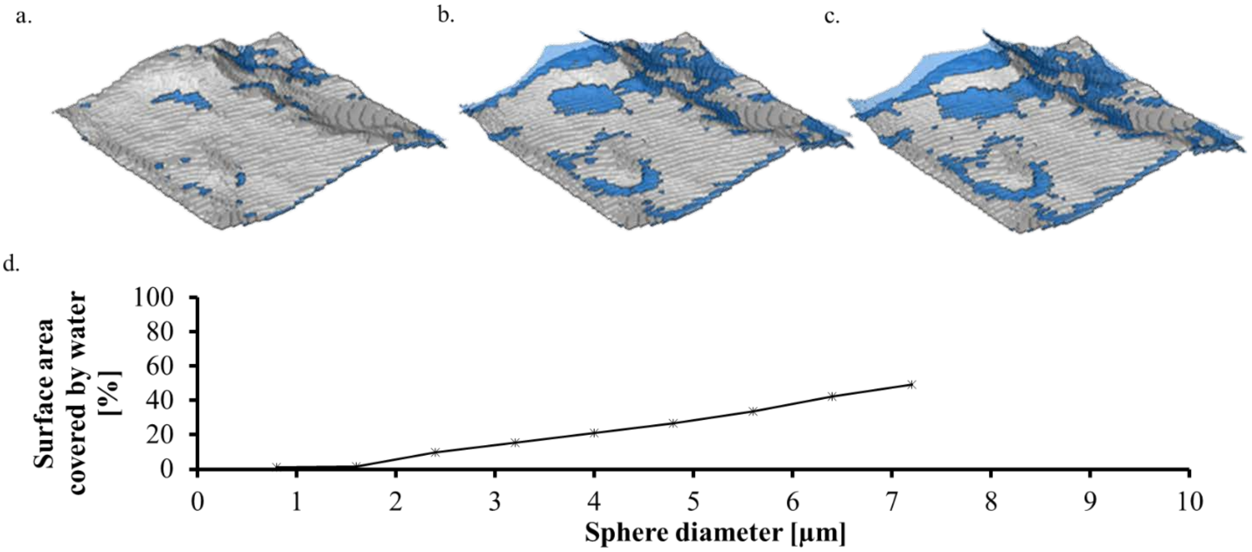

**Fig. 9.** Water films (blue) on top of a rock surface (grey) obtained from a drainage simulation based on sphere fitting (a: sphere diameter = 1.6 µm, b: sphere diameter = 5.6 µm, c: sphere diameter = 6 µm). d shows the percentage of surface area covered with brine as a function of sphere diameter [71].

wettability pattern after aging. This small-scale wettability pattern leads to a water-wet contact angle distribution at the pore-scale, while some surface show discontinuous oil layers and a mixed-wet core-scale response leaning towards the water-wet side.

Furthermore, nano-scale simulations showed that the higher the capillary pressure, the larger the oil-rock contact area. Once the oil film becomes continuous the core scale response for the same system appears oil-wet at the pore- and core-scale.

This study demonstrates that for predictions of the core-scale wettability response, the nano-scale surface structure of the rock needs to be considered.

## Acknowledgments

We would like to acknowledge the staff of UGCT, Ghent, Belgium for support for the spontaneous imbibition experiment and the Paul Scherrer Institute, Villigen, Switzerland for the provision of synchrotron radiation beamtime at TOMCAT beamline of the SLS and for assistance during the session. Furthermore, we would like to thank Anne Bonnin, Christian Hinz, Arne Jacob, Christian Wagner, Steven Henkel and Frieder Enzmann for support during the beamline experiments. We would like to acknowledge Alex Schwing and Rob Neiteler for the design of the setup and instrumentation, Fons Marcelis for sample preparation, Holger Ott, Ryan Armstrong and James McClure, Alex Winkel, Hayley Meek, Matthew Leivers, Tannaz Pak, the Shell Digital Rock team at Imperial and the team from Math2Market for helpful discussions. We gratefully acknowledge Shell Global Solutions International B.V. for their permission to publish this work.

## References

1. R. J. S. Brown and I. Fatt, "Measurements Of Fractional Wettability Of Oil Fields' Rocks By The Nuclear Magnetic Relaxation Method," presented at the Fall Meeting of the Petroleum Branch of AIME, Los Angeles, California, 1956.

2. E. C. Donaldson and W. Alam, "CHAPTER 1 - Wettability," in *Wettability*: Gulf Publishing Company, 2008, pp. 1-55.

3. R. A. Salathiel, "Oil Recovery by Surface Film Drainage In Mixed-Wettability Rocks," *Journal of Petroleum Technology,* vol. 25, no. 10, pp. 1216-1224, 1973, Art. no. SPE-4104-PA.

4. W. Anderson, "Wettability Literature Survey- Part 1: Rock/Oil/Brine Interactions and the Effects of Core Handling on Wettability," *Journal of Petroleum Technology,* vol. 38, no. 10, pp. 1125-1144, 1986, Art. no. SPE-13932-PA.

5. W. Abdallah *et al.*, "Fundamentals of wettability," *Schlumberger Oilfield Review,* vol. 19/2, pp. 44-61, 2007.

6. E. C. Donaldson and W. Alam, "CHAPTER 3 - Wettability and Production," in *Wettability*: Gulf Publishing Company, 2008, pp. 121-172.

7. W. Anderson, "Wettability Literature Survey- Part 4: Effects of Wettability on Capillary Pressure," *Journal of Petroleum Technology,* vol. 39, no. 10, pp. 1,283 - 1,300, 1987, Art. no. SPE-15271-PA.

8. W. Anderson, "Wettability Literature Survey Part 5: The Effects of Wettability on Relative Permeability," *Journal of Petroleum Technology,* vol. 39, no. 11, pp. 1453-1468, 1987, Art. no. SPE-16323-PA.

9. T. Hassenkam, L. L. Skovbjerg, and S. L. S. Stipp, "Probing the intrinsically oil-wet surfaces of pores in North Sea chalk at subpore resolution," *Proceedings of the National Academy of Sciences,* vol. 106, no. 15, pp. 6071-6076, 2009.

10. T. Hassenkam *et al.*, "Could Atomic-Force Microscopy Force Mapping Be a Fast Alternative to Core-Plug Tests for Optimizing Injection-Water Salinity for Enhanced Oil Recovery in Sandstone?," *SPE Journal,* vol. 21, no. 03, pp. 720 - 729, 2015, Art. no. SPE-169136-PA.

11. J. Matthiesen *et al.*, "How Naturally Adsorbed Material on Minerals Affects Low Salinity Enhanced Oil Recovery," *Energy & Fuels,* vol. 28, no. 8, pp. 4849-4858, 2014.

12. N. R. Morrow, "The Effects of Surface Roughness On Contact: Angle With Special Reference to Petroleum Recovery," *Journal of Canadian Petroleum Technology,* vol. 14, no. 04, pp. 0021-9487, 1975.

13. M. Andrew, B. Bijeljic, and M. J. Blunt, "Pore-scale contact angle measurements at reservoir conditions using X-ray microtomography," *Advances in Water Resources,* vol. 68, pp. 24-31, 2014.

14. A. L. Herring, E. J. Harper, L. Andersson, A. Sheppard, B. K. Bay, and D. Wildenschild, "Effect of fluid topology on residual nonwetting phase trapping: Implications for geologic CO2 sequestration," *ADV WATER RESOUR,* vol. 62, pp. 47-58, 2013.

15. A. L. Herring, A. Sheppard, L. Andersson, and D. Wildenschild, "Impact of wettability alteration on 3D nonwetting phase trapping and transport," *International Journal of Greenhouse Gas Control,* vol. 46, pp. 175-186, 2016.

16. R. T. Armstrong, M. L. Porter, and D. Wildenschild, "Linking pore-scale interfacial curvature to column-scale capillary pressure," *Advances in Water Resources,* vol. 46, pp. 55-62, 2012.

17. T. Bultreys *et al.*, "Validation of model predictions of pore-scale fluid distributions during two-phase flow," *Physical Review E*, vol. 97, no. 5, p. 053104, 2018.

18. S. Berg *et al.*, "Connected pathway relative permeability from pore-scale imaging of imbibition," *Advances in Water Resources*, vol. 90, pp. 24-35, 2016.

19. F. C. Benner, W. W. Riches, and F. E. Bartell, "Nature and Importance of Surface Forces in Production of Petroleum," presented at the Drilling and Production Practice, Amarillo, Texas, 1938.

20. K. Kumar, E. Dao, and K. Mohanty, "Atomic force microscopy study of wettability alteration," presented at the SPE International Symposium on Oilfield Chemistry, The Woodlands, Texas 2005.

21. M. A. Fernø, M. Torsvik, S. Haugland, and A. Graue, "Dynamic Laboratory Wettability Alteration," *Energy & Fuels*, vol. 24, no. 7, pp. 3950-3958, 2010.

22. J. S. Buckley, "Effective wettability of minerals exposed to crude oil," *Current Opinion in Colloid & Interface Science*, vol. 6, no. 3, pp. 191-196, 2001.

23. M. S. Akhlaq, D. Kessel, and W. Dornow, "Separation and Chemical Characterization of Wetting Crude Oil Compounds," *Journal of Colloid and Interface Science*, vol. 180, no. 2, pp. 309-314, 1996.

24. M. White, K. Pierce, and T. Acharya, "A Review of Wax-Formation/Mitigation Technologies in the Petroleum Industry," *SPE Production & Operations*, vol. 33, no. 03, pp. 476 - 485, 2017, Art. no. SPE-189447-PA.

25. T. Fan, J. Wang, and J. S. Buckley, "Evaluating Crude Oils by SARA Analysis," presented at the SPE/DOE Improved Oil Recovery Symposium, Tulsa, Oklahoma, 2002.

26. B. Derjaguin and L. Landau, "Theory of the stability of strongly charged lyophobic sols and of the adhesion of strongly charged particles in solutions of electrolytes," *Acta Physico Chimica URSS*, vol. 14, no. 633, 1941.

27. J. T. G. Overbeek and E. Verwey, *Theory of the Stability of Lyophobic Colloids: The interaction of Sol Particles Having an Electric Double Layer*. New York-Amsterdam: Elsevier Publishing Company., 1948.

28. J. N. Israelachvili, "17 - Adhesion and Wetting Phenomena," in *Intermolecular and Surface Forces (Third Edition)*San Diego: Academic Press, 2011, pp. 415-467.

29. G. J. Hirasaki, "Wettability: Fundamentals and Surface Forces," *SPE Formation Evaluation*, vol. 6, no. 02, pp. 217 - 226, 1991, Art. no. SPE-17367-PA.

30. C. Drummond and J. Israelachvili, "Fundamental studies of crude oil–surface water interactions and its relationship to reservoir wettability," *Journal of Petroleum Science and Engineering*, vol. 45, no. 1-2, pp. 61-81, 2004.

31. W. B. Bartels, H. Mahani, S. Berg, and S. M. Hassanizadeh, "Literature review of low salinity waterflooding from a length and time scale perspective," *Fuel*, vol. 236, pp. 338-353, 2019.

32. J. S. Buckley, Y. Liu, X. Xie, and N. R. Morrow, "Asphaltenes and Crude Oil Wetting - The Effect of Oil Composition," *SPE Journal*, vol. 2, no. 02, pp. 107-119, 1997, Art. no. SPE-35366-PA.

33. P. Purswani, M. S. Tawfik, and Z. T. Karpyn, "Factors and Mechanisms Governing Wettability Alteration by Chemically Tuned Waterflooding: A Review," *Energy & Fuels*, vol. 31, no. 8, pp. 7734-7745, 2017.

34. A. Mennella, N. R. Morrow, and X. Xie, "Application of the dynamic Wilhelmy plate to identification of slippage at a liquid-liquid-solid three-phase line of contact," *Journal of Petroleum Science and Engineering*, vol. 13, no. 3, pp. 179-192, 1995.

35. Y. Deng, L. Xu, H. Lu, H. Wang, and Y. Shi, Direct measurement of the contact angle of water droplet on quartz in a reservoir rock with atomic force microscopy," *Chemical Engineering Science*, vol. 177, pp. 445-454, 2018.

36. R. Giro, P. W. Bryant, M. Engel, R. F. Neumann, and M. B. Steiner, "Adsorption energy as a metric for wettability at the nanoscale," *Scientific Reports*, vol. 7, p. 46317, 2017.

37. L. E. Treiber and W. W. Owens, "A Laboratory Evaluation of the Wettability of Fifty Oil-Producing Reservoirs," *SPE Journal*, vol. 12, no. 06, pp. 531 - 540, 1972, Art. no. SPE-3526-PA.

38. R. O. Leach, O. R. Wagner, H. W. Wood, and C. F. Harpke, "A Laboratory and Field Study of Wettability Adjustment in Water Flooding," *Journal of Petroleum Technology*, vol. 14, no. 02, pp. 206-212, 1962, Art. no. SPE-119-PA.

39. F. G. McCaffery and N. Mungan, "Contact Angle And Interfacial Tension Studies of Some Hydrocarbon-Water-Solid Systems," *Journal of Canadian Petroleum Technology*, vol. 9, no. 03, pp. 185-196, 1970.

40. O. S. Hjelmeland and L. E. Larrondo, "Experimental Investigation of the Effects of Temperature, Pressure, and Crude Oil Composition on Interfacial Properties," *SPE Reservoir Engineering,* vol. 1, no. 04, pp. 321-328, 1986.

41. A. W. Neumann and R. J. Good, "Techniques of Measuring Contact Angles," in *Surface and Colloid Science: Volume 11: Experimental Methods,* R. J. Good and R. R. Stromberg, Eds. Boston, MA: Springer US, 1979, pp. 31-91.

42. D. Broseta, N. Tonnet, and V. Shah, "Are rocks still water-wet in the presence of dense CO2 or H2S?," *Geofluids,* vol. 12, no. 4, pp. 280-294, 2012.

43. R. N. Wenzel, "RESISTANCE OF SOLID SURFACES TO WETTING BY WATER," *Industrial & Engineering Chemistry,* vol. 28, no. 8, pp. 988-994, 1936.

44. A. Fogden, "Effect of Water Salinity and pH on the Wettability of a Model Substrate," *Energy & Fuels,* vol. 25, no. 11, pp. 5113-5125, 2011.

45. E. E. Santiso, C. Herdes, and E. A. Müller, "On the Calculation of Solid-Fluid Contact Angles from Molecular Dynamics," *Entropy,* vol. 15, no. 9, pp. 3734-3745, 2013.

46. A. R. Kovscek, H. Wong, and C. J. Radke, "A pore-level scenario for the development of mixed wettability in oil reservoirs," *AIChE Journal,* vol. 39, no. 6, pp. 1072-1085, 1993.

47. D. Quéré, "Wetting and Roughness," *Annual Review of Materials Research,* vol. 38, no. 1, pp. 71-99, 2008.

48. S. Herminghaus, "Roughness-induced non-wetting," *Europhysics Letters,* vol. 52, no. 2, pp. 165-170, 2000.

49. M. Rücker *et al.*, "The Effect of Mixed Wettability on Pore-Scale Flow Regimes Based on a Flooding Experiment in Ketton Limestone," *Geophysical Research Letters,* vol. 46, no. 6, pp. 3225-3234, 2019.

50. J. S. Buckley, C. Bousseau, and Y. Liu, "Wetting Alteration by Brine and Crude Oil: From Contact Angles to Cores," *SPE Journal,* vol. 1, no. 03, pp. 341-350, 1996, Art. no. SPE-30765-PA.

51. A. Scanziani, K. Singh, M. J. Blunt, and A. Guadagnini, "Automatic method for estimation of in situ effective contact angle from X-ray micro tomography images of two-phase flow in porous media," *Journal of Colloid and Interface Science,* vol. 496, pp. 51-59, 2017.

52. A. AlRatrout, A. Q. Raeini, B. Bijeljic, and M. J. Blunt, "Automatic measurement of contact angle in pore-space images," *Advances in Water Resources,* vol. 109, pp. 158-169, 2017.

53. A. M. Alhammadi, A. AlRatrout, K. Singh, B. Bijeljic, and M. J. Blunt, "In situ characterization of mixed-wettability in a reservoir rock at subsurface conditions," *Scientific Reports,* vol. 7, no. 1, p. 10753, 2017.

54. S. Iglauer, M. Fernø, P. Shearing, and M. Blunt, "Comparison of residual oil cluster size distribution, morphology and saturation in oil-wet and water-wet sandstone," *Journal of colloid and interface science,* vol. 375, no. 1, pp. 187-192, 2012.

55. R. I. Al-Raoush, "Impact of Wettability on Pore-Scale Characteristics of Residual Nonaqueous Phase Liquids," *Environmental Science & Technology,* vol. 43, no. 13, pp. 4796-4801, 2009.

56. K. Singh, B. Bijeljic, and M. J. Blunt, "Imaging of oil layers, curvature and contact angle in a mixed-wet and a water-wet carbonate rock," *Water Resources Research,* vol. 52, no. 3, pp. 1716-1728, 2016.

57. Q. Lin, B. Bijeljic, S. Berg, R. Pini, M. J. Blunt, and S. Krevor, "Minimal surfaces in porous media: Pore-scale imaging of multiphase flow in an altered-wettability Bentheimer sandstone," *Physical Review E,* vol. 99, no. 6, p. 063105, 2019.

58. P. Lehmann *et al.*, "Impact of geometrical properties on permeability and fluid phase distribution in porous media," *Advances in Water Resources,* vol. 31, no. 9, pp. 1188-1204, 2008.

59. V. Joekar-Niasar, S. M. Hassanizadeh, and A. Leijnse, "Insights into the Relationships Among Capillary Pressure, Saturation, Interfacial Area and Relative Permeability Using Pore-Network Modeling," *Transport in Porous Media,* journal article vol. 74, no. 2, pp. 201-219, 2008.

60. H. J. Vogel, U. Weller, and S. Schlüter, "Quantification of soil structure based on Minkowski functions," *Computers & Geosciences,* vol. 36, no. 10, pp. 1236-1245, 2010.

61. S. Schlüter *et al.*, "Pore-scale displacement mechanisms as a source of hysteresis for two-phase flow in porous media," *Water Resources Research,* vol. 52, no. 3, pp. 2194-2205, 2016.

62. R. T. Armstrong *et al.*, "Porous Media Characterization Using Minkowski Functionals: Theories, Applications and Future Directions," *Transport in Porous Media,* journal article 2018.

63. A. L. Herring, J. Middleton, R. Walsh, A. Kingston, and A. Sheppard, "Flow rate impacts on capillary pressure and interface curvature of connected and disconnected fluid phases during multiphase flow in sandstone," *Advances in Water Resources,* vol. 107, pp. 460-469, 2017.

64. S. Zou, R. T. Armstrong, J.-Y. Arns, C. H. Arns, and F. Hussain, "Experimental and Theoretical Evidence for Increased Ganglion Dynamics During Fractional Flow in Mixed-Wet Porous Media," *Water Resources Research,* vol. 54, no. 5, pp. 3277-3289, 2018.

65. Q. Lin, B. Bijeljic, R. Pini, M. J. Blunt, and S. Krevor, "Imaging and Measurement of Pore-Scale Interfacial Curvature to Determine Capillary Pressure Simultaneously With Relative Permeability," *Water Resources Research,* vol. 54, no. 9, pp. 7046-7060, 2018.

66. E. C. Donaldson, R. D. Thomas, and P. B. Lorenz, "Wettability Determination and Its Effect on Recovery Efficiency," *SPE Journal,* vol. 9, no. 01, pp. 13 - 20, 1969.

67. E. Amott, "Observations Relating to the Wettability of Porous Rock," *Petroleum Transactions, AIME,* vol. 216, pp. 156-162, 1959, Art. no. SPE-1167-G.

68. C. C. Mattax and J. Kyte, "Imbibition oil recovery from fractured, water-drive reservoir," *SPE Journal,* vol. 2, no. 02, pp. 177-184, 1962, Art. no. SPE-187-PA.

69. S. Ma, N. Morrow, and X. Zhang, "Generalized scaling of spontaneous imbibition data for strongly water-wet systems," presented at the Technical Meeting/Petroleum Conference of The South Saskatchewan Section, Regina, Canada, 1995.

70. K. S. Schmid and S. Geiger, "Universal scaling of spontaneous imbibition for arbitrary petrophysical properties: Water-wet and mixed-wet states and Handy's conjecture," *Journal of Petroleum Science and Engineering,* vol. 101, pp. 44-61, 2013.

71. M. C. Leverett, "Capillary Behavior in Porous Solids," *Transactions of the AIME,* vol. 142, no. 01, pp. 152-169, 1941.

72. S. Zou and R. Armstrong, "Multiphase Flow Under Heterogeneous Wettability Conditions Studied by Special Core Analysis and Pore-Scale Imaging," *SPE Journal,* vol. 24, no. 03, pp. 1234-1247, 2019.

73. M. J. Blunt, *Multiphase flow in permeable media: a pore-scale perspective*. Cambridge, UK: Cambridge University Press, 2017.

74. M. Rücker, "Wettability and wettability alteration at the pore- and nano- scales," PhD Thesis, Imperial College London, 2018.

75. W. Bartels, "Pore scale processes in mixed-wet systems with application to low salinity waterflooding," PhD PhD Thesis, UU Dept. of Earth Sciences, 2018.

76. W. B. Bartels *et al.*, "Fast X-Ray Micro-CT Study of the Impact of Brine Salinity on the Pore-Scale Fluid Distribution During Waterflooding," *Petrophysics,* vol. 58, no. 01, pp. 36-47, 2017.

77. W. Bartels *et al.*, "Pore-scale displacement during fast imaging of spontaneous imbibition " presented at the International Symposium of the Society of Core Analysts, Vienna, Austria, 2017.

78. H. Mahani, A. L. Keya, S. Berg, W.-B. Bartels, R. Nasralla, and W. R. Rossen, "Insights into the Mechanism of Wettability Alteration by Low-Salinity Flooding (LSF) in Carbonates," *Energy & Fuels,* vol. 29, no. 3, pp. 1352-1367, 2015.

79. E. Flügel, *Microfacies of carbonate rocks: analysis, interpretation and application*. Springer Science & Business Media, 2013.

80. K. Singh *et al.*, "Dynamics of snap-off and pore-filling events during two-phase fluid flow in permeable media," *Scientific Reports,* vol. 7, p. 5192, 2017.

81. M. Andrew, H. Menke, M. J. Blunt, and B. Bijeljic, "The Imaging of Dynamic Multiphase Fluid Flow Using Synchrotron-Based X-ray Microtomography at Reservoir Conditions," *Transport In Porous Media,* journal article vol. 110, no. 1, pp. 1-24, 2015.

82. M. Andrew, "Reservoir-Condition Pore-Scale Imaging of Multiphase Flow," PhD PhD Thesis, Earth Science and Engineering, Imperial College London, London, 2015.

83. J. Kokkedee, W. Boom, A. Frens, and J. Maas, "Improved special core analysis: scope for a reduced residual oil saturation," presented at the Society of core analysis conference paper, Montpellier, France, 1996.

84. S. Berg, A. W. Cense, J. P. Hofman, and R. M. M. Smits, "Two-Phase Flow in Porous Media with Slip Boundary Condition," *Transport in Porous Media,* journal article vol. 74, no. 3, pp. 275-292, 2008.

85. C. McPhee, J. Reed, and I. Zubizarreta, *Core Analysis: A Best Practice Guide*. Amsterdam, The Netherlands: Elsevier, 2015.

86. L. Dake, *Fundamentals of Reservoir Engineering., 1978*. Elsevier, New York, 1983.

87. B. Masschaele *et al.*, "HECTOR: A 240kV micro-CT setup optimized for research," *Journal of Physics: Conference Series,* vol. 463, p. 012012, 2013.

88. T. Bultreys, W. De Boever, and V. Cnudde, "Imaging and image-based fluid transport modeling at the pore scale in geological materials: A practical introduction to the current state-of-the-art," *Earth-Science Reviews,* vol. 155, pp. 93-128, 2016.

89. Q. Lin *et al.*, "A New Waterflood Initialization Protocol With Wettability Alteration for Pore-Scale Multiphase Flow Experiments," *Petrophysics,* vol. 60, no. 02, pp. 264-272, 2019.

90. M. Rücker *et al.*, "A time-resolved synchrotron X-ray micro-tomography dataset of a waterflood in an altered mixed-wet Ketton limestone," ed: Digital Rocks Portal, 2019.

91. D. Paganin, S. Mayo, T. E. Gureyev, P. R. Miller, and S. W. Wilkins, "Simultaneous phase and amplitude extraction from a single defocused image of a homogeneous object," *Journal of Microscopy,* vol. 206, no. 1, pp. 33-40, 2002.

92. I. Arganda-Carreras *et al.*, "Trainable Weka Segmentation: a machine learning tool for microscopy pixel classification," *Bioinformatics,* vol. 33, no. 15, pp. 2424-2426, 2017.

93. J. Schindelin *et al.*, "Fiji: an open-source platform for biological-image analysis," *Nature Methods,* Perspective vol. 9, p. 676, 2012.

94. M. Hilpert and C. T. Miller, "Pore-morphology-based simulation of drainage in totally wetting porous media," *Advances in Water Resources,* vol. 24, no. 3, pp. 243-255, 2001.

95. N. Alyafei and M. J. Blunt, "The effect of wettability on capillary trapping in carbonates," *Advances in Water Resources,* vol. 90, no. Supplement C, pp. 36-50, 2016.

# Is contact angle a cause or an effect? – A cautionary tale

*Douglas* Ruth

University of Manitoba, Winnipeg, Manitoba, Canada

**Abstract.** The most influential parameter on the behavior of two-component flow in porous media is "wettability". When wettability is being characterized, the most frequently used parameter is the "contact angle". When a fluid-drop is placed on a solid surface, in the presence of a second, surrounding fluid, the fluid-fluid surface contacts the solid-surface at an angle that is typically measured through the fluid-drop. If this angle is less than 90°, the fluid in the drop is said to "wet" the surface. If this angle is greater than 90°, the surrounding fluid is said to "wet" the surface. This definition is universally accepted and appears to be scientifically justifiable, at least for a static situation where the solid surface is horizontal. Recently, this concept has been extended to characterize wettability in non-static situations using high-resolution, two-dimensional digital images of multi-component systems. Using simple thought experiments and published experimental results, many of them decades old, it will be demonstrated that contact angles are not primary parameters – their values depend on many other parameters. Using these arguments, it will be demonstrated that contact angles are not the cause of wettability behavior but the effect of wettability behavior and other parameters. The result of this is that the contact angle cannot be used as a primary indicator of wettability except in very restricted situations. Furthermore, it will be demonstrated that even for the simple case of a capillary interface in a vertical tube, attempting to use simply a two-dimensional image to determine the contact angle can result in a wide range of measured values. This observation is consistent with some published experimental results. It follows that contact angles measured in two-dimensions cannot be trusted to provide accurate values and these values should not be used to characterize the wettability of the system.

## 1 Introduction

This paper will discuss various considerations of the interface between a gas, a liquid, and a solid surface. The fundamental principle of a force balance between the gas and the liquid, if they are separated by a curved surface, is that the difference in pressure across that surface, $\Delta P$, is given by

$$\Delta P = \sigma_{lg}\left(\frac{1}{R_1}+\frac{1}{R_2}\right) \qquad (1)$$

Here $\sigma_{lg}$ is the interfacial tension between the gas and the liquid, and $R_1$ and $R_2$ are the two radii of curvature of the surface. If a drop of fluid is placed on a flat, solid surface, a balance of forces requires that (Young's equation)

$$\sigma_{lg}\cos\theta = \sigma_{sg} - \sigma_{sl} \qquad (2)$$

Here $\sigma_{sg}$ is the interfacial tension between the solid and the gas, $\sigma_{sl}$ is the interfacial tension between the solid and the liquid, and $\theta$ is the angle that the liquid-gas surface makes with the solid surface, termed the "contact angle". If the solid is a circular capillary tube, then the pressure difference across the surface is termed "capillary pressure", $P_c$, and simple rules of geometry lead to the expression

$$P_c = \frac{4\,\sigma_{lg}\cos\theta}{\delta} \qquad (3)$$

Here $\delta$ is the diameter of the tube. These three equations are all that is required to demonstrate the characteristic behaviors of contact angles.

Generally, Equation 2 is used to determine the wettability of a three component (liquid-gas-solid) system. Specifically, if $\theta$ when measured through the liquid is found to be much less than 90˚, the system is said to be strongly "liquid wet"; a typical liquid wet system is water/ air/ glass. If $\theta$ is near 90˚ the system is said to be "neutrally wet". If $\theta$ is much greater than 90˚, the system is said to be "gas wet"; a typical gas wet system is mercury/ air/ glass. For very simple cases, such as a drop of water on a horizontal solid surface, this definition of wettability is universally accepted. Unfortunately, this definition has become dogmatic and it has been extended to mean that the contact angle directly defines the wettability in all situations. In particular, with the advent of high resolution imaging methods, apparent contact angles can be measured *in-situ* in both static and dynamic situations. In the present paper, published results and simple thought experiments are to demonstrate that contact angles are not always characteristic of wettability. Furthermore, it is demonstrated that direct measurement of *in situ* contact angles is difficult without sophisticated interpretation methods.

This paper is not a condemnation of the ability to determine contact angles on the microscopic scale – it is a cautionary statement that such determinations must be done with great care. However, this paper does demonstrate that interpreting wettability from direct contact angle measurements is not always a meaningful activity.

## 2 The Contact Angle and Wettability

It is a tacit assumption that if a contact angle can be measured, then the wettability of a system can be determined. However, there are many cases where this assumption is obviously wrong. One of these cases is demonstrated in the classic monograph by Craig [1].

---

* Corresponding author: douglas.ruth@umanitoba.ca

His Fig. 2.3 clearly demonstrates that even in the case of a static contact angle measurement, it can take many hundreds of hours to obtain an equilibrium contact angle. The illustration is for an oil/water/solid surface and it could be argued that such systems are susceptible to complex chemical factors. However, even this simple case provides a cautionary note. Modelling of displacement processes generally utilize capillary pressure data that is time-independent. But if the contact angle is time dependent, then it follows from Equation 3 that the capillary pressure must be time dependent. Therefore, all displacement processes are potentially time dependent, an issue rarely considered when analyzing such processes.

A second case of interest is that of a drop on a surface, when the surface is gradually tilted from the horizontal. This case has been studied since at least the late 1930s [2]. A more recent paper by Krasovitski and Marmur [3] provides a succinct description of this case. What they found is that the drop distorts but does not move until the plate is tilted to a critical angle, the "slip angle". Assuming, a gas/ water/ solid system, when the drop distorts, the contact angle at the up-tilt end of the drop, $\theta_u$, decreases and the contact angle at the down-tilt end of the sample, $\theta_d$, increases. Using the conventional interpretation, this would mean that simply tilting the surface causes the up-tilt end of the system to become more water-wet while the down-tilt end of the system moves toward neutral-wettability

It is found both experimentally and theoretically that the slip angle, $\alpha$, is related to the two contact angles by the relation

$$\sin\alpha = C\,\sigma_{lg}(\cos\theta_u - \cos\theta_d) \qquad (4)$$

Here $C$is a constant that depends on the densities of the fluids, gravitational acceleration, and drop shape. Krasovitski and Marmur also document that once the drop begins to move, the values of $\theta_u$ and $\theta_d$ do not remain constant. An argument can be made that these changes are due to the fact that the up-tilt contact line is receding over a surface which was in contact with water, while the down-tilt contact line is advancing over a surface that was in contact with gas, and that this difference accounts for the difference between "advancing contact angles" and "receding contact angles". However, at tilt angles less than the slip angle, this argument does not apply because the drop has not yet moved.

Next, consider a water/ air/ solid system in a vertical capillary tube with one end immersed in a tray of liquid and the other open to air. The well-known behavior is that water will rise in the tube until a force balance obtains between the hydrostatic and capillary forces. The pressure in the water at the water-surface in the tray must be equal to the pressure in the air at this point. Therefore, this force balance requires that

$$\frac{4\,\sigma_{lg}\cos\theta}{\delta} = (\rho_l - \rho_g)\,g\,h \qquad (5)$$

Here $\rho_l - \rho_g$ is the difference between the densities of water and air, $g$ is the acceleration of gravity, and $h$ is the height of the liquid/ air interface in the capillary tube relative to the height of the liquid/ gas interface in the tray.

Now consider what would happen if the tube is gently removed from the tray and a second water/ air surface is created at the bottom of the tube. The pressure below the bottom water/ air surface differs from the pressure above the top water/ air surface by $\rho_g\,g\,h$. Therefore, the hydrostatic pressure of the water in the tube just makes up for the capillary pressure at the upper surface and the pressure difference at the bottom water/air surface must remain at zero. But this implies that the bottom surface is flat and that $\theta$ is 90°. Using our conventional definition of wettability means that the top surface is strongly water-wet and the bottom surface is neutrally-wet.

Continuing this line of reasoning, various amounts of water can be forced from the tube to obtain force balances that would require

$$\frac{4\,\sigma_{lg}}{\delta}(\cos\theta_{top} - \cos\theta_{bottom}) = (\rho_l - \rho_g)\,g\,h \qquad (5)$$

Therefore, by implication, the contact angle at the bottom water/air surface would have values given by the equation

$$\theta_{bottom} = \operatorname{arcos}\left(\cos\theta_{top} - \frac{\delta\,(\rho_l - \rho_g)\,g\,h}{4\,\sigma_{lg}}\right) \qquad (6)$$

This equation implies that wettability at the bottom of the tube varies continuously with height of water.

The above description is an approximation to what would actually happen experimentally. The bottom of the tube includes a flat surface which complicates the situation. Water can spread across this surface resulting is a convex-up surface that increases the pressure at the bottom surface, hence the pressure at the top surface. However, the conclusion remains the same – the contact angle at the top surface cannot be the same as the contact angle at the bottom surface or the tube will drain and experimentally it is found that the tube does not drain.

A variation on the above reasoning can be made for a horizontal tube that is spun in a centrifuge. The equation describing the capillary pressure in this system is

$$P_{co} - P_{ci} = (\rho_g - \rho_l)\frac{\omega^2}{2}({r_o}^2 - {r_i}^2) \qquad (7)$$

Here $r$ is the radius of rotation, the subscript $i$ denotes the variables at the fluid interface closest to the center of rotation, $o$ denotes the variables at the interface farthest from the center of rotation, and $\omega$ is the angular velocity. At zero angular velocity, the pressures in the water at the two ends of the tube are the same. As the angular velocity is increased, the equilibrium condition requires that the capillary pressures at the two ends of the tube must differ. Using Equation 3, this difference can be expressed in terms of contact angles:

$$\frac{4\,\sigma_{lg}}{\delta}(\cos\theta_o - \cos\theta_i) = \left(\rho_g - \rho_l\right)\frac{\omega^2}{2}\left({r_o}^2 - {r_i}^2\right) \tag{8}$$

We can conclude from this that the contact angle for the interface farthest from the center of rotation varies with angular velocity; hence, following conventional reasoning, the wettability at this point, is a function of angular velocity which is not true.

There are also many reports in the literature of how the contact angle at the interface of two fluids in a tube differ with the velocity of the interface. It is well known that the problem of a moving contact angle cannot be solved analytically because a singularity arises in the equations at the contact point of the two fluids and the solid surface. This singularity is generally treated by assuming that there is “slip” at the contact line. Based on this model, the classic paper by Cox [4] showed that the apparent contact angle was related to the static contact angle as a function of the capillary number. This behavior was verified experimentally in such works as Fermigier and Jenffer [5]. It is found that, above a capillary number of approximately $10^{-3}$, the apparent contact angle can vary significantly, going from static values of 30° to values approaching 180°. In terms of wettability, these contact angles imply a variation from strongly water wet to strongly oil wet. Therefore, for dynamic displacements in capillary tubes, the contact angle cannot be used to characterize the wettability. If this is true for flow in capillary tubes, it must also be true for flow in porous media.

## 3 In-Situ Measurements of Contact Angles

There has been a recent interest in measuring contact angles in-situ by means of micro-imaging techniques (*e.g.* Andrew *et al* [5], Held *et al* [6]). However, of porosity by means of two-dimensional images, in-situ measurements of contact angles are problematic. similar to the measurement. This will be illustrated by using the case of an interface in a vertical capillary tube.

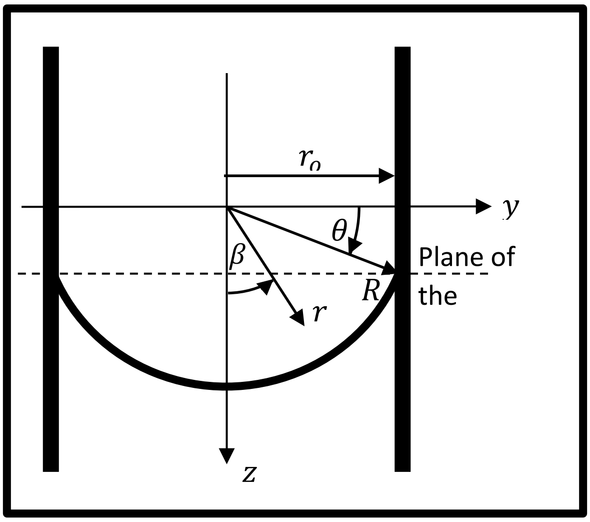

Fig. 1a Nomenclature for an interface in a vertical tube (elevation view).

Fig. 1 shows the nomenclature for an interface in a vertical tube. The interface is assumed to have a spherical shape with a radius of curvature, $R$. Two coordinate systems will be used: a Cartesian system with coordinates $x, y, z$ and a spherical coordinate system with coordinates $r, \alpha, \beta$. The origin of both coordinate systems is the center of curvature of the surface. Here, $z$ is assumed positive downward.

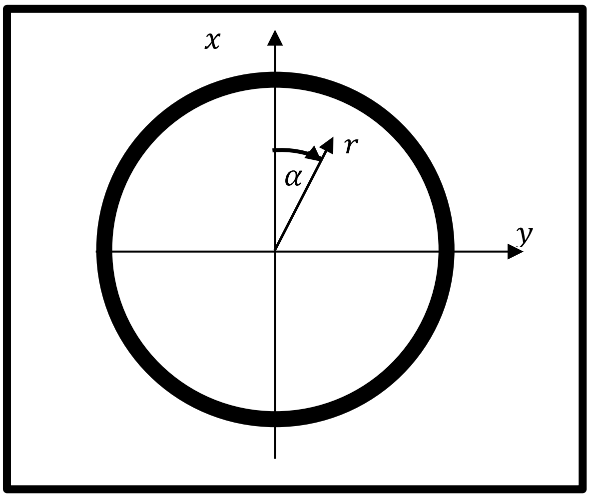

Fig. 1b Nomenclature for an interface in a vertical tube (plan view).

The equations of the surface in the Cartesian coordinate system in terms of the spherical system are

$$x_s = R\sin\beta\cos\alpha \tag{9a}$$

$$y_s = R\sin\beta\sin\alpha \tag{9b}$$

$$z_s = R\cos\beta \tag{9c}$$

The equations for the wall in Cartesian coordinates in terms of the spherical system are

$$x_w = R\sin\theta\cos\alpha \tag{10a}$$

$$y_w = R\sin\theta\sin\alpha \tag{10b}$$

$$z_w = z \tag{10c}$$

It is next assumed that the interface is cut by a plane, as shown in Fig. 2, such that the cross-section of the interface can be examined in a two-dimensions plane, $u - w$. (This plane is meant to represent the observation plane in a two-dimensional imaging experiment.) The equations for this plane in terms of the Cartesian coordinate system are

$$x_p = u \tag{11a}$$

$$y_p = y_e - w\cos\gamma \tag{11b}$$

$$z_p = z_e + w\sin\gamma \tag{11c}$$

The equations for the surface in the two-dimensional plane in terms of the spherical system can be found by combining Equations 9 and 11. The result is

$$u = R\sin\beta\cos\alpha \tag{12a}$$

$$w = \frac{R\cos\beta - z_e}{\sin\gamma} \tag{12b}$$

$$w = \frac{y_e - R\sin\beta\sin\alpha}{\cos\gamma} \tag{12c}$$

The two equations for $w$ require that

$$\begin{aligned}(\cos\beta - z'_e)\cos\gamma &= \\ &(y'_e - \sin\beta\sin\alpha)\sin\gamma\end{aligned} \tag{13}$$

where $y'_e$ is $y_e/R$ and $z'_e$ is $z_e/R$.

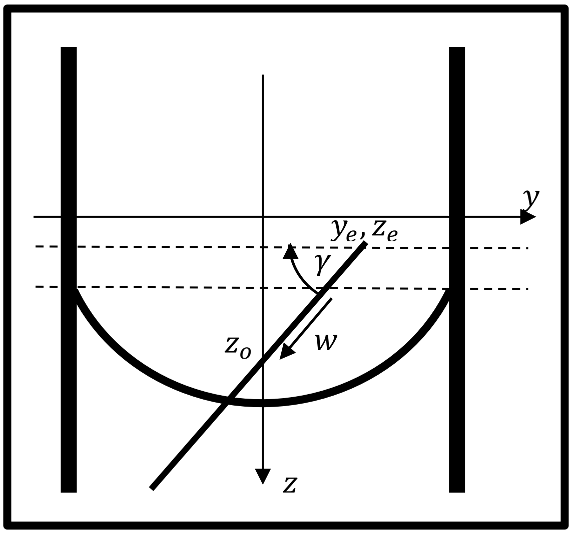

Fig. 2 A two dimensional plane that intersects the surface and the wall.

The two-dimensional surface can be characterized by the point where the plane crosses the $z$- axis, $z_o$, and the angle the plane makes with the horizontal, $\gamma$. This will allow the calculation of the coordinates where the plane crosses the surface in the cross-section shown in Fig. 2. Provided that the plane intersects the plane of contact, the minimum $\beta$-value, denoted by $\beta_1$, will always be $\pi/2 - \theta$ (the point where the surface contacts the wall). For this condition,

$$\begin{gathered} w = \frac{R\sin\theta - z_e}{\sin\gamma} = \frac{y_e - R\cos\theta}{\cos\gamma} \\ \tan\gamma > \frac{z_o}{r_o} \end{gathered} \tag{14}$$

If the intersecting plane does not intersect the plane of contact, then the $\beta$-value can be found using Equation 13 and setting the $\alpha$-values to $\pi/2$; this $\beta_1$-value is given by

$$\begin{aligned}\sin\beta_1 &= \left(z'_e\cos\gamma + y'_e\sin\gamma\right)\sin\gamma - \\ &\cos\gamma\sqrt{\left(1 - \left(z'_e\cos\gamma + y'_e\sin\gamma\right)^2\right)}\end{aligned} \tag{15}$$

The second point where the plane intersects the surface, $\beta_2$, is also given by Equation 13. Again setting the $\alpha$-values to $\pi/2$, this time the solution is

$$\begin{aligned}\sin\beta_2 &= \left(z'_e\cos\gamma + y'_e\sin\gamma\right)\sin\gamma + \\ &\cos\gamma\sqrt{\left(1 - \left(z'_e\cos\gamma + y'_e\sin\gamma\right)^2\right)}\end{aligned} \tag{16}$$

Furthermore, Equation 13 can be used to generate $\alpha$-values that correspond to $\beta$-values

$$\begin{aligned}\alpha &= \\ &\sin^{-1}\left(\frac{y'_e\sin\gamma + z'_e\cos\gamma - \cos\beta\cos\gamma}{\sin\beta\sin\gamma}\right)\end{aligned} \tag{17}$$

The shape of the surface in the intersecting plane can therefore be calculated for various $\beta$-value between the minimum and the maximum.

For the wall, the coordinates in the intersecting plane become

$$u = R\cos\theta\cos\alpha \tag{18a}$$

$$w = \frac{y_e - R\cos\theta\sin\alpha}{\cos\gamma} \tag{18b}$$

The shape of the wall in the intersecting plane can therefore be calculated for any $\alpha$–value. For the wall, $\alpha$–values range from 0 to $2\pi$.

A special case is when the intersecting plane is vertical. Then the equation for the plane is

$$x = R\cos\beta\cos\alpha \tag{19a}$$

$$y = y_o \tag{19b}$$

$$z = z_p \tag{19c}$$

the intersection of the surface in the plane is

$$R\cos\beta\sin\alpha = y_o \tag{20a}$$

$$y_p = R\sin\beta \tag{20b}$$

the maximum $\beta$-value is

$$\beta = \cos^{-1}\left(\frac{y_o}{R}\right) \tag{21}$$

and the $\alpha$–values are given by

$$\alpha = \sin^{-1}\left(\frac{y_o}{R\cos\beta}\right) \tag{22}$$

The apparent contact angle can be found from

$$\left(\frac{dw}{du}\right)_{surface} - \left(\frac{dw}{du}\right)_{wall} = \tan\theta_a \tag{23}$$

evaluated at the wall. This is a complex derivative best done numerically.

## 4 Typical Interface Shapes

Fig. 3 through 9 show typical interface shapes for planes that intersect the interface at various positions. These figures were calculated assuming that $\theta = 30°$. In each figure, the left panel shows a schematic of the intersection and the right panel shows what would be observed in the intersecting plane, that is, the plane of observation in an imaging experiment.

Fig. 3 shows the case where the plane intersects the interface horizonally. The conclusion that could be drawn from the image is that gas is flowing as an encapsulated phase and that the water is perfectly wetting with an apparent contact angle of $\theta_a = 0$. In this case, the intersection of the plane with the wall is circular.

Fig. 4 shows the case where the plane intersects the interface before it intersects the wall. The conclusion that could be drawn from the image is that gas is flowing as an encapsulated phase, that the water is perfectly wetting with an apparent contact angle of $\theta_a = 0$, and perhaps water is trapped in a pore space located at the bottom of the image. In this case, the intersections of the plane with the wall is elliptical and the plane with the interface is circular.

Fig. 5 shows the case where the plane intersects the surface at the point where the interface contacts the wall. In this case, $\gamma \cong 20°$ and the apparent contact angle that would be measured in the image is $\theta_a = 0$. In this case, the intersections of the plane with the wall is elliptical and the plane with the interface is circular.

Fig. 6 shows the case where the plane intersects the surface at the point such that $= 45°$ ; the apparent contact angle that would be measured in the image is $\theta_a = 24.5°$. In this case, the intersection of the plane with the wall is elliptical.

Fig. 7 shows the limiting case where the plane is vertical,$\gamma = 90°$; the apparent contact angle that would be measured is the true contact angle $\theta_a = 30°$. In this case, the intersection of the plane with the wall is elliptical; however, the ellipse is infinitely extended such that the wall appears as two vertical lines.

Fig. 8 shows the case where the plane is vertical, $\gamma = 90°$, but is offset from the *z*-axis half the distance to the wall. In this case the apparent contact angle that would be measured is $\theta_a = 33.7°$. The wall still appears as two vertical lines; however, the spacing between the lines is less than for the previous case. This could be interpreted to mean that the image is for a capillary tube with a smaller diameter than in the previous case.

Fig. 9 shows the case where the plane is vertical, $\gamma = 90°$, but is offset from the *z*-axis by 95% of the distance to the wall. In this case the apparent contact angle that would be measured is $\theta_a = 61.6°$. The wall still appears as two vertical lines; however, the spacing between the lines is much less than for the previous case. This could be interpreted to mean that the image is for a capillary tube with a much smaller diameter than in the previous case.

The implications of the last two cases is obvious. Simply examining the images to obtain apparent contact angles, it could be concluded that the contact angles for smaller sized capillary tubes increase and approach $\theta_a = 90°$ in the limit. This would suggest that smaller capillary tubes are neutrally wet while larger tubes are water wet. This conclusion is, of course, specious.

In summary, using intersecting planes for various positions, it is possible to measure apparent contact angles anywhere in the range $0° \leq \theta_a \leq 90°$. This conclusion is completely supported by the work of Andrew *et al* [6]. They used what they called a "resampling plane" that could be reoriented relative to the grain surface. They found that the measured angle could vary from approximately $10°$ to $110°$ (their Fig. 10) by repositioning the resampling plane.

The above analysis considers the very simple example of a straight, circular capillary tube. Real porous media have flow passages that diverge, converge, twist and turn. An analysis of such passages is beyond the scope of the present paper. However, it is obvious that the measurement of true contact angles in such passages would be much more complex than that for the simple model considered here.

## 5 A Way Forward

It should be no surprise that the contact angle must be an effect, not a cause. Examining Young's equation, there are four parameters $\sigma_{lg}, \theta, \sigma_{sg},$ and $\sigma_{sl}$. Basic principles of functions requires that only three of these variables can be independent. The interfacial tensions are assumed to be properties of the substances, related to how various species of molecules interact across a surface. They can therefore be assumed to be the independent variables. This implies that the contact angle is the dependent variable and

$$\theta = f\left(\sigma_{lg}, \sigma_{sg}, \sigma_{sl}\right) \tag{24}$$

Furthermore, Young's equation depends on a static force balance and other force terms must affect that balance if they are present. It is unreasonable to expect the values of the interfacial tensions to change with the additional forces; hence, the contact angle must change. In fact, many theoretical studies utilize a modified Young's equation that includes body forces and fluid stresses.

I emphasize that this paper is not a condemnation of the ability to determine contact angles on the microscopic scale – it is a cautionary statement that such determinations must be done with great care. The work of Andrew *et al* [6] shows how the measured contact angle varies depending on how the plane of investigation is oriented. Their work could be taken one-step further. Using multiple images, a three-dimensional interface model could be reconstructed and this model could then be interpreted to determine a unique contact angle that characterizes the system, assuming that such an angle exists. Based on observations made in the Andrew *et al* work, such a process would require much more detailed images than they acquired. They found that there was insufficient accuracy in the digital data to determine contact angles computationally and they resorted to a manual process.

This would be impractical if reconstructions of interfacial surfaces are performed, particularly in a dynamic experiment. It would appear that one more level of sophistication in image analysis must be achieved before contact angles can be systematically interpreted from micro-imaging experiments. There is evidence that this type of work is being pursued (AlRatrout *et al* [8]).

## 6 Conclusions

The present work supports the following conclusions:

1. Contact angles are dependent variables, functions of fluid/ solid properties (interfacial tensions), displacement velocities, history (time, hysteresis, and externally applied body forces and viscous stresses) – they are effects not causes.
2. Wettability can be defined dependably by the contact angle only for the static case with no externally imposed forces. Contact angles measured in dynamic and complex systems may not be good indictors of wettability.
3. It is not possible to measure accurately a contact angle in a simple two-dimensional image. Such measurements would require detailed reconstruction and interpretation of the three-dimensional interface.

## 7 References

1. F.F.Craig, jr., *The Reservoir Engineering Aspects of Waterflooding*, (SPE Monograph Series**, 3**, 1971).
2. G.Macdougall, and C.Ockrent, "Surface energy relations in liquid/solid systems. I. The adhesion of liquids to solids and a new method of determining the surface tension of liquids", PRSA **180**, 981, 151-173, (1942).
3. B.Krasovitski and A.Marmur,"Drops down the hill: Theoretical study of limiting contact angles and the hysteresis range on a tilted plate", Langmuir, **21**, 3881-3885, (2005).
4. R.G.Cox, "The dynamics of spreading of liquids on a solid surface. Part 1. Viscous flow", JFM, **168**. 169-194, (1986).
5. M.Fermigier and P.Jenffer, "An experimental investigation of the dynamic contact angle in liquid-liquid systems", JCIS, **146**, 1, 226-241, (1991).
6. M.Andrew, B.Bijeljic, and M.J.Blunt, "Pore-scale contact angle measurements at reservoir conditions using X-ray microscopy", AWR, **68**, June, 24-31, (2014).
7. R.Held, N.Schleifer, L.Genolet, and A.Fogden, "Added insight from image-based wettability characterization", E3S Web Conference, **89**, (International Symposium of the Society of Core Analysts, 2018).
8. A.AlRatrout, A.Q.Raeini, B.Bijeljic, and M.Blunt, "Automatic measurement of contact angle in pore-scale images", AWR, **109**, 158-269, (2017).

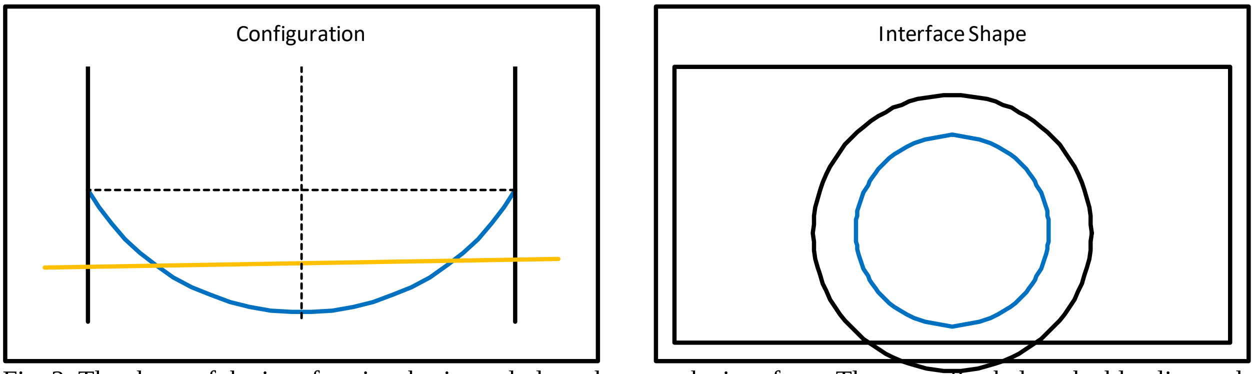

Fig. 3  The shape of the interface in a horizontal plane that cuts the interface.  The water lies below the blue line and the air above.

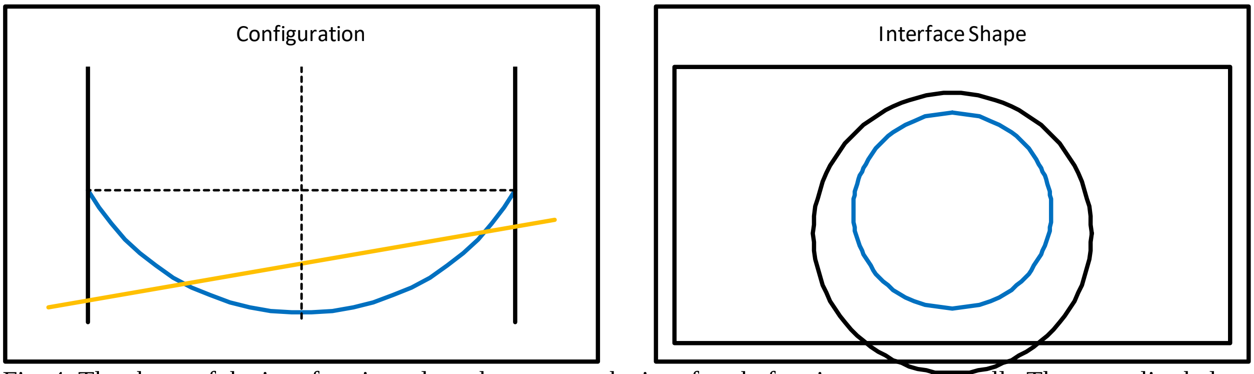

Fig. 4  The shape of the interface in a plane that crosses the interface before it crosses the wall.  The water lies below the blue line and the air above.

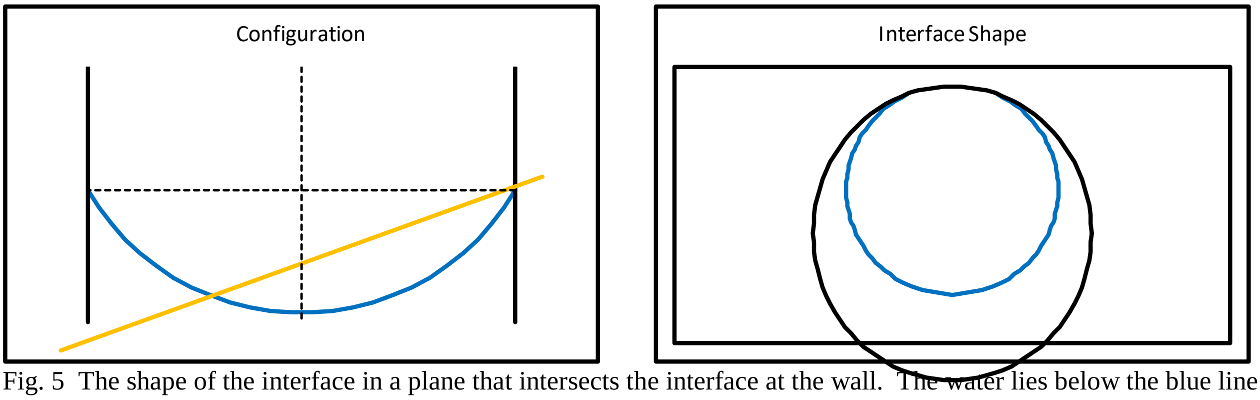

Fig. 5  The shape of the interface in a plane that intersects the interface at the wall.  The water lies below the blue line and the air above.

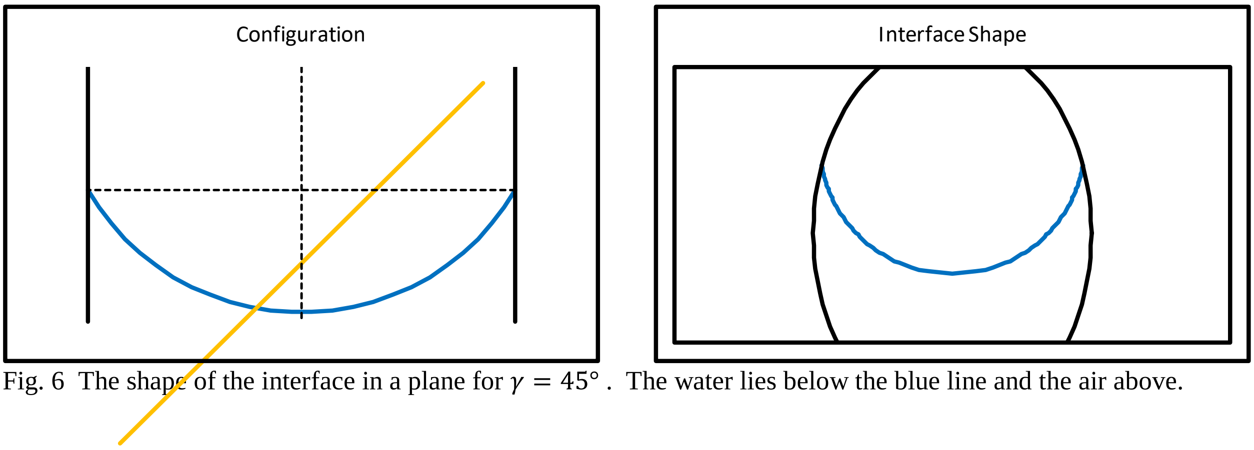

Fig. 6  The shape of the interface in a plane for $\gamma = 45°$ .  The water lies below the blue line and the air above.

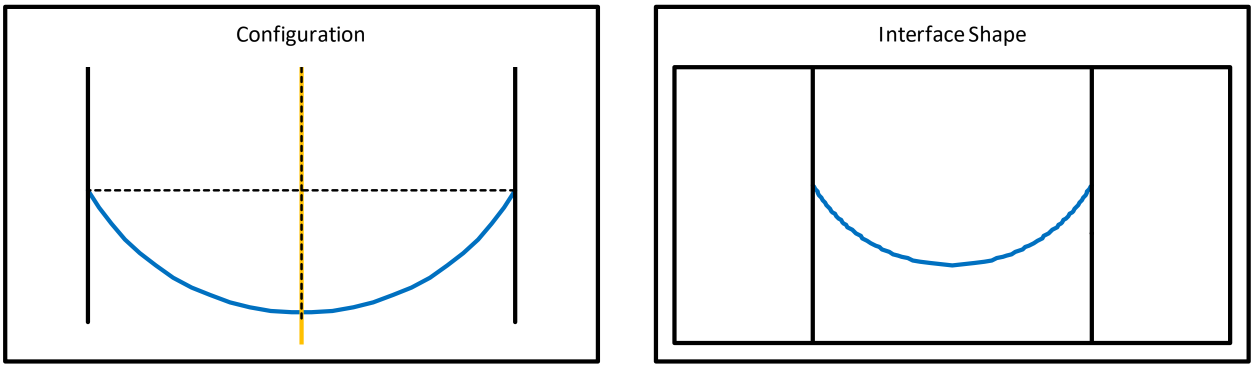

Fig. 7  The shape of the interface in a vertical plane.  The water lies below the blue line and the air above.

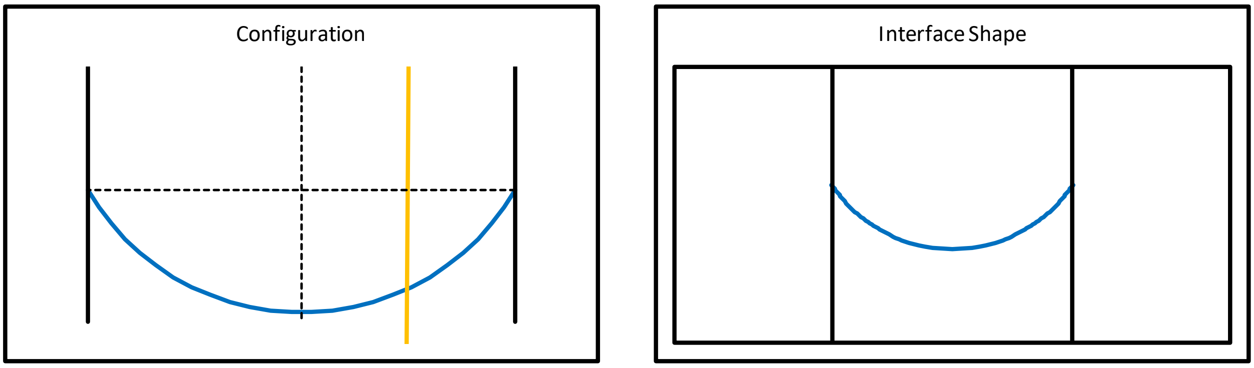

Fig. 8  The shape of the interface in a vertical plane offset from the *z*-axis half the distance to the wall.  The water lies below the blue line and the air above.

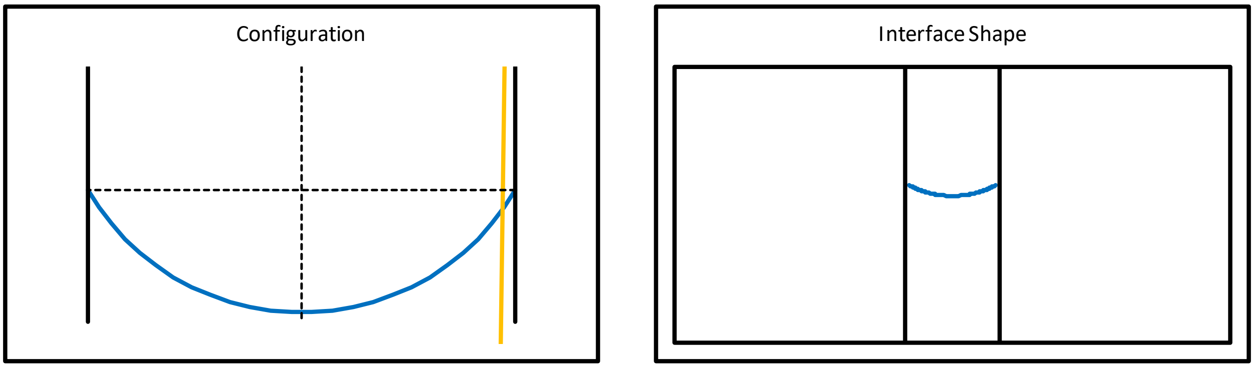

Fig. 9  The shape of the interface in a vertical plane offset from the *z*-axis is 95% of the distance to the wall. The water lies below the blue line and the air above.

# The link between microscale contact angle measurements and corescale wettability

*Chenhao* Sun[1], *James* McClure[2], *Mehdi, Shabaninejad*[3], *Peyman* Mostaghimi[1], *Steffen* Berg[4] and *Ryan T.* Armstrong[1,*]

[1]University of New South Wales, Minerals and Energy Resources Engineering, Sydney, NSW, Australia.
[2]Virginia Polytechnic Institute and State University, Advanced Computing, Blacksburg, Virginia, USA.
[3]Australian National University, Applied Maths, Canberra, ACT, Australia.
[4]Shell Global Solutions International BV, Rock and Fluid Sciences, Amsterdam, The Netherlands.

**Abstract.** Wettability is an important parameter for assessing the performance and optimum recovery scenario for hydrocarbon reservoirs. Relative permeability and capillary pressure-saturation functions show a high sensitivity to wettability. At the core-scale, wettability is defined via the capillary pressure drainage and imbibition cycle, e.g. as Amott-Harvey or USBM indices. At the microscale, the concept of contact angle is used, which until recently was not experimentally possible to determine in a porous rock at reservoir conditions. In this work, the Gauss-Bonnet theorem is used to provide a link between *Pc(Sw)* and measured distributions of microscale contact angles. We propose that the wettability of a porous system can be described by geometrical constraints that define the state of immiscible fluids. The constraint describes the range of possible contact angles and interfacial curvatures that can exist for a given system. We present measurements on a sandstone rock for which the USBM index, *Pc(Sw)*, and pore-scale contact angles are measured. The results show that pore-scale contact angle measurements can be predicted from capillary pressure data within 4-8% error. This provides a general framework on how petrophysical data can be used to describe the geometrical state of fluids in a porous media.

## 1. Introduction

In a multiphase system, wettability refers to the relative preference between two fluids to coat the solid materials as a consequence of the associated surface energies. This physical consequence is important for special core analysis because it influences relative permeability, end-point saturations, capillary pressure, capillary-end effect and other advanced multiphase flow processes, such as counter-current imbibition [1,2,3,4]. While various laboratory methods can be employed to define the wetting state of a rock there lacks a fundamental framework to incorporate wettability into Darcy scale models. Phenomenological approaches can be applied, such as correlations between Corey exponents and wettability. Common laboratory methods that define wettability are USBM or Amott wettability indices or sessile drop experiments [5]. More recent advances have also allowed for contact angle measurements in a porous rock with fluids at reservoir conditions [6,7]. These measurements bring about an exciting new tool to study the wettability of reservoir rocks. They also raise various fundamental questions regarding the physical meaning and uniqueness of these measurements.

Of particular interest is the link between microscale contact angle and macro-scale wettability indices. Microscale measurements provide the wetting angle formed between a fluid and solid defined by Young's equation,

$$\sigma_{F_1/S} = \sigma_{F_2/S} + \sigma_{F_1/F_2} \cos\theta \qquad (1)$$

where $\theta$ is the angle formed along the common line in the orthogonal plane when the fluid/solid ($\sigma_{F_1/S}$, $\sigma_{F_2/S}$) and fluid/fluid ($\sigma_{F_1/F_2}$) interfacial tensions are in balance at equilibrium. This measurement is not necessarily practical for macroscale quantification of wettability.

The measurement of $\theta$ in porous rock requires experiments at reservoir conditions and X-ray computed microtomography imaging followed by a sequence of image processing steps that introduce user-biases and have their own inherent difficulties with precision and accuracy. The measurement is only along the 3-phase common line on the rock surface. The variation of surface roughness and chemical heterogeneity on the rock surface that leads to a wide variation of surface energies is not necessarily quantified adequately. The location of the common line and observed $\theta$ is dependent on the system parameters. A high versus low capillary number experiment would push the common line into different regions of the pore space. Drainage versus imbibition experiments would produce various distributions of advancing and receding contact angles. Contact angle hysteresis, interface pinning, and the time allotted for the

---

[*] Corresponding author: ryan.armstrong@unsw.edu.au

system to reach equilibrium prior to imaging would also influence the observed pore-scale contact angles. Overall, these microscale measurements are an outcome of the dynamical system.

Macroscale indices provide an alternative bulk measurement for porous systems. Methods such as the USBM are based on the drainage and imbibition *Pc(Sw)* curves. The USBM provides a single measurement of wettability, which is essentially the ratio of positive to negative work required for saturation. Alternatively, the Leverret J-function can be used to rescale *Pc(Sw)* data to match the curve for another rock by adjusting the assigned contact angle given that all other terms are known. This approach would provide a single "average" contact angle for the rock. What these macroscale indices mean in terms of microscale fluid arrangements is unclear.

There currently exists no fundamental link between microscale contact angles and macro-scale wettability indices. Herein, we provide the link by using a theorem from integral geometry that explains the geometrical state of oil clusters in a porous rock in terms of curvature and contact angle. We utilize *Pc(Sw)* data to infer the geometrical state of fluid clusters in a sandstone rock to predict the distribution of pore-scale contact angles. This will require an advance review of integral geometry and theorems not commonly applied to porous systems.

### 1.1 Gauss-Bonnet Theorem

The Gauss-Bonnet Theorem [8] can be used to relate the total curvature of an oil cluster (C) to its topology ($\chi$),

$$2\pi\chi(\delta C) = \int \kappa_T dA + \int \kappa_g \, dL \qquad (2)$$

where $\delta C$ is the bounding surface of the cluster, $dA$ is an area element on the cluster surface, $\kappa_T = {}^{1}\!/_{r_1 r_2}$ is the Gaussian curvature along the surface, $r_1$ and $r_2$ are the two principal radii of curvature at any given location on the surface, $dL$ is a line element (common line) along the boundary formed by the cluster and solid, and $\kappa_g$ is the geodesic curvature along $dL$. This is an exceptional statement regarding differential surfaces that relates geometry (curvature) to topology (connectivity). The topological term used is the Euler characteristics ($\chi$), which can be decomposed into the number of objects, loops and holes that a given cluster or set of clusters have,

$$\chi(C) = Objects - Loops + Holes. \qquad (3)$$

Take for example the bounding surface of a sessile drop, which is a single object with no loops and one hole, resulting in $\chi(\delta C)$ =2. There is one hole because we are considering only the bounding surface (manifold) of the droplet not the drop as a solid object. The Euler characteristic for the solid droplet would be $\chi(C)$ =1 (no holes or loops). The Gauss-Bonnet theorem provides an important link between local geometrical properties and global topological properties, which explains the geometrical state of a bounding surface. Further details on the Gauss-Bonnet theorem and other important aspects of integral geometry applied to porous systems are provided in a recent review paper [8].

The simplest way to understand the implications of Eq. (2) and its utility for porous systems is to study a sessile drop. We can use piecewise integration for this purpose. The bounding surface, *A,* can be partitioned into fluid/fluid and fluid/solid interfaces. There is also a common line separating the two bounding surfaces. Average curvature of the fluid/fluid interface can be defined as $\kappa_{F1/F2}$ and likewise for the fluid/solid interface $\kappa_s$. The geodesic curvature along the common line is defined from two reference planes, i.e. the fluid/fluid interface ($\kappa_{g_{F1/F2}}$)and fluid/solid interface ($\kappa_{g_{F1/S}}$). The latter is the contact angle that is measured during a sessile drop experiment. The former is the angle over which the common line deviates from being straight.

From the previous definitions, we arrive at the following formula,

$$2\pi\chi(\delta C) = A_{F1/s}\kappa_s + A_{F1/F2}\kappa_{F1/F2} + \kappa_g L \qquad (4)$$

where $A_{F1/s}$ is the area between fluid 1 and solid, $A_{F1/F2}$ is the fluid/fluid area and $L$ is the length of the common line. The geodesic curvature ($\kappa_g$) of the common line can be partitioned into its curvature components $\kappa_{g_{F1/S}}$ and $\kappa_{g_{F1/F2}}$. Here we assume that $\kappa_{g_{F1/S}} \gg \kappa_{g_{F1/F2}}$. The implications of this assumption will be discussed in the results section. The Euler characteristic for the bounding surface of a single droplet is two,

$$\kappa_{g_{F1/S}} = [4\pi - A_{F1/s}\kappa_s + A_{F1/F2}\kappa_{F1/F2}]/L. \qquad (5)$$

Eq. 5 explains how contact angle ($\kappa_{g_{F1S}}$) could change for any homeomorphic deformation of an oil cluster. This is a geometrical constraint. There are no requirements for equilibrium and thus, the result is independent of any force being applied to the droplet and is purely geometrical.

Homeomorphic deformation means that no topological change occurs. Oil droplets that have undergone various homoeomorphic deformations are displayed in **Fig. 1**. By inspection it is evident that all of the bounding surfaces are single objects with no loops and one hole. Euler characteristic is the same for all cases despite each having a distinctly different geometrical shape. The implication is that total curvature must be conserved for these droplets, see Eq. 2. For the 2D droplet, the total curvature in the fluid/fluid interface is *2*π with zero geodesic curvature. For the 2D sessile droplet, the total curvature in the fluid/fluid interface is *2*π(1–*x)* where *x* is the fraction of the droplet area that is hypothetically extended into the solid substrate. The remaining curvature is in the common points represented by θ since the fluid/solid interface is flat with zero curvature. A similar situation occurs for the droplet in a capillary tube. For the dynamic droplet on a decline, the total curvature in the fluid/fluid interface is not trivial and the fluid/solid curvature is zero.

However, the same geometric constraint must apply meaning that any curvature that is not in the fluid/fluid and fluid/solid interfaces must be in the common points representing the advancing and receding contact angles.

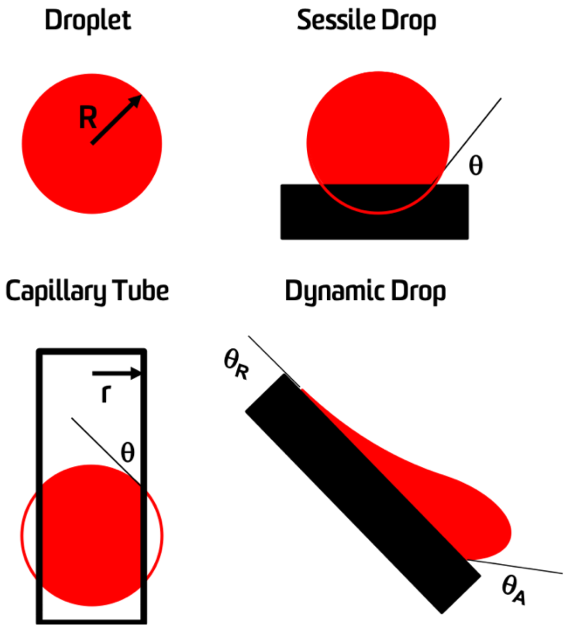

***Fig. 1.*** *An oil droplet with radius* R *(top left) The droplet is placed in a solid surface such that* the *radius of curvature remains* 1/R *with contact angle* θ *(top right). The droplet is placed in a capillary tube such that contact angle remains* θ *with radius of curvature* cos(θ)/r *(bottom left). A droplet moves along a decline with advancing angle* $\theta_A$ *and receding angle* $\theta_R$ *(bottom right).*

An additional example can be provided by considering an oil droplet captured in a microfluidic device, as shown in **Fig. 2**. Here the oil cluster has the same Euler characteristic as the previous examples in **Fig. 1**. The multi-colored curves represent the interfaces. The fluid/fluid interfaces curve outward with positive curvature while the fluid/solid interfaces curve inward with negative curvature. From the segmented image, we cannot resolve the contact of oil with the solid surface. However, regardless of a wetting film existing along the grain surfaces or direct contact of the grains with the solid, the oil always curves away from the solid surface creating negative curvature in regions adjacent to grains. Experimental evidence of this can be found elsewhere [14,15,16,17]. To determine contact we evaluate $\int \kappa_T dA$ over the multicoloured curves and then subtract the value from $4\pi$. The result, *Re,* is equal to $\int \kappa_g \, dL$. For the 2D image provided in **Fig. 2**, $dL$ represents the 20 common points marked by the red stars. The average contact angle (or geodesic curvature) for all common points would be determined by *Re/20*.

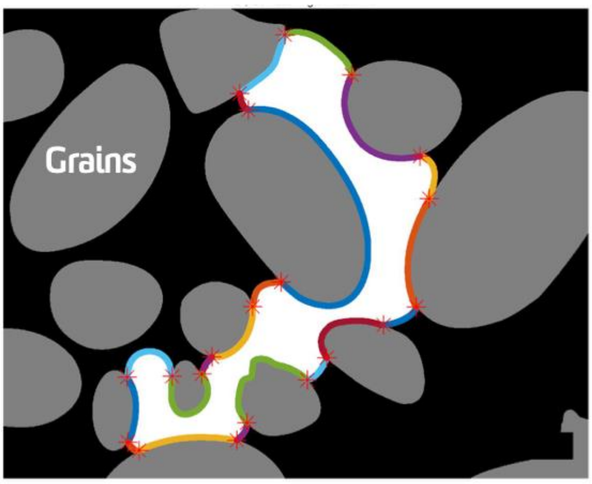

**Fig. 2.** An oil cluster trapped in a microfluidic device. The topology of the cluster is the same as the sessile drops displayed in **Fig. 1**.

## 2. Materials and Methods

We developed a workflow to generate multi-mineral models that can be assigned spatially heterogeneous wetting conditions. These models are used for multiphase flow simulations using the lattice Boltzmann method. A sandstone rock is first imaged with micro-CT followed by impregnation of epoxy and thin sectioning. The thin section is then imaged with Quantitative Evaluation of Minerals by Scanning Electron microscopy, known as QEMSCAN [9]. The analysis provides a high-resolution image of the rock with spatially defined mineral content in 2D. These data are then spatially registered to the 3D micro-CT data [10]. Grey-scale micro-CT values are correlated to mineral content to identify “seed points”. Then sequential sequences of converging active contours are applied by using the seed points as initial positions that advance based on the local image gradient [11]. The final outcome is a segmented 3D image of defined mineralogical information that can be used to assign spatially varying wetting [12]. The workflow is presented in **Fig. 3**.

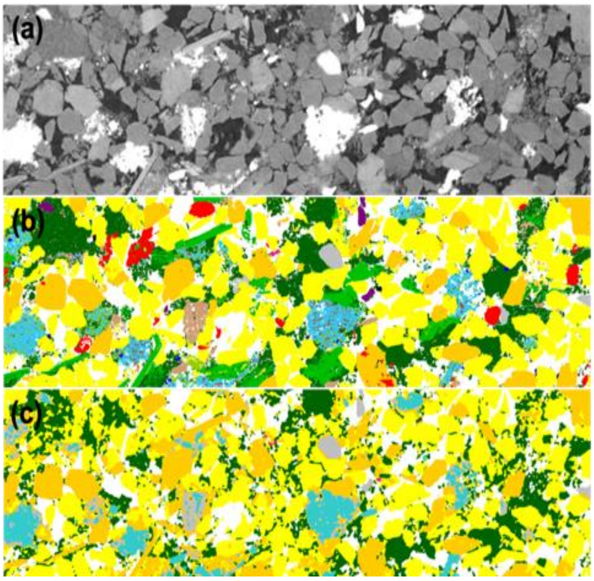

**Fig. 3.** An example of the image processing workflow for generation of the multi-mineral model. Micro-CT image (a), QEMSCAN image (b) and segmented data (c).

We used the 2-phase flow lattice Boltzmann method to simulate drainage and imbibition for various wetting states [12]. Details on the LBM and validation studies are presented elsewhere [13,14,15,16]. We tested two wetting states – one with an overall wettability of 0.1 (neutral wet) and the other with an overall wettability of 0.75 (strongly water wet). Overall wettability, *W*, is defined as the summation of the cosine of the contact angles assigned to the mineral surfaces,

$$W = \sum_{i=1}^{n} \frac{\gamma_{iF1} - \gamma_{iF2}}{\gamma_{F1F2}} \phi_i \qquad (6)$$

where $\gamma$ is interfacial tension with subscripts for each fluid (F) or mineral ($i$) pair and $\phi_i$ is the solid voxel fraction.

For each *W* there were four cases:

1) ***Homogeneous*** - constant wettability everywhere.
2) ***Corner wet*** - corners were water wet, remainder of grain surfaces were oil wet with a constant value.
3) ***Mineral heterogeneity*** - heterogeneous wetting based on the mineral type.
4) ***Corner wet with mineral heterogeneity*** - heterogeneous wetting based on the mineral type, but with water wet conditions applied in the corners.

These cases were designed to mimic commonly assumed conditions for digital rock simulations and/or restored state cores that are aged in crude oil [3,5]. All simulations were initiated from a morphological-based (maximum inscribed spheres) drainage state of *Sw~0.2*. Water flooding was simulated until the production curves starts to level off. Once the curves level off at ~1M timesteps, a second set of simulations for secondary drainage were conducted starting from the end-point of the water flood. This provided the hysteretic drainage and imbibition curves required to calculate the USBM index [3]. The phase distributions were then used to measure contact angles and the curvature of interfaces. For direct contact angle measurements, we used the method explained by [6,7]. This is an apparent contact angle for the visualized fluid clusters. For curvature measurements, we used the approach explained by [17].

## 3. Results and Discussion

Contact angle distributions for the simulations near residual oil saturation are presented in **Figs. 4** and **5**. The corner-wet cases resulted in lower contact angles, which could be characterized as a more water-wet state than the homogeneous and heterogeneous cases. Interestingly the heterogeneous and homogeneous wet cases resulted in similar contact angles distributions and also provided similar *Pc(Sw)* curves (data not shown). The largest influence on the pore-scale contact angles appeared to be dictated by the corners and cervices of the rock remaining water wet. This suggests that connate water saturation plays a significant role in the overall observed wettability.

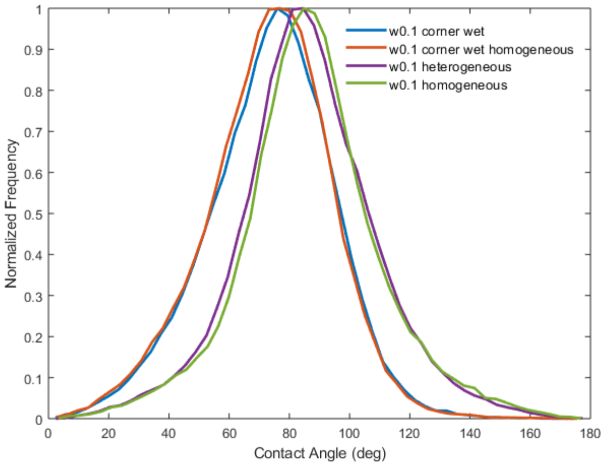

**Fig. 4.** Contact angle distributions for the model systems where the total summation of the cosine of the contact angles for the mineral surfaces are 0.1 (see Eq. 6).

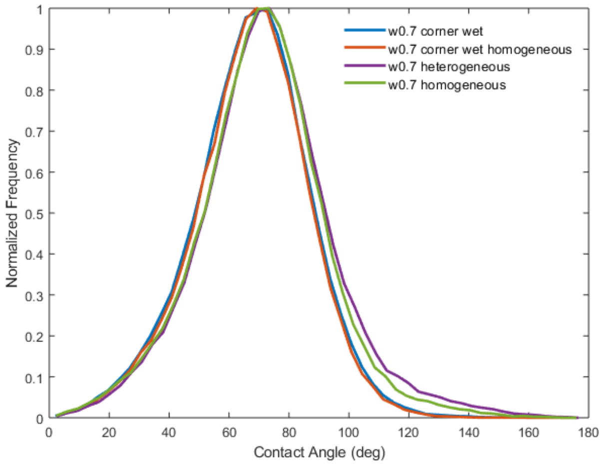

**Fig. 5.** Contact angle distributions for model systems where the total summation of the cosine of the contact angles for the mineral surfaces are 0.7 (see Eq. 6).

For the homogeneous case there was not a unique contact angle with a standard deviation of zero. Indeed, for the homogeneous case, the cosine of the contact angles assigned to each voxel was constant suggesting that the measured contact angle should be constant. A single contact angle was not observed for various reasons. Firstly, the surfaces of the grains are not uniformly smooth, and the direct contact angle measurement does not necessarily account for voxel-by-voxel roughness. The method measures the local angle of the fluid interface and grain surface near the common line by taking a regional approximation [6,7]. The reported values are apparent angles. Secondly, contact angle hysteresis must be considered. During flow there are complex sequences of cooperative dynamics where interfaces are advancing and receding providing a range of various contact angles. Lastly, the measured data was not collected at equilibrium conditions. The data analyzed was collected at residual oil saturation under flowing conditions.

The measured contact angle distributions represent advancing and receding contact angles in addition to local regions were interface could be pinned, such as the entrance to a pore body. Distributions, such as these have been reported for experimental data in carbonate rocks where the surface chemistry is considered to be homogeneous [6]. If or how long it takes an interface to return to its equilibrium condition along the common line after an advancing or receding displacement is an open question. One advantage of using the Gauss-Bonnet theorem to predict the distribution of possible microscale contact angles, as explained later on, is that the methodology is purely geometrical. One also has to keep in mind that using geometric measures probes contact angles within the contact angle hysteresis loop, and not simply the intrinsic contact angle. The outcome therefore provides all of the possible geometrical states for fluid clusters regardless of the underlying dynamics. This applies in particular to techniques assessing contact angles from microscale fluid distributions which are a consequence of flow that are in most cases a superposition of processes with advancing and receding contact lines and various other dynamic effects.

The *Pc(Sw)* data for the *W=0.1* homogeneous and *W=0.7* corner-wet cases are provided in **Fig. 6**. The simulations were initiated from a morphological-based (maximum inscribed spheres) drainage state of *Sw~0.2*. Only the primary imbibition and secondary drainage processes were simulated. The simulation data were also fitted to the Van Genuchten equation to provide a means for determining the USBM index. Connate water saturation was based on the initial state of the simulation, which was determined by the maximum inscribed spheres method. The USBM indices and corresponding contact angle measurements for all of the models are reported in **Table 1**.

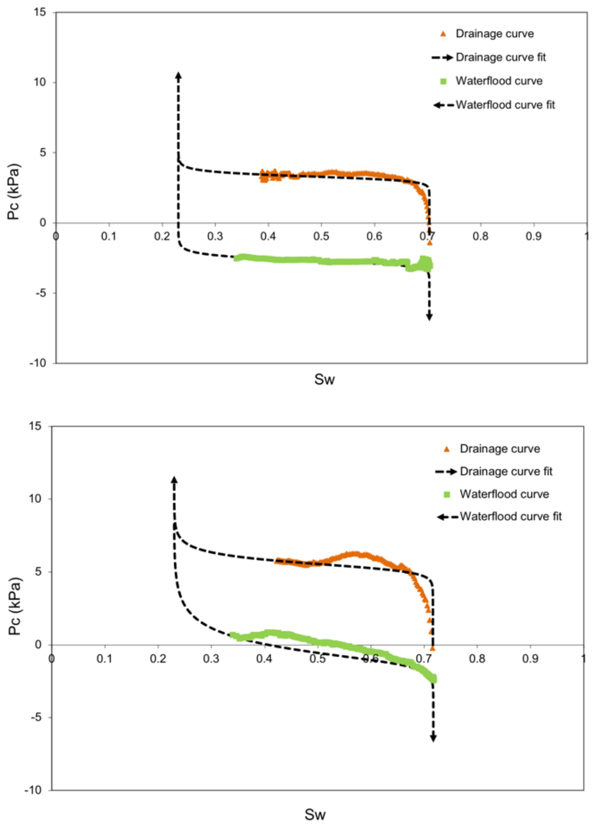

**Fig. 6.** Simulated capillary pressure versus saturation data for the W=0.1 wetting case (top). Simulated capillary pressure versus saturation data for the W=0.7 wetting case (bottom). Regression analysis was used to fit the Van Genuchten equation to the simulated data.

***Table. 1.*** *Summary of pore-scale contact angle measurements and macro-scale USBM wettability indices.*

| **Case** | **USBM*** | | **Mean θ (deg)** | | **Standard Deviation (deg)** | |
|---|---|---|---|---|---|---|
| **W** | **0.1** | **0.7** | **0.1** | **0.7** | **0.1** | **0.7** |
| **1** | 0.62 | 1.00 | 73.7 | 67.4 | 21.0 | 19.5 |
| **2** | 0.76 | 0.96 | 73.0 | 67.2 | 20.8 | 19.0 |
| **3** | 0.19 | 0.84 | 86.2 | 72.9 | 23.0 | 22.7 |
| **4** | 0.10 | 0.88 | 87.4 | 70.9 | 23.4 | 21.6 |

USBM indices near 1.0 result in contact angles less than 70 degrees while indices around 0.5 or less result in contact angles greater than 70 degrees. It is interesting that Case 4 with USBM indices of 0.10 and 0.88 resulted in only a 16.5-degree difference in contact angle. The measured contact angles are a sampling of the grain surfaces where the common line exists. The finding is only a statement as to where on the grain surface the common line prefers to be located under the prevailing conditions. We also find that for a single overall wetting state (*W*) there was variability in the standard deviation of the measured contact angles. Models with more heterogeneous distributions of surface energies resulted in a wider range of contact angles. The trend, however, is minimal because of the previously discussed reasons regarding dynamics, hysteresis and numerical errors that also result in the observed contact angle distributions.

Next, we attempt to predict all of the possible pore-scale contact angles and their associated probabilities for a system of fluid clusters. The prediction is provided by applying a statistical mechanics approach to Eq. 5. First, we define a probability density function for the apparent fluid/fluid curvatures, $\kappa_{F1/F2}$, based on *Pc(Sw)* data. We assume that a given fluid cluster can be located in any pore region of the rock based on the associated area under the *Pc(Sw)* curve. Through the Young-Laplace equation capillary pressure can be related to mean curvature. For axisymmetric interfaces, Gaussian curvature can also be determined since the two principal curvatures are equal. The *Pc(Sw)* curve is then divided into local ranges of Gaussian curvatures with associated probabilities.

We consider that an oil cluster of a given volume could be located anywhere in the porous system based on the probability density function of $\kappa_{F1/F2}$. Eq. 5 then provides a distribution of possible $\kappa_{g_{F1/S}}$ for a cluster. The $\kappa_{g_{F1/S}}$ distributions for each cluster size that spans the entire power law distribution of cluster sizes are then determined. To determine the final distribution for a system of clusters, we then consider the volume distribution of clusters. We combined the distributions of $\kappa_{g_{F1S}}$ for individual cluster volumes using a weighted function based on cluster frequency,

$$X_T(i) = \sum w_j x_j(i) \qquad (7)$$

where $x_j(i)$ is the counts for each contact angle $i$, and $w_j$ is the weight for each cluster size $j$. Here,

$$w(j) = N_j/N_T \qquad (8)$$

where $N_j$ is the number of clusters of size j and $N_T$ is the total number of clusters. The result provides a distribution of apparent $\kappa_{g_{F1S}}$ that can be compared to direct pore-scale contact angle measurements presented in **Figs. 4** and **5**.

The predicted and measured contact angle distributions for *W=0.1* homogeneous and *W=0.7* corner-wet cases are presented in **Figs. 7** and **8**. The results are comparable with less than 4% difference for the average contact angle. We also compare the entire distributions as quantile differences and observe the largest difference of ~8% for smaller contact angles.

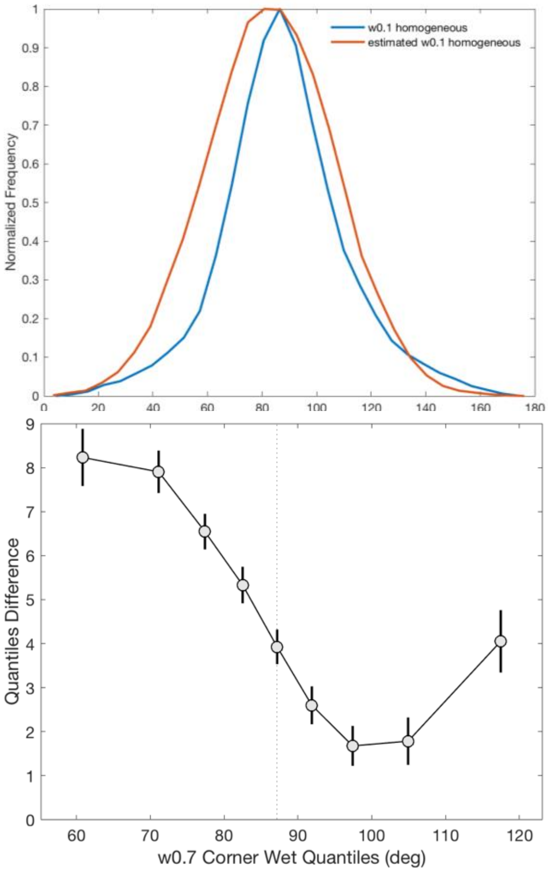

**Fig. 7.** Measured pore-scale contact angles compared to those predicted by Eq. 5 using *Pc(Sw)* data (top). Percent differences for each quantile of the contact angle distributions (bottom). The black dashed line represents the mean contact angle.

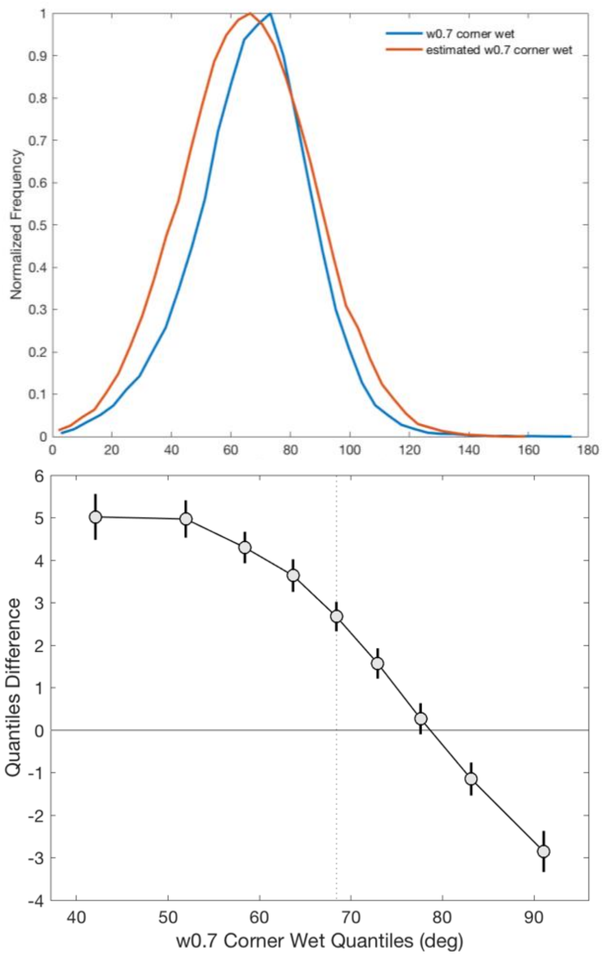

**Fig. 8.** Measured pore-scale contact angles compared to those predicted by Eq. 5 using *Pc(Sw)* data (top). Percent differences for each quantile of the contact angle distributions (bottom). The black dashed line represents the mean contact angle.

## 4. Conclusions

By using the Gauss-Bonnet theorem, we are able to understanding how *Pc(Sw)* and cluster size distributions are related to the geometrical state of the fluids [8,18]. This provides a direct link between the USBM method measured from *Pc(Sw)* data and microscale contact angle measurements. Our predictions of microscale contact angle distributions are within 4% difference for mean contact angle and around 8% difference for the smaller contact angles. The proposed method utilizes two assumptions that could have resulted in these differences. Firstly, we assume that the interfaces in pores are axisymmetric, which is not necessary the case for all porous systems. Secondly, we assume that all clusters could exist in all microscopic states of the porous media. This may occur (open question) at infinite time and space but for our limited observation this is questionable. In addition, it should be noted that the actual pore-scale contact angle measurements also have error and these errors would likely increase for smaller contact angles near rough surfaces. Thus, the assumed benchmark should also be questioned. Despite these issues the results are within a reasonable error margin and the developed framework provides new insights on the geometrical state of fluids [18] and how core analysis measurements can be used to understand these states [14]. The tested wetting cases demonstrate how the spatial variability of water-wet regions can influence the wetting state of the rock. By using the proposed framework, we can provide a reasonable distribution of microscale contact angles within a dynamical system without the need for direct measurements. These distributions could be used for network models, other modelling approaches, guiding the interpretation of special core analysis results and/or the development of more advanced theories for multiphase flow in porous media.

Acknowledgements: This research used resources of the Oak Ridge Leadership Computing Facility, which is a DOE Office of Science User Facility supported under Contract No. DE-AC05-00OR22725. We also thank the members of the ANU/UNSW DigiCore Consortium.

## References

1. W. G. Anderson, "Wettability literature survey-part 2: Wettability measurement", Journal of Petroleum Technology, **38** (11) (1986).
2. W. G. Anderson, "Wettability literature survey part 5: The effects of wettability on relative permeability", Journal of Petroleum Technology, **39** (11) (1987).
3. H. Kovscek, C. Wong, A. Radke, "Pore-level scenario for the development of mixed wettability in oil reservoirs", AIChE Journal **39** (6) (1993).
4. Donaldson, E. C., Thomas, R. D., Lorenz, P. B. et al., "Wettability determination and its effect on recovery efficiency", Society of Petroleum Engineers Journal, **9** (01) (1969).
5. C. McPhee, J. Reed, I. Zubizarreta, "Core analysis: a best practice guide", Vol. 64, *Elsevier* (2015).
6. M. Andrew, B. Bijeljic, M. J. Blunt, "Pore-scale contact angle measurements at reservoir conditions using x-ray microtomography", Advances in Water Resources, **68** (2014).
7. A. AlRatrout, A. Q. Raeini, B. Bijeljic and M. Blunt, "Automatic measurement of contact angle in pore-scale images", Advances in Water Resources, **109**, 158-269 (2017).
8. R. T. Armstrong, J. McClure, V. Robins, Z. Liu, C. Arns, S. Schlüter, S. Berg, "Porous media characterization using Minkowski functionals: theories, applications and future directions", Transport in Porous Media, 1-31 (2018).
9. D. Pirrie, A. R. Butcher, M. R. Power, P. Gottlieb, G. L. Miller, "Rapid quantitative mineral and phase analysis using automated scanning electron microscopy (QEMSCAN); potential applications in forensic geoscience", *Geological Society*, London, Special Publications **232** (1) (2004).

10. S. Latham, T. Varslot, A. P. Sheppard et al., “Image registration: enhancing and calibrating x-ray micro-CT imaging”, *Proc. of the Soc. Core Analysts*, Abu Dhabi, UAE (2008).
11. A. P. Sheppard, R. M. Sok, H. Averdunk, "Techniques for image enhancement and segmentation of tomographic images of porous materials”, Physica A: Statistical mechanics and its applications **339** (1-2) (2004).
12. M. Shabaninejad, J. Middleton, S. Latham, A. Fogden, “Pore-scale analysis of residual oil in a reservoir sandstone and its dependence on water Flood salinity, oil composition, and local mineralogy”, Energy & Fuels, **31** (12) (2017).
13. J. McClure, J. F. Prins, C. T. Miller, “A novel heterogeneous algorithm to simulate multiphase Flow in porous media on multicore cpu-gpu systems”, Computer Physics Communications **185** (7) (2014).
14. Z. Liu, J. McClure, R. T. Armstrong, “The influence of wettability on phase connectivity and electrical resistivity”, Physical Review E, **98** (4) (2018).
15. R. T. Armstrong, J. McClure, M. Berill, M. Rücker, S. Schlüter, S. Berg, “Flow regimes during immiscible displacement”, Petrophysics, **58** (01) (2017).
16. R. T. Armstrong, J. McClure, M. Rücker, S. Schlüter, M. Berill, S. Berg, “Beyond Darcy’s law: The role of phase topology and ganglion dynamics for two fluid flow”, Physical Review E, **94** (4) (2016).
17. R. T. Armstrong, M. L. Porter and D. Wildenschild, “Linking pore-scale interfacial curvature to column-scale capillary pressure”, Advances in Water Resources, **46**, 55-62 (2012).
18. J. McClure, R. T. Armstrong, S. Schlüter, M. Berrill, S. Berg, W. Gray, C. T. Miller, “A geometric state function for two-fluid flow in porous media”, Physical Review Fluids, **3**(8), 084306 (2018).
19. N. R. Morrow, “The effects of surface roughness on contact angle with special reference to petroleum recovery”, The Journal of Canadian Petroleum Technology 14(04), 42-53, 1975.

# Effect of fractures on hot solvent injection in viscous oil: a study using HP-HT micromodel

*Igor* Bondino[1,*], *Gerardo Emanuel* Romero[1], *Jean-Philippe* Chaulet[1], *Anne* Brisset[1] and *Marelys* Mujica[2]

[1]TOTAL, Avenue Larribau, 64018 Pau Cedex, France
[2]CHLOE, Avenue de l'Université, UFR Sciences et Techniques, 64013 Pau Cedex, France

**Abstract.** In this study, a transparent glass micromodel is used to study the physico-chemical behaviour of a solvent / viscous oil system with pressures and temperatures in the range [8-100] bar and [60-110] °C respectively, allowing the visual observation of the phenomena at the actual P, T reservoir conditions of interest. The experiments, covering immiscible, miscible and supercritical conditions, reveal the influence of pressure, temperature, connate water and fractures, on the oil recovery and flow behaviour. A physico-chemical interpretation is performed, by both analytical and numerical methods, resulting in deep understanding of the miscible process at microscopic scale. It is found that the most interesting behaviour in terms of oil recovery (for the type of solvent used in this work) is given by the ratio of fracture permeability to intact matrix permeability (which is commonly referred to as excess permeability index). Being the micromodel vertically oriented with the lighter solvent injected from the top, the stability of the experiments is also classified: although solvent fingers are expected as buoyancy is not strong enough to prevent their initiation and growth, in reality they are only seen in a minority of experiments. This behaviour is explained due to the contributions of the transverse dispersion (which smooths out the fingers as they grow) and to the fractures on the stabilization of the flow inside the matrix.

## 1 Introduction

Miscible-flood studies started in the early 1950's. Since then, several improvements have been achieved to make miscible flooding economical and technically applicable. By consequence, more complex processes such as miscible WAG, CO2 miscible displacement and foam addition have been applied at reservoir scale. Solvent injection can be used as a secondary or tertiary oil recovery method and is normally implemented in order to achieve miscible displacement, which implies that the solvent and reservoir fluid mix in all proportions and that all mixtures remain in single phase. This also means absence of interfacial tension, hence no capillary pressure and no interface. However, miscible injection has not been as widely applied as water flooding due to process and solvent cost or solvent availability issues: for example, the incremental oil recovery must be sufficiently large and timely to withstand the added operational costs. Obviously such evaluation requires a good understanding of the mechanisms: but the processes that happen in a reservoir at microscopic scale and in-situ conditions of pressure and temperature, are still not very well understood.

The micromodel technology remains today the best tool to visualize the physico-chemical behaviour of a solvent/oil system at different conditions. A large set of investigations was for example carried out for the specific problem of heavy oil recovery by means of vaporized hydrocarbon solvents, VAPEX (see Chatzis [1] for one of the early examples). A micromodel is an idealized transparent representation of a rock to visualize how a recovery mechanism works at a pore scale. The principle of a micromodel experiment is similar to that of a traditional core flooding experiment, with the exception that the pore pattern is manmade and 2D and that the volumes involved are very small (tens to a few hundred microliters). State-of-the-art optical cameras (as in this paper) can be used to capture the fluid displacements within the pore network while the displacing fluid is injected. A number of investigators have used this tool for solvent studies.

Campbell and Orr [2] studied the injection of CO2 and refined oil respectively, at 8.3 bar and 25°C in crude and refined oil. The experiments were conducted in water-wet and oil-wet media. It was found that oil gets trapped in the region that was first penetrated by the viscous fingers. This is due to oil's impoverishment and loss of its miscible condition. For refined oil as solvent, the oil-wet medium facilitates the residual oil/solvent contact as the crude oil wets the pore walls while the solvent passes through them. In the water-wet medium, CO2 dissolves in water and reaches out more trapped oil, reducing its viscosity and allowing it to be produced. Crude oil/CO2 systems are not first contact miscibility, and present capillary forces that favour the removal of oil from dead end pores, which increases the recovered oil.

---

[*] Corresponding author: igor.bondino@total.com

Sohrabi et al. [3] observed the performance of gravity stable CO2 injection for extra-heavy crude oil at 41.46 bar and 44°C, applying different sequences of water-alternating-gas injection (WAG). Starting with CO2 injection, the highest recovery factor is obtained after the first CO2/water cycle, where oil swelling is observed. CO2 displaces oil by a double drainage mechanism, which means gravity stable displacement of the solvent while dissolving into the oil and reducing its viscosity. Gravity stability refers to the inhibition of fingers formation due to a compensation of the viscous forces with gravity forces.

Saidian et al. [4] investigate the matrix-fracture interaction in glass micromodels during miscible displacement considering different injection rates, viscosity ratios and solvents. It is demonstrated that oil recovery increases with injection rate when the oil/solvent viscosity ratio equals one. But when the viscosity ratio is greater than one, the ultimate oil recovery decreases when the injection rate increases. This is due to the channelization of the solvent in the fracture that leaves the fracture-matrix interaction as diffusion dominated. One conclusion is that the viscosity ratio affects the "dispersion" in the matrix and in the fractures: nevertheless, considering the mixing-cell theory [5], dispersion refers to a phenomenon that happens in a porous medium and the term does not apply for the observations in the fracture. However, for the matrix only, dispersion increases when the viscosity ratio (oil/solvent) decreases.

Marciales and Babadagli [6] analyse the solvent retrieval process at atmospheric conditions for different wettabilities using two types of solvent: heptane and distilled oil. In their case, the micromodel has fractures and the process is non isothermal. It is observed that solvent entrapment is more frequent in non-oil wet media than in oil-wet media (no water saturation is present). This behaviour is explained considering the stability of the solvent film that forms on the pore walls of the oil-wet media. This allows the interconnection of the solvent drops and their flow. In oil-wet media, the solvent gets into the smaller pores and oil recovery increases. Distilled oil is proved to be more efficient for heavy oils.

Shokrlu and Babadagli [7] studied the formation of residual oil (kerosene) saturation for solvent injection (n-heptane) after and before water injection (WAG) at ambient conditions. It was concluded that solvent injection before any water injection increases drastically the oil recovery. Moreover, in order to prevent viscous instabilities, it was proposed that water injection should be always performed after solvent injection. Otherwise, viscous fingers form and recovered oil may decrease.

Qi et al. [8] analysed the condensing solvent extraction process, using propane and butane for bitumen extraction at pressures from 3 bar to 18 bar and temperatures from 70°C to 115°C, applying different flow rates. Three regions were identified: (1) vapor-solvent chamber, (2) condensing edge, (3) liquid solvent zone: the highest recovery factor was observed in zone (2) by a combination of bitumen dilution and vapour fingering.

Furthermore, interesting observations also emerge from literature on core experiments, as follows. Burger and Mohanty [9] analysed the mass transfer mechanisms from bypassed zones during gas injection, for a homogeneous and a heterogeneous core with different orientations and different enrichment levels of C3H8. The conditions were: miscible, first contact miscibility (FCM) and multi-contact miscibility (MCM), near-miscible and immiscible. It was then proved that the higher the enrichment level, the higher the recovery factor. Orientation affects the performance of the tests, which are dominated by different mass transfer mechanisms: gravity driven, capillary driven and so on. For horizontal orientation, MCM tests give higher recovery factors than FCM due to less gravity override.

Wylie and Mohanty [10] describe the gas injection as two in-series processes: gas flooding and oil bypassing, and mass transfer from the bypassed oil. Therefore, the impact of wettability on each is studied. Mass transfer is enhanced under oil-wet conditions (OW) and it is less effective as capillary forces increase. In OW, water saturation does not greatly affect mass transfer because it occupies the larger pores and does not block the flowing gas from contacting the oil. For OW, vertical gas flood (VGF), gravity stable, has a slightly lower recovery than for water-wet (WW). Horizontal gas flood (HGF) has lower recovery than VGF due to gravity override. For HGF, recovery increases monotonically with solvent enrichment for OW, while it barely increases for WW. This is the most remarkable conclusion and it is explained hypothesizing that water is redistributed in WW and shields the oil-solvent contact, while it remains trapped in the larger pores in OW.

Hopstaken [11] tested CO2, N2 and flue gas injection for a natural fractured reservoir core at (a) miscible and (b) immiscible conditions and different orientations. The lower recovery factor was obtained at immiscible conditions. When vertically oriented, the increase of the core size was proved to influence gravity forces and improve the recovery. Gravity drainage and mixing are the proposed mechanisms responsible for enhancing the recovery, while the oil entrapment due to capillary hold is pointed to diminish it.

From this literature analysis on microscopic recovery we therefore notice that solvent injection at microscopic scale presents still some questions, mainly on how the reservoir parameters, like water presence, wettability, pore pattern, fractures presence and type of solvent, impact on the behaviour of the fluid flow and the recovery at microscopic scale.

The objective of this paper is to provide a qualitative interpretation, from a physical and chemical point of view, of the results from 8 high pressure high temperature (HP-HT) micromodel experiments to determine the effects of temperature, pressure, connate water saturation, and fractures at reservoir conditions: HP-HT conditions were simultaneously applied on micromodels whose pore patterns have complex pore geometry and fractures. Each parameter was tested separately to give a thorough description of microscale solvent performance at reservoir conditions for continuous solvent injection.

# 2 Materials and methods

## 2.1. Micromodels

Three types of micromodels were manufactured by S.A.S KLEARIA (France) and utilized here (see also tables 1 and 2):

1. "Sandstone-like" with 28 inlets/outlets and 3 fractures spaced by 2.5cm (Chip 1).
2. "Sandstone-like" with 20 inlets/outlets and 3 fractures spaced by 2.5cm (Chip 2).
3. "Bi-modal carbonate-like" with 20 inlets/outlets and 2 larger than above fractures spaced by 5 cm (Chip 3)

The typical channel's cross section of glass (wet-) etched micromodels is shown in figure 1: fractures also have this characteristic cross section.

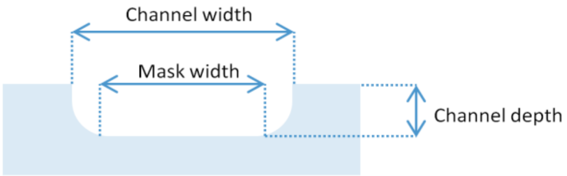

**Fig. 1.** Typical pore cross section in a glass micromodel (by wet etching technique): the pore cross section is not a true rectangle but a half ellipsoid due to acid etching.

**Table 1.** Characteristics of pore matrix dimensions.

| | Chip 1, 2 | Chip 3 | |
|---|---|---|---|
| | | Matrix-1 (macro pores) | Matrix-2 (micro pores) |
| Channel depth | 40 μm | 40 μm | 1 μm |
| Mask width | 40-320 μm | 75-200 μm | 10 μm<br>Constant value everywhere |

### 2.1.1. Sandstone-like micromodels (Chips 1 and 2)

Chips 1 and 2 are essentially equal, the sole difference lies in the amount and size of inlets/outlets. Chip 2 has fewer inlets/outlets but they are wider. This change was made during the course of the experimental program and allowed the viscous fluid to flow more easily during the oil saturation phase facilitating the set-up of the test.

The matrix pattern (figure 2) was created by repeating periodically an identical "tile" of dimensions approximately 3mmx3mm, derived from a 2D slice of a x-ray tomography dataset of 1 Darcy Clashach sandstone, which was manually edited, on a subjective empirical basis, to enhance its connectivity and guarantee percolation in the 2D space.

The pore pattern, excluding inlet/outlet channels, has size 5 cm x 5 cm x 40 μm (length x width x depth), and is constituted by D263 glass. The pore volume was experimentally estimated to be around 150 μl, without inlet/outlet channels. Permeability was not measured experimentally: but matrix permeability was estimated using CFD simulation, as will be explained in Section 5.

**Table 2.** Position of fractures and their dimensions. The three blue lines indicate the positions of the fractures in Chips 1 and 2 whilst the thicker red lines give the position in Chip 3.

| | 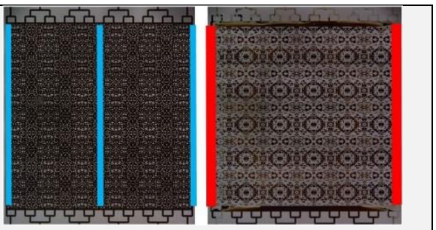 | |
|---|---|---|
| | Chips 1 and 2 | Chip 3 |
| Channel depth | 40 μm | 40 μm |
| Mask width | 200 μm | 1000 μm |
| Channel width | 280 μm | 1080 μm |

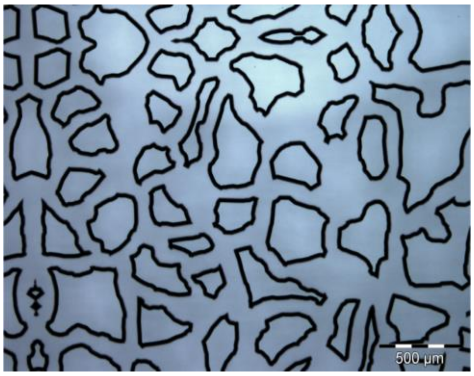

**Fig. 2.** Optical microscope image of pore pattern (Chips 1 & 2).

### 2.1.2. Bi-modal carbonate-like micromodels

The matrix pattern was created from a 2D slice of a x-ray tomography dataset of a 250mD Estaillades limestone, similarly to what explained above: in this case though the x-ray dataset produced only a representation of the intergranular porosity (and not of the intragranular microporous regions). As before, the image was treated digitally in order to qualitatively reproduce two types of porosities, which we name for convenience as "macro-porosity" and "micro-porosity" (figure 3). The macro-pores alone (which are represented by the thick black lines in figure 3) do not form a connected percolating pore network. It is the "micro-porosity" that assures global percolation (see figure 4 for details of mask construction). The pore pattern dimensions are identical to Chips 1 and 2 (5cmx5cm). Pore volume and permeability were not estimated.

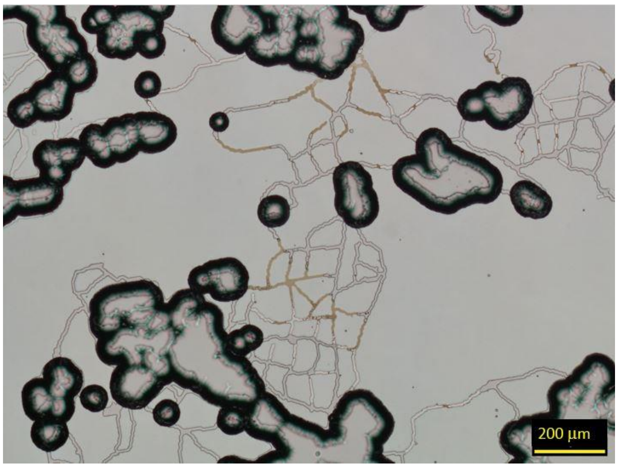

**Fig. 3.** Optical microscope image of pore pattern (Chip 3). Picture taken at the end of the experiment in a region close to a fracture: some residual oil is visible in the "micro-porosity" channels.

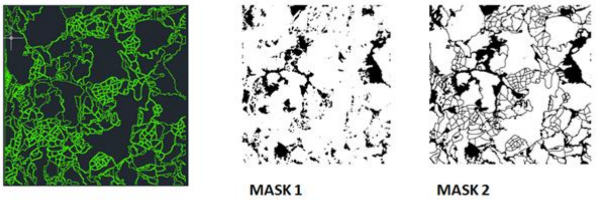

**Fig. 4.** Chip 3: on the left, the construction mask ("tile") of dimensions ~4mmx4mm that was repeated periodically across the 5cmx5cm surface of the pore pattern. The green lines track the contours of the porous system. The final "tile" (and micromodel) is actually composed by joining together the etched sides of two glass plates, one etched with pore depth 40um (from Mask 1) and one with depth 1um (from Mask 2).

### 2.1.3. Fractures

Chips 1 and 2 have three fractures (see table 2), parallel to the flow, which can be considered as channel type open aperture fracture [12]: two smooth fractures at each side of the pore pattern and a non-smooth one in the center (bounded by the rounded pore shapes of the matrix). The fractures' size is 0.2 mm, categorized as "capillary fractures" [13]. The fracture to matrix permeability ratio is estimated to be around 3 (matrix permeability was assessed using CFD software as explained in section 5). Chip 3 has only two smooth fractures at the sides, but of larger diameter (1mm, "supercapillary fracture"): the fracture to matrix permeability ratio is not available as the same image analysis and numerical CFD approach could not be used for this more complex matrix. In terms of behavior characterization of the systems under exam, considering the three fractures of Chip 1 and 2 and corresponding matrix, we can write the following flow equation:

$$Q = \Delta P \left( \frac{3}{8}\frac{\pi r^4}{\mu L} + \frac{k A}{\mu \Delta x} \right) \tag{1}$$

Which can be written as:

$$Q = \Delta P \left( \frac{1}{8\,\mu L / 3\,\pi r^4} + \frac{1}{\mu \Delta x / k A} \right) = \frac{\Delta P}{8\mu L / (3\pi r^4 + 8k A)} \tag{2}$$

For Chip 3, the bimodal pore matrix has two types of permeability acting in series and two parallel fractures along with the flow direction. The corresponding flow equation becomes:

$$Q = \Delta P \left[ \frac{1}{4}\frac{\pi r^4}{\mu L} + \frac{k_a k_b A_a A_b}{\mu (k_b \Delta x A_b + k_a \Delta x A_a)} \right] \tag{3}$$

Which again becomes:

$$Q = \Delta P \left( \frac{1}{4\,\mu L / \pi r^4} + \frac{1}{\mu (k_a \Delta x A + k_b \Delta x A) / k_a k_b A^2} \right) = \frac{\Delta P}{4\mu L\,(k_a + k_b) / (\,(k_a + k_b)\pi r^4 + 4 k_a k_b A)} \tag{4}$$

Equation (4) shows that the flow resistance of the matrix is inversely proportional to the product of both permeabilities and is dominated by the smallest permeability of the system

### 2.2. Experimental procedures

A recently built in-house HP-HT micromodel rig for use up to P=500 bar, T=150°C has been utilized, which makes use of a high pressure cell containing the micromodel. The flow cell is immersed in a mineral oil bath which is heated at the required temperature. Two experimental procedures have been utilized during the experimental work (table 3): the second one, used for the last 3 experiments, is an improved version and is the one which is described here. The authors consider that the modification in the protocol (made to enhance the robustness of the manipulation) has not changed the qualitative nature of the results and corresponding observations.

Without entering the details of single experiment P,T variations, the experimental procedure "EP2" (table 3) for a P=30 bar, T=60°C experiment, can be generalized as, referring to the scheme in figure 5:

1. Micromodel vertically placed
2. Pull the vacuum in all the circuit including the micromodel.
3. Open the valve V1 while V2, V3, V4 are closed and inject oil in the circuit from the bottom with the oil pump at P=2 bar, until the oil level reaches the top end.
4. Use the 'air' reservoir at P=30 bar to pressurize all circuit.
5. Open all valves to have P=30 bar everywhere.
6. Close V1 and V2 and maintain V3 open. Inject propane from «propane pump» to saturate dead volumes on top.
7. Finally inject propane at 100 µl/h until it enters the micromodel, opening V2 and closing V3.

An optical camera (Phase One) with a detector 10328x7760 pixels was used to capture images at a resolution of approximately 9 µm/pixel. This allows

*Table 3. Experiment description list: EP is experimental procedure; SS is solvent state: gas, liquid, supercritical SC; the miscibility state (MS) for all the experiments is shown by comparison to the minimum miscibility pressure (MMP).*

| Exp N. | Chip N. | EP | SS | P bar | T °C | Q µl/h | $S_{or}$ % | $S_{wi}$ % | MMP bar | MS |
|---|---|---|---|---|---|---|---|---|---|---|
| 1 | 1 | 1 | Gas | 8,5 | 60 | 100 | ~ 20 | 0 | 21.51 | Immiscible |
| 2 | 1 | 1 | Liq | 30 | 60 | 1000 - 100 | ~ 0 | 0 |  | First Contact M. |
| 3 | 1 | 1 | Liq | 100 | 60 | 100 | ~ 0 | 0 |  |  |
| 4 | 1 | 1 | Liq | 30 | 60 | 100 | ~ 0 | 0 |  |  |
| 5 | 1 | 1 | SC | 50 | 110 | 100 | ~ 10 | 0 | 50.74 | Near Miscible |
| 6 | 2 | 2 | Liq | 30 | 60 | 100 | ~ 0 | ~ 20 | 21.51 | First Contact M. |
| 7 | 2 | 2 | Liq | 30 | 60 | 100 | ~ 0 | 0 |  |  |
| 8 | 3 | 2 | Liq | 30 | 60 | 100 | > 80 | 0 |  |  |

observing details at the pore scale whilst also imaging the full extension of the pore pattern (25cm$^2$). The image capture frequency was kept at a rate of 4 images/minute, which was the maximum possible capture rate for this large image size. From experiment 6 onwards, inlet/outlet channels were also almost completely captured in the images. A second camera (IMPERX) is used to capture a video of the experiment, mainly for QC purposes, at higher time resolution but lower spatial resolution.

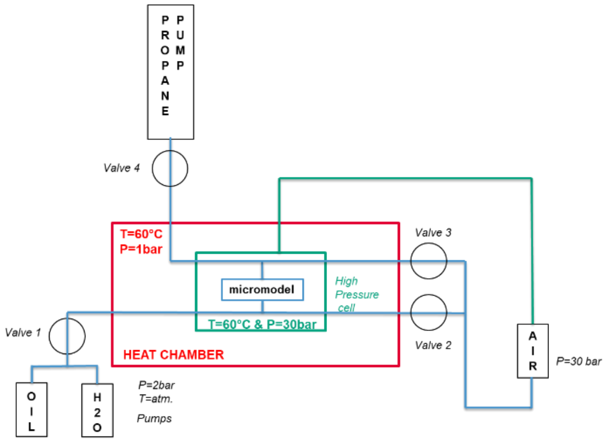

**Fig. 5.** Schematization of the experimental set-up for HP-HT micromodel experiments. Case of P=30 bar, T=60°C experiment.

### 2.2.1 Fluids

The fluids employed in the experiments were:

- Viscous oil (viscosity 135cp @ T=60° ; density 909kg/m$^3$; asphaltene content 4.4% weight )
- Solvent: Pure propane ($P_{crit}$ : 42bars ; $T_{crit}$=97°C)
- Brine (45g/L Nacl, 5g/L CaCl)
- Air (Nitrogen)

Depending on the P, T conditions the solvent was injected as gas, liquid or supercritical state.

## 3 Organisation of experiments

Table 3 reports the characteristics of the 8 experiments. Residual oil saturation (Sor) is estimated qualitatively by visual inspection. Note that the rate in experiment 2 was of 1000 µl/h until solvent breakthrough, then dropped to 100 µl/h. Experiment 7 is the repetition of experiment 6 in exactly the same conditions, apart from presence of connate water, $S_{wi}$. Experiment 7 also repeats experiments 2 and 4 in terms of identical P,T conditions.

## 4 Interpretation of the experiments

### 4.1. Pore-level visual observations

The following general observations on the displacement can be made:

- No oil is trapped in the miscible tests, all is produced.
- Experiment 1 (immiscible, solvent in gas state) and experiment 5 (supercritical near miscible) both show trapped oil ganglia, but of different sizes (figure 6).
- At miscible conditions, precipitation of asphaltenes is normally observed (dark black phase in figure 7).
- Solvent breakthrough always takes place via a fracture, except for experiment 7, where instead a finger through the matrix travels faster than the one in the fracture (figures 8, 9).
- Experiment 8 has solvent flow only in fractures: the matrix is largely unaffected, with exception of the areas near the fracture (figure 10).

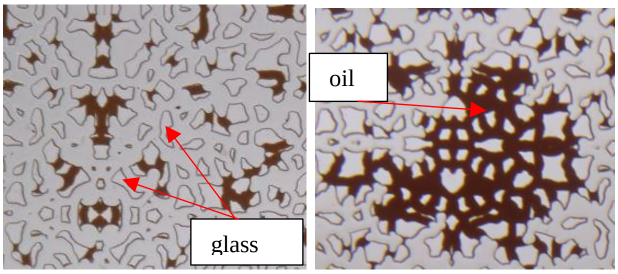

**Fig. 6.** Trapped oil configurations in experiment 5, left, (supercritical, near miscible) and experiment 1, right, (gas state, immiscible): in the latter larger blobs are present. See also figure 11 and 14.

### 4.2. Pressure and temperature

The definition of the miscible condition is the first aspect to define. Thus, for a given solvent, the temperature of the system defines the minimum miscibility pressure (MMP) that must be attained to have either multi-contact or first contact miscibility. These values were calculated with an in-house PVT software and the resulting miscible conditions are detailed in table 3.

In this section, experiments 1, 3, 4 and 5 (highlighted in orange in table 3) are specifically studied to observe how pressure and temperature conditions impact on the fluids behaviour (figures 11, 12, 13, 14). We observe that:

- The behaviour of the experiments changes drastically once the minimum miscibility pressure is achieved (first contact miscibility in these cases).
- The pressure in experiment 1 is below the MMP, by consequence oil gets trapped due to capillary forces. Solvent goes preferentially through the left fracture where the solvent breakthrough takes place rapidly. Oil keeps being produced until percolation takes place in all 3 fractures: only when all three fractures are conducting, the oil production stops. The residual oil is about 20%, located mostly at the bottom.
- The pressures of experiments 3 and 4 are above the MMP. Therefore, they are in first contact miscible regime and no capillary forces exist. All the oil is produced in these cases and fluids' behaviour is almost the same in both experiments.
- Experiment 5 retains approximately 10% of the oil. This is due to the presence of capillary forces that trap the oil. However, oil is produced quicker (less PVs of solvent injected) than for the first contact miscible experiments. The reduction of oil viscosity due to a higher temperature (110°C instead of 60°C) explains this observation. It might be considered too that, according to [13], capillary forces may be a source of mixing that enhance the oil recovery of dead-end pores while in near-miscible or multi-contact miscible conditions. The same effect is observed by [1] in their work with CO2 injection. Although controversial, this mechanism has been observed in several works [8, 9] and could be another reason to explain the observed behaviour.

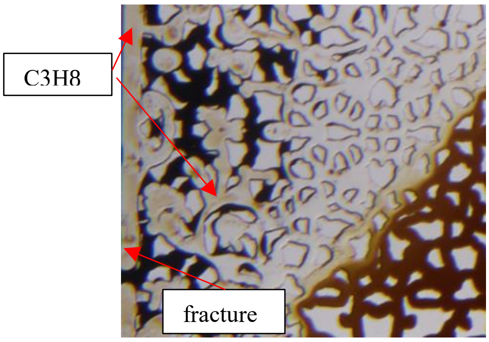

**Fig. 7.** "Black" asphaltene deposits at a late stage of experiment 2. The fracture is visible on the left hand side. The front of miscibility in the matrix is also seen (change in oil colour).

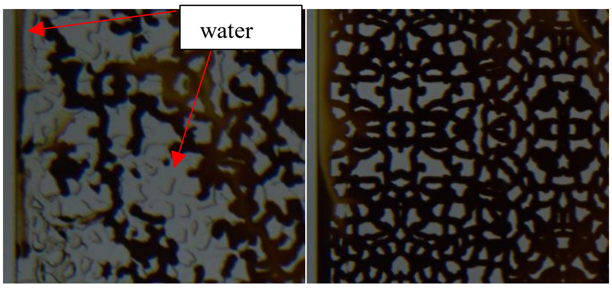

**Fig. 8.** Early stage of the experiments 6 and 7. Left: snapshot right after solvent breakthrough in fracture for experiment 6 (with Swi). Right: snapshot of solvent finger in fracture for experiment 7 (no $S_{wi}$), just seconds before the breakthrough, which will happen at another location.

**Fig. 9.** Moment of breakthrough for the solvent finger in experiment 7 which has travelled through the matrix (see also figure 17).

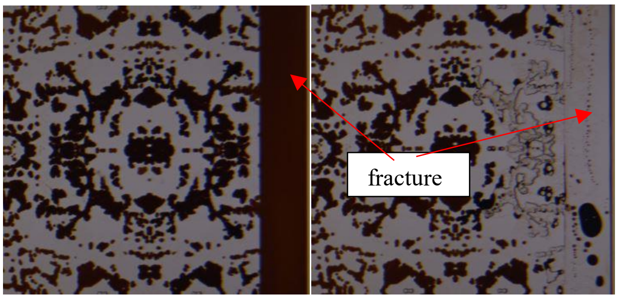

**Fig. 10.** Detail of the fracture region for experiment 8. The fracture is visible on the right. Left: snapshots at the start of the experiment. Right: at the end of the experiment after 1 day (right). The state remained nearly identical even after 13 more days of continuous solvent flooding.

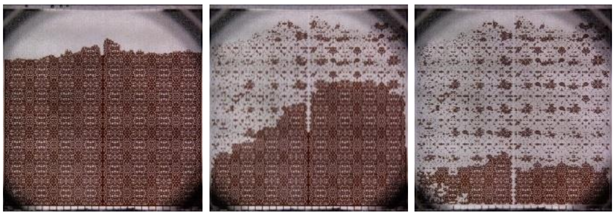

**Fig. 11.** Experiment 1 at different stages: from left to right, start of the test, after 4.38h and after 166.27h respectively, which in this case represents the very end of the experiment. Note that the right hand side image also represents the situation at the very end of the experiment: the matrix in the bottom part of the micromodel could not be swept. (Note: an instantaneous pressure fluctuation at the very start of the experiment made the oil level slightly raise which explains the different height of oil between the snapshot at the start and that after 4.38h).

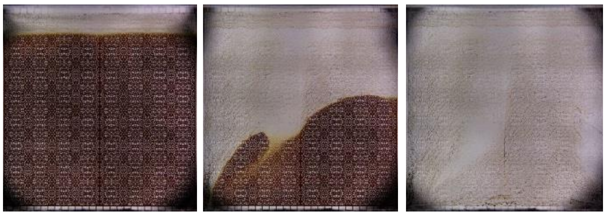

**Fig. 12.** Experiment 3 at different stages: from left to right, start of the test, after 1.2h, and after 3.32h respectively, at experiment completed. A finger developed at some point.

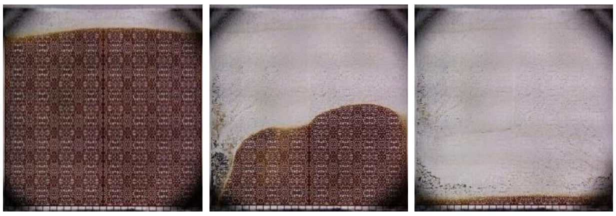

**Fig. 13.** Experiment 4 at different stages: from left to right, start of the test, after 0.43h and after 1.73h respectively, at experiment nearly completed.

**Fig. 14.** Experiment 5 at different stages: from left to right, start of the test, after 0.28h and after 0.73h respectively, at experiment nearly completed.

### 4.3. Injection rate and amount of inlets/outlets

Experiments 2 (figure 16), 4 (figure 13) and 7 (figure 18) were performed at 30 bar and 60°C in the "sandstone-like" micromodel but with different injection rates (experiment 2 vs experiment 4) and with different inlets/outlets characteristics (experiment 7 vs experiment 4). The differences are detailed in table 4.

**Table 4.** Experimental details defining the peculiarities of experiments 2, 4 and 7.

| Parameter | Exp. 2 | Exp. 4 | Exp. 7 |
|---|---|---|---|
| Injection rate (µl/h) | 1000 and 100 after solvent breakthrough | 100 | |
| Amount of inlets/outlets | 28 narrower inlets/outlets | | 20 wider inlets/outlets |

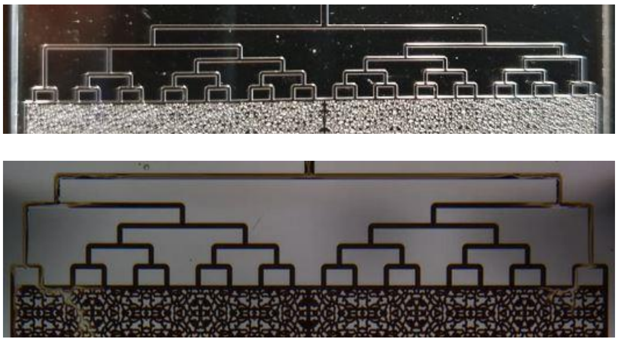

**Fig. 15.** Detail of inlet/outlet channels. Top image: 28 inlet/outlet channel configuration: this does not favour solvent entry through the sides. Bottom image: 20 inlet/outlet channel configuration: this tends to favour solvent entry via the sides (as can be seen, by the colour change).

The observations are:

- Experiment 2: Increasing injection rate (compared to experiment 4), whilst the viscosity ratio between oil and solvent is higher than 1000, has the sole effect of speeding up solvent breakthrough favouring the channelization. This is also observed by [4]. Nonetheless, the injection rate is decreased after the solvent breakthrough and the final performance becomes similar to that observed in experiment 4.
- The 28 inlet/outlet channel configuration does not favour solvent entry through the sides (as the 20 channel configuration does): nevertheless, solvent still travels via the edge of the micromodel (in the fractures).
- Experiment 7: Solvent fingers are clearly observed in the matrix and are parallel and close to the side fractures. Their growth is later damped by transverse dispersion but these early invaded zones control the solvent path through the matrix and contribute to the solvent breakthrough. This radically different behaviour of percolation in the matrix and not in fractures could be explained considering that experiment 7 has less but wider inlet channels. Thus, for the same total injection rate, each inlet has a higher "individual injection rate", which may trigger sustained finger growth in the matrix (see also section 4.6).

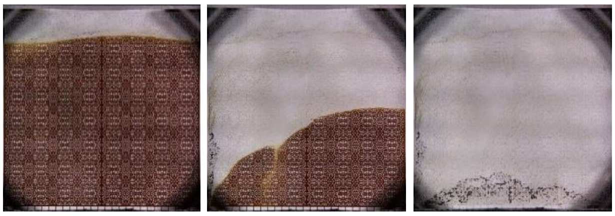

**Fig. 16.** Experiment 2 at different stages: start of the test, after 0.93h and after 2.1h, end of the experiment, from left to right.

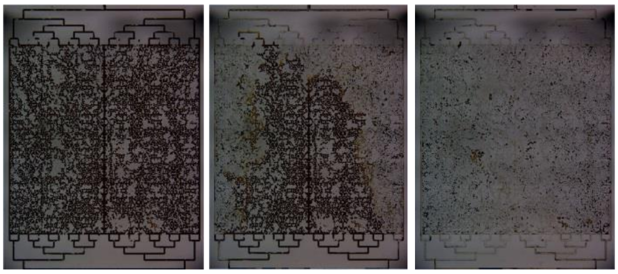

**Fig. 17.** Experiment 6 with Swi (Chip 2) at different stages: start of the test, after 5.6h and after 15.15h, from left to right.

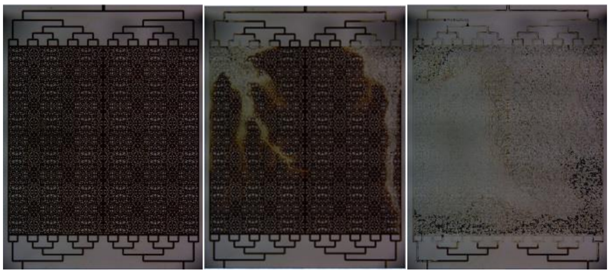

**Fig. 18.** Experiment 7 with no water (Chip 2) at different stages: start of the test, after 0.1h and after 2.0h, from left to right.

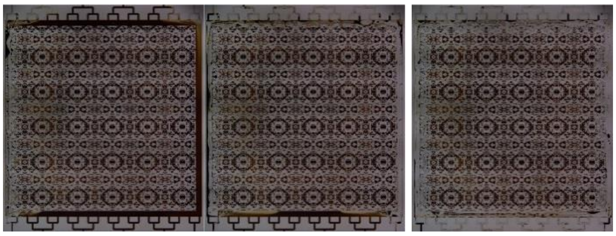

**Fig. 19.** Experiment 8 in Chip 3 ("Bi-modal carbonate-like") at different stages: start of the test, after 0.37h and after 16.32h, from left to right.

### 4.4. Immobile water presence

The effect of immobile water on miscible behaviour is studied comparing experiments 6 (figure 17, with connate water) and 7 (figure 18, without connate water), both performed on the same Chip 2. Both were performed at the same pressure and temperature, 30 bar and 60°C, which implies first contact miscible conditions. The main observations and conclusions are:

- The dynamics of oil recovery is slower. As the medium is water-wet, immobile water acts as a mass transfer barrier that retards the contact between oil and solvent and interrupts the mixing mechanisms. This is observed by several authors [2, 10, 14]. If the medium were oil-wet, then oil would wet the pore walls and form a film. This would allow the oil-solvent mass transfer through it. Consequently, water presence would not have a great impact on the mixing mechanisms as it does, on the contrary, on the water-wet media used here.
- On the other hand, early solvent channelization and breakthrough through the two lateral fractures is observed if $S_{wi}$ is present (compared to experiment 7, without water). Considering equation (2), it is observed that decreasing the effective matrix cross sectional area of flow ('A'), which is now partially occupied with water, increases the matrix resistance for the solvent to flow. This favours the passage of solvent through the less resistance paths, which in this case are the two lateral fractures.

### 4.5. Comparison with double porosity, larger fracture case

Experiment 8 (figure 19) was performed in a bi-modal "carbonate-like" micromodel (Chip 3). It has two types of porosities, which we can define as macro- and micro-porosity. The latter connects the macro-pores with each other and to the rest of the medium. The observations are compared with those from experiment 7 ("sandstone-like", single-type matrix porosity, figure 18), which was performed at the same pressure and temperature conditions (30 bar and 60°C, implying first contact miscibility). The same experimental procedure (EP2) is used.

The main observations for experiment 8 are:

- Estimated residual oil is approximately 80%, even after 13 days of continuous solvent injection, and is very high compared to that of Experiment 7 which instead sweeps all the oil in 2.0 hours. Oil is only recovered at the lateral borders near the two lateral fractures, where solvent breakthrough was instantaneous: solvent goes through the fractures and barely invades the matrix.
- Almost no oil is produced after 30 minutes from the start of the experiment.
- Some mass transfer takes place between the fractures and the regions next to it.

This behaviour can be explained comparing equations (2) and (4) and considering the connectivity of the medium (production allocation in the matrix and the fractures) as well as the mixing mechanisms (matrix-fracture and matrix-matrix interactions), which are very different than those of Chips 1 and 2. The resistance to flow due to the fractures and matrix can be seen as:

$$\delta = \frac{R_{fractures}}{R_{matrix}} = \frac{{}^{8\,\mu\,L}/_{\pi r^4}}{{}^{\mu\,\Delta x}/_{k\,A}} = 8\,\frac{k\,A}{\pi r^4} \qquad (5)$$

Therefore experiment 7 ("sandstone-like") has a greater value of δ than experiment 8 ("carbonate-like"), consequence of a smaller fracture characteristic size and a bigger matrix permeability: experiment 8 has a resistance ratio δ such that only production through the fractures prevails.

In terms of mixing mechanisms, considering equation (6),

$$\frac{D_{eff}}{D} = \frac{\emptyset}{\tau} \qquad (6)$$

the effective diffusion coefficient for experiment 8 is smaller than for experiment 7 and the mass transfer by diffusion between the fractures and the matrix is slower as observed in the experiment.

Considering microscopic dispersion, since both transverse and longitudinal dispersion depend on the interstitial velocity (Perkins and Johnston [15]), which is practically zero inside the matrix for experiment 8, then dispersion mechanisms must be absent inside the matrix. However, the zones of the matrix next to the fractures have a higher interstitial velocity and then, the diffusion coefficient plays a role. According to the discussion in [15], the mixing mechanisms that take place in the zones next to the fractures are diffusion dominated and very slow.

On top of the observations above it is worthy reporting that solvent is again percolating preferentially through the left hand side fracture: this general behaviour of our experiments might be due to a slight tilting of the vertically positioned micromodel.

### 4.6. Viscous fingering analysis

Viscous fingering refers to the onset and evolution of morphological instabilities that occur at the interface of two fluids while they displace each other in a porous medium. Their formation and growth depends on the balance of viscous and gravity forces, the dispersion mechanisms and the heterogeneities of the medium. These three parameters are analysed in order to understand the results of these experiments. Gravity forces may improve the sweepout and oil recovery by preventing an early breakthrough of the lighter solvent and the formation of bypassed areas. This is achieved when the solvent is injected from the top and the production rate (equal to the injection rate in these cases) is low enough for gravity to keep solvent and oil segregated, avoiding the formation of the solvent fingers. In order to define the stability of the displacement, the injection rate of all the experiments was compared to the critical velocity defined by Dumoré [16] in:

$$u_c = \frac{(\rho_o-\rho_s)}{(\mu_o-\mu_s)} k * g = Critical\ velocity \qquad (7)$$

The expression above was developed assuming that injection is from the top, the solvent/oil interface is horizontal with a negligible transition zone. According to this criterion, the injection rate (100ul/hr, resulting in 5,96 ft/day) is too rapid, that is, higher than the critical velocity, which is less than 1 ft/day for any of our experiments: it means all the experiments should show solvent fingers as buoyancy is not strong enough to prevent their initiation and growth by viscous/advection forces. On the other hand, instabilities in the matrix were only observed in two experiments (for example, experiments 7, figure 18). This behaviour can be explained due to the contributions of the transverse dispersion (which smooths out the fingers as they grow) and to the stabilizing role of the fractures, in relation to the flow inside the matrix. The presence of fractures simply reduces the effective flow rate inside the matrix, as fractures and matrix compete in the production of oil (parallel system). In other words the actual velocity in the matrix is slower than the injection rate, and therefore the system tends to stabilize, i.e. we don't observe fingers in the matrix.

## 5 Simulation exercise on "sandstone-like" pattern

We finally report a simulation exercise whose objective is to verify that the set of equations embedded in the simulator is able to reproduce the obtained experimental results, with the available information, and even at these small scales. This is a two edge situation in which both equation system and data must prove to be adequate, since a unique set of inputs must be able to reproduce the different observations as P,T change. The benefit of adding this study is to give confidence in future sensitivity analysis that can be run to forecast possible outcomes and propose future experimental set-ups, even at core scale.

The simulator STARS CMG was used. For the construction of the grid, the values of matrix permeability for the Chip 1 and 2 were obtained numerically by means of the Stokes solver OPENFOAM applied to a segmented portion of the chip, as seen in figure 20 [17]. The permeability was estimated to be around 42D, which should be considered a qualitative estimate also in light of the large uncertainty on the segmentation of the experimental image. Porosity used in the grid for the matrix is 66%. The diffusion coefficient was estimated from published data for similar solvent types as D= 2.7*10-7 m$^2$/day.

Simulations were not carried out for Chip 3 (experiment 8) as it was not possible to obtain the permeabilities of the matrix, "macro-" and "micro-porosities".

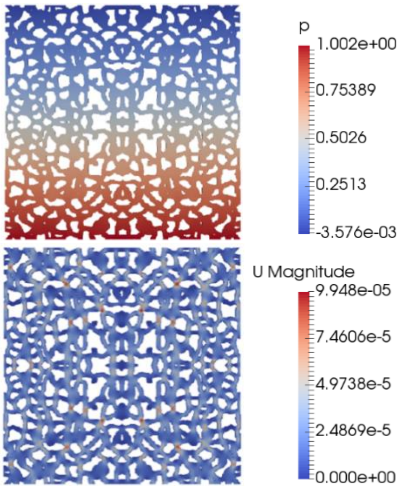

**Fig. 20.** CFD simulation on a sample from the Chip 1 (2): pressure field on top; velocity field at the bottom. Legend in SI units (for an arbitrary pressure drop of 1 Pa across the model).

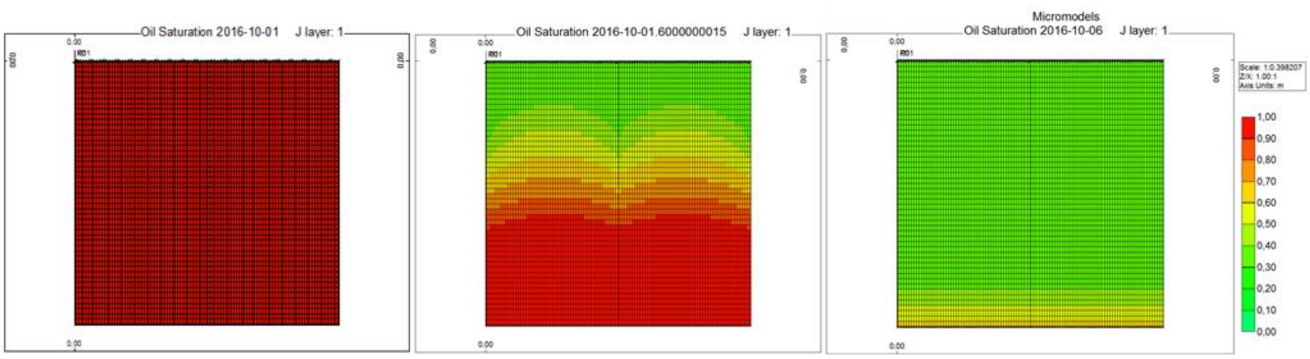

**Fig. 21.** Experiment 1 (P=8.5 bar; T=60°C) flow simulation. Oil saturation at different stages (after 0 days, 0.6 days, and 5 days).

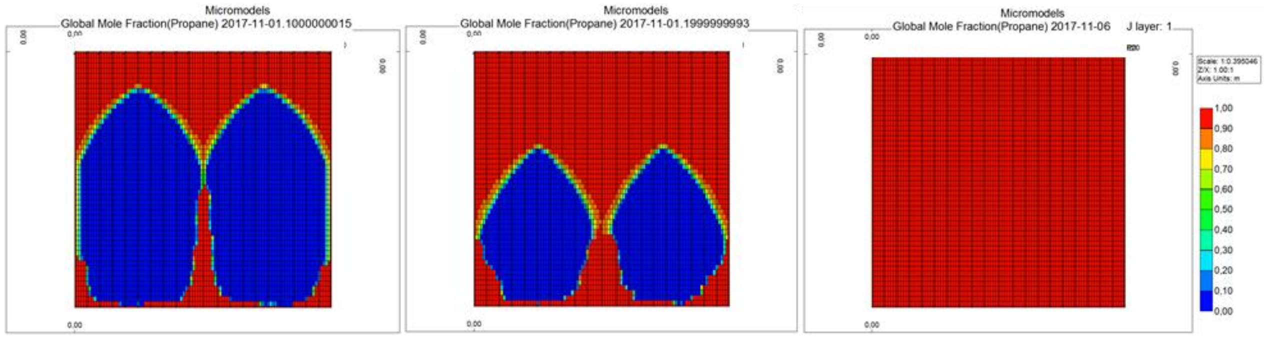

**Fig. 22.** Experiment 3 (P=100 bar; T=60°C) flow simulation. Global mole fraction of propane at different stages (after 0.1 days, 0.19 days, and 5 days).

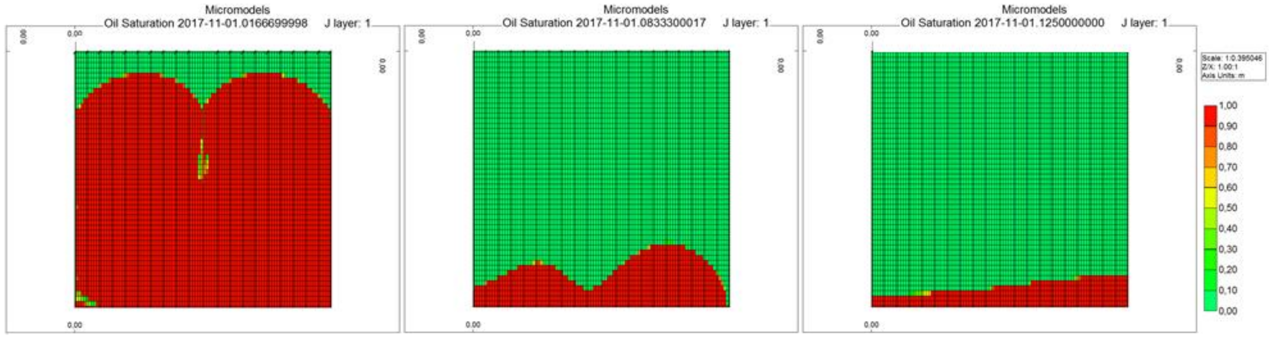

**Fig. 23.** Experiment 5 (P=50 bar; T=110°C) flow simulation. Oil saturation at different stages (after 0.01 days, 0.08 days and 0.12 days).

### 5.1. Experiment 1 (P=8.5 bar; T=60°C)

It was decided to simulate experiment 1 with one "producer" and one "injector well" (using common reservoir engineering terminology that will also be used in the next two paragraphs), to mimic the chip's inlet/outlet ports. Capillary pressure and relative permeabilities were taken into account because it is an immiscible displacement case. This simulation could not reproduce the complex dynamics of experiment 1 (figure 21): as mentioned above, there is some residual oil left (in the form of a bottom layer) at the end of the experiment. In the simulation, the solvent does not percolate through the fractures in the same (complex) way as instead it does in the experiment. In the experiment the left fracture is first percolated, followed by the right fracture and finally the central one: only when the total conductivity of the fractures is large enough, the matrix is cut out. In the simulation, the solvent front gets only deformed by the fractures.

### 5.2. Experiment 3 (P=100 bar; T=60°C)

The numerical set-up includes now 20 "producers" and 20 "injectors": this change allowed to better represent the visual "history of production" for this experiment. The relative permeabilities are considered as equal to the phase saturation [14] for first contact miscibility cases (experiments 3, 4, 6 and 7). Observations: all the oil is recovered as observed in the experiment. It was later also verified that relative permeabilities do not impact flow in the simulation: this is because the solvent, propane, is a liquid and the simulator solves the case as monophasic flow of liquid oil. This is also why figure 22 shows the global mole fraction of propane instead of the oil saturation. The same exercise was conducted to reproduce the experiment 4 (P=30 bar; T=60°C) leading to nearly identical outcome as well as for Experiment 6, where connate water was not seen to change the picture (cases not reported here).

### 5.3. Experiment 5 (P=50 bar; T=110°C)

This is the experiment performed in supercritical conditions. The numerical set up is similar to the previous case as well as the relative permeabilities. Capillary pressure is not taken into account because CMG STARS has convergence problems (so it is then set to "zero" for any saturation). A residual oil saturation of 8% was obtained, similar to the experiment. The asymmetry seen in figure 23 is due to a negative skin attributed to the wells on the left side, in order to try to represent as close as possible the experimentally observed asymmetry.

Overall the simulation exercise conducted at these small scales has proven that it is possible to reproduce the main qualitative features of the experiments.

## 5 Conclusions

The topic of investigation of this paper has been the injection of a solvent (propane) in viscous oil using HP-HT glass micromodels.

The experiments show that for an isothermal process, for a given pore pattern and solvent, pressure modifies drastically the displacement behaviour, as an indication of how far the oil-solvent system is from miscibility. A miscible displacement is observed once the miscibility pressure is surpassed. Above that value, the behaviour of the system will not change any more as long as pressure stays in the range of multi-contact miscibility or first contact miscibility.

Water presence, for the water-wet media used in this work, acts as a barrier to solvent-oil contact and affects the apparent pore size distribution available for solvent flow paths and mass exchange. The effective matrix cross sectional area available to flow becomes now partially occupied with water, increasing the matrix resistance for the solvent to flow (whilst fractures have remained water-free during oil drainage) and the recovery becomes slower. However, the overall performance does not change as all oil is recovered despite the water presence.

An important effect of fracture characteristic size was seen. The ratio between fracture and matrix permeability is considered to have highly affected the displacement efficiency: once a certain threshold is surpassed, the recovered oil drops drastically despite being a miscible displacement. This can also happen once solvent has broken through a high enough number of fractures, as seen in the immiscible case (experiment 1). These behaviours can be hard to predict a priori.

According to criteria defined in the literature, the experiments are classified as having unstable displacement. By consequence, solvent fingers are expected as buoyancy is not strong enough to prevent their initiation and growth by viscous/advection forces. But this happened to be the case only in a minority of experiments. This behaviour is explained as being a consequence of the contributions from transverse dispersion (which smooths out the fingers as they grow) and from the presence of fractures which in fact aid in stabilizing the character of the flow inside the matrix, since they "absorb" most of the instability. Changes in inlet boundary conditions from one chip to another also play a role.

Finally a numerical simulation exercise with CMG STARS simulator was conducted which allowed to qualitatively reproduce the main behaviours observed in the experiments, with a unique set of petrophysical and PVT inputs. There is a hint though that complex fracture matrix completion might not be easily predictable by simulation, as it was the case for experiment 1. Nevertheless, this exercise being satisfactory, it provides confidence for future numerical applications.

The authors would like to acknowledge TOTAL for permission to publish this paper and Drs Clément Varloteaux and Igor Bogdanov (CHLOE) for the technical discussions and help on simulation. Richard Rivenq (TOTAL) is also gratefully acknowledged for improving the quality of the manuscript with his comments.

## Nomenclature

Q = total flow rate, $m^3/s$
$\Delta P$ = delta pressure, Pa
r = fracture one chracateristic size, m
L = fracture and pore pattern length, m
$\mu$ = oil viscosity, Pa.s
k = permeability of the matrix, $m^2$
A = matrix cross sectional area of flow, $m^2$
$\Delta x$ = matrix length through which $\Delta P$ is measured, m
$k_a$ = permeability of the macropores, $m^2$
$k_b$ = permeability of the micropores, $m^2$
$D_{eff}$ = effective diffusion coefficient, $m^2/s$
D = bulk diffusion coefficient, $m^2/s$
Ø = fractional porosity, dimensionless
$\tau$ = tortuosity, dimensionless
$\rho o$, $\rho s$ = oil and solvent density, $kg/m^3$
$\mu o$, $\mu s$ = oil and solvent viscosity, Pa.s
g =standard acceleration due to gravity = 9.81 ($m^2/s$)

## References

1. I. Chatzis, Pore scale phenomena of heavy oil recovery using vapor extraction, SCA n° 2002-26, *Society of Core Analysts*, Monterey, CA, USA, (2002)
2. B.T. Campbell and F. M. Orr Jr, Flow Visualization for CO2/Crude-Oil Displacements, *Society of Petroleum Engineers*, https://doi.org/10.2118/11958-PA (1985)
3. M. Sohrabi, A. Emadi, M. Jamiolahmady, S. Ireland, C. Brown, Mechanisms of extra-heavy oil recovery by gravity stable CO2 injection, SCA n° 2008-20, *Society of Core Analysts*, Abu Dhabi, UAE (2008)
4. M. Saidian, M. Masihi, M. H. Ghazanfari, R. Kharrat, S. Mohammadi, An Experimental Study of the Matrix-fracture Interaction During Miscible Displacement in Fractured Porous Media: A

Micromodel Study, *Energy Sources, Part A: Recovery, Utilization, and Environmental Effects*, 36:3, 259-266, https://doi.org/10.1080/15567036.2010.536828 (2014)

5. F. Civan, *Porous media transport phenomena* (Wiley, 2011)
6. A. Marciales, T. Babadagli, Pore scale visual investigations on solvent retrieval during oil recovery at elevated temperatures: A micromodel study, *Chemical Engineering Research and Design,* Vol. 106, 59-73, https://doi.org/10.1016/j.cherd.2015.12.007 (2016)
7. Y. H. Shokrlu, T. Babadagli, Pore-Scale Investigation of Phase Distribution and Residual-Oil Development During Secondary and Tertiary Solvent Injection, *SPE Reservoir Evaluation & Engineering, 18, 01, https://doi.org/10.2118/173180-PA (2015)*
8. Z. Qi, A. Abedini, P. Lele, N. Mosavat, A. Guerrero, D. Sinton, Pore-scale analysis of condensing solvent bitumen extraction, *Fuel*, 193, 284-293, https://doi.org/10.1016/j.fuel.2016.12.070 (2017)
9. J. E. Burger, K. K. Mohanty, Mass transfer from bypassed zones during gas injection, *SPE Reservoir Engineering,* 12, 02, https://doi.org/10.2118/30768-PA (1997)
10. P. Wylie, K. K. Mohanty, Effect of Wettability on Oil Recovery by Near-miscible Gas Injection. *Society of Petroleum Engineers,* doi:10.2118/39620-MS, https://doi.org/10.2118/39620-MS (1998)
11. K. M. Hopstaken, The effect of miscibility conditions on Gas Oil Gravity Drainage; an experimental study in a simulated fractured medium using CO2 as a displacement agent, *Msc Thesis*, Faculty of Geosciences, Utrecht University, https://dspace.library.uu.nl/handle/1874/278654 (2013)
12. M. S. Ameen, Fracture and in-situ stress patterns and impact on performance in the Khuff structural prospects, eastern offshore Saudi Arabia, *Marine and Petroleum Geology,* Vol. 50, Pages 166-184 (2014)
13. G. V. Chilingarian, S. J. Mazzullo, H. H. Rieke, Carbonate reservoir characterization: a geologic-engineering analysys, part I, *Developments in petroleum science* 44 (Elsevier, 1992)
14. F. I. Stalkup Jr, Miscible displacement, *SPE Monograph and Richardson*, Society of Petroleum Engineers (1983)
15. T. K. Perkins, O. C. Johnston, A review of diffusion and dispersion in porous media, *SPE J.*, 3, 1, (1963)
16. J. M. Dumoré, Stability considerations in downward miscible displacement, *SPE Journal*, 356-317 (1964)
17. C. Varloteaux, I. Bondino, I. Bogdanov, Rock absolute permeability analysis using image-based direct pore-scale simulations. *InterPore 10th Annual Meeting and Jubilee*, May 14 – 17 2018, New Orleans, LA (2018)

# Screening of EOR potential on the pore scale by statistical and topological means

*Holger* Ott[1*], *Ahmad* Kharrat[1], *Mostafa* Borji[1], *Thorsten* Clemens[2], *Pit* Arnold[1]

[1]Department Petroleum Engineering, Montanuniversität Leoben, 8700 Leoben, Austria.
[2]OMV E&P, Vienna, Austria.

**Abstract.** Chemical EOR processes modify properties of fluid-fluid and rock-fluid interfaces in the pore space with the aim of mobilizing additional oil. The initial mobilization takes place on the scale of the individual pore. Therefore, observations on the pore scale provide valuable insights into water-oil displacement mechanisms; the understanding of these mechanisms enables an efficient design of the injection water chemistry. In this article, we present a first step towards a statistical and topological fingerprint of EOR processes used to characterize and optimize EOR processes. We use microfluidics to observe changes in the oil distribution in the pore space and the formation of emulsion phases. The oleic phase was analyzed by statistical and topological means showing a systematic change as a function of alkali concentration. In particular, Lorenz diagrams and the normalized Euler characteristic appeared as sensitive to changes in the water chemistry. It turned out that the displacement processes are influenced by emulsion formation, especially at low and high alkali concentrations. This is implicitly reflected in the statistical and topological analysis, but has not yet been explicitly taken into account.

## 1 Introduction

Alkaline flooding is a chemical Enhanced Oil Recovery (EOR) method, which is often combined with surfactant and polymer flooding [1-3]. The addition of an alkaline agent to the injection water results in a high pH and can lower the interfacial tension when the crude contains a substantial amount of fatty acids, which is reflected in the total acid number (TAN). At high pH values, hydroxide ions and acidic oil components saponify at the oil-water interface, resulting in the generation of in-situ surfactants. The resulting decrease in interfacial tension commonly leads to emulsification and an increasing displacement efficiency, leading to additional oil recovery.

Complex chemical EOR processes such as alkali or surfactant flooding are typically optimized for their phase behavior and by conventional core flooding experiments. However, the information from core floods is rather limited, as there are no direct insights into details of oil mobilization and displacements. As a rule, cumulative oil production and differential pressure are measured. These are rather one-dimensional information from which complex displacement processes must be understood. On the other hand, the phase behavior, respectively the degree of emulsification, is often analyzed in test-tubes and not under realistic flow, respectively mixing conditions as in porous media.

Chemical EOR processes modify fluid-fluid and rock-fluid interfacial properties in the pore space in order to mobilize additional oil. There are several techniques by which oil mobilization can directly be observed in the pore space, such as micro-CT imaging [4, 5] and microfluidics [6-9]. It has further been demonstrated that both techniques, but especially microfluidics, allow as well the identification of emulsion phases and hence give access to combined information on flow and phase behavior [7, 9].

In the recent years, fluid distributions on the pore scale have been analysed by statistical and topological means, deriving information that is more sophisticated and may provide more insight into EOR displacements than e.g. recovery curves and differential pressure measurements alone. Cluster-volume and cluster-length distributions have been used to characterize fluid phases and have been linked to fluid-phase mobility [4, 5, 10-12]. These distributions are characteristic, but their interpretation with respect to oil mobility depends on the tail end of the distribution, which may be influenced by the limited field of view [11], respectively the largest clusters that may not be statistically represented in the observed volume. However, the distributions themselves are fairly independent of the tail end and thus of the field of view and may be robust displacement characteristics.
Another very recent development is the description of the microscopic fluid-phase distribution by topological means using Minkowski functionals [13, 14]. Fluid phase topology is linked to classical parameters like fluid saturation, capillary pressure, capillary pressure hysteresis and the wetting state [14, 15]. The advantage of a topological description is that it assigns these parameters a well-defined physical and mathematical meaning. Of particular interest in this context is the Euler characteristic, which describes the connectivity of a fluid phase and may be associated with wetting properties [14].

In the frame of the present study, we investigate displacements of crude oil by water and alkali solutions. We use microfluidics (MF) to screen the performance of the injection water as a function of alkali concentration.

---

[*] Corresponding author: holger.ott@unileoben.ac.at

The advantage of using MF for EOR screening is (a) that MF devices are chemically very well defined, (b) that MF experiments are relatively fast performed and cost competitive, and (c) MF can easily be parallelized and is therefore an ideal screening tool. There are of course shortcomings with respect to interactions of fluids with mineral phases and with mimicking realistic rock structures. In the present work, we focus on fluid-fluid interactions and use therefore MF according to its strength.

We take advantage of the high spatial and temporal resolution achievable in MF to observe fluid displacement processes like the breaking of oil clusters, changes of wetting states and the formation of emulsion phases. We analyze fluid-phase distributions by means of a statistical and topological description of oil clusters, and link the observations to the injection water chemical composition.

The study shows (a) that cluster analysis can be used for EOR screening, which is a first step towards a statistical fingerprinting for optimizing EOR processes, (b) that classical phase-behavior experiments do not reflect the phase behavior under flow conditions, and (c) that emulsion formation might be of disadvantage and may lead to oil phase pinning.

# 2 Materials and methods

## 2.1. Porous medium

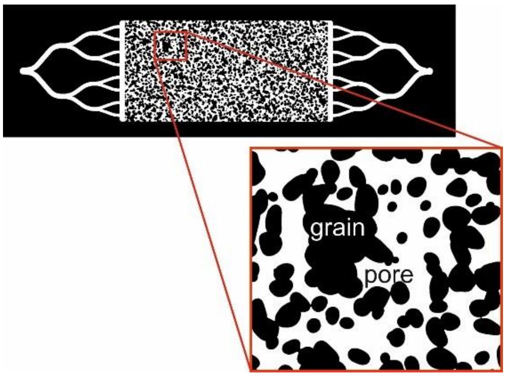

**Fig. 1:** 2D pore structure etched in glass microfluidic chips. The porous domain is contacted on the left and right by channel systems for fluid injection and production resulting in a linear flow geometry.

Experiments were performed with microfluidic chips made from borosilicate glass, representing a 2D porous media. The pattern is characterized by a homogeneous etching depth of 20 µm and a lateral definition of pores and pore throats. Porosity and permeability have been determined to $\phi = 0.57$ and $K = 2.5$ D and total pore volume to 2.3 $\mu l$. The total porous domain is 1 cm × 2 cm with channel systems at the inlet and outlet for a proper fluid distribution and fluid collection as displayed in Fig. 1. The lateral porous structure is rather open and homogeneous with all features larger than the etching depth, and with the simulated capillary pressure curve showing an extended plateau.

## 2.2 Instrumentation

The flooding experiments were performed at ambient conditions with a constant flow rate boundary condition at the inlet, and a constant pressure boundary condition at the outlet. Fluids were injected with a high precision Chemyx Fusion 200 syringe pump. For each fluid type, a separate syringe was used. On the downstream side, a constant pressure boundary condition was realized by producing fluids into a vessel at atmospheric pressure. For preparation purpose, a vacuum pump was installed on the downstream side to evacuate the micromodel and the flow lines, and for pre-saturation.

For imaging the fluid phases in the pore space, a Leica DMi 8 high-end microscope with a wide-range automated xy table and an image stitching option was used, providing a high spatial resolution and a time resolution that allows for detailed investigation of displacement processes and fluid phase configurations. The images were recorded with a Leica DMC2900 camera.

## 2.3 Fluids

Experiments with three different oil samples from the Vienna Basin were performed in order to investigate the variability of displacement patterns in water flooding. The samples were characterized by the viscosity (µ), interfacial tension to water (IFT) and the total acid number (TAN) as listed in Table 1. The bulk of experiments and all alkaline floods have been performed with crude 8. As injection water, deionized (DI) water was used. Alkaline solutions were prepared on basis of DI water with $Na_2CO_3$ as alkali agent in concentrations in between 200 ppm and 12000 ppm. In this range, the pH varies monotonically in between 10.6 and 11.6 as shown in Table 1. IFT of Crude 8 to the various alkaline solutions are not reported here; emulsion phases separate in the capillary of the spinning-drop tensiometer, leading to an instable three-phase system making a reliable IFT measurement impossible. However, the phase behavior indicates that IFT monotonically decreases with increasing alkali concentration leading to an increasing miscibility.

Table 1: Crude oil properties; IFT was measured to DI water by spinning-drop tensiometry. The API gravity indicates medium heavy oil. Crude 8 and 16 show relatively high TAN, which indicates that the respective fields are potential targets for alkaline flooding. Bottom row: measured pH of water as function of the $Na_2CO_3$ concentrations.

| Crude | Viscosity [cP] at 20 °C | IFT [mN/m] at 20 °C | TAN [mg KOH /g oil] | API Gravity [°] |
|---|---|---|---|---|
| 8 | 331 | 0.7±0.1 | 1.96 | 19.88 |
| 16 | 80 | 12.7±1 | 1.56 | 23.79 |
| F | not measured | 5.5±0.7 | 0.34 | 30.14 |
| Inj. water pH | 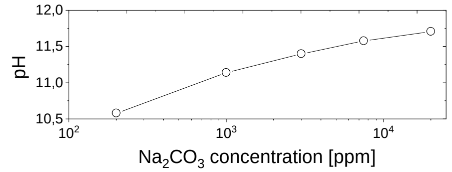 | | | |

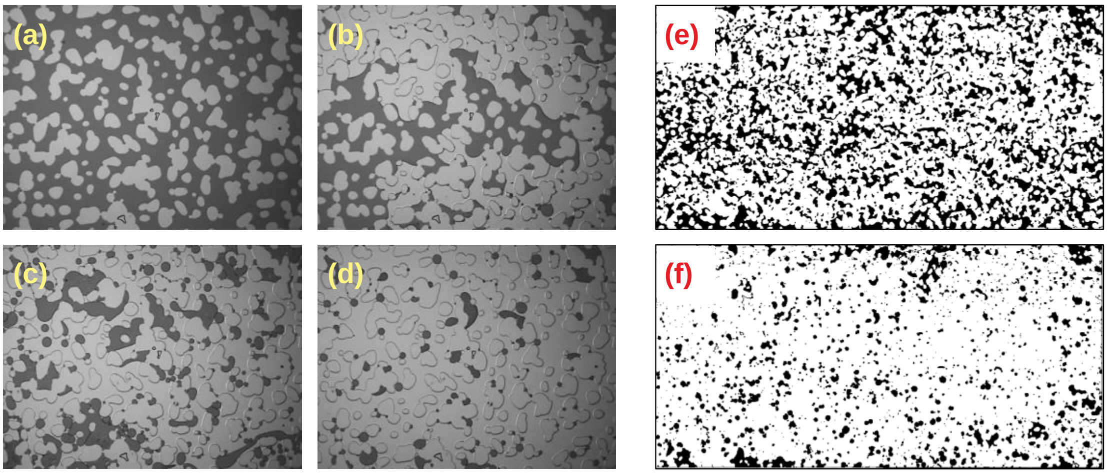

**Fig. 2:** Left images: Water flood and subsequent alkaline flood with a $Na_2CO_3$ concentration of 950 ppm. (a) to (d): images of a subvolume during an experimental sequence. (a) oil saturated micromodel, (b) the same section during water flooding, (c) during alkaline flooding and (d) after alkaline flooding. Right images: Segmented images showing the oil phase in black. The images cover the total flooding domain. Image (e) was taken after water flooding and (f) after alkaline flooding.

### 2.4 Sample preparation

The microfluidic chips were cleaned before each experiment by injecting 250 pore volumes (PV) of distilled water at high flow rate and subsequently a sequence of solvents at low flow rate to allow for efficient displacement and mixing with the fluids in place: 50 PV of acetone followed by 50 PV of toluene followed by another 50 PV of acetone to clean out the toluene. In a final step, vacuum was applied to vaporize the acetone. After cleaning, no fluids or colouring were visible in the micromodels, nor in the injection and production lines. After cleaning, oil was injected under vacuum conditions until the sample was oil saturated – no connate water was present at the beginning of the experiments.

### 2.5 Flooding experiments

The starting point of each experiment was a fully oil saturated sample with $S_o = 1$. To mimic a tertiary recovery process, firstly water was injected immiscibly displacing oil from the porous domain. The flooding time was always in between 22 h to 24 h, longer than the time to reach steady stead with no detectable change of the oil saturation in the porous medium at the end of each flood. Subsequently, the samples were flooded with alkaline solutions in order to study tertiary displacement effects. The alkaline-flooding time did not exceed 24 h either. For both, water and alkaline flooding, an injection rate of 0.01 ml/h have been chosen, leading to an interstitial velocity of about $2.4 \cdot 10^{-5}$ m/s (~ 6.9 ft/day). The total injected volume corresponds to approximately 100 PV. This relatively high flow rate corresponds to velocities in the vicinity of injection wells, where initial oil mobilization may take place prior to oil-bank formation.

Optical images of the flood domain were taken under flow conditions; in some cases, with a relatively small field of view and a high time resolution of about 100 ms to 1 s, in most cases with a field of view that covered the entire flood area with high spatial resolution, resulting in a lower time resolution of the order of 30 s to 1 min. The statistical and topological analysis was carried out mainly on the final image in the stationary state.

## 3 Fluid displacements – visual observations

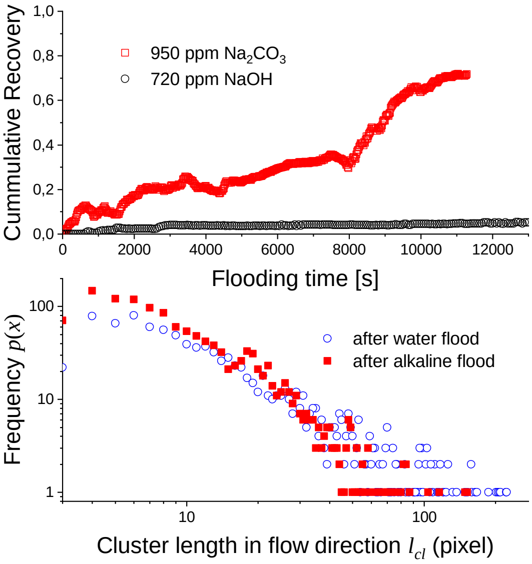

**Fig. 3:** Top panel: tertiary recovery curves of alkaline flooding with 950 ppm $Na_2CO_3$ and 720 ppm NaOH. The data were calculated from the subvolume in the left panel in Fig. 2. Bottom: cluster length distributions of experimental sequences: water followed by alkaline flooding.

The left panel of Fig. 2 shows typical microscopic images of a subvolume during an experimental sequence. The initial state of all experiments is $S_o = 1$ as shown in (a). The “grains” appear in light grey and the oil saturated pore volume in dark grey with a good optical contrast for image segmentation. To study tertiary recovery processes, the samples are at first water flooded to a state close to residual saturation as shown in Fig. 2 (b). During water flooding, water is invading by displacing the oil. Remaining larger clusters are pinned to the “grains” as a result of the initial “oil-wet” state. In time, larger clusters break down by snap-off effects producing smaller

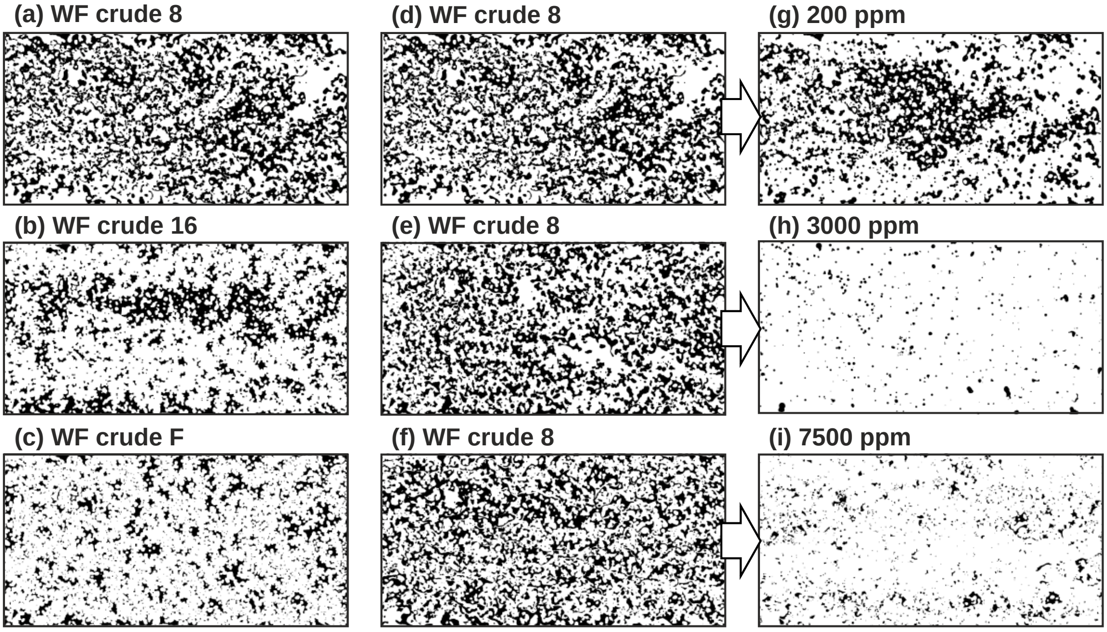

**Fig. 4:** Left: Secondary water floods of three different crude oils. Middle: Secondary water floods of crude 8; three repeat experiments at identical conditions. Right: Tertiary floods in sequence to the water floods in the respective left image (middle column). The alkali agent was $Na_2CO_3$ with concentrations of 200, 3000 and 7500 ppm.

droplets/ganglia that are mobile and are produced by the injected water. After a certain time, a steady state is reached, with a stationary remaining oil phase.

During the subsequent injection of an alkalic solution with 950 ppm $Na_2CO_3$ [16], interfacial tension between oil and water is lowered and the remaining clusters break further down with the fragments being produced. As a result, after alkaline flooding, the oil saturation is substantially lower, and the oil-cluster sizes are further reduced. The respective tertiary production curve is shown in the upper panel of Fig. 3; the data is calculated from the time dependent saturation states of the subvolume shown in Fig. 2 (b) to (d).

The lower panel of Fig. 3 shows the cluster length distribution $p(l_{cl})$ determined from the whole flooding domain (Fig. 2 (e) and (f)) after water and alkaline flooding, respectively; the breakdown of the clusters is reflected in the change of $p(l_{cl})$ to a larger number of smaller, and a smaller number of larger clusters, resulting in a narrower distribution after EOR.

### 3.1 Final displacement patterns and repeatability

Repeating individual experiment did not result in exactly the same displacement pattern and recovery factor. What means "being repeatable"? The middle column of Fig. 4 compares the oil saturations after water flooding performed with the same fluids under the same conditions. The patterns show some similarity, but are different. To spot the similarity, we compare them to displacement patterns obtained for different crude oils under otherwise the same conditions (crude properties are listed in Table 1). Comparing the displacement patterns, some statements can be made, e.g. that crude 16 with highest interfacial tension to water shows the most heterogeneous displacement pattern, with large clusters dominating the oil saturation. In general, we observe substantially different displacement patterns for the different crude oils. Repeat experiments with crude 8 (middle column) show in comparison relatively homogeneous and similar patterns. All the following experiments were performed with crude 8.

The final displacement pattern after tertiary flooding with 200, 3000, 7500 ppm $Na_2CO_3$ solutions are shown in the right column of the same figure. The final oil saturations, i.e. the displacement efficiencies, varies substantially as indicated by the respective black covered areas. While at 200 ppm some additional oil is recovered, the displacement efficiency appears to be best at 3000 ppm. For the two higher concentrations, the trend to smaller cluster sizes is observed.

### 3.2 Effects of emulsification

An important and noteworthy observation is that under flow conditions only very little emulsion formation was observed. This is in contrast to phase-behavior experiments which show strong emulsification. Under flow conditions, emulsion phases formed at relatively low and high concentrations, i.e. outside the optimum. This can be explained by the intensity of the contact between the oil and the alkali agent taking into account the alkali concentration and the contact time between the phases.

The effect of emulsification may be illustrated for low, but comparable concentration of NaOH (720 ppm in DI water), which is a stronger alkali agent, in comparison to the case discussed above (950 ppm $Na_2CO_3$) [16]. Under otherwise the same conditions, minor oil production was observed, associated with stagnant oil clusters and slow but extensive formation of an emulsion phase. Microemulsions are known to allow extremely low interfacial tension between oil and water, but have a high viscosity, which may be detrimental to displacement efficiency. In the present case, microemulsions form at the oil-water interfaces and appear to be immobile and pin clusters in the pore space. Even if the clusters break by snap off, the fragments remain largely immobile, resulting in a low tertiary recovery factor (Fig. 3).

## 4 Recovery factors

### 4.1 Displacement process

After water flooding, the remaining oil phase is dominated by rather large oil clusters as can be seen in Fig. 2 (b) and (e). The system appears as partially wetted by water and partially by oil and may be described as mixed wet. In this specific experiment, an oil recovery of 0.52 has been reached. During subsequent alkaline flooding, these clusters broke down in droplets, which appeared to be mobile and are displaced by the injection water and 0.72 of the afore remaining oil was recovered. In comparison to the water flood, the remaining oil phase after alkaline flooding can rather be described by small dispersed droplets that are trapped in the pore structure.

### 4.2 Recovery calculations

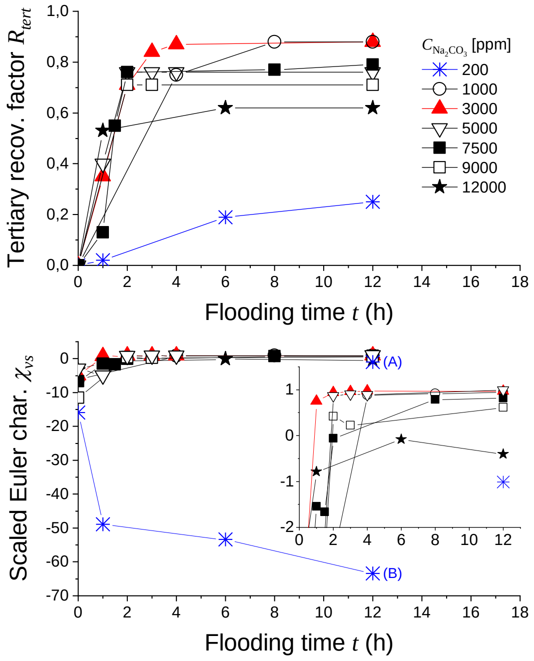

**Fig. 5:** Top: recovery factors, $\boldsymbol{R_{tert}}$, as function of flooding time for different $Na_2CO_3$ concentrations. Bottom: the respective normalized Euler characteristic. (A) and (B) correspond to different interpretations of the 200-ppm experiment as described in the text. The inset shows a zoon-in of the main panel.

The recovery factors of the secondary water floods, $R_{sec}$, were calculated from the remaining oil in the pore space, represented by the dark area, $A_{oil}$, after image segmentation: $R_{sec} = 1 - \frac{A_{oil}}{A_{pore}}$, where $A_{pore}$ corresponds to the porosity, which is measured from the initial state, $S_o = 1$, in the same way as later $A_{oil}$. For tertiary floods, we calculate the additionally recovered oil $R_{tert}$, which is defined as: $R_{tert} = 1 - \frac{A_{oil}}{A_{oil,sec}}$, and which refers to the volume of oil in place after the preceding water flood.

The recovery curves show differences in the displacement efficiency for different $Na_2CO_3$ concentrations; in the upper panel of Fig. 5, $R_{tert}$ is plotted as function of time. Different ultimate recoveries as well as different time dependencies were observed; while, e.g., at 1000 ppm and 3000 ppm similar ultimate recovery factors were reached, the 3000-ppm recovery curve appears steeper and ultimate recovery was reached much earlier. Above and below this range, ultimate recovery decreases.

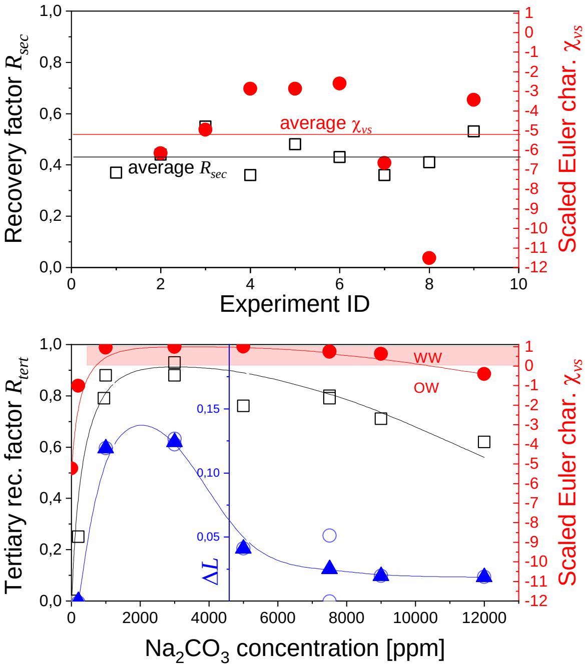

**Fig. 6:** Top: recovery factors (volumetric property) and the normalized Euler characteristic (topological property) after water-flooding experiments performed under identical conditions. Bottom: the same quantities for alkaline experiments as a function of the $Na_2CO_3$ concentration. The blue Symbols represent the difference in the Lorenz factor $\boldsymbol{\Delta L}$ as calculated from the cluster-volume distribution (statistical property).

Fig. 6 shows the ultimate recovery factors after water flooding (top panel) and after alkaline flooding (bottom panel). The recovery factor by water flooding varies with an average of 0.43 (±0.1) with a standard deviation of 0.1. The scatter may be a result of the relatively small flooding domain; the porosity-based REV of the used micromodel corresponds to an area of $5 \times 5\ \mathrm{mm}^2$, which is smaller than the total flooding domain of $20 \times 10\ \mathrm{mm}^2$. However, it is known that in two-phase flow, the REV can be larger, not only depending on the pore structure, but also on the distribution of the fluids therein [11]; if a system is dominated by large oil clusters, the cluster-size distribution may be truncated by the system size, or the largest clusters are not statistically represented in the flooding domain. In these cases, the observed recovery factor may still be scale dependent.

The bottom panel of Fig. 6 shows the final tertiary recovery factor as a function of $Na_2CO_3$ concentration. According to the definition, at zero concentration, no additional oil is recovered. With increasing $Na_2CO_3$ concentration, the recovery factor increases steeply with a maximum in the range between 1000 to 3000 ppm. At higher concentrations, the recovery factor decreases again. This behaviour will be further characterized in terms of wettability and is affected by emulsion formation. After alkaline flooding, the oil cluster sizes are generally smaller, and the REV is therefore smaller than for the respective water flood.

## 5 Euler Characteristic

From Fig. 2 it becomes obvious that the wetting state of the sample changes during the experimental sequence. Initially, the system is in an oil wet state. This is due to the fact, that we start the experiments with $S_o = 1$ and oil is initially wetting the glass surface. During water flooding, oil is partially displaced by water. In the swept areas, wettability changes to a more water-wet state, however, large clusters are still connected over several pores, partially covering the "grains" – we may call this a mixed-wet system. During alkaline flooding, larger clusters are pinned by their contacts to the grains, but successively break up by viscous forces into smaller non-wetting droplets; the system turns successively water wet where internal surfaces got in contact with the injection water.

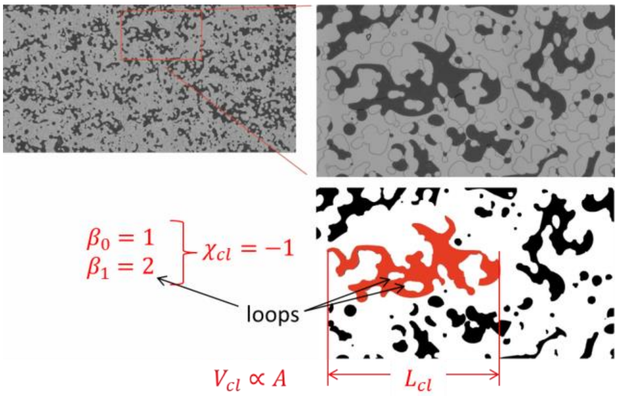

**Fig. 7:** Determination of cluster properties. Left: oil distribution after a water flood. Right: zoom-in and corresponding segmented image. The red labeled oil cluster has a Euler characteristic of $\boldsymbol{\chi_{cl} = -1}$, corresponding to one object and two loops.

It has recently been shown that the wetting state is closely linked to the Euler characteristic ($\chi$), which describes the connectivity of a fluid phase [14]. In the following, we make use of this link to characterize the change of the wetting state during displacements. The Euler characteristic, $\chi$, can be calculated from the Betti numbers, $\beta_i$: $\chi = \beta_0 - \beta_1 + \beta_2$. $\beta_0$ refers to the number of objects, i.e., the number of clusters in the system, $\beta_1$ is the number of loops or holes in the structure and $\beta_2$ refers to the number of inclusions. In 2D systems, inclusions do not exist and $\beta_2 = 0$.

According to the definition, $\chi$ scales with the number of objects, and tiny droplets may contribute with the same weight as large clusters, which are more significant for oil production. Therefore $\chi$ is not a good measure in the present case, because recovery does not refer to the number of objects, but to oil volumes, and larger clusters contribute more than small droplets. We therefore propose an alternative Euler characteristic, $\chi_{vs}$, scaled by cluster volumes:

$$\chi_{vs} = \frac{\sum_{n_{cl}} \chi_{cl} V_{cl}}{\sum_{n_{cl}} V_{cl}},$$

with $n_{cl}$ being the number of clusters, $\chi_{cl}$ the Euler characteristic of an individual cluster and $V_{cl}$ the volume of this cluster. As a result, the most water-wet state corresponds to individual droplets with $\chi_{cl} = 1$ and has $\chi_{vs} = 1$. The most oil wet state then corresponds to $\chi_{vs} = 1 - N_{grains}$ with $N_{grains}$ being the number of "rock grains", which is then equal to the number of loops. The determination of $\chi_{cl}$ is illustrated in Fig. 7.

The evaluated $\chi_{vs}$ after the different water and alkaline floods have been plotted together with the recovery factors in Fig. 6. Referring to oil wet as $\chi_{vs} < 0$ and to water wet as $\chi_{vs} > 0$, we can state that after water flooding, generally an oil-wet behavior has been observed, changing towards a more water-wet state during alkaline flooding. This development $\chi_{vs}(t)$ is shown in the lower panel of Fig. 5. The exception for low alkali concentrations is a matter of phase behavior and will be discussed further below. For the range of favorable alkali concentrations (high recovery factor), the $\chi_{vs}$ indicates a strongly water-wet state.

It is noticeable that $\chi_{vs}$ show larger scatter for water flooding than for alkaline flooding. This is explained with the same argument we used to explain the scatter in the recovery data; if the system is dominated by large clusters with high volumes and many loops, then a single cluster, which may statistically not be represented in the observed domain, may dominate the recovery factor and the $\chi_{vs}$. It appears to be even more sensitive to the REV than all the other quantities deduced in the frame of this work. This is the case after water flooding, but not after alkaline flooding, where we generally observe small clusters and a smooth dependency as a function of alkali concentration.

## 6 Lorenz analysis

The data presented so far, indicate a plateau of the recovery factor and the Euler characteristic as a function of the alkali concentration. The optimum can be found in a range between 1000 and 3000 ppm $Na_2CO_3$ with a mild decline to higher concentrations. Both quantities are associated with uncertainties, which are a result of the investigated domain size versus the largest clusters, which are statistically not well represented in the domain.

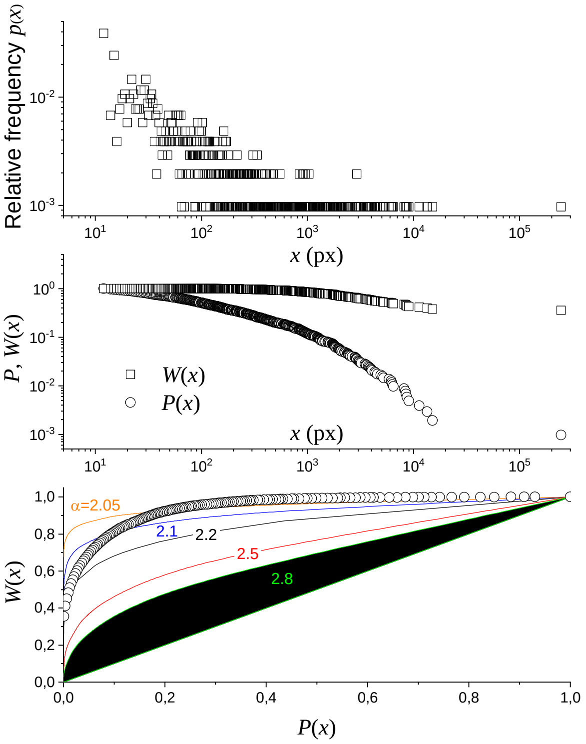

**Fig. 8:** Data taken from a water flood. Top: cluster volume distribution (CVD) ($\boldsymbol{p}$) (relative frequency as function of cluster size). Middle: cumulative CVD ($\boldsymbol{P}$) and volume weighted cumulative CVD ($\boldsymbol{W}$). Bottom: Lorenz plot $\boldsymbol{W}(\boldsymbol{P})$. For comparison, Lorenz plots for fractal distributions with different exponents $\boldsymbol{\alpha}$ are given in the same panel. The area under the curves, as indicated for $\boldsymbol{\alpha} = \mathbf{2.8}$, is a measure of "heterogeneity". In the present case, $\boldsymbol{P}(\boldsymbol{x})$ corresponds to the largest fraction of clusters, and $\boldsymbol{W}(\boldsymbol{x})$ to the total oil volume associated with this fraction of clusters. For fractal distributions: $\boldsymbol{W} = \boldsymbol{P}^{(\boldsymbol{\alpha}-\mathbf{2})/(\boldsymbol{\alpha}-\mathbf{1})}$.

In contrast to the recovery factor and the Euler characteristic, the displacement characteristic may be more robustly reflected in the cluster size distribution, which is less sensitive to individual clusters at the tail end of the distribution. Fig. 8 illustrates various cluster-volume distribution plots as applied in the following to all data sets; the top row of Fig. 9 shows the cumulative cluster size distributions $P(x)$ at the end of the respective floods. The data were calculated from the cluster size distribution, $p(x)$, by integration [17, 18]:

$$P(x) = \int_x^\infty p(y)dy.$$

As a first observation, the results on water flooding (blue symbols) show a very consistent behavior despite the scatter in the recovery data and the Euler characteristic. Comparing the individual data sets to the subsequent alkaline floods, we find that $P(x)$ has a much narrower distribution to smaller clusters after alkaline flooding, consistent with the visual observations. Assuming for a moment a fractal distribution, $p(x) = cx^{-\alpha}$, an exponent $\alpha$ can be determined by a maximum likely hood approach [11, 17, 18]. In a double logarithmic plot, $\alpha$ appears as slope of a straight line fit, which is shown as lines in the upper row of Fig. 9; we find that $\alpha$ becomes generally larger after alkaline flooding, consistent with a narrower CVD, and deviates strongest in cases where we find high recovery and positive $\chi_{vs}$ and are rather similar for the cases we consider outside optimum. However, this signature is not very robust, because the range, over which the data show fractal behavior is about one order of magnitude and hence rather limited.

It is evident that the size of an individual cluster directly refers to (a) phase mobility (cluster length) and (b) to recovery (cluster volume). Therefore, an imbalance of the cluster size distribution to larger clusters may be beneficial for the mobilization of oil, i.e. there is a higher EOR potential. Such an imbalance may be described by Lorenz diagrams. This concept refers back to Max Otto Lorenz (1880–1962), who was a US Economist and described with his concept the distribution of wealth in society [19]; next to $P(x)$, we calculate the volume-weighted cluster size distribution by integration:

$$W(x) = \frac{\int_x^\infty yp(y)dy}{\int_{x_{min}}^\infty yp(y)dy},$$

with $x_{min}$ being the lower bound of the distribution. Plotting $W\big(P(x)\big)$ results in the Lorenz plot. We translate the economic interpretation – $P$ being the richest fraction of the population and $W$ the associated fraction of the total wealth – to the problem of oil production – $P$ being the largest fraction of clusters and $W$ being the total volume of oil associated with this fraction of clusters. The closer the Lorenz curve tends to be a straight line (the diagonal), the more equal the oil is distributed over the different classes of clusters. The more the curve deviates from the diagonal to the upper left corner, the more the large clusters are dominating the oil volume – an imbalance of wealth.

We may associate larger clusters with higher EOR potential, since large clusters are easier to be mobilized, or, in the present case, may be subject to clusters breakup by viscous forces. The lower row of Fig. 9 compares the Lorenz plots after water flooding and alkaline flooding. We observe in all cases (but 200 ppm, where no change has been observed) a deviation of the Lorenz curve to a more uniform distribution due to alkaline flooding. Together with the decrease of absolute cluster sizes, this indicates a decrease in further EOR potential. The signature is most pronounced in the range where highest recovery and highest Euler characteristic is observed. The effect of alkaline flooding in the Lorenz plots appears to be a robust indication of a working EOR process, which can be quantified by the difference of the Lorenz factor of

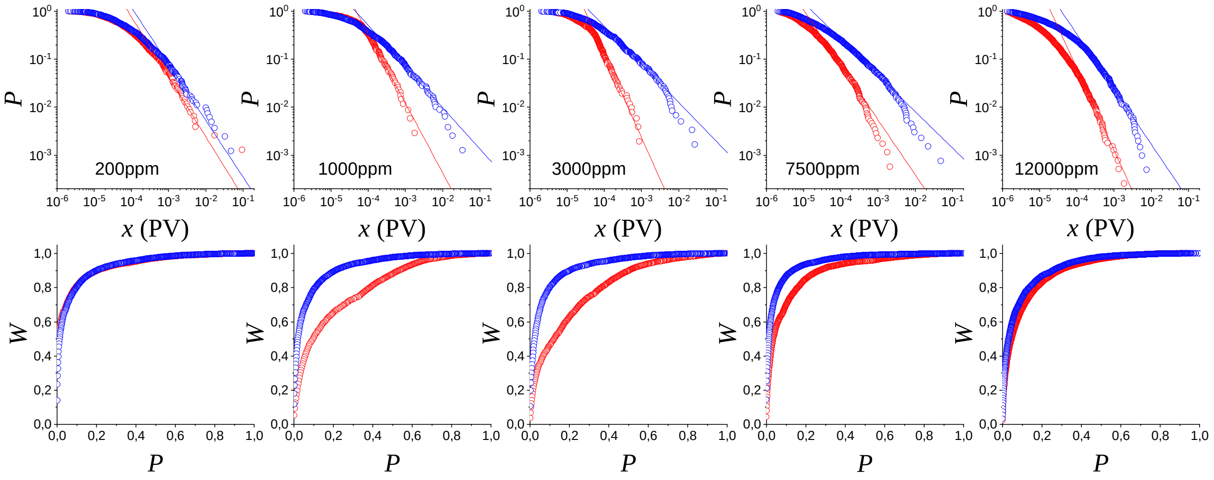

**Fig. 9:** Top row: cumulative cluster size distributions for three experimental sequences of water floods (blue) and alkaline floods (red) with 200, 1000, 3000, 7500 and 12000 ppm $Na_2CO_3$. The lines correspond to power law fits by a maximum likelihood approach. Bottom row: Lorenz plots for the same data sets.

water flooding and alkaline flooding $\Delta L$, with $L = 2\left(\int_0^1 W dP - \frac{1}{2}\right)$, which varies in between $\Delta L = 0$ at 200ppm and $\Delta L = 0.12$ at optimum performance. Its dependency on the $Na_2CO_3$ concentration is compared to the recovery factor and the Euler characteristic in Fig. 6; it shows a stronger decline to higher concentrations than the other quantities and therefore defines the optimum better.

## 7 Texture of oleic and emulsion phases

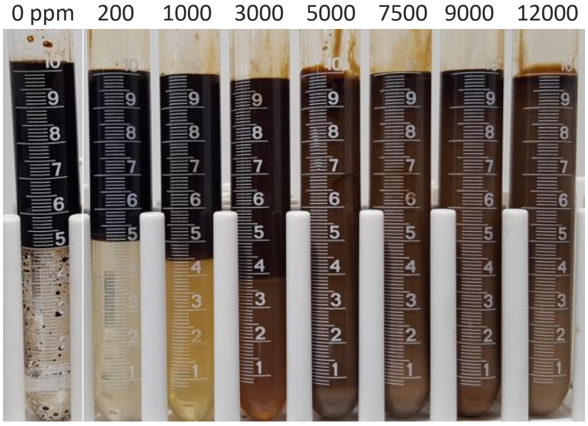

**Fig. 10:** Phase behavior after mixing crude 8 with water of different $Na_2CO_3$ concentrations in ppm as indicated in the picture.

Bringing the high-TAN oil (crude 8) in contact with an alkalic solution, the interfacial tension is lowered to a degree that emulsions are forming. This is shown in Fig. 10 for a series of experiments with different $Na_2CO_3$ concentrations in test tubes; the same volumes of crude oil and alkali solution were brought in contact to each other, the fluids were mixed by shaking the tubes and subsequently put for 48 h at rest. At rest and with time, the fluids separate by gravity to their equilibrium state and stable fluid phases may be observed. In the present case, oil-in-water and water-in-oil emulsions have been observed simultaneously as visible by a coloring of the aqueous phase and a decrease of the oil-water contact line, which indicates a swelling of the oil phase. No separate micro emulsion phases were observed in between the oleic and the aqueous phase as for optimized surfactant solutions, which may be a result of the variety of surfactants generated from the crude oil by saponification. The contrast between the oleic and the aqueous phase became gradually less with increasing alkali concentration; we may say, the degree of emulsification is monotonically increasing as function of $C_{Na2CO3}$.

In contrast, only water-in-oil emulsions were observed in the respective microfluidic experiments and this just to a limited extend. Examples of resulting textures are given in Fig. 11. Up to this point, emulsification has not been taken into account in the cluster analysis; the approach to identify the oil phase distribution, as discussed so far, is based on two-phase grey-scale image segmentation; we discriminated the light grey aqueous phase from a dark oil phase by essentially setting a threshold in between the respective grey values. With this approach, we ignore effects of emulsification. Different types of textures have been identified as a result of emulsification. We distinguish in the following between emulsions and conglomerates.

### 7.1 Effect of emulsification

In the presented series of experiments, emulsification was predominantly observed for rather low and high alkali concentrations and just to a minor extend in between. A possible explanation will be given below. Emulsion phases appear darker as the oil phase and become darker and expand in time. As can be seen in the lower left image of Fig. 11, the grey scale between emulsions and the oil phase changes gradually and a phase segmentation between them may not be useful. With the present segmentation approach, we partly ignore emulsion phases. This is because water participates in emulsions to a certain volume, which we account for as oleic phase – the oil phase is swelling. As a consequence, our material

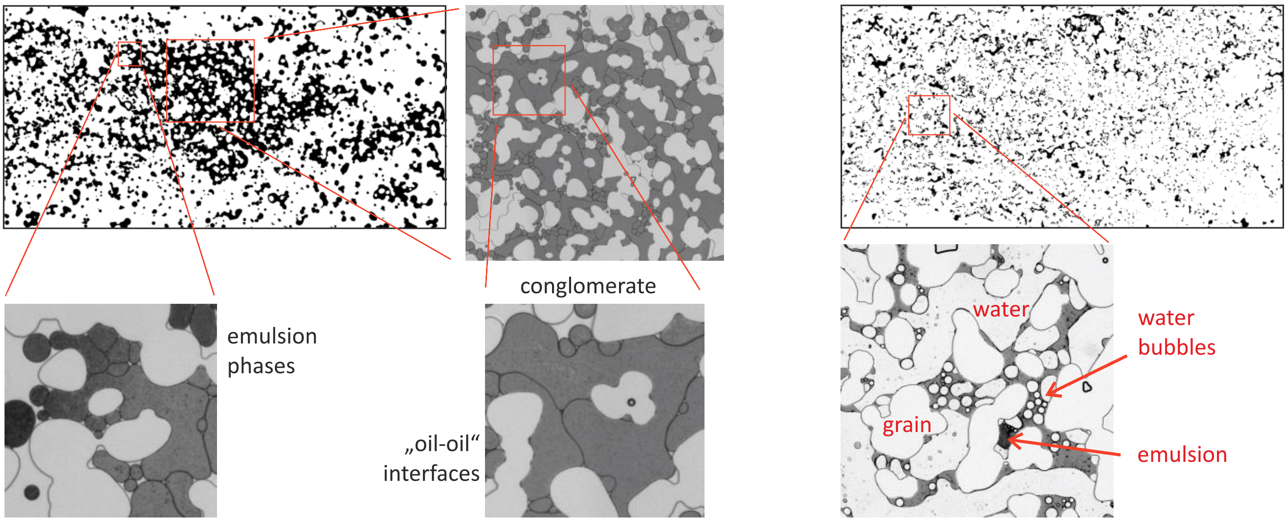

**Fig. 11:** Left side: segmented oil pattern after alkaline flooding with 200 ppm $Na_2CO_3$. The zoom in shows the formation of conglomerates and a detailed view on the observed "oil-oil" interfaces. The lower left image shows the boundary of the conglomerate with emulsion formation; darker grey values indicate water-in-oil emulsion phases. Right side: emulsion phases at 12000 ppm $Na_2CO_3$ concentration; the texture, respectively the various bubble sizes, makes it difficult to discriminate between emulsions and bubbles/clusters.

balance may not be perfect and the oil saturation may be slightly overestimated in the respective cases. We consider the associated error on the recovery curves as small. On the other hand, emulsions have been found to pin oil clusters, i.e., to demobilize the oleic phase; because emulsification influences cluster mobility, it is implicitly reflected (and accounted for) in the cluster topology and cluster statistics as given above.

### 7.2 Conglomerates

During displacements, mobile oil clusters may come into contact with each other. Depending on interfacial properties they may merge forming larger clusters. This has been observed in several pore scale displacement studies using model oils [4, 5, 20]. Such coalescence events have been observed for higher alkali concentrations (i.e. lower interfacial tension) in the current study. Sometimes, especially at low alkali concentrations, bubbles adhere together without merging. This is illustrated in Fig. 11; such conglomerates are stable configurations of oil droplets separated by dark appearing interfaces, which might be interpreted as emulsion. Even appearing to the eye as individual droplets, conglomerates may behave as large clusters with a highly negative $\chi_{vs}$, even in cases that we would not call "oil wet". At that point it is too simple to talk about a single connected cluster or individual droplets. It also may be too simple to link the Euler characteristic to the wetting state, but still reflect phase connectivity. In Fig. 5, the Euler characteristic for two alternative interpretations of the 200-ppm experiment is given; (A) accounts for individual droplets, even if they form conglomerates, (B) treats conglomerates as objects. Conglomerates may be exceptional and leaving room for interpretation with respect to cluster size distribution and $\chi_{vs}$, depending on whether they are accounted for as individual small clusters, or rather as super cluster (as we do).

### 7.3 Emulsification at low and high ppm – a hypothesis

It is quite remarkable that emulsification was observed for high and low alkali concentration, but not for concentrations in between that we consider as optimum condition – emulsification and the recovery factor behave non-monotonic. This in contradiction to the phase behavior experiments shown in Fig. 10 in which the degree of emulsification is monotonically increasing as function of $C_{Na2CO3}$. Emulsion phases are known to influence displacements due to various aspects; Emulsions may facilitate ultra-low interfacial tension between oil and brine, improving the displacement efficiency. On the other hand, emulsions have typically a substantially higher viscosity than their constituents, which may oppose displacement.

A first attempt to understand the degree of emulsification in the present case requires to consider not only the bulk phase behavior, but also the flow regimes: At *low alkali concentrations*, the displacement efficiency is not much improved compared to the preceding water flood and just a minor fraction of the remaining oil is mobilized; most of the oil clusters are stagnant. These clusters are contacted by multiple PVs of alkali solution and over time, emulsions are forming, pinning the clusters even more due to the increasing viscosity of the oleic phase by emulsification. At very *high alkali concentrations*, emulsification is fast – faster than the mobilization of the clusters. Emulsions are forming nearly instantaneously, pinning the oil phase by the low mobility of the emulsion phase at the boundaries of the oil clusters. At a certain degree of emulsification, the oleic phase becomes stagnant (trapped). For concentrations in between – *at optimum conditions* – the alkali concentration is high enough to mobilize the oil, but not too high to lead to fast emulsion formation. Once mobilized, oil droplets move with the injection water and the droplet does no come in contact with multiple PVs as in case of a stagnant oil phase – the relative velocity between the mobile oil clusters and the injection water may be close to zero.

## 8 Summary and conclusions

In the present study, we use microfluidics as a screening tool to optimize the composition of injection water for alkaline flooding. We use the high spatial and temporal resolution to study the respective displacement processes and changes in the displacement efficiency on the pore scale. Due to the limited size of the flooding domain, the recovery factor alone is not a sufficient criterion for evaluating displacements. This is especially true for the results of water flooding, where the remaining oil phase consists of relatively large-volume clusters that dominate the system. To make robust predictions, we analyze the remaining oil phase based on its steady-state cluster size distribution and Euler characteristic at the end of each flood.

What are the signatures of an ideal alkaline flood or – more general – an ideal EOR displacement? By changing the capillary number, larger clusters break up into smaller clusters. It has been observed that these smaller clusters are non-wetting and mobile. On this basis, we define the EOR potential: (1) the initial cluster size distribution (volume distribution) shows a strong imbalance toward large clusters. As a measure of this imbalance we use Lorenz diagrams and for quantification the Lorenz factor, and (2) in the present case, the large clusters are predominantly pinned to the solid phase, i.e. being in a wetting state. To analyse the wetting state, we introduced a volume weighted Euler characteristic. These statistical and topological phase properties may change from water flooding to the subsequent alkaline flooding; on this basis we optimize the injection water composition. We find the following criteria: The system lowers its EOR potential, which is reflected in the following factors:

- a high tertiary recovery factor is reached on a short time scale,
- the tendency for a positive volume-scaled Euler characteristic that reflects water-wet condition,
- the tendency to smaller clusters, which are reflected in a narrower cumulative cluster-volume distribution, and
- a more even distribution of oil cluster volumes, which tends to reflect a lower Lorenz factor.

Using these criteria and for the present case, a plateau with optimum alkali concentration around 3000 ppm $Na_2CO_3$ has been identified. Interestingly, no significant emulsification was observed in this range, which stays in contrast to the classical phase-behavior experiments performed with the same fluid pairs. Outside this optimal EOR range, emulsification was observed, interestingly for higher *and* lower alkali concentrations. A first attempt of explanation was made on the basis of the alkali concentration and the contact time based on droplet/cluster mobility.

The authors acknowledge the OMV AG, Vienna, Austria for funding this project. Furthermore, we would like to thank Ryan Armstrong for insightful discussions on fluid topology and Hassan Mahani, Steffen Berg and Hendrik Rohler for reviewing and commenting the manuscript.

## References

1. L. W. Lake, *Enhanced oil recovery*. Prentice Hall, 1989.
2. G. Hirasaki, C. A. Miller, and M. Puerto, "Recent Advances in Surfactant EOR", *SPE Journal*, vol. 16, no. 04, pp. 889-907, 2011.
3. A. A. Olajire, "Review of ASP EOR (alkaline surfactant polymer enhanced oil recovery) technology in the petroleum industry: Prospects and challenges", *Energy*, vol. 77, pp. 963-982, 2014.
4. S. Berg *et al.*, "Onset of Oil Mobilization and Nonwetting-Phase Cluster-Size Distribution", *Petrophysics*, vol. 56, no. 01, pp. 15-22, 2015.
5. M. Rücker *et al.*, "From connected pathway flow to ganglion dynamics", *Geophysical Research Letters,* vol. 42, no. 10, pp. 3888-3894, 2015.
6. V. A. Lifton, "Microfluidics: an enabling screening technology for enhanced oil recovery (EOR)", *Lab on a Chip,* vol. 16, no. 10, pp. 1777-1796, 2016.
7. E. Unsal, M. Broens, and R. T. Armstrong, "Pore Scale Dynamics of Microemulsion Formation", *Langmuir,* vol. 32, no. 28, pp. 7096-7108, 2016.
8. W.-B. Bartels, H. Mahani, S. Berg, R. Menezes, J. A. van der Hoeven, and A. Fadili, "Oil Configuration Under High-Salinity and Low-Salinity Conditions at Pore Scale: A Parametric Investigation by Use of a Single-Channel Micromodel", *SPE Journal*, vol. 22, no. 05, pp. 1362-1373, 2017.
9. M. Broens and E. Unsal, "Emulsification kinetics during quasi-miscible flow in dead-end pores", *Advances in Water Resources*, vol. 113, pp. 13-22, 2018.
10. S. Iglauer, S. Favretto, G. Spinelli, G. Schena, and M. J. Blunt, "X-ray tomography measurements of power-law cluster size distributions for the nonwetting phase in sandstones", *Physical Review E,* vol. 82, no. 5, p. 056315, 2010.
11. A. Georgiadis, S. Berg, A. Makurat, G. Maitland, and H. Ott, "Pore-scale micro-computed-tomography imaging: Nonwetting-phase cluster-size distribution during drainage and imbibition", *Physical Review E,* vol. 88, no. 3, p. 033002, 2013.
12. R. T. Armstrong, A. Georgiadis, H. Ott, D. Klemin, and S. Berg, "Critical capillary number: Desaturation studied with fast X-ray computed microtomography", *Geophysical Research Letters,* vol. 41, no. 1, pp. 55-60, 2014.
13. R. T. Armstrong, J. E. McClure, M. A. Berrill, M. Rücker, S. Schlüter, and S. Berg, "Beyond Darcy's law: The role of phase topology and ganglion dynamics for two-fluid flow", *Physical Review E,* vol. 94, no. 4, p. 043113, 2016.

14. R. T. Armstrong *et al.*, "Porous Media Characterization Using Minkowski Functionals: Theories, Applications and Future Directions", *Transport in Porous Media*, 2018.
15. J. E. McClure *et al.*, "Geometric state function for two-fluid flow in porous media", *Physical Review Fluids,* vol. 3, no. 8, p. 084306, 2018.
16. M. Borji and H. Ott, "suppl. material", 2019.
17. A. Clauset, C. R. Shalizi, and M. E. J. Newman, "Power-Law Distributions in Empirical Data", *SIAM REVIEW,* vol. 51, no. 4, pp. 661-703, 2009.
18. Y. Virkar and A. Clauset, "Power-law distributions in binned empirical data", *The Annals of Applied Statistics*, vol. 8, no. 1, pp. 89-119, 2014.
19. M. O. Lorenz, "Methods of Measuring the Concentration of Wealth", *Publications of the American Statistical Association,* vol. 9, no. 70, pp. 209-219, 1905.
20. S. Youssef *et al.*, "Oil ganglia dynamics in natural porous media during surfactant flooding captured by ultra-fast X-ray microtomography", International Symposium of the Society of Core Analysts, SCA2014-023, 2014.

# An experimental investigation of surface-modified silica nanoparticles in the injection water for enhanced oil recovery

*Alberto* Bila[1, *], *Jan* Åge Stensen[1, 2], and *Ole* Torsæter[1]

[1]PoreLab Research Center, Department of Geoscience and Petroleum-Norwegian University of Science and Technology (NTNU), S. P. Andersens veg 15a, 7031, Norway
[2]Sintef Industry, S. P. Andersens veg 15a, 7031, Norway

**Abstract.** Extraction of oil trapped after conventional water flooding still poses huge challenges in the oil industry. Therefore, innovative enhanced oil recovery (EOR) technologies are required to run the production more economically. Recent advances suggest renewed application of surface-modified nanoparticles (NPs) for oil recovery. The advantages of these NPs include improved properties (e.g. stability, stabilisation of emulsions, etc.), which make them appropriate to improve microscopic sweep efficiency of water flood. However, the EOR mechanisms of NPs are not well understood. This work evaluates the effect of four types of polymer-coated silica NPs as additives to the injection water for EOR. The NPs were examined as tertiary recovery agents using water-wet Berea sandstone rocks at 60 °C. Crude oil was obtained from North Sea field. The NPs were diluted to 0.1 wt. % in seawater before injection. The transport behaviour of the NPs and their interactions with the rock system were also investigated to reveal possible EOR mechanisms. The flooding experiments showed that the NPs could effectively increment oil recovery in water-flooded reservoirs. The incremental oil recovery was up to 14% of original oil in place (OOIP). Displacement studies revealed that oil production was affected by interfacial tension reduction and wettability effect; however, the migration behaviour of the NPs through the rock suggested that log-jamming effect and formation of NP-stabilized emulsions were relevant explanations for the mobilisation of residual oil.

## 1. Introduction

The oil production rates of the existing fields are declining, and the occurrence of new discoveries has been scarce [1, 2]. Therefore, improving the recovery rates from mature oil fields is a priority for oil companies. The oil recovery factor from oil fields is typically around 20-40% of OOIP [3], the remaining oil is in some cases amenable for further developments. However, before the design of any production strategy, it is important to understand the mechanisms that have led to the entrapment of the oil during the early stages of oil production. After secondary water flooding in water-wet reservoirs, oil remains in the larger pores, where it can snap-off and become trapped [4]. This oil or residual oil saturation dwells in the reservoir pore spaces as capillary-trapped and/or by-passed oil [2, 5]. Mobilisation of the capillary-trapped oil requires increasing the viscous forces or decreasing the capillary forces [5, 6]. Increasing the viscous forces may result in fracturing of a reservoir; hence, decreasing the capillary forces becomes an assertive option; this can be achieved through the reduction of interfacial tension between the reservoir fluids. Conversely, the by-passed oil or the oil located in unswept areas of the reservoir can be mobilised by pore plugging and diversion of the normal flow of the injected fluids [5-8].

For this purpose, experimental and numerical studies suggest that properly designed nanoparticles (NPs) can change the physical or chemical behaviour of an oil reservoir, thereby increasing microscopic sweep efficiency of water flood. This is because NPs have small diameter size (1-100 nm) and large surface area-to-volume ratio. These properties enhance the NPs mobility and surface activity, particularly at elevated temperature, thus making them suitable to modifying the fluid-rock properties [9, 10]. Furthermore, NPs can easily travel through and reach untouched zones of a reservoir with no severe impact to the rock permeability [1, 8, 10]. The NPs are injected into the reservoir in the form of suspended particles in designed carrier fluid (e.g. water, ethanol, etc.). The suspension system must remain stable under reservoir conditions throughout the duration of oil recovery process to perform effectively such a task.

Thus far, silica NPs are the most studied nano-materials. They naturally occur in sandstone formations and are costly effective [1, 11]. Additionally, silica NPs can be synthesized and surface functionalised to meet particular reservoir conditions [9, 10].

Promising oil recovery results have been reported in the literature due to silica NPs [11-18] under a variety of experimental conditions. The experiments varied from the

---

[*] Corresponding author: alberto.bila@ntnu.no

use of silica NPs with different size, composition, surface functionalities, etc., suspended in aqueous solutions with diverse ionic strength [11-17] or in non-aqueous solutions [16]. The concentration of the NPs in the continuous phase is also varied. Furthermore, the injection flowrate, temperature, evaluation criteria of oil recovery, etc., are often selected randomly, even if the NP suspension system is intended for particular oil field application. The variation of the experiments makes it difficult to adequately grasp the oil recovery mechanisms of silica nanoparticles. Nevertheless, studies aiming at explaining the oil recovery due to silica NPs injection have suggested multiple EOR mechanisms such as; i) interfacial tension (IFT) reduction and wettability alteration [12, 16, 17, 19], ii) structural disjoining pressure [26], iii) formation of in-situ emulsions [20-22], and iv) Pore blocking and microscopic flow diversion [6-8, 14, 23-25].

In nanofluid flooding EOR, NPs are expected to decrease the IFT between the flowing aqueous and oil phases. Thus, promoting deformation and breakup of oil into small drops that can easily be produced. This implies redistribution of flowing fluids within the reservoir and modification of the fluid’s relative permeability, which is a manifestation of wettability effect. When there is no tendency for NPs to adhere to the solid surface, the oil recovery occurs through so-called structural disjoining pressure effect proposed by Wasan and Nikolov [26]. Furthermore, the flow dynamics and the interactions occurring between NPs and rock system can boost emulsification of oil. On the other hand, small NPs can block larger pore spaces, prompting the pressure to increase and forcing the injected water to find new paths, resulting in increased oil recovery. Verification of the contribution of each of the proposed NP’s mechanisms for oil recovery has not been established yet. More studies are needed to realise optimum conditions for a significant increase in oil recovery to make nanotechnology robust for field applications.

The goal of this work was to evaluate the efficacy of surface modified silica NPs for EOR in water-wet reservoirs and identify possible oil recovery mechanisms. The NPs suspension was prepared at 0.1 wt. % in synthetic seawater. After which, the nanofluids were evaluated as tertiary EOR agents at 60 °C.

## 2. Experimental materials

### 2.1 Silica nanoparticles and synthetic seawater

Four types of hydrophilic silica NPs were used. The particles were spherical and hydrophilic with surface coated by polymer molecules to render them stable in synthetic North seawater. The main component of the NPs was silicon dioxide ($SiO_2$>98.3%), additional components such as aluminium oxide ($Al_2O_3$) and mixed oxides (MOX) were present. The NPs are special research and development (R&D) products from Evonik Industries and were supplied to us as AERODISP®, which is AEROSIL® particles in liquid solution. The properties of the NPs suspended in distilled water, as received, are given in **Table 1**.

**Table 1.** Properties of silica NPs dispersed in distilled water.

| NF | Basis | wt. % | Size (nm) |
|---|---|---|---|
| 02-3 | $SiO_2$ (sol gel cationic) | 38.6 | 107 |
| 02-4 | $SiO_2$ (sol gel anionic) | 26.0 | 32 |
| 02-6 | $SiO_2/Al_2O_3$/MOX | 21.6 | 218 |
| 02-8 | $SiO_2/Al_2O_3$/MOX | 25.6 | 145 |

The concentrated solutions of the NPs were diluted to 0.1 wt. % in synthetic North seawater (SSW), here referred to as nanofluid (NF). The number in front of “NF” is used to identify the nanofluid type hereafter. The composition of prepared SSW by wt. % was NaCl (74.4), KCl (1.85), $NaHCO_3$ (0.57), $Na_2SO_4$ (10.62), $CaCl_2·6H_2O$ (4.24), $MgCl_2·6H_2O$ (8.25) and $Sr_2·6H_2O$ (0.07). The total dissolved salts were approximately 38,318 ppm. The density, viscosity and pH of SSW was 1.008 g/cm$^3$, 0.53 cP and 7.97, respectively. The nanofluid density was 1.007-1.009 g/cm$^3$ and the viscosity ranged from 0.51-0.67 cP. All measurements were performed at 60 °C using Anton Paar Density meter and Anton Paar Rheometer, respectively

### 2.2 Oleic phase

A North Sea reservoir crude oil was used in this work. It was a light oil (30 °API, 6 cP at 60 °C) with 71.57 wt. % saturates, 20.81 wt. % aromatics, 7.44 wt. % resins and 0.18 wt. % of asphaltenes. The crude oil was filtered twice through a 5-µm Millipore filter to remove any suspended particles that can block the lines and the pores spaces and or change the oil composition. Normal decane with density of 0.73 g/cm$^3$ and viscosity of 0.92 cP at 20 °C was used for wettability experiments.

### 2.3 Core characterization and preparation

Ten core plugs initially at water-wet conditions were used in this work. The cores were drilled from the same block of Berea sandstone; their mineral composition was measured with X-ray diffraction and were composed of 93.7 vol % quartz, 5 vol % of Microcline (Alkali feldspar) and 1.3 vol % Diopside. The core plugs were prepared to have similar dimensions of 3.8 cm diameter and length of 10 cm. They were cleaned with methanol through Soxhlet extractor and then dried at 60 °C for 2-3 days. Afterwards, gas porosity and permeability were measured on dried core plugs. The next step was to evacuate the core plugs for 2 hours and saturate them with SSW at 100 mbar vacuum pressure for 2-3 hours. The saturated cores were left soaked in the same SSW for at least 10 days for ionic equilibration with the rock constituents. The weight of the wet and dried core plugs was used to calculate the porosity and pore volume (PV), and these data are given **Table 2**.

**Table 2.** Properties of Berea sandstone core plugs.

| Core | Porosity (%) | $K_{abs}$[1] (mD) | PV (ml) |
|---|---|---|---|
| L1 | 18.7 | 404 | 21.4 |
| L2 | 17.4 | 537 | 21.8 |
| L3 | 15.9 | 460 | 17.6 |
| L4 | 16.2 | 411 | 17.9 |
| L5 | 17.1 | 367 | 18.9 |
| L6 | 16.8 | 333 | 18.5 |
| L7 | 18.4 | 384 | 20.3 |
| L8 | 18.3 | 184 | 20.3 |

[1]Klinkenberg corrected permeability.

### 2.4 Core flooding equipment

**Fig**. **1** presents a schematic of core flooding rig with its main components labelled. It utilizes an injection pump, three cylinders containing oil, synthetic sea water and nanofluid each. All cylinders were assembled vertically inside a temperature-controlled oven.

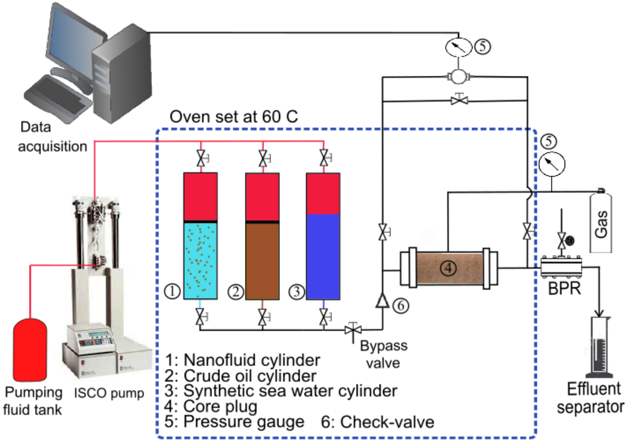

**Fig. 1.** Schematic of core flooding apparatus.

The core was loaded in the core-holder and oriented horizontally at a confining pressure held within 18-22 bar. A check valve and a backpressure regulator (BPR) were used to prevent back-flow of produced fluids and maintain the pore pressure constant during the core flooding experiments. The BPR was set to 5-bar pressure. The core flooding experiments were performed at 60 °C.

## 3. Experimental methodology

### 3.1 Core-flooding

Eight flooding tests were conducted with nanofluids as tertiary EOR-agents (two parallel tests for each nanofluid type). First, the 100% SSW saturated core plug was injected with fresh SSW for 1-2 PVs to ensure a complete removal of gas bubbles. Second, the drainage process was conducted by successively increasing the crude oil injection flowrate, from 0.5, 1.5 to 3 ml/min, for 15 PVs. This procedure ensured that there was no SSW production and the irreducible water saturation ($S_{wir}$) was achieved. The direction of the injection was reversed after half of the total PVs injected to even the distribution of the fluids within the core. This procedure also established the OOIP reported in **Table 3**. It is worth note that the drainage step was conducted at ambient conditions.

Before starting the experiments, the flooding system was heated while injecting crude oil at low rate of 0.02 ml/min until the temperature stabilised at 60 °C. Then, water (SSW) flood followed at constant flowrate of 0.2 ml/min until there was no oil production for 1-2 PVs. Thereafter, the flowrate was increased ten-fold (bump rate) for ≈1PV to overcome the capillary end-effects. In the following step, the injection was continued with nanofluid at 0.2 ml/min until there was no more oil production for 2-4 PVs. Then, the flowrate was bumped for ≈1PV. During the flooding experiments, the volume of oil produced was collected every ¼ PV and corrected for the flooding system dead volume. When the oil production was occurring at low pace, a camera with automated capturing was used to record the production in a graded line overtime, while the total production was being collected in a large effluent separator. The recorded pictures were then analysed to measure the amount of oil produced overtime. This oil was compared to the total volume of oil produced in the large effluent separator.

The differential pressure (dP) and oil recovery were recorded versus PVs injected, and the residual oil saturation ($S_{or}$) was calculated for each flooding stage.

### 3.2 Interfacial tension measurement

The interfacial tension (IFT) between crude oil and SSW or nanofluids was determined with pendant drop and spinning drop techniques at 60 °C.

For the pendant drop method, a Kruss drop shape analyser (DSA) 100 assembled with a J-shape syringe-needle of 1.0047 mm of inner diameter was used to dose the oil drops. With the oil drop hanging from the needle in the bulk phase, the measurements were taken every 20 seconds until static IFT value was reached. The IFT was calculate using Young-Laplace model. For the spinning drop method, a SVT20N (Data Physics) spinning video tensiometer was used. Crude oil was injected drop-wise into a capillary tube filled with SSW or nanofluid. The tube was rotated at speed varying from 6,000 to 10,000 rpm. The IFT was calculated based on the model by Than, et al. [27], at equilibrium. The refractive index measured for both SSW and nanofluids was 1.338.

### 3.3 Amott-wettability test

The wettability of the cores was evaluated before and after nanofluid flooding at ambient conditions using Amott-test. The core plugs were set at $S_{wir}$ before placing each core plug in the Amott cell filled with SSW. The SSW was allowed to imbibe spontaneously into the core displacing oil over time. The oil production was recorded stepwise until the equilibrium was reached and the total denoted as $V_{o1}$. The remaining mobile oil ($V_{o2}$) was forcibly displaced by core flooding method, i.e. by injecting SSW at high flowrates (1 ml/min to 3 ml/min).

Then, the core was removed from the core-holder and dipped in the Amott cell filled with oil to assess whether the oil could spontaneously displace water phase. At equilibrium, the amount of SSW produced was recorded as $V_{w1}$. The remaining mobile SSW in the core ($V_{w2}$) was displaced by injecting oil at high flowrates. Decane was used as the oleic phase.

The wettability index (WI) was calculated as the difference between the displacement-by-water ratio (water index, $I_w = V_{o1}/(V_{o1}+V_{o2})$) and displacement-by-oil ratio (oil index, $I_o = V_{w1}/(V_{w1}+V_{w2})$). Categorisation of wettability based on WIs is given in ref. [28]

## 4. Experimental results

### 4.1 Oil recovery

Eight core flood tests were conducted at 60 °C. Two core plugs were used for each nanofluid type to reproduce the results and reduce experimental errors. To overcome the capillary end-effects and ensure that any additional oil recovery was a result of nanofluid effect, the flow rate was increased from 0.2 to 2 ml/min at the end of the floods (procedure described in section **3.1**). The oil recoveries achieved by conventional water flooding varied from 47.2 to 56.1% of OOIP. The incremental oil recovery due to nanofluid flooding ranged from 7.0 to 14% of OOIP. The production of first oil due to nanofluid injection was observed for approximately 1.5 to 4 PVs. This was found to depend on NP type, and it was also affected by core properties. Significant oil production was observed after several PVs of nanofluid were injected. An example of oil recovery profile (water and nanofluid flood) at low- and high flow-rates is presented in **Fig. 2** as function of PVs injected for samples NF02-4 and NF02-6. The inset in **Fig. 2a** illustrates the effluent production from nanofluid flooding. It shows the emulsification of oil in water phase, especially when the flowrate was increased during the injection of NF02-4. Alike effluent was observed for sample NF02-3 under the same injection procedure. These samples (NF02-3 and NF02-4) had insignificant effect on pressure compared to the reference case, i.e. the injection pressure remained at the level of water flood pressure (see **Fig. 7a**) throughout the duration of the process.

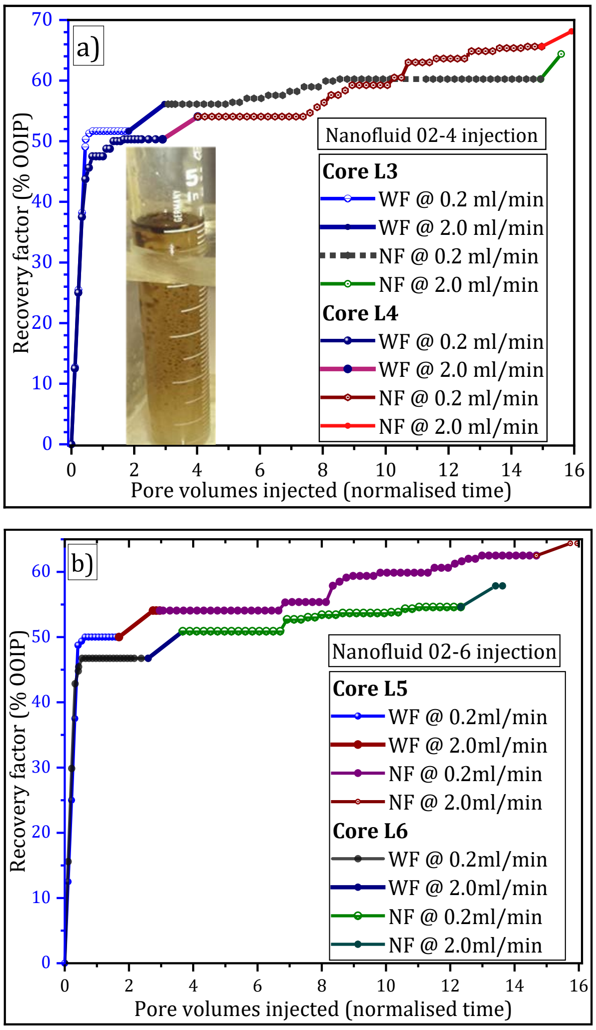

**Fig. 2.** Oil recovery factors (RFs) versus PVs injected: a) NF02-4 and, b) NF02-6 injection. In both cases, the first oil production was observed after 3 PVs of nanofluids injection.

The injection of NF02-6 and NF02-8 caused the pressure to increase and no visible signs of formation of emulsions were observed, even when the flowrate was increased. The pressure was higher than reference case (see **Fig. 7b).** At the end of the test, a filtered NP "cake" was observed at the core inlet for both NF02-6 and NF02-8 showing that filtration of large NPs and pore blocking was happening during the floods. **Table 3** summarizes

**Table 3.** Oil recovery factors (expressed as % of OOIP) achieved at each injection rate. The $RF_1$ and $RF_2$ represent the oil recovery factors at low flowrate (0.2 ml/min) and high flowrate (2 ml/min), respectively.

| NF | Core | $S_{wir}$ (%) | OOIP (ml) | **Water flood** | | | $S_{or1}$ (%) | **Nanofluid flood** | | | $S_{or2}$ (%) | $E_D$ (%) | Total RF |
|---|---|---|---|---|---|---|---|---|---|---|---|---|---|
| | | | | $RF_1$ | $RF_2$ | RF | | $RF_1$ | $RF_2$ | RF | | | |
| 02-3 | L1 | 24.7 | 16.1 | 44.7 | 2.5 | 47.2 | 39.8 | 8.6 | 1.4 | 9.9 | 33.6 | 15.6 | 57.1 |
| | L2 | 32.2 | 14.8 | 43.9 | 4.1 | 48.0 | 35.3 | 7.0 | 4.1 | 11.1 | 27.7 | 22.0 | 59.1 |
| 02-4 | L3 | 10.5 | 15.7 | 51.7 | 4.4 | 56.1 | 39.3 | 5.3 | 3.0 | 8.3 | 31.9 | 19.0 | 64.4 |
| | L4 | 10.6 | 16.0 | 50.3 | 3.8 | 54.1 | 41.1 | 11.6 | 2.5 | 14.1 | 28.5 | 31.0 | 68.2 |
| 02-6 | L5 | 15.5 | 16.0 | 50.0 | 4.1 | 54.1 | 38.8 | 8.4 | 1.9 | 10.3 | 30.1 | 22.4 | 64.4 |
| | L6 | 16.7 | 15.4 | 46.8 | 4.2 | 51.0 | 44.3 | 4.7 | 2.3 | 7.0 | 35.1 | 21.0 | 58.0 |
| 02-8 | L7 | 18.8 | 16.5 | 49.4 | 4.2 | 53.6 | 37.7 | 8.2 | 0.9 | 9.1 | 30.0 | 20.4 | 62.7 |
| | L8 | 18.7 | 16.5 | 52.4 | 2.7 | 55.2 | 36.5 | 7.3 | 3.0 | 10.3 | 28.1 | 23.0 | 65.5 |

the main core flooding results used to evaluate the nanofluid samples. The displacement efficiency due to nanofluid was evaluated by equation:

$$E_D = \left[1 - \left(\frac{S_{or2}}{S_{or1}}\right)\right] \times 100\% \qquad (1)$$

Here, $S_{or1}$ and $S_{or2}$ represent the residual oil saturation at the end of water- and nanofluid-flooding (low and high flow rate injection), respectively.

## 4.2 Interfacial tension

The interfacial tension (IFT) between crude oil and NF02-3 and NF02-4 was measured with both pendant drop and spinning drop methods. Nanofluids NF02-6 and NF02-8 were very sensitive at elevated temperature; the solutions immediately precipitated at 60 °C and became opaque, thus making it impossible to use the pendant drop method for IFT analysis. The spinning drop was used instead. **Fig. 3** shows the crude oil drop hanging from a needle within sample NF02-6 at 22 °C and 60 °C. When the temperature was increased, the NPs quickly agglomerated at the oil and water (o/w) interface. The agglomerates or layers of NPs deposited on the bottom of the cuvette due to gravity force.

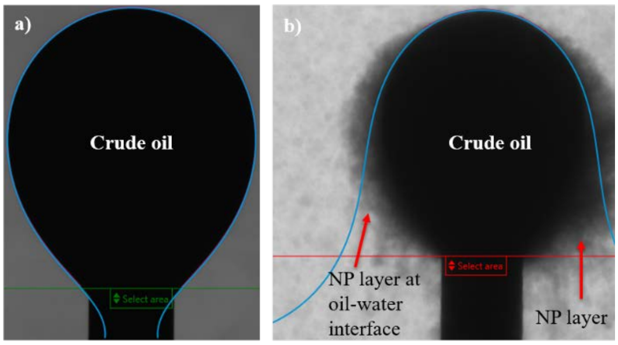

**Fig. 3.** Crude oil drop suspended in NF02-6: a) at 22 °C, and b) at 60 °C, NPs self-assembled at the w/o interface.

This effect was viewed thanks to a high-resolution pendant drop camera. The measured values of interfacial tension are presented in **Table 4**.

**Table 4.** Interfacial tension values measured at 60 °C.

| Fluid | Interfacial tension (mN/m) | |
|---|---|---|
| | Pendant drop | Spinning drop |
| SSW | 11.0 | 10.0 |
| NF02-3 | 3.5 | 3.1 |
| NF02-4 | 3.3 | 2.9 |
| NF02-6 | - | 6.8 |
| NF02-8 | - | 4.7 |

The spinning drop was also used to confirm the IFT values obtained from pendant drop method for samples NF02-3 and NF02-4. **Fig. 4** shows a crude oil droplet dipped in the capillary tube spun at 7,000 rpm and at 60 °C. Due to the high rotational speed, there were no visible aggregates of NPs and the IFT could be measured for all samples.

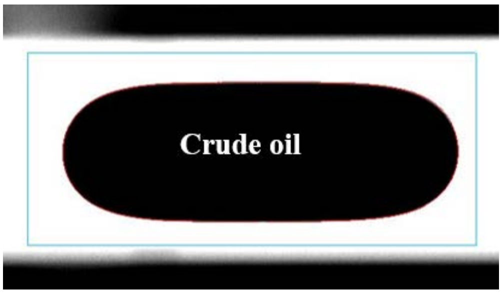

**Fig. 4.** Crude oil drop shape inside the capillary tube filled with NF02-6 and spun at 7,000 rpm for IFT analysis using STV20 spinning drop video tensiometer.

## 4.3 Core wettability

Two core plugs were used to investigate the initial wettability of the cores (i.e. before nanofluid injection). The measured wettability index of the cores was, WI = 0.86, on average, showing strongly water-wet condition. The core plugs used afterwards were considered water-wet. This assumption was made because all the core plugs were drilled from the same block and followed the same preparation and cleaning procedures.

After nanofluid flooding was completed, each core (at $S_{or}$) was flooded with decane using high flowrates (1 to 3 ml/min) until residual nanofluid saturation was achieved. Thereafter, each core plug was dipped into the Amott cells following the procedure described in section 3.3. **Fig. 5** shows the oil recovery from SSW spontaneous imbibition (SI) during 30-days test. It was observed that the rate of water imbibition decreased slightly in cores injected with nanofluids compare with original ones (not injected with NPs). At the beginning of the test, the oil was produced from all the faces of the core plugs.

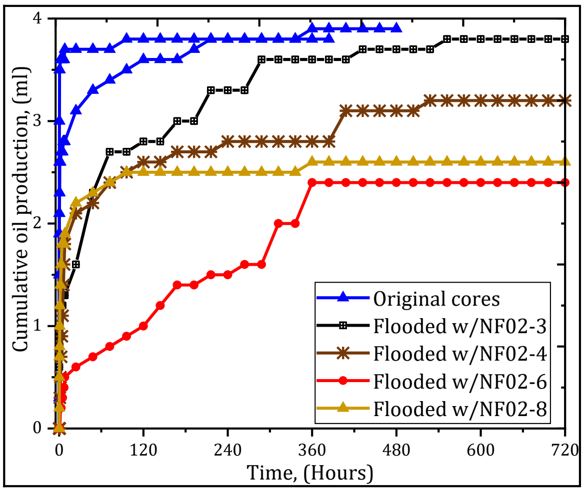

**Fig. 5.** Water spontaneous imbibition performed on cores flooded with nanofluids (at ambient conditions).

After 2-3 days, the oil production was observed from the top of the core plugs. The produced oil, at this stage,

---

[*] Corresponding author: alberto.bila@ntnu.no

remained on the top surface of the cores and detached from it after several days or by gently shaking the Amott cells. These events are depicted by rapid increase in oil recovery at some points in **Fig. 5**. At equilibrium, the measured water indexes ($I_w$) varied from 0.5 to 0.89.

In the second cycle of spontaneous imbibition, oil did not imbibe into the core or displace water, implying that the Amott oil index is zero, $I_o = 0$. Therefore, the Amott-test was not completed, and the obtained water indexes were used to assess the effect of NPs on the rock surface.

### 4.4 Permeability and porosity

After nanofluid flooding and wettability evaluation tests, the cores were cleaned with toluene and methanol for several days with Soxhlet extraction and dried at 60 °C for 2-3 days. Then, the gas permeability and porosity were measured. The results are presented in **Table 5**. The objective was to determine and quantify the changes of initial values of permeability and porosity as result of NPs adsorption or retention during the nanofluid flooding process. The negative values, in **Table 5**, indicate permeability or porosity impairments; otherwise, it would indicate improvement.

## 5. Discussion of the results

### 5.1 Nanofluid stability analysis

The approaches used to study the stability of the NPs solutions at 0.1 wt. % were: i) the particle size distribution (PSD), ii) zeta potential, and iii) sedimentation test.

Malvern Zetasizer instrument was used to characterise the PSD and zeta potential of the NP solutions. After setting the temperature at 60 °C, the average particle diameter size for NF02-3 was 94 nm and 32 nm for NF02-4. A comparison of the measured particle size shows that the size is in the range claimed by manufacturer (i.e. 107 nm for NF02-3 and 32 nm for NF02-4). Hence, it suggests that the NPs were stable in seawater solution, at least for the measured period. The measurements for samples NF02-6 and NF02-8 resulted in high values of polydispersity index indicating formation of large NP aggregates, thus not suitable for the characterisation of particle size with dynamic light scattering technique. The measurements of zeta potential of the NPs gave unreliable values, for unknown reasons.

Visual observations were conducted to confirm the results obtained from particle size measurements. The nanofluids were placed in the oven at 60 °C and monitored daily. It was immediately observed that NF02-6 and NF02-8 were aggregating at 60 °C, as also noted during measurements of interfacial tension. The formed NPs structures deposited to the bottom of the ampules within the couple of hours. The stability analysis for NF02-3 and NF02-4 was conclusive after 4 days. After which, the nanofluid samples also started to flocculate and gradually settled out of solution and forming large NPs aggregates. **Fig. 6** illustrates the NPs in the aggregated form on the bottom of the ampules (white) after four-day test. It was interesting to observe, visually, (for sample NF02-4) the stretching and flocculation of polymer chains in solution. Possibly, this was caused by hydrolysis and the polymers precipitated in the presence of divalent cations (e.g. $Mg^{2+}$, $Ca^{2+}$) at the elevated temperature [29]. Consequently, the desired repulsion forces between the NPs in the solution vanished between the particles.

**Fig. 6** Visual analysis of NPs stability. The white colour at the bottom of each ampule indicates the aggregated NPs. Stretched polymers in SSW were observed in NF02-4.

**Table 5**. Permeability and porosity measured before and after nanofluid flooding on core plugs.

| **Core** | **Injected nanofluid** | **Permeability (mD)** | | | **Porosity[2] (%)** | | |
|---|---|---|---|---|---|---|---|
| | | before | after | % difference | before | after | % difference |
| L1 | 02-3 | 404 | 350 | -13 | 19 | 17 | -10 |
| L2 | | 537 | 452 | -16 | 20 | 16 | -19 |
| L3 | 02-4 | 460 | 446 | -3 | 17 | 15 | -11 |
| L4 | | 411 | 370 | -10 | 18 | 16 | -15 |
| L5 | 02-6 | 367 | 232 | -37 | 18 | 13 | -25 |
| L6 | | 331 | 246 | -26 | 18 | 14 | -25 |
| L7 | 02-8 | 384 | 292 | -24 | 18 | 15 | -18 |
| L8 | | 265 | 193 | -20 | 20 | 17 | -16 |

[2] Measured with Helium porosimeter

Based on sedimentation test, it was concluded that NF02-3 and NF02-4 were stable for approximately 4 days whereas NF02-6 and NF02-8 became readily unstable at 60 °C. The primary observation is that the injection of these NPs will increase the pressure and oil production costs. Therefore, they may not be suitable for EOR at field-scale. Therefore, the surface modification of these particles still needs to be optimized to remain stable for extended periods of injection (expected at field-scales). This should not only focus on the particle stability, but also on the surface chemistry and other possible interactions that may occur between NPs and an oil-field.

### 5.2 Evaluation of oil recovery

An accurate evaluation of tertiary oil recovery not only requires the reproducibility of experimental results, but also to properly determine the waterflood $S_{or}$ and to ensure that any additional oil is solely due to EOR effect. To achieve this, twin core plugs were used for each nanofluid type; the injection of water at low rate was changed after it did not produce more oil for 1-2 PVs, thereafter the flowrate was bumped for 1 PVs.

It was observed that the nanofluids at a concentration of 0.1 wt. % could mobilise the residual oil, but it was delayed compared to breakthrough of nanofluids. The arrival of first oil at the core outlet varied among the samples. It occurred after 1.5 to 4 PVs were injected of nanofluids. The oil production due to NF02-6 (**Fig. 2b**) and NF02-8 was observed at late injection times compared to NF02-3 and NF02-4 (**Fig. 2a**); at this stage, the produced oil consisted of small droplets that merged with the oil in the separator. For all samples, the main oil occurred after large amount of nanofluid were injected. In **Fig. 2**, we see several points were oil increases due to nanofluid injection. The amount of oil recovered stepwise varied as the NPs injection advanced and the NPs interacted with the rock system. The late occurrence of oil production with nanofluid injection is attributed to differences between the viscosities of nanofluids and crude oil ($\mu_o/\mu_{nanofluid} \approx 6$). Additionally, oil production was affected by number of pore volumes injected during the water flood stage and variations in core properties. Therefore, for the nanofluids to produce an additional oil, an extra energy or physicochemical interactions between the nanoparticles and the oil system was needed. This shows that injected NPs in the reservoir need to decrease the surface energy to deform and break large oil drops and/or to block enough pores to build up enough pressure across the core to detach and mobilise the residual oil in the adjacent pores.

Despite the late occurrence of oil production, the core flooding tests have revealed that surface modified silica NPs can extract more oil efficiently in water-wet water flooded Berea sandstone formations. The EOR potential of the NPs was revealed after the injection of large amounts of nanofluids. However, if these results are directly compared to a field-scale injection, it may appear economically unfeasible because of the cost of NPs. But, to better simulate the injections at field-scale, large pore volumes of nanofluids must be injected at core scale [30]. **Table 3** reports the oil recoveries achieved at the end of water and nanofluid flooding. The oil recovery achieved by water flood varied from 47.2% to 56.1% of OOIP after the flowrate was bumped. When the nanofluid system was injected at low rate, the incremental oil recovery varied from 4.7% to 11.6% of OOIP. Increasing the flowrate tenfold for ≈1 PV, the ultimate incremental recoveries reached 7.0% to 14.1% of OOIP. The oil recovery during the bump rate is shown in **Fig. 2** by a "linear" segment. This was because it was difficult to record the amount of oil produced per step during the bump rate, as it was a quick and short process. Additionally, oil was produced as droplets. Therefore, the total volume of oil was measured at the end of injection and added to that recovered at low rate injection. It should be noted that the "linear" segments in **Fig. 2** do not indicate linear production of oil.

The twin cores produced comparable results; the variation was below 5%. The thin gap between the core plug and the end plug may be the main source of capillary end effects, thus affecting the obtained results. In addition to the core heterogeneity and the criteria chose to switch from low to high rate (2 PVs of no oil production), probably it was not optimal to reach the equilibrium. Consequently, additional oil production may occur with the bump rate (producing bypassed oil in the core).

Conjugating the data from **Table 1** and **Table 3**, one can see that the highest incremental oil recovery was achieved by the smallest NPs size. The increased oil recovery with decreasing the NP size is also consistent with measured IFT values shown in **Table 4**, where it is shown that NPs of small size were efficient in lowering the o/w interfacial tension, thus resulting in higher oil recovery than the large sized NPs. The results are also in agreement with previous findings reported in the literature [13, 20], but are also in contrast to the positive correlation observed between the NP size and oil recovery reported by Aurand, et al. [23]. The NPs at 0.1 wt.% had no significant effect on the viscosity of the SSW solution, thus unable to improve the mobility ratio. The maximum pressure was achieved from NPs of large size. This observation supports the notion that increasing the NPs size decreases the rock permeability [13], and reduces the surface functionalities of the NPs at the oil-water-rock interfaces [31, 32], thus resulting in low oil recovery.

The small variations observed in oil recoveries (<5%) ensured reproduced results in this work; it proved that the surface-modified silica NPs can improve oil recovery efficiently in water-wet water flooded reservoirs under the experimental conditions.

### 5.3 Evaluation of EOR mechanisms

This work reports promising results for the application of surface-modified silica NPs for EOR. In section **1**, we reviewed possible mechanisms of silica NPs based on the mechanisms responsible for entrapping the oil after water flooding in water-wet reservoirs. We observed that for each nanofluid type different recovery mechanisms are operating for maximum oil recovery. This implies that additional studies are needed to quantify the contribution of the involved EOR mechanisms. The actual oil recovery mechanisms are discussed in the following sections to gain knowledge and suggest the probable dominant mechanisms of the surface modified nanoparticles

### *5.3.1 Interfacial tension and rock wettability*

In nanofluid flooding applications, NPs are needed to improve water flooding microscopic sweep efficiency. When injecting the NPs, the major expectation is that the differential pressure across the core exceed the capillary forces trapping the oil. This can be achieved if the NPs adsorb to the o/w interface, which will in turn decrease the IFT between oil and injection water. Capillary number, $N_c$, describes the balance between the oil mobilising forces (viscous forces) and the oil trapping forces, and it provides a mean to evaluate how effective the NPs are for mobilizing the residual.

$$N_c = \frac{\mu v}{\gamma} \qquad (2)$$

Here, $\mu$ and $v$ are the viscosity and velocity of the displacing fluid, respectively, and $\gamma$ is the interfacial tension between the displacing and displaced phases.
The $N_c$ for water flooding calculated in this work is of order of $10^{-6}$. It is generally recognized that the critical capillary number for the onset of mobilization of residual oil in water-wet reservoirs is of orders of $\approx 10^{-5}$ [8, 33] above which, a complete mobilisation of residual may take place. Moreover, this condition can be met if any additive to the injection fluid can decrease the IFT between oil and water down to $<10^{-3}$ mN/m [34].

In this work, it was observed that the modified silica NPs reduced the o/w interfacial tension. In **Table 4**, one can see that the nanofluids had a moderate effect on the o/w interfacial tension, and the IFT values are not low enough to produce the desired $N_c$ to significantly mobilise the residual oil. These findings are consistent with earlier research [23, 35]. The current results indicate poor surface activity performance of the NPs onto the o/w interface. The reasons for that might be i) the high temperature that increased the degree of collision between the NPs in solution and the aggregation tendency at the o/w interface (see **Fig. 3**); ii) the surface modification with polymer was lost due to solubility effect of polymers in water, especially at elevated temperature, thus destabilizing the silica particles in the presence divalent ions. Particularly, the aluminium present in samples NF02-6 and NF02-8 would form sulphates in the solution and prompting the formation of precipitates.

In addition to decreasing the oil and water IFT, the injection of nanofluids explored the interactions occurring at the fluid-rock interface. This is because NPs can modify the fluid distribution and flow-ability of fluids within the reservoir and improve the microscopic displacement efficiency. For this purpose, we explored the rate of water imbibition and the Amott indexes to evaluate the effect of the injected NPs on the solid surface. From **Fig. 5**, one can see that the rate of water imbibition was relatively low especially on cores flooded with samples NF02-3 and NF02-6 compare with original cores (not injected with NPs). Furthermore, we see a sudden increase in oil recovery with time from all the cores indicating a progressive alteration of wettability. This indicates that the adsorbed oil was released as the pore spaces became increasingly water-wet due to NPs, thus resulting in increased oil recovery by spontaneous water imbibition. The measured Amott water indexes ranged from 0.5 to 0.86. The overall results suggest that the wettability was affected by nanofluids to water-wet condition. These results were expected because the injected NPs were hydrophilic, and when exposed to a substrate of like wettability or surface charge such as Berea sandstone, they could adsorb physically or confine themselves on the pores in response to the applied injection pressure. Thus, developing new hydrophilic surface roughness on the pores where the particles were lodged. This results show agreement with previous studies [14, 36] that studied the wettability alteration using hydrophilic silica NP types.

Owing to small effects of NPs on IFT and wettability alteration, the studied NPs are not expected to mobilise residual oil and increase oil recovery by solely reducing the IFT and/or by affecting the wettability. But, the moderate effect of NPs on fluid-rock properties still plays a predominant role for stabilisation of emulsions [21, 37, 38]. This effect or the emulsion formation will be discussed in the following section, especially for samples NF02-3 and NF02-4, that achieved the lowest IFT reduction among the studied nanoparticles.

### *5.3.2 Differential pressure profile analysis*

The differential pressure (dP) was recorded during the flooding experiments using a Keller PD-33X with range of 0-30 bar instrument. The dP behaviour may indicate whether emulsions were formed [20] or microscopic flow diversion was occurring during NPs flooding. Gathering these data one can comprehend the migration behaviour and the EOR mechanisms of NPs.

During the flood of nanofluids NF02-3 and NF02-4, it was observed that the dP increased slightly for ≈1PV, then it decreased and finally it levelled to the reference waterflood value. This behaviour of dP is presented in **Fig. 7a** for NF02-4. The slow rise of dP is thought to be caused by physical confinement of the particles at the core entrance. Then, the pressure decreased as the injection advanced indicating propagation of the NPs through the pore spaces without clogging or causing significant damage to the rock permeability. The reduction of core absolute permeability varied from 3% to 16%, which confirmed low retention and the ease with which the NPs travelled through the core. Furthermore, the low pressure also provided an indication of generation of in-situ emulsions with nanofluid flooding. This was confirmed by increasing the flowrate; oil-in-water emulsions were visible in the effluent vials as illustrated by the inset picture in **Fig. 2a.** The yellowish colour of the effluent is attributed to the solubilisation of oil during the displacement process. The collected effluent production contained significant fraction of discrete oil droplets in the water phase. These droplets merged upwards with the oil in the vials after a couple of hours due to gravity effect. Previous studies that investigated the EOR effect of polymer-coated silica NPs, such as used in this work, have highlighted the formation of NPs-stabilised emulsions for oil recovery. The studies argued that NP-stabilized emulsions can easily be transported out of the cores with low retention, and increase oil recovery [14, 21, 37].

The generation of emulsions, in this work, concurs with the reduction of IFT, especially for NF02-3 and NF02-4 (with the lowest IFT reduction among the studied samples). In addition to the high temperature that was enhancing the oil and water interactions within the core resulting in flow of emulsion, particularly, when the flowrate was increased. This is because increasing the flowrate can provide an extra energy required to break up oil phase, thus allowing more NPs to adsorb at the oil-water interface [22]. Additionally, NF02-3 and NF02-4 had surfactant agents present in their composition, thus favourable to generating emulsions. It is most likely that samples NF02-3 and NF02-4 improved oil recovery by affecting the effective mobility to oil (oil relative permeability) due to generation of NP-stabilised oil-in-water emulsions.

The contrasting results were observed during the injection of samples NF02-6 and NF02-8, little to no formation of emulsions were observed, even with the increased flowrate. The injection of these samples was accompanied with continuous increased pressure. From approximately 5 PVs of nanofluid injection the dP showed high degree of oscillation until the tests were stopped. At the end of the flooding test, a filtered NP “cake” was observed at the core inlet indicating that a cross-flow filtration, blockage of the pores was occurring, which is likely the primary source for pressure increase. This is because the NPs were hydrated and were unstable in SSW, so the particle size has increased and creating favourable conditions for blockage of small pores from start of the injection. An example of the pressure profile is shown in **Fig. 7b**; the inset picture illustrates the formed filtered NP “cake” due to NF02-6. Accordingly, the permeability reduction was in the range of 20% to 37%, and it was higher than that measured on cores injected with samples NF02-3 and NF02-4. As mentioned earlier, NF02-6 and NF02-8 produced the first oil at the latest injection time of all tested NFs and progressively increased pressure. The pressure pattern also indicated that pore blocking was also happening inside the core until an extreme pore blockage was reached. The effect of pore blocking is likely the diversion of the injection water and the mobilization of bypassed residual oil. **Fig. 7b** also shows periods of an abrupt increase and decrease of dP caused by pore blockage and un-blockage of the jammed NPs. These periods of high spikes (pump effect) supported the notion that the NPs were further retained or aggregating within the core; as a result, the pressure was redistributed within the pores to assist the diverted water to reach and detach the by-passed oil in the adjacent pores. As the production of oil and the detachment of weakly adsorbed NPs on the pore walls was occurring, the local pore pressure was temporarily relieved. Thus, restoring the normal flow of water. This behaviour was reflected on events of sudden pressure drops (in **Fig. 7b)**. As the blockage continued on the available pore channels, the injected water was continuously forced to find new paths. Due to the high pressure generated with advancing of the injection and subsequent confinement of NPs in the pores, the oil was detached from the surface and produced before the pores were relocked. However, not all cases the pressure increase was accompanied by oil production.

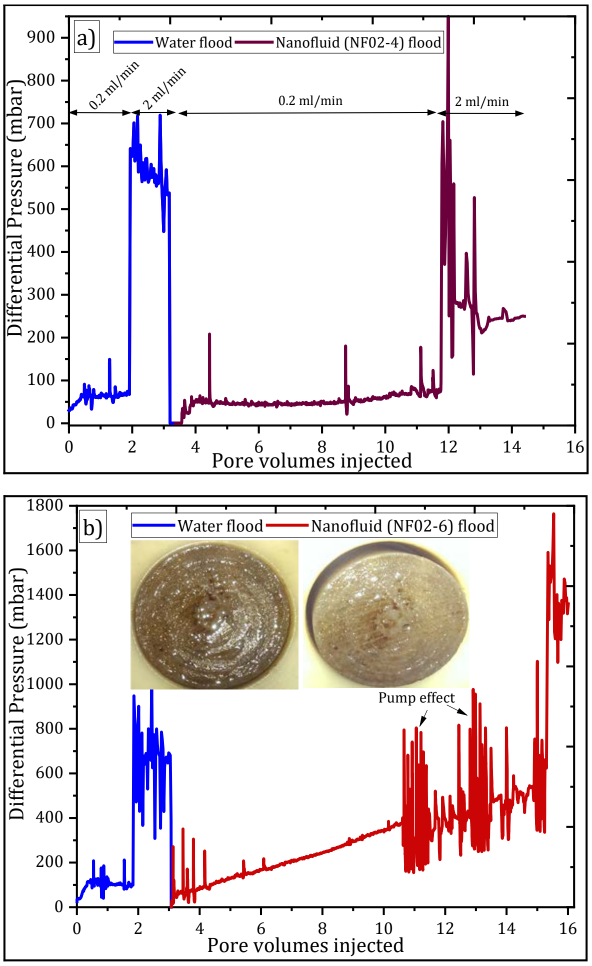

**Fig. 7.** Differential pressure profiles as a function of PVs of injected fluids: a) NF02-4 injection and b) The inset is the NPs “cake” formed at the core inlet during the injection of NF02-6.

The primary recovery mechanisms for NF02-6 and NF02-8 is possibly the pore blocking and flow diversion also referred to as log-jamming effect [7, 8, 23]. According to Spildo, et al. [5] and Skauge, et al. [7] this phenomenon can be explained by mass difference between the NPs and water. This is because the hydrated NPs become heavy and their flow ability is decreased, hence causing the particles to accumulate at the pore entrance during the core injection. In this work, the log jamming effect finds further support because the NPs were aggregating in SSW solution before the injection. Therefore, further injection would promote accumulation and retention of NPs at the core inlet and within the core and increase the pressure. The main particle retention mechanism is mechanical rather than chemical adsorption. This is supported by the late occurrence oil recovery and subsequent increased oil production with progressive increase in pressure during the flood process.

Due to the synergistic effect of IFT reduction and wetting effect, the increased dP also contributed for the mobilization of both by-passed and capillary-trapped oil. However, quantifying the contribution of pore blocking and fluid flow diversion mechanisms in the mobilisation of residual oil based on differential pressure is complex.

### 5.4 Effect of NPs on permeability and porosity

To evaluate the influence of NPs on rock properties, the permeability and porosity were evaluated after nanofluid flooding. The results are presented in **Table 5**. The results revealed both permeability and porosity reduction for all cores after nanofluid flooding. This was due to retention or adsorption of NPs within the cores. The cores injected with nanofluids containing small-sized NPs diameter (NF02-3 and NF02-4) resulted in the lowest reduction in permeability and porosity. The observed permeability reduction was from 3% to 16% and the porosity reduction ranged from 10% to 19%. For these samples the retention may be due to chemical adsorption of NPs owing to their small size [12]. The slightly high values of porosity reduction suggested that adsorption and blockage due to NPs were relevant in the large pores.

Nanofluids NF02-6 and NF02-8 with large initial size and tendency to form large structures of NPs resulted in the largest permeability and porosity impairments. The permeability reduction was from 20% to 37% and the porosity reduction was from 16% to 25%. As the NPs aggregated before the injection, significant permeability and porosity reductions were expected. It is possible that the NPs were desorbed from the pore walls and produced during the preparation of the cores for wettability tests.

## 6. Conclusions

This work investigated the effect of surface-modified silica NPs for enhanced oil recovery applications. Flooding experiments were performed by injecting the nanofluids in water-wet core plugs at 60 °C in tertiary recovery mode. The NPs were prepared at 0.1 wt. % in seawater. The main EOR mechanisms due to silica NPs were also evaluated. Based on the experimental results, the following conclusions were obtained:

- The core flooding experiments have shown that oil recovery is enhanced with surface modified silica nanoparticles, despite the limited stability. The NPs increased oil recovery up to 14% of OOIP in water-wet rocks at 60 °C;
- The IFT between water and crude oil was decreased with surface modified silica NPs, but the reduction is not in orders of magnitude to contribute significantly to the remobilisation of residual oil;
- The wetting properties of Berea sandstone rocks were moderately affected with nanoparticles towards to water-wet condition;
- An analysis of EOR mechanisms of the studied nanofluid systems suggest that NF02-3 and NF02-4 improved microscopic sweep efficiency by generation of in-situ oil-in-water emulsions, while NF02-6 and NF02-8 recovered oil by pore blocking and microscopic flow diversion (log-jamming effect).

Based on the current findings, further work is underway aiming at evaluating the EOR potential of the same NPs in neutral-wet cores and improving the evaluation procedure of oil recovery mechanisms of the nanoparticles.

**Acknowledgements**: The authors gratefully acknowledge Evonik Industries for providing the nanoparticles used in this work and the Research Council of Norway for their financial support through PoreLab, Centre of Excellence, project number 262644.

## References

1. X. Sun, Y. Zhang, G. Chen, and Z. Gai, "Application of Nanoparticles in Enhanced Oil Recovery: A Critical Review of Recent Progress," *Energies*, vol. 10(3), 2017, pp. 345.
2. A. Muggeridge *et al.*, "Recovery rates, enhanced oil recovery and technological limits," *Philosophical transactions. Series A, Mathematical, physical, and engineering sciences*, vol. 372(2006), 2014, pp. 20120320-20120320.
3. I. Sandrea and R. Sandrea, "Recovery factors leave vast target for EOR technologies," *Oil & Gas Journal*, vol. 105(41), 2007, pp. 44-47.
4. W. Abdallah *et al.*, "Fundamentals of wettability," *Technology*, vol. 38(1125-1144), 1986, pp. 268.
5. K. Spildo, A. Skauge, M. G. Aarra, and M. T. Tweheyo, "A New Polymer Application for North Sea Reservoirs," *SPE Reservoir Evaluation & Engineering*, vol. 12(03), 2009, pp. 427-432.
6. M. A. E. Kokubun, F. A. Radu, E. Keilegavlen, K. Kumar, and K. Spildo, "Transport of Polymer Particles in Oil–Water Flow in Porous Media: Enhancing Oil Recovery," *Transport in Porous Media*, vol. 126(2), 2018, pp. 501-519.
7. T. Skauge, K. Spildo, and A. Skauge, "Nano-sized Particles For EOR," in *SPE Improved Oil Recovery Symposium*, Tulsa, Oklahoma, USA, 2010, pp. 10. https://doi.org/10.2118/129933-MS.
8. Z. Hu, S. M. Azmi, G. Raza, P. W. J. Glover, and D. Wen, "Nanoparticle-assisted water-flooding in Berea sandstones," *Energy & Fuels*, vol. 30(4), 2016, pp. 2791-2804.
9. S. Ayatollahi and M. M. Zerafat, "Nanotechnology-Assisted EOR Techniques:

New Solutions to Old Challenges," in *SPE International Oilfield Nanotechnology Conference and Exhibition*, Noordwijk, The Netherlands, 2012, pp. 15. https://doi.org/10.2118/157094-MS.

10. M. V. Bennetzen and K. Mogensen, "Novel Applications of Nanoparticles for Future Enhanced Oil Recovery," in *International Petroleum Technology Conference*, Kuala Lumpur, Malaysia, 2014, pp. 14. https://doi.org/10.2523/IPTC-17857-MS.
11. M. I. Youssif, R. M. El-Maghraby, S. M. Saleh, and A. Elgibaly, "Silica nanofluid flooding for enhanced oil recovery in sandstone rocks," *Egyptian Journal of Petroleum*, vol. 27(1), 2018, pp. 105-110.
12. M. Zallaghi, R. Kharrat, and A. Hashemi, "Improving the microscopic sweep efficiency of water flooding using silica nanoparticles," *Journal of Petroleum Exploration and Production Technology*, vol. 8(1), 2018, pp. 259-269.
13. L. Hendraningrat, S. Li, and O. Torsater, "Effect of Some Parameters Influencing Enhanced Oil Recovery Process using Silica Nanoparticles: An Experimental Investigation," in *SPE Reservoir Characterization and Simulation Conference and Exhibition*, Abu Dhabi, UAE, 2013, pp. 10. https://doi.org/10.2118/165955-MS.
14. B. A. Suleimanov, F. S. Ismailov, and E. F. Veliyev, "Nanofluid for enhanced oil recovery," *Journal of Petroleum Science and Engineering*, vol. 78(2), 2011, pp. 431-437.
15. K. Xu, D. Agrawal, and Q. Darugar, "Hydrophilic Nanoparticle-Based Enhanced Oil Recovery: Microfluidic Investigations on Mechanisms," *Energy & Fuels*, vol. 32(11), 2018, pp. 11243-11252.
16. N. A. Ogolo, O. A. Olafuyi, and M. O. Onyekonwu, "Enhanced Oil Recovery Using Nanoparticles," in *SPE Saudi Arabia Section Technical Symposium and Exhibition*, Al-Khobar, Saudi Arabia, 2012, pp. 9. https://doi.org/10.2118/160847-MS.
17. L. Hendraningrat, S. Li, and O. Torsæter, "A coreflood investigation of nanofluid enhanced oil recovery," *Journal of Petroleum Science and Engineering*, vol. 111(2013, pp. 128-138.
18. A. Bila, Å. J. Stensen, and O. Torsæter, "Experimental Investigation of Polymer-Coated Silica Nanoparticles for Enhanced Oil Recovery," *Nanomaterials*, vol. 9(6), 2019.
19. R. Li, P. Jiang, C. Gao, F. Huang, R. Xu, and X. Chen, "Experimental Investigation of Silica-Based Nanofluid Enhanced Oil Recovery: The Effect of Wettability Alteration," *Energy & Fuels*, vol. 31(1), 2017, pp. 188-197.
20. M. Adil, K. Lee, H. M. Zaid, N. R. A. Latiff, and M. S. Alnarabiji, "Experimental study on electromagnetic-assisted ZnO nanofluid flooding for enhanced oil recovery (EOR)," *PloS one*, vol. 13(2), 2018, pp. e0193518.
21. T. Zhang, D. Davidson, S. L. Bryant, and C. Huh, "Nanoparticle-Stabilized Emulsions for Applications in Enhanced Oil Recovery," in *SPE Improved Oil Recovery Symposium*, Tulsa, Oklahoma, USA, 2010, pp. 18. https://doi.org/10.2118/129885-MS.
22. I. Kim, A. J. Worthen, K. P. Johnston, D. A. DiCarlo, and C. Huh, "Size-dependent properties of silica nanoparticles for Pickering stabilization of emulsions and foams," *Journal of Nanoparticle Research*, vol. 18(4), 2016, pp. 82.
23. K. R. Aurand, G. S. Dahle, and O. Torsæter, "Comparison of oil recovery for six nanofluids in Berea sandstone cores," in International Symposium of the SCA, France, 2014, vol., no., pp. 1-12.
24. A. I. El-Diasty and A. M. Aly, "Understanding the Mechanism of Nanoparticles Applications in Enhanced Oil Recovery," in *SPE North Africa Technical Conference and Exhibition*, Cairo, Egypt, 2015, pp. 19. https://doi.org/10.2118/175806-MS.
25. A. Bila, J. Å. Stensen, and O. Torsæter, "Experimental Evaluation of Oil Recovery Mechanisms Using a Variety of Surface-Modified Silica Nanoparticles in the Injection Water," in *SPE Norway One Day Seminar*, Bergen, Norway, 2019, pp. 19. https://doi.org/10.2118/195638-MS.
26. D. T. Wasan and A. D. Nikolov, "Spreading of nanofluids on solids," *Nature*, vol. 423(6936), 2003, pp. 156-159.
27. P. Than, L. Preziosi, D. D. Josephl, and M. Arney, "Measurement of interfacial tension between immiscible liquids with the spinning road tensiometer," *Journal of colloid and interface science*, vol. 124(2), 1988, pp. 552-559.
28. W. G. Anderson, "Wettability Literature Survey Part 5: The Effects of Wettability on Relative Permeability," *Journal of Petroleum Technology*, vol. 39(11), 1987, pp. 1453-1468.
29. R. S. Seright, A. Campbell, P. Mozley, and P. Han, "Stability of Partially Hydrolyzed Polyacrylamides at Elevated Temperatures in the Absence of Divalent Cations," *SPE Journal*, vol. 15(02), 2010, pp. 341-348.
30. K. H. Hosseinzade and O. Torsæter, *Injected pore volume on lab and field scales* (9th International Conference on Porous Media & Annual Meeting). Rotterdam, Netherlands: International Society for Porous Media, Interpore, 2017.
31. A. Habibi, M. Ahmadi, P. Pourafshary, s. Ayatollahi, and Y. Al-Wahaibi, "Reduction of Fines Migration by Nanofluids Injection: An Experimental Study," *SPE Journal*, vol. 18(02), 2012, pp. 309-318.
32. P. Bacchin, Q. Derekx, D. Veyret, K. Glucina, and P. Moulin, "Clogging of microporous channels networks: role of connectivity and

tortuosity," *Microfluidics and Nanofluidics,* vol. 17(1), 2014, pp. 85-96.

33. K. J. Humph ry, B. M. J. M. Suijkerbuijk, H. A. van der Linde, S. G. J. Pieterse, and S. K. Masalmeh, "Impact of Wettability on Residual Oil Saturation and Capillary Desaturation Curves," *Petrophysics,* vol. 55(04), 2014, pp. 313-318.
34. J. J. Sheng, "Status of surfactant EOR technology," *Petroleum,* vol. 1(2), 2015, pp. 97-105.
35. C. Dai *et al.*, "Spontaneous Imbibition Investigation of Self-Dispersing Silica Nanofluids for Enhanced Oil Recovery in Low-Permeability Cores," *Energy & Fuels,* vol. 31(3), 2017, pp. 2663-2668.
36. S. Li and O. Torsaeter, "The Impact of Nanoparticles Adsorption and Transport on Wettability Alteration of Intermediate Wet Berea Sandstone," in *SPE Middle East Unconventional Resources Conference and Exhibition*, Muscat, Oman, 2015, pp. 14. https://doi.org/10.2118/172943-MS.
37. H. ShamsiJazeyi, C. A. Miller, M. S. Wong, J. M. Tour, and R. Verduzco, "Polymer-coated nanoparticles for enhanced oil recovery," *Journal of Applied Polymer Science,* vol. 131(15), 2014.
38. D. A. DiCarlo, B. Aminzadeh, M. Roberts, D. H. Chung, S. L. Bryant, and C. Huh, "Mobility control through spontaneous formation of nanoparticle stabilized emulsions," *Geophysical Research Letters,* vol. 38(24), 2011.

# Permeability Prediction using multivariant structural regression

*Matthew* Andrew[1],*

[1]Carl Zeiss Microscopy, 4385 Hopyard Rd., Pleasanton, CA, 94588, USA

**Abstract.** A novel method for permeability prediction is presented using multivariant structural regression. A machine learning based model is trained using a large number (2,190, extrapolated to 219,000) of synthetic datasets constructed using a variety of object-based techniques. Permeability, calculated on each of these networks using traditional digital rock approaches, was used as a target function for a multivariant description of the pore network structure, created from the statistics of a discrete description of grains, pores and throats, generated through image analysis. A regression model was created using an Extra-Trees method with an error of <4% on the target set. This model was then validated using a composite series of data created both from proprietary datasets of carbonate and sandstone samples and open source data available from the Digital Rocks Portal (www.digitalrocksporta.org) with a Root Mean Square Fractional Error of <25%. Such an approach has wide applicability to problems of heterogeneity and scale in pore scale analysis of porous media, particularly as it has the potential of being applicable on 2D as well as 3D data.

## 1 Introduction

Flow and transport in porous media are fundamentally rooted at the scale of the tiny tortuous pore pathways through which the flow takes place. As such, pore scale investigation is now a widely adopted tool across a range of disciplines associated with the examination of flow and transport. Such an approach has applications ranging from understanding the flow properties of porous ceramics (used as a catalytic substrate for vehicle emission reduction) [1], [2], examining battery electrolyte exchange [3], [4], characterizing geological formations for the purpose of understanding groundwater flow [5], carbon capture and storage [6]–[8] and (in its most industrially applied application) oil and gas recovery [9]–[12]. One of the most useful results from a holistic pore-scale characterization is the prediction of effective medium properties, such as permeability [13], relative permeability [14], capillary pressure curves [15], and effective acoustic and electrical properties [16], [17]. Traditional approaches to the prediction of effective properties from porous media (e.g. permeability, diffusivity or effective conductivity) focus on coupling the 3D structural imaging of porous media with the full physical simulation of the partial differential equations governing the property of interest [13], [18]. Once the domain and physics have been defined (with appropriate boundary conditions), the physics then converges over multiple iterations. Such an approach is contrasted to more traditional (legacy) approaches for effective property estimation, such as Kozeny-Carman or Kuwabara [19], [20] techniques which feed a relatively limited and difficult to measure set of structural properties into quasi-analytical models to make flow estimations. These are typically inaccurate (e.g. [21]), may require significant (and arbitrary) correction factors and are challenging to effectively apply to real problems [22]. For example, different variants of the Kozeny-Carman equation require the knowledge of characteristic particle size, tortuosity or effective channel diameter – something typically ambiguous to measure in a real system of arbitrary pore network type.

The past 10 years have seen an explosion in the availability of open source machine learning and computer vision tools, enabling both in-depth multivariant classification and analysis of porous media structure [23], [24] and powerful new regression techniques, facilitating the usage of such multivariant statistics for effective prediction [25]. The application of these tools and techniques to flow and transport in porous media has been limited. In this study these techniques are used to present a new technique for prediction of Stokes flow (viscous dominated) permeability from pore-scale images of rocks using multivariant statistical regression coupled with extensive synthetic geometry generation and pore-scale computational simulation. Pore structures were parameterized using 34 distinct statistical parameters, derived from specific discretized structural properties. This multivariant model is validated on an extensive open source digital rock dataset, comprising carbonate and sandstone pore geometries, giving an average prediction error of around 25% for predicted permeability values ranging over 6 orders of magnitude (10µD to 10D).

## 2 Materials and Methods

One of the biggest challenges in the application of machine learning based computer vision techniques to

---

* Corresponding author: matthew.andrew@zeiss.com

digital rock analysis is that of data. Pore networks are complex, and the range of tools available for characterizing them is broad, so any multivariant characterization and prediction will require many datasets (potentially many thousands or millions) to effectively train while avoiding model overfitting, a difficult feat when each 3D image may take several hours to acquire. To overcome this obstacle, synthetic pore network generation techniques were used to generate a more extensive training set than would be available for real (imaged) structures. Early digital rock studies used synthetic pore space generation extensively to examine simple rock systems at the pore scale. While such an approach has been largely supplanted by direct imaging, synthetic techniques do present specific advantages, especially when examining mechanisms behind various processes while controlling the amount of heterogeneity [26], [27], or when trying to develop an holistic understanding of systems which are extremely challenging to characterize experimentally, such as the organic hosted pore networks present in unconventional shale reservoirs [28]. Synthetic pore spaces can either be constructed physically, usually by glass beads or etchings in glass (e.g. [29], [30]) or numerically using a pore space generator, using stochastic or object-based techniques, subject to  with various constraints (e.g. [31]–[33]).

Two thousand, one hundred and ninety (2,190) synthetic intergranular pore networks were generated by modelling grains as convex polyhedral [34], randomly placed within the pore space under a range of packing conditions and statistical descriptions. Polyhedra were defined by picking vertices around a bounding ellipse, defined by 3 axes ($L_1$, $L_2$ & $L_3$, such that $L_1 < L_2 < L_3$). All geometries were given a nominal voxel size of 1μm – a single nominal voxel size was used as the resulting permeability simulation results were then scaled across multiple nominal voxel sizes using the Hagen-Poisseuille equation as described below.

To allow for a range of granular aspect ratios the axis lengths for each grain were picked from a normal statistical distribution, each defined by an average and standard deviation ($\mu_1$, $\mu_2$, $\mu_3$ and $\sigma_1$, $\sigma_2$, $\sigma_3$). For simplicity the same distribution was used for the two shortest axes ($\mu_1 = \mu_2$ and $\sigma_1 = \sigma_2$). The ratio $L_3/L_{1,2}$ (defining average grain aspect ratio) was randomly defined at the beginning, being a uniformly distributed random variable between 1 and 3. Similarly target porosity (φ) was a uniformly distributed random variable in the range $0.05 < \varphi < 0.7$, as were $\mu_{1,2}$ (in the range 15-60 voxels). $\sigma_1$ and $\sigma_2$ were determined using a coupled random variable in the range 5-35 voxels, and $\sigma_3$ an independently determined variable in the same range. Multiple geometric packing strategies were used, including (in order of increasing computational expense) allowing grains to overlap [28], removing grain overlap and the explicit physical modelling of gravitational settling. The entire range of target porosities could be effectively modelled when allowing grain overlap; however when using the other techniques (which achieved higher grain packing densities than when allowing overlap) once the maximum packing density was reached grain networks were eroded and dilated to extend the networks over a wider array of porosities. Computationally cheaper techniques allowed for more complex statistical descriptions (along with larger total geometries) to be used, including multi size component grain distributions. A set of various different synthetic images are shown in figure 1.

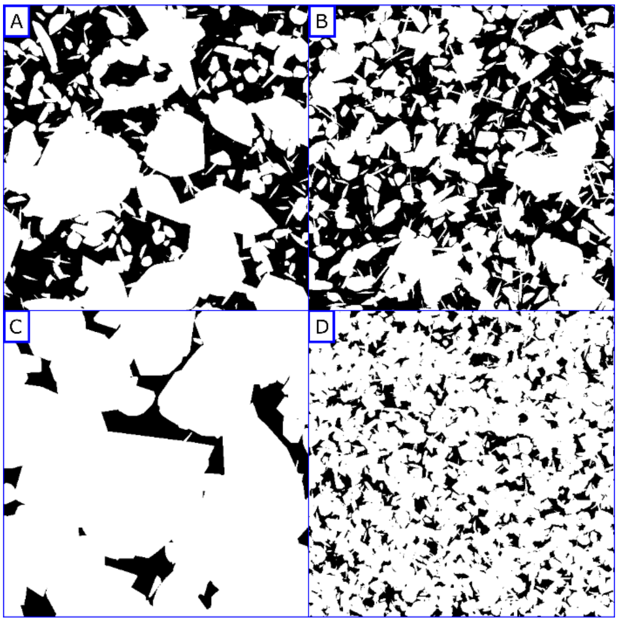

Figure 1 - A) A dual grain size system, with one grain population having a largest axis of 25μm and one population having a largest axis of 43μm. B) A dual grain size system, with one grain population having a largest axis of 22μm and one population having a largest axis of 35μm. C) A dual grain size system, with one grain population having a largest axis of 56μm and one population having a largest axis of 86μm. D) A single grain size system with a largest axis length of 19μm.

Structural statistics were calculated on a range of 2D slices through each 3D volume. It was decided  to make measurements in 2D rather than on the full 3D network as it was more computationally tractable (and trivially parallelizable) and allows for the same model to be applied on 3D networks (acquired with XRM and FIB-SEM) and 2D structures (such as those characterized using light or electron microscopy). The application of these techniques to 2D systems is an interesting target of future work, but beyond the scope of this paper. Inherent biases and errors associated with 2D rather than 3D measurements are inherently accounted for in the relative weightings of different measurements during statistical multivariant regression. Grains and pores were then separated using a watershed algorithm operating across an Euclidian distance map [35], [36], with object seeds filtered using the “h-maxima” algorithm (figure 2). While such a technique has its limitations when dealing with complex network geometries [37], relatively simple networks can be effectively characterized [38]. Perhaps more important was that a perfect granular separation was not required, just that any object separation errors were consistent between training and validation series of data. For example, differential errors in grain separation for systems with large grains (relative to the voxel size) relative to systems with smaller grains (relative to the voxel size) are implicitly accounted for by the large array of different grain sizes in the training set. The same errors will be present in both the training and the final (imaged) datasets, and therefore the impact of any errors on prediction will be minimized.

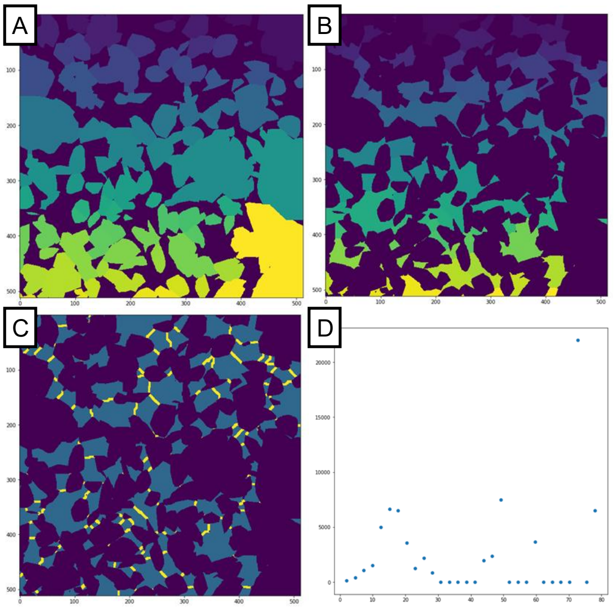

Figure 2 - Feature vector extraction. A) Grain separation. B) Pore separation. C) Throat identification (throats shown in yellow). D) Grain size distribution, showing a multimodal population distribution.

Once grains and pores were separated, population statistics were computed on features from these different populations, including grain, pore and pore throat sizes, shape averages, distributions, and network connectivity. This created a large (34 component) feature vector set for each network. The range of structural feature vectors (as well as their relative importance is shown in figure 3. The relative feature importance is defined as fraction of the decision tree associated with the permeability prediction decision tree [39], or the number of nodes in the decision graph associated with that feature. The 21 most important features had feature importances larger than 10% of the most important feature vector in the set (the standard deviation in the inscribed throat radius). Such a broad distribution in importances is an indication of both the complexity of the problem and the power of such a multivariant approach – a large number of different structural metrics are required to achieve a high quality prediction. An extensive evaluation of specific feature impacts in such a complex multivariant model, as well as an examination of the impact of changing numbers of input parameters and parameter selection on model performance would be an interesting target for future work. The requirement of the use of a large number of network characteristics is unsurprising, particularly given the requirement to make predictions using only features extracted in 2D. The goal for this approach is ultimately to generate a model which can be applied on 2D data (for example light or electron microscopy), and a greater exploration of this is the target for future work. It is likely that, should features be extracted in 3D, a more accurate prediction could be made, potentially with a smaller number of extractable features, but this model would not have the potential of being (ultimately) transferred to 2D analytical techniques.

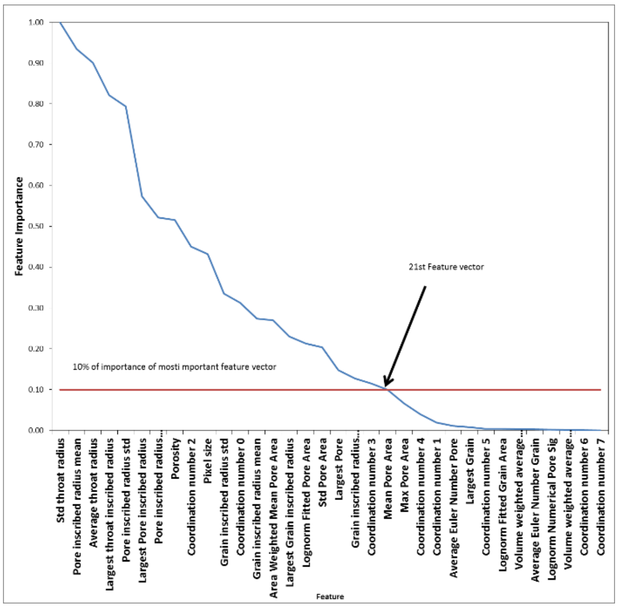

Figure 3 - distribution of feature vector importances.

It is interesting that the most important parameter (the parameter which is responsible for the greatest number of nodes in the forest of decision trees) is that of the standard deviation in inscribed pore throat radii. This corresponds to whether or not the porous medium is homogenous (has a uniform fluid velocity distribution) or heterogeneous (has a more channelized fluid flow distribution). As the flow rate is non-linearly sensitive to changes in throat size (equation 1, below) it is not surprising that the distribution in throat size has a strong control on flow rate. Similarly it is unsurprising that the second and third most important features are the average inscribed pore and pore throat radii respectively.

Flow was then simulated on each of these synthetic volumes using traditional digital rock techniques [40], giving the permeability for each network. Each of the synthetic networks had a nominal voxel size of 1µm; however, a much broader range of pore network statistics (with associated permeabilities) could be generated by examining analytical solutions to the Navier-Stokes equation within the viscous dominated regime (such as the Hagen-Poiseuille equation, equation 1)

$$\frac{\Delta P}{\Delta L} = \frac{8\mu}{r^2} v \qquad (1)$$

where $\Delta P/\Delta L$ is the pressure gradient, $\mu$ is the viscosity, r the pipe radius and v the (linear) fluid average velocity. For any (defined) structure, a Stokes flow solution to the Navier-Stokes equation will predictably scale as the square of the spatial length scale. As such any change in nominal voxel size (for a topologically and topographically defined network) should change permeability values similarly. An arbitrarily extended set of network statistics could therefore be created, scaling each (dimensioned) measure appropriately with the voxel size, and the permeability values with its square. An extended set of 219,000 network statistics were created using this technique, with nominal voxel sizes ranging from 10nm to 10um and predicted permeability values varying over 10 orders of magnitude (from from $10^{-25}$m$^{-2}$ to $10^{-7}$m$^{-2}$, with a 10-90 percentile range of $1.2\times10^{-18}$m$^{-2}$ – $9.25\times10^{-12}$m$^{-2}$) (figure 4).

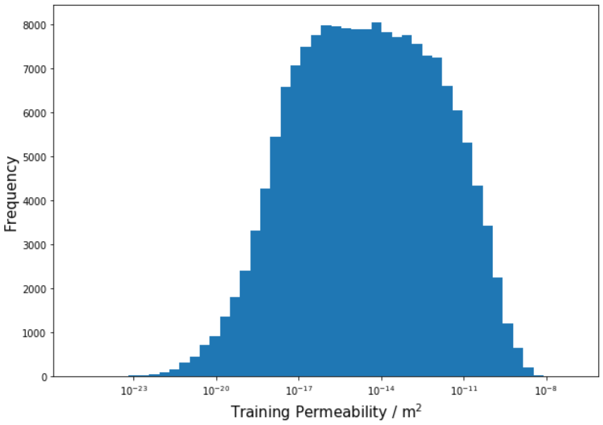

Figure 4 - distribution of training permeability values.

At first inspection it seems like such an approach adds little to the overall training dataset – they are just generated by extrapolation. The key to understanding its utility is that the regression is designed to be performed on real (measured) datasets with real pixel sizes. The same network will have different permeability values if you change its nominal voxel size, and any model must be trained on volumes spanning the entire range of pixel sizes of interest. One way to extend the pixel size range of the training set is to randomly assign pixel sizes, however this will decrease the training dataset density at any specific spatial length scale. Instead Hagen-Poiseuille extrapolation was used as it allows for all the training datasets to be available to the training algorithm at all spatial lengthscales.

## 3 Results and discussion

This extended dataset of multivariant structural statistics was split into "training" and "testing" sets (with 80% of the data belonging to the training set, and 20% belonging to the test set). The training set was then regressed against the natural logarithm of the permeability using open-source machine learning tools (www.scikit-learn.org) using a randomly seeded Extra-Trees (decision tree based) ensemble algorithm [41]. Total training time on a 40-core workstation was around 12 seconds. A natural logarithmic representation of permeability was used for regression as it allowed prediction errors to be evenly distributed across the entire range of permeability – a linear representation would have concentrated prediction errors strongly towards the largest permeabilities, overfitting these values and underfitting the rest of the dataset. Another way of viewing this is that a logarithmic representation essentially forces the algorithm to minimize fractional (rather than absolute) errors in the regression model. This model was then tested on the test set, finding a Root-Mean-Square-Fractional-Error (RMSFE) of <4% (figure 5).

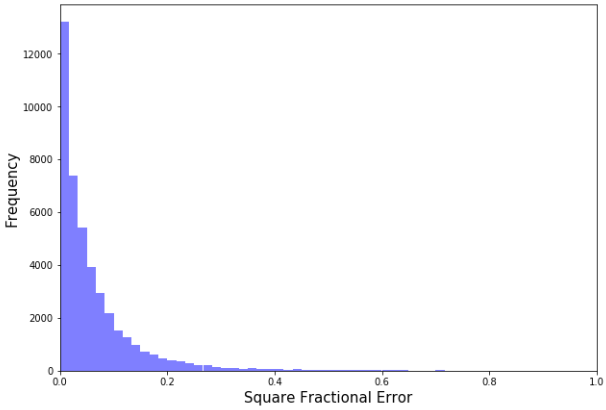

Figure 5 - Root Mean Square Fractional Error (RMSFE) distribution

One major question when applying this model (trained on synthetic networks) to real datasets is whether the synthetic images really represent real imaged pore networks. A composite set of real digital rock images to validate the predictive model for more general use. This composite set of 36 images consisted of a range of open source volumes taken from the Digital Rock Portal (www.digitalrocksportal.org), previously published data, and new nano-CT datasets from micritic carbonate microporosity. This constituted two qualitatively different pore networks (the intergranular pore networks common in sandstones and micritic microporosity common in dual porosity carbonate reservoirs. While there are significant differences in chemistry and scale for the networks, in both cases the grain networks consist of euhedral to sub-hedral sub-angular clasts, so they may have a similar relationship between pore structure and flow properties and have grains which are well represented by convex polyhedra.

The unsegmented datasets were segmented using state-of-the-art machine learning based segmentation [24] (Zen Intellesis). Flow was then simulated on each of the segmented datasets, with predicted permeabilities ranging over 6 orders of magnitude (10µD to 10D). These predictions were then compared with multivariant predictions with a RMSFE of <25% across the entire range (figure 6).

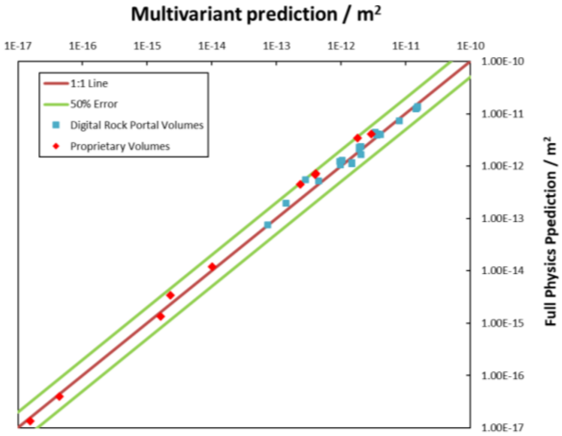

Figure 6 - correlation between simulated permeabilities and permeability predicted using multivariant regression.

Such a result is extremely encouraging – while the prediction error was higher in the (real) validation datasets than the (synthetic) test datasets, the prediction error was still relatively small. Predictions were accurate across multiple pore network types (both intergranular sandstone pore networks and micritic microporosity), and a wide range of length scales and permeability values.

This technique offers multiple advantages over both traditional (full physics) simulations and legacy estimation techniques. First, while analysing and simulating flow on the thousands of training images was computationally expensive, applying it to each imaged dataset was relatively cheap. As such it is significantly faster to apply than traditional techniques, with a large volume prediction taking less than a minute on standard lab computational resources, where a full physics simulation of the same result might take many hours. Perhaps the most important advantage of this technique, however, is it has the potential of greatly expanding the forms of data applicable to quantitative flow prediction, as the features used for both regression and prediction can be extracted in 2D as well as 3D. This allows for effective property prediction from structural analysis of 2D data (e.g. light or electron microscopy), which can be acquired over much larger areas (allowing a much better characterization of structural heterogeneity), can be acquired much faster, and offers qualitatively richer data (giving information about mineralogy, geochemistry or texture not present when using 3D imaging techniques).

A significant drawback to traditional techniques for permeability estimation (like Kozeny-Carman) is the challenging and arbitrary nature of the measurement of their constituent parameters [42]. A significant advantage of multivariant regression-based techniques is that all inherent errors in measurement are included when performing the regression - the minimization of the prediction error implicitly includes the minimization of the impact of any systematic measurement errors. The general approach for the prediction of effective medium properties based on multivariant structural statistics can be extended to other systems through the incorporation of either other synthetic pore network generation routines or re-enforcement learning with real (imaged) data. There is also significant scope for future development in the extraction of structural statistics, including the usage of multi-point statistical characterization [43] or recently developed persistent homology metrics [44]. Future work will focus on the examination of the usage of such large area predictive statistical techniques to validate and inform upscaling techniques, allowing for integration of multiple scales of data in single predictive models.

## 4 Conclusions

A novel method for permeability prediction using multivariant statistical regression is presented. Over 2,000 synthetic geometries were created by modelling granular media using convex polyhedral. Full physical simulations were performed on all of these datasets. The resulting permeability values were used as a target function for a high dimensional description of the volumes, created from structural statistics of rock grains, pores and throats. The regression model was trained with an error of less than 4% in the test data. Validation of this model was performed on a composite series of 36 independent datasets , taken from both an open source data source (www.digitalrocksportal.org) and proprietary data from carbonate microporosity. These datasets range in pore system from carbonate microporosity to intergranular sandstone pores, with pixel sizes ranging from 10µm to 32nm and permeabilities ranging over 6 orders of magnitude from 10µD to 10D. Predictions in this validation set showed a RMSFE of less than 25% over the entire range.

Differences in error between the validation and test data provide an interesting insight into the validity of the synthetic datasets in training multivariant models – while they do not perfectly represent real (imaged) data, they are close enough to accurately predict data across length scales. Interesting future work could focus on expanding the training dataset to include networks representative of other pore systems, either through an expansion of synthetic generation techniques or through the incorporation of real imaged geometries.

Such an approach to permeability prediction is extremely promising for addressing many problems associated with pore scale analysis of geological materials, particularly those associated with scale and heterogeneity. By reducing the relative computational complexity of simulation larger geometries can be efficiently analysed. Perhaps more exciting is the application of these tools (trained on 2D slices through 3D volumes) to other pore structural analytical technologies operating in 2D. These techniques are able to address much larger linear length scales, thereby enabling for a much more effective assessment of structural heterogeneity. They also allow for the incorporation of analytical information not accessible in 3D.

## Acknowledgements

I thank ZEISS microscopy and Math2Market Gmbh. for the equipment and software access required for this work. Many thanks to Dr. Hannah Menke for assistance in the preparation of this manuscript.

## References

1. G. Bruno, A. Efremov, B. Wheaton, I. Bobrikov, V. G. Simkin, and S. Misture, "Micro- and macroscopic thermal expansion of stabilized aluminum titanate," *J. Eur. Ceram. Soc.*, 2010.
2. G. Bruno *et al.*, "On the stress-free lattice expansion of porous cordierite," *Acta Mater.*, 2010.
3. P. R. Shearing, L. E. Howard, P. S. Jørgensen, N. P. Brandon, and S. J. Harris, "Characterization of the 3-dimensional microstructure of a graphite negative electrode from a Li-ion battery," *Electrochem. commun.*, 2010.
4. D. Kehrwald, P. R. Shearing, N. P. Brandon, P. K. Sinha, and S. J. Harris, "Local Tortuosity Inhomogeneities in a Lithium Battery Composite Electrode," *J. Electrochem. Soc.*, 2011.
5. R. Dann, M. Turner, M. Close, and M. Knackstedt, "Multi-scale characterisation of coastal sand aquifer media for contaminant transport using X-ray computed tomography," *Environ. Earth Sci.*, 2011.
6. H. P. Menke, M. G. Andrew, M. J. Blunt, and B. Bijeljic, "Reservoir condition imaging of reactive transport in heterogeneous carbonates using fast synchrotron tomography - Effect of initial pore structure and flow conditions," *Chem. Geol.*, vol. 428, pp. 15–26, 2016.
7. M. Andrew, B. Bijeljic, and M. J. Blunt, "Pore-by-pore capillary pressure measurements using X-ray microtomography at reservoir conditions: Curvature, snap-off, and remobilization of residual CO2," *Water Resour. Res.*, vol. 50, no. 11, pp. 8760–8774, 2014.
8. S. Iglauer, S. Favretto, G. Spinelli, G. Schena, and M. J. Blunt, "X-ray tomography measurements of power-law cluster size distributions for the nonwetting phase in sandstones," *Phys. Rev. E - Stat. Nonlinear, Soft Matter Phys.*, vol. 82, pp. 10–12, 2010.
9. M. J. Blunt *et al.*, "Pore-scale imaging and modelling," *Adv. Water Resour.*, vol. 51, pp. 197–216, 2013.
10. A. V. Ryazanov, K. S. Sorbie, and M. I. J. van Dijke, "Structure of residual oil as a function of wettability using pore-network modelling," *Adv. Water Resour.*, vol. 63, pp. 11–21, 2014.
11. J. Schmatz, J. L. Urai, S. Berg, and H. Ott, "Nanoscale imaging of pore-scale fluid-fluid-solid contacts in sandstone," *Geophys. Res. Lett.*, p. n/a-n/a, 2015.
12. D. Silin, L. Tomutsa, S. M. Benson, and T. W. Patzek, "Microtomography and Pore-Scale Modeling of Two-Phase Fluid Distribution," *Transp. Porous Media*, vol. 86, pp. 495–515, 2011.
13. H. Andrä *et al.*, "Digital rock physics benchmarks-part II: Computing effective properties," *Comput. Geosci.*, vol. 50, pp. 33–43, 2013.
14. T. Ramstad, N. Idowu, C. Nardi, and P. E. Øren, "Relative Permeability Calculations from Two-Phase Flow Simulations Directly on Digital Images of Porous Rocks," *Transp. Porous Media*, 2012.
15. I. Shikhov and C. H. Arns, "Evaluation of Capillary Pressure Methods via Digital Rock Simulations," *Transp. Porous Media*, 2015.
16. M. A. Knackstedt, S. Latham, M. Madadi, A. Sheppard, T. Varslot, and C. Arns, "Digital rock physics: 3D imaging of core material and correlations to acoustic and flow properties," *Lead. Edge*, 2009.
17. Y. Keehm, T. Mukerji, and A. Nur, "Computational rock physics at the pore scale: Transport properties and diagenesis in realistic pore geometries," *Lead. Edge*, 2002.
18. H. Andrä *et al.*, "Digital rock physics benchmarks-Part I: Imaging and segmentation," *Comput. Geosci.*, vol. 50, pp. 25–32, 2013.
19. P. C. Carman, "Fluid flow through granular beds," *Trans. Inst. Chem. Eng.*, vol. 15, pp. 150–166, 1937.
20. S. Kuwabara, "The Forces experienced by Randomly Distributed Parallel Circular Cylinders or Spheres in a Viscous Flow at Small Reynolds Numbers," *J. Phys. Soc. Japan*, 1959.
21. S. Mauran, L. Rigaud, and O. Coudevylle, "Application of the carman-kotenzy correlation to a high-porosity and anisotropic consolidated medium: The compressed expanded natural graphite," *Transp. Porous Media*, 2001.
22. P. N. Singh and W. W. Wallender, "Effects of Adsorbed Water Layer in Predicting Saturated Hydraulic Conductivity for Clays with Kozeny–Carman Equation," *J. Geotech. Geoenvironmental Eng.*, 2008.
23. L. Mosser, O. Dubrule, and M. J. Blunt, "Reconstruction of three-dimensional porous media using generative adversarial neural networks," *Phys. Rev. E*, 2017.
24. M. Andrew, "A quantified study of segmentation techniques on synthetic geological XRM and FIB-SEM images," *Comput. Geosci.*, vol. 22, no. 6, pp. 1503–1512, 2018.
25. O. Sudakov, E. Burnaev, and D. Koroteev, "Driving digital rock towards machine learning: Predicting permeability with gradient boosting and deep neural networks," *Comput. Geosci.*, vol. 127, pp. 91–98, 2019.
26. J. Bear, "Dynamics of Fluids in Porous Media," *Soil Sci.*, 2006.
27. P. S. Ringrose, a. W. Martinius, and J. Alvestad, "Multiscale geological reservoir modelling in practice," *Geol. Soc. London, Spec. Publ.*, vol. 309, no. 1, pp. 123–134, 2008.
28. M. Andrew, "Comparing organic-hosted and intergranular pore networks: topography and topology in grains, gaps and bubbles," *Geol. Soc. London, Spec. Publ.*, vol. 484, pp. SP484--4, 2018.
29. T. Phenrat, H. J. Kim, F. Fagerlund, T. Illangasekare, R. D. Tilton, and G. V. Lowry, "Particle size distribution, concentration, and magnetic attraction affect transport of polymer-modified Fe0 nanoparticles in sand columns," *Environ. Sci. Technol.*, 2009.

30. F. De Smedt and P. J. Wierenga, “Solute Transfer Through Columns of Glass Beads,” *Water Resour. Res.*, 1984.
31. P. E. Øren and S. Bakke, “Process based reconstruction of sandstones and prediction of transport properties,” *Transp. Porous Media*, vol. 46, no. 2–3, pp. 311–343, 2002.
32. S. Bakke and P.-E. Øren, “3-D Pore-Scale Modelling of Sandstones and Flow Simulations in the Pore Networks,” *SPE J.*, vol. 2, no. 02, pp. 136–149, 1997.
33. T. Lerdahl, P. E. Oren, and S. Bakke, “A predictive network model for three-phase flow in porous media,” *SPE/DOE Improv. Oil Recover. Symp.*, 2000.
34. P. A. Cundall, “Formulation of a three-dimensional distinct element model-Part I. A scheme to detect and represent contacts in a system composed of many polyhedral blocks,” *Int. J. Rock Mech. Min. Sci.*, 1988.
35. A. Rabbani, S. Jamshidi, and S. Salehi, “An automated simple algorithm for realistic pore network extraction from micro-tomography images,” *J. Pet. Sci. Eng.*, vol. 123, pp. 164–171, 2014.
36. M. G. Andrew, H. P. Menke, M. J. Blunt, and B. Bijeljic, “The Imaging of Dynamic Multiphase Fluid Flow Using Synchrotron-Based X-ray Microtomography at Reservoir Conditions,” *Transp. Porous Media*, vol. 110, pp. 1–24, 2015.
37. A. Q. Raeini, B. Bijeljic, and M. J. Blunt, “Generalized network modeling: Network extraction as a coarse-scale discretization of the void space of porous media,” *Phys. Rev. E*, vol. 96, no. 1, 2017.
38. H. Dong and M. J. Blunt, “Pore-network extraction from micro-computerized-tomography images,” *Phys. Rev. E - Stat. Nonlinear, Soft Matter Phys.*, vol. 80, no. 3, 2009.
39. Gilles Louppe, “Understanding Random Forests: From Theory to Practice,” 2014.
40. S. Linden, A. Wiegmann, and H. Hagen, “The LIR space partitioning system applied to the Stokes equations,” *Graph. Models*, vol. 82, pp. 58–66, 2015.
41. P. Geurts, D. Ernst, and L. Wehenkel, “Extremely randomized trees,” *Mach. Learn.*, 2006.
42. H. P. Menke, Y. Gao, S. Linden, and M. G. Andrew, “Using nano-XRM and high-contrast imaging to inform micro-porosity permeability during Stokes-Brinkman single and two-phase flow simulations on micro-CT images,” *Adv. Water Resour.*
43. H. Okabe and M. J. Blunt, “Prediction of permeability for porous media reconstructed using multiple-point statistics,” *Phys. Rev. E - Stat. Physics, Plasmas, Fluids, Relat. Interdiscip. Top.*, 2004.
44. A. L. Herring, V. Robins, and A. P. Sheppard, “Topological Persistence for Relating Microstructure and Capillary Fluid Trapping in Sandstones,” *Water Resour. Res.*, 2019.

# A fast FFT method for 3D pore-scale rock-typing of heterogeneous rock samples via Minkowski functionals and hydraulic attributes

*Han* Jiang[1] and *Christoph H.* Arns[1,*]

[1]UNSW, School of Minerals & Energy Resources Engineering, Sydney 2052 NSW, Australia

**Abstract.** The integration of numerical simulation and physical measurements, e.g. digital and conventional core analysis, requires the consideration of significant sample sizes when heterogeneous core samples are considered. In such case a hierarchical upscaling of properties may be achieved through a workflow of partitioning the sample into homogeneous regions followed by characterization of these homogeneous regions and upscaling of properties. Examples of such heterogeneities are e.g. fine laminations in core samples or different micro-porosity types as consequence of source rock components and diagenesis. In this work we utilize regional measures based on the Minkowski functionals as well as local saturation information derived through a morphological capillary drainage transform as a basis for such a classification/partitioning. An important consideration is the size of the measurement elements utilized, which could be considerable in the case of larger heterogeneities; in such case the calculation of the regional measures can be computationally very expensive. Here we introduce an FFT approach to calculate these measures locally, utilizing their additivity. The algorithms are compared against direct summation techniques and shift-overlap approaches for a selection of different averaging supports to illustrate their speed and practical applicability. We consider a range of artificial Boolean models to illustrate the effect of including hydraulic information on the resulting classifications scheme. This allows the determination of bias, since for these model systems local classes are known ab-initio. The classification framework is tested by comparing to the known initial micro-structure distribution and relative bias quantified in terms of choice of averaging elements (size and shape). Importantly, depending on the actual morphological transition between micro-type partitions, partitions including hydraulic attributes differ from pure morphological partitions with applications to electrofacies and hydraulic unit definitions.

## 1 Introduction

Rock type classification is an important topic in reservoir characterization and spans a large range of scales from seismic interpretation (meter scale [1]) to well logging (down to centimeter scale [2]) and further down in scale to core analysis. It forms part of an upscaling strategy involving the correlation of classes of different type, purpose, or origin; e.g. lithofacies vs. electrofacies (distinguishable classes based on well-logs). However, reservoir heterogeneity extends to even smaller scales.

The rapid development of (micro-) X-ray CT techniques exposes rock heterogeneity down to the order of microns, at the pore-scale, in 3D. While the calculation of petrophysical properties and correlations has been demonstrated for a range of properties including e.g. electrical conductivity, elastic moduli, mercury intrusion capillary pressure, and permeability [3]-[7], this is for homogeneous sandstones of limited clay content. For more complex carbonates cross-variograms between porosity and permeability and multiple imaging length scales [8] may be utilized. Often one may however want to utilize a hierarchical upscaling approach based on core-scale rock-types to integrate several length scales and multiple physical properties, including for thinly laminated sandstones. While petrophysical rock-types may include such laminations and thus anisotropy caused, describing fluid flow leads to a homogenization problem which can be approached at the Darcy scale [9], or numerically through partial homogenization [10] by solving the Brinkmann equation. Either way, a classification technique for scale separation is required.

Classification techniques targeting petrophysical interpretation are not new. Archie developed a method of skeleton classification with a few petrophysical parameters in [11]. Skalinski and his colleagues used pore throat distributions as the main parameter for pore type classification with mercury injection pressure measurement data of many rock samples [12]. Characteristics of fractures and vugs of carbonate rocks were extracted from micro-CT images in [13]. Dernaika et al. [14] calculated porosity and mineralogy of core samples from advanced dual energy XCT imaging and linked to plug data after upscaling.

Schmitt and colleagues considered pore shapes (length, width, thickness, orientation) in reservoir rock from 3-D X-ray micro-CT images [15], limiting themselves to large pores due to the higher resolution

---

[*] Corresponding author: c.arns@unsw.edu.au

requirements for deriving these measures. Alternately, one may characterize microstructure utilizing the additive morphological measures volume, surface area, mean and total curvature, namely the Minkowski functionals [16], which can be evaluated easily on a segmented tomogram [17], [18] and have been used in the past as sensitive descriptors of morphology [17]-[22]. The strong correlation of physical properties of Boolean models to morphological properties, the Minkowski functionals [23],[24], motivates the use in rock-typing approaches. This was done in [25] for a thinly laminated sandstone using a 1D sliding measuring window approach and in 3D using non-overlapping regions of the image. A high-resolution field of morphological regional measure could not be computed due to computational cost. In [26] a support shift technique was utilized for the computations, which however still does not scale to large supports, as we require in this work. We define as support of a measurement a small (regional) volume within the sample, and over which an average is taken. A larger support is desirable to reduce the standard deviation of such a measure.\\

Another relationship often used in rock-typing approaches is given by mercury intrusion capillary pressure (MICP) curves [27]. In terms of micro-CT approaches this type of information can be gained either by direct imaging approaches [28], or by modeling the MICP process numerically [29],[30]. Capillary pressure heterogeneity was also inferred from regional saturation distributions in [31], while [32] considered non-wetting phase cluster distributions.

The resulting question we target in this work is whether the inclusion of hydraulic information – taken to be local fluid saturation – changes rock-types defined on the basis of the Minkowski functionals alone as basis for petrophysical rock-types due to their strong relationship to physical properties. We utilize the decomposition of the Minkowski functionals into histograms over vertex configurations to implement (fast) calculations of the Minkowski measures over large support via Fast Fourier Transforms (FFTs). The technique is compared against more direct implementation schemes on a set of artificial microstructures and applied to the classification of laminated Boolean composites. Classifications based on the Minkowski measures alone are compared with ones including a saturation attribute and resulting bias is discussed.

## 2 Methodology

In this section we review the basic techniques utilized in this work. We introduce the Minkowski functionals and measures as a full set of additive measures of 3D space, regional measures based on these definitions over a finite support, as well as resulting curvature density fields and algorithms to calculate them. Finally, for demonstration of the algorithms we introduce a set of Boolean composites featuring forming layered media.

### 2.1 Minkowski functionals

In this work we follow the notation of [26]. Consider a body $Y$ in $\mathbb{R}^3$ with sufficiently smooth surface $\partial Y$. Then the additive geometrical characteristics are volume $V(Y)$, surface area $S(Y)$, integral of mean curvature $M(Y)$ and integral of total curvature $K(Y)$ with surface integrals

$$\begin{aligned} S(Y) &= \int_{\partial Y} ds\,, \\ M(Y) &= \int_{\partial Y} \frac{1}{2}\Big(\frac{1}{r_1(s)} + \frac{1}{r_1(s)}\Big)\, ds\,, \\ K(Y) &= \int_{\partial Y} \frac{1}{r_1(s)\, r_2(s)}\, ds\,. \end{aligned} \tag{1}$$

Here $r_1(s)$ and $r_2(s)$ are the maximum and minimum curvature radii in $s$. The above characteristics are related to the intrinsic volumes via

$$\begin{aligned} V_0(Y) &= \frac{1}{4\pi}K(Y)\,, \\ V_1(Y) &= \frac{1}{\pi}M(Y)\,, \\ V_2(Y) &= \frac{1}{2}S(Y)\,, \\ V_3(Y) &= V(Y)\,. \end{aligned} \tag{2}$$

On the segmented tomogram the intrinsic volumes can be determined by evaluating the histogram of the individual vertex configurations. Excellent illustrations of this process have been given in [17], [33]. Here we consider the grain phase as the phase of interest; all other phases are merged for this calculation and the characteristic function of the structure takes the value of 1 for the granular phase and 0 otherwise. A vertex made up of eight voxels can then be in $2^8 = 256$ different configurations, where each configuration has a certain contribution to volume, surface area, mean, and total curvature. Lookup tables for these contributions has been given in [17], [33]. We use the 8-neighbourhood for 2D connectivity and 26-neighbourhood for 3D connectivity as given in [17]. For a recent review of the applications of integral geometry in porous media see [19].

### 2.2 Regional curvature measures

To define a measure over a finite volume we consider the average over regions of spherical and ellipsoidal shape. For a given position of this support in the actual tomographic images we then evaluate all vertices of the discrete tomogram, where the centers of the vertices are within the measurement window.

Consequently, the regional measures can then be derived from the local configuration histogram over the given spatial support. Evaluating the regional measures for a regular grid of support vectors will generate a set of morphological fields *V(**r**), S(**r**), M(**r**), K(**r**)*. We report all measures as curvature densities, e.g. normalized by the averaging volume.

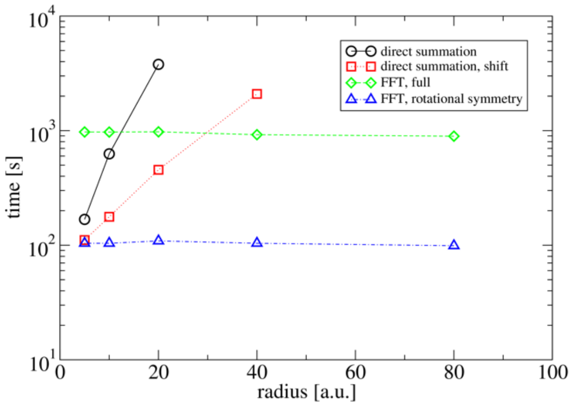

**Fig. 1.** Computational times for the Minkowski measure field generation for a $400^3$ sub-volume of a segmented Bentheimer sandstone sample as function of radius of a spherical support (radius in voxel, single processor).

### 2.2.1 *Curvature density fields by direct summation*

The most direct approach for calculating the curvature density fields simply places the spatial support at a position-of-interest, evaluates the configuration histogram, and stores the result at the respective position, looping over the curvature measure grid. For dense strides of the support this leads to significant overlap of support volumes for adjacent evaluations; thus, large numbers of vertices are evaluated multiple times for large measurement support, e.g. large radii of a spherical support. This naïve approach therefore does not scale well with increasing support size, as it scales with support volume.

### 2.2.2 *Curvature density fields by support-shift algorithms*

A somewhat more efficient way recognizes this partial support overlap and only evaluates vertices anew which are added to the support volume after a shift on the lattice, e.g. stride along a lattice direction with a fixed step size; the same number of vertices will be removed and added from the histogram for each support shift when shifting in the same direction. This approach scales significantly better, and essentially scales with the surface "area" of the support for small strides; it takes direct advantage of the additivity of the Minkowski measures.

### 2.2.3 *Curvature density fields by FFT methods*

The additivity of the curvature measures allows a much more efficient approach to deriving regional measures. This approach utilizes a convolution of the support with the vertex configuration field, thus deriving the curvature density fields by a series of Fast Fourier Transforms (FFTs) and adding up the curvature contributions to each regional measure according to the lookup table of [17]. In this case the size of the support has essentially no influence on the speed of the algorithm. Very large support volumes and arbitrary support shapes can be utilized this way.

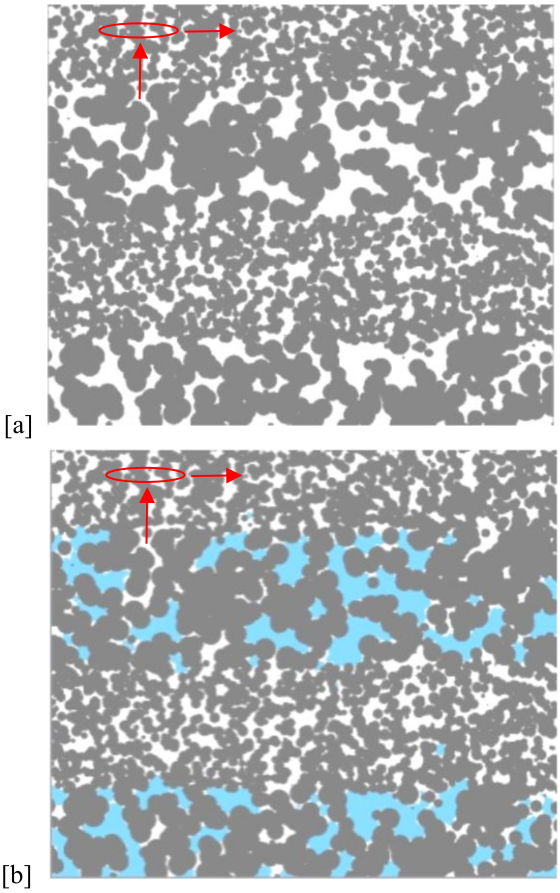

**Fig. 2.** 2D slice through a layered Boolean model with two generating sphere processes, one for each layer. [a] generated microstructure, [b] microstructure partially saturated by a non-wetting phase with invasion radius $r_i = 6.6$. Sphere radii are $r_1 = 13$ and $r_2 = 26$. The microstructure has dimensions of 1200 x 1000 x 800 voxels after removal of boundary regions in arbitrary units. Blue denotes the invading non-wetting phase.

A comparison of the relative performance of the algorithms is given in Fig. 1 for a sub-volume of a segmented tomogram of Bentheimer sandstone. Clearly, using large averaging volumes becomes very costly with the non-FFT based algorithms applied here, while the FFT approach scales well, e.g. is independent of averaging volume. A significant speedup of the FFT method can be achieved by utilizing the rotational symmetry of the possible vertex configurations [17]. For the FFT method we consider both spherical and ellipsoidal measure supports. In practice the size and shape of the measurement support may be chosen through structural analysis, utilizing variograms [26], and considering that the resulting rock-types should be compact, e.g. do not have too many holes. Due to additivity and the availability of parallel FFT libraries for various architectures the proposed technique easily scales to largest datasets.

## 2.3 Boolean model

We generate layered synthetic micro-structures by controlling the generating grains of a Boolean (or Poisson particle) process according to an initial (known) layered distribution of two rock-types: after choosing a **Table. 1**

Structural details of dry sample in Figure 2. The generating shape for both layers is spheres.

| Formation | Thickness (voxel) | Porosity | Particle Radius (voxel) |
|---|---|---|---|
| **Layer 1** | 300 | 0.242 | 13 |
| **Layer 2** | 300 | 0.244 | 26 |

random location to place a particle the particle shape and size is decided by the corresponding pre-defined rock-type: Similar microstructure modeling approaches were presented in [10], [25], [30] for a more general 3D case, which was not required here for the demonstration of the technique. Placing a spherical particle of radius *r* at a random location results in a decrease of porosity. Particles can overlap into adjoining rock-types and the particle placement process is stopped when both rock-types achieve their target porosity. A 2D slice through a 3D realization of a Boolean layered system with two different sphere sizes of $r_1 = 13$ voxels and $r_2 = 26$ voxels is given in Fig. 2a. The structure parameters are summarized in Table 1.

### 2.4 Simulated non-wetting fluid invasion

We model the invasion of the synthetic rock with a non-wetting fluid by utilizing the capillary drainage transform [7], [24] with a fixed saturation chosen to provide additional contrast between the different rock-types. This is achieved by selecting an invasion radius below the critical radius of percolation for the larger-scale porosity, but above the critical radius of percolation for the smaller-scale porosity. A 2D slice through the saturated medium at $S_w = 0.38$, corresponding to an invasion radius of $r_i = 6.6$ is given in Fig. 2b. The critical radii for the two sphere composites making up the layers are $r_{c1} = 4$ and $r_{c2} = 9$. Note that the original samples were 1600 x 1200 x 1600 voxels. We selected the inner 1200 x 1000 x 800 region for further analysis in order to avoid boundary effects resulting from simulated capillary pressure fluid distributions.

### 2.5 Rock-type classification

We carry out the classification into different rock-types on the regional curvature measures and saturation field. This is achieved by defining the centroids of a Gaussian Mixture Model (GMM) in a supervised way by selecting the central zones of the layers as can be seen visually. The GMM centroids have cross-variance matrices of size 4 x 4 each (curvature measures only) or 5 x 5 (including saturation), which together with the respective means are derived upfront from statistics of unambiguous regions.

## 3 Results

The application of an ellipsoidal measurement support with half-axes of a=120, b=30, c=120 and resulting curvature and saturation fields is given in Fig. 3. The averaging support size and shape was chosen to avoid generating holes in the resulting classification and respecting the evident layering. The corresponding histograms of the regional measures are given in Fig. 4. Recall that the porosity of the two rock-types is essentially the same. Consequently, there is no real contrast in the solid volume measure (Fig. 4a). The different color scales (Fig. 3b) are a consequence of different grain sizes, the larger structure showing the more extreme values. We observe a clear separation of rock-types in the surface area density as one would expect (Fig. 3c, Fig. 4b), with small spheres corresponding to the larger surface area contributions. The 2D slice illustrates the strong layering detected by surface area, while the histogram illustrates a good separation with a moderate area one could interpret as overlap region. An equally sharp contrast in layers is visible in Fig. 3d, corresponding to mean curvature. The smaller values (larger in magnitude) correspond to the small spheres. The corresponding histogram (Fig. 4c) shows an excellent separation with only a small area between peaks. Consider now the total curvature measure (Fig. 3e, Fig. 4d). The smaller sphere regions show a stronger connected behavior expressed by the more negative total curvature measure. Compared to this, the larger sphere regions exhibit a negative peak suggesting connectivity of both phases, but with some values becoming positive. Even larger measurement supports may lead to an even better separation of layers for this measure. Finally, the saturation field offers an approach to generate contrast between different rock-types by capillary pressure, here in a static sense; we consider this a hydraulic attribute for rock-typing. The measure is potentially attractive for low resolution image classification as such contrast can be generated either by simulation or by actual differential tomographic imaging (dry & wet imaging). From the 2D cross-section of the saturation map we observe that for the given invasion radius the rock-type with smaller features remains largely fully saturated with wetting fluid, with some exceptions close to the boundary, making the interface between rock-types less consistent (Fig. 3f). The corresponding histogram shows a huge spike for $S_w = 0$ (truncated), and a somewhat distributed peak with a significant transition zone otherwise.

The distribution of the curvature and saturation measures is further summarized in Fig. 5 through a 1D profile. We emphasize that the procedures introduced here are general for 3D; however, given the special nature of the laminated samples it is logical to also provide a corresponding 1D log.

Consider now the resulting rock-type classifications of the laminated microstructure for the case of the ellipsoidal measurement support of a=c=120 voxel and b=30 voxel via the GMM procedure. We illustrate the sharpness of the boundary both by taking 2D slices perpendicular to the bedding direction (Fig. 6) and by illustrating the resulting classification as 1D log (Fig. 7). For the case of using the Minkowski measures only as basis for the classification the recovered interface between the rock-types is sharp and coincides well with the original interface. Adding water saturation to the classification basis results in a somewhat smoother

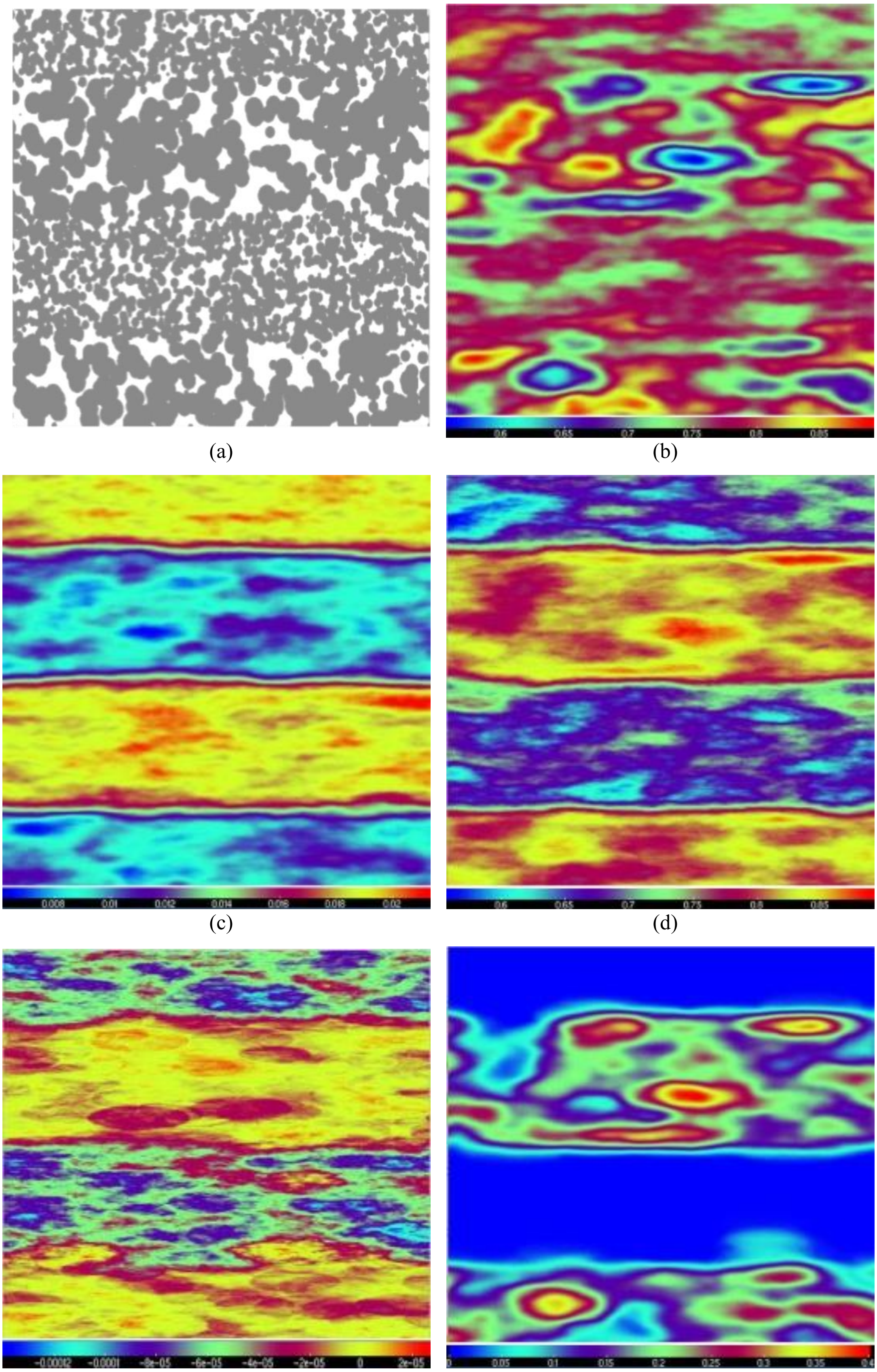

(a) (b)

(c) (d)

(e) (f)

**Fig. 3.** 2D-cuts through fields of the regional Minkowski measures and hydraulic property. The averaging support is of ellipsoid shape with half-axes of a=120, b=30 and c=120 voxels. (a) original sample, (b) solid volume solid, (c) surface area, (d) integral of mean curvature, (e) integral of total curvature, and (f) fluid saturation over total volume. All volumes are 960 x 940 x 560 voxels corresponding to all locations where the full size of the measuring window is contained within the sample (see also Fig. 2). Scales are given at the bottom of the figures; for distribution of the values in (b-f) see Fig. 4.

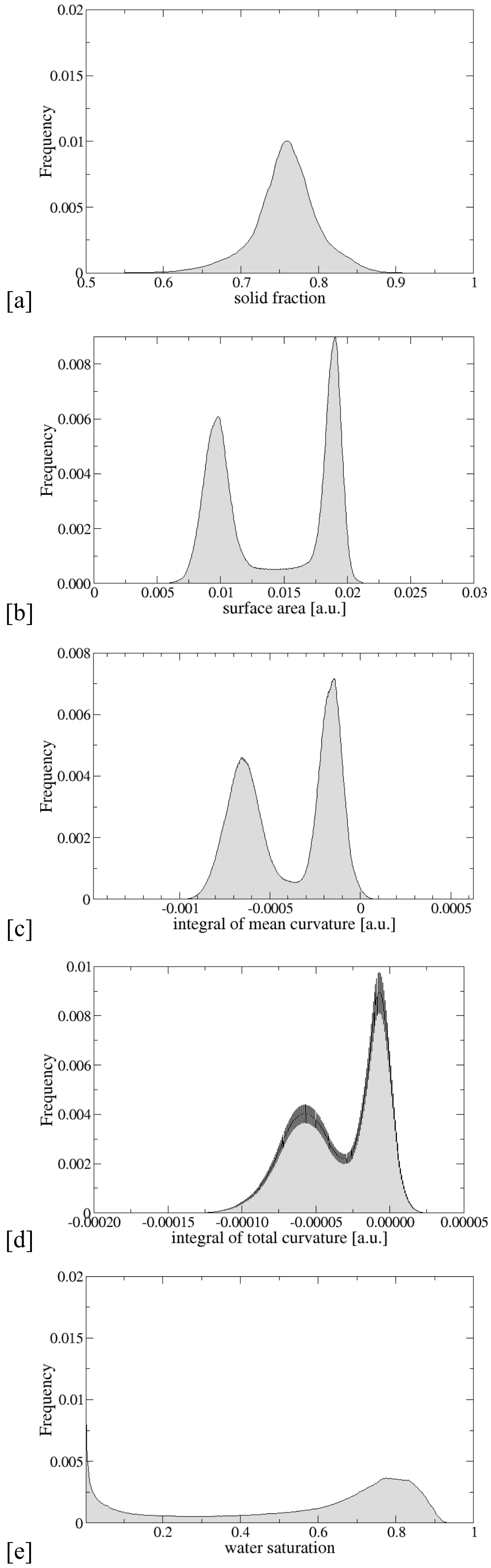

**Fig. 4.** Regional curvature measure and saturation distribution functions for the Boolean layered model. Ellipsoidal averaging element with a=c=120 voxels and b=30 voxels. [a] Solid volume, [b] surface area, [c] mean curvature, [d] total curvature, [e] defending phase saturation (point at zero saturation of 0.16 is truncated, e.g. of the scale).

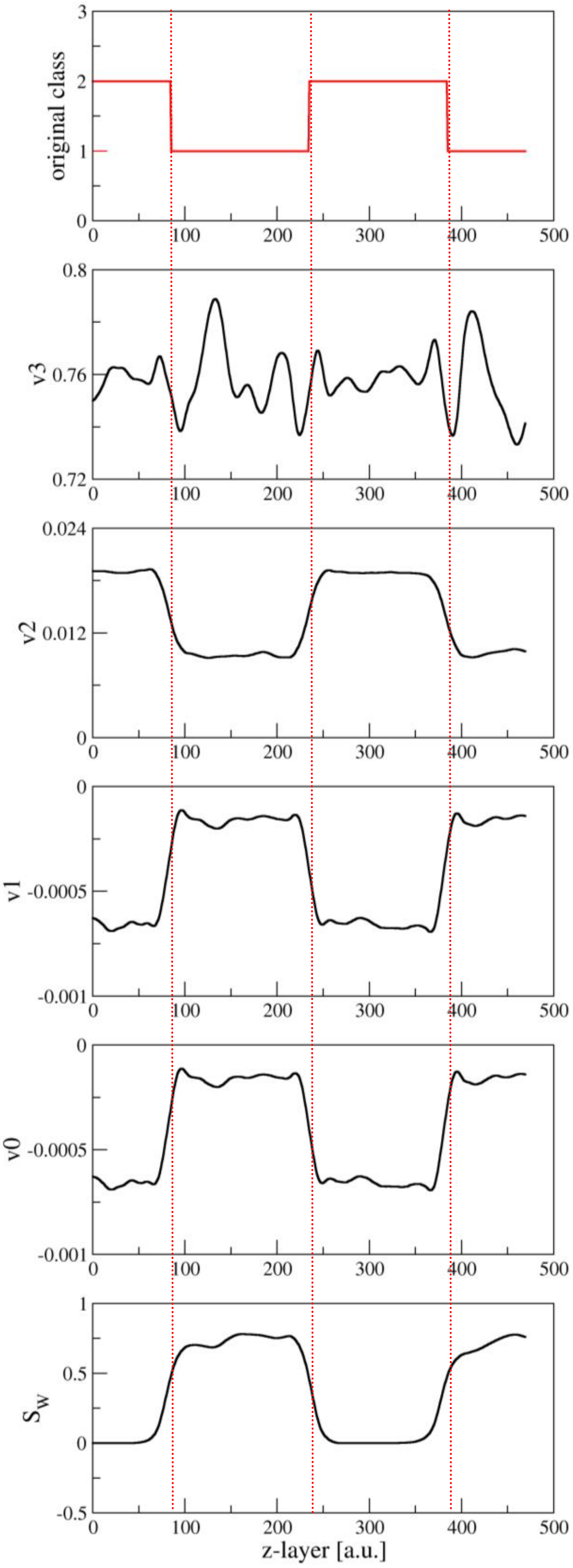

**Fig. 5.** Profile of the curvature and saturation measures along the y-dimension, e.g. averages over slices parallel to the layering. Ellipsoidal averaging element with a=c=120 voxels and b=30 voxels. The red lines indicate the actual rock types and their boundaries. For a cut through the corresponding 3D fields of regional measures in color see Fig. 3b-f. All measures are given in lattice units.

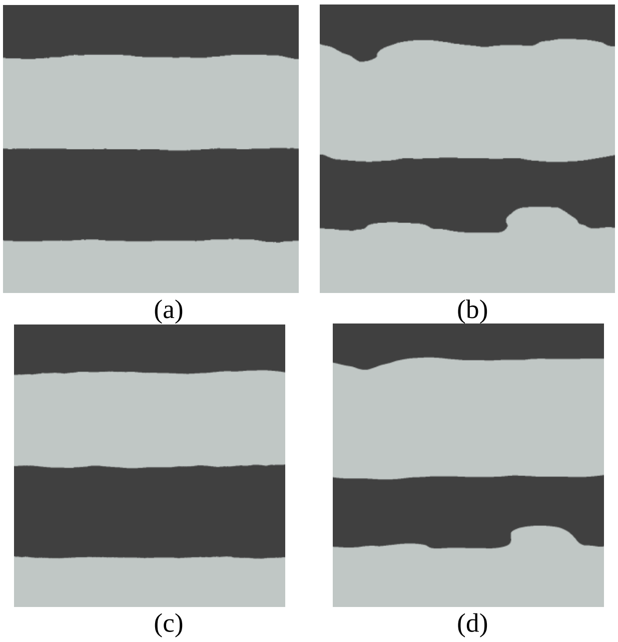

**Fig. 6.** 2D slices through the recovered layer systems from morphological descriptors and fluid saturation with different measuring window size. *Left:* classification based on Minkowski descriptors only. *Right:* combination of Minkowski descriptors and fluid saturation. (a,b) ellipsoidal averaging elements with a=c=120 and b=30 voxels, (c,d) a=c=160 voxels and b=40 voxels.

transition of the rock-types; furthermore, an apparent bias in the position of the boundary is introduced. We attribute this to an internal invasion boundary condition, e.g. a pore-scale saturation transition zone. This interpretation is supported by Fig. 6b and Fig. 6d, showing local misclassifications likely due to local heterogeneities in structure, allowing invasion of the boundary at lower capillary pressure. This local variation in saturation is also evident in Fig. 7.

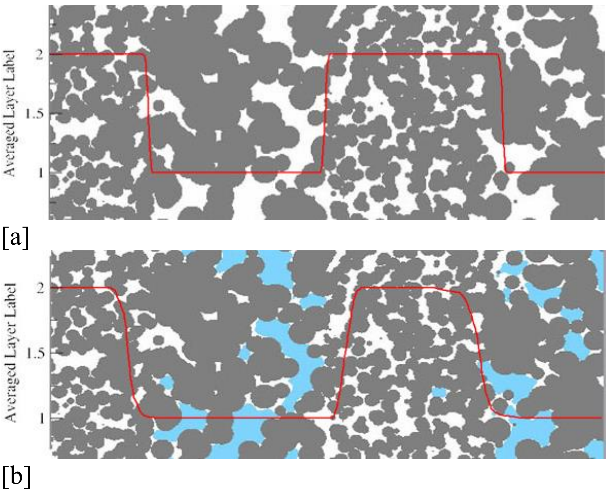

**Fig. 7.** 2D slices through the recovered 3D layer type distribution along Y dimension, overlapping original sample. The curve in (a) is recovered from the four Minkowski descriptors while (b) is recovered from Minkowski descriptors and fluid saturation. The blue color depicts the non-wetting phase saturation calculated by a MICP simulation.

We further quantify the relative boundary bias by scanning through each x-z column along the y-axis, calculating both the mean and standard deviation of the interface location for the case two different averaging element sizes and the Minkowski measures only versus including water saturation as additional hydraulic discriminator. The respective measures are reported in Table 2. The curvature measures alone recover the thickness of all layers almost exactly for both averaging ellipsoidal supports (b = 30 and b = 40, a = c = 4b). There is little variation in the location of the interface as well, e.g. no significant undulations are introduced, which is visible in the small standard deviation. Adding water saturation to the classification basis increases standard deviation significantly and introduces considerable bias towards the larger-scale rock-type.

**Table 2.** Boundary information of different descriptors under various window sizes.

| b | | | Layer 1 | Layer 2 | Layer 3 | Layer 4 |
|---|---|---|---|---|---|---|
| 30 | Original | | 170 | 300 | 300 | 170 |
| | MFs | Mean | 168 | 298 | 300 | 173 |
| | | Std | 4 | 6 | 6 | 10 |
| | MFs + Sw | Mean | 132 | 367 | 225 | 216 |
| | | Std | 7 | 9 | 15 | 17 |
| 40 | Original | | 160 | 300 | 300 | 160 |
| | MFs | Mean | 155 | 299 | 293 | 172 |
| | | Std | 15 | 29 | 29 | 72 |
| | MFs + Sw | Mean | 122 | 374 | 220 | 204 |
| | | Std | 16 | 33 | 29 | 63 |

## 4 Conclusions

In this work we introduced a fast FFT based algorithm for the calculation of regional curvature fields in 3D for the case of large measurement supports. The algorithm was demonstrated on a layered Boolean microstructure mimicking a laminated sandstone. It provides linear scaling with sample size and does not depend on the spatial support size. This allows the use of large spatial supports for rock-typing purposes utilizing the Minkowski functionals.

We further illustrated the classification bias introduced by including hydraulic information into the classification basis. For the given model rock, the strongest discriminator in terms of interface sharpness was regional mean curvature, followed by regional surface area. Including hydraulic information into the classification basis resulted in a smoother boundary transition which overestimated the relative fraction of the larger scale porosity.

CHA thanks the Australian Research Council (ARC) for funding through grant DP160104995 and through an ARC Future Fellowship (FT120100216). HJ and CHA thank the Chinese Scholarship Council (CSC) for their support. This research was undertaken with the assistance of resources and services from the National Computational Infrastructure (NCI), which is supported by the Australian Government. We thank reviewers Ryan Armstrong and Steffen Berg for a careful review, which further improved the quality of this manuscript.

## References

1. W. Xu, T. Tran, R. Srivastava, A. G. Journel, et al., Srivastava, R. M. "Reservoir characterization with probability field simulation," in *Proc. SPE Annu. Tech. Conf. Exhib,* Society of Petroleum Engineers, 1992.
2. M. Pirrone, A. Battigelli, L. Ruvo, et al., "Lithofacies Classification of Thin-Layered Turbidite Reservoirs Through the Integration of Core Data and Dielectric-Dispersion Log Measurements," *SPE Reservoir Eval. Eng.*, vol. 19, no. 2, pp. 226-238, Apr. 2016, Art. no. SPE-170748-PA.
3. C. H. Arns, M. A. Knackstedt, M. V. Pinczewski, and W. Lindquist, "Accurate estimation of transport properties from microtomographic images," *Geophysical Res. Lett.*, vol. 28, no. 17, pp. 3361-3364, Sep. 2001.
4. C. H. Arns, M. A. Knackstedt, W. V. Pinczewski, and E. J. Garboczi, "Computation of linear elastic properties from microtomographic images: Methodology and agreement between theory and experiment," *Geophys.*, vol. 67, no. 5, pp. 1396-1405, Sep. 2002.
5. C. H. Arns, M. A. Knackstedt, W. V. Pinczewski, and N. S. Martys, "Virtual permeametry on microtomographic images," *J. Petroleum Sci. Eng.*, vol. 45 no. 1-2, pp. 41-46, Nov. 2004.
6. J. Fredrich, A. DiGiovanni, and D. Noble, "Predicting macroscopic transport properties using microscopic image data." *J. Geophysical Res.: Solid Earth*, vol. 111, no. B3, Mar. 2006.
7. C. H. Arns, M. A. Knackstedt, and N. S. Martys, "Cross-property correlations and permeability estimation in sandstone," *Phys. Rev. E*, vol. 72, no. 4, pp. 046304, Oct. 2005.
8. A. Dehghan Khalili, J.-Y. Arns, F. Hussain, Y. Cinar, W.V. Pinczewski, and C.H. Arns, "Permeability upscaling for carbonates from the pore-scale using multi-scale Xray-CT images," *SPE Reservoir Eval. Eng.*, vol. 16, no. 4, pp. 353, Mar. 2012.
9. A. Fadili, and R. Ababou, "Dual homogenization of immiscible steady two - phase flows in random porous media," *Water Resour. Res.,* vol. 40, no. 1, pp. 1-18, Jan. 2004.
10. S. Norouzi Apourvari and C. H. Arns, "Image-based relative permeability upscaling from the pore scale," *Adv. Water Resour.*, vol. 95, pp.161-175, Sep. 2016.
11. G. E. Archie, "Classification of carbonate reservoir rocks and petrophysical considerations," *AAPG Bull.*, vol. 36, no. 2, pp. 278-298, Feb. 1952.
12. M. Skalinski, J. Kenter, S. Jenkins, et al., "Rock type definition and pore type classification of a carbonate platform, Tengiz Field, Republic of Kazakhstan," in *Proc. SPWLA 50th Annu. Logging Symp.,* Society of Petrophysicists and Well-Log Analysts, 2009, SPWLA-2009-62185.
13. B. Li, X. Tan, F. Wang, P. Lian, W. Gao, and Y. Li, "Fracture and vug characterization and carbonate rock type automatic classification using X-ray CT images," *J. Petroleum Sci. Eng.*, vol. 153, pp. 88-96, May. 2017.
14. M. Dernaika, Y. N. Uddin, S. Koronfol, O. Al Jallad, G. Sinclair, Y. Hanamura, K. Horaguchi, et al., "Multi-scale rock analysis for improved characterization of complex carbonates," in *Proc. SPE Reservoir Characterisation Simul. Conf. Exhib.,* Society of Petroleum Engineers, 2015, SPE-175598.
15. M. Schmitt, M. Halisch, C. M¨uller, and C. P. Fernandes, "Classification and quantification of pore shapes in sandstone reservoir rocks with 3-D X-ray micro-computed tomography," *Solid Earth,* vol. 7, no. 1, pp. 285-300, Feb. 2016.
16. K. R. Mecke, T. Buchert, and H. Wagner, "Robust morphological measures for large-scale structure in the universe," *arXiv preprint astro-ph/9312028*, Dec. 1993.
17. C. H. Arns, M. A. Knackstedt, W. V. Pinczewski, and K. R. Mecke, "Euler-Poincaré characteristics of classes of disordered media," *Phys. Rev. E*, vol. 63, no. 3, pp. 031112, Feb. 2001.
18. C. Arns, M. Knackstedt, and K. Mecke, "3D structural analysis: sensitivity of Minkowski functionals," *J. Microsc.,* vol. 240, no. 3, pp. 181-196, Dec. 2010.
19. R. T. Armstrong, J. E. McClure, V. Robins, et al., "Porous Media Characterization Using Minkowski Functionals: Theories, Applications and Future Directions," *Transport in Porous Media,* pp. 1-31, Nov. 2018.
20. J. Schmalzing and K. M. G´orski, "Minkowski functionals used in the morphological analysis of cosmic microwave background anisotropy maps," *Monthly Notices Roy. Astronomical Soc.*, vol. 297, no. 2, pp. 355-365, Jun. 1998.
21. C H Arns, MA Knackstedt, KR Mecke, "Characterisation of irregular spatial structures by parallel sets and integral geometric measures," *Colloids and Surfaces A: Physicochemical and Engineering Aspects,* vol. 241, no. 1-3, pp. 351-372, Jul. 2004.
22. S. Winitzki and A. Kosowsky, "Minkowski functional description of microwave background Gaussianity," *New Astron.*, vol. 3, no. 2, pp. 75-99, Mar. 1998.
23. C. H. Arns, M. A. Knackstedt, and K. R. Mecke, "Reconstructing complex materials via effective grain shapes," *Phys. Rev. Lett.* Vol. 91, no. 21, pp. 215506 Nov. 2003, doi: 10.1103/PhysRevLett.91.215506.
24. C. H. Arns, M. A. Knackstedt, and K. R. Mecke, "Boolean reconstructions of complex materials: Integral geometric approach," *Phys. Rev. E*, vol. 80, no. 5, pp. 051303, Nov. 2009, doi: 10.1103/PhysRevE.80.051303.

25. N. I. Ismail, "Rock-typing using the complete set of additive morphological descriptors, " Ph.D. dissertation, School of Minerals and Energy Resour. Eng., Univ. New South Wales, Sydney, NSW, Australia, 2014.
26. C. H. Arns, J. Mecke, K. R. Mecke, and D. Stoyan, "Second-order analysis by variograms for curvature measures of two-phase structures," *Europ. Phys. J. B: Cond. Matt.,* vol. 47, no. 3, pp. 397-409, Oct. 2005.
27. J. A. Rushing, K. E. Newsham, and T. A. Blasingame, "Rock typing: Keys to understanding productivity in tight gas sands," in *Proc. 2008 SPE Unconventional Reservoirs Conf.*, Keystone, Colorado, Jan. 2008.
28. M. Turner, L. Knuefing, C. Arns, A. Sakellariou, T. Senden, A. Sheppard, R. Sok, A. Limaye, W. V. Pinczewski,and M. Knackstedt, "Three-dimensional imaging of multiphase flow in porous media," *Physica A: Statistical mechanics and its applications*, vol. 339, no. 1-2, pp. 166-172, Aug, 2004.
29. M. Hilpert and C. T. Miller, "Pore-morphology-based simulation of drainage in totally wetting porous media," *Adv. Water Resour.,* vol. 24, no. 3-4, pp. 243-255, Feb. 2001.
30. I. Shikhov and C. H. Arns, "Evaluation of capillary pressure methods via digital rock simulations," *Transport in Porous Media*, vol. 107, no. 2, pp. 623-640, Mar. 2015.
31. R. Pini, S. C. Krevor, & S. M. Benson, "Capillary pressure and heterogeneity for the CO2/water system in sandstone rocks at reservoir conditions," *Adv. Water Resour.*, vol. 38, pp. 48-59, Mar. 2012.
32. A. Georgiadis, S. Berg, A. Makurat, G. Maitland, and H. Ott, "Pore-scale micro-computed-tomography imaging: Nonwetting-phase cluster-size distribution during drainage and imbibition," *Phys. Rev. E*, vol. 88, no. 3, pp. 033002, Sep. 2013, doi: https://doi.org/10.1103/PhysRevE.88.033002
33. S. T. Hyde, I. S. Barnes, B. Ninham, "Curvature energy of surfactant interfaces confined to the plaquettes of a cubic lattice," *Langmuir*, vol. 6, no. 6, pp. 1055-1062, Jun. 1990.

# Estimation of Gas Condensate Relative Permeability using a Lattice Boltzmann Modelling approach

*Josephina* Schembre-McCabe[1,*], *Jairam* Kamath[1], *Andrew* Fager[2] and *Bernd* Crouse[2]

[1]Chevron Energy Technology Company, Reservoir and Production Engineering, USA
[2]Dassault Systèmes, USA

**Abstract.** Predicting well deliverability loss due to condensate banking requires imbibition gas/oil relative permeability as a function of capillary number. These measurements can be difficult to conduct and are often unavailable. It would be of benefit if reasonable estimates of the imbibition relative permeability can be obtained from commonly available drainage data. We use a multiphase Lattice Boltzmann method to compute drainage and imbibition gas/oil relative permeability for a Berea sandstone core. The computations are done on a 3D digital pore space of the core constructed for micro-CT-scan images. The imbibition calculations are for both displacement and dropout processes, and for a range of capillary numbers. These results are then compared to experimental measurements reported in literature as a function of krg/kro and capillary number Nc, and they showed agreement with experimental results for different sandstones.

## 1 Introduction

A gas condensate system is typically single-phase gas at time of discovery. As the gas/condensate system pressure decreases below the dew point in the near-wellbore region, condensate saturation increases leading to "condensate banking." The effective gas permeability decreases in the near well region, and this often leads to a large reduction of well productivity [**1,2**]. The ratio of forces expressed as capillary number (Eq. 1) plays a key role in the degree of impairment [**3,4,5**].

$$N_c = \frac{U\mu}{\sigma} \quad \text{(Eq. 1)}$$

The imbibition relative permeability data needed to model condensate banking phenomena are difficult to measure. They are often obtained by performing steady-state or "pseudo-steady-state" experiments. Reservoir condition steady-state relative permeability tests that capture the effect of rock type, flow velocities and near-well bore conditions are especially complex and time consuming. "Pseudo-steady state" relative permeability experiments with reservoir and synthetic fluids that match liquid concentration, viscosity ratio and interfacial tension of the condensate [**6,7**] are often used. These experiments require fitting to a relative permeability model to obtain curves as function of saturation. In general, imbibition data to model condensate banking are often unavailable. It would be of benefit if reasonable estimates of the imbibition relative permeability can be obtained from commonly available drainage data.

The objective of this work is to test the capabilities of Lattice Boltzmann based multi-phase fluid flow simulation to model drainage and imbibition gas/oil relative permeability, to investigate the effects of different methods of establishing condensate saturation at the pore scale (displacement, dropout), and the effects of capillary number. A high-resolution 3D image of a Berea sandstone is used to test the simulation method, and the results are compared with data obtained from literature.

## 2 Methodology

### 2.1 Sample Imaging

We use a micro-CT device to create a 3D image of a Berea Sandstone sample. Figure 1-left shows one 2D slice perpendicular to flow (1024x1024 pixels) in original grey scale. The slice represents a 5mm diameter plug and has a resolution of 2.6 µm/voxel. Figure 1-right shows the same slice in binary scale after segmentation. The segmentation of the image was performed using an in-house enhanced histogram thresholding method [**8**].

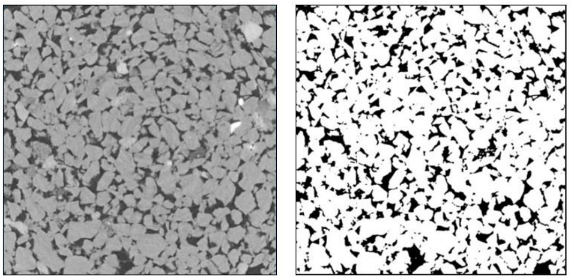

**Fig. 1.** Two-dimensional section of scans for the Berea Sandstone used in this work: original grey scale (left) and segmented image (right)

The simulations described in the next section were performed for a sub-volume (600x600x600) whose grain- and pore- space visualizations are shown in Figure 2.a (grain space) and 2.b (pore space). The sub-volume had a connected porosity of 17.8% with a critical pore throat radius of 8.3µm (3.2 voxels). The critical pore throat radius is a measure of pore size. It is defined as the radius of the largest sphere that can start from a face of the rock and find its way within the pore space to the other,

---

[*] Corresponding author: jschembremccabe@chevron.com

opposing face. Any sphere with a radius larger than the critical throat radius will becomes stuck within the pore space. For a cubic 3D geometry, it is measured in all 3 directions. Here the critical throat radius is only reported for the flow direction. The simulated permeability and total porosity was 670 mD and 22 %.

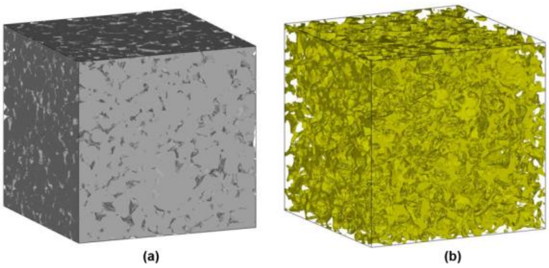

**Fig. 2:** Visualization of (a) grain and (b) pore space of the 3D model used for all simulation.

## 2.2 Numerical Modelling Approach

The numerical modelling approach used in this study consists of a multiphase Lattice Boltzmann method (LBM) where condensate dropout and its effects on two-phase flow are investigated and compared to a traditional displacement-based method. LBM has been recently used for directly solving flow scenarios at pore-scale within porous media, particularly for petroleum reservoir rock systems [**9,10**].

LBM is based on kinetic theory and solves a discrete form of the Boltzmann transport equation. The explicit method often operates on a cubic lattice. This allows for local compute operations with good parallel efficiency. LBM based fluid solvers are considered competitive alternatives to traditional Navier-Stokes PDE-based numerical methods [**11-16**].

The solver used for this work is based on an extension of the multiphase Shan-Chen model (SC-LBM) [**17**]. The model used here was recently extended to improve numerical stability and accuracy under the operating conditions required for digital rock workflows, low resolution and low numerical viscosity [**18,19**]. In the model fluid phase separation is the result of interaction forces between fluid components while wettability is determined by interaction forces between fluid and pore walls.

The pore-solid interface is defined by triangular surface elements, or surfels, which allows for high fidelity representation of the surface. The usage of surfels increases accuracy of near-wall fluxes and is a unique feature of the model used in this work [**20,21**]. This allows for a relatively coarse number of grid cells to be used for resolving the critical throats of a rock volume, making computational cost of practical rock volumes manageable.

## 2.3 Numerical Modelling Setup

Two multi-phase flow modelling setups were used to generate gas/condensate relative permeability curves. The first corresponds to steady-state relative permeability displacement. In the second setup, the drop-out of condensate is modelled, and the effective permeability of both gas and condensate is calculated as a function of saturation and capillary number.

### *2.3.1. Relative Permeability -- Displacement*

A steady-state relative permeability displacement method is used here to simulate both drainage and imbibition displacements. Gas displaces condensate in drainage, while condensate displaces gas in imbibition. Periodic boundary conditions and a driving force are applied in the flow direction, while no-flow boundary conditions are used in the direction transvers to flow. Additional details for this method can be found in [**9**].

### *2.3.2 Relative Permeability -- Dropout*

In a physical gas condensate system, the liquid condensate phase develops through the spontaneous condensation or dropout of components initially in gas. The dropout of the liquid condensate phase occurs from a state change (typically a pressure reduction) of the system. To model this mechanism in this simulation methodology, condensate mass is uniformly introduced into the gas filled pore space as a new fluid component using a volumetric exchange process. In each voxel a source term introduces condensate mass while a sink term simultaneously removes an equal amount of gas. This is done with a uniform rate of exchange in all gas phase voxels. Initially, the condensate component remains dissolved as the minor component in the gas phase, but as the described exchange process continues to introduce condensate mass and increase condensate density, the interaction forces between the gas and condensate components naturally lead to the spontaneous formation of a liquid condensate phase. F**igure 3** shows a diagram of the condensation model in which condensate is introduced in the gas filled pores. .

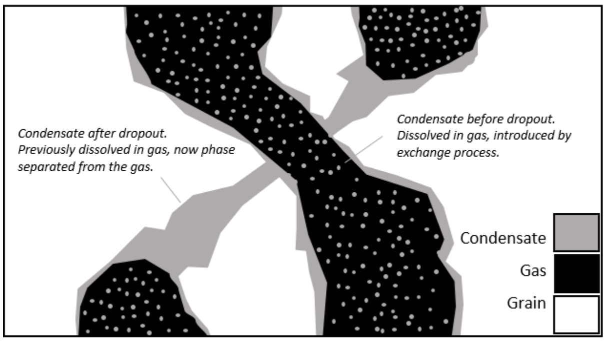

**Fig. 3**. Diagram of the condensate dropout method

The little condensate points in the gas phase indicate dissolved condensate component in the numerical simulation that have been introduced by the exchange process. After forming a separate phase (i.e. dropping out) the condensate phase is shown to have migrated to and collected along the pore walls. This is representative of condensate being the wetting phase and in agreement with the film-wise process observed in micromodels [**22**]. Similar to the displacement method a body force is used to drive flow through the rock over the course of a dropout simulation.

**Figure 4** describes the progression of a dropout simulation. The simulation starts at the initial saturation state. The dropout method is initially off. During this step the time behaviour of relevant flow quantities are measured. When these quantities are determined to be converged in time the permeability of all phases, gas and condensate, is measured. Typically, only gas is mobile at the initial saturation state. After measuring permeability, the dropout method is turned on. When the dropout method is on the condensate saturation increases and gas saturation decreases correspondingly. The dropout process continues until a predefined saturation is achieved. When the saturation threshold is achieved the dropout method is turned off and the convergence and permeability measurement step is performed again. The saturation remains constant during this step. Once this step is complete the dropout method is turned on again. The simulation continues to alternate the dropout step and the convergence step until only the condensate phase is mobile and the gas phase is determined to be immobile.

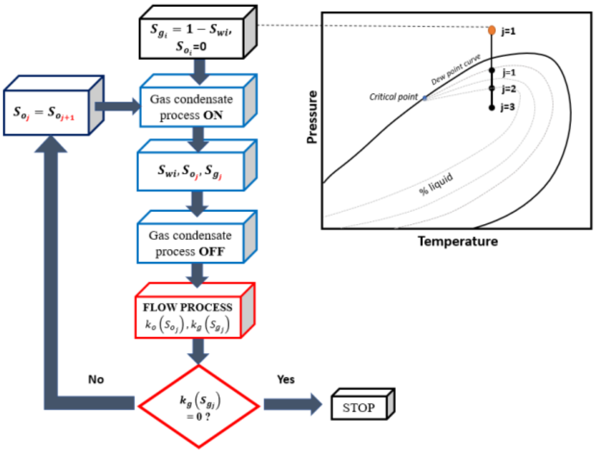

**Fig. 4.** Diagram showing process for computing Gas/Oil (dropout) relative permeabilities

### *2.3.3 Modelling Conditions*

In this study 5 simulations were performed using the Berea Sandstone 3D model shown in **Figure 2. Table 1** provides a list of the simulations performed. In all simulations the liquid condensate is assigned to be the wetting fluid while the gas is assigned as the non-wetting fluid. Pressure, temperature and overall composition will make viscosities different for different fluid systems, in this case the average of the range considered for condensate dynamic viscosity to gas viscosity ratio is 10.

Using the steady-state displacement method both drainage and imbibition condensate/gas simulations are performed. In the drainage simulation gas is the displacing fluid. In the imbibition simulation the liquid condensate is the displacing fluid. Three condensate dropout simulations are also performed. **Table 1** shows the prescribed gas capillary number used for each simulation. The gas capillary number is defined as:

$$N_{c,gas} = \frac{U_t \mu_{gas}}{\sigma} \qquad \text{(Eq. 2)}$$

Where the total Darcy velocity ($U_t$) is the sum of the gas and condensate Darcy velocities (Eq. 3). This is held constant throughout a simulation to maintain constant flow rate.

$$U_t = U_g + U_c \qquad \text{(Eq. 3)}$$

The total Darcy velocity is chosen so that the prescribed gas capillary number is achieved when the condensate phase is immobile and only the gas phase is flowing. For drainage this occurs at the end of the displacement, when all mobile oil has been removed. For both the imbibition displacement and dropout simulations this occurs at the beginning of the simulation when only gas is flowing.

**Table 1 :** List of Runs performed on Berea 3D Model (**Fig. 2)**

| Run | Method | $N_{c,gas}$ |
|---|---|---|
| 1 | Steady-State Drainage | $1\text{x}10^{-5}$ |
| 2 | Steady-State Imbibition | $1\text{x}10^{-6}$ |
| 3 | Condensate Dropout | $1\text{x}10^{-6}$ |
| 4 | Condensate Dropout | $1\text{x}10^{-5}$ |
| 5 | Condensate Dropout | $5\text{x}10^{-5}$ |

## 3 Results

### 3.1 Numerical Simulations on 3D Berea Model

In this section, results from the simulations described above are presented and discussed. **Figure 5** compares the result of a drainage gas/oil relative permeability simulation for a capillary number of 1x10$^{-5}$ with results from literature representing low and high capillary numbers [**23,24**]. The results from simulation are in the range between these two boundaries.

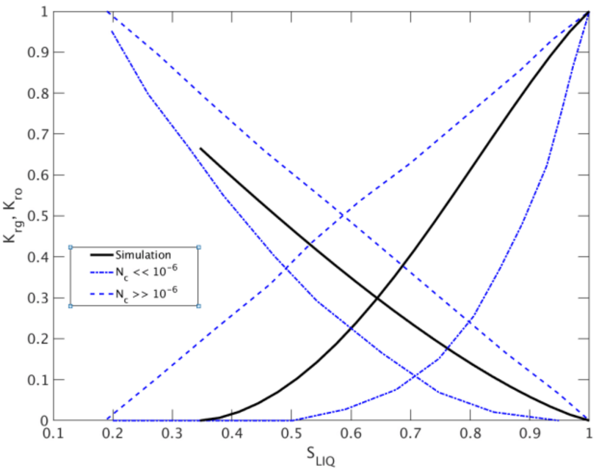

**Fig. 5**. Comparison of Drainage Oil/Gas relative permeability obtained from run 1 (black) and ranges suggested for sandstones between low capillary number (solid blue line) and high capillary number (dashed blue line).

**Figure 6** compares imbibition gas and condensate relative permeabilities obtained from different mechanisms at same capillary number: the dashed line depicts curves where displacement of gas by liquid condensate occurs (run 2); while the solid line shows curves for the case where gas is replaced by liquid condensate using the dropout method (run 3).

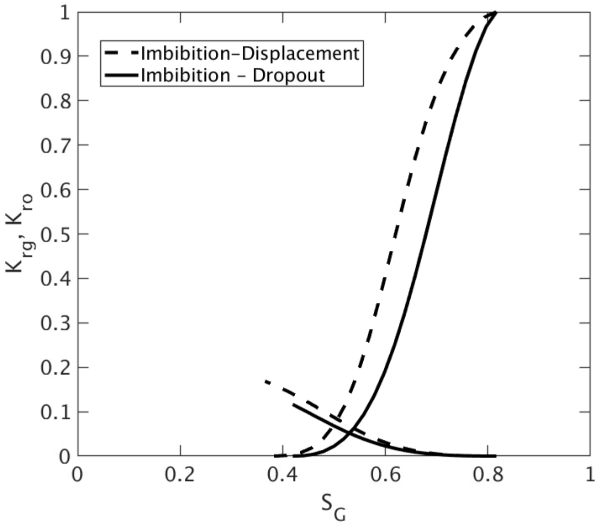

**Fig. 6.** Comparison of Oil/Gas Relative Permeabilities obtained by Displacement (run 2) and Gas Condensate formation (run 3) at $N_c = 1x10^{-6}$

Condensate relative permeability is lower in the dropout case. This could be due to more regions of disconnected condensate saturation. Dropout gas relative permeability values are also lower. This could be due to the relatively uniform introduction of condensate into both large and small pores by the dropout method. This would cause the gas phase to breakup sooner than in the displacement method where the preference is for condensate to fill small pores first and preserve the connectivity of the gas phase.

**Figure 7** compares krg/kro data for drainage displacement, imbibition displacement, and imbibition dropout. The drainage displacement values are much higher than the imbibition values, and the differences between the two methods of imbibition are relatively minor. At the end of each simulation shown in figure 6, when the displaced fluid is trapped, the capillary number based on the displacing fluid is the same. For drainage (run 1) this is $N_{c,gas}=1x10^{-5}$. For both imbibition simulations (run 2 & 3) this is $N_{c,cond}=1x10^{-5}$ .

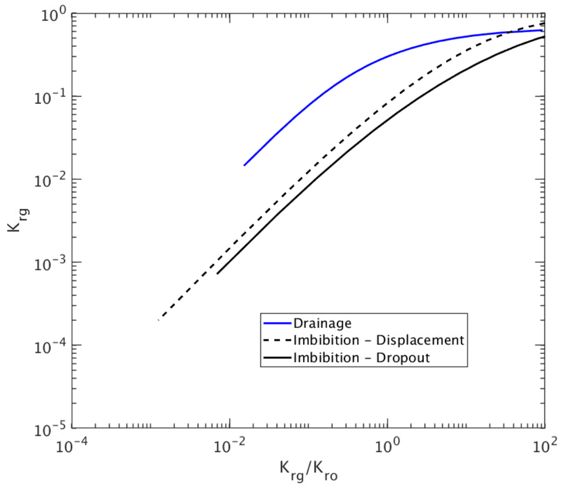

**Fig. 7.** Gas Relative permeability as a function of $k_{rg}/k_{ro}$ for drainage and imbibition (displacement, dropout)

Our findings of small differences between displacement and dropout imbibition data are consistent with those of Henderson et al. [**4**].

**Figure 8** shows four snapshots of gas and liquid dropout distribution for run 3 at four different saturations steps; liquid dropout appears in different regions of the 3D volume as the simulation progresses towards increased liquid condensate saturations.

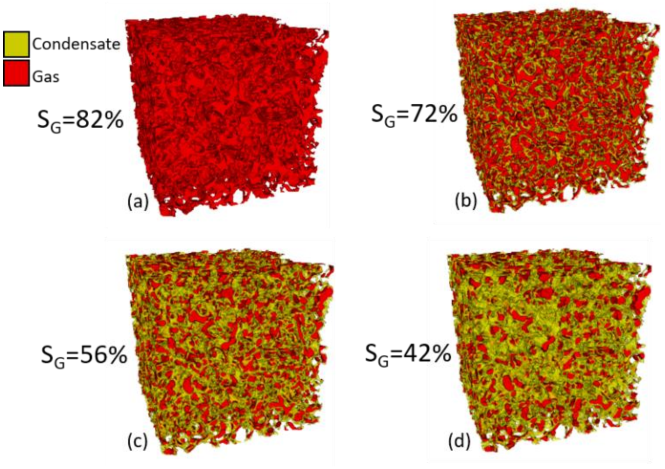

**Fig. 8.** Snapshot of gas and liquid dropout distribution at different gas saturation stages in run 3 at Nc=1x10$^{-6}$ (**Table 1**).

**Figure 9** shows gas and condensate relative permeability for different capillary numbers (runs 3, 4 and 5 in **Table 1**). **Fig. 10** plot same data from Fig. 8 in semilog scale, which shows critical condensate saturation in the range of 20% for the lowest capillary number tested in this study ($N_c=1x10^{-6}$); because we set a target condensate saturation in this range, the evolution towards lower critical condensate saturations at larger capillary numbers is not resolved; however, the trend of the condensate relative permeability in this plot suggests that critical condensate saturation decreases with increasing capillary number.

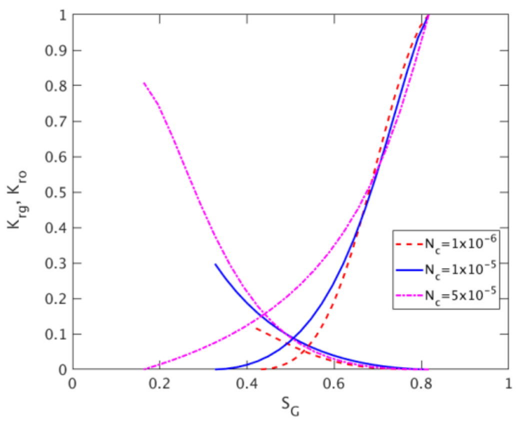

**Fig. 9.** Gas Condensate Relative Permeability obtained from runs 3, 4 and 5 (**Table 1**).

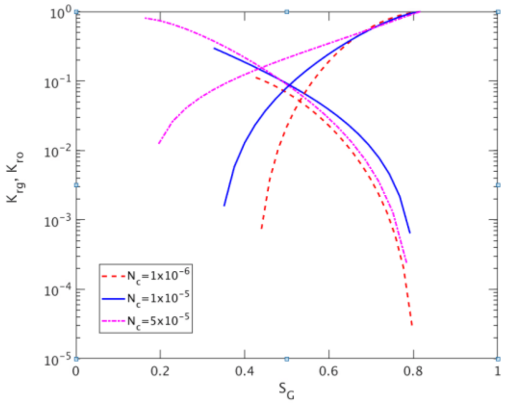

**Fig. 10**. Gas Condensate Relative Permeability from **Fig. 8** (semi log).

**Fig. 11** shows data from **Fig. 8** in the $k_{rg} = f(k_{rg}/k_{ro})$ which is used to model gas condensate by developing relative permeability at different capillary numbers [**1, 5**]. It shows that gas mobility increases with increasing capillary number, which is an expected well-known trend [**2,5,7**]. There is some discrepancy in the high $k_{rg}/k_{ro}$ space and this needs to be further explored.

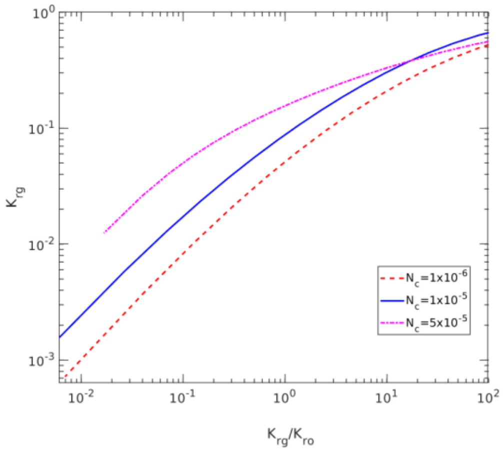

**Fig. 11**. Gas Relative permeability as a function of Gas/Oil Relative Permeability ratio from relative permeability obtained from runs 3, 4 and 5 (**Fig. 4**, **Table 1**).

**Figure 12** shows visualizations of the gas phase at the residual gas condition of each capillary number simulated with the dropout method. The visual shows that much of the gas is disconnected and that the amount of gas decreases with increasing capillary number.

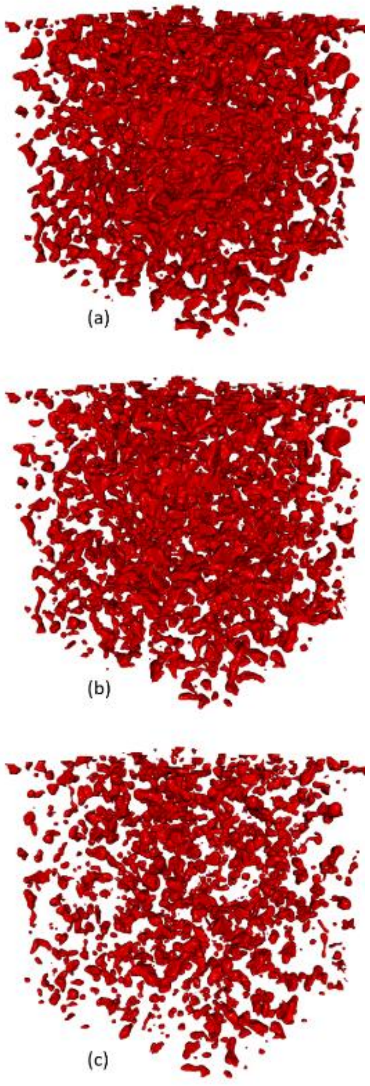

**Fig. 12.** Visualization showing locations of trapped gas for (a) run #3 at Nc=1e-6, (b) run 4 at Nc=1e-5, and (c) run 5 at Nc=5e-5.

**Figure 13** shows the average blob volume measured at the same residual gas conditions. As capillary number increases the size (volume) of gas blobs decreases. The range of values of trapped gas saturations are in line with the 25-45% range reported in the literature [**23**].

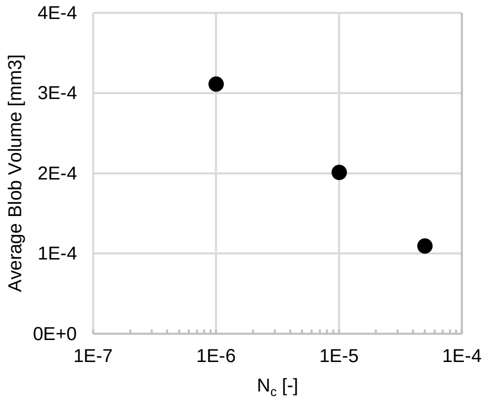

**Fig. 13.** Average blob volume for each capillary number simulated with the dropout method (run 3 to 5). Blob volume measured at the residual gas condition of each simulation.

**Figure 14** shows iso-surface visualizations of the gas blob locations. These are shown for both the displacement and dropout method. A gas saturation of $S_G$=48% is shown. These are intermediate saturation states where both gas and condensate are still flowing. The blob color denotes blob volume with the largest gas blobs colored as red and the smallest colored as blue. The deep red colored gas blobs represent the largest gas blobs. These blobs are often fully connected from inlet to outlet and associated with high gas relative permeability. It is observed that the displacement method leads to a gas phase that has a better connectivity than the dropout method. This is consistent with the observation that the gas permeability curve generated by the displacement method is overall higher than that generated by dropout method as shown in **figure 6**.

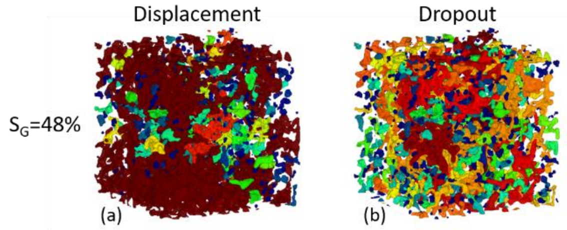

**Fig. 14.** Visualization showing locations and volume of gas blobs. Color denotes blob volume. Largest gas blobs colored red. Smallest gas blobs colored blue. (a) shows displacement (run #2) while (b) shows dropout (run #3).

## 3.2 Comparison with published data

In this section, the results presented in the previous section in **Fig. 11** are compared with results reported in literature for sandstone in the form of $k_{rg} = f(k_{rg}/k_{ro})$. The comparison covers the range of capillary numbers [**4,26,27,28**] that include the capillary number used in this study (**Table 2**). The data compiled was collected in Berea or reservoir sandstone with porosity ranging between 17 and 25%, and permeabilities between 50 and 500 mD. Most of the data were obtained using the Steady State method, generally by fixing target gas condensate ratio (GCR) at each step. Cable et al [**25**] and Kumar el al [**28**], used pseudo-state method to measure relative permeability. Regarding the fluid properties, some of these studies used mixtures match fluids at reservoir conditions and/or reservoir fluids, the oil/gas viscosity ratio ranged between 7 and 40 for the cases we used for comparison.

**Figure 15** compares run 3 ($N_c$=1x10$^{-6}$) with data reported for capillary numbers ranging between $1\text{x}10^{-6}$ and $5\text{x}10^{-6}$ [**4,26,27, 28,31**]. We see good agreement between the data reported for this range and the simulation results.

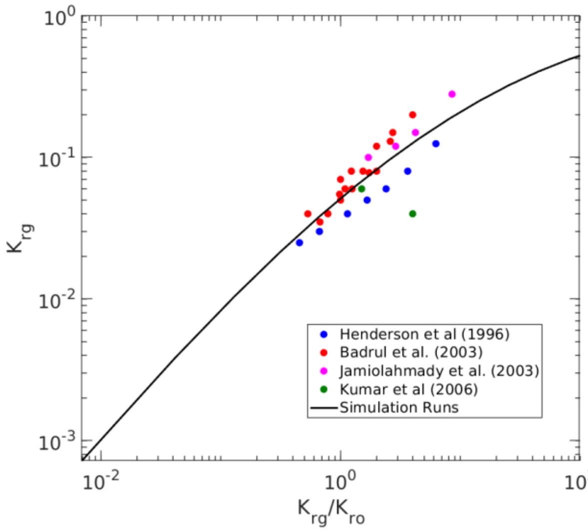

**Fig. 15.** Gas Relative permeability as a function of $k_{rg}/k_{ro}$. Comparison of Simulation run # 3 ($N_c$ = 1x10$^{-6}$) with data published in the literature for range covering the capillary number condition ($1\text{x}10^{-6} \leq N_c < 5\text{x}10^{-6}$)

**Figure 16** compares run 4 ($N_c$=1x10$^{-5}$) with data reported for capillary numbers ranging between $5\text{x}10^{-6}$and $2\text{x}10^{-5}$ [**4,26,28,30,31**]. For this range, we observed more variability in the data reported in literature compared to the previous case at lower capillary number. And yet, the simulation results show good agreement with the results reported in literature

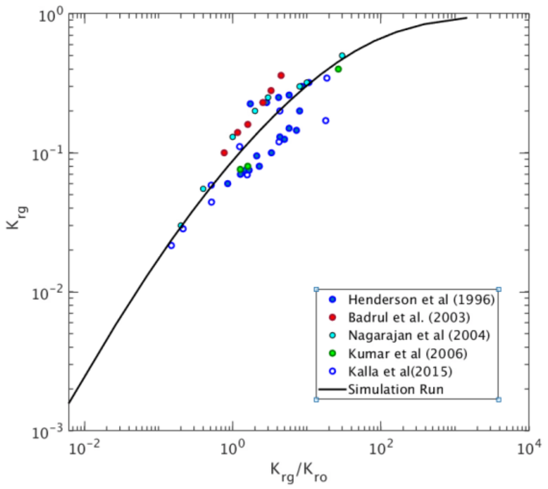

**Fig. 16.** Gas Relative permeability as a function of $k_{rg}/k_{ro}$. Comparison of Simulation run 4 ($N_c$ = $1\text{x}10^{-5}$) with data

published in the literature for range covering the capillary number condition ($5x10^{-6} \leq N_c < 2x10^{-5}$).

**Figure 17** compares run 5 with data reported for capillary numbers larger than $2x10^{-5}$ [**25,31**]. Even though we have less data to compare in this range and experimental data shows uncertainty, we see a good agreement between the simulation results and the range of data reported

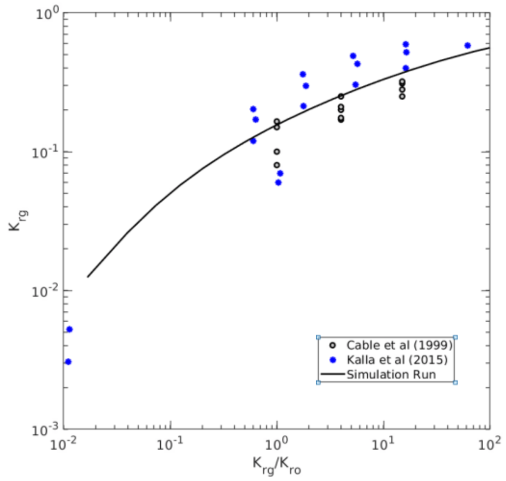

**Fig. 17.** Gas Relative permeability as a function of $k_{rg}/k_{ro}$. Comparison of Simulation run 5 ($N_c = 5x10^{-5}$) with data published in the literature for range covering the capillary number condition ($N_c \geq 2x10^{-5}$).

## 4 Conclusions

Multiphase flow LBM calculations of imbibition gas/oil relative permeability for a Berea sandstone gave promising results -

- The calculated gas relative permeability as a function ($k_{rg}/k_{ro}$, $N_c$) was in line with experimental results for different sandstones
- There were minor differences between displacement and dropout methods of establishing a wetting condensate saturation. This is as expected and consistent with the literature.

Future work will need a careful comparison where there is computed and measured drainage and imbibition data on the same sample. If the results are still promising, LBM offers a way to calculate the imbibition gas/oil relative permeability data needed to model effects of condensate banking from commonly available drainage experiments.

## 5 Nomenclature

$k_{rg}$ = gas relative permeability
$k_{ro}$ = oil or gas condensate relative permeability
$S_{LIQ}$= liquid saturation
$S_g$ = gas saturation
$S_{gr}$ = residual gas saturation
$S_{oc}$ = critical gas condensate saturation
$S_{org}$ = residual oil (to gas) saturation
$U$ = velocity
$\mu$ = viscosity
$\sigma$ = interfacial tension
$N_c$= capillary number

## Acknowledgments

We would like to acknowledge the support of Chevron Corp and Dassault Systèmes to allow the publication of this work.

## References

1. H. L. Chen, S. D. Wilson, and T. G. Monger-McClure, "Determination of Relative Permeability and Recovery for North Sea Gas Condensate Reservoirs," SPE 30769, *SPE Annu. Tech. Conf. and Exhib.*, Dallas, TX, USA, Oct 22-25, 1995.
2. J. Kamath, "Deliverability of Gas-Condensate Reservoir – Field Experiences and Prediction Techniques," *JPT*, pp 94- 99, Apr 2007.
3. W. Boom, K. Wit, A. M. Shulte, S. Oedai, J.P.W. Zeelenberg and J. G. Maas, "Experimental Evidence for Improved Condensate Mobility at Near-wellbore Flow Conditions," SPE 30766, *SPE Annu. Tech. Conf. and Exhib.*, Dallas, TX, USA, Oct 22-25, 1995.
4. G. D. Henderson, A. Danesh, D. H. Tehrani, S. Al-Shaidi, and J. M. Peden, "Measurements and Correlation of Gas Condensate Relative Permeability by the Steady-State Method," *SPE J.*, vol 6, pp 191-201, 1996.
5. G. A. Pope, W. Wu, G. Narajanaswamy, M. Deslhad, M. Sharma, and P. Wang, "Modeling Relative Permeability Effects in Gas Condensate Reservoirs," SPE 49266, *SPE Annu. Tech. Conf. and Exhib.*, New Orleans, LA, Sept 27-30, 1998.
6. C. H. Whitson, Ø. Fevang, and A. Sævareid, "Gas condensate Relative Permeability for Well Calculations," *Transport in Porous Media*, vol. 52, pp 279-311, 2003.
7. V. Kumar, V. Bang, G.A. Pope, M.M. Sharma, P.S. Ayyalasomayajula, and J. Kamath, "Chemical Stimulation of Gas/Condensate Reservoirs," SPE 102669, *SPE Annu. Tech. Conf. and Exhib.,* San Antonio, Texas, USA, Sept 24-27, 2008.
8. J. M. Schembre-McCabe and J. Kamath, "Using Digital Rock Technology to Quality Control and Reduce Uncertainty in Relative Permeability Measurements," *Petrophysics*, vol 59, no. 1. pp 44-53, 2018.
9. G. R. Jerauld, J. Fredrich, N. Lane, Q. Sheng, B. Crouse, D. M. Freed, A. Fager, and R. Xu, "Validation of a Workflow for Digitally Measuring Relative Permeability," SPE 188688*, 2017 SPE Abu Dhabi Int. Pet. Exhib. & Conf.,* Abu Dhabi, U.A.E., Nov. 13-16, 2017.
10. H. Andrä, N. Combaret, J. Dvorkin, E. Glatt, J. Han, M. Kabel, Y. Keehm, F. Krzikalla, M. Lee, C. Madonna, M. Marsh, T. Mukerji, E. H. Saenger, R. Sain, N. Saxena, S. Ricker, A. Wiegmann, X. Zhan, "Digital rock physics benchmarks—part II:

Computing effective properties," *Comp. Geosci.*, vol. 50, no. 33, pp 33-43, 2013.

11. S. Chen and G. Doolen, "Lattice Boltzmann method for fluid flows," *Annu. Rev. Fluid Mech.*, vol. 30, no. 1, pp 329-264, 1998.
12. S. Chen, H. Chen, D. Martinez, and W. Mattheus, "Lattice Boltzmann model for simulation of magnetohydrodynamics," *Phys. Rev. Lett.*, vol. 67, no. 27, pp. 3776-3779, Dec. 1991.
13. H. Chen, S. Chen, W. Matthaeus, "Recovery of the Navier - Stokes equations using a lattice-gas Boltzmann method," *Phys. Rev. A*, vol. 45, no. 8, pp R5339-R5342, Apr. 1992.
14. Y. Qian, D. d'Humieres, P. Lallemand, "Lattice BGK models for Navier-Stokes equation," *Europhys. Lett.,* vol. 17, no. 6, pp 479-484, Feb. 1992.
15. H. Chen, C. Teixeira, and K. Molvig, "Digital physics approach to computational fluid dynamics: some basic theoretical features," *Intl. J. Mod. Phys. C*, vol. 8, no. 4, pp. 675-684, 1998.
16. H. Chen, "Volumetric formulation of the lattice Boltzmann method for fluid dynamics: Basic concept," *Phys. Rev. E*, vol. 58, no. 3, pp. 3955-3963, Sep. 1998.
17. X. Shan and H. Chen, "Lattice Boltzmann model for simulating flows with multiple phases and components," *Phys Rev E*, vol. 47, no. 3, p. 1815-1819, Mar. 1993.
18. H. Otomo, H. Fan, R. Hazlett, Y. Li, I. Staroselsky, R. Zhang, R., and H. Chen, H., "Simulation of Residual Oil Displacement In A Sinusoidal Channel With The Lattice Boltzmann Method," *Comptes Rendus Mécanique*, vol. 343, no. 10, pp. 559–570, 2015.
19. H. Otomo, H. Fan, Y. Li, M. Dressler, I. Staroselsky, R. Zhang, and H. Chen, "Studies Of Accurate Multi-Component Lattice Boltzmann Models On Benchmark Cases Required For Engineering Applications," *Jour. Comp. Sci.*, vol 17, pp. 334–339, 2016.
20. H. Chen, C. Teixeira, and K. Molvig, "Realization of Fluid Boundary Conditions via Discrete Boltzmann Dynamics," *Int. J. Mod. Phys. C*, vol. 9, p. 1281, 1998.
21. B. Crouse, D. M. Freed, N. Koliha, G. Balasubramanian, R. Satti, D. Bale, and S. Zuklic, "A Lattice-Boltzmann Based Method Applied to Digital Rock Characterization of Perforation Tunnel Damage*,".* SCA 2016-058, *Int. Symp. Soc. Core Analysts*, Snow Mass, CO, USA., Aug. 2016.
22. A. Danesh, G. D. Henderson, and J. M. Peden, "Experimental Investigation of Retrograde Condensation in Porous Media at Reservoir Conditions," SPE 18316, *SPE Annu. Tech. Conf. and Exhib.*, Houston, TX, Oct.2-5, 1988.
23. G. Jerauld, "Prudhoe Bay Gas/Oil Relative Permeability," *SPE Res. Eng.*, Feb 1, pp. 66-73, 1997.
24. S. C. M. Krevor, R. Pini, L. Zuo, and S. M. Benson, "Relative Permeability and trapping of $CO_2$ and water in Sandstone rocks at reservoir conditions," *Water Resour. Res.*, vol. 48, no. 2, Feb. 2012.
25. A. Cable, R. Mott, and M. Spearing, "Experimental Techniques for the Measurement of Relative Permeability and In-Situ Saturation in Gas Condensate Near Wellbore and Drainage Studies," SCA 9928, *Int. Symp. Soc. Core Analysts*, Golden, CO, USA, 1999.
26. M. J. Badrul, W. S. Ucok, and L. L Robert, "Effect of Permeability Distribution and Interfacial Tension on Gas Condensate Relative Permeability: An Experimental Study," SPE 80551, *SPE Asia Pacific Oil and Gas Conf. and Exhib.,* Jakarta, Indonesia, Apr. 15-17, 2003.
27. M. Jamiolahmady, A. Danesh, G. Henderson, and D. Tehrani, D., "Variations of Gas-Condensate Relative Permeability with Production Rate at Near Wellbore Conditions: A General Correlation," SPE 83960, *SPE Offshore Europe Conf.*, Aberdeen, UK, Sep. 2-5, 2003.
28. V. Kumar, G. A. Pope, and M. M. Sharma, "Improving the Gas and Condensate Relative Permeability Using Chemical Treatments," SPE 100529, *SPE Gas Technol. Symp.*, Calgary, Alberta, Canada, May 15-17, 2006.
29. A. Sævareid, C. H. Whitson, and Ø. Fevang, "An Engineering Approach to Measuring and Modeling Gas Condensate Relative Permeabilities," SCA 9930, *Int. Symp. Soc. Core Analysts*, Golden, CO, USA, 1999.
30. N. R. Nagarajan, M. M. Honarpour, and K. Sampath, "Comparison of Gas-Condensate Relative Permeability using live fluid vs. Model Fluids," SCA 2004-009, *Int. Symp. Soc. Core Analysts*, Abu Dhabi, UAE, Oct. 5-9, 2004.
31. S. Kalla, S. A. Leonardi, D. W. Berry, L. D. Poore, H. Sahoo, R. A. Kudva, and E. M. Braun, "Factors That Affect Gas-Condensate Relative Permeability," SPE Res. Eval. and Eng., vol. 18, no. 1, pp 5-10, Feb. 2015.
32. A. Orangi, N. R. Nagarajan, M. M. Honarpour and J. Rosenzweig, "Unconventional Shale Oil and Gas-Condensate Reservoir Production, Impact of Rock, Fluid, and Hydraulic Fractures," SPE 140536, *SPE Hydraul. Fracturing Technol. Conf. and Exhib.*, Woodlands, Texas, USA, Jan. 14-26, 2011.

# Low permeability measurement on crushed rock: insights

*Sandra* Profice[1,*], and *Roland* Lenormand[2]

[1]TOTAL CSTJF, avenue Larribau, 64018 Pau Cedex, France
[2]CYDAREX, 31 avenue Gabriel Péri, 92500 Rueil-Malmaison, France

**Abstract.** The Gas Research Institute (GRI) method enabling permeability measurement on crushed samples or drill cuttings was proposed by Luffel *et al.* in the early 90's. This paper presents the study led by Cydarex and Total to (i) Analyze the validity of permeabilities determined with GRI methods applied in the industry (ii) Collect information about these methods (iii) Explain the discrepancies between the results collected for similar rocks. Three materials were selected: one homogeneous outcrop rock and two reservoir rocks having absolute permeabilities ranging from 1 to 50 nD and anisotropy ratios varying from 1 to 3. For each rock, the permeabilities delivered by three commercial laboratories having their own GRI techniques were compared to the permeabilities we derived with the DarcyPress and Step Decay techniques. In addition to use different methods, the companies worked on diverse samples going from the plug of a few centimeters to the pack of millimetric particles. It was highlighted that the dispersion in the permeability data increases when the sample characteristic length decreases. To better understand the observations, the results were analyzed considering many things: literature, laboratories' crushed samples, laboratories' data and information, permeability values from GRI tests we undertook, numerical simulations…

## 1 Introduction

In the early 90's, Luffel *et al.* [1] developed the method of permeability measurement on crushed rock or drill cuttings, named Gas Research Institute (GRI) method. In this method, a pressure pulse is emitted at the surface of the particles and the signal due to fluid flow in the sample pore network is recorded over time. As a consequence, a GRI test is nothing more than a pycnometry test. The GRI or pycnometry device generally found in the industry is schematically represented on Figure 1.

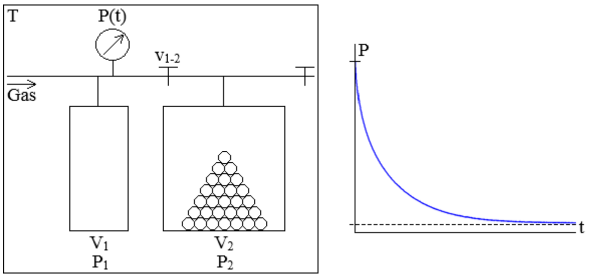

**Fig. 1.** GRI or pycnometry device and recorded pressure signal

The sample is in a chamber of volume $V_2$ connected to a chamber of volume $V_1$ via a valve $v_{1-2}$. Initially, the valve $v_{1-2}$ is closed and the pressure in the dead volume of the chamber $V_2$ as well as the pressure in the sample pore volume are at $P_2$. The test starts with the pressurization of the chamber $V_1$ at a pressure $P_1$ higher than the pressure $P_2$. At time t=0, the valve $v_{1-2}$ is opened and the recording of the pressure transient P(t) is triggered simultaneously. The temperature T of the system is kept constant either by regulating the laboratory temperature or by placing it in a temperature-controlled oven.

The option to work on rock particles is attractive as the test duration is considerably shortened by the increase of the medium exchange area with the invading fluid and the decrease of the medium characteristic penetration depth [2]. Moreover, this option should also drastically reduce the test cost considering that only a few grams of cuttings recovered while drilling are theoretically enough. Another argument defended by Luffel *et al.* [1] is the elimination during crushing of the coring-induced microfractures. The authors maintain that the microfractures remain open even when confining the core sample, which creates a bias in the estimated matrix permeability. However, the fact that tests under realistic confining pressures are not possible with the GRI method is as problematic as the existence of microfractures, low permeable media being very sensitive to stress [3]. Recent papers from the literature pointed out additional issues. Passey *et al.* [4] observed a significant dispersion of the permeabilities determined for identical samples by different commercial laboratories having their own devices, experimental procedures and interpretative models. The discrepancies between the values reached up to several decades. The reasons of these discrepancies are not discussed in the paper maybe because the authors did not have the elements needed to analyze the results.

Among the elements which could be responsible for the discrepancies, the rock pore network alteration during crushing could be a possibility. In his experimental work on the GRI method, Tinni [5] demonstrated the influence

---

[*] Corresponding author: sandra.profice@total.com

of the mean particle size on the estimated permeability. He noticed permeability increases of more than two orders of magnitude in the worst cases, when the mean particle diameter square increases from 0.1 to 100 mm$^2$. Tinni [5] assessed the influence of several other parameters on the permeability: amount of rock particles in the chamber $V_2$, initial pressure in the chamber $V_1$, gas nature, initial free water content in the particles and flushing of the system with the test gas before analysis. He highlighted that, in addition to the particle size, the sample pore volume and the pressure level act considerably on the permeability.

The permeability is also possibly affected by the rock anisotropy [3] and the thermal perturbations occurring at early times after opening the valve $v_{1-2}$ [2, 6]. A GRI test does not give a directional permeability, the gas invading the rock particles in the three space directions. This means that, for anisotropic samples such as laminated shales for instance, the permeability resulting from a GRI test is a combination of the permeabilities in the three directions. The thermal effects are of two types [6]. The first effect appears when the gas quickly expands from the chamber $V_1$ to the chamber $V_2$. The second one, known as Joules-Thomson effect, originates from the slow expansion of the gas through the porous medium. Both effects create biases in the pressure values recorded at early times.

The last element impacting permeability estimation is the model used to interpret P(t). Few models are reported in the literature and the consequences of the simplifying assumptions made, when modeling the physical problem, are rarely easy to evaluate. The most usual simplification regards the sample geometry. The sample consists of rock particles with arbitrary shapes and variable sizes covering an interval depending on the way it was prepared. While Luffel *et al.* [2] assimilated the sample to a monodisperse pack of cylinders, many other authors who focused later on the GRI method assimilated it to a monodisperse pack of spheres [2, 5, 7].

We studied the GRI methods used routinely by three commercial laboratories. The first objective was to check the coherence between the permeabilities delivered by the laboratories and the permeabilities we measured with our techniques: the DarcyPress [6] applied on small pieces of rock (10*5 mm) and the Step Decay [8] implemented on core plugs (23*25 mm). The second objective was to try to find the reasons explaining the discrepancies between the results. In order to do this, we considered many things such as: the literature, the laboratories' crushed samples as well as the data and information they accepted to share with us (raw pressure data, characteristics of the devices, experimental procedures…), the results from GRI tests we did with a device we specially designed for this study, the results from numerical simulations…

## 2 Study and results

### 2.1 Selected rocks

The three commercial laboratories which participated in the study are named Lab 1, Lab 2 and Lab 3 in the paper. Each of them received a set of samples including a piece of pyrophyllite rock, a piece of shale rock and a piece of clayey sandstone rock.

Pyrophyllite is an outcrop rock which is interesting to test methods dedicated to low permeability measurement given that it has ideal characteristics: high homogeneity, low anisotropy, low dependence on the mechanical stress and low dependence on the humidity of the ambient air. The pieces of shale rock and clayey sandstone rock were cut out from reservoir cores.

CT-scans were acquired and measurements conducted to appraise rock homogeneity and rock anisotropy. Only the reservoir cores were scanned as the pyrophyllite block was too bulky to be scanned completely. The images can be seen on Figure 2. Different layers perpendicular to the longitudinal axis are clearly identifiable on the shale core. Lamination is less visible and more discontinuous for the clayey sandstone core. The anisotropy ratio was assessed from permeability measurements for the three rocks. The results are in § 2.3.1.

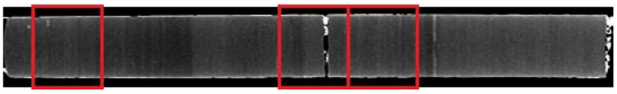

Shale core

Clayey sandstone core

**Fig. 2.** CT-scans of the reservoir cores

In Table 1 are presented the values of total porosity $\varphi_t$ and solid density $\rho_s$ from the laboratories along with the values we measured. The $\varphi_t$ values agree in a satisfactory manner for the three rocks. The $\rho_s$ values are coherent for the pyrophyllite and the shale. For the clayey sandstone, our value of 2.650 g.cm$^{-3}$ diverges from the other values varying between 2.705 to 2.710 g.cm$^{-3}$. We performed a second $\rho_s$ measurement on a sample $S_2$ taken far from the sample $S_1$ having 2.650 g.cm$^{-3}$ for $\rho_s$ value. The samples $S_1$ and $S_2$ are located along the core on Figure 2. The new value of 2.672 g.cm$^{-3}$ was obtained. The results reveal that $\rho_s$ is not uniform along the clayey sandstone core. This is possibly justified by local cementation knowing that the white spots disseminated over the whole scan are the core zones where the densities are the highest ones.

**Table 1.** $\rho_s$ and $\varphi_t$ values for the three rocks

| $\rho_s$ (g.cm$^{-3}$) | | | | |
|---|---|---|---|---|
| Rock | Cyd./Tot. | Lab 1 | Lab 2 | Lab 3 |
| Pyro. | 2.832 | 2.824 | 2.834 | 2.825 |
| Shale | 2.573 | 2.578 | 2.563 | 2.569 |
| Sand. | 2.650 | 2.705 | 2.710 | 2.707 |
| $\varphi_t$ (frac) | | | | |
| Rock | Cyd./Tot. | Lab 1 | Lab 2 | Lab 3 |
| Pyro. | 0.042 | 0.044 | 0.053 | 0.045 |
| Shale | 0.141 | 0.135 | 0.118 | 0.129 |
| Sand. | 0.044 | 0.035 | 0.033 | 0.040 |

For the pyrophyllite and the shale, the fact that the $\rho_s$ and $\varphi_t$ values are slightly dispersed tends to confirm that comparable pieces of rock were sent to the laboratories. The homogeneity of the clayey sandstone core is not easy to evaluate. On one hand, the consistency of the $\varphi_t$ values would suggest that the laboratories' pieces of rock have similar permeabilities. On the other hand, the variability of the $\rho_s$ values cast doubt upon this point.

### 2.2 Experimental procedures

Each laboratory received a letter of instructions with the set of three rock samples. In this letter were indicated the operations to be done on the rocks as well as the data and information needed in addition to the results and crushed samples. The experimental procedure to be followed was voluntarily simple in order that any alteration of the rock pore structure can be attributed to the crushing technique only. Notably, no solvent cleaning was demanded. Each rock had to be dried at 65 °C until mass stabilization, prior to crushing and characterization.

The letter mentioned nothing about crushing, sieving or testing to let the laboratories free to apply their standard procedures. All of them used a mechanical rock crusher and sieved the crushed materials in order to limit particle size distribution. In Table 2 are listed the specificities of the laboratories' experimental procedures.

**Table 2.** Characteristics of the experimental procedures

| Parameter | Lab 1 | Lab 2 | Lab 3 |
|---|---|---|---|
| Sieving | | | |
| US mesh | 20/35 | 12/20 | Not given |
| Testing | | | |
| T (°C) | 20.5 | 20 | 20 |
| Injected gas | Helium | Helium | Nitrogen |

### 2.3 Crushed samples

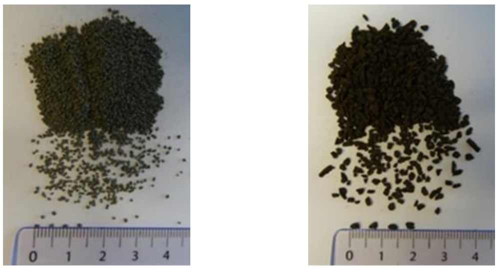

**a.** Lab 1 - Pyrophyllite **b.** Lab 2 - Shale

**c.** Lab 3 - Clayey sandstone

**Fig. 3.** Crushed samples

On Figure 3 are provided some photos of the laboratories' crushed samples. Unsurprisingly, the samples are packs of non-uniform rock particles. The sample from Lab 1 is visually different from the other laboratories' samples as the particles look clearly finer and more homogeneous in terms of shape and size.

The main features of the samples are in Table 3: bulk volume $V_t$ and mean particle diameter D. The D value of 0.671 mm was not measured by Lab 1. The parameter was assumed to be equal to the mean value of the range of D values fixed by the mesh sizes chosen for sieving. Lab 2 derived D by Laser Particle Size Analysis (LPSA) on the shale crushed sample. The data are plotted on Figure 4.

**Table 3.** Characteristics of the crushed samples

| Pyrophyllite | | | |
|---|---|---|---|
| Parameter | Lab 1 | Lab 2 | Lab 3 |
| $V_t$ (cm$^3$) | 32.328 | 11.181 | 31.516 |
| D (mm) | 0.671 | 1.780 | 1.900 |
| Shale | | | |
| Parameter | Lab 1 | Lab 2 | Lab 3 |
| $V_t$ (cm$^3$) | 34.945 | 13.278 | 37.997 |
| D (mm) | 0.671 | 1.780 | 1.766 |
| Clayey sandstone | | | |
| Parameter | Lab 1 | Lab 2 | Lab 3 |
| $V_t$ (cm$^3$) | 17.971 | 11.450 | 32.705 |
| D (mm) | 0.671 | 1.780 | 1.576 |

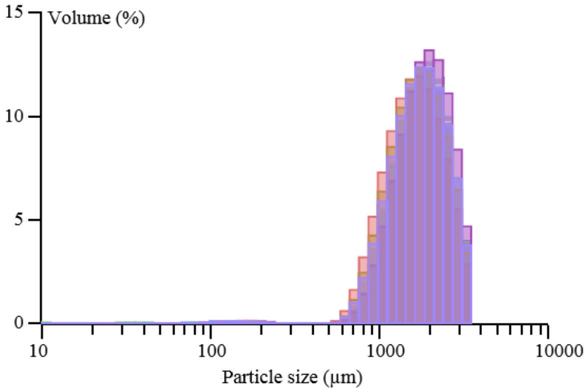

**Fig. 4.** Results of the LPSA for the shale

The graph reveals that the particle size distribution law is not centered on the mean value of the diameter interval. The mean D value of 1.780 mm coming from the LPSA is higher than the maximum mesh size selected by Lab 2 for sieving. This incoherence still necessitates to be clarified. Maybe sieving was not as efficient as expected owing to the irregular particle shapes. One can easily imagine that the particles will hardly be held back by the sieve screens if they are elongated.

$V_t$ and D are both inputs of the interpretative model. $V_t$ is as complicated as D to estimate, notably in the case where the laboratory receives cuttings or a sample already crushed [9]. How do the uncertainties on these parameters affect the results coming from the interpretation? A huge work would be needed to answer this question.

## 2.3 Permeability results

### *2.3.1 $k_l$ and b values from Cydarex and Total*

For the three rocks, we measured the absolute or intrinsic permeability $k_l$ and the Klinkenberg coefficient b, by Step Decay [8] for Total and DarcyPress [6] for Cydarex.

The orientation of the bedding plane was obvious for the reservoir cores but not for the pyrophyllite block. This is the reason why the sampling directions are identified, in the paper, in relation to the space directions (numbered from 1 to 3) for the pyrophyllite and to the bedding plane for the shale and the clayey sandstone. We will talk about sampling parallel (//) or perpendicular (⊥) to bedding for the reservoir cores. We supposed that the rock properties are equivalent in the two directions parallel to bedding.

Total performed the tests on plugs having a diameter of 23 mm and a length of 25 mm, injecting nitrogen only. Four plugs were taken from the pyrophyllite block. One plug was sampled in each space direction to orientate and quantify the anisotropy. A last plug was sampled far from the three others to check the homogeneity. The results are reported in Table 4. They were determined at an effective confining pressure $P_{eff}$ of around 80 barg. The plugs were not dried before analysis because the pyrophyllite proved to be quite insensitive to the humidity of the ambient air. The results demonstrate that the rock is homogeneous and slightly anisotropic, the anisotropy ratio reaching about a factor of 2. The $k_l$ value in Direction 2 is the lowest one and the $k_l$ values in Direction 1 and Direction 3 are very close. When the study was started, all the unconventional reservoir cores stored at Total's core house were no longer cylinders but half-cylinders. Plug sampling perpendicular to bedding was not feasible, as a consequence. Sampling parallel to bedding was problematic too knowing that the volume of rock available per facies was small according to the laboratories' needs. In the end, only one plug could be taken per reservoir core, parallel to bedding. The data are also in Table 4. Those corresponding to the shale plug were not validated since CT-scans evidenced fractures in the plug. The test on the clayey sandstone was conducted at a low $P_{eff}$ value of around 60 barg to limit the effect of the confinement on the permeability. Prior to testing, the plug was dried in an oven at 65 °C until mass stabilization, to respect the instructions passed on to the laboratories.

**Table 4.** $k_l$ and b values measured by Total

| | | | |
|---|---|---|---|
| Pyrophyllite | | | |
| 23*25 mm cylinders - Nitrogen - $P_{eff} \approx 80$ barg | | | |
| Plug | Direction | $k_l$ (nD) | b (bara) |
| 1 | 1 | 55 | 31 |
| 2 | 2 | 28 | 31 |
| 3 | 3 | 58 | 30 |
| 4 | 1 | 61 | 29 |
| Clayey sandstone | | | |
| 23*25 mm cylinder - Nitrogen - $P_{eff} \approx 60$ barg | | | |
| Plug | Direction | $k_l$ (nD) | b (bara) |
| $S_1$ (§ 2.1) | // to bedding | 19 | 21 |

Cydarex prepared for the tests small rock cylinders of 10 mm of diameter and 5 mm of length embedded in resin discs of 25 mm of diameter and 5 mm of length. Sampling was undertaken in Direction 2 and in Direction 3 for the pyrophyllite, parallel and perpendicular to bedding for the reservoir rocks. The results are in Table 5. The tests were run at an axial confining pressure $P_{axial}$ of about 100 barg, with nitrogen for the three rocks and with helium as well for the reservoir rocks. The samples were dried at 65 °C until mass stabilization. Total received from Cydarex two DarcyPress samples for characterization by Step Decay. The cylinders of shale and clayey sandstone were taken perpendicular to bedding. The diameter of the resin discs was reduced from 25 to 23 mm so that the samples fit in the core holder of the Step Decay device. The results are in Table 5 again. The tests were conducted with nitrogen, at a $P_{eff}$ value of about 60 barg.

**Table 5.** $k_l$ and b values measured by Cydarex and Total

| | | | |
|---|---|---|---|
| Cydarex - Pyrophyllite | | | |
| 10*5 mm cylinders - Nitrogen - $P_{axial} \approx 100$ barg | | | |
| Sample | Direction | $k_l$ (nD) | b (bara) |
| 1 | 2 | 32 | 32 |
| 2 | 3 | | |
| Cydarex - Shale | | | |
| 10*5 mm cylinders - Nitrogen - $P_{axial} \approx 100$ barg | | | |
| Sample | Direction | $k_l$ (nD) | b (bara) |
| 1 | // to bedding | 28 | 18 |
| 2 | ⊥ to bedding | 8 | 28 |
| Total - Shale | | | |
| 10*5 mm cylinders - Nitrogen - $P_{eff} \approx 60$ barg | | | |
| Sample | Direction | $k_l$ (nD) | b (bara) |
| 3 | ⊥ to bedding | 6 | 7 |
| Cydarex - Shale | | | |
| 10*5 mm cylinders - Helium - $P_{axial} \approx 100$ barg | | | |
| Sample | Direction | $k_l$ (nD) | b (bara) |
| 1 | // to bedding | 24 | 61 |
| 2 | ⊥ to bedding | 11 | 51 |
| Cydarex - Clayey sandstone | | | |
| 10*5 mm cylinders - Nitrogen - $P_{axial} \approx 100$ barg | | | |
| Sample | Direction | $k_l$ (nD) | b (bara) |
| 1 | // to bedding | 4 | 13 |
| 2 | ⊥ to bedding | | |
| Total - Clayey sandstone | | | |
| 10*5 mm cylinders - Nitrogen - $P_{eff} \approx 60$ barg | | | |
| Sample | Direction | $k_l$ (nD) | b (bara) |
| 3 | ⊥ to bedding | 0.8 | 41 |
| Cydarex - Clayey sandstone | | | |
| 10*5 mm cylinders - Helium - $P_{axial} \approx 100$ barg | | | |
| Sample | Direction | $k_l$ (nD) | b (bara) |
| 1 | // to bedding | 4 | 28 |
| 2 | ⊥ to bedding | | |

When two lines are merged in Table 5, it means that Sample 1 and Sample 2 have comparable $k_l$ or b values. In other words, the discrepancies were too low compared to the uncertainties so that one value can be differentiated from the other.

For the pyrophyllite, there is a satisfactory agreement between the values of $k_l$ derived for the 23*25 mm plugs by Total and those determined for the 10*5 mm plugs by Cydarex. The same observation applies to the b values.

The data collected for the small shale plugs highlight that: (i) The $k_l$ values from tests run on different samples and with different methods are coherent, contrary to the b values. (ii) The $k_l$ values obtained with different gases are coherent. (iii) The shale rock has an anisotropy ratio of 3 approximately. (iv) The ratio of the b value measured with helium to the b value measured with nitrogen is not so far from the expected value of 2.9, parallel and perpendicular to bedding. The theoretical value of 2.9 was computed by applying the following relationship:

$$\frac{b_{helium}}{b_{nitrogen}} = \frac{\mu_{helium}}{\sqrt{M_{helium}}} \frac{\sqrt{M_{nitrogen}}}{\mu_{nitrogen}} \qquad (1)$$

The expression of b, true for any gas, was drawn from the reference [10]:

$$b = \frac{4c\mu}{r}\sqrt{\frac{\pi RT}{M}} \qquad (2)$$

In Equation (1), M is the gas molecular weight and µ the gas viscosity. In Equation (2), c is a coefficient close to 1, r is the radius in mm of the capillary tubes used to model the pore network and R is the universal gas law constant.

For the clayey sandstone, the precedent remarks made for the shale change as follows: (i) The $k_l$ values from tests involving different samples and methods are not coherent, as well as the b values. (ii) The $k_l$ values estimated with different gases are similar. (iii) The sandstone rock has a negligible anisotropy ratio. (iv) The ratio of b is close to 2.9.

To sum up, the DarcyPress and Step Decay $k_l$ values converge for the pyrophyllite and the shale while, for the clayey sandstone, discrepancies reaching until a factor of 5 were noted. Regarding our b values, they are consistent for the pyrophyllite only. The discrepancies range from a factor of 1.6 to a factor of 3, for the shale and the clayey sandstone. Finding the reasons why the $k_l$ and/or b values are dispersed for the reservoir cores would be a complex task. Lack of representativity of the small samples due to the heterogeneity of the rocks at small scale? Anisotropy? Multiplicity of the methods and experimental conditions? More tests would be needed to answer these questions.

### *2.3.2 $k_{app}$ values from the commercial laboratories*

Values of apparent permeability $k_{app}$ were collected from the three commercial laboratories although $k_l$ values were demanded in the letter of instructions. Graphs of apparent permeability $k_{app}$ plotted against the inverse of the mean pore pressure $P_m$ were built to enable the comparison of our results to the laboratories' results. They are shown on Figure 5, Figure 6 and Figure 7. Two graphs are given per type of rock, the first one for nitrogen and the second one for helium. On each graph is delimited the area covering the possible $k_{app}$ values expected for the rock and the gas considered, when neglecting the effect of the confinement on $k_{app}$. The upper and lower limit lines were drawn using Klinkenberg law [10]:

$$k_{app} = k_l\left(1 + \frac{b}{P_m}\right) \qquad (3)$$

Notably, every potential lower or upper limit was plotted to have the maximal area in which the laboratories' $k_{app}$ values should lie, according to all of our pairs of $k_l$ and b values. The lower limits are based on the pairs of values associated to the least permeable samples. These samples are those taken parallel to Direction 2 for the pyrophyllite and perpendicular to bedding for the reservoir rocks. On the opposite, the upper limits rely on the pairs of values corresponding to the most permeable samples, which are parallel to Direction 3 for the pyrophyllite and parallel to bedding for the reservoir rocks. When no tests were done with helium on the samples characterized with nitrogen, the limits were plotted on the graph for helium with the $k_l$ values for nitrogen and b values equal to 2.9 times those for nitrogen.

The notations "D." and "D.s" appearing in the legends of the graphs of Figure 5, Figure 6 and Figure 7 stand for "Direction" and "Directions" respectively.

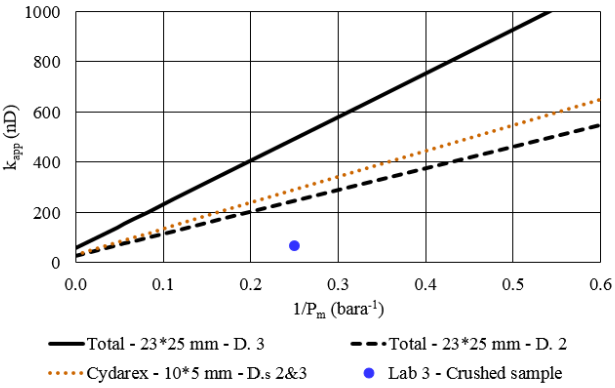

**a.** Nitrogen

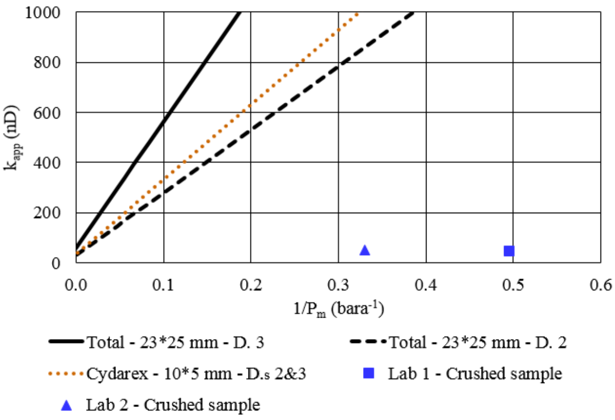

**b.** Helium

**Fig. 5.** $k_{app} = f(1/P_m)$ graph for the pyrophyllite

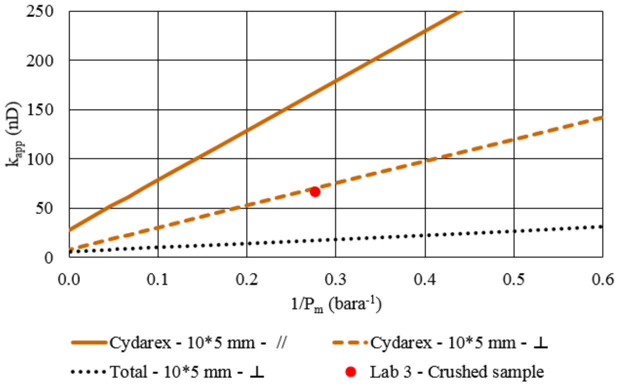

**a.** Nitrogen

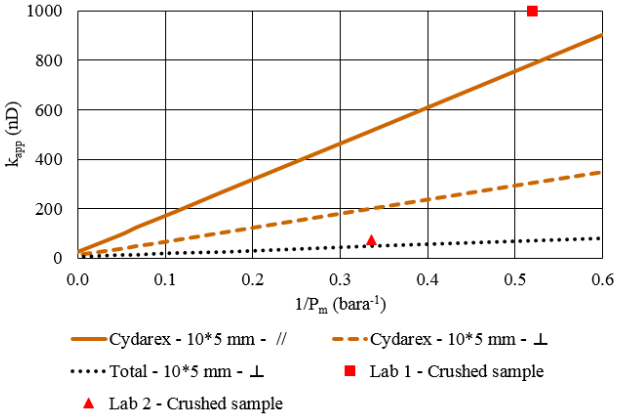

**b.** Helium

**Fig. 6.** $k_{app} = f(1/P_m)$ graph for the shale

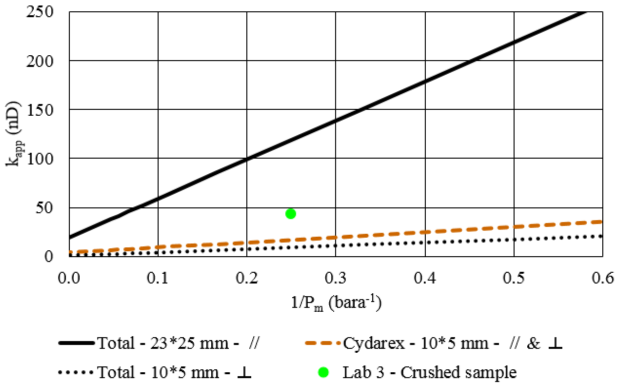

**a.** Nitrogen

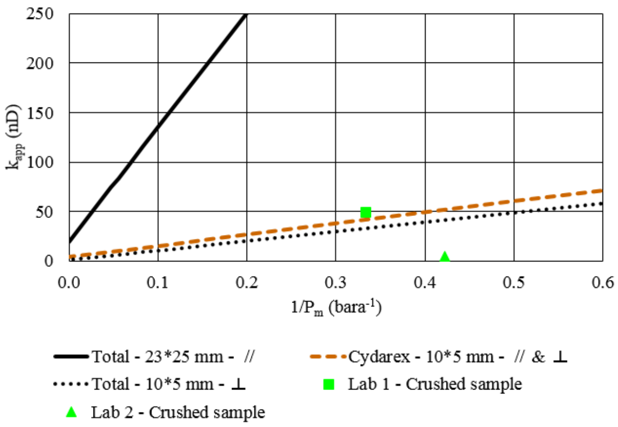

**b.** Helium

**Fig. 7.** $k_{app} = f(1/P_m)$ graph for the clayey sandstone

The $k_{app}$ values from the laboratories were reported on the graphs by associating them to the $P_m$ values computed from Equation (4). $P_2$ is the initial absolute pressure in the rock particles and $P_{f,1+2}$, the final one.

$$P_m = \frac{P_2 + P_{f,1+2}}{2} \tag{4}$$

It must be noted that the value deduced from Equation (4) is an approximation. In a classical steady-state test, $P_m$ is the mean pore pressure recorded at steady-state. In a GRI test where no steady-state regime is reached, what is the $P_m$ value to be assigned to the $k_{app}$ value? This question is not easy to answer. At least, $P_m$ cannot be taken equal to the mean pressure recorded at the surface of the particles.

Less than 50 % of the laboratories' $k_{app}$ values are in the areas of expected values. Hence, working on crushed samples generates even more dispersion in the values of permeability. The $k_{app}$ values tend to be at the bottom of the areas or to be below their lower limits. Discrepancies from a factor of 3.5 to a factor of 28 can be noted between the measured $k_{app}$ values and the lowest predicted values.

One argument extracted from the literature [1] which could explain the observations is that crushing eliminated the micro-fractures whereas such fractures were present in the DarcyPress and Step Decay samples. Given that the highest discrepancies were observed for the pyrophyllite, this rock was selected for SEM imaging at plug scale and at particle scale. The rock particles came from the crushed samples prepared by the three laboratories. The images of Figure 8 reveal the existence of fractures in some particles but not in the piece of plug. This piece of plug seems to be more intact than the particles, which goes against the argument drawn from the reference [1].

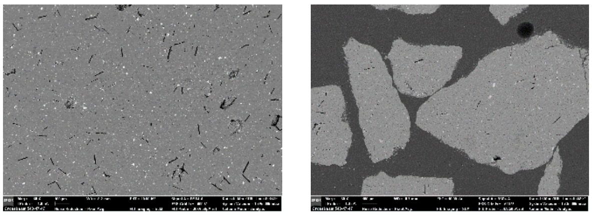

**a.** Plug **b.** Particles from Lab 1

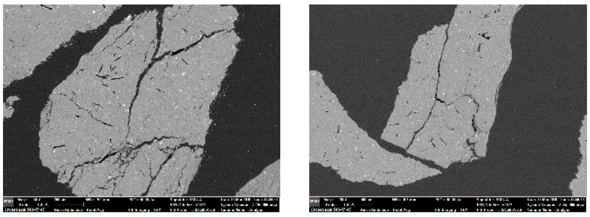

**c.** Particles from Lab 2 **d.** Particles from Lab 3

**Fig. 8.** SEM images on plug and particles for the pyrophyllite

### 2.4 Experimental devices

While Lab 1 and Lab 2 worked with experimental devices similar to the GRI device represented on Figure 1, Lab 3 developed a different device by removing the chamber $V_1$ and connecting the valve $v_{1\text{-}2}$ to the gas source. The valve opens for a fraction of second at the beginning of the test in order that the pressure pulse is directly produced in the dead volume of the chamber $V_2$. The initial pressure at the surface of the particles is better controlled in this way. The three laboratories reduced at maximum the dead volume around the crushed sample by placing calibrated billets in the chamber $V_2$. In Table 6 are detailed the specificities of the laboratories' devices. DV designates the dead volume remaining in the chamber $V_2$ after filling with the sample and the billets.

**Table 6.** Characteristics of the devices

| Pyrophyllite | | | |
|---|---|---|---|
| Volume | Lab 1 | Lab 2 | Lab 3 |
| $V_1$ (cm$^3$) | 24.985 | 59.381 | - |
| $V_2$ (cm$^3$) | 144.382 | 67.754 | 105.510 |
| $V_{billets}$ (cm$^3$) | 57.617 | 30.667 | 38.220 |
| DV (cm$^3$) | 54.437 | 25.906 | 35.774 |
| Shale | | | |
| Volume | Lab 1 | Lab 2 | Lab 3 |
| $V_1$ (cm$^3$) | 24.985 | 59.381 | - |
| $V_2$ (cm$^3$) | 144.382 | 67.754 | 106.810 |
| $V_{billets}$ (cm$^3$) | 54.043 | 27.451 | 41.090 |
| DV (cm$^3$) | 55.394 | 27.025 | 27.723 |
| Clayey sandstone | | | |
| Volume | Lab 1 | Lab 2 | Lab 3 |
| $V_1$ (cm$^3$) | 24.985 | 59.381 | - |
| $V_2$ (cm$^3$) | 144.382 | 67.754 | 105.510 |
| $V_{billets}$ (cm$^3$) | 82.722 | 29.045 | 35.280 |
| DV (cm$^3$) | 43.689 | 27.259 | 37.525 |

### 2.5 Experimental signals

Figure 9 shows the laboratories' raw pressure signals.

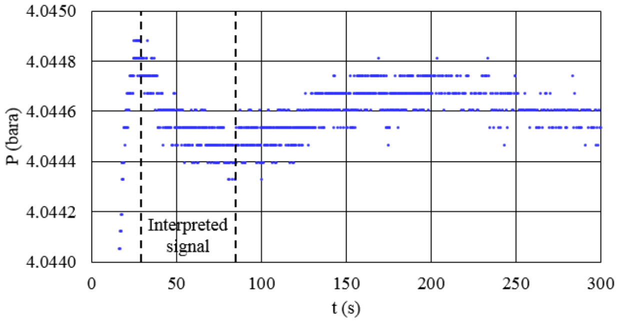

**a.** Pyrophyllite - Lab 1

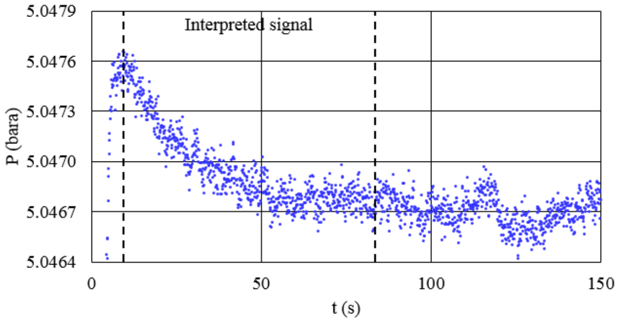

**b.** Pyrophyllite - Lab 2

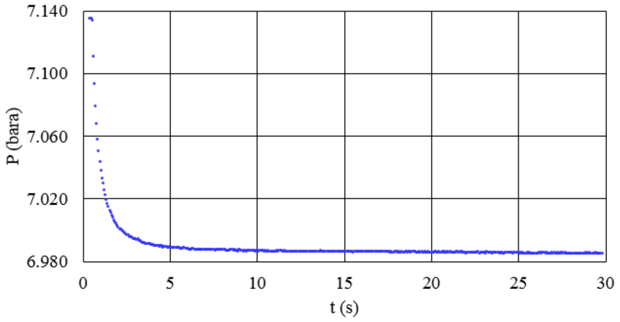

**c.** Pyrophyllite - Lab 3

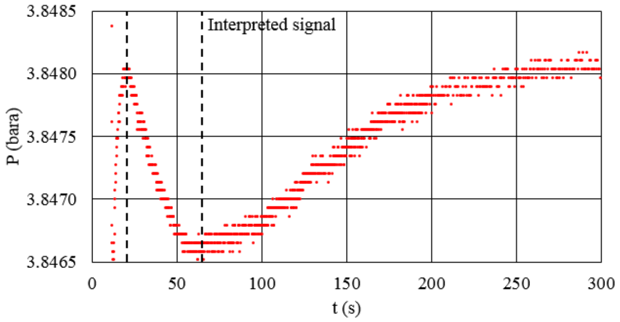

**d.** Shale - Lab 1

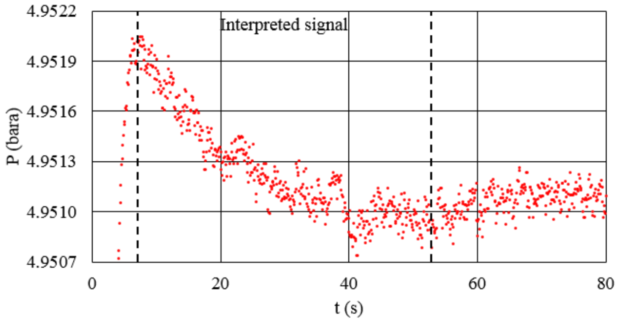

**e.** Shale - Lab 2

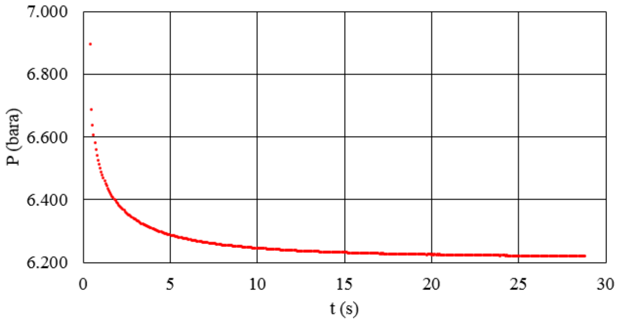

**f.** Shale - Lab 3

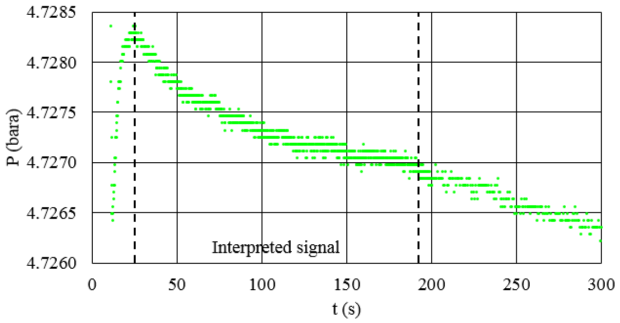

**g.** Clayey sandstone - Lab 1

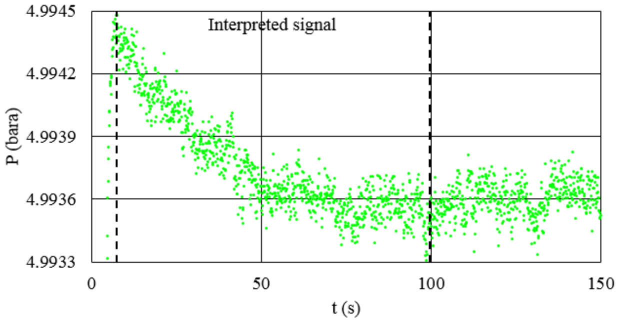

**h.** Clayey sandstone - Lab 2

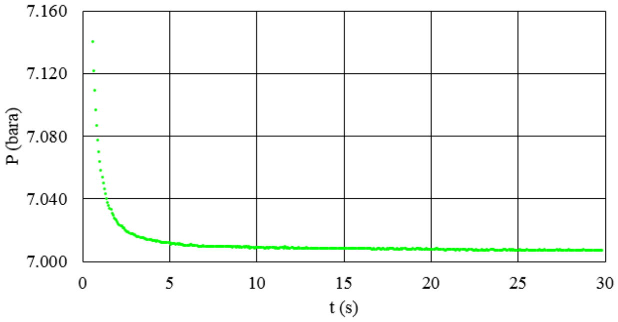

**i.** Clayey sandstone - Lab 3

**Fig. 9.** Pressure signals

The signals tend to be short and noisy, short because of the small particle sizes and noisy because of the small pressure variations due to the small sample pore volumes. The signal durations range from about 1 to 150 s and the signal amplitudes from less than 1 mbar to a few hundreds of millibar, according to the data in Table 7.

**Table 7.** Characteristics of the pressure signals

| Pyrophyllite | | | |
|---|---|---|---|
| Parameter | Lab 1 | Lab 2 | Lab 3 |
| $P_1$ (bara) | 13.103 | 6.853 | - |
| $P_2$ (bara) | 0 | Ambient | Ambient |
| $P_{i,1+2}$ (bara) | 4.0449 | 5.0477 | 7.1353 |
| $P_{f,1+2}$ (bara) | 4.0445 | 5.0467 | 6.9856 |
| θ (mbar) | 0.414 | 0.737 | 149.628 |
| Δt (s) | ≈ 50 | ≈ 100 | ≈ 15 |
| Shale | | | |
| Parameter | Lab 1 | Lab 2 | Lab 3 |
| $P_1$ (bara) | 13.108 | 6.854 | - |
| $P_2$ (bara) | 0 | Ambient | Ambient |
| $P_{i,1+2}$ (bara) | 3.8480 | 4.9520 | 6.8965 |
| $P_{f,1+2}$ (bara) | 3.8466 | 4.9511 | 6.2197 |
| θ (mbar) | 1.379 | 0.869 | 676.802 |
| Δt (s) | ≈ 50 | ≈ 50 | ≈ 30 |
| Clayey sandstone | | | |
| Parameter | Lab 1 | Lab 2 | Lab 3 |
| $P_1$ (bara) | 13.121 | 6.853 | - |
| $P_2$ (bara) | 0 | Ambient | Ambient |
| $P_{i,1+2}$ (bara) | 4.7284 | 4.9945 | 7.1605 |
| $P_{f,1+2}$ (bara) | 4.7270 | 4.9935 | 7.0075 |
| θ (mbar) | 1.379 | 0.971 | 152.990 |
| Δt (s) | ≈ 150 | ≈ 100 | ≈ 15 |

Regarding the notations in Table 7, $P_{i,1+2}$ is the initial pressure recorded just after opening the valve $v_{1-2}$ in the chamber $V_1$ and in the dead volume DV of the chamber $V_2$ while $P_{f,1+2}$ is the equilibrium pressure in the system at the end of the test. Furthermore, θ and Δt are respectively the amplitude and the duration of the pressure signal. The θ value in Table 7 is an approximate value, the pressure $P_{i,1+2}$ being affected by an error generated by the thermal effect produced at the opening of the valve $v_{1-2}$.

The quality of the pressure signals varies depending on the laboratory. Because of their very low amplitudes, the signals from Lab 1 suffer from the lack of resolution of the pressure sensor while those from Lab 2 suffer more from the noise affecting pressure acquisition. Resolution and noise do not impact as much the signals from Lab 3, the errors they engender being relatively low compared to the pressure variations. In other words, the good quality of the signals from Lab 3 is due to their high amplitudes. These high amplitudes are themselves related to the high amounts of crushed materials considered for the tests and to the limited volume (namely, the dead volume DV of the chamber $V_2$, no chamber $V_1$ being used) depleted during the gas flow in the sample pore volume.

For any type of rock, the pressure signal from Lab 3 is systematically the shortest one. This is not coherent with the fact that the particle sizes chosen by Lab 1 and Lab 2 are smaller or comparable to those chosen by Lab 3. This is also not coherent with the fact that Lab 3 worked with nitrogen while Lab 1 and Lab 2 injected helium. Indeed, the pressure signal is expected to be shorter with helium since the lower the gas molar mass, the higher b and thus, the higher $k_{app}$. The signals from Lab 1 and Lab 2 never stabilize, contrary to those from Lab 3. This suggests that they could be impacted by experimental artifacts, thermal effects or something completely different? It is difficult to identify the causes of this behavior.

## 2.6 Interpretative models

Only Lab 3 accepted to reveal information regarding the model used to interpret the GRI tests. The crushed sample was assimilated to a monodisperse pack of homogeneous and isotropic spheres. Moreover, the gas was supposed to be ideal, to have a constant viscosity and to propagate in isothermal conditions. Lab 3 solved the physical problem analytically and in Laplace space. The gas compressibility was assumed to be independent of pressure in order that a solution can be computed. This solution is at the center of the interpretative procedure implemented to estimate $k_{app}$ by history matching the simulated pressure signal with the recorded pressure signal. It is inverted numerically using Stehfest algorithm to be given in time space.

# 3 Discussion

## 3.1 GRI tests by Cydarex and Total

### *3.1.1 Device, sample, procedure and interpretation*

To better understand the limits of the GRI technique, we developed our own device for permeability measurement on crushed rock. Our device is similar to that sketched on Figure 1. The test is run following the standard procedure described in the introduction but with the material in the chamber $V_1$. The response recorded after opening of the valve $v_{1\text{-}2}$ is no longer a pressure decay. It increases over time while the gas flows out from the medium. Figure 10 shows an example of experimental signal obtained with our device on a pyrophyllite crushed sample.

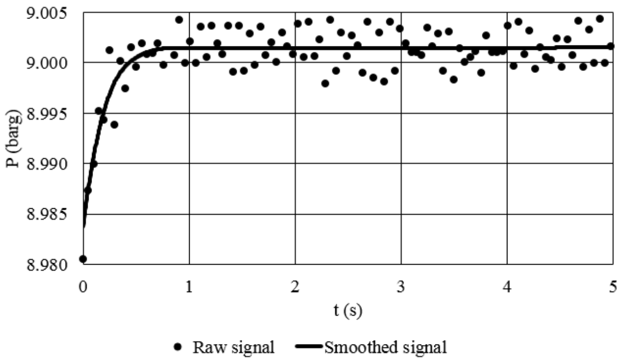

**Fig. 10.** Example of recorded and smoothed pressure signals

The signal is noisy owing to small pressure variations but it properly stabilizes at long times. A meticulous work aiming at reducing as much as possible the experimental and thermal artifacts was done over the whole prototype elaboration phase. This work was essential to ensure the reliability of the small recorded signals. The noise is not so problematic knowing that it can be eliminated with an appropriate signal processing method. Such a method was systematically implemented to smooth the signal prior to interpretation. An example of smoothed signal appears on Figure 10.

The model intervening in the interpretative procedure is based on two hypotheses. First, the crushed sample is assumed to be a monodisperse pack of homogeneous and isotropic spheres. Second, the gas is supposed to be ideal, to have a constant viscosity and to propagate in isothermal conditions. The model is a numerical model which takes into account the gas compressibility. It is at the center of a history matching procedure providing an estimation of $k_{app}$ at the end of the interpretation. Determining $k_l$ and b values instead of a $k_{app}$ value would not be feasible as the two properties are correlated [2]. The approach adopted to discriminate $k_l$ from b was to conduct tests at increasing $P_m$ values and to deduce $k_l$ and b from the coefficients of the linear regression on the points of $k_{app}$ plotted against $1/P_m$. Refer to § 2.3.2 for the comments about the $P_m$ value to be assigned to the $k_{app}$ value. Figure 11 is an example of $k_{app} = f(1/P_m)$ graph for a shale crushed sample.

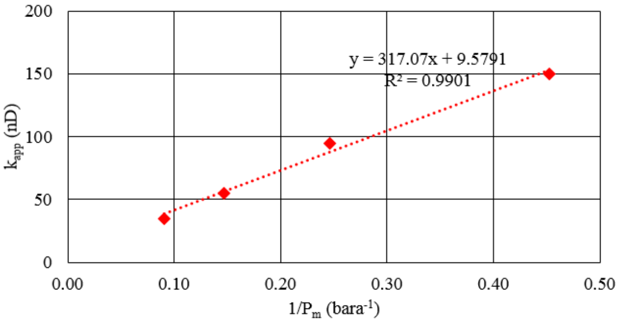

**Fig. 11.** $k_{app} = f(1/P_m)$ graph for the shale

### *3.1.2 Validity domain*

As previously mentioned in the introduction, the pressure signal is impacted by thermal effects at early times. These effects were not introduced in the interpretative model. It is then obvious that the signal due to the gas flow out from the sample must be more significant than the signal due to the thermal perturbations so that the estimated $k_{app}$ value can be validated. The period over which errors affect the recorded pressures when injecting nitrogen was assessed experimentally. A highly permeable material called BLM was chosen for the tests. Its $k_l$ value is equal to 7 mD. For such a $k_l$ value and a mean particle diameter of 1.720 mm, the pressure signal related to the gas flow in the sample pore network vanishes quite instantaneously. This means that the entire recorded signal can be attributed to thermal effects. The signal acquired for BLM with nitrogen is on Figure 12.

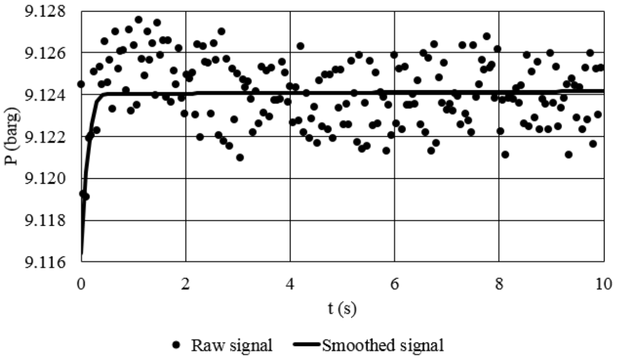

**Fig. 12.** Pressure signal recorded for BLM with nitrogen

The signal persists approximately 0.5 s. This duration was taken as a criterion to propose a graph of $k_{app}$ plotted against $\varphi_t$ where is delimited, in a specific experimental configuration, the validity domain of the GRI technique applied with our device. Figure 13 is an example of such a graph, where the validity domain is delimited for three mean particle sizes. The graph was built from numerical simulations undertaken with the parameters defining the experimental configuration adopted for the tests tackled in § 3.1.3. For a given D value, the couples of $\varphi_t$ and $k_{app}$ values lying on the associated curve ensure the recording of a pressure signal which is long enough compared to that acquired for BLM. A test is validated when the ($\varphi_t$, $k_{app}$) couple is below the curve and disregarded in the opposite case.

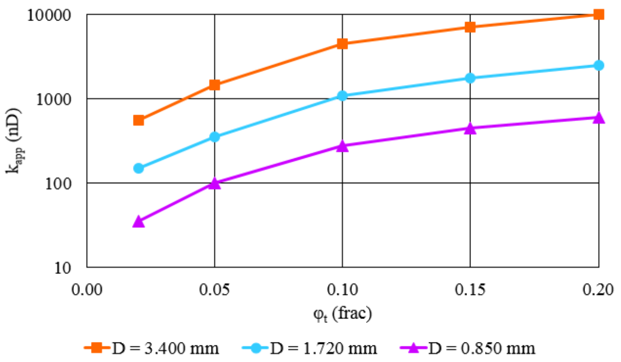

**Fig. 13.** $k_{app} = f(\varphi_t)$ graph for nitrogen

### *3.1.3 Results*

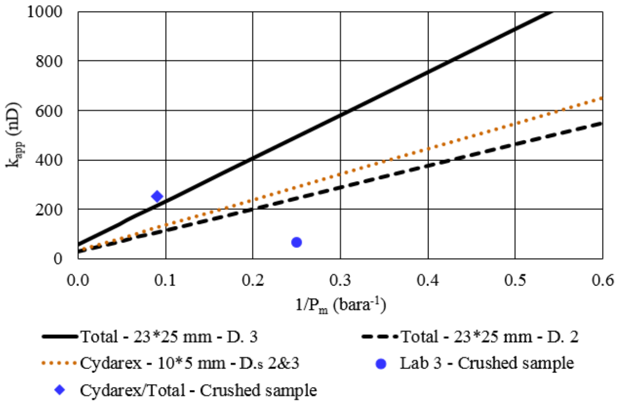

**Fig. 14.** $k_{app} = f(1/P_m)$ graph for the pyrophyllite

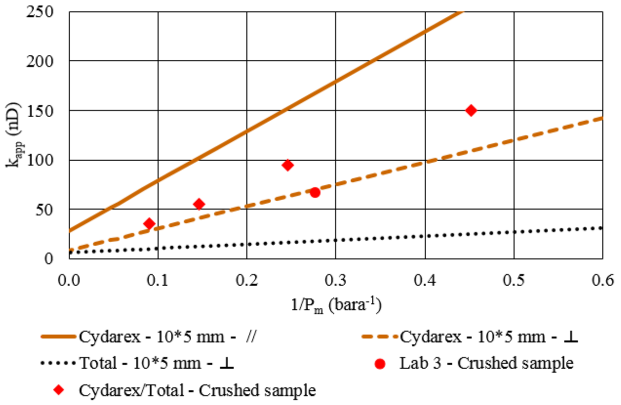

**Fig. 15.** $k_{app} = f(1/P_m)$ graph for the shale

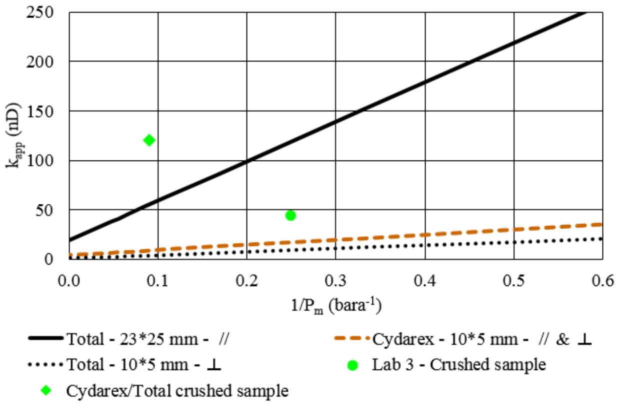

**Fig. 16.** $k_{app} = f(1/P_m)$ graph for the clayey sandstone

We carried out GRI tests on one crushed sample of each type of rock injecting nitrogen. The graphs for nitrogen of Figure 5 to Figure 7 were completed with our $k_{app}$ values. The new graphs are those of Figure 14 to Figure 16.

Our $k_{app}$ values lie in the predicted area for the shale and a bit above the upper limit for the pyrophyllite. The $k_{app}$ value for the clayey sandstone is quite equal to twice the upper limit value. Paying attention to eliminate at best the experimental and thermal artifacts altering the signal quality probably contributed to decrease the dispersion of the results. For the pyrophyllite and the clayey sandstone, one could think that the higher than expected $k_{app}$ values are maybe due to a problem of validity of the tests. This justification would not be absurd, both rocks being poorly porous and then bad candidates to acquire long signals. However, the graph of Figure 17 highlights that, as well as the ($\varphi_t$, $k_{app}$) couples for the shale, the couples for the pyrophyllite and the clayey sandstone are in the validity domain of the method.

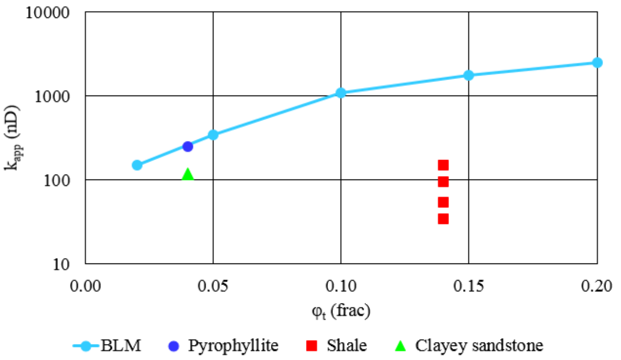

**Fig. 17.** Cydarex/Total results on $k_{app} = f(\varphi_t)$ graph for nitrogen and D = 1.720 mm

## 3.2 Cydarex/ Total model versus laboratories' models

As the laboratories sent all of the parameters concerning their samples and devices, it was possible to predict with our model the pressure signal expected from a GRI test in a specific experimental configuration and for specific $k_l$ and b values. The exercise was done for the pyrophyllite, using the parameters coming from Lab 2. On the graph of Figure 18, the signal recorded by Lab 2 when testing the pyrophyllite crushed sample with helium is compared to two numerical signals. The first one was simulated with the $k_l$ and b values from Total and, more exactly, with the $k_l$ value for nitrogen and the b value for nitrogen increased by a factor of 2.9. The second one was simulated with the $k_{app}$ value from Lab 2. There is no coherence between the experimental and numerical signals. It is not surprising to see that the recorded signal does not match with the signal simulated from Total's $k_l$ and b values since the existence of discrepancies between the laboratories' results and our results is known. It is more problematic to notice that the signal simulated with the $k_{app}$ value from Lab 2 is faster than the recorded signal. This suggests that Lab 2 works with a model differing from ours.

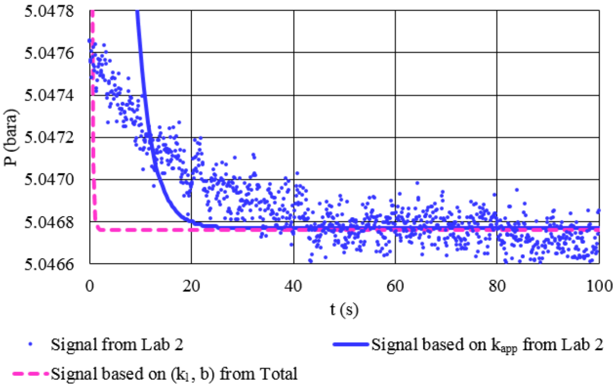

**Fig. 18.** Recorded signal versus simulated signals

# 4 Conclusions

Reconciling permeability data determined on samples of different sizes and by different laboratories having their own methods and experimental procedures is challenging. This is illustrated in the present paper for three materials: one homogeneous and slightly anisotropic outcrop rock named pyrophyllite and two reservoir rocks which were fairly homogeneous and moderately anisotropic.

The study started with the comparison of our methods dedicated to low permeability measurement: DarcyPress for small cylinders (10*5 mm) and Step Decay for bigger cylinders (23*25 mm). Consistency was noticed between the $k_l$ values as between the b values for the pyrophyllite only. For the reservoir cores, the results were dispersed. The discrepancies reached at maximum a factor of 5 for $k_l$ and a factor of 3 for b.

Three commercial laboratories having their own GRI techniques were contacted to characterize the three rocks following their standard procedures. The crushed samples they prepared were made up with particles having mean diameters between 0.7 and 1.9 mm. The three laboratories provided $k_{app}$ values instead of the demanded $k_l$ values. A range of possible $k_{app}$ values was hence defined for each rock from the $k_l$ and b values we estimated. About 50 % of the delivered $k_{app}$ values were in the predicted ranges and rather close to the lowest limits. The remaining $k_{app}$ values were mostly lower than the lowest expected values. Discrepancies ranging from a factor of 3.5 to a factor of 28 were noted. The $k_{app}$ values from the GRI tests created hence more dispersion in the permeability data. The fact that the $k_{app}$ values for the crushed samples tend to be low is not justified by the elimination of microfractures during crushing. Indeed, SEM images done for the pyrophyllite showed fractures in some particles of the crushed samples but not in the plug. Crushing seems to damage the rock.

The comparison of the permeabilities drawn from the Step Decay, DarcyPress and GRI tests evidenced that the dispersion of the results increases when the characteristic length of the medium decreases. Thus, one of the reasons explaining why many laboratories' $k_{app}$ values are out of the ranges of expected values would be the heterogeneity of the materials at small scale. This means that the crushed samples are potentially not representative of the rocks. A second reason could be the bad quality of the raw pressure signals. For two laboratories out of three, the signals were clearly affected by experimental or thermal artifacts since they were long and not stabilized at equilibrium. The third laboratory acquired signals having good amplitudes and durations by acting simultaneously on the sample features and on the device design. A third possible reason would be the diversity of the laboratories' interpretative models and the difficulty to define some input parameters such as the mean particle size for instance. A crushed sample is a complex system to model. The impacts of the simplifying assumptions made when building the model are generally hard to appraise.

We developed a GRI device especially for the study and we performed tests with it on the pyrophyllite and on the reservoir rocks. We spent time to eliminate at best the experimental and thermal artifacts impacting the pressure signal. This was indispensable to ensure the reliability of the recorded pressure values. Besides, we carried out tests on a highly permeable rock to identify the minimal signal duration needed with our device to ensure the validity of the test and of the results. The derivation of $k_l$ and b values from several tests run at increasing mean pore pressures proved to be satisfactory. Moreover, our $k_{app}$ values were closer to the expected values than the $k_{app}$ values from the laboratories. Being careful to the signal quality probably contributed to decrease the dispersion of the permeability data.

We do not pretend that our results are more accurate than those provided by the commercial laboratories. It is hard to know if the discrepancies are due to experimental issues, the interpretative models or the representativity of the samples. We believe that it is essential to continue the analysis of the GRI method and launch other benchmarks before considering it as a “routine” laboratory method. If we refer to the study of the centrifuge method historically initiated by the SCA [11], it could be fruitful to compare the numerical models used for interpretation on synthetic data.

# References

1. D. L. Luffel, C. W. Hopkins and P. D. Shettler, “Matrix permeability measurement of gas productive shales”, presented at the 68th SPE Annu. Tech. Conf. and Exhibition, Houston, TX, USA, Oct. 3 - 6, 1993, Paper SPE 26633.
2. S. Profice, D. Lasseux, Y. Jannot, N. Jebara and G. Hamon, “Permeability, porosity and Klinkenberg coefficient determination on crushed porous media”, *Petrophysics*, vol. 53, n° 06, Dec. 2012.
3. O. Kwon, A. K. Kronenberg, A. F. Gangi and B. Johnson, “Permeability of Wilcox shale and its effective pressure law”, *J. Geophys. Res.*, vol. 106, n° B9, pp. 19,339 - 19,353, Sep. 10, 2001.

4. Q. R. Passey, K. M. Bohacs, W. L. Esch, R. Klimentidis and S. Sinah, “From oil-prone source rock to gas-producing shale reservoir - Geologic and petrophysical characterization of unconventional shale-gas reservoirs”, presented at the CPS/SPE Int. Oil & Gas Conf. and Exhibition, Beijing, China, Jun. 8 - 10, 2010, Paper SPE 131350.
5. A. Tinni, E. Fathi, R. Agarwal, C. H. Sondergeld, I. Y. Akkutlu and C. S. Rai, “Shale permeability measurements on plugs and crushed samples”, presented at the SPE Canadian Unconventional Resources Conf., Calgary, AB, Canada, Oct. 30 - Nov. 1, 2012, Paper SPE 162235.
6. R. Lenormand, F. Bauget and G. Ringot, “Permeability measurement on small rock samples”, presented at the SCA Int. Symp., Halifax, NS, Canada, Oct. 04 - 07, 2010, Paper SCA2010-32.
7. P. Egermann, R. Lenormand, D. Longeron and C. Zarcone, “A fast and direct method of permeability measurements on drill cuttings”, *Petrophysics*, vol. 44, n° 4, pp. 243 - 252, Jul. - Aug. 2003.
8. D. Lasseux, Y. Jannot, S. Profice, M. Mallet and G. Hamon, “The “Step Decay”: a new transient method for the simultaneous determination of intrinsic permeability, Klinkenberg coefficient and porosity on very tight rocks”, presented at the SCA Int. Symp., Aberdeen, Scotland, Aug. 27 - 30, 2012, Paper SCA2012-25.
9. R. Lenormand and O. Fonta, “Advances in measuring porosity and permeability from drill cuttings”, presented at the SPE/EAGE Reservoir Characterization and Simulation Conf., Abu Dhabi, U. A. E., Oct. 28 - 31, 2007, Paper SPE 111286.
10. L. J. Klinkenberg, “The permeability of porous media to liquids and gases”, *Drilling and Production Practice*, pp. 200 - 213, Jan. 1, 1941.
11. P. Forbes, “Centrifuge data analysis techniques: a SCA survey on the calculation of drainage capillary pressure curves from centrifuge measurements”, presented at the SCA Int. Symp., Calgary, AB, Canada, Sep. 8 - 10, 1997, Paper SCA-9714.

## Nomenclature

| | | |
|---|---|---|
| b | Pa | Klinkenberg coefficient |
| c | - | Coefficient close to 1 |
| D | m / - | Diameter / Direction |
| DV | - | Dead volume |
| k | $m^2$ | Permeability |
| M | $g.mol^{-1}$ | Molecular weight |
| P | Pa | Pressure |
| r | m | Radius |
| R | $J.mol^{-1}.K^{-1}$ | Universal gas law constant |
| S | - | Sample |
| t | s | Time |
| T | K | Temperature |
| v | - | Valve |
| V | $m^3$ | Volume |
| $\Delta t$ | s | Duration |
| $\theta$ | Pa | Amplitude |
| $\mu$ | Pa.s | Viscosity |
| $\rho$ | $kg.m^{-3}$ | Density |
| $\varphi$ | - | Porosity |
| // | - | Parallel |
| $\perp$ | - | Perpendicular |

Subscripts

| | | |
|---|---|---|
| app | - | Apparent |
| eff | - | Effective |
| f | - | Final |
| i | - | Initial |
| l | - | Absolute |
| m | - | Mean |
| s | - | Solid |
| t | - | Total / Bulk |

# Towards Relative Permeability Measurements in Tight Gas Formations

*Denis* Dzhafarov[1], and *Benjamin* Nicot[1*]

[1]Total SA, 64018 Avenue Larribau PAU cedex, France

**Abstract.** Relative permeability is a concept used to convey the reduction in flow capability due to the presence of multiple fluids. Relative permeability governs the multiphase flow, therefore it has a significant importance in understanding the reservoir behavior. These parameters are routinely measured on conventional rocks, however their measurement becomes quite challenging for low permeability rocks such as tight gas formations.

This study demonstrates a methodology for relative permeability measurements on tight gas samples. The gas permeability has been measured by the Step Decay method and two different techniques have been used to vary the saturations: steady state flooding and vapor desorption.

Series of steady-state gas/water simultaneous injection have been performed on a tight gas sample. After stabilization at each injection ratio, NMR T2, NMR Saturation profile and low pressure Step Decay gas permeability have been measured. In parallel, progressive desaturation by vapor desorption technique has been performed on twin plugs. After stabilization at each relative humidity level the NMR T2 and Step Decay gas permeability have been measured in order to compare and validate the two approaches.

The techniques were used to gain insight into the tight gas two phase relative permeability of extremely low petrophysical properties (K<100 nD, phi < 5 pu) of tight gas samples of Pyrophillite outcrop.

The two methods show quite good agreement. Both methods demonstrate significant permeability degradation at water saturation higher than irreducible. NMR T2 measurements for both methods indicates bimodal T2-distributions, and desaturation first occurs on low T2 signal (small pores).

Comparison of humidity drying and steady-state desaturation technique has shown a 12-18 su difference between critical water saturation (Swc) measured in gas/water steady-state injection and irreducible saturation (Swirr) measured by vapor desorption.

## 1 Introduction

In tight-gas sandstone, the productivity of a well is sometimes quite different from that of a nearby well. Wells also can be very sensitive to small amounts of water, whether from an aquifer associated with the reservoir, from hydraulic fracturing, or from other completion operations. In tight rocks, in case of small porosity and very small permeability, a significant influence water saturation on gas phase permeability is expected [1].

Relative permeability governs the multiphase flow; therefore, it has a significant importance in understanding the reservoir behavior. These parameters are routinely measured on conventional rocks, however their measurement becomes quite challenging for low permeability rocks such as tight gas formations.

Tight gas rocks generally have various initial water saturation values. Due to tight nature of the rock, a significant transition zone above gas water contact exists. In this case, presence of water can have a big impact on the effective permeability and, therefore, on the wells productivity. Thus, a proper measurement of effective permeability over different partial water saturations is an important subject for the reservoir characterization and production forecast.

### 1.1 Literature review and Issues of Kr tight gas

Liquid distribution in a tight gas reservoir controls the flow of gas more critically than in conventional systems [2]. Earlier experimental studies [3, 4] on tight gas sandstone show that the relative permeability to gas decreases dramatically as water saturation increases. While this implies that measurements relating to two-phase flow in tight sands should be performed under carefully controlled conditions of stress and water saturation, such elaborate experiments are difficult and time-consuming because of the extremely small flow rates involved.

It was indicated [3, 5] that in low-permeability reservoir irreducible water saturation and critical water saturation can be dramatically different. “Permeability jail” concept in low-permeability reservoir was introduced, there is a

---

[*] Corresponding author: benjamin.nicot@total.com

broad range of water saturations in which neither gas nor water can flow.

Convention holds that connate water has little effect on oil or gas permeability because it occupies the smaller pores [1].

In the recent study [2], by use of laboratory scale experiments and modelling, it was shown that capillary driven transport is an important mechanism that helps to redistribute the water within the tight gas rock samples. Strong effect of water dissipation due to capillary suction (during shut-in period) was demonstrated.

Effect of water saturation on the effective permeability to gas has been the subject of numerous experiments [6,4,3]. The common laboratory practice is to use evaporation to desaturate samples, effective gas permeability is measured by either the steady-state or the pulse technique at various levels of water saturation established by evaporation.

However, one can argue that the nature of water distribution resulting from evaporation has certain disadvantages of heterogeneity of water distribution and possible salt precipitation of brine.

## 2 Samples and Methods

### 2.1 Our methods

In this study, we demonstrate a methodology for relative permeability measurements on tight gas samples, with particular attention to the monitoring (quality control) of desaturation process, using NMR T2 and NMR saturation profiles measurements. Two different techniques were used to vary the saturations: steady state flooding and vapor desorption. The gas-phase effective permeability at certain water saturation has been measured by the Step Decay method [7].

Steady-state gas/water simultaneous injection has been performed at elevated pressure drop across the sample in order to achieve faster stabilization. After stabilization at each injection ratio, NMR T2, NMR Saturation profile has been measured to control the water saturation homogeneity.

In parallel, progressive desaturation by vapor desorption (humidity drying) technique has been performed on twin plugs. The experimental technique implies the samples saturation equilibration in a series of relative humidity levels. Saturation is then determined gravimetrically and by NMR T2 volume measurements.

After stabilization at each relative humidity level, NMR T2 and Step Decay gas permeability have been measured in order to compare and validate two approaches.

The Step Decay method is an advanced technique allowing the determination of absolute permeability of tight permeability samples (<0.1 mD) that is not possible or very long in time with standard methods under steady-state flow using Darcy's equation The principle of the Pulse Decay method consists in applying a pulse of pressure on one face of the plug and recording the differential pressure $\Delta P$ calculated from measurements taken at both extremes of the plug. The Step Decay method is based on the application of several consequently increasing pressure pulses [7]. The principal schema of Step Decay experimental set up is shown on Figure 1.

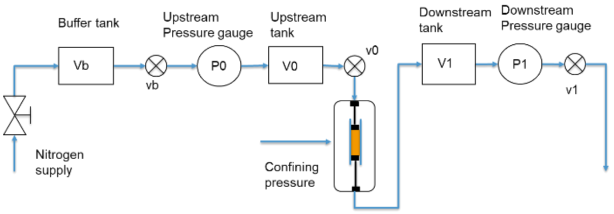

**Fig. 1.** Schematic of Step Decay experimental device

Step-Decay allows the simultaneous determination of intrinsic permeability (Kl), Klinkenberg coefficient (b) and porosity in one test only, speeding up the laboratory measurement.

Currently, the Step Decay method is used for absolute permeability determination (gas monophasic condition) of permeability of tight rock /gas shale.

Step Decay permeability measurements, performed at different gas/water saturations provides gas relative permeability data. In this case, the procedure of experiment is complicated by several steps of sample (de)saturation and have been performed using the following two methods:

- Steady-state gas/water simultaneous injection
- Vapor Desorption (humidity drying)

### 2.2 Steady-state gas/water simultaneous injection

The experiment concerns the progressive desaturation of the rock sample by the steady-state technique

In the steady state test, a sequence of fixed ratios of water/gas fluids is injected through the core sample until saturation and pressure equilibrium is established at each ratio.

Since the permeabilty involved is extremely low (<100 nD,), extremely low flow rates are required (< 5 µL/min). To ensure such injection requirements an ultra high pressure pump has been employed.

Humid nitrogen gas and brine are injected to displace gradually the water from the initially fully saturated tight rock sample at constant temperature. Prior to each fractional flow stage, the sample is fully saturated every time by water flooding.

Injection of gas is conducted at constant pressure drop across the core. The water injection is conducted at imposed flow rate on one side of the core (injection). Pressures at the inlet and outlet and the gas flow rate at the outlet of the core sample are monitored with time. The pressure differential to gas and water is assumed to be equal to the measured total pressure drop. Figure 2 shows a schematic of the experimental setup.

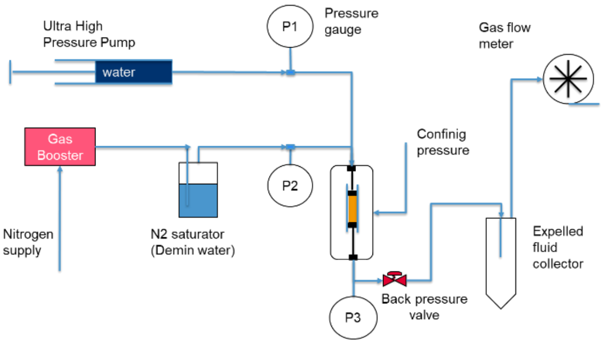

**Fig. 2.** Schematic of steady-state gas/water injection experimental set up

Each time when stabilization is achieved, injection is stopped and equipment is progressively depressurized. The sample is taken out from the cell and water saturation is determined by gravimetric measurements. NMR T2 and NMR Saturation profiles are also measured to ensure water saturation uniform distribution.

Capillary end effects are a particular problem in gas floods and the potential presence, influence and impact of end effects should be carefully considered when designing a gas displacement relative permeability test program [8]. Steady state water displacing experiments are not generally recommended unless one is aware of the limited saturation range expected from these analyses and of the potential saturation inaccuracies because of disequilibria effects [9]. Thus, the steady-state set up in this case is used only for saturation variation and the gas phase effective permeability is measured by Step Decay method.

## 2.3 Vapor Desorption (humidity drying)

The fundamental principal of vapor desorption method is the observation that the vapor pressure (Pv) above a liquid's curved surface is a function of the liquid surface curvature. Since the capillary pressure (Pc) is a function of the liquid surface curvature as well, both capillary and vapor pressure are the functions of saturation (Sw). Pc, therefore, can be calculated from Pv by controlling the relative humidity in the rock pores [10,11].

Initially fully saturated samples are placed in a sealed environment with relative humidity control (Humidity drying)

The test sequence represents a drainage type test (water is displeased by gas) where the wetting phase saturation Sw (water) is reduced as the humidity of the chamber is reduced. In practical manner, water is removed sequentially from the largest pores down through the smallest pores. Figure 3 schematically illustrates how the water vapor condenses within the pores of different size at different RH conditions.

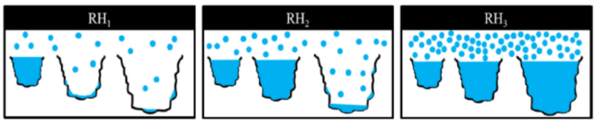

**Fig. 3.** Vapor desorption/condensation in pores of different size at different relative humidity environments RH1<RH2<RH3, after [11]

An electronically controlled humidity chamber is used. It allows investigating the relative humidity from 10 % to 95 % at room temperature. At each humidity level the mass stabilization is achieved and NMR T2 and Step Decay permeability are measured. Water saturation is determined by gravimetric techniques.

The main advantage of this method is the ability to achieve very high capillary pressures (the case for tight gas samples). The salinity increase or probable salt crystallization are the main problems of vapor desorption method that can potentially influence the Pc curve and permeability measurements especially at low saturations. The stabilization time may be several weeks/months.

## 2.4 Samples description and preparation

Identical plugs of Pyrophyllite quarry have been used to perform the test. Pyrophyllite is a homogeneous quarry rock sourced from the United Sates. The samples have preferential water wet wettability. They are mostly composed of clay and consequently has a low permeability (10-200 nD).

A Mercury Injection Capillary Pressure (MICP) and scanning-electron-microscope (SEM) analysis have been carried out on the fragments of the rock (Figures 4 and 5). In Figure 4, the pore throat distribution obtained by MICP shows a continuous distribution of pores approximately in the range between 2 and 30 nm. SEM images analysis shows that two types of pores coexist in this rock: interconnected system of small elongated pores and big pores weakly connected to the main pore system.

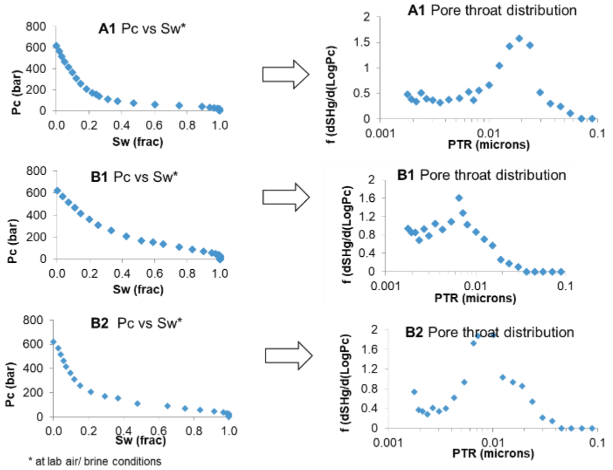

**Fig. 4.** Capillary pressure (Pc) and Pore throat size distribution (PSD) of Pyrophillite quarry rock

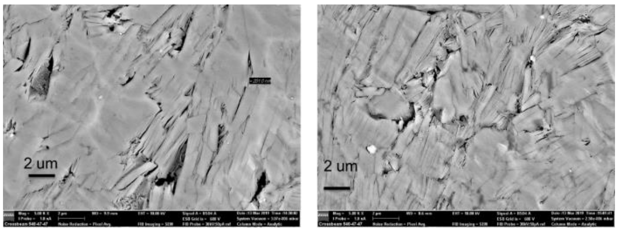

**Fig. 5.** Scanning scanning-electron-microscope (SEM) typical images of Pyrophillite quarry rocks

Before starting the experiments the Step Decay permeability (Kl) of each plug were measured at initial “as received” conditions. In this case, the significance of the “as received” condition is that the samples are at the same saturation conditions as in the quarry (atmospheric water) and do not contain hydrocarbons.

Next, the plugs were subjected to Soxhlet cleaning with isopropanol and gentle oven drying at 60 °C until mass stabilization. Then plugs were fully saturated by 70 g/l NaCl water brine at 500 bar during two weeks, after having created a vacuum over a period of four days.

Total of five pyrophyllite plugs with diameter 23 mm and height 25 mm have been prepared:

- 1 plug A1 (Permeability-230 nD and Porosity-5.6 pu) has been used for Steady-State flooding experiment
- 4 plugs B1/B2/B3/B4 (Permeability- 80 – 350 nD and Porosity 4.6 - 6.6 pu) have been used for Vapor desorption experiment.

## 3 Results

### 3.1 Steady-state desaturation experiment results

The experiment started by only water injection to fully water saturated sample in order to determine brine permeability.

Before each fractional flow stage the sample was fully re-saturated to 100 % Sw. Every fractional flow stage starts by one phase water injection cycle. As soon as the water stabilization is achieved, the gas at higher pressure is applied, while water is continuously injected at the same rate.

Four different gas /water injection ratios have been applied, they are listed in Table 1.

At the final stage, only gas has been injected. For this stage the sample has again fully re-saturated (100% Sw) and the only gas injection has been applied until pressure and gas rate stabilization.

**Table 1.** Main parameters of gas/water steady-state experiment (sample A1).

| TEST | Water rate, ml/hr | Water Pres, bars | Gas Pres, bars | NMR Vol, ml | Sw, su |
|---|---|---|---|---|---|
| Only water | 0.10 | 100 | - | 0.59 | 100.0 |
| 1 | 0.30 | 260 | 310 | 0.52 | 87.5 |
| 2 | 0.20 | 205 | 310 | 0.45 | 75.8 |
| 3 | 0.13 | 120 | 310 | 0.40 | 68.3 |
| 4 | 0.03 | 53.6 | 310 | 0.34 | 57.3 |
| Only Gas | - | - | 150 | 0.34 | 56.8 |

Back pressure for all tests has been set to 32 bars. Net overburden stress has been set to 100 bars.

Critical water saturation (Swc) has been defined at -57 su. High Swc value is expected due to tight nature of the rock (high capillary pressure)

NMR Saturation profile has been performed after each injection ratio:

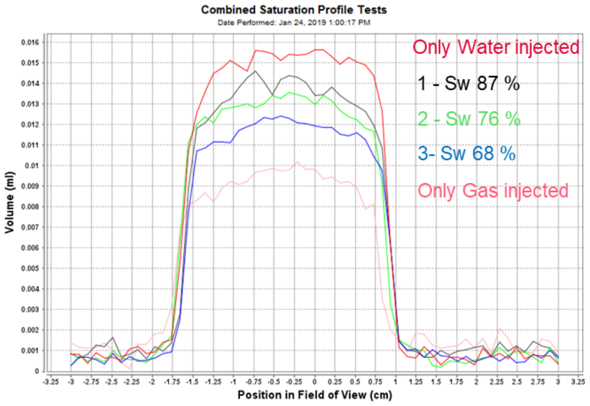

**Fig. 6.** NMR Saturation profile. Measurements performed after each injection ration at ambient conditions.

Based on Figure 6, saturation profiles appear relatively flat. NMR Saturation profiles do not have any evidence of pronounced capillary end effects. Such saturation behavior could be explained by the combinations of following phenomenon that potentially could influence the saturation distribution and reduce the capillary end effect:

- Water capillary suction. There is around 10 min time lag between the experiment and NMR saturation measurements, so the water is redistributed by capillarity
- Drying effect
- Effect of gas expansion/compression

The results of Step-Decay gas phase effective permeability measurements over different partial saturation are presented in Figure 7.

It is assumed that use of low pressure step decay method is not influenced by the capillary end effects, as it does not require the water flooding during the experiment.

Water phase effective permeability has been calculated assuming steady-state water flow (see table above). Water phase effective permeability should be treated with caution since it may be biased by saturation disequilibria effects [9]

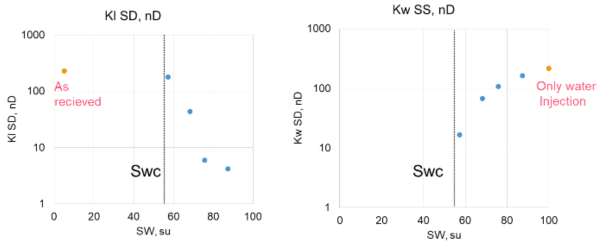

**Fig. 7.** Gas phase effective permeability measurements by Step-Decay technique. Steady-state gas/water flooding was used to vary the saturation. Water phase effective permeability have been measured by steady-state gas/water simultaneous injection.

Step-Decay gas phase permeability measurements revealed insignificant difference (by factor 1.2-1.5) between the permeability in "as received" conditions and at critical water saturation (Swc). At the same time significant permeability degradation was observed at water saturation being higher than critical. The water phase effective permeability did not show significant decay over Sw decrease (about a decade).

NMR T2 distribution has been measured at each injection ratio. Combined T2 plot is shown on Figure 8.

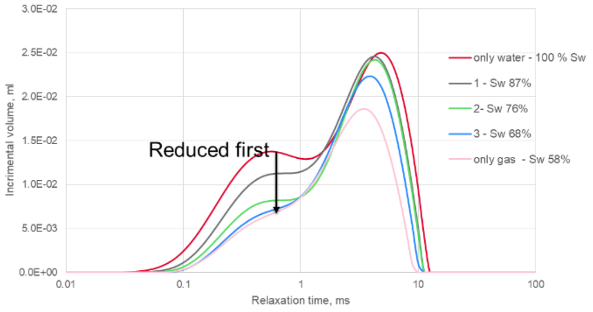

**Fig. 8.** NMR T2 distribution for different water saturations during steady-state gas/water simultaneous injection

One notes bimodal T2-distributions with higher intensity on second pic. As it can be seen from Figure 8, the desaturation first occurs on low T2 signal. Initially, first decrease of low T2 signal was not expected, as it implies that water desaturation occurs first in low porosity. This could be explained by the assumptions that gas initially flows the path of interconnected system of small elongated pores and desaturates bigger pores at the later stages.

### 3.2 Vapor desorption results

Low permeability sample B1 (76.4 nD) and high permeability samples B2, B3, B4 (230-350 nD) have been used to perform the vapor desorption test.

Initially, fully saturated samples were subjected to four different relative humidity (RH) levels: 90%, 85%, 80%, 75%. After stabilization at each relative humidity level the NMR T2 and Step Decay gas permeability have been measured in order to compare the two approaches. Step-decay permeability measurements results are shown on Figure 9.

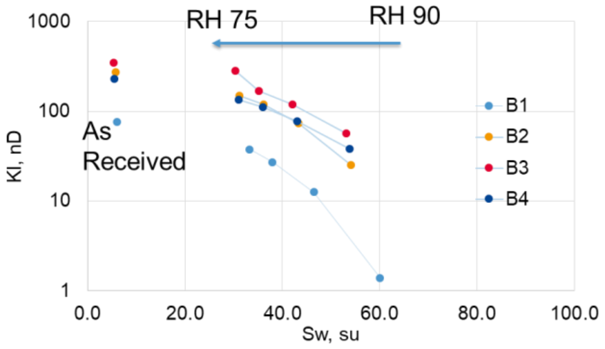

**Fig. 9.** Gas phase effective permeability measurements by Step-Decay technique. Humidity drying was used to vary the saturation

Effective gas permeability decay was observed with saturation increase, but less pronounced compared to steady-state desaturation (see Figure 7), since the gas effective permeability high water saturation was not measured (the maximum measured water saturation is limited to RH 90%).

At Relative Humidity of 75 % saturation levels ranged from 40 su (for B3 sample) to 46 su (for B1 sample). According to the Kelvin equation (Newsham et al 2003), RH 75 % corresponds to approximately 400 bars of capillary pressure in laboratory air/ brine conditions. So, it is assumed that at this pressure irreducible saturation (Swirr) is achieved. Swirr values appear systematically smaller by 12-18 su compared to Swc measured by steady-state desaturation (see Figure 7).

NMR T2 distribution at each humidity level is shown on Figure 10.

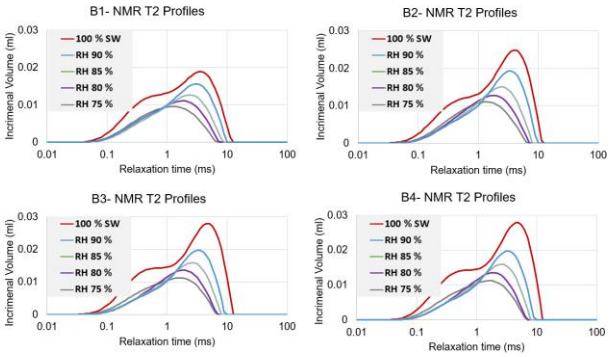

**Fig. 10.** NMR T2 distribution for different water saturations during vapor desorption desaturation process

NMR T2 distribution during vapor desorption process (Figure 10) confirms that desaturation first occurs on low T2 signal, which was previously observed at steady-state gas/water desaturation experiment (Figure 8).

## 4 Discussion

This study aims at developing new method of tight gas relative permeability measurement and gain insights into the tight flooding specific features. Steady-state regime has been achieved at elevated pressure drop and low injection volumes (see table 1). In this case the direct determination of effective gas phase permeability from experiment is complicated by numerous effects: gas compression/expansion effects, end scale effect, gas viscous instability, etc. On top of that, it is extremely difficult to monitor the downstream fluids production. Thus, the steady-state gas water set-up was used only for the saturation variation. Effective permeability at known saturation was measured by low pressure Step Decay technique. In such way it helps us to avoid many problems related to steady-state relative permeability determination. However, the sample is exposed to the atmosphere which can lead to different undesired influences such as drying and capillary suction. In this case, it is important to control the homogeneity of water saturation. We use NMR Saturation profile measurements to prove the saturation homogeneity.

NMR T2 Monitoring at each saturation level was used to perform analysis of fluids distribution within the pore medium. Despite the fact that the gas is non-wetting phase and it initially flows the path of least resistance through the largest pores, we observe first decrease of low T2 signal at high saturation. Detailed analysis and explanation of this observation is yet to be done.

Comparison of humidity drying and steady-state desaturation technique has shown the difference in critical water saturation (Swc) measured by steady-state gas/water injection and irreducible saturation (Swirr) measured by vapor desorption is 12-18 su. This difference appears mainly in high T2 signal (big pores).
Sharp permeability decrease (about a decade) with saturation increase has been observed for both desaturation methods.

## 5 Conclusion

In this study, we demonstrate a methodology for relative permeability measurements on tight gas samples of extremely low petrophysical properties (K<100 nD) of Pyrophillite outcrop. We pay particular attention to the monitoring (quality control) of desaturation process, using NMR T2 and NMR saturation profiles measurements. The gas permeability has been measured by the Step Decay method, and two different techniques have been used to vary the saturations: steady state flooding and vapor desorption. The following conclusion can be made:

- Step-Decay gas phase permeability measurements revealed insignificant difference (by factor 1.2-1.5) between the permeability in “as received” conditions and at critical water saturation (Swc). At the same time significant permeability degradation was observed at water saturation being higher than critical (about a decade).

- NMR T2 measurements indicate bimodal T2-distributions and that desaturation first occurs on low T2 signal (small pores). First decrease of low T2 signal was not expected and further detailed analysis of this phenomenon is required

- Comparison of humidity drying and steady-state desaturation technique has shown the difference in critical water saturation (Swc) measured in steady-state and irreducible saturation (Swirr) measured by vapor desorption is 12-18 su. This difference appears mainly in high T2 signal (big pores).

## References

1. S. Motealleh, S. L. Bryant, “Quantitative Mechanism for Permeability Reduction by Small Water Saturation in Tight-Gas Sandstones,” *SPE Journal*, vol. 14, no. 2, pp. 252-258, June 2009, doi:10.2118/107950-PA
2. D. H. Le, H. N. Hoang, J. Mahadevan, “Gas Recovery From Tight Sands: Impact of Capillarity,” *SPE Journal*, vol. 17, no. 4, pp. 981-991, December 2012, doi:10.2118/119585-PA.
3. K.W. Shanley, R.M. Cluff, J.W. Robinson, “Factors controlling prolific gas production from low-permeability sandstone reservoirs: Implications for resource assessment, prospect development, and risk analysis,” *AAPG Bull*, vol. 88, pp.1083-1121, 2004, doi:10.1306/03250403051
4. P. Chowdlah, “Influence of Water-Desaturation Technique and Stress on Laboratory Measurement of Hydraulic Properties of Tight Sandstones” *SPE Formation Evaluation*, vol. 3, no. 4, pp. 679-685, December 1988, doi:10.2118/15210-PA
5. R. M. Cluff, A. P. Byrnes, “Relative Permeability In Tight Gas Sandstone Reservoirs - The “Permeability Jail” Model,” presented at the SPWLA 51st Annual Logging Symposium, Perth, Australia, June19-23, 2010, Paper SPWLA-2010-58470
6. J. S. Ward, N. R. Morrow, “Capillary Pressures and Gas Relative Permeabilities of Low-Permeability Sandstone,” *SPE Formation Evaluation*, vol. 2, no.3, pp 345-356, September 1987, doi:10.2118/13882-PA
7. D. Lasseux, Y. Jannot, S. Profice, M. Mallet, G. Hamon, “The ‘Step Decay’: A New Transient Method for the Simultaneous Determination of Intrinsic Permeability, Klinkenberg Coefficient and Porosity on Very Tight Rocks,” presented at the International Symposium of the Society of Core Analysts, Aberdeen, Scotland, 27-30 August, 2012, Paper SCA2012-25
8. C. McPhee, J. Reed, I. Zubizarreta, “Relative Permeability,” in *Core Analysis: A Best Practice Guide*, vol. 64, 1st ed., Amsterdam, Netherlands: Elsevier B.V., 2015, pp. 561-562
9. A. Cense, J. Reed, P. Egermann, “SCAL for gas reservoirs: a contribution for Better experiments”, presented at the International Symposium of the Society of Core Analysts, Snowmass, Colorado, USA, 21-26 August, 2016, Paper SCA-2016-23
10. K. E. Newsham, J. A. Rushing, P. M. Lasswell, “Use of Vapor Desorption Data to Characterize High Capillary Pressures in a Basin-Centered Gas Accumulation with Ultra-Low Connate Water Saturations,” presented at SPE Annual Technical Conference and Exhibition, Denver, Colorado, 5-8 October, 2003, Paper SPE-84596-MS
11. A. Zolfaghari, H. Dehghanpour, “Pore Size Distribution from Water Adsorption Isotherm,” presented at SPE Annual Technical Conference and Exhibition, Houston, Texas, USA, 28-30 September, 2015, Paper SPE-175155-MS

# Storing $CO_2$ as solid hydrate in shallow aquifers: Electrical resistivity measurements in hydrate-bearing sandstone

*Jarand* Gauteplass[*], *Stian* Almenningen, and *Geir* Ersland

Department of Physics and Technology, University of Bergen, 5007 Bergen, Norway

**Abstract.** A recent proposed carbon dioxide ($CO_2$) storage scheme suggests solid $CO_2$ hydrate formation at the base of the hydrate stability zone to facilitate safe, long-term storage of anthropogenic $CO_2$. These high-density hydrate structures consist of individual $CO_2$ molecules confined in cages of hydrogen-bonded water molecules. Solid-state storage of $CO_2$ in shallow aquifers can improve the storage capacity greatly compared to supercritical $CO_2$ stored at greater depths. Moreover, impermeable hydrate layers directly above a liquid $CO_2$ plume will significantly retain unwanted migration of $CO_2$ toward the seabed. Thus, a structural trap accompanied by hydrate layers in a zone of favorable kinetics are likely to mitigate the overall risk of $CO_2$ leakage from the storage site. Geophysical monitoring of the $CO_2$ storage site includes electrical resistivity measurements that relies on empirical data to obtain saturation values. We have estimated the saturation exponent, $n$ in Archie's equation for $CO_2$ and brine saturated pore network ($n \approx 2.1$), and for hydrate-bearing seal ($n \approx 2.3$ for $S_H < 0.4$), during the process of storing liquid $CO_2$ in Bentheimer sandstone core samples. Our findings support efficient trapping of $CO_2$ by sedimentary hydrate formation and show a robust agreement between saturation values derived from PVT data and from modifying Archie's equation.

## 1 Introduction

Carbon capture and storage (CCS) technologies are expected to play a substantial role in the transformation of the energy sector toward reduced emissions of anthropogenic greenhouse gases [1]. Captured $CO_2$ is typically injected and stored in a supercritical state [2] in aquifers and depleted reservoirs at great depths. Once injected, $CO_2$ is retained in the sediments by physicochemical processes including structural trapping, capillary trapping, fluid dissolution, and mineral reactions. The contribution from each trapping process varies greatly with time [3]. Structural and capillary trapping are highly relevant from the onset of injection, while fluid dissolution and mineral reaction are believed to have a significant impact at a later stage.

More recently, an additional trapping mechanism suggests liquid $CO_2$ stored and contained by an upper $CO_2$ hydrate layer located at the base of the gas hydrate stability zone (GHSZ). This self-sealing hydrate layer makes an artificial cap rock that can prevent upward migration of $CO_2$ [4]. Cooler storage conditions enhances the $CO_2$ storage capacity due to increased $CO_2$ density, increased mobility control (important if long inter-well distance), and increased $CO_2$ solubility in water compared to storage of supercritical $CO_2$.

Experimental work has verified that $CO_2$ hydrate can form at the base of the GHSZ and reduce the $CO_2$ diffusion rate significantly in unconsolidated media [5]. Furthermore, high-density storage of $CO_2$ hydrate in silica sand has been demonstrated [6], as well as $CO_2$ hydrate acting as permeability barriers and successfully sealing off the pore space [7]. $CO_2$ immobilization by hydrate formation was directly visualized using MRI and micromodels [8]. A substantial GHSZ is ideal to make sure escaped liquid $CO_2$ is immobilized and converted to solid hydrate before reaching the seabed, and thus extending the hydrate sealing layer. Predicted thickness of the GHSZ for offshore Western Europe is nearly 0.5 km of the upper sediments [9], showing great potential for liquid $CO_2$ storage at shallow depths.

Resistivity measurements are routinely used to determine presence of sedimentary hydrates both in the field and in the laboratory. However, relevant empirical data are needed for saturation quantifications. These can be obtained and calibrated based on controlled laboratorial experiments. For a medium with uniform cross-section transmitting a uniform flow of electric current, resistivity is found from:

$$R_t = Z\frac{A}{L}\cos(\theta) \tag{1}$$

where $R_t$ is the bulk resistivity, $Z$ is the measured impedance, $A$ is the cross-sectional area of the sample, $L$ is the length of the sample, and $\theta$ is the phase angle. The Formation Factor ($F$) relates empirically to porosity through [10]:

$$F = \frac{R_0}{R_w} = a\phi^{-m} \tag{2}$$

---

[*] Corresponding author: Jarand.Gauteplass@uib.no

where $R_0$ is the resistivity of a fully brine-saturated sample, $R_w$ is the resistivity of the brine, $\phi$ is the porosity of the sample, $m$ is the cementation exponent and $a$ is the tortuosity factor. $R_w$ is calculated using a standard conversion [11]:

$$R_w = 0.0123 + \frac{3647.5}{[C]^{0.955}} \tag{3}$$

where $C$ is the ion content of brine. The $R_w$ value is corrected for temperature variations by [12]:

$$R_w(2) = R_w(1) * \frac{(T_1 + 21.5)}{(T_2 + 21.5)} \tag{4}$$

where $T_1$ is ambient temperature and $T_2$ is sample temperature. The Resistivity Index ($RI$) that applies to sediments partially saturated with a non-conductive material such as oil, gas, or hydrate, is defined as:

$$RI = \frac{R_t}{R_0} = S_w^{-n} \tag{5}$$

where $R_t$ is the measured bulk resistivity, $S_w$ is the brine saturation and $n$ is the saturation exponent.

Hydrate growth is accompanied by an effective reduction of the pore space as well as a salinity increase of the remaining brine that is not converted to solid hydrate. Both of these processes results in a continuous change in $R_0$ as hydrate grows, and a dynamic $R_0*$ needs to be implemented in eq. 5. This $R_0*$ is calculated from eq. 2 by adjusting $R_w$ and $\phi$ as hydrate grows. $R_w$ is found from eq. 3-4 by keeping track of the salinity increase during hydrate growth from PVT data. PVT data is also used to monitor the hydrate saturation during hydrate growth, and $\phi_{eff}$ is then found from the following relation:

$$\phi_{eff} = \phi(1 - S_H) \tag{6}$$

where $S_H$ is the hydrate saturation. The cementation exponent $m$ is calculated by eq. 2 when the sample (with known porosity) is completely filled with brine. This $m$ is then assumed constant as hydrate grows in the pore space [13]. The tortuosity factor $a$ is set to 1 to ensure that $R_w = R_0$ in the limiting case where $\phi \rightarrow 1$.

Finally, the saturation exponent $n$ is derived during hydrate growth by a modified version of eq. 5:

$$\log\left(\frac{R_t}{R_0 *}\right) = -n \log S_w \tag{7}$$

The $n$ is found as the slope when plotting the left side of eq. 7 as a function of –log $S_w$.

The majority of hydrate resistivity studies presented are related to $CH_4$ hydrate in the context of mapping and production of natural gas through various dissociation processes [13-16]. To the best of the authors' knowledge, this paper presents the first reported resistivity measurements on sedimentary $CO_2$ hydrate. We provide the saturation exponent $n$ during $CO_2$ injection into brine-filled cores and subsequent $CO_2$ hydrate formation. Saturation values derived from resistivity measurements are compared with PVT derived saturations to investigate the applicability of using resistivity measurements to monitor the evolving $CO_2$ hydrate seal in subsurface carbon storage.

## 2 Materials and methods

Homogenous and quartz-dominated Bentheimer sandstone (95.5% quartz, 2.0% kaolinite, 1.7% K-feldspar, 0.8% other [17]) was used in this study. Average porosity and absolute permeability were measured to 0.22 and 1.1 D, respectively. Twin samples, all with diameter of 5 cm and length 15 cm, were cleaned, dried at 70 °C for 24 hours, and fully saturated with brine (3.5 or 5.0 weight% NaCl) under vacuum. The brine-saturated cores were positioned in a core holder containing a rubber sleeve, fixed upstream end-piece, and floating downstream end-piece (see Fig. 1). A nitrogen-supported back-pressure regulator was connected downstream and an effluent sample collector measured brine production. A refrigerated circulator supplied the system with cooling fluid. Precise high-pressure pumps regulated overburden and pore pressure. The laboratory setup allowed pressure differences and bulk resistivity (Hewlett-Packard LCR-meter; 1 kHz, two-electrode setup) across the core sample to be logged.

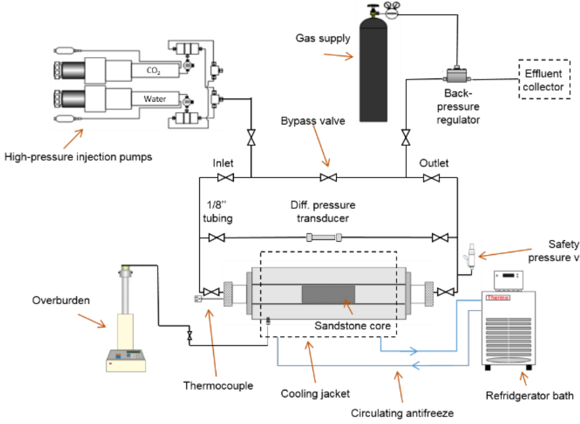

**Fig. 1.** Coreflooding laboratory setup including sandstone core sample, core holder, cooling system, pressure and temperature measurements, back-pressure regulator, and high-pressure pumps to regulate pore pressure and overburden. Modified from [18].

The pore space was pressurized with brine to 7.0 MPa, while the confinement pressure was set to 10.0 MPa. The core was then flooded with brine ($\mu$=1.07 cP) over a range of injection rates and absolute permeability was calculated. The waterflood was followed by liquid $CO_2$ ($\mu$=0.07 cP) injection at constant volumetric flow rate (0.5, 5 or 10 $cm^3$/min) to achieve a mixture of water and $CO_2$ in the pore space mirroring $CO_2$ invasion into an aquifer.

Two different hydrate growth conditions were designed in the laboratory: i) hydrate formation at constant pressure ($CO_2$ pressurized from both core ends, bypass valve open) and ii) flow-induced hydrate formation during $CO_2$ injection with constant volumetric flow rate. Onset of hydrate formation within the pore space was determined from the increase in resistivity, temperature, and differential pressure.

## 3 Results and discussion

### 3.1 $CO_2$ – brine system (outside GHSZ)

The $CO_2$ injection rate into a porous media affects the displacement efficiency and fluid saturations within the pore network. Achieving substantial $CO_2$ storage capacity in a multiple well scenario relies on an efficient displacement process from injector to producer(s). Though supercritical $CO_2$ can recover about the same amount of water at core-scale, the more optimum mobility ratio between liquid $CO_2$ and water is likely to be important at long interwell distances.

Fig 2 shows the rate dependency on macroscopic sweep efficiency, which govern the initial fluid distribution before hydrate formation. Three experiments with $CO_2$ injection rate of 0.5 $cm^3$/min (circles), 5 $cm^3$/min (diamonds) and 10 $cm^3$/min (triangles) were conducted outside of the GHSZ (20 °C) at 7.0 MPa. Injection rate (capillary number) affects both overall $S_w$ and pore-level fluid distribution. A linear production profile is valid before $CO_2$ breakthrough (BT), supplemented with water production measurements. Delayed $CO_2$ BT (indicated with broken vertical lines) for 5 and 10 $cm^3$/min implies improved sweep compared to the low injection rate (0.5 $cm^3$/min). However, doubling the injection rate from 5 to 10 $cm^3$/min had insignificant effect on the displacement process, reaching a plateau where approximately 50% of the brine remained after injecting several pore volumes (PV) of liquid $CO_2$. Though the experiments were designed to minimize capillary end effects by increasing the core length and using relatively high flow rates, the lowest rate (0.5 $cm^3$/min) experiment is prone to a more heterogeneous saturation profile due to reduced displacement efficiency. At breakthrough, saturation fractions in the pore space were $S_w$= 0.77 and $S_{CO2}$= 0.23 (0.5 $cm^3$/min), $S_w$= 0.59 and $S_{CO2}$= 0.41 (5 $cm^3$/min), and $S_w$= 0.57 and $S_{CO2}$= 0.43 (10 $cm^3$/min).

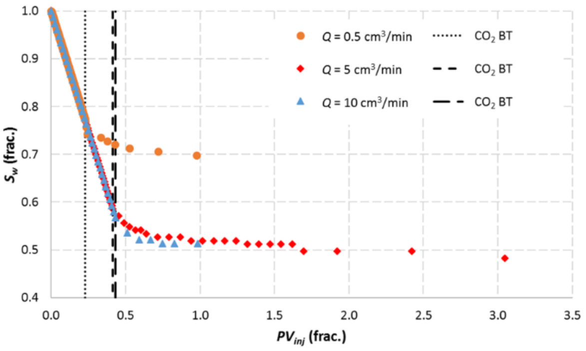

**Fig 2**. Drainage of initial water by liquid $CO_2$ in Bentheimer core samples at different injection rates; 0.5 $cm^3$/min, 5 $cm^3$/min, and 10 $cm^3$/min.

The bulk resistivity increased with increasing $CO_2$ saturation because electrically conductive brine was replaced by insulating $CO_2$ in the pore space. Fig 3 presents a logarithmic cross plot of water saturation ($S_w$) and resistivity index ($RI$) during $CO_2$ injection into the cores. The saturation exponent $n$ was found as the slope of the curves, with emphasis on the first saturation point ($S_w = 1$) and the last saturation points (after $CO_2$ BT in the cores) when determining the slope of the curves (solid filled markers). The use of Archie's equation is not applicable until $CO_2$ has reached the end of the core, achieving a predominantly uniform two-phase saturation profile throughout the entire core length. This is illustrated by the data points (no fill) obtained before $CO_2$ BT, which deviate from the linear trend lines in Fig. 3.

The saturation exponent $n$ increased with decreasing $CO_2$ flow rate, and was 1.9 for 10 $cm^3$/min, 2.1 for 5 $cm^3$/min, and 2.3 for 0.5 $cm^3$/min. This again reflects the different macroscopic sweep efficiencies that were achieved for the different flow rates, and highlights that $n$ is sensitive to the displacement history. The $n$ values identified in our $CO_2$-brine systems corroborate with $n$ values reported for similar conditions [19,20]. $CO_2$ is a highly reactive fluid that can influence resistivity measurements through i) dissolution and dissociation where new ions are provided to the solution, and ii) contribution of surface conductivity – even in clay free rocks [19,21]. Both processes lead to increased electrolytic conductivity and may thus overestimate the water saturation if not accounted for. These effects are negligible if the water is highly saline [22]. In the next section, we will compare the water saturation derived from Archie's using the estimated $n$ values with measured PVT data, to find if these effects are relevant to our systems with seawater salinity or higher.

### 3.2 $CO_2$ hydrate – brine system (within GHSZ)

To simulate the conditions of shallow $CO_2$ storage sites in offshore Western Europe, a temperature and pressure regime of 4 °C and 7.0 MPa pore pressure were chosen. This puts the system well within the GHSZ for $CO_2$ hydrate. Two hydrate growth scenarios were tested; i) static hydrate formation at constant pressure and ii) flow-induced hydrate formation under continuous $CO_2$ injection. Both approaches resulted in formation of $CO_2$ hydrate and subsequently immobilization of the injected $CO_2$ over a range of thermodynamic conditions.

Fig 4 shows a logarithmic cross plot of water saturation ($S_w$) and resistivity index ($RI$) during $CO_2$ hydrate formation in the pore space. The saturation exponent $n$ is derived from the slope of the best-fit linear model to all measured data points during $CO_2$ hydrate formation. Final hydrate saturation depended on initial displacement of water by $CO_2$, and the more efficient displacement (improved macroscopic sweep), the more hydrates were formed. Increasing the initial $CO_2$ flow rate from 0.5 $cm^3$/min to 10 $cm^3$/min, increased the final hydrate saturation by almost a factor of 2. When hydrates, water and $CO_2$ were present simultaneously in the pore space, $n$ took the value of 1.7 when $S_H = 0.37$ ($S_w = 0.21$),

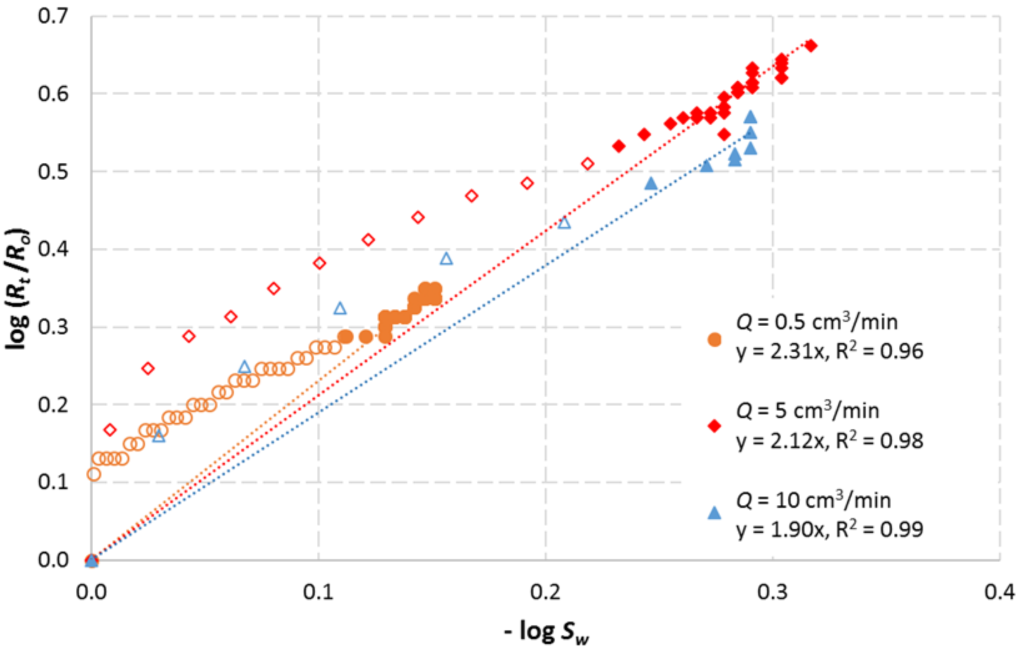

**Fig 3.** Logarithmic cross plot of RI and $S_w$ during $CO_2$ injection in brine-filled Bentheimer core samples at injection rates: 0.5, 5 and 10 $cm^3$/min at experimental conditions of 7.0 MPa and 20 °C. Data point markers with no fill (non-uniform saturation profile) were excluded from the linear trend lines. The saturation exponent *n* ranged between 1.9 – 2.3.

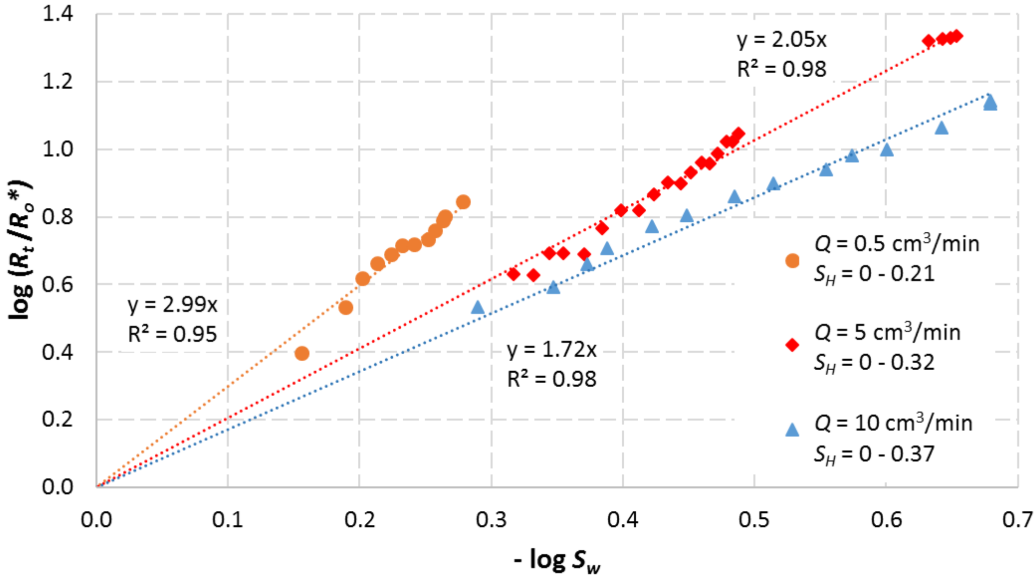

**Fig 4.** Logarithmic cross plot of RI and $S_w$ during $CO_2$ hydrate formation in Bentheimer core samples from a range of initial brine saturations caused by varying $CO_2$ injection rates: 0.5, 5 and 10 $cm^3$/min at 7.0 MPa and 4 °C. Depending on the saturation profiles, the saturation exponent *n* ranged from 1.7 to 3.0.

2.1 when $S_H = 0.32$ ($S_w = 0.22$), and 3.0 when $S_H = 0.21$ ($S_w = 0.53$). Compared to the $CO_2$-brine system, hydrate formation changed the *n* value for the 0.5 $cm^3$/min drainage experiment (least uniform saturation distribution) from 2.3 to 3.0, for 10 $cm^3$/min from 1.9 to 1.7, while for 5 $cm^3$/min *n* remained unchanged (2.1). The dispersion in obtained saturation exponents increased with the additional complexity of hydrate formation and dynamic hydrate growth in the pore space. This caused the mean value of *n* to increase from 2.1 to 2.3 during $CO_2$ hydrate formation. The obtained *n* values are nonetheless in good agreement with recent studies for natural gas hydrate in coarse-grained reservoirs [13], and for glass bead specimen [23].

The next three figures show a direct comparison of saturation values derived from Archie's and from measured PVT data.

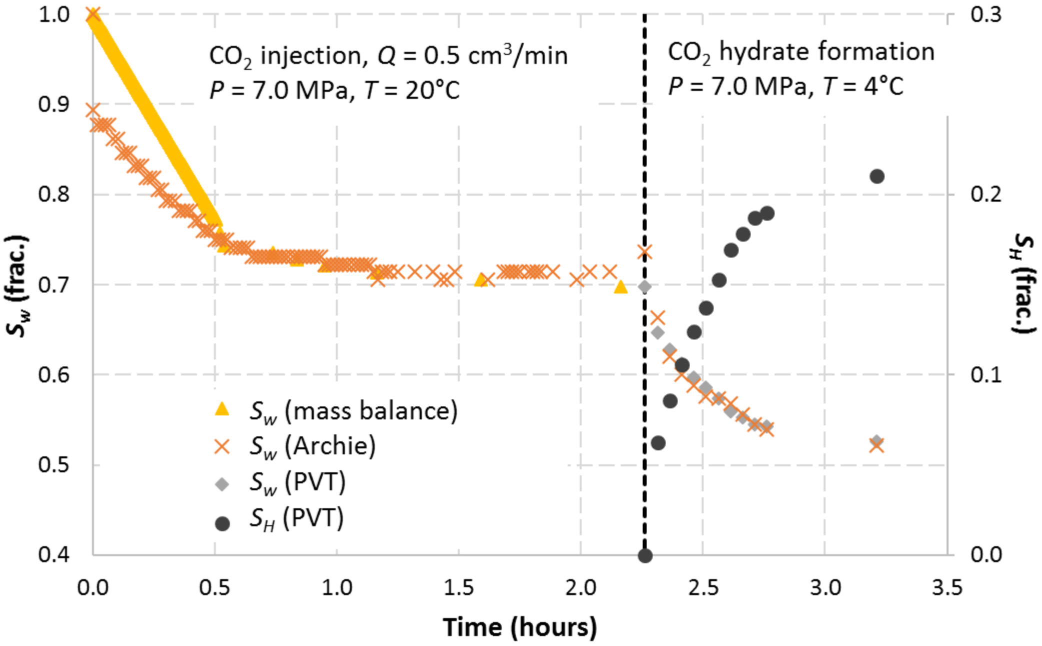

**Fig 5.** Comparison of saturation calculations from Archie and measured PVT data for injection rate 0.5 cm$^3$/min during initial displacement of water by $CO_2$ (7.0 MPa and 20 °C) and the following $CO_2$ hydrate formation (7.0 MPa and 4 °C). Obtained saturation values correlates very well after $CO_2$ breakthrough as a uniform saturation profile is established, and throughout $CO_2$ hydrate formation.

In Fig 5, saturation profiles during the initial displacement and the following hydrate nucleation and growth are displayed for flow rate 0.5 cm$^3$/min. The aforementioned unsteady-state regime occurring before $CO_2$ breakthrough, leads to severe deviation between the Archie saturation and correct linear displacement (mass balance) due to temporarily non-uniform saturation profiles. Once $CO_2$ breaks through at the outlet end of the sample, the saturation values from Archie's match actual PVT values very well at the plateau ($S_w$≈0.7). The onset of hydrate formation is indicated with a vertical line (broken). At this point, Archie's overestimate the water saturation somewhat compared to actual measurements. This apparent increase in water saturation is likely due to a short drop in resistivity linked to hydrate nucleation as reported in the literature [7,14,24]. Another possibility is the aforementioned $CO_2$ effects that may overestimate the water saturation, although the effects are most likely inhibited by the saline brine present. For the following hydrate growth process there is a very good agreement between the two water saturation profiles.

In Fig 6, drainage of water by $CO_2$ at injection rate of 5 cm$^3$/min and subsequent hydrate formation is displayed. Again, we observed a deviation in saturation profiles before $CO_2$ BT, and a good agreement after the $CO_2$ front reached the outlet end of the sample. The consistency continues from the onset of hydrate formation until hydrates occupy approximately 15% of the pore space. At this point the hydrate formation rate decreased substantially and the saturation profiles temporarily plateaued (for 0.2 hours). This period of hampered hydrate growth is not captured using Archie's saturation calculations, thus underestimating the water saturation here. Accelerated hydrate formation followed next and this "normalization" caused the end-point saturation values from PVT data and resistivity measurements to match once again.

Fig 7 shows saturation profiles during the initial displacement, and the following hydrate nucleation and growth for flow rate of 10 cm$^3$/min. The remaining water saturation in the core after $CO_2$ breakthrough was almost identical to the 5 cm$^3$/min experiment. There is a good agreement between the water saturation profiles after this point including the whole hydrate formation period in Fig 7.

$CO_2$ dissociation effects are highly sensitive to salinity. The 3.5 weight% NaCl solution used in Fig 5-7, belongs in a "high-salinity regime" where the conductivity was actually reduced by up to 15% due to reduced ion mobility [25]. This $CO_2$ dissolution effect, if not accounted for, will underestimate the water saturation derived from resistivity measurements. At the time-scale investigated in our study, no consistent impact of $CO_2$ dissociation on resistivity measurements was observed. Modifying Archie's equation by accounting for reduced effective porosity and increased salinity of the remaining water for each time step [14], resulted in resistivity saturation values agreeing very well with independent PVT measurements.

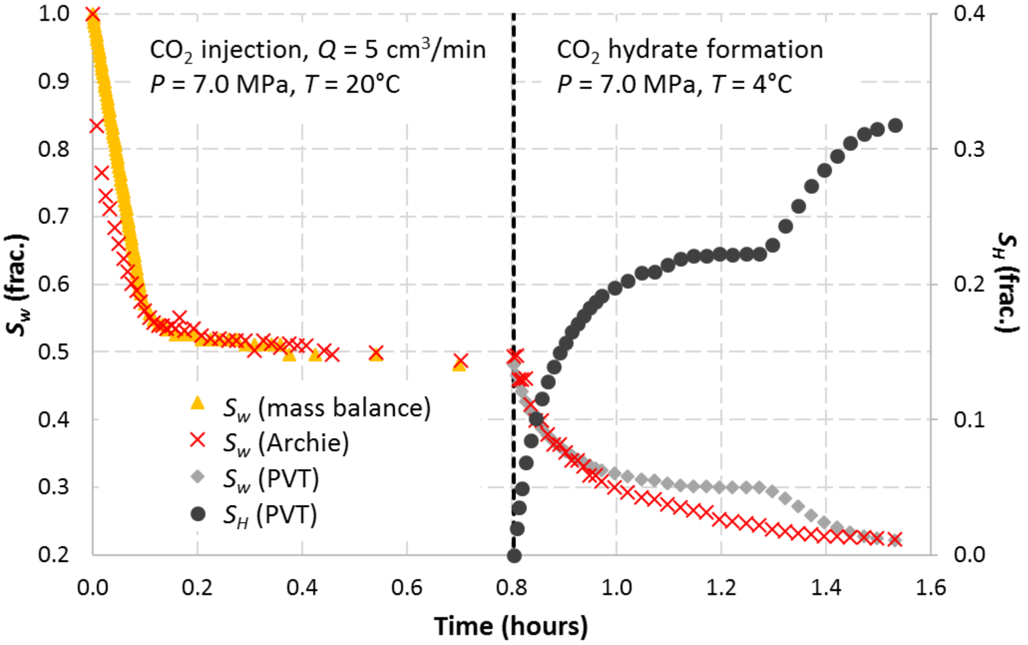

**Fig 6.** Comparison of saturation values obtained from Archie and measured PVT data for injection rate 5 cm$^3$/min during drainage (7.0 MPa and 20 °C) and during the following CO$_2$ hydrate formation (7.0 MPa and 4 °C).

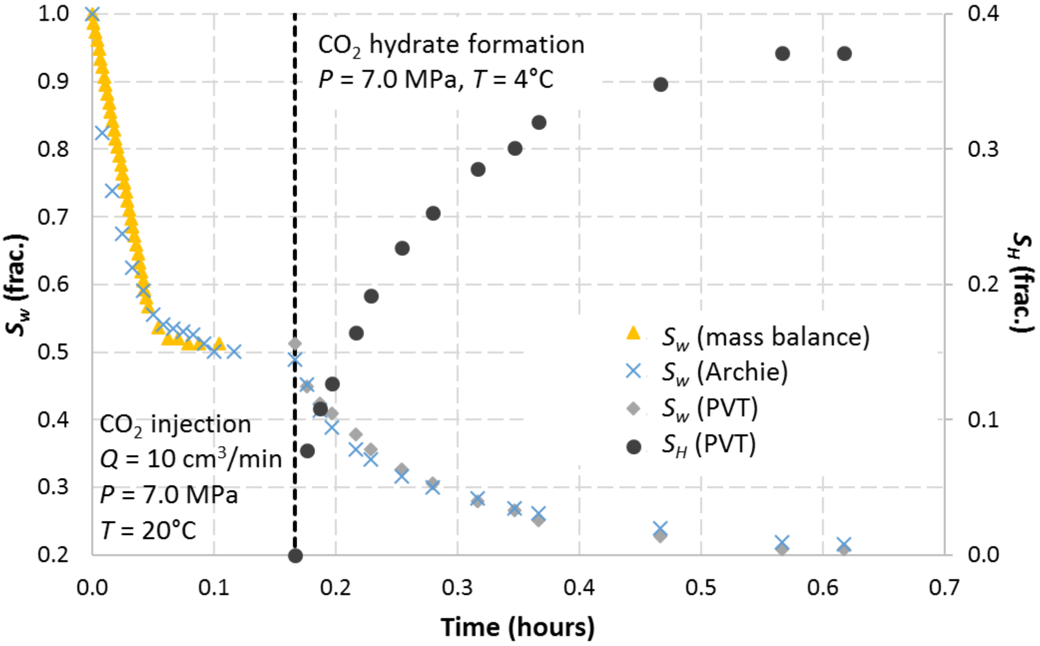

**Fig 7.** Comparison of saturation calculations from Archie and measured PVT data for injection rate 10 cm$^3$/min during initial displacement of water by CO$_2$ (7.0 MPa and 20 °C) and the subsequent CO$_2$ hydrate formation (7.0 MPa and 4 °C).

In addition to the constant pressure experiments, a series of flow-induced $CO_2$ hydrate formation experiments were tested for various thermodynamic conditions (within the GHSZ). $CO_2$ was injected into fully brine-saturated core samples at 7.0 MPa pore pressure and aquifer temperature of 4 °C or 6 °C. In Fig 8, resistivity profiles for different $CO_2$ flow rates, and salinity and temperature regimes are compared as a function of time. Here, increased flow rate (from 0.5 to 5 $cm^3$/min) accelerated hydrate formation and subsequent $CO_2$ trapping and immobilization. However, in terms of pore volumes (PV) $CO_2$ injected, we observed no effect of injection rate on hydrate induction time. The initial displacement of brine by liquid $CO_2$ increased the bulk resistivity from approximately 5 Ωm to 10 Ωm in all four corefloods. Two experiments were flooded with $CO_2$ at a constant rate of 5 $cm^3$/min at 7.0 MPa and 4 °C, where one core contained 3.5 weight% NaCl (red curve) and the other 5 weight% NaCl (yellow) – to demonstrate the effect of salinity increase on hydrate formation. Furthermore, two experiments were flooded with $CO_2$ at a constant rate of 0.5 $cm^3$/min at 7.0 MPa and salinity of 3.5 weight% NaCl, one experiment at 4 °C (blue) and the other at 6 °C (light blue) - to demonstrate the effect of temperature increase.

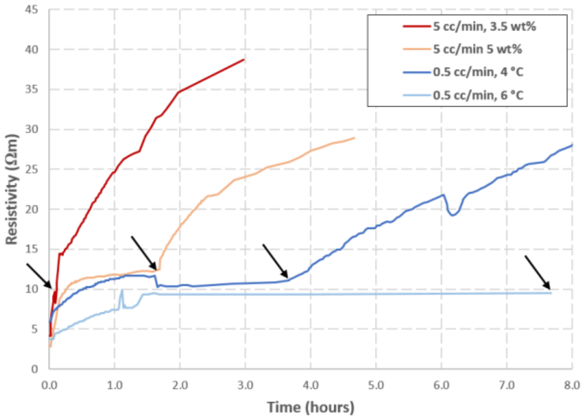

**Fig 8**. Resistivity profiles for various temperature and salinity conditions. Arrows indicate hydrate nucleation detected by a combination of pressure, resistivity, and temperature readings. Increase in salinity/temp caused a delayed $CO_2$ hydrate seal formation during continuous flow experiments.

The 5 $cm^3$/min constant rate experiment at lowest salinity (Fig 8 – red curve) started forming solid hydrates in the pore space shortly after $CO_2$ breakthrough (nucleation indicated with black arrows). By increasing the brine salinity from 3.5 to 5 weight% (yellow curve), we observed a prolonged induction time of approx. 1.5 hours (factor 9 increase) from flow-induced hydrate formation. When injecting $CO_2$ at 0.5 $cm^3$/min at 3.5 weight%, the effect of increasing the sandstone temperature from 4 °C to 6 °C was a factor 2 increase in induction time from 3.8 hours (blue) to 7.6 hours (light blue – resistivity data beyond this point is missing, however point of hydrate nucleation was identified from pressure and temperature logs).

The flow-induced hydrate induction time was evidently sensitive to salinity and temperature variations. All four experiments led to solid $CO_2$ hydrate formation eventually. The steady increasing resistivity profiles after nucleation demonstrated hydrate growth in the pore network and decreased effective porosity and permeability. All corefloods experienced significant differential pressure build-up across the samples after hydrate formation, effectively stopping the $CO_2$ production at the outlet. These observations suggest that the injected $CO_2$ phase is made discontinuous by pore-spanning hydrate layers acting as permeability barriers, and thus successfully obstruct viscous $CO_2$ flow in the core sample for the time investigated.

## Conclusions

Electrical resistivity measurements providing fluid saturations relevant to $CO_2$ hydrate storage, resulted in the following key experimental observations:

For two-phase $CO_2$-brine systems, the saturation exponent $n$ ranged from 1.9 – 2.3 (average $n$=2.1) depending on the $CO_2$ injection rate used during the drainage process. Because the saturation exponent is sensitive to the saturation profile along the core length, it is not recommended to rely on saturation values derived from resistivity measurements using a 2-electrode setup in non-uniform fluid distribution processes.

During $CO_2$ hydrate formation, the saturation exponent $n$ ranged from 1.7 – 3.0 (average $n$=2.3) depending on the initial distribution of brine, which resulted in different final $CO_2$ hydrate saturations. The estimated values of $n$ may be used to map the brine saturation $S_w$ and the $CO_2$ hydrate saturation ($S_H = 1 - S_w$) in excess water conditions, and are in good agreement with previously measured $n$ values during methane hydrate growth. Resistivity measurements are increasingly important for $S_H < 0.4$, as acoustic methods currently cannot obtain sufficient velocity contrasts in zones of low hydrate saturation.

$CO_2$ hydrates effectively blocked the $CO_2$ flow path and sealed off the sandstone pore network during flow-induced hydrate formation for different injection rates and thermodynamic conditions. Moderate increase in brine salinity or aquifer temperature resulted in significantly prolonged induction time before $CO_2$ hydrate formed under constant flow rate. Once stored, unwanted $CO_2$ re-mobilization/migration was obstructed by formation of sedimentary hydrate layers. This observed mechanism could act as an additional safety factor against leakage from geological stored $CO_2$ located below the gas hydrate stability zone.

The authors gratefully acknowledge financial support from Equinor and the Research Council of Norway. One of the authors is supported by CLIMIT grant number 255490.

## Nomenclature

$a$ = tortuosity constant
$A$ = area, $L^2$, $m^2$
$C$ = ion content of brine, ppm
$F$ = formation factor
$L$ = length, L, m
$m$ = cementation exponent
$n$ = Archie's saturation exponent
$RI$ = resistivity index
$R_o$ = resistivity of fully water saturated sample, $(mL^3)/(tq^2)$, Ωm
$R_t$ = resistivity of sample, $(mL^3)/(tq^2)$, Ωm
$R_w$ = resistivity of brine, $(mL^3)/(tq^2)$, Ωm
$S_{CO2}$ = saturation of $CO_2$, fraction
$S_H$ = saturation of hydrate, fraction
$S_w$ = saturation of water, fraction
$S_{wi}$ = initial saturation of water, fraction
$T$ = temperature, T, °C
$Z$ = impedance, $(mL^2)/(tq^2)$, Ω
$\Delta P$ = differential pressure, $m/(Lt^2)$, bar
$\Theta$ = phase angle, °
$\varphi$ = porosity, fraction
$\varphi_{eff}$ = effective porosity, fraction
$\mu$ = viscosity, cP

## References

1. International Energy Agency (IEA/OECD), "20 years of Carbon Capture and Storage - Accelerating future deployment." Review report (2016)
2. O. Eiken, P. Ringrose, C. Hermanrud, B. Nazarian, T. A. Torp and L. Høier, "Lessons learned from 14 years of CCS operations: Sleipner, In Salah and Snøhvit." Energy Procedia **4**, 5541-5548 (2011)
3. S. Benson and D. R. Cole, "CO2 Sequestration in Deep Sedimentary Formations." *Elements* **4**, 325-331 (2008)
4. H. Koide, M. Takahashi, H. Tsukamoto and Y. Shindo, "Self-trapping mechanisms of carbon dioxide in the aquifer disposal." *Energy Conversion and Management* **36**, 505-508 (1995)
5. B. Tohidi, R. Anderson, B. Clennell, R. W. Burgass and A. Biderkab, "Visual observation of gas-hydrate formation and dissociation in synthetic porous media by means of glass micromodels." *Geology* **29**, 867-870 (2001)
6. M. Massah, D. Sun, H. Sharifi and P. Englezos, "Demonstration of gas-hydrate assisted carbon dioxide storage through horizontal injection in lab-scale reservoir." *Journal of Chemical Thermodynamics* **117**, 106-112 (2018)
7. J. Gauteplass, S. Almenningen, G. Ersland and T. Barth, "Hydrate seal formation during laboratory CO2 injection in a cold aquifer." *International Journal of Greenhouse Gas Control* **78**, 21-26 (2018)
8. S. Almenningen, J. Gauteplass, P. Fotland, G. L. Aastveit, T. Barth and G. Ersland, "Visualization of hydrate formation during CO2 storage in water-saturated sandstone." *International Journal of Greenhouse Gas Control* **79**, 272-278 (2018)
9. C. A. Rochelle, A. P. Camps, D. Long, A. Milodowski, K. Bateman, D. Gunn, P. Jackson, M. A. Lovell and J. Rees, "Can CO2 hydrate assist in the underground storage of carbon dioxide?" *Geological Society* **319**, 171-183 (2009)
10. G. E. Archie, "The Electrical Resistivity Log as an Aid in Determining Some Reservoir Characteristics." *AIME* **146**, 54-62 (1942)
11. Baker-Hughes. *Introduction to Wireline Log Analysis* (1992)
12. J. J. Arps, "The Effect of Temperature on the Density and Electrical Resistivity of Sodium Chloride Solutions." *Journal of Petroleum Technology* **5**, 17-20 (1953)
13. A. E. Cook and W. F. Waite, "Archie's Saturation Exponent for Natural Gas Hydrate in Coarse-Grained Reservoirs." *Journal of Geophysical Research: Solid Earth* **123**, 2069-2089 (2018)
14. K. A. Birkedal, G. Ersland, L. P. Hauge, A. Graue, K. Hester, J. Stevens and J. Howard, "Electrical resistivity measurements of CH4 hydrate-bearing sandstone during formation." *7th International Conference on Gas Hydrates* (2011)
15. A. E. Cook, B. I. Anderson, J. Rasmus, K. Sun, Q. Li, T. S. Collett and D. S. Goldberg, "Electrical anisotropy of gas hydrate-bearing sand reservoirs in the Gulf of Mexico." *Marine and Petroleum Geology* **34** (2012)
16. Y. F. Sun, and D. Goldberg, "Dielectric method of high-resolution gas hydrate estimation." *Geophysical Research Letters* **32** (2005)
17. T. Ramstad and H. Rueslåtten, "Pore scale numerical analysis for geological sequestration of $CO_2$." Technical report, 1-63 (2013)
18. C. Hågenvik, "CO2 Injection in Hydrate Bearing Sandstone with Excess Water." University of Bergen, MSc thesis (2013)
19. D. Bosch, J. Ledo, P. Queralt, F. Bellmunt, L. Luquot and P. Gouze, "Core-scale electrical resistivity tomography (ERT) monitoring of CO2–brine mixture in Fontainebleau sandstone." *Journal of Applied Geophysics* **130**, 23-36 (2016)
20. M. Han, S. Youssef, E. Rosenberg, M. Fleury and P. Levitz, "Deviation from Archie's law in partially saturated porous media: Wetting film versus disconnectedness of the conducting phase." *Physical Review E* **79** (2009)
21. J. H. Börner, V. Herdegen, J.-U. Repke and K. Spitzer, "The impact of CO2 on the electrical properties of water bearing porous media – laboratory experiments with respect to carbon capture and storage." *Geophysical Prospecting* **61**, 446-460 (2013)
22. M. Fleury and H. Deschamps, "Electrical Conductivity and Viscosity of Aqueous NaCl Solutions with Dissolved CO2." *Journal of Chemical & Engineering Data* **53**, 2505-2509 (2008)
23. E. Spangenberg and J. Kulenkampff., "Influence of methane hydrate content on electrical sediment properties." *Geophysical Research Letters* **33** (2006)
24. Y. Liu, W. Zhang, Y. Liu, S. Ren, "Experimental characterization and modelling of acoustic and electrical resistance in hydrate bearing sediments." *6th International Conference on Gas Hydrates* (2008)

25. J. H. Börner, K. Spitzer, J.-U. Repke and V. Herdegen, "The electrical conductivity of CO2-bearing pore waters at elevated pressure and temperature: a laboratory study and its implications in CO2 storage monitoring and leakage detection." *Geophysical Journal International* **203**, 1072-1084 (2015)

# Multiphase flow imaging through X-ray microtomography : Reconsideration of capillary end-effects and boundary conditions

*Franck* Nono[1,*], *Peter* Moonen[1,2], *Hélène* Berthet[3] and *Richard* Rivenq[3]

[1]CNRS/UNIV Pau & Pays Adour/E2S UPPA, Développement des Méthodologies Expérimentales-IPRA UMS3360, Pau, France
[2]CNRS/Total/UNIV Pau & Pays Adour/E2S UPPA, Laboratoire des fluides complexes et leurs réservoirs-IPRA UMR5150, Pau, France
[3]TOTAL S.A., Pau, France
[*]*now with Modis, Pau, France*

**Abstract.** We focus on capillary end-effects and boundary conditions during multiphase flow experiments. To that extent, we performed drainage and imbibition experiments on Bentheimer plugs with various wettabilities and for various flow rates. For each case, we studied the fluid distribution inside the pore space by means of X-ray microtomography. Experimental observations focus on three main aspects: (i) fluids distribution in the diffusers, (ii) saturation profiles and, (iii) cluster dynamics near the outlet-end interface.

It is shown that there is always an end-effect near the last cm/mm which cannot be investigated by many routine SCAL devices. Furthermore the outlet saturation varies significantly with flow rate, which disagrees the widely used zero capillary pressure ($P_c$) condition at the outlet corresponding to very little variation of the outlet-end saturation. In a standard configuration (inlet end piece – rock – outlet end piece) the observed filling states of the rock's interfaces contradict usual mathematical boundary conditions imposed on flow equations and the outlet end-piece may act (depending on geometry) as an obstacle to the flow direction thus generating perturbations and disturbing saturation profiles.

These experimental observations confirm the general conclusions that the physics of multiphase flow towards the boundaries in DRP and traditional SCAL experiments may be insufficiently known.

## 1 Introduction

Digital rock physics (DRP) has undergone remarkable developments these last years. Multiphase flow can directly be visualized at the pore scale under reservoir conditions and processes such as ganglion dynamics and snap-off can be investigated in great detail [1]-[3]. Nevertheless, the properties derived through DRP experiments still suffer from large uncertainties when compared to Special Core Analysis Laboratory (SCAL) data. Scarce studies [4], [5] succeeded in obtaining comparable experimental data via DRP routines as by classic SCAL measurements. One of the many reasons why there are large uncertainties associated to DRP routines is related to the sample size which is typically one or two orders of magnitude smaller than for SCAL. This raises questions about the representativeness of the results and more specifically the impact of experimental artefacts, mainly capillary end-effects (C.E.E) on the multiphase flow properties measured. On mm-scale plugs, these effects are expected to be emphasized. Analytical investigations [6], [7] have highlighted a clear relationship between the sample's length and the extent of C.E.E.

In this paper, we investigate C.E.E during classical oil-brine unsteady-state flow (USS) displacements at the pore-scale by means of 3D X-ray microtomography. Even though mathematical boundary conditions of a plug during USS flow displacement ((i) constant inlet injection rate, (ii) constant outlet pressure, (iii) zero Pc just outside the outlet face) and experimental considerations (total wetting of the inflow face by the injected phase) are widely used and mentally granted, there is little direct visual evidence to support these theories. This experimental study shows directly in a core flooding scenario and in agreement with a few conceptual and theoretical studies [8], [9] that our understanding of the boundary conditions during multiphase flow displacements may be less solid than that generally assumed. Before reporting our experimental results, we present a state of the art about end-effects. This concise literature survey includes a number of studies which report results that contrast with the general vision of boundary conditions. All along this paper, the discussion will be limited to USS flow displacements in homogeneous core samples.

## 2 State-of-the-art on capillary end-effects

C.E.E are essentially related to the boundary conditions of a plug during multiphase flow. At laboratory scale they arise due to the finite length of plugs and are most of the time significant whereas at the field scale they are negligible [10]. Capillary pressure being the difference in

---

[*] Corresponding author: franck.nono@external.total.com

the pressure in the non-wetting phase and that in the wetting phase, leads to be coupled with saturation inside the rock while this coupling does not exist outside the rock. A mathematical condition of Pc = 0 is then imposed at these boundaries (mainly outside the outlet end of the plug for USS flow) to solve flow equations.

Different causes for the saturation distortions at the inlet have been proposed. Nooruddin and Blunt [11] explained that some degree of counter-current flow of the non-wetting fluid is encountered across the inlet boundary during the injection of the wetting phase because the non-wetting phase may easily escape back through the inlet at the beginning of the test due to the capillary suction of the wetting phase by the rock, which impacts the saturation profile provided that water wetness is significant. Virnovsky et al. [12] argued based on numerical simulations that oil counter-current flow effects during waterflooding of a water-wet rock could be drastically reduced using a hydrophilic semi-permeable disk at the inlet. Other parameters such as (i) viscous fingering, (ii) plug's length and (iii) inlet end-piece geometry and properties are known to affect inlet end saturation. As the measured transient pressure drop over the overall plug length also depends on the inlet saturation, this artefact may cause non-negligible uncertainties on derived multiphase flow properties [13].

The most well-known capillary end-effects are related to the boundary conditions at the outlet-end. This subject has been extensively studied, especially in view of accounting for C.E.E during relative permeability ($K_r$) calculations using directly SCAL measurements or history matching of production and pressure data [12], [14]-[18]. A long-standing hypothesis in many SCAL studies is that the capillary pressure at the outlet-end (just outside the core's outflow face) equals zero, as it is assumed that the fluids exit the porous medium at equal pressure. This hypothesis has a number of logical consequences: (i) where both fluids are in contact at the outlet, the curvature must be negligible, (ii) the saturation being solely dependent on the capillary pressure, the outlet-end saturation must vary within very narrow limits thus be nearly independent on the flow rate, and (iii) at least the displaced phase must be continuous at the outlet-end. A small number of studies exist which report contradicting observations.

We start our introduction to this topic with the studies of Levine [19]. His set-up was one of the first attempts to measure the capillary pressure gradient over the plug's length during USS flow. A linear extrapolation of the measured $P_c$ gradient to the outlet end seemed to indicate that the outlet $P_c$ was not null at equilibrium. Later, Houpeurt [20] reported results of experiments performed by Delclaud for a private communication. Delclaud achieved vertical gas/oil drainage with gas (non-wetting phase) injected from the bottom of the sample and the outlet submersed in a large oil (wetting phase) volume. Under these conditions, he observed non-flat interfaces with gas bubbling out, indicative for non-null capillary pressure. Furthermore, he observed that an increase in gas pressure at the inlet generates an increase of the number of outlet pores occupied by gas. He argued that the outlet capillary pressure must at least be equal to the displacement pressure [21]. More recently, some authors [22] benchmarked various flow simulators including CYDAR ® [http://www.cydarex.fr] and the open source simulator SCORES [23]. They investigated the impact of different ways of imposing the outlet mathematical condition zero capillary pressure on the simulated production data and pressure gradient. SCORES is especially built in a way that it allows the outlet saturation to be flowrate dependent. Though, the outlet saturation variation range is too limited to observe an influence on production data or gradient pressure. It came out from this study that there were no impact on the different outputs.

From another perspective, when using conventional configurations of the outlet diffuser (i.e. an end-piece with grooves), mathematical boundary conditions may be very difficult to realise. Firstly, the end-piece acts as obstacle to the flow and generates perturbations as the flow stream lines near the interfaces are no longer straight [24]. Secondly, as pointed out by Ramakrishnan and Capiello [25], the outlet diffuser can unexpectedly become 100% saturated with one phase. For example, let us consider a stable vertical oil/brine primary drainage with oil injected from the top in a water-wet core. At equilibrium, a long time after breakthrough, there will be no brine in the diffuser and the rock's outlet-end will then be wetted by oil. Capillary pressure ($P_c$) at the outlet will therefore be impossible to characterize as there will be no interface. The semi-dynamic method [24] was implemented to correct this bias. With an optimized apparatus, the displaced phase is reinjected in the outlet diffuser through a different channel than that of normal flow at a very low rate so as to wash the core's outlet face and maintain its continuity from inside the plug to the diffuser, without disturbing the flow inside the core. The comparisons made by the authors with numerical simulations showed good agreements especially at low flowrates. However, at higher rates, the saturation gradient near the outlet end interface (where $P_c$ is relatively small) does not match well. Unfortunately, we are not aware of any experimental verification of the actual saturation distribution in the immediate vicinity of the outlet-end for the semi-dynamic method.

Standard in-situ saturation monitoring (ISSM) does not always provide information enabling to verify the outlet $P_c$ mathematical condition on the last cm of the sample and not at all on the last mm. The saturation profiles in these locations are always simulated, whereas the pressure gradient is measured along the rock's total length. If they exist, C.E.E in these last centimetres/millimetres may contribute significantly to the measured pressure gradient thus to the calculated relative permeability especially when using analytical approaches.

At this point, a parallel can be drawn with observations made regarding capillary pressure curves determined by the centrifuge method. The outlet boundary condition termed “zero capillary pressure” is the key assumption to derive $P_c$ curves. For primary drainage curves, 100% of brine saturation is expected at the outlet. Some studies show that the zero capillary pressure assumption is not valid above a specific bond number or when using specific end-pieces [26]-[28]. They reveal a large number of issues and show that accurate criteria enabling a direct experimental observation and quantification of these effects is lacking.

The difficulty in accessing the direct visualization of these phenomena is unlocked thanks to 3D X-ray microtomography. The drawback of using this technique is a matter of sample size. In practice, targeting higher resolution (tens of µm or less) imposes the use of millimetre-sized plugs and with small lengths (up to 10cm). Capillary end-effects are thus expected to be emphasized. Reducing C.E.E can be achieved by using long cores, high flowrates or high viscosity ratios. These choices are reflected in the Rapoport criterion ($N_R$) [29]:

$$N_R = L.v.\mu \geq 1 \text{ to } 5 \quad (\text{in } cm^2.min^{-1}.cP) \qquad (1)$$

Where L represents the sample length (cm), v the rate of displacement ($cm.min^{-1}$), and µ the displacing phase viscosity (cP). This factor is widely used in petrophysical applications mainly for the design phase when trying to set configurations reducing the impact of C.E.E. Many other factors can impact C.E.E such as permeability or rock-type. This is why even after Rapoport scaling, C.E.E may not be sufficiently minimised [18].

Recent studies [3] have evidenced different fluid flow configurations and cluster morphologies which are flowrate dependent (ganglion dynamics and connected pathway flow) and highlighted their important impact on $K_r$ in some cases. The Rapoport criterion enables estimating that one would need to analyse samples in the order of at least one-half meter in length, to mimic in example waterflooding at reservoir rates (1ft/day) in the lab with negligible C.E.E. This sample size can't be used in conventional micro-CT devices. This example clearly illustrates that: i) We do not have a lot of flexibility, ii) We can't avoid to really understand C.E.E mechanisms and their impact on small cores, and iii) Depending on the rock/fluids/rates system, the entire rock length could be in the C.E.E.

The aim of the current study is to take a close look to what really happens near the sample boundaries in a conventional configuration (plug and diffusers) during oil and brine flooding at various wettability conditions and to understand the impact these phenomena may have on multiphase flow properties.

## 3 Materials and methods

The experimental set-up is similar to the one used by Berthet et al. [4].

### 3.1 Porous media

Flooding experiments were performed on eight cylindrical Bentheimer sandstone plugs (6 with diameter 4mm and 2 with diameter 1cm, lengths ranging from 1 to 5cm and modal pore size ranging from 60µm to 80µm). Bentheimer sandstone is widely used in the field of digital rock physics because only a small fraction of the pore volume is below the resolution of conventional X-ray micro-tomographs. Moreover, this rock-type is known to be homogeneous as illustrated by Figure 1 which represents porosity and permeability profiles along the full length of all eight plugs used in this study. Porosity was determined through 3D image processing. The porosity held in the clay fraction is below image resolution (4µm – 5µm) and is not taken into account. Differences between the calculated and the true porosity are estimated to be in the range of 1-2 porosity units (p.u.). Permeability was obtained using simulation on segmented images via OpenFoam ® software (Volume Of Fluid method implemented). Every permeability point is calculated over 500 µm length of the sample. Samples permeability varied between 1.3D and 2D with homogeneous profiles and an increase in the last 500µm due to trimming. With homogeneous profiles of permeability and porosity, the samples used in this study can be considered to be homogeneous.

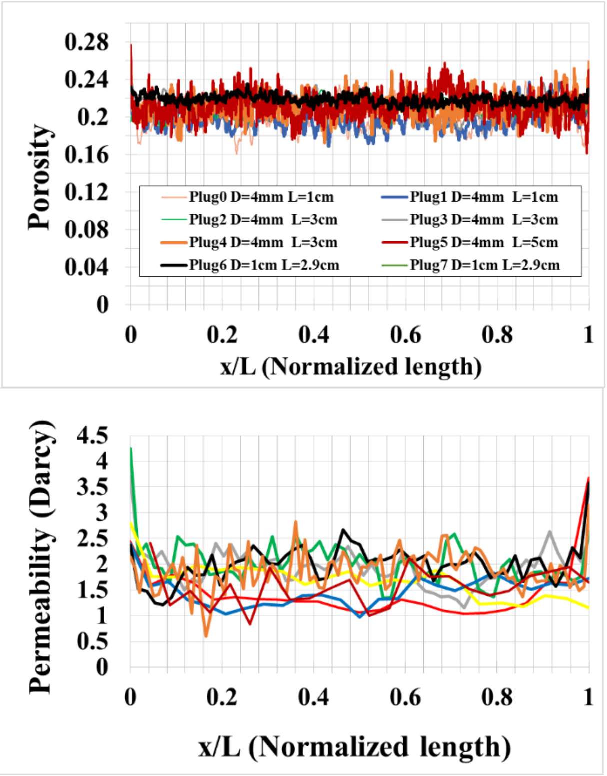

**Fig. 1.** Porosity and permeability profiles obtained via 3D image processing of the Bentheimer plugs used in this study and numerical simulation using segmented images on OpenFoam ® respectively. For porosity, the uncertainty on segmentation is estimated at +/- 0.4 p.u. and we must add +1 to 2 p.u. for the clay part.

### 3.2 Fluids

In this study, we focus on two phase flow (oil/brine) displacements. We use a brine made of 70 g/l of potassium iodide (KI) diluted into distilled water. This concentration enables sufficient X-ray contrast between oil, brine and rock. Decane was used as oil ($\mu_o$ = 0.93 cP and $\rho_o$ = 0.73 $g.cc^{-1}$ at 25°C).

### 3.3 Wettability modification

Fresh Bentheimer sandstones are water-wet. For a certain number of tests (4), the natural rock wettability was altered after primary drainage following the protocol proposed by Tweheyo et al. [30]. The procedure consists in replacing the decane present in the plug by a mixture of decane and Hexadecylamine and letting the plug age for 24h at ambient temperature. The modified oil mixture is prepared by dissolving 8g/l of Hexadecylamine (acid additive) into decane for about two weeks. This period of time (2 weeks) is due to the fact that there was some excess amine which needed more time as it remained undissolved during the first days [30].

### 3.4 End-pieces (diffusers)

Two different geometries were manufactured in PEEK (Figure 2).

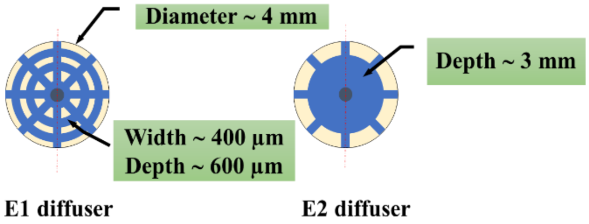

**Fig. 2.** Diffuser's geometry

i. The first diffuser (**E1**) features a pattern consisting of concentric circular grooves and straight radial grooves. The depth and width of the grooves are larger than the pore sizes in Bentheimer sandstone. Variants of this geometry are widely used in many laboratories worldwide.

ii. The second diffuser (**E2**) features a large central hole with a diameter nearly equal to the sample diameter and a depth (~3-5mm) much larger than the typical pore size of Bentheimer sandstone. This geometry causes minimal disturbance for the displaced fluid. Moreover, it allows live visualization of the fluids at the free-outlet interface of the plug during the experiment. Finally, as will be shown, **E2** end-pieces also help imposing mathematical boundary conditions at the outlet i.e. ensuring the continuity of the displaced phase and the permanent contact between the injected and the displaced phase at the oulet (see Delclaud experiments explained in the **State of art of capillary end effect** previously).

### 3.5 Image acquisition and processing

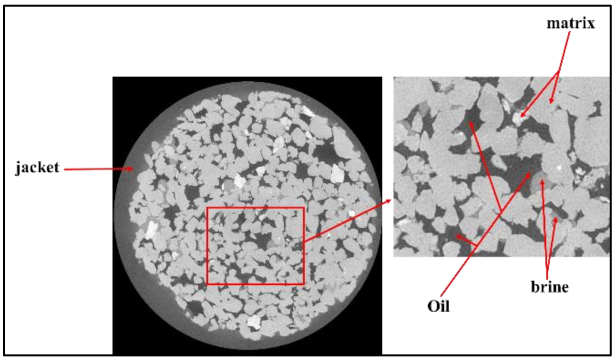

**Fig. 3.** Colour code for the reconstructed data

Figure 3 illustrates the colour code for reconstructed data ranging from dark grey for oil, light grey for the matrix. Intermediate grey levels correspond to brine.

Two different types of acquisitions were performed:

i. 3D scans of the whole plug after reaching steady-state conditions using end-pieces **E1**, and

ii. dynamic 2D and 3D scans of the plug's end faces during multiphase flow using end-pieces **E2**.

3D images were acquired using a Zeiss Xradia Versa 510. Energy settings were chosen between 80kV and 90kV while power varied between 7W and 8W. The voxel size was 4 µm for the 4 mm diameter plugs and 5 µm for the 1 cm diameter plugs. This meant we had to stitch 9 segments which would take 18 hours in total (2h per segment).

Image processing was realized using Avizo Fire 9.0 ® and the free software ImageJ. An illustration of the different stages of the image processing pipeline is presented in Figure 4. The raw images are already corrected automatically from beam hardening and ring artefacts in the upstream of the process by the software.

The 3D images of the wet plug were first registered to the dry images so as to be perfectly stackable. The matrix didn't change during the whole flooding protocols and it was verified during all registrations steps. The Viton® sleeve which had a specific greyscale level is isolated on the dry scan images using ImageJ and is used as mask for the entire dataset.

The main advantage is that the full cross section of the cylindrical sample can be analysed. The later stages involved filtering (non-local means filter), watershed segmentation and 3D labelling to dissociate and quantify the different phases/clusters at each flooding step.

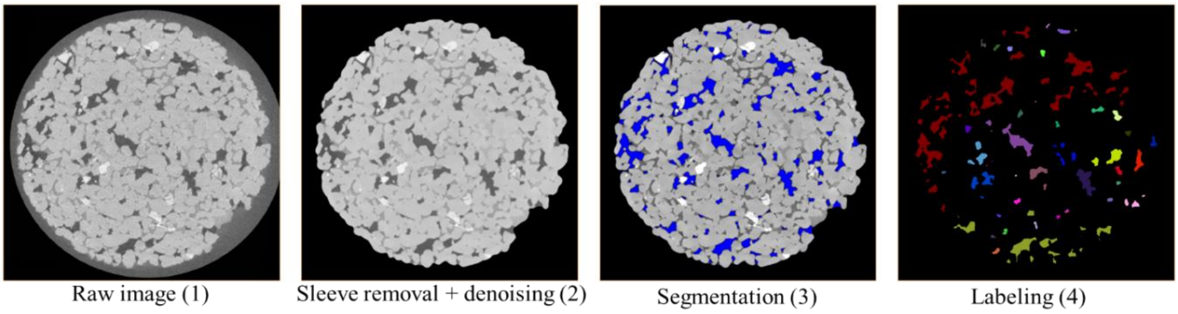
Raw image (1) Sleeve removal + denoising (2) Segmentation (3) Labeling (4)

**Fig. 4.** Image processing of a Bentheimer sandstone

### 3.6 Experimental procedures

The following experimental procedure was used (end-pieces **E1**):

1. Dry 3D scan of the whole plug
2. Vacuum-saturation and flushing with 40 pore volumes (PVs) of brine
3. Vertical primary drainage with decane injected from top at different injection rates. At least 10PVs are injected at each rate. When steady-state conditions are reached, the flow is stopped and a 3D scan is taken under constant and stabilized pore pressure (15 bar). Dynamic scanning under steady state conditions was not possible due to limitations in capacity of the injection pumps.

**N.B.** Some tests were carried in the beginning of the project to evaluate the speed of redistribution of fluids in the core after stopping the flow during primary drainage steady-state. The conservation of saturation profiles was found to last more longer than the overall sample scanning time (18h).

4. Vertical waterflooding with brine injected from bottom at different injection rates. Similar to primary drainage, at least 10 PVs per step are injected and 3D scans are taken under stabilized pore pressure (15 bar).

Optionally, the wettability of the rock is altered in between steps 3 and 4. The flowrates used in this study are reported in terms of capillary number ($C_a$) expressed as below in equation 2:

$$C_a = v.\mu/\gamma \qquad (2)$$

Where v represents the superficial fluid velocity ($m.s^{-1}$), μ the displacing phase viscosity ($P_a.s$) and γ the interfacial tension ($N.m^{-1}$). The range of capillary numbers investigated is from $2.5x10^{-8}$ to $1.35\ x10^{-5}$.

## 4 Results and discussions

Results are divided into three topics:

i. Observations at the interfaces between the plugs and the **E1** end-pieces (inlet and outlet) at equilibrium
ii. Saturation profiles at steady state conditions (with **E1** end pieces)
iii. Experiments with **E2** end-pieces

All observations were well reproducible. The 8 samples followed almost the same procedure during primary drainage with similar qualitative observations. Saturation ranges (mostly the plateau of saturation profiles) varied within 5-6 units. Average saturations and saturation profiles during waterflooding for the 8 samples (4 in water-wet conditions and 4 in altered wettability conditions) varied within a narrower range (3 units max) than that for primary drainage with very similar qualitative observations.

However, in order not to overload the paper, each observation will only be illustrated for a single plug.

Regarding saturation profiles, they will always be illustrated with inlet at the left of the plot and outlet at right. Every point on saturation profiles represents an average over the diameter of the plug (4mm or 1cm) and a length which is the acquisition resolution (4µm or 5 µm).

### 4.1 Interfaces between plugs and E1 end-pieces

In Figure 5 we illustrate oil/brine distributions on 2D cross-sections during primary drainage at equilibrium for $C_a = 2.5x10^{-8}$ on strongly water-wet sample. The top left figure shows the inlet **E1** diffuser, and the other figures correspond to cross-sections at increasing distance from the inlet. The bottom right figure shows the outlet **E1** diffuser. The images show that the inlet and outlet diffusers are completely saturated with oil. This observation holds for different injection rates. Specifically concerning the presence of oil at the outlet, our observations confirm the expectations of Ramakrishnan and Capiello [25] and disagree the hypothesis that the outlet interface between the rock and the diffuser is almost 100% brine-filled. The cross-section with the highest brine saturation is located at almost 1 to 2 mm from the outlet diffuser, inside the plug and no connected brine flow path to the outlet could be identified.

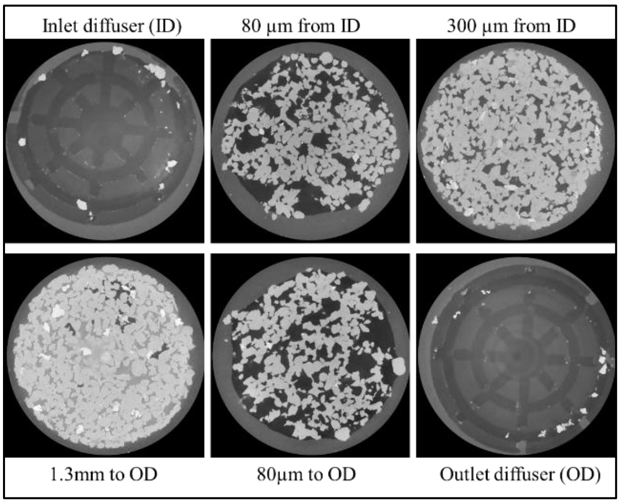

**Fig. 5.** From inlet (ID) to outlet (OD) during primary drainage of a 4mm diameter Bentheimer plug

Figure 6 uses a similar representation to illustrate the results after waterflooding. For the water-wet case (Figure 6a) the inlet is full of oil trapped in the diffuser due to (i) counter-current flow and (ii) the presence of large pores near the end-faces, leading to oil trapping in the first 100µm of the plug. Oil and brine co-exist inside the plug, oil occupying the large pores and brine the smaller ones as expected for this wettability. Near the outlet, a large fraction of the diffuser is oil filled while at 80µm from the outlet surface, brine fills the majority of pores. The filling in the diffuser could be for the most relevant due to the imperfect contact between the plug and the end-piece (trimming) or rock's wettability. As will be shown in Figure 6b, diffuser's wettability seems to have a negligible impact on fluid's repartition.

For the altered wettability case (Figure 6b), the inlet diffuser is full of brine (as expected) contrary to the water-wet case. Inside the sample, brine occupies the larger pores, while oil is found in the smaller ones. Close to the outlet of the plug we observe an accumulation of oil as expected due to the capillary end effect. The diffuser is however full of brine.

These reproducible observations per rock's wettability show that the inlet diffuser, as well as the space between the inlet diffuser and the sample, is not necessarily filled with the injected phase. On the contrary, rock's wettability seems to be the determining factor. When comparing tests at different flow rates (not shown) for the waterflooding in the water-wet case, we observe that once a preferential flow path is formed through the whole plug at low flow rate, it becomes very difficult to evacuate the trapped oil phase at the inlet even when we increase the flow rate within 2 orders of magnitude. A full contact between the injected phase and the entire area of the plug's inlet face may thus be difficult to obtain and control during unsteady-state flow experiments depending on rock's wettability.

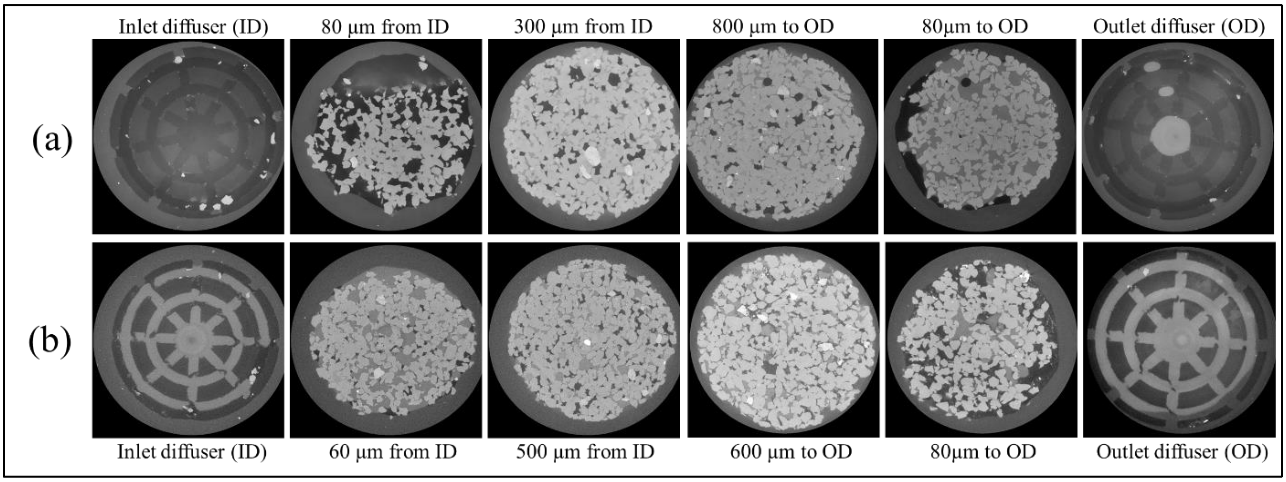

**Fig. 6.** From inlet to outlet during waterflooding of Bentheimer: (a) water-wet case at $Ca=1.35x10^{-7}$ ; (b) altered wettability case at $C_a=1.35x10^{-7}$

Important observations are also made near the outlet end. At this interface just inside the plug, saturation is expected to tend to the corresponding zero capillary pressure saturation and just outside the plug, a permanent contact between both fluid phases is expected. Our observations show that this is not necessarily true as for example in the primary drainage case, the outlet volume is 100% filled with oil and oil wets the entire outlet face of the plug. These observations hold regardless of the rock wettability, the diameter-to-length ratio of the sample and the investigated flowrate. Repeatability tests were performed as well. All these results seem to indicate that mathematical boundary conditions are not necessarily satisfied during drainage and imbibition experiments on micro-plugs in this particular configuration.

## 4.2 Saturation profiles

### *4.2.1 Primary drainage of water-wet samples*

Figure 7 and Figure 8, illustrate primary drainage saturation profiles at different oil injection rates (characterised by the capillary number) for two water-wet samples of respectively 4 mm and 1 cm in diameter. Both samples have a length of 29 mm. Each saturation profile curve is obtained after the injection of a sufficient number of pore volumes to ensure dynamic equilibrium. The flow takes place from left to right (representing the sample top and bottom respectively).

All profiles exhibit a brine saturation increase towards the end of the plug, which is the typical signature of C.E.E. As expected, C.E.E. decreases with increasing injection rate. We observe 100% oil saturation at the injection face. Few grains after the injection face just inside the core plug, saturation values exhibit an apparent plateau which level depends on the injection rate. This observation shows that the plug is entirely in C.E.E which then could invalidate an analytical approach [18] of determining relative permeability. It is similar from what reported in [18] for their case0 (also entirely in C.E.E). Very close to the outlet face of the plug, all brine saturation profiles exhibit a steep drop. This observation is coherent with the displacement of all the brine by oil in the outlet diffuser as shown on Figure 5. Note these saturation gradients occur over a very short distance, less than 10 mm, which is too small to be detectable by some routine SCAL devices and could erroneously be interpreted as a plateau without capillary end effects.

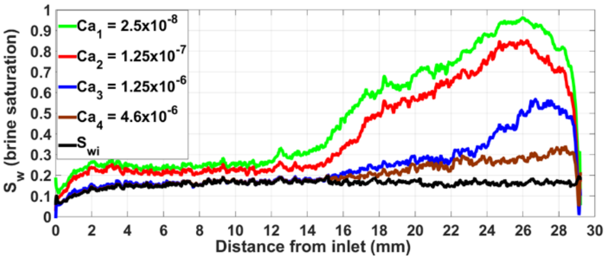

**Fig. 7.** Example of brine saturation profiles during primary drainage at varying injection rates of a Bentheimer plug (sample diameter = 1cm)

C.E.E in these zones could engender additional pressure gradient which may not be negligible for an interpretation using analytical methods. A final observation is that all saturation curves exhibit dependency on the injection rate: both the saturation level of the plateau in the first part of the plug (as expected) and the peak of maximum brine saturation in the second part of the plug are both capillary number dependent.

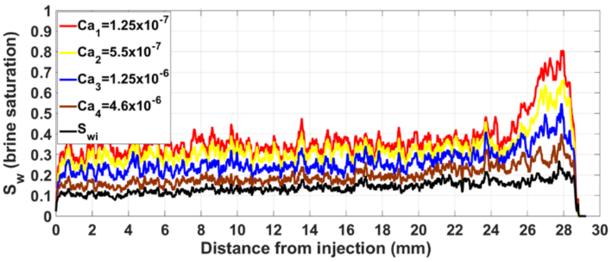

**Fig. 8.** Example of brine saturation profiles during primary drainage at varying injection rates of a Bentheimer plug (sample diameter = 4mm)

This second point contradicts the assumption that the peak saturation (point of maximum wetting phase saturation → outlet saturation in SCAL experiments) is independent of the injection rate (outlet $P_c \sim 0$ → outlet $S_w \sim$ constant) during primary drainage [24].

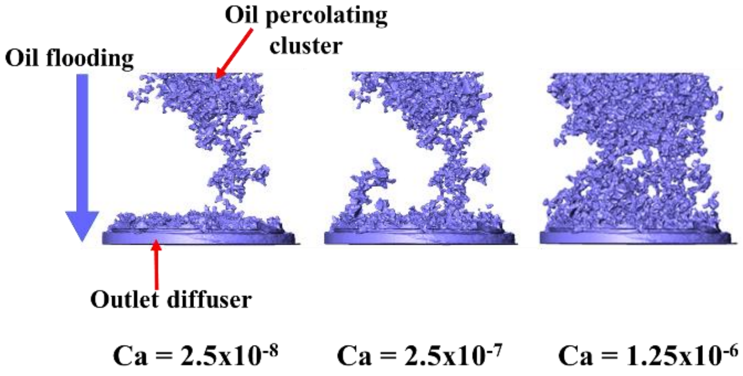

**Fig. 9.** Oil cluster spreading out and accumulating at the outlet during primary drainage of a Bentheimer plug (diameter = 4mm) at various rates. Magnification is the same in both directions and the diffuser is 4 mm diameter.

At this stage, the most plausible cause for the difference between our observations and the expected saturation profiles seems to be that our boundary conditions differ from the mathematical ones. One can argue that the final average brine saturations obtained in our study during primary drainage with the flooding method (in the range of 10% to 15%) are greater than what obtained Lin et al. [31] on similar sample (7% - 10%) with centrifugation method meaning that we still have a mobile brine saturation on the last drainage rate. Initialization by flooding is known to not be an efficient method for SCAL protocols but here, it doesn't have an impact on our interpretations as the main points highlighted here occur before we reach our apparent irreducible brine saturation.

We first seek to understand the dependency of the peak saturation with the injection rate. To that extent, the last few mm of the plug are analysed in detail. Figure 9 is a 3D representation of the (percolating) oil phase near the plug outlet. We clearly observe a very high oil content at the outlet next to the diffuser, corresponding to zero brine saturation and consistent with the observations made on figure 5. Slightly inward, we observe less oil, corresponding to the peak in water saturation. At increasing injection rates (i.e. capillary number), we observe the development of oil counter-current flow, leading to a local decrease in brine saturation. This was observed for all plugs investigated.

We assume that this phenomenon may be caused by perturbations at the outlet-end due to the diffuser. Lombard [24] argued that the distance affected by this perturbation could be estimated as the distance between the grooves of the diffuser. Our experiments seem to indicate that the counter-current flow can impact the saturation profiles at much larger distances from the outlet. When the capillary number is increased, the counter-current oil fingers grow and reconnect with the large percolating oil cluster in the bulk of the sample. Rather than only being controlled by the inter-groove distance, the phenomenon also seems to be pressure controlled. Our tests with an alternative diffuser, reported in section **4.3** seem to confirm this hypothesis.

### *4.2.2 Waterflooding of water-wet samples*

Figure 10 depicts brine saturation profiles of a 1cm diameter plug for various brine injection rates. These profiles are well reproducible, both qualitatively and quantitatively. As expected for water-wet plugs, the saturation is rather constant along the plug length and the flowrate does not have any impact on the measured residual oil saturation for the considered range. The average residual oil concentration $S_{orw}$ lies between 40% and 45% for all the plugs investigated, and this range is consistent with literature data on Bentheimer sandstone [32]. As it was the case for primary drainage, we also observed distortions of saturation profiles near both end faces during waterflooding. The distortions at the inlet are consistent with counter-current flow and the presence of large pores near the inlet surface (Figure 6a) and thus we expected low brine saturation at low rates. At high injection rates, the oil cluster at the inlet is fractioned and transported downstream. Towards the outlet we surprisingly observe a reproducible brine saturation gradient (brine saturation increases along the plug). A detailed analysis of oil clusters over the plugs' length (see Figure 11) revealed that a large number of small clusters are trapped in the last 4-5 mm of the plug. This phenomenon is not yet explained.

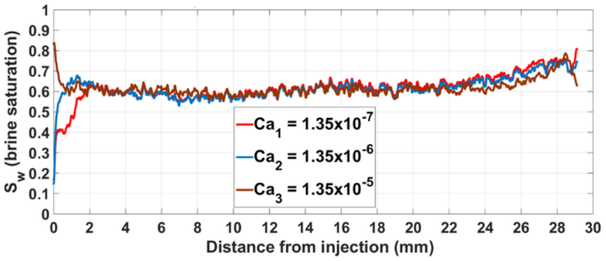

**Fig. 10.** Waterflooding of a Bentheimer sandstone operated at water-wet conditions : diameter = 1cm, length = 2.9cm

Among the possible causes, we cite: i) perturbations of the end-piece causing multidirectional flow near the last millimetres or ii) re-imbibition of brine after breakthrough. A simulation work is required to fully understand this phenomenon.

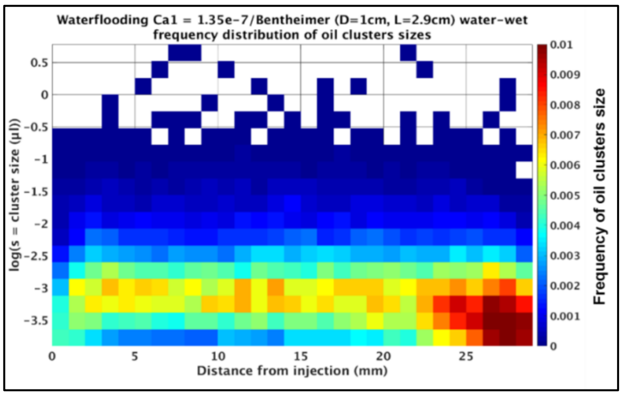

**Fig. 11.** Distribution of oil clusters size over the plug's length. Clusters smaller than 1000 voxels are not considered as they might be related to imaging artefacts. Every cluster is positioned according its center of mass

### *4.2.3 Waterflooding of altered-wet samples*

The results of waterflooding experiments on a sample of Bentheimer with altered wettability are presented in Figure 12. As for the case of waterflooding on water-wet rocks, we observe a rather constant brine saturation level along the plug length which seems to be quite invariant with flowrate. The average remaining oil saturation (ROS) is lower than for the water-wet case (between 20% and 32% for all the plugs investigated and for all capillary numbers). These results are reproducible among all plugs investigated.

Close to the plug outlet-end, a peak in oil saturation (or a decrease in brine saturation) is observed. This end-effect moves towards the outlet end face as capillary number increases. Note that the average oil saturation decreases as rate increases. As the saturation gradient is concentrated over the last 3 mm, it would not be captured by conventional 1D ISSM (In Situ Saturation Monitoring). Our observation might explain the puzzling results of Heaviside [33] on macro cores: he reported decrease in average oil saturation with rate on intermediate wet samples without any saturation gradient. We can see here an analogy in observations with the primary drainage phase of the water-wet case. At both end surfaces of the plug, a high brine saturation is found, which is consistent with the saturation state of the diffusers (Figure 6b).

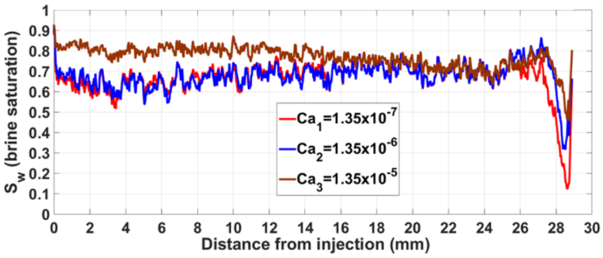

**Fig. 12.** Example of brine saturation profiles during waterflooding of a Bentheimer sandstone operated at modified wettability conditions, diameter = 4mm , Length = 2.9cm

These observations on brine saturation profiles clearly show that our end-pieces have a significant impact on the distribution of the fluids in place. The resulting profiles do not match with the conventional theory of zero capillary pressure at the outlet face hence raising future, undeniable and quantitative investigations on the real impact of this phenomenon on relative permeability ($K_r$) or capillary pressure ($P_c$) curves determination in similar conditions.

### 4.3 Experiments with E2 end-pieces

To confirm the important impact of the end-pieces, we performed a series of drainage and imbibition tests with an alternative exit diffuser design. Furthermore, the microfluidics system was adapted to generate continuous flow during X-ray monitoring. Dynamic 2D radiographic imaging was performed as well as 3D imaging of the steady-state equilibrium configuration. Steady-state was assumed to be reached as soon as the pressure gradient remained constant over a time scale we fixed at 30 min.

In view of minimizing perturbations of the flow (and thus to impose near-ideal outlet flow conditions), **E2** outlet-end pieces feature a large free space and minimize contact with the sample. Secondly, the flow direction is reversed with respect to the conventional direction. This means that during primary drainage, oil is injected from bottom to top so as to maintain a large brine filled outlet on top of the sample over which the exiting oil floats. For waterflooding experiments, we altered rock wettability first and injected the brine from top to bottom so as to maintain contact between oil and the sample's outlet end by capillary affinity, while the exiting water sinks due to gravity.

Experiments were performed on two samples of 1 cm in diameter and 3 cm in length. This size is an intermediate length between plugs typically used in micro-CT experiments and those used in SCAL experiments. We first performed primary drainage and focussed on the outlet with 3D dynamic scans for three different steady-state flow rates without stopping oil flooding. Figure 13 shows a number of cross sections near the outlet surface of the plug for three different injection rates.

It is clear that the brine saturation increases towards the end of the plug. The outlet surface is nearly 100% brine

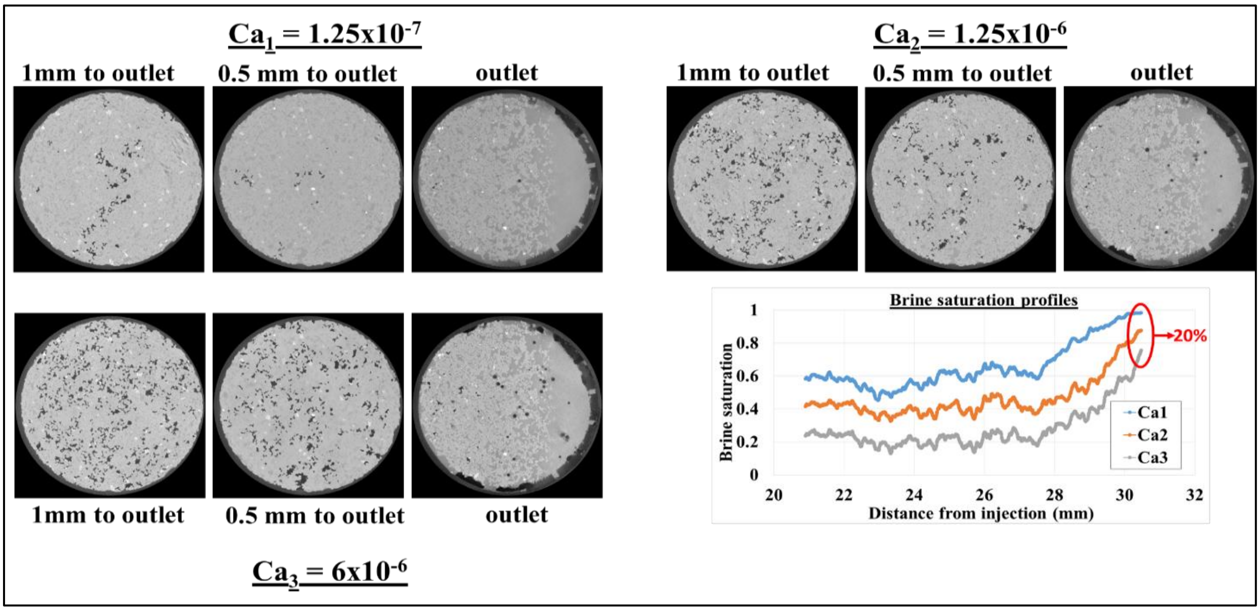

**Fig. 13.** 2D slices (from 3D reconstructed images) of the outlet-end interface with **E2** end-pieces during ascending primary drainage of a water-wet Bentheimer sandstone after reaching steady-state conditions for different injection rates. Saturation profiles are incorporated. One can see that the profiles follow a practically monotonic trend and a change of up to 20% of brine saturation is encountered at the outlet between the lowest and the highest capillary numbers investigated in this experiment. Though the range of capillary numbers investigated in this experiment is small so we expect more variations of the outlet saturation with greater ranges of capillary numbers.

saturated at the lowest rate. The maximum saturation is found at the exit plane, as expected. Here, brine is in permanent contact with the sample. The **E2** end pieces thus enable enforcing the expected boundary conditions (maximum water saturation at the outlet), and the resulting saturation profiles are much closer to the theoretical expected profiles. However, the decrease of the outlet brine saturation with increasing oil flowrate, disagrees with the theory of nearly constant outlet saturation. It would be interesting to check whether this inconsistency is also present in the semi-dynamic method.

For the second test, a plug was drained with decane until irreducible brine saturation. After 2 days of ageing with modified decane [sufficient to alter wettability, see [30]], waterflooding was performed from top to bottom. 2D projections of the outlet were continuously acquired (at 1 Hz) after reaching steady-state conditions without stopping the flow. Characteristic projection images for three injection rates are shown in Figure 14.

As expected, at low Capillary number oil wets the majority of the plug’s outlet surface. At a number of discrete locations, brine droplets exit the sample. Once they reach a critical size, these droplets detach and sink. When the brine flowrate is increased, we observe an increase in the number of brine exit points. This implies that the brine saturation at the outlet plane increases with increasing flowrate. This result is similar to the observations reported by Houpeurt [20] in the gas-oil

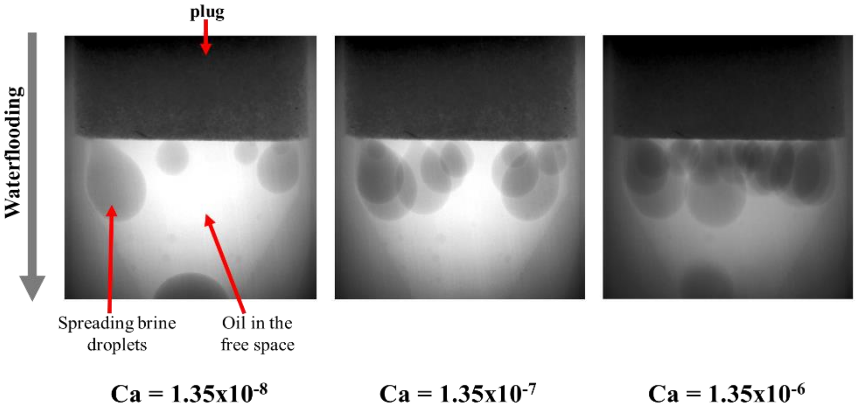

**Fig. 14.** 2D projections of the outlet-end interface with **E2** end-pieces during waterflooding of Bentheimer sandstone after reaching steady-state conditions for different injection rates. The wettability in this case is modified using the mixture of decane and hexadecylamine at $S_{wi}$. Brine is dark grey and oil is light grey in opposite to 2D tomograms (e.g. Fig.2.) where brine is light grey and oil is black.

system during gas injection. Furthermore, in this dynamic configuration, the interface curvature of each droplet is constantly changing. One can measure the droplets curvatures to: (i) determine the true outlet boundary condition, (ii) relate the capillary pressure calculated to a Pc–$S_w$ curve. In primary drainage mode with oil injected from bottom to top and a free outlet full of brine, oil droplets were very difficult to capture due to their small sizes and rapid motion thus impossible to measure a curvature. We did measure manually brine droplets curvatures for wettability conditions depicted in figure 14 (altered wettability state) as the motion was slower and brine droplets were bigger. Unfortunately, we didn't achieve measurements of capillary pressure curve at this wettability.

In real time, the brine droplets are in a dynamic motion, increasing their volume then breaking and falling down the diffuser due to gravity forces. Though for measurements, we assumed them to be static and axi-symmetrical. The highest capillary pressure measured was found when the droplets just appeared at the interface. Values of almost 4 to 5 mbars of capillary pressure were measured. When the droplets grow, the curvatures become wider and Pc decreases to negligible values (0.2 mbars) before collapse. They all (brine droplets) had similar curvature values even when their number increased. One reason could lie on the fact that the zero capillary pressure zone on the Pc curve may be very flat and a little variation of capillary pressure could head to a great variation of brine saturation at the outlet.

### 4.4 Attempt to Darcy-scale simulation of experimental saturation profiles

In other to investigate the possible impact of misunderstanding capillary end effect behaviour on the determination of multiphase flow properties, we first tried to understand if our saturation profiles obtained during primary drainage (case with most available data in the literature) could be simulated with a Darcy scale approach. The main idea here is to simulate saturation profiles during primary drainage using literature data (primary drainage Pc– $S_w$ curves and relative permeability curves of Bentheimer sandstone can be found in [31] and [34] respectively) and compare them to our experimental profiles. For indication, we used: irreducible brine saturation of $S_{wi}$ = 7%, Corey fit exponents of $n_w$ = 4.1, $n_o$ = 3.2 and end-point $K_{row}$ of 0.98. The softwares **CYDAR** ® and **SCORES** were used to simulate saturation profiles and both simulators outputs were also compared. However some considerations needed first to be taken into account. As the sharp decrease of brine saturation near the outlet during primary drainage can't be simulated at the Darcy-scale, the last 2mm of the sample are truncated (beginning at the peak of brine saturation, see Figure 15 which are saturation profiles from Figure 8). The choice of saturation profile on the last 2mm is then let free to the simulators. The first comparisons between simulation and experiments didn't work that well because the capillary pressure used was found to be high.

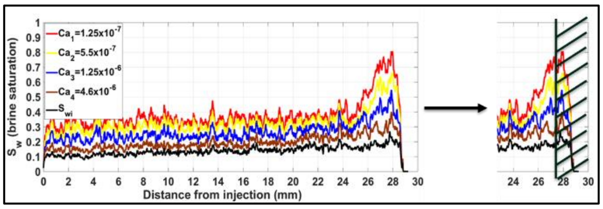

**Fig. 15.** Preparing experimental saturation profiles for history matching

History matching of experimental saturation profiles shown that the best capillary pressure curve explaining our data was almost half in values than that of Lin et al. [31]. This may be due to differences in IFT values used. The authors reported an IFT of 51.5 mN/m in their experiments. In our study, we used n-decane and unfortunately, we couldn't measure the true brine/decane IFT. The expected value is nearly 35 mN/m.

Comparisons of simulated saturation profiles and experimental data are reported in figure 16 in the top figure. The experimental data is well matched (apart from the lowest capillary number) and both simulators gave similar results although different implementations of mathematical boundary conditions as expected in [22].

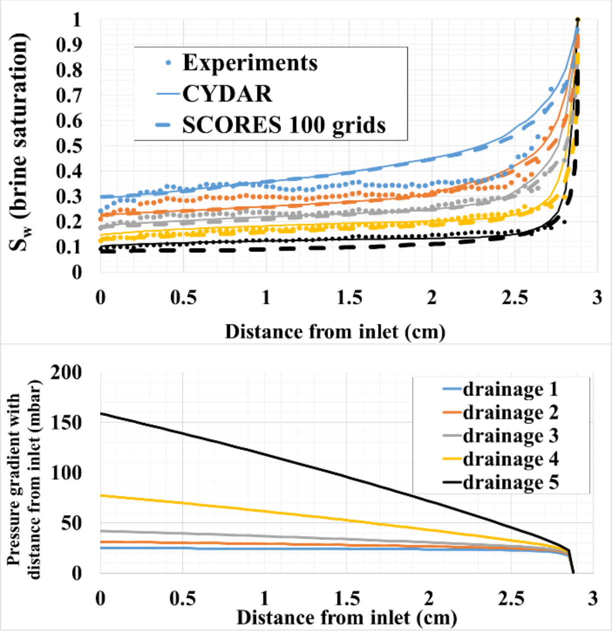

**Fig. 16.** top figure - comparisons of simulated saturation profiles (results from CYDAR and SCORES) with experimental data; bottom figure - pressure gradient function of the position in the plug.

However, when we look at the gradient pressure profiles determined using CYDAR ® (figure 16, bottom figure), we can notice that at lower rates, the last millimeters of the plug gather an important part of the total gradient pressure. When the injection rate increases, this zone has less and less impact but still, at the highest capillary number, the last 2mm gradient pressure represents almost 10% of the total gradient pressure. Though, this is a simulated gradient pressure related to the simulated saturation profile. In reality, during experiments we observe a sharp decrease of brine saturation and not an increase towards 100% $S_w$. We then expect the simulated gradient pressure in these last millimeters to be different from the experimental measurements, but to what extent ? This can only be answered through additional experiments and some pore-scale numerical simulations.

## 5 Conclusions

This paper presents a detailed analysis of capillary end effects during unsteady-state flow. The study relies on 3D X-ray microtomography and uses a microfluidic setup. We focus on multiphase flow in homogeneous Bentheimer sandstones and the observations were reproducible on all eight plugs investigated.

The main conclusions of this study are:

- Capillary-end effects always exist in the last centimeters or millimeters of the plug, i.e. at locations which might be invisible to some usual SCAL devices. The presence of Capillary end effects is systematic and may have an impact on the measured pressure difference over the plug.
- Outlet end saturation varies with flow rate. The theoretical concept of a zero capillary pressure boundary condition may be questionable. At low rates (nearer to field rate), this assumption can be applied without causing much errors. At higher rates, saturation distortion may have to be taken into account. The question remains to what extent they impact multiphase flow properties derived through interpretation by simulation;
- With the end-faces configuration used in this study, the expected boundary conditions were not guaranteed. Diffuser geometry and rock wettability are shown to have a critical impact on the obtained saturation profiles, and thus should be taken into account when interpreting multiphase flow experiments.
- Outlet end-pieces act as obstacles to the flow even though their geometry was intended to avoid that and it doesn't seem to be a matter of diffuser's wettability. They generate counter-current flow of the injected phase and thus drastically affect saturation profiles close to the outlet, which complicates history matching. Without an optimized apparatus, the best way to maintain theoretical wetting conditions and to avoid counter-current flow is adapt the diffuser geometry. The results obtained with our free outlet diffuser (**E2**) showed that saturation profiles are monotonic till the end faces.
- A Darcy-scale simulation of our experimental data shows that our saturation profiles are nearly in line with what is expected from the literature but the distortion of the profiles in the last millimetres occurs in a zone which could gather depending on rate, an important amount of the gradient pressure. It becomes therefore important to clarify the real impact of this **systematic** distortion on the experimentally measured gradient pressure as it could also have an impact on interpretation by simulation.

Beyond a perspective of investigating the real impact of these observations on SCAL studies, one must keep in mind that a future best description of these systems should incorporate pore scale modelling in plugs AND in the whole outlet taking into account their geometry.

We thank TOTAL for their financial support and the permission to publish this paper. We also acknowledge Dr. G. Hamon, Dr. C. Caubit, Dr. Clement Varloteaux, Mme M. Hebert and Mr R. Brugidou for their insightful discussions and contributions.

## References

1. M.G. Andrew, H. Menke, M.J. Blunt, and B. Bijeljic, “The imaging of dynamic multiphase fluid flow using synchrotron-based x-ray microtomography at reservoir conditions,” in *Transport in porous media*, 110(1), 1-24, (2015)
2. S. Berg, H. Ott, S. A. Klapp, A. Schwing, R. Neiteler, N. Brussee, A. Makurat, L. Leu, F. Enzmann, J. O. Schwarz, M. Kersten, S. Irvine, and M. Stampanoni, “Real-time 3D imaging of Haines jumps in porous media flow,” *Proceedings of the National Academy of Sciences*, 110(10), 3755–3759, (2013)
3. M. Rücker, S. Berg, R. T. Armstrong, A. Georgiadis, H. Ott, A. Schwing, R. Neiteler, N. Brussee, A. Makurat, L. Leu, M. Wolf, F. Khan, F. Enzmann, and M. Kersten, “From connected pathway flow to ganglion dynamics,” *Geophysical Research Letters*, **42**(10), 3888–3894, (2015)
4. H. Berthet, P. Andriamananjaona, S. Barbouteau, M. Hebert, R. Farwati, R. Meftah, G. Quenault, J.P. Chaulet, , R. Brugidou, and R. Rivenq, “Capillary desaturation curves and insights on trapped oil at the pore-scale, in water-wet and oil-wet sandstones,” *International Symposium of the Society of Core Analysts*, SCA2018 Trondheim, Norway, (2018)
5. S. Zou, F. Hussain, J. Arns, Z. Guo, and C. Arns, “Computation of relative permeability from in situ imaged fluid distributions at the pore scale*,” SPE Journal*, n°189453, (2018)
6. D.D. Huang, and M.M. Honarpour, “Capillary End Effects in Coreflood Calculations,” Paper SCA 9634 presented at the International Symposium of the Society of Core Analysts, Montpellier, France, 8-10 September, 1996.
7. R.Gupta, and D. R. Maloney, “Intercept Method - A Novel Technique to Correct Steady-State Relative Permeability Data for Capillary End-Effects,” Society of Petroleum Engineers, (November 10, 2014), doi:10.2118/171797-MS.
8. E. Unsal, G. Mason, N.R. Morrow, D.W. Ruth, “Bubble snap-off and capillary-back pressure during counter-current spontaneous imbibition into model pores,” Langmuir 25(6):3387–3395, 2009.
9. E. Unsal, “Impact of Wetting Film Flow in Pore Scale Displacement,” SCA 2013–016 (2013)

10. R. Gupta, P. Lu, and R. Glotzbach, “A Novel Field-Representative Enhanced Oil Recovery Coreflood method,” Improved oil recovery Symposium, Tulsa, 12-16 April. *Society of Petroleum Engineers*, http://dx.doi.org/10.2118/169088-MS (2014)
11. H.A. Nooruddin, , and M.J. Blunt, “Analytical and numerical investigations of spontaneous imbibition in porous media”, *water Resour. Res.*, 52, 7284–7310, http://dx.doi.org/10.1002/2015WR018451, (2016)
12. G.A. Virnovsky, Y. Guo, S.M. Skjaeveland, and P. Ingsoy, “Steady-State Relative Permeability Measurements and Interpretation with Account for Capillary Effects,” *Society of Core Analysts,* SCA1995-02, (1995)
13. C. Shen and D.W. Ruth, “Impact of inlet boundary conditions on the numerical simulation of one-dimensional coreflooding,” *J. Can. Pte. Technol.,* **35**, 1, pp. 19-24, (1966)
14. R. Gupta and D. R. Maloney, “Intercept method-A novel technique to correct steady-state relative permeability data for capillary end effects,” *Society of Petroleum Engineers*, http://dx.doi.org/10.2118/171797-PA, (2016)
15. G. F. Hadley, and L. L. Handy, “A theoretical and experimental study of the steady state capillary end effect,” *Society of Petroleum Engineers*, http://dx.doi.org/10.2118/707-G, (1956)
16. S. Qadeer, K. Dehghani, D.O. Ogbe, and R.D. Ostermann, “Correcting Oil/Water Relative Displacement Experiments,” *Society of Petroleum Engineers,* SPE 17423, presented at the SPE California Regional Meeting held in Long Beach, March 23-25, (1988)
17. R. Gupta, and D. Maloney, “Applications of the Intercept Method to Correct Steady State Relative Permeability for Capillary End Effects,” Paper SCA2015-001 presented at the SCA International Symposium, St. John’s Newfoundland and Labrador Canada, 16–21 August, 2015.
18. J. Reed, and J. Maas, “Review of the intercept method for relative permeability correction using a variety of case study data,” In The International Symposium of the Society of Core Analysts, Trondheim, Norway , 2018.
19. J.S. Levine, “Displacement experiments in a consolidated porous system,” *Trans. AIME* **201**, 57, (1954)
20. A. Houpeurt, « Mécanique des fluides dans les milieux poreux - Critiques et recherches, » Editions Technip, Paris, (1974)
21. J. P. Delclaud, “New results on the displacement of a fluid by another in a porous medium,” http://dx.doi.org/10.2118/4103-MS, *Society of petroleum engineer*, (1972)
22. R. Lenormand, K. Lorentzen, J.G. Maas, and D. Ruth, “Comparison of four numerical simulators for SCAL experiments,” International Symposium of the Society of Core Analysts (August 2016), Snowmass, USA, SCA-2016-006, 2016.
23. J.G. Maas, and A.M. Schulte, “Computer Simulation of Special Core Analysis (SCAL) Flow Experiments Shared on the Internet,” Reviewed Proceedings of the 1997 International Symposium of the SCA, Calgary, Canada, September 7-10, 1997.
24. J.M. Lombard, P. Egermann, and R. Lenormand, “Measurement of capillary pressure curves at reservoir conditions,” SCA n° 2002-09, *Society of Core Analysts*, Monterey, California, (2002)
25. T. S. Ramakrishnan, and A. Cappiello, “A new technique to measure static and dynamic properties of a partially saturated porous medium,” *Chem. Eng. sci.* **46**, 1157−1163, (1991)
26. D.J.Jr. O’Meara, G.J. Hirasaki, and J.A. Rohan, “Centrifuge Measurements of Capillary Pressure: Part 1-Outflow boundary condition,” *SPE Res Eng* 7(1): 133-142, SPE-18296-PA, http://dx.doi.org/10.211 8/18296-PA, (1992)
27. D. Ruth and Z. Chen, “On the measurement and interpretation of centrifuge capillary pressure curves: The SCA survey data,” *The log Analyst*, 36, 21, (1995)
28. R. W. Wunderlich, “Imaging of Wetting and Non-Wetting Phase Distributions- Application to Centrifuge Capillary Pressure Measurements,” 60th Annual Technical Conference and Exhibition, September 22-25, Las Vegas, Nevada, *Society of Petroleum Engineers,* SPE Paper 14422, (1985)
29. L. A. Rapoport, and W. J. Leas, “Properties of linear waterfloods,” *Trans AIME* **198**, 139-148, (1953)
30. M.T. Tweheyo, T. Holt, and O. Torsaeter, “An experimental study of the relationship between wettabilty and oil production characteristics,” *J. Pet.Sci. Eng.* **24** (2-4): 179-188, http://dx.doi.org/10.1016/S0920-4105(99)00041-8, (1999)
31. Q. Lin, B. Bijeljic, , S. Berg, R. Pini, M. J. Blunt, and S. Krevor, “Minimal surfaces in porous media: pore-scale imaging of multiphase flow in an altered-wettability Bentheimer sandstone,” https://doi.org/10.1103/PhysRevE.99.063105, 2019, March 28.
32. X. Nie, Y. Mu, R. Sungkorn, V. Gundepalli and J. Toelke, “Numerical Investigation of the Dependence of Residual Oil Saturation on Geometry, Wettability, Initial Oil Saturation and Porosity,” Proceedings of the International Symposium of the Society of Core Analysts, SCA2014-042, Avignon, France.
33. J. Heaviside, C.E. Brown and I.J.A. Gamble, “Relative permeability for intermediate wettability reservoirs,” paper SPE 16968 presented at the 62th Annual technical Conference and Exhibition of SPE, Dallas, TX, Sep. 27-30, (1987)
34. M. Blunt, “Multiphase Flow in Permeable Media: A Pore-Scale Perspective,” Cambridge University Press. doi: 10.1017/9781316145098, 2017.

# Local Capillary Pressure Estimation Based on Curvature of the Fluid Interface – Validation with Two-Phase Direct Numerical Simulations

*Takashi* Akai[1,*], *Branko* Bijeljic[1], and *Martin* Blunt[1]

[1]*Imperial College London, Department of Earth Science and Engineering, London, SW7 2AZ, United Kingdom*

**Abstract.** With the advancement of high-resolution three-dimensional X-ray imaging, it is now possible to directly calculate the curvature of the interface of two phases extracted from segmented CT images during two-phase flow experiments to derive capillary pressure. However, there is an inherent difficulty of this image-based curvature measurement: the use of voxelized image data for the calculation of curvature can cause significant errors. To address this, we first perform two-phase direct numerical simulations to obtain the oil and water phase distribution, the exact location of the interface, and local fluid pressure. We then investigate a method to compute curvature on the oil/water interface. The interface is defined in two ways. In one case the simulated interface which has a sub-resolution smoothness is used, while the other is a smoothed interface which is extracted from synthetic segmented data based on the simulated phase distribution. Computed mean curvature on these surfaces are compared with that obtained from the fluid pressure computed directly in the simulation. We discuss the accuracy of image-based curvature measurements for the calculation of capillary pressure and propose the best way to extract an accurate curvature measurement, quantifying the likely uncertainties.

## 1 Introduction

Capillary pressure, $P_c$, is a pressure discontinuity across the interface between oil and water, defined as $P_c = P_o - P_w$, where $P_o$ and $P_w$ are the pressures of oil and water phase, respectively. Traditionally, capillary pressure for oil/water systems has been measured in a laboratory using the porous plate method in which the pressure of each phase is measured using two external pressure transducers. Based on the Young-Laplace equation, capillary pressure locally is defined as:

$$P_c = 2\sigma\kappa_m, \tag{1}$$

where $\sigma$ is the interfacial tension between two phases and $\kappa_m$ is the mean curvature of the interface.

With the advancement of high-resolution three-dimensional X-ray imaging, it is now possible to directly measure the curvature of the interface extracted from segmented CT images during two-phase flow experiments to derive capillary pressure. Armstrong et al. [1] demonstrated this approach using synchrotron-based tomographic datasets of oil/water drainage and imbibition cycles on a bead pack structure [2]. They compared the capillary pressure obtained from curvature measurements with that obtained from pressure transducers. Fairly good agreement was obtained for imbibition, whereas the curvature measurement showed a systematically lower value than that obtained from the transducers for drainage cycles. Later, using the same dataset, Li et al. [3] presented that their proposed curvature measurement method improved the agreement with the transducer based capillary pressure. Using a similar curvature measurement method, Herring et al. [4] estimated the capillary pressure for a range of curvature between 0 and 0.225 voxel$^{-1}$ based on their air/water drainage and imbibition experiments on a Bentheimer sandstone. However, there is an inherent difficulty of this image-based curvature measurement: the use of voxelized image data for the calculation of curvature can cause significant errors, resulting in a wide range of measured values, with some negative curvature values, which are not expected in a water-wet system. Hence, it is not clear how the distribution of measured curvature values represents the true range of local capillary pressure.

We investigate the accuracy of curvature measurement on the basis of pore-by-pore comparison using direct numerical simulations of two-phase flow. The color-gradient lattice Boltzmann method is employed to generate an oil and water phase distribution in pore structures of a bead pack and Bentheimer sandstone. From the simulated phase distribution, synthetic segmented data is generated, then curvature computation on the interface extracted from this segmented data is performed by employing several smoothing methods. These curvature values are then compared with those obtained from the simulated local fluid pressure. We discuss the accuracy of image-based curvature measurements for the calculation of capillary pressure and suggest the best method with associated errors for capillary pressure estimation.

---

[*] Corresponding author: t.akai17@imperial.ac.uk

## 2 Methods

### 2.1 The color-gradient lattice Boltzmann method

The color-gradient LB model proposed by Halliday et al. [5] was used. Our LB model was constructed with a 3D19Q lattice model which consists of a set of 19 discrete lattice velocity vectors, $\mathbf{e}_i$, in three-dimensional space. We defined particle distributions of two immiscible fluids, labeled red and blue, as $f_i^r$ and $f_i^b$, respectively. The fluid density, $\rho_r$ and $\rho_b$, and velocity, $\mathbf{u}$, at position $\mathbf{x}$ and time $t$ are obtained by:

$$\rho^k = \sum_i f_i^k(\mathbf{x},t), \tag{2}$$

$$\rho\mathbf{u} = \sum_i f_i \mathbf{e}_i , \tag{3}$$

where $f_i$ is the total particle distribution given by $f_i = f_i^r + f_i^b$; $\rho$ is the total fluid density given by $\rho = \rho_r + \rho_b$. The lattice Boltzmann equation for the total particle distribution is written as:

$$f_i(\mathbf{x} + \mathbf{e}_i\delta t, t + \delta t) = f_i(\mathbf{x},t) + \Omega_i(\mathbf{x},t) + \phi_i , \tag{4}$$

where $t$ denotes the lattice time step which was set to unity and $\Omega_i$ and $\phi_i$ are the collision operator and the body force term, respectively. For the collision operator, we used the Multiple-relaxation-time (MRT) collision operator [6] expressed as:

$$\Omega_i = -\left(\mathbf{M}^{-1}\mathbf{S}\mathbf{M}\right)_{i,j}\left(f_i - f_i^{eq}\right), \tag{5}$$

where $\mathbf{M}$ and $\mathbf{S}$ are the transformation matrix and the diagonal relaxation matrix, respectively. $f_i^{eq}$ is the equilibrium distribution function which is obtained by a second order Taylor expansion of the Maxwell-Boltzmann distribution with respect to the local fluid velocity. The location of the interface was tracked using a color function $\rho^N$ defined by:

$$\rho^N(\mathbf{x},t) = \frac{\rho_r(\mathbf{x},t) - \rho_b(\mathbf{x},t)}{\rho_r(\mathbf{x},t) + \rho_b(\mathbf{x},t)}, \quad -1 \le \rho^N \le 1 . \tag{6}$$

Using the color function, the interfacial tension between two fluids was computed as a spatially varying body force, $\mathbf{F}$, based on the continuum surface force (CSF) model [7] given by:

$$\mathbf{F} = -\frac{1}{2}\sigma\kappa\nabla\rho^N , \tag{7}$$

where $\sigma$ is the interfacial tension and $\kappa$ is the curvature of the interface. This spatially varying body force $\mathbf{F}$ was incorporated into the lattice Boltzmann equation through the body force term $\phi_i$. For the MRT model, this was performed by transforming the forcing term proposed by Guo et al. [8] using the scheme presented in Yu and Fan [9]. After the application of the interfacial tension ($\mathbf{F}$) to the particle distributions, the recoloring algorithm proposed by Latva-Kokko and Rothman [10] applied to these distributions to ensure phase segregation and maintain the interface. This results in a slightly diffusive interface whose thickness is about 2 to 3 lattice units. Further details of our LB model can be found in Akai et al. [11, 12]. The only difference is that we used the MRT collision operator, while the single-relaxation-time (SRT) collision operator [13] was used in Akai et al. [11].

At solid-fluid boundary lattice nodes, a full-way bounce back boundary condition was implemented to achieve a non-slip boundary condition. In addition, the wettability of solid surface was modeled by specifying contact angles using the wetting boundary condition presented in Akai et al. [11]. This wetting boundary condition accurately assigns contact angles for 3D arbitrary geometries with smaller spurious currents compared to the widely-used fictitious density boundary condition [11].

### 2.2 Curvature computation on voxelized images

There are mainly two approaches to compute curvature from voxelized data such as micro-CT images. One approach calculates curvatures from the gradient of 3D float data (e.g., raw or processed grayscale data), while the other approach estimates curvature through the fitting of a quadratic form locally to a surface extracted from voxelized, segmented data [14]. We used the latter approach as this has been presented in previous studies [14, 1, 15, 4, 3, 16].

We started with three-phase segmented label data (oil, water and solid) obtained from raw grayscale CT images. Using the marching cubes algorithm [17], the oil/water interface was extracted from the label data. Since this surface had a staircase shape, it had to be smoothed before computing curvature. In this study, we compare three smoothing methods: Constrained Gaussian smoothing (CGS), Laplacian smoothing (LPS) and boundary preserving Gaussian smoothing (BPGS). CGS is applied when the surface is extracted using the marching cubes algorithm. A Gasussian kernel filter with different kernel sizes is applied to label data, then isosurface is extracted. In this process, the constraint to preserve the location of an original label is imposed.

LPS [18] and BPGS [19] are applied after the extraction of the surface with the marching cubes algorithm. The extracted surface with a staircase shape is modeled as a triangulated surface. Then, the vertices of the triangle elements are moved with these smoothing methods. In LPS, the position of a vertex is moved to the average position of its neighboring vertices. BPGS also moves the position of a vertex based on the position of its neighboring vertices. A scale factor which determines the degree of the movement in one iteration is defined. Two consecutive smoothing steps with a positive and negative scaling factor are performed in one iteration. This smoothing produces a surface which preserves the original boundary without shrinkage [19]. The degree of the smoothing in LPS and BPGS is controlled by the number of iterations. In this study, CGS and BPGS were performed with commercial image processing software, Avizo, while LPS was performed with Paraview.

After the generation of a smoothed triangulated surface, the elemental triangles were fitted by a quadratic form:

$$ax^2+by^2+cz^2+2exy+2fyz+2gzx \\ +2lx+2my+2nz+d=0. \tag{8}$$

Then, the principal curvature values and directions of principal curvature were obtained from the eigenvalues and eigenvectors of the fitted quadratic form in Eq. 8 [1]. Avizo was used to perform this computation. Users can choose the number of neighboring triangles to be used for the fitting at the center of a triangle. We used a fixed value of 4 neighbors in the following analyses.

## 3 Results

In section 3.1, we provide validation of our direct numerical simulations for different grid resolutions. Next, in section 3.2, using a single oil droplet test case, we investigate the accuracy of the curvature computation method described in section 2.2. Here, a smoothed interface which was extracted from synthetic segmented data based on the simulated phase distribution is used to compute curvature, then the resultant values are compared with those obtained from the simulated fluid pressure. Finally, in section 3.3, the same approach is applied to the simulated phase distributions in two realistically complex pore structures of a bead pack and Bentheimer sandstone.

### 3.1 Validation of the two-phase lattice Boltzmann model

To validate our two-phase lattice Boltzmann model and investigate its accuracy as a function of grid resolutions, the oil/water interface in a corner of triangular pore space was simulated. A 2D pore structure with an isosceles triangle shape as shown in Fig. 1 was used. Here, the length of $L_x$ and $L_y$ were set to 70 µm. $R$ is the radius of curvature of the interface; $\theta$ is the contact angle; $\beta$ is the half angle of the corner of the triangle, which is given by: $\tan\beta=L_x/2L_y$. This pore structure was modeled with 4 grid sizes of Δ=1.0, 2.0, 3.5 and 5.0 µm.

The identical density and viscosity of the water and oil phases were set to 1,000 kg/m$^3$ and 1 mPa, respectively. The interfacial tension and contact angle were set to 18 mN/m and 45°, respectively. Initially, the lower part of the pore structure was filled with oil to a specified oil saturation, while the other part at the top corner was filled with water. Then, simulations were performed for 50,000 time steps until they reached equilibrium.

In this pore geometry, the radius of curvature, $R$, can be analytically derived based on the geometrical relationship, which is given by:

$$R^2=\frac{S_w L_x^2}{4\tan\beta}\left(\frac{\cos^2\alpha\cos\beta}{\sin\beta}+\sin\alpha\cos\alpha-\left(\frac{\pi}{2}-\alpha\right)\right)^{-1}$$

$$\alpha=\theta+\beta, \tag{9}$$

where $S_w$ is the water saturation and the other parameters are shown in Fig 1. This analytically derived radius of curvature was used to compare with the simulated radius of curvature obtained using the input contact angle of $\theta$=45°. Based on the simulated fluid configurations, the exact location of the interface corresponding to $\rho^N=0$ (see Eq. 6) was extracted as shown in Fig. 2. Then, the radius of the curvature of this interface was obtained by fitting a circle to the interface, since in 2D in equilibrium the analytical shape of the interface is a part of a circle. Table 1 shows the comparison between the radius of curvature obtained from the analytical solution and that obtained with a circle fit to the simulated interface for different grid sizes. The relative error in the radius of curvature is less than 3% for these grid resolutions. This suggests that good agreement in capillary pressure is also obtained since the capillary pressure is directly linked to the radius of curvature through Eq. 1.

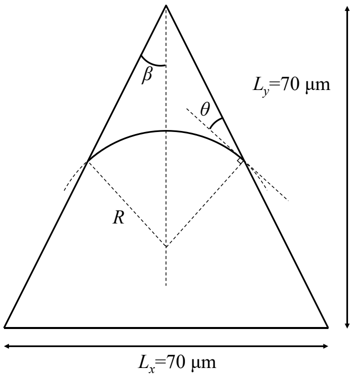

**Fig. 1**. A schematic of the isosceles triangle pore used for the simulations.

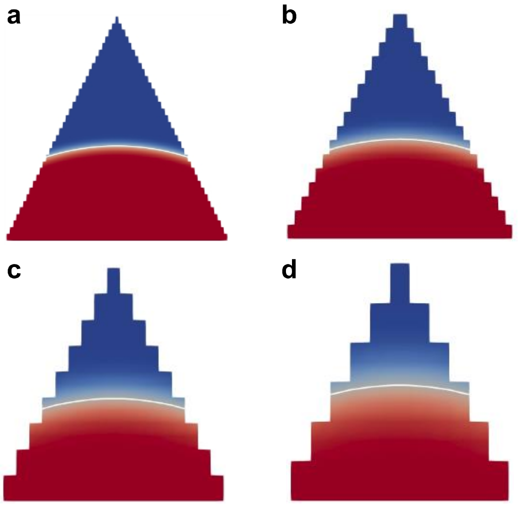

**Fig. 2**. Simulated fluid configurations for grid sizes of (a) Δ=1.0 µm, (b) Δ =2.0 µm, (c) Δ =3.5 µm and (d) Δ =5.0 µm. Here, oil and water are shown in red and blue, while the exact location of the oil/water interface is shown by the white line.

**Table 1.** Comparison between the radius of curvature obtained from the analytical solution and that obtained with a circle fit to the simulated interface for different grid sizes.

| grid size<br>µm | $S_w$<br>% | analytical<br>$R$<br>µm | simulated<br>$R$<br>µm | %Diff.<br>% |
|---|---|---|---|---|
| 1.0 | 35.9% | 70.3 | 70.9 | 0.9% |
| 2.0 | 35.6% | 69.9 | 68.2 | -2.4% |
| 3.5 | 36.0% | 70.3 | 68.3 | -3.0% |
| 5.0 | 32.7% | 67.0 | 65.9 | -1.7% |

**Table 2.** Parameters used for Constrained Gaussian smoothing (CGS), Laplacian smoothing (LPS) and boundary preserving Gaussian smoothing (BPGS).

| smoothing method | parameters | smoothing level<br>level 1 | <br>level 2 | <br>level 3 |
|---|---|---|---|---|
| CGS | kernel size | 1 | 3 | 9 |
| LPS | number of iterations | 200 | 600 | 1800 |
| BPGS | number of iterations | 50 | 150 | 450 |

## 3.2 Curvature of a single oil droplet in triangular pore space

To investigate the curvature computation algorithm described in section 2.2, a simple 3D test case was performed. A cylindrical pore structure with the length of 171.5 µm with an isosceles triangular cross-section as in the previous test case was used. This pore structure was modeled with a grid size of 3.5 µm. The same fluid properties and contact angle as in the previous section were used. Initially, oil was placed in the central region of the pore space as shown in Fig. 3a. Then, simulations were performed for 50,000 time steps until they formed a single oil droplet after equilibrium (Fig. 3b).

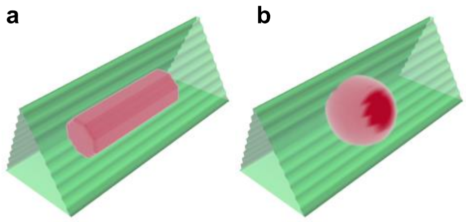

**Fig. 3.** An oil droplet in a 3D triangular pore space. (a) Initial condition. (b) Equilibrium condition. Here, solid is shown in transparent green and the oil phase is shown in red.

Two types of the oil/water interface were prepared based on the simulation results: a “simulated interface” and a “smoothed interface”. The simulated interface was obtained by extracting the contour line of the color function $\rho^N=0$. This surface originally had a sub-resolution smoothness. The other surface, the smoothed interface, was obtained from synthetic voxelized label data. The simulated distribution of the color function was segmented into label data with the threshold of $\rho^N=0$, then the oil/water interface was extracted using the marching cubes algorithm. This surface has a staircase shape due to the shape of a voxelized grid system. Therefore, it needs to be smoothed before computing curvature. As discussed in section 2.2, three smoothing methods were applied: Constrained Gaussian smoothing (CGS), Laplacian smoothing (LPS) and boundary preserving Gaussian smoothing (BPGS). The parameters used for the smoothing are summarized in Table 2.

Based on the simulated fluid pressure, the capillary pressure was obtained using:

$$P_c^{sim} = P_o^{avg} - P_w^{avg} = \frac{1}{N_o}\sum_{\rho^N>0.9} P - \frac{1}{N_w}\sum_{\rho^N<-0.9} P \qquad (10)$$

where $P_o^{avg}$ and $P_w^{avg}$ are the average fluid pressure in the oil and water phases, respectively; $N_o$ and $N_w$ are the number of grid blocks having $\rho^N>0.9$ and $\rho^N<-0.9$, respectively; $P$ is the simulated fluid pressure in each grid block. Here, to exclude the interface region, we computed an average pressure for each phase for $|\rho^N|>0.9$. Then, $P_c^{sim}$ was converted to the simulated mean curvature using Eq. 1. We refer to this mean curvature as the fluid pressure derived mean curvature, $\kappa_m^P$.

Fig. 4 shows the oil/water interface after smoothing, colored by computed mean curvature. For all of the smoothed surfaces, we see a variation in the computed mean curvature, although the correct mean curvature should give a uniform value as shown in the curvature computed on the simulated interface, Fig. 4(j), because the oil droplet is in capillary equilibrium. Furthermore, we see errors around the edge of the interface (close to the three-phase contact lines) for all of the smoothed interfaces, Fig. 4(a)~(i). Therefore, we decided to discard the data points whose distance from solid surface is fewer than 3 voxels. This 3 voxels distance cutoff was used for all of the following analyses. Table 3 summarizes the average and standard deviation of the computed mean curvature and the relative difference to the fluid pressure derived mean curvature, $\kappa_m^P$ =0.133 voxel$^{-1}$ for the smoothing level 2 as shown in Fig. 4(b), (e), (h). We note that Li et al. [3] proposed that in addition to the distance cutoff, taking an average weighted by the distance from the solid surface further improves the accuracy of curvature measurement using synthetic test cases of the interface in a cylindrical structure with a circular-cross section; however, taking a distance-weighted average did not improve the estimation of curvature in our cases as we can conclude from the overestimated curvature values observed in the central region of the oil droplet in Fig. 4(a) ~ (i).

In fact, the optimum smoothing method and its level of smoothing is dependent on the shape and the size of an object. Therefore, here, we only provide the qualitative features of the three smoothing methods. CGS preserves the shape of an object, but significant smoothing cannot be applied even with increasing the kernel size, because the resultant surface is constrained by the original voxel data. As a result, CGS tends to give a wider range of variation. LPS can apply significant smoothing by

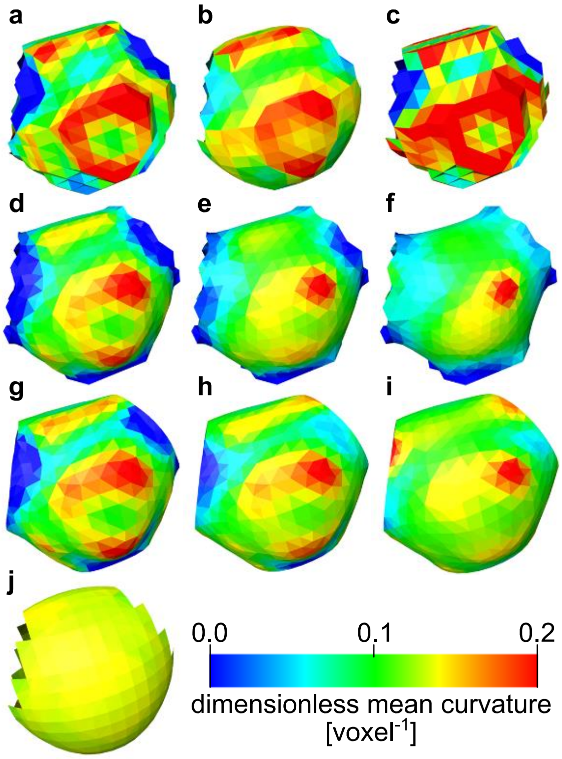

**Fig. 4.** The oil/water interface after the application of the several smoothing methods with different smoothing levels. CGS with a kernel size of (a) 1 voxel, (b) 3 voxels and (c) 9 voxels. LPS with (d) 200 iterations, (e) 600 iterations and (f) 1800 iterations. BPGS with (g) 50 iterations, (h) 150 iterations and (i) 450 iterations. (j) The simulated interface. Here, the surface is colored by the value of mean curvature. The correct surface should present uniform mean curvature as seen in the simulated interface since the droplet is in capillary equilibrium for which the capillary pressure is uniform.

increasing the number of iterations; however, this could change the shape of the interface as shown in a top part of the interface in Fig. 4(f) where we see the bending of the interface towards the opposite direction. This is caused by the propagation of errors in the three-phase contact line through many iterations. However, combining with the distance cutoff, this erroneous part can be effectively removed while preserving a well smoothed surface in the middle of the interface. BPGS gives the similar results to LPS, while better keeping the shape of an object compared to LPS.

For the simulated interface which was directly obtained from the simulated color function without any smoothing, the computed curvature showed good agreement with the fluid pressure derived curvature with a smaller standard deviation (Table 3). Moreover, since this surface did not show the errors close to the three-phase contact line, the average and standard deviation without the distance cutoff also gave similar values, i.e., the average of 0.132 voxel$^{-1}$ and standard deviation of $3.99\times10^{-3}$ voxel$^{-1}$.

**Table 3.** Voxel based interfaces with the smoothing level 2 (see Table 2) and a distance cutoff of 3 voxels. Here, the relative difference was computed to the fluid pressure derived mean curvature of $\kappa_m^P$=0.133 voxel$^{-1}$.

| surface | computed curvature avg. [voxel$^{-1}$] | std. [voxel$^{-1}$] | relative difference [%] |
|---|---|---|---|
| simulated interface | 0.134 | $3.23\times10^{-3}$ | 0.7% |
| smoothed with CGS | 0.149 | $3.23\times10^{-2}$ | 12.1% |
| smoothed with LPS | 0.132 | $2.40\times10^{-2}$ | -0.1% |
| smoothed with BPGS | 0.139 | $2.68\times10^{-2}$ | 5.0% |

## 3.3 Local capillary pressure estimation for complex porous media

Two realistically complex pore structures were used: a synthetic bead pack pore structure and micro-CT images of Bentheimer sandstone. For these structures, simulation domains were composed of 256×256×256 voxels with a grid size of 3.56 µm as shown in Fig 5. For the analysis of the simulation results, the pore structures were divided into pore regions using the separate pore algorithm in Avizo, resulting in 402 and 272 pore regions for the bead pack and Bentheimer sandstone, respectively. The mean pore radius which accounts for 50% of the pore volume was 37 µm and 30 µm for the beadpack and Bentheimer sandstone, respectively.

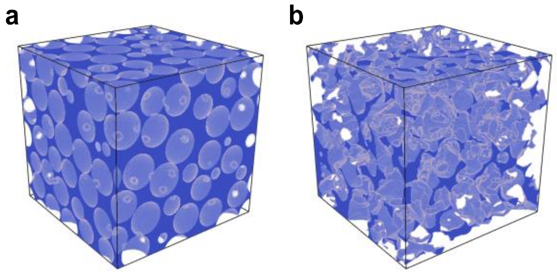

**Fig. 5.** Pore structures of (a) the bead pack and (b) the Bentheimer sandstone.

The identical density and viscosity of water and oil phase were set to 1,000 kg/m$^3$ and 1 mPa, respectively. The interfacial tension and contact angle were set to 25 mN/m and 45°, respectively. All 6 faces of the cubic simulation domain were covered with solid voxels, i.e., a no-slip boundary condition was applied to all 6 faces. Initially, 50% of oil and 50% of water were randomly placed in pore voxels, then the simulations were performed with no external force for 250,000 time steps (corresponding to 0.1 seconds) until they reached equilibrium conditions.

Fig. 6 shows the simulated phase distribution at the equilibrium condition. Similar to the analysis presented in the previous section, the simulated interface and the smoothed interface were prepared from the simulation results. Curvature computation was performed on these surfaces. Figs. 7 and 8 show the histogram of the computed curvature for the bead pack and Bentheimer sandstone, respectively. The fluid pressure derived mean

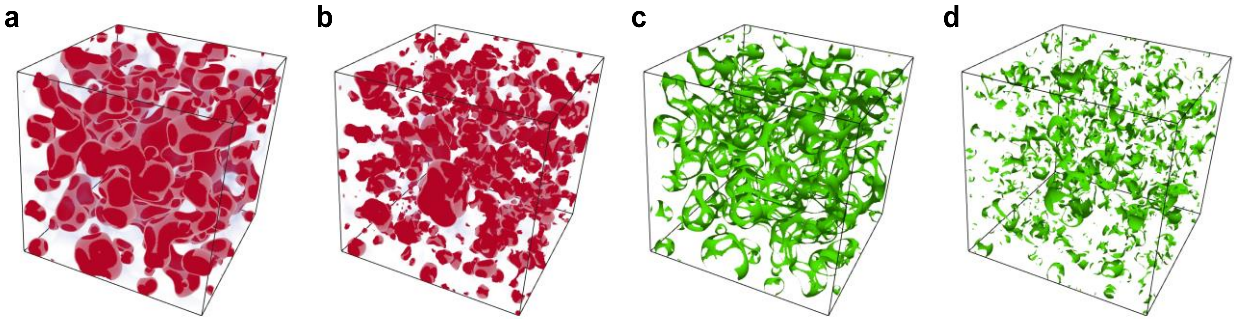

**Fig. 6.** The simulated phase distribution of (a) the bead pack pore structure and (b) the Bentheimer sandstone pore structure. Here, only oil is shown in red, while water and solid are transparent. The extracted interface based on the simulation results for (c) the bead pack and (d) the Bentheimer sandstone. This was performed extracting the contour line of $\rho^N$=0.

curvature, $\kappa_m{}^P$, obtained with Eq. 10 is also shown by the vertical line. In both figures, the histograms obtained from the smoothed interface without and with the distance cutoff are shown in (a) and (b), while those obtained from the simulated interface without and with the distance cutoff are shown in (c) and (d). The average and standard deviation of these distributions are summarized in Table 4 for the bead pack and Table 5 for the Bentheimer sandstone.

Here, we discuss the following two key observations. First, the computed curvatures obtained with the smoothed interface show the wide range of the distribution when the cutoff is not applied, while the curvatures obtained with the simulated interface show a much narrower range. For the histograms without the cutoff, the difference between the distributions obtained with the smoothed interfaces and the simulated interface suggests that there are many erroneous values in curvature computation on the smoothed surfaces. The histograms obtained with CGS appeared to have the most similar distribution to that obtained with the simulated interface. However, as shown in Table 4 and 5, their average values are much higher than that obtained from the fluid pressure and simulated interface because of the long tails of their distribution toward values higher than 0.3, which are not shown in Figs. 7 and 8. Second, after the application of the distance cutoff, all the histograms obtained with the smoothed interface become similar to that obtained with the simulated interface. However, in both the smoothed and the simulated interface, the data points of high curvature values have been lost. This is because the distance cutoff removes the data points of not only the edges of the interface but also the entire parts of the interface in small pores, which tend to give a high curvature value. Although a high curvature value is not captured when the distance cutoff is applied, the smoothed interface seems to provide a good estimate of local mean curvature values of the interface. This will be

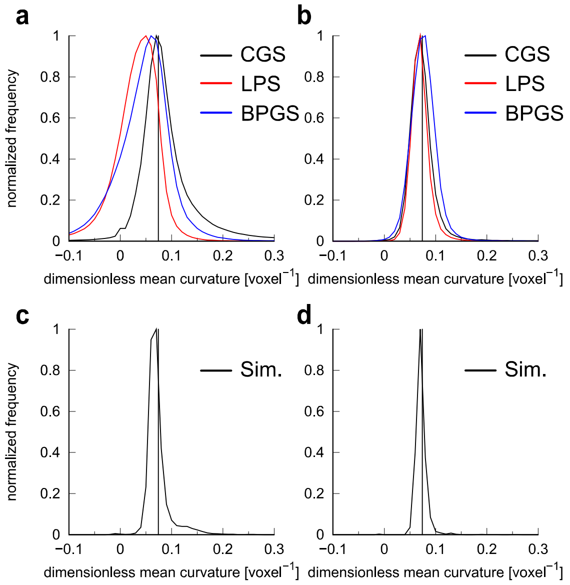

**Fig. 7.** The histogram of computed mean curvature for the bead pack. The histograms computed on the smoothed interface without and with the distance cutoff (a and b). The histograms computed on the simulated interface without and with the distance cutoff (c and d). The fluid pressure derived mean curvature obtained with Eq. 10 is also shown by the vertical line.

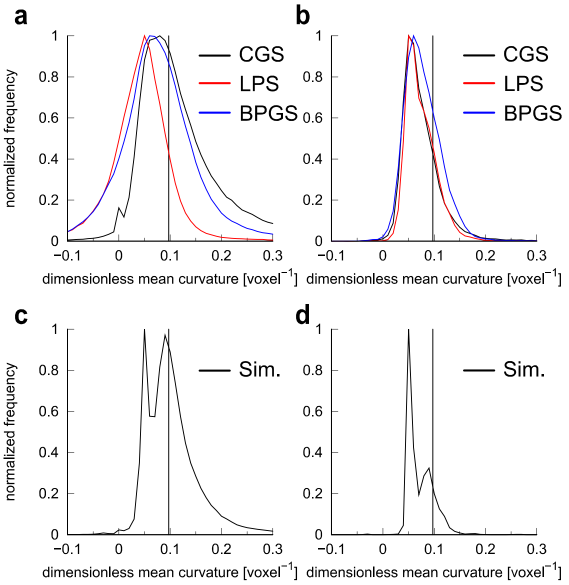

**Fig. 8.** The histogram of computed mean curvature for the Bentheimer sandstone. The histograms computed on the smoothed interface without and with the distance cutoff (a and b). The histograms computed on the simulated interface without and with the distance cutoff (c and d). The fluid pressure derived mean curvature obtained with Eq. 10 is also shown by the vertical line.

**Table 4.** The average and standard deviation of the distribution of computed mean curvature for the bead pack shown in Fig. 7.

| | computed curvature avg. [voxel$^{-1}$] | std. [voxel$^{-1}$] |
|---|---|---|
| simulated fluid pressure | $7.40 \times 10^{-2}$ | N/A |
| without the cutoff | | |
| simulated interface | $7.36 \times 10^{-2}$ | $4.25 \times 10^{-2}$ |
| smoothed with CGS | $11.5 \times 10^{-2}$ | $16.1 \times 10^{-2}$ |
| smoothed with LPS | $3.06 \times 10^{-2}$ | $5.63 \times 10^{-2}$ |
| smoothed with BPGS | $4.54 \times 10^{-2}$ | $6.87 \times 10^{-2}$ |
| with the cutoff | | |
| simulated interface | $7.12 \times 10^{-2}$ | $1.22 \times 10^{-2}$ |
| smoothed with CGS | $8.02 \times 10^{-2}$ | $8.43 \times 10^{-2}$ |
| smoothed with LPS | $7.01 \times 10^{-2}$ | $2.03 \times 10^{-2}$ |
| smoothed with BPGS | $7.62 \times 10^{-2}$ | $2.54 \times 10^{-2}$ |

**Table 5.** The average and standard deviation of the distribution of computed mean curvature for Bentheimer sandstone shown in Fig. 8.

| | computed curvature avg. [voxel$^{-1}$] | std. [voxel$^{-1}$] |
|---|---|---|
| simulated fluid pressure | $9.73 \times 10^{-2}$ | N/A |
| without the cutoff | | |
| simulated interface | $11.1 \times 10^{-2}$ | $8.20 \times 10^{-2}$ |
| smoothed with CGS | $19.3 \times 10^{-2}$ | $27.0 \times 10^{-2}$ |
| smoothed with LPS | $4.24 \times 10^{-2}$ | $7.64 \times 10^{-2}$ |
| smoothed with BPGS | $8.51 \times 10^{-2}$ | $10.8 \times 10^{-2}$ |
| with the cutoff | | |
| simulated interface | $7.17 \times 10^{-2}$ | $2.51 \times 10^{-2}$ |
| smoothed with CGS | $8.16 \times 10^{-2}$ | $8.48 \times 10^{-2}$ |
| smoothed with LPS | $7.45 \times 10^{-2}$ | $3.12 \times 10^{-2}$ |
| smoothed with BPGS | $7.81 \times 10^{-2}$ | $3.60 \times 10^{-2}$ |

further discussed in the following analysis. Among the three smoothing methods, when the cutoff is applied, LPS gave the closest average value of the mean curvature to that obtained from the simulated interface with the smallest standard deviation.

To further investigate the accuracy of curvature computation on the interface, the comparison was made on a pore-by-pore basis. First, we computed local capillary pressure applying Eq. 10 for each pore region. This local capillary pressure was converted to the mean curvature for each pore region using Eq. 1. Next, we also obtained the mean curvature for each pore region by taking the average of the computed curvature values on the interfaces in that pore region. Figs. 9 and 10 show the comparison between the dimensionless mean curvature obtained from the simulated fluid pressure and that obtained from the computed curvature on the interface for the bead pack and Bentheimer sandstone, respectively. In both, the curvature computed on the simulated interfaces gave consistent values with those obtained from the fluid pressure. This means that when the interface is reasonably smooth, the curvature computation gives an accurate estimation of local capillary pressure. For the curvature computed on the smoothed interface, CGS shows highly overestimated curvature values for some pore regions, while LPS and BPGS estimate curvature within a range of about ±20% difference from the curvatures obtained with the fluid pressure for the mean curvature smaller than

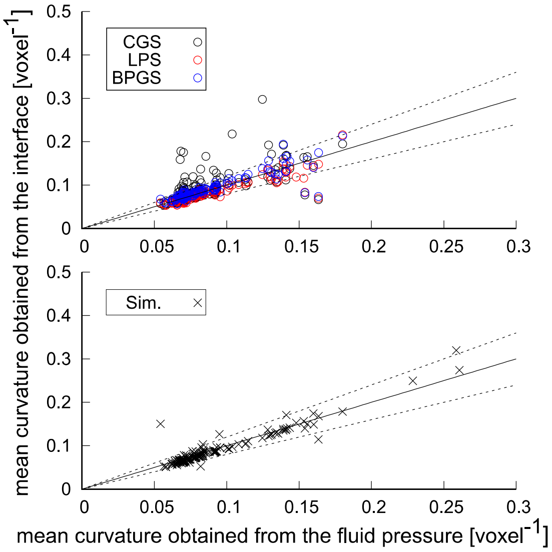

**Fig. 9.** Comparison of local mean curvature for the bead pack on pore-by-pore basis. X-axis shows the dimensionless mean curvature obtained from the simulated fluid pressure, while the Y -axis shows that computed on the interface. A unit slope indicating perfect agreement in these values is shown by a black solid line, while, ±20% difference is shown by black dotted lines.

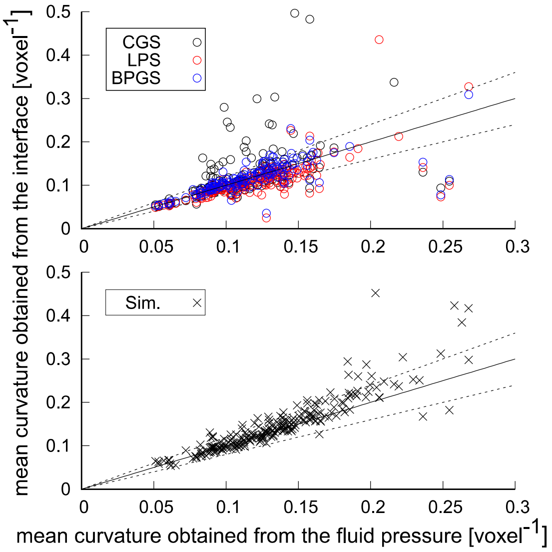

**Fig. 10.** Comparison of local mean curvature for the Bentheimer sandstone on pore-by-pore basis. X-axis shows the dimensionless mean curvature obtained from the simulated fluid pressure, while the Y -axis shows that computed on the interface. A unit slope indicating perfect agreement in these values is shown by a black solid line, while, ±20% difference is shown by black dotted lines.

about 0.15 voxel$^{-1}$. Therefore, with LPS or BPGS incorporating the distance cutoff of 3 voxels, local capillary pressure can be measured with a ±20% error up to 0.15 voxel$^{-1}$ at this resolution.

## 4 Conclusions

Direct numerical simulations were conducted to obtain oil and water phase distribution, the exact location of the oil/water interface and local fluid pressure. From the simulation results, two types of the oil/water interface were generated. One is a simulated interface which has a sub-resolution smoothness, while the other is a smoothed interface. The smoothed interfaces were generated by applying three types of smoothing methods to a staircase shape surface extracted from synthetic segmented data based on the simulated phase distribution. Then, curvature computation was performed on these surfaces. The resultant mean curvature value from these surfaces was compared with that obtained from the simulated fluid pressure. This was performed to find the best way to extract accurate curvature measurement, and to quantify the likely uncertainties.

First, we tested our approach using a single oil droplet in triangular pore space. Computed curvature values on the simulated interface showed a narrow distribution whose average value was consistent with that obtained from the fluid pressure. This means that when the surface is sufficiently smooth, the fitting of a quadratic form equation to the surface properly computes local curvatures. On the other hand, computed curvature values on the smoothed interface showed a wide distribution with erroneous values close to the three-phase contact lines. Therefore, we discarded values whose distance from solid surface was fewer than 3 voxels. After the application of the distance cutoff, the average of computed mean curvature values became closer to that obtained from the fluid pressure. However, their standard deviation was on the order of $10^{-2}$ voxel$^{-1}$ against the mean curvature value of 0.133 voxel$^{-1}$, which was 10 times higher than that obtained from the simulated interface. These deviated values were caused by error, since an oil droplet in capillary equilibrium should give a uniform value of mean curvature.

Next, realistically complex pore structures of a bead pack and Bentheimer sandstone were used to simulate oil droplets in capillary equilibrium. When the distance cutoff was not applied, curvature computed on the simulated interface gave an average value of mean curvature consistent with that obtained from the fluid pressure for both the bead pack and Bentheimer sandstone. However, when the distance cutoff was applied, the average value became lower than that from the fluid pressure. This is because the distance cutoff removes the data points of not only the edges of the interface but also the entire parts of the interface in small pores, which tend to give a high curvature value. For the smoothed interface, the distributions obtained without the cutoff were quite different from that obtained from the simulated interface. Many negative values of computed mean curvatures suggest significant errors in these cases. After the application of the distance cutoff, the distribution became closer to that obtained with the simulated interface.

Finally, we compared computed mean curvature on a pore-by-pore basis. As opposed to the test case performed on the single oil droplet, oil droplets with different mean curvature values corresponding to different pore sizes can be obtained in these simulations. Therefore, we need to investigate whether the range of computed mean curvature is caused by error or it reflects a variation in local capillary pressure. Good agreement between mean curvature obtained from the fluid pressure and that computed from the simulated surface for each pore region suggested that the range of distribution observed in the simulated surface properly captures variation in local capillary pressure. For the smoothed interface with the cutoff, LPS and BPGS estimated curvature within a range of about ±20% difference from the curvatures obtained with the fluid pressure for mean curvatures smaller than about 0.15 voxel$^{-1}$, while CGS showed highly overestimated curvature values for some pore regions.

In conclusion, the application of the distance cutoff is necessary to remove the errors close to the three-phase contact line. Among the three tested smoothing methods, LPS appeared to be the best method since it gave the closest average of mean curvature values to that obtained from the simulated interface with the smallest standard deviation. In addition, it gave good estimates of the local mean curvature for each pore with a ±20% error up to 0.15 voxel$^{-1}$ at this resolution.

Currently, we are using the similar approach to quantify the accuracy of curvature computation for drainage and imbibition events on the bead pack and Bentheimer sandstone. This will be discussed in a future publication.

## Acknowledgements

The authors gratefully thank Japan Oil, Gas and Metals National Corporation (JOGMEC)

## References

1. R. T. Armstrong, M. L. Porter, and D. Wildenschild, “Linking pore-scale interfacial curvature to column-scale capillary pressure,” Adv. Water Resour., vol. 46, no. 6, pp. 55–62, Sep. 2012, doi: 10.1016/j.advwatres.2012.05.009.
2. M. L. Porter, D. Wildenschild, G. Grant, and J. I. Gerhard, “Measurement and prediction of the relationship between capillary pressure, saturation, and interfacial area in a NAPL-water-glass bead system,” Water Resour. Res., vol. 46, no. 8, pp. 1–10, Aug. 2010, doi: 10.1029/2009WR007786.
3. T. Li, S. Schlüter, M. I. Dragila, and D. Wildenschild, “An improved method for estimating capillary pressure from 3D microtomography images and its application to

the study of disconnected nonwetting phase," Adv. Water Resour., vol. 114, pp. 249–260, 2018, doi: 10.1016/j.advwatres.2018.02.012.

4. A. L. Herring, J. Middleton, R. Walsh, A. Kingston, and A. Sheppard, "Flow rate impacts on capillary pressure and interface curvature of connected and disconnected fluid phases during multiphase flow in sandstone," Adv. Water Resour., vol. 107, pp. 460–469, 2017, doi: 10.1016/j.advwatres.2017.05.011.
5. I. Halliday, A. P. Hollis, and C. M. Care, "Lattice Boltzmann algorithm for continuum multicomponent flow," Phys. Rev. E, vol. 76, no. 2, p. 026708, Aug. 2007, doi: 10.1103/PhysRevE.76.026708.
6. D. D'Humieres, I. Ginzburg, M. Krafczyk, P. Lallemand, and L.-S. Luo, "Multiple-relaxation-time lattice Boltzmann models in three dimensions," Philos. Trans. R. Soc. A Math. Phys. Eng. Sci., vol. 360, no. 1792, pp. 437–451, Mar. 2002, doi: 10.1098/rsta.2001.0955.
7. J. Brackbill, D. Kothe, and C. Zemach, "A continuum method for modeling surface tension," J. Comput. Phys., vol. 100, no. 2, pp. 335–354, Jun. 1992, doi: 10.1016/0021-9991(92)90240-Y.
8. Z. Guo, C. Zheng, and B. Shi, "Discrete lattice effects on the forcing term in the lattice Boltzmann method," Phys. Rev. E, vol. 65, no. 4, p. 046308, Apr. 2002, doi: 10.1103/PhysRevE.65.046308.
9. Z. Yu and L.-S. Fan, "Multirelaxation-time interaction-potential-based lattice Boltzmann model for two-phase flow," Phys. Rev. E, vol. 82, no. 4, p. 046708, Oct. 2010, doi: 10.1103/PhysRevE.82.046708.
10. M. Latva-Kokko and D. H. Rothman, "Diffusion properties of gradient-based lattice Boltzmann models of immiscible fluids," Phys. Rev. E, vol. 71, no. 5, p. 056702, May 2005, doi: 10.1103/PhysRevE.71.056702.
11. T. Akai, B. Bijeljic, and M. J. Blunt, "Wetting boundary condition for the color-gradient lattice Boltzmann method: Validation with analytical and experimental data," Adv. Water Resour., vol. 116, no. March, pp. 56–66, Jun. 2018, doi: 10.1016/j.advwatres.2018.03.014.
12. T. Akai, A. M. Alhammadi, M. J. Blunt, and B. Bijeljic, "Modeling Oil Recovery in Mixed-Wet Rocks: Pore-Scale Comparison Between Experiment and Simulation," Transp. Porous Media, vol. 127, no. 2, pp. 393–414, Mar. 2019, doi: 10.1007/s11242-018-1198-8.
13. Y. H. Qian, D. D'Humières, and P. Lallemand, "Lattice BGK models for Navier-Stokes equation," EPL (Europhysics Lett., vol. 17, no. 6, p. 479, 1992.
14. R. T. Armstrong, C. H. Pentland, S. Berg, J. Hummel, D. Lichau, and L. Bernard, "Estimation of curvature from micro-CT liquid-liquid displacement studies with pore scale resolution," Int. Symp. Soc. Core Anal., vol. SCA2012-55, no. August, p. 6, 2012, doi: 10.1109/CVPR.1994.323794.
15. M. Andrew, B. Bijeljic, and M. J. Blunt, "Pore-by-pore capillary pressure measurements using X-ray microtomography at reservoir conditions: Curvature, snap-off, and remobilization of residual CO 2," Water Resour. Res., vol. 50, no. 11, pp. 8760–8774, Nov. 2014, doi: 10.1002/2014WR015970.
16. Q. Lin, B. Bijeljic, R. Pini, M. J. Blunt, and S. Krevor, "Imaging and Measurement of Pore-Scale Interfacial Curvature to Determine Capillary Pressure Simultaneously With Relative Permeability," Water Resour. Res., vol. 54, no. 9, pp. 7046–7060, Sep. 2018, doi: 10.1029/2018WR023214.
17. W. E. Lorensen and H. E. Cline, "Marching cubes: A high resolution 3D surface construction algorithm," in Proceedings of the 14th annual conference on Computer graphics and interactive techniques - SIGGRAPH '87, 1987, pp. 163–169, doi: 10.1145/37401.37422.
18. L. R. Herrmann, "Laplacian-isoparametric grid generation scheme," J. Eng. Mech. Div., vol. 102, no. 5, pp. 749–907, 1976.
19. G. Taubin, "Curve and surface smoothing without shrinkage," in Proceedings of IEEE International Conference on Computer Vision, 1995, pp. 852–857, doi: 10.1109/ICCV.1995.466848.

# Determination of Critical Gas Saturation by Micro-CT

*Steffen* Berg[1,3], *Ying* Gao[1,3], *Apostolos* Georgiadis[1,3], *Niels* Brussee[1], *Ab* Coorn[1], *Hilbert* van der Linde[1], *Jesse* Dietderich[2], *Faruk Omer* Alpak[2], *Daniel* Eriksen[1], *Miranda* Mooijer-van den Heuvel[1], *Jeff* Southwick[1], *Matthias* Appel[1], *Ove Bjørn* Wilson[1]

[1]Shell Global Solutions International B.V., Grasweg 31, 1031 KC Amsterdam, The Netherlands
[2]Shell International Exploration and Production Inc., 3333 Highway 6 South, Houston, TX 77210, USA
[3]Department of Earth Science & Engineering, Imperial College London, Kensington SW7 2AZ, UK

**Abstract.** The critical gas saturation was directly determined using micro-CT flow experiments and associated image analysis. The critical gas saturation is the minimum saturation above which gas becomes mobile and can be produced. Knowing this parameter is particularly important for the production of an oil field that during its lifetime falls below the bubble point which will reduce the oil production dramatically. Experiments to determine the critical gas saturation are notoriously difficult to conduct with conventional core flooding experiments at the Darcy scale. The difficulties are primarily related to two effects: The development of gas bubbles is a nucleation process which is governed by growth kinetics that, in turn, is related to the extent of pressure drawdown below the bubble point. At the Darcy scale, the critical gas saturation at which the formed gas bubbles connect to a percolating path, is typically probed via a flow experiment, during which a pressure gradient is applied. This leads not only to different nucleation conditions along the core but also gives no direct access to the size and growth rate of gas bubbles before the percolation. In combination, these two effects imply that the critical gas saturation observed in such experiments is dependent on permeability and flow rate, and that the critical gas saturation relevant for the (equilibrium) reservoir conditions has to be estimated by an extrapolation. Modern Digital Rock related experimentation and modelling provides a more elegant way to determine the critical gas saturation. We report pressure depletion experiments in mini-cores imaged by X-ray computed micro-tomography (micro-CT) that allowed the direct determination of the connectivity of the gas phase. As such, these experiments enabled the detection of the critical gas saturation via the percolation threshold of the gas bubbles. Furthermore, the associated gas- and oil relative permeabilities can be obtained from single-phase flow simulations of the connected pathway fraction of gas and oil, respectively.

## INTRODUCTION

The critical gas saturation is the saturation at which the gas that comes out of solution below the bubble point of a hydrocarbon mixture becomes mobile inside of porous rock (“critical gas”). This is relevant for the production of oil fields that during their lifetime fall below the bubble point which will reduce the oil production dramatically. The critical gas saturation is also an important parameter for correct dynamic modelling. Experimentally observed critical gas saturations range between 0.5-50% depending on fluid and rock properties, pressure decline rate and experimental protocols [1,2]. Such experiments are notoriously difficult to conduct [3-6]. The development of gas bubbles is a nucleation process at a growth rate related to pressure drawdown below the bubble point and associated supersaturation [3,8-12]. When operating at a constant pressure decline rate there is an interplay between supersaturation of the liquid, the rate of gas bubble nucleation [5,18], growth kinetics [3] and the rate of pressure decline [1]. Thus critical gas saturations observed under experimentally achievable decline rates ranging from 10-50% [1-6] are extrapolated to the pressure decline rate in the field resulting in critical gas saturations in the range of typically 3-15% [1,2,8-12]. The wide range of observed critical gas saturations occurs not only because of differences in decline rate but also because of different regimes [3]. For pressure depletion mode without any significant flow reflecting a nucleation process one would expect a critical gas saturations in the same range as a residual gas saturation, i.e. above 20-30% [16,17] which is consistent with typical percolation thresholds in 3D between 20-32% [21-25]. Experiments where the saturation at which gas becomes mobile is probed by a flow measurement observe typically much lower critical gas saturations. Due to the low viscosity the gas phase is significantly more mobile than a liquid which can cause viscous fingering at the pore scale [27] and lead to a connected pathway significantly below percolation thresholds. Viscous fingering may be significantly enhanced at near-miscible conditions where interfacial tension is very low [28,29]. In the field flow and gas

---

* Corresponding author: steffen.berg@shell.com

expansion processes can be coupled e.g. in solution gas drive [19,20]. The critical gas saturation depends on exactly how depletion and flow are coupled which can vary from field to field and by the distance from the well-bore. The experimentally observed critical gas saturation therefore depends on the respective experimental protocol and the associated pore scale fluid distribution [17].

Most Darcy scale experiments involve substantial instrumental complexity and efforts while the results are still impacted by protocols and interpretation methodology [6,7]. Saturation monitoring by X-ray [6,7,18] has improved the interpretation. For instance, in low-permeability rock the (significant) pressure gradient crosses the bubble point in the rock at a location that can be determined via saturation monitoring by X-ray [6] allowing to infer the critical gas saturation. Still one of the main shortcomings of Darcy-scale experiments is that the critical gas saturation is inferred from either flow or saturation (gradients). It is difficult to clearly separate the regimes of quasi-static nucleation and unstable flow. Using micro-CT imaging allows to determine directly the connectivity of the gas phase inside the pores at the point of critical gas (phase fraction) where non-percolating gas bubbles can be already observed above the bubble point and the critical gas saturation is detectable via the percolation threshold. This study provides a proof-of-concept where methodology and workflow are assessed. Two central questions are addressed: (1) is the natural contrast between gas and liquid large enough to segment gas and liquid without any contrast agent and (2) can pressure and gas nucleation controlled precisely enough in a small rock sample suitable for µCT such that the percolation threshold i.e. the critical gas saturation can be determined.

## METHODS AND MATERIALS

The experimental methodology is based on imaging the gas distribution directly inside the pore space by X-ray computed micro-tomography. A Bentheimer sandstone sample (porosity = 19.1%, permeability = 2500 mD, 4 mm diameter and 20 mm length) is enclosed in a rubber sleeve and mounted into a custom-built core holder shown in **Figure 1** which is made from PEEK which can operate to a pressure of 30 bar and a temperature of 60 °C. Note that this setup is meant for a proof-of-concept and the operating envelope of this experiment can be extended to higher pressures and temperature to correspond to reservoir conditions. A mixture of n-decane and n-propane was chosen as gas-liquid model system that has an extended two-phase region within the operating envelope of the setup. The phase behaviour including the liquid-vapour split is displayed in **Figure 2**. The phase split has been computed with Shell's proprietary STFlash tool using the Shell modified Redlich-Kwong (SMIRK) equation of state (EOS) [26]. Based on the flash calculations a 50% molar fraction of propane was chosen, for ambient temperature (22°C in the laboratory and pumps, and 27°C inside the µCT). The EOS calculated bubble point pressure for that experimental condition is 4.77 bar at an interfacial tension of 17 mN/m (at 4.69 bar, using a parachor approach). Given the experimental uncertainties on mixing and thermal equilibration we would expect a bubble point between 2 and 5 bar.

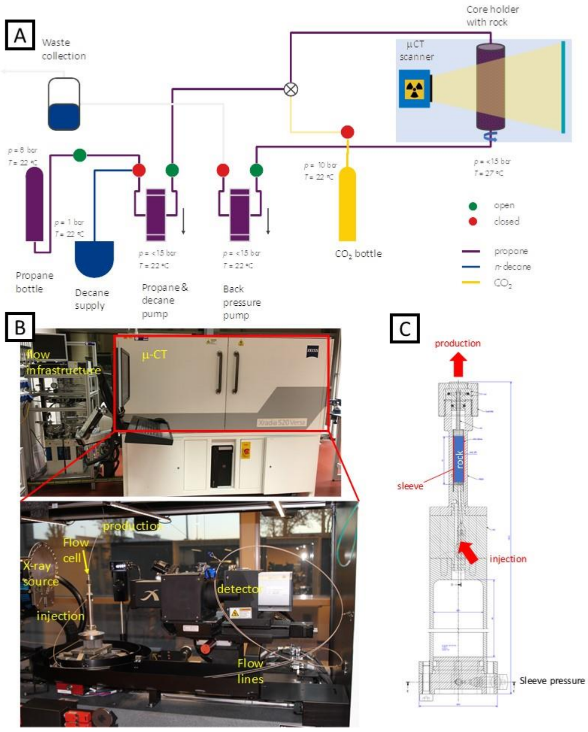

**Figure 1.** Schematic overview of the experimental setup (A) consisting of the flow infrastructure and the micro-CT scanner (B) and the core holder with the rock sample (C). Injection occurs from bottom to top.

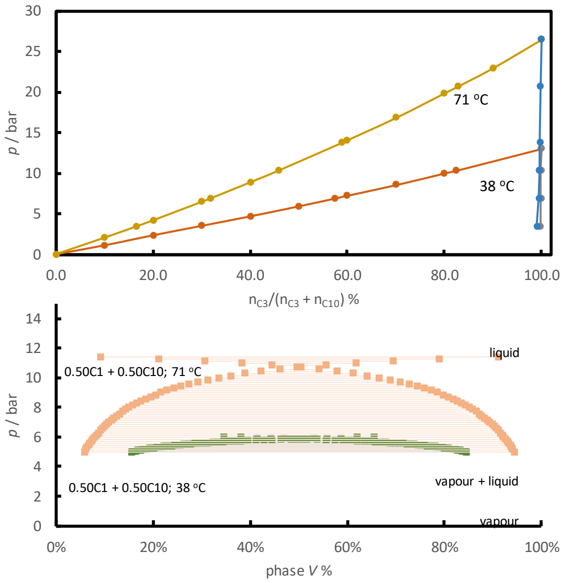

**Figure 2.** Phase envelopes of the propane-decane mixture for different temperatures as a function of composition (top) and liquid-vapor phase split (bottom).

Micro-CT imaging has been conducted with a Zeiss Versa 520 micro-CT scanner at 0.4x magnification at 80 kV and a power of 7W. A 2x2 binning of the detector was used at an exposure time of 1.3 s. 1401 projections have been used for reconstruction, leading to an overall scan time of about 1 hour. This protocol was determined by systematic variation of resolution, number of projections and integration time in order to arrive at a reconstructed image where the gas can be segmented. µCT scans were always taken at pressure equilibrium conditions. During post-processing, no indications of fluid moment during the scanning time was observed. For image processing (Avizo 9, ThermoFisher) all images are registered on the dry scan. Then a cylinder is cropped to remove the rubber sleeve encapsulating the sample within the confining pressure. A non-local means filter [34] (search window: 21px; local neighbourhood: 4 px; similarity value: 3) is applied twice to remove image noise. Each scan is then segmented by the watershed region growing method.

## RESULTS

The first set of experiments has been conducted in either pressurization or pressure depletion modes of the pore fluids in absence of any external flow. In experiments where the pressure was lowered in small (0.1 bar) increments with significant equilibration time at each step, the observed bubble point was typically below 2 bar, and once reached, a significant amount of gas came out of solution leading to instantaneous percolation from top to bottom. This is consistent with the observation of a bubble point depression [3] which basically prevents us from probing the percolation threshold in a very gradual way.
In the following we present two strategies to overcome this observation challenge. In both cases, the pressure is initially drawn significantly below the bubble point to initiate bubble nucleation. In the first mode, the *pressurization mode*, the pore pressure has been initially drawn down such that a significant fraction of gas came out of solution and became immediately connected. Subsequently, the pore pressure was increased in steps to gradually reduce the size of gas bubbles and eventually reach the percolation threshold for the gas phase. The second mode, *the pressure depletion mode*, aims at nucleating bubbles rapidly but then bringing the pressure quickly back to the expected bubble point in order to prevent the formation of large percolating gas bubbles. The percolation threshold is then reached upon further pressure depletion.

### *Pressurization mode*

Experiment 1 was conducted in pressurization mode. The pore pressure as a function of time is shown in **Figure 3** which also shows the micro-CT scan intervals. The dry scan was taken before start of the experiment. A fully liquid-saturated scan was taken right before the start of the pressure depletion which is the first scan interval shown in **Figure 3**. After the initial pressure drawdown, a significant amount of gas is nucleated which – as we will see later - percolates across the whole pore space. In **Figure 4**, pressure vs. volume for Experiment 1 is displayed. On can clearly see the initial fluid compressibility effect and the suppressed nucleation similar to what is reported in the literature [3]. Upon further drawdown the gas is nucleated and then compressed during pressurization. Extrapolating the liquid-gas p-V line during the re-pressurization to the intersect with the liquid p-V line during initial pressure depletion gives an indication of the bubble-point, which is consistent with experimental observation of bubble points around 3 bar. The area under the liquid-gas line would be characterized by the supersaturation and nucleation regime where the system is not in a phase equilibrium [3].

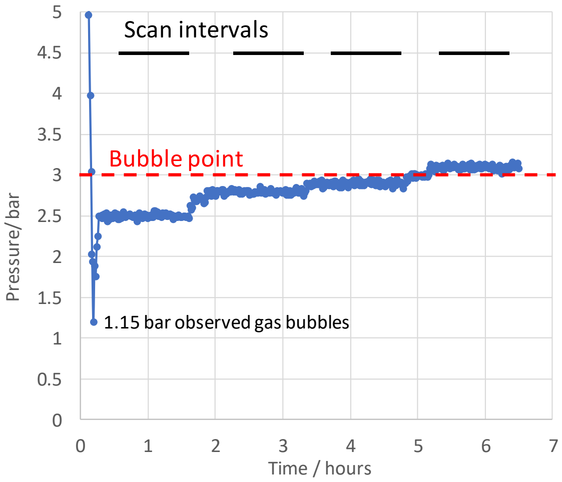

**Figure 3.** Pressure during experiment 1. The initial pressure drawdown below the bubble point causes a large amount of gas coming out of solution which percolates through the whole pore space. The gas is compressed and dissolves in the liquid until it is not connected anymore. The intervals where micro-CT scans were taken are indicates by black lines.

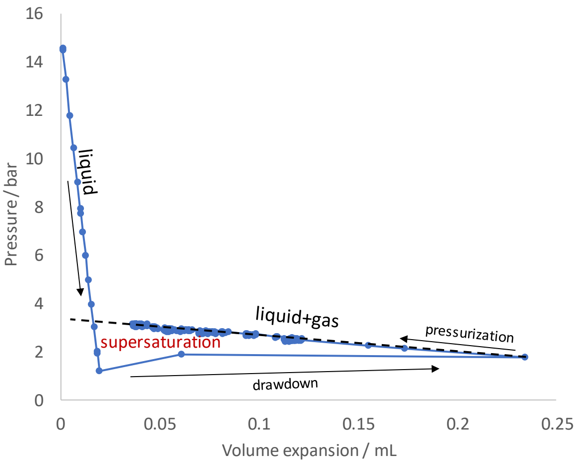

**Figure 4.** Pressure vs. volume for experiment 1 which was conducted in pressurization mode. The initial pressure depletion leads to a supersaturation without nucleation of gas [3]. The percolation threshold is reached upon pressurization.

The 3D images of the experiment shown in **Figure 5** are consistent with the pressure-volume signature from **Figure 3** and **Figure 4**. The initial depletion and equilibration lead to a large volume of gas coming out of solution which percolates from inlet to outlet. Most of the clusters are connected. In **Figure 5** a cluster analysis was performed, and each gas cluster is labelled and displayed in a different colour. The scan displayed in **Figure 5A** represents the first equilibration step after pressure drawdown. The gas phase forms one large cluster which percolates through the whole pore space. Upon pressurization the gas saturation decreases, gas clusters shrink and lose more and more their connectivity as shown in **Figure 5 B-D** (more colours appear indicating more disconnected clusters).

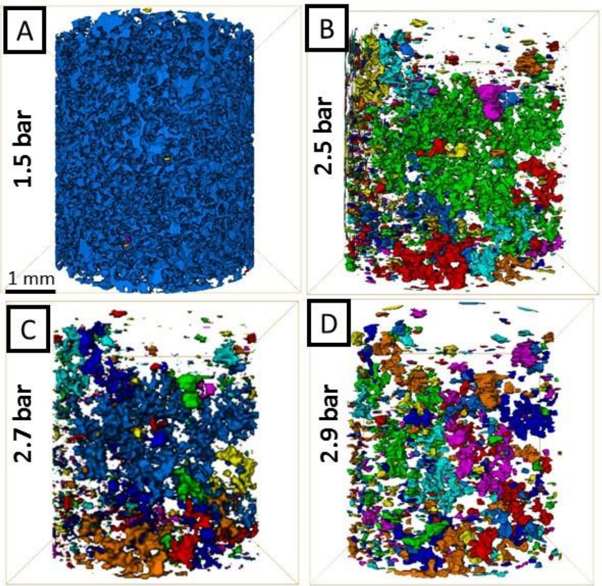

**Figure 5.** Micro-CT images taken during experiment 1. Each connected gas cluster is shown in a different colour. After the initial pressure drawdown to 1.5 bar almost the whole pore space is filled by gas, which is almost entirely connected (A). Upon pressurization the gas saturation decreases, and gas clusters shrink losing more and more their connectivity (B-C) until at 2.9 bar the top-bottom connectivity is finally lost (D).

### *Pressure depletion mode*

Experiment 2 is conducted in pressure depletion mode. In order to nucleate small, non-percolating gas bubbles, the pressure is initially drawn down to 1.6 bar and then quickly raised again to 3.0 bar which is approximately the bubble point as shown in **Figure 6**.

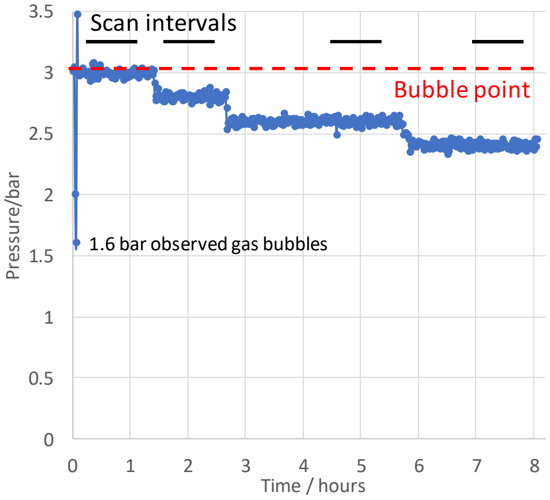

**Figure 6.** Pressure during experiment 1. The initial pressure drawdown below the bubble point causes a large amount of gas coming out of solution which percolates through the whole pore space. The gas is increasingly compressed until it is not connected anymore.

In **Figure 7.** pressure vs. volume for Experiment 1 is displayed. After initial depressurization and fluid compressibility effects, gas is nucleated by a brief pressure drawdown and immediate re-pressurization followed by pressure depletion. The regime where phase equilibrium is still visible but less pronounced than in experiment 1 (**Figure 4**). This is apparently an effect of the quick drawdown and respective rapid bubble nucleation. Overall the applied protocol is indeed successful.

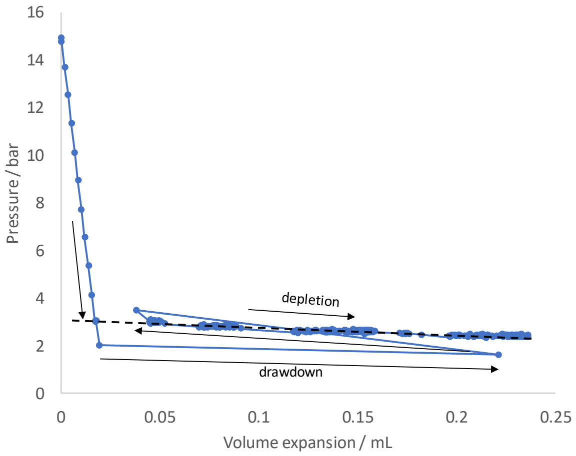

**Figure 7.** Pressure vs. volume for experiment 2 which was conducted in pressure depletion mode. Due to the very quick drawdown the supersaturated regime where nucleation of bubbles is suppressed and there is no phase equilibrium is avoided to a large extent.

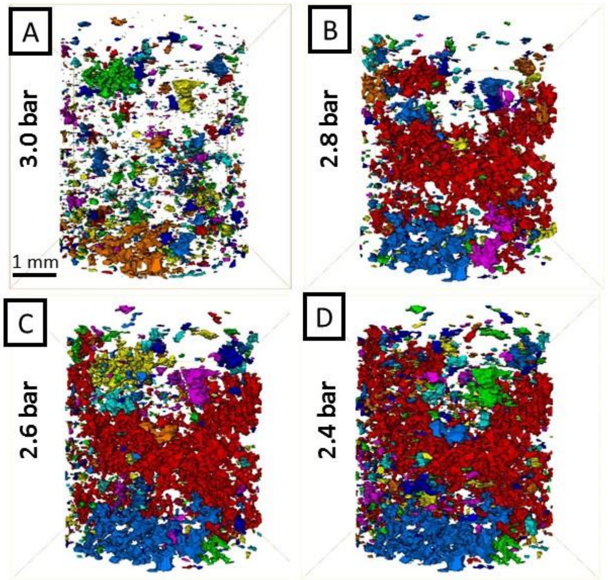

**Figure 8.** Micro-CT images taken during experiment 2. After the very quick initial pressure drawdown during which small gas bubbles are nucleated, the pore pressure is raised again to 3.0 bar leaving a set of small, not-connected gas bubbles (A). Upon pressure depletion, the gas saturation increases, and gas clusters grow increasing their connectivity (B-D).

The successful experimental protocol is also supported by the 3D images displayed in **Figure 8**. **Figure 8A** was taken right after pressure drawdown and re-equilibration at the expected bubble point. Small, not-connected gas bubbles were observed. Upon closer inspection of **Figure 7.** we observe that the one data point at 1.6 bar is associated with a volume expansion of 2.2 mL, which is similar to the volume expansion in experiment 1 (**Figure 4**). This data set suggests that the expanding gas fills nearly the entire pore space as shown in **Figure 5A.** One can, therefore, conclude that the gas was nucleated and almost fully expanded into all available pore space and then re-compressed in two subsequent steps arriving at a non-percolating distribution of gas bubbles as shown in **Figure 8A.** Upon pressure depletion the gas saturation increased again, and gas clusters grew increasing their connectivity (**Figure 8B-D**). Connectivity of the gas in the horizontal direction is already encountered at 2.8 bar (**Figure 8B**) but vertical connectivity is observed only at 2.4 bar displayed in **Figure 8D**.

### Fluid Connectivity and Percolation Threshold

The connectivity of the gas phase in experiments 1 and 2 was assessed via the Euler characteristic $\chi$ , which is a measure of connectivity and state variable for multiphase flow in porous media [30-32]. For our case the Euler characteristic for the gas phase can be defined as [30]

$$\chi = objects - loops \qquad \text{eq. 1}$$

The Euler characteristic is directly computed on the segmented image using Avizo [32]. Note that $\chi$=0 is an indication for the percolation threshold and is therefore a convenient measure to determine the critical gas saturation $S_{gc}$. The Euler characteristic as a function of gas saturation is displayed in **Figure 9**, indicating that $S_{gc}$=0.25 for the pressurization mode and $S_{gc}$=0.2 for the pressure depletion mode. That is consistent with the range of typical percolation thresholds of 3D structures as listed in Table 1.

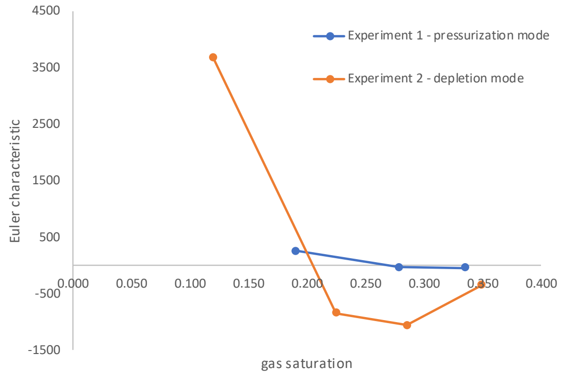

**Figure 9.** Euler characteristic as a function of gas saturation for experiments 1 and 2. The zero-crossing of the Euler characteristic indicates the percolation threshold, which is around $S_{gc}$=0.25 for the pressurization mode and $S_{gc}$=0.2 for the pressure depletion mode.

The difference in critical gas saturation in pressurization and depletion mode ultimately reflects that re-pressurisation is not simply the reverse of primary depletion, as the previously developed phase does not simply retract from the latest pores invaded during depressurization. Rather, the process exhibits a large degree of hysteresis in both local super saturation and gas phase distribution [10].

**Table 1.** Percolation Threshold in 3D

| Structure | Coordination number | Percolation threshold | Ref. |
|---|---|---|---|
| Simple cubic lattice | 6 | **0.30-0.31** | 18-23 |
| BCC lattice | 8 | **0.243-0.246** | 18-23 |
| FCC lattice | 12 | **0.195-0.199** | 24 |
| Random sphere pack | 6 | **0.31** | 25 |

Note that the top-bottom connectivity does not always coincide with the zero crossing of the Euler characteristic. This might be related to the fact that the Euler characteristic is a measure of isotropic connectivity.

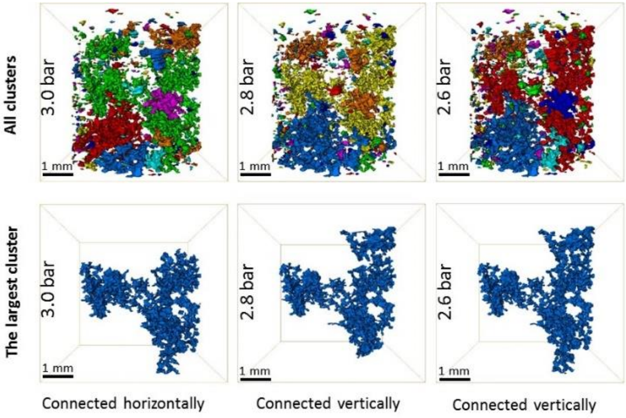

**Figure 10.** 3D fluid distribution in a pressure depletion experiment (similar to experiment 2) showing all clusters on the top panel and only the largest cluster at the bottom.

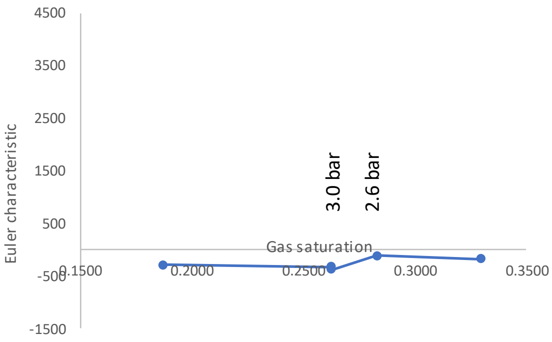

**Figure 11.** Euler characteristic for the 3D fluid distributions from **Figure 10** plotted at the same scale as in **Figure 9**.

In **Figure 10** the 3D fluid distribution in a pressure depletion experiment (similar to experiment 2) is displayed showing all clusters on the top panel and only the largest cluster at the bottom. The respective Euler characteristic χ is shown in **Figure 11**. At 3.0 bar the largest cluster percolates horizontally, but not vertically. The Euler characteristic values shown in **Figure 11** are all negative, indicating connectivity, which is aligned with the visual inspection of the identified gas clusters.

### Relative Permeability

Apart from the critical gas saturation, the associated relative permeability of gas and liquid are the key parameters of interest [6-7,40]. Traditionally, relative permeability is determined by flow experiments. However, in practical situations the applied pressure gradients and associated viscous instabilities would likely impact the fluid distribution which results in large uncertainties in the determination of relative permeability via flow experiments. Instead, here the 3D spatial distribution of liquid and gas phases from the segmented micro-CT scans were used to compute (connected pathway) relative permeability following a similar methodology as in [36] using a multi-relaxation time lattice Boltzmann method running on distributed GPU [35]. That is possible because the flow regime of connected pathway flow dominates, and -at least in water-wet rock- the flux contribution of ganglion dynamics is expected to be small [37,38].

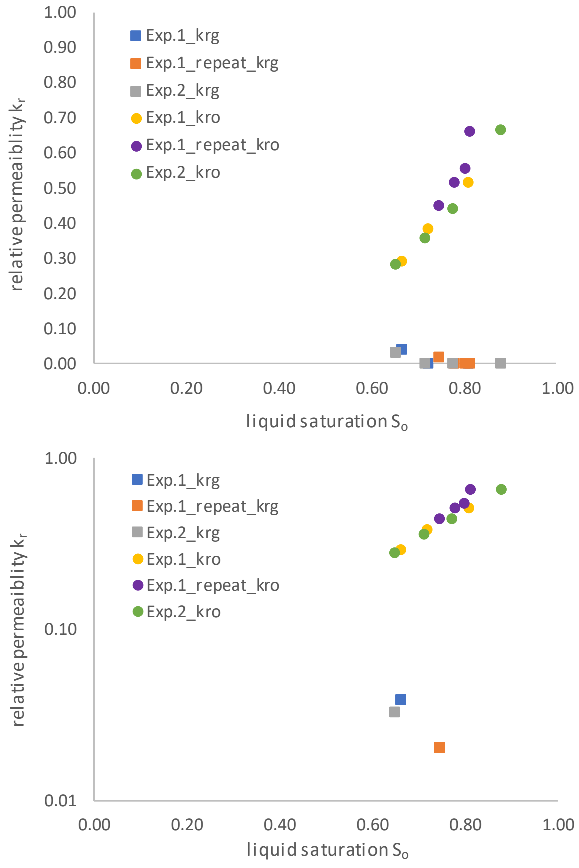

**Figure 12.** Relative permeability for liquid ("oil", o) and gas (g) computed with a single-phase multi-relaxation time lattice Boltzmann code based on the 3D fluid distribution from the experiments measured by micro-CT on a linear (top) and logarithmic scale (bottom).

The results are displayed in **Figure 12** on a linear (top) and logarithmic scale (bottom). The relative permeability curves are not straight lines as in a near-miscible situation [40]. That is consistent with a interfacial tension of approximately 17 mN/m derived from the PVT EOS calculations. The simulated relative permeability curves appear to be more compatible with a typical Corey behaviour [28] with exponents $n_w>1$ and $n_o>1$. The relative permeabilities of experiment 1 and a repeat experiment both conducted in pressurization mode, as well as experiments 2 carried out in pressure depletion mode overlap within the experimental uncertainty. That is somewhat surprising because the pressurization mode is in the widest sense an imbibition process while the pressure depletion is in the widest sense a drainage process, and hysteresis is expected. However, the saturation range is too narrow to clearly identify hysteresis. The fact that no hysteresis was observed could also be explained by the nature of the pores affected. In this case we remain at high gas saturation within or around the percolation threshold and it is likely that hysteresis here could play a minor role.

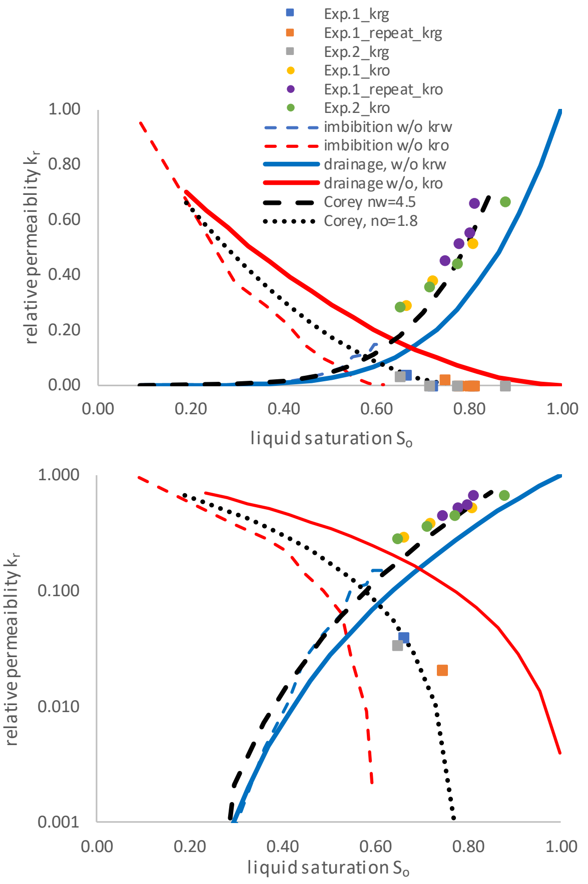

**Figure 13.** Gas-liquid relative permeability from **Figure 12** on a linear (top) and logarithmic scale (bottom). For comparison, wetting and non-wetting phase relative permeability for water-oil (w/o) are added, both in drainage and imbibition mode (solid and dashed red and blue lines). The gas relative permeability falls right between drainage and imbibition data. The liquid relative permeability seems to follow an extension of the water-relative permeability (dashed black line).

We observe $k_{r,g}>0$ only for Euler characteristic $\chi<0$ which supports the view that the Euler characteristic $\chi$ is a meaningful measure for the critical gas saturation. The dynamic range covered in these experiments was not sufficient to establish a $k_{r,g}(\chi)$ relationship as in [33]. In **Figure 13** water-wet water-displacing-oil drainage and imbibition relative permeabilities from a steady-state special core analysis measurement were added for comparison. The measurements were conducted on a 1.5" twin sample using brine-decalin on water-wet (cleaned) rock. The drainage data is shown as solid red and blue lines, the imbibition data is shown as dashed lines. In that comparison the water relative permeability is the wetting phase and oil is the non-wetting phase. In the gas-out-of-solution micro-CT experiment, oil is the wetting phase (because in absence of water it is a liquid and therefore the wetting phase) while gas is the non-wetting phase. Hence, we should compare the gas-out-of-solution liquid relative permeability with the water/oil relative permeability, and gas with oil, respectively. One would expect the liquid relative permeability to follow a primary drainage water line because gas-out-of-solution seems to be associated more with a drainage process. Interestingly the liquid relative permeability does not follow a primary drainage wetting phase relative permeability but rather the same trend as an imbibition relative permeability shown as dashed black line in **Figure 13** (which is an extension of the water imbibition relative permeability using a Corey representation with an exponent $n_w$=4.5). The gas relative permeability does not seem to follow either a primary drainage or a first imbibition trend. This reflects the fact that gas can come out of solution before a percolation threshold is reached. When comparing with an imbibition data set, this gas saturation would be therefore automatically below the residual oil saturation and hence the relative permeability cannot follow the imbibition line, at least not without re-normalizing the mobile saturation range. A primary drainage oil relative permeability would not be compatible because in primary drainage the non-wetting phase becomes mobile immediately while in the gas-out-of-solution study mobile gas is only possible from the critical gas saturation on. Therefore, the critical gas saturation of $S_{o,crit}$=0.21 is a logical value for a irreducible non-wetting phase saturation. And indeed, when using this re-normalization of the mobile saturation range the gas relative permeability is consistent with a drainage relative permeability as shown in the dotted black line in **Figure 13** (using $S_{or}=S_{o,crit}$=0.21 and $n_o$=1.8 which is consistent with both drainage and imbibition oil $k_r$). The liquid relative permeability could also just be a matter of re-scaling to the right end-point saturation, but it is not $S_{gc}$.

### *Injection mode*

The experiments shown so far were all conducted in absence of external flow addressing the expected slow depletion deep in the reservoir. There is certainly some flow because of expansion (or compression) of gas, but no external gas injection or flow via a pressure gradient was applied. In order to address the scenario near the wellbore, i.e. where gas flows in a potentially unstable fashion, a series of experiments were conducted where pure propane was injected into the propane-decane mixture. The first experiment was conducted at a pressure below the calculated bubble point but above the bubble point observed in previous experiments.

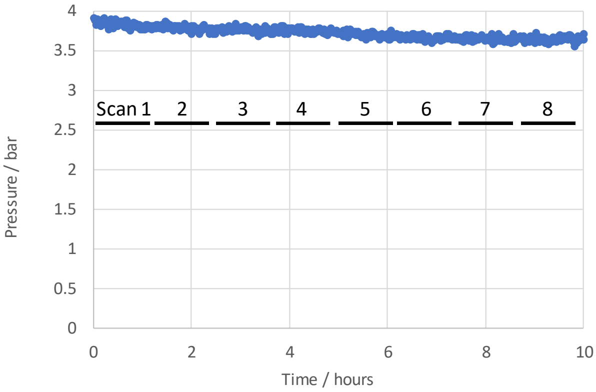

**Figure 14.** Pressure during flow at low Pe. At nearly constant pressure propane is injected into the Bentheimer core at constant rate of 0.03 ml/h. Respective micro-CT scan intervals are indicated as black lines.

The pressure data of experiment 3 and respective scan intervals are shown in **Figure 14**. Scans were taken continuously where the first scan was taken right after injection started but before gas entered the rock. Propane was injected into the ~50:50 propane-decane mixture at a rate of 0.03 ml/hour. That translates into a Darcy velocity of 2.39 mm/h and a capillary number of $Ca=6\cdot10^{-8}$ (for a liquid viscosity of 0.296 mPa s, calculated from the EOS). The 3D distribution of gas (and respective cluster analysis) is shown in **Figure 15**. Even though there is no visible connectivity from top-to-bottom, already at the first scan there is disconnected gas present in the whole sample. All values of the Euler characteristic $\chi$ are near-zero as shown in **Figure 16** indicating a near-percolating situation.

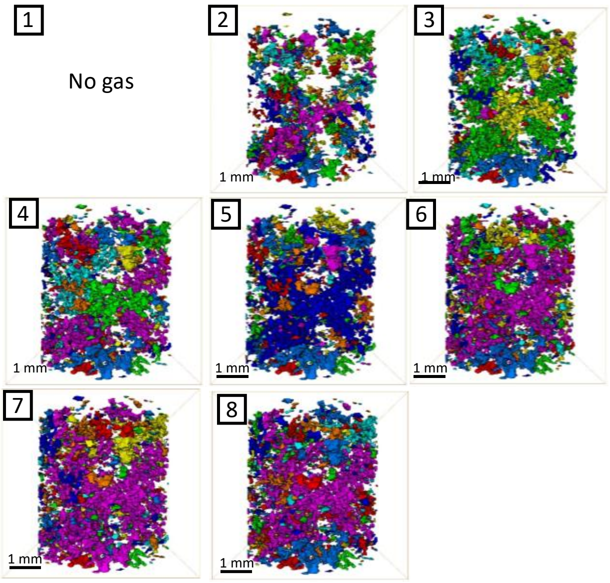

**Figure 15.** 3D visualization of the gas phase during the constant rate propane injection for the scan intervals from **Figure 14**. From scan 6 on there is top-bottom connectivity.

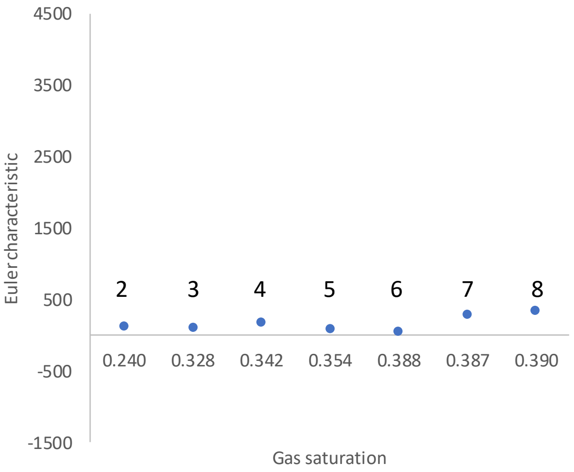

**Figure 16.** Euler characteristic $\chi$ for the 3D gas distribution from **Figure 15**. $\chi>0$ indicating a lesser degree of connectivity.

Actual top-to-bottom connectivity was observed from scan 6 onwards. One the one hand we have to keep in mind that permanent connectivity is not a necessary pre-requisite for flow. Processes such as snap-off in drainage [41] have been observed both experimentally [42] and in direct numerical calculation [43]. Cooperative dynamics such as ganglion dynamics [44] can lead to saturation distributions without permanent connectivity or connected pathway flow to inlet or outlet. Such a situation has been observed in previous synchrotron-beamline based studies with significantly higher time resolution (see Fig. 4 in [42]). Even at a few seconds time resolution the relatively fast snap-off processes which last only few milliseconds were not resolved. With the very limited time resolution of benchtop-based µCT it is difficult fully reveal the microscopic displacement mechanisms. Only a significantly higher time resolution would be able to resolve the exact processes leading to the gas distributions in **Figure 15** before a permanent top-bottom connectivity has been established.

What is striking is that an extended 3D spatial distribution is not only observed in scan 1 but also in the subsequent scans including up to scan 5. Permanent top-bottom connectivity is only observed form scan 6 on. That degree of saturation changes in 3D without permanent connectivity is beyond of what has been observed in simple drainage experiments where only occasionally a connection through a single pore throat was missing [42]. Therefore, the question arises whether there are additional mechanisms at play. One possible hypothesis is that during injection of propane the composition changes locally to a higher propane concentration which would lead to an increase in the bubble point. Therefore, even at a pressure above the bubble point experimentally observed in the previous constant-rate depletion experiments, the pressure would be below the local bubble point which could lead to an unstable growth and propagation of gas bubbles. This mechanism is possible because the Péclet number $Pe=L\cdot v/D\sim 4\cdot 10^{-2}$ for a characteristic length scale $L\sim 60$ µm (typical pore body diameter for Bentheimer sandstone), a typical molecular self-diffusion coefficient for hydrocarbon mixtures of $D\sim 5.8\cdot 10^{-9}$ m$^2$/s [45] and an interstitial flow velocity of $v\sim 3.5$ µm/s. With $Pe$ much smaller than one the diffusive processes dominate over convection which means that propane could indeed diffuse into the liquid (faster than the flow) and increase the local propane concentration substantially. For the given diffusion coefficient, diffusion across a 60 µm large pore would take about 1 s. To which extent exactly the local composition really changes and how much that really leads to an increase in local bubble point pressure is difficult to estimate without a detailed computation of transport and mass transfer which is beyond the scope of this work.

However, at a higher injection rate the flow would be more convection dominated and less diffusion dominated. By increasing the injection rate by a factor of 30 the Péclet number increases to $Pe\sim 1$ which essentially means that the diffusion is only about as fast as the flow. In comparison with the lower flow rate the onset of a more convection dominated regime and the effect of local compositional changes might be less. Therefore, the injection experiment was repeated at a 30 times higher flow rate of 0.9 ml/h which translates into a Darcy velocity of 72 mm/h and respective capillary number of $Ca=1.8\cdot 10^{-6}$. The pressure and micro-CT scan intervals are indicated in **Figure 17**. The respective 3D gas distribution is displayed in **Figure 18**.

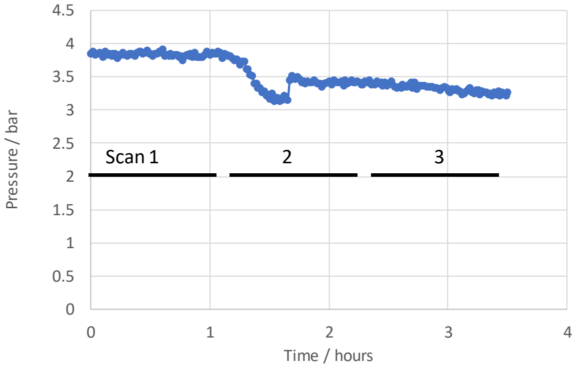

**Figure 17.** Pressure during experiment 4. Propane is injected into the Bentheimer core at a constant rate of 0.9 ml/h. Respective micro-CT scan intervals are indicated as black lines.

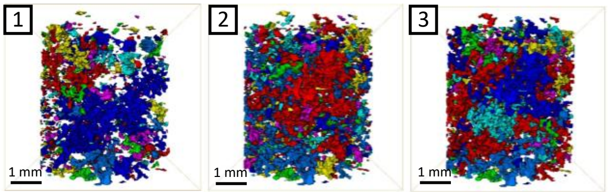

**Figure 18.** 3D visualization of the gas phase during the constant rate propane injection for the scan intervals from **Figure 17**. Note that in scan 2 and 3, there is permanent top-bottom connectivity.

Note that for the 3D gas distribution displayed in in **Figure 18** scan 2 and 3 have permanent top-to-bottom connectivity and even though no top-bottom connection has been made yet the overall connectivity of scan 1 is already higher than scan 2 or 3 in **Figure 15** (which has a comparable gas saturation). The connectivity is still higher than even scan 5 in **Figure 15** which is the last scan before permanent top-bottom connectivity was established. Also judging from the Euler characteristic χ displayed in **Figure 19**, which is negative, there is an overall higher degree of connectedness than in the lower flow rate injection experiment from **Figure 16**, i.e. less gas distribution without obvious connectivity to inlet.

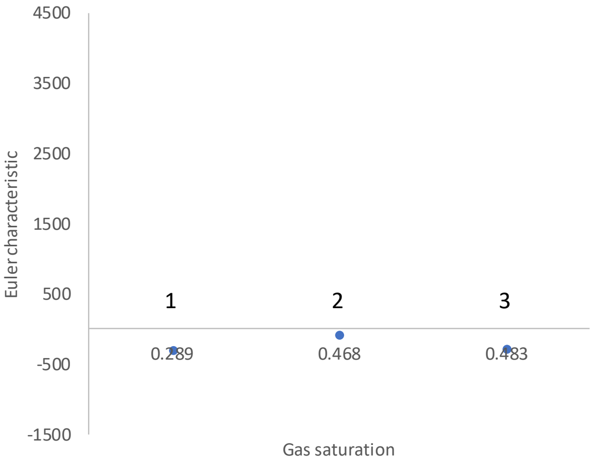

**Figure 19.** Euler characteristic χ for the 3D gas distribution from **Figure 18**. χ<0 indicating a higher degree of connectivity.

The robust conclusion is that the two injection experiments conceptually differ in terms of fluid connectivity. The increase in flow rate by a factor of 30 does not change the flow regime in terms of capillary number (Ca=$6 \cdot 10^{-8}$ and *Ca*=$1.8 \cdot 10^{-6}$ are both still in the capillary dominated regime) but does change the regime in terms of Péclet number (from *Pe*<<,1 to *Pe*~1). The more convection dominated regime has the higher degree of permanent connectivity. That supports to some extent the hypothesis of the unstable character of gas injection based on local compositional changes at the *Pe*<<1 case. Potentially the *Pe*<<1 process could also contribute to some observation classically made during tertiary gas injection (below miscibility) with the formation of an oil bank ahead the gas breakthrough. Injecting gas at higher pressure than the bubble pressure could lead, in addition to the standard swelling to sweeping the pore space. Further investigations and modelling work could help to further elucidate the phenomenon.

## Relative Permeability

In **Figure 20** the Gas-liquid relative permeability data from the flow experiments were super-imposed on the pressurization and depletion experiments without flow. While the liquid relative permeability is following closely the trend of the pressurization/depletion experiments, the gas relative permeability is clearly different, which could be caused by the fact that the gas is mobile without a permanent connectivity.

When plotting in **Figure 21** all gas relative permeability data vs. Euler characteristic χ there are two distinct populations: All pressure depletion and also high-rate injection experiments show χ<0 as expected for a highly connected phase, whereas for the low rate injection (and presumably diffusion dominated case) χ>0 Indicating a less connected situation.

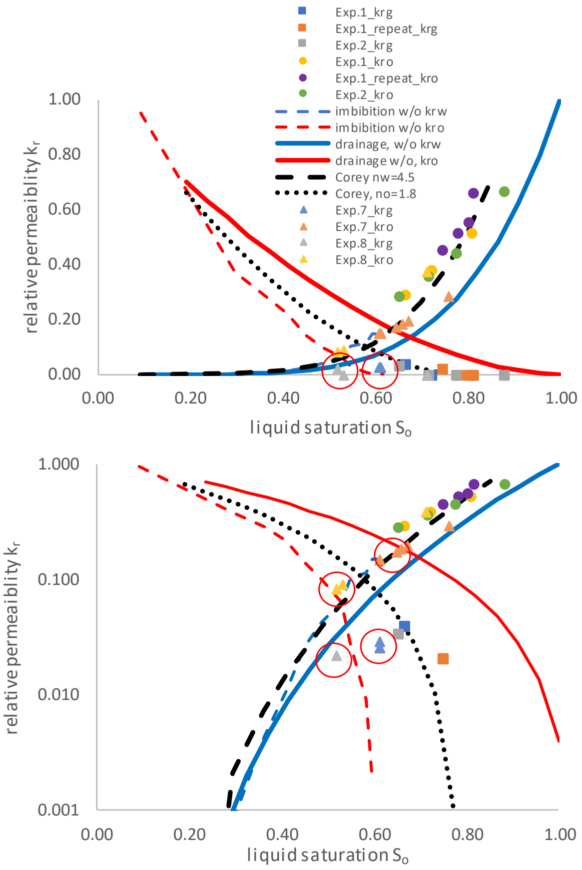

**Figure 20.** Gas-liquid relative permeability from the flow experiments super-imposed on the pressurization and depletion experiments without flow from **Figure 13**.

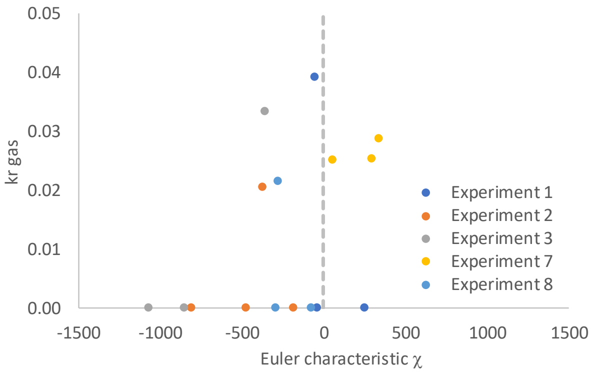

**Figure 21.** Gas relative permeability vs. Euler characteristic χ. For all pressure depletion (exp. 1-3) and high rate injection experiments (exp 8) χ<0 indicating a connected gas phase. Only for the low rate gas injection case (exp. 7) which is presumably diffusion dominated, χ>0 indicating a non-connected gas phase.

## SUMMARY AND CONCLUSIONS

The critical gas saturation has been assessed experimentally via a series of micro-CT flow experiments on a hydrocarbon model system where a gas phase drops out of solution upon pressure depletion. Pressure depletion in absence of flow provides a proof-of-concept that such critical gas experiments can be indeed conducted via pore scale experimentation. The pore scale distribution of gas was directly imaged by μCT. Consistent with the body of literature, in the porous medium the observation of the bubble point is depressed. The consequence is that nucleation eventually occurs and due to the associated supersaturation [3] the volume of gas dropping out of solution leads to instantaneous percolation, thereby masking the onset of connectivity, i.e. the critical gas saturation. That is an artefact of the experiment conducted at much faster pressure decline rates than the reservoir in the field case [1]. To accommodate for this effect, two protocols were developed where the first protocol operates in pressurization mode (somewhat similar to an imbibition type of experiment) and in the second protocol gas bubbles were first nucleated by rapid pressure drawdown and then re-pressurization to the bubble point followed by subsequent pressure decline (somewhat similar to a drainage process). The observed critical gas saturations were in the range of known percolation thresholds of 3D structures like random sphere packs. Pressurization and pressure depletion led to noticeably different critical gas saturations which might be related to the underlying difference in pore scale displacement events between drainage and imbibition processes [39]. A so far unresolved question is how the fast depletion – re-pressurization affects the depletion mode experiments.

Respective relative permeability curves were computed from the 3D gas and liquid distributions imaged by micro-CT using an in-house developed multi-relaxation time lattice Boltzmann method. They were then compared with drainage and imbibition water/oil relative permeability from steady-state SCAL data conducted on a (water-wet) twin sample. In that comparison the liquid relative permeability is consistent with an extension of the (wetting) water relative permeability from a water-oil imbibition experiment. The gas relative permeability is not compatible with either a drainage or an imbibition oil relative permeability from SCAL. The main reason is that a critical gas saturation is required before gas becomes mobile, i.e. a relative permeability can be defined. Therefore, the mobile gas saturation range starts at critical gas saturation which is larger than zero (hence the gas relative permeability cannot be compatible with a primary drainage curve) and smaller than a typical residual oil saturation (hence not compatible with a first imbibition relative permeability). However, rescaling the oil primary drainage relative permeability to the mobile saturation range for the gas case using the measured percolation threshold $S_{o,crit}=0.21$ as saturation endpoint does provide good consistency with the gas relative permeability.

The methodology of imaging the gas distribution in a flow experiment was extended to different flow regimes. Injecting gas at a low flow rate led to a 3D gas distribution without any obvious permanent connectivity to the inlet and a positive Euler characteristic $\chi>0$, i.e. below the percolation threshold. In direct comparison, at high injection rate, the connectivity at similar saturations was higher with $\chi<0$, i.e. above the percolation threshold. This could indicate a potentially unstable displacement scenario for the low injection rate case. While the low and the high injection rate experiments fall both within the same flow regime in terms of capillary number, they differ in terms of Péclet number $Pe$. For the low injection rate $Pe<<1$ meaning a much more diffusion-dominated regime, where the gas injected above the bulk liquid bubble point pressure can dissolve into the liquid phase at the injection front and change the respective composition such that the bubble point pressure increases. That can lead to a potentially unstable flow regime, where displacement scenarios become thinkable that do not require permanent connectivity. At the high injection rate, $Pe\sim1$ a higher degree of connectivity above the percolation threshold was observed which is more representative for a typical drainage type of displacement scenario. Note here the self-diffusion coefficient has been used to estimate the diffusive flux. Mutual diffusion coefficients in concentration gradients can be substantially higher which would increase the diffusive flux.

In order to develop the concept for quantifying critical gas saturation using pore scale imaging further, more detailed injection studies need to be conducted at different regimes e.g. in the supersaturated range below the observed bubble point but before gas can nucleate, at an even lower injection rate, and at faster time resolution to identify movement of discontinuous gas clusters. The underlying assumption of most of the current work is the steady movement of a continuous, sample spanning, gas phase at critical gas saturation. That assumption is widely accepted but may not fully cover all possible flow regimes such as gas clusters moving as a discontinuous phase [14-15] somewhat similar to the ganglion dynamics phenomena in immiscible 2-phase flow [37,38]. Relatively high interfacial tension of the chosen model system and the short core would likely suppress the movement of gas clusters. In order to study dynamic phenomena, the fast acquisition of a synchrotron beamline based μCT facility would be required. In low interfacial tension system, at increased time resolution intermittent gas production during gas depletion experiments on cores before the period of sharp gas-oil-ratio increase could be observed.

Our experiments have demonstrated that the hybrid methodology of pore scale experimentation and pore scale modelling provides a useful approach to address complex special core analysis problems that are difficult to achieve or even inaccessible for traditional special core analysis experimentation.

**Acknowledgements:** Arjen Cense, Keith Love and Birol Dindoruk are acknowledged for helpful discussions that guided the experiments. Willem-Bart Bartels and Hassan Mahani are acknowledged for designing and testing the micro-CT flow cell. Gerald Hamon and Patrick Egermann are gratefully acknowledged for the constructive comments during the review.

## References

1. SCHERPENISSE, W., WIT, K., ZWEERS, A.E., SNOEI, G., AND VAN WOLFSWINKEL, A., "Predicting Gas Saturation Build-up During Depressurisation of a North Sea Oil Reservoir". Presented to the SPE Europec Meeting, London, Oct. 1994. SPE 28842 (1994).
2. LIGTHELM, D.J., REIJNEN, G.C.A.M., WIT, K., WEISENBORN, A.J., SCHERPENISSE, W., Critical Gas Saturation During Depressurisation and its Importance in the Brent Field, 1997 Offshore Europe Conference held in Aberdeen, Scotland, 9-12 September 1997, SPE-38475 (1997).
3. FIROOZABADI, A., OTTESEN, B., MIKKLESEN, M., Measurements and Modelling of Supersaturation and Critical Gas Saturation, SPE 19694, San Antonio, October 1989.
4. KAMATH, J., BOYER, R.E., Critical Gas Saturation and Supersaturation in Low-Permeability Rocks, SPE 26663, SPE Formation Evaluation, 247-253, December 1995.
5. DU, C., YORTSOS, Y. C., A Numerical Study of the Critical Gas Saturation in a Porous Medium, Trans. Porous Med. 35, 205-225 (1999).
6. EGERMANN, P., VIZIKA, O., Critical Gas Saturation and Relative Permeabilty During Depressurization in the Far Field and the Near-Wellbore Region, 2000 SPE Annual Technical Conference and Exhibition held in Dallas, Texas, 1-October 2000, SPE-63149 (2000)
7. EGERMANN, P., VIZIKA, O., A New Method to Determine Critical Gas Saturation and Relative Permeability During Depressurization in the Near-wellbore Region, Petrophysics 42(4), 352-361 (2001).
8. PICCAVET, N., LONG, J., HAMON, G., BONDINO, I. MCDOUGALL, S.R., Depletion of Near-Critical Oils : Comparison between Pore Network Model Predictions and Experimental Results, International Symposium of the Society of Core Analysts held in Trondheim, Norway, 12-16 September 2006, SCA2006-32 (2006).
9. BONDINO, I., MCDOUGALL, S.R., HAMON, G., Pore network modelling of heavy oil depressurisation: a parametric study of factors affecting critical gas saturation and 3-phase relative permeabilities, SPE Journal 196-205 (2005), SPE-78976.
10. BONDINO, I., MCDOUGALL, SR., EZEUKO, CC., HAMON, G., Pore-Scale Simulation of Hysteresis Effects During Repressurization of Gas-Oil Systems, SPE Annual Technical Conference and Exhibition held in Florence, Italy, 19-22 September 2010. SPE-134525.
11. GRATTONI, C.A., HAWES, R.I., DAWE, R.A., Relative Permeabilities for the Production of Solution gas from Watereflood Residual Oil, 1998 Annual Symposium of the Society of Core Analysts, SCA-9817 (1998).
12. PETERSEN JR, E.B., AGAEV, G.S., PALATNIK, B., RINGEN, J.K., ØREN, P.E., VATNE, K.O., Determination of Critical Gas Saturation and Relative Permeabilties Relevant to the Depressurization of the Statfjord Field, International Symposium of the Society of Core Analysts held in Abu Dhabi, UAE, 5-9 October, 2004, SCA2004-33 (2004).
13. JI, W., DAHMANI, A., AHLFELD, DP., LIN, JD., HILL, E. III, Laboratory study of air sparging: air flow visualization, Groundwaetr Monitoring & Remediation 13(4), 115-126, 1993.
14. PLUMMER, CR., NELSON, JD., ZUMWALT, GS., Horizontal and vertical well comparison for in-situ air sparging. Ground Water Monitoring Review 17(1), 91-96, 1997.
15. MUMFORD, KG., Spontaneous expansion and mobilization of gas above DNAPL, PhD Thesis, McMaster University, 2008.
16. BULL, O., BRATTELI, F., RINGEN, JK., MELHUUS, K., BYE, AL., IVERSEN, JE., The Quest for the True Residual Gas Saturation - An Experimental Approach, International Symposium of the Society of Core Analysts held in Austin, Texas, USA, 18-21 September, 2011, SCA2011-03 (2011).
17. CENSE, A., REED, J., EGERMANN, P., SCAL for Gas Rservoirs : A Contribution for Better Experiments, International Symposium of the Society of Core Analysts held in Snowmass, Colorado, USA, 21-26 August 2016. Paper SCA2016-023.
18. KIM, T.W., KOVSCEK, A.R., The Effect of Voidage-Displacement Ratio on Critical Gas Saturation, SPE Journal 24(01), 178-199 (2019).
19. SATIK, C., ROBERTSON, C., KALPACKI, B., GUPTA, D. , "A Study of Heavy Oil Solution Gas Drive for Hamaca Field": Depletion Studies and Interpretations", SPE paper 86967 presented at the SPE International Thermal Operations and Heavy Oil Symposium and Western Regional Meeting, Bakersfield, CA, 16-18, March (2004).
20. SAHNI, A., GADELLE, F., KUMAR, M., TOMUTSA, L., KOVSCEK, A., "Experiments and Analysis of Heavy Oil Solution Gas Drive", SPE Reservoir Evaluation & Engineering, pp 217-229, June (2004).
21. XU, X., WANG, J. LV, J.-P., DENG, Y., Simultaneous analysis of three-dimensional percolation models, Frontiers of Physics 9(1), 113-119 (2014).
22. JAN, N., STAUFFER, D., Random Site Percolation in Three Dimensions, International Journal of Modern Physics C 09(02), 341-147 (1998).
23. SYKES, M.F., ESSAM, J.W., Critical percolation probabilities by series method, Physical Review 133(1A), A310-A315 (1964).

24. VAN DER MARCK, S.C., Calculation of Percolation Thresholds in High Dimensions for FCC, BCC and Diamond Lattices, International Journal of Modern Physics C, 9(4), 529-540 (1998).
25. POWELL, M.J., Site Percolation in Randomly Packed Spheres, Physical Review B 20(10), 4194-4198 (1979).
26. VAN WAGENINGEN, W.F.C., MAAS, J.G., Reservoir Simulation and Interpretation of the RECOPOL ECMB Pilot in Poland, 2007 International Coalbed Methane Symposium, Paper 072 (2007).
27. LENORMAND, R., TOUBOUL, E., ZARCONE, C., Numerical models and experiments on immiscible displacements in porous media, J. Fluid Mecha. 189, 165-187 (1988).
28. BERG, S., OEDAI, S., LANDMAN, A.J., BRUSSEE, N., BOELE, M., VALDEZ, R., VAN GELDER, K., Miscible displacement of oils by carbon disulfide in porous media: Experiments and analysis, Physics of Fluids 22, 113102 (2010).
29. BERG, S., OTT, H., Stability of CO2-Brine Immiscible Displacement, International Journal of Greenhouse Gas Control 11, 188-203 (2012).
30. HERRING, A.L., ANDERSSON, L., SCHLÜTER, S., SHEPPARD, A., WILDENSCHILD, D.: Efficiently engineering pore-scale processes: the role of force dominance and topology during nonwetting phase trapping in porous media. Adv. Water Resour. 79, 91 (2015)
31. MCCLURE, J.E., ARMSTRONG, R.T., BERRILL, M.A., SCHLÜTER, S., BERG, S., GRAY, W.G., MILLER, C.T., A geometric state function for two-fluid flow in porous media, Phys. Rev. Fluids 3(8), 084306, 2018.
32. ARMSTRONG, R.T., MCCLURE, J.E., ROBINS, V., LIU, Z., ARNS, C.H., SCHLÜTER, S., BERG, S., Porous Media Characterization Using Minkowski Functionals: Theories, Applications and Future Directions, Transport in Porous Media, 2018 in press doi:10.1007/s11242-018-1201-4
33. LIU, Z., HERRING, A., SHEPPARD, A., ARNS, C., BERG, S., ARMSTRONG, R.T., Morphological characterization of two-phase flow using X-ray microcomputed tomography flow-experiments, Transport in Porous Media 118(1), 99-117, 2017.
34. BUADES, A., COLL, B., MOREL, J.-M., A Non-Local Algorithm for Image Denoising, 2005 IEEE Computer Society Conference on Computer Vision and Pattern Recognition (CVPR'05) 2, 60-65 (2005).
35. ALPAK, F.O., GRAY, F., SAXENA, N., DIETDERICH, J., HOFMANN, R., BERG, S., A Distributed Parallel Multiple-Relaxation-Time Lattice Boltzmann Method on Graphic Processing Units for the Rapid and Scalable Computation of Absolute Permeability from High-Resolution 3D Micro-CT Images, Computational Geosciences 22(3), 815–832 (2018).
36. BERG, S., RÜCKER, M., OTT, H., GEORGIADIS, A., VAN DER LINDE, H., ENZMANN, F., KERSTEN, M., ARMSTRONG, R.T., DE WITH, S., BECKER, J., WIEGMANN, A., Connected Pathway Relative Permeability from Pore Scale Imaging of Imbibition, Advances in Water Resources 90, 24-35, 2016.
37. ZOU, S., ARMSTRONG, R.T., ARNS, J.Y., ARNS, C.H., HUSSAIN, F., Experimental and Theoretical Evidence for Increased Ganglion Dynamics During Fractional Flow in Mixed-Wet Porous Media, Water Resources Research 54 (5), 3277-3289, 2018.
38. ARMSTRONG, R.T., MCCLURE, J.E., BERRILL, M.A., RÜCKER, M., SCHLÜTER, S., BERG, S., Beyond Darcy's law: The Role of Phase Topology and Ganglion Dynamics for Two Fluid Flow, Physical Review E 94, 043113 (2016).
39. SCHLÜTER, S., BERG, S., RÜCKER, M., ARMSTRONG, RT., VOGEL, H.-J., HILFER, R., WILDENSCHILD, D., Pore scale displacement mechanisms as a source of hysteresis for two-phase flow in porous media, Water Resources Research 52(3), 2194-2205, 2016.
40. ALZAYER, A., VOSKOV, D.V., TCHELEPI, H.A., Relative Permeability of Near-Miscible Fluids in Compositional Simulators, Trans. Porous Med. 122(3), 547-573 (2018).
41. ROOF, J.G., Snap-off of oil droplets in water-wet pores. SPE J 10(1):85–90 (1970).
42. BERG, S. ARMSTRONG, R.T., OTT, H., GEORGIADIS, A., KLAPP, S., A., SCHWING, A., NEITELER, R., BRUSSEE, N., MAKURAT, A., LEU, L., ENZMANN, F., SCHWARZ, J.-O., WOLF, M., KHAN, F., KERSTEN, M., IRVINE, S., STAMPANONI, Multiphase flow in porous rock imaged under dynamic flow conditions with fast X-ray computed microtomography, Petrophysics 55 (4), 304-312, 2014.
43. EVSEEV, N., ARMSTRONG, R.T., BERG, S., DINARIEV, O., KLEMIN, D., KOROTEEV, D., SAFONOV, S., Modeling of pore-scale two-phase flow phenomena using density functional hydrodynamics, Transport in Porous media 112(3), 577-607, 2016.
44. RÜCKER, M., BERG, S., ARMSTRONG, R.T., GEORGIADIS, A., OTT, H. SCHWING, A., NEITELER, R., BRUSSEE, N., MAKURAT, A., LEU, L., WOLF, M., KHAN, F., ENZMANN, F., KERSTEN, M., From Connected Pathway Flow to Ganglion Dynamics, Geophysical Research Letters 42, 3888-3894, 2015.
45. REAMER, H.H., OPFELL, J.B., SAGE, B.H., Diffusion Coefficients in Hydrocarbon Systems, Methane-Decane-Methane in Liquid Phase, Ind. Eng. Chem. 48(2), pp 275–282, 1956.

# Inverted bucket centrifugation with fluorinated oils and its applications to $T_2$ cut-offs

*Ben* Anger[1,*], *Stefan* Hertel[2], *Keith* Love[3], *Michael* Ehiwario[3], *Matthias* Appel[1]

[1]Shell Global Solutions International B.V., Shell Technology Centre Amsterdam, Amsterdam, Netherlands
[2]Shell International Exploration and Production Inc., Shell Technology Center Houston, Houston, TX, USA
[3]Shell Exploration & Production Company, Shell Woodcreek, Houston, TX, USA

**Abstract.** Hydrocarbon reservoirs with a large column height as well as tight gas rocks require a large range of capillary pressures to describe the saturation of fluids present in these formations. While mercury injection capillary pressure (MICP) can achieve high equivalent capillary pressures, the tests are destructive to the core plugs. Centrifuge techniques have gained in popularity since they are faster than the porous plate technique, but they are limited in the achievable pressure range. Here, we propose the use of fluorinated oils to extend the achievable capillary pressure of the air-brine centrifuge technique by a factor of two. We use Fluorinert FC-70 in an inverted bucket configuration which doubles the radius of rotation and keeps the density contrast comparable to an air-brine system. Furthermore, we show the application to NMR $T_2$ cut-off determination as a function of capillary pressure. Since Fluorinert does not contain any hydrogen, there is no signal overlapping with the brine in the core plugs. Furthermore, in the inverted bucket configuration, the outlet face of the plug is not in contact with a drainage surface so that the Hassler-Brunner boundary condition of Pc = 0 is satisfied. Additionally, the method allows the storage under a liquid Fluorinert phase, which prevents evaporation and significantly extends the available time for NMR measurements at low water saturations.

## 1 Introduction

The interactions between wetting and non-wetting fluids in a porous rock are controlled in large part by capillary forces [1, 2, 3, 4]. These forces determine fluid distributions and control the ease with which pore fluids can be recovered during production. The relationship between fluid saturations and capillary pressure is represented in capillary pressure curves. Lab measurements of these curves provide information on important petrophysical properties such as irreducible water saturation and residual oil saturation as well as insight into the initial hydrocarbon saturation in a reservoir. Reliable estimations of petroleum reserves depend on a complete understanding of the capillary pressure curves for a given reservoir.

Capillary pressure is defined as the pressure difference between the wetting and non-wetting phases as a function of the saturation of the wetting-phase in a porous medium. This pressure difference arises thanks to the interfacial tension that exists at the boundary between two immiscible fluids. Together with gravity, the capillary pressure in a porous medium controls both the distribution of fluid saturations as well as the ease with which fluids can move within the rock. As such, the capillary pressure distribution within a reservoir has a strong influence on the producible hydrocarbon volume.

Several methods exist to measure capillary pressure curves in porous rock through the displacement of the wetting fluid phase with a non-wetting phase [5]. Mercury intrusion capillary pressure (MICP) is a fast method for determining saturation as a function of capillary pressure, but rock samples are destroyed during MICP measurements. Steady-state displacement against a saturated porous plate provides an accurate measurement of saturations, but since the time required for equilibration at each capillary pressure can be on the order of several weeks, steady-state measurements are extremely time consuming.

A third common technique for the determination of capillary pressure curves is the use of a high-speed centrifuge to displace one reservoir fluid with another [6]. This method is non-destructive and is significantly faster than steady-state methods. However, accurate interpretation of high-speed centrifuge data is dependent on a series of assumptions that can lead to uncertainty [7]. Efforts have been made to address these inherent uncertainties using novel non-wetting fluids [8] or the use of magnetic resonance imaging. Green *et al.* [9], combined the saturation gradient inherent in centrifuge measurements with one-dimensional NMR images to extract capillary pressure data from a sample that had been exposed to only one centrifuge speed [9, 10].

---

[*] Corresponding author: benjamin.anger@shell.com

Proton magnetic resonance provides a powerful and non-destructive method for probing the plug saturation and fluid distributions within a rock sample. The combination of NMR methods and the high-speed centrifuge techniques allows for the determination of bound and free fluid volumes through the measurement of a quantity called the $T_2$ cut-off [11]. As illustrated in **Figure *1***, the $T_2$ cut-off is the boundary in $T_2$ space between movable and bound fluids at a given capillary pressure. NMR data from sample desaturated at a given capillary pressure is compared to the fully saturated NMR data to determine the $T_2$ cut-off.

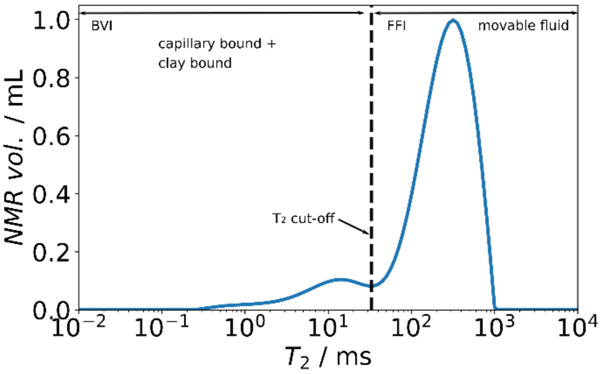

**Figure 1.** Fluid distribution and $T_2$ cut-off.

Generally, a single cut-off value is used as an input for NMR logging curves, which allows for separation of NMR $T_2$ distributions into the movable fluid fraction and the bound fluid fraction. However, it is not always clear which capillary pressure should be used to determine the irreducible water saturation and hence the $T_2$ cut-off value. It would therefore be desirable to develop a method to rapidly determine cut-off values at a range of capillary pressures.

In this work we present a method for rapid determination of movable and bound fluid volumes as a function of capillary pressure through a combination of NMR relaxometry and centrifuge primary drainage experiments in which formation brine is displaced by a dense fluorinated oil (Fluorinert FC-70). Because the non-wetting FC-70 is denser than the displaced brine, an inverted bucket configuration can be used in the centrifuge. The combination of comparable density contrast and the larger distance of the sample from the axis of rotation allows for desaturation at twice the capillary pressures compared to standard centrifuge methods. Further, in the inverted bucket configuration, the outlet face of the plug is not in contact with a drainage surface so the Hassler-Brunner boundary condition of $P_c=0$ is satisfied.

NMR $T_2$ measurements were made on a group of samples after multiple centrifuge speeds to produce $T_2$ cut-offs as a function of capillary pressure. This work showed that for this sample set, the commonly used cut-off of 33 ms should be replaced with a cut-off value of approximately 5 ms at the maximum capillary pressure achieved in the reservoir.

## 2 Experimental methods

### 2.1 Samples

The samples used in this work were sourced from a sandstone formation. All plugs were 2.54 cm in diameter. They were cleaned according to API RP 40 protocols, including UV fluorescence of solvent effluent and silver nitrate testing for salt content and then pressure saturated with 90 kppm NaCl equivalent synthetic formation brine. Klinkenberg-corrected permeability, helium porosity and MICP measurements were performed on twin plugs in a vendor lab. MICP saturations were calculated based on the normalization of the volume of Hg injected to the He porosity. Closure corrections and Hill-Shirley-Klein corrections were applied to correct for surface roughness and the presence of clay-bound water respectively. Sample details can be found in **Table *1***.

**Table 1**. Sample details, d = 2.54 cm for all plugs.

| Sample | Klinkenberg Perm. (mD) | He porosity (frac.) | Length (cm) |
|---|---|---|---|
| C04 | 1.82 | 0.148 | 1.765 |
| C05 | 2.43 | 0.178 | 1.602 |
| C06 | 2.62 | 0.170 | 1.816 |
| C07 | 2.96 | 0.174 | 2.034 |
| C08 | 3.02 | 0.160 | 1.583 |
| C09 | 3.26 | 0.158 | 1.836 |

### 2.2 Desaturation techniques

*2.2.1 Steady-state displacement*

Several methods were tested for the displacement of brine with a fluorinated oil (Fluorinert FC-70.) Standard NMR 2 MHz relaxometers are insensitive to FC-70, so an experiment in which brine is displaced by a fluorinated oil provides maximum contrast. At any given capillary pressure, the only fluid present after the displacement that is visible in the NMR measurements is the brine remaining in the plug.

Steady-state displacement methods against a brine-saturated porous plate produces a uniform saturation distribution throughout the sample. While the results of these experiments are very robust, this type of desaturation can be extremely time consuming due to the very low flow rates typically associated with steady-state displacement. Our initial attempts were performed in hydrostatic Hassler-type core holders. These measurements were complicated by the fact that we were required to unload and reload each sample between each injection pressure in order to measure the brine saturation with NMR. During our initial attempts at this method, we determined that extraneous brine entered the samples during the process of unloading and loading as a result of the removal of the confining stress. This unavoidable ingress of brine added an unacceptable amount of uncertainty to the NMR brine volumes.

We then successfully performed a steady-state desaturation against a saturated porous plate in an NMR pressure cell. Since the core flood was performed in the NMR instrument, there was no need to remove the sample between subsequent desaturation steps. This effort led to generally satisfactory results, but several complications led us to abandon these efforts. The presence of the brine-saturated porous plate made precise determination of the saturation values at each injection pressure difficult since signal from the porous plate and core plug were combined in the NMR response. Separation of the two signal sources through subtraction is possible, but can lead to a significant decrease in signal to noise and an increase in uncertainty. Further, covering the full range of desired capillary pressures required more than two months for a single sample. The long measurement time combined with the fact that the NMR spectrometer was unavailable for other work during the experiment led us to seek alternative solutions.

### *2.2.2 Centrifuge desaturation*

In order to achieve the desired range of capillary pressures on a realistic number of samples in an acceptable time frame, we turned to high-speed centrifuge displacement of the synthetic formation brine with FC-70. Two centrifuges were used in this work. The first was a Beckman Coulter Optima L-80XP Ultracentrifuge, and the second was a Beckman Coulter Optima L-90K. For all samples the inverted bucket orientation was used (see **Figure *2***), with the inlet face at a radius of 16.66 cm from the axis of rotation. Samples were centrifuged in sets of three or six simultaneously for 4-7 days per capillary pressure at rotation speeds of 1000, 1500, 2250, 3200, 3900, 5515, 10000 and 15000 RPM.

There are two main benefits to the use of the inverted bucket orientation. The distance of the plug from the axis of rotation is roughly double that of the radius in conventional buckets leading to a factor of two increase in the obtainable $P_c$ values. Further, no end piece is required with inverted buckets. Since the outlet face of the plug is not in contact with another surface, the Hassler-Brunner boundary condition of $P_c$=0 at the outlet face is satisfied.

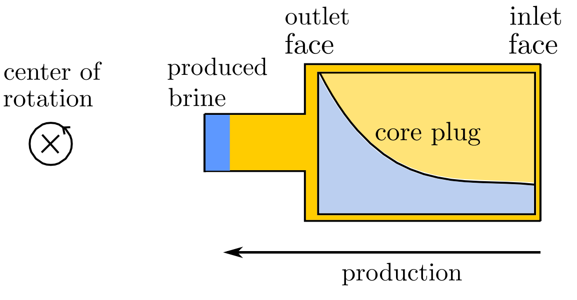

**Figure 2**. Inverted bucket orientation. In the plug, the remaining brine is blue and the FC-70 is yellow.

In the centrifuge, synthetic formation brine ($\rho$ = 1.057 g/cm$^3$, $\eta$ = 0.99 cP) was displaced by FC-70 ($\rho$ = 1.93 g/cm$^3$, $\eta$ = 24 cP). The change in weight of each plug was measured after each centrifuge speed to provide an independent measurement of the change in saturation at each capillary pressure. At all times during the series of measurements, the brine-saturated plugs were submerged in FC-70. This is important because the produced brine was never in contact with the plugs at any time, preventing brine from being imbibed into the samples and introducing uncertainty.

In order to correlate the FC-70/ brine capillary pressure dependent data with the Hg/air from the MICP measurements, we measured the contact angle of FC-70 in brine and the IFT to be 140$^o$ and 55.47 dynes/cm respectively. Each centrifuge speed produced a range of Hg/air equivalent capillary pressures dependent on plug length. A list of pressure ranges can be found in **Table *2***.

## 2.4 Nuclear magnetic resonance

### *2.4.1 Bulk NMR*

Bulk $T_2$ NMR measurements were performed on each sample after each centrifuge speed. Relaxation distributions were obtained via CPMG measurements at 2.3 MHz in Oxford Instruments GeoSpec2 relaxometers with TE = 400 µs (chosen to match common logging tool values), 12,500 echoes and a recycle delay of 7.5 s. The NMR response of the samples were compared to a calibration sample of known water volume to calculate brine saturations. All NMR experiments were performed with the plugs submerged in a clean bath of NMR-silent FC-70. This provided the opportunity for extended signal averaging without the worry of the loss of brine through evaporation – an important consideration since the total brine volume present in plugs after high rotation speeds was on the order of 0.5 cm$^3$ or less.

### *2.4.2 1D NMR imaging*

A uniform saturation distribution is not expected as a result of centrifuge desaturation experiments. To quantify this, one-dimensional saturation profiles were acquired at 12.7 MHz on an Oxford Instruments spectrometer using a simple frequency encode one-dimension profiling sequence.

# 3 Results and discussion

All samples were centrifuged at the range of speeds described earlier. An example of the results for a single plug at all centrifuge speeds can be found in **Figure 3**. This plot shows a continued decrease in the total brine saturation as irreducible brine saturation is obtained at all capillary pressures. Further, the main peak of the $T_2$ distributions shifts to shorter times as brine in larger pores and more loosely bound brine is expelled from the sample.

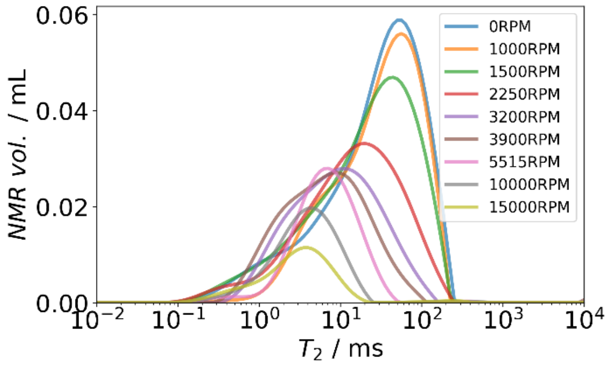

**Figure 3.** *$T_2$* spectra for all capillary pressures for sample C09.

Since the synthetic brine was displaced by NMR-silent FC-70, the calibrated NMR volume after each rotation speed corresponds to the remaining water volume in the plug at a given capillary pressure and all movable brine has been displaced by Fluorinert. From this brine volume, a water saturation $S_w$ can be calculated for each plug as a function of capillary pressure. A comparison of NMR saturations to vendor-supplied MICP saturation data is shown in **Figure *4***. The Fluorinert-brine capillary pressures were averaged over the core plug and converted to the mercury/air capillary pressure through the well-known conversion

$$P_{Hga} = P_{Fb}\frac{\sigma_{Hga}\cos(\theta_{\mathrm{Hga}})}{\sigma_{Fb}\cos(\theta_{Fb})} \qquad (1)$$

where $\sigma_{Hga}$ and $\sigma_{Fb}$ are are the interfacial tensions for mercury/air and FC-70 brine and $\theta_{Hga}$ and $\theta Fb$ are the contact angles for mercury/air and Fc-70/brine.

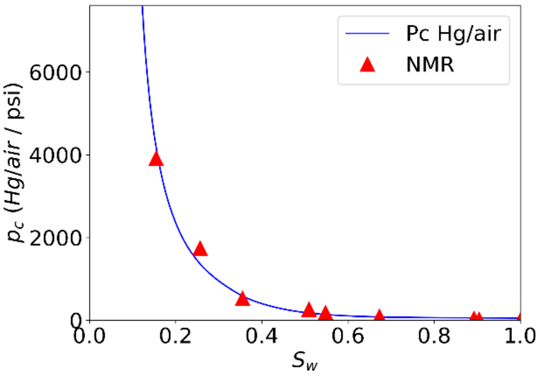

**Figure 4.** Comparison of NMR and MICP saturations for sample C09.

There is excellent agreement between the MICP and NMR data over the entire range of capillary pressures.

As seen in the comparison of NMR brine volumes to brine volumes calculated from the change in plug mass after centrifuging in **Figure 5**, there was good agreement between the two measurement methods.

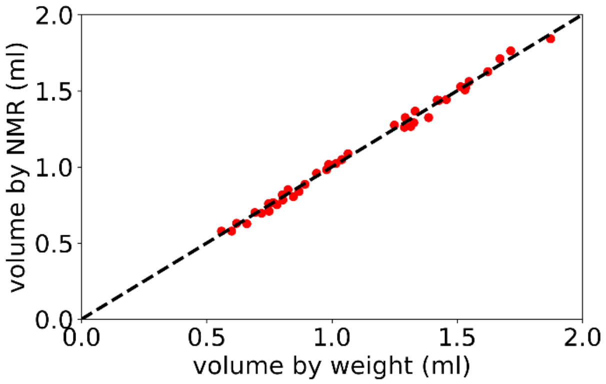

**Figure 5.** Comparison of NMR brine volume to calculated brine volume from change in sample mass.

A representative one-dimensional NMR saturation profile is shown in **Figure *6***. As expected $S_w$ approaches 100% at the outlet face.

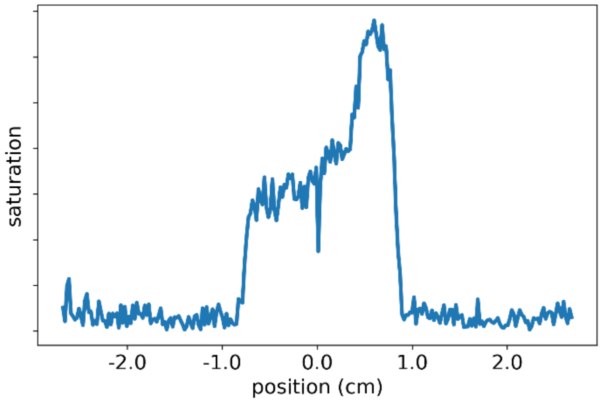

**Figure 6.** Saturation profile for sample C09 after centrifuging. Brine saturation approaches 100% at the outlet face on the right side of the plot.

As observed in the 1D NMR images, brine saturation in the plug after centrifugation is not uniform. If the Hassler-Brunner boundary condition of $P_c$=0 at the outlet phase is assumed, the variation in capillary pressure as a function of position along the plug is given by:

$$P_c(r) = \frac{\Delta\rho\omega^2}{2}(R_1^2 - r^2) \qquad (2)$$

where $\Delta\rho$ is the density contrast between FC-70 and the expelled brine, $\omega$ is the angular velocity of the centrifuge and $R_1$ is the distance of the inlet face from the axis of rotation. Given this distribution of capillary pressures and the one-dimensional profiles observed in several samples, an integrated average of the distribution described in equation 1 was calculated for each sample. The average Pc value is given by:

$$\overline{P_c} = \frac{\Delta\rho\omega^2}{2(R_2 - R_1)^2}\int_{R_1}^{R_2}(R_1^2 - r^2)dr \qquad (3)$$

where $R_2$ is the distance of the outlet face from the axis of rotation. A range of Pc values were calculated for each centrifuge speed and each sample used in this work. These values can be found in **Table *2***.

**Table 2.** Equivalent FC-70/brine and Hg/air $P_c$ ranges for all centrifuge rotation rates.

| Rotation Speed (RPM) | $P_c$ (Fc-70/brine, psi) | $P_c$ (Hg/air, psi) |
|---|---|---|
| 1000 | 3- 5 | 15-19 |
| 1500 | 7-10 | 34-43 |
| 2250 | 18-22 | 77-97 |
| 3200 | 36-45 | 155-196 |
| 3900 | 54-68 | 231-291 |
| 5515 | 108-134 | 461-581 |
| 10000 | 443-354 | 1515-1910 |
| 15000 | 504-636 | 3410-4297 |

As shown in **Figure 7**, the $T_2$ cut-off at a given capillary pressure can be determined by comparing the cumulative NMR signal at $S_w$=100% to the cumulative NMR signal from the desaturated sample. The $T_2$ cut-off is the value at which a horizontal line drawn through the final cumulative volume of the desaturated sample intersects with the cumulative volume of the fully saturated sample.

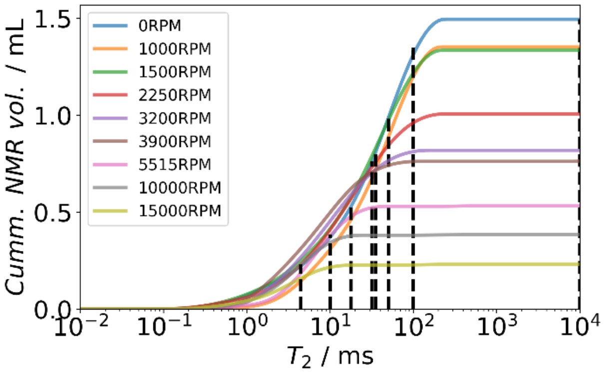

**Figure 7.** $T_2$ cut-off determination for sample C09.

Pressure dependent cut-off values were extracted for all samples. The results for sample C09 can be found in **Figure 8**. The commonly used sandstone cut-off of 33 ms is indicated by a dashed vertical line. While there is good agreement with the C09 data at a Hg/air equivalent of about 300 psi, it is clear that for higher capillary pressures the cut-off value between movable and bound fluid is much lower. For all samples in this work, the asymptotic $T_{2irr}$ value was 4-5 ms. In this case, use of the standard cut-off value would lead to large errors in the estimates of movable fluid volumes.

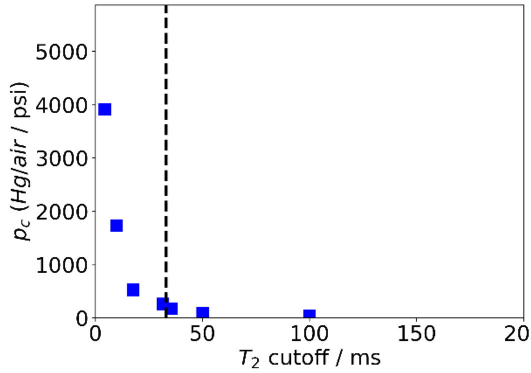

**Figure 8.** $T_2$ cut-off as function of Hg-air capillary pressure for sample C09. The dotted line is the standard 33 ms cut-off.

A modified Brooks-Corey model was applied to the data to extract asymptotic $T_2$ cut-off values for each sample. The standard Brooks-Corey *[12]* model relates capillary pressure to brine saturation as:

$$P_c = P_e\left(\frac{S_{w100} - S_{wi}}{S_w - S_{wi}}\right)^n \tag{4}$$

where $P_e$ is the capillary entry pressure, $S_{wi}$ is the irreducible water saturation and $S_{w100}$ (typically given as 1) is the maximum saturation. Following the recently published work of Al-Harbi *et al. [13]*, this relationship can be recast in terms of relaxation times as:

$$P_c = P_e\left(\frac{T_{2\max} - T_{2irr}}{T_{2cut} - T_{2irr}}\right)^n \tag{5}$$

where $S_{w100}$ is replaced by $T_{2max}$ (longest $T_2$ value in the fully $T_2$ distribution of the saturated sample), $S_w$ is replaced by$T_{2cut}$ ($T_2$ cut-off), and $S_{wi}$ is replaced by $T_{2irr}$ ($T_2$ cut-off at irreducible saturation). $T_{2max}$ was between 300-400 ms for all samples.

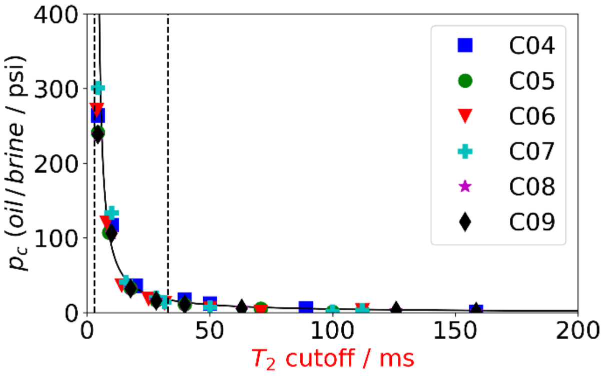

**Figure 9.** Brooks-Corey $T_2$ cut-off model applied to samples C04-C09 with $T_{2irr}$ = 3.3 ms, $P_e$ = 1 psi and $n$ = 1.1. Dashed lines are drawn at $T_{2irr}$ and at 33 ms.

The application of the modified Brooks-Corey model to a selection of samples can be found in **Figure 9**. For all samples in this set, an asymptotic cut-off value in the range of 4-5 ms was found to provide a more accurate measure of the division between mobile and immobile pore fluids at irreducible water saturation at capillary pressures corresponding to those found in the reservoir from which the samples were obtained.

## 5 Conclusions

In this work we presented a novel method for quantifying movable fluid volumes as a function of capillary pressure through a combination of NMR relaxometry and primary drainage experiments in a centrifuge in which the formation brine is displaced by Fluorinert FC-70. The combination of a large density contrast between the wetting and non-wetting fluid phases and the increased distance of the sample from the axis of rotation allows for significantly larger capillary pressures compared to standard air-brine displacement measurements. This method allows for the storage and measurement of samples submerged in Fluorinert, which prevents evaporation and significantly extends the available time for NMR measurements at low saturations.

The samples measured in this work showed asymptotic cut-off values in the range of 4-5 ms, significantly shorter than the commonly used cut-off value of 33 ms. The determination of a more accurate division between mobile and immobile fluid allows for more accurate estimates of movable fluids in place.

This work is directly applicable to reservoirs with large transition zones. In this specific case, it will be useful to produce a model in which the $T_2$ cut-off depends on capillary pressure and hence on the height above free water level. In a future paper, we will present the application of this method to the determination of a saturation model in which the $T_2$ cut-off varies as a function of the height above free water level.

Work is also currently underway to incorporate spatially resolved relaxation measurements of plugs after centrifuging using the 1D NMR profiling method developed by Hertel *et al.* [14]. This technique provides a snapshot of fluid distributions within a centrifuged plug on short time scale compared to standard 1D MRI methods. With this method, a significantly smaller number of centrifuge speeds will be needed to determine cut-off values at a full range of relevant capillary pressures.

The authors would like to thank Shell management for the permission to use the samples, and Kirk Smith, Aaron Dhaemers and Vivian Morah for their technical assistance.

## References

1. J. Schön, Physical Properties of Rocks, Amsterdam: Elsevier, 2015.
2. E. Thomas, "Capillary Pressure Tutorial: Part 1 - It's a Jungle in Here," *Petrophysics,* vol. 59, no. 4, pp. 421-427, 2018.
3. E. Thomas, "Capillary Pressure Tutorial: Part 2 - The Path Out of the Jungle," *Petrophysics,* vol. 59, no. 5, pp. 557-563, 2018.
4. E. Thomas, "Capillary Pressure Tutorial: Part 3 - The Jungle Gives Us Many Things," *Petrophysics,* vol. 59, no. 6, pp. 739-747, 2018.
5. C. McPhee, J. Reed and I. Zubizarreta, Core Analysis: A Best Practice Guide, Amsterdam: Elsevier, 2015.
6. G. Hassler and E. Brunner, "Measurement of capillary pressures in small core samples," *Trans. of AIME,* vol. 160, pp. 114-123, 1945.
7. D. O'Meara, G. Hirasaki and J. Rohan, "Centrifuge Measurements of Capillary Pressure: Part 1-Outflow Boundary Condition," *SPE Reservoir Engineering,* vol. 7, no. 1, pp. 133-142, 1992.
8. C. Straley and G. Leu, "Low-field NMR profiles for verification of oil and water saturations in cores," *Proc. Soc. Core Anal.,* pp. SCA2006-31, 2006.
9. D. Green, J. Gardner, B. Balcom, M. McAloon and J. Cano-Barrita, "Comparison Study of Capillary Pressure Curves Obtained Using Traditional Centrifuge and Magnetic Resonance Imaging Techniques," in *SPE Symposium on Improved Oil Recovery*, Tulsa, OK, 2008.
10. Q. Chen and B. Balcom, "Measurement of rock-core capillary pressure curves using a single-speed centrifuge and one-dimensional magnetic-resonance imaging," *J. Chem. Phys.,* vol. 122, p. 214720, 2005.
11. A. Timur, "Effective Porosity and Permeability of Sandstones Investigated Through Nuclear Magnetic Principles," *The Log Analyst,* vol. 10, no. 1, 1969.
12. R. Brooks and A. Corey, "Hydraulic Properties of Porous Media," *Hydrology Papers,* no. 3, 1964.
13. A. Al-Harbi, G. Hursan, H. Kwak and J. Gao, "A New NMR-based Height Saturation Model of a Low Permeability Carbonate Reservoir," *Saudi Aramco Journal of Technology,* pp. 49-59, 2018.
14. S. Hertel, D. de Kort, I. Bush, A. Sederman, L. Gladden, B. Anger, H. de Jong and M. Appel, "Fast spatially-resolved T2 measurements with constant-gradient CPMG," *Magnetic Resonance Imaging,* vol. 56, pp. 70-76, 2019.

# A New Apparatus for Coupled Low-field NMR And Ultrasonic Measurements in Rocks at Reservoir Conditions

*Paul R. J.* Connolly[1], *Joël* Sarout[2], *Jérémie* Dautriat[2], *Eric F.* May[1], *Michael L.* Johns[1]

[1]Department of Chemical Engineering, M050, The University of Western Australia, 35 Stirling Highway, CRAWLEY WA 6009, Australia.

[2]CSIRO Energy, ARRC Laboratories Kensington, Perth 6151, WA, Australia.

**Abstract.** Models which describe the effect of pore fluids on elastic wave propagation in rocks are the basis for quantitative reservoir analysis. Laboratory ultrasonic measurements conducted on rock cores are often used to test the applicability of the various models and adapt them as required. Current saturation-wave velocity models usually require some description of fluid saturation and/or distribution, pore aspect ratio, wettability and fluid viscosity. These are often measured indirectly at different experimental conditions to the reservoir or simply assumed. Hydrogen ($^1$H) Nuclear magnetic resonance (NMR) is a technique that can be used to quantitatively describe some of these important parameters. Here we report the design and performance of a novel NMR-compatible core holder system allowing for the measurement of both ultrasonic P-wave velocities and NMR relaxation parameters in rock cores at reservoir pressure and at variable fluid saturation conditions. Successful validation against a conventional benchtop ultrasonic measurement system was performed using a dry Berea sandstone core, whilst sequential NMR and ultrasonic measurements were performed on a Bentheimer Sandstone core at reservoir pressures and as a function of variable brine saturation (core flooding conditions). To the authors' knowledge, this new apparatus represents the first documented example of coupled high temperature NMR and ultrasonic measurements conducted at the same experimental conditions on the same rock specimen, and allows for a new approach to study pore scale saturation effects on elastic wave propagation in rocks.

## 1 Introduction

Low field Hydrogen ($^1$H) Nuclear Magnetic Resonance (NMR) is an important tool in petrophysics and is readily used to determine important reservoir parameters such as porosity, permeability, fluid type and saturation. Measurements are made both *in situ* in reservoirs using well logging tools, and *ex situ* on recovered reservoir plugs using benchtop spectrometers [1]. For quantitative assessment, low-field NMR employing magnetic field strengths less than 0.5 T have been shown to be more robust than higher fields as the impacts of internal magnetic field gradients are minimized [2], [3]. Furthermore, due to the technological challenge of operating well logging tools on long wire lines in harsh reservoir conditions, only low magnetic fields (e.g. ~<0.1T) are currently attainable [4].

Another key toolbox used in quantitative reservoir assessment and dynamic reservoir monitoring is seismic attribute analysis. The propagation of elastic waves in rocks can be related to their key lithological and geomechanical properties [5], and is also sensitive to the properties of the pore fluids [6]. Regional scale seismic surveys are used to map subsurface structures and delineate economic concentrations of hydrocarbons [7]. Furthermore, with improvements in 4D seismic techniques, effective monitoring of reservoir fluids during hydrocarbon production [8], [9] and $CO_2$ sequestration [10], [11] has been demonstrated. The interpretation of seismic data requires seismic inversion, which is generally constrained by rock physics models based on calibrated laboratory measurements. These rock physics models relate the elastic properties of rocks to effective stress, rock anisotropy, lithological and geomechanical properties, and also consider the impact of pore fluids (e.g. [5], [12]–[14]). A critical aspect in the application of these models to seismic reservoir characterisation and time lapse monitoring is their ability to predict the elastic response of rocks partially saturated with multiple pore fluids.

---

[*] Corresponding author: paul.connolly@uwa.edu.au

By combining laboratory ultrasonic and NMR measurements to directly quantify important parameters like wettability, pore surface-to-volume ratios and saturation, we aim to provide new insight on elastic wave propagation in saturated and partially saturated rocks. Furthermore, the ability to calibrate these measurements directly against *in situ* reservoir ultrasonic and NMR measurements made by wireline logging tools may also offer a novel approach to improving well log interpretation. Here, we present, as far as the authors are aware, the first example of an NMR compatible core flooding system capable of measuring ultrasonic wave velocities at high temperature and pressure conditions. The system has been designed to fit within the constraints of a 53mm borehole which is typical for low field NMR instruments used for rock core analysis. Only one other example of combined NMR and ultrasonic measurements of geological material was cited in the literature where the authors utilised a small animal Magnetic Resonance Imaging (MRI) system (85.7 MHz $^1$H or 2.0 T magnet) to study the formation of methane hydrates in sand packs. We have conducted a series of preliminary tests in a 2 MHz $^1$H NMR spectrometer up to temperatures and pressures of 45°C and 21 MPa. The design challenges and noise considerations are discussed, comparisons to a well-established ultrasonic measurement standard are made, and initial results are reported for a dry Berea sandstone and for a Bentheimer sandstone saturated with variable amounts of brine and supercritical $CO_2$.

## 2 Materials and Methods

### 2.1 Rock samples

Two quartz-dominated sandstone rock cores widely considered as petro-physical standards, Berea and Bentheimer, were used in this study. For comparison purposes, ultrasonic data on a dry Berea sandstone were acquired with both our novel apparatus and a well-established instrument, namely, the Autonomous Triaxial Cell (ATC) available at the Commonwealth Scientific and Industrial Research Organisation (CSIRO) in Perth, Australia [12]–[15]. The gravimetrically determined porosity for this core sample was 19.4%. The original Berea sandstone core had an original diameter of 3.81 cm and a length of 4.60 cm. The P-wave velocity in this dry core was first measured on a benchtop ultrasonic system. To adapt this core to our new NMR-Ultrasonic core holder (and with the desire to repeat the experiments on the same sample), its diameter was reduced to 2.54 cm using a diamond grinding wheel. For the core flooding tests a Bentheimer core was used due to its lower clay content and well-established NMR response [16], [17]. The core sample used had a diameter of 2.54 cm and was 11.45 cm long, with a gravimetrically-determined porosity of 21% and a permeability (to brine) of 3.4 D.

### 2.2 NMR relaxation time measurements

NMR signal or magnetisation ($\mathbf{M}_{(0)}$) decay occurs via two mechanisms, namely spin-spin ($T_2$) and spin-lattice ($T_1$) relaxation, corresponding to the transverse and longitudinal components of the magnetic field, respectively. Longitudinal recovery is described by:

$$\frac{\mathbf{M}_{(t)}}{\mathbf{M}_{(0)}} = 1 - exp\left\{-\frac{t}{T_1}\right\}, \tag{1}$$

while the transverse component decay is described by:

$$\frac{\mathbf{M}_{(t)}}{\mathbf{M}_{(0)}} = exp\left\{-\frac{t}{T_2}\right\}. \tag{2}$$

Measuring $T_2$ relaxation times can be achieved significantly faster than measuring $T_1$ relaxation times, whilst providing similar pore scale information. Hence $T_2$ times are a standard measurement approach for reservoir rock characterisation. When bound in a porous medium, proton ($^1$H) spins interacting with pore walls undergo enhanced relaxation due to increased dipolar interactions and/or restrictions to molecular mobility. Brownstein and Tarr [18] showed that for a fluid contained in a restricted environment, $T_2$ measured using a CPMG sequence can be modelled as:

$$\frac{1}{T_2} = \frac{1}{T_{2,bulk}} + \rho_s \frac{S}{V} + D_0 \frac{(\gamma G t_e)^2}{12}, \tag{3}$$

where $S/V$ is the surface-to-volume ratio of the pores; $\rho_s$ is the surface relaxivity constant representing the magnitude of proton ($^1$H) relaxation enhancement from surface interactions; $D_0$ is the fluid's self-diffusion coefficient; $\gamma$ is the gyromagnetic ratio of a proton nuclei; $G$ is any magnetic field gradients (in fluid-saturated rocks these are induced by the difference in magnetic susceptibility between phases); and $t_e$ is the time between NMR spin echoes. Typically, the impact of diffusive decay is negligible for conventional porous sandstones analysed with low magnetic field instruments (such as the 0.049 T system used here) and where sufficiently short echo times are used [19].

Considering $T_2$ times as a proxy for fluid-filled pore sizes is well-established [20]. This correlation assumes that diffusive exchange between pores is slow compared to the timescale of a measurement. For heterogeneous porous materials such as rocks, the observed $T_2$ response is represented by a convolution of exponentially decaying signals arising from pores of different sizes:

$$\frac{\mathbf{M}_{(t)}}{\mathbf{M}_{(0)}} = \frac{1}{V_0}\sum_{i}^{n}\left(V_i \times \left(e^{-t/T_{2,i}}\right)\right), \tag{4}$$

where $V_0$ and $V_i$ are the total sample volume and the *i$^{th}$* pore volume contribution respectively; $n$ is the number of pores; $\mathbf{M}_{(0)}$ is the equilibrium magnetisation; and $T_{2,i}$ is the relaxation rate for the *i$^{th}$* pore [21]. To solve for the probability distribution of relaxation times the raw NMR data must be inverted. Tikhonov's regularisation [22] is well suited to this ill-posed problem and has been used here. This method differs from a simple minimisation of residual norms in that an additional penalty term is added to balance the impact of noise. A more detailed description of Tikhonov's regularisation, as implemented here, can be found in Connolly *et al.* [23].

All NMR measurements presented here were made using a Magritek (New Zealand) Rock Core Analyzer (RCA) with a magnetic field strength of 0.049 T (corresponding to a $^1$H Larmor frequency of 2 MHz) and a 54 mm r.f. probe with a minimum echo time of 100 µs. To demonstrate the combination of NMR and ultrasonic velocity measurements on a sample at reservoir conditions, NMR transverse ($T_2$) relaxation time measurements were made on a Bentheimer sandstone core after sequential injection of brine and supercritical carbon dioxide. The calibrated NMR signal amplitude determines the brine filled porosity and the $T_2$ times are indicative of the pore sizes the brine occupies [4], [22]. All $T_2$ relaxation time measurements were made using a standard CPMG pulse sequence [24 - 25].

### 2.3 Ultrasonic pulse transmission measurements

The velocity of the primary compression ($V_P$) and secondary shear ($V_S$) waves in a homogeneous, isotropic and elastic medium are related to its elastic moduli through [5],

$$V_P = \sqrt{\frac{K + \frac{4}{3}\mu}{\rho_m}}, \tag{5}$$

$$V_S = \sqrt{\frac{\mu}{\rho_m}}, \tag{6}$$

where $K$ and $\mu$ stand for the bulk and shear moduli, respectively; and $\rho$ is density.

Here we apply one of the most widely applied methods to measure wave velocities in rocks, the pulse transmission technique where travel times of a single-pulse wave are measured over a known length [26]. In the physics of wave propagation, velocities can be referred to as the phase or group (or energy, or ray) velocity. For the majority of laboratory apparatuses described in the literature, including our new apparatus, the phase velocity is estimated from pulse travel time measurements conducted along the axis of a cylindrical rock specimen. Only in cases for which substantial rock anisotropy exists and/or very small sensor widths (<2mm) are used, can the pulse travel times yield a group velocity [27].

In practice, one transducer is used as the source of mechanical vibration while an opposing transducer is the sensor that converts the propagated mechanical energy back into an electrical signal. Our design utilized ring shaped piezo-ceramics that were nominally P-wave type (polarised along the ring's symmetry axis, which corresponds to the propagation direction) and produce clear first arrival times. These P-wave piezo-ceramics also generate some shear energy, although they are not designed for that purpose. Hence, shear wave arrival times were not determined from our data. Using dedicated shear wave piezo-ceramics allowing for an unambiguous determination of the shear wave velocity is possible and will be a focus for future apparatus development.

Electrical excitation of the source transducer was made using square wave pulses generated by an Olympus 5077PR pulse generator, which can generate pulses up to 400 V at frequencies from 0.1 to 20 MHz. Resulting waveform signals generated at the sensing transducer were captured using an oscilloscope and averaged (stacked) 128 times at a pulse rate of 100 Hz to enhance the signal to noise ratio (SNR). Due to the compliant nature and acoustic impedance compatibility of the PEEK spacers, no additional coupling fluid was required in our new apparatus.

## 3 Apparatus Design and Calibration

### 3.1 Core holder

A FCH series Core Labs NMR-compatible core holder was retrofit with custom-designed fluid distribution plugs made of PEEK, incorporating custom-built ring piezo-ceramics (**Figure 1**). The piezo-ceramic rings and associated electrical connections was designed to ensure the integrity of the fluid distribution plugs. Coaxial cables run through the confining oil ports using Kelmon™ K-25 series high-pressure feed-throughs. A NMR-inert fluorocarbon oil (Fluorinert™ FC-70) was used as the confining medium, and was circulated in the annulus between the primary fluid sealing sleeve and a fluorinated ethylene propylene (FEP) heat shrink sleeve covering the rock core sample. Sealing O-rings made of chemically inert fluroelastomer (Kalrez®) capable of handling corrosive fluids like supercritical $CO_2$ were used. The distribution plugs move freely with an O-ring seal on the injection lines, meaning that at elevated pressure the rock is subject to isotropic stress conditions. The range of operational conditions for the altered design was tested from ambient conditions to a confining pressure of 22 MPa at 45 °C.

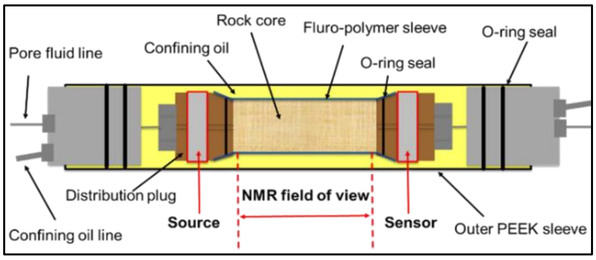

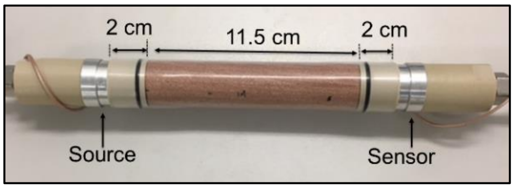

**Figure 1**. Schematic of the assembled core holder (top) and picture of assembled distribution plugs with piezo ceramic source and sensor transducers incorporated (bottom). Sensitive region of the magnet is 10 cm.

Electrically conductive components placed in or near NMR instrumentation usually result in residual eddy currents causing undue electrical noise in the recorded NMR data [28]. Initially, when the assembled core holder was placed inside the magnet borehole residual background noise on the order of 7-8 μV was observed. This level of background noise is approximately two orders of magnitude greater than when the core holder is not present. This noise level is commensurate with the signal typically arising from a fully saturated rock core, making meaningful relaxation time measurements impossible without overly excessive signal averaging. A solution to this problem was obtained by earthing the coaxial lines connected to the ultrasonic transducers, and all metallic components of the core holder and associated injection lines to the base plate of the magnet, effectively reducing the RMS background noise to ~ 0.15 μV, which is only ~ 0.09μV greater than the background RMS noise of an empty system (without core holder). Consequently, the NMR and ultrasonic measurements could be performed sequentially (with a switching time of less than 1 second) with no sample manipulation required ensuring that both measurements were performed at exactly the same stress-pressure-temperature conditions for the respective rock core sample.

Another concern for NMR measurements was the potential distortion of the applied magnetic field ($\mathbf{B_0}$) by having the ultrasonic transducers in or near the homogeneous magnetic field region where the NMR signal is detected (the NMR field of view as shown in the apparatus schematic in **Figure 1**). In the apparatus configuration reported here, the ultrasonic transducers remain on the outer edges of the NMR field of view and did not significantly affect the homogeneity of $\mathbf{B_0}$ within this region (i.e., no change in the full width at half maximum (FWHM) of the NMR spectrum was observed). This was not the case when the transducers were positioned within the NMR field of view, where severe distortions in the $\mathbf{B_0}$ field were observed. Shorter rock cores than used here could be accommodated in this apparatus by simply extending the length of the PEEK distribution plugs, which would ensure that the transducers remained outside the NMR field of view.

### 3.2 Piezo-ceramic Transducers

The characteristic ultrasonic frequencies generated by the piezo-ceramic transducers are defined by their resonant vibrational modes, which are determined by their piezo-elastic and geometric properties. The geometry of the ring-shaped piezo-ceramics used here had dimensions of 19.0 mm OD, 12.0 mm ID and were 2.5 mm thick. The directionally-dependent wave velocities within the piezo-ceramic material as quoted by the manufacturer are 1500, 2040, and 1980 m/s for the planar, axial and radial modes, respectively. The first harmonic vibration modes for flexural motion (in and out of plane bending), and radial and axial contraction were calculated to have frequencies of 104, 429 and 816 kHz, respectively. These ceramics were housed in custom-built aluminium casings while PEEK was used as electrical insulation to shield terminal connections **Figure 2**.

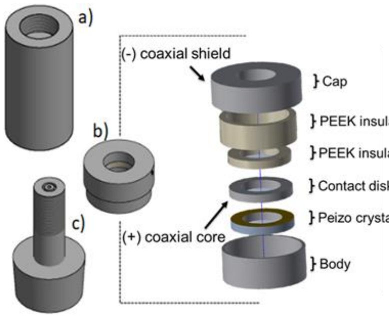

***Figure 2**. a,c) PEEK fluid distribution plugs, b)* custom piezo-ceramic transducer made of aluminium and PEEK. The transducer's electrical contacts rely on mechanical force only (pressure), with the design allowing for PEEK insulation and piezo-ceramic crystals with different dimensions (hence, resonant frequencies) to be interchanged.

The power spectrum of the transducers was measured by placing two transducers in direct contact (face-to-face) and conducting a calibration pulse-transmission test. Single excitation square wave pulses at 400 V with durations of 10, 1 and 0.1 μs at a repetition rate of 100 Hz were used, with the results shown in **Figure 3**. Using piezoelectric charge constants reported by the manufacturer the unconstrained (free) static displacement expected at 400 volts in the axial direction and radial direction are 0.160 μm and 0.029 μm, respectively. The observed frequency response is a convolution of the multiple modes of vibration of the ring-shaped piezo-ceramics (geometry and intrinsic properties), the interface coupling between the piezo-ceramic and the spacer (PEEK), and the body effects of the transducers' casing. Despite this complexity, comparison to the first nodal vibrations the simple calculations mentioned above were reasonable, with peaks at about 80 kHz, a broader band response around 400 kHz and a minor contribution at 830 kHz. When the length of the excitation pulse was increased from 0.1 to 10 μs, the preference for exciting the lower frequency vibrational modes is shown by the increase in the peak at around 80 kHz in **Figure 3**.

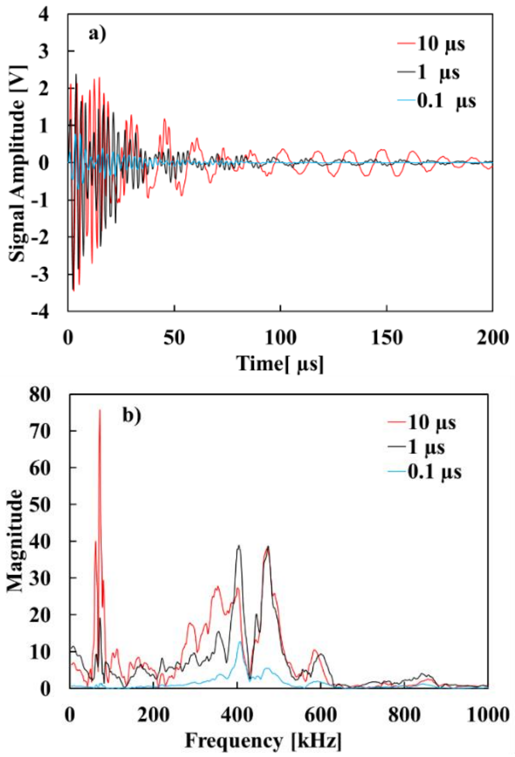

**Figure 3.** a) Time domain signal and b) power spectrum of ring piezo-ceramic transducers in direct contact with one another.

To account for contributions from the PEEK distribution plugs and aluminium casing to the total wave travel times, a calibration of the empty system in which the PEEK distribution plugs were in direct contact (without rock specimen) was conducted. Measurements were taken at temperatures between 25 and 48 °C, and pressures between 1 and 22 MPa. A linear elastic response was observed and fitted with a two-parameter linear model in the form: $ax + by + c$. The resultant fit had a correlation coefficient ($R^2$) of 0.9938 and a Root Mean Square Error (RMSE) of 0.0125 μs. A list of coefficients with corresponding 95% confidence intervals are listed in ***Table 1***. Pressure and temperature inputs to the model were made in Mpa and °C respectively, with the output in μs. Using this calibration mode, the instrument's inherent contribution to the ultrasonic travel times could then be subtracted from measurements carried out on actual rock cores.

***Table 1.*** *Fitting parameters for P-wave PEEK distribution plug time of flight calibration model.*

**Equation: $f(p,T) = ap + bT + c$**

| Coefficient | Value | 95% confidence bounds | |
|---|---|---|---|
| a | -0.001 | 0.001 | -0.001 |
| b | 0.017 | 0.016 | 0.017 |
| c | 15.8 | 15.78 | 15.82 |

## 4 Results and Discussion

### 4.1 Comparison test

Examples of ultrasonic waveforms acquired with the new NMR-Ultrasonic apparatus in a dry Berea sandstone for increasing confining pressures up to 21 MPa are shown in **Figure 4**. The excitation source was a 400 V 1 μs single-pulsed square wave with a pulse repetition rate of 100 Hz. The SNR of the initial peak amplitude was greater than 1000.

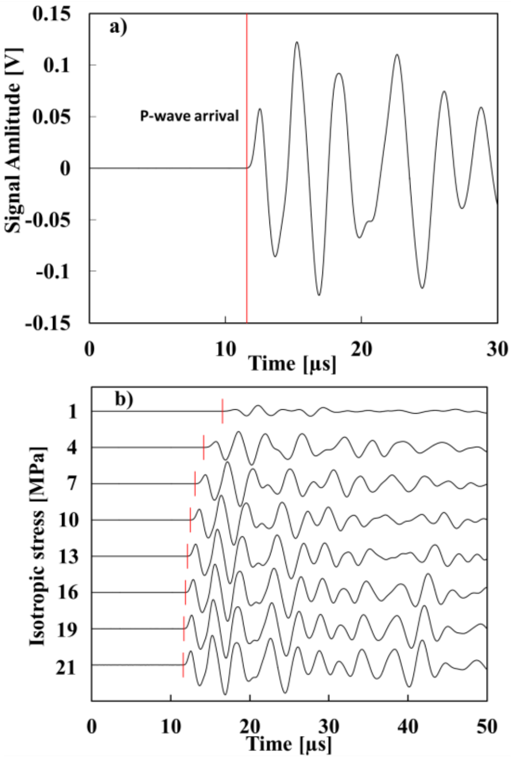

**Figure 4.** a) example of P-wave arrival time and b) response as a function of increasing effective stress. Clear P-wave arrivals are observed with excellent signal-to-noise ratio. Each waveform is typically the average of 128 repeated pulse-transmissions tests at a given pressure condition.

To evaluate the accuracy of P-wave velocities recorded in this new NMR-Ultrasonic apparatus, we conducted comparison measurements on the same rock sample using a well-established Autonomous Triaxial Cell (ATC)[12]–[15]. P-wave velocities were measured at 25°C with a stepwise increase in the confining pressure (3 MPa increments) up to 21 MPa, with repeated measurements at the same confining pressures during unloading. The results of the comparison are shown in **Figure 5** and agree remarkably well for both the loading and the unloading parts of the applied pressure cycle. Increasing wave velocity in rocks with increasing pressure is expected [5] and relates to the compaction of compliant porosity, grain boundaries and matrix defects leading to an increase in the stiffness of the rock frame. Note also that some amount of P-wave velocity hysteresis is observed between the loading and unloading parts of the pressure cycle, which is also a well-documented behaviour [5].

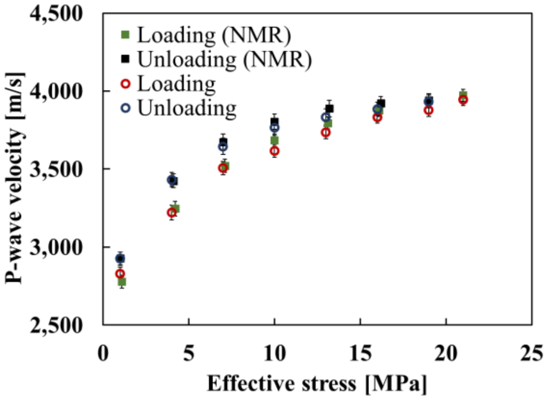

**Figure 5.** Comparison of the P-wave velocity as a function of effective stress for dry Berea sandstone measured using the new NMR-Ultrasonic apparatus (closed squares,) and the well-established Autonomous Triaxial Cell (open circles). The error bars correspond to uncertainties in length and arrival time measurements and typically correspond to ~1% of the estimated P-wave velocity.

### 4.2 Core flooding test

To demonstrate the combined application of NMR and ultrasonic measurements using the new apparatus, a series of core flooding tests involving supercritical $CO_2$ and brine were conducted on the Bentheimer sandstone rock core. The core was vacuumed for 12 hours before dead 3 wt% NaCl brine was injected to a pressure of 10 MPa. Following this, 10 pore volumes of 'live' $CO_2$-saturated brine was injected through the core to achieve an initial 100% brine saturated state. Prior to injection, the 'live' brine was exposed to Bentheimer sandstone for 12 hours to chemically equilibrate the solution, minimising the risk of mineral dissolution effects. The temperature of all fluid pumps, vessels and the core holder were maintained at 40 °C throughout the core flooding experiment. Pressure at the outlet of the core was maintained at 10 MPa with a backpressure regulator. A complete description of the core flooding system used can be found in reference [23]. A series of 10 pore volume aliquots of supercritical $CO_2$ were then injected at flow rates ranging between 20 and 40 ml/min resulting in a number of different partial $CO_2$-brine saturation states. Following this step several pore volumes of $CO_2$-saturated brine were injected at 1 ml/min until a stable saturation was reached, with a portion of the pore space occupied by capillary trapped $CO_2$. After each injection aliquot, NMR transverse relaxation ($T_2$) times and ultrasonic P-wave travel time measurements were carried out. The acquisition and processing of the P-wave arrival times followed the same procedure as the effective stress test on the dry Berea sandstone. Changes in brine saturation were calculated from the decrease in NMR signal relative to the fully saturated state.

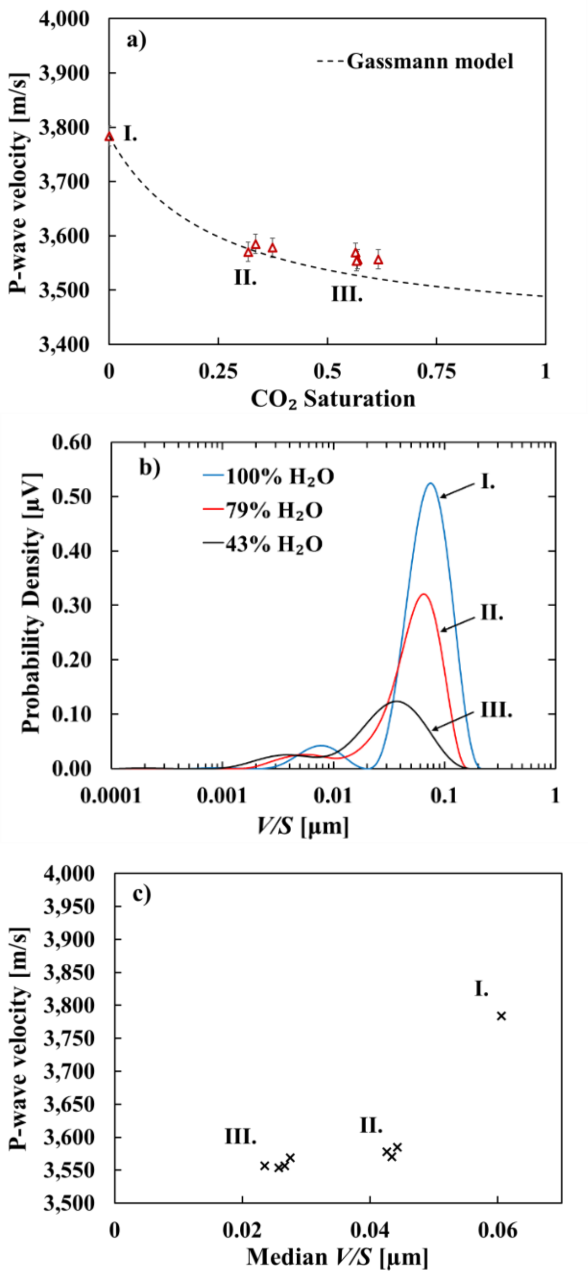

**Figure 6**. a) P-wave velocity in the Bentheimer sandstone at varying levels of supercritical $CO_2$ saturation as determined by NMR signal intensity, b) examples of *V*/*S* ratio distributions (converted $T_2$ time distributions) of brine-invaded pores at three particular saturation states, i.e., 100%, 79% and 43% brine saturation, and c) corresponding median *V*/*S* of the brine-invaded pores. Roman numerals indicate data pertaining to saturated (I.), after forced brine imbibition (II.), and after drainage by $CO_{2(sc)}$ injection (III.) respectfully.

**Figure 6** shows the change in P-wave velocity and corresponding change in $T_2$ relaxation times with increasing fraction of supercritical $CO_2$ content. The reduction in $T_2$ relaxation times is direct evidence of pore scale fluid occupation of pores with various surface-to-volume ratios. As the surface relaxivity of Bentheimer sandstone is well-known and quite consistent between samples, we have converted the $T_2$ times to $V/S$ ratios using a surface relaxivity $\rho_s$ value of 9.5 μm/s [17]. P-wave velocity was observed to decrease with increasing $CO_2$ content as the effective pore fluid compressibility increased. To aid demonstration, we have included the Gassmann's fluid substitution model which remains the most widely used model in the oil & gas industry for predicting P-wave velocity for variable pore fluid compressibility [29], [30]. The largest change in velocity coincides with the preferential displacement of brine from the largest pores, as indicated by the decrease in signal from pores with a larger $V/S$ ratio, and an increase in median relaxation rate ($1/T_2$) (Figure 5). Furthermore, the change in the distributions of $T_2$ times corresponds to the transition between a rock with pores fully saturated with water to one with pores partially occupied by water. Future work will focus on testing NMR determined petro-physical and pore scale saturation properties against the current understanding of how fluid impacts the ultrasonic wave properties in sedimentary rocks.

## 4 Conclusion

A novel design for an NMR compatible rock core holder is presented which allow for the combined measurement of P-wave velocity and NMR fluid responses of rocks at reservoir conditions. The P-wave velocities measured in this system for Berea sandstone at varied effective stress were compared to results from a well-established tri-axial test instrument and showed excellent agreement. Furthermore, pulse transmission velocity measurements of rocks at reservoir conditions are presented for which NMR has been utilised to quantify varied fluid saturation states. This was demonstrated using sequential NMR $T_2$ time relaxation and P-wave velocity measurements on a Bentheimer sandstone that was both fully saturated and partially saturated with brine and supercritical $CO_2$. By converting the $T_2$ times to $V/S$ ratios, these measurements allow for the study of pore fluid effects on elastic wave propagation as a function of fluid occupation in different sized pores. To the author's best knowledge, this is the first example of NMR being used to monitor effects of saturation state whilst recording the P-wave velocity response of a rock at reservoir pressure and temperature conditions. Future work will include extending the application of NMR relaxation, diffusion-weighted and spatially-resolved measurements to further the understanding ultrasonic wave propagation in saturated and partially saturated rocks, and the installation of transversely polarised piezo-ceramic transducers to include the ability to quantitatively determine shear wave velocities.

## 5 References

1. K. Dunn, D. Bergman, and G. LaTorraca, "Chapter 5 NMR logging applications," *Handb. Geophys. Explor. Seism. Explor.*, vol. 32, pp. 129–164, 2002.
2. C. Straley, D. Roosini, H. J. Vinegar, P. Tutunjian, and C. E. Morriss, "Core analysis by low-field NMR," *Log Anal.*, vol. 38, no. April, pp. 84–94, 1997.
3. J. Mitchell, T. C. Chandrasekera, M. L. Johns, L. F. Gladden, and E. J. Fordham, "Nuclear magnetic resonance relaxation and diffusion in the presence of internal gradients: The effect of magnetic field strength," *Phys. Rev. E - Stat. Nonlinear, Soft Matter Phys.*, vol. 81, no. 2, pp. 1–19, 2010.
4. J. Mitchell and E. J. Fordham, "Contributed review: Nuclear magnetic resonance core analysis at 0.3 T," *Rev. Sci. Instrum.*, vol. 85, no. 11, pp. 0–17, 2014.
5. G. Mavko, T. Mukerji, and J. Dvorkin, *The Rock Physics Handbook, Second Edition*. 2009.
6. M. Batzle and Z. Wang, "Seismic properties of pore fluids," *Geophsyics*, vol. 57, pp. 1396–1408, 1992.
7. R. E. Sheriff and L. P. Geldart, *Exploration Seismology*. Cambridge University Press, 1995.
8. R. J. Greaves and T. J. Fulp, "Three-dimensional seismic monitoring of an enhanced oil recovery process," *Geophysics*, vol. 52, no. 09, pp. 1175–1187, 1987.
9. D. Lumley, "Time-lapse seismic reservoir monitoring," *Geophysics*, vol. 66, no. 1, pp. 50–53, 2001.
10. D. Lumley, D. Adams, R. Wright, D. Markus, and S. Cole, "Seismic monitoring of CO2 geosequestration: reaslistic capabilities and limitations," *Annu. Soc. Explor. Geophys. Conf. Expand. Abstr.*, pp. 2841–2845, 2008.
11. R. Arts, A. Chadwick, O. Eiken, S. Thibeau, and S. Nooner, "Ten years' experience of monitoring CO2 injection in the Utsira Sand at Sleipner offshore Norway," *First Break*, vol. 26, no. 1, pp. 65–72, 2008.
12. J. Sarout, C. Delle Piane, D. Nadri, L. Esteban, and D. N. Dewhurst, "A robust experimental determination of Thomsen's δ parameter," *Geophysics*, vol. 80, no. 1, pp. A19–A24, 2015.
13. J. Dautriat, J. Sarout, C. David, D. Bertauld, and R. Macault, "Remote monitoring of the mechanical instability induced by fluid substitution and water weakening in the laboratory," *Phys. Earth Planet. Inter.*, vol. 261, pp. 69–87, 2016.
14. L. Pimienta, L. Esteban, J. Sarout, K. Liu, J. Dautriat, C. Delle Piane, and M. B. Clennell, "Supercritical CO2injection and residence time in fluid-saturated rocks: Evidence for calcite dissolution and effects on rock integrity," *Int. J. Greenh. Gas Control*, vol. 67, no. September, pp. 31–48, 2017.
15. C. Delle Piane and J. Sarout, "Effects of water and supercritical CO2on the mechanical and elastic properties of Berea sandstone," *Int. J. Greenh. Gas Control*, vol. 55, pp. 209–220, 2016.
16. H.-K. Liaw, R. Kulkarni, S. Chen, and a. T. Watson, "Characterization of fluid distributions in porous media by NMR techniques," *AIChE J.*, vol. 42, no. 2, pp. 538–546, 1996.
17. K. E. Washburn, M. Sandor, and Y. Cheng, "Evaluation of sandstone surface relaxivity using laser-induced breakdown spectroscopy," *J. Magn. Reson.*, vol. 275, pp. 80–89, 2017.
18. K. R. Brownstein and C. E. Tarr, "Spin-lattice

relaxation in a system governed by diffusion," *J. Magn. Reson.*, vol. 26, no. 1, pp. 17–24, 1977.

19. J. Mitchell, T. C. Chandrasekera, M. L. Johns, L. F. Gladden, and E. J. Fordham, "Nuclear magnetic resonance relaxation and diffusion in the presence of internal gradients: The effect of magnetic field strength," *Phys. Rev. E*, vol. 81, no. 2, pp. 1–19, 2010.
20. R. L. Kleinberg, "Pore size distributions, pore coupling, and transverse relaxation spectra of porous rocks," *Magn. Reson. Imaging*, vol. 12, no. 2, pp. 271–274, 1994.
21. O. Mohnke and B. Hughes, "Jointly deriving NMR surface relaxivity and pore size distributions by NMR relaxation experiments on partially desaturated rocks," *Water Resour. Res.*, vol. 50, no. 6, pp. 5309–5321, 2014.
22. A. N. Tikhonov, "Solution of Incorrectly Formulated Problems and the Regularisation Method.pdf," *Sov. Math. Dokl.*, vol. 4, no. 4, pp. 1035–1038, 1963.
23. P. R. J. Connolly, S. J. Vogt, S. Iglauer, E. F. May, and M. L. Johns, "Capillary trapping quantification in sandstones using NMR relaxometry," *Water Resour. Res.*, pp. 1–16, 2017.
24. H. Y. Carr and E. M. Purcell, "Effects of diffusion on free precession in nuclear magnetic resonance experiments," *Phys. Rev.*, vol. 94, no. 3, pp. 630–638, 1954.
25. S. Meiboom and D. Gill, "Modified spin-echo method for measuring nuclear relaxation times," *Rev. Sci. Instrum.*, vol. 29, no. 8, pp. 688–691, 1958.
26. F. Birch, "The velocity of compressional waves in rocks to 10 kilobars: Part 1," *J. Geophys. Res.*, vol. 65, no. 4, pp. 1083–1102, 1960.
27. J. Delllinger and L. Vernik, "Do core sample measurements record group or phase velocity?," *SEG Tech. Progr. Expand. Abstr. 1992*, no. May 2009, pp. 662–665, 1992.
28. M. Terpstra, P. M. Andersen, and R. Gruetter, "Localized eddy current compensation using quantitative field mapping.," *J. Magn. Reson.*, vol. 131, no. 1, pp. 139–143, 1998.
29. F. Gassmann, "Über die Elastizität poröser medien.," *Vierteljahrsschrift der Naturforschenden Gesellschaft Zürich*, vol. 96, pp. 1–23, 1951.
30. F. Yan and D. H. Han, "Effect of pore geometry on Gassmann fluid substitution," *Geophys. Prospect.*, vol. 64, no. 6, pp. 1575–1587, 2016.

# Defining a sample heterogeneity cut-off value to obtain representative Special Core Analysis (SCAL) measurements

*Jos G.* Maas [1,*], *Niels* Springer [2], and *Albert* Hebing [1]

[1]PanTerra Geoconsultants BV, Weversbaan 1-3, 2352 BZ Leiderdorp, The Netherlands
[2]GEUS, Øster Voldgade 10, 1350 København, Denmark

**Abstract.** Recently we published a method to quantitatively assess a heterogeneity number V that indicates the variability of the absolute permeability in a core plug. At that time, however, we could not provide a suitable cut-off for V. Therefore, the risk remained that SCAL measurements could be conducted on samples with a local distortion dominating flow and water cut behaviour. Subsequent use of the extracted relative permeability data in a reservoir simulation model would cause the field behaviour to be dominated in the same way, generating significantly wrong forecasts. In the present study, more than 70 scenarios for synthetic heterogeneous core plugs were simulated to study the impact of heterogeneity onto flow parameters measured in SCAL experiments. Both Unsteady-State and Centrifuge experiments on these synthetic plugs were simulated in 3-D. Subsequently, the simulated production data were history matched with a newly developed AutoSCORES software package to extract the relative permeability and capillary pressure in an objective manner. A rigorous statistical analysis was applied to determine a cut-off value for the heterogeneity number V for each listed scenario. The cut-off proved to be strongly dependent on the number of samples available in a SCAL study. First experimental results of measurements on actual rock samples are in line with predictions. A table is presented to assist SCAL experimentalists in deciding which SCAL samples reliably can be used for a SCAL study unaffected by the effects of heterogeneities, based on V of a sample.

## 1 Introduction

Special Core Analysis (SCAL) data are used as input in reservoir simulation models to predict long term oil and gas field behaviour as part of field development planning. State-of-the-art interpretation-by-simulation of the data, as well as conventional analytical data analysis (e.g. “JBN” [1], “Hassler-Brunner” [2]) requires the core plugs to be homogeneous. Today, no industry accepted methods exist to deal with heterogeneous plugs, while the common belief is that hardly any core plug is perfectly homogeneous.

A serious problem develops when SCAL measurements are conducted on core plugs with a local distortion dominating flow and water cut behaviour. Subsequent use of the extracted relative permeability data in a reservoir simulation model would cause the field behaviour to be dominated in the same way, generating significantly wrong forecasts. The problem was addressed by several authors already many years ago [3, 4, 5], but only qualitative results were presented in the absence of a heterogeneity number at the time.

Building on earlier work where we identified a heterogeneity number V [6], we now have conducted a detailed study into the effect of various possible heterogeneity scenarios onto measured relative permeability, such as stochastically distributed heterogeneities throughout the whole plug, a thin high-permeability zone, etc. We used SCORES3D (a 3D version of license-free SCAL simulator SCORES [7, 8]), to study in total more than 70 synthetic scenarios, covering what we believe are typical heterogeneity occurrences in core plugs.

The paper first discusses the general design of the study, clarifying the necessity to follow primarily a simulation approach. Subsequently, the heterogeneity scenarios are presented, followed by a discussion of the automatic history matching tool AutoSCORES we developed to achieve objective evaluations of the relative permeabilities impacted by the heterogeneities.

Central to the work is the interpretation of the results following a rigorous statistical analysis. This is explained in detail in a separate Section.

Finally, laboratory SCAL experiments are presented that were conducted in support of the analysis of the simulation study.

## 2 General design of the study

We will first present the outline for the study in determining a cut-off value for heterogeneity number V as it could happen in an ideal world where no budget or time restrictions play a role. Subsequently, we show how from this ideal study program we derived the workflow followed in this study.

---

[*] Corresponding author: jgmaas@euronet.nl

## 2.1 Ideal approach studying effect of heterogeneity on SCAL measurements on core plugs

In an ideal, unconstrained world one could set up a measurement program with the following steps:

1. Identify a base case set of perfectly homogeneous samples, i.e. samples with V=0. The heterogeneity number V is defined in our earlier paper [6] as

$$V = \frac{d}{a}\sigma_{HU} \quad (1)$$

   with *d* determined from an exponential correlation between porosity and permeability from routine core analysis (RCA) data and parameter *a* determined from a linear correlation between porosity and Hounsfield numbers from CT-images of the plugs. $\sigma_{HU}$ is the standard deviation of the Hounsfield values in the CT-image of the plug.
   To improve the statistical accuracy of the selection, the set should consist of at least 10 plugs, preferably 100 or more plugs (see Section 5).
2. Collect samples with increasing V numbers and of different topologies (i.e. layered, or containing impermeable spots or streak, open vugs, etc.). At least 10, preferably 100 samples or more per chosen V and chosen topology are required for reliable statistics (see Section 5).
3. Conduct RCA on all samples for porosity φ and absolute permeability K.
4. Conduct CT scanning on all samples to assess the individual V numbers, using Eq. 1.
5. Restore wettability through aging at representative initial water saturation and conduct imbibition SCAL experiments on all samples with a combination of UnSteady-State (USS) for relative permeability and Multispeed Centrifuge measurements for capillary pressure. Note that although SCAL data are primarily used to determine relative permeabilities, the capillary pressure function needs to be determined to be able to account properly for end-effects in the measurements.
6. Extract the water relative permeability krw, oil relative permeability kro and capillary pressure Pc using an interpretation-by-simulation technique.
7. Determine the cut-off value for V, beyond which the extracted relative permeabilities are found to be significantly different from the homogeneous base case, using sample statistics.

Clearly, the above approach is impossible to carry out because of practical limitations in time and budget.

## 2.2 Approach followed in this study

We have chosen to use synthetic core plugs constructed in software rather than real rock. The software employed is a newly developed extension into 3 dimensions of the license-free SCAL simulator SCORES built on DuMux [7, 8]. Simulations were conducted on a grid of 16 x 16 x 50 grid blocks. The capabilities of SCORES3D are described in Section 4. Our workflow has been set-up staying close to the ideal approach discussed above:

1. A homogeneous base case was defined as a core plug with K=10 mD, and φ=0.17.
   Relative permeabilities were defined using the Corey parameters listed in Table 1. We use the following Corey formulations for the water and oil relative permeabilities krw and kro respectively:

$$k_{rw}(S_w) = k_{rwor}\left(\frac{S_w - S_{wc}}{1 - S_{wc} - S_{or}}\right)^{n_w} \quad (2)$$

$$k_{ro}(S_w) = k_{rowc}\left(\frac{1 - S_w - S_{or}}{1 - S_{wc} - S_{or}}\right)^{n_o} \quad (3)$$

   A capillary pressure function Pc(Sw) was constructed similar to case 0, as used by Reed and Maas [9] (see also Gupta and Maloney [10]).
2. A range of heterogeneity scenarios was built with SCORES3D, based on experience in the laboratory. In total more than 70 heterogeneous plugs were constructed in software. Details of the scenarios are described in Section 3.
3. RCA is replaced by a numerical approach to calculate the effective K and φ for each synthetic plug.
4. CT scans are replaced by numerical calculation of V for each scenario, i.e. each individual synthetic plug.
5. SCAL is replaced by simulation in 3-D of each scenario using SCORES3D for a synthetic
   a. USS imbibition experiment with 2 bump floods
   b. Multispeed Centrifuge imbibition experiment, with 6 speeds
6. Data analysis was conducted
   a. Analytically - JBN [1] on selected scenarios to obtain an indication of the effect of V on the relative permeabilities.
   b. By interpretation-by-simulation - history matching using the newly developed numerical tool AutoSCORES to obtain relative permeabilities and Pc.

7. A rigorous statistical analysis of the results has been carried out, using data sets of up to 1000 AutoSCORES runs (thus simulating up to 1000 laboratory measurements for a single synthetic plug). In this way cut-off values for V could be identified beyond which relative permeability data are significantly different from the perfectly homogeneous base case.

**Table 1.** Corey parameters used for the scenario runs

| Swc | Sor | krwor | krowc | nw | no |
|---|---|---|---|---|---|
| 0.1 | 0.2 | 0.3 | 1.0 | 5 | 3 |

## 3 Details of scenarios

More than 70 synthetic scenarios have been investigated in this study. An overview is presented in Tables 2a-2g.

The base porosity ($\varphi_1$) was set to 0.17, and the base permeability was set to 10 mD. Scenario A0 represents a perfectly homogeneous plug. The SCAL simulator SCORES3D has been fitted with a random number generator [11], to generate normally distributed porosities assigned randomly to each grid block. The absolute permeability in each grid block was then derived from a standard exponential correlation [6], while the capillary pressure in each grid block was derived through a Leverett-J correlation [6].

**Table 2a.** Characteristics of heterogeneity scenarios: no layers, $\sigma_\varphi$: standard deviation of porosity distribution; $\varphi_{eff}$: effective (average) porosity; $K_{eff}$: effective permeability; V: heterogeneity number [6]. Note: $9.87 \times 10^{-15}$ m$^2$ = 10 mD.

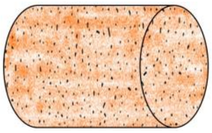

| Id | $\sigma_\varphi$ | $\varphi_2$ | $\varphi_{eff}$ | $K_{eff}$ ($10^{-15}$m$^2$) | V |
|---|---|---|---|---|---|
| B1 | .001 | - | .17 | 9.87 | .02 |
| B2 | .01 | - | .17 | 9.76 | .21 |
| B3 | .02 | - | .17 | 9.52 | .44 |
| B33 | .03 | - | .17 | 9.20 | .69 |
| B34 | .04 | - | .17 | 8.84 | .99 |
| B4 | .05 | - | .17 | 8.47 | 1.4 |

**Table 2b.** Characteristics of heterogeneity scenarios: "speckled" plug (see text), $\sigma_\varphi$: cut-off factor (see text) for standard deviation of porosity distribution; $\varphi_{eff}$: effective (average) porosity; $K_{eff}$: effective permeability; V: heterogeneity number [6]. Note: $9.87 \times 10^{-15}$ m$^2$ = 10 mD.

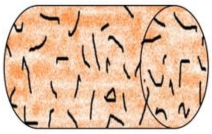

| Id | $\sigma_\varphi$ | $\varphi_2$ | $\varphi_{eff}$ | $K_{eff}$ ($10^{-15}$m$^2$) | V |
|---|---|---|---|---|---|
| C1 | x1 | - | .12 | 2.52 | .68 |
| C2 | x2 | - | .16 | 8.53 | .22 |
| C225 | x2.25 | - | .17 | 9.13 | .16 |
| C250 | x2.5 | - | .17 | 9.51 | .11 |
| C275 | x2.75 | - | .17 | 9.70 | .08 |
| C3 | x3 | - | .17 | 9.79 | .05 |

**Table 2c.** Characteristics of heterogeneity scenarios: 2-layers of equal thickness, $\sigma_\varphi$: standard deviation of porosity distribution; $\varphi_{eff}$: effective (average) porosity; $K_{eff}$: effective permeability; V: heterogeneity number [6]. Note: $9.87 \times 10^{-15}$ m$^2$ = 10 mD.

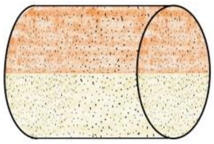

| Id | $\sigma_\varphi$ | $\varphi_2$ | $\varphi_{eff}$ | $K_{eff}$ ($10^{-15}$m$^2$) | V |
|---|---|---|---|---|---|
| D01 | .001 | .16 | .17 | 8.73 | .11 |
| D1 | .001 | .15 | .16 | 7.77 | .21 |
| D2 | .01 | .15 | .16 | 7.69 | .30 |
| D3 | .02 | .15 | .16 | 7.50 | .49 |
| D4 | .05 | .15 | .16 | 6.71 | 1.4 |
| D5 | .001 | .19 | .18 | 13.0 | .21 |
| D6 | .01 | .19 | .18 | 12.9 | .30 |
| D7 | .02 | .19 | .18 | 12.5 | .49 |
| D8 | .05 | .19 | .18 | 11.2 | 1.4 |
| D9 | .001 | .21 | .19 | 17.7 | .39 |
| D10 | .01 | .21 | .19 | 17.5 | .45 |
| D11 | .02 | .21 | .19 | 17.1 | .61 |
| D12 | .05 | .21 | .19 | 15.2 | 1.5 |

---

* Corresponding author: jgmaas@euronet.nl

**Table 2d.** Characteristics of heterogeneity scenarios: plug with 3-layers of equal thickness, $\varphi_2$: porosity of middle layer; $\sigma_\varphi$: standard deviation of porosity distribution; $\varphi_{eff}$: effective (average) porosity; $K_{eff}$: effective permeability; V: heterogeneity number [6]. Note: $9.87 \times 10^{-15}$ m$^2$ = 10 mD.

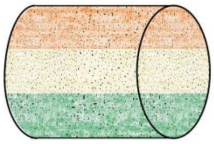

| Id | $\sigma_\varphi$ | $\varphi_2$ | $\varphi_{eff}$ | $K_{eff}$ ($10^{-15}m^2$) | V |
|---|---|---|---|---|---|
| E01 | .001 | .16 | .17 | 9.12 | .10 |
| E1 | .001 | .15 | .16 | 8.47 | .20 |
| E2 | .01 | .15 | .16 | 8.38 | .29 |
| E3 | .02 | .15 | .16 | 8.19 | .48 |
| E4 | .05 | .15 | .16 | 7.34 | 1.4 |
| E5 | .001 | .19 | .18 | 11.9 | .21 |
| E6 | .01 | .19 | .18 | 11.8 | .31 |
| E7 | .02 | .19 | .18 | 11.5 | .50 |
| E8 | .05 | .19 | .18 | 10.4 | 1.4 |
| E9 | .001 | .21 | .19 | 14.9 | .42 |
| E10 | .01 | .21 | .19 | 14.8 | .48 |
| E11 | .02 | .21 | .19 | 14.4 | .64 |
| E12 | .05 | .21 | .19 | 13.0 | 1.6 |

**Table 2e.** Characteristics of heterogeneity scenarios: plug with 3-layers, middle layer with $\varphi_2$ of about 4 mm thickness, $\sigma_\varphi$: standard deviation of porosity distribution; $\varphi_{eff}$: effective (average) porosity; $K_{eff}$: effective permeability; V: heterogeneity number [6]. Note: $9.87 \times 10^{-15}$ m$^2$ = 10 mD. For layer with $\varphi_2 = 0$, $\sigma_{\varphi 2}=0$.

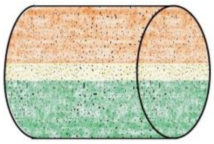

| Id | $\sigma_\varphi$ | $\varphi_2$ | $\varphi_{eff}$ | $K_{eff}$ ($10^{-15}m^2$) | V |
|---|---|---|---|---|---|
| F1 | .001 | .15 | .17 | 9.50 | .12 |
| F2 | .01 | .15 | .17 | 9.40 | .24 |
| F3 | .02 | .15 | .17 | 9.19 | .46 |
| F4 | .05 | .15 | .17 | 8.27 | 1.4 |
| F5 | .001 | .19 | .17 | 10.5 | .16 |
| F6 | .01 | .19 | .17 | 10.4 | .27 |
| F7 | .02 | .19 | .17 | 10.1 | .47 |
| F8 | .05 | .19 | .17 | 9.09 | 1.4 |
| F9 | .001 | .21 | .18 | 11.3 | .37 |
| F10 | .01 | .21 | .18 | 11.2 | .43 |
| F11 | .02 | .21 | .17 | 10.9 | .59 |
| F12 | .02 | .21 | .17 | 9.82 | 1.5 |
| F13 | .001 | .0 | .15 | 8.76 | .37 |
| F14 | .01 | .0 | .15 | 8.67 | .43 |
| F15 | .02 | .0 | .15 | 8.47 | .59 |
| F16 | .05 | .0 | .15 | 7.60 | 1.5 |

---

[*] Corresponding author: jgmaas@euronet.nl

**Table 2f.** Characteristics of heterogeneity scenarios: plug with 3-layers, middle layer with $\varphi_2$ of about 2 mm thickness, $\sigma_\varphi$: standard deviation of porosity distribution; $\varphi_{eff}$: effective (average) porosity; $K_{eff}$: effective permeability; V: heterogeneity number [6]. Note: $9.87 \times 10^{-15}$ m$^2$ = 10 mD. For layer with $\varphi_2 = 0$ and with $\varphi_2 = 0.5$: $\sigma_{\varphi 2}=0$.

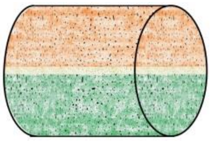

| Id | $\sigma_\varphi$ | $\varphi_2$ | $\varphi_{eff}$ | $K_{eff}$ ($10^{-15}$m$^2$) | V |
|---|---|---|---|---|---|
| G1 | .001 | .15 | .17 | 9.70 | .09 |
| G2 | .01 | .15 | .17 | 9.60 | .23 |
| G3 | .02 | .15 | .17 | 9.37 | .45 |
| G4 | .05 | .15 | .17 | 8.38 | 1.4 |
| G5 | .001 | .19 | .17 | 10.2 | .12 |
| G6 | .01 | .19 | .17 | 10.1 | .25 |
| G7 | .02 | .19 | .17 | 9.83 | .46 |
| G8 | .05 | .19 | .17 | 8.79 | 1.4 |
| G9 | .001 | .21 | .17 | 10.6 | .29 |
| G10 | .01 | .21 | .17 | 10.5 | .36 |
| G11 | .02 | .21 | .17 | 10.2 | .54 |
| G12 | .02 | .21 | .17 | 9.15 | 1.4 |
| G13 | .001 | .0 | .16 | 9.34 | .25 |
| G14 | .01 | .0 | .16 | 9.25 | .33 |
| G15 | .02 | .0 | .16 | 9.02 | .52 |
| G16 | .05 | .0 | .16 | 8.03 | 1.4 |
| G170 | .001 | .5 | .19 | 49.6 | 3.9 |

**Table 2g.** Characteristics of heterogeneity scenarios: plug with 3-layers, middle layer with $\varphi_2$ of about 0.3 mm thickness, $\sigma_\varphi$: standard deviation of porosity distribution; $\sigma_{\varphi 2}=0$; $\varphi_{eff}$: effective (average) porosity; $K_{eff}$: effective permeability; V: heterogeneity number [5]. Note: $9.87 \times 10^{-15}$ m$^2$ = 10 mD.

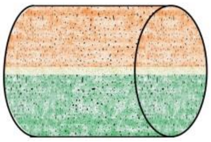

| Id | $\sigma_\varphi$ | $\varphi_2$ | $\varphi_{eff}$ | $K_{eff}$ ($10^{-15}$m$^2$) | V |
|---|---|---|---|---|---|
| G17 | .001 | .5 | .17 | 38.1 | 10 |
| G18 | .001 | .6 | .17 | 53.1 | 11 |
| G19 | .001 | .7 | .17 | 56.1 | 11 |
| G20 | .001 | .8 | .18 | 56.5 | 11 |

The B scenarios (Table 2a) represent heterogeneous core plugs without any layering, but with porosity normally distributed over the grid blocks (and therefore permeability follows a log-normal distribution [6]) throughout the whole plug. The standard deviation of the porosity distribution was varied as indicated.

The settings for the standard deviation for the C scenarios (Table 2b) are shown as multipliers for $\sigma_\varphi$. SCORES3D uses this information to adjust any porosity that would be selected by the random number generator to be outside e.g. 2$\sigma$, back to the value of 0.001, while setting all other porosity values to a flat value of $\varphi_1$ (0.17). For that reason, the C scenarios are called "speckled", because this is how these would show up in a CT image: many white spots representing impermeable spots. This is seen in the laboratory e.g. if disseminated pyrite or glauconite nodules are present.

D scenarios (Table 2c) have two layers of equal thickness into the direction of flow, the porosity of the second layer was set to $\varphi_2$. E scenarios (Table 2d) have three layers of equal thickness, with the porosity of the middle layer set to $\varphi_2$ and for the third layer set equal to $\varphi_1$. Scenarios F (Table 2e) and G (Table 2f) have a thin middle layer. Scenarios F13 through F16 and G13 through G16 have a non-permeable layer into the direction of flow.

Scenarios G170 (Table 2f), G17 to G20 (Table 2g) represent a core plug with a thin or very thin open fracture in the flow direction. Permeability in the fracture was set to 1000 times the base permeability.

The heterogeneity number V is calculated internally in SCORES3D and listed in Tables 2a-2g as well.

# 4 AutoSCORES

As discussed above, we have developed AutoSCORES to conduct automatic history matching of SCAL laboratory experiments. AutoSCORES currently allows history matching of SS (Steady-State), USS, Centrifuge and Porous Plate experiments, simultaneously or in isolation. As part of AutoSCORES, the experiments (real or synthetic) are simulated with SCORES [7,8] in one dimension (SCORES1D) to account for the interference between capillary pressure and relative permeabilities.

History matching is conducted by searching for the least square deviation between experimentally measured production data and production data generated by SCORES1D, through varying the input relative permeability and capillary pressure. The Levenberg-Marqardt (LM) method [11] is used as search algorithm, similar as used by SENDRA [12, 13] or Cydar [14].

Input relative permeabilities are defined in a 6-parameter Corey formulation (see Eqs. 2 and 3): Swc, Sor, krwor, krowc, no and nw. The relative permeabilities are then submitted as tables to SCORES1D. The saturation tables are refined near low relative permeability.

The input capillary pressure is defined through a specially constructed 11 point table. We tested first LET [15] and other formulations [16] for capillary pressure but these proved to have insufficient flexibility to deal with very sharply bending imbibition capillary pressure curves as seen in the laboratory. Within SCORES1D all saturation tables are interpolated by monotonous cubic spline functions [17].

The capillary pressure table is generated between Swc and 1-Sor, so it has two points in common with the Corey relative permeability formulation. This results in AutoSCORES searching for an optimal 6+9=15 component "state vector" [11; Chapter 15.4] delivering a match between the experimental production curves and the production curves generated by SCORES1D.

## 4.1 Brief overview of the design of AutoSCORES

The LM method can be seen as a special strategy in a Newton-Raphson (NR) process that seeks the zero value of a function [11]. NR requires the calculation of the derivative of the function. For the case at hand, the function is constructed comparing a selection of points on the production curves generated by SCORES1D, against a corresponding set of points on the experimental (or synthetic as the case may be) production curves perturbed with a certain noise level [11; Chapter 15.1]. This selection is used to construct a so-called Chi-square function. The LM method then searches for the minimum Chi-squared value while varying the state-vector. Generally, the selection of points consists of several 1000's of data points Ndata (automatically selected within AutoSCORES)..

The derivative consists of 15 partial derivatives, one for each component in the state vector. So-called 2-sided derivatives are used to increase stability of the search algorithm.

For our study we conducted history matching of a USS and a multi-speed centrifuge (numerical) experiment simultaneously, requiring a base run and 30 "derivative" runs per iteration, per experiment, so in total 62 runs per iteration. The LM method usually converged after 5 to 10 iterations.

A major advantage of this approach is that the minimum Chi-square has a known expectation value: this value is equal to Ndata [11; Chapter 5.1]. Searching for a minimum value of a function of a multicomponent state-vector can never be guaranteed to deliver the correct answer. A local minimum in the multi-dimensional space can be found instead. However, at least wrong, way too large or too small, values found after convergence can be rejected, based on the expectation value and based on the known standard deviation of the Chi-square function. AutoSCORES rejects results deviating more than 4 standard deviations, corresponding to a probability of less than 0.006% for being a correct result. After testing, the convergence tolerance for Chi-square was set to 0.001, normalised to Ndata. For a tighter tolerance setting, the distributions of the extracted Corey parameters did not change significantly from the values found with 0.001.

As an example, we present in Fig. 1 a typical matched production profile for a multispeed centrifuge run as used in our study. The data of the (numeric) experiment include the noise added. The above mentioned convergence and tolerance settings clearly prove to be effective.

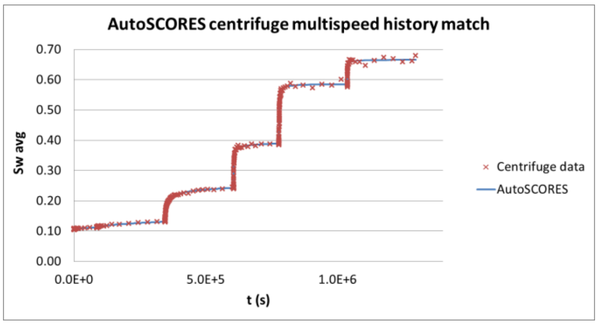

**Fig. 1.** Example of AutoSCORES matching a production profile of a multi-speed imbibition centrifuge experiment. Average water saturation is plotted as a function of time (s).

In view of the large amount of AutoSCORES runs required for this study, dedicated hardware was set-up with two DELL R-815 32-core servers, with 128 GB memory each, which allows parallel processing of all 62 runs per iteration. This brought about a significant reduction in run time. AutoSCORES was written in C++ and was run on a Windows platform that controlled the two servers for parallel processing. We found that the servers were not fully loaded during the LM iterations. This allowed us to run up to four Windows machines with AutoSCORES, in parallel, feeding the servers and we obtained thus a further reduction in turn-around time in this research project. AutoSCORES is designed to run also in sequential mode on a single Windows platform in case no massive amount of history matching is required.

# 5 Statistical Analysis

First, the performance of the tools (SCORES3D and AutoSCORES) developed in this study has been evaluated through statistical analysis. A short but excellent introduction to statistical data analysis can be found in Numerical Recipes [11].

A large number of simulations confirmed that SCORES3D produces stochastically distributed heterogeneities that we can be confident to follow a normal distribution which means that parametric statistics [18] can be used in data analysis. Subsequently, a Chi-squared (goodness of fit) test [11; Chapter 14.3] was used to test whether an observed distribution of parameters extracted by AutoSCORES, such as Corey parameters, deviated from a normal distribution having the same mean and standard deviation.

A students t-test [11; Chapter 14.2] was used to test for significant differences between the heterogeneity scenarios (Tables 2a-2g) and a corresponding isotropic homogeneous base case scenario, see the example in the Section below. An F-test was conducted [11; Chapter 14.2] to check for equal variances before the t-statistic could be calculated. The significance of the calculated statistics was evaluated against tables of significant test levels of the respective probability density distributions [19].

With the performance of SCORES3D and AutoSCORES proven statistically reliable, we proceeded to use the tools to study the impact of heterogeneity on SCAL parameters.

### 5.1 Analysing the impact of heterogeneity

Ignoring the effect of the V cut-off would allow the plug to be part of a SCAL program and its relative permeabilities and Pc to be extracted. The impact of the actual heterogeneities of a certain scenario Z therefore is best judged by comparing the relative permeabilities extracted for Z with the relative permeabilities extracted for a corresponding homogeneous base case A0_Z.

A0_Z is a SCORES3D run with V=0, and permeability and porosity set equal to the effective permeability and porosity of scenario Z[a].

As an example of how we investigated the heterogeneity cut-off values, we discuss here the B-scenarios, representing a single layer with random scatter in φ (Table 2a). Each scenario was tested against the corresponding base case scenarios labelled A0_BX. For instance, consider heterogeneity scenario B1. According to Table 2a, the average porosity and permeability of B1 are 0.17 and $9.87 \times 10^{-15}$ m$^2$ respectively. Therefore a homogeneous run labelled A0_B1 was executed with SCORES3D with all grid blocks set to a single porosity and permeability value of 0.17 and $9.87 \times 10^{-15}$ m$^2$ respectively. The results from the A0_B1 run would have been observed in the laboratory if the core plug indeed would have been perfectly homogeneous. Any differences between interpretation-by-simulation of A0_B1 and B1 therefore are directly the result of B1 being heterogeneous. In Table 3 we present results found for the Corey nw parameter for all B scenarios.

While testing AutoSCORES, a number of scenarios have been run with N different seeds for the noise added to the production data (see Section 4.1), with N set to 10, 100 and even 1000 for selected cases. However, in a laboratory environment a realistic number of SCAL samples is likely to be much lower, and a case for N=3 has been settled for in this example, i.e. small sample statistics shall be used in analysis.

First a so-called null hypothesis H0 of "no difference between the average nw found for BX and A0_BX" is formulated and tested using a t-test (Table 3). The t-test considers the difference between two averages (X1 and X2), using the standard deviations (s1 and s2) and the number N of simulations in the SCAL experiment. The calculated t-value $t_{calc}$ is then compared against the critical test value $t_{crit}$ (at a 5% or 1% test level) found from a table of the t probability density distribution [19]. If we find $t_{calc} \leq t_{crit}$ then H0 stands and we accept there is no significant difference between the two scenarios. For $t_{calc} > t_{crit}$, H0 is rejected and we can be more than 95% or 99% sure they are different.

Consider scenario B4 vs. A0_B4: the calculated t=8.07 is greater than the 5% and 1% test levels having critical $t_{95}$=2.78 and $t_{99}$=4.60, i.e. we can be more than 99% sure that B4 is different from the perfectly homogeneous A0_B4 scenario. However, the remaining B-scenarios with the test levels we have decided for (5% and 1%), are not seen as significantly different from the equivalent perfect homogeneous scenario even for a coefficient of variation V close to 1. This may look as a surprising result but is closely related to the t-probability distribution and the calculation of the t-statistic. Both are very sensitive to the number of samples N if N is small, as shown in Table 4.

In effect, with a larger number of samples, the accuracy improves with which the mean value of e.g. nw is determined. At improved accuracy, a statistical analysis will then detect reliably a smaller difference between nw of a heterogeneous plug and a homogeneous one [11; Chapter 14.2]. In the ideal case of 100 or more plugs, the t-distribution approaches the normal distribution having the minimal critical $t_{95}$=1.96 and $t_{99}$=2.58 and thus the maximum strength in testing the significance of difference between means.

From the scenarios listed in Tables 3 and 4 it is clear that an increase in the number of samples from 3 to 10 can reduce the cut-off for V to around 0.5. This means that only the three scenarios B1-B3 in Table 4 would qualify as homogeneous in SCAL measurements if 10 samples were available.

---

[a] Effective permeability of the synthetic heterogeneous sample was determined either by a separate 3-D simulation of brine injection into a fully brine saturated sample, or from the pressure drop in the simulated 3-D USS experiment at early times, given the known (inputted) end point of the oil relative permeability at initial water saturation. Both methods agreed within 0.25%.

**Table 3.** Statistical test of the difference between Corey nw's calculated from different BX scenarios vs. their corresponding base case A0_BX at N=3. When the null hypothesis is 'True' the result is said to be non-significant (non-S), when it is 'False' the result is significant (S), i.e. the 2 scenarios are different.

| Statistic → | $X_1$ | $X_2$ | $s_1$ | $s_2$ | df | $t_{calc.}$ | $H_0$ | Result | $H_0$ | Result | V |
|---|---|---|---|---|---|---|---|---|---|---|---|
| Scenario ID ↓ | | | | | | | [5%] | [5%] | [1%] | [1%] | |
| | | | | | | | | | | | |
| B1 vs A0_B1 | 4.967 | 4.945 | 0.063 | 0.056 | 4 | 0.438 | True | non-S | True | non-S | 0.021 |
| B2 vs A0_B2 | 4.933 | 4.954 | 0.062 | 0.062 | 4 | 0.410 | True | non-S | True | non-S | 0.21 |
| B3 vs A0_B3 | 4.950 | 5.017 | 0.065 | 0.094 | 4 | 1.018 | True | non-S | True | non-S | 0.44 |
| B33 vs A0_B33 | 4.872 | 5.061 | 0.098 | 0.140 | 4 | 1.917 | True | non-S | True | non-S | 0.69 |
| B34 vs A0_B34 | 4.916 | 5.126 | 0.067 | 0.172 | 4 | 1.972 | True | non-S | True | non-S | 0.99 |
| B4 vs A0_B4 | 4.945 | 5.526 | 0.066 | 0.105 | 4 | 8.07 | False | S | False | S | 1.37 |
| | | | | | | | | | | | |
| *Conditions :* | $N_1=N_2=3$ | | | $t_{95}$ = | *2.78* | | $t_{99}$ = | *4.60* | | *df=deg. of freedom* | |
| | $X_1$ : | *Avg A0_BX* | | $X_2$ : | *Avg BX* | | $s_1$ : | *Stdev A0_BX* | | $s_2$ : | *Stdev BX* |

**Table 4.** Statistical test of difference between Corey nw's calculated from different B scenarios vs. their base case A0_BX at N=10. Compare with the cut-off value of V for N=3 in Table 3 above.

| Statistic → | $X_1$ | $X_2$ | $s_1$ | $s_2$ | df | $t_{calc.}$ | $H_0$ | Result | $H_0$ | Result | V |
|---|---|---|---|---|---|---|---|---|---|---|---|
| Scenario ID ↓ | | | | | | | [5%] | [5%] | [1%] | [1%] | |
| | | | | | | | | | | | |
| B1 vs A0_B1 | 4.967 | 4.945 | 0.063 | 0.056 | 18 | 0.799 | True | non-S | True | non-S | 0.021 |
| B2 vs A0_B2 | 4.933 | 4.954 | 0.062 | 0.062 | 18 | 0.748 | True | non-S | True | non-S | 0.21 |
| B3 vs A0_B3 | 4.950 | 5.017 | 0.065 | 0.094 | 18 | 1.859 | True | non-S | True | non-S | 0.44 |
| B33 vs A0_B33 | 4.872 | 5.061 | 0.098 | 0.140 | 18 | 3.50 | False | S | False | S | 0.69 |
| B34 vs A0_B34 | 4.916 | 5.126 | 0.067 | 0.172 | 18 | 3.60 | False | S | False | S | 0.99 |
| B4 vs A0_B4 | 4.945 | 5.526 | 0.066 | 0.105 | 18 | 14.7 | False | S | False | S | 1.37 |
| | | | | | | | | | | | |
| *Conditions :* | $N_1=N_2=10$ | | | $t_{95}$ = | *2.10* | | $t_{99}$ = | *2.88* | | *df=deg. of freedom* | |
| | $X_1$ : | *Avg A0_BX* | | $X_2$ : | *Avg BX* | | $s_1$ : | *Stdev A0_BX* | | $s_2$ : | *Stdev BX* |

**Table 5.** Cut-off values for V, per scenario, established for a small number of samples (N≈3). For plugs with V below the cut-off, heterogeneities will have a non-significant impact on the relative permeabilities extracted through interpretation-by-simulation of the SCAL experiments.

| Scenario | Short description | V cut-off |
|---|---|---|
| B | stochastically distributed Gaussian porosity distribution | 0.9 |
| C | "speckled" (see Section 3) core plug | 0.2 |
| D | dual layer in flow direction | 0.15 |
| E | three layers in flow direction, equal thickness | 0.1 |
| F | three layers in flow direction, middle layer thickness ≈4 mm | 0.1 |
| G [G1-G8] | three layers, middle layer ≈2 mm | 0.8 |
| G [G9-G12] | three layers, middle layer ≈2 mm, and of significantly higher porosity | 0.1 |
| G [G13-G15] | three layers, middle layer ≈2 mm, and impermeable | 0.4 |
| open fracture | one or more open fractures in flow direction | 0 |

## 6 Results on synthetic data

A detailed analysis has been conducted on the 70+ scenarios listed in Table 2a-2g. Through interpolation and extrapolation of V versus $t_{calc}$, cut-off values were defined in a straightforward manner for scenarios B, C, D and G and listed in Table 5.

The results for scenarios E and F proved to be more difficult to interpret. We noticed e.g. that scenarios E1, E2 and E3 showed False, while E4 showed True, i.e. E4 is not significantly different from a homogeneous case with the same effective permeability and porosity, while E1-3 are different. A similar situation occurred for F1-4. This behaviour is due to the fact that with increasing $\sigma_\varphi$, the E and F scenarios in the 1-4 sequence are changing character from a clearly layered system into a more evenly stochastically distributed porosity/permeability distribution. In other words: changing from E1 to E4, the core plug looks more and more like a B3 or B4 scenario. As shown in Table 5, the B scenarios have a very high cut-off, meaning that up to V=0.9 the samples behave like homogeneous samples. In fact, it will be impossible from CT images to make a distinction between an E4 or F4 scenario and a B4 scenario. Scenarios can only be used in determining a cut-off value for V if these can be recognised in the images in the first place.

So, we interpret the results for the E and F scenarios as follows: if a layering is visible in the CT images, the cut-off is 0.1, both for E and F scenarios.

Note that E and F scenarios represent three-layered plugs of which the middle layer has a thickness of several mm. The middle layer in the G scenarios has a thickness of only 2 mm (G1-G15). Our results indicate that for G1-G8, the cut-off is 0.8. In fact, G1 to G8, with only a small porosity difference between the middle layer and layers 1 and 3, behave similar to the B scenarios. However, if the middle layer has a porosity of at least 0.04 larger than layers 1 and 3, the cut-off is 0.1 (G9-G12).

For thin layers with no porosity, as modelled by G13-15, we see a cut-off of 0.4.

If the middle layer is an open fracture (G170 and G17-G20), the cut-off is basically zero: no plug with that scenario will behave like an unfractured, homogeneous plug.

Finally, we investigated a limited number of sensitivities. We checked how the cut-off values would change for the B and G13-G15 scenarios if absolute permeability was set to 1 mD, 100 mD and 1000 mD, or if the capillary pressure was changed to a much sharply bent imbibition curve, i.e. an imbibition curve showing hardly any spontaneous water imbibition. We found no significant difference with the cut-off values seen before.

We have not tested sensitivity with respect to the chosen Corey parameters. At first glance, a change of e.g. a water Corey exponent from 5 as used in this study to 3 would bring about a higher water mobility and therefore could accelerate break-through. However, since in our scenarios, all layers have the same Corey parameters, the overall net effect is probably of second order: all layers would see similar acceleration of break-through, cancelling a net effect.

## 7 Laboratory experiments

In support of conclusions derived from synthetic data, USS laboratory experiments were conducted with gas-brine in drainage mode. Out of a set of 12 Oberkirchener (OBKN) sandstone samples, three samples were selected (G2, G3 and B2), with a porosity around 0.17 and permeability of about 10 mD. CT DICOM-images were analysed and we found that the heterogeneity numbers V for all three samples were around 0.26. Sample B2 (Fig. 2) had two stylolites filled with higher density material, but still had overall porosity, absolute permeability and V similar to G2 and G3. Samples G2 and G3 had no stylolites or other distinct features observable by the naked eye or in CT images and therefore fall into a class B scenario. Sample B2 falls into a class G13 scenario. According to the results presented in Section 6, SCAL parameters extracted by AutoSCORES should deliver similar results for these three samples, given V≈0.26.

The three samples were measured in UnSteady-State mode, at constant pressure drop as is customary for gas-brine drainage experiments [20]. Gas was equilibrated with brine at injection pressure by bubbling the gas through a PanTerra-designed humidifier mounted in-line. The humidifier consists of two cylinders, partially brine filled that are connected at the bottom. Gas is injected at the top of one cylinder and escapes at the top of the other. Residence time of the gas in the brine is in the order of 20 to 2 seconds, dependent on the flow rate. Back pressure was set fixed at 190 psi, and initial pressure drop was set to 20 psi. This value was determined using SCORES as a design tool. In design mode, one uses guestimated relative permeabilities and capillary pressure. Relative permeabilities were chosen as typical for drainage in a water-wet plug (the OBKN plugs had been soxhlet-cleaned before the experiments) and the drainage capillary pressure was chosen similar to the curve found in OBKN centrifuge drainage experiments on other OBKN plugs several years ago.

The experiments were run into a gas-brine separator that had been mounted upstream of the back-pressure regulator, so that this regulator only dealt with a gas flow. Production data were automatically recorded with a data logger connected to an electronic balance collecting the cumulative water production and to electronic gas flow sensors. Once that the gas-cut reached 99.95% (vol/vol, at standard conditions), the differential pressure was increased to 40 psi and subsequently to 100 psi, as bump floods, in order to reduce the capillary end-effects. The cumulative water production and gas flow rate of the USS experiments in conjunction with the production curve from the primary drainage centrifuge experiment mentioned before, were history matched with AutoSCORES.

The centrifuge data were brought-in to constrain the results of AutoSCORES: i.e. the Corey parameters of relative permeability, together with an assessment of the drainage capillary pressure. Using 10 to 100 different seeds for the applied noise level in AutoSCORES, statistics were obtained for all parameters to allow assessment of similarity (the H0 hypothesis as mentioned in Section 5) between the three plugs. Tables 6 and 7 summarise the results for the Corey parameters.

Note that these experiments were conducted in primary drainage, so Srg does not play a role. Rather a percolation threshold exists that we assumed fixed at 0.02. For the same reason the Corey parameter krwgr was fixed at 0.98.

Except for krgwc, plugs B2, G2 and G3 are characterised by the same Corey parameters with a confidence level of 99%, despite the presence of impermeable stylolites in plug B2. This result is obtained using small number of samples statistics (N=3) as above. Analysis shows that in order to see a possible difference at confidence levels 95% and 99%, one would need some 10 plugs or more.

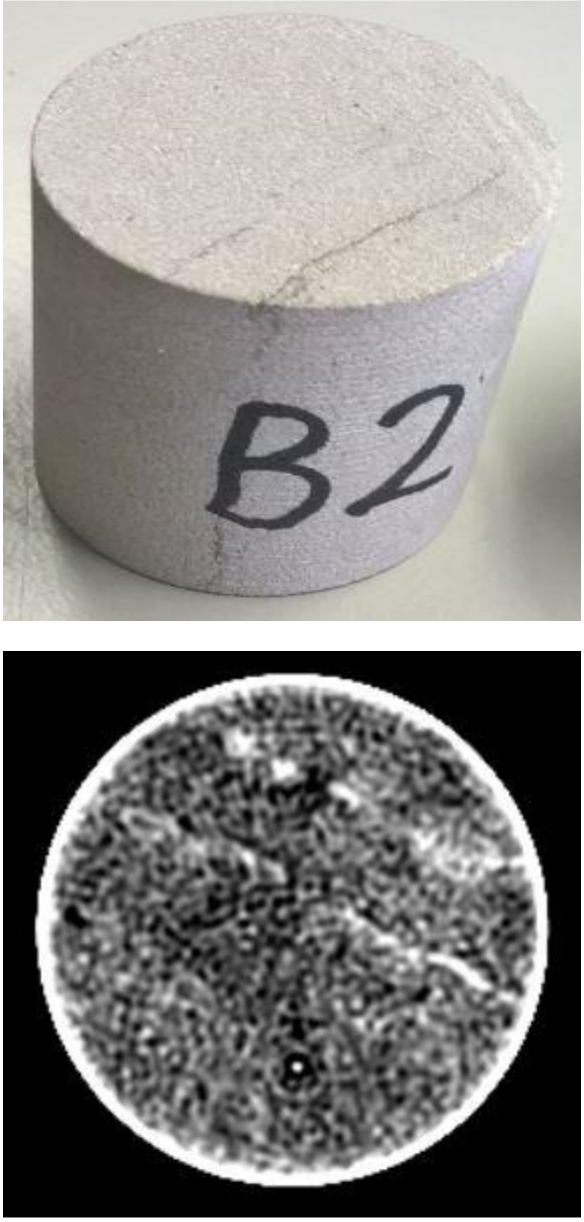

**Fig. 2.** Sample B2 with two stylolites visible, and a CT tomogram of B2. The stylolites appear as white streaks in CT, because high densities are translated into white pixels.

**Table 6.** nw, ng, krgwc, Swc results on OBKN G2 and G3, conditions similar to Table 3. σ: standard deviation.

| Statistic : → | Avg. G2 | Avg. G3 | σ(G2) | σ(G3) | df | $t_{calc.}$ | $H_0$ | Result | $H_0$ | Result |
|---|---|---|---|---|---|---|---|---|---|---|
| OBKN G2 vs G3: ↓ | | | | | | | [5%] | [5%] | [1%] | [1%] |
| | | | | | | | | | | |
| **nw** | 4.19 | 3.85 | 0.23 | 0.17 | 4 | 2.04 | True | non-S | True | non-S |
| **ng** | 2.69 | 2.95 | 0.23 | 0.15 | 4 | 1.66 | True | non-S | True | non-S |
| **krgwc** | 0.52 | 0.58 | 0.03 | 0.03 | 4 | 2.52 | True | non-S | True | non-S |
| **Swc** | 0.05 | 0.05 | 0.02 | 0.01 | 4 | 0.04 | True | non-S | True | non-S |

**Table 7.** nw, ng, krgwc, Swc results on OBKN B2 and G2, conditions similar to Table 3. σ: standard deviation.

| Statistic : → | Avg. B2 | Avg. G2 | σ(B2) | σ(G2) | df | $t_{calc.}$ | $H_0$ | Result | $H_0$ | Result |
|---|---|---|---|---|---|---|---|---|---|---|
| OBKN B2 vs G2: ↓ | | | | | | | [5%] | [5%] | [1%] | [1%] |
| | | | | | | | | | | |
| **nw** | 4.26 | 4.19 | 0.30 | 0.23 | 4 | 0.32 | True | non-S | True | non-S |
| **ng** | 2.44 | 2.69 | 0.18 | 0.23 | 4 | 1.41 | True | non-S | True | non-S |
| **krgwc** | 0.36 | 0.52 | 0.03 | 0.03 | 4 | 6.34 | False | S | False | S |
| **Swc** | 0.06 | 0.05 | 0.03 | 0.02 | 4 | 0.65 | True | non-S | True | non-S |

Krgwc is shown to be significantly different between B2 and the two other plugs. This parameter is derived mainly from the production data at the end of the experiment, i.e. from the last bump flood. The experiment on the G2 and G3 plugs were terminated earlier than on the B2 plug where we had additional focus on late time behaviour. This may well have caused salt precipitation in plug B2 to be more significant than in the G2 and G3 experiments. B2 showed a reduction in absolute permeability after the experiment of about 25% while G2 and G3 showed a reduction of only 5%. Note that the reduction in permeability is similar to the reduction observed for krgwc. We do not know when the reduction in permeability of B2 occurred, but if it indeed would have been during the later phase of the experiment, later time data would have been affected most. As a result, krgwc would then be strongly affected: AutoSCORES was not set to use the absolute permeability as an adjustable parameter, so a reduction in the lab of the absolute permeability translates into a correspondingly lower value for krgwc. If one would be allowed to correct for this effect, an adjusted value for krgwc of B2 would bring the H0 at the 5% level to True, i.e. no significant difference in krgwc can be observed anymore between B2 and the two other samples.

Finally, it is of interest to note that the analytical JBN calculation on B2, G2 and G3 showed $ng \approx 2$ , $nw \approx 3$ and $Swc \approx 0.2$. Moreover, Dean-Stark extraction on the plugs after the experiments showed average final water saturations in the order of 0.2. This demonstrates how end-effects, even at high differential pressure in a gas-brine drainage experiment may still dominate the results and that history matching the production data makes a real difference in interpreted results.

# 8 Conclusions

A cut-off value for the heterogeneity value V of a core sample represents the value beyond which flow parameters measured in SCAL experiments will be significantly affected by heterogeneity. When that happens, the plug needs to be discarded because no reliable SCAL data can be measured on that core plug. Using such data would compromise simulations on the field scale with possibly serious effects on development plans.

In summary we have:

- Cut-off values for the heterogeneity number V have been defined now for many scenarios as these come about in laboratory practice.
- The cut-off value for V is strongly dependent on the heterogeneity scenario seen in CT images of plug.
- Layering in a plug strongly reduces the cut-off value for V.
- The recommended work flow is to conduct RCA and CT-scanning and establish the heterogeneity number V for all candidate plugs. Based on the observed heterogeneity scenario, the cut-offs presented in Table 5 can then be used to select the plugs that have V below the cut-off value.
- Cut-off values for V are dependent on the number of plugs available for a study. This is caused by the fact that if 10 or more plugs per flow unit are used, the critical test value for the evaluation of the student-t analysis changes substantially from the value used if only 3 samples are available.
- The first laboratory experiments to test the results derived for the synthetic plugs were promising.

A core plug with visible stylolites showed flow parameters similar to an unperturbed plug, as predicted by our heterogeneity analysis.

- AutoSCORES allows for history matching multiple experiments simultaneously. All SCAL laboratory experiments can be addressed.

The CT-scans of the OBKN material were made available courtesy of Prof. Pacelli Zitha, TUDelft, and conducted expertly by Mrs. Ellen Meijvogel-de Koning.

We acknowledge the accurate work by Xiangmin Zhang, PanTerra Geoconsultants, who conducted the UnSteady-State experiments.

## References

1. E.F. Johnson, D.P. Bossler, V.O. Naumann, “Calculation of relative permeability from displacement experiments,” AIME **216,** 370–372 (1959)
2. G. Hassler, E. Brunner, “Measurement of capillary pressures in small core samples”, Trans. AIME **160**, 114-123 (1945)
3. A. Sylte, T. Manseth, J. Mykkeltveit, J.E. Nordtvedt, “Relative permeability and capillary pressure: effects of rock heterogeneity”, SCA-9808 (1998)
4. A. Zweers, W. Scherpenisse, K. Wit, J. Maas, “Relative permeability measurements on heterogeneous samples. A pragmatic approach”, SCA-9909 (1999)
5. D. Fenwick, N. Doerler, R. Lenormand, "The effect of heterogeneity on unsteady-state displacements", SCA2000-30 (2000)
6. J.G. Maas, A. Hebing, “Quantitative X-ray CT for SCAL plug homogeneity assessment”, SCA 2013-004 (2013)
7. J.G. Maas, B. Flemisch, A. Hebing, “Open source simulator DuMux available for SCAL data interpretation”, SCA 2011-08 (2011)
8. R. Lenormand, K. Lorentzen, J. G. Maas and D. Ruth, “Comparison of four numerical simulators for SCAL experiments”, SCA 2016-06 (2016)
9. J. Reed, J.G. Maas, “Review of the intercept method for relative permeability correction using a variety of case study data”, SCA 2018-030 (2018)
10. R. Gupta, D. Maloney, ”Intercept Method – A novel technique to correct steady-state relative permeability data for capillary end-effect”, SPE Reservoir Evaluation & Engineering, SPE 171797, doi:10.2118/171797-MS (2014)
11. W.H. Preuss, B.P. Flannery, S.A. Teukolsky, W.T. Vetterling, *Numerical Recipes in C++, The Art of Scientific Computing*, 2nd Edition, Cambridge University Press, Cambridge (2002). See also http://www. numerical.recipes
12. E. Ebeltoft, A. Sylte. E.B. Petersen Jr., “Simultaneous determination of relative permeability and capillary pressure from several types of experiments”, SCA2004-17 (2004)
13. A.T. Watson, P.C. Richmond, P.D. Kerig, T.M. Tao, "A regression-based method for estimating relative permeabilities from displacement experiments", SPE Reservoir Engineering, Aug. 1988, p 953 (1998)
14. CYDAR user manual, see http://www.cydarex.fr
15. F. Lomeland, E. Ebeltoft, “A new versatile capillary pressure correlation”, SCA2008-08
16. D. Loeve, F. Wilschut, R.H. Hanea, J.G. Maas, P.M.E. van Hoof, P.J. van den Hoek, S.G. Douma, J.F.M. Van Doren, “Simultaneous determination of relative permeability and capillary pressure curves by assisted history matching several SCAL experiments”, SCA2011-35 (2011)
17. F.N. Fritsch, R.E. Carlson, "Monotone piecewise cubic interpolation", SIAM J. Numer. Anal. **17(2)**, 238-246 (1980)
18. R.A. Fisher, *Statistical Methods for Research Workers,* Edinburgh, Oliver & Boyd (1962)
19. R.A. Fisher, F. Yates, *Statistical tables for biological, agricultural and medical research*, London, Oliver & Boyd (1963)
20. Potter, G. and G. Lyle, “Measuring unsteady-state gas displacing liquid relative permeability of high permeability samples”, SCA 9419 (1994)

# Digital core repository coupled with machine learning as a tool to classify and assess petrophysical rock properties

*Vanessa* Hébert[1*], *Thierry* Porcher[1], *Valentin* Planes[1], *Marie* Léger[1], *Anna* Alperovich[2], *Bastian* Goldluecke[2], *Olivier* Rodriguez[1] and *Souhail* Youssef[3]

[1]Voxaya, Cap Oméga, rond-point Benjamin Franklin, CS 39521, 34960 Montpellier, France

[2]University of Konstanz, Universitätsstraße 10, 78464 Konstanz, Germany

[3]IFP Energies Nouvelles, 1-4 Avenue du Bois Préau, 92852 Rueil-Malmaison, France

**Abstract.** To make efficient use of image-based rock physics workflow, it is necessary to optimize different criteria, among which: quantity, representativeness, size and resolution. Advances in artificial intelligence give insights of databases potential. Deep learning methods not only enable to classify rock images, but could also help to estimate their petrophysical properties. In this study we prepare a set of thousands high-resolution 3D images captured in a set of four reservoir rock samples as a base for learning and training. The Voxilon software computes numerical petrophysical analysis. We identify different descriptors directly from 3D images used as inputs. We use convolutional neural network modelling with supervised training using TensorFlow framework. Using approximately fifteen thousand 2D images to drive the classification network, the test on thousand unseen images shows any error of rock type misclassification. The porosity trend provides good fit between digital benchmark datasets and machine learning tests. In a few minutes, database screening classifies carbonates and sandstones images and associates the porosity values and distribution. This work aims at conveying the potential of deep learning method in reservoir characterization to petroleum research, to illustrate how a smart image-based rock physics database at industrial scale can swiftly give access to rock properties.

## Introduction

Digital rock analysis recently becomes an important part of the laboratory services in oil and gas industry. Numerical properties accelerate and improve the understanding of the reservoir behavior.

Computed tomography scans from rocks associated with Digital Rock Physics (DRP) analysis receives considerable and extended use in the oil and gas laboratory services. Computed micro-tomography (MCT) scans of rocks record multiple structural information such as the texture and the rock fabric. A 3D image of a rock sample gives access to the actual representation of the mineral phase and the pore space. Rock images with voxel size down to the micrometer resolution allow to extract the topology of the pore space. Once segmented in two (usually pore and solid) or more phases of interest, the MCT images can be used to simulate porous media physical properties such as fluids transport, electrical and geo-mechanical properties as well as processes like enhanced oil recovery simulation [1, 2]. Ongoing improvements in MCT systems and image analysis software quickly provide increasing amounts of data. Properties computed from rock images accelerate and improve the understanding of the reservoir behavior.

In DRP analysis, key elements are the voxel size and the representative elementary volume (REV) determined during the acquisition phase. A too low image resolution can restrict the pore space reconstruction, causing bad pore space topology determination and rock properties estimation as demonstrated in [3]. Al-Raoush [4] and Papadopoulos reveals that the minimal REV for particle size distribution and coordination number is larger than the minimal REV for porosity. This technical restriction results in a permanent search of increasing resolution and volume size of the acquired images. At the same time the constant progress of acquisition technique leads to more and more image acquisition generating dozen terabytes of data needing to be processed afterward. As a consequence, standard image processing techniques become more and more limited and need to be automated to work with an efficient workflow.

Recent advances in high performance computing and machine learning (ML) will probably lead to new and more efficient computations. At the present time, research carried out on deep learning produces various frameworks easily accessible that particularly democratize its uses. Deep neural network provides excellent results for X-ray computed tomography (Wang [5], Würfl *et al.* [6]). Convolution neural network (CNN) is an important deep learning architecture. It can extract the image features automatically and has high classification accuracy. CNNs have achieved a wide range of applications such as plant classification, face recognition, handwritten Chinese character recognition and so on Mikia *et al.* [7] and Lopes *et al.* [8].

---

[*] Corresponding author: vanessa.hebert@voxaya.com

Naranjo Leon *et al.* [9] provided a permeability-porosity relationship for each rock type, allowing to complement the reservoir characterization in the un-cored wells. Chen *et al.* [10] demonstrated the capability of machine learning in rock facies classification from wireline log scalar attributes improving by feature augmentation. Compared to conventional image segmentation methods, machine-learning segmentation could come closer to the ground truth for determining the porosity from noisy MCT images (Berg *et al.* [11]). Karimpouli [12] and Tahmasebi revealed that a CNN algorithm improves the accuracy of a segmentation comparing with a multiphase thresholding segmentation. Their network also produced valid results for unseen images with a categorical accuracy of about 96%. Araya-Polo *et al.* [13] used a deep learning architecture to instantaneously predict permeability of clastic rocks from high resolution Scanning Electron Microscopy images. Sudakov *et al.* [14] validated a 3D CNN method for predicting permeability of digital Berea sandstone volume subsets.

In this study we pursue tests on the CNN potential for DRP predictions. We provide some proofs of concept and discuss how they could be designed to be integrated in a more global usual analysis workflow. The typical size of a MCT image, a few dozen gigabytes, is huge in comparison to hardware capacity (some gigabytes for GPU) and time consuming. That is why the CNN is relevant to emphasize relevant features with a reasonable time and standard computing resources.

The goal of this study is thus to explore and evaluate the contribution of machine learning as a tool to evaluate geological and petrophysical properties directly from grayscale MCT scan images. The purpose is to deploy an automated workflow directly after the reconstruction of 3D rock images.

The paper is organized as follow: we first introduce the basics of CNN algorithms and the selected image database used for this study. Second, we present the classification of reservoir sedimentary rock types from grayscale MCT images using an adapted version of the Inception-V3 network, named RockClass model. Then an optimized regression-CNN network, named RegPhi model, is used to estimate the total porosity from MCT scan images without segmentation. The porosity is evaluated thanks to an AutoEncoder model realizing an automated segmentation from the grayscale images and associating the total porosity. Finally, the results are discussed.

## Workflow description

### Machine learning concepts

Convolutional neural networks (CNNs) are a powerful tool widely used in various computer vision problems, like image classification [15], object detection [16], segmentation [17] and image enhancement. As convolutional networks assume that pixels that are close to one another are semantically related, they seem a good candidate to extract physical properties from MCT images.

During the last decade, many network architectures (types of layers, size of layers, interconnexion of layers) have been experimented. In this paper, we use 3 types of networks.

The first one is a customization of the Inception-V3 network as presented in [18] developed by Google to solve the ImageNet Large Scale Visual Recognition Challenge [19]. This network has been trained on a very large dataset (1.2 million 2D 299 x 299 images) and is able to classify 1,000 kinds of images. The output of the network is a vector of probabilities for the image to belong to a specific class.

Then we use a network proposed by Sudakov *et al.* [14] to estimate the porosity from a MCT image. This network has fewer layers than Inception-V3 but is able to accept 3D 100 x 100 x 100 voxel images. Instead of providing a classification, this network is trained to fit a function (porosity in our case). The output of the network is a scalar.

Finally, an AutoEncoder (or encoder-decoder) network is used to produce a pixel-wise output. The key idea is to extract a relatively small set of features (bottleneck) from the input image data and then decode those features into the desired output.

Although this kind of CNNs is able to model complicated phenomena due to a large number of parameters, it is still hard to predict the behavior of neural network on “unfamiliar” test examples. There are various techniques to overcome this difficulty: for instance, semi-supervised learning where a mathematical model is incorporated into CNN architecture or loss function as demonstrated in [20 – 22].

### Dataset

The petroleum reservoir rocks are widely composed of two main lithological classes, sandstones and carbonates [23]. The original database is made of a series of reservoir analogue samples including 2 carbonates from Estaillades [24, 25] and Savonnieres [26-28] formations, and 2 sandstones from Fontainebleau [29, 25] and Berea [30-33] formations. For each sample, the rock type and the rock formation are notified in the generated database which will provide the predicted class of rock type.

See below Table 1 for a description and illustrations of the image collection.

The core plugs are imaged in 3D with a voxel size of 3 to 4 µm. Having the same voxel size ensures a consistent learning of the patterns. This voxel size proposed by most of micro-CT scanners is commonly used for imaging rock porous media. 3-µm voxel size enables the internal fine structures to be imaged accurately, though this is the limit between macropore and micropore for the Estaillades sample. Although it remains a challenge to accurately predict porosity from subresolved imaged porous media, we choose to disregard the porosity resolution influence (Saxena *et al.* [34]). We use only 2-phase segmentation which totally ignores the subresolved porosity. The 2-phase segmentation handed by an expert user reflects the most common arbitrary segmentation and its known sensibility.

Sub-resolution porosity involves low contrast and blurred limits between the different phases, which can partly cause a dispersion of the results. These segmented images are taken as references for the training network predicting the porosity. The goal is to try to predict an estimation based on particular subjective expert appreciation, which may differ from the ground truth porosity. For monomineral sample, it is possible to take into account grey levels reported to microporosity thanks to a mean grey segmentation method [25].

**Table 1**: List of the selected rock images, a collection based on sandstones and carbonates, associated to the CT image information and to the lab and computed basic measurements.

| **Rock type & formation** | **Lab measurements** | **Cross-section of the CT image, CT image information and Property estimations** | |
|---|---|---|---|
| Carbonate<br>Estaillades | Porosity: 25%<br>Permeability: 273 mD | 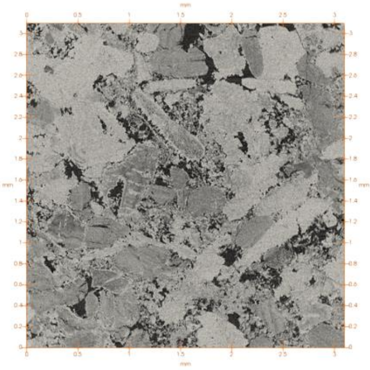 | Voxel size: 3.1 µm<br>Image size: 1000 x 1000 x 1000 voxels<br>Porosity: 15%<br>Permeability: 475 mD |
| Carbonate<br>Savonnieres | Porosity: 22%<br>Permeability: 115 mD |  | Voxel size: 3.8 µm<br>Image size: 1000 x 1000 x 1000 voxels<br>Porosity: 22%<br>Permeability: 50 mD |
| Sandstone<br>Berea | Porosity: 20%<br>Permeability: 500 mD<br>[35] | 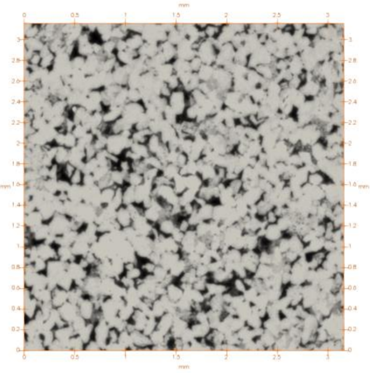 | Voxel size: 3.2 µm<br>Image size: 1000 x 1000 x 1000 voxels<br>Porosity: 21%<br>Permeability: 620 mD |

| | | | |
|---|---|---|---|
| Sandstone<br>Fontainebleau | Porosity: 12%<br>Permeability: 320 mD | 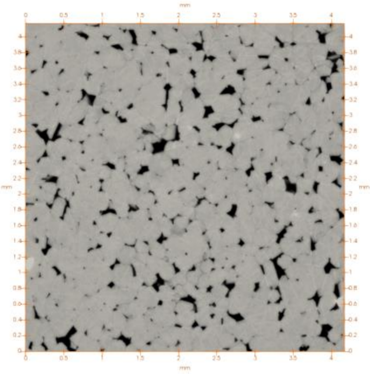 | Voxel size: 3.2 µm<br>Image size: 1000 x 1000 x 1000 voxels<br>Porosity: 12%<br>Permeability: 380 mD |

Voxaya's software Voxilon [36] is used to extract a dataset of 18 images of size up to 1000 x 1000 x 1000 voxels from those 4 digital plugs. An expert user generates the 3D binary segmented images by selecting the threshold values. The total porosity and absolute permeability are computed from each segmented image. From these large blocks, small 100 x 100 x 100 voxels non-overlapping images are extracted using Python scripting tools [36], leading to a database with more than 36,000 images (18,000 CT and 18,000 segmented). For each segmented image, related pore volume fraction, related permeability and tortuosity are computed, the last two properties not being presented in this paper. For each study, part of the database is used for training and some data is always kept aside for evaluation (training assessment) and testing (model assessment).

## Rock classification

Convolution neural network (CNN) can automatically extract image features and presents high classify accuracy.

The goal is to prove that the rock types and formations classification can be realized using existing technologies for image classification.

### Network architecture

Here we choose to use the pre-trained Inception version 3 (Inception-V3) model specialized in 2D image classification by feature extraction, provided by the TensorFlow framework. This network is quite optimized and contains 48 layers (see Figure 1 below). A specialized algorithm for training is designed to overcome the limitations of usual algorithms.

### Transfer Learning Concept

All the power of the inception approach lives in the Transfer Learning concept. The inception network model is a complex network, so training the model directly from the beginning would cost at least a few days. However, using the method of Transfer Learning, the parameters of the first layers are kept unchanged and only the last layer from the network is adapted to the use case and trained. The last layer is a softmax classifier, a mathematical function which outputs a probability distribution [37]. The porosity for a patch 100 x 100 x 100 is individually estimated. To evaluate the porosity for the whole rock sample one could compute porosity for every patch and average the result. It is replaced by a layer with as many neurons as there are classes to choose from. The network has to be retrained to update the weights of this layer using a back propagation algorithm and the cross entropy loss function. In our case, we use 4 classes: Berea, Fontainebleau, Estaillades and Savonnieres.

### Training

As input data, we use 4,000 grayscale 2D slices (1,000 per class) resized to be compatible with the network (initially 1000 x 1000 resized to 299 x 299) and rescaled between 0 and 1.0. Training duration is about 6 minutes on a 32 cores Intel Xeon(R) CPU E5-2667 v3 @ 3.20GHz system.

### Results

For testing, 1,200 slices (300 slices per class) from images were analyzed and the computation took 64 seconds. Eventually the data for testing reveals a final accuracy of 100% for the selected rock typing classification. Recognition between the 2 lithological rock types (sandstone and carbonate) is 100% and recognition of the 4 rock formations is also 100%.

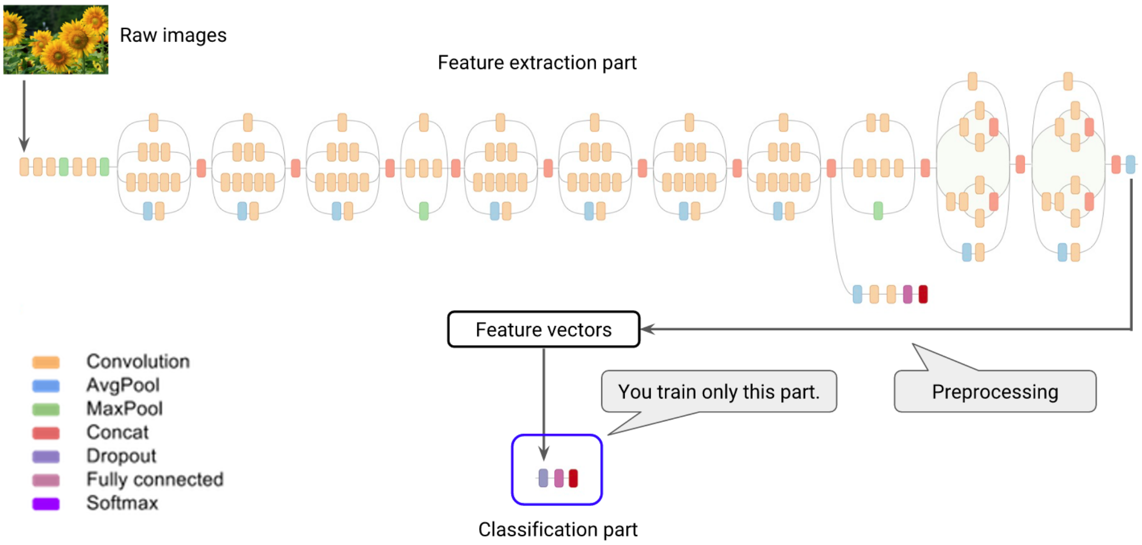

**Figure 1**: Inception V3 architecture (source: Google codelabs).

# Porosity estimation

## Porosity from CT scan without segmentation

In this paper we try to predict porosity from grayscale 3D images. Araya *et al.* [13] already used grayscale SEM image as input for DL-based permeability predictions avoiding the segmentation, the highest sensitive step linked to the resolution, and speeding-up processing workflows.

Following that work, we focus on the Berea sandstone sample for training and prediction imaged in 3D. For the network architecture we take inspiration from Sudakov *et al.* [14]. Using this network, the authors try to predict permeability by Linear Regression and CNN from segmented images. Our model RegPhi is implemented using the Keras framework [38] and is described in Table 2.

### *Training*

In our study we use non-overlapping sub-blocks (100 x 100 x 100 voxels) from 2 Bera CT images. We have 8,000 of these sub-blocks, 3,500 being used for training while keeping 600 blocks for validation.

**Table 2**: The RegPhi Network Architecture.

| Layer type | Parameters |
|---|---|
| 3D Convolution | [ filters=32, kernel_size=(5, 5, 5), strides=(2,2,2), padding='valid', activation='relu') ] |
| 3D Convolution | [ filters=32, kernel_size=(5, 5, 5), strides=(2,2,2), padding='valid', activation='relu') ] |
| 3D Max Pooling | [ pool_size=(2, 2, 2) ] |
| 3D Convolution | [ filters=32, kernel_size=(3, 3, 3), padding='valid', activation='relu' ] |
| 3D Convolution | [ filters=32, kernel_size=(3, 3, 3), padding='valid', activation='relu' ] |
| 3D Max Pooling | [ filters=32, kernel_size=(3, 3, 3), padding='valid', activation='relu' ] |
| Dense | [ units=128, activation='relu' ] |
| Dense | [ units=64, activation='relu' ] |
| Flatten | |
| Dense | [ units=1 ] |

### *Results*

Figure 2 shows the distribution of the relative error on porosity prediction compared to the reference.

$$Error = 100 * | \varphi_{RegPhi} - \varphi_{Reference} | / \varphi_{Reference}$$

These predictions are realized on a set of 1,000 sub-blocks of 100 x 100 x 100 voxels from grayscale Berea sandstone images without any segmentation or improvement process. We use a REV-independent approach in order to provide prediction on large amount of images. Here we can see encouraging results about the porosity prediction, the median of the series is under 15% despite a mean relative error of 18% (see Figure 3).

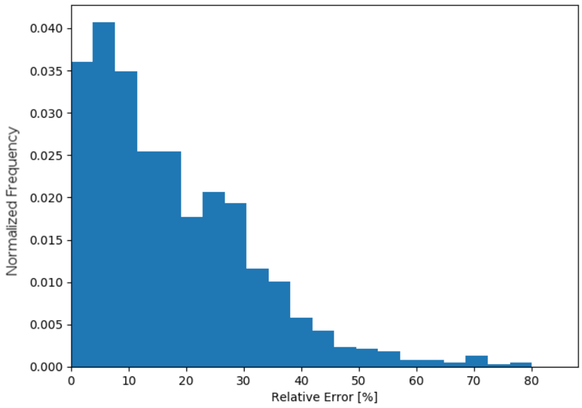

**Figure 2**: Distribution of absolute error for porosity prediction in percentage from the same Berea sandstone image.

---

[*] Corresponding author: vanessa.hebert@voxaya.com

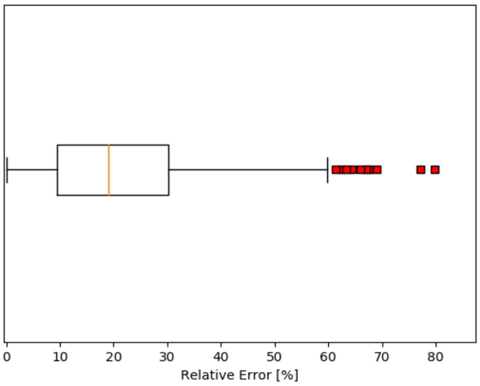

**Figure 3:** Corresponding box plot of absolute error for porosity prediction in percentage from the same Berea sandstone image.

## Porosity from automated segmentation

### Network architecture

In this work, we propose an AutoEncoder network that segments pores in 3D rock images (see Figure 4 for a detailed description of the network architecture).

The idea is to compute the high-level features from the input 3D volume that already contain information about porosity in the training example and then decode those features into the segmentation mask, where every value corresponds to the probability of the voxel being a pore. To make sure that the bottleneck layer captures information about porosity, we predict it as an additional pathway in the decoder. We believe that this type of guidance helps the network to cope well with the segmentation task since it already takes the porosity into account while decoding.

Theoretically speaking, we should have trained network with the loss function for porosity and without. Nevertheless we could in general argue that some guidance for the bottleneck is shown to be a promising technique in deep learning. For instance, variational autoencoders are good example how this type of guidance improves the robustness of classification problem (Pu *et al.* [39]).

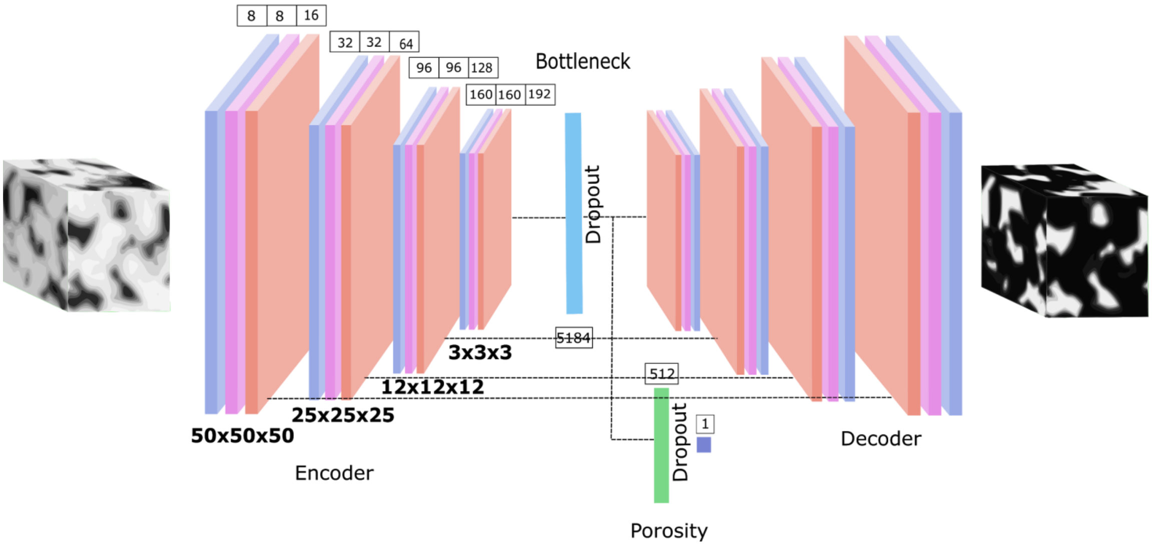

**Figure 4**: Network architecture with 12 convolutional layers, bottleneck, and 12 corresponding upsampling layers. The layers are organized in 4 blocks with 3 layers each. On top of the encoder part, we show the number of features after each layer. On the bottom of the encoder, we show the tensor size. With dashed lines, we illustrate skip connections [40], where encoder features are copied to the corresponding decoder layers. This helps to bring small details that were lost after downscaling. The decoder part has two pathways, the first one recovers the segmentation mask and the second one computes the porosity.

### Computational framework

The input data of the network is a set of grayscale CT image volumes of dimension 100 x 100 x 100 voxels. Larger images are segmented into these patches, so that our network can deal with input data of any shape.

The basic ingredients for the encoders and decoders are residual blocks. To decrease resolution, we employ strided convolutions with stride 2, so that our network is fully convolutional. The choice of this architecture is well supported in the literature [41, 42] as it allows to speed up the training process and deals with "vanishing gradients", which is a common problem in deep learning. The residual blocks have a very simple structure and allow direct pass-through of the batch normalized input, see Figure 4.

In the encoder pathway, four groups of three residual blocks are chained together, 12 blocks in total. In the first three groups, every third block reduces the patch resolution via strided convolution while increasing feature depth, with the overall goal of gradually reducing dimensionality. Others keep spatial resolution the same while increasing the number of features. In the last group, both blocks decrease spatial resolution such that the output shape is 3 x 3 x 3 x 192, see Figure 4. The feature output at the representation level is concatenated. This is the final output of the encoder, and the bottleneck of the network.

After passing the bottleneck, the low-dimensional representation is decoded again by a chain of residual layers. The latent variables enter two decoder pathways. One is the path that predicts the porosity and another one outputs the segmentation mask. Decoder pathways that lead to the segmented 3D volume use transposed convolutions to exactly revert the encoder on the corresponding level. However, the only link between them is through the latent representation and skip connections, see Figure 5. To prevent overfitting, we apply dropout layers on the bottleneck with 0.2 probability of each node to be discarded.

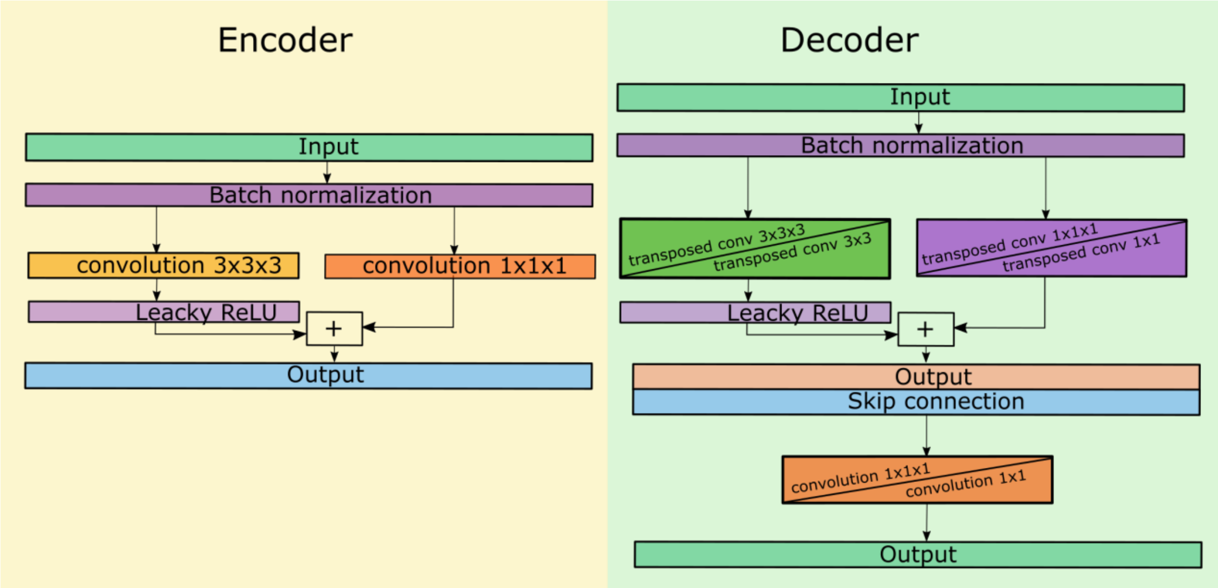

**Figure 5**: Single residual block of the encoder and decoder networks. After batch normalization, a first path leads through a (possibly strided) convolution or up-sampling layer and a leaky ReLU. A second path either keeps the input or passes it through a strided (transposed) convolution in case it needs to be resampled. Both paths are added together to produce the final output. In the decoder block we skip connect the corresponding encoder features to the output of the decoder. The idea is that it is much easier for such blocks to learn the identity transformation, or perform only small modifications to the input [42], which helps the encoder-decoder paths to gradually add details.

### *Loss function*

In the classical supervised machine learning used to train the model, we need training data together with a label or target. By observing the random variable $X$ and its label $Y$ in the training set, the supervised learning tries to fit the model $f$ to the training samples $(x_0, y_0), \ldots, (x_n, y_n)$.

Test data has similar structure as training data, but the network never sees it.

The training process can be considered as learning the mapping $f$ to predict label $y^*$ from the new instance $(x^*, y^*)$ of the test data via $f(x^*) = y^*$.

A typical cost function for image classification and segmentation tasks is cross-entropy with logits.

Let $p(x_i) = f(x_i)$ be the probability that point $x_i$ is a pore. Thus $p(x_i) \in [0,1]$ with $p(x_i)$ close to 0 if the probability is low. The cross-entropy between $p(x)$ and $y$ is given by:

$$E_{cross-entropy}(y, p) = -\sum_{i\in\Omega} y_i \log(p(x_i)) \quad (1)$$

with $\Omega$ being a set of all points in the training example.

In order to predict the porosity from the bottleneck, we use the standard mean squared error (MSE):

$$E_{MSE} = ||\phi_y - \phi_e||^2 \quad (2)$$

where $\phi_y$ denotes the target porosity and $\phi_e$ is the predicted porosity computed at the bottleneck level.

Finally, to link the predicted porosity $\phi_e$ and final output we compute $\phi_{out} = \sum_{i\in\Omega} p(x_i)/|\Omega|$ and introduce another loss function:

$$E_{model} = ||\phi_{out} - \phi_e||^2 \quad (3)$$

that ensures that the porosity computed from the segmentation mask equals the predicted porosity obtained from the bottleneck features.

Final loss function is the sum of the previously defined loss functions (1), (2) and (3):

$$E = E_{cross-entropy} + E_{MSE} + E_{model} \quad (4)$$

### *Training the CNN model*

From the training data, we leave aside 10% for a validation set whereas the rest is used for training. Several images are also completely held back and used only for testing. We implement the network using TensorFlow in Python3, and train it on an Intel Xeon(R) CPU E5-2667 v3 @ 3.20GHz system with one Nvidia Quadro M6000. Weights are initialized using the same strategy as for residual networks [40]. Stochastic optimization using the Adam optimizer [43] took roughly two days, after which loss remained stable. We train with batch size 10 and learning rate 1-e4. Reconstruction of a single pathway during evaluation requires about 0.5 - 1.5 seconds for the 3D volume of size 100 x 100 x 100. The complete segmentation of a 1000 x 1000 x 1000 voxels image takes about 15 - 20 minutes.

### *Results*

Figures 6 and 7 show the source CT image and resulting segmentations using Hysteresis segmentation and the AutoEncoder network. Globally, AutoEncoder segmentations tend to be sharper than the binary thresholding but also thinner (one voxel difference on the boundaries). Thus, porosity computed on the AutoEncoder images will always be smaller than the reference obtained by Hysteresis segmentation.

| **CT image** | **Reference** | **AutoEncoder segmentation** |
|---|---|---|
| <br>Cross-section | <br>Cross-section segmented image | <br>Cross-section segmented image |
| 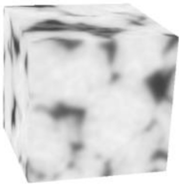<br>3D volume | 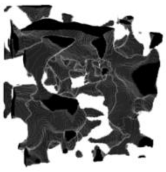<br>3D volume of pore space | 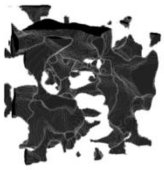<br>3D volume of pore space |
|  | Computed porosity volume: 20% | Computed porosity volume: 15% |

**Figure 6**: Comparison between Hysteresis segmentation (Reference) and AutoEncoder model methods: original CT image in grayscale, segmented image with black pixels for pore and greyish for solid.

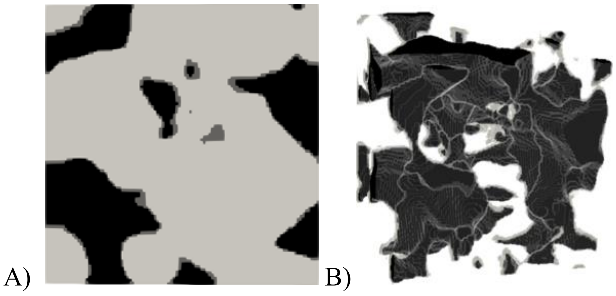

**Figure 7**: Cross-section (A) and 3D volume (B) images resulted from the comparison of segmentation methods: Hysteresis segmentation and AutoEncoder model. The black voxels are joint porosity of both segmentations and dark grey voxels are supplementary pore voxels in the Hysteresis segmentation.

# Discussion and perspectives

## Computing resources

The most time-consuming task is the training part of the networks. GPU runs (using one Nvidia Quadro M6000 graphics card) are 15 faster than CPU runs (on a 32 cores Intel Xeon workstation).

## Rock classification

In this study, 4 classes of lithological rock formations are distinguished with a highly successful recognition rate.

This work will be extended to numerous classes of reservoir rock facies. All authors [4, 10, 12, 14] referring to machine learning mentioned the importance of the quality of the dataset and required a massive amount of data. This database generation with various available reservoir rock formations imaged at several voxel sizes will be a crucial step.

Rock classification using Inception-V3 (RockClass) proves to be a very promising tool. It can be used for pre-calibrating geological-oriented workflow in digital rock analysis proposing a suitable image processing and analysis workflow. The classification rate could be used as a quality control indicator for validating the image quality before any numerical computations. Then a rock class recognition is interesting to offer a fast estimation of the numerical properties already processed from similar rock class.

To further improve digital rock classification, additional physical attributes as mineralogy and pore fabric could probably enhance RockClass capability in detailing geological rock types. For example, pore fabric is directly related to the hydraulic radius size distribution, which is the key parameter for the permeability computation.

## Porosity estimation

The porosity is computed on 1,000 sub-blocks of 100 x 100 x 100 voxels by 3 porosity modules: Hysteresis segmentation, RegPhi an AutoEncoder networks.

The porosities estimated from Hysteresis segmentation are used as reference values. They are computed from segmented images obtained by binary thresholding. Porosity estimation obtained by Hysteresis segmentation is benchmarked and validated in several studies with diverse partners (IFPEN, Geosciences Montpellier, [2]).

Figure 8 illustrates the porosity distribution obtained by these 3 methods on 1,000 juxtaposed blocks of size 100 x 100 x 100 voxels belonging to the same 1000 x 1000 x 1000 voxels image.

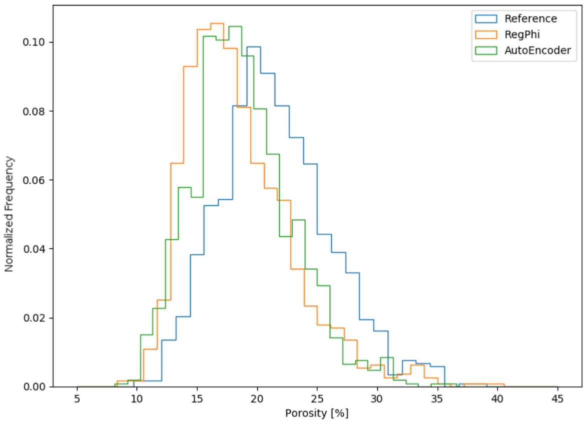

**Figure 8**: Porosity distribution computed by image analysis (reference), RegPhi and AutoEncoder models for Berea Sandstone sub-blocks.

The reference porosity values indicate that the porosity ranges from 9 to 36% with a mean value of 21.5%. This large distribution is mostly due to variation of the pore-solid ratio along the series of small REV of 100 x 100 x 100 voxels with a high voxel size. The RegPhi and AutoEncoder results present a wider porosity distribution, respectively, from 8 to 41% with a mean value of 18.6% and from 8 to 37% with a mean value of 18.8%. The AutoEncoder model is considered being a more reliable network for predicting porosity values close to the values obtained by conventional image analysis.

RegPhi model allows to estimate the porosity without segmentation whereas AutoEncoder generates a segmented image to assess the porosity. Both networks seem to predict similar porosity distributions and from 2.7% (AutoEncoder) to 2.9% (RegPhi) under evaluate the porosity compared to the reference one. This promising result validates improbable capabilities of both models to evaluate porosity directly from grayscale images. An intensified training is required to enhance their performance.

RegPhi and AutoEncoder networks are both trained on these similar subs-volumes of Berea grayscale image. This similarity of results demonstrates how efficient and accurate segmented images are generated by the AutoEncoder model in this study. From these automated segmented images, series of numerical petrophysical properties could be swiftly computed. A complete digital petrophysical workflow can thus be proposed, here for Berea sandstone.

## Conclusion

In this study we aim at demonstrating the potential of neural network algorithms to make digital rock analysis simple. We work on implementing an automated workflow from MCT images to digital petrophysical measurements without operator intervention.

The numerical petrophysics workflow is based on a 3-step approach. First, a rock classification from grayscale MCT images using RockClass model is investigated in the two main lithological rock reservoirs types, carbonates and sandstones. Then RegPhi model is used to predict the total porosity from grayscale MCT images.

An AutoEncoder network allows to automatically generate the pore space segmented image and then evaluate the total porosity.

The results of this study are not limited to 4 reservoir rock classes and porosity estimation, but the proposed workflow can be adapted for any CT rock types in order to deliver a complete series of numerical analysis.

This work was supported by the ERC Starting Grant ``Light Field Imaging and Analysis'' (LIA 336978, FP7-2014).

## References

1. P. Gouze and L. Luquot, “X-ray microtomography characterization of porosity, permeability and reactive surface changes during dissolution”, J. of Contaminant Hydrology, **120-121**, pp. 45–55, doi: 10.1016/j.jconhyd.2010.07.004, (2011)

2. L. Luquot, V. Hebert and O. Rodriguez, “Calculating structural and geometrical parameters by laboratory measurements and X-ray microtomography: a comparative study applied to a limestone sample before and after a dissolution experiment”, Solid Earth, **7**, pp. 441-456, doi: 10.5194/se-7-441-2016 (2016)

3. S. Youssef, E. Rosenberg, N. Gland, S. Bekri and O. Vizika, “Quantitative 3D characterisation of the pore space of real rocks: Improved μ-CT resolution and pore extraction methodology”, Int. Symp. Soc. Core Analysts, Calgary, Canada, Sept. 10-12, Paper SCA2007-17 (2007)

4. R. Al-Raoush and A. Papadopoulos, “Representative elementary volume analysis of porous media using X-ray computed tomography”, Powder Technology, 200, pp. 69-77, doi: 10.1016/j.powtec.2010.02.011 (2010)

5. G. Wang, “A Perspective on deep imaging”, IEEE Access, 4, 8914-8924, Nov. 3, doi: 10.1109/ACCESS.2016.2624938 (2016)

6. T. Würfl et al., “Deep learning computed tomography: Learning projection-domain weights from image domain in limited angle problems”, IEEE Trans. Med. Imaging, 37, pp. 1454-1463 (2018)

7. Y. Mikia et al., “Tooth labelling in cone-beam CT using deep convolutional neural network for forensic identification”, Computers in Biology and Medicine, 80, pp. 24-29 (2017)

8. A. T. Lopes, E. de Aguiar, A. F. de Souza, T. Oliviera-Santos, “Facial expression recognition with convolutional neural networks: Coping with few data and the training sample order”, Pattern Recognition, 61, pp. 610-628 (2017)

9. M. A. Naranjo Leon et al., “Rock typing mapping methodology based on indexed and probabilistic self-organized map in Shushufindi field”, SPE Latin American and Caribbean Petroleum Engineering Conf., Rio de Janeiro, Brazil, Nov 18-20, Paper SPE-177086-MS, doi: 10.2118/177086-MS (2015)

10. J. Chen and Y. Zeng, “Application of machine learning in rock facies classification with physics-motivated feature augmentation”, Machine Learning, Geophysics, arXiv: 1808.09856 (2018)

11. S. Berg, N. Saxena, M. Shaik and C. Pradhan, “Generation of ground truth images to validate micro-CT image-processing pipelines”, The Leading Edge, Advancements in image processing, 37, pp. 412-420 (2018)

12. S. Karimpouli and P. Tahmasebi, “Image-based velocity estimation of rock using convolutional neural networks”, Neural Networks, 111, pp. 89-97 (2019)

13. M. Araya-Polo, F. O. Alpak, S. Hunter, R. Hofmann and N. Saxena, “Deep learning-driven pore-scale simulation for permeability estimation”, ECMOR XVI, Barcelona, Spain, Dec. 3 (2018)

14. O. Sudakov, E. Burnae and D. Koroteev, “Driving digital rock towards machine learning: Predicting permeability with gradient boosting and deep neural networks”, Computer and Geosciences, 127, pp. 91-98 (2019)

15. A. Krizhevsky, I. Sutskever and G. E. Hintonn, “Imagenet classification with deep convolutional neural networks”, Advances in neural information processing systems, 25 (2012)

16. Z. Zhao, P. Zheng, S. Xu and X. Wu., “Object detection with deep learning: A review”, IEEE Transactions on Neural Networks and Learning systems, Apr. 19, arXiv: 1807.05511v2 (2018)

17. Y. Guo, Y. Liu, T. Georgiou and M. S. Lew, “A review of semantic segmentation using deep neural networks”, Int. J. of Multimedia Information Retrieval, 7, pp. 87-93 (2018)

18. C. Szegedy, V. Vanhoucke, S. Ioffe, J. Shlens and Z. Wojna, “Rethinking the inception architecture for computer vision”, IEEE Conf. on Computer Vision and Pattern Recognition, pp. 2818-2826 (2016)

19. ImageNet. http://www.image-net.org

20. A. Alperovich, O. Johannsen, M. Strecke and B. Goldluecke, “Light field intrinsics with a deep encoder-decoder network”, poster, Proc. CVPR (2018)

21. W. Shi et al., “Real-time single image and video super resolution using an efficient sub-pixel convolutional neural network”, Proc. CVPR, pp. 1874–1883 (2016)

22. A. Alperovich, O. Johannsen and B. Goldluecke, “Intrinsic light field decomposition and disparity estimation with a deep encoder-decoder network”, IEEE European Signal Processing Conf. (2018)

23. S. N. Ehrenberg and P. H. Nadeau, “Sandstone vs. carbonate petroleum reservoirs: A global perspective on porosity-depth and porosity-permeability relationships”, AAPG Bulletin, 89, pp. 435-445 (2005)

24. J. Dautriat, N. Gland, A. Dimanov and J. Raphanel, “Hydromechanical behavior of heterogeneous carbonate rock under proportional triaxial loadings”, J. of Geophysical Research, 116, B01205 (2011)

25. S. Youssef et al., “High resolution μ-CT combined to numerical models to assess electrical properties of bimodal carbonates”, Int. Symp. Soc. Core Analysts, Abu Dhabi, UAE, Paper SCA2008-37 (2008)

26. T. Bultreys, W. De Boever, L. Van Hoorebeke and V. Cnudde, “A multi-scale image-based pore network modeling approach to simulate two-phase flow in heterogeneous rocks”, Int. Symp. Soc. Core Analysts, St. John’s Newfoundland and Labrador, Canada, Paper SCA2015-027 (2015)

27. H. Derluyn, J. Dewanckele, M. N. Boone, V. Cnudde, D. Derome and J. Carmeliet, “Crystallization of hydrated and anhydrous salts in porous limestone resolved by synchrotron X-ray microtomography”, Nuclear Instruments and Methods in Physics Research, DOI: 5 10.1016/j.nimb.2013.08.065 (2014)

28. S. Roels, J. Elsen, J. Carmeliet and H. Hens, “Characterization of pore structure by combining mercury porosimetry and micrography”, Materials and Structures, 34, pp. 76-82 (2001)

29. T. Bourbié and B. Zinszner, “Hydraulic and acoustic properties as a function of porosity in Fontainebleau sandstone”, J. of Geophysical Research, 90, pp. 1524-1532 (1985)

30. A. Sinnokrot, H. J. Ramey and S. Marsden, “Effect of temperature level upon capillary pressure curves”, Soc. Petroleum Engineering, 11, pp. 13-22 (1971)

31. P.L. Churcher, P. R. French, J. C. Shaw and L. L. Schramm, “Rock properties of Berea sandstone, Baker dolomite, and Indiana limestone”, SPE Int. Symp. Oilfield Chemistry, Anaheim, California, Paper SPE-21044-MS, Feb. 20-22 (1991)

32. P.-E. Oren and S. Bakke, “Reconstruction of Berea sandstone and pore-scale modeling of wettability effects”, J. Petroleum Science and Engineering, 39, pp. 177-199 (2003)

33. S. Youssef, D. Bauer, Y. Peysson and O. Vozoka, “Investigation of pore structure impact on mobilization of trapped oil by surfactant injection”, Int. Symp. Soc. Core Analysts, Avignon, France, Sept. 11-18, Paper SCA2014-64 (2014)

34. N. Saxena, R. Hofmann, F.O. Alpak, J. Dietderich, S. Hunter and R.J. Day-Stirrat, “Effect of image segmentation & voxel size on micro-CT computed

effective transport & elastic properties", Marine and Petroleum Geology, 86, pp. 972-990 (2017)

35. S. Cyprien et al., "The impact of sub-resolution porosity of X-ray microtomography images on the permeability", Transport in Porous media, 113, pp. 227-243 (2016)

36. O. Rodriguez, T. Porcher, V. Planes, G. Mecuson and R. Bouvier, "Non destructive testing of CMC engine internal parts from X-ray tomographic images", 9th Int. Conf. Industrial Computed Tomography, Padova, Italy, Feb. 13-15 (2019)

37. A. Krizhevsky, I. Sutskever and G. E. Hinton, "ImageNet classification with deep convolutional neural networks", Advances in Neural Information Processing Systems, 25, pp. 1097-1105 (2012)

38. F. Chollet et al., https://keras.io (2015)

39. Y. Pu et al., "Adversarial symmetric variational autoencoder", Advances in Neural Information Processing Systems, 30, pp. 4330-4339 (2017)

40. X.-J. Mao, C. Shen and Y.-B. Yang, "Image restoration using very deep convolutional encoder-decoder networks with symmetric skip connections", Proc. Neural Information Processing Systems, arXiv: 1603.09056 (2016)

41. K. He, X. Zhang, S. Ren and J. Sun, "Deep residual learning for image recognition", Proc. Int. Conf. Computer Vision and Pattern Recognition, arXiv: 1512.03385 (2016)

42. J. Springenberg, A. Dosovitskiy, T. Brox and M. Riedmiller, "Striving for simplicity: The all convolutional net", Proc. 3rd Int. Conf. Learning Representations, workshop track (2015)

43. D. Kingma and J. Ba, "Adam a method for stochastic optimization", Proc. 3rd Int. Conf. Learning Representations (2015)

# Using Capillary Condensation and Evaporation Isotherms to Investigate Confined Fluid Phase Behavior in Shales

*Elizabeth* Barsotti[1,*], *Evan* Lowry[1], *Mohammad* Piri[1], and *Jin-Hong* Chen[2]

[1]Center of Innovation for Flow through Porous Media, Petroleum Engineering Department, University of Wyoming, Laramie, Wyoming, USA
[2]Aramco Services Company, Aramco Research Center-Houston, Houston, Texas, USA

**Abstract.** The abundance of nanopores (pores with diameters between 2 and 100 nm) in shale and ultra-tight reservoirs precludes the use of common pressure-volume-temperature (PVT) analyses on reservoir fluids. The small sizes of the pores cause capillary condensation, which is a nanoconfinement-induced gas-to-liquid phase change, that can occur at pressures more than 50% below the corresponding bulk phase change of the fluid due to strong fluid-pore wall interactions. We quantify this phenomenon by measuring propane isotherms both in a synthetic nanoporous medium and a core from a shale gas reservoir. Comparison of our results in the two porous media indicates the occurrence of capillary condensation in shale rock. At the same time, we observe capillary condensation hysteresis for shale, in which the density of the fluid is significantly lighter during desorption than adsorption. This indicates structural changes to the rock matrix caused by the phase behavior of the confined fluid. We use scanning electron microscopy to corroborate our findings. These results have significant implications for determining the PVT properties, porosity, and permeability of shale and ultra-tight formations for use in reservoir modeling and production estimations.

## 1 Introduction

Current methods of shale reservoir evaluation do not account for (i) capillary condensation, a confinement-induced gas-to-liquid phase change, or (ii) continuous pore filling, a sharp increase in the density of supercritical fluids, that occur in nanopores. [1] Even though it has been shown that accounting for nanoconfinement-induced phase phenomena such as capillary condensation could increase reserves estimates by 600%, [2] the current prevailing opinion only considers the existence of an adsorbed, or physisorbed, phase on the pore walls and free gas in the pore bodies. [3]

The primary reason for this is misinterpretation of isotherms measured in shale. Throughout the literature, isotherms measured for both hydrocarbons and gases, such as $CO_2$, do not exhibit the distinct capillary condensation step defined in the IUPAC Type IV isotherm [4] or the continuous filling step that has recently been elucidated by Tan et al. [5] and Barsotti et al. [6] Instead, they appear similar to IUPAC Type I and II isotherms, [7], [8] which are attributed to mono-layer and multi-layer adsorption, respectively. [4] Therefore, they are given the same interpretation even though the IUPAC isotherms rely on fundamental assumptions about the adsorbate and adsorbent that are not true of shale rock. The Type I isotherm assumes a microporous material, while the Type II isotherm assumes a macroporous or non-porous surface. [4] Both of these cases are far removed from the wide pore size distributions, complex wettabilities, unpredictable pore geometries, and complex fluid compositions in shale. Even so, the ease with which longstanding, simplistic adsorption theories, such as Langmuir and BET, can be fit to shale adsorption isotherms has led to their widespread incorporation into shale characterization [9], [3], [10], [11] and reservoir modeling. [12]-[14]

However, we prove here that despite the fact that the shapes of shale isotherms are often similar to IUPAC isotherms, the underlying physics are generally not the same. By creating controlled pore size distributions with a synthetic nanoporous medium called MCM-41 and comparing the isotherms measured in them to those measured in shale, we show that the broad pore size distribution of shale can alter the appearance of capillary condensation and continuous pore filling such that they manifest much differently from the traditional IUPAC Type IV isotherm. We further demonstrate this with desorption measurements where hysteresis belies the underlying phase change. Closer scrutiny of the hysteresis loop in combination with scanning electron microscopy not only confirms the occurrence of capillary condensation but also provides evidence that just as the nanopores can alter the phase behavior of fluids, so can the nanoconfinement-induced phase behavior of the fluids impart irreversible changes to the rock, including fractures. Our observations of capillary condensation and continuous pore filling cast significant doubt upon the

---

[*] Corresponding author: ebarsott@uwyo.edu

ability of simple adsorption theories to accurately model phase behavior in shale.

## 2 Materials and Methods

### 2.1. Isotherm Measurements

All isotherms were measured using a novel gravimetric apparatus. [15], [16] Unlike other systems available commercially and in the literature, our apparatus is compatible with macro-scale cores enclosed in core holders. [15] All core holders employed in this study were ¾" in internal diameter and 7" long and comprised a titanium body with stainless steel endcaps. During the isotherm measurements, the core holders were suspended from Mettler Toledeo XPE505C mass comparators inside of an environmental chamber (Thermotron). The environmental chamber uses air as the thermostating fluid such that experiments between 5.4 and 16.1°C were characterized by a temperature control of +/- 0.1°C. In other words, the experimental fluid resided solely in the core holder, while the temperature and pressure of the thermostatic air were constant throughout all experiments. Therefore, no correction for buoyant force had to be made, [16] underscoring another unique feature of our apparatus.

By injecting or retracting the experimental fluid into or out of the core holders, its pressure could be changed, such that the change in mass and pressure at constant temperature could be used to plot an isotherm. Equilibrium was defined as the time at which the pressure of the fluid became constant as read by a Rosemount pressure transducer (Emerson). [16] At equilibrium, pressure and mass data points were generated by averaging data collected at a rate of 1/sec over a timespan of 1 minute. [16] Statistical analyses of these time series showed the standard error for mass and pressure to be less than 0.008 g and 0.008 psi, respectively, for all measurements. Because these errors are negligible, no error bars are included in the isotherm plots. We refer interested readers to our previous publications for more comprehensive discussions of the operating principle, repeatability, and accuracy of the apparatus. [15]-[17]

For adsorbents, both synthetic silica nanopores (MCM-41) and shale cores from a gas reservoir in the Middle East were used. The shale used here is from the same core that was used in our previous work. [18]

MCM-41 is a synthetic nanoporous silica popular for use in capillary condensation experiments because its singular pore size distribution and cylindrical pores simplify data analysis. Three different pore sizes of MCM-41 (Glantreo, Ltd.) were characterized using Non-Local Density Functional Theory analysis of nitrogen isotherms measured at 77K. [6] The characteristic pore diameters of the samples were 2.90 nm, 4.19 nm, and 8.08 nm. [6] Henceforth, the small, medium, and large pore sizes of MCM-41 will be referred to as MCM-41-S, MCM-41-M, and MCM-41-L to be consistent with our previous work. [6] To create controlled pore size distributions, known amounts of the different adsorbents were mixed together. In one core holder, 8.2946 grams of MCM-41-S were packed. [6] In a second core holder, 4.96016 grams of MCM-41-S were mixed with 3.51795 grams of MCM-41-M. In a third core holder, 5.02250 grams of MCM-41-S were mixed with 2.31973 grams of MCM-41-L. The three different core holders allowed us to determine how large and small differences in pore size affect the shape of an isotherm.

As received shale cores were crushed by hand following the same procedure in our previous work. [18] Pieces of the crushed rock were randomly selected for characterization using a Helios 650 (ThermoFisher Scientific) focussed ion beam scanning electron microscope (FIB-SEM). Energy dispersive X-ray scattering revealed the mineralogy to comprise kerogen and calcite with minor amounts of quartz, pyrite, and illite. [18] High resolution imaging using a Through-the-Lens detector in downhole vision mode showed the kerogen to be highly nanoporous, as shown in Figure 1. Approximately 67 grams of the shale rock were packed into a titanium core holder for the isotherm measurement.

Propane (99%, AirGas) was used as an adsorbate for the measurements in both types of porous media.

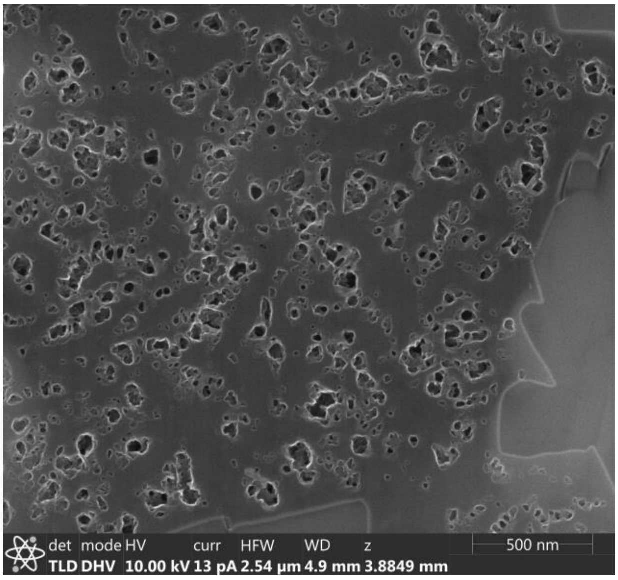

**Figure 1.** Scanning electron micrograph of kerogen nanopores in the shale rock taken at a voltage of 10kV and a current of 13 pA with an instrument resolution of 0.8 nm.

### 2.1. SEM Imaging

One piece of the crushed shale was randomly selected for FIB-SEM imaging to determine whether the fluid phase behavior in the rock affected the rock properties. The sample was mounted on a 45-degree, pre-tilted aluminium stub (Ted Pella) using carbon tape and silver paint (Ted Pella). Then, a 20 µm by 20 µm cross-section of the sample was polished with the FIB-SEM's gallium ion beam. Subsequently, a 1 µm diameter, 2 µm deep circular hole was milled into the kerogen in the rock using the ion beam. Imaging of the surface was done prior to and after exposure to propane. To expose the sample to propane, it was removed from the sample stub, and placed into a pressure cell. The pressure cell was first vacuumed out using a Welch vacuum pump to remove any air and then pressurized to 6.9 bar with propane at 20°C. After approximately 1.5 hrs, the pressure of the cell was reduced to atmospheric and the rock sample was removed, re-mounted on the 45-degree, pre-tilted stub, and imaged again. The circular hole was to determine whether any permanent changes to the kerogen structure, such as irreversible swelling, had occurred.

## 3 Results and Discussion

### 3.1. Isotherms in MCM-41

The isotherms measured in all three of the MCM-41 packs are shown in Figure 2. Isotherms were measured at 5.4°C. Note that the bulk saturation pressure for propane at this temperature is 5.5766 bar, as reported by NIST. [19] In Figure 2, the bulk saturation pressure is measured as the rightmost abrupt increase in amount adsorbed as indicated in the plots. In all three cases, the measured bulk saturation pressure fell within 2% (percent difference) of that reported by NIST, affirming the accuracy of our measurements.

In all three isotherms, the initial increase in the amount adsorbed is propane adsorption on the pore walls. The downward concavity indicates that the propane is a wetting fluid [4] to the MCM-41.

At higher pressures capillary condensation or continuous pore filling occurs. For the pure MCM-41-S, only a single step in the isotherm is observed, indicating filling of the pores with a dense supercritical phase. Of the three pore sizes only MCM-41-L was sufficiently large to exhibit the subcritical phase transition, capillary condensation. [5] Therefore, in the mixture of MCM-41-S and MCM-41-L, the two distinct steps in the isotherm indicate continuous pore filling for MCM-41-S and capillary condensation in MCM-41-L. When the pore sizes were closer together in the case of the mixture of MCM-41-S and MCM-41-M, the continuous pore filling in both blended together into a single step.

This has significant implications for shale rock, where the pore size distribution is broad but consecutive sizes are close together. It is often assumed that, because a distinct capillary condensation or continuous pore filling step cannot be observed in shale isotherms, neither of the nanoconfined phase phenomena is occurring. However, if we extend our understanding from the MCM-41 experiments, the absence of a step in the isotherm does not indicate the absence of capillary condensation or continuous pore filling; rather it indicates the absence of a distinct, singular pore size. In other words, phase phenomena occur gradually in the different pore sizes giving rise to a gently sloping isotherm that may be easily mistaken as an IUPAC Type I or II isotherm.

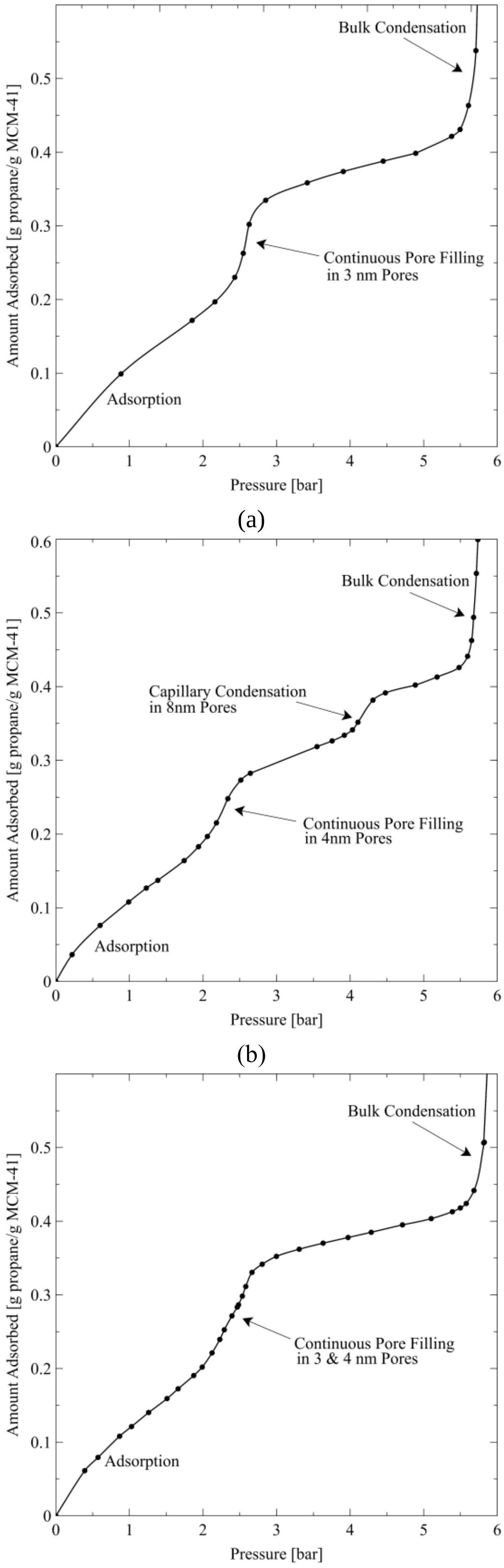

(a)

(b)

(c)

**Figure 2.** Propane adsorption isotherms measured at 5.4$^{o}$C in the core holders containing (a) MCM-41-S, (b) MCM-41-S and MCM-41-L, and (c) MCM-41-S and MCM-41-M. Figure (a) adapted with permission from Barsotti et al. [6] Copyright 2018 American Chemical Society.

Likewise, the presence of both a sub-critical and supercritical phase in the nanopores, may not only further reduce the relevance of current modeling efforts but also make accurate modeling more difficult as many equations of state are not well-equipped to work with supercritical fluids.

### 3.1. Isotherms in Shale Rock

This behavior is evident in Figure 3, where no apparent capillary condensation or continuous pore filling step is observed during adsorption, and the isotherm does, indeed, appear similar to the IUPAC Type I and II isotherms. However, the occurrence of capillary condensation in the shale sample can be verified by also measuring desorption. Upon desorption, hysteresis is observed. Hysteresis at relatively high pressures is commonly attributed to capillary condensation. [4] Therefore, because we observe hysteresis occurring at pressures as high as 90% of the bulk saturation pressure, which is approximately 7.5 bar in Figure 3, we interpret it as indicating the occurrence of capillary condensation. This interpretation is consistent with other studies in the literature where any hysteresis occurring above 50% of the bulk saturation pressure was defined as a key indicator of capillary condensation. [20] Therefore, we show that capillary condensation can occur in shale rock, even when it is not immediately apparent from the adsorption part of the isotherm.

Interestingly, the hysteresis loop for shale also appears to differ from those types classified by IUPAC. Rather than desorption occurring at larger amounts adsorbed than adsorption, [4] we observe it to occur at smaller amounts. This indicates that the fluid in the pore space is less dense during desorption than during adsorption. This can be interpreted to mean that the pore size is larger during desorption than adsorption. Thus, it may be possible not only that the shale nanopores are affecting the phase behavior of the fluid but also that the fluid can affect the morphology of the pores. In addition to our observation of hysteresis at high pressures, our observation of hysteresis at low relative pressure supports this, as it has been found in the literature to indicate adsorbent deformation. [4]

Further evidence for deformation is given by the dips observed in the isotherm at intermediate pressures. In isotherms measured for coal, these dips are often interpreted to indicate swelling of the adsorbent. [21]

To prove this, a polished cross section of the shale was visualized both before and after contact with propane at 0 °C and ~6.9 bar. Both images are presented in Figure 4. After the propane capillary condensation, large fractures were observed in the rock. Our initial hypothesis was that permanent swelling of the kerogen induced the fractures. But comparison of the 1 μm diameter holes milled into the kerogen before and after propane exposure shows no change to the diameter or shape of the hole. We, therefore, hypothesize that reversible kerogen swelling causes fracturing. In essence, the kerogen swells during adsorption. During desorption, as the kerogen returns to its initial configuration, differences in the elasticities of the inorganic (i.e., calcite, quartz, and pyrite) and organic minerals result in fractures. Kerogen swelling has been observed previously during capillary condensation, [18], [22] but to the best of our knowledge, this is the first observation of fracturing during capillary condensation.

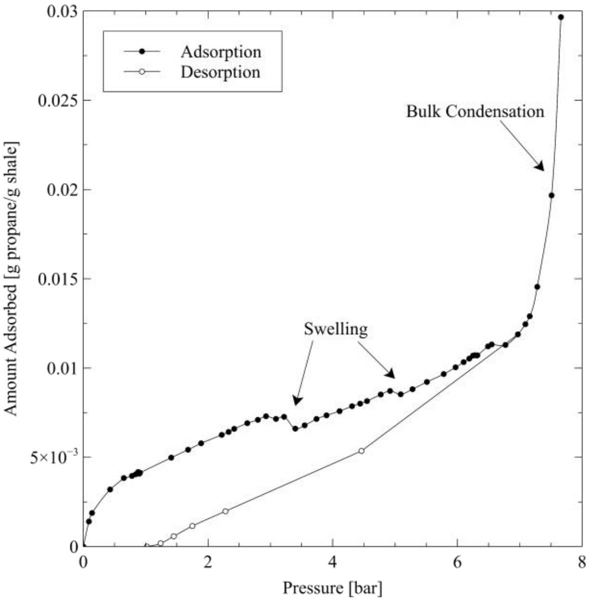

**Figure 3.** Propane capillary condensation isotherms measured in shale rock at 16.1°C. Note that the bulk saturation pressure for propane at 16.1°C is 7.5379 bar as reported by NIST. [19] Therefore, the percent difference between our measurement and theirs is less than 1%, also affirming the accuracy of this measurement.

## 4 Conclusions

By measuring isotherms both in controlled pore size distributions of MCM-41 and shale rock, we show that complexities of the adsorbent, such as a wide pore size distribution, can cause the shape of the isotherm to appear significantly different from ideal cases presented in the literature for simple porous media. This discrepancy can lead to the misinterpretation that capillary condensation or continuous pore filling do not occur in shale. However, our observations of capillary condensation occurring gradually at different pressures across the range of pore size both in the MCM-41 and shale disprove this. Observations of hysteresis in the shale further indicate the occurrence of capillary condensation. Indeed, the complex mineralogy of shale may lead to capillary condensation-induced fractures. This indicates that the rock and fluid properties are interrelated and that current methods of PVT and core analysis that do not account for capillary condensation may lead to erroneous estimates of rock and fluid properties. The degree to which capillary condensation affects these phenomena is highly dependent upon the chemical compositions and physical morphologies of the fluid and the rock. We have proven

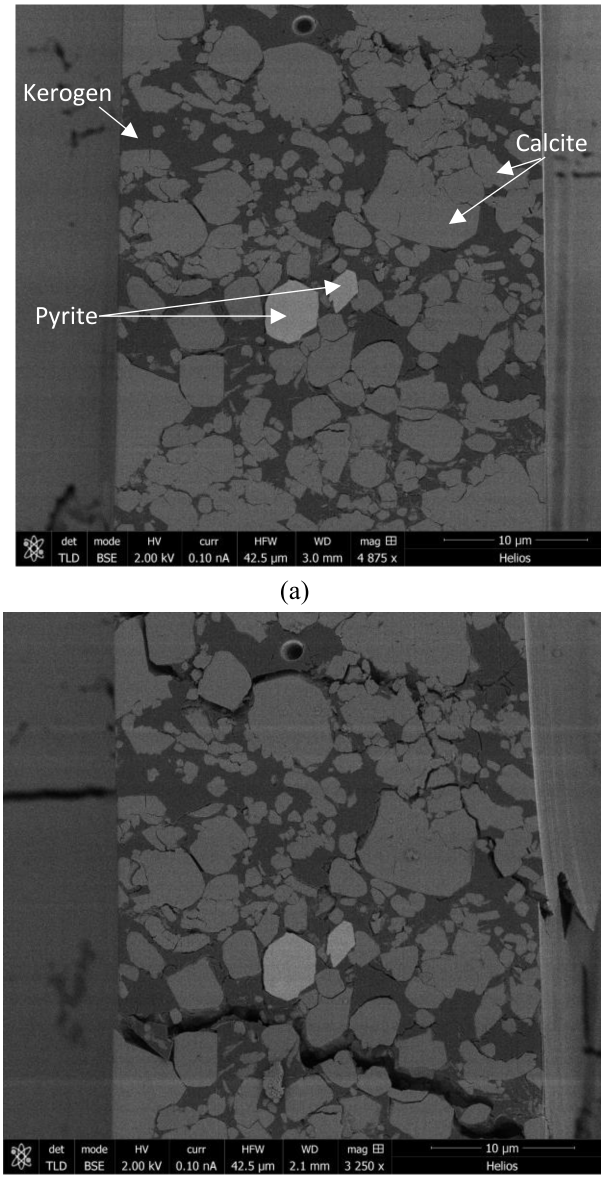

(a)

(b)

**Figure 4.** SEM images of a polished cross-section of the shale (a) before and (b) after exposure to propane at 20$^{o}$C and ~6.9bar. The low, medium, and high greyscale intensity minerals are kerogen, calcite, and pyrite, respectively.

this both experimentally [16], [23] and theoretically [24] in MCM-41, where selective adsorption occurs and can affect the phase transition. Future work must include more complex mixtures in different types of reservoir cores to fully characterize this phenomenon.

We gratefully acknowledge the financial support of Saudi Aramco, Hess Corporation, and the School of Energy Resources at the University of Wyoming.

## References

1. E. Barsotti, S. P. Tan, S. Saraji, M. Piri and J.-H. Chen, “A review on capillary condensation in nanoporous media: Implications for hydrocarbon recovery from tight reservoirs,” *Fuel,* pp. 344-361, 2016.
2. J.-H. Chen, A. Mehmani, B. Li, D. Georgi and G. Jin, “Estimation of total hydrocarbon in the presence of capillary condensation for unconventional shale reservoirs,” in *SPE Middle East oil and gas show and conference*, Manama, Bahrain, 2013.
3. J. Richardson and W. Yu, “Calculation of Estimated Ultimate Recovery and Recovery Factors of Shale-Gas Wells Using a Probabilistic Model of Original Gas in Place,” *SPE Reservoir Evaluation & Engineering,* pp. 638 - 653, 2018.
4. M. Thommes, K. Kaneko, A. V. Neimark, J. P. Olivier, F. Rodriguez-Reinoso, J. Rouquerol and K. S. Sing, “Physisorption of gases, with special reference to the evaluation of surface area and pore size distribution (IUPAC Technical Report),” International Union of Pure and Applied Sciences & De Gruyter, 2015.
5. S. P. Tan, E. Barsotti and M. Piri, “Criticality of Fluids Confined in Nanopores Based on the Liquid Spinodal,” *Under Review,* 2019.
6. E. Barsotti, S. P. Tan, M. Piri and J.-H. Chen, “Phenomenological Study of Confined Criticality: Insights from the Capillary Condensation of Propane, n-Butane, and n-Pentane in Nanopores,” *Langmuir,* pp. 4473-4483, 2018.
7. S. Duan, M. Gu, X. Du and X. Xian, “Adsorption Equilibrium of CO2 and CH4 and Their Mixture on Sichuan Basin Shale,” *Energy & Fuels,* p. 2248–2256, 2016.
8. S. Rani, B. K. Prusty and S. K. Pal, “Methane adsorption and pore characterization of Indian shale samples,” *Journal of Unconventional Oil and Gas Resources,* pp. 1-10, 2015.
9. W. Yu, K. Sepehrnoori and T. W. Patzek, “Modeling Gas Adsorption in Marcellus Shale With Langmuir and BET Isotherms,” *SPE Journal,* pp. 589 - 600, 2016.
10. S. Rani, E. Padmanabhan and B. K. Prusty, “Review of gas adsorption in shales for enhanced methane recovery and CO2 storage,” *Journal of Petroleum Science and Engineering,* pp. 634-643, 2019.
11. M. Eliebid, M. Mahmoud, S. Elkatatny, M. Abouelresh and R. Shawabkeh, “Adsorption Role in Shale Gas Recovery and the Feasibility of CO2 in Shale Enhanced Gas Recovery: A Study on Shale Gas from Saudi Arabia,” in *SPE Kuwait Oil & Gas Show and Conference,* Kuwait City, Kuwait, 2017.
12. V. Nguyen-Le and H. Shin, “Development of reservoir economic indicator for Barnett Shale gas potential evaluation based on the reservoir and

hydraulic fracturing parameters," *Journal of Natural Gas Science and Engineering,* pp. 159-167, 2019.

13. S. Yang, K. Wu, J. Xu, J. Li and Z. Chen, "Roles of multicomponent adsorption and geomechanics in the development of an Eagle Ford shale condensate reservoir," *Fuel,* pp. 710-718, 2019.
14. H. Belyadi and M. Smith, "A Fast-Paced Workflow for Well Spacing and Completions Design Optimization in Unconventional Reservoirs," in *SPE/AAPG Eastern Regional Meeting,* Pittsburgh, Pennsylvania, USA, 7-11 October 2018.
15. E. Barsotti, S. Saraji and M. Piri, "Nanocondensation Apparatus". United States of America Patent US15/588,094, 2017.
16. E. Barsotti, S. Saraji, S. P. Tan and M. Piri, "Capillary Condensation of Binary and Ternary Mixtures of n-Pentane–Isopentane–CO2 in Nanopores: An Experimental Study on the Effects of Composition and Equilibrium," *Langmuir,* p. 1967–1980, 2018.
17. E. Barsotti, S. P. Tan, M. Piri and J.-H. Chen, "Capillary-Condensation Hysteresis in Naturally-Occurring Nanoporous Media," *Under Review,* 2019.
18. E. Barsotti, S. P. Tan, M. Piri and J.-H. Chen, "Capillary-Condensation Hysteresis in Naturally-Occurring Nanoporous Media," *Under Review,* 2019.
19. E. Lemmon, M. McLinden and D. Friend, *NIST Standard Reference Database Number 69,* P. Linstrom and W. Mallard, Eds.
20. H. Bu, Y. Ju, J. Tan, G. Wang and X. Li, "Fractal characteristics of pores in non-marine shales from the Huainan coalfield, eastern China," *Journal of Natural Gas Science and Engineering,* vol. 24, pp. 166-177, 2015.
21. R. Pini, S. Ottiger, G. Storti and M. Mazzotti, "Role of Adsorption and Swelling on the Dynamics of Gas Injection in Coal," *Journal of Geophysical Research Solid Earth,* vol. 114, no. 84, 2009.
22. M. Pathak, H. Kweon, M. Deo and H. Huang, "Kerogen Swelling and Confinement: Its implication on Fluid Thermodynamic Properties in Shales," *Scientific Reports,* vol. 7, 2017.
23. E. Barsotti, M. Piri, J.-H. Chen and S. Althaus, "Solution Gas Drive in Tight Oil Reservoirs: New Insights from Capillary Evaporation Experiments," in *SPE/AAPG/SEG Unconventional Resources Technology Conference,* Houston, Texas, USA, 2018.
24. S. P. Tan, E. Barsotti and M. Piri, "Application of material balance for the phase transition of fluid mixtures confined in nanopores," *Fluid Phase Equilibria,* 2019.

# Methane Isotherms and Magnetic Resonance Imaging in Shales

*M. J.* Dick[1,*], *D.* Heagle[2], *D.* Veselinovic[1] and *D.* Green[1]

[1]Green Imaging Technologies, Fredericton, NB, Canada
[2]Natural Resources Canada, Canmet Energy – Ottawa, ON, Canada

**Abstract.** Adsorption isotherms of light hydrocarbons on reservoir rocks are key data used to quantify the total gas content in reservoirs and isotherms are now being used to improve our understanding of the processes affecting subsurface gas flow associated with gas injection from Enhanced Oil Recovery techniques. This project combined elements of the traditional pressure-volume gas adsorption isotherm technique and an NMR-based adsorption isotherm approach to determine the adsorption isotherms of light hydrocarbons on to tight rocks from oil and gas reservoirs. The new approach allows isotherms to be derived from NMR data. First, a $T_2$ distribution of the gas is determined over a range of gas pressures. Next, the volume of pore gas is estimated using the pore volume of the rock and the Van der Waals gas equation. The adsorbed gas content is then calculated by subtracting pore gas content from the total gas content. This is repeated for a range of gas pressures to determine the adsorption isotherm. This project used the NMR method described above and measured the gas pressure decay in the NMR cell. This combined approach includes the advantages of the NMR method but it also produces a pressure-time curve that can be used to identify when equilibrium is attained in low permeability rocks and can be used to compare adsorption kinetics of different gases. The advantages of our approach are that 1) the samples remain intact and the measurements provide information on the pore size distribution; 2) analyses can be carried out at reservoir pressures; 3) isotherms can be measured for any gas containing hydrogen atoms; and 4) the results can be used to examine the processes controlling gas flow through the rock. Future work to develop this technique will improve our quantification of the amount of pore gas in the cell, which will improve our partitioning between adsorbed gas and pore gas as well as allow for an improved analysis of the pressure response of the sample after degassing.

## 1 Introduction

Adsorption of gases to rocks is an important process for evaluating natural gas resource potential, coalbed methane recovery, as well as secondary and tertiary enhanced oil recovery techniques. State-of-the-art models are used to evaluate resource potential and enhanced oil recovery but these models require inputs including gas transport processes and adsorption isotherms to help describe the mobility and storage of gasses on the rocks. Gas transport through low-permeability rock, also referred to as tight rock, is a significant factor for evaluating how much of a resource is recoverable and how effective gas injection into a tight reservoir might be. Gas transport by diffusion is a slow process while transport by advection, or Darcy flow, may be orders of magnitude greater. Assessing the contribution of each component to the gas flux requires sophisticated experiments at a variety of pressures and/or multiple gases and for the most part does not lend itself to routine analyses [1].

Adsorption isotherms for rocks commonly report data on the volume of gas contained within the pore space, referred to here as pore gas, and the gas adsorbed on to the surface of the pore walls referred to here as adsorbed gas. Our use of the term adsorbed gas is equivalent to the term excess gas that has been used in some other adsorption isotherm studies [2].

The quantity of pore gas and adsorbed gas is traditionally measured volumetrically using a system of two cells, a sample cell and a reference cell, which are separated by a valve. A crushed rock sample is placed in the sample cell and the reference cell is filled with a gas at a known pressure. The valve is opened and the gas from the reference cell expands into the sample cell and the pressures in the two cells equalize. The procedure is performed first with a non-adsorbing gas, such as helium, to determine the void volume, or free gas content, in the rock sample via the difference in temperature and pressure before and after opening of the valve between the two cells. Then the system is evacuated at below-atmospheric pressures to remove the gas, and the reference cell is filled with an adsorbing gas. The valve is opened again and the adsorbing gas expands into the sample cell, it will fill the

---

[*] Corresponding author: mjdick@greenimaging.com

void volume and adsorb on the sample. The amount of adsorption can be calculated by subtracting the free gas content. The expansion of the gases is repeated at numerous pressures to generate isotherms. The disadvantages of this method include 1) the sample is crushed for the measurement which alters the structure of the sample; 2) no information is acquired on the size of the pores occupied by the gas; and 3) many analyses do not examine the processes controlling gas flow through the rock.

Low Pressure Gas Adsorption (LPGA) is another technique used to determine adsorption isotherms, pore size distributions and surface area. This technique also uses dry powdered samples that are evacuated of all gas and cooled so that the equilibrium gases, typically $N_2$ or $CO_2$, can adsorb to the surface of the sample. After the absorbing gas is added to the sample the change in pressure over time is analyzed to determine the adsorption isotherm as well as the pore size distribution and surface area or the sample. There are disadvantages with this method that impact analysis of low permeability rock including drying and powdering the samples that may change the sample characteristics. Also, the isotherms are carried out at low pressures (< 20 psi) which prevents an analysis of the isotherms at reservoir conditions and the number of gas adsorption sites is related to the gas pressure [2] so conducting the isotherms at lower pressures may underestimate the adsorption capacity of a reservoir or source rock. Finally, the isotherms are not determined using methane or any of the other light hydrocarbon gases, so the interaction between the hydrocarbon gas and organics in the rocks may not be addressed with this method.

Measuring gas in shales is challenging with NMR due to the low hydrogen index of gas and the small pore volume of shales, both of which result in low NMR signal. However, with recent advances in NMR hardware, gas measurements in shales are possible. Low-field NMR can be used to measure gas isotherms with hydrocarbon gases of interest (e.g. methane or ethane), which is important for evaluating gas in place or determining adsorption of hydrocarbon gases during gas injection for Enhanced Oil Recovery (EOR) strategies [3]. The advantages of NMR measurements include 1) the samples remain intact and the measurements provide information on the pore size distribution; 2) analyses can be carried out at reservoir pressures; and 3) isotherms can be measured for any gas containing hydrogen atoms; and 4) the results can be used to examine the processes controlling gas flow through the rock.

Gas adsorption to nanoporous materials and shales have has been previously studied [4,5]. These studies showed it was possible to identify three distributions of methane including 1) methane adsorbed in the micropores, 2) adsorbed methane in fast exchange with the surrounding mesopore network, and 3) adsorbed methane in exchange with the interparticle void space of the adsorbent beds by characteristic relaxation times and pressure dependencies in the relaxation time distributions.

In this study we use low-field NMR to generate methane isotherms by measuring the total gas in the rock and distinguishing the amount of free gas and adsorbed gas in a rock. We calculate the pore gas volume using Van der Waals gas equation to determine the methane adsorption isotherm. We also combine pressure measurements with NMR measurements to carry out an initial assessment of the transport processes controlling gas flow in a shale.

## 2 Method

The method for determining gas isotherms from NMR data is as follows:

1) Record the $T_2$ distribution of the dry shale sample (95C for 7 days in vacuum oven) with 0 psi of methane. Shale samples often have NMR signal from organic content present in the rock and should not be included in the gas isotherm analysis. It is assumed that this signal will be invariant with methane pressure and should be subtracted from all subsequent $T_2$ distributions at higher methane pressures.

2) Equilibrate the sample at a range of methane pressures (i.e. 500, 1000, 1500 psi etc.). At each pressure record the $T_2$ distributions as a function of time. This is necessary as it will take time for the methane to fully penetrate all the pores of the sample. Continue to record the distributions until the observed NMR signal has stabilized.

3) Subtract the background (0 psi methane) echo train from each of the echo trains measured for the various pressures (500, 1000, 1500 psi etc.) to account for the $T_2$ distribution of the rock and any liquids or gases present in the sample before the experiment began. Retrieve the observed methane signal from each background subtracted distribution by summing the area under each distribution. This will yield the observed methane content in units of equivalent water volume (ml) as the NMR spectrometer has been calibrated using water.

4) Convert the observed methane content in units of equivalent water volume to gas content (GC as $scm^3$ of methane/ $cm^3$ sample) of observed methane using the following equation:

$$GC = \frac{PVT_{STP}}{TP_{STP}H_{index}V_{bulk}} (1)$$

Where P, V and T are the pressure (psi), volume ($cm^3$) and temperature (307 °K) of methane during the experiment. $H_{index}$ is the hydrogen index of methane. $P_{STP}$ and $T_{STP}$ are standard temperature and pressure (14.7 psi and 292 °K). $V_{bulk}$ is the bulk volume ($cm^3$) of the core sample.

5) Plot the gas content measurements for each pressure of methane observed as a function of time. This plot should show that the gas content stabilizes over time. After stabilization, retrieve the gas content for each pressure and plot the gas content as a function of pressure. This will yield the total gas isotherm.

6) To retrieve the pore gas isotherm employ the pore volume of the core sample (measured in a separate NMR experiment with a 100% brine saturated sample) and the Van der Waals gas equation and the compressibility of methane were used to calculate the pore gas content (scm$^3$/cm$^3$).

$$Pore\ Gas\ Content = \frac{PnT_{STP}c}{P_{STP}V_{bulk}T} \quad (2)$$

Where P is the pressure (psi) of the cell; n is the porosity (unitless) of the rock; $T_{STP}$ is the standard temperature (292 °K); c is the compressibility (unitless) of methane at 307 °K; $P_{STP}$ is the standard pressure (psi); $V_{bulk}$ is the bulk volume of the core; and T is the temperature (307 °K) of the magnet and cell. This assumes that the pore gas behaves like any standard gas in a container of fixed volume (i.e. an individual pore).

7) To retrieve the adsorbed gas isotherm subtract the pore gas isotherm from the total gas isotherm.

# 3 Experiment

The method for determining gas isotherms via NMR data was tested in three different experiments on three different shale samples. For the first two experiments, the NMR data was recorded on Oxford Instruments GeoSpec 2-75 rock core analyzer [6] equipped with Oxford Instruments P5 overburden NMR probe [7]. All data was then processed using GIT Systems Advanced software [8].

## 3.1 Experiment 1

The first experiment determined the gas isotherm for a Barnett shale (BN 1). The Mississippian Barnett Shale is an organic rich, thermally mature source rock for oil and gas produced from Paleozoic reservoir rocks in the Bend arch–Fort Worth Basin area of Texas [9]. Mean TOC for core samples averages between 4% and 5% [9] and a porosity of 6% [10]

Figure 1 shows the experimental setup employed for this experiment. Table 1 summarizes the properties of the sample while Table 2 summarizes the NMR parameters employed.

| **Core Sample** | **BN 1** | **LHSVL** | **Bakken** |
|---|---|---|---|
| Origin | Barnett | Lower Haynesville | Bakken |
| Core Diameter (cm) | 3.81 | 2.51 | 2.49 |
| Core Length (cm) | 4.79 | 2.57 | 1.67 |
| Bulk Volume (mL) | 54.61 | 12.9 | 8.1 |
| Dry Core Mass (g) | 129.16 | - | - |
| Pore Volume (mL) | 2.60 | 1.137 | 0.19 |
| Porosity (p.u.) | 4.76 | 8.80 | 2.3 |

**Table 1.** Sample Information

| **Measurement** | **$T_2$ , BN-1** | **$T_2$ , LHSVL** | **$T_2$, Bakken** |
|---|---|---|---|
| Recycle delay (ms) | 750 | 7500 | 2250 |
| Tau (µs) | 50 | 50 | 54 |
| Number of Echoes | 5000 | 5000 | 13889 |
| Filter Width (kHz) | 125 | 125 | 125 |
| 90° Pulse Length (µs) | 7.5 | 9.31 | 6.63 |
| 180° Pulse Length (µs) | 15.2 | 18.88 | 13.71 |

**Table 2.** NMR Parameters

The experiment can be summarized as follows, sample BN 1 was confined hydrostatically with FC-40 (CAS Number 86508-42-1), and NMR-inert fluid, to a pressure of 2500 psi in the overburden NMR probe. The system was examined for gas leaks but no obvious leak was detected. The probe was then inserted into the rock core analyzer. The sample was evacuated with a vacuum pump, then as received or dry $T_2$ measurements were taken before the introduction of methane. Next, methane was introduced to the sample at 500 psi. $T_2$ measurements were acquired at 2-minute intervals for the first hour, then at 15-minute intervals for the following 3 hours, and at 60 minute intervals for the remainder of the experiment. The pressure was continuously monitored via Arduino micro-controller [11]. The Arduino then reported the pressure to an internal website and a computer program running on our server logs all the system pressures. In addition, a Raspberry Pi [12] computer monitors the overburden pressure via the same internal website and turns a pump on or off depending if the overburden pressure was too high or too low. This ensured the overburden pressure remained constant throughout the experiment. The $T_2$ measurements were then employed to retrieve the total gas content present in the rock as a function of time

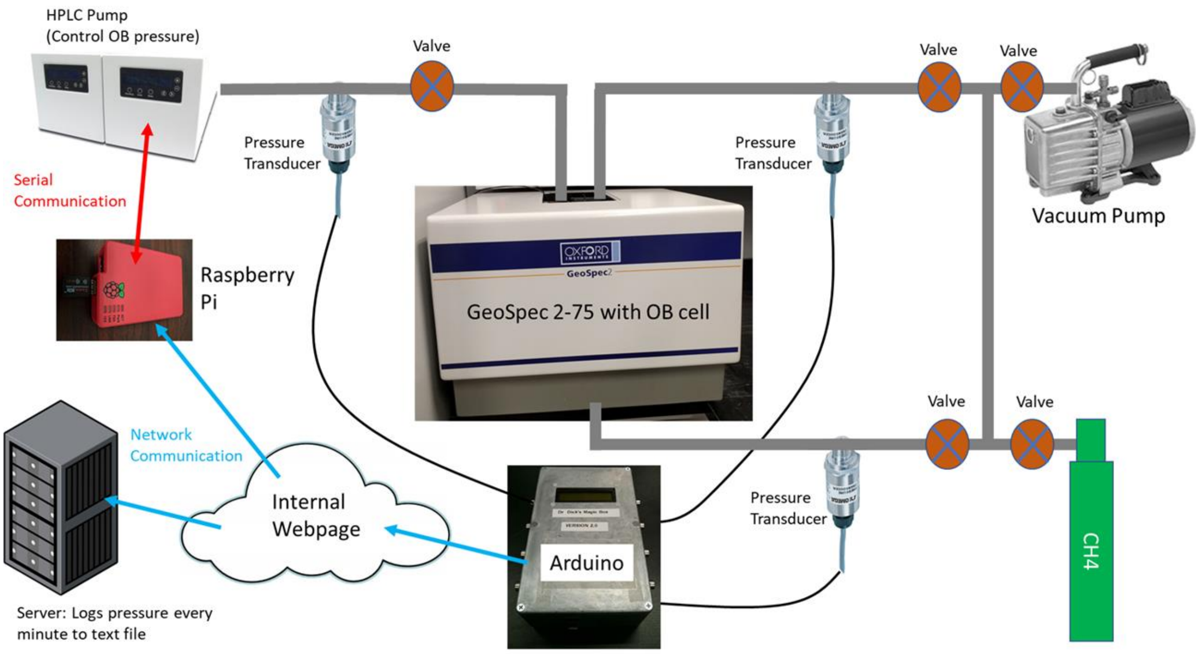

**Figure 1** - Experiment 1 Setup

following the procedure outlined in Section 2 of this paper.

### 3.2 Experiment 2

The second experiment determined the gas isotherm for a Lower Haynesville shale (LHSVL). The Upper Jurassic Haynesville Shale is an organic- and carbonate-rich mudrock deposited in a deep-water environment on the margins of the Gulf of Mexico, with average porosities around 11%. The average TOC of the Haynesville formation is 2.5% [13] with a range of 3% to 14% [14,15].

Table 1 summarizes the properties of the sample while Table 2 summarizes the NMR parameters employed. Sample LHSVL was not a solid core sample as sample BN 1. Instead this sample was made up of three irregularly shaped fragments (Figure 2).

**Figure 2**: LHSVL Sample

Coring is an issue with most shale samples so the goal of this experiment was to prove that the NMR gas isotherm determination can be employed on samples regardless of shape including crushed and powdered samples. In order to get the fragments into the overburden probe a new Teflon holder with the same outer dimensions as a standard core sample was built. Previous testing with Teflon using a GeoSpec 2-75 rock core analyzer has shown the digital filters remove the fluorine signal, thereby removing the signal from the Teflon core holder from the results. As shown in Figure 2, the samples were then placed into the new holder. The holder and the samples were then placed into the overburden NMR probe and the probe then inserted into the rock core analyzer. As in Experiment 1, the sample was evacuated with a vacuum pump, then as received or dry $T_2$ measurements were taken before the introduction of methane.

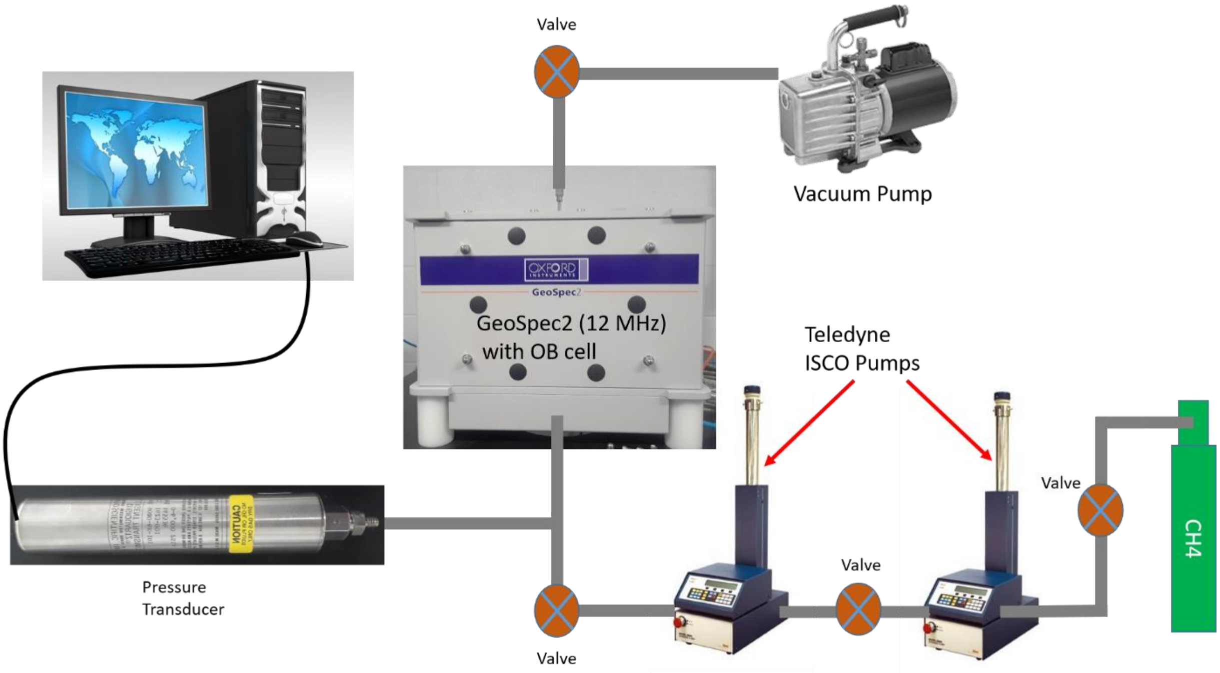

**Figure 3**: Experiment 3 Setup

No confining fluid was used in this experiment. Instead methane filled the confining volume of the probe. This simplified the experiment as it eliminated the need to use a second pump and an additional fluid as confining fluid. However, as a result of filling the probe with methane, the $T_2$ distributions recorded at elevated methane pressures had large amounts of signal from free methane. As will be outlined in the Results section of this paper, this added a step to the gas isotherm determination method outlined in the previous section.

### 3.2 Experiment 3

The experimental design for experiment 3 (Figure 3) was similar to experiment 2 except the core sample was one solid piece of rock and the Teflon core holder was not used. Table 1 shows the rock sample properties for the Bakken core used in this experiment. The Bakken shale sample was collected from the Viewfield area in Saskatchewan, Canada. The Upper and Lower members of the Bakken are black organic-rich shales the Upper Member shale have average TOC of 17.6% with an average porosity of 3% [16].

The methane gas supply was connected to an ISCO 260HL pump and an ISCO 260D pump. The pressure in the overburden cell was controlled using the valves and the constant pressure setting of the ISCO pumps. Independent pressure measurements of the overburden cell were obtained using a Paroscientific 9000K model pressure transducer.

The overburden cell and sample were evacuated using a vacuum pump, then the initial NMR $T_2$ distribution was obtained using an Oxford Instruments Geospec2 12 MHz rock core analyzer [17]. All data was again processed using GIT Systems Advanced Software. NMR parameters used for all $T_2$ measurements are shown in Table 2. Adsorption isotherms were determined at the following pressures (psi): 242, 494, 997 and 1593. Adsorption isotherms were carried out by raising the pressure in the cell to the desired pressure, setting the pumps to the constant pressure, and monitored through the course of the experiment. The NMR $T_2$ distributions were taken minutes apart for the first hour of the experiment and then hours apart as the experiment proceeded for 24 or more hours.

Following measurement of the gas isotherms for the Bakken sample, an experiment was completed examining the desorption isotherm of methane from the shale. This experiment was meant to improve our understanding of the processes controlling methane movement in the rock matrix. After the $T_2$ data collection was completed at the highest pressure (1593 psi), the overburden cell was allowed to degas over a period of minutes and when the pressure in the cell reached atmospheric pressure, the cell was re-sealed using the valves. The pressure was monitored over the next several days and $T_2$ measurements were obtained over that time.

## 4 Results

The left-hand panel of Figure 4 shows three $T_2$ distributions recorded for sample BN 1. The black trace is the background or as received distributions recorded at 0 psi of methane. The red and blue traces were recorded with a methane pressure of 2000 psi, with the red trace recorded within minutes of methane being introduced to the sample, and the blue trace was recorded hours after the introduction of methane. As expected, the blue trace has more signal than the red trace as methane has more time to penetrate the pores of the sample. If there was free methane surrounding the core then a relatively large peak should be observed near $10^3$ ms (see LHSVL and Bakken results below).

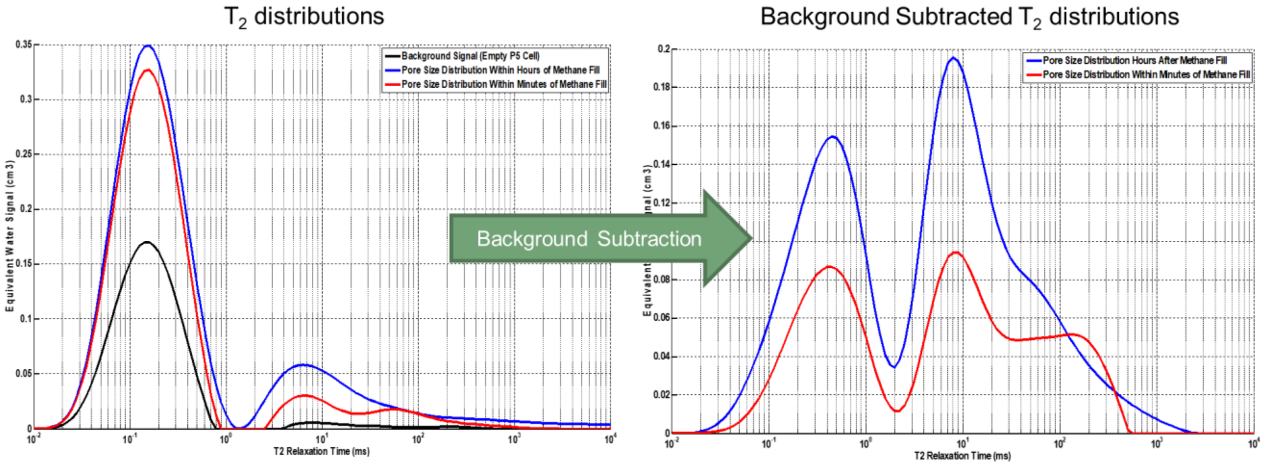

**Figure 4**: T$_2$ distributions For BN 1 Sample

The right-hand panel in Figure 4 shows the same T$_2$-distributions as the right-hand panel, but with the background T$_2$ distribution (black line in the right-hand panel) subtracted. The bimodal distribution of the subtracted T$_2$ distributions shows methane occupying small pores ($T_2 < 2$ ms) and methane occupying relatively larger pores ($T_2 > 2$ ms). The area under each of the blue curve and the red curve is the methane content in units of equivalent water volume. These volumes are converted to methane gas content and plotted as a function according to Step 4 of the procedure outlined in Section 2 of this paper.

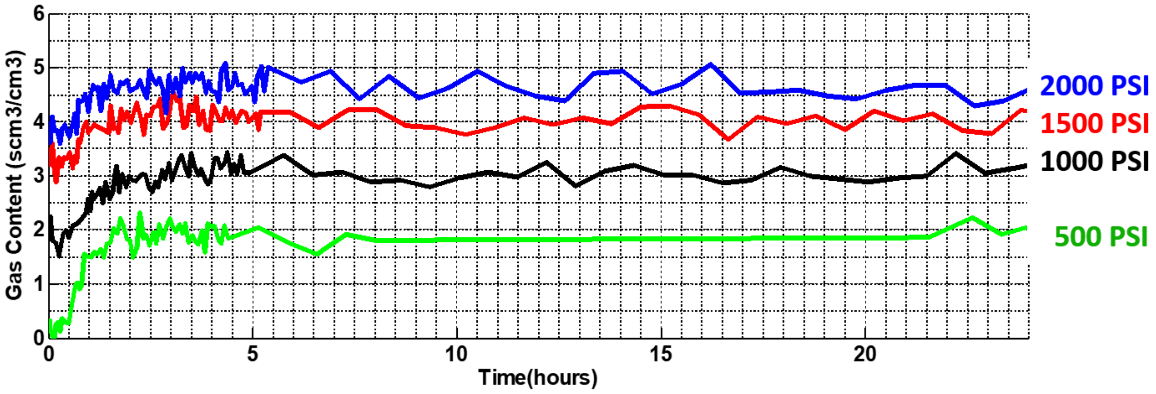

Figure 5 shows the plot of calculated gas content versus time for sample BN1. The figure shows that for each fill pressure of methane (green 500 psi, black 1000 psi, red 1500 psi, and blue 2000 psi) approximately 4 hours are required for methane to fully penetrate the pores of the sample and the amount of methane to stabilize. After 4 hours the measured gas content remained relatively constant (± 1%). The variability in the gas contents decreases after 5 hours but this is likely due to a reduced sampling frequency.

The average amount of methane after four hours was used to calculate the total gas isotherms for each pressure and is plotted as the blue trace in Figure 6. The green trace in Figure 6 is the calculated pore gas isotherm using equation 2 above while the red trace is the adsorbed gas isotherm and is calculated as the difference of the total gas content and the pore gas content. Each were calculated according to the procedure outlined in Section 2 of this paper. The pore gas content increases relatively linearly with pressure and only deviates from linearity at higher pressures where its behaviour begins to deviate from the ideal gas law according of the Van der Waals equation. The adsorbed gas content on the other hand is not linear. The amount of adsorbed gas increases quickly at lower pressures due to the large number of adsorption sites still available but there are a finite number of adsorption sites available so the change in gas content with increasing pressure declines with increasing pressure. Finally, the total gas isotherm is simply the sum of the pore gas isotherm and adsorbed isotherms and has properties similar to each. The adsorbed methane content for BN1 reaches 1.3 scm$^3$/cm$^3$ or 0.02 mmol/g of rock at 1500 psi, which is within the reported range of methane adsorption of 0.007 to 0.1 mmol/g [2].

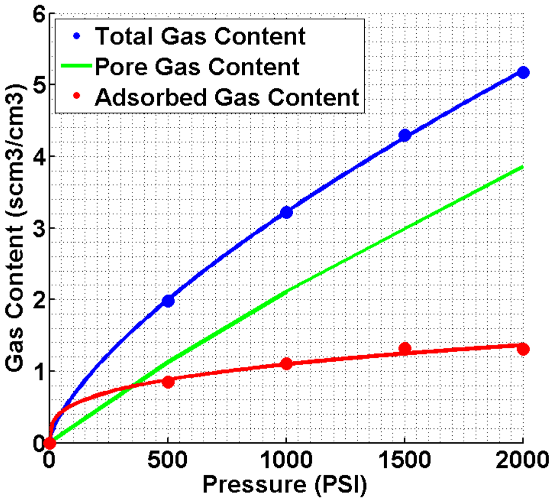

**Figure 6**: Gas Isotherm For Sample BN1

Figure 7 shows background subtracted $T_2$ distributions recorded for the fragmented LHSVL sample. The blue trace shows the distribution recorded with a pressure of 500 psi of methane while the red trace shows the distribution recorded at a pressure of 2000 psi. As expected, there is more methane present in the sample at 2000 psi than at 500 psi. What is more interesting about Figure 7, is the large signals present at slow $T_2$ (i.e. above 100 ms). This signal is too late to be originating in the pores of the shale sample. Typical shales have $T_2$ distributions with peak values around 0.1 to 10 ms. These late $T_2$ peaks are instead due to free methane present in the experiment. This was further confirmed in a T1-T2 map in experiment 3, where a large peak appeared at T1 = ~1000 ms, T2 = ~1000 ms and it was assumed to be bulk methane. As mentioned in the previous section, there is significant free methane in the LHSVL experiment because the confining volume of the overburden probe was filled with methane. To calculate the gas isotherm analysis for this sample, the free methane was removed from the $T_2$ distributions recorded at each pressure. From Figure 7, it is obvious that the removal of signal from free methane can be accomplished by simply applying a cut off to the $T_2$ distributions. For example, in Figure 7, only the signal below 223 ms (shown by the vertical green line) is included, which removes the free methane signal from the analysis. Once the distributions have the free methane signal removed, the gas isotherm calculation continues according to the method laid out in Section 2 of this paper.

The final gas isotherms generated from the NMR data for LHSVL are shown in Figure 8 and the shape of the curves are similar to what was observed in the BN 1 sample above. The adsorbed methane content for LHSVL reaches 4.0 $scm^3/cm^3$ or 0.07 mmol/g of rock at 1500 psi, which is close to other reported data 0.09 mmol/g [18].

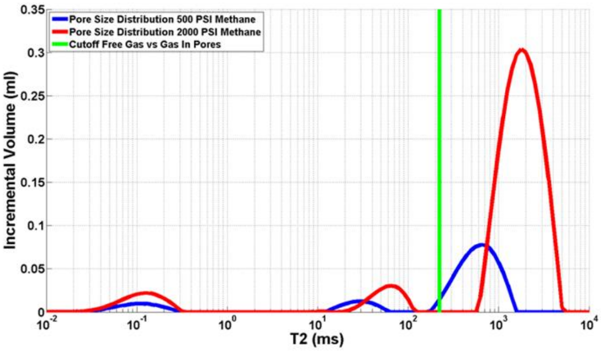

**Figure 7**: $T_2$ Distributions for Sample LHSVL

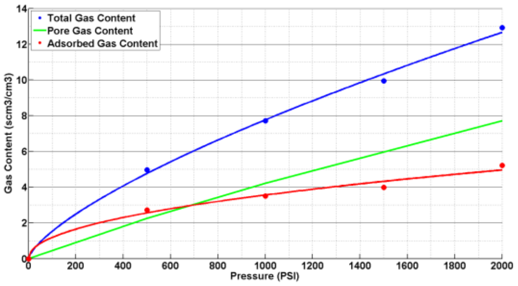

**Figure 8:** Gas Isotherm For Sample LHSVL

Figure 9 shows a background subtracted $T_2$ distribution recorded for the Bakken sample at pressure of 1500 psi. $T_2$ measurements ended before the relaxation was complete because the focus was on characterizing the signal between 0 and 100 ms, the methane associated with the rock. The peak above 200 ms is caused by free methane and was removed to complete the gas isotherm analysis similar to the LHSVL sample described above.

Figure 10 shows the gas isotherm generated for the Bakken core, which is different from the two cores described above. The adsorbed gas content of the Bakken core is greater than the Haynesville core, which is likely due to the higher %TOC in the Bakken core, and TOC preferentially adsorbs hydrocarbon gases. The pore gas content of the Bakken core is significantly lower than the other two cores. The adsorbed gas for the LHSVL sample was approximately 4 $scm^3/cm^3$ at 1000 psi whereas the pore gas content at 1000 psi for the Bakken sample was approximately 1 $scm^3/cm^3$. This is consistent with the lower porosity of the Bakken sample compared to the Hayneville sample (Table 1), which limits the volume available for pore gas. The adsorbed methane content for this Bakken core is 0.3 mmol/g of rock at 1500 psi, which is below the reported range of $CO_2$ adsorption isotherms 1.0 to 3.5 mmol/g [19]. LPGA results for the Bakken were between 1.75 and 3.25 $cm^3/g$ [20], which is less than the adsorption reported here (approximately 7 $scm^3/g$) but the LPGA analysis was carried out with $N_2$ at nearly 1500 psi less than the experimental conditions here.

A review of the BN-1, LHSVL and Bakken isotherms shows that the results are consistent with published literature and the distribution of peaks can be used to quantify methane in tight rocks. The results are limited at low pressures because the relatively small amount of methane is insufficient to produce a reliable signal, though the examination of hydrocarbon gases and source or reservoir rocks is typically carried out at higher pressures. Further work is also required to determine the accuracy of the pore gas content using Van der Waals equation as well as exploring employing a Langmuir isotherm to fit to the adsorption isotherm data.

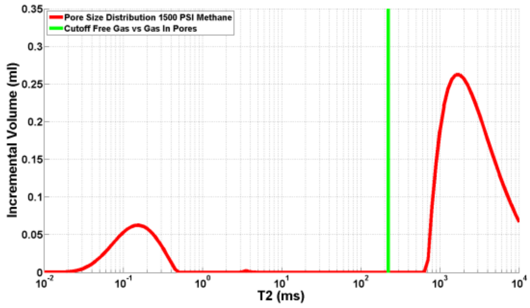

**Figure 9**: $T_2$ distribution At 1500 psi for Bakken Sample

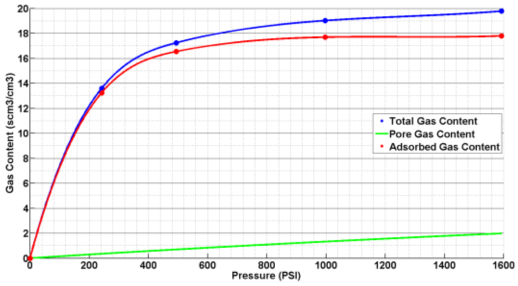

**Figure 10**: Gas Isotherm for the Bakken Sample

The experiments with the Bakken core continued beyond the measurement of the gas isotherm. $T_2$ distributions were recorded as the core degassed. Figure 11 shows the final background subtracted $T_2$ distributions recorded during the degassing stage of the experiment. The upper panel shows the $T_2$ distributions recorded on the same y-axis scale as the data recorded with a pressure of 1500 psi (Figure 9) where as the lower panel shows the $T_2$ distributions plotted with a more reduced y-axis scale making it easier to see the peaks. Comparing the upper panel with Figure 9, it is obvious that the amount of gas in the pores (peak near 0.1ms) has been reduced during degassing but gas is still present. This methane signal is most likely now from residual adsorbed gas that is taking time to leave the pore walls.

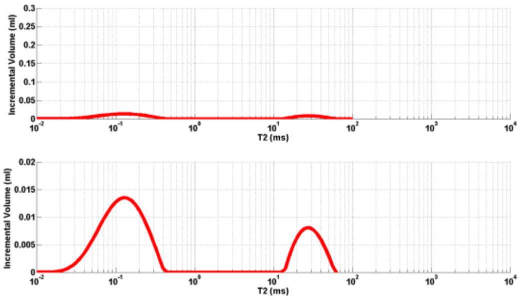

**Figure 11**: $T_2$ Distribution Measured For Bakken Sample at the End of Degassing

Further evidence that the methane signal is coming from residual adsorbed gas can be observed by plotting the total gas content determined from the NMR measurements during degassing as a function of time, which is presented in Figure 12. The amount of gas in the core declines to approximately 15 scm$^3$/cm$^3$ in the first 12 minutes followed by a gradual decrease in total gas content. The methane is slowly moving out of the core. Once the methane is out of the core it is no longer present in the total gas content calculation as it becomes free methane and is removed from the calculations. The total gas content remains near 15 scm$^3$/cm$^3$ after almost two days of degassing. Based on the isotherm (Figure 10), the remaining methane in the core is likely adsorbed to the pore walls but some methane may remain in the pores. .

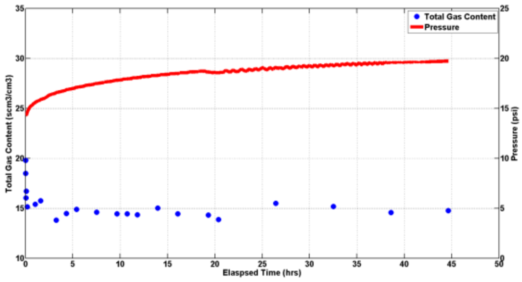

**Figure 12**: Total Gas Content and Pressure During Degassing for Bakken Sample

Further evidence of this degassing behavior can be interpreted from the experimental pressure that was recorded simultaneously with the total gas content and is also plotted in Figure 12. As expected, the pressure is increasing over time during degassing as the adsorbed gas leaves the pore walls where it does not contribute to measured gas pressure in the overburden cell and migrates to pore gas or free methane resulting in an increase in gas pressure in the cell. After the cell was opened, gas pressure declined to atmospheric pressure (14.3 psi) and increased during the degassing period to 19.7 psi. Future work will determine the volume of the NMR cell so that the declining core gas content can be compared to the rising cell pressure and an improved approach can be used to examine the transport processes controlling methane degassing from the core.

Another interesting result from Figure 11, is the appearance of a second peak between 10 and 100 ms that was not present during the gas isotherm measurement. We believe that this is signal from methane in a fracture within the core. This signal was not present in Figure 9 as the confining pressure was high enough (1500 psi) to close this fracture. Releasing the confining pressure during degassing has caused the fracture to open allowing gas from the smaller pores to migrate into it. In addition, if you look closely at Figure 9 you see a small peak at approximately 2.5 ms. This small peak was present in all the 1500 psi $T_2$ distributions recorded during the gas isotherm measurement and might be the same fracture as observed in the degassing experiment. At 1500 psi, the fracture would be closed leading to a decrease in the amount of gas in it and a decrease in its $T_2$ relaxation time.

Figure 13 shows the total gas content of the core as it degases (blue circles) as well as the gas content of the first

$T_2$ peak (black circles) and the gas content of the second $T_2$ peak from 10 to 100 ms (grey circles). The total gas content and gas content of the first $T_2$ peak follow the same pattern. The first $T_2$ peak represents the majority of the gas in the core, which is corroborated by the larger $T_2$ peak in Figure 11. The first peak represents the adsorbed gas on the core and the gas in the small pores. The second $T_2$ peak, contains less gas than the first peak, and increases over time. The higher $T_2$ value for this peak suggests this peak represents gas filling larger secondary porosity, possibly a fracture that developed in the core during the pressure-depressure cycle and that future degassing phases may need to be carried out at a slower rate to avoid the creation of such features. However, degassing at too slow a rate may miss important information regarding gas transport at early time.

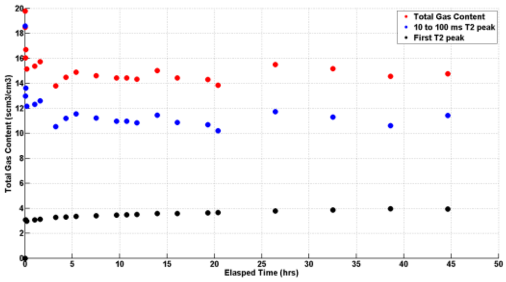

**Figure 4**: Calculated Total Gas Content For The Core Sample And Calculated Gas Content Both $T_2$ Peaks Observed.

The change in the total gas content over time shown as blue circles in Figure 13 is the rate that methane adsorbed on to the core and methane in the pores of the core are able to escape the core. The calculated total gas content desorbed from the core was calculated by subtracting the total gas contents from the total gas content of the core at the completion of the 1593 psi adsorption isotherm (19.8 $scm^3/cm^3$) and are shown in Figure 14 as the experimental data.

The rate of methane loss from the core was examined using the diffusion equation shown by [21].

$$Q(t) = Q_{tot}\sqrt{1 - e^{-BKt}}$$

Where Q(t) is the desorbed gas content ($scm^3/cm^3$) at time t (s); $Q_{tot}$ is the total desorbed gas content from the beginning of the experiment to the end; $B = 4\pi^2 D/d^2$; and D the diffusion coefficient ($m/s^2$); d the radius of the sample (m); and K is a unitless correction factor. When the B-value ranges between $6.58 \times 10^{-3}$ to $6.58 \times 10^{-6}$, which was the case for this work, the K-value is 0.96 [21]. The calculated total degassed contents are shown as blue circles in Figure 14. The calculated gas loss by diffusion matches the pattern of the experimental data suggesting the equation is adequate to examine gas loss from the core. The diffusion coefficient used for this calculation was $2.6 \times 10^{-9}$ $m^2/s$, which is significantly lower than $2.1 \times 10^{-5}$ $m^2/s$ for methane in air, but greater than the $10^{-12}$ $m^2/s$ values obtained for coal [21]. The calculated diffusion coefficient suggests that while diffusion may play a role in the rate of methane lost from the core, another process (e.g. advection) may be a significant process. This is not surprising given that at the beginning of the degassing phase the core was at least near equilibrium with 1593 psi and surrounded by atmospheric pressure, which should result in some amount of gas flow out of the core.

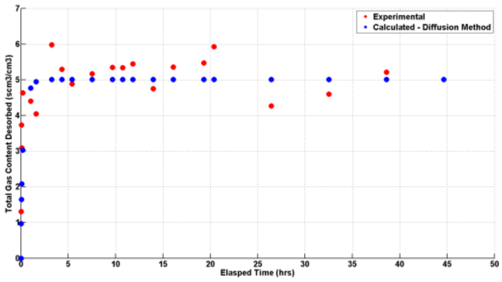

**Figure 5**: Total Gas Content ($scm^3/cm^3$) Removed From The Core And Calculated Total Gas Content Removed From Core Using The Diffusion Equation.

## References

1. X. Cui, A.M.M. Bustin, and R.M. Bustin, “Measurements of gas permeability and diffusivity of tight reservoir rocks: different approaches and their applications,” *Geofluids*, vol. 9, no. 3, Aug. 2009, doi: 0.1111/j.1468-8123.2009.00244.x.
2. M. Gasparik, P. Berier, Y. Gensterblum, A. Ghanizadeh, B.M. Kroos and R. Littke, “Geological controls on the methane storage capacity in organic-rich shales,” *Int. J. Coal Geol.*, vol. 123, no. 1, pp 34-51, Mar. 2014, 10.1016/j.coal.2013.06.010.
3. T. Alexander, J. Baihly, C. Boyer, B. Clark, G. Waters, V. Jochen, J. Le Calvez, R. Lewis, C.K. Miller, J. Thaeler, and B.E. Toelle, “Shale Gas Revolution,” *Oilfield Rev.*, vol. 23, no. 3, pp. 40-55, Sep. 2011.
4. C. Horch, S. Schlayer, F. Stallmach, “High-pressure low-field 1H NMR relaxometry in nanoporous materials,” *J. of Magn. Reson.*, vol. 240, pp 23-33, Mar. 2014, doi: 1 0.1016/j.jmr.2014.01.002.
5. Y. Liu, C. Wang, “Determination of the Absolute Adsorption Isotherms of $CH_4$ on Shale with Low-Field Nuclear Magnetic Resonance,” *Energy Fuels*, vol. 32, no. 2, pp. 1406-1415, Jan. 2018, doi: 10.1021 /acs.energyfuels.7b03428.
6. *Geo-Spec 2-75 Rock Core Analyzer User Manual*, Version 1.8, Oxford Instruments, Tubney Woods, Abingdon, Oxon, UK, 2018.
7. *P5 Overburden Probe User Manual*, Version 1, Oxford Instruments, Green Imaging Technologies, Oxford Instruments, Tubney Woods, Abingdon, Oxon, UK 2016.
8. *GIT Systems and LithoMetrix User Manual*, Version 1.9, Green Imaging Technologies, Fredericton, NB, Canada, 2016.
9. R.M. Pollastro, D.M. Jarvie, R.J. Hill, “Geologic framework of the Mississippian Barnett Shale, Barnett-Paleozoic total petroleum system, Bend

arch–Fort Worth Basin, Texas," *AAPG Bull.*, vol. 91, no. 4, pp. 405-436, doi: 10.1306/10300606008.

10. K.A. Bowker, "Recent developments of the Barnett Shale play, Fort Worth Basin" *W. Texas Geol. Soc. Bull.*, vol. 42, no. 6, pp 4-11. Art. No. 10126.
11. Arduino Microcontroler Homepage, www.arduino.cc (accessed Feb. 1, 2018).
12. Raspberry Pi Computer Homepage, www.raspberrypi.org (accessed Feb. 1, 2018).
13. N.R. Jabri, "Chemostratigraphy and paleoenvironment of the Haynesville Formation, Harrison County, Texas," M.Sc. thesis, Geol. Dept., Univ. Houston, Arlington, Texas, 2013.
14. F.P. Wang F.P. and U. Hammes, "Effects of reservoir factors on Haynesville fluid flow and production," *World Oil*, vol. 231, pp. D3-D6.
15. U. Hammes, H.S. Hamlin, and E.E. Thomas, "Geologic analysis of the Upper Jurassic Haynesville Shale in east Texas and west Louisiana," *AAPG Bull.*, vol. 95, no. 10, pp. 1643-1666, Oct. 2011, doi: 10.1306/02141110128.
16. L.K. Kreis, A.L. Costa and K.G. Osadetz, "Hydrocarbon potential of Bakken and Torquay formations, southeastern Saskatchewan," in *Saskatchewan and Northern Plains Oil & Gas Symposium* C.F. Gilboy and S.G. Whittaker, Eds. 2006 , pp. 118-137.
17. *Bench-top Imager Hardware User Manual*, Version 1.1, Oxford Instruments, Tubney Woods, Abingdon, Oxon, UK, 2006, pp. 1-32.
18. A. Merkel, R. Fink and R. Littke, "The role of pre-adsorbed water on methane sorption capacity of Bossier and Haynesville shales," *International J. Coal Geol.*, vol. 147-148, no.1, pp. 1-8, Aug. 2015.
19. S. Kumar, "Rock-fluid interaction and phase properties of fluids in nano- and sub-nanopores of shales: sorption-based studies." Ph.D. dissertation, Dept. Petrol. Eng., Colorado School of Mines, 2016.
20. Y. Liu, B. Shen, Z. Yan, P. Zhao, "Structure characterization and the controlling factors of the Bakken Formation," *Energies*, vol. 11, no. 11, pp. 2879-2894, Oct. 2018, doi: 10.3390/en11112879.
21. G. Ni, B. Lin, C. Zhai, Q. Li, S. Peng, X. Li, "Kinetic characteristics of coal gas desorption based on the pulsating injection," *Int. J. Min. Sci. Tech.*, vol. 24, no. 5, pp. 631-636, Sep. 2014, doi: 1 0.1016/j.ijmst.2014.03.023.

# Dielectric Polarisation In Partially Saturated Shales

*Paul R.J.* Connolly[1], *Matthew* Josh[2], *Keelan* O'Neill[1], *Eric F.* May[1], *Michael L.* Johns[1]

**1**Department of Chemical Engineering, M050, The University of Western Australia, 35 Stirling Highway, Crawley WA 6009, Australia.

**2**CSIRO Energy, ARRC Laboratories Kensington, Perth 6151, WA, Australia.

**Abstract.** Dielectric measurements of reservoir rocks are used to estimate important petrophysical properties such as water filled porosity and pore surface textures. However, complex dielectric polarisation processes that occur in rocks are strongly dependent on frequency, making physically meaningful interpretation of broadband dielectric data difficult. Here we demonstrate the application of Tikhonov regularisation methods to compute dielectric relaxation time distributions from broadband (40Hz to 110MHz) dielectric data for a shale sample at varying partial saturation. Furthermore, via the Kramers-Kronig relation the contribution from in phase conduction currents to the imaginary component of the dielectric response was quantified. The evolution of dielectric polarisation processes with increasing moisture content was analysed directly from changes in relaxation time distributions. It was found that the dominant polarisation mechanism up to a critical partial saturation occurred exclusively in the electrical double layer (EDL). Above this critical partial saturation electro-diffusion mechanisms acting between the diffuse layer and the bulk electrolyte controlled the low frequency response. This work provides valuable insight into dielectric polarisation mechanisms in shales, and demonstrates such measurements are sensitive to EDL properties and electro-diffusion length scales that are relevant to characterising pore properties in shales.

## 1 Introduction

The complex broadband (Hz to GHz) dielectric response of moist rocks arises from a range of polarisation processes related to individual molecules, interfacial charge phenomena and electrochemical potentials [1], [2]. Several authors have highlighted the potential of using electrical relaxation times to extract important hydraulic properties of rocks such as permeability [3], [4], textural properties of pore surfaces [5] and pore and pore throat sizes [6], [7]. However, despite many experimental studies [8] and theoretical considerations [9], a complete model for broadband dielectric polarisation in permeable rocks is still yet to be realised [10]. A limiting factor in this lack of physical insight is the widespread application of empirical models that are based on dielectric relaxation for a single dipole [11]–[13]. The alternative, and more physically appropriate approach, of fitting broadband dielectric dispersion data with a continuous distribution of relaxation times [14]–[16], of which there are only few examples in the literature that involved spectral induced polarisation measurements [17]–[19].

Here we demonstrate the successful application of Tikhonov regularisation methods to compute continuous distributions of dielectric relaxation times directly from broadband (40 Hz – 110 MHz) frequency domain data for a shale rock at varied partial saturation. The evolution of dielectric relaxation distributions was studied as a function of water content, with measurements of 6 incremental saturation states ranging from dry to fully saturated. Analysis of the relaxation time distributions obtained as moisture content increased reveals new insights into the consequent changes in EDL polarisation processes. Furthermore, we attempt to quantify the contribution of in-phase conduction currents by using the inverted relaxation time distribution models and the Kramers-Kronig relation to link the solutions obtained for the real and imaginary components of the dielectric response.

## 2 Background and Theory

### 2.1 Effective Electrical Properties

In an applied electrical field ($\vec{E}$), the effective current density ($\overrightarrow{J_E}$) of a homogenous material is composed of two parts: conduction currents ($\overrightarrow{J_C}$) and displacement currents ($\overrightarrow{J_D}$),

---

[*] Corresponding author: paul.connolly@uwa.edu.au

$$\overrightarrow{J_E} = \overrightarrow{J_C} + \overrightarrow{J_D} \tag{1}$$

where,

$$\overrightarrow{J_C} = \sigma \vec{E} \tag{2}$$

and,

$$\overrightarrow{J_D} = \varepsilon \frac{\partial \vec{E}}{\partial t} \,. \tag{3}$$

Here $\sigma$ is the electrical conductivity and $\varepsilon$ the dielectric permittivity [20]. Conduction currents are defined as an ordered translation of free charge, which for rocks corresponds primarily to the translation of charge carrying ions present in fluids within the pore space. The magnitude of conduction is related to the charge, charge density and drift velocity [21] of the free charges being translated. Displacement currents relate to the time dependent polarisation processes of bound charges [22], which can occur from an atomic scale to macro assemblages of molecules. The extent of electrical polarisation is related to the density of effective dipoles, their polarizability and mobility.

In a time varying electrical field ($\vec{E}$) with angular frequency $\omega = 2\pi f$ , the relationship between the complex frequency dependence of conductance and displacement currents can be derived from Maxwell's equations [22],

$$\overrightarrow{J_E}(\omega) = \sigma^*(\omega)\vec{E} = \varepsilon^*(\omega)\frac{\partial \vec{E}}{\partial t} \tag{4}$$

where,

$$\varepsilon^*_{(\omega)} = \left[\varepsilon'_{(\omega)} + \frac{\sigma''_{(\omega)}}{\omega\varepsilon_0}\right] - i\left[\varepsilon''_{(\omega)} + \frac{\sigma'_{(\omega)}}{\omega\varepsilon_0}\right] \tag{5}$$

and

$$\sigma^*_{(\omega)} = \left[\sigma'_{(\omega)} + \varepsilon''_{(\omega)}\omega\right] + i\left[\sigma''_{(\omega)} + \varepsilon'_{(\omega)}\omega\right] \tag{6}$$

Here the effective dielectric permittivity ($\varepsilon^*_{(\omega)}$) The imaginary and real components of the permittivity ($\varepsilon''_{(\omega)}$) and conductivity ($\sigma'_{(\omega)}$) relate to ohmic conductance or the translation of charges, respectively, while real permittivity ($\varepsilon'_{(\omega)}$) and imaginary conductivity ($\sigma''_{(\omega)}$) components relate to the capacitive susceptance or the displacement of charges [20]. The measured electrical quantities $\sigma^*(\omega)$ and $\varepsilon^*(\omega)$ are in fact composites of complex conduction and polarisation processes. It is also useful to normalise $\varepsilon^*(\omega)$ by the dielectric permittivity of free space $\varepsilon_0$ and report the relative permittivities $\varepsilon_r = \varepsilon^*/\varepsilon_0$.

## 2.2 Dielectric Relaxation Time

For a single dipole, the frequency dependent complex dielectric permittivity, $\varepsilon^*_{(\omega)}$, is given by the Debye model.

$$\varepsilon^*_{(\omega)} - \varepsilon_\infty = \frac{\Delta\varepsilon}{1 + i\omega\,\tau} \tag{7}$$

Here $\tau$ is the characteristic relaxation time, $\varepsilon_\infty$ is dielectric permittivity at the high frequency limit and $\Delta\varepsilon$ is the difference in permittivity between the high and low frequency limits. While the Debye model eloquently describes the response of a single dipole, heterogenous rocks represent complex and non-ideal dielectric systems where multiple dielectric processes occur because of strong surface-electrolyte charge interactions, highly varied compositions and complex pore structures. To better represent the ensemble of relaxation processes that occur in many complex dielectrics, the most widely used approach has been to empirically alter the exponential form of the Debye model by broadening [11] or combining broadening with functional asymmetry [13]. The Havriliak-Negami (HN) adaptation is one such model and takes the form,

$$\varepsilon^*_{(\omega)} - \varepsilon_\infty = \frac{\Delta\varepsilon}{(1 + (i\omega\,\tau)^\alpha)^\beta} \tag{8}$$

where both $\alpha$ and $\beta$ are empirical fitting parameters ranging between 0 and 1. Note that if $\beta$ is set to 1 the HN equation reduces to the Cole-Cole equation [11], and if $\alpha$ is set to one it reduces to the Cole Davidson equation [12]. Although capable of fitting some complex dielectric data, the relationship of the values obtained for these empirical fitting parameters with physical processes is ambiguous. Furthermore, for broadband dielectric data covering frequency ranges that span many orders of magnitude, a combination of several such functions are usually required to fit the experimental data obtained, requiring a priori assumptions about the number of relaxation processes and approximate relaxation times[23]–[25].

Alternatively, broadband dielectric dispersion data can be described by a continuous distribution of Debye-like processes,

$$\frac{\varepsilon^*_{(\omega)} - \varepsilon_\infty}{\Delta\varepsilon} = \int_{\tau_{\min}}^{\tau_{\max}} \frac{g(\tau)}{1 + i\omega\,\tau}\,d\tau \tag{9}$$

where $g(\tau)$ represents the probability distribution of characteristic relaxation times. Analysis of the dielectric response data using this form provides distinct benefits over parametrised methods as dispersion processes can be assessed directly from relaxation time distributions. Numerically, however, this analysis is more difficult as the solution to the integral equation is ill-conditioned (i.e., many of the solutions for $g(\tau)$ are linearly dependent and small changes in the signal can disproportionately impact the solution). One way to overcome the numerical problems associated with the ill-conditioned nature of the integral equation and to manage contributions of experimental noise is through the use regularisation methods, as developed for example by Tikhonov [26].

### 2.3 Dielectric Polarisation in Complex Materials

Dielectric dispersion observed in moist rocks arises from several polarisation mechanisms of effective dipoles that vary in mobility and size. At high electric field frequencies (>1 GHz) only small mobile dipoles, which typically correspond to individual molecules, and atomic and ionic structures can be polarised. As frequency is reduced, less mobile and larger effective dipoles related to restricted molecules, assemblages of molecules, and surface effects start contributing to the measured dielectric permittivity, as do electro-diffusion processes. Loewer et al. [23] provides a good overview and graphical representation of these polarisation mechanisms and their relationship to the frequency of applied electric field. Numerous models have been developed to describe electrical processes in rocks, which can be broadly divided into those derived from bulk properties [27]–[31] and those that incorporate surface related mechanisms (i.e. conduction and polarisation of surface charges) [1], [9], [32], [33].

Experimentally, Maxwell-Wagner-Bruggeman-Hanai (MWBH) theories have been shown to successfully describe experimental results well for most moist rocks at frequencies above 10 MHz [34]. However, at frequencies lower than this, contributions from surface processes to conduction and displacement currents can be much stronger than those accounted for by bulk effect models alone [35].

Surface polarisation and conduction models attempt to account for charged ions and effective dipoles, whose behaviour and assembled structure is defined by their interactions with an active surface. When a solid, charged surface is in contact with an ion-containing solution, an electrical double layer (EDL) will form in the vicinity of that surface. The EDL structure consists of tightly bound, immobile inner layer of ions with the opposite charge to that of the surface known as the Stern layer. Beyond the Stern layer, an ionic atmosphere called the diffuse layer is formed by ions of both charges, with a slightly higher concentration of those with the charge opposite to the surface [36].

O'Konski (1960) considered polarisation of charge carriers within an EDL moving tangentially along the surface of a spherical particle with radius *a*. In this approach, the surface conductivity ($\sigma_s$) is considered to account for the mobility of charges in the EDL and displacement normal to the surface is not permitted. The relaxation time ($\tau_s$) for establishing polarisation was hence derived,

$$\tau_s = \frac{a(\varepsilon_2 + 2\varepsilon_1)}{8\pi\sigma_s} \qquad (10)$$

where $\varepsilon_1$ and $\varepsilon_2$ are the dielectric permittivities in the low frequency limit corresponding to the electrolyte and particle respectively. Schwarz (1962) argued that O'Konski's approach of expanding MW theory to include ohmic surface conductance around the particle was not enough to account for experimental observations, with dielectric permittivities many orders of magnitude higher than their constituents found for some composite materials. Instead, the relaxation time for polarisation in the EDL should be considered as controlled by the diffusion of surface bound ions ($D_s$) [37],

$$\tau_s = \frac{a^2}{2D_s} \qquad (11)$$

Comparisons of such models to experiments with suspensions of polystyrene spheres in an electrolyte solution showed improved agreement [32]. However, for polarisation in an time-dependent field, the surface ion diffusion interpretation is only valid in the limit of small particle size; for large particles the observed relaxation time is better described by the surface conductivity description [35]. Models which define the polarisation as occurring exclusively in the EDL (i.e. no interaction with the bulk electrolyte) are sometimes term *closed EDL* models [35]. Although applicable to a wide range of materials, these fixed layer models fail to capture the very large low frequency dielectric response observed in, for example, colloidal systems [38] and clay rich sands [39].

The boundary conditions of the *closed* double layer models can be altered to allow for diffusional flux of counter and co-ions from the EDL to the bulk electrolyte [37], [40], with the resulting formalism sometimes referred to as an *open* double layer model **Figure 1**. The driving force for this flux is a result of electrochemical potentials that arise between the bulk electrolyte and the distorted charge distribution of the polarised electrical double layer. These diffusive fluxes of ions can occur out of phase with the applied field and result in very large displacement currents, which is consistent with many experimental observations [39]. The characteristic relaxation times for these systems are also controlled by diffusion; however, in this case it is the bulk diffusion of counter and co-ions across a length scale *a,* which reflects the compositional front associated with the electrochemical potential,

$$\tau_D = \frac{a^2}{2D} \qquad (12)$$

The exact dielectric polarisation mechanisms that occur in clay rich rocks are complex and likely to be a convolution of multiple different phenomena dependent on various length and time scales. Having a better fundamental understanding of the different polarisation process enables the interpretation of observed relaxation times in terms of various length scales. This in turn may lead to more accurate applications of dielectric relaxation time models to determine various key properties of rock samples that are otherwise difficult to determine.

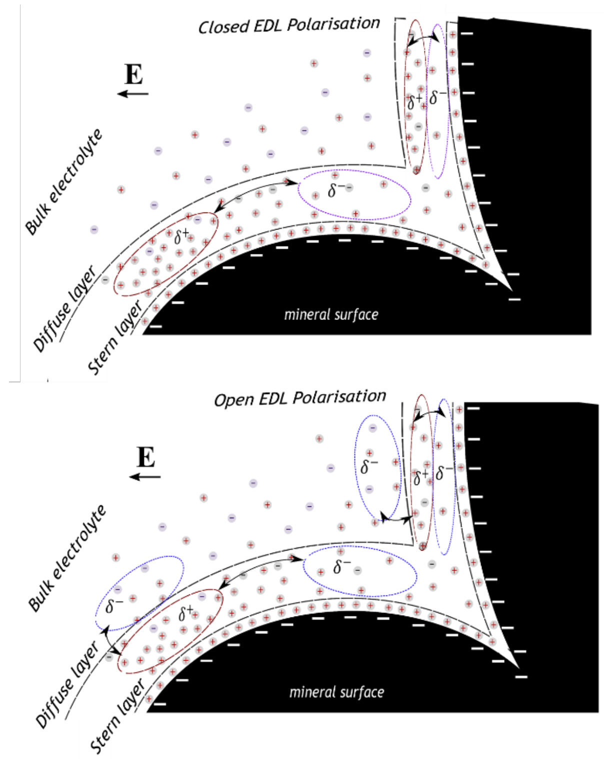

***Figure 1**. schematic of open and closed EDL polarisation processes. Arrows indicate charged ion transfer between positive and negative domains of effective dipoles.*

# 3 Method

## 3.1 Samples

This study involved an American shale sample, which after acquisition from a well the sample was air dried, and thus still contained remnant formation salt. Dielectric measurements were made on a thin disc 8 mm thick and 25.4 mm in diameter which was cut from the original plug. The flat surfaces of the samples were cut with a tolerance of ±0.08 mm.

**3.2 Saturation Protocol** The sample was measured at 6 saturation states ranging from dry to 100% saturated. First, the ‘as received’ shale sample was left in four different RH environments allowing for it to reach several different partial saturation states. Specifically, RH conditions of 99%, 75%, 43% and 23% were generated by placing saturated salt solutions of potassium sulfate, sodium chloride, potassium carbonate and potassium acetate, respectively, into temperature-controlled glass desiccators. The sample was removed periodically for weighing and equilibrium saturation was determined when the mass had stabilised to within approximately $\pm$ 0.0005 g; this process typically took 6 weeks. The effect of exposing shale to different RH environments was to vary its saturation state by the addition of pure $H_2O$ vapour, which effectively diluted or concentrated any electrolytes in the pore space.

Following this, the samples were placed under vacuum for 48 hrs and then pressure saturated (150 bar) with 1% NaCl solution, after which they were left for a further 48 hrs at pressure. Finally, the samples were dried in a vacuum oven at 105˚C for 3 weeks.

## 3.3 Dielectric Measurements

To remove the effects of ohmic conduction and electrode polarisation we made measurements with a regenerated cellulose sheet that acted as a blocking film in place between the sample and electrodes [41]. Repeat measurements were also made without the blocking film in place to record the equivalent conductivity. After each measurement the sample was rotated 180° and a repeat measurement was made, with the average of the two measurement reported here. Hence, a total of 24 individual test were conducted on this sample over the course of the experimental procedure.

At each saturation state, capacitance and resistance measurements were made using the three terminal parallel plate method, which includes the addition of a guarding electrode that minimises stray edge effects. Samples were placed in between the two platens (20 mm sensing diameter) with a small compression force applied using a manual hydraulic pump to ensure a firm surface contact. The dielectric measurement cell was connected to an Agilent 4294A impedance analyser which has a basic impedance accuracy of $\pm 0.08\%$ and covers a broad frequency range of 40 Hz to 100 MHz. Parasitic capacitance contributions associated with the transmission lines and terminals were subtracted from the experimental data by conducting calibration measurements at the beginning of each experimental run.

## 3.4 Regularisation

To solve for $g(\tau)$ from logarithmically spaced data we first introduce the following normalization condition,

$$\int_{\tau_{max}}^{\tau_{min}} g(\tau) d(\ln \tau) = 1 \qquad (16)$$

Then, through the Kramers-Kronig relation, the measured real and imaginary components of the dielectric permittivity can be represented by a calculation based on a specified $g(\tau)$,

$$\varepsilon'_{(\omega)} = \varepsilon_\infty + (\Delta\varepsilon) \int_{\tau_{max}}^{\tau_{min}} \frac{g(\tau)}{1+\omega^2\tau^2} d(ln\tau) + s_n(\omega) \qquad (17)$$

$$\varepsilon''_{(\omega)} = (\Delta\varepsilon) \int_{\tau_{max}}^{\tau_{min}} \frac{g(\tau)\omega\tau}{1+\omega^2\tau^2} d(ln\tau) + s_n(\omega) \qquad (18)$$

Here $s_n(\omega)$ is the noise associated with the experimental measurement. This more mathematically complex representation is a Fredholm integral of the first kind. The task then becomes to solve the inverse problem to determine $g(\tau)$ from the measured complex dielectric permittivity. Regularisation methods, such as minimizing the residual norm, can be used to solve these Fredholm integrals for approximate solutions but discrete noisy signals can lead to unrealistic, highly oscillatory solutions. A well-established method for generating robust solutions for noisy data is Tikhonov regularisation

[26] where the minimisation quantity, $H$, is defined as [42],

$$H(\alpha) = \sum_{j} \left[\varepsilon_j^{exp} - \varepsilon_j^{est}\right]^2 + \alpha \|g(\tau)\| \tag{19}$$

where $\varepsilon_j^{exp}$ are the experimental data, $\varepsilon_j^{est}$ is the estimated solution and $\alpha\|g(\tau)\|$ is the penalty term which balances the impact of noise to the fidelity of the final answer. The summation extends over both the real and imaginary components (i.e. contains 2N elements where N is the number of frequencies at which $\varepsilon_j^{exp}$ were measured). This method allows for the simultaneous regression real and imaginary data for a single $g(\tau)$ solution. However, regression of a single N element (i.e. for either real or imaginary component only) is also easily implemented. Relaxation time models can then be translated between real and imaginary permittivity via the Kramer-Kronig relation.

In our implementation the penalty term is proportional to the second derivative of $g(\tau)$ with respect to $(\ln \tau)$,

$$\|g(\tau)\| = \int_{D}^{0} [g"(\tau)]^2 d(\ln \tau) \tag{20}$$

The magnitude of the penalty term is governed by the smoothing coefficient $\alpha$. Translating this to matrix form we get,

$$H(\alpha) = |\boldsymbol{Rg} - \boldsymbol{b}|^2 + \alpha\|\boldsymbol{Lg}\| \tag{21}$$

$\boldsymbol{R}$ is the transfer matrix, $\boldsymbol{g}$ is the probability distribution of dielectric relaxation times, $\boldsymbol{b}$ is the measured signal inclusive of noise, and $\|\boldsymbol{Lg}\|$ is the penalty term.

The selection of the smoothing parameter is an important step. If the magnitude of penalty function is too small then the solution appears under regularised, often highly oscillatory and generally unphysical. Conversely, if the penalty function is too large, then not enough weight is given to the exact analytical solution resulting in very broad, under-defined distributions [43]. To select the alpha value we have used an automated method of generalized cross validation (GCV), which is described in detail elsewhere [44]–[46]. The basis of the GCV method is to sequentially remove data from $\boldsymbol{s}$ and determine which value of $\alpha$ for the regularised solution best predicts the omitted data. Scores are assigned to a defined range of $\alpha$ values, with the $\alpha$ that minimizes the GCV score being the optimal smoothing parameter.

## 4 Results

**Figure 2** shows experimental data for the real and imaginary relative permittivity of the shale sample at the six saturation conditions measured. In the dry state, the real part of the dielectric response was relatively flat ranging from about 7 at 100 MHz to about 10 at 40 Hz. At the first RH condition (23%), at frequencies < 10 MHz, the real part of the dielectric response rapidly increased to several hundred as frequency decreased to ~1 KHz, where a low frequency plateau was observed. In the high frequency range (10-100 MHz) the real part of the dielectric response began to converge toward a plateau. With increasing saturation the plateau in the low frequency region remained fairly constant, until at a critical saturation (typically occurring for samples exposed to greater than RH 75-99%) the real part of the dielectric response began to increase again at frequencies around 1 kHz and lower. At full saturation this effect was greatest, with some real relative permittivity values at 40 Hz reaching several tens of thousands for some samples. This low frequency transition to higher real permittivity as moisture content increased was coupled with a sharp increase in the imaginary component of the permittivity at sub-kHz frequencies.

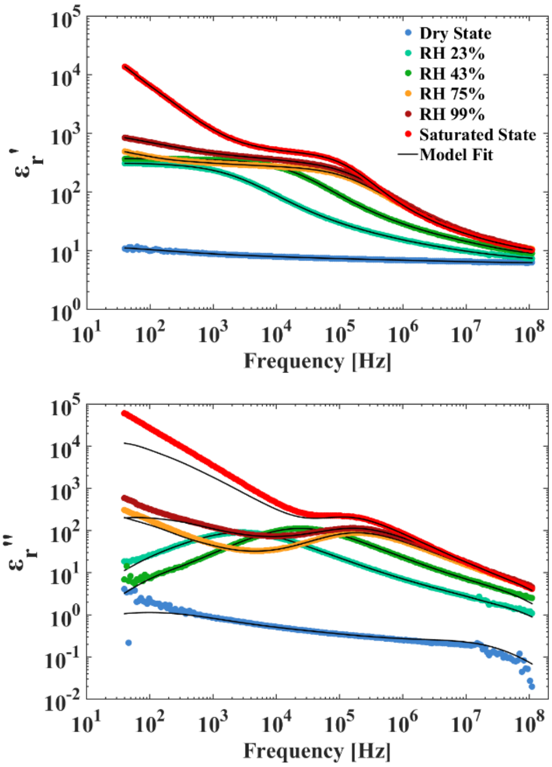

***Figure 2.*** *Measured real and imaginary dielectric permittivity of shale sample at varied saturation conditions. The real permittivity is fitted with the g(τ) regularised solutions (Model fit). The imaginary data is compared against the equivalent KK model derived from the real permittivity g(τ) solution.*

Using the regularisation steps previously outlined, we minimise a solution of $g(\tau)$ against the real permittivity data (i.e. $\varepsilon'_{(\omega)}$ only). Then, via the Kramers-Kronig relation we generate the model solution, $\varepsilon''^{(KK)}_{(\omega)}$, for the imaginary component of the permittivity using the $g(\tau)$ solution derived from on the real part of the permittivity data. This model solution, $\varepsilon''^{(KK)}_{(\omega)}$, is then compared against the measured values for the imaginary permittivity (i.e. $\varepsilon''_{(\omega)}$) (**Figure 2**). Assuming $\frac{\sigma''_{(\omega)}}{\omega\varepsilon_0} \gg \frac{\sigma'_{(\omega)}}{\omega\varepsilon_0}$, which to a first order approximation should be true at frequencies $< 1\,\mathrm{MHz}$, then the differences between

$\varepsilon''^{(KK)}_{(\omega)}$ and the experimental data will be related to in phase conduction current (equation 5). By subtracting the difference between $g(\tau)$ and the imaginary data, the in phase conduction at low frequency could be quantified **Figure 3**.

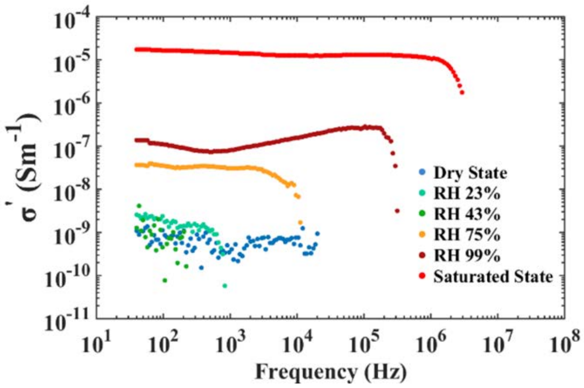

***Figure 3.*** *Values of σ' extracted from the differences between g(τ) solutions from real component of the dielectric permittivity and imaginary permittivity data plotted as function of frequency.*

The increase in a sample's moisture content driven by humidity produced negligible contributions to in-phase conductivity up to a RH of 45%. At higher values of RH, conduction increased appreciably at frequencies below a critical value which also increased with moisture content. Above RH 45 %, the conduction magnitude increased appreciably with each increment in moisture content and was largely independent of frequency. We suspect the observed onset of conduction arises from counter diffusion currents between the bulk electrolyte and the polarised diffuse layer within the EDL (open EDL). In this case, the electrochemical potential that results from a deformed EDL drives the mass diffusion of ions as the system moves to electro-neutrality [47]. The magnitude of the conduction relates to the number of charge carriers involved, and the critical frequency to the electrostatic activation energy a charge carrier needs to overcome to exchange from the diffuse layer to the bulk (i.e. when EDL counterion diffusivity > time EDL is polarised).

The evolution of dielectric relaxation time distributions with increasing moisture are shown in **Figure 4**. At the lowest RH condition (23%), the magnitude of Δε dramatically increased and the dominant relaxation time observed ranged from $10^{-3}$ – $10^{-4}$ s. Subsequent increases in moisture resulted in a downward shift of the dominant relaxation time, while the magnitude of Δε contribute by this polarisation process remained relatively constant. This observation is better described by the phenomenological model for EDL polarisation [32], [48] than by a MW-type polarisation. Increased water vapour saturation will result in a decrease in charge concentration, which in turn will result in the expansion of diffuse part of the EDL [36] and an increase in the counterion diffusivity [49]. From numerical studies of the Debye- Falkenhagen dynamics, a decrease in charge density would result in an increased characteristic relaxation time (opposite to that observed) while an increased counterion diffusivity would reduce the apparent relaxation time [50]. Hence, our experimental results suggest that the increased diffusivity of charge carriers in the EDL is the controlling factor in the observed shift in relaxation times between $10^{-3}$-$10^{-6}$ s. The relatively constant magnitude of Δε suggests that for relative humidities between 23% and 45%, the polarisation process is constrained to within the EDL (i.e. a closed EDL with no exchange to the bulk).

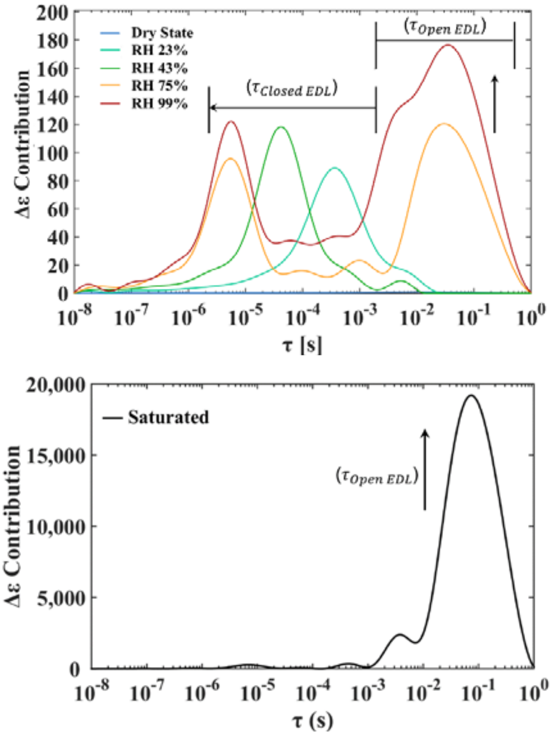

***Figure 4.*** *Evolution of dielectric relaxation time distributions after exposure to different RH environments. Domains with dominate polarisation mechanisms closed electrical double layer ($\tau_{closed\ EDL}$) and open electrical double or diffusion fluxes ($\tau_{open\ EDL}$) are identified. Arrows indicate trend with increasing saturation. The Δε contribution from $\tau_{open\ EDL}$ for the fully saturated states is much larger and hence it has been presented separately for clarity.*

At around the saturation state incurred at RH 75% there was a sharp increase in Δε that is related to a polarisation process with characteristic relaxation times ~$10^{-2}$-$10^{-1}$ s. Furthermore, at a fully saturated conditions this polarisation mechanism completely dominates (**Figure 4**). This very large low frequency dielectric response is consistent with *open* EDL polarisation (often referred to as membrane polarisation) where a coupled electro-diffusional mechanism is acting between the diffuse part of the EDL and the bulk electrolyte, giving rise to large in-phase displacement currents and slow relaxation times ($\tau_D$) [39]. This polarisation mechanism is driven by the difference in electrochemical potential between a polarised EDL and the bulk, which causes diffusive fluxes of oppositely charged ions.

## 5 Conclusion

Here we demonstrate the application of Tikhonov regularisation methods to compute dielectric relaxation time distributions from broadband (40Hz to 110MHz) dielectric data for a shale sample at varying partial saturation. The evolution in the dielectric response with moisture content was driven by polarization processes within the EDL (closed EDL) up to an apparent critical partial saturation. Thereafter, the polarisation was dominated by diffusion between the EDL and the bulk electrolyte (open EDL). Future work will extend the analysis such that the relaxation time analysis can be readily converted into diffusion lengths, hence allowing for microstructure quantification. Furthermore, including a greater range of measurement frequencies (i.e. mHz – Hz and GHz) will assist in developing complete electrical property models for rocks and will also be a focus of future work.

## References

1. R. Knight *et al.*, “Geophysics At the Interface : Response of Geophysical Properties To Solid - Fluid , Fluid - Fluid , and Solid - Solid Interfaces,” *Rev. Geophys.*, vol. 48, no. 2007, pp. 1–30, 2010.
2. D. P. Lesmes and F. D. Morgan, “Dielectric spectroscopy of sedimentary rocks,” *J. Geophys. Res. Earth*, vol. 106, no. B7, pp. 13329–13346, 2001.
3. K. Titov, A. Tarasov, Y. Ilyin, N. Seleznev, and A. Boyd, “Relationships between induced polarization relaxation time and hydraulic properties of sandstone,” *Geophys. J. Int.*, vol. 180, no. 3, pp. 1095–1106, 2010.
4. A. Revil and N. Florsch, “Determination of permeability from spectral induced polarization in granular media,” *Geophys. J. Int.*, vol. 181, no. 3, pp. 1480–1498, 2010.
5. W. E. Kenyon, “Texture effects on megahertz dielectric properties of calcite rock samples,” *J. Appl. Phys.*, vol. 55, no. 8, pp. 3153–3159, 1984.
6. G. Osterman, K. Keating, A. Binley, and L. Slater, “A laboratory study to estimate pore geometric parameters of sandstones using complex conductivity and nuclear magnetic resonance for permeability prediction,” *Water Resour. Res.*, vol. 52, pp. 4321–4337, 2016.
7. A. Revil, “Effective conductivity and permittivity of unsaturated porous materials in the frequency range 1 mHz-1GHz,” *Water Resour. Res.*, vol. 49, no. 1, pp. 306–327, 2013.
8. R. D. Swanson *et al.*, “Anomalous solute transport in saturated porous media: Relating transport model parameters to electrical and nucleur magnetic resonance properties,” *Water Resour. Res.*, vol. 51, pp. 1264–1283, 2015.
9. A. Revil and P. Leroy, “Constitutive equations for ionic transport in porous shales,” *J. Geophys. Res.*, vol. 109, no. B3, p. B03208, 2004.
10. A. Binley, S. Kruschwitz, D. Lesmes, and N. Kettridge, “Exploiting the temperature effects on low frequency electrical spectra of sandstone: A comparison of effective diffusion path lengths,” *Geophysics*, vol. 75, no. 6, pp. A43–A46, 2010.
11. K. S. Cole and R. H. Cole, “Dispersion and absorption in dielectrics I. Alternating current characteristics,” *J. Chem. Phys.*, vol. 9, no. 4, pp. 341–351, 1941.
12. D. W. Davidson and R. H. Cole, “Dielectric relaxation in glycerol, propylene glycol, and n-propanol,” *J. Chem. Phys.*, vol. 19, no. 12, pp. 1484–1490, 1951.
13. S. Havriliak and S. Negami, “A complex plane analysis of α-dispersions in some polymer systems,” *J. Polym. Sci. Part C Polym. Symp.*, vol. 14, no. 1, pp. 99–117, 1966.
14. S. M. Usmanov, “Use of the tikhonov regularization method in automated mathematical analysis of dielectric spectrometry data,” *Sov. Phys. J.*, vol. 34, no. 10, pp. 931–936, 1990.
15. F. D. Morgan and D. P. Lesmes, “Inversion for dielectric relaxation spectra,” *J. Chem. Phys.*, vol. 100, no. 1, pp. 671–681, 1994.
16. H. Schäfer, E. Sternin, R. Stannarius, M. Arndt, and F. Kremer, “Novel approach to the analysis of broadband dielectric spectra,” *Phys. Rev. Lett.*, vol. 76, no. 12, pp. 2177–2180, 1996.
17. A. Tarasov and K. Titov, “Relaxation time distribution from time domain induced polarization measurements,” *Geophys. J. Int.*, vol. 170, no. 1, pp. 31–43, 2007.
18. S. Nordsiek and A. Weller, “A new approach to fitting induced-polarization spectra,” *Geophysics*, vol. 73, no. 6, p. F235, 2008.
19. M. Tong, L. Li, W. Wang, and Y. Jiang, “Determining capillary-pressure curve, pore-size distribution, and permeability from induced polarization of shaley sand,” *Geophysics*, vol. 71, no. 3, p. N33, 2006.
20. N. Wagner, K. Emmerich, F. Bonitz, and K. Kupfer, “Experimental Investigations on the Frequency- and Temperature-Dependent Dielectric Material Properties of Soil,” *Ieee Trans. Geosci. Remote Sens.*, vol. 49, no. 7, pp. 2518–2530, 2011.
21. A. Revil and P. Glover, “Theory of ionic-surface electrical conduction in porous media,” *Phys. Rev. B - Condens. Matter Mater. Phys.*, vol. 55, no. 3, pp. 1757–1773, 1997.
22. B. D. Fuller and S. H. Ward, “Linear System Description of the Electrical Parameters of Rocks,” *IEEE Trans. Geosci. Electron.*, vol. 8, no. 1, pp. 7–18, 1970.
23. M. Loewer, T. Günther, J. Igel, S. Kruschwitz, T. Martin, and N. Wagner, “Ultra-broad-band electrical spectroscopy of soils and sediments-a combined permittivity and conductivity model,” *Geophys. J. Int.*, vol. 210, no. 3, pp. 1360–1373, 2017.
24. D. P. Lesmes and F. D. Morgan, “Dielectric spectroscopy of sedimentary rocks,” *J. Geophys. Res. Solid Earth*, vol. 106, no. B7, pp. 13329–13346, 2001.

25. G. Goracci, M. Monasterio, H. Jansson, and S. Cerveny, “Dynamics of nano-confined water in Portland cement - Comparison with synthetic C-S-H gel and other silicate materials,” *Sci. Rep.*, vol. 7, no. 1, pp. 1–10, 2017.
26. A. N. Tikhonov, “Solution of Incorrectly Formulated Problems and the Regularisation Method.pdf,” *Sov. Math. Dokl.*, vol. 4, no. 4, pp. 1035–1038, 1963.
27. J. C. Maxwell, *A treatise on electricity and magnetism*. New York: Dover Publ. Inc., 1891.
28. K. W. Wagner, “Erklarung derDielectrishenNachwirkungsvorgange auf grund Maxwellscher vorstellungen,” *Arch. Electrotech.*, vol. 2, pp. 371–381, 1924.
29. D. Bruggeman, “Berechnung Verschiedeneren Physicalischer Konstanten von Heterogenen Substanzen,” *Ann. Phys.*, vol. 24, pp. 636–679, 1935.
30. R. W. Sillars, “The properties of a dielectric containing semiconducting particles of various shapes,” *Inst. Electr. Eng. - Proc. Wirel. Sect. Inst.*, vol. 12, no. 35, pp. 139–155, 1937.
31. T. Hanai, “Dielectric properties of emulsions IV. Dielectric Behavior of Nitrobenzene-in Water Emulsions,” *Kolloid-Zeitschrift*, vol. 184, no. 2, pp. 143–148, 1962.
32. G. Schwarz, “A Theory of the Low-Frequency Dielectric Dispersion of Colloidal Particles in Electrolyte Solution,” *J. Phys. Chem.*, vol. 66, no. 12, pp. 2636–2642, 2007.
33. C. T. O’Konski, “Electric properties of macromolecules. V. Theory of ionic polarization in polyelectrolytes,” *J. Phys. Chem.*, vol. 64, no. 5, pp. 605–619, 1960.
34. T. L. Chelidze, Y. Guéguen, and C. Ruffet, “Electrical spectroscopy of porous rocks: a review-II. Experimental results and interpretation,” *Geophys J Int*, vol. 137, no. August, pp. 16–34, 1999.
35. T. L. Chelidze and Y. Guéguen, “Electrical spectroscopy of porous rocks: a review- I. Theoretical models,” *Geophys J Int*, vol. 137, no. April, pp. 1–15, 1999.
36. H. L. Bohn and B. L. Mcneal, “A qualitative derivation of the diffuse double layer 1,” *J. Agron. Educ.*, vol. 12, p. 2628, 1983.
37. S. S. Dukhin and V. N. Shilov, *Dielectric Phenomena and Double Layer in Disperse Systems and Polyelectrolytes*. New York: John Wiley & Sons, 1974.
38. L. A. Rosen, J. C. Baygents, and D. A. Saville, “The interpretation of dielectric response measurements on colloidal dispersions using the dynamic Stern layer model,” *J. Chem. Phys.*, vol. 98, no. 5, pp. 4183–4194, 1993.
39. O. De Lima and M. Sharma, “A generalized Maxwell-Wagner theory for membrane polarization in shaly sands,” *Geophysics*, vol. 57, no. 3, pp. 431–440, 1992.
40. M. Fixman, “Charged macromolecules in external fields . I . The sphere,” vol. 5177, no. 1980, 1993.
41. M. Josh, B. Clennell, M. Cauchefert, and T. Han, “Dielectric permittivity and anisotropy of intact multi-saturated organic shales,” *SPWLA 57 th Annu. Logging Symp. June 25 - 29*, no. June, p. 14, 2016.
42. B.-G. Kim and J.-J. Kim, “Application of tikhonov regularization to dipole glass relaxation function,” *Ferroelectrics*, vol. 206, no. 1, pp. 79–91, 1998.
43. P. R. J. Connolly, S. J. Vogt, S. Iglauer, E. F. May, and M. L. Johns, “Capillary trapping quantification in sandstones using NMR relaxometry,” *Water Resour. Res.*, pp. 1–16, 2017.
44. G. Wahba, “Practical Approximate Solutions to Linear Operator Equations When the Data are Noisy,” *SIAM Journal on Numerical Analysis*, vol. 14, no. 4. pp. 651–667, 1977.
45. J. D. Wilson, “Statistical approach to the solution of first-kind integral equations arising in the study of materials and their properties,” *J. Mater. Sci.*, vol. 27, no. 14, pp. 3911–3924, 1992.
46. K. G. Hollingsworth and M. L. Johns, “Measurement of emulsion droplet sizes using PFG NMR and regularization methods,” *J. Colloid Interface Sci.*, vol. 258, no. 2, pp. 383–389, 2003.
47. V. N. Shilov, A. V Delgado, F. Gonz, and J. Horno, “Polarization of the Electrical Double Layer . Time Evolution after Application of an Electric Field,” *J. Colloid Interface Sci.*, vol. 148, pp. 141–148, 2000.
48. J. M. Schurr, “On the Theory of the Dielectric Dispersion of Spherical Colloidal Particles in Electrolyte Solution1,” *J. Phys. Chem.*, vol. 68, no. 9, 1964.
49. I. C. Bourg and G. Sposito, “Molecular dynamics simulations of the electrical double layer on smectite surfaces contacting concentrated mixed electrolyte (NaCl – CaCl2) solutions,” *J. Colloid Interface Sci.*, vol. 360, no. 2, pp. 701–715, 2011.
50. M. B. Singh and R. Kant, “Debye-Falkenhagen dynamics of electric double layer in presence of electrode heterogeneities,” *J. Electroanal. Chem.*, vol. 704, pp. 197–207, 2013.

# CT-scan in-situ investigation of waterflood front instabilities during immiscible displacements: effect of viscosity contrast and flow rate

*Matthieu* Mascle[1,*], *Elisabeth* Rosenberg[1], *Berit* Roboele[2], *Espen* Kowalewski[2], and *Souhail* Youssef[1]

[1]IFP Energies Nouvelles, Geofluids & Rock Department, 92852 Rueil-Malmaison Cedex, France
[2]Equinor ASA, 7005 Trondheim, Norway

**Abstract.** In this work, unstable displacements were conducted using special equipment designed to run in-situ CT-scanner experiments. All the displacements were conducted on a strongly water-wet Bentheimer sandstone full-size plug, of 10cm in diameter and 40cm in length. It was found that the oil recovery at brine breakthrough (%PV) shows a good correlation with the viscous fingering number as defined by Doorwar. Early water breakthrough appears to be boosted by high injection flow rate and less favorable fluids mobility ratio. The local saturation monitoring provides new insight to characterize the finger shapes and analyze the production mechanisms, for the different flowing conditions. In water-wet conditions, the capillary forces contribute to stabilize the front against viscous instabilities. If the viscous forces become too dominant, the capillary forces are overcome and fingering may occur for displacement with unfavorable fluids ratio. A diagram has been constructed to separately quantify the contribution of the viscous fingering and the capillary fingering. Results have shown that capillary fingering was the main mechanism responsible for the water early breakthrough.

## 1. Introduction

Unstable displacements can occur when a fluid is displaced by any fluid of different nature. The driving force of these instabilities can either be a viscosity contrast, a density contrast or capillary forces when the two considered fluids are immiscible. As these complex flows lead to poor fluids mixing or sweeping efficiency and early fluid breakthrough (BT), they have been discussed in an extensive number of publications of various engineering fields [1–4].

When the displacing and displaced fluids are immiscible, the front instabilities take the form of fingering. Their shape and magnitude are governed by various parameters, including the fluids and rock properties and structure, the injection conditions or the system dimensions and heterogeneities. Previous authors have suggested dimensionless scaling parameters aiming to account for all these contributions. Among the first, Peters and Flocks [5] have constructed a dimensionless number ($I_{sc}$) using Chuoke's stability theory [6] to predict the onset of front instabilities. Later, Lenormand et al. [7] proposed a phases-diagram using two dimensionless numbers to dissociate the capillary and the viscous contributions ($C$ and $M$, respectively). Their diagram provided a better characterization of the different flow instabilities forms, with 3 identified regimes: (1) a piston-like displacement in the stable flow domain, (2) high magnitude tree-like fingerings in the viscous dominated flow domain and (3) low magnitude loop-like fingering in the capillary dominated flow domain. More recently, Doorwar [8] combined Lenormand two dimensionless numbers and added a tertiary contribution to account for the core dimensions and petrophysical properties. This contribution was already expressed in Peters and Flocks instability number. The resulting dimensionless number $N_I$ has demonstrated good results to predict total fluids recovery at BT (BTR) for water-wet displacement, but provide no forecast for fluids fingering shape.

Fingering occurs at different scales ranging from the phases by-pass at pore level to the phases partitioning at reservoir level. The magnitude of their dimensions variation causes its modelling to be a perilous task using Darcy's scale models [9]. One solution is to upscale flow dynamics properties from laboratory experiments, to account for the complexity of these flows at higher scale resolution. In recent works, various authors [10–12] have used and adapted Fayers' phenomenological approach of viscous fingering [13] to upscale relative-permeabilities. These models, referred as lumped-finger, rely on the merging of all fingering in a unique finger, described by various physical parameters. This approach allows to obtain a satisfying match of the global experimental data (mean saturation or total pressure drop). Yet, the local saturations and the equivalent finger shape is rarely studied. The phenomenological modelling demonstrates the necessity to have a 2D or 3D flow visualization to characterize front inabilities forms. Glass micro-models had provided a useful tool for visual inspection but they are limited in dimensions and connectivity [12, 14]. Slab

---

[*] Corresponding author: matthieu.mascle@ifpen.fr

experiments conducted on Bentheimer samples have allowed to look further in the 2D fingerings characterization [9, 15]. However, the core width is restricted with these experiments, leading to high dimensions ratio. It has been demonstrated that this dimensions ratio strongly affect the fingers growth [12]. Molding techniques using epoxy resin have been used on real cores in the past [16] to show the complexity of the fluids front. But this method obviously does not allow for any dynamic monitoring.

In this work, unstable displacements were conducted using special equipment designed to run experiments combined with a CT-scanner. All the displacements were conducted on a strongly water-wet Bentheimer sandstone full-size plug, of 10cm in diameter and 40cm in length. A set of waterflood displacements have been conducted in a coreflood cell with different oil viscosity (from 5 to 330 cP) and injection flowrate (from 85 cc/h to 420 cc/h) to assess their effect on the front stability. The purpose of this work is to characterize the finger shapes and analyze the production mechanisms, for the different flowing conditions.

## 2. Materials and methods

### 2.1 Coreflood set-up

An overview of the experimental set-up is given Fig. 1. Experiments were conducted using a special equipment designed to run in-situ experiments under a CT scanner. The equipment is composed of an X-ray transparent core holder and a mobile rig able to inject different fluids at up to 100bar. The core holder is designed to handle cylindrical samples of 10cm in diameter and up to 60cm in length. The core holder body is made of a 5mm thickness aluminum alloy which allows good X-ray transmission at an energy of 140kVP.

A multi-pump system is used, allowing to inject different fluids without need of changing pump fluid and thus avoid fluid pollution. The low viscosity fluids are injected using Vindum VP-12K pumps. The high viscosity fluids are injected using 5L piston cylinders, connected to a Vindum pump to drive the pistons. The back pressure (BPR) is regulated to 20bars. The confining pressure is imposed to 50bars using an Isco syringe pump, fed with deionized water (MilliQ). Experiments are conducted at scanner room temperature, regulated by an air conditioner at 19.5°C.

**Fig. 1.** Overview of the IFPEN medical CT Scan GEHC Discovery 750HD and the experimental setup

The differential pressure is monitored using two 150 bar Keller absolute pressure transducers connected to the upstream and downstream static fluids lines. The fluids saturation is monitored using a medical CT scanner GEHC Discovery 750HD dual energy. It is operated at 140kVP with a beam current of 260mA to minimize signal/noise ratio. This equipment imposes the coreflood cell to be installed horizontally. The produced effluents are collected and gravity-separated in a vertical graduated burette to support the saturation computation.

### 2.2 Rock sample and fluids

A 4inch diameter, 40cm long water-wet Bentheimer core is used for the coreflood (Table 1). The core was analyzed with the dual energy mode of GEHC called GSI (Gemstone Spectral Imaging) to assess the saturation homogeneity (Fig. 2). It suggests the saturation is slightly increasing from the left to the right (from inlet to outlet). A small heterogeneity shaped as a 1cm radius sphere is visible near the center of the core. This centimeter-scale heterogeneity won't impact the flooding experiments. Still, it shows the Bentheimer rock-type can exhibit some heterogeneities. The mean porosity was estimated to 22.2%, giving a core pore volume (PV) of 722cc. The core permeability *K* was measured with the brine at a confining pressure of 50bar and a pore pressure of 20bar. The resulting permeability is estimated to 2530mD.

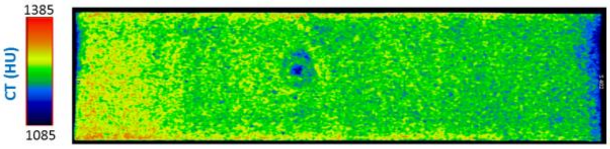

**Fig. 2**. CT Sagittal cross section rendering of the 10 cm diameter core. High CT values (hot shades) indicates lower porosities.

**Table 1.** Core dimensions and petrophysical properties

| | |
|---|---|
| Dimensions (D, L) | 10cm, 40cm |
| Mean porosity *Φ* | 22.2% |
| Absolute permeability *K* | 2530mD |
| Dispersion *D* | $2.7\ 10^{-9} m^2/s$ |

Experiments have been conducted using a 70 g/l TDS brine and mineral oils with different viscosities (Isopar L, Primol and Drakeol). The brine water is a mixture of NaCl (30g/L) doped with NaI (40g/L) to increase the CT contrast. The viscosity of the different mineral oils was estimated at 19.5°C. The resulting viscosities are respectively for the Drakeol, the Primol and the Isopar L: 321cP, 168cP and 4.7cP. The estimated viscosity for brine using tabulated data is 1.18cP. Deionized water (MilliQ) and isopropyl alcohol (IPA) were used for cleaning and miscible fluids exchange. Viscosities and densities of the different fluids used in this study are summarized Table 2. The interfacial tension (IFT) of the mineral oil in contact with the brine has been measured using the Wilhelmy plate method.

**Table 2.** Fluid properties at 19.5°C, and interfacial tension (IFT in contact with the brine water).

| Fluid | Viscosity (cP) | Density (g/cc) | IFT (mN/m ) |
|---|---|---|---|
| Brine | 1.18 | 1.05 | - |
| Drakeol | 321 | 0.86 | 51 |
| Primol | 168 | 0.86 | 30 |
| Isopar L | 4.7 | 0.76 | 45 |

The core homogeneity is assessed using a tracer test. The brine water was injected at 7.0cc/min in the core saturated with the MilliQ water. The tracer concentration is monitored using the CT-scanner. Concentration profiles are given Fig. 3, with the local value displayed on the sagittal core section (see section 2.4). They show a homogenous displacement with limited phases dispersion during the sweeping. This core dispersion is fitted to $D = 2.7 \cdot 10^{-9} m^2/s$ using an analytical solution [17] (Fig. 4).

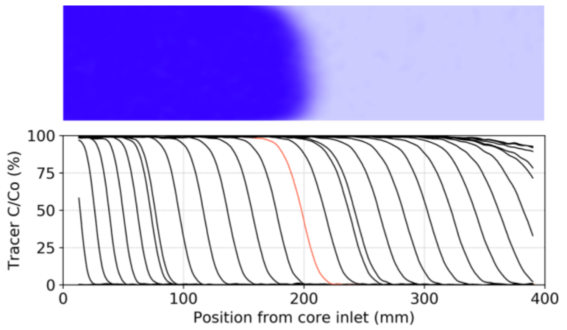

**Fig. 3**. Tracer concentration profiles during a tracer injection. The red profile and the sagittal section are taken after 0.5PVinjected.

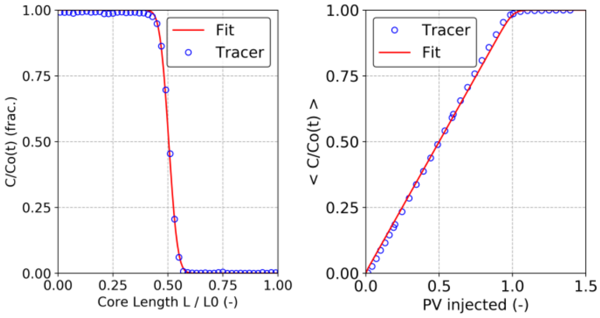

**Fig. 4**. Core dispersion fitted using an analytical solution [17]. The dispersion is fitted using the concentration profile after 0.5PV injected (left plot) and total tracer concentration (right plot). Dispersion is fitted to $2.7 \cdot 10^{-9}$ m²/s.

### 2.3 Experimental procedure and design

Five waterflood displacements have been conducted on the same Bentheimer core using varying injection flow-rates and oil viscosities. All the fluids were injected from the same inlet face. Corefloods with the Primol (CF2 and CF3) were conducted first, followed by the coreflood with the Isopar L (CF1). Corefloods with the Drakeol (CF4 and CF5) were conducted at last due its higher viscosity. All experiments start at *Swi*, reached by injecting the oil at 180cc/h, until pressure and saturation stability are obtained. From *Swi*, the brine is injected for a minimum of 5 pore-volumes. Both the differential pressure and the fluids saturation are monitored during this displacement. After the water flooding, the oil used in the next coreflood is directly injected to reach *Swi* and replace the oil from the previous experiment. For CF1, *Swi* is set by flooding with the Primol first, followed by Isopar L injection to replace the Primol. This intermediate step is conducted with the Isopar L oil to have comparable *Swi* for all experiments, considering its low viscosity possibly leading to unfavorable displacement.

The core entry face is swept with brine before proceeding with the injection in the core, using a dedicated outlet port in the inlet face. Homogenous sweeping is ensured by an injection diffuser carved with a double spiral. During the sweeping phase, the flow rate is set to 50cc/h for at least 2h. This step is monitored using the CT-scan for quality-checking. The experimental design of the presented experiments is given in Table 3. Peters & Flocks instability number $I_{sc}$ [5] is computed for each displacement, using equation 1, where $\mu_o$ and $\mu_w$ respectively expressed the oil and brine water viscosity, $v$ is the brine superficial velocity, $K$ is the core absolute permeability, $\sigma_{ow}$ is the fluids interfacial tension and $C^*$ is the dimensionless wettability number, taken to 306 for water-wet core [5]. In their theory, they predicted unstable displacements for $I_{sc} > 13.56$. Following this, all waterflood displacement excepted CF1 are expected to show instabilities.

$$I_{sc} = \left(\frac{\mu_o}{\mu_w} - 1\right)\frac{v\mu_w D^2}{C^*\sigma_{ow}K} \qquad (1)$$

**Table 3.** Experimental corefloods design, with the $I_{sc}$ instability number computed (see equation 1).

| Coreflood | Oil (viscosity) | Injection flow rate (cc/min) | $I_{sc}$ |
|---|---|---|---|
| CF1 | Isopar L (4.7cP) | 7.0 | 4 |
| CF2 | Primol (168cP) | 1.4 | 50 |
| CF3 | Primol (168cP) | 7.0 | 250 |
| CF4 | Drakeol (321cP) | 1.4 | 56 |
| CF5 | Drakeol (321cP) | 7.0 | 280 |

### 2.4 Saturation monitoring

The full core is scanned in 30sec which allowed to acquire 3D images with a time interval of 3min until breakthrough and 20min after. Voxel resolution was 0.33x0.33x1.25mm. The local saturation is computed from the CT-scans using a linear scaling of the fluids X-ray contrast between its two extreme saturation states (referred to as CT-references), given by equation 2. Illustrations of 2D of the local saturation is given Fig. 5, in sagittal and transverse slicing. A mean-filter is used with a kernel of $3^3$ voxels to reduce the noise.

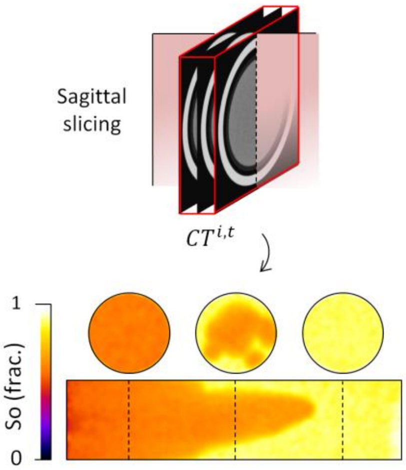

**Fig. 5.** Illustration of sagittal and transverse slicing processing from raw data.

CT-references are acquired for all the fluids under consideration, with the core saturated with the corresponding fluid (Fig. 6). The average CT-contrast between the brine and the oils is 157HU (Hounsfield Unit) for the Isopar L and 135HU for the Drakeol and Primol.

$$S_o^{i,t} = (CT^{i,t} - CT^i_{oil}) / (CT^i_{brine} - CT^i_{oil}) \qquad (2)$$

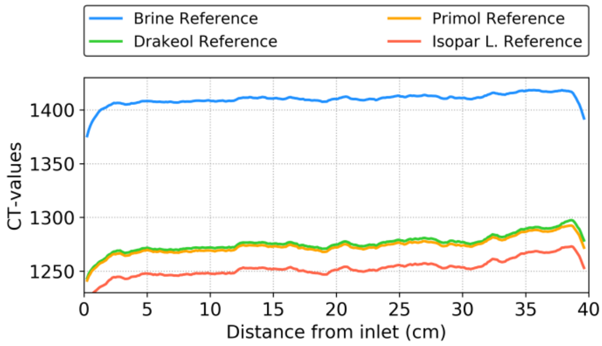

**Fig. 6.** CT-references of the brine water and the mineral oils

Repeatability and stability measurements conducted on the CT-scanner have given a standard error $\delta CT$ equal to 1HU. An estimation of the standard error $\delta So$ can be done according to equations 2 and 3. The standard error is lower than 1% for all experiments. Confidence intervals (IC95) are plotted Fig. 7 for the 3 mineral oils. IC95 (and therefore the standard error) is lower for the Isopar L oil due to its higher CT-contrast with the brine.

$$\delta S_o^{\,2} = \delta CT^2 \left( {\frac{\delta S_o}{\delta CT^i}}^2 + {\frac{\delta S_o}{\delta CT_{brine}}}^2 + {\frac{\delta S_o}{\delta CT_{oil}}}^2 \right) \qquad (3)$$

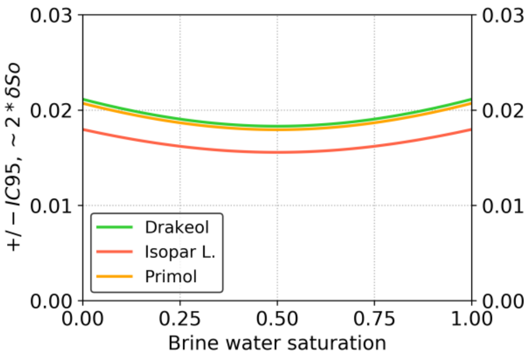

**Fig. 7.** Saturation confidence intervals (IC95) computed for the different minerals oil. IC95 is computed as twice the standard error $\delta So$. $\delta So$ is computed using equations 2 and 3.

The scanner resolution prevents us to 3D render the water fingering occurring at low scale (< 1.25mm). Consequently two types of fingerings are considered here: 1, the macroscopic fingering that has a higher magnitude than the scanner resolution and 2, the local fingering that has a lower magnitude than the scanner resolution. The macroscopic fingering is easily characterized using the CT-images. The local fingering (interpreted capillary fingering) is characterized using the local oil saturation in the swept areas.

## 3. Results and discussion

### 3.1 Water breakthrough (BT)

The dynamic core oil saturations measured using the CT-scanner during waterflood are compared in Fig. 8 for the 5 corefloods. The differential pressures recorded during the flooding are given in Fig. 9. The *Swi* reached after oil drainage are comparable for all corefloods, ranging from 11.3 to 12%. The water flooding with the lowest oil viscosity (CF1) shows a remarkable piston-like displacement, with no oil produced after breakthrough (BT). All other corefloods (CF2 to CF5) show early BT compared to CF1, with a different arrival time for each. These observations are consistent with Peter & Flocks instability number $I_{sc}$, that predicted stable displacement for CF1, and unstable displacements for the others corefloods (Table 3).

Results obtained in this study show that the fingering increases by increasing water injection flow rate or decreasing fluids viscosity ratio (defined as $\mu_w/\mu_o$). This is in agreement with most of the results found in the literature for the water-wet case [12]. Still, it is not clear why the fingering is boosted with high injection flow rate at constant mobility ratio, as the opposite trend was observed for the oil-wet case [11].

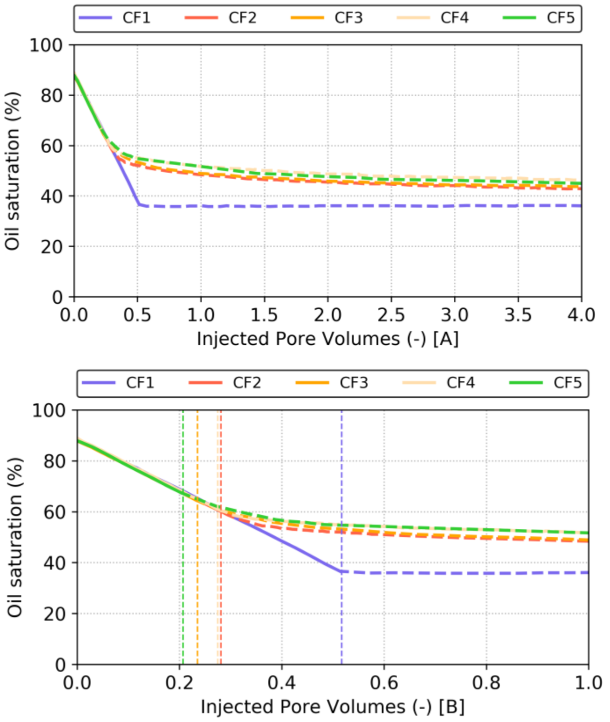

**Fig. 8.** Core oil saturation comparison during the coreflood [A], zoomed on the 1 first injected pore volume [B]. Plain lines are before breakthrough, dashed lines are after breakthrough (separation is indicated by the vertical dotted lines).

The differential pressure (dP) recorded during CF1 coreflood shows a specific trend with an increase of the pressure losses from *Swi* to *Sorw*, despite the oil being replaced by a less viscous fluid (Fig. 9). A similar behavior was observed by Doorwar [12] for the most favorable displacement ($\mu_w/\mu_o = 1$). This behavior can be explained by the water-wet nature of the core and the piston-like displacement. For the other cores, the oil viscosities being substantially higher than the brine water's, the dP decreases as the oil is swept.

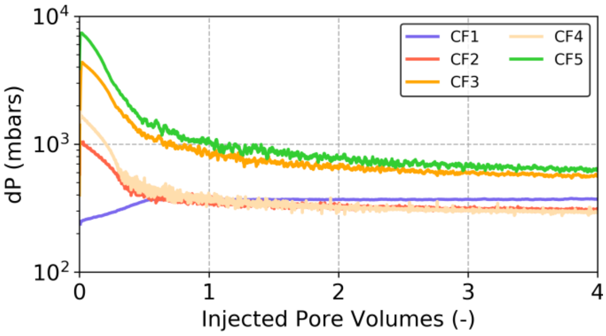

**Fig. 9.** Differential pressure (dP) recorded during the corefloods.

The easiest and standard way to quantify the breakthrough time is to measure the quantity of water injected in the core until BT (PV@BT). This quantity is referred in this paper as the oil recovery at breakthrough (%PV). It is calculated using the oil saturation reached at breakthrough *So@BT* (see equation 4). These values are measured and summarized Table 4 for all corefloods. They are plotted in Fig. 10 as function of the instability number $N_I$ defined by Doorwar in his thesis [8] (see equation 5).

$$Oil\ recovery\ @BT = 100 - Swi - So@BT \quad (4)$$

$$N_I = \frac{v\mu_w}{\sigma_{ow}}\left(\frac{\mu_o}{\mu_w}\right)^2\frac{D^2}{K} \quad (5)$$

Results from Doorwar thesis of coreflood experiments conducted on a water-wet Boise sandstone (*Φ, D, L, K* = 29%, 5cm, 30cm, 6D, respectively*)* are included in the plot for comparison. Results obtained in this study demonstrate a comparable trend but do not align with Doorwar's data. A possible improvement of the Doorwar number, to scale all data, could be to integrate the fluids mobilities upstream and downstream of the front vicinity (referred as the shock mobility ratio), as suggested by previous authors [3, 18]. This shock mobility ratio may provide a better prediction of the front instability than the fluids viscosities solely.

**Table 4.** Saturations reached during the corefloods. The oil recovery at breakthrough is measured as: *Oil recovery @BT = 100 – Swi – So@BT*

| Coreflood | Swi (%) | So@BT (%) | *Oil recovery @BT (%PV)* |
|---|---|---|---|
| CF1 | 11.7 | 38.05 | 50.25 |
| CF2 | 11.7 | 60.4 | 27.9 |
| CF3 | 12 | 66 | 22 |
| CF4 | 11.9 | 61.2 | 26.9 |
| CF5 | 11.3 | 69.45 | 19.25 |

Here, the monotonous increase of the breakthrough timing with respect to $N_I$ has been fitted with a logarithmic regression to underline the global trend in the data. The number of data points presented here and considering its uncertainty associated is not sufficient to truly demonstrate the consistency of this regression. Logarithmic trends can be easily mistaken with power-law trend [19].

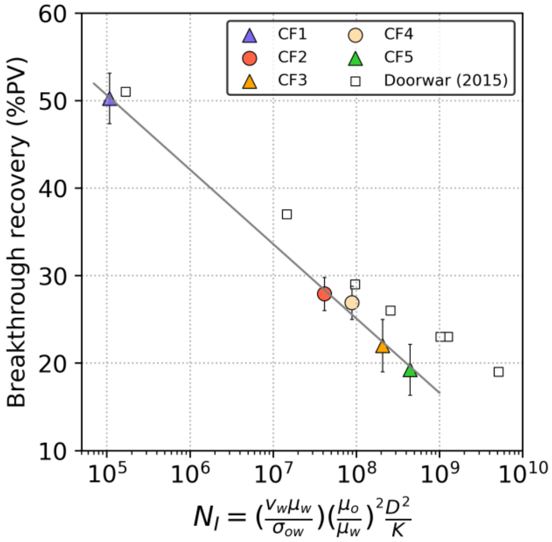

**Fig. 10.** Oil recovery at breakthrough (%PV) versus the Doorwar instability number $N_I$. The displayed bars errors account for the saturation confidence intervals and the temporal resolution of the

CT-monitoring. Circle and triangle markers respectively refer to corefloods conducted at 1.4 and 7.0 cc/min.

The saturation profiles, derived from the CT-scans, are given Fig. 11 for different time steps. They provide a beginning of answer to explain the early breakthrough for CF2 to CF5. The saturation profiles of these corefloods suggest a displacement far from being piston-like, especially when compared to CF1. The saturation profiles for CF1 provide additional insight to explain the increasing differential pressure observed during the displacement (Fig. 9). The piston-like displacement results in a spatially short transition of local saturations from *Swi* values, ahead the water-front, to *Sorw* values, behind it. In this configuration, mainly oil is flowing head of the front, and mainly brine-water is flowing behind the front. The pressure drop from inlet to outlet is consequently driven by two values: the oil relative permeability at *Swi* and the water relative permeability at *Sorw*, respectively referred as $k_{rom}$ and $k_{rwm}$. An increasing differential pressure during a piston-like flooding, simply requires to have $k_{rwm} < k_{rom} * \mu_w/\mu_o$.

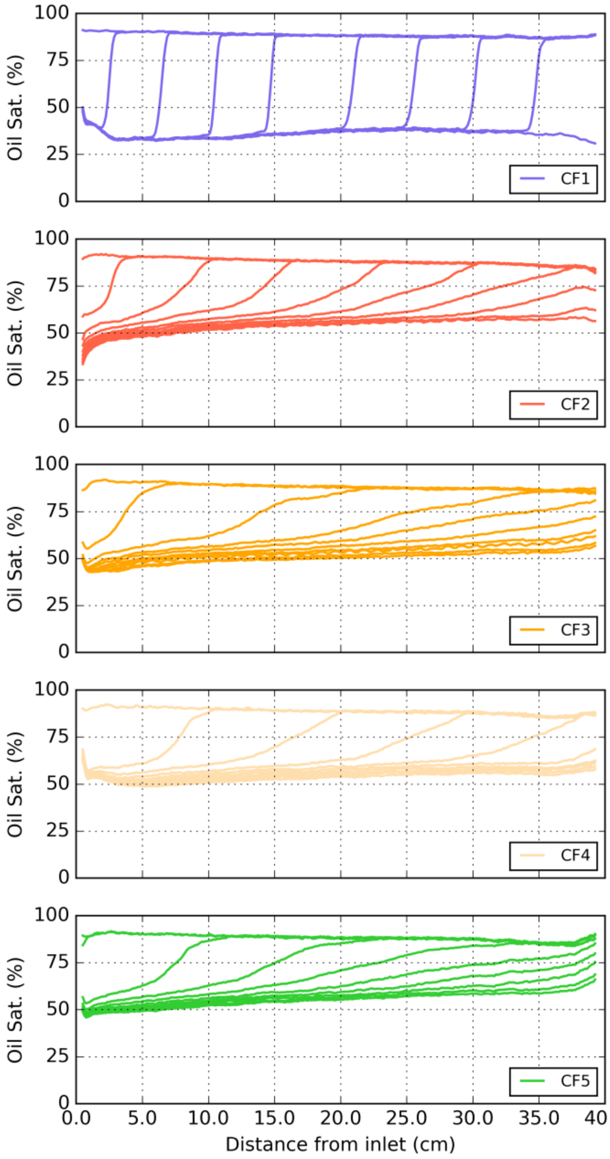

**Fig. 11.** Oil saturation profiles along the core axis for all corefloods.

The saturation profiles alone provide a poor characterization the finger's shapes. The next section uses the 3D CT-scans to better visualize the front instabilities.

### 3.2 Front instability shape

2D visualizations of the fingering are presented in Fig. 12 using sagittal and 3 transverse slicing. Positions of the transverse slicing are marked by the dotted black lines, at 8, 20 and 32cm from the core inlet. The sagittal slicing is illustrated in Fig. 5. Visualizations are given at breakthrough (on the right) and around half the breakthrough (on the left).

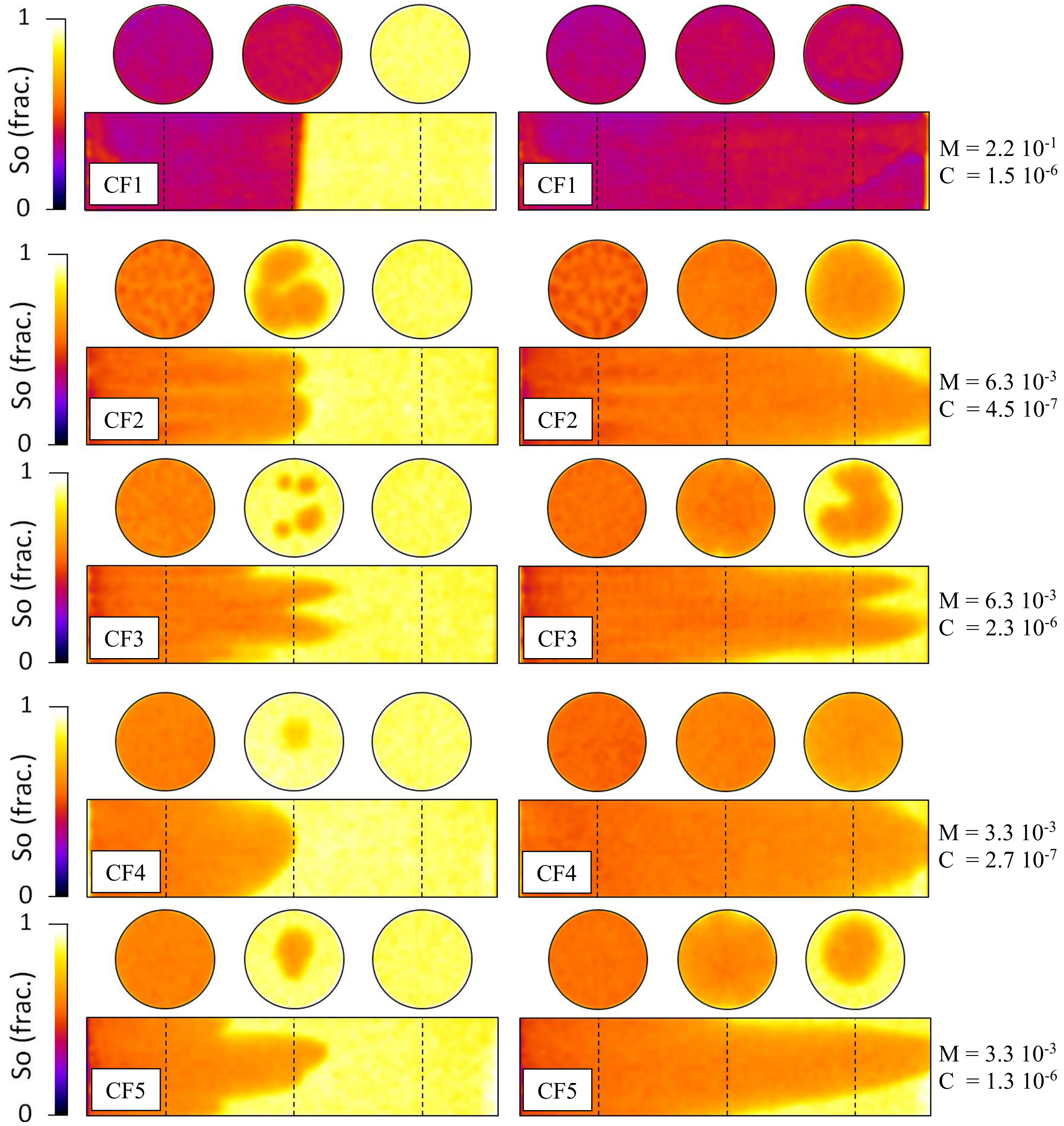

**Fig. 12.** 2D visualization if the front instability using sagittal and transverse slicing. The displacement is displayed at half the breakthrough on the left and at breakthrough on the right. Positions of the transverse slicing are marked by the dotted black line. The sagittal slicing is illustrated Fig. 5. M and C values are given on the right for each experiment.

The piston-like displacement is clearly visible for the coreflood CF1. The water front is completely stable, resulting in a homogenous sweeping of the core. This coreflood was expected to show the best oil recovery but not to have a perfect front stability, as the fluids mobility ratio is still unfavorable ($\mu_w/\mu_o$ < 0.25 for CF1). This dynamic behavior may be explained by strong capillary forces, caused by the preferential core's wettability to water. Capillary forces generate a spontaneous invasion of the water in the core that overcomes the viscous instabilities and stabilizes the water front. It results in a front sharper than the monophasic fluids dispersion observable during a miscible displacement (see Fig. 3). Here, capillary forces have a dual contribution as they improve the sweeping efficiency at core-scale but are responsible for oil trapping at pore-scale (final *Sorw* is measured to 38%).

Results given Table 4 showed greater fingering as the flow rate is increased. This observation is consistent with the previous explanation: when the flow rate is increased, the capillary forces are overcome by the viscous forces. They can no longer stabilize the water front, resulting in more viscous fingerings. As capillary forces are related to the core's wettability, the trend suggested by our experiments between the breakthrough earliness and injection flow rate may only be valid for the water-case.

All others corefloods from this study (CF2 to CF5) show front instabilities taking the form of a main large finger or multiple fingers. CF2 and CF3, conducted with the Primol, have fingering slightly more complex than the fingering obtained with the Drakeol (CF4 and CF5). Experiments with the Primol exhibit up to 4 distinct fingers while it takes the form of a main, central finger with the Drakeol. It should be noted that the shape of the front is changing during the flooding leading to the progressive fingers merging. Despite the visible front instabilities for CF2 to CF5, the core is overall well swept at breakthrough. For all corefloods, the middle core cross-section shows a complete sweeping at breakthrough (Fig. 5). fingering is not as severe as it can be seen in slab experiments or in micro-models [7, 9, 15], where oil recovery at breakthrough (%PV) < *0.1* can be achieved. The comparison of the oil recoveries behind the water front (in the swept area) suggests that the early breakthrough is possibly mainly due to a lower oil recovery in the swept areas. Oil saturation behind the water front is measured around 38% for CF1 while it comes close to 60% for the others corefloods.

The experiments conducted here are represented on Fig. 13 in a manner following a Lenormand et al. phase-diagram [7]. This diagram represents the displacement regimes that may be expected according to two dimensionless numbers: the capillary and the viscous numbers (*C* and *M*, respectively). This diagram is probably too simplistic as it excludes the viscous and capillary fingering mechanisms to occur at the same time. It does provide, however, a global representation of the prevailing fingering mechanism which may occur during immiscible displacement of oil by water. This diagram has been originally constructed and validated using simulations and experiments conducted on micro-models only. The scale, the geometry and the dimensions of the porous media used here are very different.

On the diagram, the experiments of this study fall in (or at the fringe) of the capillary fingering region, not so far from the viscous fingering region for CF2 to CF5. *M* and *C* values are given Table 5.These predictions are compatible with our observations, but the result of CF1 falling in the same domain as the other experiments is questionable, as it demonstrated a stable front. However the residual oil saturation in the swept zones (around 37%) demonstrates the high capillary forces. The stable displacement region they defined should be seen as a region of near complete oil recovery, reached beyond the standard capillary desaturation curve transition, at very high capillary number. Predictions for CF2 to CF5 are relatively consistent with experimental results, as they show a combination of both viscous and capillary fingering mechanisms. The contribution of the two mechanisms can't be done using the visual inspection only. In the following section, the CT-images has been processed to quantify their contribution alone to the breakthrough earliness.

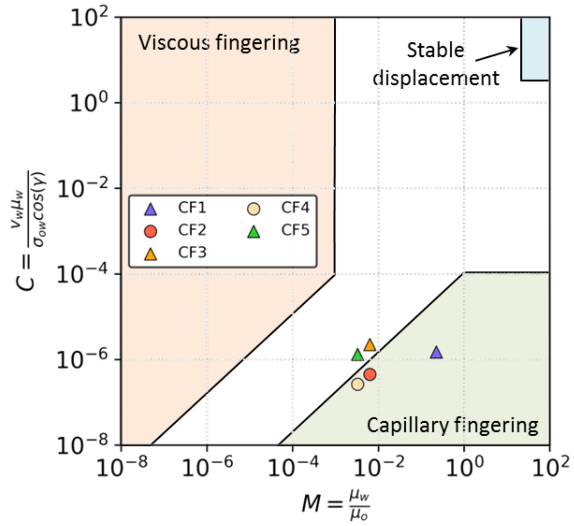

**Fig. 13.** Corefloods positioning on Lenormand et al [7] fingering domains diagram. *M* and *C* are the dimensionless viscosity and capillary numbers. Circle and triangle markers respectively refer to corefloods conducted at 1.7 and 7.0 cc/min. *M* and *C* values are given Table 5.

**Table 5.** Viscous and capillary (*M, C*) dimensionless numbers defined by Lenormand et al. $M = \mu_w/\mu_o$ and $C = v\mu_w / \sigma_{ow} cos\theta$, where $\theta$ is the contact angle, taken to 0°, water-wet case.

| | CF1 | CF2 | CF3 | CF4 | CF5 |
|---|---|---|---|---|---|
| *M* | 2.2E-01 | 6.3E-03 | 6.3E-03 | 3.3E-03 | 3.3E-03 |
| *C* | 1.5E-06 | 4.5E-07 | 2.3E-06 | 2.7E-07 | 1.3E-06 |

### 3.3 Fingering mechanisms

Following the Lenormand et al. phase-diagram theory [7], the volume of water injected at breakthrough can be expressed as the product of two distinct contributions (see equation 6): (i) the fraction of the core pore volume swept by the water at BT ($PV^{swept}$) and (ii) the oil-recovery in this swept areas $S_o^{swept}$. This oil recovery is defined as the fraction of oil produced (or displaced) in the swept areas. The sweeping efficiency $PV^{swept}$ account for fingering observable at macro-scale. The microscopic recovery $S_o^{swept}$ account for the capillary trapping, occurring at the pore-scale. They can be respectively identified as the viscous fingering and the capillary fingering.

$$PV@BT = PV^{swept} * S_o^{swept} \qquad (6)$$

The volume swept by the water at a certain time is obtained by subtracting the initial CT-scan (at *Swi*) to the corresponding CT-scan. Swept and unswept areas are segmented using a threshold applied on the subtracted saturations. Fig. 14 shows the core local saturations measured using the CT-scanner during the flooding. Two populations of local saturations can be clearly identified: (1) in red, high oil saturation, corresponding to local *Swi* values and (2) in blue, lower oil saturations defining the swept area. After phases segmentation, the volume swept at BT ($PV^{swept}$) and the microscopic oil recovery $S_o^{swept}$ in this area are easily derived (see illustration Fig. 15).

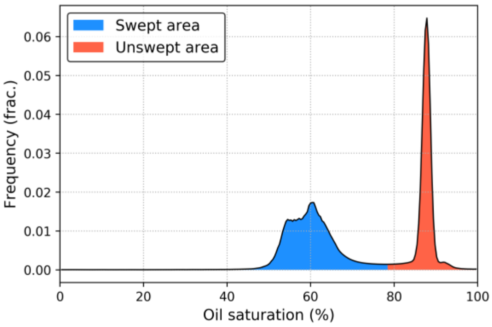

**Fig. 14**. CT-scan local saturations distribution due core flooding (CF5@14.5%PV. The red and blue areas refer to the unswept and swept areas.

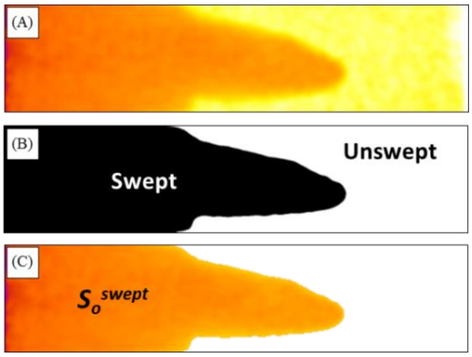

**Fig. 15**. Swept and unswept areas segmentation (CF5@14.5%PV, sagittal slicing). (A) is the original image, (B) is after swept and unswept areas segmentation (see details in Fig. 14) and (C) is the saturation displayed in the swept area, used to compute the microscopic oil recovery.

$PV^{swept}$ and $S_o^{swept}$ values are computed for all corefloods and summarized Table 6. They are plotted and compared Fig. 16. Plain curves represent constant pore-volume curves: they show the solutions of $S_o^{swept}$ and $PV^{swept}$ resulting in equivalent pore volume at breakthrough (see equation 6). This diagram allows to dissociate the contribution of the waterflood sweeping and the microscopic recovery to better characterized the fingering mechanisms underlying the early BT. Above the $x = y$ diagonal is the region of capillary fingering, with poor microscopic oil recoveries. Below the $x = y$ diagonal is the region of viscous fingering, with poor sweeping efficiencies. High $PV^{swept}$ and $S_o^{swept}$ values is the region of stable displacement.

**Table 6.** $PV^{swept}$ and $S_o^{swept}$ values measured at BT, respectively quantifying the viscous fingering and the capillary fingering (see equation 6).

| | CF1 | CF2 | CF3 | CF4 | CF5 |
|---|---|---|---|---|---|
| $S_o^{swept}$ (%) | 51.3 | 31.5 | 30.6 | 30.2 | 29 |
| $PV^{swept}$ (%) | 98.0 | 88.6 | 71.9 | 89.1 | 66.4 |

The 5 corefloods show good sweeping efficiency and intermediate to poor microscopic oil recovery. As expected from the piston-like displacement, CF1 coreflood shows a near-perfect sweeping efficiency at BT, with all the remaining oil trapped by capillary forces. The corefloods CF2 to CF5 demonstrate lower microscopic oil recoveries, with a sweeping efficiency close to 90% for experiments conducted at 1.4cc/min and around 70% for the experiments conducted at higher velocity (7cc/min). The strong reduction of microscopic oil recoveries between CF1 and the other cores seems mainly explained by the fluid mobility ratios.

For coreflood CF2 to CF5, the difference in sweeping efficiency at BT is not controlled by the fluids mobility ratio: CF2-CF3 (and CF4-CF5) are conducted using the same fluids but show different sweeping values. It is on the other hand controlled by the injection flow rate. This result illustrates the effect of the flow velocity discussed above for water-wet cores, with the fluids front being less stabilized at increasing flow rates.

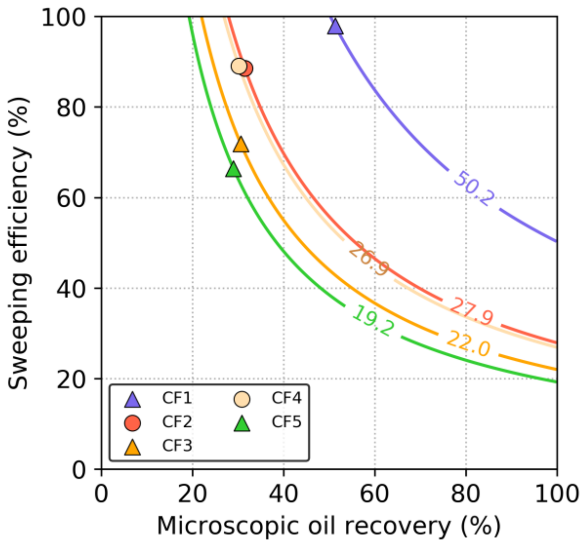

**Fig. 16.** Sweeping efficiency and microscopic oil recovery at breakthrough ($S_o^{swept}$ and $PV^{swept}$). Plain curves are iso-injected pore volume line, plotted for each coreflood (see equation 6). Circle and triangle markers respectively refer to corefloods conducted at 1.7 and 7.0 cc/min.

## 4. Conclusion

In this study, effect of the oil viscosities and injection flow rates on the water-breakthrough have been investigated using in-situ saturation imaging. It was found that the oil recovery at brine breakthrough (%PV) shows a good correlation with the viscous fingering number as defined by Doorwar [8]. Early water breakthrough appeared boosted by injection flow rate and less favorable fluids mobility ratio.

The local saturation monitoring provides new insight to characterize the finger shapes and analyze the production mechanisms, for the different flowing conditions. In water-wet conditions, the capillary forces contribute to stabilizing the front against viscous instabilities. If the viscous forces become too dominant, the capillary forces are overcome and fingering may occurs for displacement with unfavorable fluids ratio.

A diagram has been constructed to separately quantify the contribution of the viscous fingering and the capillary fingering. Capillary fingering is defined as the fingering occurring at low scale, below the scanner resolution. Viscous fingering is defined as the macroscopic fingering, visible using the CT-images. Our results indicate that although both fingerings were seen in our corefloods, capillary fingering was responsible for more oil trapping than the viscous fingering.

For further work, additional experiments should be conducted to compare the fingering mechanisms for oil-wet or intermediate-wet core.

## Acknowledgement

Experiments have been conducted with the technical expertise of M.C. Lynch for the CT-scanner and F. Martin for the corefloods.

## References

1. P. van Meurs, C. van der Poel, A Theoretical Description of Water-Drive Processes Involving Viscous Fingering, *SPE-931-G*, **213**, 103-112 (1958)
2. T. K. Perkins, O. C. Johnston, A Study of Immiscible Fingering in Linear Models, *SPE-8371-PA 9*, **01**, 39–46 (1969)
3. J. Hagoort, Displacement Stability of Water Drives in Water-Wet Connate-Water-Bearing Reservoirs, *SPE-8371-PA 14*, **01**, 63–74 (1974)
4. Y. C. Yortsos, A. B. Huang, Linear-Stability Analysis of Immiscible Displacement: Part 1-Simple Basic Flow Profiles, *SPE-12692-PA* 1, **04**, 378–390 (1986)
5. E. J. Peters, D. L. Flock, The Onset of Instability During Two-Phase Immiscible Displacement in Porous Media, *SPE-8371-PA 2*, **02**, 249–258 (1981)
6. R. L. Chuoke, P. van Meurs, C. van der Poel, The Instability of Slow, Immiscible, Viscous Liquid-Liquid Displacements in Permeable Media, *SPE-1141-G,* **216**, 188-194 (1959)
7. R. Lenormand, E. Touboul,C. Zarcone, Numerical models and experiments on immiscible displacements in porous media, *Journal of Fluid Mechanics*, **189**, 165–187 (1988)
8. S. Doorwar, Understanding unstable immiscible displacement in porous media, *Thesis*, University of Texas at Austin (2015)
9. R. D. Loubens, G. Vaillant, M. Regaieg et al., Numerical Modeling of Unstable Water Floods and Tertiary Polymer Floods into Highly Viscous Oils, *SPE-182638-PA*, **23**, (2017)
10. H. Luo, K. K. Mohanty, M. Delshad, Modeling and Upscaling Unstable Water and Polymer Floods: Dynamic Characterization of the Effective Viscous Fingering, *SPE-179648-PA 20*, **04**, 779–794 (2017)
11. T. Worawutthichanyakul, K. K. Mohanty, Unstable Immiscible Displacements in Oil-Wet Rocks, *Transport in Porous Media* **119**, 205–223 (2017)
12. S. Doorwar, K. K. Mohanty, Viscous-Fingering Function for Unstable Immiscible Flows (includes associated Erratum), *SPE-173290-PA 22*, **01**, 19–31 (2017)
13. F. J. Fayers, An Approximate Model With Physically Interpretable Parameters for Representing Miscible Viscous Fingering, *SPE-12692-PA 3*, **02**, 551–558 (1988)
14. J. Sharma, S. B. Inwood, A. Kovscek, Experiments and Analysis of Multiscale Viscous Fingering During Forced Imbibition, *SPE-173290-PA 17*, **04**, 1142–1159 (2012)
15. A. Skauge, P. A. Ormehaug, T. Gurholt et al., 2-D Visualisation of Unstable Waterflood and Polymer Flood for Displacement of Heavy Oil, *Society of Petroleum Engineers*, 12 (2012)

16. D. Pavone, Observations and Correlations for Immiscible Viscous-Fingering Experiments, *SPE-12692-PA* 7, **02**, 187–194 (1992)
17. D. R. F. Harleman, R. R. Rumer, Longitudinal and lateral dispersion in an isotropic porous medium, *Journal of Fluid Mechanics*, **3**, 385–394 (1963)
18. S. Bouquet, S. Leray, F. Douarche, et al., Characterization of Viscous Unstable Flow in Porous Media at Pilot Scale - Application to Heavy Oil Polymer Flooding, *EAGE* (2017)
19. A. Clauset, C. R. Shalizi, M. E. J. Newman, Power-Law Distributions in Empirical Data. *SIAM Rev, 51*, **4**, 661–703 (2009)

# Core-scale sensitivity study of $CO_2$ foam injection strategies for mobility control, enhanced oil recovery, and $CO_2$ storage

*Zachary Paul* Alcorn[1*], *Sunniva B.* Fredriksen[1], *Mohan* Sharma[2], *Tore* Føyen[1,3], *Connie* Wergeland[1], *Martin A.* Fernø[1], *Arne* Graue[1], *and Geir* Ersland[1]

[1]Dept. of Physics and Technology, University of Bergen, Norway
[2]National IOR Centre of Norway, University of Stavanger, Norway
[3]SINTEF Industry, Trondheim, Norway

**Abstract.** This paper presents experimental and numerical sensitivity studies to assist injection strategy design for an ongoing $CO_2$ foam field pilot. The aim is to increase the success of *in-situ* $CO_2$ foam generation and propagation into the reservoir for $CO_2$ mobility control, enhanced oil recovery (EOR) and $CO_2$ storage. Un-steady state *in-situ* $CO_2$ foam behavior, representative of the near wellbore region, and steady-state foam behavior was evaluated. Multi-cycle surfactant-alternating gas (SAG) provided the highest apparent viscosity foam of 120.2 cP, compared to co-injection (56.0 cP) and single-cycle SAG (18.2 cP) in 100% brine saturated porous media. $CO_2$ foam EOR corefloods at first-contact miscible (FCM) conditions showed that multi-cycle SAG generated the highest apparent foam viscosity in the presence of refined oil (*n*-Decane). Multi-cycle SAG demonstrated high viscous displacement forces critical in field implementation where gravity effects and reservoir heterogeneities dominate. At multiple-contact miscible (MCM) conditions, no foam was generated with either injection strategy as a result of wettability alteration and foam destabilization in presence of crude oil. In both FCM and MCM corefloods, incremental oil recoveries were on average 30.6% OOIP regardless of injection strategy for $CO_2$ foam and base cases (i.e. no surfactant). $CO_2$ diffusion and miscibility dominated oil recovery at the core-scale resulting in high microscopic $CO_2$ displacement. $CO_2$ storage potential was 9.0% greater for multi-cycle SAGs compared to co-injections at MCM. A validated core-scale simulation model was used for a sensitivity analysis of grid resolution and foam quality. The model was robust in representing the observed foam behavior and will be extended to use in field scale simulations.

## 1. Introduction

A major challenge in carbon dioxide ($CO_2$) enhanced oil recovery (EOR) is poor macroscopic $CO_2$ sweep efficiency caused by the low viscosity and density of injected $CO_2$ [1, 2]. These adverse properties can result in viscous fingering and gravity override, greatly hindering oil recovery and sweep efficiency [3, 4]. Reservoir heterogeneity can also cause injected $CO_2$ to channel through high permeability zones (layers or fractures) resulting in early $CO_2$ breakthrough, high $CO_2$ recycling, and low incremental oil recoveries. $CO_2$ foam injection is a laboratory verified and field-validated technique proven to mitigate poor $CO_2$ sweep efficiencies through effectively increasing $CO_2$ viscosity and reducing its relative permeability [5].

Foam is a dispersion of gas ($CO_2$, in this case) in liquid where the liquid phase is continuous and at least some of the gas phase is discontinuous and separated by lamella [6]. The discontinuous $CO_2$ phase becomes trapped between lamella [7], effectively reducing its relative permeability. Foam apparent viscosity is used as a measure of foam strength in laboratory experiments, where a stronger foam corresponds to a higher apparent viscosity. Entrapment of $CO_2$ in foam and $CO_2$-surfactant emulsification also increases $CO_2$ apparent viscosity and reduces $CO_2$ mobility [8, 9]. These combined effects are capable of diverting flow from high permeability, well-swept regions, into less permeable areas with higher oil saturations, thereby increasing macroscopic displacement and oil recovery.

$CO_2$ foam generation and stability are influenced by oil composition and wettability. The presence of oil can destabilize some foams [10] and it has also been reported that foam can only be generated at strongly water-wet conditions [11]. At strongly water-wet conditions, water-wet films covering the pore surfaces maintain the continuous foam structure [12]. A shift to oil-wet can cause the lamellas to detach from the pore walls and foam may be destabilized. Schramm and Mannhardt (1996) confirmed reduced foam effectiveness at intermediate to oil-wet conditions [13] and Fredriksen et al. (2019) induced surfactant wettability alteration in oil-wet fractures to generate $CO_2$ foam in matrix below a critical oil saturation [14]. The impacts of wettability and the presence of oil on foam stability are areas under active investigation.

---

[*] Corresponding author: zachary.alcorn@uib.no

Foam is generated in porous media by injecting a water (or $CO_2$) soluble foaming agent (surfactant) with gas, such as $CO_2$, either simultaneously (co-injection) or in alternating slugs (SAG). The injection strategy must balance *in-situ* foam generation, propagation, and injectivity constraints. In practice, there are two main injection strategies for *in-situ* $CO_2$ foam generation [15, 16]. The first is simultaneous injection of $CO_2$ and surfactant solution known as co-injection. In this case, the quality of the foam is determined by the fraction of gas ($f_g$) and is a function of flow rate [17]. The second injection strategy is surfactant-alternating gas (SAG), where the surfactant solution and $CO_2$ are injected in alternating slugs and the quality of the foam depends on the slug sizes of $CO_2$-to-surfactant solution. At laboratory scale, alternating slugs are not typically used due to small fractional flows of gas and the inability to achieve steady-state [18]. At the field scale, operational constraints influence aspects of the injection strategy. For example, co-injection can be difficult to implement due to extremely low injectivity and associated pressure increases, which minimize throughput [19]. In addition, downhole corrosion can occur from carbonic acid during co-injection of $CO_2$ and surfactant solution. This has led to a majority of field tests using SAG injection for better injectivity control, especially when operating close to the fracture pressure [20, 21, 22].

Few attempts have been made to characterize unsteady-state *in-situ* $CO_2$ foam behavior. Therefore, this study attempts to begin establishing a knowledge base for investigating core-scale $CO_2$ foam injection strategies. The aim is to reduce $CO_2$ mobility, through the generation of foam, in experiments that are representative of the near wellbore region. This work is part of an ongoing field pilot research program utilizing $CO_2$ foam for mobility control, EOR, and $CO_2$ storage in the Permian Basin of West Texas. Miscible $CO_2$ foam injection will be implemented to reduce high producing gas-oil-ratios, $CO_2$ recycling, and to provide mobility control for increased $CO_2$ sweep efficiency. The reservoir pressure in the pilot area is 220 bars, which is close to the formation fracture pressure of 269 bars [23]. An injection strategy must be selected that will not fracture the formation, which would cause problems beyond any remediation by the foam. Thus, the primary objective of this work is to evaluate co-injection and a variety of SAG injection strategies for $CO_2$ foam mobility control, EOR, and $CO_2$ storage to assist in the design of the field pilot. A secondary objective is to investigate the impacts of miscibility conditions on *in-situ* foam generation and stability. For more detailed information on the field pilot program see Alcorn et al. (2019).

$CO_2$ foam was evaluated based upon apparent foam viscosity and its impact on oil recovery. In addition, $CO_2$ storage potential was measured for each injection strategy. Experimentally, foam behavior by co-injection, single-cycle SAG, and multi-cycle SAG were performed in brine saturated systems to generate foam *in-situ* without the presence of oil. $CO_2$ foam EOR corefloods were then conducted at first-contact miscible (FCM) and multi-contact miscible (MCM) conditions using *n*-Decane and crude oil, respectively, after waterflooding. A local-equilibrium foam model was fitted from foam stability scans, and experimental results from a $CO_2$ foam EOR coreflood were used to validate a core-scale numerical model to investigate effects of grid resolution, foam quality, and surfactant. The main objective of the numerical sensitivity study was to validate the foam model in representing the observed foam behavior, which is being extended for use in ongoing field-scale simulations.

## 2. Materials and Fluids

Outcrop limestone core plugs were used as reservoir analogues due to limited reservoir cores available from the field. Core plugs were drilled with a 2-inch diameter from larger slabs, cut, cleaned and dried before being 100% saturated with synthetic Permian Basin brine under vacuum. Values of porosity and pore volumes were calculated based on weight differential before and after fluid saturation. Absolute permeability was measured by injecting brine until a stable differential pressure was obtained for three different flood rates. Permeability measured for the single core plugs varied between 8mD to 73mD and porosities from 19 to 35%.

Synthetic Permian Basin brine was made based upon water analysis from the field, whereas a light North Sea crude oil was used. The North Sea crude oil has an API of 33.6° (calculated from specific gravity), a little above the API gravity of the Permian Basin crude of 31° at standard conditions. Compositions of brine and crude oil are reported elsewhere [14, 24]. The North Sea crude oil is considered MCM with $CO_2$ at 60°C and 180 bar, with a minimum miscibility pressure (MMP) of 125 bar [25]. Reservoir conditions for the field test are well above MMP for $CO_2$ and crude oil. To investigate the effects of miscibility conditions on foam generation and stability a refined oil, *n*-Decane ($C_{10}H_{22}$), was also selected for the first set of EOR corefloods to obtain FCM conditions with $CO_2$.

A non-ionic surfactant (i.e. Huntsman L24-22) was previously selected for the $CO_2$ foam field pilot from a surfactant screening study that quantified adsorption on reservoir rock with and without $CO_2$ present [26]. The non-ionic surfactant was also screened for its ability to alter wettability of oil-wet carbonate rocks to weakly oil-wet conditions in favor of foam generation [14]. The non-ionic surfactant was used at a 1.0 wt% concentration in Permian Basin Brine.

## 3. Procedure

### 3.1 Coreflood Set-up

The core-scale system was composed of two stacked core plugs providing a total nominal length of 25 cm to generate foam *in-situ*. Cores with similar porosity and absolute permeability were paired and stacked. An overview of experiments and their stacked system properties are presented in Table 1.

**Table 1** – Experimental overview and core properties

| ID | Experimental overview | Oil phase | Length [cm] | Porosity [%] | $K_{abs}$ [mD] | $S_{wi}$ |
|---|---|---|---|---|---|---|
| **D1** | Foam Scan: Co-injection | - | 7.5 ± 8.8E-03 | 24.2 ± 0.2 | 20.5 ± 0.3 | 1.00 ± 0.01 |
| **D2-D3** | Foam Scan: Co-injection | - | 12.7 ± 3.5E-03 | 26.2 ± 0.8 | 31.6 ± 0.2 | 1.00 ± 0.01 |
| **E2** | Foam Stability: SAG | - | 12.7 ± 2.0E-03 | 25.4 ± 0.2 | 42.3 ± 0.1 | 1.00 ± 0.01 |
| **E3-E4** | EOR: Co-injection 1.0 ft/day | n-Decane | 24.4 ± 2.8E-03 | 22.3 ± 1.9 | 15.5 ± 0.2 | 0.24 ± 7.22E-03 |
| **E5-E6** | EOR: Co-injection 2.0 ft/day | n-Decane | 24.9 ± 2.8E-03 | 25.8 ± 0.3 | 21.4 ± 0.3 | 0.31 ± 7.28E-03 |
| **E7-E8** | EOR: Single cycle SAG | n-Decane | 27.5 ± 2.8E-03 | 30.7 ± 2.8 | 24.0 ± 0.0 | 0.38 ± 7.59E-03 |
| **E9-E10** | EOR: Multi-cycle SAG | n-Decane | 24.8 ± 2.8E-03 | 25.1 ± 1.5 | 38.4 ± 0.4 | 0.29 ± 7.27E-03 |
| **E13-E14** | Foam Scan/EOR: Co-injection 1.0 ft/day | Crude oil | 24.7 ± 2.8E-03 | 27.5 ± 0.4 | 31.4 ± 0.5 | 0.24 ± 7.13E-03 |
| **E15-E16** | Foam Scan/EOR: Co-injection 1.0 ft/day (base case[1]) | Crude oil | 27.4 ± 2.8E-03 | 22.5 ± 2.3 | 14.3 ± 1.3 | 0.15 ± 7.04E-03 |
| **E17-E18** | EOR: Multi-cycle SAG 1.0 ft/day | Crude oil | 24.9 ± 2.8E-03 | 28.4 ± 1.7 | 31.6 ± 0.2 | 0.25 ± 7.20E-03 |
| **E21-E22** | EOR: Multi-cycle WAG 1.0 ft/day (base case[1]) | Crude oil | 25.0 ± 2.8E-03 | 25.8 ± 1.8 | 21.3 ± 0.7 | 0.24 ± 7.18E-03 |

[1] Base case without surfactant solution.

[2] Uncertainty calculated as standard deviation of the mean

The cores were mounted in a horizontally oriented Hassler type core holder and experimental conditions were set to 60°C, to avoid crude oil wax precipitation. Pore pressure was set to 180 bars for $CO_2$ to be MCM with the North Sea crude oil. At these conditions $CO_2$ is supercritical and will create an emulsified phase (liquid-in-liquid) with the surfactant solution. A differential pressure transducer and two absolute pressure transducers (i.e. one downstream and one upstream) measured pressure response. The standard setup for high-pressure/high-temperature $CO_2$ foam injection can be found in [27].

*In-situ* foam generation, strength, and stability is evaluated by its apparent viscosity, which is quantified from flow rate and pressure drop during foam injection [28]. Foam apparent viscosity is calculated by;

$$\mu_{app} = \frac{k\nabla p}{(u_l + u_g)} \tag{1}$$

where, $k$ is the absolute permeability of the porous media, $\nabla p$ is the pressure gradient measured, and $u_l$ and $u_g$ are the superficial velocities of liquid and gas, respectively [17].

### 3.2 Unsteady-State Foam Stability Scan by SAG

Foam generation and stability was investigated for two modes of SAG injection in a foam stability scan. Single-cycle SAG was run at 100% brine saturated conditions prior to multi-cycle SAG on the same core (E2). A waterflood to re-establish initial conditions with close to zero $CO_2$ saturation was run in between the foam stability scans. For both SAG injections, pre-determined slug sizes were injected for 4.0 pore volumes (PVs) targeting a gas fraction ($f_g$) of 0.70. For single-cycle SAG, a single slug of surfactant solution was injected (1 PV) before $CO_2$ was introduced for 3 PVs. For multi-cycle SAG, 12 rapid cycles were run: each cycle consisting of a surfactant slug of 0.11 PVs and a $CO_2$ slug of 0.22 PVs. Un-steady state apparent foam viscosities were calculated as a function of time (i.e. PVs injected) using Equation 1.

### 3.3 Steady-State Foam Quality and Rate Scans by Co-injection

Foam generation and stability during co-injection was assessed by foam quality and rate scans. Tests were run in 100% brine saturated cores, where one system was composed of a single core (D1) and the other a stacked system (D2-D3). Scans were also performed at residual oil saturation after $CO_2$ foam EOR to investigate the effect of residual oil on foam stability (E13-E14), and equivalently for a base case without surfactant (E15-E16). See Table 1 for experimental overview.

Foam quality scans determine the optimal gas fraction ($f_g$) that will generate the highest apparent viscosity during co-injection. $CO_2$ fractions were changed from 0.0 to 0.90 for drainage-like co-injection (i.e. increasing $CO_2$ fraction) at a total superficial injection rate of 1.0 ft/day. Each fraction was injected until steady state pressure drop was achieved before increasing to the next fraction. The apparent foam viscosity was calculated from Equation 1. Rate scans were performed following foam quality scans on the same core(s) to estimate rate-dependency on shear-thinning behavior. Rate scans for co-injection were run by increasing the total injection rate at the optimal $CO_2$ fraction from quality scans. Starting at a superficial velocity of 1.0 ft/day, the injection rate was increased to 2.0, 3.0, and 4.0 ft/day after reaching steady-state conditions.

### 3.4 $CO_2$ Foam EOR

Core plugs were initially 100% brine saturated, stacked, and drained with either *n*-Decane or dead crude oil to irreducible water saturation ($S_{wi}$) at a constant pressure drop of 2 bar/cm. A waterflood was performed for 1 PV prior to $CO_2$ foam injection. Injection strategies during $CO_2$ foam were either co-injection, single-cycle, or multi-cycle SAG. $CO_2$ foam was injected for no more than 2 PVs, considering volumetric and economic limitations at the field-scale. Produced fluids were measured at ambient conditions as stock tank volumes. Density and compressibility were considered negligible for the specific dead crude oil and refined oil used in these experiments. Saturations were calculated based upon the difference in initial oil in place and oil produced divided the total pore volume.

$CO_2$ foam EOR was performed at FCM conditions using *n*-Decane and at MCM conditions using North Sea crude oil. At FCM conditions, $CO_2$ foam co-injection used two injection rates (1.0 ft/day for E3-E4 and 2.0 ft/day for E5-E6) to investigate the shear-thinning behavior of foam during EOR. Co-injection results were then compared with single cycle (E7-E8) and multi cycle SAG (E9-E10). The most promising (highest apparent foam viscosity and oil recovery) injection strategies were evaluated at MCM conditions, with crude oil, and compared with base case experiments without surfactant solution.

### 3.5 Core-Scale Model Set-up

Laboratory data from a co-injection experiment (E13-E14) was utilized for a core-scale simulation model. The model was initialized to represent the stacked system during waterflood and co-injection. For the waterflood, simulations were conducted with ECLIPSE 100 Blackoil simulator while the compositional simulator E300 (Schlumberger, 2015.2) was used for co-injection. Experimental data validated the model through matching bottom hole pressure (BHP) and cumulative oil/water production. The validated model was used to conduct a sensitivity analysis on the effect of grid cell size, foam quality, and surfactant on oil recovery and $CO_2$ mobility reduction. The main objective was to ensure model robustness at representing the observed foam behavior, which is extended to use in ongoing field scale simulations.

The base case model consisted of a rectangular grid with dimensions 1 x 1 x 100 (x, y, z). The length of the model was identical to the experimental core system length of 24.7 cm. The model and individual grid cells were also consistent with the core diameter of 4.8 cm thus, each individual grid cell measured 4.8 x 4.8 cm in the x- and y-directions. The injector was located in the first grid block (inlet), while the producer was located in the last grid block (outlet). The production well was placed on BHP control and the injector was controlled by rate both of which were measured in the laboratory. Relative permeability data for the waterflood was derived from JBN analysis of oil and water displacement during the laboratory experiment [29]. Oil and water densities and viscosities were available from PVT-analysis of the crude oil. The model was initiated with $S_{wi}$ of 0.24 at a system pressure of 182 bars.

The co-injection was initialized at pressure and saturations from the history-matched waterflood. The grid size, orientation, well completions and controls were kept identical, except two injection wells were used to represent the single co-injection well from the experiment (one for $CO_2$ and one for surfactant solution). A compositional simulation case was generated which contained 14 oil components and 2 water components (water and surfactant). Relative permeability curves were derived from $CO_2$/brine displacement experiments on similar core material described elsewhere [23]. Despite their influence on foam behavior, capillary pressure effects were not included in this study. This is an area, which merits further investigation.

The injection schedule was identical to the experimental procedure and a foam quality of 70% was targeted using a surfactant solution concentration of 1.0 wt%. The effect of foam was modeled using an empirical local-equilibrium approach where the gas relative permeability in the presence of foam is modified by multiplying the gas relative permeability without foam by a mobility reduction factor (MRF) [30]. The mobility reduction factor is dependent upon water saturation, oil saturation, surfactant concentration and shear rate. A maximum gas mobility reduction (*fmmob*) is also used to set the maximum mobility reduction that can be achieved by foam. These parameters were derived from foam quality and rate scans and fit to the empirical model by curve fitting regression [23, 30].

## 4. Results and Discussion

Apparent viscosities and incremental oil recoveries were used to evaluate foam generation, stability, and EOR performance during $CO_2$ foam injection. Several mechanisms contribute to the foam apparent viscosity (and pressure response) including foam generation, trapped gas, and $CO_2$-surfactant emulsification.

### 4.1 Unsteady-State Foam Stability by SAG

$CO_2$ foam stability scans by single-cycle and multi-cycle SAG injections were compared in initially brine saturated systems without oil present (Figure 1). Foam apparent viscosity during single-cycle SAG was 18.2 ± 2.7 cP (dashed curve, Figure 1), and 120.2 ± 0.3 cP for multi-cycle SAG (solid curve, Figure 1). Based upon the increase in apparent viscosity, foam was generated when the first $CO_2$ slug was injected for both injection modes (Figure 1).

During single-cycle SAG, foam generation occurred within the first PV of $CO_2$ injected and foam remained stable for the next 2 PV with only a slight dry-out effect towards the end of injection (black dashed curve, Figure 1). Injecting multiple alternating slugs of surfactant solution and $CO_2$ improved conditions for foam generation and stability. During multi-cycle SAG, surfactant solution was introduced to the system in an imbibition process, which caused a decrease in capillary pressure, likely triggering foam generation. This change in capillary pressure is advantageous for foam generation since the creation of lamella requires exceeding a minimum pressure gradient. Hence, a decrease in capillary pressure during the surfactant slugs improved conditions for foam generation. Increased wetting-phase saturation during surfactant solution slugs also may have mitigated foam dry-out. The growth and propagation of a stable high apparent viscosity foam was clear during multi-cycle SAG (solid curve, Figure 1).

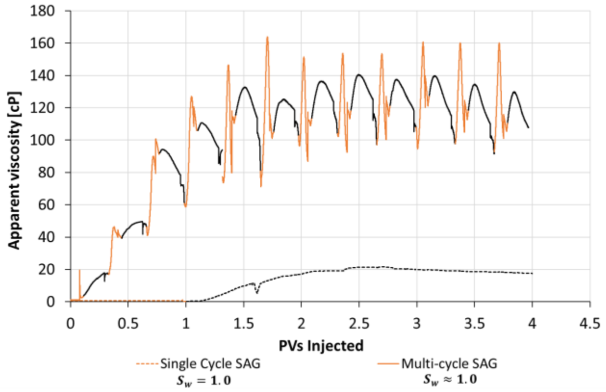

**Fig. 1.** Foam apparent viscosity as a function of pore volumes injected during single-cycle SAG (dashed curve) and multi-cycle SAG (solid curve). Orange curves represent surfactant solution slugs and the black curves are $CO_2$ slugs. Single cycle SAG was initiated at $S_w = 1.0$ (no trapped $CO_2$), whereas multi-cycle SAG injection was initiated with a nominal amount of trapped $CO_2$ in the core, $S_w \approx 1.0$.

The first $CO_2$ injection during multi-cycle SAG (from 0.11 to 0.33 PV) is equal to the first $CO_2$ injection of the single-cycle SAG (from 1 to 1.22 PV), except the amount of surfactant injected (which should benefit single-cycle). We can therefore directly compare the first cycle of the experiments, and evidently, the foam generation is much more immediate and rapid in the multi-cycle experiment, resulting in 15 cP increase in apparent viscosity when 0.22 PV is injected, compared with < 5 cP during the single-cycle. It took 5 cycles to reach peak foam strength of 120 cP during the multi-cycle SAG, where each step had an average increase in apparent viscosity of 25 cP. Extrapolating the observed behavior of the first 0.22 PV of the single-cycle experiment for five consecutive cycles to reach peak apparent viscosity, would result in final apparent viscosity of 25 cP.

Despite efforts to return the core to 100% water saturation, the presence of trapped $CO_2$ from the previous single-cycle SAG experiment likely reduced $CO_2$ relative permeability and increased the pressure drop during multi-cycle SAG. This would result in higher foam apparent viscosities. A decrease in effective water permeability was observed for E2 from 42.3 mD to 19.8 mD by capillary trapped $CO_2$ prior to multi-cycle SAG foam stability. However, during multi-cycle SAG, the step-wise increase in differential pressure and significantly increased apparent viscosity compared to single-cycle SAG suggest that the alternating injection scheme did improve conditions for foam generation and stability.

## 4.2 Steady-State Foam Quality and Rate Scans by Co-injection

Figure 2 shows co-injection foam quality scans, D1 and D2-D3 (orange and green curves), which have previously been published [14, 31] and are shown here for comparison.

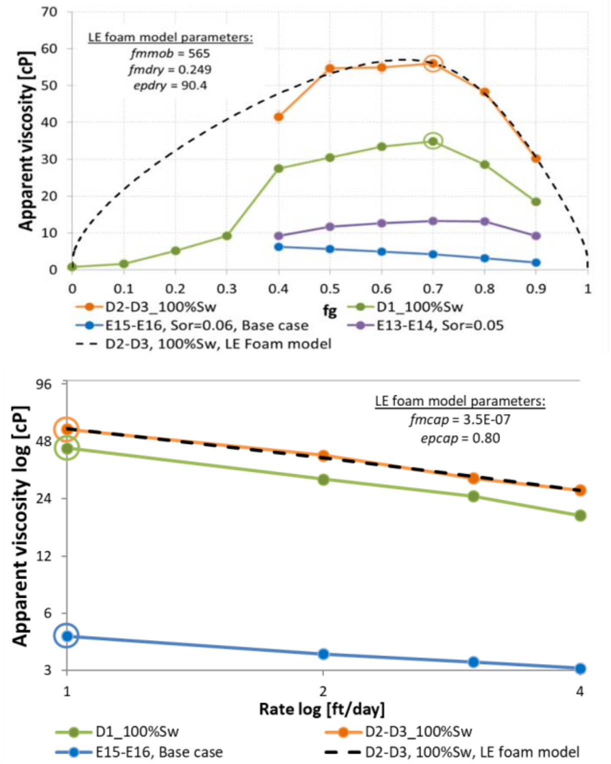

**Fig. 2.** Foam quality scans $f_g = 0.0$ to 0.90 (top) and foam rate scans at 1.0, 2.0, 3.0 and 4.0 ft/day (bottom) during co-injection of $CO_2$ and surfactant solution. Foam model parameters derived from the experiments are also shown.

Peak apparent foam viscosities at steady state for $f_g = 0.70$ was 34.9 ± 1.0 cP (D1), and 56.0 ± 1.6 cP (D2-D3), higher than single-cycle SAG (18.2 ± 2.7 cP), but lower than multi-cycle SAG (120.2 ± 0.3 cP) in Figure 1. The foam strengths measured during the two co-injections are relatively similar, considering the heterogeneous core, but discrepancy remains when comparing the three co-injection experiments to the SAGs. It is likely that the injection scheme is not the only explanation for the variation in apparent viscosities.

Foam quality scans with residual oil also investigated the influence of crude oil on foam stability. Experiment E13-E14 in Figure 2 (purple curve) was performed after $CO_2$ foam EOR at a residual oil saturation ($S_{or}$) = 0.05 (purple curve, Figure 2). A lower apparent foam viscosity was observed for every $f_g$ compared to foam quality scans conducted with 100% initial water saturation (i.e. strongly water-wet) in Figure 2 (orange and green curves). However, apparent viscosities at fg = 0.70 were 13.20 cP for experiment E13-E14 with surfactant (purple curve, Figure 2) compared to 4.19 cP for the base case (E15-E16, blue curve, Figure 2) at $S_{or}$ = 0.06, without surfactant. Hence, these experiments show that this foam system is capable of generating foam with low apparent viscosities when crude oil is present.

## 4.3 $CO_2$ Foam EOR

### 4.3.1 First-Contact Miscible Conditions

Co-injection and SAG injection strategies were evaluated based upon their apparent viscosity and oil recovery at

FCM conditions (Figure 3). The initial waterfloods recovered between 31.2 % and 47.7% OOIP and a clean water cut was observed for all experiments (left of the vertical black dashed line). The range in waterflood recovery can be attributed to core heterogeneity [32]. Recovery factors and apparent viscosity values are listed in Table 2.

$CO_2$ foam co-injections were performed at two different injection rates (1.0 ft/day and 2.0 ft/day) to investigate shear-thinning behavior during EOR corefloods (Figure 3). Foam was generated earlier at higher rate (at 1.7 PVs injected, E5-E6, orange dashed curve) compared to the lower co-injection rate (at 2.3 PVs injected, E3-E4, orange solid curve) from dynamic observations of apparent viscosity. The average apparent viscosity, however, was higher at 1.0 ft/day (28.1 cP, E3-E4) than for 2.0 ft/day (18 cP, E5-E6) for the last 0.5 PVs injected (Table 2). This is an indication of the shear-thinning behavior of foam at increasing flow rates. Shear-thinning behavior was also observed in foam rate scans shown in Figure 2 (bottom).

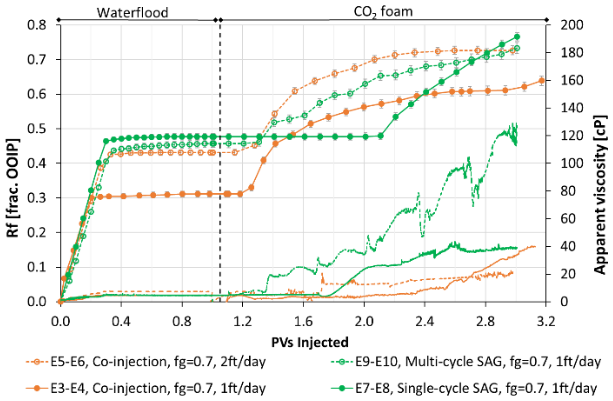

**Fig. 3.** Recovery factor vs. PVs injected for $CO_2$ foam EOR corefloods with co-injection and SAG under FCM conditions with *n*-Decane. The orange curves represent $CO_2$ foam by co-injection at rates of 1.0 ft/day (closed circles) and 2.0 ft/day (open circles), and the green curves are single-cycle SAG (closed circles) and multi-cycle SAG (open circles). The vertical dashed black line separates the waterflood to the left from the $CO_2$ foam flood to the right. The secondary y-axis shows apparent viscosity.

**Table 2**. Recovery factors for $CO_2$ foam EOR corefloods

| Core ID | Injection Strategy | Oil phase | $R_{f,\,WF}$ [%OOIP] | $R_{f,\,CO2\,foam}$ [%OOIP] | $R_{f,\,tot}$ [%OOIP] | Apparent visc. $CO_2$ foam [cP][1] | $S_o$ (after WF) |
|---|---|---|---|---|---|---|---|
| **E3-E4** | Co-injection | n-Decane | 31.2 ± 0.9 | 32.7 ± 1.7 | 63.9 ± 1.4 | 28.1 ± 7.7 | 0.48 |
| **E5-E6** | Co-injection | n-Decane | 43.1 ± 0.8 | 29.6 ± 1.5 | 72.7 ± 1.2 | 18.0 ± 1.4 | 0.39 |
| **E7-E8** | Single-cycle SAG | n-Decane | 47.7 ± 0.8 | 28.9 ± 1.5 | 76.6 ± 1.2 | 37.9 ± 1.1 | 0.48 |
| **E9-E10** | Multi-cycle SAG | n-Decane | 45.7 ± 1.1 | 27.6 ± 1.9 | 73.3 ± 1.6 | 100.7 ± 14.6 | 0.46 |
| **E13-E14** | Co-injection | Crude oil | 62.0 ± 0.9 | 31.0 ± 1.6 | 93.0 ± 1.3 | 5.5 ± 0.5 | 0.29 |
| **E15-E16** | Co-injection[2] | Crude oil | 58.6 ± 1.0 | 34.9 ± 1.7 | 93.5 ± 1.4 | 7.3 ± 0.1 | 0.35 |
| **E17-E18** | Multi-cycle SAG | Crude oil | 62.3 ± 0.9 | 30.5 ± 1.6 | 92.8 ± 1.3 | 7.0 ± 3.0 | 0.28 |
| **E21-E22** | Multi-cycle WAG[2] | Crude oil | 66.8 ± 1.0 | 33.2 ± 1.8 | 100.0 ± 1.4 | 7.3 ± 1.6 | 0.25 |

$R_{f,WF}$ = recovery factor by waterflood; $R_{f,\,CO2foam}$ = recovery factor by $CO_2$ foam; $R_{f,tot}$ = total recovery factor

[1] Mean average last 0.5PVs at the end of the $CO_2$ foam flood. Uncertainties are given as standard deviation of the mean.

[2] Base case without surfactant.

Apparent viscosity trends during SAG EOR (green curves, Figure 3) were the same as for foam stability scans without oil present (Figure 1). The increase in apparent viscosity was more rapid for each SAG injection (green curves) than either of the co-injection experiments (orange curves), likely due a faster increase in $CO_2$ saturation. However, it is possible that a higher apparent viscosity could have been obtained by continuing the co-injection at 1.0 ft/day (Figure 3, solid orange curve). $CO_2$ foam apparent viscosity for multi-cycle SAG (Figure 3, dashed green curve) increased continuously for each cycle and reached an average value of 100.7 cP at the end of injection. In terms of mobility control, multi-cycle SAG was superior in creating conditions for high viscous displacement during EOR corefloods at FCM conditions (Figure 3).

The presence of the alkane *n*-Decane oil did not negatively influence foam generation or propagation for either injection strategy (Figure 3). *N*-Decane is a non-polar oil molecule with has no ability to alter wetting-state like that of heavy polar molecules (i.e. asphaltenes and resins). Aging carbonate rock in *n*-Decane does not alter wettability [33] and so stable foam was able to be created *in-situ*, even in the presence of oil.

Accelerated oil recovery rate was observed from the start of both co-injections (Figure 3, open and closed orange circles) and most of the oil was produced after 1.0 PV of $CO_2$ foam injected. For single-cycle and multi-cycle SAG (solid green circles), no oil was recovered during the initial surfactant slug before $CO_2$ was injected. Thus, diffusion dominated oil recovery above that of viscous displacement by foam at FCM conditions. $CO_2$ diffusion is a dominant recovery mechanism at core-scale with the potential to recover nearly 100% of the oil [34, 35]. At constant $f_g$ = 0.70, $CO_2$ diffusion recovered the same amount of oil regardless of injection mode, on average 29.7 ± 2.2% OOIP. As observed in Figure 3, however, total recoveries did not reach the ultimate recovery potential of 100% OOIP. This is because stable foam lamellas can create barriers that hinder direct contact between the discontinuous $CO_2$ phase and unrecovered oil, negatively impacting oil recovery. Values of incremental oil recovery during $CO_2$ foam are listed in Table 2.

### *4.3.2 Multiple-Contact Miscible Conditions*

Viscous forces are desirable for mobility control and fluid diversion during $CO_2$ foam EOR. Co-injection at 1.0 ft/day and multi-cycle SAG gave best results in terms of both apparent viscosity and EOR at FCM conditions. These injection strategies were therefore used to determine sensitivity in presence of multicomponent crude oil at MCM conditions. Base case experiments were also performed without surfactant solution as a reference. Results are presented in Figure 4.

The initial waterflood recovered on average 62.0 ± 2.8% OOIP (blue curves, Figure 4) with two-phase production, a characteristic of less water-wet conditions [36]. The measured apparent viscosities during $CO_2$ foam experiments demonstrated little to no *in-situ* foam generation. No increase in foam apparent viscosity was observed above that of the base cases without surfactant. Two possible explanations are offered for the absence foam generation:

- Oil composition is known to influence lamella creation and foam stability, and its presence can make some foams more unstable than others. Foam stability can be reduced with decreasing carbon content in crude oils. It has also been observed elsewhere that a lower number alkanes are more destabilizing than higher number alkanes, because their shorter hydrocarbon chains are more easily imbibed into foam plateau borders to solubilize with surfactants leading to oil spreading and foam instability [10, 37-39].

- Wettability alteration by crude oil towards less water-wet conditions can hinder foam generation and strength. It has previously been reported that foam cannot be generated at wettability conditions other than strongly water-wet due to the lack of water-wet snap-off sites [40, 16, 13]. The multi-component crude oil likely induced a shift towards oil-wet conditions, which caused the lamellas to detach from the pore walls, restricting foam generation.

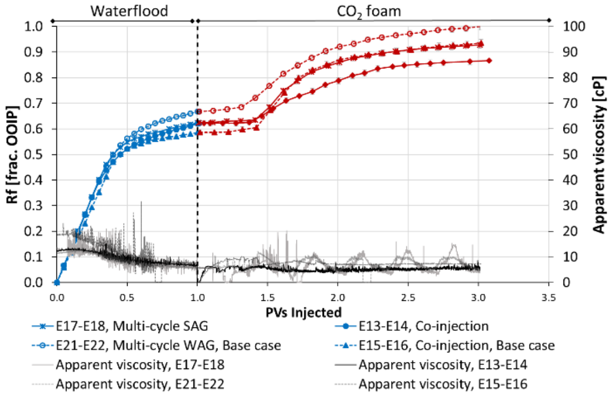

**Fig. 4.** Recovery factor vs. PVs injected for EOR corefloods by co-injection and multi-cycle SAG under MCM conditions. Left of the vertical dashed black line is waterflood (blue curves) and to the right is $CO_2$ foam (red curves). $CO_2$ foam injections are represented by the solid lined curves, while the base cases are dashed lines. The secondary y-axis shows apparent viscosity.

$CO_2$ foam oil recoveries were on average 30.6 ± 3.0% OOIP for all injection strategies with and without surfactant, at both FCM and MCM conditions. Therefore, incremental oil recoveries were also driven by $CO_2$ diffusion at MCM conditions (Figure 4). Bernard and Holm observed the same effect in their core-flood experiments with $CO_2$ foam [44]. This restricts evaluation of injection strategies in terms of production efficiency. Longer induction periods were observed, however, for continuous oil banks to develop under MCM conditions in Figure 4. Between 0.3 to 0.4 PVs of $CO_2$ foam were injected before oil production was observed (red curves). Total recoveries were higher at MCM conditions (93.2 ± 2.7% OOIP) compared to FCM conditions (71.2 ± 3.2% OOIP) as the waterfloods at MCM conditions left behind lower residual oil saturations (Table 2). Further sensitivity analysis on the effect of $CO_2$ fractions on foam behavior was considered using the history-matched core-scale simulation model.

### 4.4 Associated $CO_2$ Storage

A secondary objective for implementing $CO_2$ foam for mobility control in EOR is the potential for storing $CO_2$ as a part of carbon capture, utilization, and storage (CCUS). To calculate $CO_2$ stored, the volume of $CO_2$ produced was measured from volumetric conservation of injected and produced fluids, and subtracted from the volume of $CO_2$ injected. Calculations were made for the FCM and MCM experiments. Based upon mass balance, the value for $CO_2$ storage (given as a fraction of total PV) is equal to the saturation change of oil and water in the core after $CO_2$ foam.

Figure 5 shows $CO_2$ storage in fraction of PV for both co-injections (top) and multi-cycle SAGs (bottom). A direct correlation between the amounts of $CO_2$ stored and the water/oil saturation change was observed regardless of injection strategy. For every amount of fluid produced, the equivalent amount of $CO_2$ was stored. $CO_2$ storage potential was 9.0% greater for multi-cycle SAGs compared to co-injections at MCM. However, $CO_2$ storage potential was 17.1% greater at FCM conditions (for either injection strategy), compared to MCM, due to improved $CO_2$ foam displacement and increased $CO_2$ trapping by capillary forces in more water-wet core plugs.

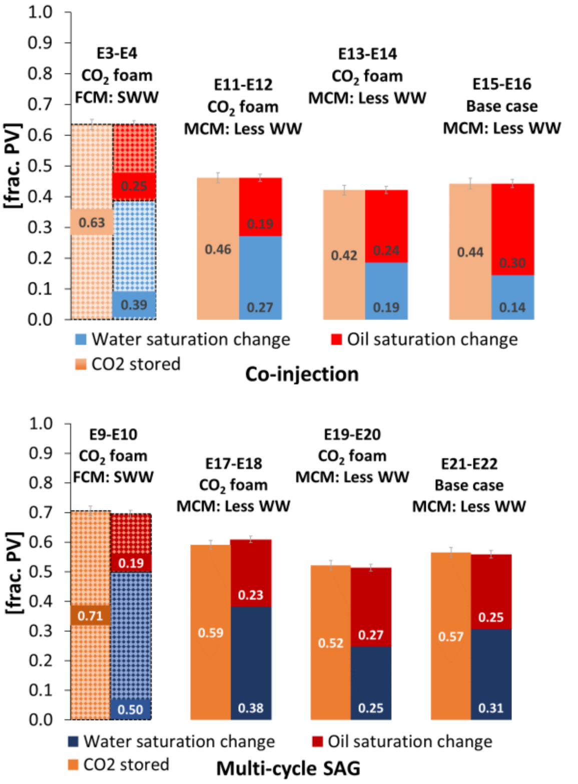

**Fig. 5.** $CO_2$ storage potential during $CO_2$ foam EOR corefloods at FMC and MCM conditions. Top: Co-injection $CO_2$ foam floods and base case (without surfactant). Bottom: Multi-cycle SAG $CO_2$ foam floods and base case. Orange bars represent $CO_2$ stored in fraction of total PV, and the blue and red bars are fractional change in water and oil saturation, respectively. Textured bars indicate FCM conditions, whereas solid bars are experiments at MCM conditions. Note wettability of cores at top of each bar.

### 4.5 Core-Scale Model Validation and Sensitivity Study

The core-scale simulation model utilized the foam stability measurements in Figure 2 to fit the empirical local equilibrium foam model by curve fitting regression [23, 30]. The value for the maximum gas mobility reduction, *fmmob*, however, was reduced to 41.5 in agreement with previous findings on field core material to reflect more realistic conditions for the field system. An acceptable history-match for experiment E13-E14 was obtained for both waterflood and co-injection. The waterflood match was achieved by tuning the oil relative permeability curve to match oil/water production rate and BHP. The co-injection was matched by tuning the oil and water relative permeabilities to match cumulative oil/water production and BHP. Figure 6 shows the history-match.

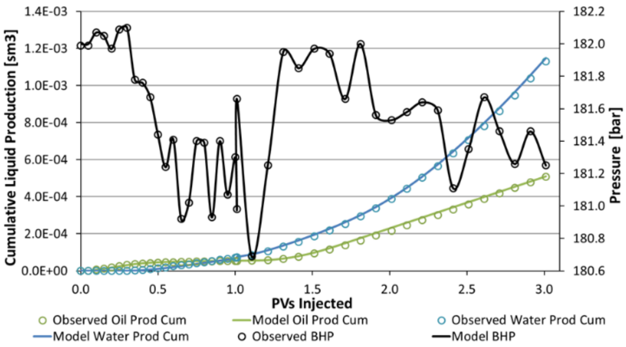

**Fig. 6.** Observed (open circles) and modeled (curves) cumulative oil/water production during waterflood and co-injection of the history-matched experiment. Production well BHP is shown on the secondary y-axis.

The validated model was first used to investigate the effect of grid resolution during co-injection. The generated case was identical to the base case history-match, but used the fine scale grid (5 times finer in the x, y, and z directions) to evaluate change in $CO_2$ mobility reduction and oil recovery. $CO_2$ mobility reduction is generally inferred from delayed $CO_2$ breakthrough and an increased response in injection pressure. However, simulation results showed limited effect of grid resolution on co-injection in terms of injection well pressures, $CO_2$ breakthrough, and cumulative recoveries. As limited variations were observed, with the fine grid model, further sensitivity studies utilized the coarser base grid.

#### 4.5.1 Effect of Foam Quality

The effect of foam quality ($CO_2$ fraction) was studied using the base grid to determine its impacts on oil recovery and $CO_2$ mobility reduction. Cases injecting higher $CO_2$ fractions were set to assess model sensitivity on amounts of $CO_2$ injected and its influence on oil recovery. The base case history-matched model used the optimal $CO_2$ fraction of 0.70 measured in laboratory. Further sensitivity cases were set to $CO_2$ fractions of 0.80, 0.90, and 0.95. Figure 7 shows cumulative oil production (solid curves) for the base case ($f_g$=0.70) and $CO_2$ fraction sensitives. With increasing $CO_2$ fractions, the oil recovery rate accelerated but all cases recovered the same volume of cumulative oil. Hence, $CO_2$ miscibility dominated oil displacement as also observed in the $CO_2$ foam EOR corefloods experiments in Figure 3 and 4.

Injection pressures for the various $CO_2$ fractions are shown in Figure 7 (dashed curves). All injection pressures followed the same trend. Higher pressures, however, were observed as the fraction of $CO_2$ decreased and the fraction of surfactant solution increased, creating a higher apparent viscosity foam (blue and red dashed curves, Figure 7). This is consistent with trends observed in foam quality scans where the optimal $CO_2$ fraction and highest apparent viscosity was observed at 0.70 (cf. Figure 2, left, green and orange circles). At fractions above this, apparent viscosities declined.

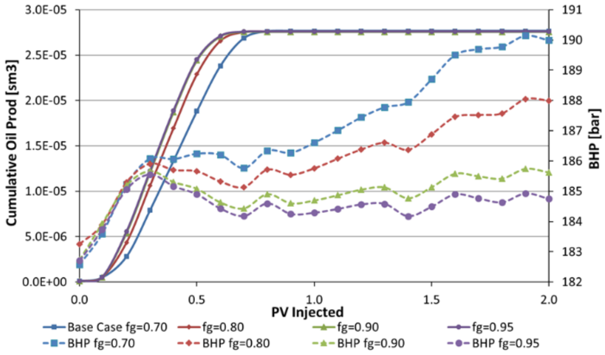

**Fig. 7.** Cumulative oil production versus time for the base case (blue solid curve), and three sensitivities with different gas ($CO_2$) fractions. Injection pressure versus time shown on the secondary y-axis for the base case (blue dashed curve), and three sensitivities with different gas ($CO_2$) fractions.

### *4.5.2 Effect of Surfactant*

$CO_2$ diffusion and miscibility are evidently the dominant oil recovery mechanisms in both simulation and laboratory experiments. Therefore, a similar case to the history-matched experiment was set-up without surfactant to investigate pure $CO_2$ versus $CO_2$ foam displacement. The injection schedule was kept identical to the base case co-injection, except only water was injected as the aqueous phase. Figure 8 shows injection pressure (dashed curves) and cumulative $CO_2$ production (solid curves) during co-injection with surfactant (blue curves) and without surfactant (red curves).

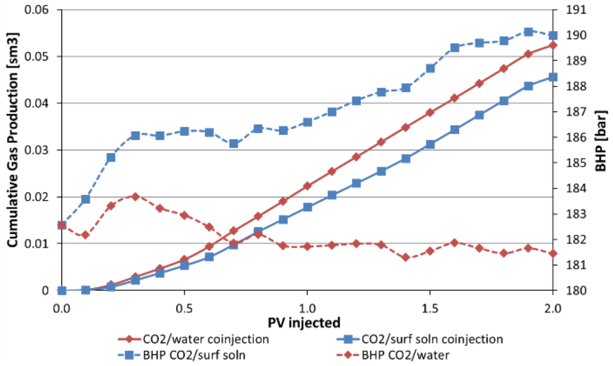

**Fig. 8.** Injection well pressure (dashed curves) and cumulative gas ($CO_2$) production (solid curves) for the base case with surfactant present (blue curve) and a case without surfactant present (red curves).

The injection well pressure was significantly lower for the case without surfactant compared to the base case with surfactant (Figure 8, red dashed curve). This indicated higher $CO_2$ mobility and increased $CO_2$ production in absence of foam (Figure 8, red solid curve). Analysis of liquid production showed the same cumulative volume of oil recovered in both cases (green curves, Figure 9), but additional water was produced during $CO_2$ foam injection (blue dashed curve). Hence, a larger storage potential for $CO_2$ was obtained with $CO_2$ foam displacement. Similar behavior was also observed in Figure 5, where $CO_2$ storage was higher for multi-cycle SAG because of increased water displacement during foam injection compared to $CO_2$ alone.

The similar volumes of oil produced with and without surfactant, demonstrated the dominance of $CO_2$ miscibility over viscous displacement by foam (green curves, Figure 9). The core-scale model is consistent with laboratory observations indicating that miscibility and diffusion are the governing displacement forces in small core-scale systems. This creates a challenge when upscaling core-scale foam behavior to the field-scale as reservoir heterogeneity and gravity effects will likely be more dominant in the field.

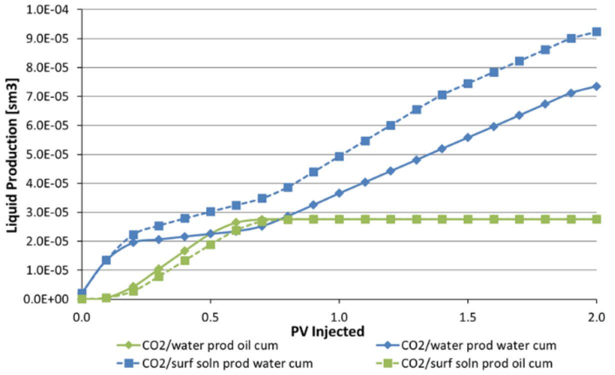

**Fig. 9.** Cumulative liquid production during $CO_2$/water co-injection (solid curves) and $CO_2$/surfactant solution (dashed curves). Green curves correspond to cumulative oil produced and blue to cumulative water.

## 5. Conclusions

This work investigated various injections strategies (co-injection and SAG) for $CO_2$ foam mobility control, EOR and $CO_2$ storage to assist in the design of a $CO_2$ foam field pilot. The sensitivity study involved both experimental laboratory work and numerical modeling. Supercritical $CO_2$ foam behavior in brine-saturated systems was investigated to generate foam *in-situ*, without the presence of oil. Additionally, $CO_2$ foam EOR corefloods were conducted in the presence of refined oil at first-contact miscible (FCM) conditions and in the presence of crude oil at multiple-contact miscible (MCM) conditions after waterflooding to investigate the impact of oil and miscibility on foam generation and stability. Key findings from this work are:

- Multi-cycle SAG resulted in the highest apparent viscosity foam of 120.2 cP during *in-situ* $CO_2$ foam stability scans compared to co-injection (56.0 cP) and single-cycle SAG (18.2 cP) without oil present. Multi-cycle SAG also achieved the highest apparent viscosity foam of 100.7 cP for the $CO_2$ foam EOR corefloods, with refined oil present, at FCM conditions.
- Incremental oil recoveries during tertiary $CO_2$ foam injections were on average 30.6% OOIP for all injection strategies, with and without surfactant, at both FCM and MCM conditions. At MCM conditions, $CO_2$ foam was not generated as a result of wettability

alteration by crude oil and foam destabilization in presence of crude oil.

- $CO_2$ diffusion and miscibility with oil were the dominant recovery mechanisms as observed in laboratory corefloods and numerical core-scale sensitivity studies on foam quality.
- A validated numerical core-scale model captured the observed foam behavior from laboratory corefloods. The foam model was not sensitive to grid resolution and corroborated laboratory observations of core-scale foam behavior. Further work is ongoing to upscale the laboratory observations to field-scale simulations.
- A direct correlation between the amounts of $CO_2$ stored and water/oil saturation change was observed in the laboratory corefloods. For every amount of fluid produced, the equivalent amount of $CO_2$ was stored regardless of injection strategy. $CO_2$ storage potential was 17.1% greater at FCM conditions, compared to MCM, due to increased displacement by $CO_2$ foam and $CO_2$ trapping by capillary forces in more water-wet core plugs. Core-scale simulations indicated higher $CO_2$ storage potential with $CO_2$ foam because of increased water displacement, compared to cases without foam.

Reservoir heterogeneity and gravity dominate displacement at the field-scale, therefore the high apparent viscosities and viscous displacement forces provided by multi-cycle SAG in the foam stability scans are favorable. The shear-thinning behavior of the foam system can also mitigate injectivity loss near the injection well, where flow rates are high. Additionally, a SAG injection scheme provides better injectivity control, when operating close to formation fracture pressure, due to the ability to switch to $CO_2$ injection for foam dry-out. Reported oil recoveries, from $CO_2$ foam EOR corefloods, cannot be upscaled to predict field performance as $CO_2$ diffusion will have less effect on displacement at the length scales existing in the field.

## Acknowledgements

The authors wish to acknowledge the Norwegian Research Council CLIMIT program for financial support under grant number 249742 - *$CO_2$ Storage from Lab to On-Shore Field Pilots Using $CO_2$-Foam for Mobility Control in CCUS* and industry partners; Shell Global Solutions, TOTAL E&P USA, Inc., and Equinor ASA. The authors also thank the field operator for cooperation.

## Nomenclature

| | |
|---|---|
| API | American Petroleum Institute |
| BHP | bottom hole pressure |
| CCUS | carbon capture, utilization, and storage |
| EOR | enhanced oil recovery |
| FCM | first-contact miscible |
| $f_g$ | gas fraction |
| fmmob | maximum gas mobility reduction |
| K | permeability |
| MCM | multiple-contact miscible |
| MMP | minimum miscibility pressure |
| MRF | mobility reduction factor (foam model) |
| OOIP | oil originally in place |
| PV | pore volume |
| PVT | pressure, volume, temperature |
| $R_{f,tot}$ | total recovery factor |
| $R_{f,WF}$ | recovery factor by waterflood |
| $R_{f,\ CO2\ foam}$ | recovery factor by $CO_2$ foam |
| SAG | surfactant-alternating-gas |
| $S_{wi}$ | irreducible water saturation |
| $S_o$ | oil saturation |
| $S_{or}$ | residual oil saturation |
| $t$ | time |
| $u_g$ | gas superficial velocity |
| $u_{liq}$ | liquid superficial velocity |
| $\mu_{app}$ | apparent viscosity |
| $\nabla p$ | pressure gradient |
| SWW | strongly water-wet |
| WW | water-wet |

## References

1. Bernard, G.G., Holm, L.W. and Harvey, C.P. (1980). Use of Surfactant to Reduce $CO_2$ Mobility in Oil Displacement. *SPE Journal* **20** (4): 281-292.
2. Latil, M. *Enhanced Oil Recovery* (1980) Paris: Editions Technip.
3. Bond, D.C. and Holbrook, O.C. Gas Drive Oil Recovery Process. (1958) United States Patent Office. 30 December. Patented number 2,866,507.
4. Nzekwu, B.I. and Bennion, D.W. (1987) Mobility Control in Dynamic Gravity Segregation Flow Systems. *Journal of Canadian Petroleum Technology* **26** (4): 80-87. JCPT87-04-08.
5. Rossen, W.R. (1996). Foams in Enhanced Oil Recovery. In Foams Theory, Measurements, and Applications. eds. Prud'homme, R.K. and Khan, S.A. **57**, ch. 11, 414-464, Marcel Dekker, Inc. New York
6. A.H. Falls, G.J. Hirasaki, T.W. Patzek, P.A. Gauglitz, D.D. Miller, and T. Ratulowski. (1988). *SPE Reserv Eng*. **3**: 844
7. Holm, L.W. (1968). The Mechanisms of Gas and Liquid Flow Through Porous Media in the Presence of Foam. *Transactions* **243**, 359-369.
8. Bernard, G.G., Holm, L.W. and Jacobs, W.L. (1965). Effect of Foam on Trapped Gas Saturation and on Permeability of Porous Media to Water. SPE Annual Fall Meeting, 3-6 October, Denver, Colorado, US. SPE-1204.
9. Emadi, A., Sohrabi, M., Farzaneh, S.A. and Ireland, S. (2013). Experimental Investigation of Liquid-CO2 and CO2-Emulsion Application for Enhanced Heavy Oil Recovery. SPE EAGE and SPE Europec, 10-13 June, London, United Kingdom. SPE-164798-MS.
10. Schramm, L.L. and Novosad. (1992). The destabilization of foams for improved oil recovery by crude oils: Effect of the nature of the oil. *Journal of Petroleum Science and Engineering* **7** (1-2), 77-90.
11. Prud'homme, R K. and Khan, S A. (1996). Foams, Theory, Measurements, and Applications. New York: Marcel Dekker Incorporated.
12. Farajzadeh, R., Andrianov, A., Krastev, R., Hirasaki, G.J. and Rossen, W.R. (2012). Foam-oil interactions

in porous media: Implications for foam assisted enhanced oil recovery. Advances in Colloid and Interface Science 183-184, 1-13.

13. Schramm, L.L. and Mannhardt, K. (1996). The effect of wettability on foam sensitivity to crude oil in porous media". *Journal of Petroleum and Engineering* **15** (1), 101-113.
14. Fredriksen, S., Alcorn, Z., Frøland, A. et al. (2019). Surfactant Prefloods During Carbon Dioxide Foam Injection for Integrated Enhanced Oil Recovery in Fractured Oil-Wet Carbonates. *SPE Journal*. SPE-190168-PA (in press; posted 5 April 2019). https://doi.org/10.2118/190168-PA.
15. Shan, D. and Rossen, W.R. (2002). Optimal Injection Strategies for Foam IOR. SPE/DOE Improved Oil Recovery Symposium, 13-17 April, Tulsa, Oklahoma. SPE-75180-MS.
16. Farajzadeh, R., Andrianov, A., Krastev, R., Hirasaki, G.J. and Rossen, W.R. (2012). Foam-oil interactions in porous media: Implications for foam assisted enhanced oil recovery. *Advances in Colloid and Interface Science* **183-184**, 1-13.
17. Jones, S.A., Laskaris, G., Vincent-Bonnieu, S., Farajzadeh, R. and Rossen, W.R. (2016). Surfactant Effect on Foam: From Core Flood Experiments To Implicit-Texture Foam Model Parameters. SPE Improved Oil Recovery Conference, 11-13 April, Tulsa, Oklahoma. SPE-179637-MS.
18. Groenenboom, J., Kechut, N.I., Mar-Or, A., Vincent-Bonnieu, S. (2017). Foam Assisted WAG: Injection Strategies to Optimize Performance. SPE/IATMI Asia Pacific Oil & Gas Exhibition, 17-19 October, Jakarta, Indonesia. SPE-186991-MS.
19. Hoefner, M.L. and Evans, E.M. (1995). $CO_2$ Foam: Results from Four Developmental Fields Trials. *SPE Reservoir Engineering* **10** (4), 273-281.
20. Chou, S.I., Vasicek, S.L., Pisio, D.L., Jasek, D.E., Goodgame, J.A. (1992). CO2 Foam Field Trial at North Ward Estes. 67th SPE Annual Technical Conference and Exhibition, October 4-7, Washington, D.C.
21. Harpole, K.J., Siemers, W.T. and Gerard, M.G. (1994). $CO_2$ Foam Field Verification Test at EVGSAU: Phase IIIC – Reservoir Characterization and Response to Foam Injection. SPE/DOE 9th Symposium on Improved Oil Recovery, 17-20 April, Tulsa, OK, USA.
22. Henry, R.L.; Fisher, D.R.; Pennel, S. P.; Honnert, M.A. (1996). Field Test of Foam to Reduce CO2 Cycling. SPE/DOE Tenth Symposium on Improved Oil Recovery, April 21–24, Tulsa, OK, US. SPE/DOE 35402
23. Alcorn, Z. P., Fredriksen, S. B., Sharma, M. et al. (2019). An Integrated Carbon-Dioxide-Foam Enhanced-Oil-Recovery Pilot Program With Combined Carbon Capture, Utilization, and Storage in an Onshore Texas Heterogeneous Carbonate Field. SPE Reservoir Evaluation & Engineering-Reservoir Engineering. SPE-190204-PA (in press; posted 27 March 2019). https://doi.org/10.2118/190204-PA.
24. Graue, A., Viksund, B G. and Baldwin, B A. (1999). Reproducible Wettability Alteration of Low-Permeable Outcrop Chalk. *SPE Reservoir Evaluation and Engineering* **2** (02), 134-140. SPE-55904-PA.
25. Steinsbø, M., Brattekås, B., Fernø, M.A., Ersland, G. and Graue, A. (2014). Supercritical $CO_2$ Injection for Enhanced Oil Recovery in Fracture Chalk. International Symposium of the Society of Core Analysts, 8-12 September, Avignon, France. SCA2014-092.
26. Jian, B., Puerto, M C., Wehowsky, A., Dong, P., Johnston, K P. and Hirasaki, G J. (2016). Static Adsorption of an Ethoxylated Nonionic Surfactant on Carbonate Minerals. *Langmuir* **32** (40), 10244-10252.
27. Steinsbø, M., Brattekås, B., Ersland, G., Bø, K., Opdal, I.E., Tunli, R., Graue, A. and Fernø, M.A. (2015). Foam as Mobility Control for Integrated CO2-EOR in Fractured Carbonates. 18th European Symposium on Improved Oil Recovery, 14-16 April, Dresden, Germany.
28. Hirasaki, G. J. and Lawson, J.B. (1985). Mechanisms of Foam Flow in Porous Media: Apparent Viscosity in Smooth Capillaries. *SPE Journal* **25** (2), 176-190.
29. Johnson, E.F., Bossler, D.P. and Naumann, V.O. (1959). Calculation of Relative Permeability From Displacement Experiments. *Trans. AIME* 1959, *216*, 370-372.
30. Sharma, M., Alcorn Z.P., Fredriksen, S.B., Fernø, M., Graue, A. (2017). Numerical Modeling Study for Designing CO2 Foam Filed Pilot. EAGE IOR Symposium, 24-27 April, Stavanger, Norway.
31. Rognmo, A.U., Fredriksen, S.B., Alcorn, Z.P., Sharma, M., Føyen, T., Eide, Ø., Graue, A. and Fernø, M. (2018). Pore-to-Core EOR Upscaling for CO2-foam for CCUS. SPE EUROPEC featured at the 80th EAGE Annual Conference and Exhibition, 11-14 June, Copenhagen, Denmark. SPE-190869-MS.
32. Eide, Ø., Haugen, Å., Svenningsen, S., Hoff, K., Ersland, G., Fernø, M.A. and Graue, A. (2012). Tertiary Liquid and Supercritical $CO_2$ injection in Chalk and Limestone at Strongly Water-Wet and Near Neutral-Wet Conditions. International Symposium of the Society of Core Analysts, 27-30 August, Aberdeen, Scotland.
33. Graue, A., Tonheim, E. and Baldwin, B. 1994. Control and Alteration of Wettability in Low-Permeable Chalk". Proceedings of the 3rd International Symposium on Evaluation of Reservoir Wettability and its Effect on Oil Recovery, 21-23 September, Laramie, WY.
34. Eide, Ø., Fernø, M.A., Alcorn, Z.P. and Graue, A. (2016). Visualization of Carbon Dioxide Enhanced Oil Recovery by Diffusion in Fractured Chalk. *SPE Journal* **21** (1), 112-120.
35. Fernø, M A., Steinsbø, M., Eide, Ø., Ahmed, A., Ahmed, K. and Graue, A. (2015). Parametric study of oil recovery during $CO_2$ injections in fractured chalk: Influence of fracture permeability, diffusion length and water saturation. *Journal of Nat Gas Sci and Eng* **27** (2), 1063-1073.
36. Jadahunandan, P.P. and Morrow, N.R. 1(995). Effect of Wettability on Waterflood Recovery for Crude-Oil/Brine/Rock Systems. *SPE Reservoir Engineering* **10** (1), 40-46.

37. Suffridge, F.E., Raterman, K.T. and Russell, G.C. (1989). Foam Performance Under Reservoir Conditions. 64th SPE ATCE, 8-11 October, San Antonio, Texas, US. SPE-19691-MS.
38. Vikingstad, A. K., Skauge, A., Høiland, H. and Aarra, M. (2005). Foam-oil Interactions Analysed by Static Foam Tests. *Colloids and Surfaces A: Physicochem. Eng. Aspects* **260** (2005), 189-198.
39. T.S. Kristiansen and T. Holt. (1992). Properties of Flowing Foam in Porous Media Containing Oil. Presented at the SPE/DOE Eighth Symposium on Enhanced Oil Recovery, Tulsa, OK, USA, April 22-24, 1992. SPE/DOE 24182.
40. Prud'homme, R K. and Khan, S A. (1996). *Foams, Theory, Measurements, and Applications*. New York: Marcel Dekker Incorporated.

# New laboratory core flooding experimental system for EOR surfactant screening, especially for foam

*Xuesong* Li[1,*], and *Matthias* Appel[1]

[1]Shell Global Solutions International B.V., Special Core Analysis Team, 1031HW Amsterdam, The Netherlands

**Abstract.** Core flooding experiments are often used to assess the performance of EOR techniques or to screen surfactants. An inherent success factor of chemical EOR processes is the choice of the optimal surfactant which is a trade-off between process performance and economic considerations. Currently, this trade-off can often not fully be evaluated with laboratory experiments because the associated experiments are time consuming which typically limits their number and, in turn, impacts the reliability of the results. For this reason, we aimed to develop an automated and parallel core flooding unit to conduct faster, cheaper and reliable tests for EOR technologies. The benefit of doing this is to dramatically increase the statistics of EOR-related experimentation while decreasing the manpower needed, leading to a much better value-to-cost ratio. As a first step, we designed a setup which is applicable for multiple EOR-related core flooding experiments, such as alkaline-surfactant polymer (ASP), low salinity, polymer flooding or foam injection. The device can be used for co- or sequential injection of gas, water and oil. For the high compressibility gas phase, it is often desirable to regulate its in-core volumetric flow rate. We control the gas flow using inline sensors and flow meters corresponding to the real time in situ core pressure. With a feedback loop, the offset of gas flow can be automatically updated within 0.1% deviation from the target setting. By miniaturizing the core sample and simplifying the experimental procedures, the automated flooding process achieved 90% efficiency gain while reducing sample consumption. This proof of concept can easily be further evolved into a parallelized system. Experience with this new core flooding system demonstrated the dramatic increase in screening capacity and added value to the EOR development workflows.

## 1 Introduction

There is general consensus about an increasing energy demand in the coming decades. Irrespective of the fact that renewable energy will play an increasing role in the energy supply, the contribution of oil for energy consumption and as feed for chemical production will remain high and is expected to grow. [1]. The current oil market requires a relatively low recovery cost for any field development [2-4] which, in turn, requires faster technology deployment and adequate evaluation of the associated technical risks.

In typical hydrocarbon recovery scenarios, after a primary and secondary recovery, there is still a larger percentage of oil (30-60%) remaining in the reservoir. This remaining oil is primarily trapped by capillary forces [5]. Enhanced oil recovery (EOR) techniques often utilize surfactants to either reduce the interfacial tension between the aqueous phase and oil phase or generate foam to increase the swept efficiency of gas injection [6]. In any of these processes, the selection of the surfactant is essential for the incremental oil recovery. From an economical point of view the cost of surfactant is also a substantial element of the cost of EOR projects [7, 8]. However, the surfactant performance depends on the reservoir fluid and rock properties at field-related temperature and pressure conditions Therefore, it would be ideal to conduct core flooding experiments which combine all these factors for surfactant selections. But when taking all the influencing parameters into account the screening matrix can be very large. For example, Table 1 illustrates the screening program for foam surfactant screening [9]. Even this fairly slimmed down screening program has a matrix size of 100, which would take a few years to complete using a conventional core flooding setup.

**Table 1.** EOR surfactant screening matrix with reduced variation of variables.

| Variables | | Variations |
|---|---|---|
| 1 | rock sample type | 1 |
| 2 | rock permeability | 1 |
| 3 | brine salinity | 1 |
| 4 | crude oil | 1 |
| 5 | surfactant type | 5 |
| 6 | surfactant concentration | 2 |
| 7 | rock sample dimension | 1 |
| 8 | flow rate | 2 |
| 9 | temperature | 1 |
| 10 | pressure | 1 |
| 11 | gas/liquid ratio in one test | 5 |
| combinations/test numbers | | 100 |

---

[*] Corresponding author: xuesong.x.li@shell.com

Conventional core flooding approaches can often take up to a month (often more than a week) to complete a single core flooding experiment and are not sufficient for the screening target [9, 10]. Keeping this in mind, a new high throughput core flooding unit was developed for the selection of EOR surfactants or related chemicals. A similar effort was published by Baldygin et al.. Their system comprised sand pack samples in combination with liquid flooding [11].

The efficiency gains of the new system presented in this study is a result of three main improvements compared to a conventional core flooding design. Firstly, a smaller core sample with a reduced diameter is used which minimizes the sample rock and fluid consumptions and responds faster to fluid injections. For this reason our new core flooding setup using a minimized rock sample was named "Lilliput" [12], which will be referred to in the following sections as the new core flooding system discussed in this paper. Secondly, in-line sensors and flow meters are used for flow control, and, together with an integrated computer program, a feedback loop enables an automatic core flooding process. Lastly, the whole setup is designed with simplified operation procedures, such as the use of an oven with a sliding base that allows for easy access to all components of the system. The high-pressure fluid vessels and core holders are designed with finger-tight nuts that simplify assembly as well as a "plug and play" design of the core sample installation. As a consequence, the Lilliput core flooding system is at least 10 times more efficient than the conventional core flooding unit in terms of required experimental duration as 2 weeks of conventional core flooding are reduced to a single-day experiment.

## 2 Detailed Design

### 2.1 Flow diagram

The Lilliput core flooding unit consist of three main parts: the fluid injections and controls, the core holder unit where fluid floods through the rock sample and the outflow of the core flooding unit including the effluent analysis and back pressure regulation. A flow diagram of the Lilliput unit is shown in Fig. 1.

Two Quizix™ pumps (QX6000 series, with 410 bar working pressure, flow rate ranging from 0.001mL/min to 50 mL/min, cylinder volume 12.3 mL) are utilized to deliver the sample fluid. One pump is connected to three parallel high-pressure vessels used as the reservoir for the aqueous phase; another pump is connected to the oil reservoir. The gas phase, either $N_2$ or $CO_2$ from gas cylinders is connected to the inlet of the core with the gas flow rate regulated by a Bronkhorst™ gas flow meter (EL-flow series, working pressure of 100 bar). Depending on the screening purposes, the injection fluid can be switched sequentially between the aqueous phase, the oil phase or gaseous phase, with two phases co-injection or three phases joint injections.

The high-pressure fluid vessels (manufactured in-house with a design pressure of 200 bar, temperature 200°C) are placed together with a core holder in an oven. Prior to any fluid injection, the fluids and rock sample are heated up to the target experimental temperature. To minimize the risk of corrosion, all the wetting parts in the oven are made of HC276™. Due to the smaller core sample and thus smaller pore volumes, the capacity of the 4 fluid vessels is sufficient to provide continued core flooding for 400 pore volumes (PV).

The fluid that comes out of the core will first pass through a cooler and then through an in-line Bronkhorst liquid mass flow meter (mini CORI-FLOW™ Coriolis) for the effluent oil fraction analysis. This meter is applicable for the liquid phase, e.g. oil and brine, or emulsion phase mass flowrate measurement A membrane type back pressure regulator is connected before the fluid is vented from the system. The maximum temperature of the setup is 120°C and the maximum operating pressure is 100 bar.

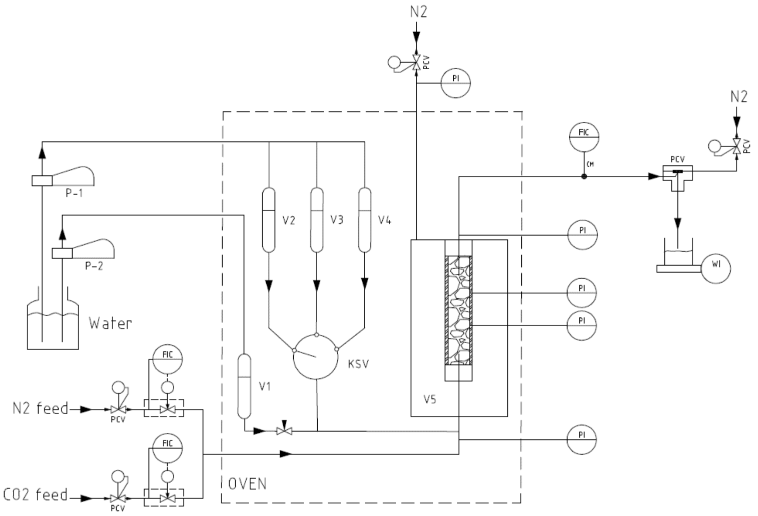

**Fig. 1.** Flow diagram of the core flooding for general EOR screening. P-1 and P-2: Quizix pump; V1, V2, V3, V4: High pressure fluid vessel with piston; KSV: switch valve; PCV: pressure control valve; FIC: flow indicator/controller; PI: pressure transducer; WI: weight indicator.

### 2.2 Core holder

The core holder is an important element of a core flooding unit. In conventional core flooding setup, there are a few typical sizes for the core, from 1 inch to 3 inches in diameter, and with a length from 5 cm to 1 m. The core samples used on Lilliput setup have a smaller diameter, 1 cm, and a variable length between 5 cm to 17 cm. The choices of core sample length depend on the available material and the purpose of the experiment. For less consolidated rock, long and slim core samples are fragile and difficult to prepare. In such cases, the rock samples are used together with two end dummy pieces made from PEEK with a 1mm inner diameter fluid pass to make up the total length of 17 cm. Due to the choice of a smaller diameter the total pore volume is significantly reduced. As a result, it takes less time to reach a steady flooding state under the same flooding condition compared to a larger core.

The core holder is placed vertically, and the flooding direction is from the bottom to the top. During a core flooding experiment the cylindrical surfaces need to be sealed to prevent fluid stream flow at the surface of the core. Often epoxy sealing or confining pressure on rubber sleeves are used in conventional core flooding setup [13, 14]. In the Lilliput unit, the “plug and play” core assemble is realized by using rubber sleeves to seal the cylindrical surface, see Fig. 2. While loading or unloading a rock sample to the core holder, vacuum pressure is applied outside of the rubber sleeve to enlarge the diameters of the sleeve. During the fluid flooding stage, confining pressure is applied outside of the sleeve with a pressure approximately 10 bar higher than the highest fluid pressure in the core. Two high pressure metal tips connected to the pressure transducers with distance of 5 cm are fixed to the rubber sleeve body. These tips are designed to avoid direct contact with the rock sample, which prevents any damage from occurring during the rock sample installation. The two pressure tips endure expansion or restriction of the rubber sleeve around the tips during the experiment. The core sleeve withstands the required 90 bar pressure difference [15], demonstrating a good sealing performance and functioning as the key time saver during the core assembling process.

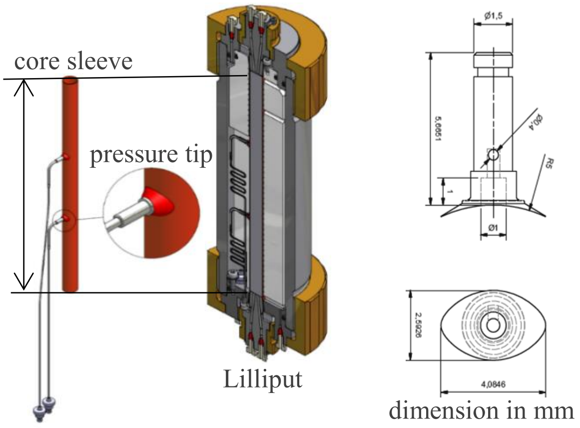

**Fig. 2.** Core holder design using rubber sleeve with moulded in mini pressure tip.

With this design of the rubber sleeve, the core installation or unloading time takes only 5 minutes, instead of typically several hours for a conventional Hassler-type core holder using sleeves, or even days if one chooses to use epoxy which involves epoxy aging, side pressure tip drilling and excess epoxy trimming. In the Lilliput unit the core changing procedure only involves opening the oven, turning the hand-tight-nuts and switching the confining pressure to vacuum, see Fig. 3. The core mounting process is dramatically simplified.

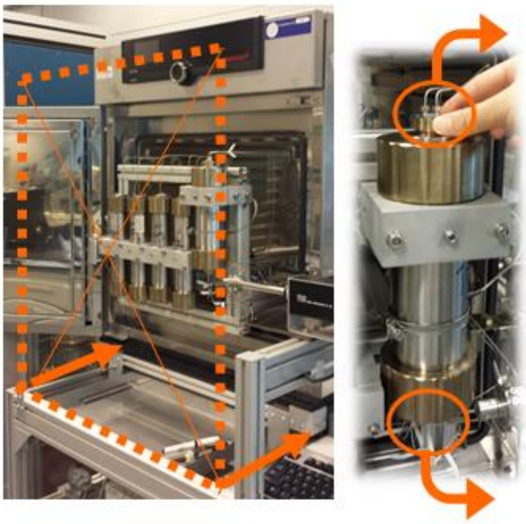

**Fig. 3.** Instruction of core holder installation on Lilliput setup with sliding oven and hand-tight nut.

### 2.3 Feedback loop control

During the core flooding experiment, the automated flooding process is regulated by a feedback loop control program, as show in Fig. 4. Depending on the purpose of the experiment, different criteria are chosen for controlling the core flooding program. First, the flooding fluids are pumped into the core with an initial flow rate given by the operator. Once the flow has started, the sensors around the core measure temperature, pressures, flowrate and effluent composition. These measurements are acquired by the computer program every 5 seconds. By reading these inputs, the computer program judges the in-situ flow status and regulates the fluid flow accordingly.

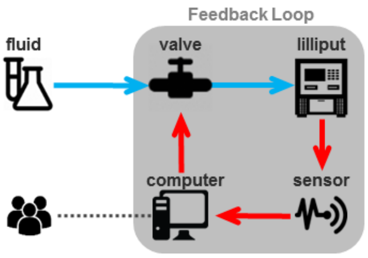

**Fig. 4.** Computer controlled feedback flow regulation on Lilliput core flooding unit.

The main benefit for the feedback loop control is enabling an automatic flooding process with limited

---

[*] Corresponding author: xuesong.x.li@shell.com

human supervision. Some of the conventional core flooding units can run through the flooding program with user-defined flooding steps. But often these approaches suffer from either long running periods for each step to ensure a steady state is reached or it requires constant monitoring by the operator.

Gases are often injected into oil reservoirs to enhance oil recovery. Due to the much lower gas viscosity compared to reservoir liquid phases, gas can have early break-through to the production well or might be fingering to the top of the reservoir without efficiently displacing the oil. Foam can achieve better conformance control. One of the important parameters used to quantify the effect of foam is by identifying the extra flow resistance created by foam.

Taking a foam resistance factor experiment as example, it would be ideal to have a constant total volumetric flow rate in the core for the performance evaluation [16]. However, due to the high gas compressibility, the manual regulation of gas flow is challenging and often introduces several percent, sometimes even 20%, uncertainty [17]. The computer-regulated foam flooding experiment is efficient and more precise as shown in Fig. 5, where the automatic fluid flow regulation by the computer program and the result of the experiment are presented. During the whole period, from 2400 s to 6500 s, there was no user-interference by the operator. All steps are completed by the computer automatically.

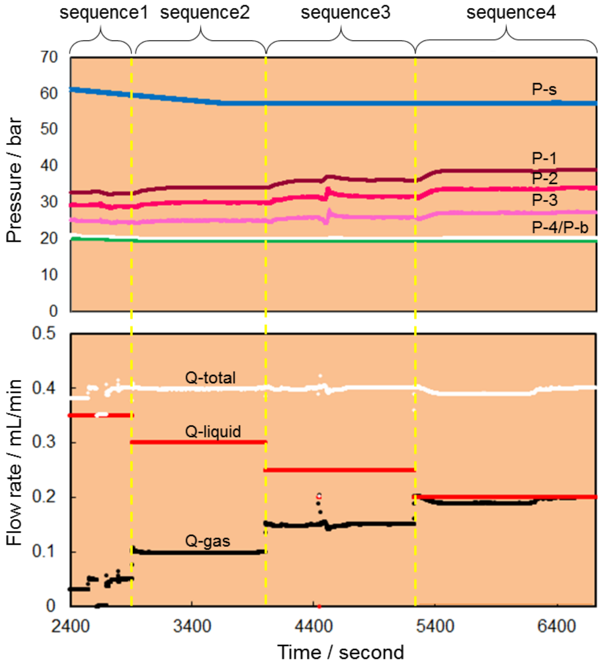

**Fig. 5.** Automatic core flooding processes for a foam resistance factor experiment. The four user-predefined flooding sequences have different foam gas/liquid ratios. The switch between sequences are done by the computer program by judging flow status criteria, here pressure stability. P-s: core sleeve confining pressure; P1, P2, P3, P4: 4 pressures point distributed along the core with the same distances; P-b: back pressure. Q-total, liquid, gas: in situ volumetric flow rate in total, for liquid and for gas, automatically regulated by the feedback flow control programme, using equation (9) below

The user input to the computer are 4 flowing sequences with constant total in-situ volumetric flow rates and changing the gas/liquid ratio. Instead of specifying the flooding, the target criteria that the program uses is that of steady flow; e.g., the stabilization criterium of the steady pressure gradient can be given as input. The four different steps are taking different times to complete, and at the end of each step both the target total in-situ volumetric is regulated within 0.5% offset and a stable flooding state are reached. The average flooding time for completing one sequence is only around 16 minutes.

A mobility reduction factor (MRF) number is often the required parameter derived from foam core flooding experiments. It is the apparent viscosity ratio of foam and gas flooding. Referring to Darcy's law, the apparent viscosity of the fluid in the core can be expressed as below,

$$Q_{v-core} = \frac{\pi R^2 \cdot K_{liquid} \cdot \Delta p}{\mu L} \tag{1}$$

$$\frac{\pi R^2 \cdot K_{liquid}}{L} = constant = \mathrm{C} \tag{2}$$

$$\frac{Q_{v-core} \cdot \mu}{\Delta p} = \mathrm{C} \tag{3}$$

$$\mu = \frac{\mathrm{C} \cdot \Delta p}{Q_{v-core}} \tag{4}$$

where, $R$ is the radius of the core, $\Delta p$ is the pressure drop over the core, and L is the length of the core, $K_{\mathrm{liquid}}$ is the permeability of the liquid in the core, $Q\mathrm{v}$ is the volumetric flow rate, and $\mu$ is the apparent viscosity, since foam is compressible, so for the same amount of gas the volume of it are different in the line and in the core. The ratio of $Q_{\text{v-core}}$ and $Q_{\text{v-line}}$ can be written as,

$$\frac{Q_{v-core}}{Q_{v-line}} = \frac{V_{gas-core} + V_{water-core}}{V_{gas-line} + V_{water-line}} \tag{5}$$

where $V$ is the volume of the fluid, with known gas fraction, *fg-line* in the line. For $N_2$ the dependency of density on pressure at the same temperature condition is nearly linear, written as below,

$$\frac{V_{gas-line}}{V_{gas-core}} = \frac{\rho_{gas-core}}{\rho_{gas-line}} = \frac{a \cdot p_{core} + b}{a \cdot p_{line} + b} \tag{6}$$

where $a$, $b$ are the known parameter of the linear relationship shown in Fig. 6 [18], and $\rho$ is the density. For a simple model below, with $p_0$ as the gas pressure in the line before entering the core, and $p_1$, $p_2$ as the pressure at the inlet and outlet of the core. The apparent viscosity can be written further as equation (7),

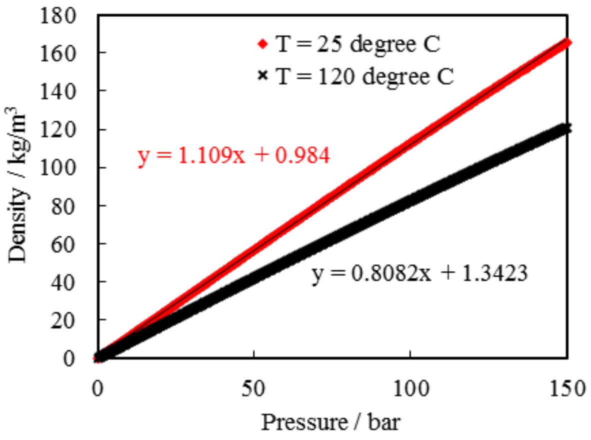

**Fig. 6.** The dependency of $N_2$ density on pressure at different temperatures.

$$\mu = \frac{C}{Q_{v-line}} \cdot \frac{p_1 - p_2}{\left[\frac{ap_0 + b}{a\left(\frac{p_1 + p_2}{2}\right) + b} - 1\right] \cdot f_{g-line} + 1} \tag{7}$$

Using conventional core flooding units, the apparent viscosity is calculated by equation (7) using the controlled gas volume in the line. For the Lilliput unit, $Q_{\text{v-core}}$ is automatically regulated to the target value. Here it is assumed that the pressure gradient in the core is constant and the in-situ core pressure can be represented by the average of $p_1$ and $p_2$. The gas fraction in line and in core has the relationship below,

$$k = \frac{ap_0 + b}{a\left(\frac{p_1 + p_2}{2}\right) + b} \tag{8}$$

$$\frac{f_{g-core}}{1 - f_{g-core}} = k \cdot \frac{f_{g-line}}{1 - f_{g-line}} \tag{9}$$

equation (9) is embedded in the computer program on Lilliput to control the in-situ gas fraction. It is a function of parameters including user defined $Q_{\text{v-core}}$, temperature. $p_1$ and $p_2$. It should be noticed that the nearly linear density dependency on pressure is only applicable to $N_2$, under the applicable working conditions. For $CO_2$, a non-linear approximation, together with the additional correction on the gas solubility in the fluid is applied.

With the above simplified core assembling procedure and the computer-controlled feedback loop, the time required for core flooding experiments using the Lilliput unit is compared with conventional larger core flooding experiments, see Table 2. In general, the efficiency gain is above 90% and the manpower requirement is dramatically reduced. In EOR surfactants or chemicals screening workflow, the rock and fluid samples are also prepared in batch to save time.

**Table 2.** Comparation of time consumption for delivering one core flooding experiment on average conventional medium size core flooding unit and on Lilliput unit.

| Procedures | conventional (*Φ*: 2inches, *L*: 30 cm) | Lilliput (*Φ*: 1 cm, *L*: 17 cm) |
|---|---|---|
| 1.Fluid sample filling to the reservoirs | 10 minutes, for 20 PV flooding | 10 minutes, for 400 PV flooding |
| 2.Core sample mounting | 8 hours for sleeve-seal; 2 days for epoxy-seal | 5 minutes |
| 3.User defined flooding sequences and criteria | 5 minutes | 5 minutes |
| 4.Execution of the flooding, foam flooding at 20 feet/day | > 2 days machine time, (50% of time needs operator's supervision) | < 4 hour, (no supervision of the operator) |
| Total time | 3 – 5 days | < 0.5 days |

Notations: *Φ*: diameter; *L*: length; PV: pore volume

## 3 Screening performance evaluation

One of the concerns with using smaller core sample is the reliability of the result, especially for those screening cases aiming to provide the highest oil recovery recipes. In principle, the smaller the sample is, the more challenging it is to measure the oil production precisely. To compensate this drawback on the setup, both an inline density meter and mass balance are used to improve the accuracy for the effluent analysis. At the same time, the system has a compact design with a shortened flowline and reduced inner diameter of tubing to minimize the dead volumes. The dead volume before the core account for about 2.5% of an average pore volume of core sample, after the core, the dead volume is 5% of the pore volume

To validate the screening reliability of the Lilliput core flooding unit, two core flooding experiments also conducted on conventional core flooding units – experiments A and B - were reproduced on the Lilliput setup. The conventional core flooding unit has a before and after core dead volume about 5% and 6%, respectively, of average pore volume.

The experimental details of these two experiments are listed in Table 3. The purpose of ASP core flooding experiments discussed here is to quantify the performance of different ASP recipes regarding their EOR protentional. In brief, significant additional oil recovery from the ASP flooding was seen in a successful ASP formula design in experiment A but not experiment B for both setups.

**Table 3.** Details of the two reference experiments

| **Experiment A – high oil recovery** | |
|---|---|
| Rock type | Berea |
| Core direction | vertical |
| Pore volume (mL) | 122 |
| Brine permeability at reservoir temp (mD) | 74 |
| Crude oil viscosity (mPa.s) | 3.9 |

|  |  |
|---|---|
| Brine viscosity at 80 °C (mPa.s) | 0.4 |
| Viscosity of ASP at 80 °C (mPa.s) | 8.5 |
| Pore volumes ASP injected (PV) | 0.4 |
| Pore volumes polymer injected (PV) | 3 |
| Viscosity of polymer at 80 °C (mPa.s) | 8.6 |
| **Saturations:** |  |
| Original oil in place (OOIP) (mL) | 67.5 ±6 |
| Oil produced waterflood (%PV): | 17±6 |
| Oil produced ASP/Polymer flood(%PV): | 34±6 |

| **Experiment B – low oil recovery** |  |
|---|---|
| Rock type | Berea |
| Core direction | vertical |
| Pore volume (mL) | 121 |
| Brine permeability at reservoir temp (mD) | 75 |
| Crude oil viscosity (mPa.s) | 0.9 |
| Brine Viscosity at T-reservoir (mPa.s) | 0.4 |
| Viscosity of ASP at 90 °C (mPa.s) | 10.7 |
| Pore volumes ASP injected (PV) | 0.4 |
| Pore volumes polymer injected (PV) | 3 |
| Viscosity of polymer at 90 °C (mPa.s) | 7.3 |
| **Saturations:** |  |
| Original oil in place (OOIP) (mL) | 75 ±6 |
| Oil produced waterflood (%PV): | 19±6 |
| Oil produced ASP/Polymer flood(%PV): | 6.6±6 |

The rock samples used for the evaluation are sandstone Berea outcrop rock with porosities of approximately 25% and permeabilities of approximately 100 millidarcy (mD). These rock samples are originally water-wet, and no pre-experiment treatment such as cleaning or aging with oil was applied to ensure consistency with the reference experiments. From an independent ASP core flooding experiment with CT-based saturation monitoring [19], no obvious capillary end effect was observed from 27 cm long cores, and capillary end effect is occurring within the 2 cm zone from 15 cm cores. In this study, the refence experiments use 30 cm long core samples, for which no significant capillary end effects during the water flood is expected. Furthermore, for the Lilliput setup, the core samples have a very slim and long shape (1cm in dimeter and 17 cm in length), where the capillary end effect is considered to have limited volumetric influence over the total pore volume. The capillary end effect correction can be made with the reference method [20], but within a screening focus in the work flow, this step was omitted. Identical oil saturation and brine flooding procedures are applied to the experiment on the Lilliput system and the reference study. In all steps, the same fluid and flooding speed was applied to both experiments. Different from the reference case, the flooding procedure on the Lilliput setup does not have an additional polymer drive after the ASP flooding, instead a slightly larger amount of 2-3 pore volumes of only ASP was injected to the core continually, with a subsequent brine drive as detailed in Table 4.

**Table 4.** Flooding procedures followed on the Lilliput setup and for reference experiment A

| Steps | Flooding speed (feet/day) | Injection volume (PV) |
|---|---|---|
| brine permeability | 60, 30, 20 | around 30 |
| Oil saturation | 10 | Around 15 |
| Brine flooding | 3 | until no additional oil recovery |
| ASP flooding | 3 | 2 to 3 |
| Brine driving | 3 | 5 |

For the re-executed experiment A, the additional oil production from ASP flooding is 1.9 mL. The additional oil recovery over the total pore volume is around 47%, see more detailed comparation are listed in Table 5,

**Table 5.** Comparing the experiment carried out on the Lilliput system with the reference experiment A

| Items | Ref exp A | Lilliput |
|---|---|---|
| Rock permeability (mD) | 74 | 105 |
| Apparent ASP viscosity (cp) | 16 | 13 - 18 |
| Core dimension, Length/Diameter (cm) | 30/5 | 17/1 |
| ASP injection (PV) | 0.4 | 3 |
| Additional oil recovery % to the total PV | 34 ± 6 | 47 ± 5 |

The pressure drop across the core during different flooding phases is another key parameter to identify the flooding behavior on the Lilliput setup. Figure 7 illustrates the apparent viscosity at the later stage of the ASP flooding period using the Lilliput system. This viscosity varies between 13 cp and 18 cp during the experiment, which is comparable to the value of the reference experiment (16 cp).

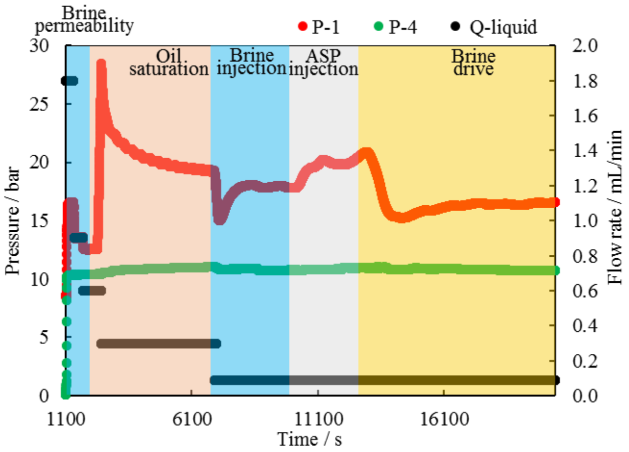

**Fig. 7.** Core flooding experiment on Lilliput unit. Four flooding periods: step 1, brine permeability measurement at three different injection rates; step 2, oil saturation period; step 3, ASP injecting period; step 4, brine drive. Steps are highlighted with different colour.

For experiment B, which was also reproduced on the Lilliput unit, the additional oil production from ASP solution flooding is approximately 0.3 mL. The additional oil recovery referenced to the total pore volume is approximately 10%, compared to the reference recovery of 6.6%. For both the conventional and the Lilliput experiment, continually increasing apparent viscosities were observed during the ASP injection. The apparent viscosities after injecting 0.4 PV of ASP solution are 80 cp and 130 cp, respectively, for the reference- and the Lilliput experiments. For the experiment with the Lilliput system, the higher length-to-diameter ratio aggravated the injectivity issue, where a higher apparent viscosity was observed.

**Table 6.** Comparing the experiment carried out on Lilliput with the reference experiment B

| Items | Ref exp B | Lilliput |
|---|---|---|
| Rock permeability (mD) | 75 | 100 |
| Apparent ASP viscosity (cp) 0.4 PV injection | 80 | 130 |
| Core dimension, Length/Diameter (cm) | 30/5 | 17/1 |
| Length/Diameter ratio | 6 | 17 |
| ASP injection (PV) | 0.4 | 3 |
| Additional oil recovery % to the total PV | 6.6 ± 6 | 10 ± 5 |

For both cases tested, the additional oil recovery determined using the Lilliput system is in good agreement with the reference experiments, but both Lilliput results are also slightly higher than the reference experiments. This could be the result of the extra 2-3 pore volume of ASP solution injected during the experiments with the Lilliput system instead of 0.4 pore volume ASP plus polymer injected during the experiment with the conventional core flooding system. Even so, qualitatively the results obtained with the Lilliput systems demonstrate that this automated core flooding system can distinguish the efficiency of ASP solutions. This capability is typically sufficient for screening purposes of chemical EOR flooding.

Regarding efficiency, each core flooding experiment is completed within 1 day (24 hours) with the sample preparation done during the day and the automatic flooding taking place during the night. The experimental results are in good agreement with the references regarding the pressure gradient/apparent viscosity across the core and the fraction of additional oil recovery. The measurement of initial oil saturation and residual oil saturation measurement, which requires real time X-ray scanning are omitted during the evaluation. The estimation of additional oil recovery is simply based on the volume of oil produced during the ASP flooding phases.

## 4 Summary

The newly designed automated core flooding using smaller core samples and a fully automated experimental control and data acquisition system has demonstrated more than 90% efficiency gain compared to conventional core flooding systems, with dramatically streamlined operation and improved control of the gas flow regulation. For foam experiments, the unit demonstrated its high precision in in-situ flow control and in-situ gas/liquid ratio. The ASP experiment carried out with the Lilliput setup verified the reliability of replacing a larger core sample by a mini core. The “plug and play” core holder design, the simplified operational procedures, the automation feedback control loop and the utilization of smart sensors can be applied to conventional core flood setups to improve the efficiency. Parallel core flooding units with the same unit design can be used to boost the screening capacity further.

The project was carried out within Shell Global Solutions International B.V. During the development of this new core flooding unit, the workshop department was heavily involved and contributed to the designing and construction of the setup.

## Reference

1. F. Fuso Nerini, J. Tomei, L. S. To, I. Bisaga, P. Parikh, M. Black*, et al.*, "Mapping synergies and trade-offs between energy and the Sustainable Development Goals," *Nature Energy,* vol. 3, pp. 10-15, 2018.
2. H. Guo, J. Dong, Z. Wang, H. Liu, R. Ma, D. Kong*, et al.*, "2018 EOR Survey in China-Part 1," presented at the SPE Improved Oil Recovery Conference, Tulsa, Oklahoma, USA, 2018.
3. B. Mukherjee, P. D. Patil, M. Gao, W. Miao, S. Potisek, and P. Rozowski, "Laboratory Evaluation of Novel Surfactant for Foam Assisted Steam EOR Method to Improve Conformance Control for Field Applications," presented at the SPE Improved Oil Recovery Conference, Tulsa, Oklahoma, USA, 2018.
4. S. Pal, M. Mushtaq, F. Banat, and A. M. Al Sumaiti, "Review of surfactant-assisted chemical enhanced oil recovery for carbonate reservoirs: challenges and future perspectives," *Petroleum Science,* vol. 15, pp. 77-102, 2018.
5. J. Chung, B. W. Boudouris, and E. I. Franses, "Surface tension behavior of aqueous solutions of a propoxylated surfactant and interfacial tension behavior against a crude oil," *Colloids and Surfaces A: Physicochemical and Engineering Aspects,* vol. 537, pp. 163-172, 2018.
6. A. B. Fuseni, A. M. AlSofi, A. H. AlJulaih, and A. A. AlAseeri, "Development and evaluation of foam-based conformance control for a high-salinity and high-temperature carbonate," *Journal of Petroleum Exploration and Production Technology,* pp. 1-8, 2018.
7. M. S. Kamal, A. Sultan, I. Hussein, S. Hussain, and A. M. AlSofi, "Screening of Surfactants and Polymers for High Temperature High Salinity Carbonate Reservoirs," in *SPE Kingdom of Saudi Arabia Annual Technical Symposium and Exhibition*, 2018.
8. N. Khazali, M. Sharifi, and M. A. Ahmadi, "Application of fuzzy decision tree in EOR screening assessment," *Journal of Petroleum Science and Engineering,* vol. 177, pp. 167-180, 2019.

9. P. Dong, M. Puerto, G. Jian, K. Ma, K. Mateen, G. Ren, *et al.*, "Exploring Low-IFT Foam EOR in Fractured Carbonates: Success and Particular Challenges of Sub-10-mD Limestone," in *SPE Annual Technical Conference and Exhibition*, 2018.
10. B. Wei, J. Ning, J. Shang, and W. Pu, "An experimental validation of a smart emulsion flooding for economic chemical EOR," in *SPE EOR Conference at Oil and Gas West Asia*, 2018.
11. A. Baldygin, D. S. Nobes, and S. K. Mitra, "New Laboratory Core Flooding Experimental System," *Industrial & Engineering Chemistry Research,* vol. 53, pp. 13497-13505, 2014.
12. J. Swift, "Gulliver's travels," in *Gulliver's Travels*, ed: Springer, 1995, pp. 27-266.
13. C. S. Gregersen, M. Kazempour, and V. Alvarado, "ASP design for the Minnelusa formation under low-salinity conditions: Impacts of anhydrite on ASP performance," *Fuel,* vol. 105, pp. 368-382, 2013.
14. M. M. Kulkarni and D. N. Rao, "Experimental investigation of miscible and immiscible Water-Alternating-Gas (WAG) process performance," *Journal of Petroleum Science and Engineering,* vol. 48, pp. 1-20, 2005.
15. S.-H. Chang and R. B. Grigg, "Laboratory Flow Tests Used To Determine Reservoir Simulator Foam Parameters for EVGSAU CO2 Foam Pilot," presented at the Permian Basin Oil and Gas Recovery Conference, 1994.
16. S. A. Jones, V. van der Bent, R. Farajzadeh, W. R. Rossen, and S. Vincent-Bonnieu, "Surfactant screening for foam EOR: Correlation between bulk and core-flood experiments," *Colloids and Surfaces A: Physicochemical and Engineering Aspects,* vol. 500, pp. 166-176, 2016.
17. R. D. Wyckoff and H. G. Botset, "The Flow of Gas-Liquid Mixtures Through Unconsolidated Sands," *Physics,* vol. 7, pp. 325-345, 1936/09 1936.
18. E. Lemmon, M. Huber, and M. McLinden, "NIST Standard Reference Database 23, Reference Fluid Thermodynamic and Transport Properties (REFPROP), version 9.0, National Institute of Standards and Technology," *R1234yf. fld file dated December,* vol. 22, 2010.
19. S. Berg, S. Oedai, D. van Batenburg, K. Elewaut, and D. Boersma, "Visualization of ASP Coreflood Experiments Using X-ray CT Imaging," in *IOR 2015-18th European Symposium on Improved Oil Recovery*, 2015.
20. D. D. Huang and M. M. Honarpour, "Capillary end effects in coreflood calculations," *Journal of Petroleum Science and Engineering,* vol. 19, pp. 103-117, 1998.

# A new CEC measurement proxy using high-frequency dielectric analysis of crushed rock

*M. Rebecca* Stokes[1], Z. *Elton* Yang[1], *Prince* Ezebuiro[1], and *Timothy* Fischer[1]

[1]Chevron Energy Technology Company, Houston, Texas, USA

**Abstract.** Measuring the cation exchange capacity (CEC) of clay bearing rocks is a useful tool to estimate smectite content, or amount of swelling clay in the rock, and is referenced across many aspects of oil and gas exploration. Measuring the CEC of a rock, however, is laborious and depending on the method used requires saturation and extraction steps, the use of multiple chemicals, titration, and spectroscopic analysis. This study, which builds on the established petrophysical link between clays and relative permittivity ($\varepsilon'_r$), outlines a work flow and set of equations that allow for bulk rock CEC to be calculated from permittivity measurements of crushed rock using a handheld dielectric probe. A series of quartz-smectite mineral mixtures were prepared and high-frequency (80 MHz-1.4 GHz) dielectric measurements collected at six relative humidity (RH) conditions ranging from 8-75%. For each RH data set, a strong linear relationship ($R^2 \geq 0.98$) exists between permittivity at 120 MHz and the lab-measured CEC of the mineral mixtures. The equations from these calibration curves were used to derive 3 RH-dependent equations. The method was validated on a variety of crushed sedimentary rocks and differences between the calculated values from this study and the lab-measured CECs range between +/- 6 meq/100g. These results demonstrate that dielectric permittivity measurements can be used as a CEC-proxy and is a fast and flexible alternative to laboratory-based CEC analysis.

## 1 Introduction

Cation exchange capacity (CEC) is a data type commonly referenced in the oil and gas industry as it holds critical information about the swelling potential of a rock which is an important component in well planning and production modeling. Specifically, quantification of clay types and their swelling behavior is used for drilling and completions planning, borehole instability mitigation, enhanced oil recovery (EOR) planning, and predicting changes in production due to damage from clay swelling. Each of these aspects of hydrocarbon production can be significantly impacted if the rocks of interest are not properly characterized with respect to the clays, and as a result there can be serious financial and Health and Environmental Safety (HES) consequences. The principal aim of this study was to develop a method to measure CEC quickly and without the use of chemicals or complicated analytical equipment so that CEC data can be available quickly to aid in decision making while drilling.

CEC is loosely related to the surface charge of a material and is the measure of the ability to reversibly adsorb cations. It is used across many geoscience and engineering fields to characterize clays. Exchangeable cations have varying hydration enthalpies due to the differences in their cation size and valence and as a result, the amount of water that can be adsorbed by a clay mineral is dependent on the total specific surface area [1], and the exchangeable cation type located in the interlayer regions and particle surfaces. While most clay minerals have some CEC *e.g.* (kaolinite, chlorite <5 meq/100g [2], illite ≈10-15 meq/100g), smectite often has significantly greater CEC, sometimes an order of magnitude higher [3].

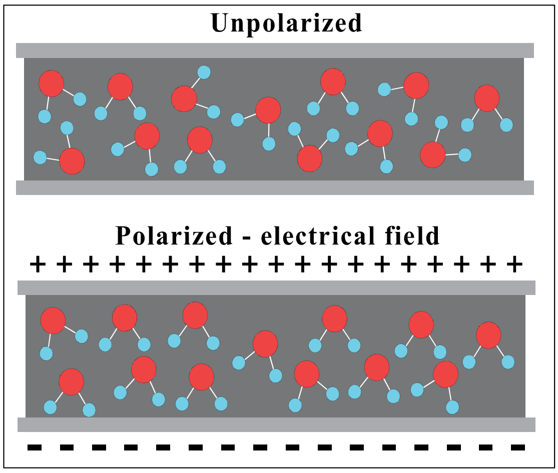

**Figure 1.** Schematic of water molecules with no electrical field versus an applied electrical field where the water molecules polarize.

---

[*] Corresponding author: rebeccastokes@chevron.com

Thus, by measuring the CEC of a rock, one can estimate the approximate amount of smectite in the rock. Several methods exist to measure the CEC of a rock, and most involve the complete exchange of cations present in the natural sample by a cationic species, such as $NH_4$, $K^+$, $Na^{2+}$, methylene blue, Co(III)-hexamine$^{3+}$, and Cu(II) ethylendiamine complex [4]. Exchange is quantified by measuring the effluent solution by spectrophotometric techniques or by measuring the change in cation concentration in the fluid through mass spectroscopy. These methods, with some limitations (*e.g.*, [5, 6]) are effective CEC measurement methods, however they are time intensive, require the use of a chemicals which involve proper disposal, and a laboratory to store chemicals and house analytical equipment.

Relative permittivity (the real part of the complex permittivity) measures the degree to which a medium resists the flow of electric charge. Water is a polar molecule with a permanent dipole moment and will rotate to align with an applied electric field (Figure 1, [7]). We take advantage of this in the frequency region where the dielectric response of the rock is governed by dipole polarization (~$10^8$ Hz). In this region, the effects of water, either in the form of adsorbed water on mineral surfaces, capillary water, or free water, makes permittivity measurements sensitive to CEC [8, 9], and thus to the amount of smectite present in the rock.

As CEC is an important mineral property to characterize in the oil and gas industry, several avenues of proxy CEC analysis have been developed, including the use of magnetic susceptibility [10] and dielectric permittivity. Specific to the use of dielectric analysis as a CEC tool, Garrouch (2018) provides a set of equations derived from dimensional analysis to calculate CEC, however these equations require surface area and porosity information to solve for CEC and these data are often not readily available [9]. Leung and Steiger (1992) also published a standard test procedure for ultimately calculating the amount of hydratable clays in shales [11]. This method involves several steps including saturating the sample in a $K^+$ solution, centrifuging twice, washing the sample with rubbing alcohol, and taking the dielectric measurement. CEC is then calculated by a simple correlation between the dielectric constant and standard mixtures, similar to those used in this study. The authors [11] have developed a portable kit that includes all the equipment necessary to make the measurements. While both methods offer ways to calculate CEC from dielectric measurements, extra labor is still required to either attain additional data to calculate CEC (Garrouch method), or to prepare the sample for dielectric analysis (Leung and Steiger method). Considering this, there is room still to generate a simplified CEC-proxy using direct dielectric permittivity measurements.

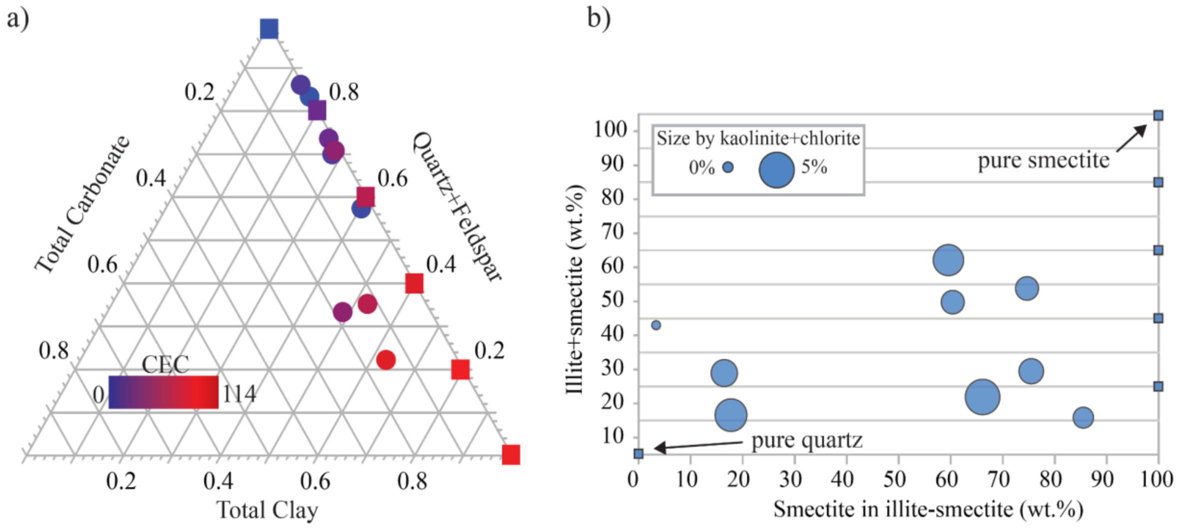

**Figure 2.** a) Summary of sample mineralogy on a ternary diagram including both quartz:smectite mixtures (squares) and rock powders (circles). Samples are colored by their CEC values from laboratory measurements. b) Illite-smectite wt.% vs. % smectite in illite-smectite (calculated using Equation (1)). Data points are sized by kaolinite+chlorite wt%.

## Materials and Methods

### 2.1 Sample selection and characterization

Two sets of samples were prepared for this study: 1) quartz-smectite mixtures and 2) rock powders from a variety of sedimentary rock types. Rock samples were selected based on their bulk mineralogy as determined by X-ray diffraction (XRD) analysis and bulk CEC values to obtain a decent range of rock types and CEC values up to 45 meq/100g (Figure 2a). Porosity data was collected on 7 of the 9 rock samples from co-located plugs by Hg porosimetry analysis on oven-dried and Dean Stark extracted material. Porosity values obtained using this method range between 7-23%. Detailed information about the clay compositions and amounts as determined by XRD analysis are shown in (Figure 2b). Figure 2b shows illite-smectite wt.% plotted against the % smectite in illite-smectite (I-S) calculated using Equation (1). In this equation, *%S in I-S* is determined by assigning the bulk rock CEC to the total illite-smectite ($CEC_{meas}$) wt.% and normalized on a difference between pure illite end member ($CEC_I$ = 15 meq/100g) and pure smectite end member ($CEC_S$ = 100 meq/100g).

$$\%S\ in\ I-S = \frac{CEC_{meas}-CEC_I}{CEC_S-CEC_I}\times 100 \tag{1}$$

Data points in Figure 2b are sized by kaolinite+ chlorite which does not exceed 5 wt.%. Both kaolinite and chlorite have a low CEC (<10 meq/100g) and are typically not considered significant contributors to bulk CEC.

The quartz-smectite standards were prepared by mechanically homogenizing 20% proportions by weight of pure quartz and a pure smectite (Tsukinuno montmorillonite JCSS-1301 distributed by The Clay Science Society of Japan) standard. Prior to homogenization the quartz was comminuted in a McCrone mill for 5 minutes so that the quartz particle size approximately matched that of the smectite standard. The rock powders were prepared by hand grinding the material in a mortar and pestle to pass through a 40 mesh (0.42 mm) sieve. This methodology for preparing the rock powders avoids common issues associated with artificially altering the CEC via sample preparation. Hand grinding minimizes shearing which might delaminate clay particles, and the particle size associated with a 40 mesh sieve is, for most rocks, larger than the average phyllosilicate grain size thus not increasing the surface area of the individual grains.

**Figure 3.** Handheld dialectic probe manufactured by Copper Mountain Technologies used in this study. The circular probe end (left side of probe) is ~1 inch in diameter.

Both the quartz-smectite mixtures and rock powders were dried in an oven at 105°C for 48 hours to ensure that the majority of clay bound $H_2O$ was removed [3]. Approximately 3 grams of material were loaded into a shallow plastic holder prior to being placed in the first relative humidity (RH) controlled desiccator. Samples were equilibrated for ~48 hours at each RH prior to dielectric analysis at each stage.

Splits were taken from all samples for CEC analysis and from the crushed rock samples for XRD analysis. These data are summarized in Figure 2a. CEC measurements were done using the Co(III)-hexamine$^{3+}$ cation exchange, spectrophotometric technique outlined by Bardon et al. (1993) [12]. The rock powders were prepared for XRD analysis following the methods described in Środoń et al. (2001) and Omotoso et al. (2006) to make randomly oriented powder mounts [13, 14]. The phase quantification was accomplished using Chevron's proprietary software, which is a modification of a technique published by Chung (1974) [15].

Relative humidity was controlled by using a series of saturated salt solutions in desiccation chambers and monitored by a barometric pressure-temperature-relative humidity data logger located inside the chamber. In increasing order of RH, the salts used in this study included lithium chlorite (LiCl), lithium iodide (LiI), potassium acetate ($CH_3CO_2K$), magnesium chlorite (MgCl), potassium carbonate ($K_2CO_3$), sodium bromide (NaBr), and sodium chloride (NaCl). To achieve the RH between LiCl and LiI (RH=11.2%), equal amounts of two saturated salt solutions (LiCl and LiI) were placed in separate containers in a desiccator. In addition, an additional RH dataset was collected by leaving the samples to equilibrate in the room RH (58.8%) for 24 hours. Room RH was monitored during the equilibration and did not deviate more than ±1.5%.

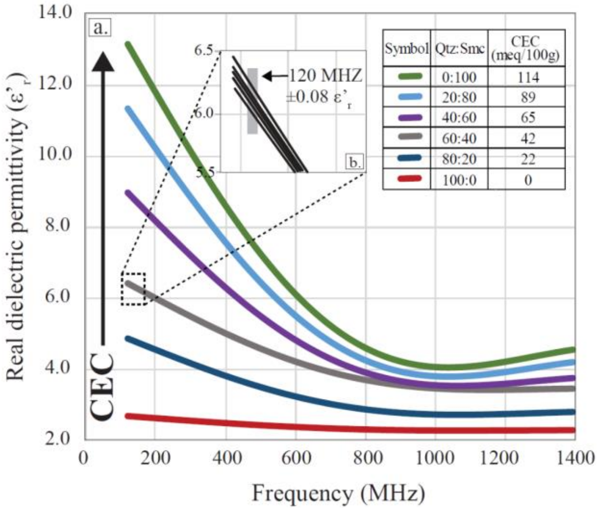

**Figure 4.** a) Real dielectric permittivity curves across the full frequency range for the 6 quartz-smectite used in this study. b) Example of the typical range observed at low frequencies between the 5 repeated dielectric analyses. Errors based on this are reported in Figure 5.

Water vapor adsorption analysis using the Dynamic Vapor Adsorption (DVS) machine developed by Surface Measurement Systems Ltd. was used to quantify the amount of water adsorbed by smectite at the specific RH conditions investigated in this study. This specific machine uses a gravimetric sorption technique that measures how quickly and how much of a solvent is adsorbed by a sample.

### 2.2 Dielectric measurement method

The Dielectric Assessment Kit System (Schmid & Partner Engineering AG, Switzerland) with a Planar R140 Vector Reflectometer (Copper Mountain Technologies vector network analyzer) and a DAK-3.5 probe was used to perform the laboratory dielectric measurements on each of the powder samples (Figure 3). The Vector Network Analyzer (VNA) operates from 85 MHz to 1.4 GHz, and the Depth of Investigation (DOI) of the DAK-3.5 probe is ~3 mm.

The dielectric probe was always calibrated at room temperature (~21°C) before usage. During the measurement at each designated RH, the probe remained vertical with the active surface area directly touching the top of the sample. A small amount of pressure was used to minimize the gap between the probe and the sample. After the permittivity readings stabilized, the values within the entire sweeping range (5 MHz resolution) were recorded (Figure 4a). The same measurement was repeated five times on each sample to ensure the reliability of the measurement and the average of those readings was used in the study. The typical observed $\varepsilon'_r$ range from 5 repeat measurements at 120 MHz is ± 0.08 (Figure 4b). Figure 4a shows the influence of CEC on the dielectric response across the full range of frequencies. The largest difference between these curves is at the lower frequencies, thus we chose to read the real dielectric permittivity at 120 MHz for this study.

It should be noted that the laboratory RH was typically ~55%, consequently collecting the data for the lower RH conditions had to be done quickly. If a sample was exposed to the room RH conditions for more than 1 minute, it was placed back in the desiccator to re-equilibrate to the low RH condition and then analyzed again. As a result, the datasets for the RH conditions <30% took many days to collect.

## 3 Results

### 3.1 Dielectric Results

### *3.1.1 Quartz-smectite mixtures*

Dielectric measurements of the quartz-smectite mixtures were collected to characterize and quantify the relationship between CEC, permittivity, and relative humidity. These results are shown in Figure 5. Each RH dataset shows a very strong correlation between permittivity and CEC with $R^2$ values >0.98. The pure quartz sample (CEC=0) has a relatively constant permittivity value of ~2.5 despite the large range of RH conditions. At this point in the study, had the slope (and y-intercept) differences between each dataset showed a linear relationship with RH, a CEC calculation would be straightforward using a line equation and a multiplication

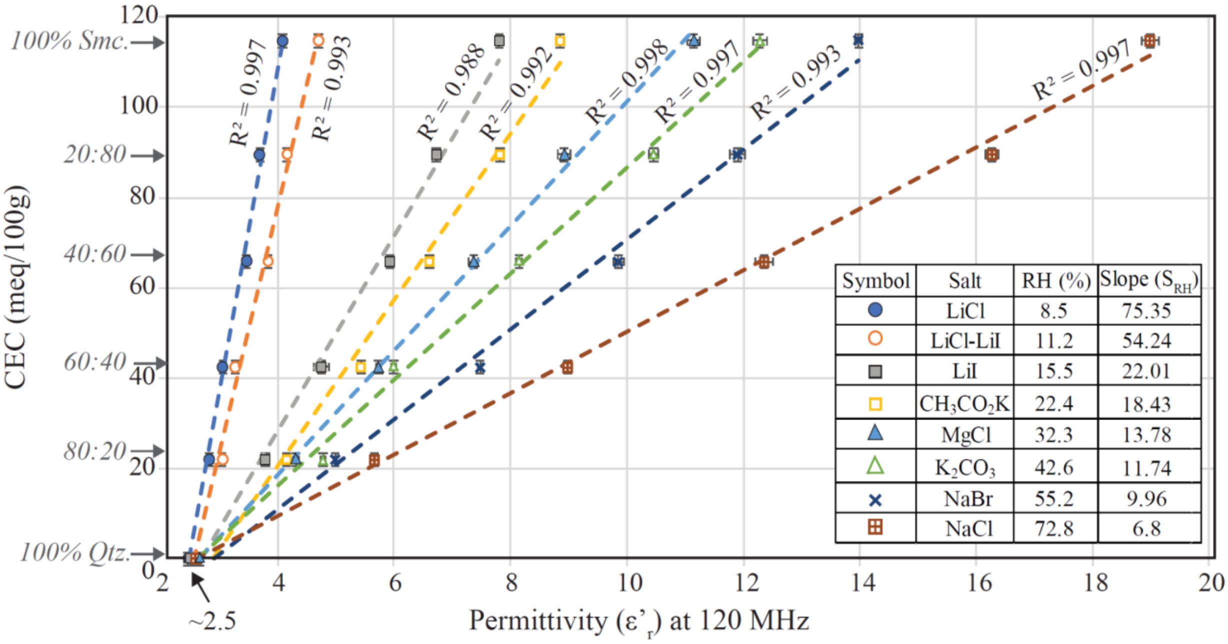

| Symbol | Salt | RH (%) | Slope ($S_{RH}$) |
|---|---|---|---|
| ● | LiCl | 8.5 | 75.35 |
| ○ | LiCl-LiI | 11.2 | 54.24 |
| ■ | LiI | 15.5 | 22.01 |
| □ | $CH_3CO_2K$ | 22.4 | 18.43 |
| ▲ | MgCl | 32.3 | 13.78 |
| △ | $K_2CO_3$ | 42.6 | 11.74 |
| × | NaBr | 55.2 | 9.96 |
| ⊞ | NaCl | 72.8 | 6.8 |

**Figure 5.** Dielectric permittivity at 120MHz results from the 6 quartz-smectite mixtures at 8 different RH conditions. All data was collected at 21°C. Dashed lines and corresponding $R^2$ values are the best fit line for each dataset. CEC error from laboratory measurements is ±1.8 meq/100g and permittivity errors are from the range of values for the 5 repeat dielectric analyses collected on every sample at each RH. Quartz:smectite ratios are noted in grey italic lettering on the left side of the plot.

factor for the slope-RH relationship. However, these datasets yield a non-linear relationship between the slope ($S_{RH}$), y-intercept constant ($c_{RH}$), and relative humidity which needs to be further constrained to successfully calculate CEC using Equation (2).

$$CEC = S_{RH}\,\varepsilon_r' + c_{RH} \tag{2}$$

The slope values (CEC/ ε'$_r$) shown in Figure 5 are plotted against their corresponding RH value in Figure 6 to establishes the relationship between CEC and permittivity as a function of RH from 8% to 72% at 21°C. It becomes apparent that there are three linearly-related regions defined by the intersection of best fit lines at low (<18%), moderate (18-35%), and high (>35%) RH conditions. The best fit lines for these regions have $R^2$ values >0.98. It should be noted that a single curve approach to fitting the data was evaluated, however, due to the sharp change in slope between the mid and high RH regions, simple exponential and power decay equations were not adequate to fit the full dataset. It should also be addressed that the mid-range RH best fit line is defined by only two data points, and we recognize that more data points would make a stronger case for the following interpretations. Despite the limited number of data points, errors ($CEC_{measured}$-$CEC_{calculated}$) of calculated CEC values reviewed in Section 3.2.1 and are reasonable, suggesting that the addition of more data points would not change the correlations.

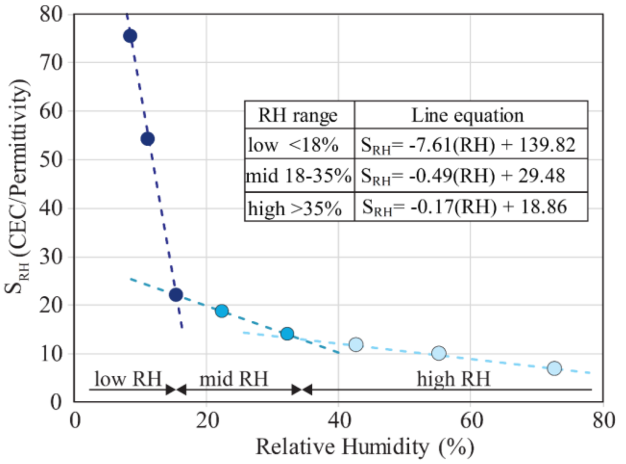

| RH range | Line equation |
|---|---|
| low <18% | $S_{RH}$= -7.61(RH) + 139.82 |
| mid 18-35% | $S_{RH}$= -0.49(RH) + 29.48 |
| high >35% | $S_{RH}$= -0.17(RH) + 18.86 |

**Figure 6.** Relationship between the slopes derived from Figure 5 and relative humidity.

The three, RH dependent, linear curves (Figure 6) provide equations that allow for $S_{RH}$ to be calculated using Equation (3).

$$S_{RH} = S_{l,m,h}(RH) + c_{l,m,h} \tag{3}$$

The parameters required to solve for $S_{RH}$ are $S_{l,m,h}$ and $c_{1,m,h}$ which are the slope and y-intercept values provided in the table embedded in Figure 6; *l*, *m*, and *h* stand for low-, mid-, and high-RH conditions. Their respective values should be substituted into Equation (3) depending on the RH recorded during permittivity data collection. Now that $S_{RH}$ can be calculated, $c_{RH}$ can be calculated using Equation (2). This is possible because the best-fit lines for each RH meet at 2.5 ε'$_r$, CEC=0 (see Figure 5) thus leaving a simple equation to solve for $c_{RH}$ (Equation 4).

$$c_{RH} = -S_{RH}(2.5) \tag{4}$$

### *3.1.2 Crushed rock samples*

Dielectric analysis results on the crushed rock samples at 32.3% and 72.8% RH are plotted in Figure 7. These data are shown together with the lower CEC quartz-smectite mixture data from the same RH conditions where the dashed lines are the same as the best-fit lines shown in Figure 5. There is good agreement between the crushed rock data and quartz-smectite mixtures despite significant differences in particle size, porosity, and mineralogy - specifically clay speciation (Figure 2a, b).

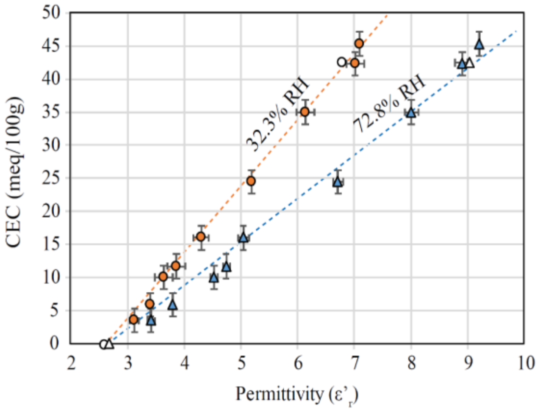

**Figure 7.** Permittivity vs. measured CEC for the crushed rock samples (filled shapes) at 32.3% and 72.8% RH. Dashed lines are the best-fit lines defined by the quartz-smectite mixtures (open shapes) shown in Figure 5.

## 3.2 Water-Vapor Adsorption Results

Water vapor adsorption results provide information about the amounts of adsorbed water and rate of adsorption that ultimately control the permittivity. In this paper we do not show the rate of water adsorption data from these experiments, however this component of the data provided valuable information regarding how quickly high CEC samples adsorb $H_2O$, thus altering the way we collected data and treated samples prior to, and during dielectric analysis. Figure 8 shows the relationship between permittivity and the amount of adsorbed $H_2O$ by smectite as a function of RH. At low RH conditions, the steep slope of the best-fit line establishes that the addition of relatively small amounts of water vapor to dry smectite has a very strong impact on the dielectric response of the material. This strong dielectric response lessens by an order of magnitude around 18% RH which, unsurprisingly, corresponds to the boundary between the low- and mid- RH regions identified in Figure 6.

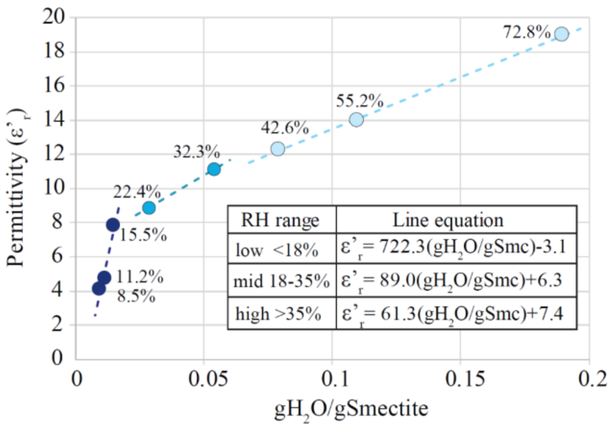

**Figure 8**. Permittivity vs. amount of water adsorbed by pure smectite at specific RH conditions (% next to circles) that match those investigated in this study.

### 3.3 Method Validation

Using Equations (2)-(4), CEC was calculated for the quartz-smectite and crushed rock samples to evaluate the method presented in this paper. There was a consistent positive offset of the calculated CEC from the lab-measured CEC of ~4 meq/100g. This correction factor (*C*) is applied to Equation (2), yielding Equation (5). The source of this error is worth investigation though it is not evaluated in this paper.

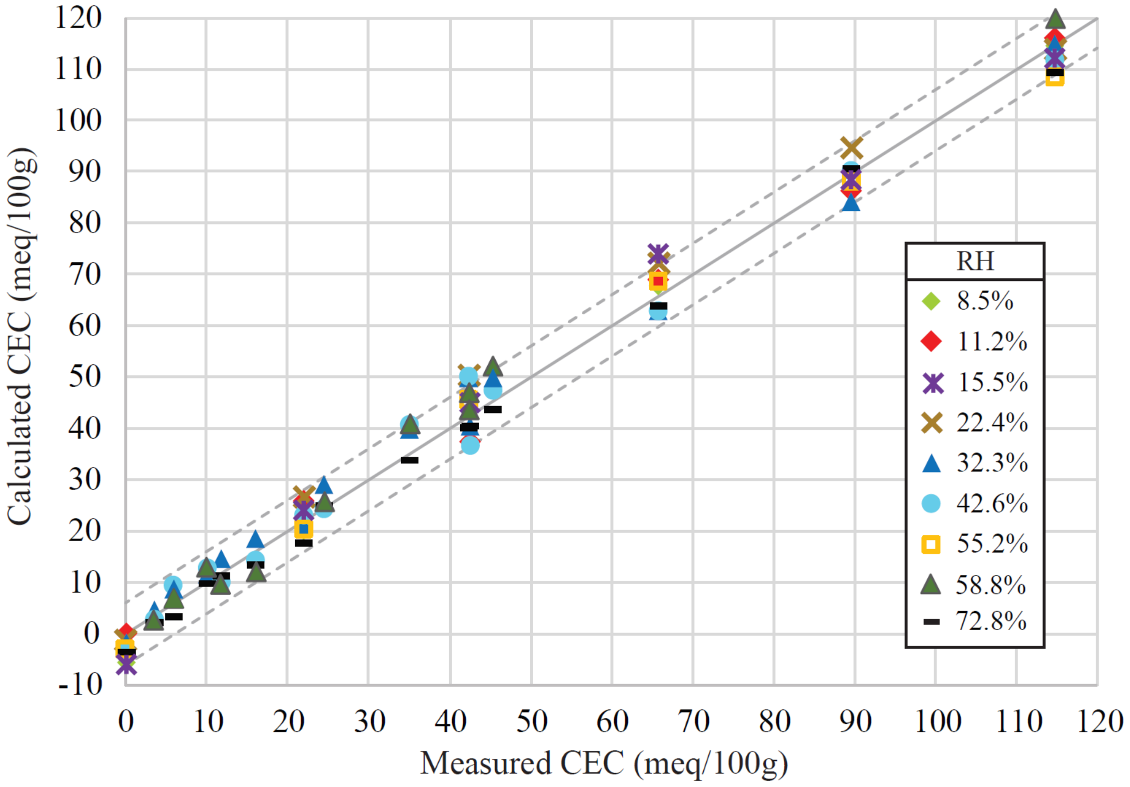

**Figure 9**. Calculated CEC using Equation 5 vs. the laboratory measured CEC for the crushed rock samples (max. CEC of 45 meq/100g) and quartz:smectite standards. Solid grey line is the 1:1 line, dashed grey lines define the ±6 meq/100g error field.

$$CEC = S_{RH}\,\varepsilon_r' + c_{RH} + C \qquad (5)$$

Adjusted calculated CEC values using Equation 5 are plotted against laboratory measured CEC in Figure 9. There is good agreement within ±6 meq/100g between calculated and measured CEC for all samples (quartz-smectite and crushed rock samples) from 8-73% RH.

## 4 Discussion

### 4.1 Method application and limitations

This study was motivated by the need for a portable CEC analysis technique that does not require significant sample preparation or the use of chemicals. Creating a method to quickly generate CEC data would be particularly useful for drilling engineers and geologists to assess changes in the swelling potential of rocks being drilled and account for potentially impacted processes in real-time. The method presented in this paper provides a procedure and set of equations for a CEC-proxy tool that can be developed for specific laboratory/field conditions where RH (and temperature) conditions are often not constant.

Identified limitations of this technique include: 1) Specific values provided for $S_{l,m,h}$, $c_{l,m,h}$, and *C* are only applicable if collecting data at the same temperature (around 21°C in this study) and frequency (120 MHz). Permittivity measurements in the high-frequency range are sensitive to changes in temperature [16], thus operating conditions outside of this will require new calibration curves similar to what are shown in Figure 5 such that new values can be calculated for $S_{l,m,h}$, $c_{l,m,h}$, and $C$. However, once established, the analyses and CEC calculations are straight forward and fast to obtain. 2) This study attempted to use a wide range of rock types to validate the method (Figure 2) however, there are some minerals/phases that were not covered and may not be suitable for this method. These include Mg-dominant smectite, certain zeolites, opal varieties, significant amounts of solid organic matter [5], and grain coating liquid hydrocarbon. Other parameters that showed surprisingly little to no impact on the dielectric response were porosity, particle size, and compositional variations of illite-smectite (*e.g.* exchangeable cations and associated variations in layer charge). 3) This method has been validated for use in RH conditions ranging from 8-73% RH. At very low RH condition, there will not be enough $H_2O$ in the system to be conducive to dielectric analysis. At very high RH conditions (>~75%) it is well documented that capillary condensation in porous media dominates water sorption mechanisms and is a phenomenon mostly independent of CEC (*e.g.* [16]). Both scenarios would significantly complicate the relationship between RH, CEC, and permittivity.

### 4.2 Clay-water interaction and dielectric response

An outcome of this study that requires further investigation are the physiochemical processes governing the relationship between $S_{RH}$ and RH as shown in Figure 6. At RH conditions below ~18%, there is a strong dielectric response to very little $H_2O$ in the environment and above this the response is not as strong relative to the ever-increasing amounts of $H_2O$ adsorbed by smectite. In the case of pure smectite, the water adsorption behavior in this RH region is largely controlled by the size and valance of the exchangeable cation in the TOT (tetrahedral-octahedral-tetrahedral) interlayers and their corresponding hydration enthalpies ($Mg^{2+} >> Ca^{2+} > Na^{+} > K^{+}$) [18]. Numerous studies have used X-ray diffraction to describe smectite swelling behavior through tracking the changes in the basal d-spacing of different smectite species at a range of RH conditions [19-22]. These results consistently show that interlayer expansion for $K^+$, $Na^+$, $Ca^{2+}$, and $Mg^{2+}$-exchanged smectite typically starts at >20%, ~20% RH, ~20% RH, ~10%RH, and <10%RH, respectively. The smectite (Tsukinuno montmorillonite) used in this study is $Na^{2+}$-dominant (>75%) with measurable amounts of $Ca^{2+}$ and $Mg^{2+}$ (Ca>Mg) [23]. Based on this information, most of the interlayer expansion via $H_2O$ adsorption starts around 20% RH which corresponds to the drastic change in the $S_{RH}$-RH relationship identified in this study at 18% RH. It follows that at RH conditions lower than ~20%, the large changes in permittivity are possibly due to $H_2O$ adsorption on high CEC mineral surfaces and edges, however this theory needs further investigation. As RH increases and smectite interlayer adsorption begins to dominate, the dielectric response decreases relative to the increased adsorption of interlayer $H_2O$.

At higher RH values, a more subtle change in the relationship between $S_{RH}$ and RH occurs at ~35% RH, and defines the boundary between the mid- to high- RH ranges shown in Figure 6. This RH value corresponds to published data that mark the prevalence of monolayer adsorption of $H_2O$ around cation/charged sites in Na-montmorillonite similar to the smectite standard used in this study [17, 19, 25]. This loose interpretation of the data from this study requires further evaluation, however if a physiochemical-based explanation for the empirical relationships identified between RH, CEC and dielectric response can be provided, it would make an even stronger case for the use of dielectric permittivity as a proxy for CEC.

## 5 Conclusions

Results of this study provide a set of equations and methodology that allow CEC to be calculated from the real part of the complex permittivity. To do this, a series of equations were developed to determine the RH dependent relationship between CEC and permittivity such that if the RH is known and the permittivity measured, bulk CEC can be calculated. Approximate error for the CEC calculation using these equations is ±6 meq/100g which for the purposes of discriminating rocks that will have issues due to clay swelling, is acceptable.

The handheld tool used for dielectric analyses is portable and relatively easy to set up and calibrate. Sample preparation only requires hand grinding the rock to pass through a 40-mesh sieve and oven drying the sample to remove any water and liquid hydrocarbons, if present, and equilibrating the sample to a single RH for at least 24 hours. This tool and set of equations are a portable and easy to use option for calculating CEC *in lieu* of traditional laboratory-based methods.

Future areas of investigation related to this study include: 1) investigate CEC-RH relationships at various frequencies and for various exchangeable cations 2) applying the learnings from this study to assess obtaining CEC data from dielectric log data, 3) the fundamental molecule-surface interactions contributing to dielectric permittivity in mineral mixtures and, 4) using this tool for CEC analysis on slabbed core.

### Acknowledgements

We would like to thank Chevron Energy Technology Company for funding this research and providing the analytical equipment and materials. We would also like to acknowledge and thank Hanming Wang, Boquin Sun, Russ Peacher, Jon Burger, and Douglas McCarty for their technical contributions and guidance on this project.

### References

1. J. Środoń, Quantification of illite and smectite and their layer charges in sandstones and shales from shallow burial depth," *Clay Miner.*, vol. 44, no. 4, pp. 421-434, Dec. 2009, doi: 10.1180/claymin.2009.044.4.421.

2. C. Ma and and R.A. Eggleton, “Cation exchange capacity of kaolinite,” *Clay Clay Miner.*, vol. 47, no. 2, pp. 174-180, Apr. 1999.
3. J. Środoń, D.K. McCarty, “Surface area and layer charge of smectite from CEC and EGME/H2O-retention measurements,” *Clays and Clay Min*., vol. 56, no. 2, pp.155-174, Apr. 2008, doi:10.1346/CCMN.2008.0560203
4. L. Meier and G. Kahr, “Determination of the Cation Exchange Capacity (CEC) of Clay Minerals Using the Complexes of Copper(II) Ion with Triethylenetetramine and Tetraethylenepentamine,” *Clay Clay Miner.*, vol. 47, no. 3, pp. 386-388, Jan. 1999, doi: 10.1346/ccmn.1999.0470315.
5. A. Derkowski, T.F. Bristow, “On the problems of total specific surface area and cation exchange capacity measurements in organic-rich sedimentary rocks,” *Clay Clay Miner.*, vol. **60**, no. 4, pp. 348-362, Aug. 2012, doi: 10.1346/CCMN.2012.0600402.
6. R. Dohrmann, S. Kaufhold, “Three new, quick CEC methods for determining the amounts of exchangeable calcium cations in calcareous clays,” *Clay Clay Miner.*, vol. 57, no. 3, pp. 338-352, Jun. 2009, doi: 10.1346/CCMN.2009.0570306.
7. M. Josh, “Dielectric permittivity: A petrophysical parameter for shales,” *Petrophysics*, vol. 55, no. 4, pp. 319-332, Aug. 2014.
8. M. Josh, B. Clennell, “Broadband electrical properties of clays and shales: Comparative investigations of remolded and preserved samples,” *Geophysics*, vol. 80, no. 2, pp. D129-D143, Feb. 2015, doi: 10.1190/geo2013-0458.1.
9. A. A. Garrouch, “Predicting the cation exchange capacity of reservoir rocks from complex dielectric permittivity measurements,” *Geophys*ics, vol. 83, no. 1, pp. MR1-MR14, Jan-Feb. 2018, doi: 10.1190/GEO2017-0035.1.
10. D.K. Potter, “Magnetic susceptibility as a rapid, nondestructive technique for improved petrophysical parameter prediction,” *Petrophysics*, vol. 48, no. 3, pp. 191-201, Jun. 2007.
11. P.K. Leung, R.P. Steiger, “Dielectric constant measurements: a new, rapid method to characterize shale at the wellsite,” presented at SPE/IADC Drilling Conference, New Orleans, LA, USA, Feb. 18-21 Paper: SPE-23887-MS.
12. C. Bardon, “Recommandations pour la détermination expérimentale de la capacité d'échange de cations des milieux argileux,” *Rev. Inst. Fr. Pét*., vol. **38**, no. 5, pp. 621-626, Sept.-Oct. 1983, doi: 10.2516/ogst:1983037.
13. J. Środoń, V. A. Drits, D. K. McCarty, J.C.C. Hsieh, D. D. Eberl, “Quantitative XRD analysis of clay-rich rocks from random preparations,” *Clay Clay Miner.*, vol. 49, no. 6, pp. 514-528, Jan. 2001, doi: 10.1346/CCMN.2001.0490604
14. O. Omotoso, D.K. McCarty, S. Hillier, R. Kleeberg, “Some successful approaches to quantitative mineral analysis as revealed by the 3rd Reynolds Cup contest,” *Clay Clay Miner.*, vol. 54, no. 6, pp.748-760, Dec. 2006, doi: 10.1346/CCMN.2006.0540609.
15. F.H. Chung, “Quantitative interpretation of X-ray diffraction patterns of mixtures. I. Matrix-flushing method for quantitative multicomponent analysis,” *J. Appl. Crystallogr*., vol. 7, no. 6, pp. 519-525, Dec. 1974, doi: 10.1107/S0021889874010375.
16. M. Hizem, H. Mehdi, B. Deville, F. Ollivier, L. Mosse, M. Simon, “Dielectric dispersion: A new wireline petrophysical measurement,” presented at the SPE annu. Tech. Conf., Denver, CO, USA, Sept. 21-24, 2008, Paper 116130.
17. W.F. Woodruff, A. Revil, “CEC-normalized clay-water sorption isotherm.” *Water Resour. Res*., vol. 47, pp. W11502, Nov. 2011, doi: 10.1029/2011WR010919.
18. T. Sato, T. Watanabe, R. Otsuka, “Effects of layer charge, charge location, and energy change on expansion properties of dioctahedral smectites,” *Clay Clay Miner.*, vol. 40, no. 1, pp. 103-113, Jan. 1992, doi: 10.1346/CCMN.1992.0400111.
19. E. Ferrage, B. Lanson, B. A. Sakharov, V. A. Drits, “Investigation of smectite hydration properties by modeling experimental X-ray diffraction patterns: Part I. Montmorillonite hydration properties,” *Am. Mineral*, vol. 90, no. 8-9, pp. 1358-1374, Aug. 2005, doi: 10.2138/am.2005.1776.
20. E. Ferrage, B. Lanson, B. A. Sakharov, N. Geoffroy, E. Jacquot, V. A. Drits, “Investigation of dioctahedral smectite hydration properties by modeling of X-ray diffraction profiles: Influence of layer charge and charge location,” *Am. Mineral*, vol. 92**,** no. 10, pp. 1731-1743, Oct. 2007, doi: 10.2138/am.2007.2273.
21. S. Morodome and K. Kawamuca, “Swelling behavior of Na- and Ca-montmorillonite up to 150C by *in situ* X-ray diffraction experiments,” *Clay Clay Miner.*, vol. 57, no. 2, pp. 150-160, 2009, doi: 10.1346/CCMN.2009.0570202.
22. R.W. Mooney, A.G Keenan, and L.A. Wood, “Adsorption of water vapor by montmorillonite, 1. Heat of desorption and application to BET theory”, *J. Am. Chem. Soc*., vol. 74, no. 6, pp. 1397-1371, Mar. 1952, doi:10.1021/ja01126a001.
23. H. Sato, “Quantification of Exchangeable Cations in Interlayer of Tsukinuno Sodium-Montmorillonite,” *MRS Proc.*, vol. 1193, pp. 529, 2009, doi: 10.1557/PROC-1193-529.
24. S. Brunauer, P.H. Emmett, & E. Teller, *J. Am. Chem. Soc*., vol. 60, no. 2, pp. 309-319, Feb. 1938, doi: 10.1021/ja01269a023.
25. H. Yamada, H. Nakazawa, H. Hashizume, S. Shimomura, T. Watanabe, “Hydration behavior of Na-smectite crystals synthesized at high pressure and high temperature,” *Clay Clay Miner.*, vol. 41,

no. 1, pp. 77-80, Feb. 1994, doi: 10.1346/CCMN.1994.0420110.

# Gas Slippage in Partially Saturated Tight Rocks and During Drainage

*Alexandra* Amann-Hildenbrand[1,*], *Mohammadebrahim* Shabani[1], *Thomas* Hiller[2], *Norbert* Klitzsch[3], *Norbert* Schleifer[4], and *Bernhard M.* Krooss[1]

[1] Institute of Geology and Geochemistry of Petroleum and Coal, Energy and Mineral Resources Group, RWTH-Aachen, Germany
[2] Leibniz Institute for Applied Geophysics, Hannover, Germany
[3] Applied Geophysics and Geothermal Energy, E.ON Energy Research Center, RWTH-Aachen, Germany
[4] Wintershall Holding GmbH, Barnstorf, Germany

**Abstract.** Effective gas permeability in partly water-saturated tight rocks is controlled by both, slippage and capillary effects. We present effective gas permeability coefficients measured on partially pre-saturated tight rock samples and during drainage starting from fully water-saturated samples. Measurements were made on Carboniferous (Westphalian D) and Permian (Rotliegend) tight sandstones with porosities <15% and permeability coefficients $<10^{-16}$ m² (0.1 mDarcy). Plugs of 30 to 38 mm in diameter and up to 40 mm in length were used in this study in "triaxial" flow cells. Confining pressures ranged from 15 to 40 MPa and differential gas pressures up to 11 MPa were applied. Drainage of initially water-saturated samples was monitored by Nuclear Magnetic Resonance (NMR) in a flow-through cell. Additionally, gas flow experiments were run on samples with defined initial water saturations of up to 60%, established either by equilibration with water vapour or by centrifuging. Effective gas permeability coefficients increased by up to three orders of magnitude with decreasing water content. The experiments revealed that above a critical water saturation the effective permeability coefficients depend on drainage- and imbibition-controlled re-distribution of the water phase. Below this critical water saturation the apparent permeability coefficients of the gas are dominated by slippage effects.

## 1 Introduction

Gas slippage is a well-known phenomenon where the flow rate in narrow pores or capillaries exceeds that calculated with the assumption of viscous flow [1-2]. In this situation, the gas layer next to the pore surface is in motion with respect to the pore surface while Poiseuille's law assumes zero velocity. The gas slippage effect increases as the mean free path length of the passing gas molecules approaches the scale of the transport pore size. It decreases with increasing gas pressure. In the "Klinkenberg diagram" the apparent gas permeability ($k_{app}$) is plotted as a function of the reciprocal mean pore pressure ($1/p_{mean}$). The Klinkenberg relationship

$$k_{app} = k_{inf} \cdot (1 + \frac{b}{p_{mean}})$$

is used to determine the intrinsic or "liquid phase" permeability ($k_{inf}$) by linearly extrapolating the apparent permeability coefficients to the y-intercept at "infinitely" high gas pressures ($1/p_{mean} = 0$) [2]. The slip factor ($b$) is determined from the slope of the regression line.

Although the slippage effect has been well documented for single-phase gas flow, only few experimental studies have investigated gas slippage in two-phase flow systems, especially for tight reservoirs [3-8]. Tight gas reservoirs contain water, either as connate/irreducible water or as imbibed water after drilling and hydraulic fracturing. Investigation of gas slippage in two-phase (gas-water) systems is therefore essential for the prediction of gas production rate from tight reservoirs [7].

In our experimental study, we have investigated the influence of water on gas flow mechanisms in tight gas reservoirs. Experiments were performed on partially pre-humidified sample plugs. Additionally, gas flow experiments (drainage and imbibition) were conducted, starting from fully water-saturated samples in an NMR flow cell. The dynamic water de- and re-saturation of the sample was continuously monitored by NMR measurements at each phase of the experiment.

---

[*] Corresponding author: alexandra.amann@emr.rwth-aachen.de

# 2 Sample preparation

## 2.1 Partial water saturation

The samples were pre-humidified in a desiccator at defined relative humidity (RH) levels by water vapour adsorption/desorption. Controlled RH in the desiccator was established by using saturated salt solutions of $MgCl_2$ (33%RH), $Mg(NO_3)_2$ (53%RH) and NaCl (75%RH). Prior to moisture equilibration the samples were dried at 105 °C to constant weight. The water content was calculated from the weight increase after humidification. Assuming a water density of 1 g/cm$^3$ the water saturation was then determined based on porosity values measured either by helium pycnometry or by saturation/buoyancy (Archimedes method).

## 2.2 Full water saturation

The sample plug after drying at 105 °C was placed overnight in a beaker inside an evacuated desiccator. The desiccator was then opened and degassed brine (here a 0.1 molar $MgSO_4$ solution) was admitted and allowed to invade the pore space at a slight overpressure (atmospheric pressure + 1 bar). The weight of the sample was monitored daily until it reached a constant value (full saturation). Due to the low permeability, the small pore diameters and the large sample size the saturation took several weeks.

# 3 Experimental procedure and results

## 3.1 Gas permeability measurements on partially saturated samples

Partially water-saturated samples were installed in a "triaxial" flow cell (Fig. 1). Axial and confining pressures were set to 20 MPa. Gas (helium) permeability measurements were performed on eight samples at a wide range of mean gas pressures (up to 12 MPa) for slip flow evaluation (Klinkenberg plot). The gas was passed through a high-pressure water reservoir (see Fig. 1) to avoid drying the samples and ensure that any changes in effective gas permeability were due only to water displacement (drainage) or slip flow. The measurements were performed using a steady state method; the upstream pressure was increased stepwise, while the downstream pressure remained atmospheric. Accordingly, also the pressure difference increased. After the gas permeability experiments the samples were weighed to determine any changes in water saturation.

The results of the apparent gas permeability measurements are shown for one selected sample at different degrees of water saturation (dry to 41%, Fig. 2). For all samples, the apparent gas permeability coefficients decreased by more than two orders of magnitude upon increase of water saturation to 30-45 % (Table 1).

Normal Klinkenberg trends, i.e. positive linear relationships between apparent gas permeability and reciprocal mean gas pressure were found for samples in the dry state and at low water-saturation (<25%). Here two different trends were observed: decrease or increase of the slippage factor $b$ with increasing water saturation, (Fig. 3). In general, the slope always decreases with increasing water saturation.

For moist samples with higher water saturations (> 30%), the Klinkenberg plot of the apparent gas permeability coefficients showed negative trends. This phenomenon is caused by capillary drainage due to the successive increase in gas pressure difference in the course of the experiment.

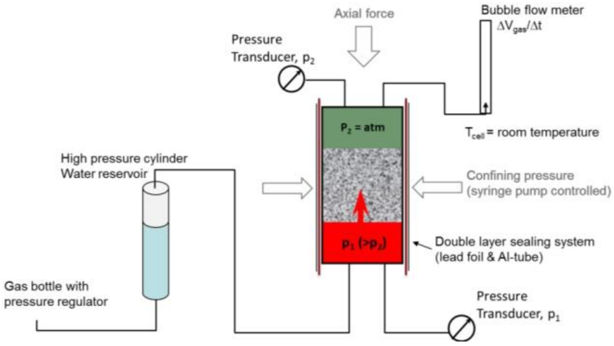

**Fig. 1.** Scheme of the experimental set-up used for permeability measurements on partially water-saturated samples

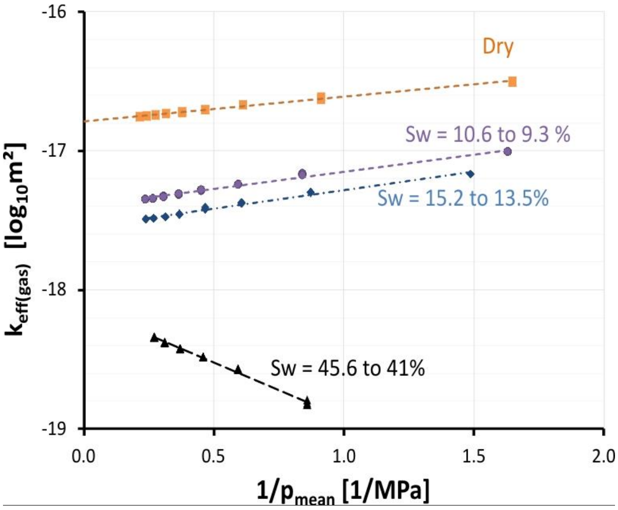

**Fig. 2.** Apparent effective gas (helium) permeability coefficients determined on the dry sample and at different water saturations.

Similar observations have been described in the literature. Rushing et al. [6] report a "decrease in gas slippage effects (as manifested by the decrease in line slope) with increasing water saturations". However, as the "line slope" is the product of $k_{inf} \cdot b$ this assertion is misleading because their slippage-factors actually still increase with increasing water saturation. Similar results are given in Li et al., Reinecke and Sleep [5, 7, 8]. Estes et al. [10] observed decreasing slip factors for most of his samples. However, at higher water saturations also higher slippage-factors were determined, as well as negative slopes of the Klinkenberg regression line.

According to slip theory, the slip factor is inversely proportional to the pore diameter. Thus, an increase in slip factor indicates decreasing mean effective transport pore sizes. In the literature this is attributed to the presence of water films on the pore walls [11, 12] ("funicular flow") [12]. In contrast, decreasing slip factors, thus increasing mean pore diameters, are considered to result from flow of gas in a completely separate network of gas-filled pores ("channel flow") [12]). As the wetting phase will occupy the smallest capillaries, gas flow occurs in the open larger pore size fraction. Dullien [12] described these flow concepts based on direct microscopic observations in synthetic porous systems. In the present study, the presence of remaining water after drainage is considered to result in a shift of the NMR T2-signal towards nominally smaller pores (see chapter 3.2, Hiller et al., [13]). Both flow types may occur simultaneously, one being the dominating process, depending on pore size distribution and mineral composition, i.e. water suction pressure. This is an issue of ongoing research, and additional measurements are under way ($N_2$ adsorption, high pressure mercury injection and Cryo-BIB/SEM).

*Table 1: Porosity and permeability coefficients of the samples analysed*

| Sample ID | Φ (%) | RH (%) | $Sw_f$ (%) | $k_{inf}$ ($m^2$) | b (MPa) |
|---|---|---|---|---|---|
| #1 | 9.7 | 0 | 0 | 2.2E-17 | 0.71 |
| | | 33 | 9.1 | 3.7E-18 | 1.08 |
| | | 55 | 13.7 | 2.4E-18 | 1.27 |
| | | 75 | 44.1 | 5.9E-19 | -1.03 |
| #2 | 9.7 | 0 | 0 | 1.54E-17 | 0.62 |
| | | 33 | 10.5 | 3.42E-18 | 1.16 |
| | | 55 | 13.5 | 2.45E-18 | 1.19 |
| | | 75 | 41.0 | 5.72E-19 | -0.88 |
| #3 | 10.6 | 0 | 0 | 4.90E-17 | 1.25 |
| | | 33 | 5.2 | 7.74E-18 | 0.86 |
| | | 55 | 8 | 6.41E-18 | 0.67 |
| | | 75 | 27 | 1.23E-18 | 0.36 |
| #4 | 6.1 | 0 | 0 | 3.60E-18 | 1.27 |
| | | 33 | 3.7 | 2.12E-18 | 0.73 |
| | | 55 | 1.2 | 2.57E-18 | 1.18 |
| | | 75 | 2.5 | 2.21E-18 | 0.95 |
| #5 | 3.4 | 0 | 0 | 6.84E-18 | 0.92 |
| | | 55 | 3.2 | 5.01E-18 | 0.70 |
| | | 55 | 3.2 | 6.31E-18 | 0.79 |
| | | 75 | 3.0 | 3.17E-18 | 1.12 |
| #6 | 5.1 | 0 | 0 | 3.3E-18 | 1.22 |
| | | 55 | 3.8 | 2.4E-18 | 1.10 |
| | | 55 | 5.7 | 2.0E-18 | 1.20 |
| #7 | 10.7 | 0 | 0 | 4.22E-15 | 0.07 |
| | | 55 | 2 | 4.2E-15 | 0.04 |
| #8 | 1.3 | 0 | 0 | 2.03E-19 | 2.17 |
| | | 55 | 62.9 | 1.06E-19 | 0.73 |
| | | 55 | 43.4 | 1.20E-19 | -0.97 |
| #9 | 12.6 | 0 | 0 | 7.83E-18 | 0.5 |
| | | 55 | 19 | 4.17E-18 | 0.3 |
| | | 75 | 54 | 6.00E-20 | -0.4 |

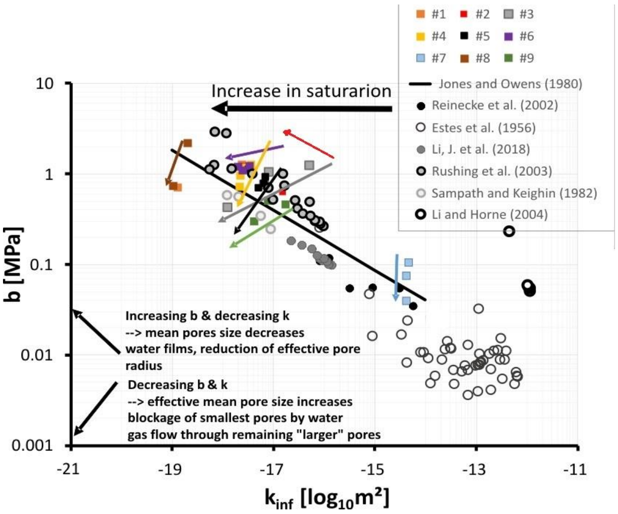

**Fig. 3.** Changes in slippage and permeability as a function of water saturation (Square symbols: data from this study for different samples, circles: Data form previous studies [4-6, 8, 10]. Arrows are inserted to guide the eye for the different trends.

### 3.2 Gas permeability measurements on initially fully water-saturated samples

Fully water-saturated samples were installed in an isostatic flow cell made out of NMR-inactive materials (Fig 4). The sample was placed between two Polyetheretherketone (PEEK) pistons surrounded by NMR-inactive confining fluid (Fluorinert FC-40). Flow-through measurements were performed at a confining pressure of 15 MPa. The flow experiments coupled with NMR measurement provide information on the dynamic water displacement in the sample plug.

The drainage experiment started by applying a constant pressure difference across the sample and monitoring NMR signal amplitudes and fluid flow. The NMR amplitudes at each stage were normalized to the NMR amplitude of the fully saturated sample to calculate water saturation. Gas permeability was determined either by a steady state (test # 1 and #2) or a non-steady state (test # 3) method. Details of the NMR flow cell setup and the technical protocol are given by Hiller et al. [13].

In the steady-state approach, the pressure difference ($N_2$ pressure up to 11MPa) across the sample was increased stepwise, resulting in successive desaturation (drainage experiment). This approach provides information on apparent gas permeability and water saturation as a function of the pressure difference. After each permeability test the sample plug was weighed and the change in water saturation compared with the water saturation measured by NMR.

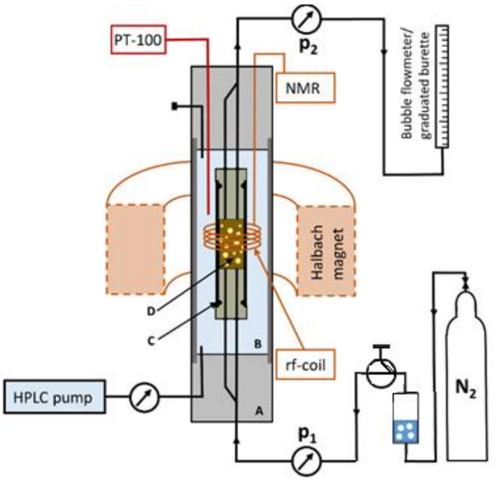

**Fig. 4.** Scheme of the NMR-inactive experimental set-up used for permeability measurements staring with fully water-saturated sample plugs. A – outer sealing system, B – confining pressure compartment filled with NMR-inactive oil, C – inner O-ring sealed sleeve system, D – sample placed between PEEK pistons.

In the non-steady state experiment, the gas pressure in the calibrated upstream volume was allowed to decrease, while downstream pressure remained atmospheric. The pressure on the upstream side was measured continuously and used to calculate the permeability coefficients. This method provides information on the spontaneous imbibition behaviour of the rock sample after gas breakthrough. Upon decrease in $\Delta p$ and $p_{mean}$ water imbibes back to the sample, resulting in an increase in saturation.

It should be noted that the pressure gradients during steady state and non-steady state experiments will result in saturation profiles along the sample, which, however, cannot be assessed/resolved with the procedures described here. The extent and consequences of these saturation profiles require further investigation.

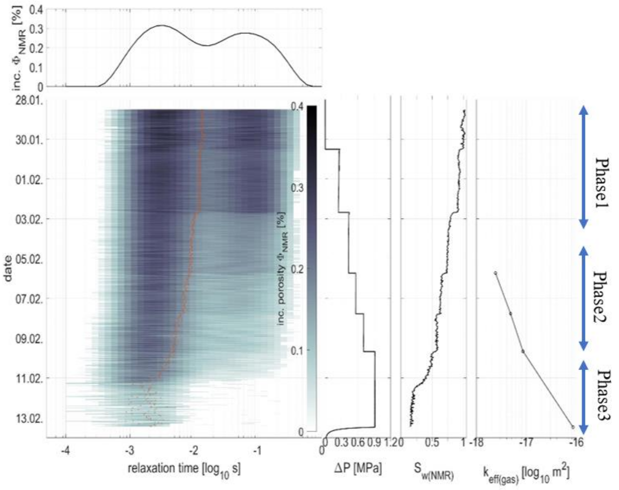

**Fig. 5.** NRM results obtained for test # 1. From left to right: Measured relaxation time distribution, Differential pressure steps, saturation apparent effective gas permeability coefficients as a function of time**.**

Figs. 5 and 6 demonstrate the results of one steady state gas permeability experiment (test # 1). Water saturation decreased during the phase I of the experiments by drainage of the largest pores. However, no significant gas flow was observed at the downstream side during this phase. After gas breakthrough, the measured gas flow rate was used to calculate the apparent gas permeability (phase 2). These permeability values are nearly two orders of magnitudes lower than those for the dry sample. Water saturation dropped significantly (to 25%) during phase 3 of the experiment leading to a one order of magnitude increase in apparent gas permeability reaching values close to the ones of the dry sample (Fig. 6). This indicates that at 25% water saturation the dominant conducting transport pathways were drained and that the remaining water-filled pores do not significantly contribute to the overall gas flow within the system.

As shown in Figure 6, apparent effective gas permeability coefficients increase with successive drainage, i.e. with increasing pressure difference, and with decreasing mean gas pressures. These observations are similar to those described in chapter 3.1 for samples with high water saturations. Two additional effects/trends were detected for other samples. For test # 2 (Figure 7) three different trends can be distinguished.

(I) The capillary pressure-controlled flow regime, where mobile water is displaced and redistributed due to the increase in differential pressure.

(II) The time delay effect, i.e. decreasing water saturation and increasing permeability until capillary pressure equilibrium has been reached.

(III) The slip flow-dominated regime were effective apparent gas permeability coefficients decrease with increasing mean gas pressure. This regime prevails at lower water saturations, i.e. where the residual water is less mobile.

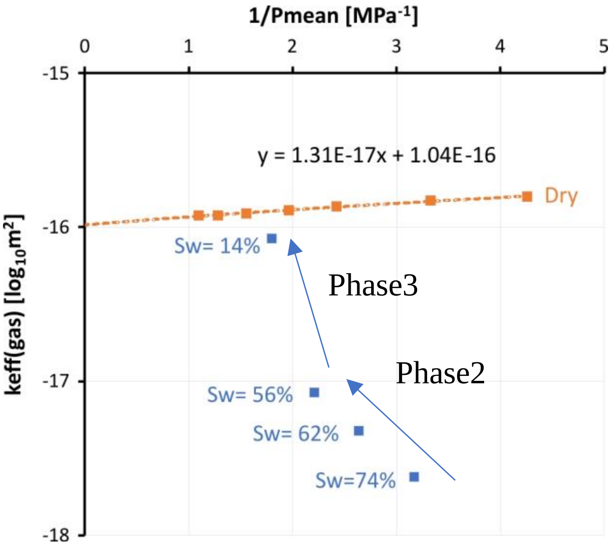

**Fig. 6.** Test # 1 - Klinkenberg plot showing apparent permeability coefficients measured on the dry sample and during the drainage experiment.

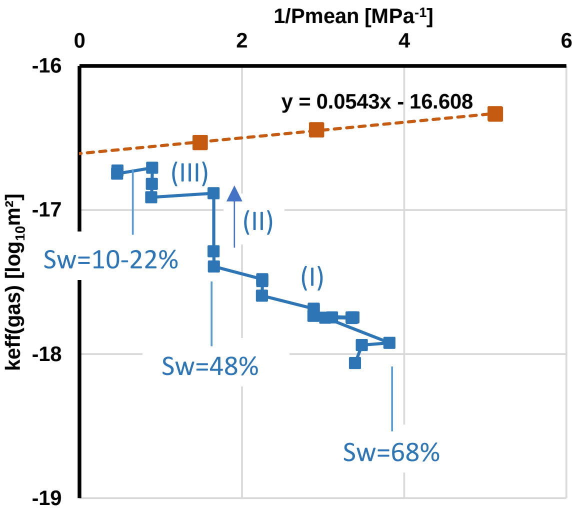

**Fig. 7.** Test # 2 - Klinkenberg plot showing apparent permeability coefficients of the dry sample and effective apparent permeability coefficients during the drainage test. (I) capillary pressure-controlled drainage due to increase in differential pressure ($S_w$=68-48%), (II) drainage – time delay, (III) slip flow-controlled gas flow at low water saturations (Sw<48%)

Five drainage/imbibition cycles (non-steady state method) were performed on test #3 (Fig. 8). The experiment was initiated by applying a constant differential pressure across the sample. The first drainage/imbition test started and changes in saturation during this cycle were monitored continuously. Due to technical problems, the gas flow was not monitored during this cycle. However, it was monitored during the other four drainage/imbibition cycles. After application of the initial pressure, gas flow starts and, as the top compartment is closed, the pressure difference across the sample decreases (Fig. 9a). As a result, water imbibes back into the pore system, resulting in an increase in water saturation and decrease of apparent gas permeability (up to two orders of magnitude, Fig. 8). The measured apparent gas permeabilitiy coefficients were up to three orders of magnitude lower than those measured on the dry sample (Fig. 9b).

As this system is controlled by capillary drainage, the negative Klinkenberg trends shown in Fig. 9b are clearly developed (cycle #4 and #5). For cycle #2 and #3 (higher water saturation), the trend is even more complex. Here, the negative slope is less pronounced at higher pressures (lower reciprocal mean pressure). Thereafter, permeability drops significantly, probably because imbibition is more efficient due to the higher amount of remaining water within the pore system. We are facing a very complex set of different processes acting simultaneously and partially with contrary effects: slip flow, drainage/imbibition, and likely some additional poro-mechanical response. Mechanical compressions at increasing effective stress, could result in a re-distribution of the pore water, i.e. driving water re-imbibition towards the compacted smaller pores.

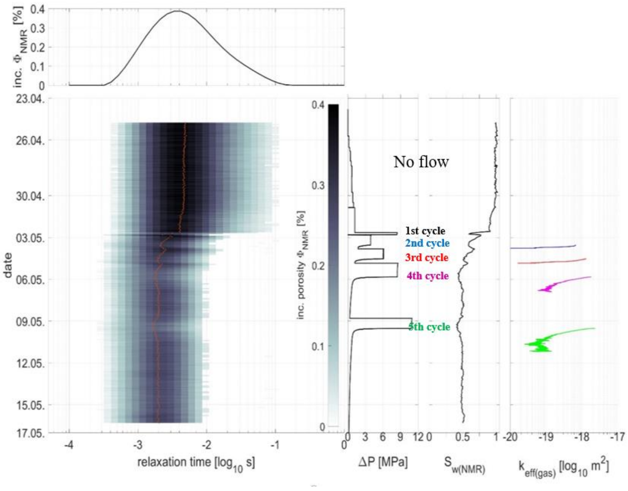

**Fig. 8.** Results from a non-steady state, imbibition test. The measured relaxation time distribution, upstream pressure, saturation, and apparent/effective gas permeability were recorded as a function of time.

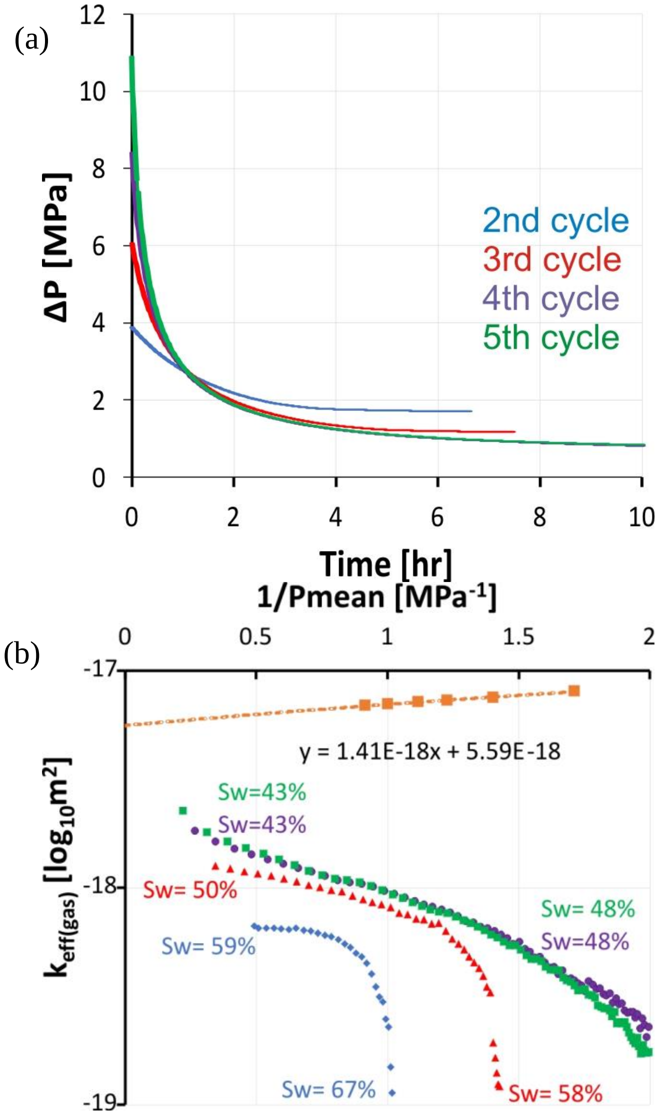

**Fig. 8:** Test # 3 - Change of differential pressure for each drainage cycle as a function of time (a), Klinkenberg plot of

measured permeabilitiy coefficients in the dry and moist state (b).

## 4 Conclusions

In this study, apparent gas permeability measurements have been performed on partially and fully water-saturated samples. In both sets of experiments the effective gas permeability coefficients decreased by more than 3 orders of magnitude upon increasing water saturation.

At higher water saturations we observed that the apparent effective gas permeability coefficients follow a negative trend in the Klinkenberg plot. This is attributed to the capillary drainage effects, i.e. the displacement of the mobile water phase within increasing pressure difference.

At lower water saturations (below 30 %), we observed that the slope within the Klinkenberg plot is continuously decreasing with increasing water saturation. In contrast the slip factor either increases or decreases. This indicates that in the first case the effective average transport pore size is getting larger, in the latter case relatively lower. This is likely attributed to different water distribution within the pore system, however, this remains speculative with the current methods applied. Further research is ongoing, e.g. analyses be Cryo-BIB/SEM on partially water saturated samples.

## 5 Acknowledgements

The authors gratefully acknowledge Wintershall Holding GmbH for funding the iLoPS research project, within which this study was conducted. We also like to thank Jonas Kaiser and Gabriel Hoder for their valuable input and help with the experimental setup in the initial stage of the project.

## References

1. A. Kundt, E. Warburg, “Über Reibung und Wärmeleitung verdünnter Gase,” Annalen der Physik 231, 1875, 337-65.
2. L. Klinkenberg, “The permeability of porous media to liquids and gases,” presented at *API In Drilling and production practice*, Tulsa, Okla., May 1941, pp. 200-213.
3. F.O. Jones, W.W. Owens, “A laboratory study of low-permeability gas sands,” *Journal of Petroleum Technology 32*, 1980, 1631-140.
4. K. Sampath, C.W. Keighin, “Factors affecting gas slippage in tight sandstones of cretaceous age in the Uinta basin,” *Journal of Petroleum Technology* 34, 1982, 2715-2720.
5. S.A. Reinecke, B.E. Sleep, “Knudsen diffusion, gas permeability, and water content in an unconsolidated porous medium*,” Water Resources Research 38*, 2002, doi: 10.1029/2002WR001278.
6. J. Rushing, K. Newsham, K. Van Fraassen, “Measurement of the two-phase gas slippage phenomenon and its effect on gas relative permeability in tight gas sands,” presented *at SPE Annual Technical Conference and Exhibition,* Denver, Colorado, USA, 5-8 Oct. 2003, SPE 84297.
7. K. Li, R.N. Horne, “Gas slippage in two-phase flow and the effect of temperature,” presented at *SPE Western Regional Meeting*, Bakersfield, California, 26-30 March 2001, SPE 68778.
8. K. Li, R.N. Horne, “Experimental study of gas slippage in two-phase flow,” presented at *SPE Western Regional Meeting*, Bakersfield, California, 26-30 March 2001, SPE 89038.
9. J. Li, Z. Chen, K. Wu, R. Li, J. Xu, Q. Liu, S. Qu, X. Li, “Effect of water saturation on gas slippage in tight rocks,” *Fuel 225*, 2018, 519-32.
10. R.K. Estes, P.F. Fulton, “Gas Slippage and Permeability Measurements,” *Journal of Petroleum Technology 207*, 1956, 69-73.
11. J. Li, Z. Chen, K. Wu, R. Li, J. Xu, Q. Liu, S. Qu, X. Li, “Effect of water saturation on gas slippage in tight rocks,” Fuel 225, 2018, 519-532.
12. F.A.L. Dullien, “Porous Media: Fluid Transport and Pore Structure”, 2nd edn, Academic Press, San Diego, 1992, 334-336
13. T. Hiller, G. Hoder, A. Amann-Hildenbrand, N. Klitzsch, N. Schleifer, „Two-Phase Fluid Flow Experiments Monitored by NMR,“ presented at *SCA2019*, Pau, France, 26-30 Aug. 2019, #117.

# Modeling Permeability in Carbonate Rocks

*Moustafa* Dernaika[1,*], *Shehadeh* Masalmeh[1], *Bashar* Mansour[2], *Osama* Al-Jallad[2], and *Safouh* Koronfol[2]

[1]Abu Dhabi National Oil Company, EOR Department, 898 Abu Dhabi, UAE
[2]Halliburton, Ingrain, 114568 Abu Dhabi, UAE

**Abstract.** In carbonate reservoirs, permeability prediction is often difficult due to the influence of various geological variables that control fluid flow. Many attempts have been made to calculate permeability from porosity by using theoretical and empirical equations. The suggested permeability models have been questionable in carbonates due to inherent heterogeneity and complex pore systems. The main objective of this paper is to resolve the porosity-permeability relationships and evaluate existing models for predicting permeability in different carbonate rock types. Over 1000 core plugs were studied from 7 different carbonate reservoirs across the Middle East region. The plugs were carefully selected to represent main property variations in the cored intervals. The data set available included laboratory-measured helium porosity, gas permeability, thin-section photomicrographs and high-pressure mercury injection. Plug-scale X-ray CT imaging was acquired to ensure the samples were free of induced fractures and other anomalies that can affect the permeability measurement. Rock textures were analyzed in the thin-section photomicrographs and were classified based on their content as grainy, muddy and mixed. Special attention was given to the diagenesis effects mainly compaction, cementation and dissolution. The texture information was plotted in the porosity-permeability domain, and was found to produce three distinct porosity-permeability relationships. Each texture gave unique poro-perm trend, where the extent of the trend was controlled by diagenesis. Rock types were defined on each trend by detailed texture analysis and capillary pressure. Three different permeability equations (Kozney, Winland, Lucia) were evaluated to study their effectiveness in complex carbonate reservoirs. The texture-diagenesis based rock types provided more insight into the effects of geology on fluid flow and saturation. Available models may not fully describe permeability in heterogeneous rocks but they can improve our understanding of flow characteristics in various rock types.

## 1 Introduction

Core laboratory measurements can have a major impact on the reservoir modeling process [1]. Such measurements often yield unrepresentative results that raise questions about the effectiveness of the core data in the reservoir model and its calibration. This is partly related to the lack of understanding of reservoir heterogeneity as well as to the unrepresentative selection of plug samples. As a result, the data is often left unexplained, and there would be no link between the macroscopic measurements and fundamental microscopic properties or geological heterogeneities in the core [2]. Carbonates have complex and multimodal pore systems, therefore variation of permeability at single porosity can be very large (three to five orders of magnitude). This leads to poor porosity-permeability relationships [3] and imposes a challenge in classifying carbonates into rock types for proper permeability prediction. The porosity-permeability relationships can be resolved by additional information about the pore system, which is mainly related to the rock microstructure (texture) being grainy, muddy or mixed. The microstructure information can be obtained from thin-section photomicrographs. The microstructure (or texture) of the rock defines the pore geometrical properties regarding flow of fluids through the core and thus largely determine absolute permeability. The pore geometrical properties are mainly related to the medium of flow (texture), tortuosity and surface area. In this study, plug samples were selected to represent statistical distribution of porosity and textures in the reservoir cores. The porosity log was initially derived from dual energy core CT scanning [4] while the different textures were identified in the X-ray CT images [5]. The microstructure information of the plugs was confirmed from thin-section photomicrographs, and was plotted in the porosity-permeability domain. Samples with grainy microstructure gave high permeability while muddy samples showed lower permeability for the same porosity. The porosity and permeability data were fitted into unique trends based on the textural analysis. The different trends were mainly controlled by the different rock microstructures whereas the extent of the trend was due to different diagenesis processes (e.g. dissolution, cementation and compaction). Different permeability models were studied and evaluated for the established rock types.

## 2 Porosity-Permeability Relationships

In an earlier investigation [6], we studied 5 carbonate reservoir cores to understand the porosity-permeability relationships. Each cored interval ranged from 300 to over 500 feet, where some of the cores represented more than one formation. The cores were mainly limestone with highly varying porosity (~5% to 33%) and permeability (~0.01 mD to 5000 mD). Plug samples of 1.5” diameter were statistically selected to represent all the cored intervals. Two more reservoir cores were later evaluated, and all the 7 reservoir core (Poro-Perm) data are shown in

---

[*] Corresponding author: mdernaika@adnoc.ae

figure 1. The data present the conventionally-measured helium porosity and gas permeability on the selected plugs. The porosity and permeability data for each plug were associated with the sample texture that was identified from the corresponding thin-section photomicrograph. Figure 1 shows three distinct porosity-permeability trends from the analysed cores in all the 7 reservoirs. The textures of the samples were classified as grainy, mixed and muddy [7]. All the textures revealed large porosity ranges, which was the result of different degrees of leaching, cementation and compaction (*i.e.* diagenesis). The different textures had clear effects on the porosity-permeability relationships. The analysed samples and the porosity-permeability relationships are believed to be representative to the reservoir properties. This was possible by applying statistical sample selection based on high-resolution dual energy CT imaging of the entire cores [4,5,9]. The plugs were also imaged by X-ray CT to ensure the samples were free of induced fractures and other anomalies that may affect the permeability data. Without the plug-scale CT image it would not be possible to ensure representative plug measurements and thus conclusive poro-perm trends. More details on the importance of the plug CT can be found in [5]. The plug CT images were also used to select representative thin-sections and MICP trims from the mother plugs. This is a crucial requirement in heterogeneous reservoirs, where heterogeneity can have dramatic effects at the centimeter scale [10]. In each of the 7 reservoirs, it was possible to establish relationships between porosity and permeability in accordance to textural variation. The grainy, mixed and muddy textures seem to be the main controlling parameters in this relationship. We can see distinct porosity-permeability trends in relation to the three identified textures. It is important to note that there was no evidence of any kind of poro-perm data cloud in any of the analysed cores [6]. All the poro-perm characteristics were classified and described based on the rock textures (and diagenesis). Although the rock microstructure appears to be the main control of flow we should also notice the effects of the porosity type. For instance, a muddy carbonate may have ‘touching vug’ porosity with a very high permeability.

## 3 Texture-Based Rock Typing

In this research, we studied the rock types of the samples within each texture trend. The rock types (along each poro-perm trend) were identified based on the link between the sample’s detailed Dunham texture [8], diagenesis and capillary pressure. Figure 2 shows examples from the effects of texture on capillary pressure (Pc) and pore-throat size distribution (PTSD) curves. The texture effect is shown for high porosity (around 25%) and low porosity (around 10%) samples (different diagenesis: here cementation). There is almost one order of magnitude (permeability) difference between the different textures at the same porosity. The grainy samples are characterised by larger pore throat sizes, lower entry pressure and higher permeability.

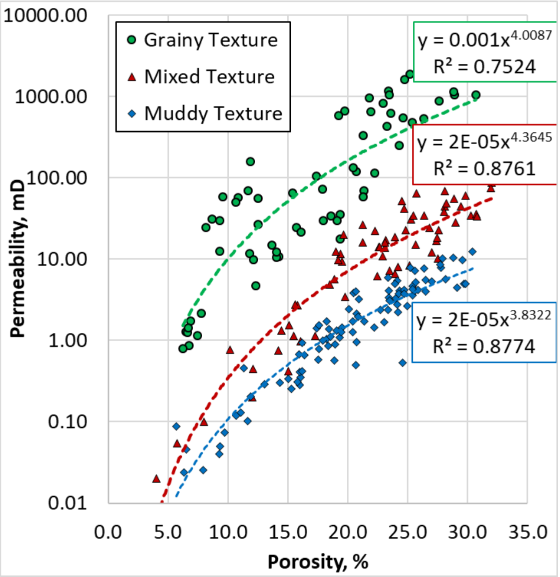

**Fig. 1.** Texture-Diagenesis based Poro-Perm trends in the 7 carbonate reservoirs in the Middle East region. Best fit along with correlation are given for each texture by power regression.

(a) high porosity (~25%)

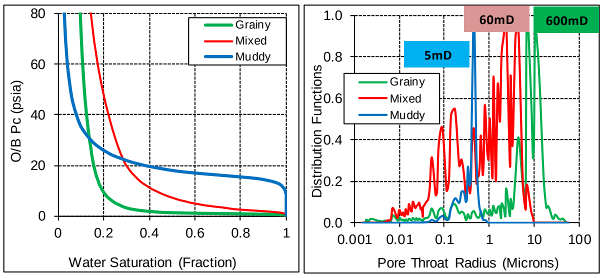

(b) low porosity (~10%)

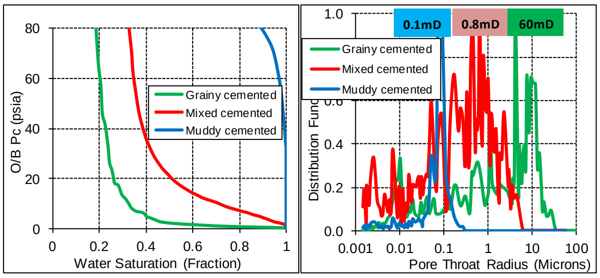

**Fig. 2.** Effect of texture on Pc and PTSD (a) at high porosity and (b) at low porosity

Initial water saturation (Swi) may not always be linked to permeability or texture in carbonates [12]. It is normally dependent on the Pc level as well as the percentage of the smallest pores in the rock beyond the applied Pc [11]. In figure 2a, for instance, the high-porosity muddy sample has lower Swi value (at high Pc) compared to the grainy and mixed texture samples. This is due to the fact that the mixed and grainy samples have more pore-throat fractions below 0.1micron as can be seen in the corresponding PTSD plot. Figure 3 shows the effect of porosity (mainly diagenesis) on the Pc and PTSD curves for each texture. It is seen that there is a good correlation between porosity and Swi within each texture: higher porosity within a single texture yields lower Swi. These plots demonstrate the influence of texture and diagenesis on petrophysical properties, hence confirming the importance of texture as a fundamental tool for rock typing. Furthermore, this analysis emphasizes the need of rock typing within single textures.

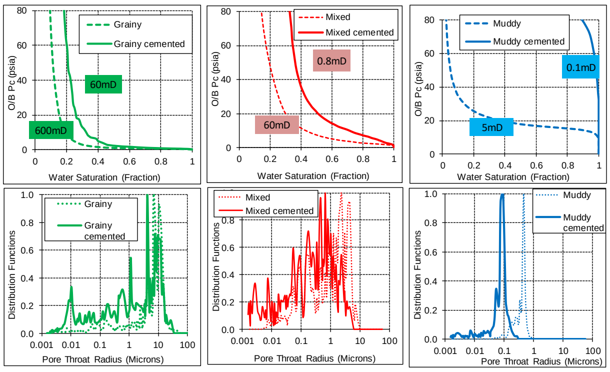

**Fig. 3.** Effect of porosity (diagenesis) on the Pc and PTSD curves for each texture

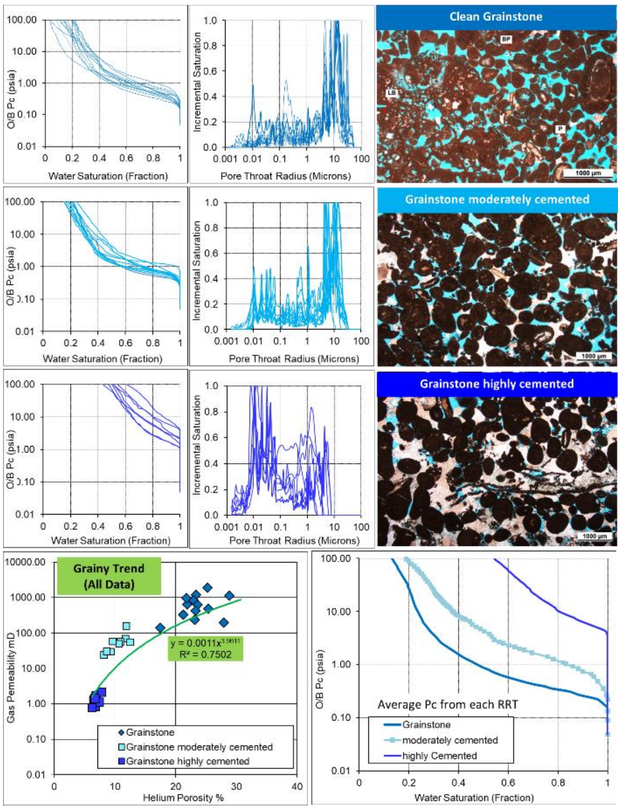

**Fig. 4.** Grainy Texture: 3 grainstone rock types. Samples from each RRT are presented with Pc/PTSD curves and a representative TS photomicrograph with Dunham classification. The poro-perm data are plotted with the main grainy trend from figure 1. Average Pc curves from all RRT's are plotted together.

## 4 The Rock Types

The rock types were established along the main texture (poro-perm) trends. They were identified over each texture based on Dunham classification and different diagenesis processes. The different geologically-defined rock types were correlated reasonably well with the poro-perm data and the MICP-derived Pc & PTSD curves. The mercury-derived Pc curves were converted to oil-water fluid system using interfacial tension of 32 mN/m. Figure 4 to figure 9 depict the main rock type characteristics found in the 7 carbonate reservoirs under study. Each figure gives all the rock types mainly within single texture classification along with their poro-perm data and mercury-derived Pc & PTSD. A representative thin-section photomicrograph is also depicted from each rock type. The main Dunham texture character of each rock type is indicated on the corresponding thin-section photomicrograph and in the legend of the poro-perm plot. The Pc curves are plotted in a semi-log format to show the capillarity behaviour more clearly. Within each rock type, all samples show consistent MICP and thin-section information with the poro-perm characteristics. A total of 25 rock types have been observed in these reservoirs. Some of the different textures may show similar drainage capillary behaviour but they can still be identified as different rock types based on the poro-perm data and other geological attributes. These rock types honour geological and static rock properties that should be further validated against dynamic data (*e.g.* imbibition capillary pressure and relative permeability) for ultimate reservoir modelling studies [12]. In this rock typing work, we indicated all the geological textures that we encountered in the studied reservoirs. Some of these textures may not have significant effects on the petrophysical properties and hence some of the identified rock types may be grouped into single RRT for practical reasons.

### Grainy Texture: Grainstone RRT's

Figure 4 shows the grainy limestone rock types from the grainstone texture. There are 3 grainstone rock types with different degrees of cementation. The poro-perm data are plotted with the main grainy trend and show higher values than the average trend. The presence of cement largely affected the poro-perm characteristics and the corresponding Pc & PTSD curves. It is seen that the percentage of microporosity increases with cementation. The microporosity in these rock types is coming from micritization in the grains.

### Grainy Texture: Rudstone RRT's

In figure 5, five rock types were identified, mainly from the Rudstone texture. The rock types show very heterogeneous PTSD curves due to large variations in grain sizes and pore sizes with different diagenetic footprints such as leaching and cementation. The best quality rock is the rudstone-to-boundstone texture while the poorest quality rock is the cemented rudstone. Two rock types were seen from the rud/bound-to-floatstone with higher percentage of floatstone in the rud/bound to floatstone2 as labelled in the corresponding legend in the figure. The higher micrite content is reflected in the PTSD curves. One more rock type was seen in this group, which is the rud-to-grainstone texture with intraparticle porosity. The rud-to-boundstone RRT show a main PTSD peak at around 100microns (~1000mD). The cemented rudstone rock type gives wide PTSD, while the rest of the rock types show bimodal PTSD.

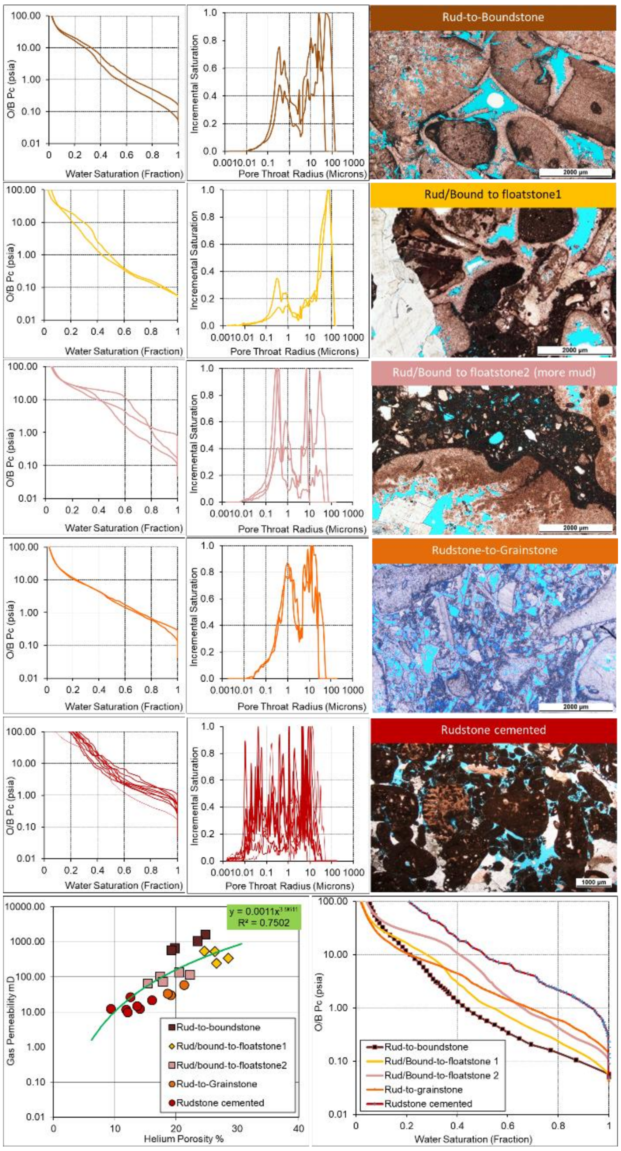

**Fig. 5.** Grainy Texture: 5 rudstone rock types.

## Grainy Texture: Dolostone RRT's

Figure 6 shows 4 dolomitic RRT's with different degrees of leaching and compaction. The poro-perm data are seen lower than the average grainy trend. The rock types show narrow and uniform PTSD curves.

## Mixed Texture: Packstone RRT's

Figure 7 shows the mixed limestone rock types from the packstone texture. There are 5 packstone rock types with different degrees of leaching, compaction and cementation. The poro-perm data are plotted with the main mixed trend. The presence of cement and compaction largely affected the poro-perm characteristics and the corresponding Pc & PTSD curves. Samples with less compaction/cementation (i.e. > 1mD) show heterogeneous PTSD.

## Mixed Texture: Floatstone RRT's

In figure 8, three rock types were identified, mainly from the Floatstone texture. The main difference in these rock types is related to detailed textural facies with floatstone-to-boundstone being the best quality with highest permeability range and lowest Pc entry pressure. The lowest quality rock type is the bioturbated floatstone-to-packstone texture. The samples show the main PTSD peak less than 1micron. The tendency towards larger pore throats is caused due to leaching and presence of boundstone texture.

## Muddy Texture: Wackstone/Mudstone RRT's

Figure 9 depicts 5 rock types from the wackstone/mudstone textures. The poro-perm data and Pc curves are largely influenced by cementation, recrystallization and compaction. All the samples have permeability less than 10mD, Pc entry pressure above 10psi (oil-water) and pore-throat radius below 1micron.

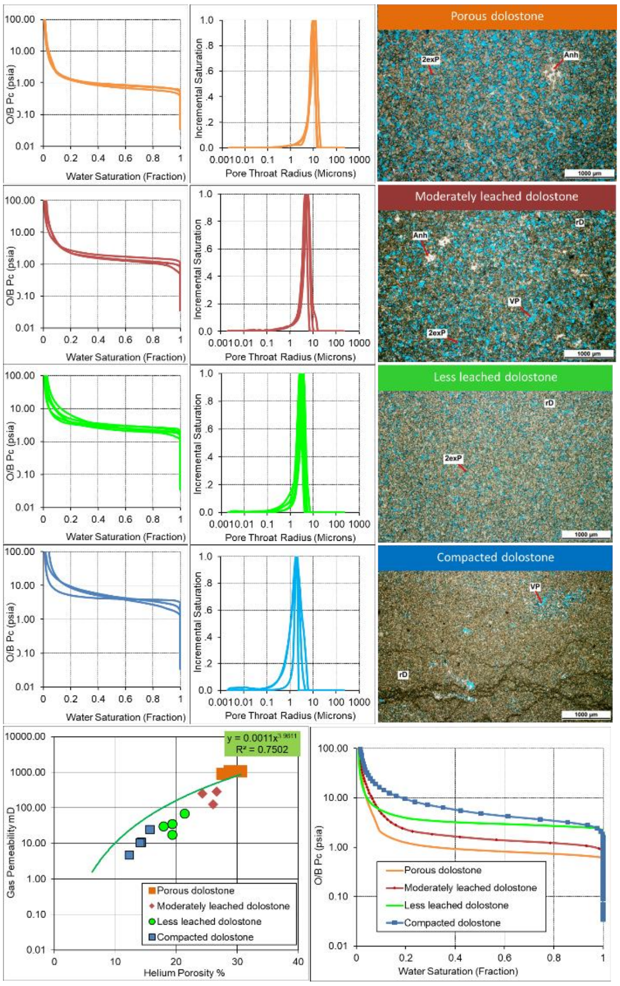

**Fig. 6.** Grainy Texture: 4 dolostone rock types.

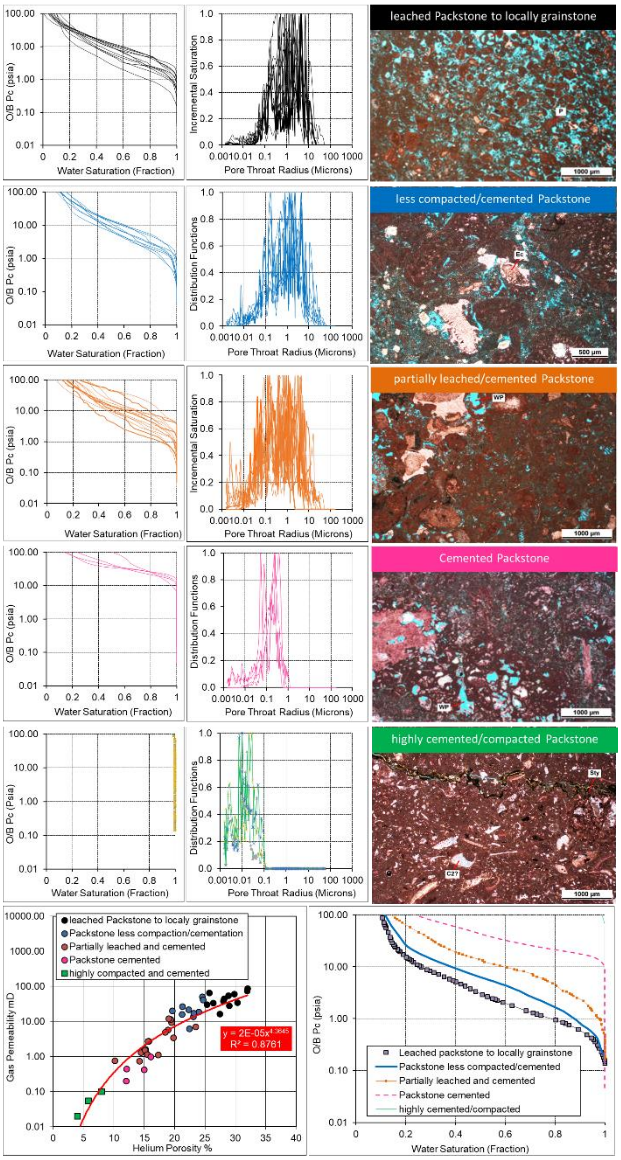

**Fig. 7.** Mixed Texture: 5 packstone rock types.

# 5 Permeability Estimation

Permeability estimation is an important step in reservoir characterisation for effective modeling of water-flood performance and subsequent Enhanced Oil Recovery (EOR) processes. The ultimate goal is to obtain permeability description as a function of reservoir space. This would require accurate determination of permeability versus depth in all logged wells in a field. This is normally achieved by the use of cross-plots of core permeability versus core porosity from log-derived porosity in uncored wells. The main aim of this research is to study the dependence of permeability on porosity and other geological attributes to provide guidelines for the establishment of accurate porosity-permeability cross-plots.

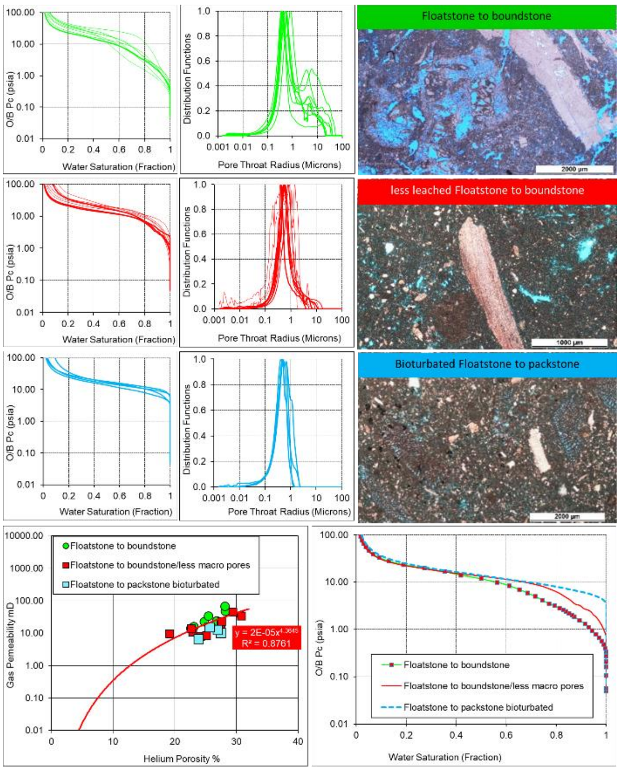

**Fig. 8.** Mixed Texture: 3 floatstone rock types.

## 5.1 Kozeny-Carmen Equation

Amaefule [13] proposed a permeability (k) model for identifying hydraulic units within mapable geological facies. The model is based on a modified Kozeny – Carmen equation and the concept of mean hydraulic radius. They derived equation (1), which indicates that for any hydraulic unit, a log-log plot of RQI versus Φz should yield a straight line with a unit slope,

$$RQI = \Phi z.FZI \qquad (1)$$

Where,

RQI is the Reservoir Quality Index (µm), $0.0314\sqrt{(k/\Phi)}$.

Φz is the Normalized Porosity Index (NPI), $\Phi/(1-\Phi)$.

FZI is the Flow Zone Indicator (µm); a unique parameter for each hydraulic unit, and is determined from the intercept of the unit slope line with Φz = 1.

Equation (1) is a reduced form of the modified Kozeny-Carmen equation below,

$$0.0314\sqrt{(k/\Phi)}=[\Phi/(1-\Phi)][1/(\sqrt{(F_s)}\ \tau.S_{gv})] \qquad (2)$$

Where,

$F_s$ stands for a shape factor (2 is for circular cylinder)

$\tau$ is the Tortuosity of the porous medium

$S_{gv}$ is the surface area per unit grain volume

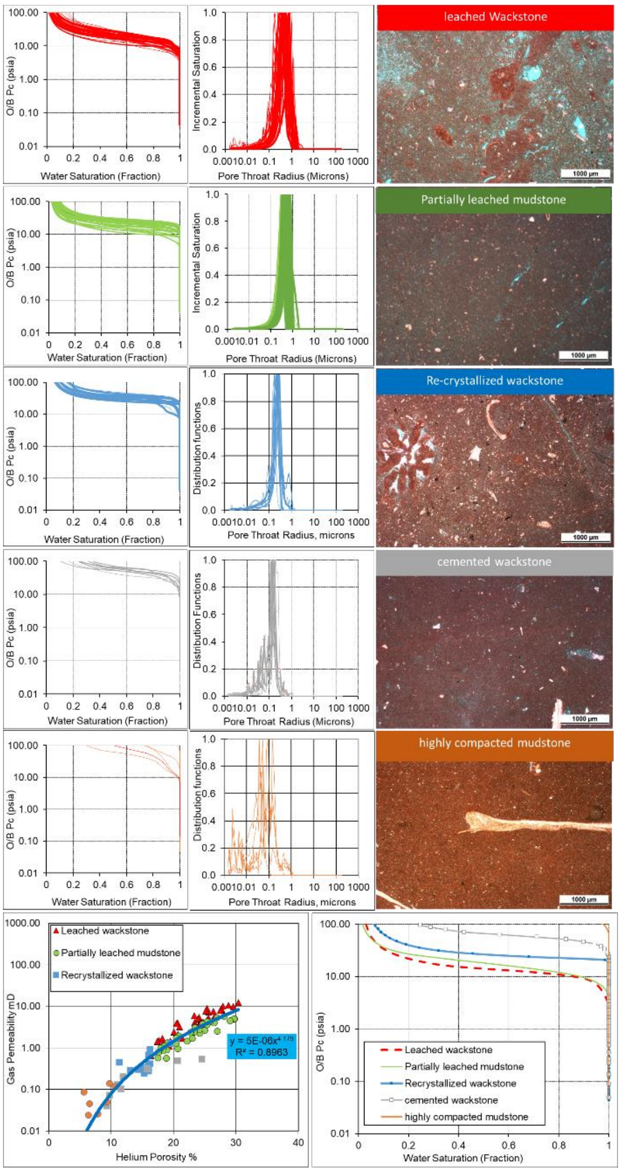

**Fig. 9.** Muddy Texture: 5 wackstone/mudstone rock types.

It is clear (from equations (1) and (2)) that FZI is related to the geological properties of the porous medium, being inversely proportional to the pore (throat) attributes. Therefore, samples with similar FZI value would constitute single hydraulic unit that is mainly defined by texture, poro-perm and capillary pressure.

Equation (3) is a developed relationship between permeability and FZI, derived from the generalized form of the Kozeny-Carmen relationship [13],

$$k=1014\,(FZI)^2\,[\Phi^3/(1-\Phi)^2] \qquad (3)$$

This permeability model has a theoretical basis with only one parameter, FZI, which offers a significant advantage over other methods for estimating permeability in uncored wells [14]. Hence, it would be an excellent opportunity to use the well-established rock type data in the earlier section to examine the effectiveness of equation (3) in carbonate reservoirs. We should bear in mind that the theoretical equation is not expected to precisely model the measured poro-perm data because the derivation of the equation was made with certain assumptions that may not necessarily hold for natural porous media; the primary assumption is that the rock is composed of a bundle of capillary tubes [14,15].

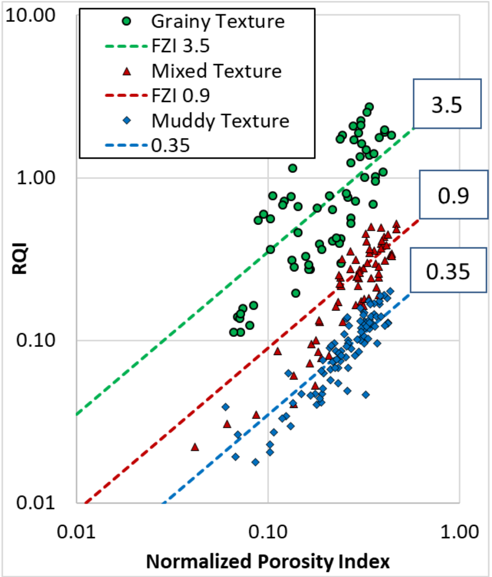

**Fig. 10.** RQI versus NPI for all the poro-perm data (from figure 1) plotted using equation 1. Grainy samples show an average FZI value of 3.5, Mixed 0.9 and Muddy 0.35.

Figure 10 plots the poro-perm data from figure 1 in the domain of RQI and NPI using equation (1). The grainy texture samples gave an average FZI of 3.5 while the mixed and muddy textures give FZI of 0.9 and 0.35, respectively. From equation (2), FZI is inversely proportional to pore shape, tortuosity and surface area. This means FZI is expected to be higher for porous media characterised by smaller surface area like the grainy texture, which is indeed consistent with the behaviour in figure 10. The pore shape factor and tortuosity may vary between textures and it would be more difficult to conclude about their effects on FZI. Actually, these pore throat attributes may vary within the same texture due to complex diagenesis processes, and this may explain the variation we already see in permeability within the same texture and porosity. Nevertheless, the strong trend we see between FZI and texture indicates the strong control of surface area on fluid flow in these carbonates. Figure 11 is rather a good representation of the FZI trends in the porosity-permeability domain by the use of equation (3). Figure 12 depicts the different grainy RRT's in the poro-perm plot. The data can be fitted with 3 different FZI values. The clean and partially cemented grainstone with Rud-to-Boundstone RRT's show similar FZI value of 6.5. The porous/leached dolomite with the Rud/Bound-to-floatstone RRT's have FZI 3.5. Less leached/compacted dolomite, highly cemented grainstone, rud-to-grainstone and cemented rudstone FZI value is 2. This clearly shows that FZI is not unique per RRT for the grainy texture samples. This statement is rather emphasized in figure 13, where the samples with similar FZI values are plotted together. Large variations are clearly seen in the Pc curves and pore structure (from thin-section photomicrographs) within samples of the same FZI (even within similar porosity range). This means FZI cannot be considered as a good parameter to characterize hydraulic units, which are normally defined by texture, porosity-permeability characteristics and capillary pressure.

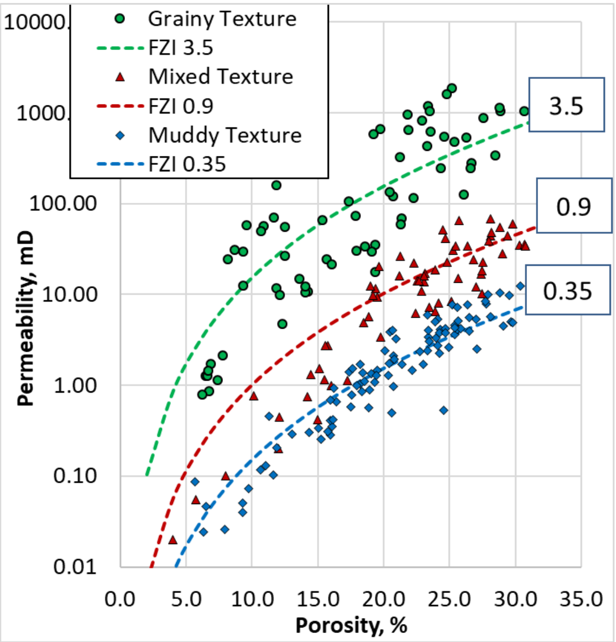

**Fig. 11.** Permeability versus porosity for all the poro-perm data (from figure 1) with FZI trends plotted from equation (3).

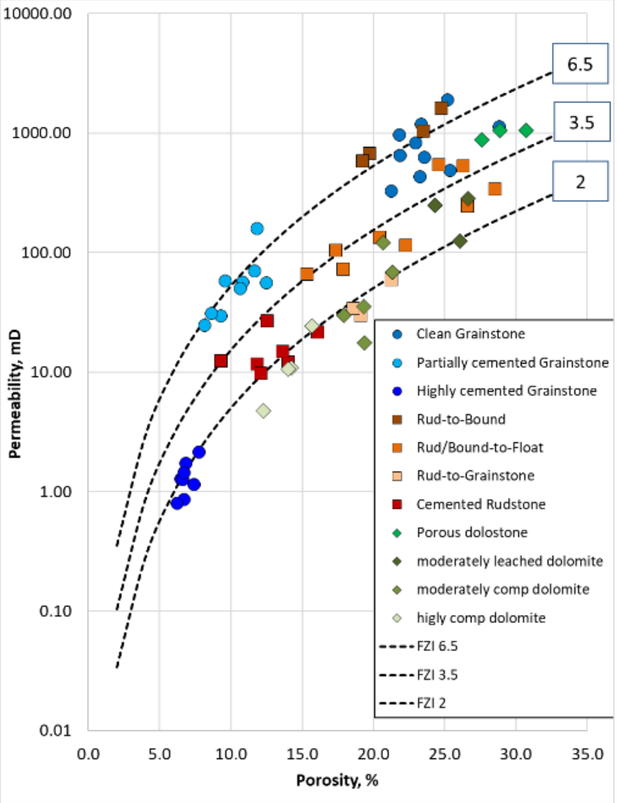

**Fig. 12.** Highlighted grainy RRT's with 3 different FZI values. Clean and partially cemented grainstone with Rud-to-Boundstone gave FZI 6.5. Porous/leached dolomite with Rud/Bound-to-floatstone FZI 3.5. Less leached/compacted dolomite, highly cemented grainstone, rud-to-grainstone and cemented rudstone FZI 2. FZI is not unique per RRT.

Figure 14 shows the mixed-texture RRT's with 2 different FZI values. The leached texture RRT's (i.e. packstone-to-grainstone, floatstone-to-boundstone and packstone) give FZI of 1 with porosity higher than 20%. The less leached textures give FZI 0.55 with the same porosity range. However, the cemented/compacted textures also give FZI 0.55 with porosity less than 20%. Figure 15(a) shows that the leached textures have similar RRT characteristics with similar FZI of 1. The less leached textures of similar porosity range (figure 15(b)) also show similar RRT characteristics and FZI of 0.55. The cemented/compacted packstone samples in figure 15(c) do not show the same consistency between FZI and the Pc curves.

(a) Grainy samples with similar FZI=6.5

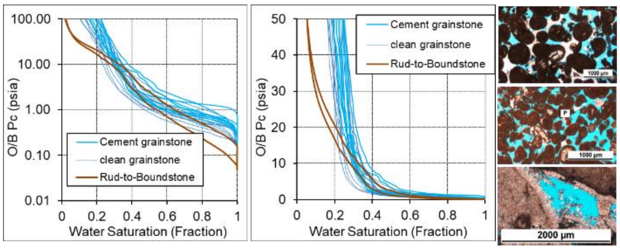

(b) Grainy samples with similar FZI=3.5

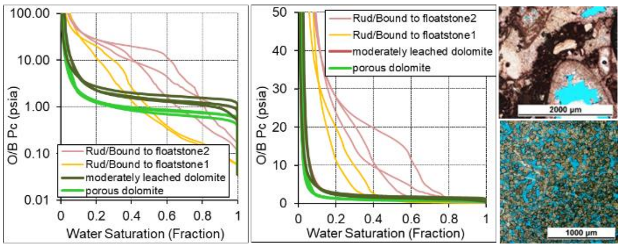

(c) Grainy samples with similar FZI=2

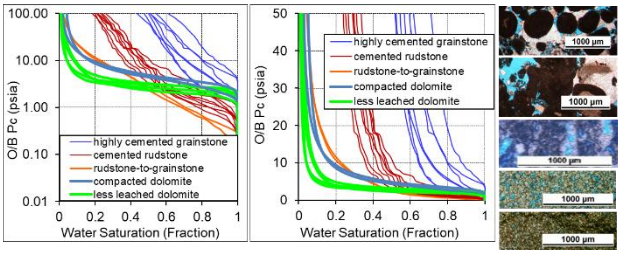

**Fig. 13.** Grainy RRT samples grouped by FZI. Samples with same FZI may not necessarily be of same RRT or demonstrate similar hydraulic flow unit.

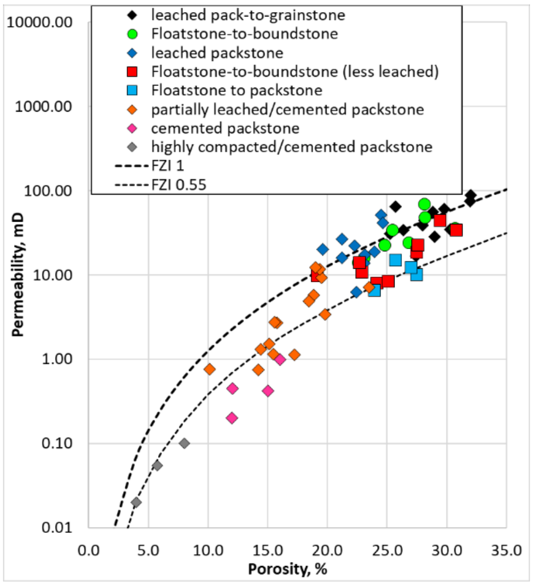

**Fig. 14.** Highlighted Mixed-texture RRT's with 2 different FZI values. Leached texture RRT's give FZI of 1 with porosity higher than 20%. Less leached textures give FZI 0.55 with the same porosity range. Cemented/compacted textures give FZI 0.55 with porosity less than 20%.

(a) Mixed-texture samples with FZI 1.0 (high porosity)

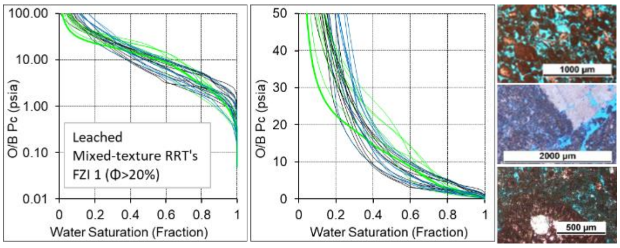

(b) Mixed-texture samples with FZI 0.55 (high porosity)

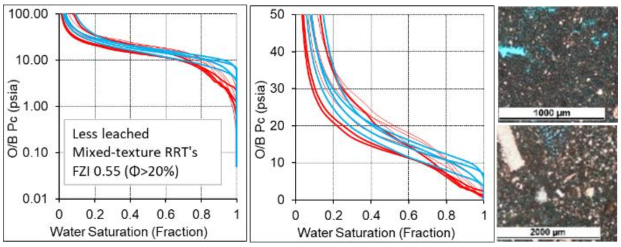

(c) Mixed-texture samples with FZI 0.55 (low porosity)

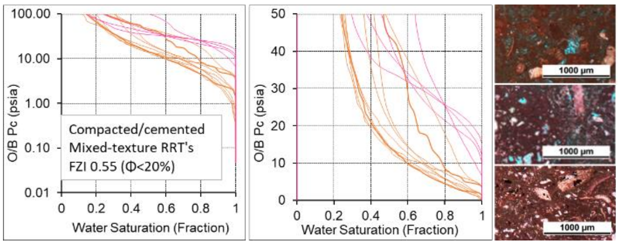

**Fig. 15.** Mixed RRT samples (from figure 14) grouped by FZI. Semi-log and linear scale Pc plots (along with corresponding TS photomicrographs). (a) Packstone-to-grainstone, floatstone-to-boundstone and leached packstone show similar RRT characteristics and FZI 1.0. (b) Less leached floatstone-to-boundstone and floatstone-to-packstone show similar RRT characteristics and FZI 0.55. (c) cemented/compacted packstone show different RRT's characteristics with similar FZI 0.55. (b) & (c) RRT's are very different and yet have similar FZI 0.55.

Moreover, samples in figure 15(b) and 15(c) do not give similar RRT characteristics although the samples have the same FZI of 0.55. Those RRT's could then be differentiated with a porosity cut-off around 20% based on the detailed Dunham classification as demonstrated in figure 14. For the muddy RRT's, figure 16 groups all the data with 3 different FZI values. The leached wackstone and the leached mudstone samples have FZI values of 0.45 and 0.35, respectively. The recrystallized, compacted and cemented wackstone and mudstone samples all have FZI of 0.25 (porosity < 17%). Figure 17 shows consistency in the Pc and FZI for the leached wackstone and mudstone RRT's. However, the tighter RRT's have shown different Pc behaviour with similar FZI of 0.25.

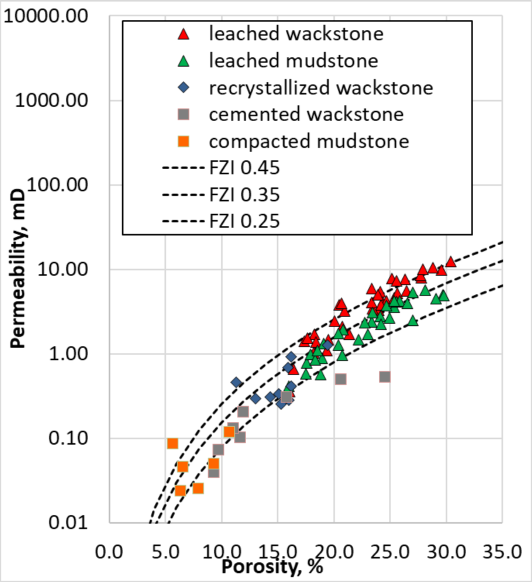

**Fig. 16.** Highlighted muddy RRT's with 3 different FZI values. Leached wackstone FZI 0.45. Leached mudstone FZI 0.35. Recrystallized/compacted/cemented wackstone and mudstone samples FZI 0.25 (porosity < 17%).

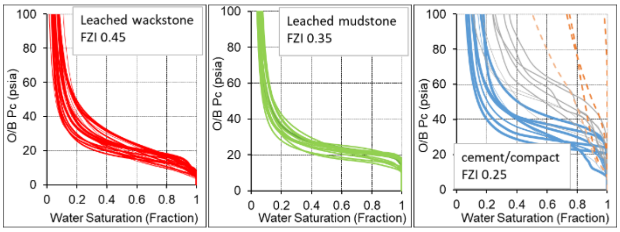

**Fig. 17.** Muddy RRT samples grouped by FZI.

### 5.2 Lucia Equation

This empirical method handles permeability in carbonates on the basis of rock-fabric classification, where the flow is related to interparticle porosity [17]. The classification is based on the so called Rock Fabric Number (RFN) that is empirically derived from porosity-water saturation relationships in a number of carbonate samples. Equation (4) and (5) give the empirical calculations of RFN (unitless) and permeability (mD), respectively,

$$\log RFN = (3.1107+1.8834\log\Phi_g+\log Swi)/(3.0634+1.4045\log\Phi_g) \quad (4)$$

$$\log k = 9.7982 - 12.0838\log RFN + (8.6711 - 8.2965\log RFN)\log \Phi_g \quad (5)$$

Where

$\Phi_g$ is the inter-grain porosity (frac)
Swi is the initial (connate) water saturation (frac)

Equation (4) is constructed on the basis that Swi decreases with porosity for every rock fabric class. Each RFN would have a unique porosity-Sw trend such that RFN increases with Swi for a given porosity. Equation (5) is designed such that permeability decreases with higher RFN for a given porosity. This would then indicate that RFN is expected to increase as we move from the grainy-texture RRT's to the muddy RRT's. In this perspective, an increase in RFN indicates an increase in surface area, hence RFN would be viewed as directly proportional to tortuosity and surface area (opposite to FZI as explained earlier). Nevertheless, the main issue with this method is the fact that it relies on a measure of inter-grain porosity excluding secondary porosity such as vuggy and moldic porosity, which is abundant in carbonate reservoirs. Figure 18 plots log-log scale permeability versus porosity for all the poro-perm data (from figure 1) with Lucia trends constructed from equation (5). Grainy samples show an average RFN 1.7, Mixed 2.85 and Muddy 3.65. Figure 19 gives the semi-log scale plot of figure 18. Because of the difficulty to quantify the interparticle porosity, the plots are given with the total porosity. As with the Kozeny-Carmen model, Lucia shows good overall match to the experimental data except the grainy texture RRT's. This is clearly caused by the high degree of heterogeneity of the grain-size and pore-size systems found in grain-dominated carbonates. The mud in the system seems to produce more unique porosity-permeability relationship, which has been well captured by both investigated models so far (*i.e.* eq. (3) & eq. (5)). Figure 20 depicts the different grainy RRT's in the poro-perm plot. The data can be fitted with 3 different RFN.

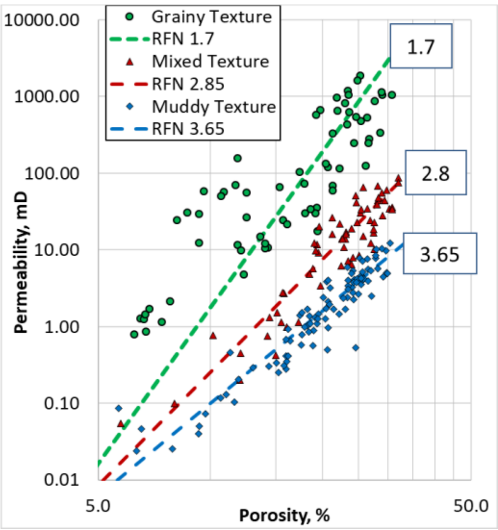

**Fig. 18.** Log-log scale permeability versus porosity for all the poro-perm data (from figure 1) with Lucia trends plotted from equation (5).

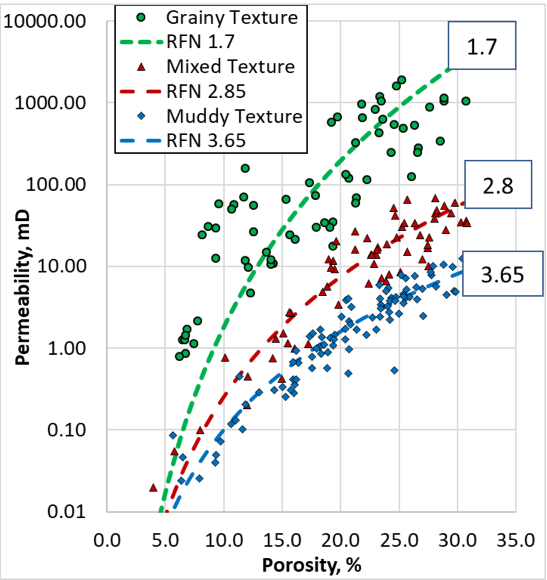

**Fig. 19.** Semi-log scale of figure 18.

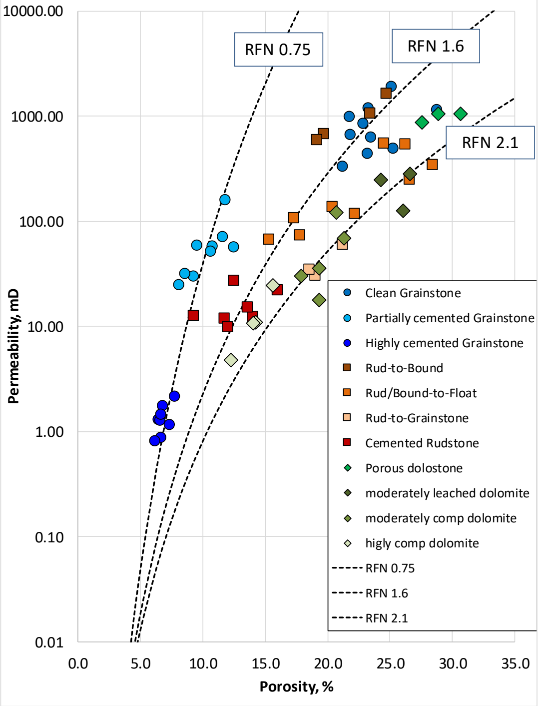

**Fig. 20.** Highlighted grainy RRT's with 3 different RFN values. Both partially & highly cemented grainstone RRT's gave RFN 0.75. Clean grainstone, Rud-to-Boundstone, low-porosity rud/bound-to-floatstone and cemented rudstone all gave RFN around 1.6. Dolomite with high-porosity Rud/Bound-to-floatstone and rud-to-grainstone gave RFN 2.1. This is a different classification to FZI from figure 12. RFN is not unique per RRT either.

The grouping seem to be different from FZI. RFN 1.6 grouped the clean grainstone RRT together with Rud-to-Boundstone, low porosity Rud/Bound to floatstone and cemented rudstone. The moderately and highly cemented grainstone RRT's were grouped together with a low RFN 0.75. RFN of 2.1 grouped the rest of the RRT's (*i.e.* all the dolomite RRT's together with the high porosity Rud/Bound-to-floatstone and the rud-to-grainstone). These rock types are very heterogeneous with diversified diagenesis processes that produce large grain and pore size variations, which may not be captured in a single model. Figure 21 shows the mixed-texture RRT's with 2 different RFN. The leached texture RRT's (i.e. packstone-to-grainstone, floatstone-to-boundstone and packstone) give RFN of 2.7. The less leached textures give RFN 3.2. This is almost a similar behaviour to the FZI model. For the muddy RRT's, figure 22 groups all the data with 2 different RFN only. The leached wackstone and the leached mudstone samples have RFN values of 3.45 and 3.75, respectively. The low porosity recrystallized, compacted and cemented wackstone and mudstone samples all have similar RFN of 3.75.

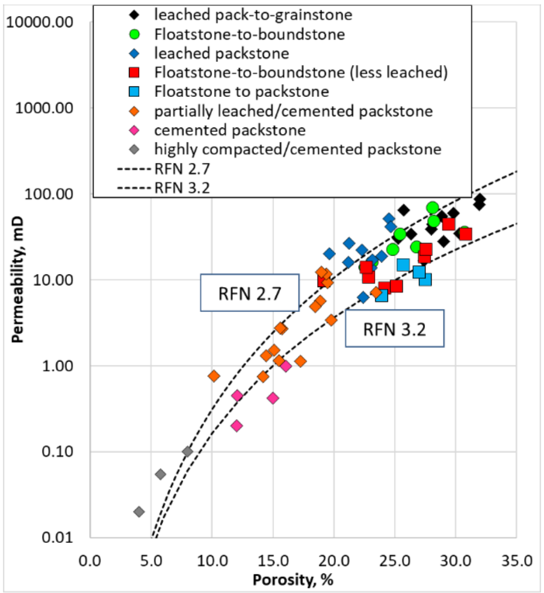

**Fig. 21.** Highlighted Mixed-texture RRT's with 2 different RFN values. Leached texture RRT's give RFN 2.7 with porosity higher than 20%. Less leached textures give RFN 3.2 with the same porosity range. Cemented/compacted textures give RFN 3.2 with porosity less than 20%.

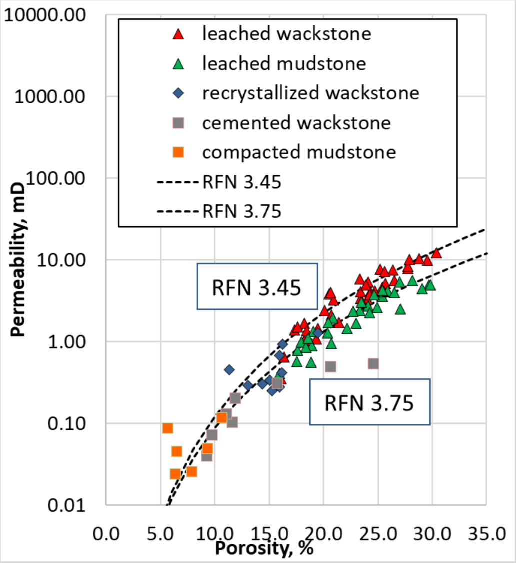

**Fig. 22.** Highlighted muddy RRT's with 2 different RFN values. Leached wackstone RFN 3.45. Leached mudstone RFN 3.75. Recrystallized/compacted/cemented wackstone and mudstone samples RFN 3.75 (porosity < 17%).

### 5.3 Winland Equation

Dale Winland of Amoco [18] used mercury injection-capillary pressure curves to develop an empirical relationship between porosity, permeability and pore throat radius (r). He tested sandstone and carbonate samples, and found that the effective pore system that dominates flow through a rock corresponds to a mercury saturation of 35%. He named that pore system r35. That pore system has pore throat radii equal to the pore throats entered when a rock is saturated 35% with a non-wetting phase. After 35% of the pore system fills with a non-wetting phase fluid, the remaining pore system does not contribute to flow. Instead, it contributes to storage. Winland never published his equation, rather it was later published by Kolodzie as in equation (6) below,

$$\mathrm{Log}(r35) = 0.732 + 0.588\log k - 0.864\log\Phi \qquad (6)$$

Where

r35 is the pore throat radius at 35% mercury saturation (micron)

$\Phi$ is the porosity (%)

k is the uncorrected air permeability (mD)

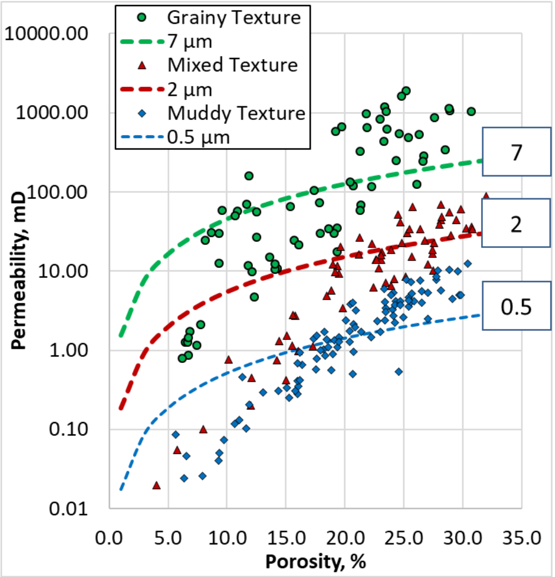

**Fig. 23.** Permeability versus porosity for all the poro-perm data (from figure 1) with r35 trends plotted from equation (6). The Winland trends have very different slopes compared to the texture-based experimental behaviour.

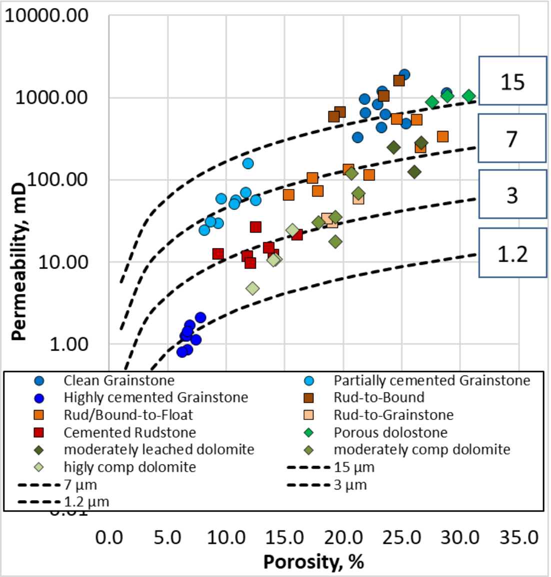

**Fig. 24.** Highlighted grainy RRT's with 4 different r35 micron values. Porous dolostone, clean grainstone, rud-to-boundstone and high porosity rud/bound-to-floatstone gave simailr r35 of 15 microns. Moderately leached dolomite with low porosity rud/bound-to-floatstone and the moderately cemented grainstone all gave r35 of 7 micron. Cemented/compacted dolomite together with cemented rudstone and rud-to-grainstone gave r35 of 3 microns. The highly cemented grainstone showed the least r35 at 1.2 microns.

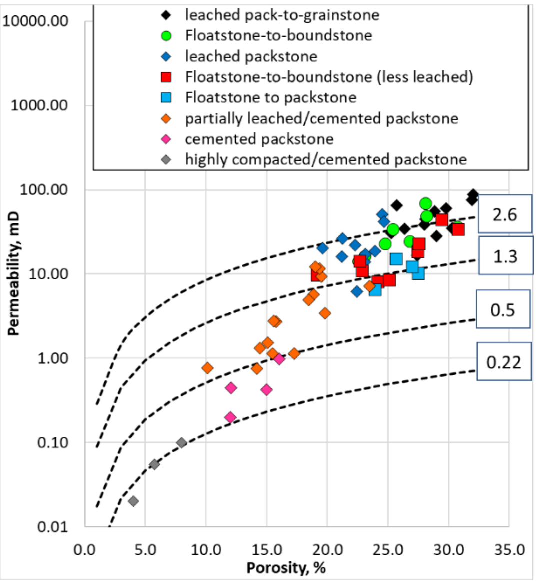

**Fig. 25.** Highlighted Mixed-texture RRT's with 4 different r35 micron values.

It is claimed that this method provides a more scientific approach for rock quality characterisation than simply using the porosity-permeability distribution. It was used to identify flow units in the reservoir by computing r35 from porosity and permeability, where the flow units are grouped by the size of the pore throats [19]. To evaluate this method, figure 23 gives the permeability versus porosity for all the poro-perm data (from figure 1) with Winland r35 trends constructed from equation (6).

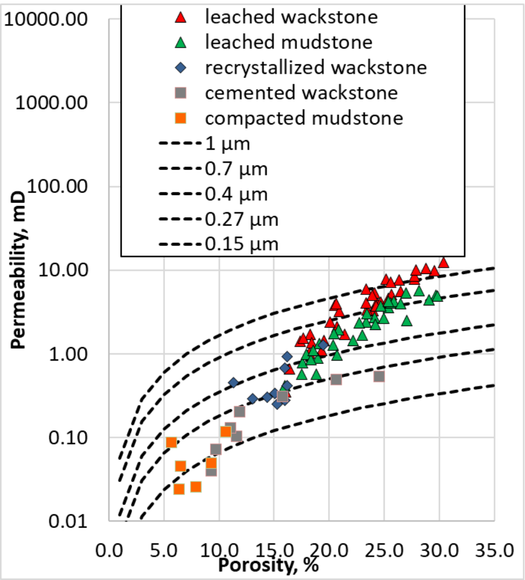

**Fig. 26.** Highlighted muddy RRT's with 5 different r35 values.

Grainy samples show an average r35 of 7 microns, Mixed 2 microns and Muddy 0.5 microns. The Winland trends have very different slopes compared to the texture-based experimental behaviour with minimal coverage of the texture trends. It is clear that r35 analysis has no strong link to the geology of the rock types. The previous approaches (FZI & RFN) seem to better honour the geology of the samples within the porosity-permeability domain. Figure 24 highlights the grainy RRT's with 4 different r35 micron values. Porous dolostone, clean grainstone, rud-to-boundstone and high porosity rud/bound-to-floatstone gave similar r35 of 15 microns. Moderately leached dolomite with low porosity rud/bound-to-floatstone and the moderately cemented grainstone all gave r35 of 7 micron. Cemented/compacted dolomite together with cemented rudstone and rud-to-grainstone gave r35 of 3 microns. The highly cemented grainstone showed the least r35 at 1.2 microns. These fitting r35 values do not necessarily reflect the true r35 of the samples and the permeability predictions based on equation (6) vary within +/- factor of 5. This method gives a very different classification to FZI and RFN from figure 12 and figure 21, respectively. R35, again, does not provide unique flow units (RRT's) in the reservoir. Figure 25 highlighted the mixed-texture RRT's with 4 different r35 micron values. Leached texture RRT's (with porosity higher than 18%) gave average micron range 2.6 to 1.3 microns, while less leached textures (with lower porosity range) gave r35 values between 0.5 and 0.22 microns. Figure 26 highlights the muddy RRT's with 5 different r35 values. Leached wackstone and mudstone RRT's gave r35 range between 1 and 0.4 microns. Recrystallized/compacted/cemented wackstone and mudstone samples show average range of r35 between 0.27 and 0.15 microns. While the porosity-permeability relationship can be described by one or two trends using FZI or RFN, Winland models the permeability with 5 trends based on varying pore sizes in the muddy RRT's.

## 6 Summary and Conclusions

Representative carbonate samples were selected from 7 reservoirs across the Middle East Region. Unique rock types were established based on porosity-permeability characteristics, capillary pressure and textural facies. Three main porosity-permeability trends were identified based on textures. Carmen-Kozeny (FZI), Lucia (RFN) and Winland (r35) permeability equations were used to model the experimental data. The following conclusions can be derived from this study,

1. Three porosity-permeability correlations were derived for the 3 main textures by (best-fit) power regression. The power equations can predict permeability with uncertainty factor of +/- 2 (figure 1).
2. Grainy RRT's showed the highest degree of permeability variation within the same porosity range. Muddy samples can be satisfactorily described by a single power correlation.
3. Three FZI trends modelled the porosity-permeability data and honoured the geological textures (figure 11). Permeability can be estimated with a factor of +/- 2 but the samples with the same FZI do not necessarily represent similar flow unit as originally claimed.
4. Three RFN trends modelled the porosity-permeability data and honoured the geological textures (figure 19). For the grainy RRT's, permeability estimation can vary +/- one order of magnitude (a factor of 10) but the prediction is much better for the mixed and muddy RRT's (factor of +/- 2). Samples with same RFN do not necessarily represent similar flow unit.
5. Winland r35 trends poorly modelled the experimental data (figure 23) and did not conform to the texture-based correlations.

The authors wish to acknowledge the support from Abu Dhabi National Oil Company (ADNOC) and Ingrain - Halliburton.

## References

1. S.K. Masalmeh and X.D. Jing, The Importance of Special Core Analysis in Modelling Remaining Oil Saturation in Carbonate Fields, SCA2008-03 (2008)
2. M. Dernaika, Z. Kalam, S. Skjaeveland, Understanding Imbibition Data in Complex Carbonate Rock Types, SCA2014-59 (2014)
3. J.J.M. Buiting, E.A. Clerke, Permeability from porosimetry measurements: Derivation for a tortuous and fractal tubular bundle, J Petrol Sci Eng, (2013) http://dx.doi.org/10.1016/j.petrol.2013.04.016i
4. M.R. Dernaika, Y. Naseer Uddin, S. Koronfol, O. Al Jallad, G. Sinclair, Multi-Scale Rock Analysis for Improved Characterization of Complex Carbonates, SCA2015-034 (2015)
5. M.R. Dernaika, B. Mansour, D. Gonzalez, S. Koronfol, F. Mahgoub, O. AlJallad, M. Contreras, Upscaled Permeability and Rock Types in a Heterogeneous Carbonate Core from the Middle East, SPE-185991-MS (2017)
6. M.R. Dernaika, and G.G. Sinclair, Resolving the Link between Porosity and Permeability in Carbonate Pore Systems, SCA2017-77 (2017)
7. M. Mousavi, M. Prodanovic, and D. Jacobi, New Classification of Carbonate Rocks for Process-Based Pore-Scale Modeling, SPE 163073, SPE J. (2013)
8. R.J. Dunham, Classification of Carbonate Rocks According to Depositional Texture. In Classification of Carbonate Rocks: A Symposium. American Association of Petroleum Geologists Memoir 1, ed. W.E. Ham, 108-121. Tulsa, Oklahoma: AAPG (1962)
9. H. Al-Owihan, M. Al-Wadi, S. Thakur, S. Behbehani, N. Al-Jabari, M. Dernaika, and S. Koronfol, Advanced Rock Characterization by Dual-Energy CT Imaging: A Novel Method for Complex Reservoir Evaluation, IPTC 17625 (2014)
10. M.R. Dernaika, B. Mansour, O. AlJallad, Characteristics of Carbonate Rock Types in the Middle East, SCA2018-65 (2018)
11. S. Serag El Din, M.R. Dernaika, M.Z. Kalam, and L. Hannon, The Effect of Rock Properties on Residual Oil Saturation in Heterogeneous Carbonate Rocks, SPE-164141 (2013)
12. S.K. Masalmeh and X.D. Jing, Improved Characterization and Modelling of Carbonate Reservoirs for Predicting Waterflood Performance, IPTC-11722-MS (2007)
13. J.O. Amaefule, M. Altunbay, D. Tiab, D.G. Kersey, and D.K. Keelan, Enhanced Reservoir Description: Using Core and Log Data to Identify Hydraulic (Flow) Units and Predict Permeability in Uncored Intervals/Wells, SPE 26436 (1993)
14. A.K. Ambastha, and T.J. Moynihan, A Simple And Accurate Method For An Integrated Analysis Of Core And Log Data To Describe Reservoir Heterogeneity, Petroleum Society of Canada. doi:10.2118/96-01-06 (1996)
15. J. Kozeny, Uber Kapillare Leitung des Wassel'S im Boden, Sitzungsberichte, Royal Academy of Science, Vienna, Proc. Class I **136**, 271-306 (1927)
16. P.E. Carmen, Fluid Flow through Granular Beds, Trans. AIChE **15**, 150 -166 (1937)
17. J.W. Jennings, and F.J. Lucia, Predicting Permeability From Well Logs in Carbonates With a Link to Geology for Interwell Permeability Mapping, SPE-84942 (2003)
18. S. Kolodzie, Analysis of Pore Throat Size And Use of the Waxman-Smits Equation To Determine OOIP in Spindle Field, Colorado, SPE 9382 (1980)
19. A.J. Martin, S.T. Solomon, and D.J. Hartmann, Characterization of Petrophysical Flow Units in Five Carbonate Reservoirs. American Association of Petroleum Geologists Bull. 81 (5):734 (1997).

# Direct Magnetic Resonance Measurement of Average Pore Size

*Florin* Marica[1], *Armin* Afrough[2], *Derrick* Green[3]*,* *Laura* Romero-Zeron[4], and *Bruce* Balcom[1,*]

[1]Department of Physics, University of New Brunswick, Fredericton, New Brunswick, E3B 5A3, Canada
[2]Centre for Oil and Gas - DTU, Technical University of Denmark, Kgs. Lyngby 2800, Denmark
[3]Green Imaging Technologies, Fredericton, New Brunswick, E3A 8V2, Canada
[4]Department of Chemical Engineering, University of New Brunswick, Fredericton, E3B 5A3, Canada

**Abstract.** Magnetic Resonance relaxation time distribution measurements, notably $T_2$ measurement, are commonly employed as a proxy measurement of pore size. They are not direct measurements of pore size and may only be converted to pore size through a separate determination of a relaxivity. In this work we employ the Brownstein-Tarr interpretation of magnetic resonance relaxation to identify non-ground modes of signal decay. These modes, most readily identified through a $T_1$-$T_2$ measurement, permit determination of an average pore size and surface relaxivities $\rho_1$ and $\rho_2$. Bulk pore size measurements are reported for three different sandstones with average pore size confirmed by electron microscopy. The pore size measurement may be spatially resolved with a spatially resolved $T_1$-$T_2$ measurement, implemented with an inversion recovery preparation for an SE-SPI $T_2$ mapping measurement. Spatially resolved pore size measurements agree with bulk measurements.

## 1 Introduction

Pore size is one of the most basic core analysis measurements. In principal magnetic resonance (MR) is ideally suited to such a measurement given sensitivity of the MR signal lifetimes to pore size through surface relaxation. A surface bound fluid layer in rapid exchange with a bulk like volume is assumed to yield an average MR signal lifetime that is proportional to the pore size. A distribution of lifetimes is thus a useful proxy for the pore size distribution [1]. Such lifetimes however require a separate calibration of surface relaxivity to permit conversion to a pore size with conventional units of size.

We have recently found that the Brownstein-Tarr approach [2] to interpreting MR relaxation rates permits a determination of average pore size in brine saturated core plugs [3,4]. The Brownstein-Tarr approach considers the competition between surface relaxation and diffusion within a pore and predicts multi-modal relaxation decay for $T_1$ and $T_2$ even for single pores. Multi-modal relaxation decay manifests itself as multiple signal lifetimes in a conventional relaxation experiment. Identifying and discriminating the ground mode signal lifetimes and the non-ground mode signal lifetimes is problematic in a conventional 1D relaxation experiment where realistic porous media have a distribution of lifetimes due to a distribution of pore sizes, in addition to short signal lifetime components due to clay bound water and other features.

Multi-modal relaxation in MR, according to the Brownstein-Tarr theory, has been recognized and understood for many years [5]. Song has emphasized the use of internal gradients to modify the non-ground mode signals [6]. The opportunity for exploiting non-ground modes to determine pore size has not been realized prior to our work.

Identifying and discriminating the ground and non-ground modes is easier in a 2D $T_1$-$T_2$ relaxation correlation experiment as described in this work. The $T_1$-$T_2$ experiment has found great utility in core analysis through its ability to discriminate molecular species [7], discriminate pore environments [8] and in more sophisticated interpretations, to measure wettability [9]. In previous work we have developed an adiabatic slice selective approach to a spatially resolved $T_1$-$T_2$ measurement [10].

Our goals in this paper are three-fold: (i) to introduce the average pore size measurement to the core analysis community, (ii) to test the measurement through application to a range of samples and (iii) to introduce a spatially resolved measurement of the pore size.

## 2 Theory

Magnetization evolution due to translational motion of spins in magnetic fields is governed by the Bloch-Torrey equations [11]. Brownstein and Tarr [2] examined the solution of these equations under conditions when diffusion does not necessarily result in uniform magnetization evolution in the pore. The Brownstein-Tarr number $BT_i$ describes the ratio of the relaxation rate at pore boundaries to the rate of diffusion in a confined geometry.

$$\mathrm{BT}_i = \frac{\rho_i l}{D} \qquad (1)$$

---

[*] Corresponding author: bjb@unb.ca

The index i in Eq. 1 discriminates between spin lattice relaxation, i = 1, with a $T_1$ time constant and spin-spin relaxation, i = 2, with a $T_2$ time constant. D is the molecular diffusion coefficient, $\rho_i$ is the surface relaxivity while l is the confinement length or pore size. Confinement length is a more general description that recognises the possibility that a pore may be only partially filled by the wetting fluid and it recognizes the possibility that a more complicated pore geometry does not permit a simple descriptor of pore size. In this work we will refer to l as the pore size.

Brownstein and Tarr identified three regimes of behaviour based on $BT_i$. $BT_i << 1$ is the fast diffusion regime. In this regime magnetization in the pore space is uniform and exchange between water at the pore surface and bulk like water in the pore centre is rapid. In this limit the observed relaxation rate depends on the pore surface to volume ratio. We note that this regime is almost universally assumed in MR petrophysics. This regime is also the rapid exchange regime of Zimmerman and Brittin [12]. $BT_i >> 10$ is the slow diffusion regime. The observed relaxation rate depends strongly on diffusion since diffusion to the pore surface is the limiting step. In this regime the relaxation behaviour depends weakly on surface relaxivity in higher order modes. The intermediate regime $1 < BT_i < 10$ is common in porous media and the observed relaxation behaviour depends on both surface relaxivity and diffusion.

The experimental data, transverse magnetization $m_+$, resulting from a 2D $T_1$-$T_2$ measurement is given by Eq. 2. In this equation $\tau_1$ is a time period of signal evolution with $T_1$ encoding, while $\tau_2$ is a time period of signal evolution with $T_2$ encoding.

$$m_+(\tau_1,\tau_2) = \int_r M_+(\boldsymbol{r},\tau_1,\tau_2)\, d\boldsymbol{r} \qquad (2)$$
$$= \sum_{q=0}^{\infty}\sum_{p=0}^{\infty} I\left(T_{1,p},T_{2,q}\right)e^{-\tau_1/T_{1,p}}e^{-\tau_2/T_{2,q}}$$

The experimental goal is to determine the 2D correlation function $I(T_{1,p}, T_{2,q})$ through inverse Laplace transformation as described in the next section. $I(T_{1,p}, T_{2,q})$ maps signal intensity to different $T_1$ and $T_2$ coordinates with p and q indexing the mode with p,q = 0 representing the ground mode and p,q = 1 representing the first non-ground mode. The $BT_i$ number determines whether significant populations exist in the non-ground mode. In simple geometries, and for arbitrary $BT_i$ values, the eigenvalues of signal lifetime for ground and non-ground modes are given by Eq. 3.

$$T_{i,n} = \frac{l^2}{4D\,\xi_{n,i}^2} \qquad (3)$$

where $\xi_{n,i}$ are functions of confinement geometry, diffusion coefficient, eigenvalue number $n$, and $\mathrm{BT}_i$. In a planar pore geometry $\xi_{n,i}$ are the positive roots of Eq. 4 [2].

$$2\xi_{n,i}\tan\xi_{n,i} = \mathrm{BT}_i \qquad (4)$$

Eqs. 1, 3 and 4, adapted from Brownstein-Tarr [2], are valid for planar pore geometries for both ground $n = 0$ and non-ground $n > 0$ eigenvalues and for longitudinal $i = 1$ and transverse $i = 2$ relaxation processes. These equations, with pore size $l$, and relaxivities $\rho_1$, $\rho_2$ determine the experimental peak locations in $T_1$-$T_2$ experiments.

This analysis yields a single pore size, rather than a distribution of pore sizes, which we interpret as an average pore size. The effect of pore shape does not significantly affect eigenvalues, and their intensities, for magnetic resonance relaxation in porous media. This is especially true for $\mathrm{BT}_i \ll 100$ [2].

## 3 Experimental

The bulk $T_1$-$T_2$ measurement was a conventional inversion recovery followed by a variable $T_1$ recovery period with a CPMG spin echo train read out, as described by Eq. 5.

$$\underbrace{\left[\pi - \tau_1 - \frac{\pi}{2}\right]}_{T_1\text{ encoding}}\underbrace{\left[-(\tau_i - \pi - \tau_i)_N\right]}_{T_2\text{ encoding}} \qquad (5)$$

The echo train data acquired is described by Eq. 2. A regularized inverse two-dimensional Fredholm integral of the first kind transforms the measured signal $m_+(\tau_1,\tau_2)$ into a 2D relaxation correlation function $I\left(T_{1,p},T_{2,q}\right)$ from which eigenvalues of magnetic resonance relaxation may be identified. This process is more commonly described as a 2D inverse Laplace transform. The inversion algorithm of Venkataramanan [13] was employed in this work. Increasing the regularization parameter $\alpha$ leads to smooth solutions whereas small $\alpha$ leads to a discretized result. A large regularization parameter, $\alpha = 1000$, was employed to identify the dominant ground mode peak. The regularization parameter was systematically decreased, usually to $\alpha = 0.1$ to yield a discretized result from which the first non-ground mode can be identified. A direct search optimization method [14] varied $\log_{10} l/\mu\mathrm{m}$, $\log_{10}\rho_1/(\mu\mathrm{m}/s)$, and $\log_{10}\rho_2/(\mu\mathrm{m}/s)$ and solved Eqs. 1, 3 and 4, to match the time constants of eigenvalues detected in $I\left(T_{1,p},T_{2,q}\right)$.

Bulk $T_1$-$T_2$ MR measurements were performed on a 8.59 MHz Maran DRX-HF imaging system (Oxford Instruments, Abingdon, UK), equipped with a 1000-watt RF amplifier (Tomco Technologies, Stepney, Australia), AE Techron 7782 gradient amplifiers (AE Techron, Elkhart, IN) and water cooled gradient coils. The 44 mm inner diameter custom-built RF probe provided 90° RF pulses with a duration of 10.6 $\mu s$ for an input RF power of 300 W. The basic experiment was repeated for 55 inversion recovery delays, spanning 500 usec to 1.9 sec. The echo time was 1 msec with 21 time domain points collected at the echo peak for signal averaging. Sixteen signal averages were collected for an overall experimental time of almost one hour. The peak SNR in the $T_1$-$T_2$ data set was more than 600.

The spatially resolved $T_1$-$T_2$ measurement was performed on a 2.21 MHz Maran DRX2 imaging system (Oxford Instruments, Abingdon, UK), equipped with a

25-watt RF amplifier and 1D vertical gradient coil. The 43 mm inner diameter probe provided 90° RF pulses with a duration of 28.5 $\mu s$. The basic experiment was repeated for 53 inversion recovery delays, spanning 100 usec to 10 sec. The first and subsequent echo times were 1 msec with sixteen time domain data points collected at the each echo peak for signal averaging. Four signal averages, each requiring 19 minutes, were collected for 16 k-space data points, yielding a final image of 16 pixels.

The samples under test, Buff Berea, Nugget, and Castlegate sandstones for bulk measurements, and Berea sandstone and Indiana limestone for spatially resolved measurement, were purchased from Kokurek Industries (Caldwell, TX). All samples had a diameter of 38 mm and were saturated with a 2% (w/v) solution of NaCl in distilled water. The Buff Berea, Nugget, and Castlegate sandstone core plugs were 50 mm in length, whereas the Berea sandstone and Indiana limestone core plugs were cut to 25 mm length to form a composite 1D sample of 50 mm length.

Natural drying was minimized by wrapping the core plugs with Teflon tape and a plastic film. The samples were maintained at 23 ºC during data acquisition.

## 4 Results and Discussion

Experimental bulk $T_1$-$T_2$ results are reported in Figs. 1-3 for brine saturated Buff Berea, Castlegate and Nugget sandstones. For each sample the three-part figure shows the $T_1$-$T_2$ distribution determined by inversion with three levels of regularization. The coarsest result, $\alpha = 1000$, permits one to identify the ground mode and its $T_1$, $T_2$ coordinates. The dominant ground mode peak is vulnerable to pearling with small values of the regularization parameter but non-ground mode peaks are not distorted by pearling. The first non-ground mode is typically less than ten percent of the intensity of the ground mode, with the second ground mode reduced still further in intensity. In some samples the second ground mode is clearly observable experimentally, but not in the data reported here. The intensity data of the non-ground modes is not at present incorporated into the data analysis. Only their lifetime coordinates are employed in the analysis.

The $T_1$ $T_2$ coordinates of the modes are connected by the pore size l, and the relaxivities $\rho_1$ and $\rho_2$ in Eqs 1, 3 and 4. Thus identifying the position of the modes permits determination of these three parameters through the optimization described above. The $T_1$ $T_2$ coordinates of the first non-ground mode, determined by optimization, are often displaced somewhat from the experimentally identified peak. The optimization process is more robust than might be imagined in part because there is a physical reality to the pore size l and the relaxivities $\rho_1$ and $\rho_2$. Values of these parameters which are too large or too small after optimization suggest a need to iterate the procedure.

Exploring the robustness of this measurement and process requires measurement of multiple samples. In the current study we focused on three similar but different sandstones as an experimental check on these procedures. Note that in each sample the $T_1$-$T_2$ data points, both experimental and predicted by optimization in Figs. 1-3, are very similar. The derived pore sizes and relaxivities are reported in Table 1 below.

Table 1: Pore size and relaxivities of samples studied.

| Sample | Pore size l, um | $\rho_1$ , um/sec | $\rho_2$ , um/sec |
|---|---|---|---|
| Buff Berea | 21 | 130 | 390 |
| Castlegate | 29 | 150 | 400 |
| Nugget | 27 | 175 | 1000 |

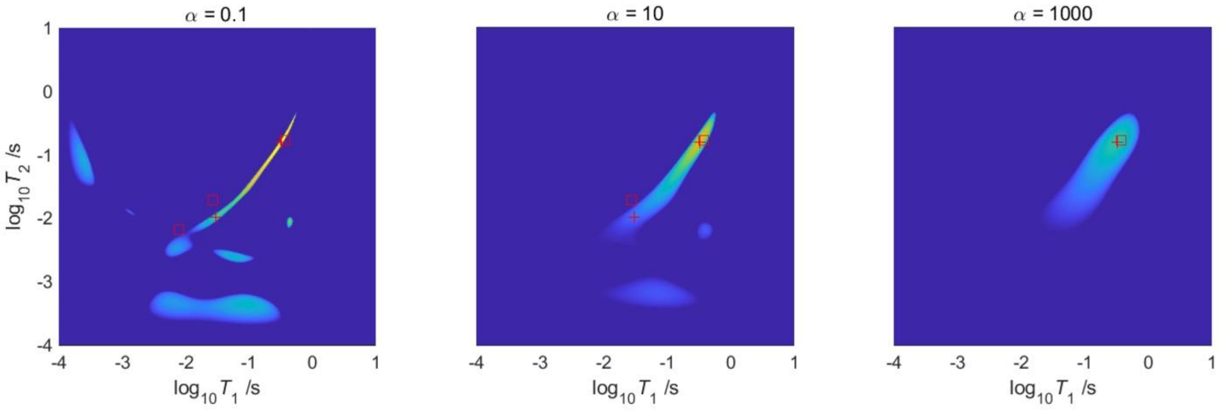

Figure 1: $T_1$-$T_2$ results for Buff Berea sandstone processed with three different values of the regularization parameter. The red crosses identify the experimental peaks of interest, the red boxes are calculated results. The peak at the longest lifetimes is the dominant ground

mode peak. The box at intermediate lifetimes identifies the first non-ground mode. The box at the shortest lifetimes is a prediction for the second non-ground mode. The display scale is logarithmic to reveal low intensity peaks.

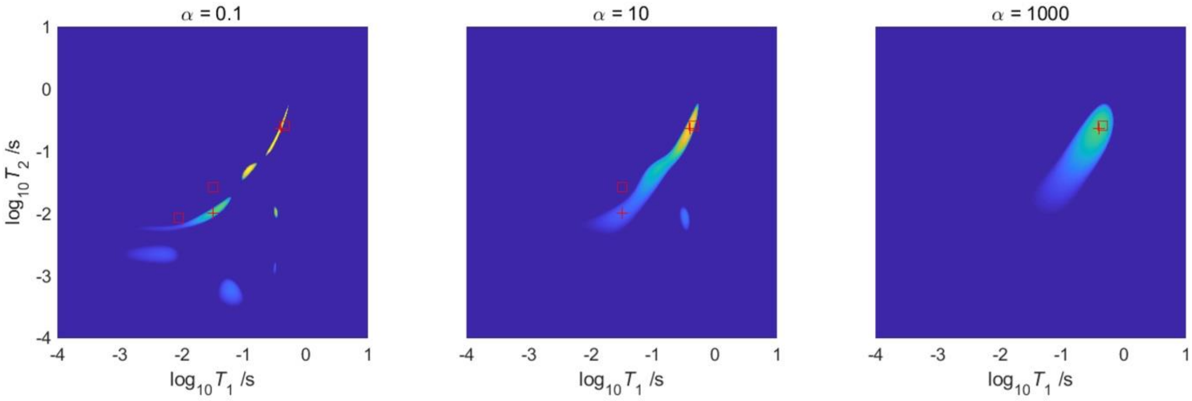

Figure 2: $T_1$-$T_2$ results for the Castlegate sandstone processed with three different values of the regularization parameter. Other descriptions are as per Figure 1.

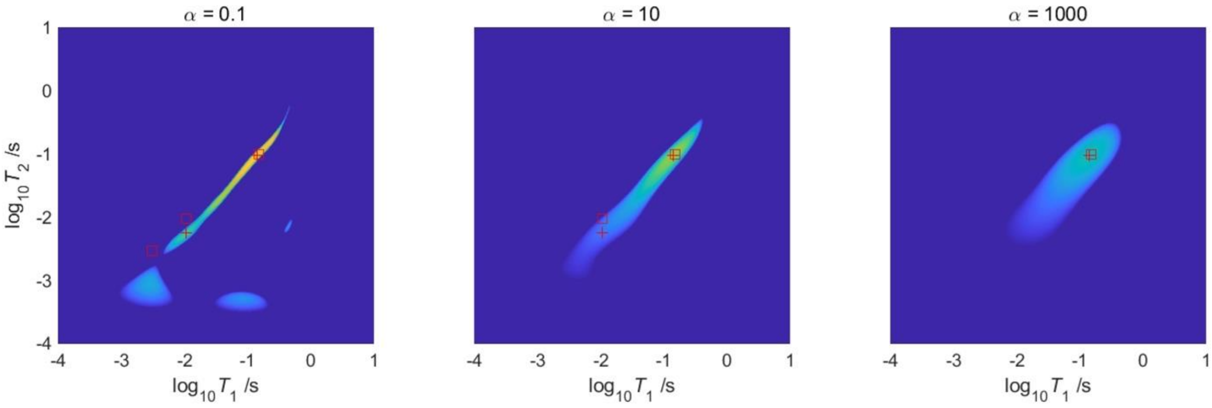

Figure 3: $T_1$-$T_2$ results for Nugget sandstone at three different values of the regularization parameter. Other parameters and descriptions are as per Figure 1.

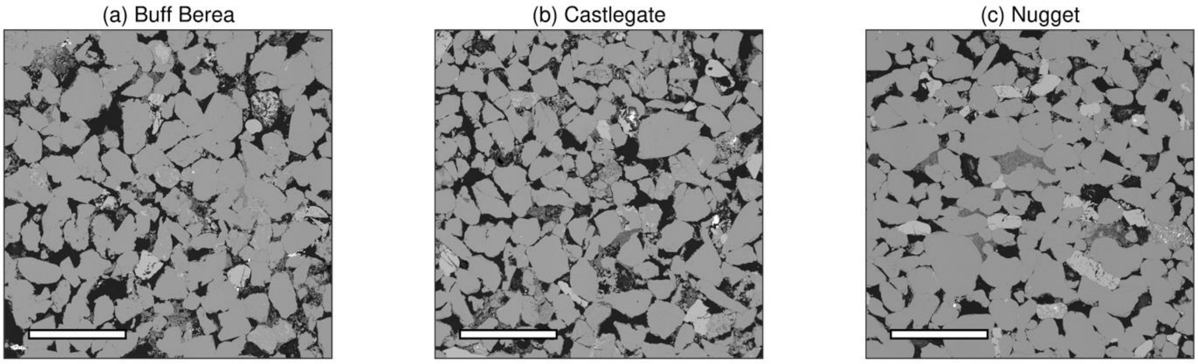
(a) Buff Berea
(b) Castlegate
(c) Nugget

Figure 4: Backscattered SEM images of resin-impregnated sandstones, with polished surfaces. The scale bar in each image indicates 500 um. The resin-filled pore space is black, quartz is medium gray, feldspar is light gray, while clay is dark gray.

The pore sizes and relaxivities of the samples reported in Table 1, in combination with the self-diffusion coefficient of water, show that all three samples exist in the intermediate regime of Brownstein-Tarr theory. $T_1$-$T_2$ derived pore sizes may be checked by ground truth electron microscopy measurements. This is critical to the validation process for this new measurement. Thin section backscattered SEM images, Fig. 4, were acquired for each of the three sandstone samples. The images show a very similar pore structure for the three samples, with average pore sizes determined to be 40 um, 35 um and 37 um for the Buff Berea, Castlegate and Nugget samples. These are very similar one to another, and they match within a factor of 2 the $T_1$-$T_2$ derived values for each sample. There is no evidence for two dominant pore sizes in the $T_1$-$T_2$ results. The SEM results confirm the pore size is single modal. Two dominant pore sizes are revealed in $T_1$-$T_2$ results by two ground mode peaks, visible even with a large regularization parameter [3].

The surface relaxivities reported in Table 1 are substantially larger, by more than an order of magnitude, than those reported by other investigators [15-17]. The minimization procedure to determine pore size and relaxivities in the Brownstein-Tarr analysis is more sensitive to the pore size that to relaxivity. The significant and systematic difference from literature values suggests however a more fundamental reason for the difference. The assumption of a planar pore geometry, as opposed to a spherical geometry, will play a role, but we believe the differences are related to the assumptions employed in the conventional determination of relaxivity as compared to the new measurement.

The Brownstein-Tarr modal analysis, and observation of non-ground modes in these experiments, is based on the combined effect of diffusion and surface relaxivity in determining the rate of change of observable magnetization. The combined effect of size, diffusion and surface relaxation is manifest in Eqs. 1,3,4. The conventional approach to determining surface relaxivity assumes rapid diffusional exchange in the pore space, and the rate of change of observable magnetization depends solely on size (S/V) and surface relaxivity. An independent measurement of S/V permits determination of $\rho$ in the conventional approach. If fluid in the pore is not in the rapid diffusion limit, and the change in observable magnetization depends on diffusion of fluid to the pore surface, the determination of $\rho$ will be in error and the estimated value in the conventional analysis will be low. The quantitative differences in $\rho$ anticipated in the two approaches will be the subject of future investigation. It is certainly true that the surface relaxivity determined through a BT analysis, assuming diffusion is important, should not be employed in the conventional analysis to determine pore size.

The utility of the $T_1$-$T_2$ measurement for various purposes has suggested the merits of developing a spatially resolved $T_1$-$T_2$ measurement. Our initial work in this area led to a slice selective method referred to above [10]. The SE SPI method developed at UNB some years ago [18] has been very successful in measurements of spatially resolved $T_2$ distributions. As an alternative to a slice selective regional $T_1$-$T_2$ we now introduce a simple modification of the SE SPI measurement through prepending an inversion pulse and variable $T_2$ recovery delay to the SE SPI method to permit $T_1$-$T_2$ profiling. This pulse sequence is illustrated in Fig. 5. In order to reduce the measurement time we limit the number of k-space data points encoded to sixteen, and thus reduce the number of image data points to sixteen as well. Spatial encoding occurs through signal phase imparted by the phase encoding gradient applied after the first 90° pulse, following partial $M_z$ recovery. The first echo in the echo train often has a longer echo time to permit gradient turn-on and turn-off in the first $\tau_i$ interval.

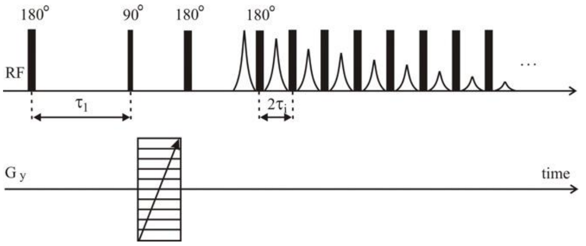

Figure 5: Inversion prepared SE SPI $T_1$-$T_2$ mapping profile measurement.

The spatially resolved $T_1$-$T_2$ weighted data sets may be processed, pixel by pixel, to yield a space resolved estimate of the pore size, via the procedures described above for bulk measurement. To test this methodology, and the analogous processing, a composite test phantom was created from half-length Berea and Indiana limestone core plugs. These fully brine saturated samples were then subjected to the inversion recovery SE SPI measurement of Fig. 5.

One $T_1$-$T_2$ weighted data set is reproduced as Fig. 6. In this data set we have position, 16 pixels, as the horizontal x axis. The image intensity is the vertical axis while the $T_2$ decay is manifest as an attenuation of the core plug profiles in the time dimension which is echo time multiplied by the echo number. This particular data set was acquired with a long $\tau_1$ value such that $M_z$ magnetization is fully recovered at the commencement of the echo train. This makes it easier to make physical sense of the $T_2$ weighted profiles that are generated for the two core plugs in the field of view. This data set is just one of 53 $T_1$ weighted data sets acquired during the measurement.

The data were analysed to yield a space resolved pore size within the two core plugs. The space resolved pore size measurement worked well, yielding a pore size of 24 um for the Berea and 53 um for the Indiana limestone. Previous bulk $T_1$-$T_2$ measurements revealed a pore size of 22 um for the Berea sample, with an SEM derived pore size of 26 um [3]. Similar bulk $T_1$-$T_2$ measurements of the Indiana limestone revealed a bimodal pore size distribution with large pores of 40 um and small pores of 10 um [3]. Complementary SEM images revealed large pores of 50 um and 10 um. The space resolved $T_1$-$T_2$ measurement does not observe the small pore size range in the Indiana limestone sample. The reasons for this discrepancy are under investigation, but probably relate to the difficulty of observing the short lifetime first non-ground mode signal in the imaging data. Nevertheless, the space resolved results are in remarkable agreement and certainly suggest the merit of analysing experimental systems where the pore occupancy and thereby confinement length will vary with position. The prolonged acquisition time of the space resolved measurement, at present, will limit measurement to systems which are in a steady state. Measurement at higher fields will of course improve the sensitivity, at the expense of potentially altering the transverse relaxation rate due to diffusion through internal field gradients.

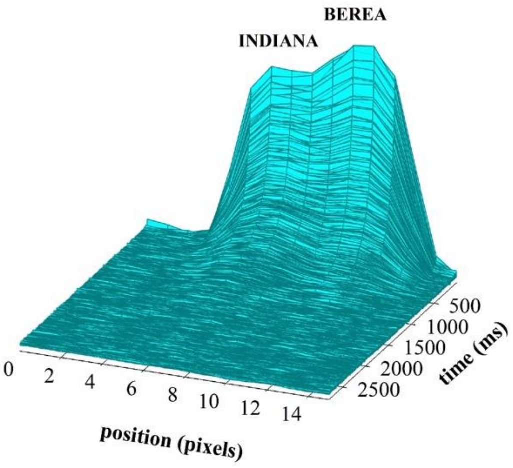

Figure 6: SE SPI based $T_1$-$T_2$ mapping profile series of a composite Berea sandstone and Indiana limestone phantom. The $\tau_1$ for this data set was 9 seconds, ensuring full $M_z$ recovery and no $T_1$ weighting of the individual profiles.

## 5 Conclusion

We have shown the application of a new $T_1$-$T_2$ measurement of average pore size to a range of sandstone samples. In accord with Brownstein-Tarr theory, non-ground modes will also appear in one dimensional relaxation experiments, but we believe non-ground modes will be easier to identify in two-dimensional experiments.

While a sophisticated data analysis stage is required, data processing is nevertheless robust. Automating the data processing is a clear goal but will require experience with a still larger cohort of samples. Future work will also explore the quantitative difference in relaxivities predicted by the new approach in comparison to a conventional analysis. If diffusion in the pore space is a common limitation on the observed relaxation rate then it is apparent that conventional estimates of relaxivity may be low as opposed to the current estimates being high.

We have also introduced a new spatially resolved $T_1$-$T_2$ measurement which is general in application, but which has particular utility for space resolved pore size measurements via the procedures described in this paper.

The authors thank NSERC of Canada for a Discovery grant and the Canada Chairs program for a Tier 1 chair in MRI of Materials.

## 6 References

1. G. Coates, L. Xiao, M. Prammer, *NMR Logging: Principles and Applications.* Houston TX, USA: Halliburton Energy Services, 1999.

2. K. Brownstein and C. Tarr, “Importance of Classical Diffusion in NMR Studies of Water in Biological Cells” *Phys. Rev. A*, vol. 19, no. 6, 2446-2453, 1979.

3. A. Afrough, S. Vashaee, L. Romero-Zeron, and B. Balcom, “Absolute Measurement of Pore Size based on Nonground Eigenstates in Magnetic Resonance Relaxation” *Phys. Rev. Appl.*, vol. 11, 2019, Art. no. 041002.

4. A. Afrough, “Magnetic Resonance Imaging of Enhanced Oil Recovery Processes in Porous Rocks” Ph.D. Dissertation, Dept. Chem. Eng., U. New Brunswick, Fredericton NB, Canada, 2019.

5. D. J. Wilkinson, D. L. Johnson and L. M. Schwartz, “Nuclear Magnetic Relaxation in Porous Media: The role of mean lifetime $\tau(\rho,D)$” *Phys. Rev. B*, vol. 44, no. 10, 4960-4973, 1991.

6. Y.-Q. Song, “Detection of the High Eigenmodes of Spin Diffusion in Porous Media” *Phys. Rev. Lett.,* vol. 85, 3878-3881 (2000).

7. M. Fleury and M. Romero-Sarmiento, “Characterization of shales using $T_1$–$T_2$ NMR maps” *J. Pet. Sci. Eng.,* vol. 137, 55-62, 2016.

8. Y.-Q. Song, L. Venkataramanan, M. Hurlimann, M. Flaum, P. Frulla and C. Straley, “$T_1$–$T_2$ Correlation Spectra Obtained Using a Fast Two-Dimensional Laplace Inversion” *J. Magn. Reson.,* vol. 154, 261-268 2002.

9. A. Valori and B. Nicot, “A Review of 60 Years of NMR Wettability” Society of Core Analysts, Trondheim Norway, August 2018, Art. no. 017.

10. S. Vashaee, M. Li, B. MacMillan, F. Marica, H. Kwak, J. Gao, A. Al-harbi and B. Balcom, “Local $T_1$-$T_2$ distribution measurements in porous media” *J. Magn. Reson.,* vol. 287, 113-122, 2018.

11. H. Torrey, “Bloch Equations with Diffusion Terms” *Phys Rev.* vol. 104, no. 3 ,563-565, 1956.

12. J. R. Zimmerman and W.E. Brittin, “Nuclear Magnetic Resonance Studies in Multiple Phase Systems: Lifetime of a Water Molecule in an

Adsorbing Phase on Silica Gel" *J. Phys. Chem.,* vol. 61, no. 10, 1328-1333, 1957.

13. L. Venkataramanan, Y.-Q. Song and M. Hurlimann, "Solving Fredholm integrals of the first kind with tensor product structure in 2 and 2.5 dimensions" *IEEE Trans. Signal Process.,* vol. 50, no. 5, 1017-1026, 2002.

14. T. Kolda, R. Lewis and V. Torczon, "Optimization by Direct Search: New Perspectives on Some Classical and Modern Methods" *SIAM Rev.,* vol. 45, no. 3, 385-482, 2003.

15. M. D. Hurlimann, K. G. Helmer, L. L. Latour and C. H. Sotak, "Restricted Diffusion in Sedimentary Rocks. Determination of Surface-Area-to-Volume Ratio and Surface Relaxivity" *J. Magn. Reson. A,* vol. 111, 169-178, 1994.

16. M. Fleury, "NMR Surface Relaxivity Determination using NMR Apparent Diffusion Curves and BET Measurements" Society of Core Analysts, Calgary, Canada, September 2017, Art. no. 035.

17. Z, X. Liao, J. Paulsen and Y.Q. Song, "Robust Determination of Surface Relaxivity from Nuclear Magnetic D-$T_2$ Measurements" *J. Magn. Reson.,* vol. 259, 146-152, 2015.

18. O. Petrov, G. Ersland and B. Balcom, "$T_2$ distribution mapping profiles with phase-encode MRI"
*J. Magn. Reson.,* vol. 209, 39-46, 2011.

# Two-Phase Fluid Flow Experiments Monitored by NMR

*Thomas* Hiller[1], *Gabriel* Hoder[2], *Alexandra* Amann-Hildenbrand[3], *Norbert* Klitzsch[3*], and *Norbert* Schleifer[4]

[1]Leibniz Institute for Applied Geophysics, Hannover, Germany
[2]SCK.CEN, Mol, Belgium
[3]RWTH Aachen University, Aachen, Germany
[4]Wintershall Holding GmbH, Barnstorf, Germany

**Abstract.** We present a newly developed high-pressure nuclear magnetic resonance (NMR) flow cell, which allows for the simultaneous determination of water saturation, effective gas permeability and NMR relaxation time distribution in two-phase fluid flow experiments. We introduce both the experimental setup and the experimental procedure on a tight Rotliegend sandstone sample. The initially fully water saturated sample is systematically drained by a stepwise increase of gas (Nitrogen) inlet pressure and the drainage process is continuously monitored by low field NMR relaxation measurements. After correction of the data for temperature fluctuations, the monitored changes in water saturation proved very accurate. The experimental procedure provides quantitative information about the total water saturation as well as about its distribution within the pore space at defined differential pressure conditions. Furthermore, the relationship between water saturation and relative (or effective) apparent permeability is directly determined.

## 1 Introduction

Petrophysical parameters play an important role in many geological applications and are subject of various research projects. For reservoir simulations, fluid flow experiments in the laboratory are crucial in order to determine parameters, which can be used for calculating fluid re-distribution in the subsurface. Regularly, core analysis is done under ambient conditions on dry plugs or completely water saturated samples, i.e., single-phase fluid flow is measured in order to derive the intrinsic permeability [1, 2]. However, when it comes to the characterization of low permeable material (tight sandstones, shales) below the mD-range, the experimental procedures need to be adapted for low flow rates and high fluid pressures. This is especially difficult for the determination of the effective permeability of a fluid in presence of another fluid, which is up to three orders of magnitude lower than the intrinsic permeability [3]. In a two-phase fluid flow system, different factors have to be accounted for, which are often strongly coupled and interdependent like stress dependence, water saturation and capillary pressure. The latter is highly important as gas flow through low permeable (partial) water saturated rocks is usually controlled by capillary pressure, i.e., as water is drained from the pores with increasing differential gas pressure [4].

In order to derive correlations between effective permeability, water saturation and capillary pressure, commonly, several experiments are carried out in different setups (core-flooding experiments, centrifuge, porous plate, mercury injection [5, 6, 7, 8, 9]. Generally, effective permeability experiments are conducted in different steps, each consisting of the pre-saturation and an effective permeability measurement. For each saturation level the flow setup has to be dis- and reassembled [10, 11]. This procedure is very time consuming and bears the risk of sample damage caused by repetitive loading / unloading cycles. Additionally, changes in water saturation during gas flow experiments cannot be directly measured in such a conventional experimental flow cell. In this work, we present a newly developed NMR flow cell, which can be loaded up to a confining pressure of 30 MPa. The apparatus allows the determination of water saturation during ongoing fluid flow experiments. Here, we introduce the experimental procedure as well as its results on an initially fully water saturated sandstone sample. After sample installation, the drainage process was continuously monitored in terms of changing water saturation and effective gas permeability. For more experimental results obtained with the introduced NMR flow cell we refer to [12].

## 2 Theoretical Background

### 2.1 Single and Two-Phase Fluid Flow

In the single-phase system, permeability depends only on the rock's intrinsic properties, i.e. pore size distribution and tortuosity [9]. In laboratory experiments, permeability can be determined on cm-sized cylindrical plugs with either water or gas. When using water as the permeating liquid, Darcy's law for incompressible media is used [13]:

$$Q = -\frac{k_{\text{water}} A}{\eta} \frac{\Delta p}{\Delta x}. \tag{1}$$

---

[*] Corresponding author: NKlitzsch@eonerc.rwth-aachen.de

Parameters are the volume flow rate $Q\ [\mathrm{m}^3/\mathrm{s}]$, the differential pressure $\Delta \mathrm{p}$ [Pa] across the sample, fluid viscosity η [Pa s], cross-sectional area $A\ [\mathrm{m}^2]$, sample length $\Delta x$ [m] and intrinsic permeability $k_{\mathrm{water}}\ [\mathrm{m}^2]$. When gas is used in the experiments, one has to account for gas compressibility (eq. 2) and slip flow (eq. 3). Assuming the validity of the ideal gas law, integration across the sample length and between the up- and downstream pressures, $p_1$ and $p_2$, yields Darcy's law for compressible media [9]:

$$Q = -\frac{k_{\mathrm{gas}} A}{\eta} \frac{(p_1^2 - p_2^2)}{2 p_2 \Delta x}. \tag{2}$$

The coefficient $k_{\mathrm{gas}}\ [\mathrm{m}^2]$ is the apparent gas permeability, which is only valid for given fluid pressure conditions. It is well known, that gas permeability increases with decreasing mean fluid pressures ($p_{\mathrm{mean}}$), which is due to the increasing molecule/pore wall interactions at low gas densities [14, 15, 16]. In single-phase flow systems, the so called "Klinkenberg" or "slip flow" correction is routinely done according to the following linear relationship with $k_\infty$ being the intercept on the y-axis, thus at infinite high gas pressure:

$$k_{gas} = k_\infty \left(1 + \frac{b}{p_{mean}}\right) \tag{3}$$

$$\text{with } b = \frac{8 c \lambda p_{mean}}{d} \tag{4}$$

In eq. 4, the slip factor $b$ [Pa] is directly related to $d$ [m], the average or mean pore diameter of the porous medium and parameters describing the property of the gas phase ($\lambda$ [m], the mean free path length of the gas molecule, $c \approx 1$, the Adzumi constant and $p_{\mathrm{mean}}$[Pa]). Accordingly, the smaller the pores, the larger the slip flow effect. In two-phase system, this is extremely difficult and so far only studied for pre-defined water saturations [10, 11, 17, 4]. This correction was not done here as it out of the scope of the present work.

In a two-phase fluid system, one distinguishes between the wetting and the non-wetting fluid. Both phases can be displaced by the other phase, which changes the saturation profile within the porous medium. Hereby, the terms drainage and imbibition are used, which refer to the displacement of the wetting phase by the non-wetting phase and vice versa. For most siliciclastic rocks, water is considered the wetting phase and gas the non-wetting phase. The mobility of both phases (effective permeability) is strongly coupled with fluid saturation and capillary pressure. Increasing capillary pressures results in a decreasing water saturation (drainage process), which in turn results in more available fluid pathways for gas flow, thus an increased effective gas permeability. The smaller the pores, the larger the capillary pressure, which has to be applied to drain water from the pore space. This relationship is described by the Washburn equation for the simplified model of cylindrical pores [18]:

$$P_{\mathrm{c}} = \frac{2\gamma \cos\theta}{R}, \tag{5}$$

with $P_c$ the capillary pressure, $\gamma$ [N/m] the interfacial tension between the wetting and non-wetting phase (here water and gas), $\theta$ [°] the surface contact angle of the wetting phase and $R$ the equivalent capillary pore radius. In non-oil contaminated reservoir rocks $\theta$ is usually assumed to be zero. In the present study, the pressures detected on the up- and downstream pressure side during the drainage experiment ($p_1$, $p_2$) correspond to the pressures of the gas and water phase, respectively. Hence, in the two-phase fluid flow experiments conducted in this study the assumption is made that $P_{\mathrm{c}}$ equals the differential pressure, $\Delta p = p_1 - p_2$.

### 2.2 NMR T₂ relaxation measurements

In this work, the principles of nuclear magnetic resonance (NMR) relaxation measurements are utilized to support petrophysical flow experiments - especially monitoring the change of water saturation $S_{\mathrm{w}}$ but also to qualitatively resolve the size of the corresponding water filled pores.

The NMR relaxation mechanism results from the interaction of a porous medium with its pore-filling fluid containing a detectable amount of hydrogen protons $^1$H (here water). In most laboratory and well-logging applications, the magnetic moments (spins) of hydrogen protons are aligned with a strong static magnetic field $\boldsymbol{B}_0$ and, therefore, yield a minute net magnetization. The characteristic precession frequency of the magnetization around the static magnetic field is called Larmor frequency $\omega_{\mathrm{L}} = \gamma_{\mathrm{H}} \boldsymbol{B}_0$ and depends solely on the strength of $\boldsymbol{B}_0$ and the gyromagnetic ratio $\gamma_{\mathrm{H}}$ of hydrogen. Larmor frequencies of commonly available applications can vary from approx. 0.2 MHz (4.7 mT) to 0.4 GHz (9.4 T) [19, 20]. A NMR relaxation measurement is started by applying an energizing electromagnetic pulse with the appropriate Larmor frequency (creating a secondary electromagnetic field $\mathbf{B}_1$) and thus tipping away all spins from their equilibrium state. After the pulse is switched off, the spins relax back into their equilibrium state. This relaxation process is measured and the resulting NMR signal is given by

$$E(t) = \sum_i \frac{V_i}{V_0} \exp\left(\frac{-t}{T_{2,i}}\right), \tag{6}$$

with $V_0$ the total water filled pore volume, and $V_i$ the volume of pore class $i$ relaxing with the characteristic relaxation time $T_{2,i}$. The sum of individual amplitudes $\sum V_i/V_0 \rightarrow E(t=0) \rightarrow E_0$ is commonly referred to as initial amplitude $E_0$ and is directly proportional to the amount of excited hydrogen protons and therewith, a direct measure for water content and, hence, saturation $S_{\mathrm{w(NMR)}}$.

The NMR $T_2$ relaxation process itself is a superposition of three independent mechanisms [19, 21]: (i) the bulk relaxation $T_{\mathrm{b}}$ of the pore fluid, (ii) the surface relaxation $T_{\mathrm{s}}$ due to the interaction of pore fluid and rock matrix and (iii) diffusional relaxation $T_\mathrm{d}$ caused by spins diffusing through a non-uniform magnetic field. In this work, we assume no internal field gradients and therefore neglect diffusional relaxation. However, in the presence of minerals that exhibit high magnetic susceptibilities, diffusional relaxation must be accounted for [22, 23, 24]. Furthermore, we also assume the so-called fast diffusion regime where $\rho_\mathrm{s} R/D \ll 1$, with surface relaxivity $\rho_\mathrm{s}$, characteristic pore size $R$ and self-diffusion coefficient of water $D$ [25]. This assumption is reasonable considering the pore sizes of the tight sandstone samples used in this study. Therefore, in a water saturated porous media the effective relaxation time $T_2$ is given by

$$\frac{1}{T_2} = \frac{1}{T_{2,\mathrm{b}}} + \frac{1}{T_{2,\mathrm{s}}} + \frac{1}{T_{2,\mathrm{d}}} \rightarrow \frac{1}{T_{2,\mathrm{b}}} + \rho_s \frac{S}{V}. \qquad (7)$$

By inspection of eq. 7 one can deduce the following straightforward relationship: the larger the pore is, the smaller is the surface-to-volume ratio $S/V$ and, hence, the longer is the relaxation time $T_2$ and vice versa. The surface relaxivity $\rho_\mathrm{s}$ is a mineral parameter and relates surface inhomogeneities to accelerated relaxation and hence has dimensions of velocity $\mathrm{m/s}$. Generally, $\rho_\mathrm{s}$ is assumed constant for a particular type of porous media and needs to be determined via calibration [26]. Depending on the knowledge of $\rho_\mathrm{s}$ and considering eqs. 6 and 7, it is possible to directly infer the pore size (or $S/V$ of the pore) from NMR relaxometry data.

To find the individual amplitudes $V_i/V_0$ as a function of relaxation time $T_{2,i}$ (cf. eq. 6), the so-called relaxation time distribution (RTD), a linear system of equations has to be solved. Generally, and because this inverse problem is ill-posed [27], this is achieved by a regularized (smoothed) least-square minimization [28] of the form

$$\min \|\mathbf{Gm} - \mathbf{d}\|_2^2 + \lambda^2 \|\mathbf{Lm}\|_2^2 \qquad (8)$$

with $\mathbf{d} = E(t)$ the NMR data vector, $\mathbf{m} = [V_i/V_0]$ the model vector and the forward operator $\mathbf{G}$ (cf. eq. 6). Here, the smoothness constraint on $\mathbf{m}$ is applied by a first-order derivative matrix $\mathbf{L}$. The regularization parameter $\lambda$ is found via the L-curve criterion and chosen such that the inversion misfit is in the order of the data noise while keeping a sufficiently smooth RTD [29, 28].

## 3 Experimental Methods & Procedures

### 3.1 NMR Flow Cell Setup

The experimental setup used in this study consists of multiple components, which allow for the combined measurement of fluid flow and NMR. An overview of the complete assembly is given in Fig. 1. The high-pressure flow cell, which is designed for samples of 30 mm in diameter and 15 − 60 mm in length, is placed vertically in the center of the Halbach magnet. The sample itself is placed between two NMR-inert PEEK (polyether ether ketone) pistons containing conduits for in- and outflow. Grooves on the pistons allow for the even distribution of the gas phase across the sample surface. A rubber sleeve encases the piston/sample arrangement. O-rings prevent influx of the confining pressure oil. The RF coil, which is a 13 mm long copper radio frequency coil (rf-coil), is located within the confining compartment surrounding the rubber sleeve and is centrally positioned around the sample plug. In order to apply a constant confining pressure, $p_\mathrm{conf}$, (up to 30 MPa) the compartment is filled with a NMR-inert synthetic oil (Fluorinert$^\mathrm{TM}$ FC-40), regulated by a HPLC pump (Shimadzu LC-6A). Temperature fluctuations within the flow cell are monitored with a resistance thermometer PT 100 with an accuracy of 0.05 K. On the outside, a wooden cylinder encases the entire setup.

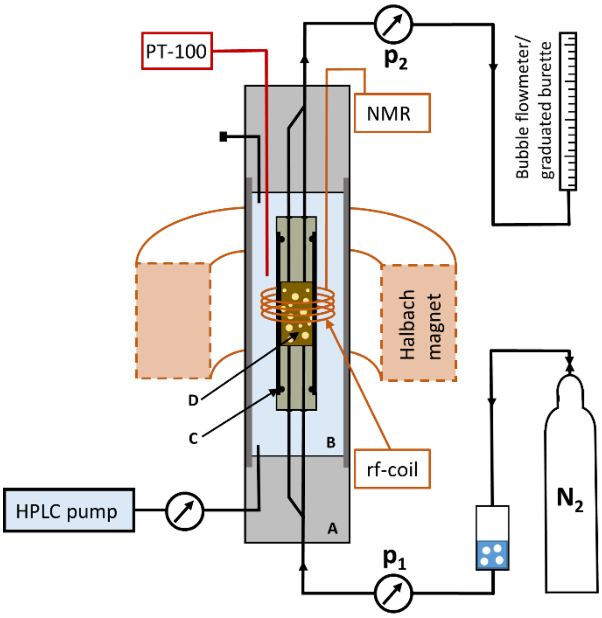

**Figure 1.** Sketch of the NMR flow cell with A – outer sealing system, B – confining pressure compartment filled with NMR-inert oil, C – inner O-ring sealed sleeve system, D – sample placed between PEEK pistons.

The flow cell is connected to a nitrogen gas bottle on the high-pressure side $p_1$ at the base of the setup. The low-pressure side $p_2$ is kept at atmospheric pressure, i.e., the gas flows opposite to gravity. In this system, gravitational forces on the water phase can be neglected as they are much smaller than the applied differential gas pressures of at least 100 kPa. A water reservoir is used to moisturize the gas stream in order to prevent drying of the sample. The downstream capillary is connected to either a bubble flow meter for gas flux measurements or a graduated pipette to determine single-phase water flux (top of the setup). Additionally, two pressure transducers (Keller, 0.05% FSO) at the inlet / outlet of the flow cell continuously monitor the pressure on both sides.

### 3.2 NMR Data Processing

All NMR relaxation measurements presented in this work are conducted with a low field Halbach NMR spectrometer with a frequency of 4 MHz [30, 31] using the Carr-Purcell-Meiboom-Gill (CPMG) pulse sequence [32, 33]. The shortest possible echo time in our setup is $TE = 320\ \mu s$ and, depending on the saturation and relaxation behavior of the corresponding sample, up to 2500 echoes were recorded, yielding signal lengths up to 0.8 s. Initially, each CPMG echo train was averaged until a signal-to-noise ratio of $S/N \sim 200$ was reached. Over the course of the drainage experiment and due to the decreasing water saturation (and hence, decreasing signal amplitude), this constraint could not be maintained while keeping an equal NMR measurement interval of 30 minutes.

According to Curie's law the magnetization is negatively correlated with temperature, i.e., for water, a temperature decrease of $1\ \mathrm{K}$ yields a magnetization increase of $\sim 0.4\ \%$ and vice versa. However, in preliminary experiments we found, that even small temperature fluctuations have a much stronger effect on the initial amplitude of the NMR signal as expected. For testing purposes, we installed a $100\ \%$ water filled dummy sample (PVC container filled with degassed tap water) in the flow cell and the confining compartment was filled with the NMR-inert oil – the confining pressure was allowed to be atmospheric. Like in a drainage experiment, the temperatures inside the flow cell $T_{\mathrm{cell}}$ and the laboratory $T_{\mathrm{room}}$ as well as the initial NMR amplitudes $E_0$ were continuously monitored over a period of 30 hours. From Fig. 2 is a strong positive correlation between the NMR amplitude ($\mathrm{NMR_{raw}}$) and the temperature measured within the flow cell ($T_{\mathrm{cell}}$) evident ($R^2 = 0.9990$, cf. inset in Fig. 2). While the temperature inside the flow cell $T_{\mathrm{cell}}$ (solid black line) varied by approximately $\pm 0.1\ \mathrm{K}$, the initial amplitude varied by about $\pm 10\ [\mathrm{a.u.}]$ or 4 %. This value is two orders of magnitude higher than the theoretical increase. As the NMR amplitude correlates linearly with the temperature fluctuation (see inset of Fig. 2), the latter can be used to correct the NMR amplitudes. The temperature-corrected signal ($\mathrm{NMR_{corr}}$) fluctuates less than 0.2 % around its mean value. For this reason, we conduct this pre-test always on the fully water saturated samples before starting the actual drainage experiment. We found, that a measurement time of approx. 48 hours yielded stable correlations between NMR amplitude and temperature fluctuations.

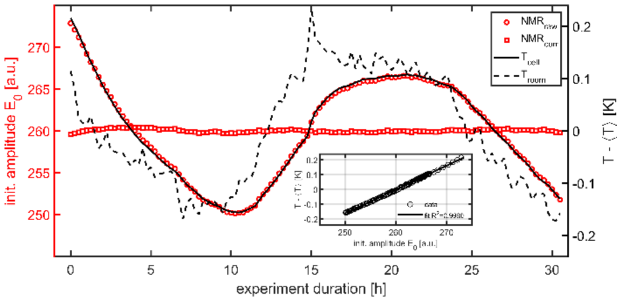

**Figure 2.** Raw (red circles) and corrected (red squares) initial NMR amplitudes $E_0$ together with the flow cell (black solid) and room temperature (black dashed) variations as a function of experiment duration for a water sample; <T> denotes the mean temperature of the flow cell or the room, respectively. The inset shows the correlation between the raw amplitude and cell temperature fluctuation.

The effect of temperature on bulk relaxation is well understood and can easily be approximated [19]. In the case of our test measurement with $100\ \%$ water, the measured bulk relaxation time follows the theoretical relation. Unlike modern NMR devices, our setup is not temperature regulated. We hypothesize that the temperature dependence of the NMR amplitude observed in our measurements is device or setup dependent, e.g., temperature effects on the electronic components of the resonant circuit. With the procedure described above, we are able to account for the temperature fluctuations and derive reliable water saturation information from our experiment.

### 3.3 Single-Phase Flow – Intrinsic Gas Permeability

To qualitatively and quantitatively compare single-phase and two-phase flow results, we use for both types of measurements the NMR flow cell under equal confining pressure conditions. To determine the intrinsic permeability $k_\infty$ the dry sample is installed into the flow cell and the capillaries on the high-pressure side are connected to a nitrogen gas source. After application of the confining pressure, the gas permeability experiments are conducted at different mean fluid pressures $p_{\mathrm{mean}}$. Here, steady state experiments are conducted at different upstream pressures $p_1$, while keeping the downstream pressure $p_2$ at ambient conditions. The volume flow $Q$, is measured on the outflow side with the attached bubble flow meter until steady state flow conditions are established. Apparent and intrinsic permeability values are determined from eqs. 2 and 3.

### 3.4 Two-Phase Flow – Effective Gas Permeability

Prior to all drainage experiments, air is removed from the sample in a vacuum desiccator. Thereafter, we saturated the sample with brine (10.6 g/L $MgSO_4$ solution) and installed it into the flow cell. There, a confining pressure of 15 MPa is established. To obtain a sufficient amount of data for the temperature correction described above, repetitive NMR measurements (30 min interval) are performed on the fully water saturated and pressurized sample for a time span of at least 48 hours.

Drainage experiments are performed according to the step-wise procedure usually applied for gas breakthrough determination of sealing lithologies [34]. The drainage experiment is conducted by increasing the gas pressure on the high-pressure side in different intervals ($p_1 = 0.3 - 2.5\ \mathrm{MPa}$), while the outflow side is constantly held at atmospheric pressure ($p_2 = \mathrm{const.}$). At low differential pressures, only water is displaced from the sample but no gas flows through it. After exceeding a threshold pressure, which equals the capillary pressure of the smallest pore along the percolation path, the gas phase breaks through and a saturation gradient establishes along the sample, i.e., along the pressure gradient. The whole drainage experiment is monitored by NMR measurements (30 min interval), temperature and pressure measurements (30 s interval). Because of the saturation gradient and the sensitive range of the NMR instrument of about 2 cm, we measure an average water saturation over this range. First gas flow being detected on the low-pressure side indicates that the capillary breakthrough pressure has been overcome. At this point, sufficient water has been displaced from the pore space and at least one gas conducting percolation path has been established. The number of percolation pathways increases with increasing gas pressure. Moreover, more pores are desaturated at the high-pressure side than at the low-pressure side, i.e., there is a saturation gradient, which changes with increasing gas pressure. Regularly, the gas outflow rate is detected with a bubble flow meter. After gas outflow and NMR signal (saturation) stabilize, the next pressure difference is applied. From the bubble flow meter and from the NMR data at stationary conditions, we calculate effective permeability of the gas phase, water saturation and relaxation time distribution, respectively. They in turn can be related to the applied pressure difference.

# 4 Results & Discussion

## 4.1 Sample Characterization & Intrinsic Properties

The test plug (R1), used in this study, was provided by the Wintershall Holding GmbH and is a tight reservoir sandstone from a depth of about 4000 m. It is a coarse-grained sandstone from the Rotliegend formation, containing illite as pore filling mineral. Some petro-physical properties of sample R1 are provided in Tab. 1.

**Table 1.** Petrophysical properties (logarithmic mean NMR relaxation time $T_{lgm}$, NMR porosity $\Phi_{NMR}$, Helium porosity $\Phi_{He}$, Archimedes porosity $\Phi_{Arch}$, intrinsic gas permeability $k_\infty$, and Klinkenberg slip factor b) of the sample used in this study.

| $T_{lgm}$ [ms] | $\Phi_{NMR}$ \| $\Phi_{He}$ \| $\Phi_{Arch}$ [%] | $k_\infty$ [m$^2$] | $b$ [MPa] |
|---|---|---|---|
| 4.8 | 5.8 \| 6.7 \| 6.9 | 4 $10^{-17}$ | 0.20 |

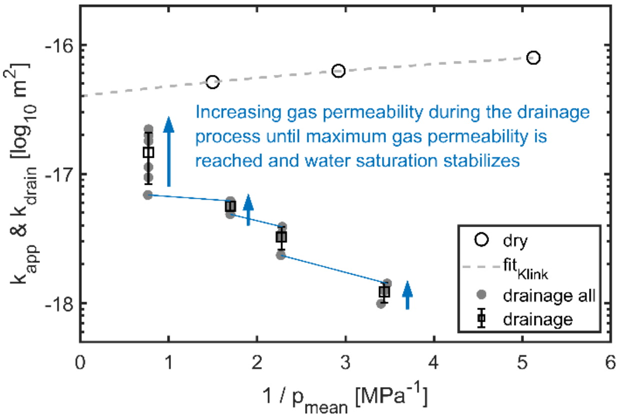

**Figure 3.** Apparent gas permeability for the dry R1 sample (circles) and effective gas permeability during drainage (squares) as a function of reciprocal mean pressure $p_{mean}$. The dashed line is a linear fit to the dry data yielding an intrinsic gas permeability of $k_\infty = 4\ 10^{-17}\text{m}^2$.

Porosity was determined via Archimedes' principle. The intrinsic (Klinkenberg corrected) permeability is $4\ 10^{-17}\text{m}^2$ and the slip factor is 0.2 MPa (cf. Tab. 1). In Fig. 3, the apparent permeability $k_{\text{app}}$ as a function of reciprocal mean pressure $p_{\text{mean}}$ is shown (black circles). The Klinkenberg fit to derive the intrinsic permeability $k_\infty$ is depicted with the gray dashed line.

In Fig. 4 shows a typical NMR measurement. The NMR transient (solid gray line) and the corresponding multi-exponential fit (solid black line) are depicted in Fig. 4a. The signal consists of 750 echoes with an inter-echo time of 320 µs. The signal-to-noise ratio (SNR) of this particular measurement is 180. Figure 4b shows the corresponding inverted relaxation time distribution (RTD). The RTD was derived as described above using a smoothed least squares fit with 20 relaxation times per decade. The regularization parameter was chosen as such, that the fitting error (rms = 0.07) is equal to the noise level of the data (dashed black line in Fig. 4a). The corresponding solid gray line in Fig. 4b represents the cumulative relaxation time distribution. The vertical dashed black line in Fig. 4b indicates the characteristic relaxation time of the RTD often referred to as logarithmic mean relaxation time $T_{\text{lgm}}$.

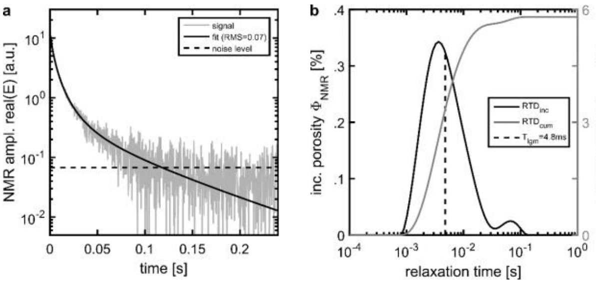

**Figure 4. (a)** T2 NMR signal (gray solid) and corresponding fit (black solid) for the full saturated sample R1; **(b)** corresponding incremental (black solid) and cumulative (gray solid) relaxation time distribution.

The RTD for sample R1 is characterized by one pronounced peak at about 4 ms and a minor peak at about 70 ms. Following the standard classification of RTDs [19] more than 95% of the signal originates from pores with relaxation times smaller than 33ms and hence, classifies as bulk volume irreducible (BVI) and clay bound water (CBW). This already indicates the tight character of the sample.

A pre-characterization of the intrinsic properties before conducting the actual drainage experiment is generally advisable. Thereafter, the experimental protocol can be adjusted accordingly, i.e., with respect to the choice of initial pressure difference or the amount of pressure steps. If, for instance, samples exhibit a narrow pore size distribution, only a few (densely spaced) pressure steps can be applied before the irreducible water saturation is reached.

## 4.2 Drainage Experiment

The drainage experiment was conducted at 15 MPa confining pressure. The differential pressure ranged from

0.2 to 2.4 MPa and the sample was drained to a $S_{\mathrm{w,irr}}$ of 0.13. The temperature over the course of the entire experiment was (19.97 ± 0.21 °C).

During the drainage experiment, we applied five distinct pressure steps (cf. Fig. 5a). At the first differential pressure of 0.2 MPa, no significant saturation decrease and no gas flow could be measured over the course of 24 h. Effective gas permeabilities were measured for the first time once breakthrough occurred and gas flow was established. This happened after approx. 50 h at a differential pressure of 0.4 MPa. In the following, differential pressure was increased approx. every 24 h depending on the equilibration of water saturation and effective gas permeability.

The temperature fluctuation inside the flow cell is depicted in Fig. 5b. The fluctuations show amplitudes of $\pm 0.5$ K over the course of the experiment and decrease towards the end of the experiment. Fig. 5c shows the raw and temperature-corrected NMR amplitudes in gray and black, respectively. There are several events (Fig. 5b, c**)** where the change of temperature clearly influences the NMR amplitudes. For instance, between 24 h and 72 h the temperature varied between $-0.5$ K and 0.5 K yielding a saturation fluctuation of $\pm 10$ %. Figure 5c visualizes the impact of the aforementioned temperature correction. Without correction, water saturation (raw in Fig. 5) increases after the onset of gas flow (≥ 48 h), which is clearly unphysical considering the given experimental setup, but slightly decreases after temperature correction (corr. in Fig. 5). Effective gas permeabilities increased by more than an order of magnitude during the entire measuring cycle from $9.9\ 10^{-19}\ \mathrm{m}^2$ to $2.2\ 10^{-17}\ \mathrm{m}^2$ at differential pressures of 0.4 MPa and 2.4 MPa, respectively.

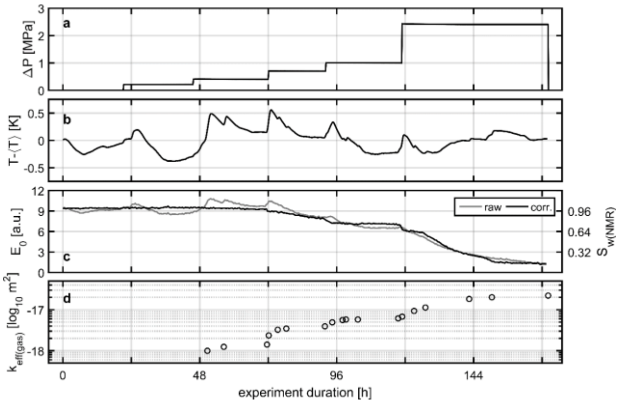

**Figure 5.** Parameters recorded during the drainage experiment: **(a)** differential pressure; **(b)** temperature fluctuation inside flow cell; **(c)** raw (gray) and temperature-corrected (black) initial NMR amplitude or water saturation; **(d)** effective gas permeability.

The increase of effective gas permeability with increasing differential pressure clearly occurs due to the drainage of successively smaller pores. This process can be visualized by contiguously plotting the RTD in a carpet plot, see panel **I** in Fig. 6. Even though we think that the drainage of successively smaller pores dominates the observed RTD changes, the shift towards shorter relaxation times with decreasing saturation might also be caused by the associated changes in the surface-to-volume ratio of drained pores. For example, water trapped in the corners of a desaturated angular pore contributes to the RTD with considerably smaller relaxation times than the originally saturated pore [35]. Panel **I** in Fig. 6 shows the relative amplitudes of the RTD (incremental porosity cf. Fig. 4b) ranging from 0.005 % (white) to 0.35 % (black) over the entire duration of the experiment. For better visualization, all amplitudes smaller than 0.005 % are not shown. The orange points in panel **I** indicate the logarithmic mean relaxation time $T_{\mathrm{lgm}}$ for every individual relaxation time distribution. It shows the change of the (logarithmic) mean size of the water saturated pores over the course of the experiment. For reference, the corresponding full saturation relaxation time distribution is shown in panel **II**. In panel **III** the temperature-corrected saturation $S_{\mathrm{w(NMR)}}$ is plotted, which is given by the ratio of the initial NMR amplitudes $E_0(t > 0)$ to the first initial NMR amplitude at full saturation $E_0(t = 0)$.

During the first 48 h of the drainage experiment, the saturation stays constant and all relaxation time distributions are very similar (cf. Fig. 4b). Like for the saturation, there is no visible change of relaxation times at the first pressure step of 0.2 MPa (after 22 h), i.e., the pressure is not high enough to establish a percolation pathway in the pore network. When increasing the differential pressure to 0.4 MPa (between $48 - 72$ h) gas breakthrough is observed and saturation, as well as $T_{\mathrm{lgm}}$, decrease only slightly. At 0.7 MPa differential pressure ($72 - 90$ h), saturation and $T_{\mathrm{lgm}}$ decrease significantly mainly due to the drainage of larger pores ($> 20$ ms). After a first strong decrease in saturation and $T_{\mathrm{lgm}}$ at 1 MPa differential pressure the decrease levels off and all values stay constant for approximately 24 h. The final increase to 2.4 MPa differential pressure yields a rather strong drainage effect and a final water saturation of $S_{\mathrm{w(NMR)}} = 0.13$. Here, the strong drainage relates to pores having relaxation times between $1 - 10$ ms. We cross-checked the final saturation by weighing the sample after the experiment and it was found to be $S_{\mathrm{w(weigh)}} = 0.15$, so comparable to the value derived from the NMR measurement.

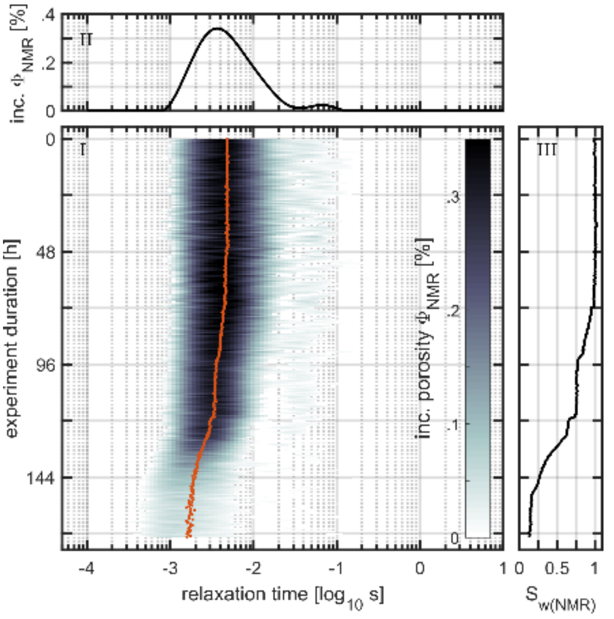

**Figure 6.** panel **(I)** RTDs over experiment duration; panel **(II)** full saturation RTD; panel **(III)** water saturation over experiment duration; orange points in panel (I) refer to the logarithmic mean relaxation time $T_{\mathrm{lgm}}$.

### 4.3 History Matching

The simultaneous recording of average water saturation (water production) and pressure gradient throughout a drainage experiment allows to history match recorded data by a two-phase flow simulator. A 1D model is used for the simulation assuming a homogeneous rock in all three dimensions. Software packages available are similar to reservoir black-oil simulators [36] and based on immiscible displacement of the fluid phases [37, 38]. They fit experimental data at distinct time steps, e.g., pressure gradient, water production by adjusting capillary pressure and relative permeability as these curves are related to pressure and saturations. Analytical functions as Corey (power law), LET, Log (beta) etc. or measured data can be selected. In this study the software Cydar© [39] was used to history match the data. In order to constrain the number of solutions, the measured relative gas permeability curve was fitted using Corey exponents and considered invariable throughout the history match. The history match was run by simulating the NMR water saturations and pressure recordings and adjusting the analytical curves of the relative permeability of water and the drainage capillary pressure. Figure 7 shows a comparison of the measured and simulated water production, the measured and simulated pressure gradients and the relative permeability curves of gas and water, as well as the drainage capillary pressure data. The capillary pressure function includes an entry pressure ($P_e$) where gas starts to enter the pore space and displaces the water phase. The value of this entry pressure is consistent with the experimental differential pressure where a decrease of the NMR water saturation was observed. The analytical functions simulating the experimental data in 1D are according to [40, 41].

$$S_{wn} = (S_w - S_{wirr})/(1 - S_{wirr}), \tag{9}$$

$$P_c = P_e - \alpha \log S_{wn}, \tag{10}$$

$$k_{rw} = k_{rw0}(S_{wn})^{Nw}, \tag{11}$$

$$k_{rg} = k_{rg0}(1 - S_{wn})^{Ng}, \tag{12}$$

with $S_w$ the measured water saturation, $S_{wirr}$ the residual water saturation, $P_e$ the pore entry pressure, $\alpha$ as fitting parameter, $k_{rw}$ and $k_{rg}$ the relative permeabilities of water and gas respectively, and $Nw$ and $Ng$ the Corey fitting parameters.

Figure 7a+b show the history match results for water saturation and differential pressure from the drainage experiment of sample R1. In Fig. 7c, the measured relative permeability (circles) is plotted. The fitted relative permeability for gas (dashed lines) and water (solid lines) are derived from history matching the monitored water saturation, pressure gradient and effective permeabilities. For the presented data, the derived Corey parameters yield a robust estimation of relative gas permeability over the entire water saturation range. Additionally, capillary pressure data can also be obtained from the history match, as shown in Fig. 7d.

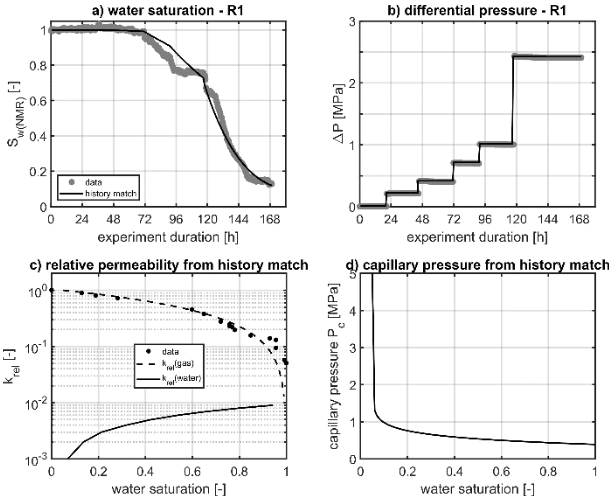

**Figure 7.** **(a)** History matched water saturation and **(b)** differential pressure for sample R1; **(c)** estimated relative permeabilities and **(d)** capillary pressure derived from history matching the monitored data for all four samples. The circles in panel a, b and c show the corresponding experimental data.

## 5 Conclusion

With the combined NMR and fluid flow measurements, we overcome the lengthy experimental series of different experiments (repetitive pre-saturation tests and permeability experiments). The test measurements proved crucial and resulted in significant improvements for the workflow and thus data quality.

The combination of NMR relaxation measurements and two-phase fluid flow experiments allows for the continuous allocation of water saturation $S_{\mathrm{w(NMR)}}$ to differential pressure $\Delta p$ (respectively capillary pressure $P_c$). Moreover, it provides information about the changing water distribution within the pore space, i.e., about the size of the water filled pores over the course of the experiment. Furthermore, with the flow cell setup, we directly measure the relationship between water saturation and effective gas permeability $k_{\mathrm{eff(gas)}}$.

After accounting for temperature fluctuations, the monitored changes in water saturation proved very accurate. However, for future experiments, it may be advantageous to place the whole setup in a temperature-controlled container.

The data, recorded with the NMR flow cell, can be utilized for the parametrization of the relations between effective permeability, water saturation and capillary pressure by an inverse simulation of the experiment, i.e., by a history match. Hence, the results can readily enter a reservoir simulation.

The authors gratefully acknowledge Wintershall Holding GmbH for funding the iLoPS research project, within this study was conducted. We also like to thank Bernhard Krooss, Jonas Kaiser and Lena Kämpfner for their valuable input and help with the experimental setup.

## References

1 E.J. Peters, *Advanced Petrophysics: Geology, Porosity, Absolute Permeability, Heterogeneity and Geostatistics,* **1**, Live Oak Book Company (2012)

2 M. Miller, B. Lieber, G. Piekenbrock and T. McGinness, “Low Permeability Gas Reservoirs How Low Can You Go?” SPWLA Middle East Regional Symposium (2007)

3 K.W. Shanley, R.M. Cluff and J.W. Robinson, “Factors controlling prolific gas production from low-permeability sandstone reservoirs: Implications for resource assessment, prospect development, and risk analysis,” AAPG bulletin, **88**, 1083-1121 (2004)

4 A. Amann-Hildenbrand, J.P. Dietrichs and B.M. Krooss, “Effective gas permeability of Tight Gas Sandstones as a function of capillary pressure–a non-steady-state approach,” Geofluids, **16**, 367-383 (2016)

5 W.R. Purcell, “Capillary Pressures - Their Measurement Using Mercury and the Calculation of Permeability Therefrom,” Trans., AIME **186**, 39-48 (1949)

6 J.S. Osoba, J.G. Richardson, J.K. Kerver, J.A. Hafford and P.M. Blair, “Laboratory Measurements of Relative Permeability,” Trans., AIME **192**, 47-56 (1951)

7 M.M. Honarpour, F.Koederitz and A. Herbert, *Relative permeability of petroleum reservoirs*, CRC Press Inc, Boca Raton, FL (1986)

8 C.L. Vavra, J.G. Kaldi and R.M. Sneider, “Geological applications of capillary pressure: a review (1),” AAPG Bulletin, **76**, 840-850 (1992)

9 D. Tiab and E.C. Donaldson, *Petrophysics: Theory and Practice of Measuring Reservoir Rock and Fluid Transport Properties*, 4th ed., Waltham (USA): Gulf Professional Publishing (2015)

10 R.K. Estes and P.F. Fulton, “Gas slippage in permeability measurements,” J. Pet. Tech, **8**, 69-73 (1956)

11 J.A. Rushing, K.E. Newsham and V.a.K.C. Fraassen, “Measurement of the Two-Phase Gas Slippage Phenomenon and its Effect on Effective Gas Permeability in Tight Gas Sands,” SPE Annual Technical Conference and Exhibition (2003)

12 A. Amann-Hildenbrand, M. Shabani, T. Hiller, N. Klitzsch, N. Schleifer and B. M. Krooss, “ Gas Slippage in Partially Saturated Tight Rocks and During Drainage,” *SCA2019, #79* (2019)

13 H.P.G. Darcy, *Les Fontaines publiques de la ville de Dijon*, Victor Dalamont (1856)

14 A. Kundt, E. Warburg, “Über Reibung und Wärmeleitung verdünnter Gase,” Annalen der Physik, **232**, 177-211 (1875)

15 M. Knudsen, “Die Gesetze der Molekularströmung und der inneren Reibungsströmung der Gase durch Röhren,” Annalen der Physik, **333**, 75-130 (1909)

16 L.J. Klinkenberg, “The permeability of porous media to liquids and gases,” Drilling and production practice (1941)

17 L. Qingjie, L. Baohua, L. Xianbing, Y. Shouguo, “The effect of water saturation on gas slip factor by pore scale network modeling,” SCA 2002 Symposium (2002)

18 E.W. Washburn, “The dynamics of capillary flow,” Phys. Rev., **17**(3),. 273-283 (1921)

19 G.R. Coates, L. Xiao, M.G. Prammer, *NMR logging: principles and applications* (1999)

20 A.A. Behroozmand, K. Keating and E. Auken, “A review of the principles and applications of the NMR technique for near-surface characterization,” Surveys in Geophysics, **36**, 27-85 (2015)

21 K.J. Dunn, D.J. Bergman and G.A. LaTorraca, *Nuclear magnetic resonance: petrophysical and logging applications* (2002)

22 K. Keating and R. Knight, “A laboratory study of the effect of magnetite on NMR relaxation rates,” J. Appl. Geophys., **66**, 188-196 (2008)

23 K. Keating and R. Knight, “A laboratory study of the effect of Fe (II)-bearing minerals on nuclear magnetic resonance (NMR) relaxation measurements,” Geophysics, **75**, F71-F82 (2010)

24 J. Mitchell, T.C. Chandrasekera, M.L. Johns, L.F. Gladden and E.J. Fordham, “Nuclear magnetic resonance relaxation and diffusion in the presence of internal gradients: The effect of magnetic field strength,” Phys. Rev. E, **81(**2), 026101 (2010)

25 K.R. Brownstein and C.E. Tarr, “Importance of classical diffusion in NMR studies of water in biological cells,” Phys. Rev. A, **19**(6), 2446-2453 (1979)

26 W.E. Kenyon, “Petrophysical principles of applications of NMR logging,” The Log Analyst, **38**(2), 21-43 (1997)

27 J. Hadamard, *Lectures on Cauchy's problem in linear partial differential equations*, Yale University Press, New York (1923)

28 R.C. Aster, B. Borchers, C.H. Thurber, *Parameter Estimation and Inverse Problems*, 2nd ed. (2013)

29 P.C. Hansen, *Rank-Deficient and Discrete Ill-Posed Problems: Numerical Aspects of Linear Inversion,* SIAM Philadelphia, (1998)

30 K. Halbach, “Design of permanent multipole magnets with oriented rare earth cobalt material,” Nucl. Instrum. Methods, **169**, 1-10 (1980)

31 S. Anferova, V. Anferov, J. Arnold, E. Talnishnikh, M.A. Voda, K. Kupferschläger, P. Blümler, C. Clauser and B.

Blümich, “Improved Halbach sensor for NMR scanning of drill cores,” Mag. Res. Imag., **25**, 474-480 (2007)

32 H.Y. Carr and E.M. Purcell, Phys. Rev., **94**(3), 630-638 (1954)

33 S. Meiboom and D. Gill, “Effects of diffusion on free precession in nuclear magnetic resonance experiments,” Rev Sci. Instrum., **29**(8), 688-691 (1958)

34 P. Egermann, J.M. Lombard and P. Bretonnier, “A fast and accurate method to measure threshold capillary pressure of caprocks under representative conditions,” *International Symposium of the Society of Core Analysts* (2006)

35 O. Mohnke, R. Jorand, C. Nordlund and N. Klitzsch, “Understanding NMR relaxometry of partially water-saturated rocks,” Hydrol. Earth Syst. Sci., 19, 2763-2773 (2015)

36 K. Aziz and A. Settari, *Petroleum reservoir simulation* (1979)

37 E.F. Johnson, D.P. Bossler and V.O. Naumann, “Calculation of relative permeability from displacement experiments,” Pet. Trans., AIME, **216**, 370-372 (1959)

38 S.C. Jones and W.O. Roszelle, “Graphical techniques for Determining Relative Permeability from Displacement Experiments,” J. Pet. Tech., **30**, 807-817 (1978)

39 R. Lenormand and G. Lenormand, *Cydar© User Manual*, Cydarex© Company Brochure (2016)

40 A.T. Corey, “The interrelation between gas and oil relative permeabilities,” Producers monthly, **19**, 38-41 (1954)

41 R.G. Bentsen and J. Anli, “Using parameter estimation techniques to convert centrifuge data into a capillary-pressure curve,” Soc. Pet. Eng. J., **17**, 57-64 (1977)

# Transport properties of the Cobourg Limestone: A benchmark investigation

*C. A.* Davy[1*], *Zhazha* Hu[2], *A.P.S.* Selvadurai[3], *Jop* Klaver[4], *M.-C.* Willemetz[1], *F.* Agostini[1], *F.* Skoczylas[1], *Jan* Dewanckele[5], *Alexandra* Amann-Hildenbrand[2] and *Roland* Lenormand[6]

[1]Centrale Lille, CS 20048, 59651 Villeneuve d'Ascq Cedex, France
[2]Energy and Mineral Resources Group, RWTH Aachen University, 52064 Aachen, Germany
[3]Department of Civil Engineering and Applied Mechanics, McGill University, Canada
[4]Microstructure and Pores GmbH, 52064 Aachen, Germany
[5]TESCAN XRE, 9052 Ghent, Belgium
[6] CYDAREX 31 Av. Gabriel Péri, 92500 Rueil-Malmaison, France

**Abstract.** Cobourg limestone formation is proposed as a possible repository site for nuclear wastes in Canada. This limestone displays significant heterogeneity, characterized by light grey calcite nodular regions, interspersed with dark grey calcite-dolomite-quartz partings containing a clay component. Mineral composition is dominated by calcite, with some minor amounts of ankerite, illite/muscovite/I-S and quartz. Analysis of the pore structure show that Cobourg limestone is extremely tight with porosities between 0.33 and 2.51%.
This paper aims at both, a comprehensive description of the transport properties of the Cobourg limestone on the nm- to cm-range, and the comparison of different experimental techniques: gas measurement using decay, quasi-static, or steady-state methods. In total four labs measured permeability, porosity and analysed the pore system by various methods (micro-CT, BIB/SEM). In all flow experiments, slip flow was accounted for by means of the Klinkenberg correction.
Effects of pore pressure, confining pressure, sample size and coring orientation are studied. For all laboratories, results range from 100 microDarcy to 1 nanoDarcy. Even for a given laboratory, results are comprised in a broad range, with several orders of magnitude differences depending on coring direction, confining pressure and sample size. Flow occurs through slit shaped pores/fractures, which are orientated along heterogeneities. Upon loading, these natural and/or artificial pores successively close, resulting in a reduced permeability and stress sensitivity.
Results are dominated by heterogeneity and anisotropy of the Cobourg limestone, so that it is delicate to select one method over another. Rather, each brings useful information to better understand this low permeability and low porosity natural material.

## 1 Introduction

### 1.1 Background

The Cobourg limestone formation is located in the eastern shores of Lake Huron in southern Ontario, Canada. The interest in the limestone stems from its potential suitability as a host rock of a Deep Geologic Repository (DGR) for storing low- and intermediate-level radioactive waste. This choice is enhanced by the proximity of the DGR to the Bruce Nuclear Facility, in Ontario, Canada. The planned depth of the DGR is approximately 680 m below ground level, within the Cobourg limestone formation of the Paleozoic sedimentary sequence that rests on a Pre-Cambrian granitic gneiss basement rock. The Cobourg limestone host rock is overlain by the upper Ordovician siltstone and grey shale extending to a thickness of approximately 200 m and underlain by argillaceous limestone and grey shale, about 150 m thick, resting on the granitic basement rock of the Canadian Shield. Despite its low clay content, the Cobourg limestone is nominally referred to as an *argillaceous limestone*. It shows fabric heterogeneity, consisting of *lighter* nodular regions of calcite and dolomite separated by *darker* argillaceous partings of a similar composition with additional quartz and low clay content (Figure 1). In the literature, the consensus is that the rock displays some nominal evidence of "stratification" resulting from the nodular fabric (the *light grey rock*) that contains calcite and dolomite interspersed by the partings (the *dark grey rock*) that contains calcite, dolomite and a clay fraction. The lighter calcite-dolomite nodular regions can have dimensions in the range of 25 mm, which places a restriction on the sample size that can capture a representative volume element (i.e. a cross-sectional area and length of flow path; Figure 1).

Previous researches on permeability testing of Cobourg limestone have been conducted by several investigators using both *in situ* packer testing and laboratory testing. In the former types of tests, the influence of scale is addressed indirectly through the selection of a packer length and borehole diameter that can capture a representative surface area. In the latter

---

[*] Corresponding author: catherine.davy@centralelille.fr

category of tests, the sample dimensions, notably the cross-sectional area of cylindrical samples is chosen to capture a representative area fraction. The length of the flow path is selected to minimize the time needed to establish a steady state.

**Figure 1.** The visual heterogeneity of the Cobourg limestone (top) cuboid measuring 300 mm (bottom) modular regions in a zone measuring 100 mm x 130 mm

The research reported by Vilks and Miller [1], Selvadurai et al. [2], Selvadurai and Jenner [3] and Selvadurai and Najari [4,5] present results of laboratory research of one-dimensional flow conducted on specimens with diameters ranging from 50 mm to 100 mm and flow paths ranging from 5 mm to 200 mm. The measured permeabilities ranged from $10^{-23}$m$^2$ to $10^{-19}$ m$^2$. The work of Selvadurai and Glowacki [6] deals with the measurement of the local permeability of the heterogeneous Cobourg limestone.

### 1.2 Aims and scopes

The determination of permeability in the nanoDarcy-range is always challenging due to the small flowrates. So far, there is no standard procedure or reference samples. Different research laboratories follow different approaches and comparing the results therefore is difficult. Differences might be induced by the use of different fluids, the flowrate measurement technique itself, sample size, sample confinement, and loading history.

This research focuses on the testing of suitable sample sizes that can satisfy the constraints imposed by the heterogeneity of the Cobourg limestone and accomplish the testing at a reasonable time duration.

This benchmark was launched by the department of Civil Engineering at McGill University who provided samples to all the involved laboratories.

A similar study was published by Profice [7] with the conclusion of good agreement between the different methods and laboratories, but that study was conducted on pyrophyllite, a very homogeneous rock with liquid permeability in the range of 100 nanoDarcy.

In the following, the methodologies for measuring permeability used by four different laboratories are presented: gas pressure decay, quasi-static, step decay or steady-state methods. We always performed the Klinkenberg correction to derive permeabilities independent of fluid nature (nitrogen, helium or brine). Further, porosity measured at ambient conditions and under stress, and permeability results are presented. Porosity and permeability results are presented and discussed with respect to the effects of pore pressure, confining pressure, sample size and coring orientation. The results are also compared to literature data, especially the liquid permeability measurements performed by McGill.

## 2 Materials and methods

### 2.1 Materials

The samples received by all participants are cored from blocks of the Cobourg limestone, that have been obtained from the Saint Mary's Quarry, located in Bowmanville Ontario, Canada. The original block samples measured approximately 2 cubic meters.

Whenever requested by the participants (McGill and RWTH Aachen University), the samples are cored out from cubical samples (measuring 100mm, 150mm, or 200mm) of the Cobourg Limestone. Each cubic sample is in an air-dry condition.

The operating speed of the corer is 600 rpm. The feed rate is at 0.127 mm per revolution. For the machining of the samples to the requested dimensions, we use a lathe with a diamond tip cutter. The lathe is operated at 550 rpm and the feed speed is at 30 mm/min. The samples are mostly cored perpendicular to the nominal bedding plane. Some participants, however, also requested samples that were cored parallel to the nominal bedding plane.

### 2.2 Experimental approach at Mc Gill University

As has been shown by Selvadurai [8], gas steady state tests needs very long time for equilibrium, while hydraulic pulse tests can be conducted in a short duration. In order to interpret the results of hydraulic pulse tests, the pore space of the sample needs to be completely saturated and parameters such as the porosity, the skeletal compressibility and solid material compressibility are needed to correctly estimate the hydraulic pulse decay in a pressurized region in contact with the Cobourg limestone.

Therefore, the research presented here involves performing one-dimensional steady state flow tests on cylindrical samples with a cross-sectional diameter of 150 mm and an axial flow path of 50 mm. The permeability tests are performed in an active GDS Triaxial Cell, which is used to apply a pressure of 5 MPa to ensure impervious contact between the sample and the enclosing rubber membrane. The sample (with stainless steel porous discs on the plane ends) is encased within the nitrile rubber sleeve exposed to vacuum desaturation for a period of two weeks in the test cell. A precision pump is used to initiate a hydraulic gradient with inlet pressures ranging from 0.5 MPa to 1.5 MPa. Figure 2 shows a typical arrangement for conducting the steady state permeability test.

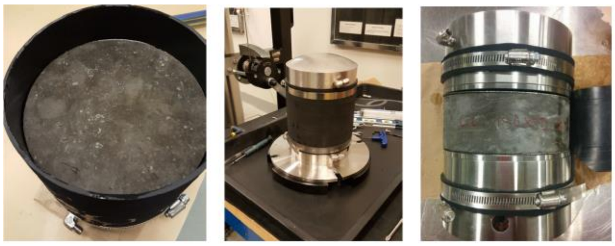

**Figure 2.** Steady state permeability tests conducted on the Cobourg limestone at Mc Gill University

The flow rate is accurately determined by measuring the volume of fluid injected for a given time.

## 2.3 Experimental approach at RWTH Aachen University

### *2.3.1 Materials*

For sample preparation, RWTH-Aachen University received a block of about 10x5x5 $cm^3$ from McGill University. Three cylindrical sample plugs of 38 mm in diameter (samples C, D and E) were drilled in this block. Additionally, we received another sample, which had been already trimmed to the required dimensions (sample B, provided by the Structural Engineering Laboratories of McGill University). The height of samples B, C, D and E are 26.48, 44.56, 42.43 and 35.04 mm, respectively

### *2.3.2 Gas transport experiments*

Samples were dried at 105 °C in a vacuum oven for at least 24 h. Subsequently, porosity and gas permeability were measured with gas. Tests are run at different confining pressure levels up to 20 MPa. In most cases, experiments are conducted on the second loading and unloading cycle. Helium is used as the gas phase.

Gas permeability is determined by the constant downstream pressure procedure, where the volume flow rate is calculated from the pressure decay in the upstream compartment (Figure 3). Due to the simultaneous decrease in mean pressure, slip flow can be accounted for by means of the Klinkenberg correction from only one pressure decay curve. Details about the experimental method are described in [9-10].

### *2.3.3 Additional analysis*

Qualitative XRD analysis demonstrates that the Cobourg limestone is dominated by calcite (79.05%), ankerite (9.31%), illite/muscovite/I-S (5.12%) and quartz (4.81%) (Table 1).

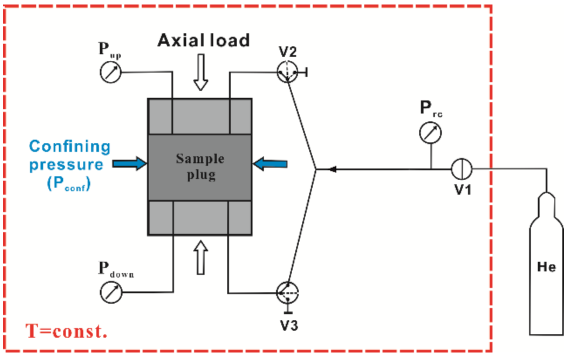

**Figure 3.** System sketch used for both pore volume and permeability measurements under defined confining pressures (The reference cell consists of the volume of the lines between valves 1, 2 and 3. The pressures in reference cell and top and bottom compartments ($P_{rc}$, $P_{up}$ and $P_{down}$) are recorded by PMP 4070 pressure transducers)

**Table 1.** XRD result of the Cobourg limestone

| Calcite (%) | Ankerite (%) | Illite/muscovite/I-S (%) | Quartz (%) | Kaolinite (%) | Pyrite (%) |
|---|---|---|---|---|---|
| 79.05 | 9.31 | 5.12 | 4.81 | 1.22 | 0.48 |

Analyses of the pore structure by micro-CT and BIB-SEM analysis show that the Cobourg limestone is extremely tight. Isolated, irregularly shaped pores up to 10th-nm to several µm-range are observed in calcite grains. In the clay matrix, slit-shaped pores of about 100 nm in width appear to be interconnected. Micro-CT imaging indicates open discontinuities in sample B, which is further identified as stylolites containing a higher percentage of clay minerals in BIB-SEM.

He-pycnometry under unconfined conditions shows that porosity values of all plugs are below 3% (Table 2). There is no measurement of porosities under stress.

**Table 2.** Porosity values of samples under unconfined conditions

| Sample | B | C | D | E |
|---|---|---|---|---|
| Porosity (%) | 1.02 | 0.98 | 2.51 | 1.83 |

## 2.4 Experimental approach at Centrale Lille

The initial cube (measuring 150mm) provided by Mc Gill University (reference S6-13) is labelled with a letter on each face (U and T, or B and D, or C and A, on parallel faces respectively). It is cored at Centrale Lille along the cube three main axis (labelled respectively U-T, B-D and C-A). This provides cylindrical samples of 65mm diameter, which are cut to a given height, comprised between 18.9 and 36.4mm (Figure 4). This location is chosen to be in the calcite-dolomite nodular regions, which can have dimensions in the range of 25 mm, or slightly bigger. No bigger sample was tested, in order to limit the duration of permeability experiments.

**Figure 4.** Sample preparation from a cube provided by Mc Gill University to cylinders of 65 mm diameter and varying height

**Table 3.** Sample volume and porosity results for 15 cylindrical samples cored out of a Cobourg limestone cube.

| | Sample height (mm) | Sample diameter (mm) | Porosity (%) |
|---|---|---|---|
| U1, U2, U3, U4, U5 | 20.6, 23.7, 17.0, 25.0, 26.9 | 65.2 | 0.93, 0.67, 0.69, 0.53, 0.33 |
| D1, D2, D3, D4, D5 | 18.7, 36.4, 17.8, 23.6, 31.3 | 65.2 | 0.99, 0.55, 0.61, 0.56, 0.33 |
| C1, C2, C3, C4, C5 | 18.5, 18.8, 32.9, 13.3, 25.6 | 65.3 | 1.21, 0.44, 0.59, 0.74, 0.43 |

As suggested by Mc Gill University, the final characteristics of the samples, i.e. their water-saturated mass, their dry mass and volume, are recorded prior to conducting the permeability tests. To this purpose, each cylinder is oven-dried at 105°C until mass stabilization.

A total of 15 samples (5 along each main axis of the initial cube) has been tested for porosity (by the water saturation method), see Table 3, out of which 4 have been tested for gas permeability. Bulk volume is determined from length and diameter of the cylinders. Standard accuracy of 1 PU is assumed for porosity.

Samples D1, D2, C3 and U5 have been tested for gas permeability. To this purpose, each sample is placed in a triaxial cell and tested at successive confining pressures of 5, 10 and 15 MPa and gas pressures of 0.5, 1.0 and 1.5 MPa (with Argon). Gas pressure is varied to quantify Klinkenberg corrected. Gas permeability is measured in the quasi-static state using either the upstream or the downstream pressure, measured just before or just after the sample (see Figure 5). The upstream gas pressure is used to analyse permeabilities down to $10^{-18}$ m$^2$ (i.e. 1$\mu$D), whereas downstream pressure is for lower permeabilities, down to $10^{-20}/10^{-21}$ m$^2$ (i.e. 1-10 nD).

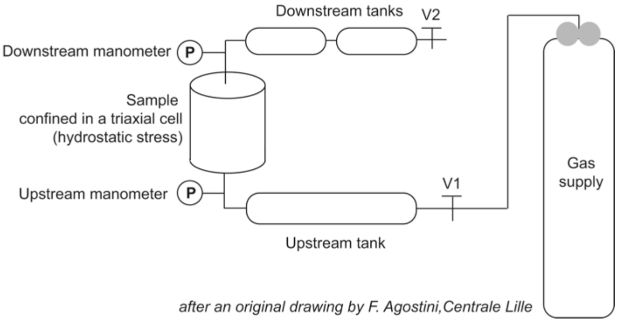

after an original drawing by F. Agostini,Centrale Lille

**Figure 5.** Quasi-static gas permeability set-up available at Centrale Lille, using either the upstream or downstream gas tanks, depending on the expected order of magnitude of permeability

The effect of sample direction and height is analysed, as well as the effect of sample confinement (hydrostatic loading) and Klinkenberg effect [11-12].

## 2.5 Experimental approach at Cydarex

A unique feature of our approach is to use small samples in order to minimize the contribution of large-scale core fractures and to reduce the durations of equilibrium before measurements and duration of measurement since all these durations are proportional to the square of the length of the samples. The principle is described in a previous SCA paper [13].

We performed two types of measurements: a measurement at different pore pressures to determine the Klinkenberg corrected permeability and the determination of a permeability profile over 7 cm to quantify the heterogeneity at the scale of 5mm.

### *2.5.1 Manufacturing of resin disks*

For the profile measurement, a cylindrical sample with diameter of 12.5 mm was embedded in resin. Once embedded in resin, several adjacent thin slices were cut parallel to the bedding plane, with thicknesses 3.4 mm (figure 6). After polishing, the slices were then put between two steel end-pieces (figure 7) and mounted in a hydraulic press (Figure 8).

**Figure 6**- Resin disk sample

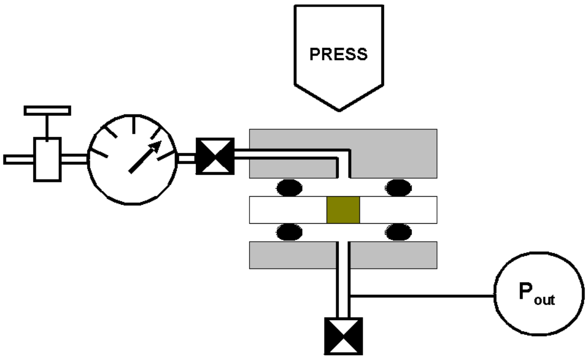

**Figure 7**- Resin disc: experimental setup with constant pressure injection (injection with a constant volume can also be used)

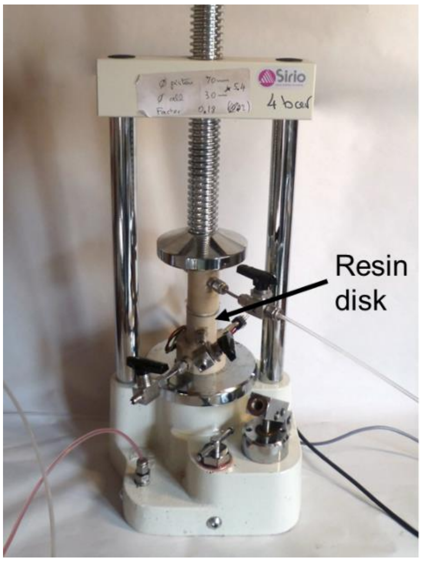

**Figure 8** – The cell under the press

*2.5.2 Principle of permeability measurements*

Because the original sample is cut parallel to the Cobourg limestone bedding planes, gas flow in the disc will be perpendicular to the bedding (vertical flow in the reservoir).

Measurements are performed with nitrogen at room temperature. Vertical pressure applied by the press acts on both the resin and the rock. Assuming that the resin is "soft" compared to the rock, the stress on the sample is around 190 bars (19 MPa).

The entry can be connected to several vessels of different volumes. The outlet is closed on a small volume. Inlet and outlet pressures are measured. By measuring the pressure at the outlet, any leakage on the high-pressure part of the apparatus is irrelevant, since the real inlet pressure is recorded and used in the numerical simulation.

The main error comes from the estimate of the surface area of the embedded sample when the shape is not circular. The overall error is estimated to be less than 10% of the measured value.

*2.5.3 Numerical simulations*

Interpretations of the results are performed using the commercial software CYDAR. The simulation is in one dimension and assumes perfect gas with Klinkenberg and Forchheimer corrections. The numerical scheme is "implicit" and the system is solved using a Newton-Raphson algorithm. Parameters such as permeability, Klinkenberg coefficient $\beta$ can be optimized using a nonlinear least-squares minimization algorithm (Levenberg-Marquardt). For the experiments performed on low permeability samples, the cost function is calculated only on outlet pressures.

*2.5.4 Porosity measurement*

The solid volume is obtained from gas expansion and pore volume is given by the difference in weight between brine saturated and dry sample. Accuracy is around 1 P.U

## 3 Accuracy of the results

In this domain of very low permeabilities, there is no reference sample that can be used to calibrate the apparatus. Accuracy must be estimated from the instruments and the procedure.

Standard error calculation accounts for errors on the size of the sample, on pressure sensors, on fluid viscosity linked to the temperature, on atmospheric pressure (not always measured). The different laboratories estimate the relative error due to the instruments and fluid properties to be less than 10% of the measured permeability values.

Another source of error is the leaks. The leaks from the upstream circuit to the atmosphere are determined by using an impermeable sample. More difficult to estimate is the leaks between the sample and the rubber sleeve. For each equipment, a minimum confining pressure is always determined.

For gas measurements, the determination of the Klinkenberg correction is always a source of error since it is based on an optimisation process or an extrapolation at origin in the Klinkenberg plot. For Cydarex, the measurements are performed with three points at different pressures and the correlation coefficient is always larger than 0.98. For the measurement reported in the next section, the extrapolated Klinkenberg corrected permeability is 0.12 nD +/- 0.01 nD. The range is determined using the extreme values calculated with only 2 points. We can consider that the Klinkenberg correction adds 10% in the error.

## 4 Results

### 4.1 Permeability at Mc Gill

Steady state tests were conducted on cylindrical samples of the Cobourg. Transverse permeability ($K_T$) is determined with bedding plane along the axis of the sample and normal permeability ($K_N$) with bedding planes perpendicular to the axis of the sample

The measured flow rates range from 4.02 x$10^{-5}$ ml/min to 6.83 x$10^{-3}$ ml/min. The experimental results gave the following:

$$K_N = (2.0 \ to \ 3.9)10^{-21} \mathrm{m}^2$$

and

$$K_T = (2.2 \ to \ 4.2)10^{-19} \mathrm{m}^2,$$

with the observation that the lower limit of permeability is obtained for the higher inlet pressure (highest pore pressure).

### 4.2 Porosity and permeability experiments under defined confining pressure conditions at RWTH Aachen University

#### *4.2.1 Porosity*

Porosity of the loaded samples was determined by He-expansion from a calibrated reference volume into the flow cell. Volume of solid is derived from the mass and the grain density. Error is around 1 PU. Porosity is ranging between 0.6 and 2.1% and decreases with increasing confining pressure. Loading from 4 MPa to 19 MPa leads to a reduction by 8-13% (Figure 8). The exponential stress sensitivity coefficient of porosity varies in between 0.004-0.010 MPa$^{-1}$. The porosity values on the first unloading path are about 92% to 100% of the corresponding values on the first loading path (Figure 9).

Klinkenberg-corrected permeabilities at 5 MPa confining pressure range in between 5x$10^{-20}$ and 1x$10^{-17}$ m$^2$ (Table 4). Sample B has the highest Klinkenberg-corrected permeability, which is related to the open discontinuities identified by micro-CT. During the first loading path from 5 MPa to 20 MPa, the Klinkenberg-corrected permeability decreases by 49-67%. The exponential stress sensitivity coefficients for permeability is much larger than those for porosity, ranging in between 0.030 and 0.071 MPa$^{-1}$.

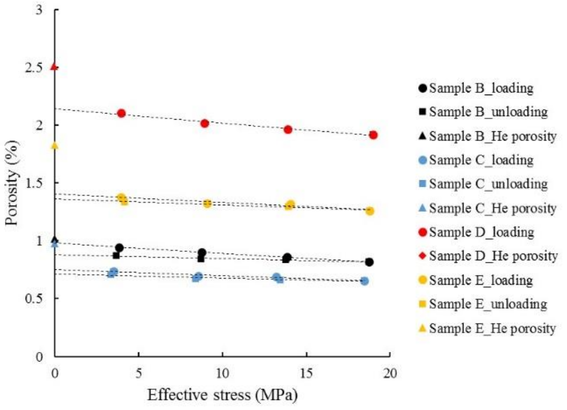

**Figure 9.** Relationship between porosity and effective stress

#### *4.2.2 Gas permeability*

**Table 4.** Klinkenberg-corrected permeabilities (m$^2$) at different confining pressures in one load-unload cycle

| Confining pressure (MPa) | B | C | D | E |
|---|---|---|---|---|
| 5 | $1.45\times10^{-17}$ | $4.64\times10^{-20}$ | $2.29\times10^{-19}$ | $1.17\times10^{-19}$ |
| 10 | $9.46\times10^{-18}$ | $2.69\times10^{-20}$ | $1.81\times10^{-19}$ | $8.43\times10^{-20}$ |
| 15 | $7.42\times10^{-18}$ | $2.30\times10^{-20}$ | $1.41\times10^{-19}$ | $7.23\times10^{-20}$ |
| 20 | $6.19\times10^{-18}$ | $1.95\times10^{-20}$ | $1.18\times10^{-19}$ | $3.84\times10^{-20}$ |
| 15 | $6.81\times10^{-18}$ | $2.03\times10^{-20}$ | - | $3.86\times10^{-20}$ |
| 10 | $8.27\times10^{-18}$ | $2.19\times10^{-20}$ | - | $4.68\times10^{-20}$ |
| 5 | $1.30\times10^{-17}$ | $3.15\times10^{-20}$ | - | $9.83\times10^{-19}$ |

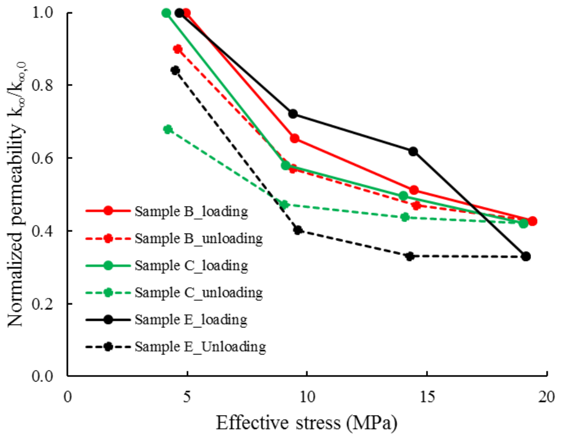

**Figure 10.** Normalized Klinkenberg corrected permeability (permeability at certain effective stress divided by permeability at initial effective stress) versus effective stress for both loading and unloading process

In view of the observed difference between permeability on the first loading path and first unloading path (Figure 10), we conclude to a large hysteresis effect.

### 4.3 Permeability experiments at Centrale Lille

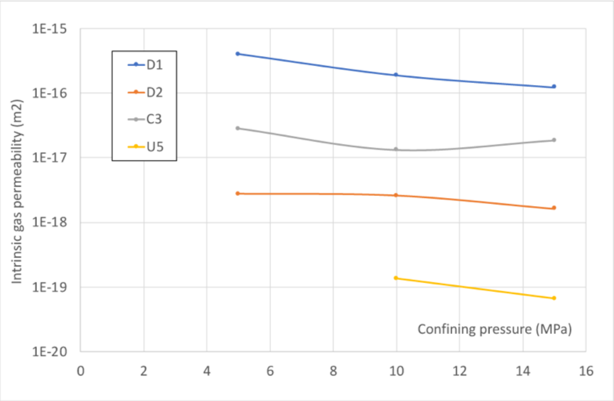

**Figure 11.** Klinkenberg corrected gas permeability (in m$^2$) for all four Cobourg limestone samples tested, as a function of confining pressure Pc (in MPa)

Klinkenberg corrected gas permeability results and associated Klinkenberg coefficient β are given for the three main axis of the original cube provided by McGill, which correspond to directions along or perpendicular to bedding planes of Cobourg limestone, for three given values of confining pressure (Table 5 and Figure 11).

As expected, gas permeability decreases with increasing confinement, meaning that the pore system is sensitive to hydrostatic stress changes. This is frequently observed for slit-like pores (or cracked materials), rather than for more rounded pore systems. In accordance, Klinkenberg coefficient β, which reputedly is proportional to the inverse of a mean pore radius, also increases with increasing confinement.

More interestingly, for the three different sample orientations, highly variable permeability orders of magnitude are obtained. The significantly smaller permeability of U5 sample compared to those in the two other directions is normal for a sample oriented perpendicularly to the bedding planes. For the two samples oriented along the same D axis, i.e. along an axis parallel to the bedding planes, a large range of permeability values were observed gas permeability changes: two orders of magnitude (between $10^{-16}$ and $10^{-18}$ m$^2$, i.e. 1 to 100 μD). This is attributed to the sample size (with a height ranging from 18.7 to 36.4 mm). It is below the biggest size of calcite-dolomite nodular regions for sample D1. The large heterogeneity of Cobourg limestone is clearly identified.

**Table 5.** Klinkenberg corrected gas permeability (in m$^2$) and Klinkenberg coefficient β (in MPa) of four cylindrical samples of Cobourg limestone, tested at three successive confining pressures

| | Sample | D1 | D2 | C3 | U5 |
|---|---|---|---|---|---|
| | Height (mm) | 18.7 | 36.4 | 32.9 | 26.9 |
| | Porosity (%) | 0.99 | 0.55 | 0.59 | 0.33 |
| $K_{int}$ at given confining pressure (MPa) | 5 | $4.0.10^{-16}$ | $2.8.10^{-18}$ | $2.8.10^{-17}$ | N/A |
| | 10 | $1.9.10^{-16}$ | $2.6.10^{-18}$ | $1.3.10^{-17}$ | $14.10^{-20}$ |
| | 15 | $1.2.10^{-16}$ | $1.6.10^{-18}$ | $1.8.10^{-17}$ | $6.6.10^{-20}$ |
| β at given confining pressure (MPa) | 5 | 3.2 | 1.1 | 0.9 | N/A |
| | 10 | 4.4 | 2.7 | 1.3 | 2.2 |
| | 15 | 4.8 | 1.2 | N/A | 2.5 |

### 4.4 Results from Cydarex

#### *4.4.1 Porosity measurement*

For four samples, porosities without confining pressure range between 2 and 3%. Accuracy of the porosity measurement is estimated to 1 PU.

#### *4.4.2 Permeability*

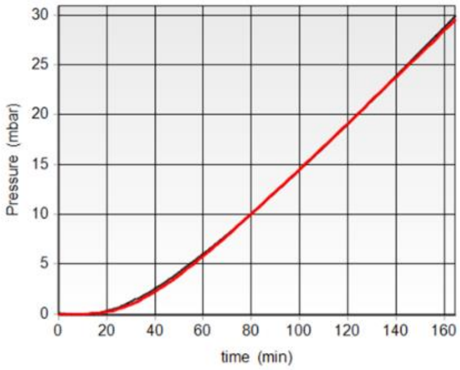

**Figure 12.** Pressure response in the downstream volume as function of time. The experiment in black and the numerical simulation in red are nearly superimposed. The transient below 60 minutes is fitted with a porosity of 1.7%.

Figure 12 shows the record of pressure in the downstream volume when a gas pressure is applied upstream. The outlet pressure shows a delay before starting to increase, due to the accumulation of gas inside the sample. The transient below 60 minutes is fitted with a porosity of 1.7%, in agreement with porosity measurement.

Measurements at different pressures are shown in figure 13. The result is a Klinkenberg-corrected permeability of 0.12 nanoDarcy (0.12 $10^{-21}$ m$^2$) and β = 20 bar (= 2 MPa).

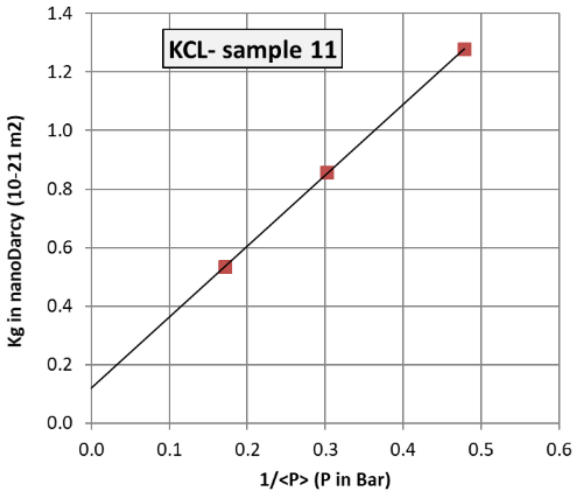

**Figure 13**- Sample 11: determination of the Klinkenberg corrected permeability (0.12 nanoDarcy or 0.12 $10^{-21}$ $m^2$) from the gas permeability measured at 3 different pore pressures. <P> is the average pressure in the sample.

### *4.4.3 Measurement of a permeability profile*

In order to determine the heterogeneity of the sample, we have measured the permeability profile on a plug, using the method of resin disks described previously with a resolution of 5 mm.

Measurements are performed with $N_2$ at room temperature and stress around 19 MPa. Injection pressure is around 10 bar (1 MPa), and the Klinkenberg correction is applied using β = 20 bar, as determined experimentally on sample 11.

The profile shows a spreading between 0.5 and 3 nD (fig. 14). The conclusion is that this sample is quite homogeneous at the scale of 5 mm. A factor 6 is often observed in samples used for core analysis.

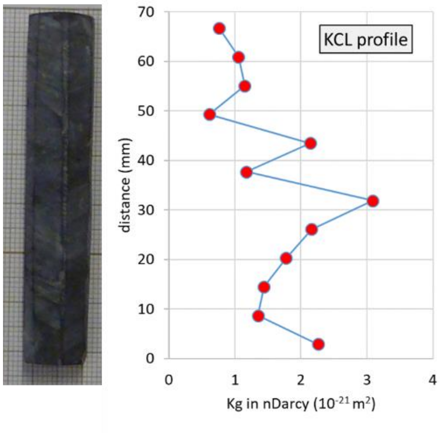

**Figure 14**- Sample and gas permeability profile measured on slices of 5mm.

## 5 Discussion - Conclusions

Performing a benchmark study on Cobourg limestone has shown that the involved teams need to possess a wide range of experimental means, enabling them to handle permeabilities from 0.1nD to 100µD, and several solutions are described to perform these measurements. Despite this wide range of permeability systems, a consistency in the results of the different partners has been found, as follows.

This benchmark study has clearly evidenced that it is a very tight rock, with porosities ranging between 0.33 and 2.51%. This porosity corresponds to a pore system sensitive to changes in hydrostatic stress, i.e. it is made of slit-like pores (similar to cracks).

The significant anisotropy of Cobourg limestone is quantified through gas permeability measurements, with values varying between $10^{-16}$ and $10^{-21}$ $m^2$ (i.e. between 1nD and 100µD) depending on the spatial direction considered.

The 1 nD order of magnitude is obtained with flow direction perpendicular to the bedding planes of Cobourg limestone.

A significant variability of Klinkenberg corrected gas permeability is observed for flow parallel to the bedding planes, with values ranging between 0.1µD ($10^{-19}$ $m^2$) and 10µD ($10^{-17}$ $m^2$). This range of variation over several decades cannot be explained by the error bar that we have estimated at around 20% (10% for the instruments and 10% for the Klinkenberg correction). The effect of stress is around a factor 2 for RWTH Aachen University (Figure 10) and 4 for Centrale Lille (Table 5); and cannot explain the differences.

This large range of permeability is attributed to the effect of heterogeneities and sample size. However, we did not found correlations with the measured permeabilities and sample size.

Coming back to the main purpose of the KCL study, that was the characterization of a nuclear repository site, the conclusion is that laboratory measurements are not at the same scale and can give results very far from field measurements with packers in the wells (that have also their own limitations).

If we want to draw a conclusion on the benchmark itself, with the purpose to compare and evaluate the equipments and interpretations of the four laboratories, it is obvious that the Cobourg limestone is too much heterogeneous and anisotropic to be a good material. The profession still needs this kind of benchmark. But it is difficult to find a good material.

**Acknowledgements.** The preparation of samples to fit the needs of the individual researchers was a challenge and a large part of the credit goes to the environmental geomechanics research team at McGill (particularly Mr. Ariel Gallagher) who spent a great deal of time performing the coring and machining them to fit the specific dimensions indicated by the investigators. Some of the participants were sent block samples, which saved a great deal of time in the end.

## References

1. Vilks, P., and Miller, N.H. (2007). Evaluation of Experimental Protocols for Characterizing Diffusion in Sedimentary Rocks, AECL. Nuclear Waste Management Division Report TR-2007-11. Toronto, Ontario.
2. Selvadurai, A.P.S., Letendre, A. and Hekimi, B. (2011) Axial flow hydraulic pulse testing of an argillaceous limestone, *Environmental Earth Sciences*, DOI 10.1007/s12665-011-1027-7.
3. Selvadurai, A.P.S. and Jenner, L. (2013) Radial flow permeability testing of an argillaceous limestone, *Ground Water*, doi: 10.1111/j.1745-6584.2012.00932.x.
4. Selvadurai, A.P.S. and Najari, M. (2016) Isothermal permeability of the argillaceous Cobourg Limestone, *Oil and Gas Science and Technology, Special Issue on Low Permeability Geomaterials*, **71**: 53-69.
5. Selvadurai, A.P.S. and Najari, M. (2017) Thermo-hydro-mechanical behaviour of the argillaceous Cobourg Limestone, *Journal of Geophysical Research* (*Solid Earth*), 122: doi:10.1002/2016JB013744.
6. Selvadurai, A.P.S. and Growacki, A. (2018) Estimates for the local permeability of the Cobourg limestone, *Journal of Rock Mechanics and Geotechnical Engineering*, https://doi.org/10.1016/j.jrmge.2018.07.002
7. Profice S, Hamon G. and Nicot B.: Low permeability measurements: Insights, SCA 2015-021, (2015).
8. Selvadurai, A.P.S. (2018) The Biot coefficient for a low permeability heterogeneous limestone, *Continuum Mechanics and Thermodynamics*, doi.org/10.1007/s00161-018-0653-7.
9. W.F. Brace, J.B. Walsh, W.T. Frangos, J. Geophys. Res. **73**, 6 (1968)
10. R. Heller, J. Vermylen, M. Zoback, Am Assoc Pet Geol Bull.98,5 (2014)
11. Chen X.T., Caratini G., Davy C. A., Troadec D., Skoczylas F., Coupled transport and poro-mechanical properties of a heat-treated mortar under confinement, Cement and Concrete Research, 49:10-20, 2013.
12. Pei Y., Agostini F., Skoczylas F., The effects of high temperature heating on the gas permeability and porosity of a cementitious material, Cement and Concrete Research, 95:141-151, 2017.
13. Lenormand R., Bauget F. and Ringot G.: Permeability measurements on small rock samples, SCA2010-32, (2010).

# Pore-scale experimental investigation of in-situ wettability and displacement mechanisms governing WAG in oil-wet carbonates

*Ziqiang* Qin[1,*], *Maziar* Arshadi[1], and *Mohammad* Piri[1]

[1]Department of Petroleum Engineering, University of Wyoming, Laramie, Wyoming 82071, United States

**Abstract.** In oil-wet carbonates, due to low oil production through conventional waterflooding, water-alternating-gas (WAG) injection is deployed to enhance oil recovery. However, to date, there is a lack of fundamental understanding of the underlying physics governing the flow at the pore scale during WAG. The advent of advanced X-ray microtomography (micro-CT) technology provides opportunities to study this complex displacement process at the pore level. In this study, a series of miniature core-flooding experiments were performed at elevated temperature and pressure conditions, using a highly-accurate core-flooding system integrated with a high-resolution micro-CT scanner. Miniature core samples were subjected to a dynamic wettability alteration process (aging) with crude oil followed by three cycles of WAG injection. The samples were X-ray imaged to generate three-dimensional fluid occupancy maps during different two- and three-phase flow stages of the WAG cycles. Pore-scale displacement mechanisms governing WAG EOR under oil-wet conditions were examined by analyzing the pore-fluid occupancy maps. The results showed that WAG flooding scheme significantly enhanced oil recovery. The sweep efficiency of both gas and brine phases were increased due to the shielding effect of the trapped gas ganglia. Oil production diminished rapidly after two waterflooding and gas injection cycles.

## 1 Introduction

More than 60% of the world's oil resources are held in carbonates [1]. It is believed that carbonate rocks were initially water-wet. However, crude oil can rupture the water layer and alter the wettability of carbonate grains during aging [2]. Therefore, carbonate reservoirs commonly demonstrate an oil-wet condition. Buckley et al. [3] reported mechanisms of wettability alteration during the aging process including surface precipitation, oil polar component interactions, acid/base interactions, and ion binding.

Due to the preferential oil-wet states and the complex pore structure, conventional waterflooding usually results in low oil production in carbonates [4,5,6,7]. Various enhanced oil recovery (EOR) techniques were proposed to further produce the remaining oil left after waterflooding. One of the most common EOR methods in the oil industry is gas injection. In North America, gas injection schemes contribute to more than 60% of the ongoing EOR projects [8]. This technique has great potential applications because of its significantly higher displacement efficiency and relatively lower cost compared to those of other chemical-based EOR methods [9]. Moreover, to alleviate the negative effect of greenhouse gases on global climate, gas injection EOR projects could also serve as underground gas storage purposes (e.g., Carbon capture and storage).

The main technical limitation of continuous gas injection is the poor volumetric sweep efficiency due to the low viscosity and density of gas compared to those of other reservoir fluids [9]. Therefore, Water-Alternating-Gas (WAG) injection strategy was developed to manipulate the gas/oil mobility ratio. Furthermore, WAG injection could improve the vertical sweep efficiency as the migration of gas to the top and that of water to the bottom in reservoirs due to gravity.

In 1975, an immiscible $CO_2$-WAG project was conducted in Lick Creek Meakin Sand Unit, AR. It was reported that about 755 Mbbl additional oil was recovered due to the WAG injection [10]. Hsie and Moore [11] reviewed the performance of a miscible $CO_2$-WAG project in a U.S. gulf coast reservoir. The project achieved an additional oil recovery of 16.9% from a water-out Miocene reservoir in sixteen months. Masoner and Wackowski [12] showed the field-application results of a $CO_2$-WAG EOR project in Range Weber Sand Unit. 50% of the Unit's remaining oil was produced.

Huang and Holm [13] studied the performance of WAG injection in both water-wet and oil-wet Berea sandstones using core-flooding experiments. They concluded that more oil was trapped in the water-wet core compared to the oil-wet sample. Sohrabi et al. [14] conducted a series of WAG flooding experiments in micromodels. The results highlighted that WAG injection led to a higher oil recovery than continuous water or gas injections. Han and Gu [15] studied the effect of WAG slug ratio on oil recovery. They concluded that the optimum slug ratio was 1:1.

---

[*] Corresponding author: zqin@uwyo.edu

Even though numerous experimental studies have confirmed the effectiveness of WAG injection for EOR, the direct evidence obtained from naturally-occurring carbonate samples on pore-scale displacement mechanisms governing the observed recovery enhancements are scarce. The advent of X-ray microtomography (micro-CT) technology provides opportunities to study the pore-scale processes of this complex displacements. In the past decades, Micro-CT imaging technology has been used widely in the petroleum engineering area, such as in-situ contact angle measurements [16,17], three-dimensional fluid visualization [18], and local displacement pattern characterization [19]. Direct characterization of in-situ pore-fluid occupancy maps provides opportunities for investigating pore-scale displacement mechanisms. In this study, a series of miniature core-flooding experiments were performed at elevated temperature and pressure conditions, using a highly-accurate core-flooding system integrated with a high-resolution micro-CT scanner. Miniature core samples were subjected to a dynamic aging process with crude oil followed by three cycles of WAG injection. The samples were X-ray imaged to generate three-dimensional fluid occupancy maps during aging and different flow stages of the WAG cycles. Pore-scale displacement physics governing WAG injection under oil-wet conditions were examined by analysing the pore-fluid occupancy maps. To the best of our knowledge, this study is the first pore-scale experimental investigation of the afore-mentioned effects in naturally-occurring carbonates under reservoir conditions.

# 2 Experiments

## 2.1 Rock and fluid properties

The rock sample used in this study was a type of carbonate outcrops named Fond du Lac. We first drilled a 1.5 inch-in-diameter core plug and measured the porosity and permeability of the sample, yielding values of 10.45% and 119.6mD, respectively. Next, a miniature core sample, 4.9mm in diameter and 43.4mm in length, was drilled from the mother core using air as a coolant. The sample was dried at 110°C in an oven for 24 hours and cooled down to room temperature in a desiccator. The dry miniature sample was then scanned by a micro-CT scanner, and the absolute porosity of 10.2% was calculated based on image analysis.

Brine solution was synthesized based on a reservoir brine analysis report. In this study, formation brine and the brine used for first waterflooding shared the same composition. Brine was degassed for 1 hour before use. Crude oil was collected from an oil field located in the Permian Basin, Texas, USA. The oil was filtered through a 0.5 µm filter to remove any possible residue and debris. Then, the filtered oil was tagged with 13 vol% 1-iodooctane to enhance the X-ray attenuation contrast between fluids in the CT images. Commercial grade nitrogen (with a purity of 99.9%) was used for gas injection. Table 1 shows the details of brine and crude oil properties.

**Table 1.** Brine and crude oil properties

| Fluids | Viscosity* (cP) | Density* (g/ml) | Salinity (ppm) | Asphaltene content(%) |
|---|---|---|---|---|
| Brine | 0.74 | 1.01 | 25416 | - |
| Crude oil | 3.79 | 0.84 | - | 0.9 |

*The viscosity and density data were measured at 40 °C and ambient pressure.

## 2.2 Experimental apparatus

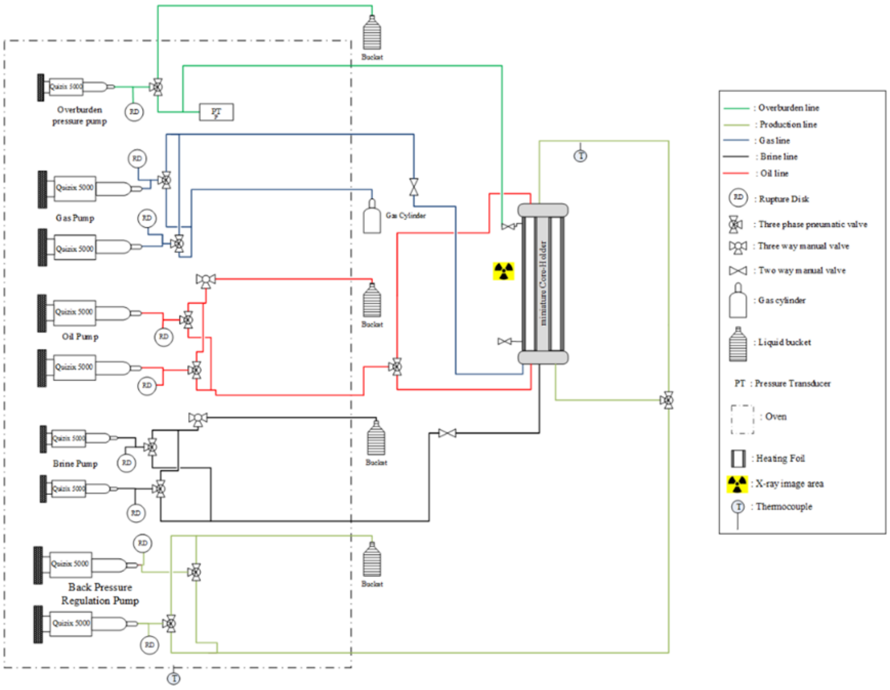

**Fig. 1** A schematic diagram of the experimental apparatus [19].

The flow experiments were conducted using a three-phase reservoir-conditions core-flooding system integrated with a high-resolution X-ray micro-CT scanner. The core-flooding system consisted of five Quizix$^{TM}$ 5000 pumps (dual-cylinder with pressure and flow rate accuracies of 0.5 psi and 1.5* $10^{-5}$ cc/min), a custom-build core-holder, a series of Rosemount$^{TM}$ differential pressure transducers, heating and isolation units, and Hastelloy tubings to minimize corrosion. Three Quizix$^{TM}$ pumps were utilized to inject brine, oil, and gas into the core-holder. The overburden pump was used to maintain the confining pressure surrounding the core sample. The back pressure regulation pump received the fluids from the core-holder at constant pressure and subsequently discharged them into a beaker. The miniature core-holder was made out of carbon fiber to minimize the X-ray attenuation and was able to sustain a pressure and a temperature up to 7000 psi and 120°C, respectively. Highly flexible peek tubing was connected to the core-holder to minimize the vibration and torque during the scan process.

A Thermo Fisher heliscan micro-CT scanner was used to image the sample. The scanner consisted of an X-ray source, a sample stage, and an X-ray detector. The core-holder was mounted vertically inside the CT scanner and rotated during the imaging process. A number of projections were collected at different angles and reconstructed to generate three-dimensional maps of the rock and residing fluids during various stages of the experiment. A resolution of 700 nm to 64 μm was attainable depending on the magnification setting. The scanning parameters were appropriately chosen to maximize the signal-to-noise ratio and improve the quality of images (Table 2). Figure 1 illustrates a schematic of the experimental apparatus used in this study.

**Table 2.** X-ray microtomography parameters used in this study

| X-ray current (uA) | X-ray voltage (kV) | Number of projections | Exposure time (s) | Voxel size (micron) | Scanning time (hours) |
|---|---|---|---|---|---|
| 52.7 | 100 | 3600 | 0.42 | 2.37 | 3 |

### 2.3 Experimental procedure

The core sample was first placed inside the core-holder with a confining pressure of 300 psi. Gaseous $CO_2$ was injected into the core to remove the bulk air, and the system was subsequently vacuumed for 24 hours. The sample was then scanned to collect a set of reference images. Afterward, the vacuumed core sample was fully saturated with brine by injecting 50 pore volume of the fluid. Subsequently, the pore pressure and the confining pressure were simultaneously increased to 600 psi and 900 psi, respectively. The system temperature was also increased to 90°C by adjusting the thermo-controller of the heating tape surrounding the core holder. The temperature and pressure conditions were maintained at these values for the rest of experiments. The system was allowed to rest for five days to achieve an ionic equilibrium between the rock surface and the brine. The experiment was continued with a primary drainage step. Crude oil was injected into the sample with a constant flow rate of 0.006 cc/min. The core was continuously imaged during the primary drainage, and the steady state was confirmed until no change was observed in pore-fluid occupancy maps, i.e., after 10pv of oil injection (Figure 2). At this point, the initial brine saturation was calculated based on image analysis. The sample was then dynamically aged by injecting crude oil at a constant flow rate of 0.0002 cc/min. Scans was taken repeatedly during the aging process to monitor the evolution of in-situ oil-brine contact angles. The aging process was considered complete once the in-situ contact angles did not change further. The aging process produced an equilibrium wettability condition in approximately fifteen days (Figure 3). After completing the aging process, a waterflooding step with a flow rate of 0.0005 cc/min was performed. Then, the brine inside the sample was displaced by doped brine (by adding 18wt% NaI as tagging agent) at the same flow rate as the one used during waterflooding. This step aimed to ensure sufficient X-ray attenuate contrast existed among brine, oil, and gas phases during gas injection. A monitoring scan was taken to make sure the fluid occupancies did not change. Subsequently, a gas injection step was conducted at an injection rate of 0.015 cc/min. The low gas rate was chosen to ensure the flow in capillary dominated regime. The experiment was further continued with another two cycles of waterflooding (with doped brine) and gas injection alternatively to probe the pore-scale displacement mechanisms governing WAG injection. A series of scans were collected during the afore-mentioned flooding processes, and each flow step was terminated until the in-situ fluid occupancy map remained constant.

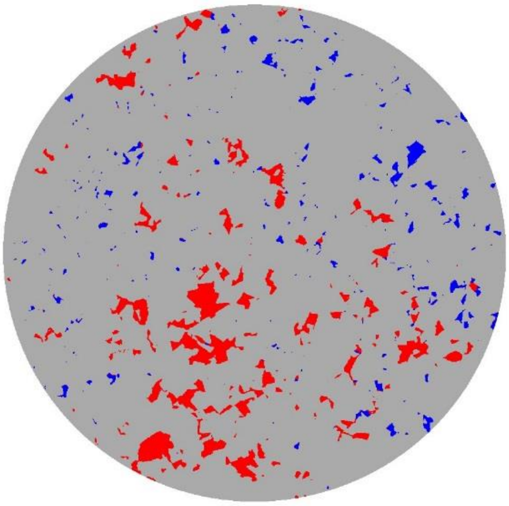

**Fig. 2** Pore-fluid occupancy map at the end of the drainage process (grain: gray, oil: red, and brine: blue).

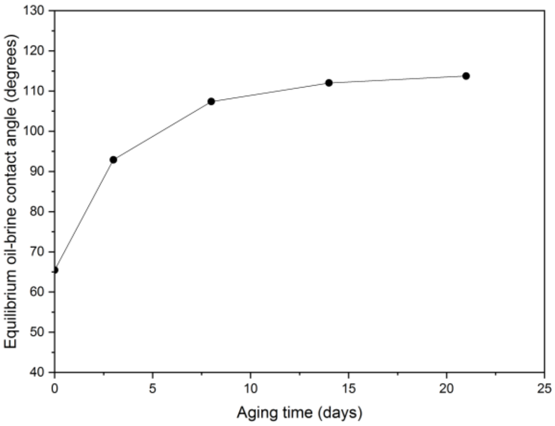

**Fig. 3** Variation of equilibrium oil-brine contact angle versus aging time (Thirty contact angles were measured at each date point).

### 2.4 Data analysis

The middle part of the sample was scanned during the experiments to avoid any possible end effect. The bulk- and pore-volume in the field-of-view were 84.22 mm$^3$ and 8.6mm$^3$, respectively. The projections acquired during imaging processes were reconstructed to generate three-dimensional internal structures of the rock-fluid systems (with an image resolution of 2.37 micrometer). Avizo 9.4.0 and PerGeos 1.7.0 software platforms were used to analyse and visualize the acquired images. The first step of image-processing workflow was applying a volume edit module to mask the area out of region-of-interest. Then, a non-local means filter was used to smoothen the data and reduce noises. Afterward, the flooded image was registered to the dry reference image pixel-by-pixel. The registered wet image was subsequently multiplied by the pore map obtained from the dry image to eliminate the solid phase. Next, the multiplied image was segmented to various fluid phases. The segmented image was used to calculate fluid saturation, measure in-situ contact angles, characterize local displacement patterns, and perform other quantitative image analysis. The details of this robust image-processing workflow can be found elsewhere [19].

## 3 Results and Discussion

### 3.1 Pore-scale displacement mechanisms of WAG injection in oil-wet carbonates

In order to study the pore-scale displacement mechanisms during WAG injection in oil-wet carbonates, we performed a total of three water-gas injection cycles following the aging process. Before waterflooding, the initial brine saturation was 0.241. After aging, first, the sample was subjected to a waterflooding process. A significant amount of oil remained un-swept at the end of this stage, as shown in Figure 2a. The residual oil saturation (calculated from segmented pore-fluid occupancy maps) reached to 0.445, which translates to an oil recovery of 41.4%. Subsequently, the experiment was further continued with alternative cycles of gas injection and waterflooding. The pore-fluid occupancy maps of the first gas injection cycle revealed that no stable spreading oil layers were formed in the system (Figure 4). Furthermore, oil, brine, and gas were identified as wetting, intermediate-wetting, and non-wetting phases based on in-situ contact angle measurements. The details of the in-situ contact angle measurement method are presented elsewhere [19]. During the first gas injection, some oil was produced and the residual oil saturation reached to 0.284 (with a gas saturation of 0.55). We also observed that some portion of the unrecovered oil was pushed by gas to the water channels that were created in the first waterflooding while the rest of oil remained un-swept due to gas fingering.

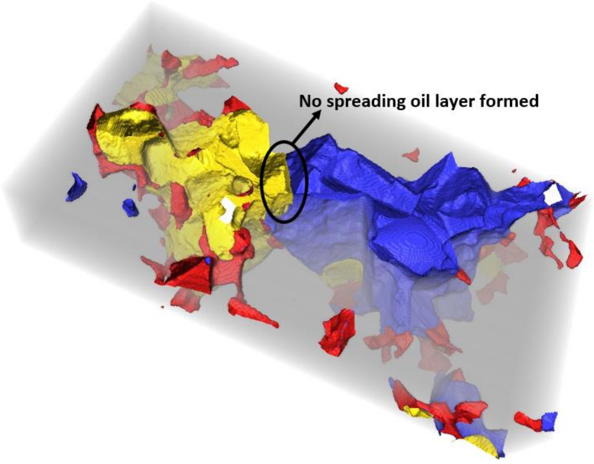

**Fig.4** Exemplary three-dimensional pore-fluid occupancy map shows the spreading phenomenon in the system (grain: gray, gas: yellow, oil: red, and brine: blue).

As it can be seen from Figure 5 (a) and (c), during the second waterflooding cycle, brine mainly flowed through the channels filled with brine in the first waterflooding. However, there were also some new brine flow channels that were created during the second waterflooding. This is mainly because gas phase partially blocked some of the previously-invaded brine channels, which subsequently allowed brine to invade more pore elements and displace additional oil from the pore space. In addition, brine also displaced some of the gas into the oil-filled pores (Figure 5 (b) and (c)), which also benefited the oil production.

As shown in Figure 5 (b)-(d), gas flow channels of the second gas injection cycle could be divided into two groups. In the first category, the gas went through the previously-invaded gas channels created by the first gas injection. During this process, trapped gas globules were reconnected, and the oil occupying these channels could be produced. The second group was some new flow channels that were not invaded by gas during the first gas injection. The formation of these channels was due to the pressure build-up of the gas phase, which resulted from the shielding effect of fragmented fluid clusters that occupied the previously-invaded gas channels as more MTM interface were involved in the displacement chain. This pressure build-up facilitated the invasion of gas into pore elements with high entry pressures. Consequently, some oil that was bypassed during the first gas injection was produced in this stage. Hence, the sweep efficiency of the gas phase was significantly increased in the second gas injection cycle compared to that in the first one, which is a crucial advantage of the WAG injection scheme.

The oil production diminished rapidly as the WAG cycles were continued. This is mainly due to two reasons: 1) the remaining oil was mostly located in small pores with high entry pressures. 2) The fluids' connectivity was very poor in this stage, which made the coalescence of the trapped oil difficult (The fluid connectivity was measured using axis connectivity module in Avizo 9.4.0).

The residual oil saturation after the first cycle of gas injection was 0.284 (with a gas saturation of 0.55), which corresponds to an additional oil recovery of 21.2%. For the second cycle of waterflooding and gas injection, the residual oil saturations were 0.188 (with a gas saturation of 0.4) and 0.122 (with a gas saturation of 0.77), which translates into the additional oil recovery of 12.6% and 8.7%, respectively. As for the third cycle, the residual oil saturations were 0.121 and 0.105, meaning the additional oil recovery of 0.1% and 2.1% (Figure 6). The pore-scale displacement mechanisms of WAG injection developed in this study could serve as a benchmark to improve the prediction capabilities of physically-based pore network models.

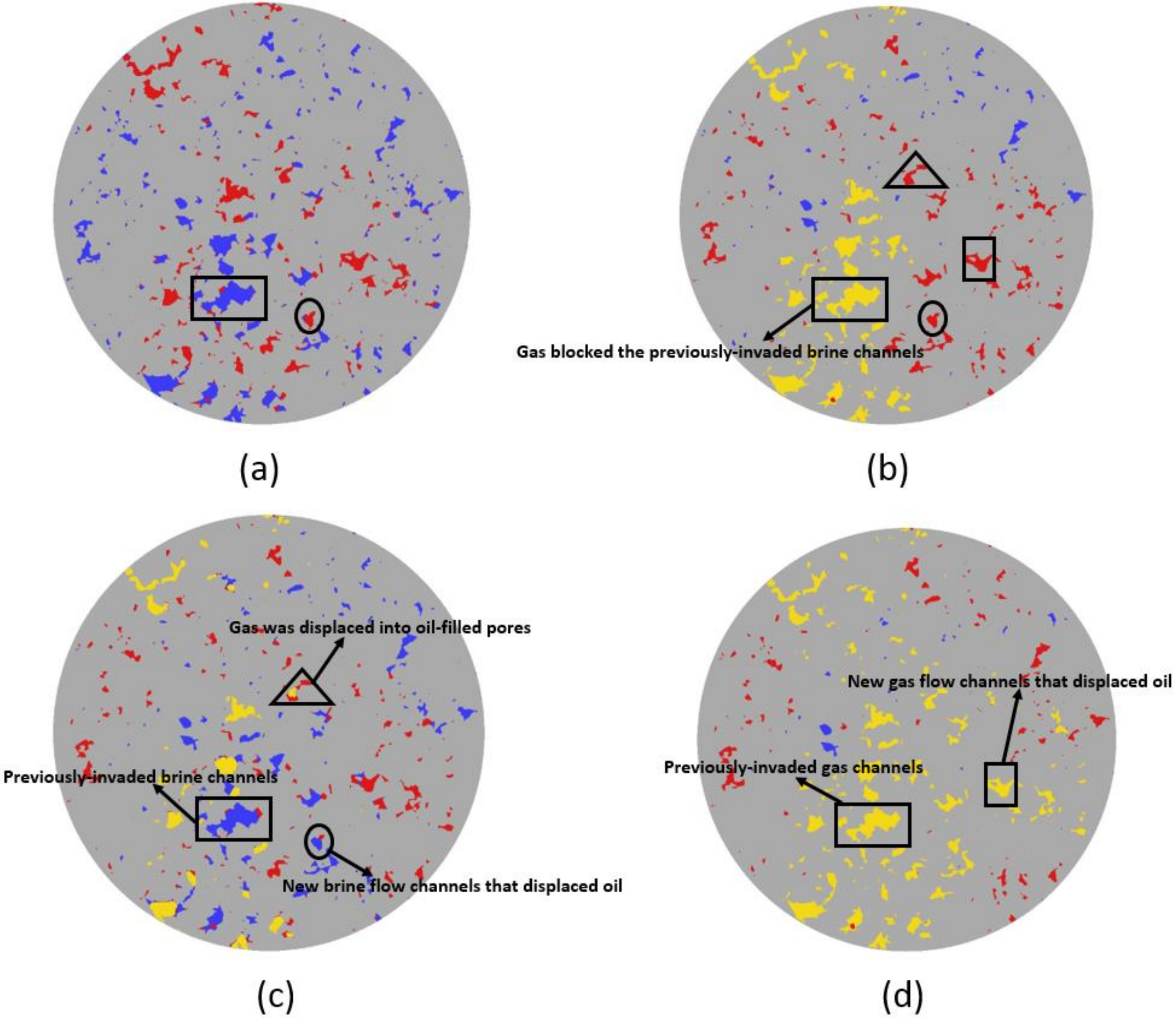

**Fig. 5** Two-dimensional cross-sectional views of in-situ fluid occupancy maps at the end of (a) the first cycle of waterflooding, (b) the first cycle of gas injection, (c) the second cycle of waterflooding, and (d) the second cycle of gas injection (grain: gray, gas: yellow, oil: red, and brine: blue).

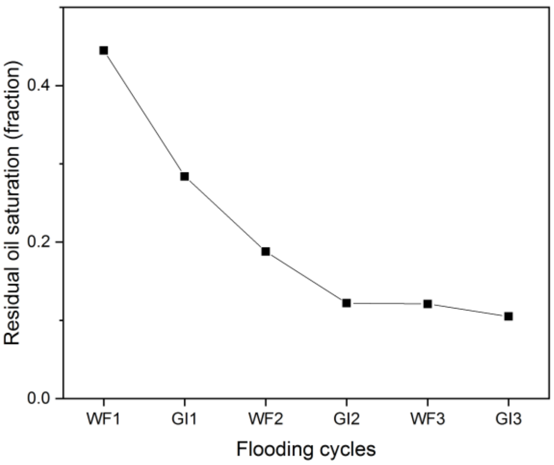

**Fig. 6** Residual oil saturation at the end of varying WAG cycles (WF: waterflooding, GI: gas injection).

## 4 Summary and conclusion

In this study, a miniature core-flooding experiments were performed in naturally-occurring carbonate at elevated temperature and pressure conditions, using a highly-accurate core-flooding system integrated with a high-resolution X-ray micro-CT scanner. Pore-scale displacement mechanisms governing WAG injection under oil-wet conditions were investigated by analyzing the in-situ pore-fluid occupancy maps. Here, we summarize the main findings:

1) WAG flooding scheme significantly enhanced oil recovery. The oil saturation was ultimately reduced from 0.759 to 0.105 during this process.
2) WAG injection scheme remarkably increased the sweep efficiency of both gas and brine phases due to the shielding effect of the trapped fluid clusters.
3) After two waterflooding and gas injection cycles, the oil production diminished rapidly as the WAG cycles were further continued.

The authors gratefully acknowledge the financial support of Thermo Fisher Scientific Company, Hess Corporation, and the School of Energy Resources at the University of Wyoming.

## References

1. Schlumberger, Carbonate reservoirs (2007).
2. N. R. Morrow, Wettability and its effect on oil recovery, Journal of Petroleum Technology **42**.12 (1990) 1–476.
3. J. Buckley, Y. Liu, and S. Monsterleet, Mechanisms of wetting alteration by crude oils, SPE journal **3**.01 (1998) 54–61.
4. J. Lai, et al. "Prediction of reservoir quality in carbonates via porosity spectrum from image logs." Journal of Petroleum Science and Engineering **173** (2019) 197-208.
5. J. Lai, et al. "Pore structure and fractal characteristics of Ordovician Majiagou carbonate reservoirs in Ordos Basin, China." AAPG Bulletin 20,190,412 (2019).
6. J. Lai, et al. "A review on pore structure characterization in tight sandstones." Earth-Science Reviews **177** (2018): 436-457.
7. W. Kuang, S. Saraji, and M. Piri. "A systematic experimental investigation on the synergistic effects of aqueous nanofluids on interfacial properties and their implications for enhanced oil recovery." Fuel **220** (2018) 849-870.
8. L. Koottungal, 2012 worldwide EOR survey, Oil & Gas Journal **110** (2012) 57–69.
9. Z. Qin, M. Arshadi, and M. Piri, "Micro-scale experimental investigations of multiphase flow in oil-wet carbonates. II. Tertiary gas injection and WAG" Fuel. (to be published)
10. T. B. Reid, and H. J. Robinson. "Lick creek meakin sand unit immiscible CO2 waterflood project." Journal of Petroleum Technology **33**.09 (1981) 1-723.
11. J.C. Hsie, and J. S. Moore. "The Quarantine Bay 4RC CO2 WAG pilot project: a postflood evaluation." *SPE reservoir engineering* **3**.03 (1988) 809-814.
12. R.K. Wackowski, and L. O. Masoner. "Rangely Weber Sand Unit CO2 Project Update: Operating History." *SPE Reservoir Engineering* **10**.03 (1995) 203-207.
13. E. T. S. Huang, and L. W. Holm. "Effect of WAG injection and rock wettability on oil recovery during CO2 flooding." *SPE Reservoir Engineering* **3**.01 (1988) 119-129.
14. M. Sohrabi, et al. "Visualization of oil recovery by water alternating gas (WAG) injection using high pressure micromodel-oil wet and mixed wet systems, SPE 71494." *Annual Technical Conference and Exhibition, New Orleans, Louisiana*. **Vol. 30**. (2001).
15. L. Han, and Y. Gu. "Optimization of miscible CO2 water-alternating-gas injection in the Bakken formation." Energy & Fuels **28**.11 (2014): 6811-6819.
16. M. Andrew, B. Bijeljic, and M. J. Blunt. "Pore-scale contact angle measurements at reservoir conditions using X-ray microtomography." Advances in Water Resources **68** (2014): 24-31.
17. H.H. Khanamiri, O. Torsæter, and J. Å. Stensen. "Effect of calcium in pore scale oil trapping by low-salinity water and surfactant enhanced oil recovery at strongly water-wet conditions: In situ imaging by X-ray microtomography." Energy & Fuels **30**.10 (2016): 8114-8124.
18. S. Youssef, et al. "4D imaging of fluid flow dynamics in natural porous media with ultra-fast X-ray microtomography." *International Symposium of the SCA, Napa Valley, California*. **Vol. 176**. 2013.
19. Z. Qin, M. Arshadi, and M. Piri, "Micro-scale experimental investigations of multiphase flow in oil-wet carbonates. I. In-situ wettability and low-salinity waterflooding" Fuel. (to be published)

SCA2019-039

# High-resolution inline density measurements: insight on multiphase flow and transport phenomena in porous media

*Jelayne* Falat[1], *Adam* Fehr[1], *Ali* Telmadarreie*[1], and *Steven* Bryant [1, 2]

[1]Univeristy of Calgary, Chemical and Petroleum Engineering Department, VP Research, 2500 University Dr. NW T2N 1N4
[2]Canada Excellence Research Chair in Materials Engineering for Unconventional Oil Reservoirs

**Abstract.** An in-line densitometer is used in core flooding applications to quantify fluid production from core samples and obtain quantitative and qualitative information such as connate water production, breakthrough times, emulsion/foam generation, and steam condensation.

A series of core floods were performed with a densitometer placed at the outlet of a sandpack. All fluids passed through the measurement cell at experiential temperatures and pressures. The second series of tests were performed at high temperature and pressure, with a densitometer placed at the inlet and outlet of a sandpack, for steam applications. In both series of experiments, data acquisition was collected at 1 hertz and the analyzed density data was compared to results from the conventional effluent analysis, including Dean-Stark, toluene separations, magnetic susceptibility measurement, and flash calculations where applicable.

The high-resolution monitoring of effluent from a flow experiment through porous media in a system with two phases of known densities enables two-phase production to be accurately quantified in the case of both light and heavy oil. The frequency of measurements results in a high-resolution history of breakthrough times and fluid behavior. In the case of monitoring steam injection processes, reliable laboratory tests show that in-line density measurements enable the determination of steam quality at the inlet and outlet of a sandpack and qualitative determination of steam condensation monitoring

The use of in-line densitometry in core flooding applications provides insight on monitoring of complex fluid flow in porous media, which typical bulk effluent analysis is not able to do. The ability to measure produced fluids at high resolution and extreme temperatures reduces mass balance error associated with the effluent collection and broadens our understanding of complex fluid flow in porous media.

## 1.0 Introduction

Traditional coreflood systems utilize two/three-phase separators or fraction collectors downstream of the core to collect effluent. While phase separators prove reliable in conventional applications, they are limited in their ability to handle highly viscous samples and complex fluids like emulsions and nanofluids. Fraction collectors may cause an error in mass balance, due to misalignment of tubes, rate of sample entering tubes, movement of the collector's arm between tubes, and more. Additionally, fraction collectors result in low temporal resolution, as all effluent is mixed in the tube, resulting in an average composition over a given tube volume. Once the effluent is collected, analyzing it can be both time-consuming and challenging [1]. The dean-stark analysis is accurate; however, the temporal resolution is very low and, in many cases, only a single end-point oil production value is obtained. Methods such as NMR, solvent extraction, Karl-Fischer, and the like are costly, time-consuming, and limited to the resolution of the effluent collection method. In-line densitometry enables real-time quantification of produced water and oil and gives a valuable qualitative understanding of phase behavior and fluid flow in porous media.

A high-temperature and high-pressure density meter can be integrated into a coreflood set-up to measure effluent density and distinguish between crude oil and injection fluid. The method discussed involves weighing the produced oil to determine the weight of the residual oil remaining. The density measurements are used along with effluent analysis to facilitate laboratory studies of enhanced oil recovery.

Olsen et al. (2017) described a method for using a densitometer for quantifying oil production in two-phase coreflood experiments and looked at the understanding obtained by in-line density data for

---

* Corresponding author: ali.telmadarreie@ucalgary.ca

dynamic events such as water breakthrough, gas breakthrough, and connate water production. They conducted immiscible displacements at constant temperature and pressure conditions using North Sea light crude oil and were able to determine that the densitometer produced comparable data to that from an acoustic separator [2].

In this paper, we look at the potential applications and the challenges of utilizing in-line densitometry in core flooding. We demonstrate the benefit of using a high temporal resolution effluent analysis technique as a tool for understanding phase behavior and fluid flow in porous media. We look at the challenges of quantifying heavy oil and assess the use of in-line densitometry in emulsion, foam, and nanofluid core flood experiments. Additionally, we look at the applications of in-line densitometry for steam flooding and the potential understanding gained from being able to determine dynamic water saturation histories during hot gas flooding, condensation monitoring for steam flooding, and real-time volumetric steam quality data. Conventionally, acquiring such information is challenging and may require complex dynamic imaging techniques (i.e. CT, MRI) which are costly. This paper introduces easy and continuous methods using high-resolution densitometry for measuring and analyzing the data that cannot be obtained with conventional core flood configurations.

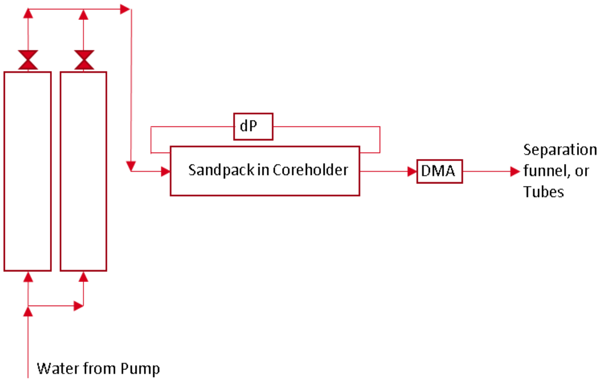

**Figure 1:** Simple schematic of multiphase core flood apparatus with the densitometer (DMA) located at the outlet of the porous media.

## 2.0 Methodology

The Anton Paar density meter (DMA HPM) operates on the principle of the oscillating U-tube, which has been used for over 50 years. The U-tube is excited by applying an electrical voltage to a Piezo element, causing it to oscillate at a characteristic frequency [3]. When fluid enters the measurement cell, the oscillation frequency is changed and is accurately detected by a second Piezo element. Each fluid has a characteristic frequency, which correlates to its density, as per the formula:

$$\rho = A\tau^2 - B \tag{1}$$

Where p is the density of the fluid, A and B are instrument constants, and $\tau$ is the oscillation period. The instrument constants A and B are determined in an instrument adjustment, where two reference standards, such as dry air and pure degassed water, are measured in order to determine the relationship between density and the period of oscillation. Using this relationship, unknown sample densities can be determined using their oscillation. The measuring cell is made from Hastelloy C-276, which can withstand high mechanical stress and is highly chemical resistant. The stated cell volume is 2 mL, however, the sensitive measuring volume is 0.35 ± 0.3 mL [2].

Multi-phase core floods were performed using a densitometer placed at the outlet of the sandpack. Density was measured at a frequency of 1 hertz and all measurements were made at the same temperature and pressure as the sandpack by using a circulating water bath and a back pressure regulator (BPR). The density meter was placed so that all fluid entering the sandpack passed through the measuring cell, before reaching the BPR and fraction collector. Flow rates used were < 0.35 mL/sec, in order to ensure that all fluid passing through the measuring cell was measured. If the flow rate exceeds the limit of the sensitive measuring volume, the accuracy of the analysis is affected.

Steam floods were performed in such a way that additives could be mixed with superheated steam resulting in wet steam laden with chemical additives that are present in the liquid phase of the injected mixture. These mixtures produced an increase in pressure drop relative to the back pressure of the apparatus which was then normalized against the pressure drops of steam of similar total heat values.

**Table 1:** The sandpack dimensions, geometry, permeability, porosity, composition, and pressure tap locations for steam foam experiments.

| **Dimensions** | 40.84cm X 2.244cm |
|---|---|
| **Geometry** | Cylindrical Unconsolidated |
| **Permeability** | 2.27 Darcy |
| **Porosity** | 40.14% |
| **Composition of Media** | Silica Sand 140-270 |
| **Tap Locations** | Absolute Pressure at 0, 10cm, dP at 10, 20, 30, 40cm |
| **Operating Pressure** | 200 psig |
| **Operating Temperature** | 200 °C |

The Experimental conditions for the steam foam floods were 200 °C 212 psia back pressure for the steam flood with four pressure taps, and 170 °C and 120 psia for the steam flood that only had pressure taps located at the inlet and outlet of the sandpack.

The dynamic saturation test was performed with nitrogen and water co-injected at a 4:1 gas to liquid ratio at varied flow rates to evaluate the equilibrium water saturation for a given flow rate at high-pressure high-temperature conditions. The back pressure of the system is adjusted in such a way that compressibility of flow is negligible and therefore unaccounted for.

**Table 2:** The sandpack dimensions, geometry, permeability, porosity, composition, and pressure tap locations for the dynamic fluid saturation experiment.

| **Dimensions** | 30.65cm X 1.5748cm |
|---|---|
| **Geometry** | Cylindrical Unconsolidated |
| **Permeability** | 35.52 Darcy |
| **Porosity** | 35.87 % |
| **Composition of Media** | Silica Sand 50-70 |
| **Tap Locations** | Inlet, Outlet |
| **Operating Pressure** | 750 psig |
| **Operating Temperature** | 100 °C |

## 2.1 Example Calculations

Olsen et al. (2017) determined a method for using in-line densitometry for quantification of produced water and oil in a two-phase system using the following equation [2]:

$$CumProdWater\,(0,N) = \sum_{0}^{N} \frac{MeasDens\,(i) - LowerEnvelope(i)}{Upper\ Envelope\,(i) - LowerEnvelope(i)} * [InjVol(i) - InjVol\,(i-1)] \quad (2)$$

Where the Lower Envelope is the density of the lightest phase, and the Upper Envelope is the density of the heaviest phase, oil and water, respectively. Alternatively, produced oil can be calculated directly using similar equation.

The produced oil fraction can then be determined by subtracting the produced water from the total injection volume

$$C(0, N) = CumInjFluid(0, N) - CumProdWater(0, N) \quad (3)$$

It is noted that the upper and lower envelopes must be carefully determined in order to ensure the accuracy of the analysis.

This equation can also be applied to miscible displacements, where the densities of the two pure phases are known.

In the case of highly viscous oil, the density measurement is dampened by a coating of oil on the walls of the measurement cell. This, in turn, lowers the apparent density. In this case, a moving upper envelope must be used. This is determined by applying a macro to the data set, which detects the change in the upper density value. If the change in density over a given produced volume is greater than a given value, in this case 0.0001 was selected as a cutoff, the upper envelope value is equal to the previously calculated value. This results in the upper envelope closely following the trend of the brine values, while accounting for slight fluctuations due to heavy oil coating the measurement cell, fines migration, fines settling in the measurement cell, changes in brine salinity, etc.

$$\begin{aligned}&Moving\ Upper\ Envelope\\ &= IF\left(\frac{Measured\ Density\ (i) - Measured\ Density\ (i-1)}{CumProdVol\ (i) - CumProdVol(i-1)}\right)\\ &> 0.001, Upper\ Envelope\ (i-1), Measured\ Density\ Value\end{aligned} \tag{4}$$

Liquid volumetric fraction calculation:

$$LVF = \frac{\rho Measured - \rho Gas}{\rho Water - \rho Gas} \tag{5}$$

Therefore, the vapor volumetric fraction can be assumed to be

$$VVF = 1 - LVF \tag{6}$$

The produced water/liquid can be calculated when the system pressure is significantly higher than the phase envelope pressure (boiling pressure) of the liquid phase. This is executed in discrete steps with each interval being each individual density measurement.

$$\begin{aligned}&Produced\ Liquid\ per\ Data\ Interval = LVF *\\ &(Total\ Volume\ Produced)/(Unit\ Time) * Unit\ Time\end{aligned} \tag{7}$$

Using the above equation, the cumulative produced liquid can be calculated as follows:

$$\begin{aligned}&Cumulative\ Produced\ Liquid =\\ &\textstyle\sum_0^N Produced\ liquid\ per\ Data\ Interval\end{aligned} \tag{8}$$

Then using that information we can calculate the liquid saturation within the porous media as follows:

$$S_w = \frac{Cumulative\ Produced\ Liquid - Cumluative\ Injected\ Liquid}{Pore\ Volume} \tag{9}$$

For steam vapor, volumetric qualities are calculated in the same way as Equation (5)

The mobility reduction of steam foams is expressed as a mobility reduction factor.

$$Residual\ Resistance\ Factor\ (RRF) = \frac{Pressure\ Drop\ of\ Steam\ with\ Additive}{Equiblibirum\ Pressure\ Drop\ of\ Saturated\ Steam} \tag{10}$$

At steady state the equation for volumetric flow rate

$$\begin{aligned}&Volumetric\ Flow\ Rate = (Mass\ )/(Unit\ Time) \times\\ &(Unit\ Volume)/(Mass\ )\end{aligned} \tag{11}$$

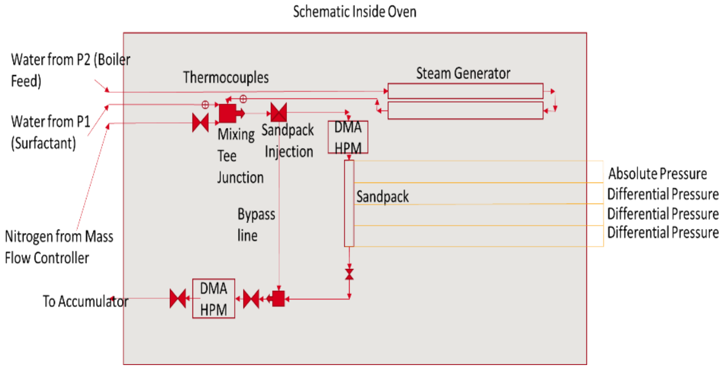

**Figure 2:** Schematic of the oven internals during steam flood/ hot gas flood experiments, the hot gas flood and the 170 °C steam flood only had one differential pressure measurement. The density measurement cell was inside the oven at 0.494 cubic centimeters of dead volume downstream the outlet of the porous media for all high-temperature experiments discussed in this paper.

## 3.0 Results and discussion

Here we summarized the capability of a high-resolution inline densitometer for flow experiments in porous media considering various condition including high temperature, high pressure, variable oil viscosity, and density differentials.

### 3.1 Oil recovery monitoring

The objective of this section is to show how we can precisely monitor the fluid production namely oil recovery in dynamic flow experiments.

The densitometer can be used to accurately determine initial oil in place (OOIP). Additionally, mass balance errors associated with the effluent collection and analysis techniques are eliminated by providing in-line results. Figure 3 to Figure 5 shows the densitometer results for conventional displacing experiments with Dodecane as the oil phase.

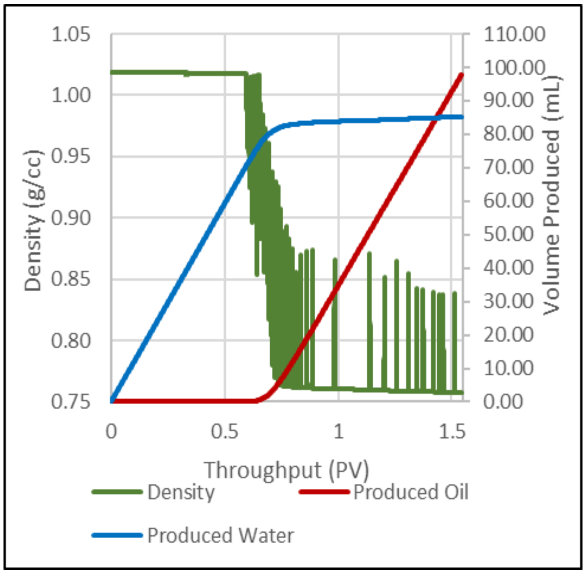

**Figure 3**: Oil displacing water in water-saturated sandpack. Density monitoring for determination of original oil in place.

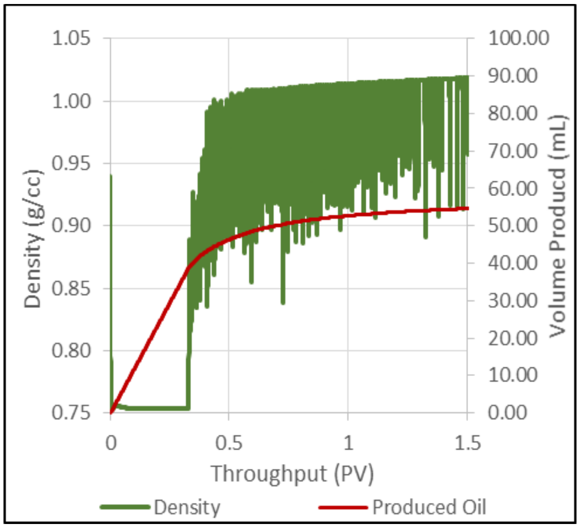

**Figure 4**: Density history of waterflood through Dodecane saturated sandpack.

As shown in Figure 4, the high-resolution monitoring of effluent from a flow experiment through porous media in a system with two phases of known densities enable oil production to be accurately quantified. The frequency of measurements results in a high-resolution history of breakthrough times and fluid behavior.

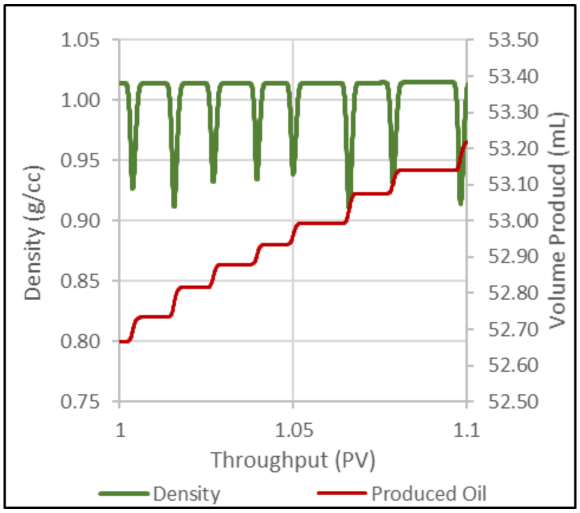

**Figure 5**: A closer look at density history of waterflood through Dodecane saturated sandpack

A closer look at the density history enables us to identify that the oil is being produced in "trains" (Figure 5) rather than as an emulsion, which is similar to the observation made by Olsen et al. [2]. This is because the density levels off at the density of the water phase, based on the calibration, before dipping down towards the density of the oil. If the oil was being produced as emulsion, there would be smaller oscillations in density, at a density representative of the quality of the emulsion.

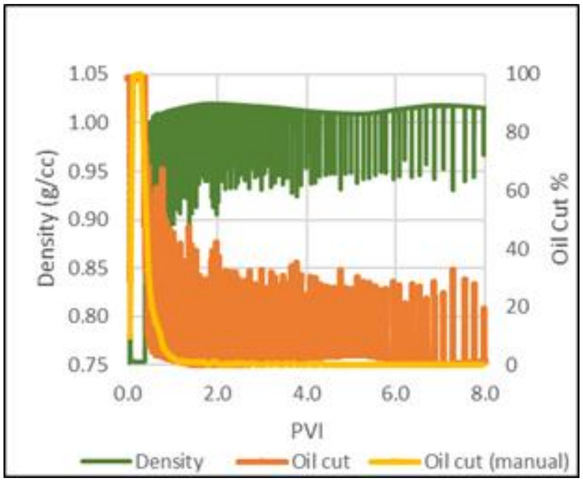

**Figure 6**: Comparison of density calculation to manual determination of oil production.

Here we demonstrate that the densitometer provides reliable results when compared to effluent fraction collection and analysis. The mass balance from the effluent analysis was 99.6% and the mass balance from calculated throughput analysis of the densitometer was 100.2%. The mass balance can be improved by utilizing a circulating water bath in the measurement cell of the densitometer, which was considered in the next section. As shown in Figure 6, effluent analysis cannot accurately capture the oil production performance especially after 2 PV. On the other hand, the oil cut from density calculation shows that the oil is still producing even after 8 PV of the injection. The change in amplitude of the density curve provides us information about the volume of oil production. The change is the frequency of the density will tell us how often oil is producing. For example, in Figure 6, the frequency of density after 5 PV is lower than that of the early time stage (1-2 PV) supporting the fact that the oil production rate decreases after 5 PV.

### 3.2 Heavy oil recovery calculation; potential and challenges

As shown above, using the density meter for oil saturation allows for a quick determination of original oil in place. This is more crucial when working with heavy crude oil. The effluent analysis is difficult with heavy oil, as it coats the collection vessel and makes visual determination inaccurate. Solvent separations are also time-consuming.

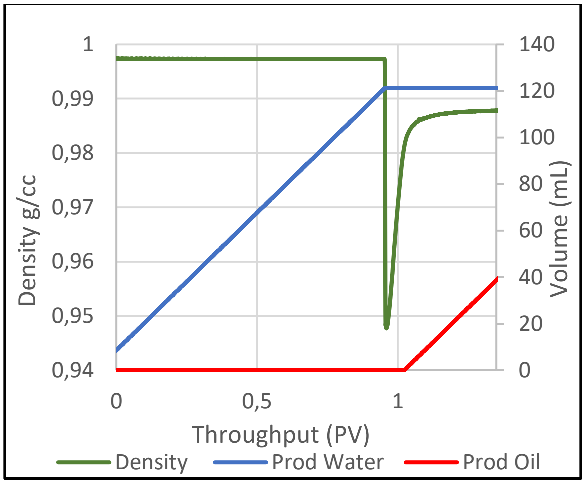

**Figure 7:** Density history of heavy oil saturation in water saturated sandpack

To verify the effectiveness of oil saturation with the density meter the effluent was passed through the measurement cell and collected into a seporatory funnel. The OOIP was 111 mL from analysis of the seporatory funnel and 113 mL by the densitometer. The negative throughput is due to dead volume production from the lines first passing through the measurement cell for both Figure 7 and Figure 8. The percent relative difference between the two methods was 1.79%.

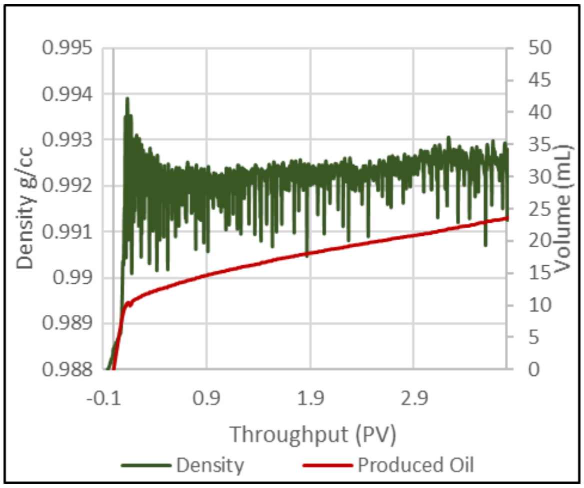

**Figure 8:** Density history of waterflood through heavy oil saturated sandpack

The quantification of heavy oil through the densitometer is challenging, due to its tendency to coat the walls of the measurement cell. However, if the upper envelope (UE) is adjusted accordingly (See equation 3- Moving upper envelope), it is possible to obtain accurate quantitation of heavy oil production. In order to verify the densitometer results, the effluent was collected into a seporatory funnel and analyzed. According to the manual method, 23.6 mL of oil was produced. According to the density meter results, 24.8 mL of oil was produced. The methods had a percent relative difference of 5.1%. It should be mentioned that several core flood tests with heavy oil were performed and the average percent relative difference was ± 10%. This error, which is due to heavy oil coating the measurement cell, could be reduced by heating the measurement cell to lower the oil viscosity and reduce coating effects. Further development of this method is required before it can be used as a stand -alone analysis of heavy oil production. However, the density meter shows potential for elimination of challenging effluent analysis, including the need for time-consuming Dean-Stark analysis.

### 3.3 Nanoparticle transport in porous media

There is a linear relationship between the density and concentration of nanofluid, enabling the densitometer to be used as an inline analyzer for quantification of nanofluid in a two-phase system. Errors could arise from adsorption of stabilizing agent to the porous media and fines migration that can be potentially detected by high-resolution density measurement. It should be mentioned that fine migration can occur in different tests and may result in additional errors.

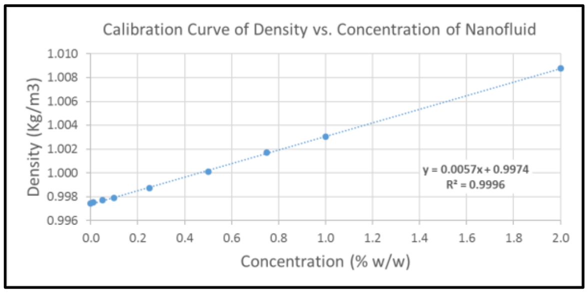

**Figure 9:** The density of silica nanoparticle at different concentrations. High-resolution density measurement allows accurate detection of nanoparticle with a relatively small increment of nanoparticle concentration.

Following is an example of densitometer capability to detect nanoparticle transport in porous media. The results were also correlated with the magnetic susceptibility measurement of the effluent samples. A suspension of iron oxide nanoparticles was injected in a water-saturated porous media (properties of porous media is mentioned in Table 2) at room condition. Thereafter, the nanofluid displaced with post flush of water. The iron oxide nanoparticles have magnetic properties so can be detected by magnetic susceptibility measurement. The magnetic susceptibility is normalized based on the magnetic susceptibility of effluent without iron oxide nanoparticles (Figure 10 b) any value above zero shows the presence of iron oxide nanoparticles. More detail on such experiments and magnetic susceptibility measurement can be found elsewhere [4].

The normalized magnetic susceptibility profile shows that the particle breakthrough occurred around 250-300 seconds. However, the density profile can accurately show the breakthrough time (260 seconds) since it is a continuous measurement with 1 Hz frequency.

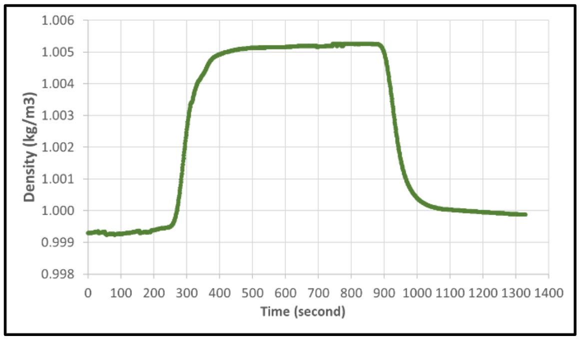

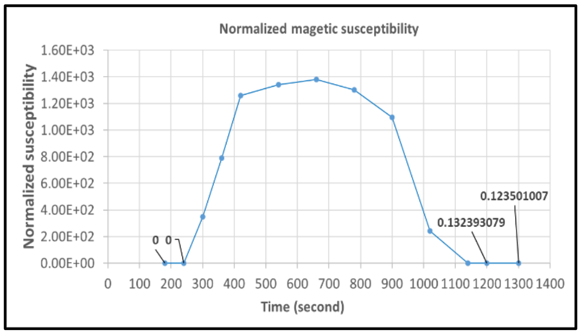

**Figure 10:** Density profile (a) and magnetic susceptibility profile (b) of iron oxide nanoparticle showing the breakthrough time and nanoparticle transport behavior. Post flush of water started at 600 seconds.

Interestingly the density profile at 1200-1300 seconds is higher than the beginning (water density) suggesting the nanoparticle are still presents in the effluent sample. The dispersed iron oxide nanoparticles in water create a very dark color liquid which is easily detectable with the naked eye even in low concentration (e.g. 0.05 wt %). The effluent sample at 1200 and 1300 seconds in Figure 10b was very clear by naked eyes, but the susceptibility measurement suggests that there is still nanoparticle in porous media supporting the density results. It is worth mentioning that monitoring transport of nanoparticles in the presence of a second fluid (i.e. oil) will add more challenges especially if the nanoparticles remain at oil-water interface.

## 3.4 Monitoring saturated steam and hot gas multiphase flow through porous media

Steam/saturated steam flow in porous media presents an especially complex multiphase flow scenario where densitometry can provide some qualitative and semi-quantitative data. High-resolution densitometry enables us to monitor –but not quantify- steam condensate production of the porous media, and we observe distinct variances during foam production as it compares to wet steam flow. Volumetric steam qualities can also be calculated from the density histories, and consequently, mass qualities are also able to be calculated when assuming the system is at steady state.

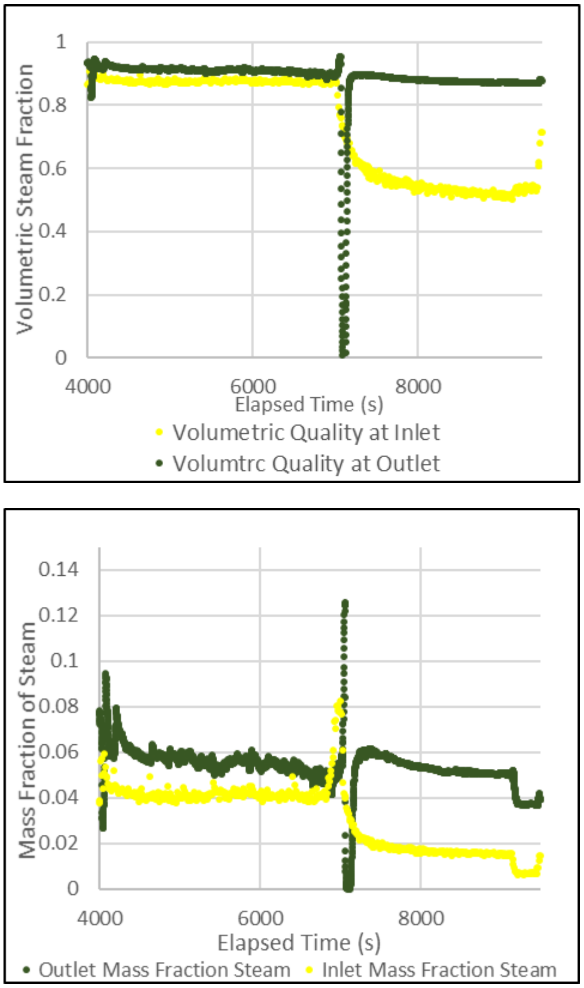

**Figures 11:** Monitoring volumetric (a) and mass (b) steam quality (inlet/outlet) with the help of inline densitometer. An ambient oven temperature of 170 °C was used.

Steam foam flood baseline is from 4000 seconds to 6850 seconds as shown in Figure 11. This flood had a flash calculated steam quality of injection of 0.4-0.6, however, the flash calculation does not account for the heat losses associated with the steam moving through the stainless steel tubing while being injected into the porous media. Densitometry enables the analyst to have experimental data to determine what the true steam qualities of injections are. In this particular scenario, the mass flow rate of the steam was 10 g/min and the thermodynamic flash calculations provide a mass quality result of 50% +/10% while the density meter results are less than 10% mass quality for both the inlet and the outlet. The density meters placed at the inlet and outlet, also enables us to observe that in this particular experiment, the outlet mass quality is higher than at the inlet due to flashing off of liquid as the absolute pressure decreases during propagation through the porous media.

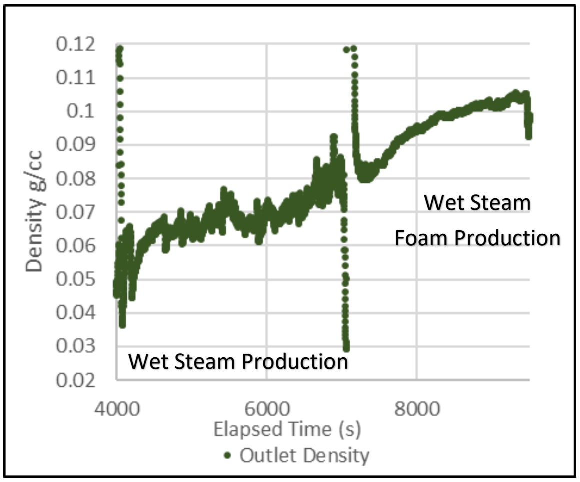

**Figure 12:** Foam/no-foam boundary identification for steam foams at the outlet of porous media. An ambient oven temperature of 170 °C was used.

Figure 12 shows the steam (4000 seconds to 6850 seconds) and steam foam flood experiment. The steam foam flow has a distinctive characteristic compared to the pure steam flow at the same steam quality. Steam foam production has a distinct lack of random fluctuations that are observed in the saturated steam production.

Steam condensation can be monitored with the density profile (Figure 13). This will enable us to evaluate the breakthrough times of steam and find out when vapor began being produced at the outlet.

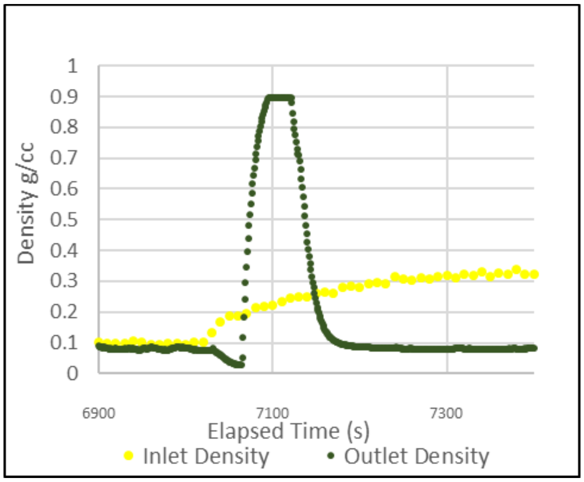

**Figure 13:** Steam condensation monitoring with the help of inline densitometer.

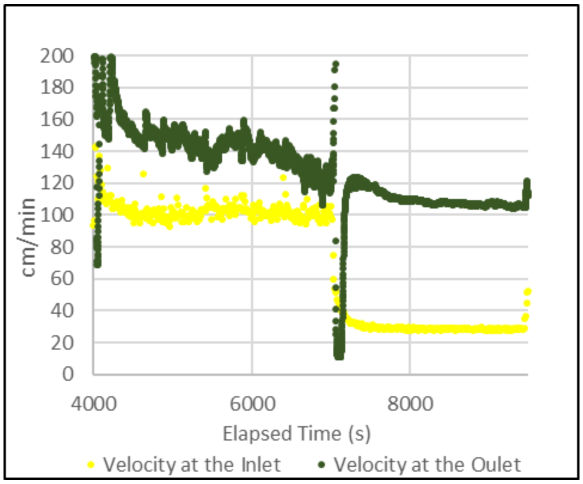

**Figure 14:** The true velocities of steam moving into the porous media. Steam flood (baseline) is from 4000 seconds to 6850 seconds. An ambient oven temperature of 170 °C was used.

The true velocities of steam cannot accurately be calculated with flash calculations and heat loss modeling. Figure 14 demonstrates the capability of calculating volumetric flow rates during steam flooding. This is not possible to calculate accurately without the use of densitometry due to the complex nature of the heat transfer that is involved with steam floods such as oven convention speeds, insulation, etc. Calculating the velocity based on flash calculations results in a falsely high velocity. The calculations all assume the system in is steady state.

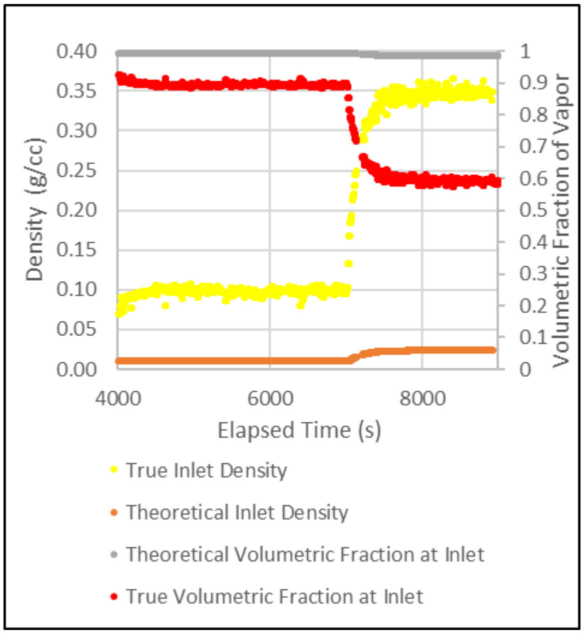

**Figure 15:** A comparison of the theoretical calculated density and volumetric fraction of the steam being injected into the porous media, highlighting the comparison between thermodynamic estimations of steam volumetric quality and measured steam volumetric quality using the DMA HPM density meter.

The true velocities of the being injected into the porous media can readily be calculated using the stream density and the mass flow rate which provides us with accurate flow velocities of steam. Using the density meter has enabled more accurate predictions of velocities than with flash calculations alone due to real time measurements of density, or specific volume of the injected phase as highlighted in Figure 15. The instrument also provides a without a doubt assurance of what phase of state the injected fluid is in which aides greatly in steam foam floods since occasionally rapid changes in pressure cause condensate production. In some cases, it's helpful to troubleshoot whether a chemicals performance is simply due to the lack of the presence of a steam phase (instrument limitation), or to distinguish that a chemical simply does not perform in the presence of the condensable gas phase.

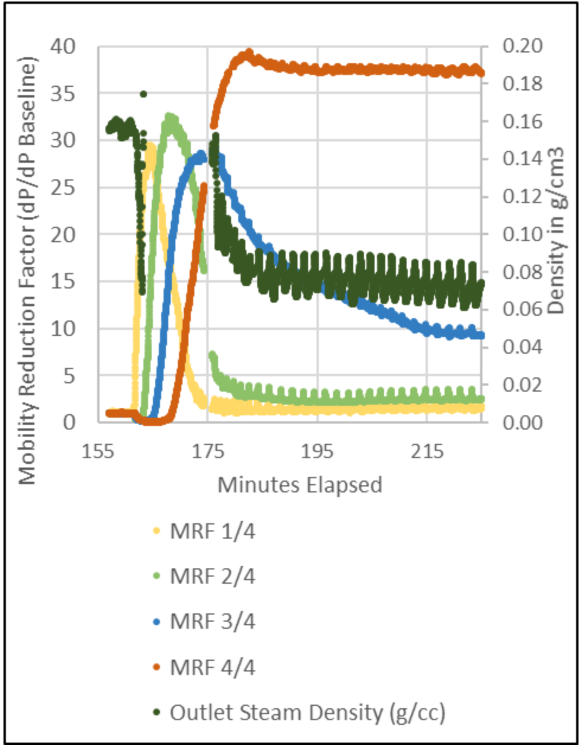

**Figure 16** mobility reduction factor and density profile during steam foam injection. The baseline was performed from 130 minutes until 165 minutes, which is only partially visible in this plot. This steam flood was performed at 200

°C with the outlet at the saturation pressure regulated with a back-pressure regulator.

As shown in Figure 16, initially we see the equilibrium steam density at baseline. The mixing water is then forced to stop mixing with the superheated steam prior to injection and is substituted by a specially designed foaming solution. Immediately a reduction in density occurs simultaneously to the increase of differential pressure in the first quarter of the sandpack. As resistance to flow increases the bubble point temperature of the steam also increases, this means that heat must be delivered to the porous media in the form of latent heat which generates condensate. We also observe the true breakthrough of the steam phase, which normally would be assumed to be at the maximum differential pressure of the last section of the sandpack, however, we can observe that steam actually begins to form at the maximum differential of the 3rd quarter of the sandpack. This is caused by the flashing of the condensate and should not be considered the actual breakthrough time of the injected steam front.

The ability to dynamically measure liquid saturation allows us to analyze the equilibrium water saturations during multiphase flow conditions as shown in Figure 16.

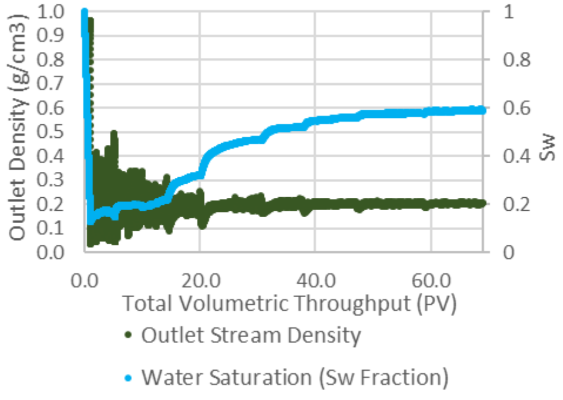

**Figure 17:** A plot demonstrating the use of densitometry to calculate dynamic fluid saturation. This test was performed at 100 °C and 750 psig back pressure. Total Volumetric flow rates were 0.5, 1.0, 1.5, 3.0, 6.0, 10.0, 15.0, 20.0 28.0 mL/min respectively

### 3.5 Quality Control of Dynamic Fluid Saturation

It should be noted that beyond ~21cc/min does not provide the density meter with enough time to measure "every molecule" that passes through it, the residence time within the DMA HPM is not long enough however the saturation values still aligned quite closely with manual mass balance performed by weighing the isolated sandpack before and after the flood. Manual mass balance results in a water saturation of 0.497 in comparison to the 0.587. The relative difference between the two methods is 16.6%. According to manual mass balance 10.66 mL of water was left within the sand pack, and according to the DMA HPM 12.56 mL of water are left inside the sand pack, this error could be due to the fact that once velocities above ~21cc/min were used at the last two velocity intervals the materials flowing through the DMA HPM did not have enough residence time to be accounted for in the cell. The error is magnified in the $S_w$ calculations because of the reduced pore volume, a larger pore volume would reduce the impact of these uncertainties. The total volume (of water) injected was 281.67cc, the total volume produced was 281.08cc. A mass balance deficit of -0.2% is obtained. The DMA HPM has proven to be an effective tool for mass balance for two-phase flow based on the data obtained. The deficit is only due to the flow rates being slightly higher than the maximum flow rate at which all material can pass through the measuring cell and have a density measurement associated with it.

## 4.0 Summary

Understanding fluid flow in porous media is challenging. Laboratory experiments at real reservoir condition are key to achieve this goal. However, the nature of experiments (pressure, temperature, fluid viscosity, multiphase flow, etc.) makes the data analysis and interpretation challenging and sometimes impossible. This study introduces the high-resolution inline density measurement at experimental condition (i.e. high pressure, high temperature) as a unique tool for understanding fluid flow in porous media. Following are some of the unique achievement of data analysis utilizing densitometer (DM):

- Beside oil recovery calculation in conventional light oil experiments, DM can significantly reduce the time, chemical usage for oil recovery calculation in tests including heavy viscous oil without compromising the accuracy.

- Valuable information in high-temperature experiments including monitoring steam condensation, steam/steam foam propagation and breakthrough time, water saturation changes, and steam front velocity calculation.
- Understanding complex fluids flow by identifying foam/no foam boundary at reservoir condition without the need for visualization.
- Monitoring and detecting nanoparticles or fine transport in porous media.

## References

1. A. Baldygin, D. S. Nobes, and S.K. Mitra. “New Laboratory Core Flooding Experimental System". Industrial & Engineering Chemistry Research 2014 53 (34), 13497-13505 (2014).

2. D. Olsen. “Using a Densitometer for Quantitative Determinations of Fluid Density and Fluid Volume in Core Flooding Experiments at Reservoir Conditions.” The International Symposium of the Society of Core Analysts, Vienna, Austria, 27 August – 1 September (2017).

3. Instruction Manual, *DMA HPM*, Document no. C34IB06A.fm, Anton Paar GmbH, Graz, Austria (2005).

4. A., Donath. “Magnetic Imaging of Nanoparticles Flow through Porous Media”. Master thesis, University of Calgary (2017).

# Pore-scale experimental study of carbonated water injection in an oil-wet carbonate: an improved insight into wettability alteration and displacement mechanisms

*Ziqiang* Qin[1,*], *Maziar* Arshadi[1], and *Mohammad* Piri[1]

[1]Department of Petroleum Engineering, University of Wyoming, Laramie, Wyoming 82071, United States

**Abstract.** Carbonated water injection (CWI) has been proposed to mitigate the poor sweep efficiency of conventional $CO_2$ flooding. Furthermore, CWI requires much less $CO_2$ that makes it more attractive for EOR projects that have access to limited quantities of $CO_2$. Even though previous experimental studies have presented data supporting the effectiveness of CWI for enhanced oil recovery, the direct evidences obtained from naturally-occurring rock samples on pore-scale displacement mechanisms responsible for the observed recovery enhancements are scarce. In the past decade, X-ray microtomography (micro-CT) technology has become more readily available and this has created numerous opportunities for pore-level investigations of complex multi-phase flow processes in natural porous media. In this study, we probed the displacement mechanisms taking place during CWI and subsequent depressurization processes through miniature core-flooding experiments at elevated pressure and temperature conditions (1400 psi and 50 °C), using a HPHT core-flooding system integrated with a high-resolution micro-CT scanner. The miniature core sample was dynamically aged with crude oil at initial water saturation and subsequently subjected to waterflooding, CWI, and a depressurization step. The sample was repeatedly imaged using the micro-CT scanner in the course of the experiments. The images were then processed to generate three-dimensional fluid occupancy maps from which the fluid saturations, in-situ contact angles, and local displacement patterns were determined. The results showed a significant incremental oil recovery due to CWI and subsequent depressurization steps compared to the unadulterated waterflooding. In-situ contact angle measurements yielded direct evidences of wettability alteration from oil-wet to neutral-wet conditions during CWI. Our observations indicated that the wettability alteration was a gradual process, which facilitates oil displacement from the medium. The swelling of oil during CWI and the displacements taking place during the subsequent depressurization process also contributed to oil production.

## 1 Introduction

$CO_2$ injection is a well-established enhanced oil recovery (EOR) scheme in oil reservoirs. However, a viscous fingering effect has always been a technical challenge for continuous $CO_2$ injection, which is amplified in carbonate reservoirs. This is mainly due to the complex pore network structure and heterogeneity of carbonate rocks [1,2]. Furthermore, most of the carbonate reservoirs were found to be in mix-wet or even oil-wet conditions [3]. Carbonated water injection (CWI) has been proposed to mitigate the poor sweep efficiency of continuous $CO_2$ flooding. In addition, CWI is an economically-efficient EOR strategy as only a small amount of $CO_2$ is consumed in this method.

Kechut et al. [4] provided experimental results showing that CWI could lead to higher oil recovery compared to unadulterated waterflooding in both secondary and tertiary modes. Also, 45%-51% of the injected $CO_2$ was stored in the porous medium at the end of the experiments, which indicates that the CWI EOR strategy could also serve for a $CO_2$ storage purpose. Sohrabi et al. [5] showed a recovery enhancement due to CWI through a series of core-flooding experiments. They reported that secondary CWI led to higher and faster oil recovery compared to that of tertiary CWI. It was also concluded that the $CO_2$ was moving ahead of the carbonated water (CW) front, which indicates successful delivery of $CO_2$ by the CW. Seyyedi et al. [6] investigated the potential of CW for enhancing the water imbibition rate and oil recovery utilizing high-pressure imbibition experiments. They reported that CW could increase the oil recovery of spontaneous imbibition in both sandstone and carbonate rocks. The oil recovery factor was a function of the initial wettability state of the rocks.

In the later period of oil production processes, CWI schemes could also result in an additional oil recovery during reservoir pressure decline stages. Riazi et al. [7] performed experiments using high-pressure micromodels and showed that a pressure blow-down period subsequent to CWI could lead to further oil production. They claimed that $CO_2$ exsolution during the depressurization caused

---

[*] Corresponding author: zqin@uwyo.edu

local flow diversions and the coalescence of isolated oil clusters, which resulted in additional oil recovery. Zuo and Benson [8] also studied the effect of depressurization after CWI on oil recovery in micromodels. They reported that a 10% additional oil recovery was achieved after reducing the pore pressure 2 MPa below the $CO_2$ liberation pressure. The main mechanisms governing the additional oil recovery were that exsolved $CO_2$ blocked the water flow channels and diverted the flow of water into the oil-filled pores. Alizadeh et al. [9] reported that $CO_2$ exsolution after CWI, as a result of depletion, led to remarkable oil recovery. A 34.6% additional recovery of the original oil in place was achieved in their experiments.

Even though previous experimental studies have presented data supporting the effectiveness of CWI for EOR and have proposed possible underlying mechanisms, the direct evidence obtained from oil-wet carbonate rocks on pore-scale displacement mechanisms responsible for the observed recovery enhancements are scarce. In the past decade, X-ray microtomography (micro-CT) technology has become more readily available, and this has created numerous opportunities for pore-level investigations of complex multi-phase flow processes in natural porous media [10]. High-resolution X-ray images have been used for capillary pressure measurements [11], in-situ contact angle measurements [12, 13, 14], relative permeability determination [15], and quantitative characterization of pore space [16]. In this study, we investigated the wettability alteration and displacement mechanisms taking place during CWI and subsequent depressurization processes through miniature core-flooding experiments at elevated pressure and temperature conditions (1400 psi and 50 °C), using a HPHT core-flooding system integrated with a high-resolution micro-CT scanner. The potential wettability alteration was probed by in-situ contact angle measurement methods. Pore-fluid occupancy maps were utilized to analyse the pore-scale displacement mechanisms.

## 2 Experiments

### 2.1 Rock and fluid properties

The rock sample used in this study was a type of carbonate outcrops named Fond du Lac. A miniature sample, 8.9 mm in diameter and 44.5 mm in length, was drilled from a rock block. The sample was dried at 110 °C for 24 hours in an oven and subsequently cooled down to the room temperature in a desiccator before use. The sample was scanned by a micro-CT scanner, and a porosity of 10.05% was calculated based on the histogram-thresholding method. An absolute brine permeability of 45 mD was measured following Darcy's law.

Brine solution was prepared using distilled water, 0.5 wt% $CaCl_2$, and 19 wt% NaI. To avoid dissolution of the carbonate matrix during flow tests, a sacrificial core plug was immersed in the brine solution for 24 hours. The connate brine and brine used for unadulterated waterflooding shared the same composition. Brine was degassed for one hour before use. Carbonated water was prepared by mixing pure $CO_2$ (with a purity higher than 99.9%) with the degassed brine in a high-pressure cell at the reservoir conditions (50 °C and 1400 psi). CW was circulated in the cell for one day and then rested for three days to make sure that $CO_2$ was fully dissolved into the brine. Crude oil was collected from an oil reservoir located in the Permian basin, Taxes, USA. The oil was filtered through a 0.5 µm filter to remove possible residue and debris [17]. Next, the oil was tagged with 12 vol% 1-iodooctane to ensure sufficient X-ray attenuation contrast between fluids in the micro-CT images (Figure 1). Table 1 provides the fluid properties.

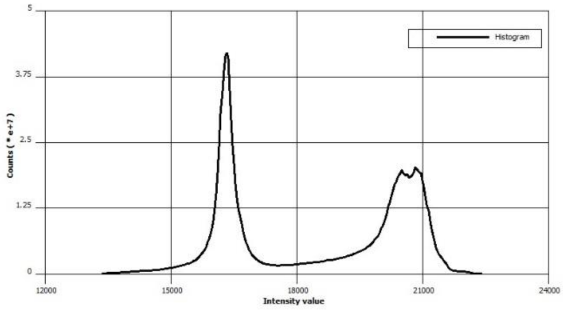

**Fig. 1.** Grey level histogram of the fluid occupancy maps at the end of the unadulterated waterflooding.

**Table 1.** Brine and crude oil properties.

| Fluids | Viscosity* (cP) | Density* (g/ml) | Salinity (ppm) | Asphaltene content (%) |
|---|---|---|---|---|
| Brine | 1.15 | 1.17 | 242236 | - |
| Crude oil | 6.5 | 0.85 | - | 0.9 |

* Viscosity and density properties were measured at ambient conditions.

### 2.2 Experimental apparatus

Flow experiments were performed using a reservoir-condition three-phase core-flooding apparatus integrated with a high-resolution X-ray micro-CT scanner. The equilibrium cell was used to prepare CW at the reservoir conditions. The core-holder was made out of carbon fibre to minimize X-ray attenuation. During the experiments, the core-holder was mounted vertically inside the CT chamber.

The X-ray imaging system was a Thermo Fisher heliscan Micro-CT scanner. Scanning was performed by collecting X-ray projections at different angles while the sample was rotating. The scanning parameters were appropriately selected to optimize image quality (Table 2). Figure 2 shows a schematic diagram of the experimental apparatus used in this study and the details of the system were explained elsewhere [18].

**Table 2.** X-ray microtomography parameters used in this study

| X-ray current (uA) | X-ray voltage (kV) | Number of projections | Exposure time (s) | Voxel size (micron) | Scanning time (hours) |
|---|---|---|---|---|---|
| 53.3 | 100 | 2880 | 1 | 3.23 | 8.3 |

### 2.3 Experimental procedure

The core sample was placed inside the core-holder with a confining pressure of 200 psi. Gaseous $CO_2$ was injected into the sample for 30 minutes to remove the bulk air from the porous medium. Then, the system was vacuumed for 24 hours. In the meantime, the sample was scanned by the micro-CT scanner to collect a set of dry reference images. Subsequently, the core was fully saturated with brine by injecting 50 pore volumes of the fluid. Afterward, the pore pressure and the confining pressure were simultaneously increased to 1400 psi and 1600 psi, respectively. The system temperature was also raised to 50 °C at this stage by adjusting the thermo-controller of the heating tape surrounding the core holder. Accordingly, brine was injected into the sample at different flow rates of 0.01 cc/min, 0.02 cc/min, 0.03 cc/min, and 0.04 cc/min to measure the absolute brine permeability. The flow rate was changed when the differential pressure across the core became stable. Next, the system was rested for five days to achieve an ironic equilibrium between the rock surface and the brine. Afterward, primary drainage was performed by injecting crude oil into the core at a constant flow rate of 0.03 cc/min. After the pressure drop across the core stabilized, the core was scanned and the initial brine saturation was determined based on image analysis. The sample was then dynamic aged with crude oil at the initial water saturation by injecting oil at a low flow rate of 0.0006 cc/min. The core was scanned frequently during aging to monitor the evolution of oil-brine contact angles. The aging process was considered complete once the in-situ oil-brine contact angles did not change further.

Subsequently, an unadulterated waterflooding was conducted with a brine injection rate of 0.005 cc/min. The experiment was further continued with a CWI step at the same flow rate as that of the unadulterated waterflooding. The core was repeatedly scanned during these processes and both flooding steps were terminated when the pore-fluid occupancy maps remained constant (a total of 15PV of CW were injected). Afterward, the injection side of the core-holder was closed. The back pressure (initially at 1400 psi) was reduced in steps to allow $CO_2$ exsolution, which represented the reservoir pressure decline during

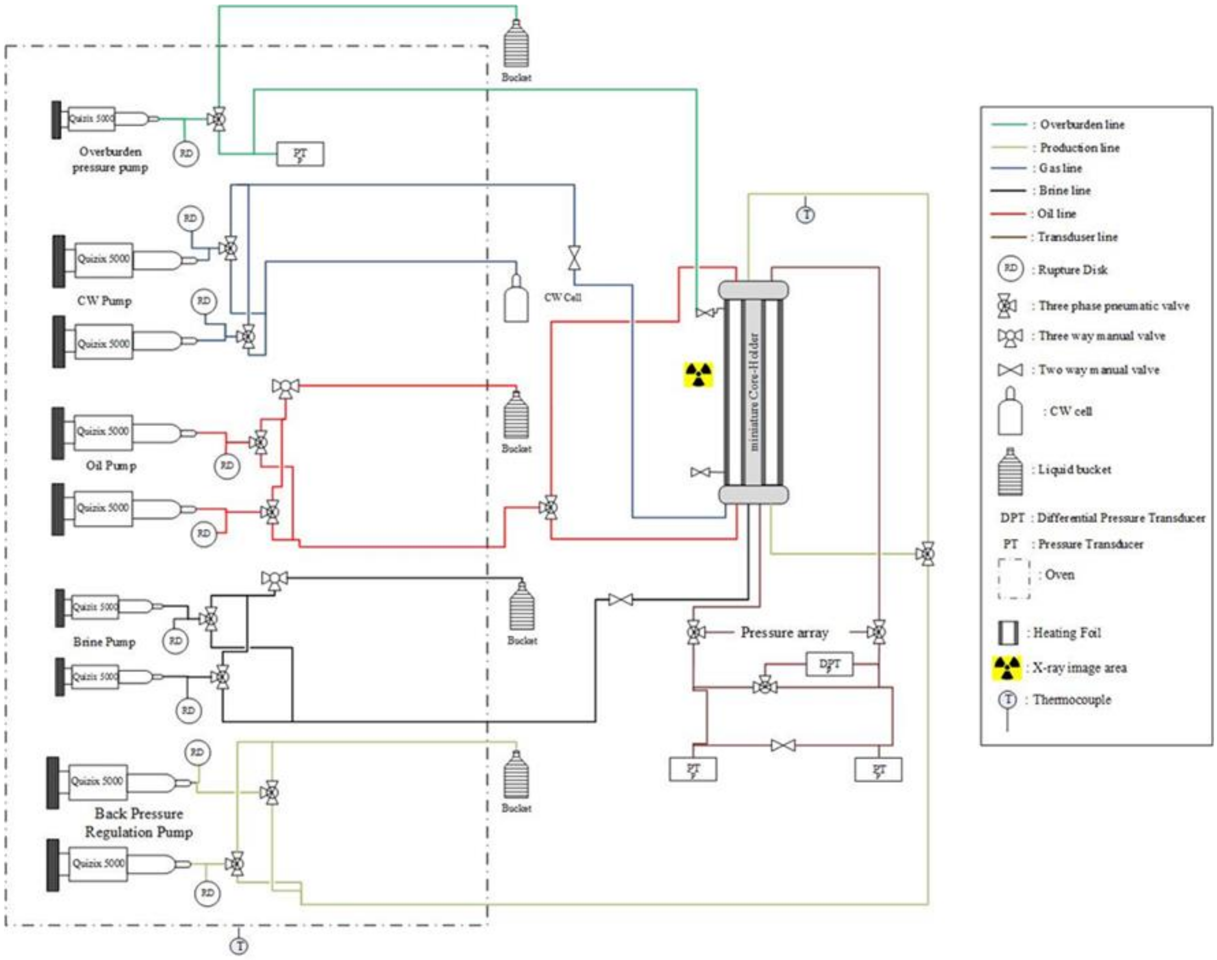

**Fig. 2.** A schematic diagram of the experimental apparatus.

depletion periods. The confining pressure was decreased at the same time to maintain the net confining pressure at 200 psi. This was done to avoid any possible pore structure deformation, as the primary focus of this study was to investigate the potential wettability alteration and displacement mechanisms of CWI and subsequent depressurization processes. The core sample was scanned at various pressure intervals during the depressurization stage. The middle part of the sample was scanned during the experiments to avoid possible end effects in the field of view (9.3mm*9.3mm*6.59mm). The projections collected during scanning were reconstructed to generate three-dimensional internal structures of the rock and residing fluids. Avizo 9.4.0 and PerGeos 1.7.0 software platforms were utilized to visualize and further process the raw images. The details of image processing workflow were explained elsewhere [13]. Figure 3 illustrates various steps of this workflow.

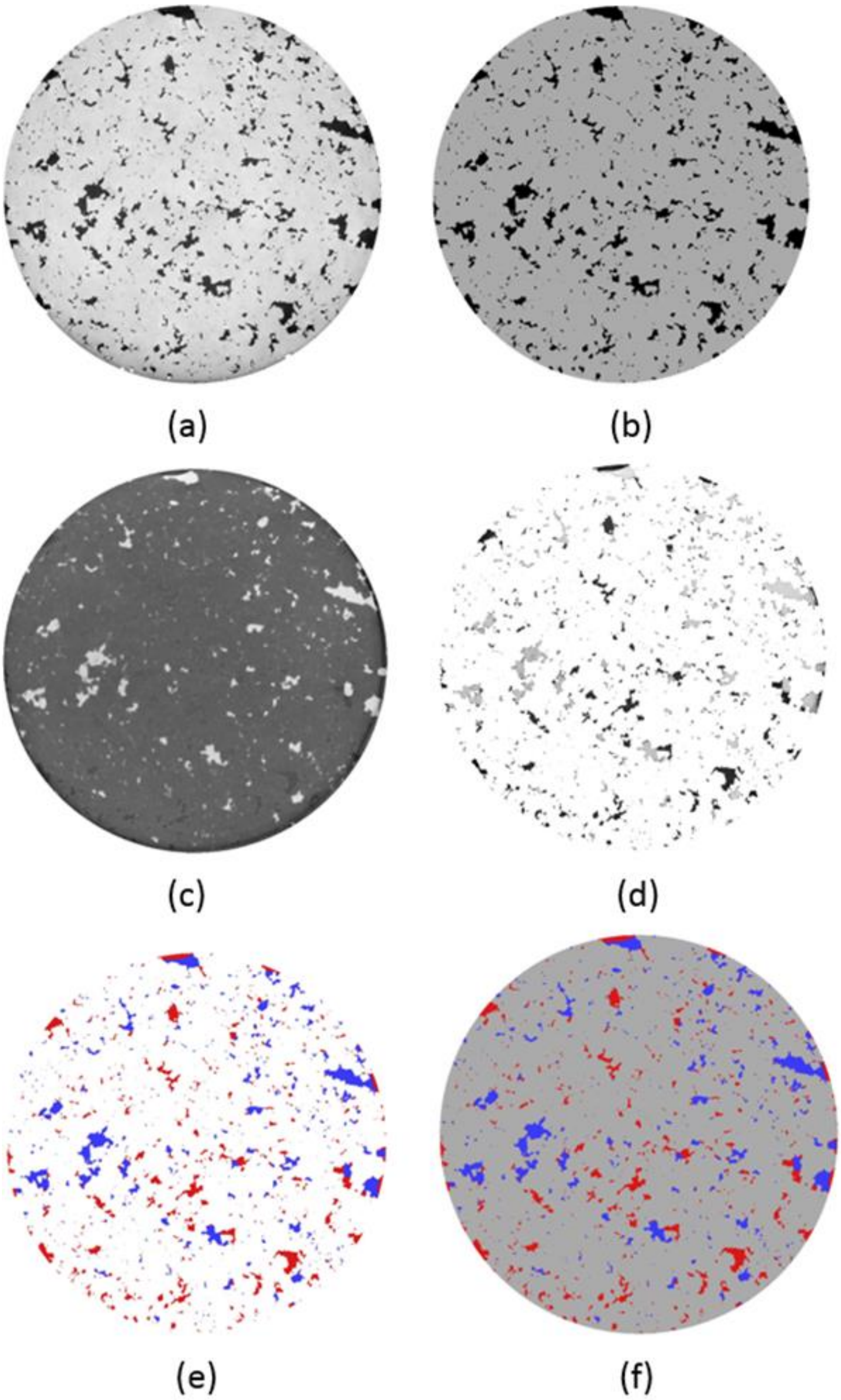

**Fig. 3.** The workflow of image processing methods: (a) filtered reference image, (b) pore map obtained from the reference image, (c) filtered flooded image, (d) multiplied image, (e) segmented pore-fluid occupancy map, (f) segmented rock-fluid system (brine: blue, oil: red, and grain: grey).

---

* Corresponding author: zqin@uwyo.edu

## 3 Results and Discussion

### 3.1 In-situ saturations

To quantify the effectiveness of CWI and subsequent depressurization processes for EOR, we calculated the fluid saturations from the segmented pore-fluid occupancy maps of various flooding stages. The initial brine saturation was 0.173 at the end of the aging process. After fifteen pore volumes of unadulterated waterflooding, the remaining oil saturation reached to 0.483, which translates to an oil recovery of 41.6%. After fifteen pore volumes of CWI, the in-situ oil saturation was reduced to 0.397 and did not change further. This is equivalent to an oil recovery of 52%. Therefore, CWI resulted in 10.4% additional recovery of original-oil-in-place compared to that at the end of the unadulterated waterflooding. Subsequently, the back pressure was reduced in steps to mimic the reservoir depletion process in later stages of production. The exsolution of $CO_2$ led to a reduction in remaining oil saturation to 0.334 as the back pressure was reduced to 130 psi. The residual oil saturation ultimately reached to 0.21 as the back pressure was further reduced to 40 psi, which corresponds to an ultimate oil recovery of 74.6%. In other words, an additional oil recovery of 22.6% was achieved as a result of the pressure blow-down process. Therefore, one can conclude that the depressurization after CWI also significantly contributed to EOR. Figure 4 demonstrates the variations of remaining oil saturation and oil recovery with respect to different flooding stages.

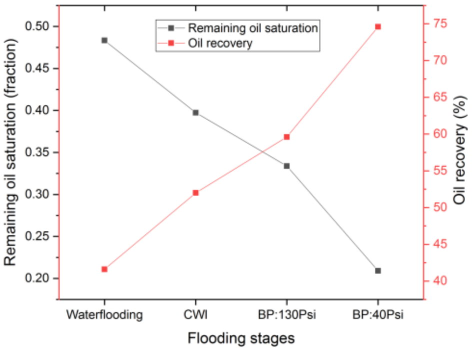

**Fig. 4.** Variations of remaining oil saturation and oil recovery with respect to different flooding stages.

### 3.2 In-situ characterization of wettability

To probe the potential wettability alteration caused by CWI, the in-situ oil-brine contact angles were measured on segmented pore-fluid occupancy maps during aging, unadulterated waterflooding, CWI, and subsequent depressurization processes. In each dataset, 30 contact angles were measured at randomly-selected locations to characterize the local wettability heterogeneity and reduce the human error. In-situ contact angle measurements might have an absolute error value of two degrees as a result of uncertainties with identifying fluid-fluid and rock-fluid interfaces and the details of this highly-accurate in-situ contact angle measurement technique were explained elsewhere [13]. The average oil-brine contact angle at the end of the unadulterated waterflood was 118.76°, which is similar to the average value of 118.15° after aging. This similarity indicates that no wettability alteration occurred during the unadulterated waterflooding process. In contrast, the average oil-brine contact angle had been reduced to 111.09° after one pore volume of CWI. The average value had reached to 107.02° after fifteen pore volumes of CWI, which reveals that the wettability alteration towards increasing water-wetness had occurred due to the CWI. The oil-brine contact angle values further decreased as the experiment was continued. At 1100 psi pore pressure during depressurization, the average oil-brine contact angle was 104.82°. This value was ultimately reduced to 95.89° by the end of the depressurization stage (i.e., 40 psi pore pressure). Our observations indicate the CW-induced wettability alteration is a gradual process that could, at least partially, impact the pore-scale mechanisms of oil recovery during CWI.

### 3.3 Pore-scale displacement mechanisms of CWI and subsequent depressurization process

Characterization of fluid occupancy maps revealed that the wettability alteration facilitated the oil displacement during CWI as a result of the increase in threshold capillary pressures (negative values in an oil-wet system). Figure 5 demonstrates the evolution of pore-fluid occupancy maps at the end of the unadulterated waterflooding (with an average oil-brine contact angle of 118.76°) and CWI (with an average oil-brine contact angle of 107.02°).

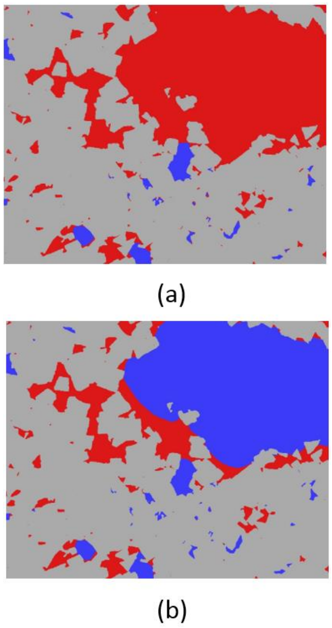

**Fig. 5.** Exemplary two-dimensional maps of fluid occupancy at the end of the (a) unadulterated waterflooding and (b) CWI (brine: blue, oil: red, and grain: grey).

Furthermore, based on in-situ fluid occupancy investigation, we found that the swelling of oil ganglia (possibly due to the diffusion of $CO_2$ from the injected CW to the oil phase) also contributed to oil production. Moreover, during the subsequent depressurization process, the displacements taking placed significantly changed the fluid occupancies and resulted in additional oil recovery. Further image analysis is being carried out at this moment to provide more insight into the pore-scale displacement mechanisms governing the observed recovery enhancements (Figure 6).

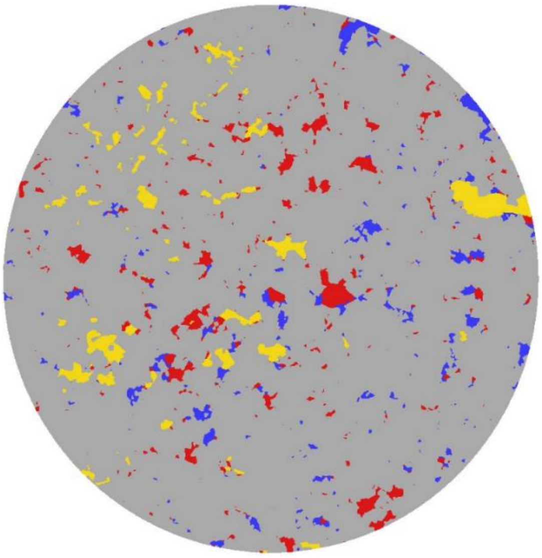

**Fig. 6.** Exemplary two-dimensional maps of fluid occupancy at the end of the depressurization process (gas: yellow, brine: blue, oil: red, and grain: grey).

## 4 Summary and conclusion

In this study, we probed the wettability alteration and displacement mechanisms taking place during CWI and subsequent depressurization processes through miniature core-flooding experiments at elevated pressure and temperature conditions, using a HPHT core-flooding system integrated with a high-resolution micro-CT scanner. The potential wettability alteration was characterized through an in-situ contact angle measurement method. Pore-fluid occupancy maps were utilized to investigate the pore-scale displacement mechanisms of CWI. Here, we summarize the main findings:

1) A significant amount of additional oil recovery was achieved during the CWI and subsequent depressurization processes compared to the unadulterated waterflooding.
2) Wettability alteration towards increasing water-wetness occurred as a result of CWI. The wettability alteration was a gradual process, which facilitates oil displacement from the medium.

The authors gratefully acknowledge the financial support of Thermo Fisher Scientific Company, Hess corporation, and the School of Energy Resources at the University of Wyoming.

## References

1. J. Lai, et al. "Prediction of reservoir quality in carbonates via porosity spectrum from image logs." Journal of Petroleum Science and Engineering **173** (2019): 197-208.
2. J. Lai, et al. "Pore structure and fractal characteristics of Ordovician Majiagou carbonate reservoirs in Ordos Basin, China." AAPG Bulletin 20,190,412 (2019).
3. P. Zhang, and T. Austad. "Wettability and oil recovery from carbonates: Effects of temperature and potential determining ions." Colloids and Surfaces A: Physicochemical and Engineering Aspects **279**.1-3 (2006): 179-187.
4. NI Kechut, M. Sohrabi, and M. Jamiolahmady. "Experimental and numerical evaluation of carbonated water injection (CWI) for improved oil recovery and CO2 storage." *SPE EUROPEC/EAGE Annual Conference and Exhibition*. Society of Petroleum Engineers, 2011.
5. M. Sohrabi et al. "Coreflooding studies to investigate the potential of carbonated water injection as an injection strategy for improved oil recovery and CO 2 storage." Transport in porous media **91**.1 (2012): 101-121.
6. M. Seyyedi and M. Sohrabi. "Enhancing water imbibition rate and oil recovery by carbonated water in carbonate and sandstone rocks." Energy & Fuels **30**.1 (2015): 285-293.
7. M. Riazi, M. Sohrabi, and M. Jamiolahmady. "Experimental study of pore-scale mechanisms of carbonated water injection." Transport in porous media **86**.1 (2011): 73-86.
8. L. Zuo, and S. M. Benson. "Exsolution enhanced oil recovery with concurrent CO2 sequestration." Energy Procedia **37** (2013): 6957-6963.
9. A. H. Alizadeh. et al. "Multi-scale experimental study of carbonated water injection: an effective process for mobilization and recovery of trapped oil." Fuel **132** (2014): 219-235.
10. J. Lai et al. "Three-dimensional quantitative fracture analysis of tight gas sandstones using industrial computed tomography." Scientific reports **7**.1 (2017): 1825.
11. R.T. Armstrong, M.L. Porter, and D. Wildenschild. "Linking pore-scale interfacial curvature to column-scale capillary pressure." Advances in Water Resources **46** (2012): 55-62.
12. M. Andrew, B. Bijeljic, and M.J. Blunt. "Pore-scale contact angle measurements at reservoir conditions using X-ray microtomography." Advances in Water Resources **68** (2014): 24-31.

13. Z. Qin, M. Arshadi, and M. Piri, “Micro-scale experimental investigations of multiphase flow in oil-wet carbonates. I. In-situ wettability and low-salinity waterflooding.” Fuel (to be published)
14. Z. Qin, M. Arshadi, and M. Piri, “Micro-scale experimental investigations of multiphase flow in oil-wet carbonates. II. Tertiary gas injection and WAG.” Fuel (to be published)
15. J. M. Schembre, and A. R. Kovscek. "A technique for measuring two-phase relative permeability in porous media via X-ray CT measurements." Journal of Petroleum Science and Engineering **39**.1-2 (2003): 159-174.
16. S. Youssef, et al. "Quantitative 3D characterisation of the pore space of real rocks: improved μ-CT resolution and pore extraction methodology." *Int. Sym. of the Society of Core Analysts* (2007).
17. W. Kuang, S. Saraji, and M. Piri. "A systematic experimental investigation on the synergistic effects of aqueous nanofluids on interfacial properties and their implications for enhanced oil recovery." Fuel **220** (2018): 849-870.
18. Z. Qin, M. Arshadi, and M. Piri, "Pore-scale experimental investigation of in-situ wettability and displacement mechanisms governing WAG in oil-wet carbonates." *Int. Sym. of the Society of Core Analysts* (2019).

# The digital rock analysis of biogenically induced reservoir heterogeneities in Cretaceous reservoirs of Saudi Arabia

*Ivan* Deshenenkov[1,*], and *Camilo* Polo[2]

[1]Geological Operations Department, Saudi Aramco, Dhahran, Saudi Arabia
[2]Northern Area Reservoir Characterization Department, Saudi Aramco, Dhahran, Saudi Arabia

**Abstract.** The characterization of the fluid-flow properties in biogenically altered formations is a key for successful exploration campaigns. This study assessed reservoir quality and evaluated permeability of the biogenically-modified Cretaceous upper Ratawi section in Saudi Arabia. When dealing with these bioturbated carbonates, characterization of sedimentary heterogeneities is often overprinted by the complex spatial geometries of burrows. The high-resolution 3D X-ray microscopy imaging and analysis of these bioturbated sections lead to a better understanding of the interconnectivity between permeable burrows and tight matrix. The analysis deploys multiscale imaging from whole core to sub-micron scale. The coarse imaging at 20-50 microns resolution helped to identify bioturbated sections to select samples for higher resolution tomography. The 3D sample tomograms were segmented to define burrows and matrix distributions, where samples were extracted for thin-sections, scanning electronic microscopy (SEM) and mercury injection capillary pressure (MICP) analyses to refine the pore sizes and rock types. The analysis showed an intricate, highly connected, mixed horizontal and inclined burrow system dominated by *Thalassinoides*. Intergranular porosity, associated with the fill of *Thalassinoides,* constitutes a mechanism for permeability enhancement in a tight matrix. Increased permeability is associated with higher dolomite content that might be used as a sweet spot identifier from wireline logs.

## Introduction

Textural and mineralogical modifications of the original sedimentary fabric by organisms at the time of sediment deposition are known as bioturbation. Biogenically driven chemical and physical alteration of the primary sedimentary fabric due to burrowing infauna in carbonate formations can result in fabric-selective dolomitization [1]. Recent studies have demonstrated that in tight carbonate formations this type of modification can lead to the enhancement of reservoir permeability [1]. Enhancement associated with bioturbation can be expressed as dual-permeability flow-media and shares some conceptual similarities to fracture systems. Sediment modifications in the primary sedimentary fabric include burrowing, churning and continuous reworking of particles. One of the fundamental input parameters into reservoir models is permeability. Commonly, biogenically induced dual-permeability flow media exhibit poor reservoir characteristics owing that only trace fossils (i.e., the permeable conduits) are able to transmit fluids, with little to none interaction with the tighter matrix [1]. This requires detailed understanding of the geological heterogeneities to characterize their impact on petrophysical and reservoir engineering studies.

This paper documents the influences of bioturbation on reservoir quality from the Cretaceous Ratawi Limestone (RL), Saudi Arabia. Permeability distributions were investigated using digital and conventional techniques to refine different rock types. We present a case study of biogenic enhancement in tight facies of a carbonate formation and provide a conceptual framework for burrow-associated permeability improvement analyzed through three-dimensional (3D) X-ray computed tomography (CT) imaging acquired at multiple scales for digital rock characterization supported by mercury injection capillary pressure (MICP) experiments and high-resolution scanning electron microscopy (SEM) imaging.

The objective of the work was to integrate the CT images, thin-section photomicrographs, MICP and SEM data to simulate permeability in high-resolution 3D images and upscale it to the plug and whole-core levels to define if permeability is linked to specific macroscale geological features of the rock.

This may only be examined through multi-scale imaging and modeling. Whole core sample analyses was essential in calculation of the reservoirs heterogeneity to assess permeability anisotropy. The comparison of permeability at different scales is necessary for

---

[*] Corresponding author: Ivan.Deshenenkov@aramco.com

upscaling laboratory-measured properties to grid cells of the full-field geological models.

## 1 Geological context

The RL is a tight formation (<1mD) in Saudi Arabia. To understand the causes of flow restriction, this study captures systematically different pore types, their relationship, distribution, connectivity and their impact on reservoir fluid flow behavior. It is observed that pores are not related to any depositional surface and are rather formed due to mesogenetic corrosion of highly micritized, tight carbonate rock bodies. Primary pores are almost completely destroyed during the process of shallow burial diagenesis. Separated larger pores are both fabric as well as non-fabric selective type. They are the main contributors to pore volume within an overall pervasive (micritic) matrix pore dominated system of wackestone and packstone.

### 1.1 Lithology

Sedimentological analysis based on core samples reveals that burrowed, tight facies range from mudstones to mud-dominated packstones and wackestones with abundant skeletal fragments and pellets.

### 1.2 Depositional environments

Overall, sediment deposition took place on a low-gradient carbonate platform along the eastern border of the Arabian Shield. The preponderance of fine-grained lithology along with intense bioturbation including well-developed *Thalassinoides* suggests deposition in sheltered lagoonal settings in the inner part of the platform during the Lower Cretaceous.

Several porosity generation and destruction events are recorded in these rocks. A eugenic phase of porosity enhancement took place initially with the dissolution of aragonite shells followed by compaction related porosity reduction. During prolonged subsidence of this passive margin sequence, a good part of the pores were occluded due to calcite cementation.

Pressure solutions are also recorded within argillaceous mudstone, which dissolved carbonate minerals locally and deposited them in the surrounding pores, causing further reduction in porosity. Mesogenic porosity enhancement is found as an important event for this formation. It is presumed that a phase of organic acid generation and carbonate mineral dissolution took place during the onset of hydrocarbon expulsion from deeper source beds. This process was very important for the RL as most of the porosities are developed through secondary pores.

## 2 Methods

### 2.1 Conventional core observations

Core descriptions, thin-section petrography and SEM assessments allowed the identification of an intricate, highly connected, mixed horizontal and inclined burrow system dominated by *Thalassinoides*. Selective dolomitization occurs in burrow fills and is commonly surrounded by a non-dolomitized lime mud matrix. This selective burrow dolomitization results in intergranular porosity and constitutes a mechanism for vertical permeability enhancement in an otherwise low-permeability matrix. Preferential vertical burrowing direction suggests that dwellings of bioturbating infauna constitute selective fluid-flow networks. Core pictures displaying oil-stained *Thalassinoides* burrows show that oil staining is concentrated preferentially in the fill of burrows (fig. 1, a). Thin-section photomicrographs provide information about rock texture and porosity types in carbonates that are essential for rock-type classification. Photomicrographs (fig. 1, b, c) illustrate dolomitized burrows, muddy matrix and intergranular porosity concentrated in the burrow fill due to preferential dolomitization associated to *Thalassinoides*. Burrows are mainly vertical with a minor horizontal component, and may span a depth of up to one meter below the sea floor, with typical diameters between five and ten millimeters.

Bioclastic material is partially leached and cemented by drusy calcite. This section of the sample shows good porosity with common fine moldic pores and micropores. A calcite cemented fracture separates the dolomitized and non-dolomitized parts of the sample. Microporosity is commonly observed in the bioclastic wackestone.

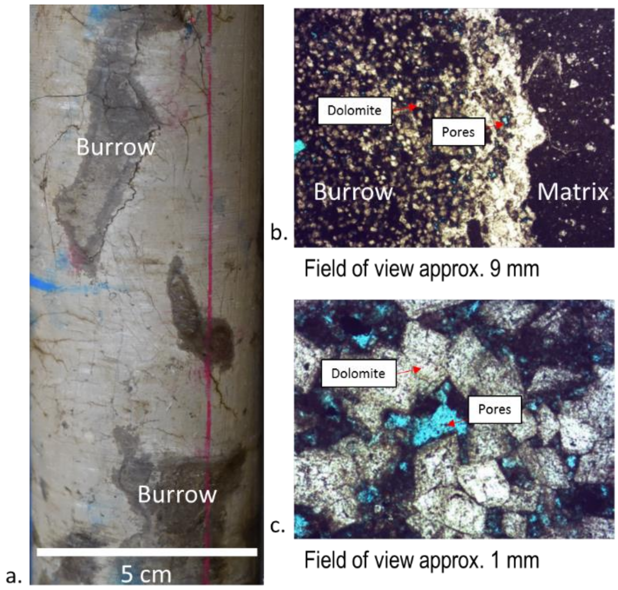

**Fig. 1.** a) Core picture and b, c) thin section photomicrography illustrating the type of biogenic enhancement of the formation.

### 2.2 Scanning electron microscopy

Samples containing burrows and matrix were selected from each whole core sample. Continuous magnification of SEM observations together with energy dispersive spectroscopy (EDS) show that most of the pores preserved in RL is moldic. Images (fig. 2, a-d) highlight the dominance of solution pores within the formation intervals. Dolomitization of grains selectively increases intercrystalline porosity locally, but this phenomenon is less common. Reservoir quality as a whole is poor due to poor connectivity of secondary dissolution or intercrystalline pores. Burrows have large dolomite grains. Matrix has tight micritic calcite as well as a few large dolomite grains.

The main goal of the SEM-EDS measurements was to establish the presence of dolomite grains in the micritic system. Fig. 2 (e, f) shows SEM-EDS points. The results demonstrate that grains are mainly calcite and dolomite.

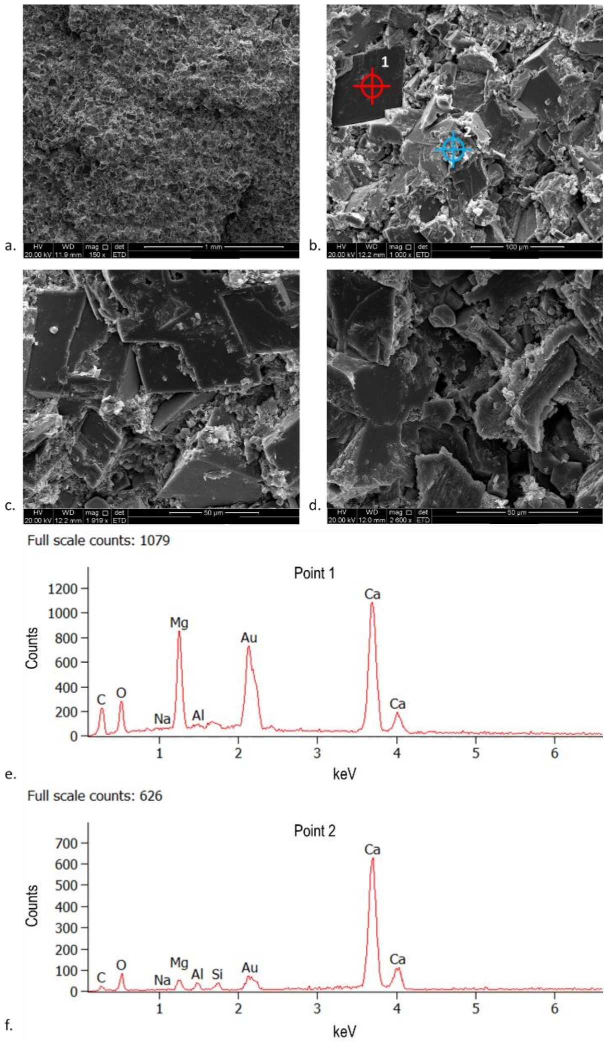

**Fig. 2.** a-d. Continuous magnification (150x-2600x) of the RL samples with SEM imaging combined with e. dolomite EDS spectrum (point 1 in b.), f) Calcite EDS spectrum (point 2 in image b.), Au peaks (gold) in the spectra are due to the gold sample coating.

## 3 Digital rock analysis of the RL bioturbated samples

The digital rock analysis workflow includes the whole core samples computed tomography analysis, burrow segmentation, identification of burrow-modified regions, and the selection of smaller samples for higher resolution work. The smaller samples were scanned at medium resolution (4 µm) to identify the matrix to burrow interface, and at high-resolution (0.5 µm) to study morphology and properties of burrows and matrix. Based on initial image analysis results, appropriate volumes were taken for MICP. Once MICP results were available, sub-samples that cover the entire porosity spectrum in the rock were selected and extracted. The next phase of the workflow involved the determination of burrow and matrix properties through high-resolution multi-scale CT imaging. In addition, a combination of high-resolution CT and SEM-EDS data were used to refine the mineralogy of the bioturbated zones. Image processing and various analyses lead to computations of porosity and permeability of the burrowed and matrix sections of the rocks. The final stage of the workflow is to integrate the properties of burrows and matrix to produce up-scaled properties. These results can also be integrated to the whole core and wireline log scale; however, this is beyond the scope of this paper.

### 3.1. Whole core samples imaging and analysis

The whole core samples were selected based on the sedimentological descriptions of 200 ft of the whole core and 1,000 ft of well logging data. Sampling locations were identified to represent variations in lithofacies, texture and porosity type. In total, thirty 25 cm long whole core samples were taken for low-resolution (25 µm) scanning. Examples of the whole core samples scans are illustrated in fig. 3.

The grayscale image of the whole core samples (fig. 3) shows that it is composed of two distinct lithology regions: matrix and longitudal circular shaped *Thalassinoides* burrows.

Based on the low-resolution scanning three type of sub-samples have been selected for the following studies: advanced high-resolution computed tomography (16 samples), MICP measurements (8 samples) and conventional core analysis to define total porosity and absolute permeability (37 samples). Visual examination of all samples was carried out to ensure the plugs were physically suitable for the measurements and free of visible fractures or anomalies.

Sub-samples were cut from representative regions in the core that preserved changes in the geological features seen in the whole core CT images to provide integrated characterization among available data. This is an effective way of understanding rock structure at multiple scales, which would lead to proper evaluation of the impact of rock quality and geological heterogeneity on the permeability of the reservoir rocks.

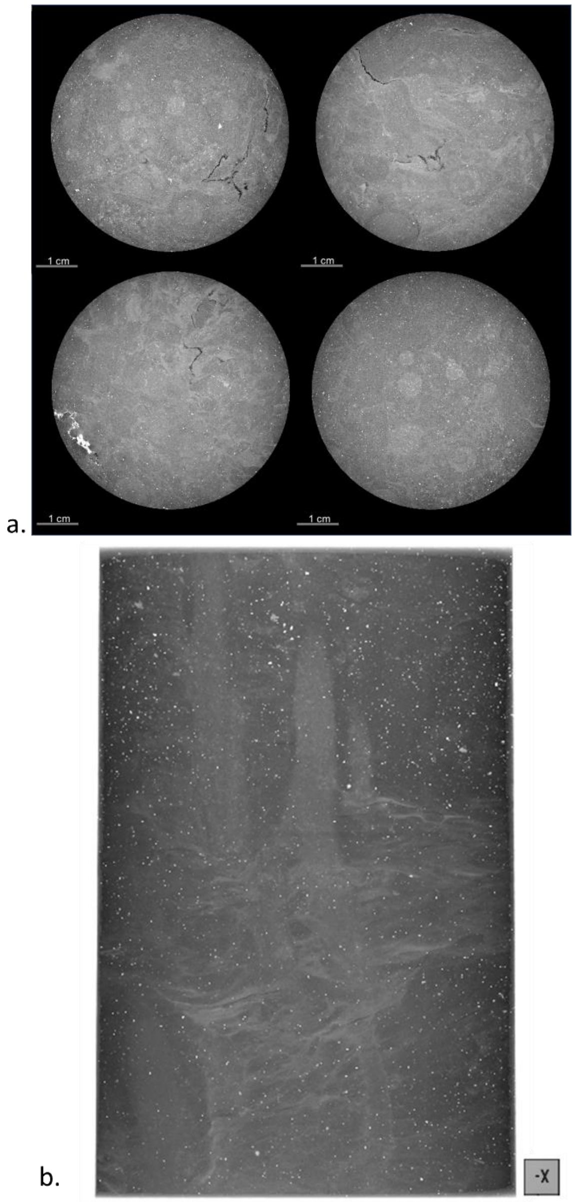

**Fig. 3.** Whole core samples tomography: a) Z-slices and b) 3D render illustrating borrows through the whole core sample.

### 3.2 Mercury injection capillary pressure data analysis

The laboratory-measured MICP samples are carefully cut from the whole core to represent each phases (burrow and matrix) in the sample (usually 1 inch diameter plug).

The MICP data indicate the prevalence of micropores in matrix (fig. 4, a) and mesopores in bioturbated regions (fig. 4, b) of the formation. MICP data show a narrow, unimodal distribution of the pore-throat radii, highlighting the development of mesopores in burrows, with the moderate entry pressure and gentle saturation gradient indicating fluid flow via mesopores. MICP data observations on the matrix sections indicate that pore-throat size distribution is bimodal, representing two types of micropores: 0.03 µm and 0.3 µm in diameter.

The difference in the pore-throat diameters is interpreted as the cause of higher permeability in the burrowed sections.

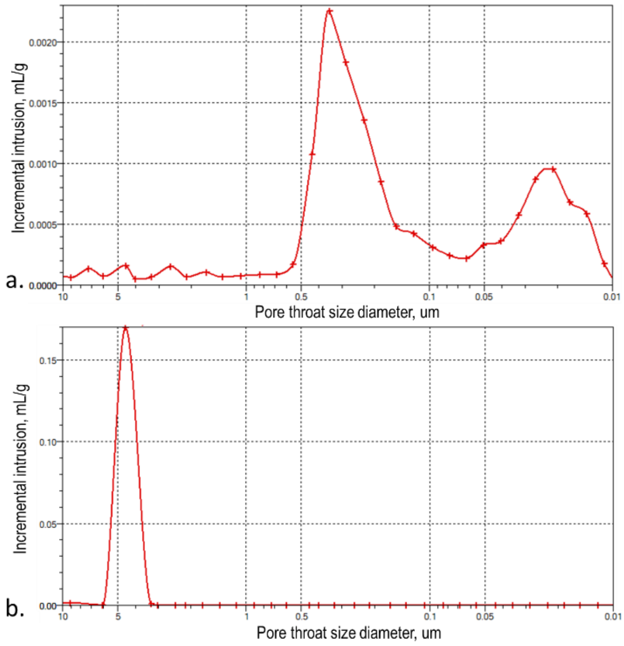

**Fig. 4.** Pore-throat size diameters distribution in a) matrix and b) burrow sections of the rock.

Absolute permeability variation associated with difference in the pore-throat size diameters has been investigated with conventional core analysis (CCAL) of the plugs.

### 3.3 Conventional core analysis of plugs

Plug samples (1.5 inch diameter) were taken from each lithology to represent the statistical property variations along the entire core length. The samples were cleaned in hot solvent extractors and were measured for helium porosity and gas permeability in standard equipment at ambient conditions using a calibrated steady-state permeameter with nitrogen gas as flowing medium.

CCAL demonstrates clear separation between bioturbated and matrix intervals on porosity-permeability graph (fig. 5). Matrix is tighter and exhibits a smaller range of porosities in comparison to the burrows porosity range. The porosity in this burrowed phase is the main contributor to the flow. On average, total porosity of these tight bioturbated plugs exceeds matrix porosity by 5-7% and permeability difference consists 1-2.5 orders of magnitude.

CCAL results underscore the importance of the bioturbated sections analyses; however, it does not provide information on permeability (k) anisotropy in vertical ($k_v$) and horizontal ($k_h$) directions. Another important task was to assess the impact of the burrow to matrix volume relationship with bulk permeability of the sample. High-resolution digital rock analysis was utilized to answer these questions.

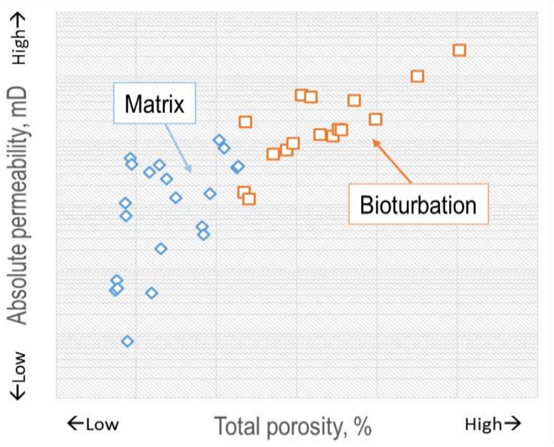

**Fig. 5.** Porosity-permeability cross-plot derived from CCAL measurements of the full (1.5 inch) plugs with embedded classification of bioturbated (orange) and matrix (blue) samples.

## 3.4 High-resolution digital rock analysis

Multi-scale digital rock analysis is conceptually well-suited for bioturbated rocks analysis and modeling [2] as it allows varying resolution and provides a systematic procedure for coarsening and refinement. Darcy's model is to approximate pressure and fluxes on a coarse grid in large-scale discontinuities, whereas fine-scale effects are captured through basis functions computed numerically by solving local Stokes-Brinkman flow problems on the underlying fine-scale geocellular grid. The Stokes-Brinkman equations give a unified approach to simulating free-flow and porous regions using a single system of equations, they avoid explicit interface modeling, and reduce to Darcy or Stokes flow in certain parameter limits [3]. The modeling demonstrates how fine-scale flow in bioturbated pore networks can be represented within a coarse-scale Darcy-flow model in fractures of the burrow to matrix interface and multi-scale elements. The flow computed solving the Stokes-Brinkman equations in burrow and matrix. This method is a promising path toward direct simulation of highly detailed rock models in bioturbated formations. The high-resolution CT imaging was conducted to build pore structures for the flow analysis.

### *3.4.1 Imaging and segmentation of full-plugs*

To perform high-resolution CT imaging, 1.5 inch samples that include a combination of burrow and matrix were extracted and scanned at 4 µm resolution. Orthogonal slices of burrow and matrix at this resolution are shown in fig. 6. It illustrates that small pores are not present at this resolution (fig. 7) within the matrix. The throat sizes distribution derived from MICP data (see fig. 4) shows that for determining the flow properties of these burrow-modified cores, the required resolution is at least 5 µm for burrow-through-flow and below 1 µm for the matrix flow unit. The higher resolutions scans are typically acquired to understand the fabric of the rock, and to define large-scale geologic objects in the samples. Therefore, a range of resolutions is needed to fully describe the plugs.

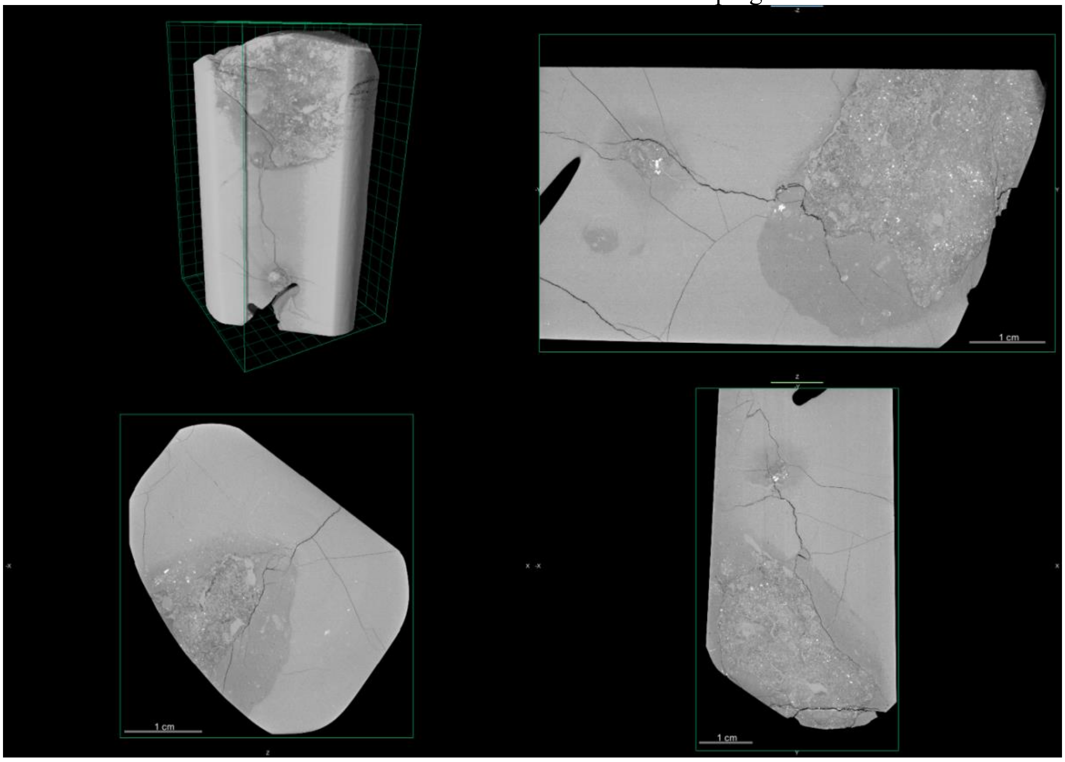

**Fig. 6.** Example of the burrowed structure, full-plug scale, 4 µm resolution: 3D render and three orthogonal projections.

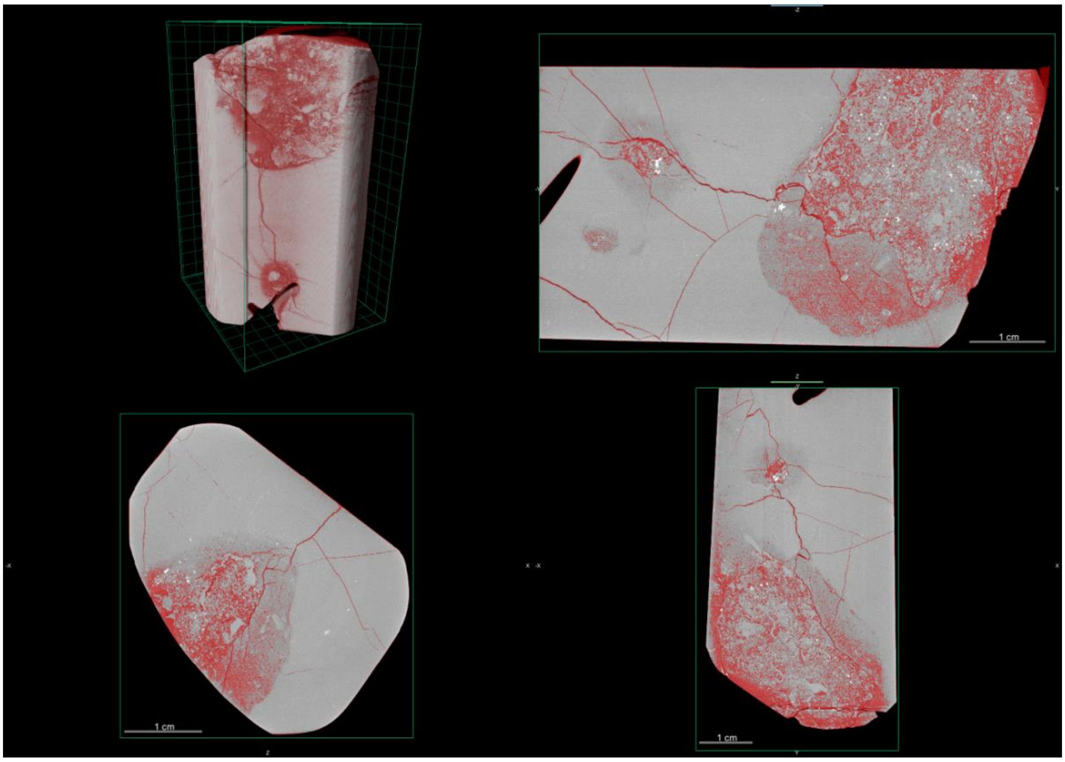

**Fig. 7.** Example of the porosity segmentation in the burrowed structure, full-plug scale, 4 µm resolution: 3D render and three orthogonal projections.

### 3.4.2 *Imaging and segmentation of sub-plugs*

The analysis of the burrow flow unit requires drilling of sub-plugs in the matrix to burrow interface locations and scanning them at 1 µm resolution; smaller separate burrow volumes were analyzed at maximum 0.5 µm that revealed a connected pore system in the burrow phase. Figure 8 shows a cross section CT slice for the burrow to matrix flow unit. The digital rock analysis confirmed the SEM data. The large dolomitic grains can be seen predominantly in the burrow phase, and the space between them is filled with micritic calcite (fig. 9). Based on the MICP data, the matrix flow unit would require imagining by focused ion beam SEM beyond the resolution of CT images. Therefore, permeability of matrix for pore-scale modeling was assigned based on the minimum CCAL of samples with matrix only. The modeling results will represent the pessimistic estimate of the whole system permeability.

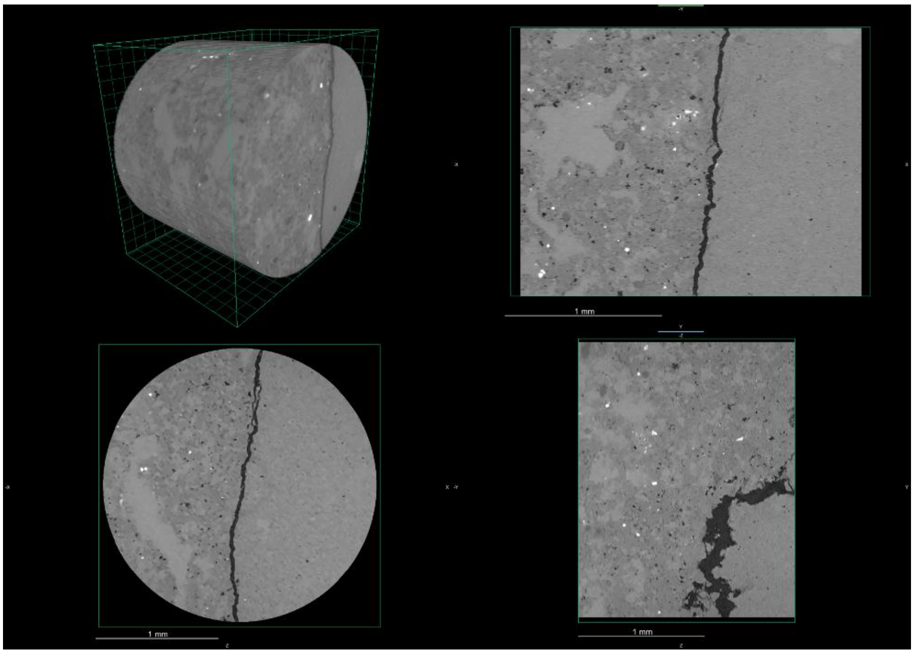

**Fig. 8.** Example of the high-resolution tomography in the matrix to burrow interface, sub-plug scale, 1 µm resolution: 3D render and three orthogonal projections.

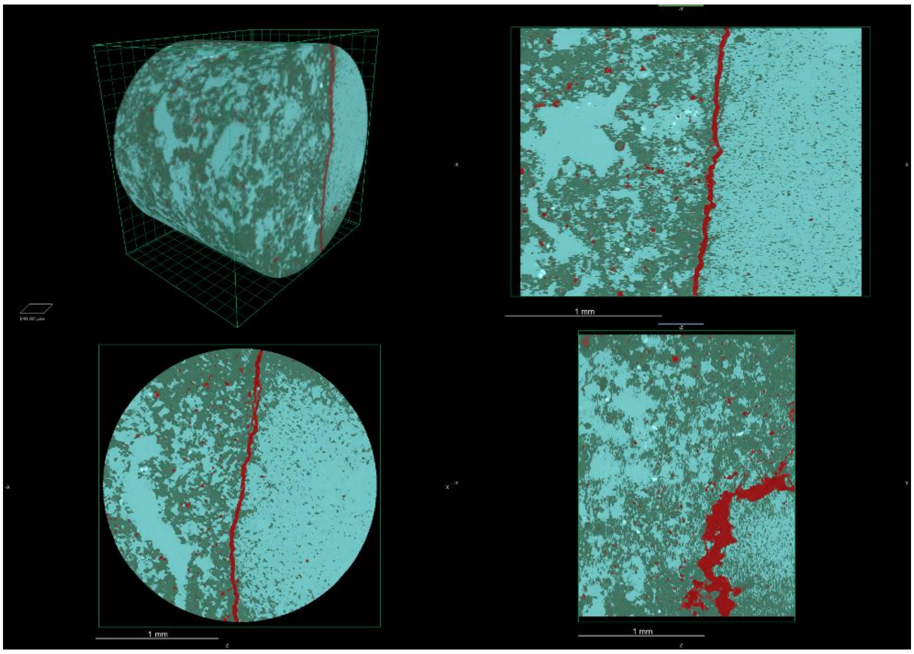

**Fig. 9.** Example of the segmentation of the high-resolution tomography in the matrix to burrow interface, sub-plug scale, 1 µm resolution: 3D render and three orthogonal projections. Color key: red – porosity, green – dolomite, cyan – calcite.

*3.4.3 Numerical modeling of the flow properties*

Numerical modeling of permeability in burrows was based on the highest magnification tomography at 0.5 µm resolution. 3D images were segmented to allow porosity and permeability computation at subsample scales. Two main phases have been identified: pores and grains.

Incompressible flow in a porous rock matrix typically obeys Darcy's law and is described by a first-order elliptic system in which Darcy's law was combined with a mass-conservation equation to relate the pressure and the total (interstitial) velocity. Incompressible flow in open domains, on the other hand, obeys the Stokes equations [3, 4]. The Stokes-Brinkman equations combine Darcy and Stokes models into a single equation. This model gives a unified approach to model flow in both the fractures and the intergranular porous subdomains using a single system of equations. In the free-flow (or fluid) domain, it is assumed that permeability tends to infinity and sets the effective viscosity equal to the fluid viscosity, otherwise it transforms into the coupled Darcy-Stokes equations, which reintroduces the requirement for interface conditions and computational intractability.

The original structure, porosity segmentation, velocity field and illuminated streamlines are illustrated in fig. 10. The porosities of burrows are in the range of 14 to 19 pu, while the permeability is in the range of 5.25 to 2.55 mD for the studied samples that compares well with literature sources [5].

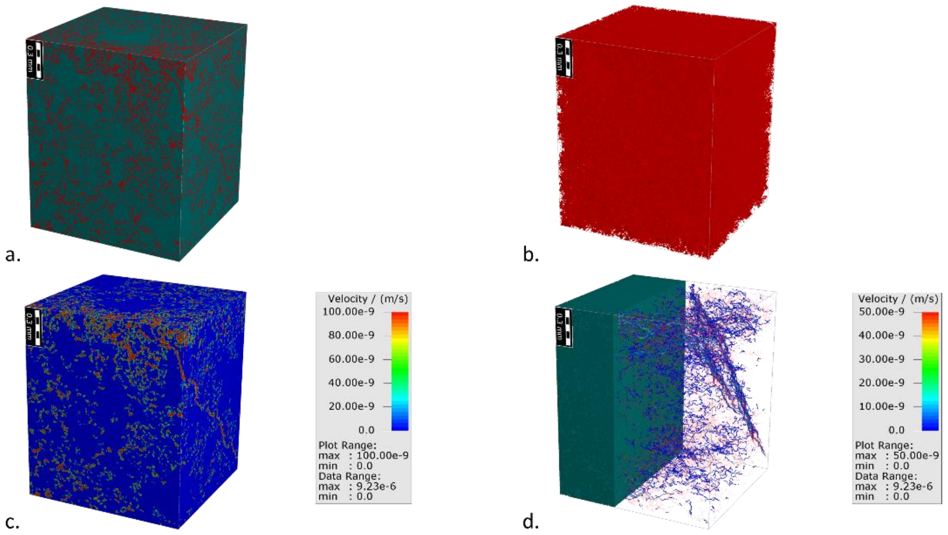

**Fig. 10.** Flow modeling in the burrow phase: a) structure, b) porosity, c) velocity field and d) structure and illuminated streamlines.

### *3.4.4 Modeling of the fluid flow through composite rocks*

Flow-based upscaling procedure based on Stokes-Brinkman equation computes effective permeability on coarser grids. To build the coarser grid, it is required to estimate permeability of the unresolved porous materials within the grid. Three sub-samples were selected to characterize the burrow and matrix system under sub-micron CT imaging (fig. 11): a) burrow phase, b) burrow to matrix interface and c) matrix.

As discussed before, permeability of 0.01 mD was pessimistically assigned to matrix based on CCAL results of the typical matrix samples. Burrow permeability was estimated with Stokes-Brinkman equation in 2.4.3.

The extracted properties of burrow and matrix then were combined into the larger scale network to evaluate permeability and interconnectivity. Two composite models were tested: 1) direct communication between burrows and matrix, and 2) inter-burrow flow through the fracture interface. In both cases, the fluid-flow was modeled with Stokes-Brinkman numerical solver under no-slip boundary conditions.

Unresolved porous burrow and tight matrix fabrics have been propagated in 3D volumes through utilization of the machine learning algorithm based on the Extra Trees engine [6] complemented with resolved porosity. This classifier implements a meta estimator that fits a number of randomized decision trees on sub-samples of the burrow and matrix grayscale dataset and uses averaging to improve the predictive accuracy and control over-fitting.

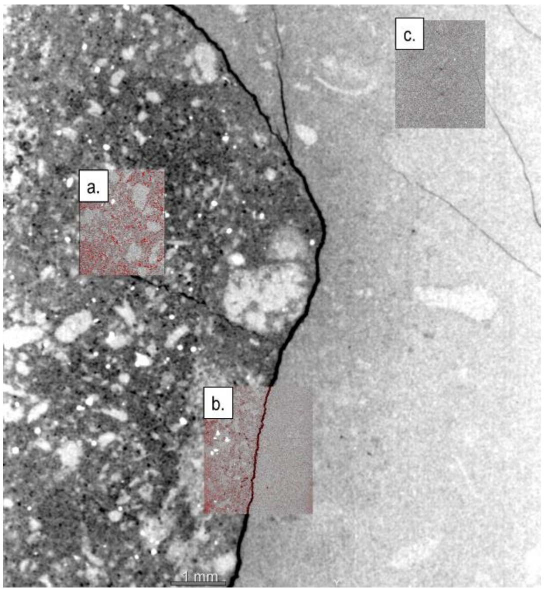

**Fig. 10.** Sub-micron volume selections for the detailed analysis: a) burrow, b) burrow to matrix interface and c) matrix.

Examples of the original grayscale image and classification results are shown on fig. 11 and fig. 12.

The results of the modeling illustrate permeability enhancement and porosity-permeability relations in the bioturbated system in three orthogonal directions. The interaction of the burrow system with the fracture network contributes to the bulk enhancement of flow between dead-end burrows and improves permeability of the system by 1-2 orders of magnitude in comparison with the case of direct communication between burrow and matrix (fig. 13).

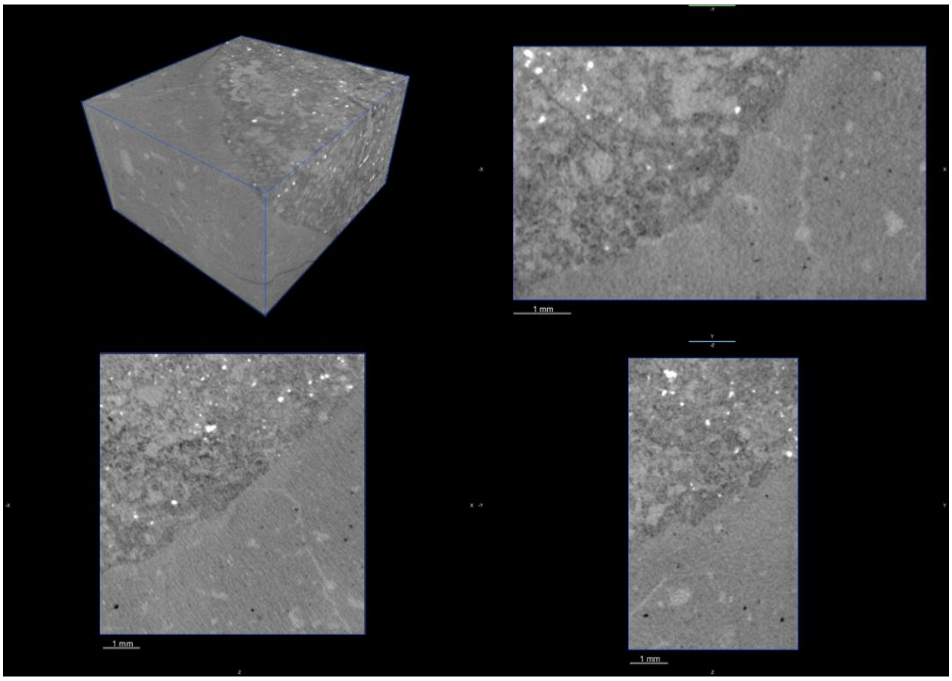

**Fig. 11.** Example of the grayscale volume used for the machine learning classification, 0.5 μm resolution: 3D render and three orthogonal projections.

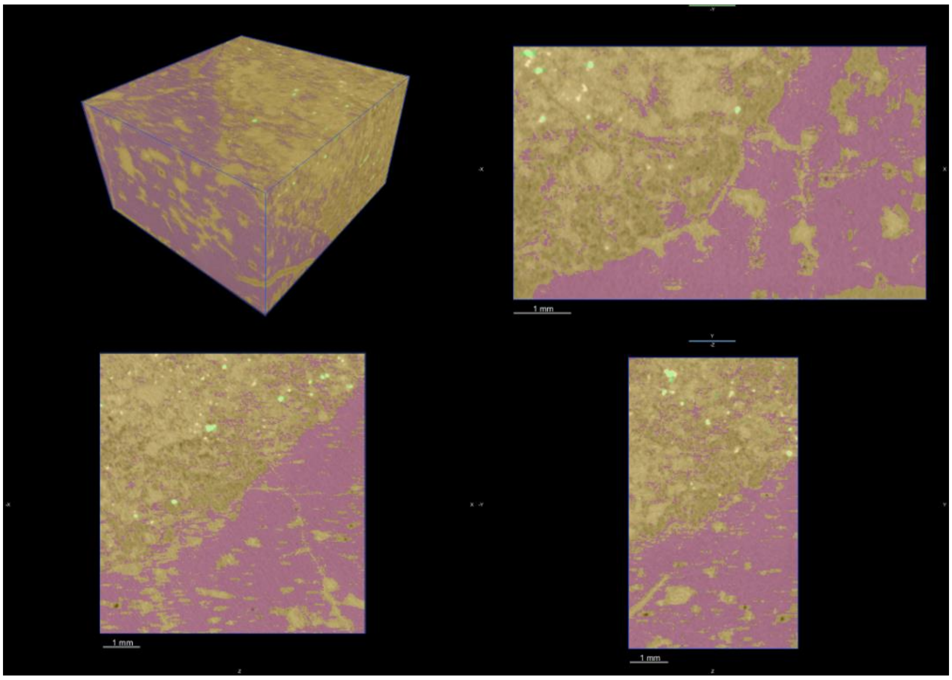

**Fig. 12.** Example of the machine learning classification, 0.5 µm resolution: 3D render and three orthogonal projections. Color key: green – high-density minerals, purple – the matrix phase and brown – the burrow phase.

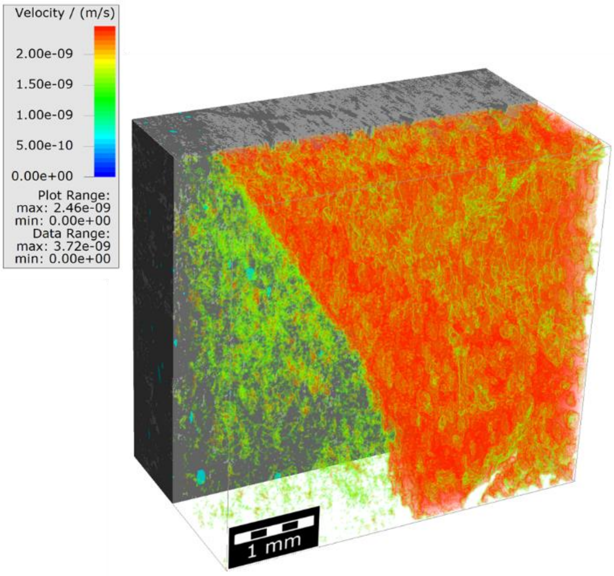

**Fig. 13.** Velocity field in composite models for both scenarios. Warmer colors show better permeability areas.

CCAL confirms enhancement of the system permeability by the fractures in the burrow to matrix interface. Highest permeability CCAL samples have been scanned and demonstrate various degrees of the fracturing. The porosity-permeability graph in fig. 14 shows five fractured samples together with the 3D render of one of them.

Comparison of the CCAL data against digital rock analysis results (see fig. 14) shows general match between two datasets with commonly underestimated porosity of matrix samples due to limitations of the scanning resolution not showing the microporosity smaller than 0.5 µm.

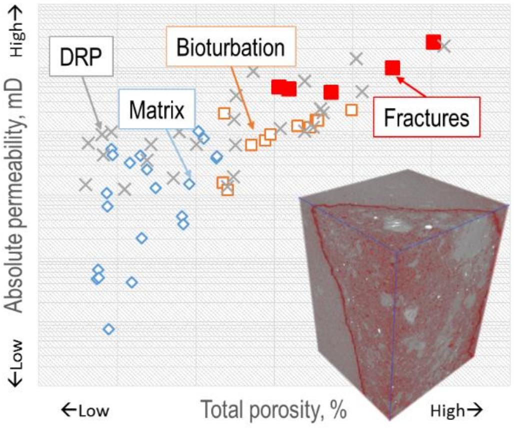

**Fig. 14.** Porosity-permeability cross-plot derived from CCAL measurements of the full (1.5 inch) plugs compared to digital rock analysis data (gray crosses). Embedded classification: fractured (red), bioturbated (orange) and matrix (blue) samples.

### *3.4.5 Relation between burrow volume fraction and permeability*

The developed digital rock model was used to simulate the permeability ratios $K_v/K_h$ as a function of burrow and dolomite volume fractions shown on fig. 15. The volume fractions of burrows vary from 0.2 to 0.75 and volume fractions of dolomite vary from 0.15 to 0.65 that is comparable with [7]. Increase of both burrow and dolomite fractions content is leading to higher $K_v/K_h$ ratios.

These relations (fig. 15) can be used for the permeability anisotropy prediction based on dolomite content derived from core or well log analysis to improve permeability simulation in the grid of geological models.

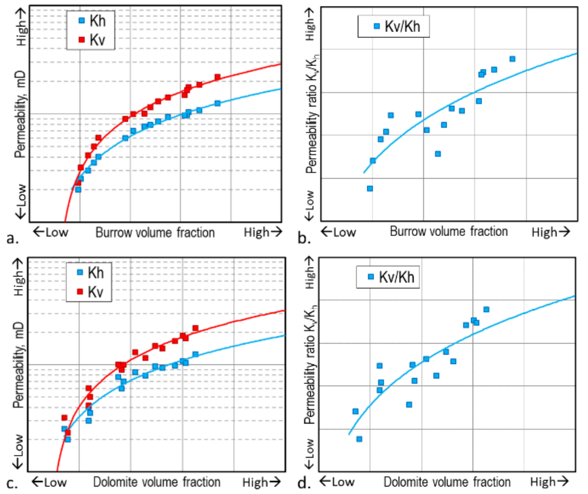

**Fig. 15.** Permeability as a function of a) burrow and c) dolomite volume fractions and permeability ratio $K_v/K_h$ as a function of b) burrow and d) dolomite volume fractions.

## Conclusions

Multiscale digital rock analysis was completed on whole core samples, full plugs and high-resolution sub-plugs to investigate the geological and petrophysical properties of the bioturbated RL at varying resolution from 25 µm to 0.5 µm. Integrated analysis of the CT images, thin-sections, CCAL and MICP data resolved permeability of burrow and matrix as well as permeability ratio in vertical and horizontal directions.

In the case study presented herein, high burrow connectivity suggests that a continuous flow network is likely to be established. The analysis shows, this is primarily influenced by the: 1) concentration and preferential orientation of permeable trace fossils; 2) degree of permeability contrast between burrows and surrounding matrix; and 3) three-dimensional connectivity of the *Thalassinoides* network system. Here, *Thalassinoides* occupy a significant volume of the rock compared to the fractures and this fact enhances the permeability and transmissivity of otherwise low-permeability matrix.

Detailed thin-section descriptions and MICP experiments improved the understanding of the geological variations in the 3D rock volume. This analysis has led to an improved geological interpretation of the diagenetically altered carbonate rocks. The overall analysis offered improved understanding of the heterogeneity in the formation and its impact on multi-scale permeability measurements.

There is at least one order of magnitude difference in permeability of burrow and matrix. Permeability of matrix appears isotropic. Permeability of the burrow fraction is one to three orders of magnitude larger than the matrix permeability; the results show enhanced burrow permeability with higher dolomite fractions. The flow between dead-end burrows occurs through the matrix or fracture interface as presented by the composite models. The $K_v/K_h$ ratio as a function of burrow and dolomite volume fractions are identified. The ratio of $K_v/K_h$ is always above one for bioturbated samples.

Increased permeability associated with the higher dolomite content resulting from intensely bioturbated intervals might be used as sweet spots identifier from wireline logs. Recognition of bioturbated intervals and the role they play in reservoir petrophysics may aid in both the optimization of secondary recovery methods and the selection of future drilling targets in similar biogenically modified intervals in the study area.

The authors acknowledge the management of the Saudi Arabian Oil Company (Saudi Aramco) for permission to publish this paper. The authors thank Jose Estevez Gonzalez and Keith MacPherson (Saudi Aramco) for their review and comments on the paper. The authors appreciate Aqeel Furaish, Hussain Alhilal and Ali Zahrani (Saudi Aramco) for their assistance with data acquisition.

## References

1. M.K. Gingras, G. Baniak, J. Gordon, J. Hovikoski, K.O. Konhauser, A. La Croix, R. Lemiski, C. Mendoza, S.G. Pemberton, C. Polo, J.P. Zonneveld, “Porosity and Permeability in Bioturbated Sediments,” *Developments in Sedimentology,* vol. 64, pp. 837-868, Dec. 2012.
2. M. Dernaika, M. Al Mansoori, M. Singh, T. Al Dayyani, Z. Kalam, R. Bhakta, S. Koronfol, “Digital and Conventional Techniques to Study Permeability Heterogeneity in Complex Carbonate Rocks,” *Petrophysics*, vol. 59, no. 3, pp. 373-396, Jun. 2018.
3. P. Popov, L. Bi, Y. Efendiev, R.E. Ewing, G. Qin, J. Li, Y. Ren. (Apr. 2009). Multi-physics and Multi-scale Methods for Modeling Fluid Flow Through Naturally-Fractured Vuggy Carbonate Reservoirs. Presented at SPE Middle East Oil and Gas Show and Conference, Bahrain. [Online]. Available: https://www.onepetro.org/conference-paper/SPE-105378-MS.
4. H.C. Brinkman, “A Calculation of the Viscous Force Exerted by a Flowing Fluid on a Dense Swarm of Particles,” *Flow, Turbulence and Combustion*, vol. 1, no. 1, p. 27, Dec. 1949.
5. M.K. Gingras, S.G. Pemberton, M. Smith, “Bioturbation: Reworking of Sediments for Better or Worse,” *Oilfield Review*, vol. 26, no. 4, pp. 46-58, Dec. 2014.
6. P. Geurts, D. Ernst, L. Wehenkel, “Extremely Randomized Trees,” *Machine Learning,* vol. 63, no. 1, pp. 3-42, Apr. 2006.
7. Y.N. Uddin, E.A. Clerke, B. Bammel, S. Koronfol, A. Grader. (May 2017). Quantitative Study of Formation Vertical Permeability in Middle East *Thalassinoides* Burrowed Carbonate Mudstone. Presented at SPE Reservoir Characterization and Simulation Conference and Exhibition, Abu Dhabi, UAE. [Online]. Available: https://www.onepetro.org/conference-paper/SPE-186001-MS.

# Novel technique to measure mutual bulk fluid diffusion using NMR 1-D gradient

*Son* Dang*, *Carl* Sondergeld, and *Chandra* Rai

Mewbourne School of Petroleum and Geological Engineering, University of Oklahoma, USA

**Abstract.** Many modelling and theoretical studies have shown that diffusion can be a significant transport mechanism in low-permeability porous media. Understanding the process allows engineers to better predict reservoir performance during both primary production and enhanced recovery in unconventional reservoirs. Direct measurement of effective diffusion in tight rocks is difficult, due to small pore volumes and the lack of techniques to actually monitor the process. Conventional diffusion measurements generally require fluid sampling, which induces a pressure transient which changes the mass transfer mechanism. Previously, we introduced a novel technique to measure tortuosity in nano-porous media by simultaneously monitoring methane versus nitrogen concentrations at high pressure using transmission Infrared Spectroscopy (IR). To complete the estimation of effective diffusion, bulk fluid diffusion coefficient also needs to be measured. In this study, we demonstrate the usage of Nuclear Magnetic Resonance (NMR) 1-D imaging to examine the dynamic change of Hydrogen Index (HI) across the interface between two bulk fluids. The experiment was conducted between a crude oil sample and methane; fluid samples were pressurized within an NMR transparent $ZrO_2$ pressure cell which operates at pressures up to 10,000 psi. The Hydrogen Index (HI) profile was continuously measured and recorded for 7 days. The results provided oil the swelling factor and the concentration profile as a function of both time and distance. These data then were fitted with Maxwell-Stefan equation to precisely back calculate the diffusion coefficient between oil and gas samples at high pressure. Accurate estimation of tortuosity and fluid diffusion is critical for the gas injection strategy in a shale formation. Greater tortuosity and smaller fluid diffusion rate lead to longer injection and production times for desirable economic recovery.

## 1 Introduction

Recent studies, including simulation works (Li et al., 2018[1]), experimentation (Li et al., 2019[2]; Dang et al., 2019[3]), and production modelling (Cronin et al., 2018[4]), suggest that matrix diffusion is a major mass transport mechanism, along with advection. Advection of a flow in porous media is governed by fluid properties (such as viscosity, density, and compressibility) and matrix permeability. Diffusion is governed by fluid diffusivity (either free diffusivity or multi-component diffusivity) and porous media' tortuosity. The Sherwood number, commonly cited in surface science and catalyst studies, is used a dimensionless factor accounting to the relative contribution between diffusion and advection in overall mass transport (Coutelieris et al., 2002[5]). With high porosity media, such as conventional rocks, the impact of advection overpowers the role of diffusion. While in tight rocks, with matrix permeability in the order of nano-Darcy, the impact of diffusion is not negligible.

With the development of unconventional shale gas and oil, the need to reevaluate these transport mechanisms, especially in nano-porous media, is essential. This does not only apply for primary production, but also for Enhanced Oil Recovery (EOR) processes. The understanding of behaviors of light gas molecules diffusing into rock matrix with included reservoir fluids, is important to optimize the efficiency of gas injection. Tortuosity measurement in nano-porous media is limited. Recently, Fleury and Brosse, 2017[6] and Dang et al., 2018[7] proposed different techniques to estimate tight matrix's tortuosity. The results suggested for rock samples with porosity, less than 7%, that tortuosity can vary from 4 to 25, a considerable range. In contrast, tortuosity values for conventional rocks, with porosity greater than 10%, are around 2 (Iversen and Jorgensen, 1993[8])

Besides matrix tortuosity, bulk fluid diffusivity also controls effective diffusion. The molecular diffusivity in the gas phase can be computed with Sigmund, 1976[9] correlation. In term of experimentation, this parameter can be estimated via several methods, including monitoring pressure profile while the oil phase contacts the gas phase inside a closed cell (Guo et al., 2009[10]). The drawback of this technique is that pressure is not maintained constant throughout the measurement.

---

* Corresponding author: dangthaison@ou.edu

Another technique is monitoring the oil phase swelling while injecting gases at a constant pressure (Jamialahmadi et al., 2016[11]). The swelling data is acquired by tracking the change in elevation of oil-gas interface. However, with the pressure above first contact minimum miscibility pressure (MMP), the interface becomes so vague to defy precise monitoring. In this study, we propose a new method using NMR 1-D gradient to monitor the dynamic change between oil-gas interfaces, from which bulk fluid diffusivity can be determined.

## 2 Experimental setup and fluid samples

For pressurization experiments, we used a Daedalus® cell, made of NMR transparent $ZrO_2$; the cell can be operated up to 10,000 psi internal pressure. The oil phase was injected into the pressure cell via a downstream port, while the gas phase would be later injected into the cell through the upstream port. The cell was then positioned inside the NMR spectrometer, in which the oil-gas interface would be aligned in the middle of the gradient scanning window. From its inlet, the cell was connected to a syringe pump system, which was used to compress gases from supply cylinders, then inject gasses into the test cell at a test pressure. The pressure was maintained constant throughout the diffusion process. **Fig. 1** illustrates major components of the experimental setup.

NMR gradient profiles were acquired using Oxford 2 MHz GeoSpec™ spectrometers, and Green Imaging acquisition and processing software. The magnet temperature was set at 35ºC throughout the experiments. The gradient scanning window was set at 7 cm, using DNK sequence. A new scan was repeated every 1 hour. Dynamic change of hydrogen index (HI) profiles across the oil-gas interface during the diffusion process, allows us to extract bulk diffusion parameters. In this study, the fluid samples included a dead oil from Meramec formation, and the injection gas is methane. **Fig. 2** represents a HI profile at the beginning of a 7-days experiment with methane injection pressure of 6000 psi, which is above minimum miscibility pressure (MMP).

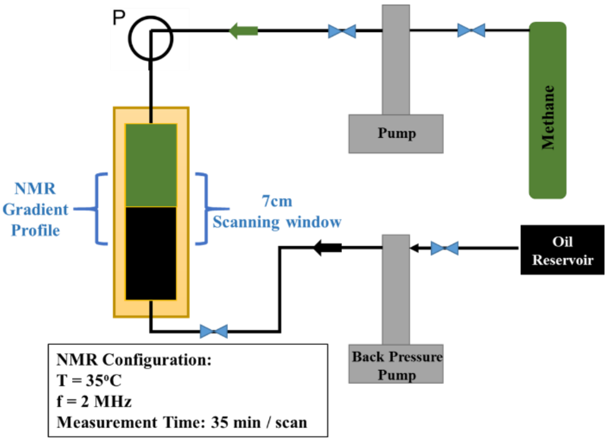

**Fig. 1**. Experimental setup, including NMR transparent $ZrO_2$ pressure cell, placed within 2 MHz NMR spectrometer. The oil phase was injected from a downstream port; the gas phase was injected through an upstream port, with the pressure controlled by a computer controlled Teledyne ISCO syringe pump system. The cell was positioned inside the spectrometer, in which the oil-gas interface was located in the middle of the gradient window.

## 3 Experimental results

With the contrast in HI between the gas and the oil phases, we can monitor the change in elevation of the interface (**Fig. 2**). During the diffusion process, in which pressure is maintained constant, methane molecules would diffuse into the oil phase at certain rate. This phenomenon dynamically changes the HI profile of the oil phase as a function of time. **Fig. 3** shows HI profile of the oil phase from the beginning of the experiment up to 7 days. HI at any point within the oil phase decreases over time, but the reduction rate is different depend of the relative position, with respect to the oil-gas interface. **Fig. 4** shows the effect of methane diffusion on HI trends at four different positions, note the marker colors correspond with the position, labeled in **Fig. 3**.

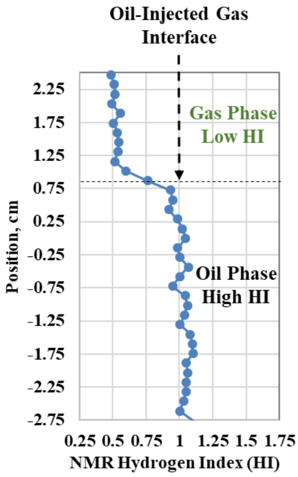

**Fig. 2**. An HI profile across the oil-gas interface. The position values are based on the relative position of the test cell in the NMR scanning window. The contrast in HI between the gas (low value) and the oil (high value) phases, allows to determine the dynamic position of the oil-gas interface during the experiment.

As expected, at the positions closest to the interface, HI decreased at the fastest rate, and quickly approached a constant value, $HI_{final}$. Moving further away from the interface, HI decreased with slower slope, but eventually reached the same $HI_{final}$. $HI_{final}$ is the result of the mixing between original oil's molecules and injection gas' molecules (methane in this case) at a particular concentration. From the experimental results, this specific concentration can be regarded as the maximum concentration of methane that can be diffused into the oil body; this parameter is a function of pressure and temperature. Using each of these HI trends, the methane diffusion coefficient can be calculated. However, with the fluctuation in the data, due to NMR signal-to-noise, the integral of HI profile is used to better estimate the diffusivity.

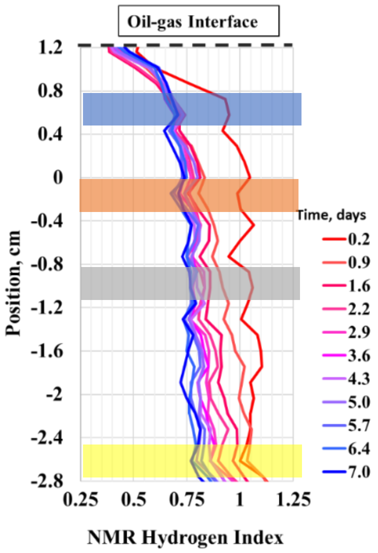

**Fig. 3**. HI profile within the oil phase as a function of time. The decreasing of the HI value within the oil phase is due to the methane diffusion. HI temporal profiles at different positions (color labels) within the oil phase are plotted in **Fig. 4**.

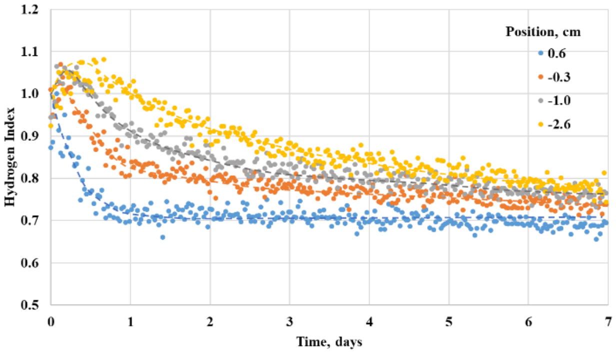

**Fig. 4**. HI profiles at different positions within the oil phase. The marker colors correspond to highlighted depths in **Fig. 3**. At the position closest to the oil-gas interface, HI decreases with the faster rate, and eventually approach a constant value, $HI_{final}$. $HI_{final}$ corresponds to the maximum concentration of diffused methane into the oil phase.

At a particular position and time, the HI value is the molar averaging between the HI value of the original oil and the HI value of methane at 6000 psi (**Eq. 1**). With the known HI value of the original oil is 1, and known HI value of methane at 6000 psi is 0.525 (both values can be extracted from the HI profile at the beginning, i.e. at t=0), relative methane concentration can be calculated, then plotted as a function of time. **Fig. 5** shows the integral of HI profile (red) and calculated methane concentration in the oil phase (blue.)

$$HI_{oil\ phase}(t) = (1-\alpha)HI_{original\ oil} + \alpha HI_{methane\ @\ 6000psi}$$

$$\alpha(t) = \frac{c_{methane}(t)}{c_{methane}(t) + c_{oil}(t)} \tag{1}$$

$$HI_{original\ oil} = 1$$

$$HI_{methane\ @\ 6000psi} = 0.525$$

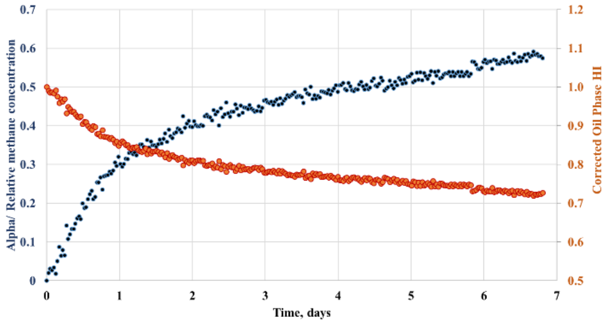

**Fig. 5**. The integral of HI respective to position, plotted as a function of time (red). Calculated relative methane concentration is also plotted (blue). The data is used to estimate methane diffusion coefficient.

## 4 Discussions

**Fig. 4** show HI trends at different positions within the oil phase. Depending on the relative position to the interface, the HI reduction rate would be different; however, they all approach a similar value of $HI_{final}$. In the other words, for a specific reservoir fluids and injection gasses, at a particular P-T condition, there is a maximum concentration of gas that can be introduced into the oil phase (Whitman, 1923[12]). While modelling the dual diffusion of injection gases into reservoir fluids and vice versa, this maximum concentration should be considered as the boundary condition; and now, we can estimate it from laboratory measurements.

Using Fick's second law (**Eq. 2**), diffusion coefficient can be estimated from the relative methane concentration profile. Note instead of using methane profile at a single position within the oil phase, we used the integral to reduce the impact of data oscillations. $C_s$ is methane concentration at the oil-gas interface. This is usually derived from the late-time diffusion data; however, with this study, $C_s$ can be directly calculated from $HI_{final}$.

$$\frac{C(x,t)}{C_s} = 1 - \mathrm{erf}(z) \tag{2}$$

$$z = \frac{x}{2\sqrt{DT}}$$

**Fig. 6** shows the fitting results of different diffusion coefficients using the relative methane concentration profile. The whole profile throughout 7 days can be fitted with diffusion coefficients ranging from $6.5\times10^{-10}$ to $8.5\times10^{-10}$ $m^2/s$; however, it is clear that the diffusion rate decreasing as a function of time. This is considered as experimental artifact. While Fick's Law was solved for infinite boundary condition, our test cell has limited volume. As soon as the first gas molecule travelling toward the oil phase, and approaches the end of the cell, the diffusion rate would be reduced.

By reviewing literature on diffusion measurements (Renner, 1986[13]; Grogan et al., 1988[14]; Jamialahmadi et al., 2006[11]), bulk diffusion rate can be varied within 2 orders of magnitude ($10^{-10}$ – $10^{-8}$ $m^2/s$). Translating this to field EOR applications, to efficiently inject a same reservoir volume, the injection time can be also varied within 2 orders of magnitude.

## 5 Conclusions

Knowing the importance of diffusion as one of major drive mechanisms in tight rocks, our studies focus on defining and estimating key parameters, allows engineers to model the process. They include porous matrix tortuosity and bulk fluid diffusivity. For example, in gas injection EOR, the combination of these two factors governs how fast injection gas molecules travel into the porous matrix to interact with a reservoir fluids' mobility, hence injection and production strategy can be optimized. In this paper, a new method to estimate fluid diffusion coefficient between methane and a crude sample was presented using NMR 1-D gradient. The technique directly captures the dynamic change of methane concentration within the oil body, reflected through the change in the HI value.

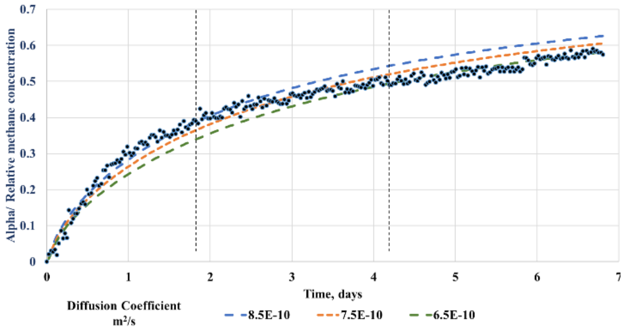

**Fig. 6**. The fitting of diffusion coefficient using the relative methane concentration profile. The diffusion rate can be precisely fitted within 25% of error, despite the experimental artifact, which makes diffusion rate decreases when gas molecules approach the end of the test cell.

This work was funded by the University of Oklahoma Unconventional Shale Consortium. We have benefitted from valuable conversations with Jairo Corredor, John Mansoori, Tom Smagala and Richard Newhart. The laboratory support of Gary Stowe, Micaela Langenvin and Jeremy Jernigen is greatly appreciated. We thank the members of Integrated Core Characterization Center (IC$^3$) for helping us during experimentation.

## References

1. L. Li, Y. Su, J. J. Sheng, "Investigation of gas penetration depth during gas huff-n-puff EOR process in unconventional oil reservoirs", Society of Petroleum Engineers, 2018
2. L. Li, Y. Su, J. J. Sheng, Y. Hao, W. Wang, Y. Ly, Q. Zhao, H. Wang, "Experimental and numerical study on $CO_2$ sweep volume during $CO_2$ huff-n-puff enhanced oil recovery process in shale oil reservoirs", Energy Fuels, 2019
3. S. T. Dang, C. H. Sondergeld, C. S. Rai, "Effects of temperature and gas pressurization on the interpretation of nuclear magnetic resonance (NMR) hydrocarbon measurements in organic rich shales", URTeC, 2019
4. M. Cronin, H. Emami-Meybodi, R. T. Johhns, "Diffusion-dominated proxy model for solvent injection in ultra-tight oil reservoirs", Society of Petroleum Engineers, 2018
5. F. A. Coutelieris, M. E. Kainourgiakis, A. K. Stubos, "The effects of Peclet on the Sherwood number in high porosity granular media", Studies in Surface Science and Catalysis, **Vol 144**, p. 753-760, 2002
6. M. Fleury, E. Brosse, "Transport in tight rocks", AGU Hydrobiogeochemical Properties of Caprock, June, 2017
7. S. T. Dang, C. H. Sondergeld, C. S. Rai, A, O. Tinni, N. Drenzek, 2018, "A first step in evaluating the role of diffusion in EOR in tight shale formations", SCA, 2018
8. N. Iversen, B. B. Jorgensen, "Diffusion coefficients of sulfate and methane in marine sediments: influence of porosity", Geochimica et Cosmochimica Acta **57**, 571–578, 1993
9. P. M. Sigmund, "Prediction of molecular diffusion at reservoir conditions, Part 1-measurement and prediction of binary dense gas diffusion coefficients", J. Can. Pet. Technol., **15**, pp. 48-57, 1976
10. P. Gou, Z. Wang, P. Shen, J. Du, "Molecular diffusion coefficients of the multicomponent gas-crude oil systems under high temperature and pressure", Ind. Eng. Chem. Res, **48**, p. 9023-9027, 2009
11. M. Jamialahmadi, M. Emadi, H. Muller-Steinhagen, "Diffusion coefficients of methane in liquid hydrocarbons at high pressure and temperature", Journal of Petroleum Science and Engineering. **Vol 52**, 1-2, p. 47-60, 2006
12. W. G. Whitman, "The two-film theory of absorption", Chem. Metall. Eng., **29**, pp. 147-152, 1923
13. T. A. Renner, "Measurement and correlation of diffusion coefficients for $CO_2$ and rich-gas applications", Society of Petroleum Engineers, 1988
14. A. T. Grogan, V. W. Pinczewski, G. J. Ruskauff, F. M. Orr, "Diffusion of $CO_2$ at reservoir conditions: models and measurements", Society of Petroleum Engineers, 1988

# A Surface Complexation Model of Alkaline-Smart Water Electrokinetic Interactions in Carbonates

*Moataz* Abu-Al-Saud[*], *Amani* Al-Ghamdi, *Subhash* Ayirala, and *Mohammed* Al-Otaibi

Saudi Aramco, EXPEC Advanced Research Center, Dhahran, Saudi Arabia

**Abstract.** Understanding the effect of injection water chemistry is becoming crucial, as it has been recently shown to have a major impact on oil recovery processes in carbonate formations. Various studies have concluded that surface charge alteration is the primary mechanism behind the observed change of wettability towards water-wet due to SmartWater injection in carbonates. Therefore, understanding the surface charges at brine/calcite and brine/crude oil interfaces becomes essential to optimize the injection water compositions for enhanced oil recovery (EOR) in carbonate formations. In this work, the physicochemical interactions of different brine recipes with and without alkali in carbonates are evaluated using Surface Complexation Model (SCM). First, the zeta-potential of brine/calcite and brine/crude oil interfaces are determined for Smart Water, NaCl, and $Na_2SO_4$ brines at fixed salinity. The high salinity seawater is also included to provide the baseline for comparison. Then, two types of Alkali (NaOH and $Na_2CO_3$) are added at 0.1 wt% concentration to the different brine recipes to verify their effects on the computed zeta-potential values in the SCM framework. The SCM results are compared with experimental data of zeta-potentials obtained with calcite in brine and crude oil in brine suspensions using the same brines and the two alkali concentrations. The SCM results follow the same trends observed in experimental data to reasonably match the zeta-potential values at the calcite/brine interface. Generally, the addition of alkaline drives the zeta-potentials towards more negative values. This trend towards negative zeta-potential is confirmed for the Smart Water recipe with the impact being more pronounced for $Na_2CO_3$ due to the presence of divalent anion carbonate $(CO_3)^{-2}$. Some discrepancy in the zeta-potential magnitude between the SCM results and experiments is observed at the brine/crude oil interface with the addition of alkali. This discrepancy can be attributed to neglecting the reaction of carboxylic acid groups in the crude oil with strong alkali as NaOH and $Na_2CO_3$. The novelty of this work is that it clearly validates the SCM results with experimental zeta-potential data to determine the physicochemical interaction of alkaline chemicals with SmartWater in carbonates. These modeling results provide new insights on defining optimal SmartWater compositions to synergize with alkaline chemicals to further improve oil recovery in carbonate reservoirs.

## 1. Introduction

Water ionic composition in the waterflooding process plays a crucial role in oil recovery for carbonate formations [1]. The chemistry of injected water strongly affects the reservoir wettability, which has been proven and observed in numerous laboratory and field studies for both carbonates and sandstones [2-4]. Modifying the water chemistry to alter the rock wettability is known as SmartWater or low salinity [5]. However, the root causes of this wettability alteration effect, which takes place at the pore-level, remain poorly understood especially for carbonates [6]. This lack of fundamental understanding of root causes of wettability alteration has resulted in conflicting studies, where some studies have observed an increase in oil recovery while other cases have not shown an increment in oil recovery [7]. Various pore-scale mechanisms have been proposed to delineate the wettability alteration process in carbonates. Some of these plausible mechanisms include electric double layer [4], in-situ soap generation (saponification effect) [8], and multi-ion exchange [9]. The surface charges of carbonate/brine and crude oil/brine are altered in such pore-scale processes, which affects the zeta-potential measurements used in understanding the rock wettability [10,11].

Recently, the synergy between tailored water salinity and enhanced oil recovery (EOR) has gained a lot of attraction [12]. For polymer EOR, it has been shown that the use of tailored salinity (SmartWater) reduces the polymer consumption used to increase the injected water viscosity [13]. For surfactant-based EOR, it has been observed that decreasing the water salinity increases the effect of surfactant on crude oil/brine through efficiently reducing the interfacial tension [14]. It is well-known that surfactants are adsorbed on carbonate rock surfaces. Therefore, a large amount of chemical surfactant is consumed before the chemical reaches the crude oil/brine

---

[*] Corresponding author: moataz.abualsaud@aramco.com

interface. To minimize surfactant adsorption on carbonate rock surfaces, alkaline is added to the injected water [15]. The alkaline chemical reacts with both crude oil/brine and calcite/brine interfaces. The reaction of alkali and naphthenic acid in crude oil generates in-situ soap that locally reduces the interfacial tension of the crude oil/brine interface. For the calcite surface, the adsorption of alkali changes the electric charges balance on the calcite/brine interface which alters the carbonate wettability towards more water-wet state [15]. Therefore, understanding the electrokinetics of brine with alkaline chemicals in carbonates is crucial to define the optimal water compositions for improving oil recovery.

There are several electrokinetic studies involving zeta-potentials that have reported the synergy effect of water salinity, crude oil, and alkaline in carbonates for crude oi/brine [17, 18] and calcite/brine interfaces [15, 16]. To the best of our knowledge, the role of individual ions in different brine compositions in the presence of alkaline chemicals for both the calcite/brine and crude oil/brine interfaces has not been previously studied using a surface chemistry model and lab measurements. In this work, we study the electrokinetics of with various brine recipes interacting with crude oil and calcite with and without alkali chemicals using a surface complexation model (SCM). We validate the modeling results with zeta-potentials of calcite/brine and crude oil/brine interfaces measured in the lab.

The outline of this work is as follows; a brief summary of the experimental setup for zeta-potential measurement is presented in section 2, followed by the surface complexation model (SCM). Then, the results of the SCM and lab measurements are shown in section 3. The conclusion and summary are included in section 4.

# 2. Materials and Methods

## 2.1. Experiment

*Rock sample:*
Pure calcium carbonate is used to represent the calcite rock sample. The purity of the calcite disk sample is measured using x-ray diffraction (XRD), which is composed of 99 wt. % of $CaCO_3$ as shown in **Figure 1**. The calcite purity confirms that there are no mineral impurities interfering with the ion adsorption on the calcite surface. The calcite disk is manually grinded using a granite mill for 30 minutes at atmospheric conditions far from contaminants to avoid surface impurities.

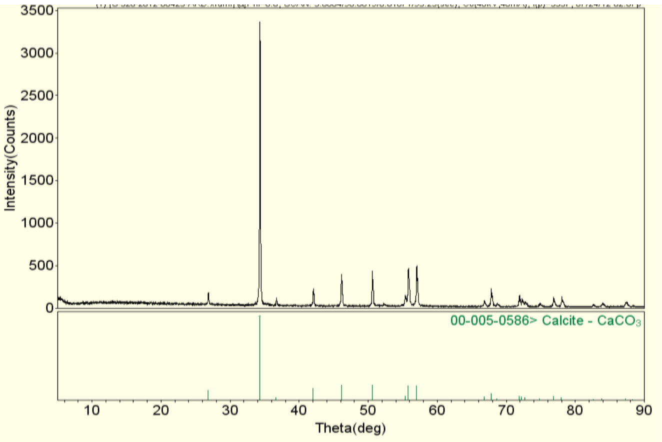

**Figure 1:** X-ray diffraction (XRD) diffractograms of calcite disk with reference patterns of pure calcite compound. The x-ray wavelength is 1.54 Å.

*Brine and Crude Oil Properties:*
Synthetic brine ionic compositions are prepared by adding different salts to deionized water. The ionic composition of the considered brine samples is listed in **Table 1**. The crude oil properties are shown in **Table 2**.

*Alkaline chemicals:*
Two types of Alkali (NaOH and $Na_2CO_3$) are added at 0.1 wt% concentration (1000 ppm) relevant to each brine recipe. Typically, alkali chemicals increase the brine pH level, which causes calcium and magnesium ions to precipitate as $Ca(OH)_2$ and $Mg(OH)_2$ respectively. Therefore, the addition of alkali to seawater is not considered to avoid precipitation, as seawater contains a high ionic concentration of hardness ions such as $Mg^{2+}$ and $Ca^{2+}$. **Table 3** lists the equilibrium pH level of different brines including alkali chemicals. The brine pH is measured after reaching equilibrium with alkaline and calcite suspensions without manually adjusting the pH level.

*Zeta-potential measurement:*
The measurement of zeta-potential is conducted using phase analysis light scattering technique (zeta PALS) applied to calcite in brine and crude oil emulsion in brine samples. 0.2 g of grinded pure calcite particles were thoroughly mixed with 50 $cm^3$ of different brines for a minimum of 48 hours to ensure suspension and equilibrium are achieved. The ratio of solid/liquid and liquid/liquid is fixed throughout the experiment to guarantee consistency in the reported values. The brine pH level is not manually adjusted. The oil droplets and calcite particles size distribution in different brines is determined using optical microscopy, similar to the approach in [19]. The average calcite particle size distribution is estimated to be around 10 μm, while the average oil droplet size is between 14-35μm**.** Sonification is used to avoid calcite particle aggregation or crude oil coalescence in brine suspensions. The zeta-potential values are determined using Smoluchowski approximation based on the electrophoretic mobility of brine suspensions. Each zeta-potential measurement is

repeated three times to ensure consistent results. The measurement variation for each reported zeta-potential value is within 3 mV. Additional details on the sample preparation and experimental zeta-potential measurement procedures can be found in [19].

**Table 1.** The composition of different synthetic brines used in this study.

| | Brine samples (concentration mg/L) | | | |
|---|---|---|---|---|
| | **Seawater** | **SmartWater** | **NaCl** | **$Na_2SO_4$** |
| **Ions** | | | | |
| $Na^+$ | 18,300 | 1824 | 2266 | 1865 |
| $Cl^-$ | 32,200 | 3220 | 3495 | - |
| $Ca^{2+}$ | 650 | 65 | - | - |
| $Mg^{2+}$ | 2,110 | 211 | - | - |
| $SO_4^{-2}$ | 4,290 | 429 | - | 3896 |
| HCO3- | 120 | - | - | - |
| Total dissolved Solids, ppm | 57,670 | 5,761 | 5,761 | 5,761 |
| pH | 7.45 | 7.4 | 6.3 | 6.11 |

**Table 2.** Crude Oil Properties

| | |
|---|---|
| API | 27.1 |
| Acid Number mg KOH/g | 0.47 |
| Base Number mg KOH/g | 0.04 |
| Saturates (%) | 50.6 |
| Asphaltenes (%) | 1.6 |
| Resins (%) | 20.7 |
| Aromatics (%) | 27.1 |

**Table 3.** Equilibrium pH values of calcite suspension in different electrolytes containing alkali.

| Type of electrolyte | pH $CaCO_3$ | pH $CaCO_3$ ( NaOH 0.1 wt.%) | pH $CaCO_3$ ( $Na_2CO_3$ 0.1 wt.%) |
|---|---|---|---|
| $Na_2SO_4$ | 9.85 | 12 | 10 |
| NaCl | 9.4 | 11.33 | 10 |
| SmartWater | 8.6 | 11.7 | 10 |
| Seawater | 7.45 | - | - |

## 2.2 Surface Complexation Model

The surface complexation model (SCM) describes the equilibrium state of ion adsorption based on specified surface reactions. The surface reactions of ions give rise to surface electric charges. For calcite/brine/crude-oil system, the adsorption of ions on crude-oil/brine and calcite/brine interfaces determine the surface charges and the corresponding zeta-potentials. The SCM has been employed to gain insight on the effect of electrokinetics on wettability in the context of brine chemistry in carbonates [20,21,24,25]. Brady *et al.* [21] used SCM based on surface reactions proposed in [22,23] to predict zeta-potentials for both rock/brine and brine/crude-oil interfaces in sandstone and carbonate rocks. However, the SCM has not been validated with experimental zeta-potential measurements. Mahani *et al.* [24] studied the electrokinetics of carbonate-based rocks with different water salinities using SCM. The SCM results were qualitatively validated with different carbonate/brine zeta-potential measurements. Song *et al.* [25] applied SCM and reported quantitative agreement with experimental zeta-potential measurements of synthetic calcite and multiple brine recipes. The SCM surface reactions are based on the model proposed in [26], which includes different SCM reactions compared to the models in [21,24]. The SCM work of Song *et al.* [25] has been recently extended to include surface reactions of organic and inorganic impurities occurring in natural carbonates [27]. In this work, we use SCM with surface reactions similar to the approach in [25] to predict zeta-potentials for pure calcite and different brine recipes with and without alkali chemicals. In addition, we determine brine/crude oil zeta-potentials by modeling SCM reactions at the brine/crude oil interface. **Tables 4 and 5** list the surface reactions and the corresponding equilibrium constants for both calcite and crude oil surfaces. The non-integer surface charge values of $> CaOH^{-0.75}$ and $> CO_3H^{+0.75}$ hydrated calcite sites is due to the structure of calcite crystal. The ionic bonding between Ca and O atoms from $(CO_3)^{-2}$ gives an effective charge of +1/3 for Ca atoms [26]. In this model, a charge of +1/4 is assumed for Ca atoms, following the approach in [25,26]. The crude oil surface reactions are similar to the models used in [20,21,28]. The SCM equations are solved using PHREEQC software [29], whereby the double layer model is specified. In the model, the concentration of adsorbed surfaces complexes (adsorbed ions) determines the total surface charge as follows:

$$\sigma = \frac{\mathrm{F}}{\mathrm{SA}} \Sigma \mathrm{z_i} c_i, \qquad (1)$$

where $\sigma$ is the surface charge density (C/m$^2$), F is the Faraday constant (96493.5 C/mol), S is the surface material mass (g), A is the specific surface area (m$^2$/g), $\mathrm{z_i}$ is the ionic electric charge, and $c_i$ is the adsorbed ion concentration (mol). The surface charge and surface-potential are related through the Gouy-Chapman model [29]:

$$\sigma = (8000\epsilon_o\epsilon_w \mathrm{RTI})^{1/2} \sinh\left(\frac{\nu F \Psi.}{2RT}\right), \qquad (2)$$

where $\epsilon_o$ is the vacuum permittivity $\left(\frac{\mathrm{C}^2}{\mathrm{mJ}}\right)$, $\epsilon_o$ is the water relative permittivity, $\Psi$ is the surface-potential (V), R is the gas constant $\left(\frac{\mathrm{J}}{\mathrm{mol\ K}}\right)$, T is the temperature (K), I is the brine ionic strength (mol/l), and $\nu$ is the electrolyte ionic charge which is assumed to be unity in PHREEQC [29]. The bulk concentration of ions interacts with the adsorbed ions at the surface due to coulombic forces. Hence, the apparent equilibrium constants are considered to include the effect of bulk concentration of the ions. The apparent and intrinsic equilibrium constants (listed in Tables 4 and 5) are described through the Boltzmann distribution [29]:

$$\mathrm{K_{app}} = \mathrm{K_{int}} \exp\left(\frac{Z_c F \Psi.}{RT}\right), \qquad (3)$$

where $Z_c$ is the net change of the surface charge at the surface due to surface reaction. The zeta-potential $\zeta$ can be approximated from the surface-potential based on the linearized Debye-Huckel theory [25], which is valid for $|\Psi| \leq 25$ mV [30]:

$$\zeta = \psi \exp(-\kappa d_s), \qquad (4)$$

where $\kappa$ is the inverse Debye length-scale, and $d_s$ is the slipping plane distance from the outer Helmholtz plane. For brines with ionic-strength of 0.1 mol/l (the considered brine recipes except for sea water), the slipping distance $d_s$ is 0.33 nm [25, 26], while the Debye length $\kappa^{-1}$ is 0.97 nm. For the seawater case (ionic strength of 1.1 mol/l), $d_s$ is 0.1 nm ($d_s = 0.1/c^{0.5}$ [26]), while $\kappa_{sw}^{-1}$ is 0.29 nm. The site density for calcite surface is 4.95 sites/nm$^2$ [26, 27], while the crude oil surface has a site density of 0.47 sites/nm$^2$ [28]. The calcite specific surface area is 1 m$^2$/g [26], while the crude oil specific area is 0.5 m$^2$/g [28]. Additional details of the above SCM equations are elaborated in [29,31].

**Table 4.** Surface Complexation Reactions and Parameters for the Calcite Surface.

| Calcite Surface Reaction | Equilibrium Constant ($\log_{10} K_{int}$) |
|---|---|
| $> CaOH^{-0.75} + H^+ \leftrightarrow\ > CaOH_2^{+0.25}$ | 0.4 |
| $> CO_3H^{+0.75} + OH^- \leftrightarrow\ > CO_3^{-0.25} + H_2O$ | 0.5 |
| $> CaOH^{-0.75} + Ca^{2+} \leftrightarrow\ > CaOH..Ca^{+1.25}$ | 1.53 |
| $> CaOH^{-0.75} + Mg^{2+} \leftrightarrow\ > CaOH..Mg^{+1.25}$ | 1.15 |
| $> CO_3H^{+0.75} + SO_4^{2-} \leftrightarrow\ > CO_3H..SO_4^{-1.25}$ | 1.5 |
| $> CO_3H^{+0.75} + CO_3^{2-} \leftrightarrow\ > CO_3H..CO_3^{-1.25}$ | 2.23 |
| $> CO_3H^{+0.75} + HCO_3^- \leftrightarrow\ > CO_3H..HCO_3^{-0.25}$ | 0.09 |
| $> CaOH^{-0.75} + Na^+ \leftrightarrow\ > CaOH..Na^{+0.25}$ | 0.22 |
| $> CO_3H^{+0.75} + Cl^- \leftrightarrow\ > CO_3H..Cl^{-0.25}$ | 0.65 |

**Table 5.** Surface Complexation Reactions and Parameters for the Crude Oil Surface.

| Crude Oil Surface Reaction | Equilibrium Constant ($\log_{10} K_{int}$) |
|---|---|
| $-COOH \leftrightarrow -COO^- + H^+$ | 6 |
| $-N + H^+ \leftrightarrow -NH^+$ | 4 |
| $-COOH + Ca^{+2} \leftrightarrow -COOCa^+ + H^+$ | -4 |
| $-COOH + Mg^{+2} \leftrightarrow -COOMg^+ + H^+$ | -4.3 |
| $-COOH + Na^+ \leftrightarrow -COONa + H^+$ | -4 |

## 3. Results and Discussion

**Figures 2 to 7** compare the SCM and experimental measurements of the zeta-potential values for different brine recipes with and without alkali. First, the zeta-potentials for brine/calcite interface are analyzed, followed by the brine/crude oil interface. The intrinsic equilibrium constants are varied in the SCM to match the measured zeta-potentials. The number of fitting parameters is equal to the number of surface reaction equations (nine equations for calcite/brine interface, and five equations for the crude oil/brine interface). The site density and specific surface area of the considered surfaces are fixed (see **Section 2.2**). For the brine/calcite interface (**Figures 2-4**), the SCM results follow the trends observed in experimental data, and quantitatively agree with the lab zeta-potential measurements especially for NaCl, SmartWater, and Na$_2$SO$_4$ brines. For the seawater case without alkali, the SCM underestimates the zeta-potential as can been seen in **Figure 2**. When NaOH alkaline is added to the brine recipes, the change in zeta-potential values of calcite/brine interface is almost negligible and in agreement with the experimental zeta-potential measurements as illustrated in **Figure 3** (within 2.5 mV difference). The addition of (OH)$^-$ ions increases the negative charge, and decreases the adsorption of H$^+$ protons while adding Na$^+$ ions increase the charge positivity resulting in an insignificant total change in the surface charge. For the Na$_2$CO$_3$ alkaline, the SCM calcite/brine zeta-potentials decrease for the considered brine recipes as displayed in **Figure 4**. This decrease in zeta-potential values is mainly due to the presence of divalent anion carbonate (CO$_3$)$^{-2}$, which forms a surface complex on the calcite surface with a -1.25 charge as illustrated in reaction 6 in **Table 3**. Calcite precipitation/dissolution has not been considered in SCM, which is likely to contribute to the slight discrepancy observed in the SmartWater recipe case in **Figure 4**. The intrinsic equilibrium constants (fitting parameters) in **Table 4** are in agreement with the work of Song et al. [25] except for the Cl$^-$ ion which has the largest discrepancy. The SCM confirms that the total surface charge and zeta-potential of calcite/brine interface strongly depend on the divalent ions (Ca$^{2+}$, Mg$^{2+}$, CO$_3^{2-}$, and SO$_4^{2-}$) due to large intrinsic equilibrium constants compared to the other ions. The SCM predicts that the most effective ion in pushing the calcite surface charge to a negative value is the divalent anion carbonate (CO$_3$)$^{-2}$, which has the largest equilibrium constant.

For the crude oil/brine interface cases, the SCM zeta-potential results qualitatively match the experimental observations. The predicted zeta-potentials are in general negatively charged as shown in **Figure 5**, which agree with the experimental results. The equilibrium constants in **Table 5** agree with the values reported in the literature [21,28] (the discrepancy in the equilibrium constants are within a value of one for each reaction). At pH > 7 (greater than the isoelectric point for crude oil/brine interface with a similar acid number [32]), the carboxylic acids in crude oil are not completely protonated (reaction 1 in **Table 5**). Also, the protonation of nitrogen bases (reaction 2 in **Table 5**) is not sufficient to switch the crude oil surface to a positive charge. When alkali is added to the brine recipe (**Figures 6 and 7**), the variation in SCM zeta-potentials is less than 2 mV. The zeta-potentials slightly increase in the positive side, especially for NaOH alkaline. This slight increase is not expected as the protonation activity decreases with the increase of the brine pH level.

However, the reactions in SCM predict that the adsorption of $Mg^{2+}$ and $Ca^{2+}$ (reactions 3 and 4) slightly compensates for the decrease in $H^+$, which results in a small increase in the zeta-potential. Based on the model predictions of calcite/brine and brine/crude oil zeta-potentials, the $Na_2SO_4$ brine with $Na_2CO_3$ alkaline provides the largest interface negative charges (**Figures 4 and 7**). The modeling results support the conclusion drawn from the experiments that the $Na_2SO_4$ brine with $Na_2CO_3$ alkaline is the preferable brine recipe to synergize with anionic surfactants due to its large negative zeta-potential. This large negative zeta-potential increases the water-wetness towards carbonate reservoir [16] and reduces the anionic surfactant retention [15]. Further improvement and refinement in the SCM will be considered as this is a starting point for ongoing research in electrokinetic modeling. Such improvements include using an SCM triple-layer model, non-linear diffuse double layer model to infer zeta-potential from the surface-potential, and adding dissolution/percipation reactions for the calcite/brine interface. Also, including the crude oil chemistry (acid/base numbers) to be part of the surface site density [33] of nitrogen base and carboxylate groups will improve the SCM for the crude oil/brine interface.

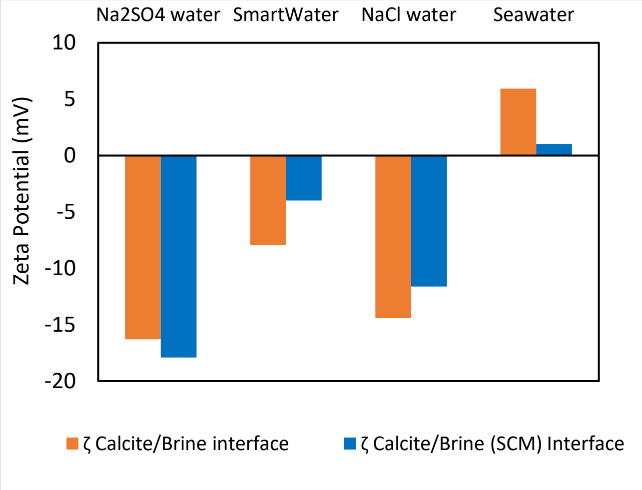

**Figure 2:** Experimental and SCM ζ- potential values at the calcite/brine interface

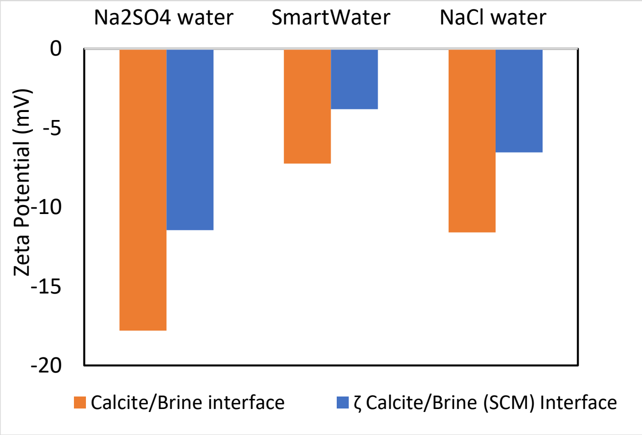

**Figure 3:** Experimental and SCM ζ- potential values at the calcite/brine interface. Brine is containing 0.1 wt.% NaOH.

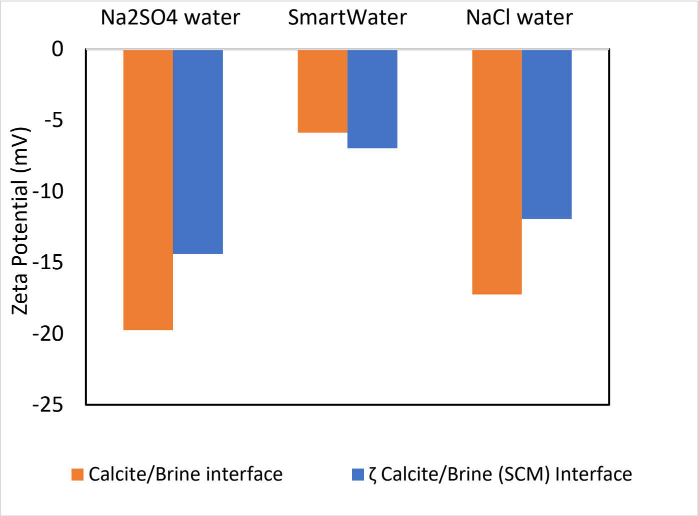

**Figure 4:** Experimental and SCM ζ- potential values at the calcite/brine interface. Brine is containing 0.1 wt.% $Na_2CO_3$.

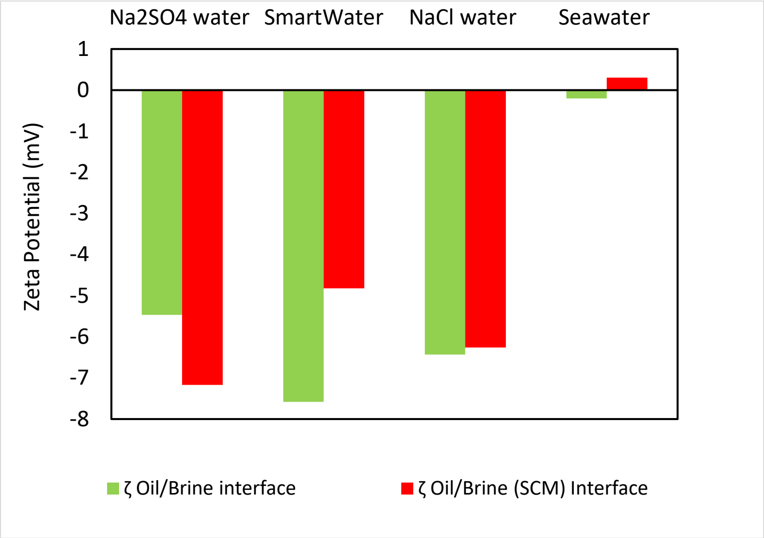

**Figure 5:** Experimental and SCM ζ- potential values at oil/brine interface.

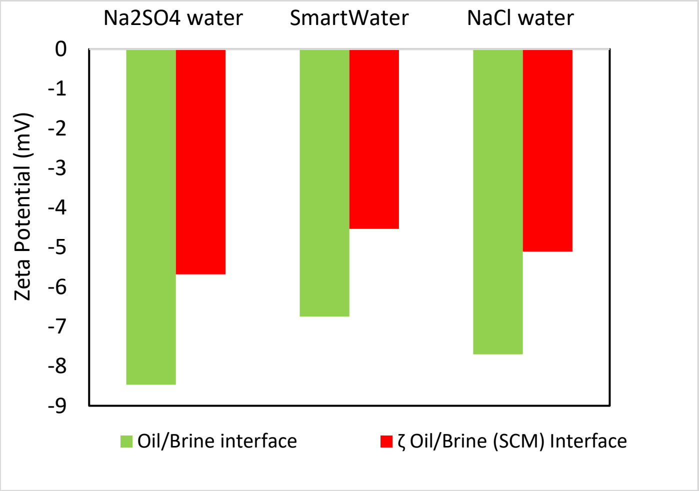

**Figure 6:** Experimental and SCM ζ- potential values at oil/brine interface. Brine is containing 0.1 wt.% NaOH.

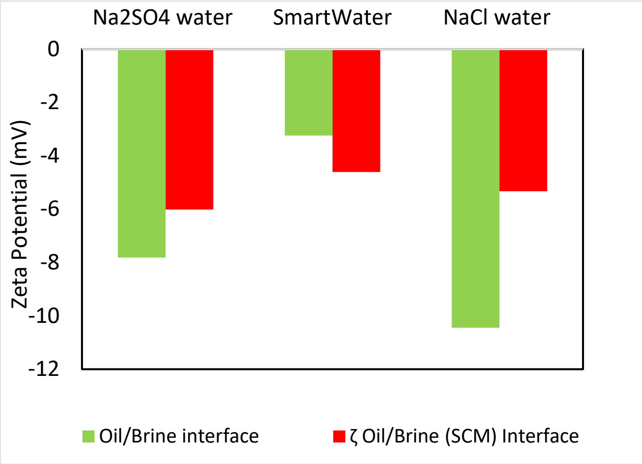

**Figure 7:** Experimental and SCM ζ- potential values at oil/brine interface. Brine is containing 0.1 wt.% $Na_2CO_3$.

## 4. Conclusions

This work explores the electrokinetic interactions of different brine recipes with and without alkali in carbonates using Surface Complexation Model (SCM). Various SCM calculations of brine/calcite and crude oil/brine zeta-potentials are conducted to evaluate the synergy between different brine recipes and alkali chemicals. The proposed SCM predicts zeta-potential results that are consistent with the experimental measurements for choosing the $Na_2SO_4$ brine with $Na_2CO_3$ alkaline to be the most suitable alkaline-based recipe due to its large negative zeta-potentials. In alkaline/surfactant EOR process, the negative electrokinetic calcite charge repels the anionic surfactant causing a reduction in surfactant retention. The modeling of zeta-potential results quantitatively agree with the experiments for the calcite/brine interface. For the crude oil/brine interface, the SCM zeta-potential results reasonably match the experimental measurements. Further correlation of the carboxylic acid group and nitrogen base crude oil active surface sites with the acid/base number is required [33] to quantitatively predict accurate zeta-potentials and gain additional insights on the electrokinetics of crude oil surfaces.

## Acknowledgements

The authors thank Hussain Saleem and Dong kyu Cha, Saudi Aramco for their help with zeta-potential measurements.

## References

1. T. Austad, S. Strand, E. Høgnesen, P. Zhang. “Seawater as IOR fluid in fractured chalk”. *In SPE international symposium on oilfield chemistry* 2005 Jan 1. Society of Petroleum Engineers.
2. A. Yousef, S. Al-Saleh, A. Al-Kaabi, M. Al-Jawfi. “Laboratory investigation of the impact of injection-water salinity and ionic content on oil recovery from carbonate reservoirs”. *SPE Reservoir Evaluation & Engineering*. 2011 Oct 1;14(05):578-93.
3. A. Yousef, J. Liu, G. Blanchard, S. Al-Saleh, T. Al-Zahrani, R. Al-Zahrani, H. Al-Tammar, N. Al-Mulhim. “Smart waterflooding: industry”. *In SPE Annual Technical Conference and Exhibition* 2012 Jan 1. Society of Petroleum Engineers.
4. D. Ligthelm, J. Gronsveld, J. Hofman, N. Brussee, F. Marcelis, H. Van der Linde. “Novel Waterflooding Strategy by Manipulation Of Injection Brine Composition”. *In EUROPEC/EAGE conference and exhibition* 2009 Jan 1. Society of Petroleum Engineers.
5. N. Morrow, J. Buckley. “Improved oil recovery by low-salinity waterflooding”. *Journal of Petroleum Technology*. 2011 May 1;63(05):106-12.
6. H. Mahani, A. Keya, S. Berg, W. Bartels, R. Nasralla, W. Rossen. “Insights into the mechanism of wettability alteration by low-salinity flooding (LSF) in carbonates”. *Energy & Fuels*. 2015 Mar 3;29(3):1352-67.
7. M. Jackson, D. Al-Mahrouqi, J. Vinogradov. “Zeta-potential in oil-water-carbonate systems and its impact on oil recovery during controlled salinity water-flooding”. *Scientific reports*. 2016 Nov 23;6:37363.
8. P. McGuire, J. Chatham, F. Paskvan, D. Sommer, F. Carini. “Low salinity oil recovery: An exciting new EOR opportunity for Alaska's North Slope”. *In SPE western regional meeting* 2005 Jan 1. Society of Petroleum Engineers.
9. A. Lager, K. Webb, C. Black, M. Singleton, K. Sorbie. “Low salinity oil recovery-an experimental investigation-1”. *Petrophysics*. 2008 Feb 1;49(01).
10. D. Al Mahrouqi, J. Vinogradov, M. Jackson. “Zeta-potential of artificial and natural calcite in aqueous solution”. *Advances in colloid and interface science*. 2017 Feb 1;240:60-76.
11. M. Jackson, J. Vinogradov, G. Hamon, M. Chamerois. “Evidence, mechanisms and improved understanding of controlled salinity waterflooding part 1: Sandstones”. *Fuel*. 2016 Dec 1;185:772-93.
12. S. Ayirala, A. Yousef. “A state-of-the-art review to develop injection-water-chemistry requirement guidelines for IOR/EOR projects”. *SPE Production & Operations*. 2015 Feb 1;30(01):26-42.
13. S. Ayirala, E. Uehara-Nagamine, A. Matzakos, R. Chin, P. Doe, P. Van den Hoek. “A designer water process for offshore low salinity and polymer flooding applications”. *In SPE Improved Oil Recovery Symposium* 2010 Jan 1. Society of Petroleum Engineers.
14. W. Alameri, T. Teklu, R. Graves, H. Kazemi, A. AlSumaiti. “Low-salinity water-alternate-surfactant in Low-permeability Carbonate Reservoirs”. *In IOR 2015-18th European Symposium on Improved Oil Recovery* 2015 Apr 14.
15. G. Hirasaki, C. Miller, M. Puerto. “Recent advances in surfactant EOR”. *SPE Journal*. 2011 Dec 1;16(04):889-907.

16. G. Hirasaki G, D. Zhang. "Surface chemistry of oil recovery from fractured, oil-wet, carbonate formations". *Spe Journal*. 2004 Jun 1;9(02):151-62.
17. Q. Liu, M. Dong, X. Yue, J. Hou. "Synergy of alkali and surfactant in emulsification of heavy oil in brine". *Colloids and Surfaces A: Physicochemical and Engineering Aspects*. 2006 Feb 1;273(1-3):219-28.
18. K. Chan, D. Shah. (1981) "The Physico-Chemical Conditions Necessary to Produce Ultralow Interfacial Tension at the Oil/Brine Interface". In: Shah D.O. (eds) *Surface Phenomena in Enhanced Oil Recovery*. Springer, Boston, MA
19. M. Alotaibi, A. Yousef. "The role of individual and combined ions in waterflooding carbonate reservoirs: electrokinetic study". *SPE Reservoir Evaluation & Engineering*. 2017 Feb 1;20(01):77-86.
20. Q. Xie, A. Sari, W. Pu, Y. Chen, P. Brady, N. Al Maskari, A. Saeedi. "pH effect on wettability of oil/brine/carbonate system: Implications for low salinity water flooding". *Journal of Petroleum Science and Engineering*. 2018 Sep 1;168:419-25.
21. P. Brady, J. Krumhansl, P. Mariner. "Surface complexation modeling for improved oil recovery". *In SPE improved oil recovery symposium* 2012 Jan 1. Society of Petroleum Engineers.
22. P. Van Cappellen, L. Charlet, W. Stumm, P. Wersin. "A surface complexation model of the carbonate mineral-aqueous solution interface". *Geochimica et Cosmochimica Acta*. 1993 Aug 1;57(15):3505-18.
23. O. Pokrovsky, J. Schott, F. Thomas. "Dolomite surface speciation and reactivity in aquatic systems". *Geochimica et Cosmochimica Acta*. 1999 Oct 1;63(19-20):3133-43.
24. H. Mahani, A. Keya, S. Berg, R. Nasralla. "Electrokinetics of carbonate/brine interface in low-salinity waterflooding: effect of brine salinity, composition, rock type, and pH on ζ-potential and a surface-complexation model". *SPE Journal*. 2017 Feb 1;22(01):53-68.
25. J. Song, Y. Zeng, L. Wang, X. Duan, M. Puerto, W. Chapman, S. Biswal, G. Hirasaki. "Surface complexation modeling of calcite zeta-potential measurements in brines with mixed potential determining ions (Ca2+, CO32−, Mg2+, SO42−) for characterizing carbonate wettability". *Journal of colloid and interface science*. 2017 Nov 15;506:169-79.
26. F. Heberling, T. Trainor, J. Lützenkirchen, P. Eng, M. Denecke, D. Bosbach. "Structure and reactivity of the calcite–water interface". *Journal of colloid and interface science*. 2011 Feb 15;354(2):843-57.
27. J. Song, S. Rezaee, L. Zhang, Z. Zhang, M. Puerto, O. Wani, F. Vargas, S. Alhassan, S. Biswal, G. Hirasaki. "Characterizing the Influence of Organic Carboxylic Acids and Inorganic Silica Impurities on the Surface Charge of Natural Carbonates Using an Extended Surface Complexation Model". *Energy & Fuels*. 2019 Jan 11;33(2):957-67.
28. T. Takeya, M. Shimokawara, Y. Elakneswaran, T. Nawa, S. Takahashi. "Predicting the electrokinetic properties of the crude oil/brine interface for enhanced oil recovery in low salinity water flooding". *Fuel*. 2019 Jan 1;235:822-31.
29. D. Parkhurst, C. Appelo. "Description of input and examples for PHREEQC version 3: a computer program for speciation, batch-reaction, one-dimensional transport, and inverse geochemical calculations". *US Geological Survey*; 2013.
30. J. Israelachvili. "Intermolecular and surface forces". *Academic press*; 2011 Jul 22.
31. D. Dzombak, F. Morel. "Surface complexation modeling: hydrous ferric oxide". *John Wiley & Sons*; 1990 Mar 16.
32. J. Buckley, K. Takamura, N. Morrow. "Influence of electrical surface charges on the wetting properties of crude oils". *SPE Reservoir Engineering*.1989. 4(03):332-340.
33. M. Bonto, A. Eftekhari, H. Nick. "An overview of the oil-brine interfacial behavior and a new surface complexation model". *Scientific reports*. 2019 Apr 15;9(1):6072.

# Effects of gas pressurization on the interpretation of NMR hydrocarbon measurements in organic rich shales

*Son* Dang*, *Carl* Sondergeld, and *Chandra* Rai

Mewbourne School of Petroleum and Geological Engineering, University of Oklahoma, USA

**Abstract.** The estimation of total hydrocarbons (HCs) in place is one of the most important economic challenges in unconventional resource plays. Nuclear magnetic resonance (NMR) has proven to be a valuable tool in directly quantifying both hydrocarbons and brines in the laboratory and the field. Some major applications of NMR interpretation include pore body size distributions, wettability, fluid types, and fluid properties. However, for tight formations, the effects of the factors on NMR relaxation data are intertwined. One purpose of this study is to review the interpretation of NMR response of HCs in a tight rock matrix through illustrated examples.

When comparing NMR data between downhole wireline and laboratory measurement, three important elements need to be considered: 1) temperature differences, 2) system response differences, and 3) pressure (mainly due to the lost gasses.) The effect of temperature on HCs would be presented with experimental results for bulk fluids. Whereas, the effect of pressure is investigated by injecting gas back into rock matrix saturated with original fluids. The experiments were performed within an NMR transparent Daedalus $ZrO_2$ pressure cell which operates at pressures up to 10,000 psi.

The results show that, at ambient temperature and pressure, NMR responds to a fraction of HCs which is volatile enough to be observed as an NMR relaxation sequence. The invisible fraction of HCs to NMR sequence at ambient condition can be up to 20% of the total extractable HCs. Molecular relaxation is impacted by fluid viscosity, pore size, and surface affinity. In other words, the fluid with higher viscosity (either due to temperature or gas loss), presenting in smaller pore, or highly affected by the pore surface, will relax faster, and would be partially invisible to NMR, especially in the field. This is critical to the interpretation of NMR response for liquid rich source rocks, in which all of the above molecular relaxing restrictions can be found. Thus, engineers can underestimate movable HCs by using routine core analysis data.

## 1 Introduction

Nuclear Magnetic Resonance (NMR) has been proven to be a useful tool to evaluate formation characteristics in both the laboratory and the field. NMR responses are induced during the relaxation of nuclear spins, for a particular pulse sequence. At a specific magnetic-field strength, scanning frequency is tuned to resonate with the Lamour's frequency of hydrogen found in reservoir fluids, such as brine, oils, gases, and bitumen (Brown 1961[1]; Bryan et al., 2002[2]; Hirasaki et al., 2003[3]). Common NMR parameters used to interpret formation properties, include $T_1$ as the longitudinal relaxation time, and $T_2$ as the transverse relaxation time. Combination of $T_1$ and $T_2$ relaxation data can provide important information about formation and fluid properties. For conventional reservoirs, NMR has been used to estimate saturated porosity, and pore size distribution (Keynon et al., 1986[4]), from which permeability can be calculated (Coates et al., 1991[5]; Kenyon et al., 1995[6][7]; Straley et al, 1994[8].)

Recently developed applications of NMR, focusing on unconventional tight rocks, include the partitioning of pore surface affinity (oil-wet versus water-wet in shales) (Odusina et al., 2011[9]; Valori and Nicot, 2019[10]) and the characterization of *in situ* fluids. However, the interpretation is not necessarily straight-forward due to the coexistence of multiples fluids within a complicated pore structure (inorganic pores versus organic pores) (Sinha et al., 2017[11]). **Fig. 1** presents an example in which the same HCs yield different NMR responses, due to its containment within different pore types. **Fig. 1-a** is the $T_1$-$T_2$ map of a preserved sample with dominant inorganic pores (TOC < 0.5w %); whereas **Fig. 1-b**is the $T_1$-$T_2$ map of an adjacent preserved sample (0.73ft away) with dominant organic pores (TOC = 5w %.)

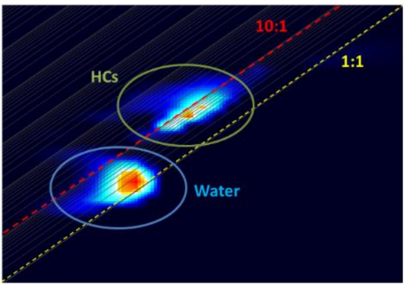

(a)

---

[*] Corresponding author: dangthaison@ou.edu

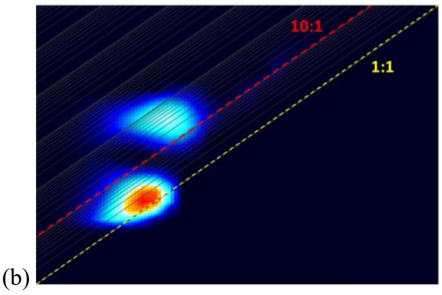

**Fig. 1.** $T_1$-$T_2$ maps of two preserved tight samples with $T_2$ is on the x-axes, and $T_1$ is on the y-axes. Brine NMR response is close to 1:1 line (yellow dash line). Sample (a) with dominant inorganic pores, HCs NMR response is between 1:1 line and 10:1 line (red dash line). Sample (b) with dominant organic pores, HCs NMR response is above 10:1 line, suggesting stronger affinity between HCs and pore surface.

It is essential to verify log-derived parameters using laboratory measurements. Besov et al., 2017[12] demonstrated how the differences in NMR configuration (such as scanning frequency, echo spacing, signal to noise ratio, and magnetic field gradient) can make the comparison between laboratory and field data complicated. Another major concern for almost all laboratory versus log comparison studies is the core condition, even for preserved samples (Blount et al., 2018[13]). In this study, we will review the understanding of NMR response to HCs in bulk fluids as a function of temperature (Dang et al., 2019[14]), as well as the new insights on how gas pressurization/ depressurization influences NMR response on organic rich tight rocks.

## 2 Experimental instrument and samples

NMR distribution, including $T_2$ relaxation and $T_1$-$T_2$ maps, were acquired at the frequency of 2 MHz, using Oxford GeoSpec™ spectrometers, and Green Imaging acquisition and processing software. The magnet temperature was set at 31°C throughout the experiments. The optimal echo spacing, of 114 µs, was chosen to capture fast relaxation components in the shale samples (including fluids in small pores and heavy HCs components), while preventing the interference of the fluorine signal from internal machine parts.

For pressurization experiments, the samples were placed inside a Daedalus® cell, made of NMR transparent $ZrO_2$; the cell can be operated up to 10,000 psi internal pressure. The cell was positioned inside the NMR spectrometer, in which samples were aligned with the uniform section of the permanent magnetic field. From its inlet, the cell was connected to a Teledyne ISCO syringe pump system, which was used to compress gases from supply cylinders, then inject gasses into the test cell at a designed pressure. To understand the dynamic response of only the HCs components in rock samples during gas pressurization and depressurization, NMR transparent gasses were chosen. Injected gas candidates include $CO_2$, $N_2$, or $CD_4$ (deuterated methane). **Fig. 2** illustrates major components of the experimental setup. Note there was no confinement applied on rock samples, gasses were injected all around samples.

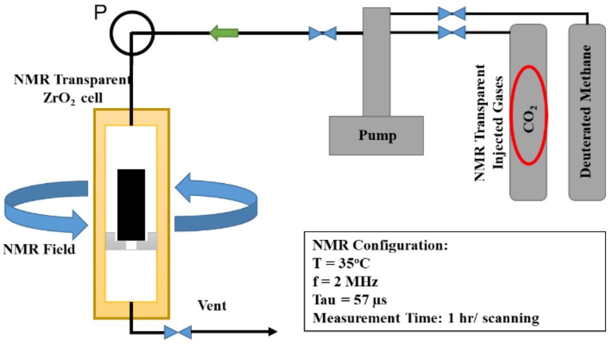

**Fig. 2.** General experimental setup, including NMR transparent $ZrO_2$ pressure cell, placed within 2 MHz NMR spectrometer. The cell was connected to a pump system to its inlet, and to a vent line from its outlet. NMR transparent injected gasses were chosen, including $CO_2$, $N_2$, or deuterated methane.

Four organic rich tight samples were selected for this study from various shale plays; two of them were preserved samples. Routine petrophysical characterizations were performed and presented in **Table. 1**, including total porosity (the sum of high pressure gas-filled porosity and NMR saturated porosity), mineralogy measured by transmission Fourier Transform Infrared (FTIR), and TOC measured with a LECO® instrument.

**Table 1.** Petrophysical characterization of four samples. These samples are from three different tight formations.

| Sample ID | Porosity | TOC | Mineralogy, w% | | | | Sample Condition |
|---|---|---|---|---|---|---|---|
| | p.u | w% | Total Clays | Total Carbonates | Quartz + Feldspars | Others | |
| **A** | 11.2 | 7.2 | 43 | 0 | 42 | 15 | **Non-preserved** |
| **B** | 5.8 | 5 | 33 | 18 | 48 | 1 | **Preserved** |
| **C-1** | 5.1 | 4.9 | 16 | 62 | 13 | 9 | **Preserved** |
| **C-2** | 8.5 | 7.2 | 32 | 45 | 15 | 8 | **Non-preserved** |

## 3 Measureable fractions of HCs under NMR spectroscopy

For $T_2$ relaxation acquisition, if a magnetization vector relaxes faster than the setup echo spacing, protons inducing those magnetization vectors cannot be observed with the NMR spectrometer. Fast relaxing components in organic tight rocks include: 1) fluid bound in small pores, 2) highly viscous fluid components (bitumen or heavy alkanes), 3) fluids with strong affinities to pore surfaces and 4) existence of paramagnetic minerals (pyrite or siderite). The existence or coexistence of these factors make the interpretation of NMR response of HCs in shale samples complicated.

**Fig.1** illustrates the impact of surface affinity or pore type on NMR response. With the same HCs, sample (a) with more inorganic pores (or weaker surface affinity), HCs signal was observed in slower relaxation region; whereas, sample (b) with more organic pore type (or stronger surface affinity), HCs signal was observed in a faster relaxation region.

Dang et al., 2019[14] synthesized a set of six oil samples from the distillation of a same produced crude under inert condition. The crude was heated to elevated temperatures to generate oil samples with successively increasing mean molecular weights. Since NMR measurements were performed at 31ºC, the results suggested that NMR response for these oil samples correlated well with < C17 fraction. **Fig. 3** shows good agreement between NMR response and Rock-Eval® $S_1$ intensity (Dang et al., 2019[14]). $S_1$ is associated with the measured fraction of total HCs with vaporization temperature equal or less than 300ºC.

Previous studies (Chakravarty et al., 2018[15]; Hirasaki et al., 2003[3]) on NMR properties of petroleum reservoir fluids also suggests that besides tool configuration and echo times, NMR response is sensitive to the mobile fraction of HCs, which is clearly a function of fluid composition and temperature.

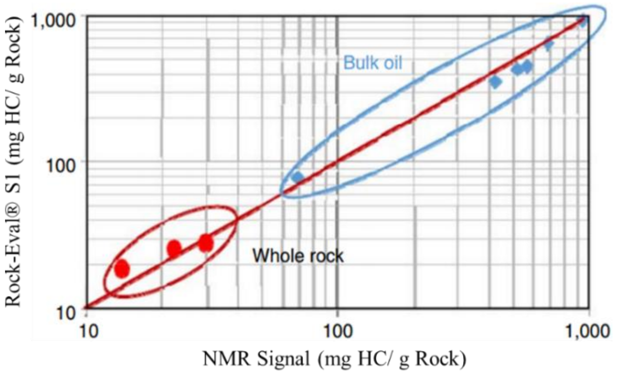

**Fig. 3.** Comparison between NMR response for HCs and Rock-Eval® $S_1$ (Dang et al., 2019.) $S_1$ intensity represents the fraction of HCs components vaporized equal to or less than 300ºC, or roughly <C17 fraction. Blue data points are from bulk oil samples; whereas red data points are from rock samples.

## 4 Impact of gas pressurization or depressurization on NMR response

As previously mentioned, the mobile fraction of HCs is governed by overall fluid composition and temperature. Since NMR response is sensitive to HCs mobility, it is critical to understand the role of gas loss while rock samples are brought up to surface conditions. Gas loss changes overall HCs composition, make the comparison between NMR benchtop measurement and downhole wireline parameters inexact. On the other hands, NMR sensitivity to fluid mobility makes it a useful tool to evaluate HCs remobilization for gas injection EOR studies.

To focus on the dynamic change of *in situ* HCs within rock matrix, experiments were performed with NMR transparent gasses. **Fig. 4** shows NMR $T_2$ spectra of sample C-1 while $CO_2$ was injected at different pressures. As injection pressure increased, $T_2$ spectra were observed to shift to the slower relaxation region (1-10ms), and signal intensity in the fast relaxation region (0.1-1ms) also decreases. These changes suggested viscosity of the original fluid was reduced, or we remobilization of HCs.

Along with the acquisition of $T_2$ relaxation, we also obtained $T_1$-$T_2$ maps, which help to separate brine from the HCs signals. HCs volume in rock matrix could be calculated by subtracting brine volume from total fluid volume. **Fig. 5** shows the normalization of HCs volume in rock matrix as a function of injection pressure. In addition to the shift toward slower $T_2$ relaxation, HCs volume detected by NMR response also increases, respectively to injection pressure. This result confirmed the existence of a fraction of HCs, which was invisible for NMR under routine laboratory condition. For some samples, the HCs volume can increase by 25vol% from initial condition to 5000 psi pressurized condition. **Fig. 6** illustrates the remobilization of HCs during gas injection, which reduce fluid viscosity and bring out a fraction of HCs originally undetectable for NMR.

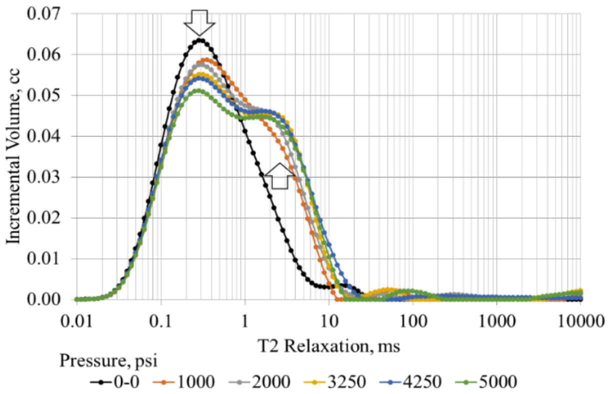

**Fig. 4.** $T_2$ spectra of sample C-1 with the injection of $CO_2$. Black spectrum is NMR response at original condition. $T_2$ were observed to shift to slower relaxation region (1-10ms), and signal intensities in the fast relaxation region (0.1-1ms) decreases. These changes suggest the reduction of fluid viscosity.

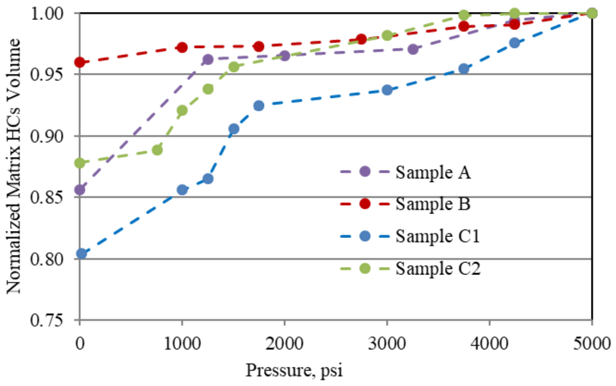

**Fig. 5**. Normalized HCs volume as a function of injection pressure. HCs volume detected by NMR increases with injection pressure. This suggest the existence of a fraction of HCs, originally invisible for NMR under routine laboratory condition.

**Fig. 7** shows the hysteresis of normalized HCs volume as a function of pore pressure between pressurization and depressurization. While pressurization data confirms the remobilization of HCs, depressurization data suggests gas trap phenomenon inside the HCs phase during depressurization. Translating to field applications, huff-n-puff EOR can be effective by increasing remaining HCs' mobility. Due to gas trapping mechanism, engineers can plan for shorter subsequent injection cycles.

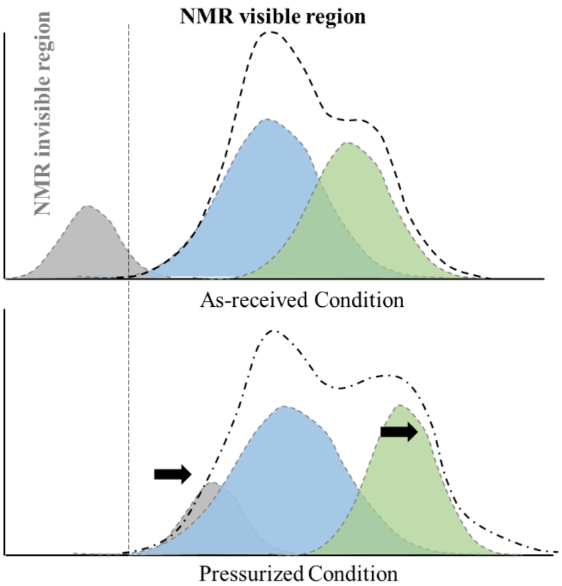

**Fig. 6.** Scheme for the remobilization of HCs during gas pressurization experiments. Blue peak corresponds to brine, green peak corresponds to light/ originally mobile HCs fraction, and gray peak corresponds to heavy HCs components. Gas pressurization reduces fluid oil viscosity, brings HCs signals toward slower relaxation regions. This makes more HCs detectable by NMR, comparing to the original condition without gas injection.

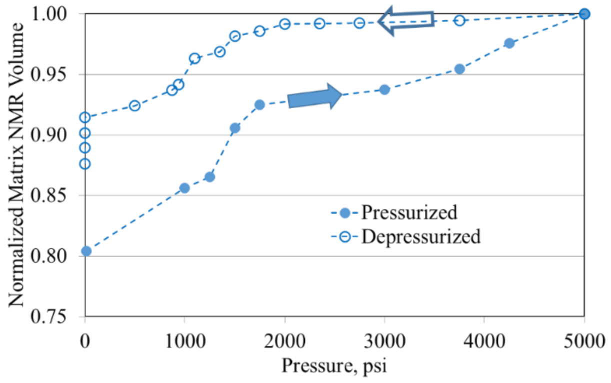

**Fig. 7.** Normalized HCs volume detectable under NMR as a function of gas pressure during pressurization and depressurization. The hysteresis between two data sets, suggest gas trapping during depressurization.

## 5 Application to study huff-n-puff in shales

The dynamic interaction between injection gas and reservoir fluid is not only a function of pressure, but also a function of injection/production strategy. With the introduction of gas into rock matrix, mobility of reservoir fluid would be enhanced, **Fig. 4**. Under a certain mass transport mechanism (convective flow or diffusion or both), additional volumes of HCs can be recovered after primary production. **Fig. 8** shows $T_2$ relaxation response of a shale sample throughout a huff-n-puff experiment with $CO_2$ as the injected gas. The experiment included four cycles with subsequent increasing of injection pressure (3750 psi, 4250 psi, 5000 psi, 5000 psi). During each cycle, gas injection was conducted for 1 day at a constant pressure, followed by 1 day production phase, in which pressure was reduced to blowdown under a controlled program. $T_2$ spectra were divided into three regions, namely non-movable fluids in matrix, movable fluid in matrix, and expelled fluids, respective to different relaxation regions. During the experiment, the signal of remaining non-movable fluid in matrix did not change; whereas, the signal of movable fluids in matrix reduced, but was volumetric balanced to the increasing of expelled fluid fractions (**Fig. 9-a and 9-b**).

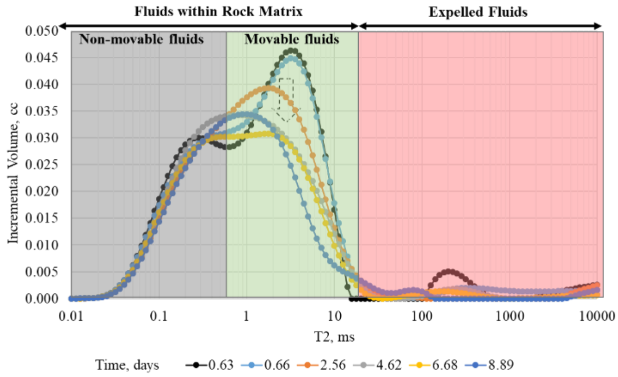

**Fig. 8.** $T_2$ relaxation response of a shale sample throughout a huff-n-puff experiment with $CO_2$ as the injected gas. $T_2$ spectra were divided into three regions, namely non-movable fluids in matrix (gray box, 0.1-1ms), movable fluid in matrix (green box, 1-10ms), and expelled fluids (red box, >10ms).

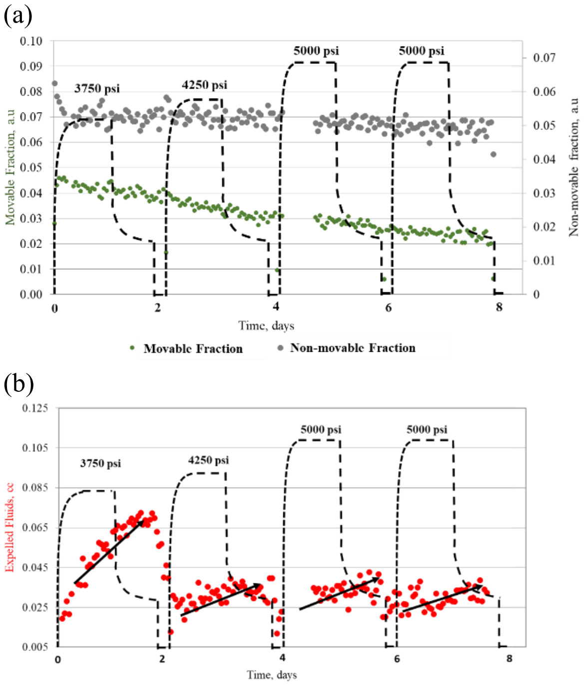

**Fig. 9.** (a) Concentration profiles of non-movable fluid in matrix (gray) and movable fluid in matrix (green). (b) Concentration profile of expelled fluids (red). While the magnitude of non-movable fluid in matrix did not change during the experiment, movable fluid fraction reduced, but volumetric balanced to expelled/ recovered fluid concentration.

## 6 Conclusions

In this study, we investigate the effect of gas pressurization by injecting gas into a rock matrix saturated with original fluids. The experiments were performed within a NMR transparent $ZrO_2$ pressure cell, placed inside a 2MHz NMR spectrometer. At a particular temperature and pressure, NMR responds to a fraction of HCs which mobile enough to be observed as an NMR relaxation sequence (roughly <C17). The invisible fraction of HCs to NMR sequence at ambient condition can be as much as 20% of the total extractable HCs. Molecular relaxation is impacted by fluid viscosity, pore size, and surface affinity. In other words, the HCs fraction with higher viscosity (either due to temperature or gas loss), presenting in smaller pore, or highly affected by the pore surface, will relax faster, and would be partially invisible to NMR. This is critical to the interpretation of NMR response for liquid rich source rocks, in which all above molecular relaxing restrictions can be found. The comparison between downhole wireline parameters and benchtop NMR measures can be incompatible. Engineers can also underestimate movable HCs by using routine core analysis data.

We also demonstrate the use of NMR spectroscopy to evaluate the efficiency of huff-n-puff EOR processes in tight rocks. This technique allows the quantification of HC recovery without compromising pressure conditions. Relaxation data also provides important knowledge on both fluid remobilization mechanism and mass transportation mechanism, during huff-n-puff.

This work was funded by the University of Oklahoma Unconventional Shale Consortium. We thank the members of Integrated Core Characterization Center (IC$^3$) for helping us during experimentation.

## References

1. R. J. S. Brown, “Proton relaxation in oils”, Nature 198: 387-388, 1961
2. J. Bryan, F. Manalo, Y. Wen, “Advances in heavy oil and water property measurements using low field nuclear magnetic resonance”, SPE International Thermal Operations and Heavy Oil Symposium and International Horizontal Well Technology Conference, Calgary, 4-7 November, 2002, SPE-78970-MS
3. G. J. Hirasaki, S. W. Lo, Y. Zhang, “NMR properties of petroleum reservoir fluids”, Magnetic Resonance Imaging, **Vol. 21**, Issues 3-4, p. 269-277, 2003
4. W. W. Kenyon, P. I. Day, C. Straley, J. F. Willemsen, “A three-part study of NMR longitudinal relaxation properties of water-saturated sandstones”, SPE Formation evaluation, 622-636, 1986, SPE 15643
5. G. R. Coates, R. C. A. Peveraro, A. Harwick, et al., “The magnetic resonance imaging log characterized by comparison with petrophysical properties and laboratory core data”, SPE ATCE, Dallas, 6-9 October, 1991, SPE-22723-MS.
6. B. R. Kenyon, B. R., C. Straley, C., G. Gubelin, G., and C, Morris, “Nuclear magnetic resonance imaging-technology for the 21st century”, Oil Field Review, 19-33, 1995
7. W.E. Kenyon, H. H. Takezaki, C. C. Straley, P. N. Sen, P. N., M. Herron, A. Matteson, M. J. Petricola, “A laboratory study of nuclear magnetic resonance relaxation and its relation to depositional texture and petrophysical properties”, Carbonate Thamama group, Mubarraz field, Abu Dhai, 1995, SPE 29886.
8. C. D. Straley, C. D. Rossini, H. Vinegar, P. Tutunjian, C. Morriss, “Core analysis by low field NMR” , 1994, SCA-9404
9. E. Odusina, C. H. Sondergeld, C. S. Rai, “An NMR study on shale wettability”, Canadian Unconventional Resources Conferences, Calgary, 15-17 November, 2012, SPE-147371-MS.
10. A. Valori, B. Nicot, “A review of 60 years of NMR wettability”, Society of Petrophysicists and Well-Log Analysts, 2019
11. A. Sinha, S. Dang, C. Sondergeld, C. Rai, “Impact of solvent extraction on surface area measurements in organic-rich shales using nitrogen adsorption”, Unconventional Resources Technology Conference, 2017, URTEC-2017-2668849
12. A. Besov, A. Tinni, C. Sondergeld, C. Rai, W. Paul, D. Ebnother, T. Smagala, “Application of laboratory and field NMR to characterize the Tuscaloosa marine shale”, Society of Petrophysicists and Well-Log Analysts, 2017
13. A. Blount, A. McMullen, M. Durand, T. Croft, B. Driskill, “Maintaining and reconstructing in-situ saturations: a comparison between whole core, sidewall core, and pressurized sidewall core in the Permian basin”, Society of Petrophysicists and Well-Log Analysts, 2018
14. S. T. Dang, C. H. Sondergeld, C. S. Rai, “Interpretation of nuclear-magnetic-resonance response to hydrocarbons: application to miscible enhanced-oil-recovery experiments in shales”, Society of Petroleum Engineers, 2019
15. A. Chakravarty, A. Tinni, C. S. Rai, C. H. Sondergeld, “NMR considerations in shales at elevated temperature”, Unconventional Resources Technology Conference, 2018, URTEC-2018-2902883

# CAUSAL PROTOCOLS TO ASSESS THE VIABILITY OF NATIVE STATE OR RESTORED STATE PREPARATION

*Jules* Reed*, Stefano* Pruno*, Izaskun* Zubizarreta*, Rolf* Solheimdal Johansen

**Abstract.** Wettability is the fundamental attribute controlling reservoir fluid saturations. It is the main parameter governing capillary pressure, which determines the distribution of the fluids, and relative permeability, which describes the fluid dynamics, within porous media. It is essential that wettability in a core study is representative of the reservoir wettability and thus, one must decide whether native (fresh or "as received") state or restored state analysis should be employed. To date, there remains debate in our industry regarding which of these two conditions should be more representative: some preferring native state (as recommended by Anderson's pivotal literature survey) and others favouring restored state core procedures, since conditions can be controlled and the processes ought to be repeatable. In recent years, it has become increasingly difficult to employ bland mud systems during coring, with additives such as; asphaltic bridging agents, emulsifying agents, surfactants, etc., that will alter wettability if invading the pore space. Use of these additives does not automatically preclude native state analysis, but inevitably complicates the process.

Some might consider that native state analysis is a relatively simpler experimental method, merely performing analyses on "as received" core samples, assuming them to be representative of native reservoir wetting conditions. However, "as received" core material may not represent native state, since wettability and saturation can be altered throughout the coring, wellsite core handling and laboratory processes, which may preclude native state analyses. If determining to employ native state core analysis, it is paramount, at an early stage in the program, to assess the impact of possible changes during the coring through to laboratory processes; considering several aspects such as: core damage, potential invasion of mud additives, saturation hysteresis, compositional change of the reservoir fluids, experimental conditions, laboratory methodologies, etc.

This paper will suggest a decision tree process, using different special core analysis protocols for different coring and core handling scenarios to determine whether native state core analysis is a viable approach for each scenario and, if not, whether restored state analysis can be applied.

# Validation of Simulated Relative Permeability Estimates in Very Low Permeability Rocks

*Nick* Drenzek, *Ryan* Antler, *Shawn* Zhang, *James* Howard

**Abstract.** Simulation of various petrophysical properties based on high-resolution images of reservoir rocks nominally requires validation with selected laboratory measurements. In the case of very low-permeability, low porosity unconventional reservoirs, the cost and time required for these validation experiments is significant. A workflow was developed that highlights the minimum in measured static and dynamic properties required to evaluate 2- and 3-phase relative permeability simulations in shale samples. A fossiliferous organic-rich shale noted by its complex fabric of large carbonate fragments floating in a fine-grain matrix of clay minerals and organic matter was used in this study. A low-resolution (~20 microns/voxel) microCT scan of the 2.5 cm diameter core plug was captured before and after measurement in a steady-state flow set up. Inspection of these images revealed faint longitudinal cracks that likely affected flow properties. Steady-state permeability to water (SSKw) measured at an effective stress of ~2500 psi was 50 nD. Subsequent gas flow and pressure decay permeability results acquired on the dried sample under significantly less effective stress were up to three orders of magnitude greater. Low-field NMR and mercury injection capillary pressure measurements indicated a bimodal distribution of pores and throats, while the NMR results show very low residual oil saturations after the SSKw test. The mercury drainage curve validated the pore geometry captured from the images. The relative permeability endpoints were defined by the SSKw and SSKo permeability and the NMR-based saturations. A 3D image volume acquired from FIB-SEM was used for the simulation of relative permeability and other basic petrophysical properties of the matrix-rich portion of the shale. These results were upscaled to a high-resolution microCT volume (~ 1 micron/voxel) that included regions of solid grains. These results were then applied to the low-resolution microCT volume, where the role of the cracks in the core plug were tested, and in some cases removed numerically.

# Composite Core – An Experimental Approach in Evaluating Ordering Criteria for Individual Cores in Composite

*Edison* Sripal*, Lesley* James

**Abstract.** Composite cores made up of core plugs typically taken from different vertical sections of a 4” core are often used for special core analysis experiments. These core plugs are typically 1-3” in length and are combined in a composite core for relative permeability and coreflooding experiments. In the seminal work, ordering of individual core samples in composite cores was presented by Huppler (1969) based on the permeability of individual cores. A harmonic averaging method was proposed by Huppler resulting in averaging the permeability of the individual core plugs to match the overall permeability. Based on a theoretical framework on North Sea sandstones, Langaas (1998) proposed ordering the core plugs from higher to lower permeability from injection to production for effective relative permeability measurements. In this paper we test the methods proposed by Huppler and Langaas. Sandstone core samples with permeability ranging from 50 mD to 2 Darcy are used for this work. Three different orientations of the core samples are tested for permeability and relative permeability with water to oil ratio of 1:6 and compared with the theoretical model developed by Langaas and Huppler. Further a new theoretical model is developed and validated with the relative permeability experimental results and compared against a data driven approach.

# Impact of Brine Spontaneous and Forced imbibition on effective permeability in gas shales

*Denis* Dzhafarov, *Benjamin* Nicot

**Abstract.** Gas shale reservoirs are developed by using hydraulic fracture technology that implies the water imbibition into the formation. In this case, it is important to understand the influence of water imbibition on effective permeability of the shale matrix.

In this study we present the impact of brine spontaneous and forced imbibition of the effective permeability to gas for a shale sample from the Vaca Muerta formation.

NMR T2 and T1T2 and Step-Decay gas permeability measurements have been performed at each step of progressive saturation by forced imbibition of brine (saturation increased by pressure steps). The techniques were used to gain insight into the effective gas permeability at different water saturation of forced imbibition process.

Permeability and NMR measurements at progressive forced brine imbibition process allow describing pore size distribution and permeability over brine saturation increase of the oil wet (organic) pores. NMR T1T2 images allow to monitor water imbibition process and determine the contribution of organic porosity to permeability at each saturation stage.

Measurements results revealed the effective permeability degradation by a factor 10 between dry and spontaneous imbibition samples states. The following forced imbibition saturation increase show effective permeability degradation up to a factor 100.

The results demonstrate that water imbibition have a strong impact on effective permeability in gas shales.

# A new approach to measure the wettability of porous media under different saturation conditions by Temperature Sensitivity of Nuclear Magnetic Resonance Relaxation Time

*Hyung T.* Kwak *and Jun* Gao

**Abstract.** The wettability, specifically the wettability of the porous structure within rocks, is one of the key parameters that determine fluid flow, which determines the potential oil producibility from reservoirs. The oil wetting preference on the pore surface of reservoir rock influences the reservoir performance in various steps of oil production, such as waterflooding and enhanced oil recovery (EOR).

The surface relaxation times of nuclear magnetic resonance (NMR) are sensitive to the wettability of pore surface since they are mainly determined by the strength of fluid-rock interaction. Thus, the surface effective activation energy (DeltaE), which is determined by the properties of fluid and pore surface, is one of the key parameters determines the NMR relaxation times. Since the DeltaE is related to temperature by Arrhenius laws for the correlation time, the wettability of pore surface is directly related to the temperature sensitivity of NMR surface relaxation times.

A new approach to measure the wettability of reservoir rocks has been developed based on this temperature dependence of NMR relaxation time. The proposed method is also capable of measuring the wettability of porous media under any saturation level which conventional method cannot provide. The proof of the concept has been conducted with a set of model mono-porous glass bead packs of various wettability. Then, the developed method has been tested to measure the wettability of multi-porous reservoir rocks with various mineralogy.

# Wettability - Combine the macroscopic approach to pore-scale analysis

*Prisca* Andriamananjaona, *Peter* Moonen, *Manuel* Chamerois, *Richard* Rivenq

**Abstract.** Fluid flow in porous media is known to be ruled by relative permeability. The relative permeability itself is dramatically impacted by the wettability state of the medium. Wettability refers to the relative preference of a solid material for one fluid in a diphasic or multiphasic system. Despite its great impact in oil recovery, a proper characterization inside the rocks, of its effect has never truly been established: until now wettability in porous media remains poorly understood. The widely used way to determine wettability in the oil industry is through empirical indices given by the Amott test or the USBM test. Those experiments give a very global idea of a given porous material's wettability, but indices do not reflect the complexity of a mixed wettability state nor the physical manifestation of wettability in the pore space. In this work, we intend to establish a correlation between measured Amott indices and the corresponding manifestation at the pore scale, to known physical properties at the pore scale, in a rock/oil/brine system.

The Amott test is usually performed on centimeter sized samples. The direct observation of fluid in the pore space is allowed by X-ray micro computed tomography (µ-CT), which give access to the very pore space in three dimensions. In order to ensure the acquisition of entire samples at a typical resolution from 2 to 3 micrometers per pixel, it is needed to work on millimeter sized sample diameters.

Here, the Amott tests are conducted on twin samples: a centimeter sized and a millimeter sized sample: respectively termed "classical Plug", and "µ-Plug". The use of twin samples allows to make sure that we compare the same wettability state. While the produced fluid volume is simply recorded on classical plugs according to Amott standard, we perform X-ray µ-CT acquisition on the µ-Plug at each endpoint of the Amott process: Primary drainage, Spontaneous Imbibition, Forced Imbibition, Spontaneous Drainage, and Forced Drainage. Obtained data allows measurements of fluid's saturation on the µ-Plug through image processing, leading to Amott indices to be compared with the classical Plug. Moreover, we propose here for the first time a deeper analysis to relate indices to corresponding pore scale properties. We intend to associate the Amott wettability indices to physical characteristics such as the fluid distribution and the interfacial properties, accounting for the porous medium complexity. In the Digital rock Physic field, this study may lead to improvement of existing simulation by including the wettability to models.

# Lithologically Controlled Core-Log-Geocell Integration Using Probabilistic Multivariate Clustering Analysis and an Expert System

*A. A.* Curtis*, E.* Eslinger*, S.* Nookala, and *F.* Boyle

**Abstract.** A workflow is presented which places far greater emphasis on formation lithology than is usual during the analysis and movement of core data to wireline log scale and then on to geomodel scale. Advanced classification techniques which utilise a consistent methodology at all scales are implemented within the new workflow. Such procedures permit more robust upscaling of petrophysical properties and thus ultimately more reliable hydrocarbon saturation estimates at geomodel scale, being consistently derived from the available core and log data. The lithological classification is also used to refine pore pressure and geomechanical understanding.

Lithological classifications are developed from core plug data and well logs using a Bayesian-based multivariate clustering analysis technique which provides a probabilistic classification at each scale. The probabilistic results at log scale are further analysed with an expert system that automatically assigns a lithology to each cluster and then predicts the probabilistic lithology at each wireline depth. The expert system can be modified for different regions and adjusted (and overruled) by an experienced analyst. The resulting multivariate models, with a consistent probabilistic lithological assignment, are used to QC and, if necessary, predict well log curves in missing intervals along the wellbore. In addition, upscaled core properties can be estimated along the wellbore using a multivariate model that combines core data with log data. Geomechanical properties such as pore pressure and minimum horizontal stress are calculated using lithology-dependent parameters for each rock type.

An example is presented for an onshore conventional gas field in which basic and saturation-dependent petrophysical properties are used to develop robust, related, lithological classifications at each of the core plug and wireline log scales. The developed wireline scale lithology then controls the development of a consistent lithology with associated properties at the geocellular model scale. The impact of different lithologies on hydrocarbon-in-place estimates and geomechanical properties can be clearly evaluated. It is concluded that such outcomes are considerably enhanced by the far better understanding and consistent inclusion of lithology at each scale.

The workflow brings more geological and petrophysical insight into the development of geocellular model properties than is usually employed. The paper outlines a readily understood workflow which fosters practical and insightful interaction between geologists, petrophysicists, and reservoir, geomechanical, and drilling engineers. It also motivates the use of available core data in a far more consistent and robust manner, thus adding value to its collection by improving project outcomes.

# An experimental and digital investigation into the impact of diagenesis above and below the oil-water contact

*Francis* Mujica*, Lesley A.* James*, Carl F.* Berg and *Derek H. C* Wilton

**Abstract.** We have investigated core samples from the Ben Nevis Formation in the Hebron field, offshore Newfoundland, Canada. This field has a short transition zone, and a clearly identified oil-water contact (OWC). Through analysis of Scanning Electron Microscope (SEM) and Cathodoluminescence (CL) images of thin sections from samples close to the OWC, we have identified different diagenesis above and below the OWC. In particular, we have observed more quartz cementation in the water zone. This observation is in agreement with the "oil retard diagenesis" theory widely discussed in the literature.

The purpose of this project was to investigate how the observed differences in diagenesis affect the pore structure and transport properties in the Ben Nevis Formation. We have evaluated the core samples' pore structure through mercury injection capillary pressure (MICP) experiments and micro-CT imaging of the core samples. Further, we have conducted digital rock simulations to evaluate the transport properties. We have simulated mercury injection by a quasi-static morphological method, electrical conductivity by solving the Laplace equation, and single-phase flow by solving the Stokes equation. Both, experimental and digital analysis were performed to eleven core samples distributed from the oil and water zones.

Our results show that despite the differences in quartz overgrowth above and below the OWC, the pore structure remains surprisingly consistent. This indicates that the diagenetic differences undergone by the rock as a result of the different pore fluids do not substantially affect the flow properties. We will discuss the experimental and digital methods and why the diagenetic differences apparently have small influence on pore structure and transport.

# Optimizing Magnetic Measurements on Drill Cuttings for Reservoir Characterization

*Michael* Bik and *David K.* Potter

**Abstract.** Magnetic measurements on drill cuttings have recently been demonstrated to give good, independently validated, estimates of certain properties (such as mineral contents and permeability) of the rocks comprising the cuttings. Cuttings are a rapid, cheap alternative to core for providing useful petrophysical information for any drilled well. This paper details how magnetic measurements on drill cuttings can be optimized for estimating petrophysical parameters. We will demonstrate via a theoretical model how mass magnetic susceptibility is essentially independent of the porosity of dry drill cuttings samples. The total porosity of drill cuttings samples comprises two components: (i) the intrinsic matrix porosity of the individual rock cuttings, and (ii) the space between individual rock cuttings. By determining mass magnetic susceptibility, which merely requires an added step of weighing the sample compared to volume magnetic susceptibility, the total porosity will essentially not affect the results of dry cuttings. In contrast, volume magnetic susceptibility is more dependent on porosity. For example, high total porosity will reduce the magnetic susceptibility of paramagnetic cuttings (such as illite), and increase the magnetic susceptibility of diamagnetic cuttings (such as quartz and calcite).

The effect of different fluids in the pore space (which includes both the intrinsic rock matrix pore space plus the space between individual cuttings) on the magnetic susceptibility of drill cuttings has also been modelled. If the pore space merely contains air then the mass magnetic susceptibility measurements are essentially independent of the total porosity. Only at total porosities of over 90% (which are unlikely to be encountered) does the model predict slight changes in the mass magnetic susceptibility. However, if the pore space contains water then the mass magnetic susceptibility is more dependent on the total porosity. Washing and drying the cuttings prior to measurement is proposed to be an optimum approach. The modelling also explains some previous experimental results where wet cuttings gave slightly different magnetic susceptibility values compared to the identical dry cuttings. Furthermore, the effect of drilling mud additives and contaminants (if present) can also be modelled, and practical steps to remove their effects will be discussed.

In summary, drill cuttings provide a vast, largely untapped resource, and the magnetic measurements described above can be used to provide petrophysical information rapidly and cost effectively. These measurements can also easily be applied to the many vials of archived drill cuttings (that are rarely studied), thus potentially adding further insights into historical datasets.

# Automated Determination of Formation Porosity from Drill Cuttings using Nuclear Magnetic Resonance

*Joel* BILLIOTTE*, Mahdi* Ammar*, Karim* Bondabou and *Jerome* Breviere

**Abstract.** Surface measurements of drill cuttings enable early-stage and low-cost access to petrophysical parameters compared with core-based laboratory measurements. Porosity measurements on cuttings using an accurate porosity measurement technique such as nuclear magnetic resonance (NMR), could be considered for petrophysical reservoir characterization, assuming a limited effect of drilling tools on effective cuttings porosity.

The recent development of rare-earth magnets and high frequency electronics technologies leads to the availability of low-cost, compact NMR spectrometers that can be used on the well site. A compact, 20-MHz NMR spectrometer can provide a signal that characterizes the fluid located inside a rock sample including weakly bound water molecules to clay particles. A typical NMR measurement is achieved in less than three minutes providing an accurate porosity measurement (with less than 0.5 point of error) by using an approximately 2-g rock sample.

Cuttings sample preparation to remove excess fluid outside the cuttings without affecting the rock texture was the main challenge. Numerous sample preparation protocols were proposed, including wiping, controlled drying, and capillary drainage. However, these methods are time-consuming and require a highly skilled operator to obtain consistent results.

In this paper, we present a new procedure based on automated analysis of the relaxation time distribution (T2) to remove contributions of the external fluid. This approach provides a first order correction of the porosity evaluation. Furthermore, we propose to perform plurality of NMR measurements during the sample preparation process of the cuttings fluid. This method enables a direct estimation of the fluid mass saturating the porous space.

To get controlled conditions, large block of cores (limestones) with different textures were used. Cuttings are produced from drilling bench experiments using real in-situ conditions and various drilling parameters. The error of porosity estimation on 25 cuttings samples with porosity ranging from 8 to 24% was less than 1 point compared to reference measurements.

The proposed workflow renders the porosity estimations on cuttings independent of the sample preparation process. Finally, the paper discusses automation of repetitive NMR measurements with a custom NMR instrument.

# Hele-Shaw setup for investigation of two-phase flow in fractures

*Martin* Raphaug*, Per* Bergmo*, Alexandre* Lavrov*, Bård* Bjørkvik*, Cathrine* Ringstad

**Abstract.** Understanding the mechanisms and the physics involved in two-phase flow in fracturs is important for optimisation of production from carbonates and gas-shale reservoirs. The amount of available research and models on this field are quite limited and has mostly been performed with single flow setups.

To obtain new experimental results on two-phase flow in fractures, in particular fluid trapping and the interplay of capillary, viscous, and gravity forces in fractures, SINTEF has developed a new transparent flow cell. Experimental results will be used for development and verification of theoretical models of two-phase flow in fractures. The cell has a dimension of 60 X 100 cm and is to our knowledge the largest existing horizontal Hele-Shaw cell for studies of two-phase flow. The cell is designed so that the following parameters can be changed:

- Fracture aperture (0.5 – 1.0 mm)
- Fracture geometry / Surface roughness
- Wettability: Oil Wet (native) to water wet (treated)
- Tilt angle: 0- 90 degrees
- Two phases can be injected simultaneously

This is achieved by constructing the main body from two interchangeable polycarbonate plates. They are distanced by a precision stainless metal spacer. The plates are supported by two 25 mm thick glass plates for avoiding deflection of the highly elastic polycarbonate material. The excellent machineability of polycarbonate material allows precise definition of the plate thickness and thereby the fracture aperture of flow setup. Surface of the plates can also be machined with a certain roughness or geometric shape. The native wettability of polycarbonate is oil-wet but by treating the plates with a hydrophilic coating the flow surface can be changed to intermediate wet or water-wet.

The experimental rig is set up with a camera for recording during the experiments, in addition flow rates and differential pressure is recorded. The recorded photos are post processed to automatically track the phase fronts, calculate phase fractions and phase velocities during the flow. A presentation of the cell and the first set of experiments will be given.

# A Review of Effects of Bedding Plane and Anisotropy on Indirect Tensile Strength Test of Rocks

*Dee* Moronkeji*, Richard* Shouse and *Rolando* Lew

**Abstract.** Indirect tensile strength (ITS) test is the recommended standard test by the International Society for Rock Mechanics (ISRM) to determine the uniaxial tensile strength of a rock sample. ITS is typically calculated from the theory of elasticity, assuming the rock to be linear elastic and homogeneous. It is estimated from the applied load and the specimen dimensions but since some rock exhibit anisotropic mechanical properties, depending on the coring direction of the disk the measurement can be greatly affected. Some of the factors that may affect ITS measurement are:

1. Bedding Plane
2. Anisotropy Angle
3. Preexisting Fractures
4. Water Content

The objective of this study is to look at available data of ITS test from different studies to see the variation in measurement in disc samples as a function of loading direction to the bedding plane and anisotropy angle. Testing were also conducted on Mountain sandstone, Clayey Sandstone, Marcellus shale, Mancos shale, Alabama limestone and Carthage limestone. Bedding plane and anisotropy can affect the mechanical properties of rocks, also preexisting fractures and water content can significantly lower ITS measurement.

Bedding plane can have a significant effect on ITS especially when the rock exhibit a vertical transverse isotropy (VTI). This is especially true in some shale plays and the ITS measured can be significantly different depending on the coring direction with respect to bedding plane. Transverse isotropy is a kind of anisotropy in which there exists an axis of symmetry so that any measured properties perpendicular to this axis appears to be the same as it is isotropic in this transverse direction. However, measured property will change at an angle to the axis of symmetry.

Based on the tests reviewed and tested it was observed that the loading direction to the bedding plane or anisotropy angle of the rock changes the measured value of ITS and these changes are more significant in anisotropic rocks. It can be seen that ITS performed on vertical samples (bedding plane parallel to the disk surface) have the highest strength because under diametrical loading, vertical samples behave isotropically. Similarly observed was that ITS measurement on disc loaded perpendicular to the bedding planes are typically higher than on core plugs loaded parallel to bedding planes.

These observations are very important for planning coring operations and should be greatly considered in selecting samples for ITS testing in rocks with bedding planes and exhibiting anisotropy.

# Pore scale visualization of Improved Sweep Efficiency During Fines Assisted Low-salinity Waterflooding Using Micro-CT Imaging

*Yamin* Wang, *Muhan* Yu, *Furqan* Hussain

**Abstract.**

Objective:

A number of studies suggest improved sweep efficiency as an enhanced oil recovery mechanism during low-salinity waterflooding (LSW). Fines migration during LSW can lead to partial blockage of pore space which diverts the injected water into unswept pores resulting in a better sweep of oil. However, there is no direct evidence of improved sweep efficiency due to fines migration. In this study, we use micro-CT imaging to visualize the changes in residual oil saturation before and after tertiary LSW.

Methodology:

Experiments were conducted on a Berea sandstone core sample. X-Ray Powder Diffraction (XRD) and X-Ray Fluorescence (XRF) were run to characterize Berea sandstone before the experiment. Scanning Electron Microscopy and Energy Dispersive X-ray Spectroscopy (SEM-EDS) analysis were run to observe changes of minerals before and after the experiment. The core sample received injection first of systematic oil, then of brine (40g/L NaCl), and finally of low-salinity water. Micro-CT images of the core sample were taken at 5 stages: (1) dry core before the experiment, (2) after synthetic oil injection, (3) after brine injection, (4) after distilled water injection and (5) dry core after the experiment. The pressure difference between the core's injection face and production face was recorded during the injection. Samples of produced water were used for ionic chromatography to measure the concentration of produced fines.

Results:

The experimental results show an extra 5% oil recovery and an order of magnitude drop in permeability after distilled waterflooding. Micro-CT images show additional swept pores after LSW.

Novelty:

The images of Micro-CT provide direct evidence of how fines assisted low salinity water flooding improves the sweep efficiency.

# New method for characterising the nano- to macro-scale voidage within black shale and for modelling shale gas recovery efficiency

*G. Peter* Matthews*, Katie L.* Jones and *G. Maurizio* Laudone

**Abstract.** We present a major new advance in the ability to characterise the nano-voidage of tight reservoirs, demonstrated using intact, rather than crushed, black shale samples.

The approach involves cleaning of 1 cm3 samples, followed by helium pycnometry and mercury intrusion. The major advance is in the subsequent modelling, which uses two new developments: (i) the correction and extension of the high pressure mercury intrusion curve to include nanoscale characteristics, recently demonstrated for nuclear reactor carbon (Jones et al., Carbon, March 2018), and (ii) a complete void size mapping based on coupled inverse and forward modelling of the full percolation characteristic (Matthews et al., Transport in Porous Media, September 2018). The approach is a major improvement on Lattice-Boltzmann and Markov chain approaches, for example that of Chen et al. (Scientific Reports 2014) which suggests an unjustified maximum number of features at 20 nm.

Important applications include:

(i) quantitative measurement of the repository void sizes in unconventional cores in the range 1 nm to 6 um,

(ii) generation of a void network which matches experimental percolation measurements, and which can be used for gas and liquid flow simulations, and

(iii) calculation of absolute permeability in the presence of trapped fluids and fines, to better understand EOR efficiency and the rate of decline of well productivity.

Shale samples are cleaned with IPA (Cornwall, 2001, SCA) since toluene can cause secondary porosity (Burger et al., 2014, SCA), followed by methanol extraction and drying. The surface accessible porosity is measured with helium pycnometry. The percolation characteristic is measured with mercury intrusion porosimetry between 4 nm and 6 um, and extended down to 1 nm using the helium pycnometry result.

Modelling is carried out with the PoreXpert software, which generates a void structure by quasi-Bayesian inverse modelling of the experimental percolation characteristic, and stochastically bridges the gap in the experimental percolation characteristic between 1 and 4 nm. Forward modelling of the percolation then allows void clusters to be identified, which are normally wrongly characterised from the slope of the percolation characteristic against applied pressure. The resulting void size mapping is a fully quantitative match to the experimental sample in terms of the volumes, cross-sections and connectivities of the voids. It is also the basis for further simulations, currently relative permeability changes caused by diethyl ether enhanced huff puff recovery in samples extracted from the kitchen zone of the Vaca Muerta shale formation, Argentina.

# Pore Structure Impact on Polymer Retention in Carbonate Cores

*Abdulkareem M.* AlSofi*, Jinxun* Wang*, Abdullah M.* Boqmi

**Abstract.** Polymer flooding can significantly improve oil recovery by increasing the injection water viscosity, hence reducing the displacing front mobility and improving the sweep efficiency. One of the major concerns in determining the feasibility of a polymer flooding project is polymer retention which is attributed to physical surface adsorption, mechanical entrapment and hydrodynamic retention. A clear understanding of the magnitude and significance of these interactions and effects for carbonates is still lacking.

In this study, we investigate the impact of pore structure on the retention of a polyacrylamide polymer in carbonates. Reservoir carbonate core samples are characterized through X-ray diffraction (XRD), nuclear magnetic resonance (NMR) and BET (Brunauer, Emmett, and Teller) surface area measurements. Polymer retention in these cores are evaluated by coreflooding experiments at reservoir conditions. The effluent polymer concentrations were analyzed by total organic carbon (TOC) method for determining polymer retentions.

Results show that the studied polymer exhibits dynamic retention in carbonates ranges from 0.155 to 0.530 mg/g-rock, and polymer inaccessible pore volume ranges from 15.2 to 20.9 % polymer volume (PV) of the studied core samples. XRD results reveal that the core samples consist mainly of calcite, with a small amount of dolomite, anhydrite and quartz, and there is no clay minerals. NMR results show that all the studied cores exhibit similar bi-modal pore size distribution, indicating they belong to a same rock type. Among the varied pore characteristics, surface area plays the most important role in polymer retention. A close relationship between polymer retention and surface area is observed. Core samples with larger BET surface area exhibit larger amount of polymer retention. Results also show tighter core sample tends to have larger value of inaccessible pore volume. This study indicates that physical surface adsorption is the main retention mechanism, and in the absence of clay minerals, surface area is a governing impact factor on polymer retention.

The results in this work help to gain insight into the interactions between the transported polymer and the carbonate pore characteristics. The governing influencing factors on polymer retention and inaccessible pore volume are investigated. This study demonstrates the potential of the studied polymer for carbonate reservoir application, as well as providing essential data for designing and evaluating polymer flooding in carbonates.

# Automated Quantitative Micromodel Image Analysis Applied to High-Pressure $CO_2$ Foam Injections

*T. L.* Føyen*, J.* Gauteplass*, Ø.* Eide*, M. A.* Fernø

**Abstract.** Porous micromodels enable multiphase pore level visualization with displacement mechanisms and flow phenomena. Imaging during fluid injection tests is typically performed as a time lap series of images, where each image contains static information such as grain size, geometry and distribution; location of pore throats, pore bodies and porosity (in field of view). Each image also contains dynamic information related to the distribution of fluids (aqueous, gaseous and oleic), interfaces between immiscible fluids and droplets of trapped fluids. The dynamic information change between each acquired image during fluid injection, generating very large image files during normal injection tests in typical micromodels. Micromodels with regular and repeated patterns (such as pillars or squares) have fewer possible fluid distributions during injection compared with irregular patterns based on real rock thin sections. The high image resolution necessary to capture a large field of view, rapidly changing fluid distributions, the presence of multiple fluid phases and moving interfaces easily generate several 100s of GB of information during a single injection test, and an effective and rigours image analysis protocol for automated quantitative analysis of observed displacement mechanisms is needed.

The rapid advancement of computer power and image analysis tools enable our research community to perform quantitative analysis of extreme amounts of image data on fluid displacement at the pore scale. An automatic, systematic interpretation that transforms images to meaningful statistics and information, minimizing biased, time-consuming manual interpretations is a valuable tool. The strength of computer vision is its high throughput, both with respect to the number of images analyzed, particularly important in dense time lap series, but also in its ability to capture all features of interest occurring in the micromodel pore structure.

We outline an automated workflow that converts time-lapsed images during $CO_2$ foam injection to quantitative analysis of important pore level phenomena such as bubble density, fluid saturations and sweep efficiency. An experimental protocol using high pressure micromodels with irregular pore space is outlined. Procedures to capture high resolution images across the micromodel and enhance the field of view, and how to prepare images for further analysis using open source software libraries for scientific image processing are discussed. Software to perform tasks as identifying, describing and counting features of interest is described, incorporating well-known and documented image processing methods. Quality control and comparison to manual analysis is presented to demonstrate the power of the new automated image processing workflow.

# Reducing Sample Heating During NMR Measurements

*M. J.* Dick*, D.* Veselinovic*,* and *D.* Green

**Abstract.** NMR-measurements (T2-distributions, T1-T2 and T2-diffusion maps) are employed to derive porosity, wettability, fluid type and other properties. These measurements are derived using the Carr Purcell Meiboom Gill (CPMG) NMR pulse sequence. This pulse sequence employs a train of radio-frequency pulses which probe the exponential decay of the NMR-signal. The rate of this decay directly leads to petrophysical information such as pore size. In order to probe the smallest pores, the pulses at the beginning of the CPMG-pulse train must be close together to properly quantify the fast-exponential decay. For larger pores, the pulse train must be long enough to fully probe the entire exponential decay.

In a typical CPMG-sequence, the pulses in the train are linearly spaced. This results in trains with a large number of pulses at high duty cycle leading to heating of the sample. Heating is an issue because as the sample's temperature increases its NMR-signal decreases. This can lead to inaccuracies in the porosity derived from the NMR-data. In addition, the petrophysical property being measured may be temperature dependent and thus there is no control of an important property. For porosity, we have explored the degree of inaccuracy and have found that heating can lead to changes in retrieved NMR-porosity of approximately 10% in both bulk fluid and core samples. We have also explored the effect of salinity of the sample fluid and strength of NMR-field on sample heating.

The processing of the CPMG-train of data is usually decimated into a much lower number of echo data. One common method reduces the echo train by logarithmically decimating the data into approximately 500 data points. These points are then processed further into the distributions and maps. One method to eliminate the unwanted heating of samples by CPMG sequences is to replace the linearly spaced pulse train with a train where the pulses are logarithmically spaced. This logarithmically spaced train will maintain the closely spaced pulses at the beginning of the sequence necessary to probe the smallest pores, while decreasing the density of the pulses as the train gets longer. This leads to a reduction in the total number of pulses and therefore a reduction in the heating of the sample. We have implemented this logarithmically spaced CPMG sequences and will show that these sequences still accurately reproduce the NMR-measurements for all samples while eliminating sample heating.

# Modeling carbonate microfractures with the lattice Boltzmann method

*Andrew* Fager, *Bernd* Crouse, *David* Freed, *Josephina* Schembre-McCabe, *Neil* Hurley

**Abstract.** The presence of fractures in an oil-bearing reservoir can have a significant impact on production. Therefore, understanding and predicting the effect of fractures on overall reservoir performance is an important endeavor. In this work, we apply the lattice Boltzmann method to high-resolution images of Indiana Limestone to investigate the effect of microfractures on fluid flow in carbonates. High-resolution imaging is used to build 3D models of pore space in the Indiana Limestone. In the original images, no fractures were observed. Microfractures of varying size and shape were then digitally overlaid on the unfractured image. By analyzing images with and without microfractures, we can study the impact of their presence on flow behavior. Both single-phase and multiphase lattice Boltzmann flow simulations are performed. Single-phase analyses show the relationship between permeability and fracture properties, such as aperture size and shape. This allows us to emulate specific features, such as the role of variable confining stress and subsequent fracture closure. Modeled trends compare favorably to laboratory measurements. In multiphase analyses, properties such capillary pressure, relative permeability, and residual oil saturation are computed for varying fracture conditions. Special attention is paid to the interaction between matrix and fracture, particularly oil production from the matrix into the fracture.

# Microscale interactions of EOR chemicals at the crude oil-water interface and their implications for oil recovery

*Zuoli* Li*, Zhenghe* Xu*, Subhash* Ayirala and *Abdulkareem* AlSofi

**Abstract.** The conventional experimental techniques used for the performance evaluation of enhanced oil recovery (EOR) chemicals, mainly polymers and surfactants, have been mostly limited to bulk viscosity and interfacial tension measurements. Furthermore, fundamental studies exploring the different microscale interactions instigated by the EOR chemicals at the crude oil-water interface are very scanty. The objective of this experimental study is to fill this existing knowledge gap and deliver an important understanding on underlying interfacial mechanisms and their potential implications for oil recovery in chemical EOR.

Different microscale interactions of EOR chemicals, at crude oil-water interface, were studied by using a suit of novel instruments such as Langmuir trough, interfacial shear rheometer and coalescence time measurement apparatus. The reservoir crude oil and high salinity injection water (57,000 ppm TDS) were used. Two chemicals, an amphoteric surfactant (at 2000 ppm) and a sulfonated polyacrylamide polymer (at 500 ppm), were chosen since they are tolerant to high salinity and high temperature conditions. Interface pressures, compression energy, interfacial viscous and elastic moduli and coalescence time between crude oil droplets are the major experimental data measured.

The results showed that interfacial pressures slightly decreased with polymer, however remained almost in the same order of magnitude as the plain high salinity aqueous brine. In contrast, a significant reduction in interfacial pressures with surfactant was observed. The interface compression energies showed the same trend and were reduced by about two orders of magnitude when surfactant is added to the aqueous brine. The surfactant was also able to retain similar interface behavior under compression even in the presence of polymer. Interfacial rheology measurements demonstrated only minor changes in interface viscous/elastic moduli (G' and G") and the absence of G'/G" crossover point with both surfactant and polymer chemicals. These insignificant effects of EOR chemicals on interface viscoelasticity can be attributed to the very low content of asphaltenes present in the crude oil. The coalescence times between crude oil droplets were slightly increased by polymer whereas substantially decreased by the surfactant. These findings indicate negligible interactions of polymer at crude oil-water interface, while demonstrating the high efficiency of the surfactant to soften the interfacial film, promote the oil droplets coalescence and mobilize substantial amounts of incremental oil in chemical EOR.

# Robust and Efficient Evaluation of Oil/Water Contact Angles and Wettability Alteration Using a Modified Washburn Method

*Alhasan B.* Fuseni*, Ziyad* Kaidar*, Abdulkareem M.* AlSofi

**Abstract.** Wettability alteration represent a potential EOR mehansims that is especially valuable for fractured media. Initial screening of surfactants for wettability-alteration purposes rely mainly on contact angle measurements prior to further spontaneous or forced displacement experiments. In this work, we evaluate a novel sorption procedure to study wettability alteration and screen surfactants. In this method, changes in wettability of carbonate rock powder when treated with various surfactants are estimated using a modified Washburn method.

Carbonate rock, synthetic brines, crude oil and four surfactants were used. Surfactants included: anionic alfa olefin sulfonate, cationic quaternary ammonium salt, an amphoteric surfactant and a nanosurfactant. Hexane was used as a reference (completely wetting) fluid. Sorption experiments were performed. In which, powdered rock with a size between 80 and 100 mesh is coated with the surfactant and compacted in the sample holder. A chamber is then raised to the bottom of the powder pack such that the fluid sorbs by capillarity. A balance measures the mass sorbed with time. Direct contact angle measurements were also performed for benchmarking.

Plotting the square of fluid mass against time gave a slope which enabled the calculation of contact angle in air. For each coating, the results (sloped) observed for the completely wetting fluid (hexane) provided the rock constant. Sorption results of crude oil coupled with the previously determined rock constant enabled estimation of the Wasburn oil/air contact angles using the modified Washburn equation. Sorption results with brine and surfactant solutions coupled with the rock constant and oil/air enabled estimation of the Washburn water/air contact angles using the modified Washburn equation. Based on water/air and oil/air contact angles, values of the conventional oil/water contact angle were estimated. This approach, enabled a robust and rapid estimation of surfactant effects on contact angles (hence wettability). Based on the benchmark contact angle results, the sorption approach yields acceptable results especially for screening purposes. Furthermore, the results demonstrated the capacity of the surfactants for wettability alteration. Among the tested surfactants, the nanosurfactant altered wettability the most.

The use of sorption to obtain contact-angle estimates provide a novel rapid and robust procedure for evaluation and screening of wettability-alteration agents. This eliminates direct contact angle measurements that are often cumbersome. It specifically eliminates the difficulties of attaching an oil drop onto a rock surface immersed in surfactant solutions where the ultra-low interfacial tension causes the oil drop to spread prematurely.

# In-situ Characterization of Mixed Wettability in Carbonate Rock: A Cryo-BIB-SEM Approach

*A.* Gmira, *S.M.* Enezi and *A. A.* Yousef

**Abstract.** Injection of SmartWater brines with tuned ionic compositions into carbonate rocks has shown a significant effect on reservoir wettability alteration from oil-wet toward a water-wet state and improved oil recovery. Multi-scale techniques have been extensively used in the last decade to decrypt the underlying mechanisms impacting rock wettability and oil mobility, although it is challenging to understand the behavior of reservoir fluids and carbonate rocks at nanoscale with conventional methods. Therefore, there is a need for advanced visualization technologies to identify fluid phases, distributions and interactions within the complex carbonate porous matrix.

Cryogenic scanning electron microscopy with broad ion beam (Cryo-BIB-SEM) is utilized to study carbonate-oil-brine interfaces at nano-scale and characterize rock porosity and connectivity. High resolution energy dispersive spectroscopy (EDS) identifies oil and brine distribution and quantifies length of oil-carbonate interfaces as well as contact angle distributions.

The study is conducted on carbonate rock samples aged in crude oil and saturated with brines with various compositions, to include the effect of salinity gradient and ionic strength. The results show the distribution and connectivity of crude oil within carbonate pore structure with clear identification of oil-brine-carbonate interfaces at nano-scale. The effect of the brine ionic composition on interfaces, fluids distribution and contact angle was monitored, bringing new insights about effect of salinity gradients and potential determining ions on carbonate wettability alteration and oil mobility.

# Core-Based Diagnostics of Sanding Prone Pay Zones in the Ordovician Sarah Sandstone Reservoir, Northern Saudi Arabia

*M. S.* Ameen*, A. Y.* Coulibaly*, A.* Rees*,* and *L.* Jihong

**Abstract.** Core-based laboratory studies and field observations are conducted on the Ordovician Sarah Sandstone reservoir in exploration wells of Northern Saudi Arabia to assess their sand production risk. The reservoir has been a target for gas exploration over the last several years.

The study was prompted by the field detection of sand production at early stage of the exploration. A comprehensive coring, logging and dynamic testing campaign was conducted to establish the driving factors for sand production, to facilitate effective prediction, mitigation, and management of sand production. The diagnosis involved rock mechanical, petrophysical, and petrographic characterization of core samples acquired from the reservoir zones, in the key wells where sanding occurred. Identifying the rock types, most at risk for sand production, was then linked to the key changes to in-situ reservoir parameters, whose change trigger sand production. Statistical geomechanical models were built to assess the pressure drawdown threshold at which sand production is likely to be triggered, and the results are calibrated against actual dynamic tests in key wells.

This paper presents the methods used and the outcomes of the integrated analysis and modeling. The results show that all reservoir zones that produced sand in the studied key wells are clean, fine- to coarse-grained sandstones with dominantly rounded to surrounded grains. They are all highly porous and permeable; poorly consolidated; poorly cemented; and mechanically weak rocks. Rock mechanical testing reveals that sand production occurs persistently when the above mentioned rock types are characterized by low Young's modulus, low unconfined compressive strength, and low cohesion. In the field, sand production in the key wells increases as the wellhead pressure decreases and as the drawdown pressure increases. Hollow cylinder (thick wall cylinder) tests on the cores acquired from sanding prone rocks confirms that rock weakening and catastrophic failure in the studied reservoirs is facilitated by the increase in confining pressure (with depletion), and the reduction in wellhead pressure due to production. Where multiphase fluids exist, sand production exponentially increases with water production, because water reduces the capillary pressure and weakens the rock, facilitating failure and sand production.

# A Pore-Level Analysis on Residual Oil Structure post Secondary and Tertiary Displacements

Lyla, *AlMaskeen;* Felix Servin, *Jesus;* AlAseeri, *Abdlrahman;* AlSofi, *Abdulkareem*

**Abstract.** The use of micromodels in displacement experiments is becoming an established methodology to study oil sweep and mobilization. Enhanced oil recovery (EOR) processes reduce the remaining oil. Yet, the evolution of this remaining oil in terms of structure and conformations has not been well described. Gaining such understanding can offer an opportunity to better optimize EOR processes. Accordingly, we perform micromodel displacements and assess the microscopic changes in remaining oil.

We use a 2D micromodel mimicking the topology of a sandstone. We establish connate brine saturation. Then, we conduct oil displacements where waterflooding is followed by a tertiary surfactant-flood. After each stage, we collect 25 microscopic images across the micromodel. We then use an in-house Matlab code to analyze the images. Based on the analyzed images, we quantify remaining-oil saturations after each stage. More importantly, we delineate the remaining-oil structures in terms of size (pore-bodies spanned), conformation (degree of roundness), and connectivity (coordination number).

In this sandstone-based micromodel, the remaining oil saturation dropped from 35% after waterflooding to 15% after surfactant injection. Initial oil saturation was 87%. Image analyses allowed in-depth characterization of the remaining oil. The size-distribution of remaining oil globules was obtained after both stages. Significant reduction of the globules size was realized post surfactant-flooding. In addition, a narrower distribution was observed. In general, most remaining globules spanned multiple pore-bodies post waterflooding while almost all were reduced to occupying a portion of single pore-bodies post surfactant-flooding. As such, the conformation of the remaining oil after waterflooding was irregular as it was dictated by the underlying topology. After surfactant-flooding, most globules were circular. Accordingly, the main trapping mechanism post surfactant-flooding is snap-off. To the contrary, the remaining oil post waterflooding was largely trapped due to bypassing (pore-doublet effects)—yet, snap-off was still observed. Obviously, globules post waterflooding exhibited higher coordination numbers as they spanned multiple-pore bodies. Surfactant-flooding enabled mobilization of these globules as the interfacial tension (IFT) was reduced, which allowed viscous forces to overcome the capillary forces required to access and deform these globules. With that, we correlate IFT reduction and the narrowest coordination path (connected pore-throat).

In summary, the evolution of remaining oil has been delineated. Differences between the remaining oil before and after surfactant-flooding is clearly outlined with respect to changes in the oil globules size, connectivity, and conformation. Such understanding might offer an opportunity to better optimize EOR processes.

# Application of digital petrophysics to Brazilian pre-salt carbonate rock: comparative study on two different facies

*Titly Farhana* Faisal (TOTAL and INRIA)*, Rodolfo* Victor (PETROBRAS)*, Rodrigo* Surmas (PETROBRAS)*, Igor* Bondino (TOTAL)

**Abstract.** Since the time Digital Rock Physics (DRP) gained momentum, a lot of attention has been dedicated in development and improvement of simulation algorithms, performance evaluation and accuracy validation against laboratory measurements etc. Thanks to these efforts we have robust understanding of associated uncertainties, limitations and assumptions. For e.g. we know that in terms of absolute values, there is a persistent overestimation of predicted elastic properties for all elastic simulators (regardless of the methodology). However what is also true, and perhaps slightly overlooked, is that we can still extract valuable trends, sensitivity ranges and data for comparative studies starting from a set of images despite these limitations.

In this work we focus on such an application to look at the variability of carbonates. Due to giant discoveries made in the past years pre-salts are of significant economic importance. We employed our DRP workflow on two Brazilian pre-salt carbonate samples with different morphology and mineralogy. A high permeability (754 mD) and porosity (14.1%) coquina sample S1 consisting primarily of calcite and quartz was chosen in contrast to a low permeability (6.15 mD) spherulite sample S2 of similar porosity (13.4%). The samples were imaged with Micro-CT at three resolutions (including a full plug image at coarse resolution) and DRP was used to characterize elastic properties, single phase flow and pore network extraction properties. As expected, numerical predictions overestimated laboratory measurements in all cases when compared. However we perform a systematic comparison between common parameters of both samples to identify if any one sample suffered a higher degree of overestimation and why? Furthermore we highlight the challenges in image processing and segmentation and the consequential effect of segmentation sensitivity on derived properties.

# Digital Core-Enabled High-Resolution Formation Evaluation via Coupled Physics and Data Analytics

*Nicholas* Drenzek, *Ryan* Antle, *Haifeng* Jiang, *Siddharth* Misra

**Abstract.** Dual energy X-ray computed tomography (DECT) scans of 30 meters of U.S. midcontinent core were acquired and post-processed to filter out imaging artefacts, align core sections, remove incongruities including core breaks and plug gaps, and erode mud-invaded zones. Mineral standard calibration curves were then leveraged to derive photoelectric (PEF) and bulk density logs at millimeter spatial (including depth) resolution, from which companion bulk mineralogy tracks of sandstone, limestone, shale, and porosity were calculated using a distributed endmember mixing model. Results demonstrate good agreement with sub-sampled x-ray fluorescence-derived PEF, helium porosity, and x-ray diffraction mineralogy measurements. Selected sections of these data were then combined with underlying DECT greyscale image stacks, 25 and 50 micron resolved visible and ultraviolet line images, respectively, of the slabbed surface of the core, and 15 centimeter resolved total and spectral natural gamma logs as inputs to a wireline petrophysics-supervised machine learning model to generate synthetic logs of rock mechanical fraccability, permeability, and fluid producibility in sections that were not used for the training dataset. Model success was largely dependent on the quantity of input data, among other factors, underpinning the value of the high resolution, high throughput, multimodal formation evaluation datasets afforded by digital core analysis methods like DECT and line imaging.

# Metre scale gas-brine coreflood investigation of plume mobility and trapping

*Michael B.* Clennell, *Cameron* White, *Ausama* Giwelli & *Matt* Myers

**Abstract.** The carbon storage concept for the Petrel basin in Northern Australia involves injection of CO2 into a high permeability sand-rich fairway of the Sandpiper Formation with a likely permeability of around 1 Darcy or more. The plume trajectory is difficult to predict with models given the potential for unconstrained gas mobility. As no suitable cores were available from the basin, we conducted experiments on uniform cores of a good petrophysical analogue. Bentheimer sandstone has been widely used in rock properties research at core to pore scales, and we took advantage of that understanding in the design of large core flood experiments in tilted and vertical orientations to study 3D flow patterns, trapping efficiency and the relative importance of capillary, viscous and gravity forces at mm to metre scale. We used the nitrogen-brine system rather than CO2-brine, given that the system is mineralogically simple and strongly water wetting. The experiments were monitored by medical x-ray CT images. The first experiment, where gas was injected into the base of a ~1 metre long x 100 mm diameter core tilted at 17 degrees, showed the minor role of gravity forces compared with capillary-viscous flow instabilities. Once formed, gas channels bypassed the majority of the brine filled volume, leading to early breakthrough and inefficient trapping. Gas injection from the base of the vertically oriented core showed the same pattern. Gas formed a preferential path and minor gravity pooling at the top of the core, while subsequent brine sweep mainly followed the remaining brine zones, and hardly displaced any of the injected gas. The third experiment involved slow injection of gas from the top of the vertical core, forming a stable cap that achieved the maximum possible original gas saturation without gas breakthrough. Secondary brine imbibition forced the gas cap downwards, as well as creating a diffuse zone of residually trapped gas. A small zone of viscous brine fingering, where the maximum velocities are realised, was also seen the inlet region. The three dimensional x-ray imaging enables excellent visualization of the gas and brine channel patterns formed in the experiments as well as enabling the residual saturation to be assessed in a range of sub-regions of the core subjected to originally high and low gas saturations. The metre-scale experiments provide a wealth of information about flow instability that occurs even in highly homogeneous rocks, and provide a guide for further experiments on more realistic systems.

# The role of heterogeneous wettability for hydrocarbon production from imbibition in a mixed multiporous carbonate reservoir rock investigated by magnetic resonance techniques

*Jun* Gao*, Hyung T.* Kwak

**Abstract.** The intermediate and/or mixed wetness of carbonate rocks is often attributed to the adsorption of oil polar components onto the pore surface over time. Many carbonate rocks have multiple pore systems with large pore size distribution and irregular pore geometry which control the access of oil to the pore surface. The previously-developed correlations between the oil mobilization and mixed and/or intermediate wettability for sandstone and mono-pore carbonate rock, such as North Sea chalk, may not be valid due to the pore system differences. Furthermore, the clear pore scale identification of the initial and residual oil distributions in multiparous carbonate rocks is imperative to improve the EOR efficiency, which are the objectives of this study.

The NMR measurements are able to provide both oil saturation distributions at core scale from imaging and at pore scale from measurements such as T2 distributions. Three types of clean reservoir core plugs composed of macropore (M), micropore (m), and both macropore and micropore (M-m) are selected based on the T2 distributions of 100% water saturated. First, the oil is saturated at different levels using a centrifuge. The samples are aged at 75°C for various time periods to create different wettabilities monitored by T2 distribution shift. Then they are immersed in D2O for imbibition with two ends open (TEO) monitored by NMR for spatial oil saturation distributions and T2 distribution shifts. Finally, a small water head (1-2 inches) is applied for further changes in saturations within samples.

The results of the aging and imbibition experiments indicate the following relations and findings: the less the initial water saturation and the longer the aging duration, the larger the wettability alteration during aging. At the pore scale, the wettability of micropore appears to be less altered due partially to the lower oil saturation. In addition, no clear progressing water fronts are observed during imbibition from MRI saturation profiles. Additional oil production is observed for some samples after applying the water head. The increase of that from micropore is mainly caused by the better contact between water and micropore impeded by local capillary barrier. In summary, the current study provides insights on the wettability heterogeneity at both core and pore scales in this multiprorous reservoir rock. The observed phenomena of the wettability alteration and oil saturation in different pore systems is the key to understand the subsequent forced imbibition and to identify residual oil distribution as the target of EOR.

# Adsorption isotherm for wettability evaluation

*Dmitry* Korobkov*, Vera* Pletneva

**Abstract.** Nowadays, digital rock technologies are successfully developed and applied in the oil industry. So, relative phase permeability and EOR scenarios can be easily simulated using microCT 3D-model of pores and wettability data. But, the most important input parameter that is wettability can be measured directly only for high permeable rock by any of Amott-based method. Data on wettability of tight rock (permeability below 1mD) is mostly unavailable. We propose using of adsorption-based methods for wettability evaluation.

Now we continue the study on rock characterization by calorimetry (presented in SCA 2018-053) where differential scanning calorimetry and gas sorption technique were used to characterize fluid/rock interaction. At the present time, we have finished jointing both setups and conducting test experiments on thermodynamic characterization of interaction between pure liquid (water, hexane) and solid (porous glasses, calcite, carbon).

In the paper we will discuss implementation of static volumetric adsorption technique and adsorption calorimetry for evaluation of wettability through free surface energy which is related to the wettability state of the surface of a formation. The both techniques and their combination were applied for characterization of artificial porous media with predefined surface properties. Experimental setup as well as results of test experiments will be presented and discussed in the paper.

# Petrophysical Parameter Prediction Utilizing Limited Core Training Data

*Ana Maria* Naranjo Pacheco and *David K.* Potter

**Abstract.** Estimates of routine and special core petrophysical parameters from logs in uncored wells rely on establishing correlations between core and log data in a nearby cored well, or by using generic database correlations for the particular reservoir type of interest. The purpose of the present study is to determine how much core training data is necessary in order to make meaningful predictions. We will demonstrate that even very limited core plug training data can produce good predictions, provided that the core plug data is representative of the reservoir(s) of interest. By using a methodology that combines machine learning with the concepts of representative genetic units and global hydraulic elements, we will show that careful selection of minimal representative core plug training data can provide predictions that are almost as good as those obtained by utilizing much larger core plug training datasets. We will demonstrate this from predictions of permeability using key well logs and different amounts of core plug training data. Specifically we compare the performance of predictors trained on data from 4 scenarios using progressively smaller numbers of core plugs as follows: (1) the entire core plug dataset in the training well, (2) core plug data from specific reservoirs in the training well, (3) core plug data from short representative genetic units (RGUs) in the training well, and (4) minimal representative core plug data selected via global hydraulic element (GHE) analysis within individual RGUs in the training well.

Remarkably, the predicted permeability values throughout the well based on scenario (4) using minimal core plug data (from just a few representative plugs – each from a different GHE) were almost as good as those from scenario (1) using the entire core plug dataset (several hundred plugs), in terms of the r2 correlation coefficient between the predicted and actual permeabilities. The r2 values from all of the scenarios were relatively high. The methodology can be applied to predicting other petrophysical parameters from minimal, representative core data, as will be discussed.

The benefits of the methodology are that it provides a rapid, cost effective way of predicting petrophysical parameters, which would potentially be useful in the exploration, appraisal, development and decommissioning phases of a field. The same approach can be used to provide rapid, cost effective predictions of petrophysical parameters from historical core, thus allowing further insights into wells drilled some time ago.

# Effects of Temperature on Fines Migration during Low Salinity Water Injection

*Yamin* Wang, *Muhan* Yu, *Furqan* Hussain

**Abstract.**

Objective:

Some experimental studies have shown that the effect of fines migration in sandstone rocks is more prominent at a higher temperature. According to these studies, the increased fines migration is generally attributed to temperature dependent zeta potential. In this paper, we investigated if mineral dissolution induced pH increase can be responsible for increased fines migration.

Methodology:

Outcrop Berea sandstone cores were used in this experimental study. X-Ray Powder Diffraction (XRD), X-Ray Fluorescence (XRF) and Scanning Electron Microscopy (SEM) analysis were run to characterize these cores. All cores were subjected to single-phase injections of water at salinities 40, 10, 2.5, 0.5, and 0 g/L NaCl. Three different temperatures were used in experiments: (1) 25°C - room temperature, (2) 50°C - represented the temperature of aquifers and (3) 80°C - represented the temperature of petroleum reservoirs. Liquid permeability of cores was measured throughout the injection experiments. Energy Dispersive X-ray Spectroscopy (EDS) was run on the post-injection SEM images to identify the mineralogy of fines blocking the pores. Samples of produced water were used to measure the concentration of produced fines, ionic chromatography and pH.

Results:

At 50°C and 80°C, a significant increase in Ca2+ ions production was observed which was accompanied by a pH increase upto 9. These observations were missing during the experiment performed at 25°C. This indicates that increasing temperature leads to cement dissolution and increases pH values. Permeability drop was highest at 80°C and lowest at 25°C which indicates that dissolution induced pH increase can stimulate fines migration and therefore, permeability drop. Analytical models were used to match the experimental data.

Novelty:

Most laboratory studies on fines-assisted low salinity water injection are conducted at room temperature. While this paper proves that increasing temperature stimulates fines migration during low salinity water injection in sandstone by rock dissolution. These observations are critical to design fines migration in aquifers and petroleum reservoirs.

# Methane Production through Combined Depressurization + Hydrate Swapping method in the Sandy Porous Medium under Permafrost Temperature Conditions

*Jyoti S* Pandey, *Nicolas* von Solms

**Abstract.** Methane Production through Combined Depressurization + Hydrate Swapping method in the Sandy Porous Medium under Permafrost Temperature Conditions.

Methane gas production recovery rate from the natural gas reservoir depends on the characteristic of porous media as well as production techniques. 70% of discovered hydrate reservoirs are in a sandy porous medium in the permafrost region. In this work, instant partial depressurization followed by Hydrate swapping combined method is applied for recovery of methane from gas hydrate reservoir by improving diffusion channels and by applying in-situ swapping of trapped methane with CO2 or Mixture of CO2/N2. The aim of the study is to investigate the dependence of methane production on the nature of the porous medium using combined method in the permafrost region.

We quantitatively investigated the methane recovery from the combined method in 3 different artificial methane hydrate-bearing sand samples in parallel in the same timeline by the use of specially designed core flooding experimental apparatus. A total of 12 experiments run are performed and effect of the combined method on methane recovery from 3 different sand medium having particle sizes (0.25mm-0.3mm, 0.33-0.4mm, 0.32-0.7mm) in the permafrost temperature conditions 269.15 -274.15K and in 20-40 bar pressure range is investigated.

The experiments result demonstrated methane recovery in permafrost region is dependent on temperature and particle sizes. Combined method generate higher methane recovery as particle size increases. Use of CO2+N2 gas mixture results into higher methane recovery compared to pure CO2. Results suggest that combined approach, is a better choice using CO2+N2 gas mixture as minimum 30% of methane has been found to be replaced from hydrate phase in most of the experiments after 120 hours from the initial exchange reaction. Gas chromatography analysis and numerical calculations show the presence of N2 allow additional recovery of methane even though driving force behind recovery reduce. High CO2% with N2 allowed further methane recovery due to an increase in driving force.

# Impact of Micro-Emulsion Phase Behavior on Near Wellbore Associated Emulsification Properties during Chemical Enhanced Oil Recovery

*Marwah M.* Alsinan, *Debora Salomon* Marques, *Hyung T.* Kwak, *Alhasan B.* Fuseni

**Abstract.** In several applications of chemical enhanced oil recovery, thermodynamically stable micro-emulsions can form under reservoir conditions. Due to reservoir pressure gradients, micro-emulsions can go through additional stresses which can change the apparent properties of micro-emulsions. These apparent changes in rheology should be accounted for in CEOR operations since they could affect the displacement efficiency.

In this paper, we compare the properties of Windsor Type I, III and II micro-emulsions before and after shearing. Alpha Olefin sulfonate (AOS) surfactant with crude oil and with a Mixture of Dodecane and Tetradecane were selected for the formation of oil-brine micro-emulsions in a 95C oven. In order to alter the phase behavior, NaCl concentration was incremented from sample to sample. In addition to the visual inspection and the viscosity measurements, micro-emulsion phase behavior studies before and after shearing were carried out using a low resolution Nuclear Magnetic Resonance (NMR) equipped with gradient coils. The average and spatial T2 along the sample length were conducted to confirm stability of micro-emulsions with temperature, oil type, and the range of salinity. In addition, pulsed field gradient (PFG) NMR technique was used to measure the diffusivity of dispersed oil and continuous water phases under the various conditions and vice versa. Also, the diffusivity measurements were used to identify discrete and bi-continuous phase structures along with the size and shape of the dispersed droplet. In order to simulate reservoir shearing forces, samples were emulsified using different techniques, which include rotor-stator homogenizer, and a micro fluidizer.

Prior to shearing, micro-emulsions exhibited two viscosity peaks at phase types III and II. Also, the viscosity was thinning by shearing around these two maxima. The Relative diffusivity of each component was calculated with respect to its free phase diffusivity. The oil and water relative diffusivity values for each sample were plotted against the corresponding salinity (phase type). The plot showed that the relative diffusivity of water was decreasing with increasing salinity while the opposite behavior was observed for the oil. Moreover, the intersection between the oil and water relative diffusivities at medium salinities (Windsor phase type III) indicated a bi-continuous structure. On the other hand, the disparity between the two components relative diffusivities at low and high salinities (Windsor phase type I and II) revealed discontinues droplet structures. Following the shearing process, the additional emulsified free phase experienced disaggregation as shearing was increased, evidenced by the droplet size reduction, which could be explained by the shear thinning viscosity behavior.

Through the current study, we demonstrated the usefulness and the robustness of PFG NMR technique for monitoring micro-emulsion phase behavior. Moreover, the changes in actual and apparent viscosity by altering the salinity and the shearing forces, respectively, where confirmed by NMR diffusivity and droplet size measurements. The findings of this paper will be important for the screening and the study of displacement efficiency of chemical EOR agents.

# Combination of computed X-ray tomography and triaxial geomechanical tests as a tool for fracture propagation prediction

*Edyta* Puskarczyk*, Paulina I.* Krakowska*, Marek* Dohnalik

**Abstract.** Nowadays combination of various lab techniques in core analysis is a way to successful and detailed complex rock interpretation. One of the imaging techniques, computed X-ray tomography, nCT, is a tool for 3D pore geometry modelling in rocks. Using these techniques is possible to identify pores and fractures, their location, size, angle and aperture. Geomechanical test can simulate the stress-strain in in situ conditions.

Computed X-ray tomography was carried out in three steps: before, during and after triaxial compression test. Firstly, sample was scanned reflecting the natural pores and microcracks geometrical system. This CT results were treated as a reference image. The second CT measurements, during the geomechanical test, reflects the geometrical system in a stage of linear stress-strain relation. At that stage we suspect elastic relations, what means that pores and cracks probably were going back to the previous positions after geomechnical test. The third CT scan, after triaxial compression test, were analyzed from the point of cracks propagation and changes in pore space development. Images combinations before and after geomechanical test give the answer about the specimen reaction on stresses, so naturally on possible hydraulic fracturing during the reservoir exploitation. Qualitative and quantitative interpretation was based on diameters, angles, azimuths, directions, volume comparison of pores and cracks before and after the test. It appeared that the tested samples were prone to fractured in defined directions. As a tested data set were used samples of different lithological types: sandstones, shales and carbonates.

As a result of a novel combination of laboratory results, 3D image of different lithological samples before, at the stage of linear relation and after the stress-strain test was obtained. Changes, crack propagation and fracture directions were analyzed. Conducted analyses contributed to better recognition of rock pore and fracture system properties and more accurate planning of the fracturing process for unconventional hydrocarbon extraction.

# Slip-flow in tight carbonate for permeability estimation using 3D digital pore space

Krakowska *P.,* Madejski *P.,* Puskarczyk *E.,* Habrat *M.*

**Abstract.** Permeability is a key parameter in reservoir description. Nowadays, computational fluid dynamics (CFD) provides chance to simulate the fluid flow in porous space. Permeability can be evaluated based on simulation results. Standard simulations are based on continuum flow regime but in the case of tight rocks the slip-flow should be applied.

First stage of the analysis was connected with building the geometrical model of the pore space. Tight carbonate was chosen as an exemplary sample in the analysis (low porosity and permeability, tight gas). Geometrical model of the pore space was generated from computed X-ray tomography data with voxel size 0.8x0.8x.08 $\mu m^3$. Digital rock model of the pore space was created and analyzed regarding geometrical parameters for each object and microfracture: volume, x, y and z-coordinate of centroid, surface area and surface mesh area, moment of inertia around shortest principal axis, middle principal axis and longest principal axis, mean thickness, standard deviation of the thickness, maximum thickness, length of best-fit ellipsoid's long radius, intermediate radius and short radius, Feret diameter, shape and also sphericity, flatness, elongation. Tortuosity was calculated based on algorithm for pore space transformation into skeleton. Geometric model was extracted on the pore space and used as an input data to create a mesh and next, finite volume elements. Fluid flow simulation was carried out using nitrogen as a working fluid to compare the results with the pulse-decay permeability measurements on the core sample. Because tight carbonate characterized with narrow pore channels, the slip-flow approach was used to perform the simulation, what reflects the molecules slip on the pore walls. As a result of the simulation several parameters were obtained, e.g. velocity and mass flow rate. Permeability was in a good agreement with the results of permeability measurement on core sample, within the 10% of error.

# A FAST AND DIRECT RCAL METHODS ON AS-RECEIVED BRAZILIAN PRE-SALT CARBONATES CORES

*Leonardo* Goncalves*; Plinio Cancio Rocha* Da Silva Junior*; Glenio* Rosinski Ribeiro*; Bernardo Coutinho Camilo* Dos Santos*; Willian Andrighetto* Trevizan

**Abstract.** Estimating petrophysical properties from rock samples in a timing suitable to support exploratory formation evaluation is challenging. This is critical for mixed-wet and oil-wet samples as Brazilian Pre-Salt carbonates, which cleaning can take several months, preventing RCAL results to be useful for initial decision making. The present work aims to cope this timing-challenge by evaluating the accuracy of a fast method to measure porosity and permeability in a few days on "as-received" carbonate samples, i.e. without previous cleaning.

A few hundred Pre-Salt reservoir carbonate oil-base-mud cores were used in this study keeping as-received samples condition. Their total porosities were measured by low-field NMR relaxometry after re-saturating the samples with filtrate-equivalent fluid. Absolute permeabilities were measured using a steady-state probe permeameter, which applies a semi-spherical gas flow from a sample plane surface. Then, the samples were cleaned and standard measurements were performed.

Results using as-received samples showed good correlation with standard measurement. While porosity deviations generally does not exceed 2 p.u., permeabilities have mostly the same order of magnitude, despite the uncertainties related to the presence of formation and drilling fluids, and the neglecting of effects like confining pressure.

The reduction of time from months to a few days have enabled these techniques to be valuable tools in supporting decision making and select candidate samples for SCAL. In addition, probe permeametry has been used to assess sample heterogeneity.

# Comparing the porous plate technique and the evaporation technique for establishing initial water saturation

*Lykourgos* Sigalas*, Hanne* Dahl Holmslykke*, Dan* Olsen

**Abstract.** Two techniques for establishing the initial water saturation, Swi, in core flooding experiments are compared, i.e. the porous plate technique and the evaporation technique. The porous plate technique is well established, and considered to conserve the wetting characteristics of the sample throughout the drainage process. The evaporation technique has the advantage of being much faster, and more precise in attaining a predetermined water saturation. However, questions have been raised, whether the evaporation technique changes the wetting characteristics of a sample because of drying the sample's surface. Results from a series of experiments indicate that sample preparation with the evaporation technique do result in lower Sorw values at the end of water-flooding experiments, and therefore affects the wetting characteristics of the samples. Processing of CT data is also in progress to quantify the water and oil distribution in the samples before and after the water-flooding experiments.

# Digital Rock Model based on nCT images as an input to Deep Learning for permeability simulation

*Edyta* Puskarczyk*, Paulina I.* Krakowska*, Magdalena* Habrat*, Paweł* Madejski*, Mariusz* Jędrychowski

**Abstract.** Computed nanotomography, nCT is one of the modern, non-destructive research methods allowing to investigate the object using X-rays and present the pore space image of the examined sample. Research material at this work constituted samples of low porosity and low permeability (shales, tight sandstones and carbonates). The 3D visualization presents qualitative interpretation including irregularity of the pore space distribution. Pore distribution graphs allow to quantitative characteristics of the rock samples and their comparison. Processing of the 3D image provides with the information about the porosity, the number and length of the pore channels, their connections, directions and structure and also possibility of permeability modelling. One of the most important petrophysical parameters is a tortuosity. Tortuosity is determined as the ratio of the capillary length measured in the flow direction to the capillary length measured in pressure gradient direction. Using modified by authors algorithm in software poROSE, tortuosity is calculated using different approaches (standard and novel approach). Using new algorithms for nCT data interpretation is possible to enhanced the correctness of the permeability calculations. In this paper the main object of the study was to simulate permeability based on the parameters obtained from nCT images processing. For permeability calculation the Deep Learning techniques, especially Artificial Neural Network (MLP and RGB) were used. As a results relation between quantitative parameters from nCT parameters and permeability was found. Results were compared to the lab measurements data. In the second step permeability obtained using Artificial Neural Networks was compared to the fluid flow simulation results. It can be concluded that the use of new CT image processing algorithms and the use of high-resolution measurements allow for a better estimation of the permeability. The use of Deep Learning is an effective tool for permeability simulation.

# Simulation and Experimental Measurements of Internal Magnetic Field Gradients and NMR Transverse Relaxation Times (T2) in Sandstone Rocks

*Paul R. J.* Connolly, *Weichao* Yan, *Daniel* Zhang, *Mohammed* Mahmoud, *Michael* Verrall, *Maxim* Lebedev, *Stefan* Iglauer, *Peter J.* Metaxas, *Eric F.* May, *Michael L.* Johns

**Abstract.** NMR T2 measurements are widely used to determine various petrophysical properties of rock cores. Internal magnetic field gradients, which occur in rock cores during NMR measurements due to magnetic susceptibility differences between the rock matrix and the pore fluid, can however distort these T2 measurements. Here we implement a FEM simulation of these internal magnetic field gradients on 3D digital μCT images for five different sandstone rocks, coupled with a random walk simulation of the T2 NMR signal relaxation process. The FEM simulations required the magnetic susceptibility of each sandstone, this was directly measured using a SQUID magnetometer over a range of magnetic field strengths. The resultant probability distributions of internal magnetic field gradients were then compared against equivalent experimental measurements; they were generally in reasonable agreement, however the simulations failed to capture the larger magnetic field gradients that were observed experimentally. By consideration of various potential reasons for this, we identify the assumption of a single mean magnetic susceptibility as being the primary source of the variation between simulated and measured results. Simulations of 2 MHz T2 relaxation process are shown however to be in good agreement with experimental measurements across the five sandstones studied.

# Computed X-ray tomography data in multiple linear regression analysis on tight rocks for permeability estimation

Krakowska *P.,* Puskarczyk *E.,* Madejski *P.,* Habrat *M.,* Dohnalik *M.*

**Abstract.** Kozeny presents one of the most useful relations between the permeability, porosity and specific surface area, assuming that the rock consists of a bundle of straight capillary tubes (porosity) and cement. But what if tight sandstone or limestone is the object of the interest? The assumption for Kozeny equation is not valid. Researches are still looking for the new equations to obtain permeability in not invasive way: by calculation or using fluid flow simulations. In the paper the equation for permeability estimation was presented based on computed X-ray tomography (CT) data and multiple linear regression analysis (MLR). Usually, most of the parameters, as SVgr in Kozeny equation, were calculated from capillary data or petrographic image analysis. Combination of high resolution laboratory technique as CT and statistical method allowed determining equation for permeability in tight reservoirs. Analysis was carried out on 60 samples of tight (low porosity and low permeability) sandstones, mudstones, limestones and dolomites (unconventional reservoirs) to get representative, general equation, free from lithology influence. Firstly, CT images for each sample were analysed quantitatively. Following parameters were calculated for objects (pores) in each sample: volume, surface area, equivalent diameter, maximum, minimum, mean, standard deviation of thickness, anisotropy, elongation, flatness, Euler number, minimum, maximum of Feret diameter, Feret Breadth, Feret Shape, ShapeVa3D, moments of inertia: I1, I2, I3, sphericity and combinations of this parameters. Summarizing, for the statistical analysis 291 parameters from CT images of pore space were analysed in each sample. In each sample analysis of: maximum, minimum, average, standard deviation, median, percentile 10, percentile 90, lower quartile, upper quartile values were carried out on all objects (pores), e.g. calculation of average value of thickness mean on all objects in the samples. Additionally, extraction of all parameters for the largest object in the sample was also made. Next, data sets for all samples, consisted of one statistical parameters and all available parameters from CT were prepared for linear correlation and MLR analysis. MLR provided the equation for permeability estimation using following parameters: Feret breadth/volume, flatness/anisotropy (from upper quartile), maximum Feret diameter/flatness, moments of inertia around middle principal axis/moments of inertia around longest principal axis, anisotropy/flatness, flatness/anisotropy (percentile 90). MLR correlation coefficient for permeability equation was 0.82, while determination coefficient was equal to 0.67. Results of MLR were compared with results of pulse and pressure decay permeability measurements on all core samples.

# Laboratory core analysis of potentially in-situ recovery amenable sandstone-hosted uranium deposits in the Morrison Formation/New Mexico/USA

*Micha Janosch* Zauner*, Matthias* Halisch*, Andreas* Weller

**Abstract.** Several core plugs from a roughly 1,000 m deep borehole penetrating the Westwater Canyon Member of the Morrison Formation in New Mexico (USA) have been investigated by various petrophysical methods in order to evaluate the potential of mining deep buried sandstone-hosted uranium deposits by in-situ recovery (ISR). Essentially, ISR is the operation of wellfields up to 1,000 m depth by continuously recycling the leaching solution after metal capture (usually by ion exchange) and subsequent refortification (chemical conditioning) before re-injection. Porosity, permeability and mineralization pattern of the host sandstone in the target aquifer are the determining parameters for ISR amenability. Mineralogy and geochemistry of the core plugs were investigated by ICP-MS (Inductively Coupled Plasma – Mass Spectrometry), XRF (X-Ray Fluorescence), XRD (X-Ray Diffraction), MLA (Mineral Liberation Analysis) and optical microscopy. Petrophysical parameters were determined by using He pycnometry, kappa bridge measurements, SIP (Spectral Induced Polarization), N2-adsorption (nitrogen gas adsorption), NMR (Nuclear Magnetic Resonance), µCT (Micro-Computed Tomography), steady state permeametry, and digital rock physics (Mercury Injection Capillary Pressure simulations). Mineralogical investigations revealed a secondary uranium mineralization mainly coating the silica grains of the arkosic sandstone and some interstitial pore fillings. The mineralized coating or seams are well visualized by optical microscopy and MLA. The differences between mineralized and non-mineralized sandstone plugs are highlighted by NMR, µCT and SIP. The NMR results show a doubling of the clay- and capillary-bound water and decrease of free-fluid porosity of mineralized samples. A correlation of mineralization grade and polarization was found through the SIP tests. Non-mineralized samples show a Gaussian pore size distribution, increased porosity and permeability, decreased magnetic susceptibility, smaller specific surface area, lower electric resistivity, and lower total chargeability. Especially the anisotropy of horizontal and vertical permeability of 3:1 shows a significant difference of mineralized samples with increased tortuosity indicating a horizontal stratification of the sandstone formation compared to isotropic and well-sorted non-mineralized core plugs from barren strata. µCT flow simulations confirm preferential horizontal flow around the mineralized grain coatings. Ore – lixiviant interaction by the leaching solution with the uranium coating is favored in horizontal flow direction generally prioritized by standard ISR operations and confirmed by column leach tests of mineralized core samples.

# Core Fracture Segmentation in CT Images by Transfer Learning

*Ryan* Antle*, Mackenzie* Dreese

**Abstract.** Fracture characterization by computer vision (CV) techniques using X-ray computed tomographic (CT) images of reservoir cores was improved by training a high accuracy (>90%) deep convolutional neural network (CNN) model for classifying images with fractures and transferring the learning to a fully convolutional network (FCN) for fracture segmentation. The analyses utilized manually feature-classified CT cross sectional images, themselves distributed sub-millimeter voxels of density- and atomic number-sensitive CT Numbers, as inputs to the CNN model for automated slice-wise classification of fractures in reservoir cores. The network layers were trained and validated using these classified images to assign probabilities of classes to subsequent images, with e.g. 'fracture' or 'no fracture' classes assigned based on corresponding class probability. The whole image classification was then extended to a pixel-wise classification by transferring the hyperparameters in the fully connected layer to a fully convolutional layer. Layers were added to the new FCN model to upscale class probabilities back to the original image dimensions, resulting in a change from an image classification output to a heatmap of object classes via a single pass pixel-wise class prediction. The transferred hyperparameters were then further refined by iteratively minimizing error between known and predicted labels in annotated images. Results showed transferred learning from CNN to FCN for fracture labeling improved accuracy (>60%) regardless of class imbalance. The improved accuracy allowed for further automation of fracture characterization including aperture and length measurements.

# STUDY OF THE EFFECTS OF NaCl REDUCTION IN OIL RECOVERY DURING THE CALIBRATED WATER INJECTION INTO DOLOMITE ROCKS

*Carlos A.* Rivas, *Alessandra* Winter, *Osvair V.* Trevisan (In memoriam)

**Abstract.** Offshore carbonate reservoirs have the seawater injection as a powerful conventional secondary recovery mechanism, not only for their availability and low operating cost but also for having active ions such as magnesium (Mg2+), calcium (Ca2+) and sulfate (SO42-). These active ions act on the surface of the carbonate rocks altering their electric charge, releasing the carboxylic components and, therefore, increasing the recovery factor. Sodium (Na+) and chlorine (Cl-) ions interfere in this ionic interaction and can have an impact on the efficiency of water injection. The creation of this ionic substitution model, related to the alteration of the carbonate wettability, also led to the idea of modifying or calibrating the composition of the injection water to cause or even increase the effect of changing the rock surface to preferentially oil wet. Several studies have been carried out seeking a better understanding of the phenomena involved, and numerous calibrated water compositions have already been investigated, however, there is still no consensus in explaining the results. Thus, this publication presents a study of the reduction of sodium chloride during the injection of seawater into dolomite rocks, once the ions Na+ and Cl- are fundamental agents in the rock/fluid interaction. For this, four coreflooding tests were carried out in two dolomite samples. In each test, a sequence of four brines was injected, starting with seawater and decreasing the composition of NaCl in 50%, 90% and 95%. In addition, effluents were collected, and by ion chromatography, the ion variation before and after the tests were compared. The first two tests used a conventional aging method, while the next two used an improved aging method on the same samples. The coreflooding tests lasted around 50 hours and were obtained high percentages of oil recovered with seawater, around 50%, in the first two experimental tests. In both tests, more than 90% of the recovered oil was obtained before the first porous volume injected, one of the possible causes indicated is that the sample was not sufficiently oil wet. The comparison of results showed a better appreciation of the ionic substitution model for the two final experimental tests. In these tests the brines with reduced NaCl concentration obtained significant oil recoveries, especially in the second brine, indicating that a 50% NaCl reduction is sufficient to achieve significant oil recoveries.

# PORTABLE XRF SPECTROMETER AS A FORMATION EVALUATION AND GEOSTEERING TOOL APPLIED IN THE POLISH PERMIAN BASIN

*Rafał* SKUPIO *Urszula* ZAGÓRSKA*, Benedykt* KUBIK*, Sylwia* KOWALSKA*, Krzysztof* WOLAŃSKI

**Abstract.** Development of hydrocarbon exploration involves sophisticated methods allowing for quick and precise reconstruction of lithological profile during drilling. Advanced geosteering procedures are set up on various methods (Morton, 2007, Stilwell et al., 2013, Yarbrough, et al. 2019). Our research was focused on Rotliegend formations from two boreholes: P4 and P5H. P4 with available archival core material was chosen as a reference borehole and P5H as a horizontal borehole for tests. Our team created a new core sampling methodology to obtain material comparable to cuttings collected on the rig site. Core data (XRF, XRD and ICP-OES/MS laboratory tests) were a basis for preparing mineralogical models built on geochemical analysis. The data were also utilised to calibrate handheld XRF spectrometer to obtain more precise geochemical results (Skupio, 2014). Lithological interpretation in whole P4 Rotliegend core section was conducted and used as a reference borehole profile. Sample preparation, XRF measurements and data interpretation were made in real time on the rig site during P5H realization. Comparison of results obtained from cuttings provided during drilling of the horizontal P5H well with core data from P4 was a basis to correct drilling trajectory of the horizontal well. XRF analyses allowed for precise lithological interpretation and showed chemical composition changes in examined profile. Real time results of P5H lithological modelling were employed for geosteering procedure. Quick sample preparation and analyses allowed for faster data acquisition than LWD measurement. Lithology interpretation for P4 and P5H boreholes was done only by modelling the XRF data according to reference well.

Morton, A.C., 2007: The role of heavy mineral analysis during drilling of high angle wells. In: Mange, M. and Wright, D.K. (eds), Heavy Minerals In Use. Developments in Sedimentology, 58, 1123-1142

Skupio R., 2014: Wykorzystanie przenośnego spektrometru XRF do pomiarów składu chemicznego skał, Nafta-Gaz nr 11, s. 771-777.

Stilwell H., Martinez N., Hildred G., Zaitlin B. 2013: Forensic Chemostratigraphy in Geosteering Multilateral Wells: An example from Devonian to Carboniferous-aged sequences in Southern Alberta Conference Paper of Unconventional Resources Technology Conference, Denver, Colorado, USA, 12-14 August 2013

Yarbrough L. D., Carr R., Lentz N.2019: X-ray fluorescence analysis of the Bakken and Three Forks Formations and logging applications. Journal of Petroleum Science and Engineering 172 (2019) 764–775

# Emulsification under different mixing conditions

*Pit* Arnold, *Ahmad* Kharrat, *Barbara* Schnöpf and *Holger* Ott

**Abstract.** Chemical EOR flooding, such as in alkaline or surfactant flooding, may lead to a complex phase behavior in the pore space; depending on the exact crude and injection-water compositions, emulsion phases may form to the advantage or disadvantage of the displacement efficiency. The injection-water composition, and hence the displacements efficiency, is typically optimized by its phase behavior and by core flood experiments. However, mixing regimes of oil and injection water are substantially different for both types of tests; while in classical test-tube experiments oil and water are mixed on a macroscopic scale and likely under turbulent conditions, we assume laminar flow – respectively mixing – conditions on the pore scale in porous media flows.

In our poster presentation, we ask the question of how representative are different measurements for the actual displacement process. For this, we compare classical test tube experiments, results from spinning-drop measurements and microfluidic experiments, representing substantially different mixing regimes. Furthermore, we discuss alkaline and surfactant systems, representing ideal and non-ideal systems. The poster builds on the paper SCA2019-011.

# Pore-scale characterization of Norwegian Continental Shelf Reservoir based on Digital Rock Simulation

*Fatime* Zekiri*, Pit* Arnold*, Jan* Steckhan*, Holger* Ott

**Abstract.** In OMV a digitalization and innovation campaign, the so called DigitUP initiative, has been kicked off to transform our business and to take it to the next technology level. The project "Digital Rock Simulation" is part of the OMV Upstream digitalization roadmap. The main goal of the project is to provide multiple realizations of reservoir properties at the pore scale efficient in time to speed up project decisions. Therefore, OMV's Petrophysics department aims to design fit-for-purpose workflows for different types of reservoirs in OMVs portfolio. The focus of the project is to simulate petrophysical and displacement properties, which are needed for static and dynamic modelling.

Furthermore, in close collaboration with the Petroleum Engineering Department of the Montanuniversität Leoben (MUL) advanced simulation concepts will be developed to optimize OMV's reservoir characterization also for enhanced recovery methods.

The first pilot project is an offshore gas-bearing sandstone reservoir with high porosity (ca. 20 – 30 %) and permeabilities above 1000 mD. Some parts of the reservoir are also of medium-to-lower quality (porosity < 15% and permeability < 100 mD). Five core samples – representatives of the variation in rock quality – have been selected and where scanned at MUL by means of laboratory- and synchrotron-based micro computed tomography. The first results have been already simulated in the past weeks and a comparison to experimental results on basic parameters show good agreement, such as porosity, permeability and capillary pressure.

The focus for the upcoming phase of the project will be to look into comparison of different simulation approaches (direct computation vs. pore network model), more complex reservoirs (e.g. carbonates) and test different approaches for upscaling.

SCA2019-090

# The Impact of Microbial Growth on Hydraulic Properties in Saturated Porous Media

*Holger* Ott*,* *Neda* Hassannayebi*,* *Frieder* Enzmann*,* *Johanna* Schritter*,* *Martin* Ferno*,* *Andreas* Loibner

**Abstract.** Understanding growth and transport of microorganisms in porous media is essential for understanding various natural subsurface systems and applications in subsurface engineering. Such applications may be related to subsurface hydrogen storage for large-scale renewable energy storage (www.underground-sun-storage.at), in-situ methanization (www.underground-sun-conversion.at), soil remediation as well as microbial EOR.

In the presented work, we investigate accumulation and growth of microbes in microfluidics and its influence on the hydraulic properties of porous media. Even though the above given examples are related to multi-phase flow, the present study focuses on saturated flow, which provides sufficient complexity and unsolved questions.

The study takes advantage of the high spatial and temporal resolution of optical microscopy in order to investigate transport and accumulation of microorganisms in microfluidics, i.e. 2D porous media etched in glass. The experiments were performed in two phases by using *Lactobacillus casei* as model organisms. In phase 1, a bacterial suspension solution in a stationary growth phase was flooded through microfluidic chips leading to initial accumulation of microbes in the pore space. In phase 2, a nutrient (substrate) solution was injected; the supply of nutrients changes bacterial growth to an exponential mode.

The change of porosity over time has been determined by image segmentation of the water-saturated pore space and the accumulated biomass in the image sequences. Furthermore, the segmented images have been used as “digital twin” – a digital representation of the experimental results – for direct numerical flow simulations; by solving the Stokes and the Navier-Stokes equations in the pore space, we determined changes of the flow field and the permeability with increasing biomass. The study indicates (a) the formation of preferred flow pathways with increasing biomass, and (b) an associated porosity-permeability relationship, with a qualitatively different behaviour in suspension flooding (phase 1) and nutrient flooding (phase 2). Furthermore, an intermittent release of biomass and subsequent filtration have been observed, leading to a stepwise local increase of biomass by filtration. A first attempt to understand and simulate transport and filtration of microbes has been started by particle-flow simulations in the Digital Twin.

# Improving oil recovery by injecting alcohol-treated $CO_2$

*Saira* Saira*, Emmanuel* Ajoma*, Furqan* Hussain

**Abstract.** Oil recovery during $CO_2$ injection is higher for near-miscible and miscible conditions compared to immiscible condition. In case of the depleted oil reservoir, reservoir pressure is not sufficient to achieve miscible or near-miscible condition. This paper investigates the impact of alcohol-treated $CO_2$ ($CO_2$ equilibrated with alcohol at reservoir Pressure and Temperature) on miscibility pressure and respective oil recovery.

Injection experiments were performed on a Bentheimer sandstone for two sets of fluid pairs (1) $CO_2$ and oil, and (2) alcohol-treated $CO_2$ and oil. A mixture of 35% Hexane and 65% Decane was used as oil. Alcohol-treated $CO_2$ prepared by mixing of 4% Ethanol in $scCO_2$ at the experimental pressure and temperature. All experiments were performed at a constant temperature of 70 ºC and two different pressures (1300 and 1700 psi). Literature studies show that 1300 psi represents immiscible condition and 1700 psi represents near-miscible condition for the selected oil and $CO_2$. To characterize the fluid pairs used in this study, we performed capillary rise experiments to measure interfacial tension (IFT) between (1) $CO_2$ and oil, and (2) alcohol-treated $CO_2$ and oil at experimental conditions. Oil recovery, differential pressure, and compositions are recorded during injection experiments.

Experimental observations reveal that alcohol-treated $CO_2$ is more effective than pure $CO_2$ for reducing IFT and miscibility pressure. Approx. 10 to 20 % oil recovery increases with the addition of 4% ethanol in $CO_2$. However, the increase in oil recovery with alcohol-treated $CO_2$ is more dominant at immiscible condition. Although it also shows some improvement at near miscible condition, its efficiency is greatly reduced.

The generated data provides a direct quantitative measurement of the reduction in miscibility pressure and improvement in oil recovery. The proposed methodology has the potential to enhance the feasibility of $CO_2$ sequestration in oil reservoirs.